Mechanisms and Machine Science 13

George Dobre *Editor*
Assisted by Mihai Robert Vladu

Power Transmissions

Proceedings of the 4th International Conference, held at Sinaia, Romania, June 20–23, 2012

Springer

Mechanisms and Machine Science

Volume 13

Series Editor

Marco Ceccarelli

For further volumes:
http://www.springer.com/series/8779

George Dobre†
Editor

Power Transmissions

Proceedings of the 4th International Conference, held at Sinaia, Romania, June 20–23, 2012

Assisted by Mihai Robert Vladu

Springer

Editor
George Dobre†
Machine Elements and Tribology
University Politehnica of Bucharest
Bucharest
Romania

ISSN 2211-0984 ISSN 2211-0992 (electronic)
ISBN 978-94-007-6557-3 ISBN 978-94-007-6558-0 (eBook)
DOI 10.1007/978-94-007-6558-0
Springer Dordrecht Heidelberg New York London

Library of Congress Control Number: 2013934722

Printed on acid-free paper

Springer is part of Springer Science+Business Media (www.springer.com)

Dedicated to the memory of
Professor George Dobre

Preface

This volume is a collection of the refereed papers selected from those submitted to the 4th International Conference on Power Transmissions (PT12), held at 20–23 June 2012, in Sinaia, Romania.

This conference aims to provide a forum for researchers, academics and industry experts to share their up-to-date findings and achievements in the field of power transmissions, and to identify the new technology requirements, needs and priorities in this field. The major conference topics, which are also reflected in the papers published in this book, include:

- Theory, Design and Experimental Researches on Power Transmissions
- Product Development, Manufacturing and Metrology
- Load capacity, structure and components
- Maintenance, operating and industrial applications
- Engineering education.

The call for abstracts stimulated excellent responses with 102 abstracts submitted, amongst of which the authors of 67 abstracts were invited for submission of full papers. All the papers submitted were peer reviewed, and, based on the review results, 59 papers were finally selected for inclusion in this book. The authors' and the referees' efforts for enhancing the quality of the papers are greatly appreciated.

This conference is jointly organised by Balkan Association of Power Transmissions (BAPT) and Romanian Association of Mechanical Transmissions (ROAMET). Their contributions and support are sincerely acknowledged. We would like to express the gratitude for the members of the Organizing Committee, for the International Scientific Committee, organisers and members of the review panels and for the help received from colleagues and staff members involved in preparation of the events, without which the success of the conference could not have been achieved. Equally, the thanks are extended to the keynote speakers and to all contributors and delegates for their support and high-quality contributions.

In this special way, we honour the contribution of distinguished Prof. George Dobre Sr., the man who inspired and influenced the most this event (passed away shortly after the Conference).

For the Local Organizing Committee
Dr. Eng. Mihai Robert Vladu

Between 20 and 23 June 2012, the town of Sinaia hosted the 4th International Conference on Power Transmissions (PT12). A hugely significant contribution to the organisation of the conference was that of Prof. George Dobre Sr., my father, who worked tirelessly for about 2 years on the general organisation of the conference and also on the many detailed arrangements (ranging from calls for papers to putting together and maintaining the website, communicating with authors, arranging reviews of submitted papers etc.).

He did all this while undergoing aggressive chemotherapy treatment for a cancer that he had been diagnosed with 2 years before. Although he was beginning to feel quite frail in the run-up to the conference, he was so committed to the meeting that he found a last reserve of energy to tap into and successfully chaired the conference, telling me at the end that he is very happy with the way it turned out. He passed away a month after that.

I am very proud to see that his labour of love, which he put so much work into, has been concluded and I am extremely grateful to his collaborators Asst. Prof. Sorin Cananau, Asst. Prof. Radu Florin Mirica and Dr. Mihai Robert Vladu for their contribution to the organisation of the conference as well as for what they have done since to ensure this volume sees the light of day. It is a wonderful tribute to my father's memory.

Dr. George Dobre Jr.

Message from Honor President of "Balkan Association of Power Transmissions"

With this 4th Conference, we celebrate the 10th anniversary of the Balkan Association of Power Transmissions (BAPT). The field of power transmissions is rather wide. Compared to structural engineering, where everything is static, mechanical engineering has everything in motion, so one could say that Power Transmissions cover the whole spectrum of Mechanical engineering.

Power Transmissions are a scientific and technological field that is not only wide, but also complex. It comprises the various driving methods—electric, hydraulic, pneumatic, etc.—as well as a multitude of transmission machine elements—shafts, bearings, couplings, gearings, belts, chains, etc. Objects of study of these machine elements are their theoretical concepts as well as calculation,

constructions, manufacturing, testing, application and maintenance. There is probably no other international organisation as much oriented towards practice, as BAPT is. BAPT puts the creator-designer in the first place.

The considerable interest in the previous three conferences of BAPT from Balkan specialists as well as representatives of other countries clearly demonstrates that an objective international demand of both Balkan and worldwide proportions has been met. One should note that conferences on the very topic of Power Transmissions and Gearings are organised in an industrially developed country like USA and France has hosted four international Gearing congresses. Germany is no less active in the field with their regular international Gearing conferences. This is a clear indication that such organisational form is needed.

It is necessary ROAMET to be specially thanked for the effort they made to organise this conference. However, ROAMET is the only national association in Europe whose focus is mechanical transmissions.

Prof. Dr. Eng. Kiril Arnaudov

Contents

Part I
Keynotes

Alternative Method for Analysis of Complex Compound Planetary Gear Trains: Essence and Possibilities

Kiril Arnaudov and Dimitar Karaivanov

Abstract An alternative method for kinematic and power analysis of compound gear train is studied, which uses the torques and lever analogy of a given gear. The method combines the accuracy of the Willis analytical method with the clarity of the graphic method of Kutzbach-Smirnov. Unlike these methods, the alternative method allows determining not only the gear ratio, but the magnitude and direction of power flows, and hence the determination of efficiency of a given compound planetary gear train. The application of the method is illustrated with examples.

Keywords Kinematic analysis · Power analysis · Ratio · Efficiency · Planetary gear trains

1 Introduction

There are various methods for analysis of planetary gear trains at all. Two, however, are most commonly used. One is the analytical method of Willis, the other is a graphical method of Kutzbach-Smirnov. Both methods have proved their worth over many years. The method of Willis (1841) is used for almost two centuries and the method of Kutzbach (1927) is there nearly a century.

The main advantage of analytical method is the accuracy. Moreover it is universal. However, it lacks any clarity, the volume of calculations, especially for the complex compound planetary gear trains, is not small, which allows and there is no simple way to check the results, but the most careful repeating of the calculations.

K. Arnaudov (✉)
Bulgarian Academy of Sciences, Sofia, Bulgaria
e-mail: k_arnaudov@abv.bg

D. Karaivanov
University of Chemical Technology and Metallurgy, Sofia, Bulgaria
e-mail: dipekabg@yahoo.com

G. Dobre (ed.), *Power Transmissions*,
Mechanisms and Machine Science 13, DOI: 10.1007/978-94-007-6558-0_1,

Undoubtedly the main advantage of the graphical method is the clarity. However, it is lost for complex compound planetary gear trains because of the tangle of lines obtained. Frankly in graphical methods we cannot speak for high accuracy.

The importance of accurate analysis of all gear trains is determined by the fact that errors in defining the correct transmit ratio or in the direction of rotation of the output shaft of the train in some cases may be fatal.

2 Need for an Alternative Method

The two main methods at use have advantages and disadvantages. This determines the need for finding another method more suitable for the practice that combine their advantages and avoid the disadvantages. The following properties are desired:

- accuracy;
- simplicity;
- maximum clarity;
- easy usability (relevance);
- easy check of the results;
- generally the opportunity to achieve more goals than with previous methods, namely—not only determining the gear ratio, but the presence or absence of internal division or circulation of power, determining the efficiency and, in particular in gearboxes, determining the load spectrum of the elements of gear train (wheels, shafts, bearings), as a prerequisite for their reliable load capacity calculation;

The need for such a method with the above mentioned features is especially pressed in practice by engineers who value the simplest, easily applied and clear methods. It must not be forgotten that clarity is the foundation of engineering thinking and is a dominant requirement in engineering work.

3 Essence of the Alternative Method

Unlike the methods of Willis and Kutzbach-Smirnov using angular velocity ω (or rotational speed n) and the peripheral velocities v, at the presented here alternative method the torques T are used. The method is based on the following well-known principles of mechanics, illustrated with the simplest case of elementary (single-carrier) gear train with three external shafts that has a very good lever analogy (Fig. 1):

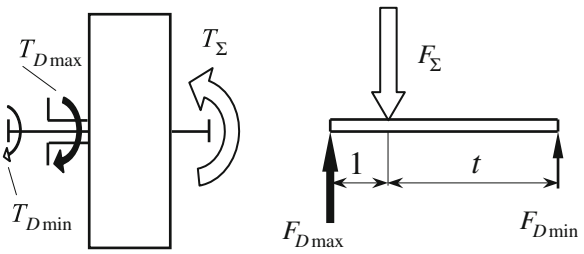

Fig. 1 Planetary gear train with three external shafts, their torques and the lever analogy

1. Equilibrium of ideal (with no account of losses) external torques acting on the three shafts

$$\sum T_i = T_{D\min} + T_{D\max} + T_{\Sigma} = 0 \tag{1}$$

where
$T_{D\min}$ and $T_{D\max}$ are the unidirectional external ideal torques (with different sizes), therefore are indicated by single lines on the figure, but with different thickness, according to their size;
T_{Σ} is the largest torque, in absolute value equal to the sum of other two torques $T_{D\min}$ and $T_{D\max}$, and therefore is marked with a double line.

2. Equilibrium of the real (considering the losses) external torques

$$\sum T'_i = T'_{D\min} + T'_{D\max} + T'_{\Sigma} = 0 \tag{2}$$

where
$T'_{D\min}, T'_{D\max}$ and T'_{Σ} are the same external torques as above, but real now considering the losses in the gear train.

3. Sum of ideal (not considering the losses) powers

For the simpler case, when the gear train is with one fixed shaft, i.e. working with F = 1 degree of freedom, the condition is

$$\sum P_i = P_A + P_B = T_A \cdot \omega_A + T_B \cdot \omega_B = 0 \tag{3}$$

where
P_A, T_A and ω_A and are the input power, torque and angular velocity;
P_B, T_B and ω_B—the output power, torque and angular velocity;

The above condition is used to determine the speed ratio

$$i = \frac{\omega_A}{\omega_B} = -\frac{T_B}{T_A} \tag{4}$$

4. Sum of real (considering the losses) powers

$$\sum P'_i = \eta \cdot P'_A + P'_B = \eta \cdot T'_A \cdot \omega_A + T'_B \cdot \omega_B = 0 \tag{5}$$

where
P'_A, T'_A and ω_A are the input power, torque and angular velocity;
P'_B, T'_B and ω_B—the output power, torque and angular velocity;

From this follows the formula for the efficiency

$$\eta = -\frac{T'_B/T'_A}{\omega_A/\omega_B} = -\frac{i_T}{i_k} \tag{6}$$

In this formula i_T means the ratio of the real external torques T'_B and T'_A at the input A and output B of gear train, as signified more as dynamic (Kreines 1947; Kudryavtsev 1966), as a power ratio or torque transformation (Looman 1996, VDI-R). The other ratio i_k is the usual speed ratio and unlike the above, if necessary, the index k—from the "kinematic" can be used.

To determine the real external torques T'_i it is necessary that the directions of relative (rolling) powers $P_{rel\,i}$ are identified in each gear train according to the respective carrier, and each gear train has its own internal efficiency (Kudryavtsev 1966; Looman 1996, VDI-R).

In most cases the direction of relative (rolling) power P_{rel} in one planetary gear train (from the sun gear 1 to the ring gear 3 and vice versa) can be determined, proceeding from the direction of the torque on the sun gear and its relative angular velocity toward the carrier $\omega_{1\,rel} = \omega_1 - \omega_H$, by the following simple criteria:

- when the directions of the torque T_1 and the relative angular velocity $\omega_{1\,rel}$ coincide i.e. $\omega_{1\,rel} \cdot T_1 > 0$—the relative power is transmitted from the sun gear 1 through the planets 2 to the ring gear 3, or in other words, the sun gear appears to be the driving one in the relative motion;
- when $\omega_{1\,rel} \cdot T_1 < 0$—the relative power is passed from the ring gear 3 to the sun gear 1;

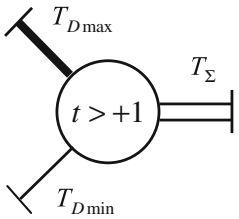

Fig. 2 Modified symbol of Wolf with three external shafts and their torques

In relatively rare cases this situation is not that clear. Then it is appropriate for determining the direction of the relative power to use the method of the samples (Seeliger 1964).

Along with the foregoing known principles of mechanics, the following two small but very useful innovations are made:

5. For the greatest possible illustration of the method the known symbol of the Wolf (1958) (Fig. 2) is used, but modified (Arnaudov 1984, 1996; Arnaudov and Karaivanov 2001, 2005a, b, 2010; Karaivanov 2000; Karaivanov and Arnaudow 2002). The each elementary (single-carrier) gear train, which has three external shafts is depicted with a circle, from which the three shafts are coming out, marked differently from the original—i.e. not with numbers, letters or inscriptions, but by the thickness of the lines corresponding to the size of the external torque, as already mentioned above. This little innovation concerning the manner of marking the shafts makes the method very clear and useful.
6. Besides using the modified symbol of Wolf, where appropriate another innovation is made. A new torque ratio is defined—the one of the unidirectional external torques (Arnaudov 1984, 1996; Arnaudov and Karaivanov 2001, 2005a, b; Karaivanov 2000).

$$t = \frac{T_{D\max}}{T_{D\min}} > +1 \tag{7}$$

because $T_{D\max} > T_{D\min}$ (Fig. 1).

This innovation is especially important. It is connected to the lever analogy.

7. Ideal external torques are always in a certain ratio, expressed with the torque ratio t

$$T_{D\min} : T_{D\max} : T_{\Sigma} = T_1 : +t \cdot T_1 : -(1+t)T_1 = 1 : +t : -(1+t) \tag{8}$$

in which always

$$T_{D\min} < T_{D\max} < |T_{\Sigma}| \tag{9}$$

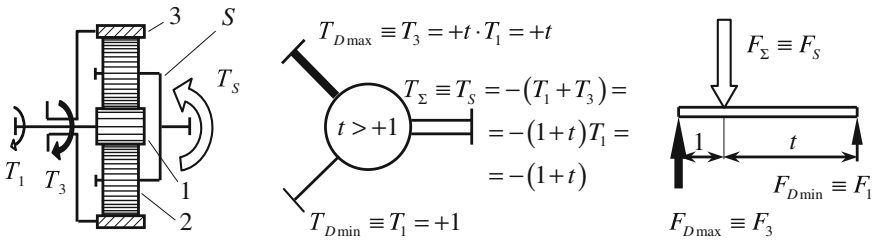

Fig. 3 The most usable simple planetary gear train, its modified symbol of Wolf and the lever analogy

however:

- How many degrees of freedom F (F = 1 or F = 2) the gear train is running with;
- Which shaft is fixed at F = 1 degree of freedom;
- What is the direction of power flow, respectively does the gear train works as a reducer or a multiplier at F = 1 degree of freedom, respectively such as a collecting or as a separating gear at F = 2 degrees of freedom, i.e. as a differential;
- Does the gear works as a single or as a component train along with others in a compound planetary gear train.

4 Application of Alternative Method

The application of the alternative method is best illustrated with the two-carrier compound planetary gear trains consisting of two of the most commonly used planetary gear trains, shown in Fig. 3. Using the modified symbol of Wolf, the linking up of the two gear trains can be done in different ways, as shown in Fig. 4

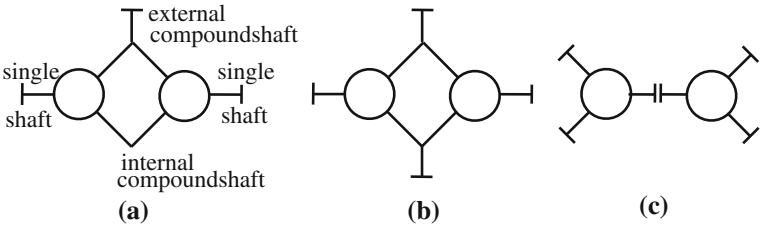

Fig. 4 Possibilities for connecting two simple planetary gear trains in two-carrier compound train. **a** With two compound and three external shafts. **b** With two compound and four external shafts. **c** With one compound and four external shafts

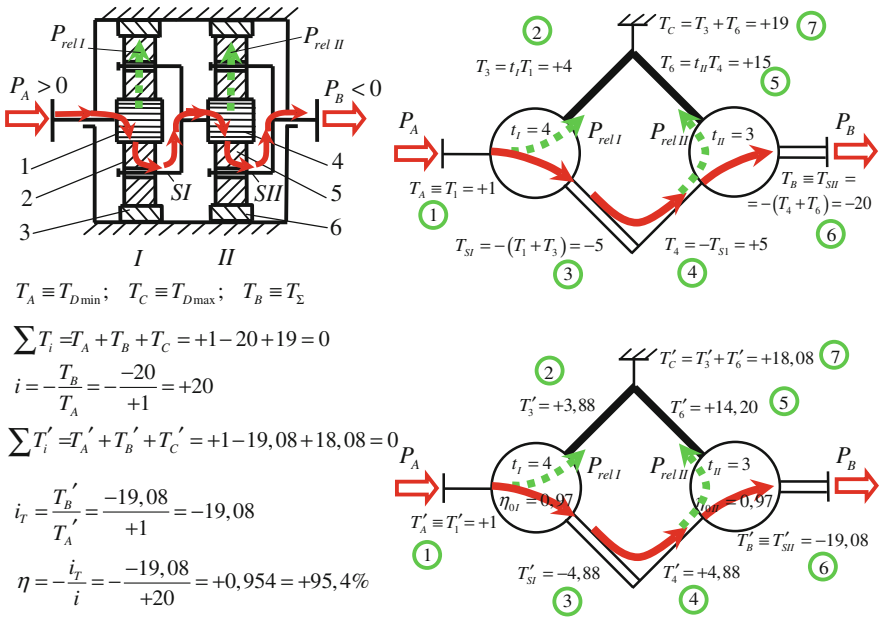

Fig. 5 Analysis of in series connected two-carrier planetary gear train

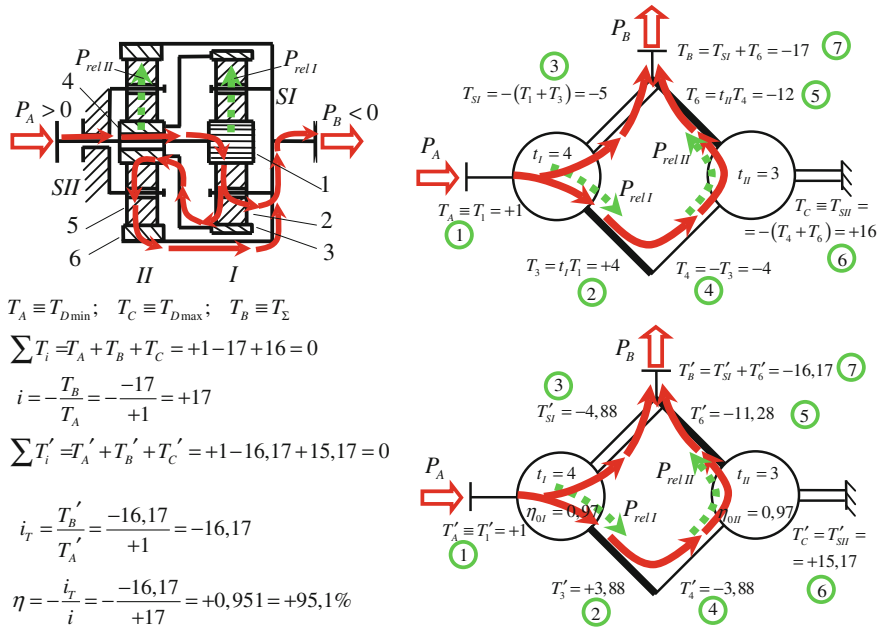

Fig. 6 Analysis of closed differential gear train with internal division of power

with structural schemes—by two or one compound shafts, where we get three-shafts, respectively four-shafts compound planetary gear train.

The most commonly used version is the first with two compound shafts and three external shafts (Fig. 4a). As seen from the figure, one of the compound shafts has no outset—it is an internal compound shaft, so that at both ends two equal sized but opposite direction torques are acting. The external torque of the other one, the external compound shaft, which has outset, equals the sum of external torques of the two coupling shafts.

The mentioned things above are illustrated by three examples:

- in series connected gear trains (Fig. 5);
- a closed differential gear train with internal division of power (Figs. 6 and 7);
- a closed differential gear train with internal circulation of power (Figs. 8 and 9);

Moreover, these are the three scenarios in this way of linking the two planetary gear trains—with two compound shafts and three external shafts. Other cases are not possible.

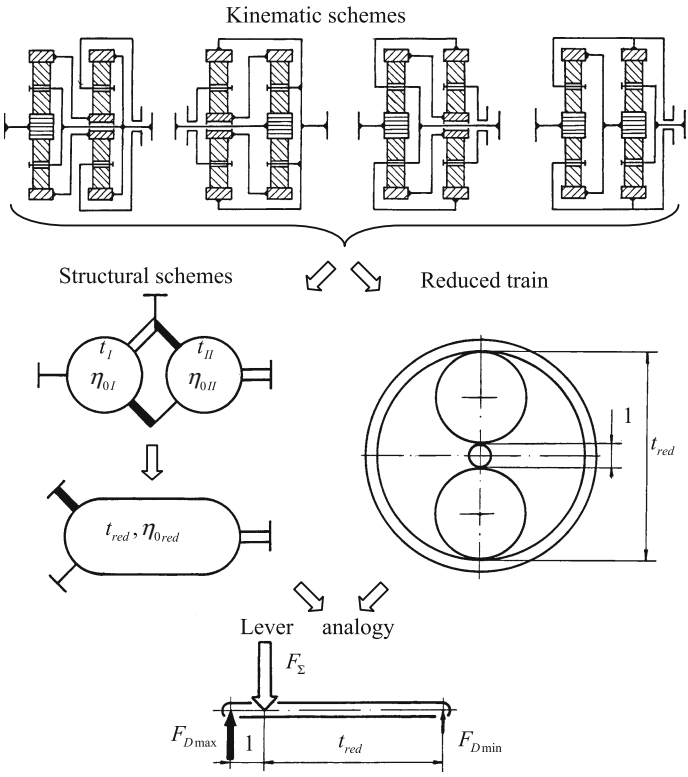

Fig. 7 Different kinematic schemes with the same structural scheme

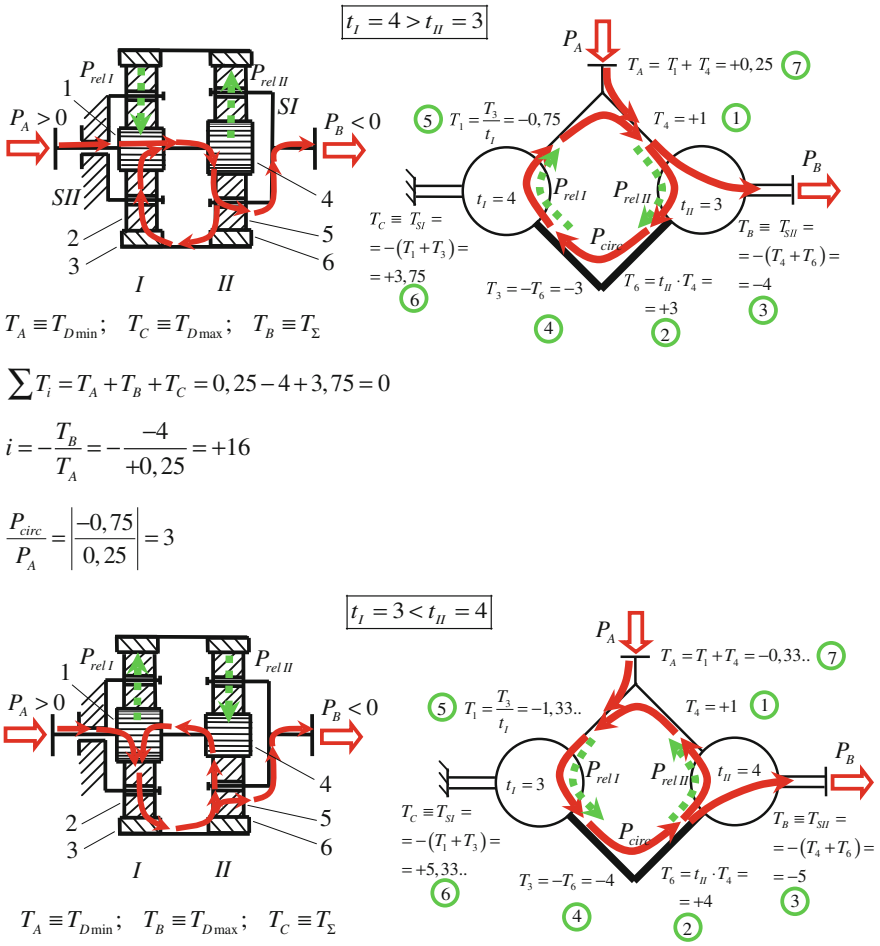

Fig. 8 Analysis of closed differential train with internal circulation of power (*I* closed train; *II* differential train; P_{circ} circulating power)

The first case (Fig. 5) is undoubtedly the simplest and most frequently used. There the whole power passes consecutively through two elementary component gear trainss. In both component trains the relative powers $P_{rel\,I}$ and $P_{rel\,II}$ are transmitted from the sun gears 1 and 4 of the ring gears 3 and 6.

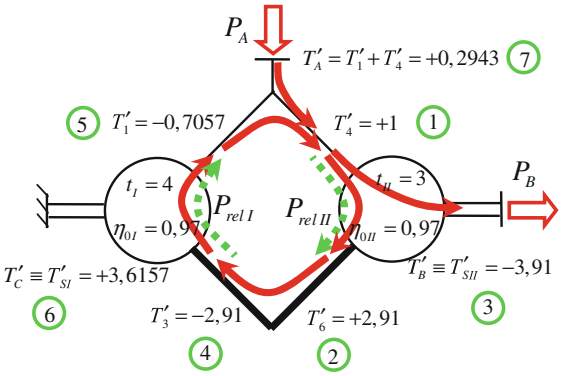

$$T'_A = +0,2943\,;\; T'_B = -3,91\,;\; T'_C = +3,6157$$

$$\sum T'_i = T'_A + T'_B + T'_C = 0,2943 - 3,91 + 3,6157 = 0$$

$$i_T = \frac{T'_B}{T'_A} = \frac{-3,91}{+0,2943} = -13,2858$$

$$\eta = -\frac{i_T}{i} = \frac{-13,2858}{+16} = 0,8304 = 83,04\%$$

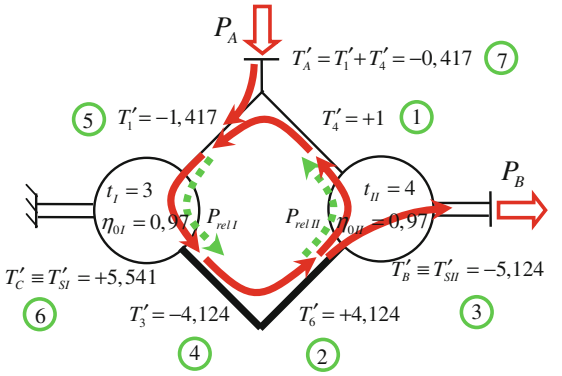

$$T'_A = -0,417\,;\; T'_B = -5,124\,;\; T'_C = +5,541$$

$$\sum T'_i = T'_A + T'_B + T'_C = -0,417 - 5,124 + 5,541 = 0$$

$$i_T = \frac{T'_B}{T'_A} = \frac{-5,124}{-0,417} = +12,2858$$

$$\eta = -\frac{i_T}{i} = \frac{+12,2858}{-15} = 0,8191 = 81,91\%$$

Fig. 9 Determination of the efficiency of planetary train from Fig. 8

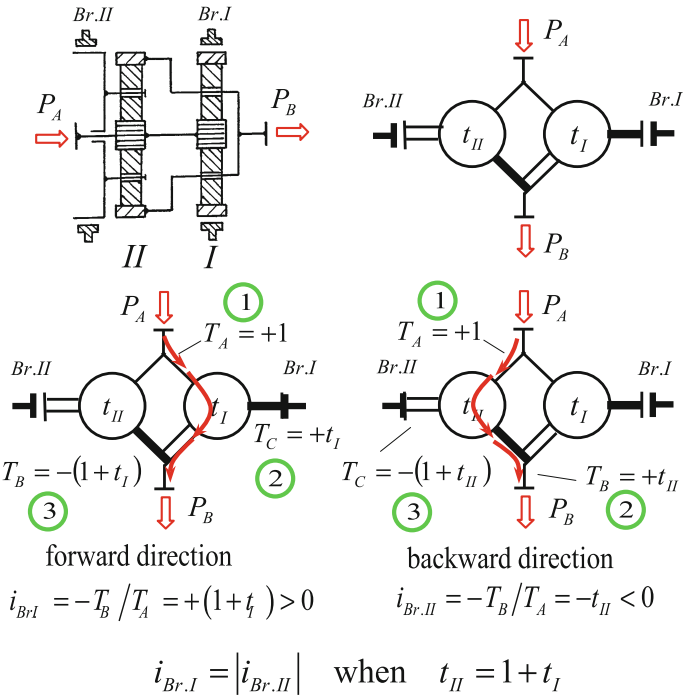

Fig. 10 Two-carrier planetary gear train with two compound and four external shafts—reverse gear train

The sequence of determination of different torques is shown on the figure with numbers in green circles. For convenience it is started with the lowest torque of the sun gear 1 or 4 of any of its component trains—I or II. In this case numerical value +1 is selected for torque of the sun gear 1 of the component train I, i.e. the first step of the compound gear train. The advantage here is that it is not just started with the lowest torque of the I component train, but the whole compound gear train. This is clearly seen from the formulas in the figure. It is quite possible however, to start with a torque of any shaft of component trains, and with any value without restriction to algebraic sign "+" or "−". The three ideal torques of each component train, which are in constant ratio are determined using the appropriate torque ratios t_I, respectively t_{II}. For both compound shafts—internal and external, the determination of the torque is done as shown above. When determining the real torques the direction of relative power $P_{rel\,I}$, respectively$P_{rel\,II}$ and the size of the internal efficiency η_{0I}, respectively η_{0II}, of each of the component trains are considered. For example, if in the first component train is begining from the real torque T_1' of the sun gear 1, for the size of the real torque T_3' of the ring gear 3 there are two options:

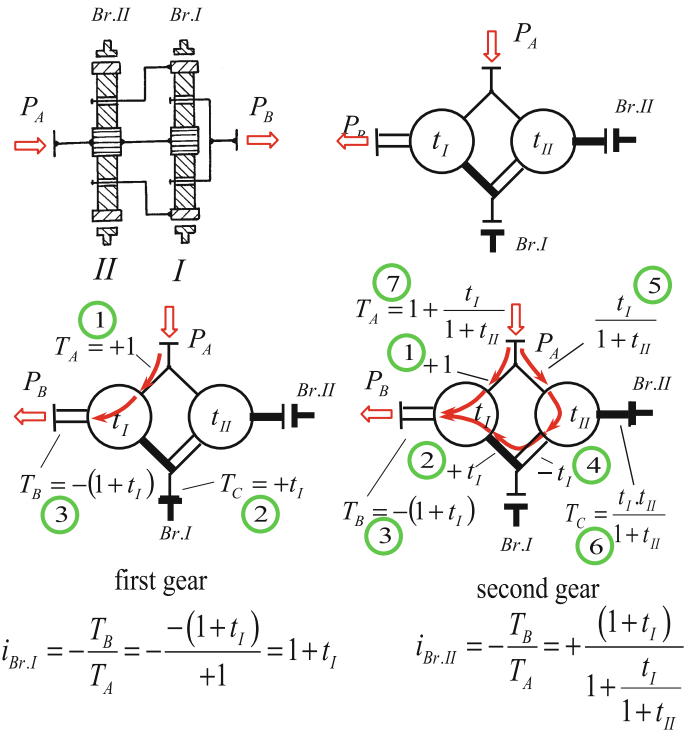

Fig. 11 Two-carrier planetary gear train with two compound and four external shafts—change-gear train (gearbox)

$T_3' = t_I \cdot T_1' \cdot \eta_{0I}$ in the direction of the relative power $P_{rel\,I}$ from the sun gear 1 to the ring gear 3;
$T_3' = t_I \cdot T_1' / \eta_{0I}$ in the direction of $P_{rel\,I}$ from the ring gear 3 to the sun gear 1;

In these formulas η_{0I} is internal efficiency of the I component gear train, i.e. in transmission of power from the sun gear 1 to the ring gear 3, with fixed carrier SI ($\omega_{SI} = 0$).

What was said up to now is true for the second component gear Fig. 5 shows:

- determination of ideal and real torques;
- check on the equilibrium of the torques, ideal and real, i.e. their correct calculation;
- determination of speed ratio i_k;
- determination of torque ratio i_T (torque transformation);
- determination of efficiency η.

The next two cases of closed differential gear trains are more interesting because in one case (Figs. 6 and 7) there is an internal division of power, which is

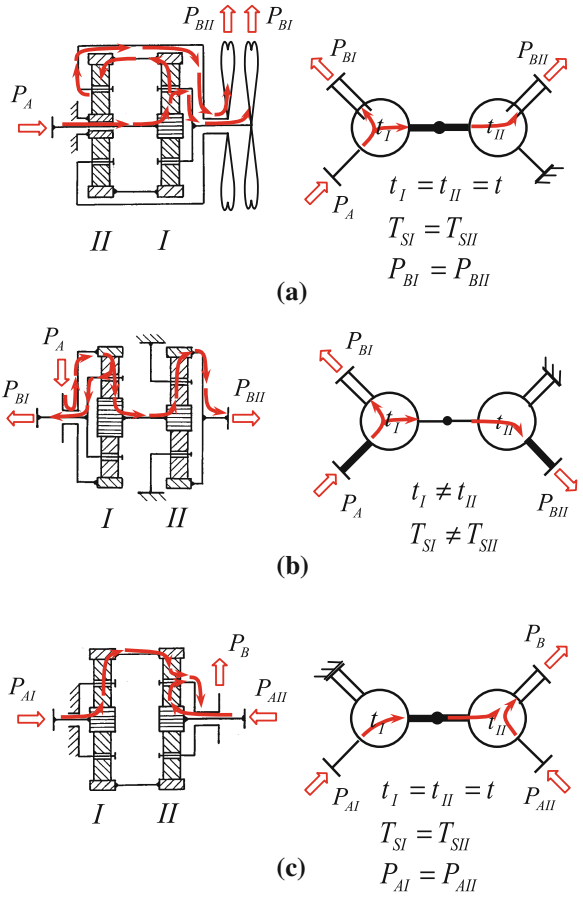

Fig. 12 Compound two-carrier planetary gear trains with one compound and four external shafts. **a** One-engine driving of two opposite rotating aircraft propellers (separating train). **b** One-engine driving of asymmetric differential of a heavy vehicle (separating train). **c** Two-engine driving of aircraft flap (collecting train)

beneficial and in the other case (Figs. 8 and 9)—internal circulation of power, which is not very beneficial.

In the literature there are, indeed, ways to determine the presence or absence of internal circulation of power. They are not simple (Kreines 1947; Kudryavtsev 1966; Tkachenko 2003; Müller 1982, 1998). Much simpler is the following rule of algebraic signs (Arnaudov 1996; 2001; Arnaudov and Karaivanov 2005a, b, 2010), which is expressed as follows:

> When the algebraic signs of the torques of two shafts, composing the external compound shaft, are the same, nevertheless "+" or "−", there is an internal division of power. In different algebraic signs there is an internal circulation of power.

The above is clearly illustrated by two examples. It is shown the direction of the circulating power, depending on torque ratios t_I and t_{II} of both component gears I and II. It is obvious that the direction may be different (Fig. 9). It can be determine as follows:

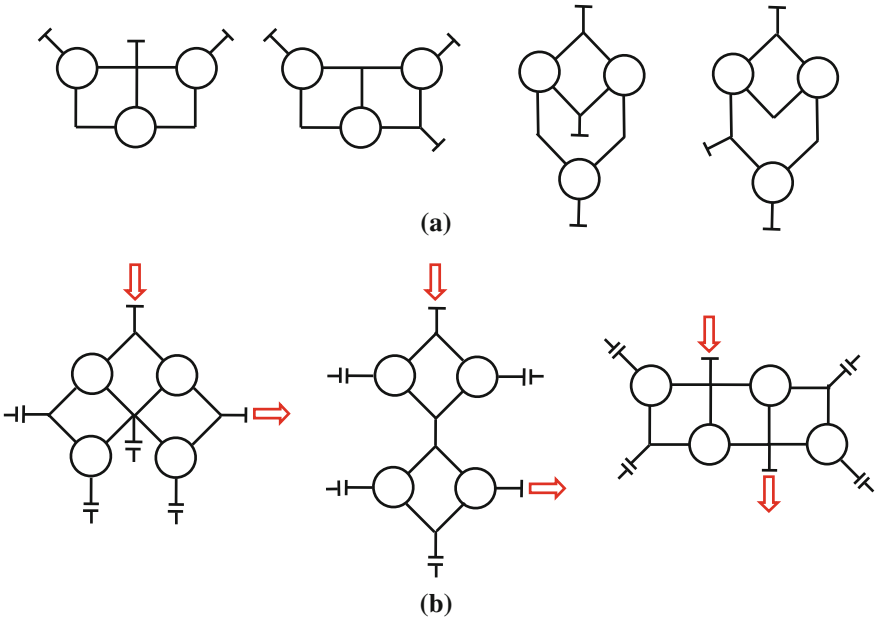

Fig. 13 Structural schemes of **a** three-carrier compound planetary gear trains, **b** four-carrier compound planetary gear trains

The direction of the circulating power P_{circ} coincides with the direction of input power P_A or output power P_B at the coupling shaft (constituting the external compound shaft) where its algebraic sign of the internal torque coincides with the algebraic sign of the torque of external compound shaft.

The directions of the relative powers $P_{rel\,I}$ and $P_{rel\,II}$ in both component trains that are important for the determination of the efficiency are shown also. In the gear trains with internal power circuits it is shown that with one and the same structural scheme, the kinematic schemes may differ (Fig. 7).

Figures 10 and 11 show two examples of the compound two-carrier planetary gear trains with two compound shafts and four external shafts. The brakes used in these gear trains can be located on different shafts—single or compound. The Fig. 10 shows a reverse gear train, carrying forward and backward. The Fig. 11 shows a change-gear (gearbox), carrying out two gear-ratio steps (speeds).

Figure 12 shows three cases of using two-carrier compound planetary gear trains with a one compound shaft, but with four external single (i.e. not-compound) shafts.

Figure 13 shows the structural schemes of three-shaft three-carrier and four-carrier compound gear trains. The first are used as reducers or multipliers, i.e. with F = 1 degree of freedom, while the second—as change-gears.

Figure 14 shows three-carrier compound gear train that works as a multiplier in the powerful wind turbine (Giger and Arnaudov 2011).

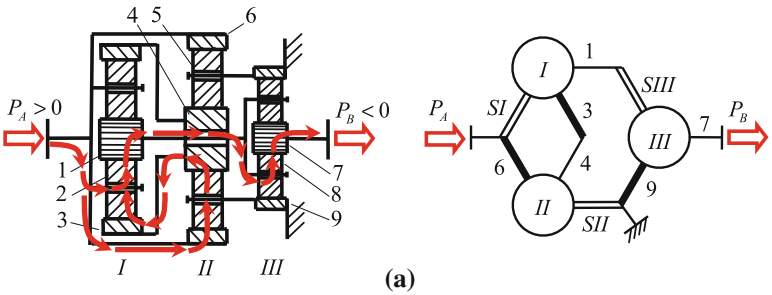

(a)

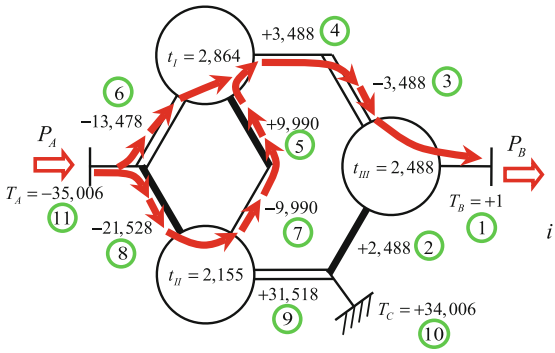

$$T_A = -35,006$$
$$T_B = +1$$
$$T_C = +34,006$$
$$\sum T_i = T_A + T_B + T_C =$$
$$= -35,006 + 1 + 34,006 = 0$$
$$i = -\frac{T_B}{T_A} = -\frac{+1}{-35,006} = +0,028566$$

(b)

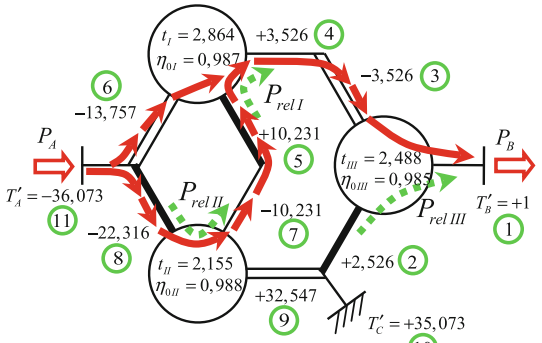

$$T'_A = -36,073$$
$$T'_B = +1$$
$$T'_C = +35,073$$
$$\sum T'_i = T'_A + T'_B + T'_C =$$
$$= -36,073 + 1 - 35,073 = 0$$
$$i_T = \frac{T'_B}{T'_A} = \frac{+1}{-36,073} = -0,02772$$
$$\eta = -\frac{i_T}{i} = -\frac{-0,02772}{+0,028566} = 0,97038 = 97,04\%$$

(c)

Fig. 14 Three-carrier planetary gear train—multiplier of wind turbine. **a** Kinematic and structural schemes. **b** Determination of speed ratio. **c** Determination of efficiency

Figure 15 shows how to determine the load spectrum of an element of four-carrier change-gear while working with different gear-ratio steps (speeds).

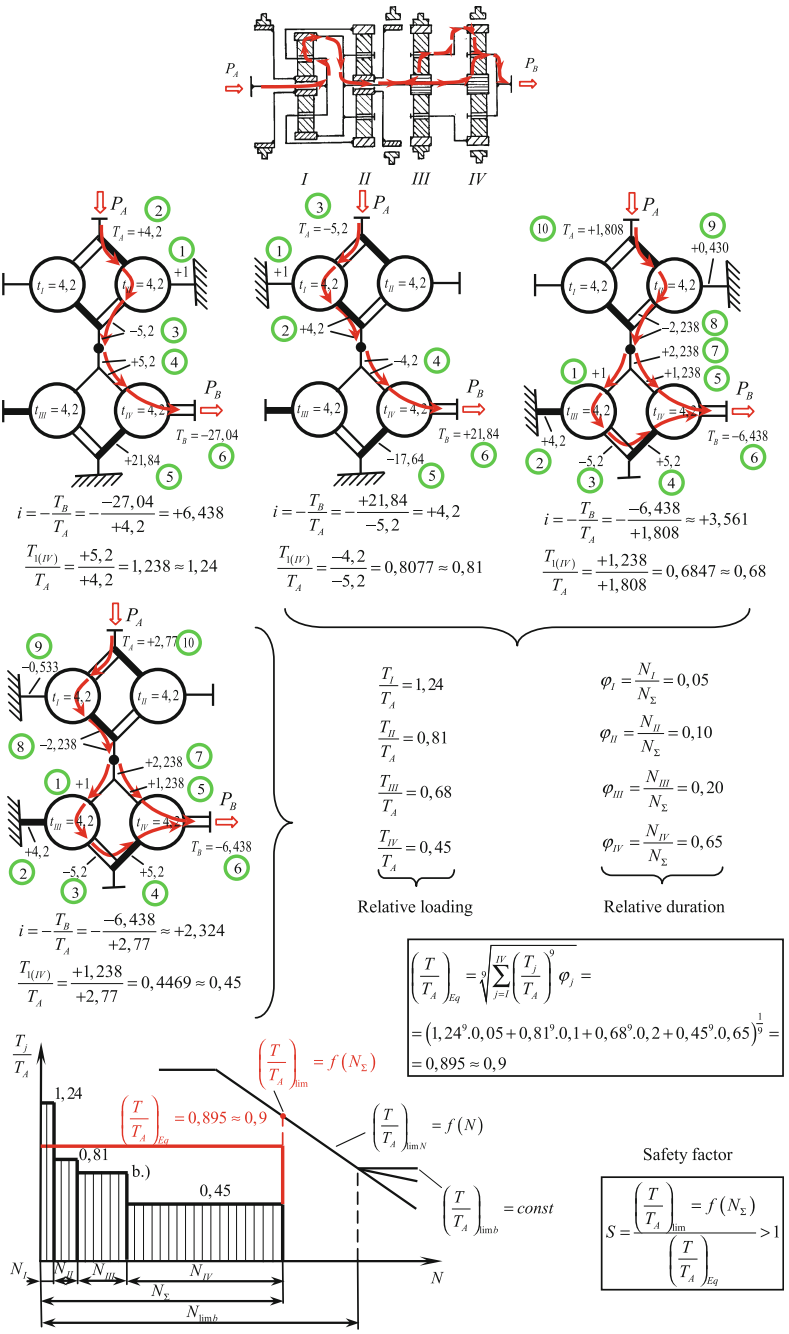

Fig. 15 Determination of load spectrum of an element of four-carrier change-gear while working with different gear-ratio steps (speeds)

5 Conclusion

Unlike the most commonly used methods of Willis and Kutzbach-Smirnov that use the angular and peripheral velocities, at the presented method here another parameter of mechanics is used—the torque. This alternative method is characterized with the following:

1. The method is characterized by simplicity, maximum clarity and ease of usability (relevance), combining in itself, accuracy and clarity, existing separately in the Willis and Kutzbach-Smirnov's methods.
2. The method allows achieving more goals than is possible with the methods of Willis and Kutzbach-Smirnov—determining not only the speed ratio, but also the internal power flows by size and direction, as a prerequisite for the determination of the efficiency. Also the determining of the load spectra of elements of the compound change-gears—gear-wheels, shafts and bearings, while working with different gear-ratio steps (speeds) as a prerequisite for their reliable load capacity calculation.
3. The dependence of the designer on a particular literary source is avoided, so he may act independently.
4. The method allows easy verification of calculations by the conditions of equilibrium of the ideal and real external torques.
5. Because of the clarity and ease applicability, the method is suitable either for industry—for engineers, or for learning process—for students.

Considering all these possibilities and the current acceptance of the method in different countries (Giger 2007; Müller 1998; Troha 2011), there is reason to believe that the alternative method can successfully compete with those of Willis and Kutzbach-Smirnov, especially in the analysis of complex compound planetary gear trains.

References

Arnaudov K (1984) Engineering analysis of the coupled (two-carrier) planetary gear trains. In: Proceedings of the national youth school of the heavy machine-building. Varna, Bulgaria (in Bulgarian)

Arnaudow K (1996) Einfaches Verfahren zur Ermittlung des Übersetzungsverhältnisses zusammengesetzter Planetengetriebe. VDI-Berichte 1230 (International Conference on Gears, Dresden), S. 313–327

Arnaudov K, Karaivanov D (2001) Engineering analysis of the coupled two-carrier planetary gearing through the lever analogy. In: Proceedings of the international conference on mechanical transmissions. China Machine Press, Chongqing, pp 44–49

Arnaudow K, Karaivanov D (2005) Systematik, Eigenschaften und Möglichkeiten von zusammengesetzten Mehrsteg-Planetengetrieben. Antriebstechnik, 5, S. 58–69

Arnaudov K, Karaivanov D (2005) Higher compound planetary gear trains. VDI-Berichte 1904 (International Conference on Gears, München), pp 327–344

Arnaudov K, Karaivanov D (2010) The complex compound multi-carrier planetary gear trains: a simple study. VDI-Berichte 2108—2 (International Conference on Gears, München), pp 673–684

Giger U (2007) Neuer Ansatz für sehr große Windkraftgetriebe. Wind Kraft Journal, 5, pp 2–4

Giger U, Arnaudov K (2011) Redesign of a gearbox for 5 MW wind turbines. In: Proceedings of the 11th ASME international power transmission and gearing conference 1–3 Sept. Washington, D.C, USA

Karaivanov D (2000) Theoretical and experimental studies of the influence of the structure of the coupled two-carrier planetary gear trains on its basic parameters. Dissertation. Sofia, Bulgaria (in Bulgarian)

Karaivanov D, Arnaudow K (2002) Die zusammengesetzten Mehrsteg-Planetengetriebe und ihre Gesetzmäßigkeiten. Zbornik radova sa Naučno-stručnog skupa Istraživanje i razvoj mašinskih elementa i sistema Jahorina—IRMES'2002, 1/2, Srpsko Sarajevo—Jahorina (Bosna i Hercegovina), 19. i 20. Sept, pp 19–26

Kreines MA (1947) Efficiency and transmit ratio of a gear mechanism. In: Proceedings of TMM seminar, vol. 1. Academy of Sciences of the USSR, Moscow, pp 21–48 (in Russian)

kudryavtsev VN (1966) Planetary trains. Mashinostroenie, Moscow (in Russian)

Kutzbach K (1927) Mehrgliedrige Radgetriebe und ihre Gesetze. Maschinenbau, H. 22, S. 1080

Looman J (1996) Zahnradgetriebe III. Auflage. Springer, Berlin

Müller HW (1982) Epicyclic drive trains. Wayne State University Press, Detroit

Müller HW (1998) Die Umlaufgetriebe 2. Auflage. Springer, Berlin

Seeliger K (1964) Das einfache Planetengetriebe. Antriebstechnik, S. 216–221

Tkachenko V (2003) Planetary mechanisms. Optimal design. HAI, Harkov (in Russian)

Troha S (2011) Analiza varijanti mjenjačkog zupčaničkog planetnog pretvarača. Doktorska disertacija. Sveučilište u Rijeci, Tehnički Facultet, Rijeka (Croatia)

Willis R (1841) Principles of mechanism. John W. Parker, London

Wolf A (1958) Die Grundgesetze der Umlaufgetriebe. Braunschweig, Friedr. Vieweg Sohn

Planetary Precessional Transmissions: Synthesis and Generation Technologies

Ion Bostan

Abstract Some problems of mechanical transmissions can be solved with special effects by developing new types of transmissions based on planetary precessional transmissions with multiple gear, that were developed by the author. Absolute multiplicity of precessional gear (up to 100 % pairs of teeth simultaneously involved in gearing, compared to 5–7 %—in classical gearings) provides increased lifting capacity and small mass and dimensions. The article presents the analysis of the main structures of precessional transmissions, the theoretical aspects of non-standard profiles generation.

Keywords Precessional transmission · Gear · Tooth profile

List of Symbols

i	Gear ratio
Ψ	Semi product angle of rotation
$\Delta\Psi_3$	Diagram error
δ	Pitch angle of the roller axis
θ	Nutation angle
β	Roller taper angle
z	Number of teeth
α	Gearing angle

I. Bostan (✉)
Technical University of Moldova, Chişinău, Moldova
e-mail: bostan@adm.utm.md

G. Dobre (ed.), *Power Transmissions*,
Mechanisms and Machine Science 13, DOI: 10.1007/978-94-007-6558-0_2,

1 Introduction

A problem for engineering companies (especially in the metalworking industry, automotive, chemical and metallurgical industries) is to satisfy the ever-increasing requirements to the transmissions used in majority of industrial machinery and technological equipment related to bearing capacity, compactness, mass and dimensions, low cost of production, etc., and, in particular, to kinematical characteristics, structural compatibility with other aggregates of the equipment, etc. Gearings are considered the most sophisticated components of machines. Machine reliability depends very much on the gearing mechanical transmission operation, in general. The quality indices of traditional gears were increased largely by changing involute gearings, and by creating new gearings, such as Novikov-Hlebanija (Krasnoshhekov et al. 1976) Symark (Kaabushiki 1977), etc.

In the field of planetary transmission it was considered properly to follow the way of developing new types with increased performances. Scientific analysts consider that in the field of technical sciences worldwide an essentially new type of mechanical transmission is being invented every 20–25 years. Thus, the German engineer L. Braren developed the cycloid planetary transmission "CYCLO" in 1923 (A Unique Concept 2012). The Russian engineer A. Moskvitin invented the harmonic friction transmission in 1944 (Tzejtlin and Tzukerman 1969), and in 1959 the American engineer C. W. Musser developed the harmonic gear transmission (Tzejtlin and Tzukerman 1969).

In the late seventies a new type of mechanical transmission has been developed at the Polytechnic Institute of Chisinau (now the Technical University of Moldova). The new type of mechanical transmission entered into international terminology circuit as planetary precessional transmission (PPT). The first patent was issued under this name in 1983. Planetary precessional transmission differs from the classical one by the new principle of motion and load transformation and transmission, i.e. by using sphere-spatial motion of the satellite and variable convex—concave profile. Due to these innovative features gearing multiplicity in planetary precessional transmission reaches 100 % (in classical transmissions - 3–7 %) which provides increased bearing capacity, reduced dimensions and weight, extended kinematical range ±10 … ±3,599 (in harmonic transmissions 79 … 300), high kinematical accuracy, etc. The research team involved in research on precessional planetary transmissions published over 800 scientific articles, obtained about 170 patents, implemented about 20 practical achievements in the field of fine mechanics and specialized technological equipment, in robotic complexes for the exploration of ferro—manganese concretions from the World Ocean bottom (USSR concept), in spaceflight technique, etc.

Know-how in the elaboration of multicouple precessional gear, manufacturing technology and control methods, and a range of precessional transmission diagrams belong to the research team from the Technical University of Moldova.

- The specific character of sphere-spatial (precessional motions of the precessional transmissions pinion make impossible the utilisation of classical involute

teeth profiles. This fact requires the elaboration of new profiles adequate to the sphere-spatial motion of pinion, which would ensure high performances to the precessional transmission. Carrying out on the principle of the transfer function continuity and gear [5] based on the principles of the transfer function continuity and gear multiplicity which aims to:

- the elaboration of the gear mathematics model with account of the peculiarities;
- the analytical description of teeth profiles by a system of parametric equations on spherical surface and normal teeth section for inner and plane gear;
- CAD determination of geometrical and cinematic parameters influence of the gear upon the teeth profiles shape and the justification of their rational limits of variation;
- the elaboration of the theoretical basis evaluation of teeth gear multiplicity in precessional transmissions;
- area definition of gear multiplicity existence by 100 % teeth couples.
- the production of non-standard teeth profiles requires a new manufacturing technology. In the complexity of problem "*gear-synthesis-profile study- manufacturing*" the elaboration of efficient methods of teeth manufacturing which ensures a maximum productivity and reduced cost while satisfying the requirements related to the gear with precessional motion plays an important role. To solve this problem the following has been done:
- we elaborated the mathematical model of teeth generation which shows the interaction of teeth in precessional gear;
- we investigated the kinematics of the mechanism of method realisation for teeth generation;
- we determined the tool path of motion and the family envelope of the generating surface by using the computer;
- we elaborated and manufactured from metal milling and tooth grinding tools, inclusively their longitudinal modification.

2 Synthesis of Planetary Precessional Transmissions

2.1 Kinematical Structure

Depending on the structural diagram, precessional transmissions fall into two main types—*K-H-V* and *2K-H* (according to Kudreavtzev's classification), from which a wide range of constructive solutions with wide kinematical and functional options that operate in multiplier regime come out.

Planetary precessional transmissions K-H-V. Kinematical structure of precessional transmission *K-H-V* (Fig. 1a) has four components: planet (wheel) carrier *H*, satellite gear *g*, central wheel *b* and the casing (framework). Satellite gear *g* and the central wheel *b* are under internal gearing, and their teeth generators cross in a

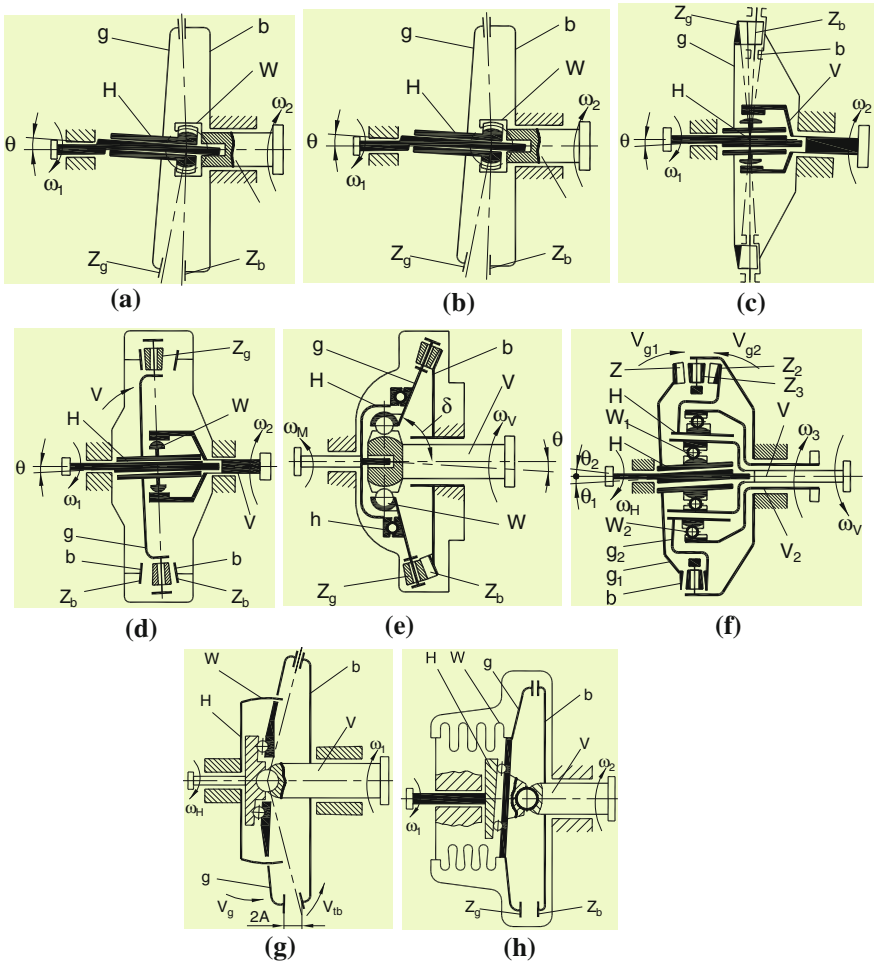

Fig. 1 Kinematical diagram of precessional transmission K-H-V

point called *the centre of precession*. Satellite gear g is mounted on the planet carrier H, designed as a reclined crank, which axis forms with the axis of the central wheel a certain angle θ. The reclined crank H, spinning, forwards a sphere-spatial motion to the satellite gear in relation to the ball joint installed in the centre of precession.

To analyze the kinematics of these transmissions, with an additional connection of the satellite g with the body: At a rotation of the drive shaft (planet carrier H), central wheel b will rotate with a certain angle $\Delta\psi_b$. To determine the position of the driven shaft V depending on the position of the drive shaft H, it is necessary to define the equation of the satellite gear motion. At a constant angular speed of the drive shaft, sphere-spatial motion of the satellite g is described by a system of equations, expressed by Euler angles $\psi = \omega_H t, \phi = \phi(t), \theta = const$, where ψ is

the angle of precession (the rotation of axis $O'O'$ of the satellite wheel g with regard to axis OO of the central wheel b); φ—is the angle of the satellite rotation itself around its axis $O'O'$; θ—is the nutation angle (pitch of axis $O'O'$ of the satellite wheel to the central wheel axis OO). It should be noted that the equation of free rotation of the satellite wheel $\varphi = \varphi(t)$ is determined by type of kinematical connection between the satellite gear and the frame. For the transmission with connection mechanism in the form of a toothed coupling (Fig. 1b) gear ratio varies in the limits:

$$i^g_{HV} = -\frac{z_g \cos\theta - z_b}{z_b};\ i^g_{HV} = -\frac{z_g \cos\theta - z_b}{z_b \cos\theta}, \tag{1}$$

reaching extreme values 4 times for each rotation of the drive shaft H. If necessary, this drawback can be eliminated using as connection mechanism double universal joint, ball synchronous couplings, etc. Average gear ratio will be:

$$i^g_{HV_{med}} = -\frac{z_g - z_b}{z_b}. \tag{2}$$

for $z_g = z_b + 1, i^g_{HV} = -1/z_b$, i.e. the drive and driven shafts have opposite directions. For $z_g = z_b - 1, i^g_{HV} = 1/z_b$, i.e. the shafts rotate the same direction. Precessional transmissions *K-H-V* fall under two basic types:

- with satellite wheel fixed to the casing;
- with central wheel fixed to the casing.

Precessional transmissions diagrams, where the central wheel b is fixed to the casing (bed), and the satellite gear g is fixed to the driven shaft V, are shown in (Fig. 1a–d). In precessional transmissions *K-H-V* with the fixed central wheel an important component is the connection device W of the satellite gear with the driven shaft V.

Device W performs transmission of motion between the shafts with parallel axes of the satellite-wheel and the central wheel that have the difference of teeth $z_g = z_b \pm 1$. Average gear ratio of these transmissions is determined from the relationship:

$$i^b_{HV} = -\frac{z_g}{z_b - z_g}; \tag{3}$$

$i^b_{HV} = -z_g$ for $z_b = z_g + 1; i^b_{HV} = z_g$ for $z_b = z_g - 1$.

A very important feature of precessional planetary transmissions K-H-V is the possibility of transmitting rotary motion in tight (hermetic) spaces. To this end, Fig. 1, g and h shows two kinematical structures of hermetic precessional transmission.

Based on the structural scheme (Fig. 1c), the demonstrational model of precessional reducer was developed, designed and manufactured (Fig. 2a, b). Manufacture of gear cover made of transparent material allows viewing the operating principle of precession gear.

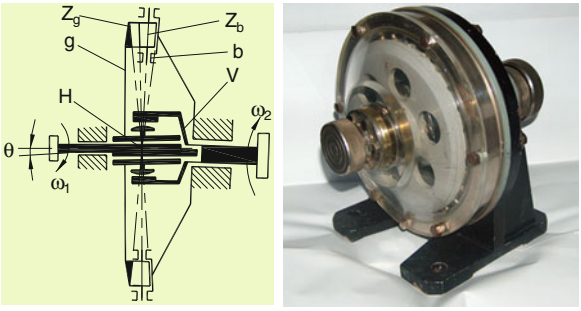

Fig. 2 The first (1983) demonstrational model of planetary precessional reducer K-H-V ($i = -29$)

In planetary precessional transmission (Fig. A, d) the satellite-wheel is placed between two fixed gear wheels, bearing the same number of teeth. This transmission has high bearing capacity and ensures reduced diametric dimensions

Advantages of planetary precessional transmissions K-H-V:

- high bearing capacity due to gearing multiplicity;
- wide range of speed reduction $i = 8\ldots60$, and in special structures $i = 60\ldots3{,}600$;
- operation in reducer and multiplier regimes;
- ensure the transmission of motion in tight spaces via membranes.

Planetary precessional transmissions 2K-H. Precessional transmissions *2K-H* can be developed following two basic schemes: one-side or bilateral location of the central wheels. In the case of bilateral arrangement (Fig. 3a, b, e, f), axial dimensions increase; and at unilateral location (Fig. 3c)—radial dimensions increase. The choice of structural diagram depends on the beneficiary needs. The diagram in Fig. 3c, b shows that the fixed wheel b and the movable wheel a are arranged on the same side of the satellite wheel—g. Pulleys Z_{g1} and Z_{g2} can be placed on separate or joint axes. In the case of location on the same axis, i.e. when $Z_{g1} = Z_{g2}$, the gear ratio is determined from the relation:

$$i_{HV}^{b} = -\frac{z_g}{z_b - z_a}. \tag{4}$$

if $Z_a = Z_{g2} - 1$ and $Z_b = Z_{G1} + 1$, then $i_{HV}^{g} = \frac{z_a}{2}$, and if $Z_a = Z_{g2} + 1$ and $Z_b = Z_{g1} - 1$, then $i_{HV}^{g} = -\frac{z_g}{2}$.

Precessional transmissions *2K-H* have higher performances, inclusive kinematical ones (Fig. 3a). Precessional transmissions *2K-H* comprise the satellite-wheel g, with two crown gears Z_{g1} and Z_{g2}, that are in gear with the fixed b and movable a central wheels. The gear ratio is determined from the relation:

$$i = -\frac{z_{g_1} z_a}{z_b z_{g_2} - z_{g_1} z_a}. \tag{5}$$

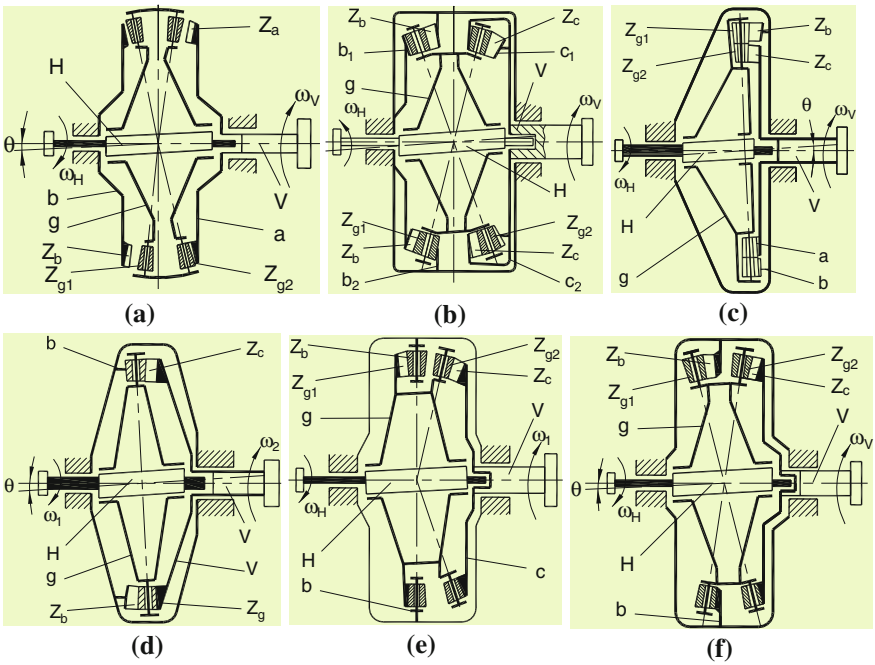

Fig. 3 Kinematical diagram of precessional transmissions 2K-H

Analysis of relation (5) shows that precessional transmissions *2K-H* provide achievement of a larger range of gear ratio. Maximum kinematical effect is reached for the teeth relations:

$$z_b = z_{g_2}; z_{g_1} = z_{g_2} + 1; z_a = z_{g_2} - 1;$$
$$i^b_{HVmax} = z^2_{g_1} \, pentru \, z_a = z_{g_1}, z_{g_2} = z_{g_1} + 1, z_b = z_{g_1} - 1.$$

The proposed gears allow obtaining maximum kinematical effect for other numbers of gear ratios, for example:

$$\begin{aligned} i_{max} &= z^2_{g_1} \, pentru \, z_a = z_{g_1}, z_{g_2} = z_{g_1} - 1, z_b = z_{g_1} + 1, \\ i_{max} &= z^2_{g_2} - 1 \, pentru \, z_b = z_{g_2}, z_{g_1} = z_{g_2} - 1, z_a = z_{g_2} + 1 \end{aligned} \tag{6}$$

While developing precessional transmissions 2K-H a problem comes out related to the selection of the optimal number of wheel teeth, which ensures the obtaining of certain gear ratio. To facilitate the rational selection of the number of teeth by relation (5), possible variants of their choice for the range of gear ratio $i = -13 \ldots 2{,}401$ were determined using computer. Calculations were performed for the ratio numbers of teeth: $z_{g_1} = z_b + 1; z_{g_2} = z_a + 1; z_{g_1} = z_{g_2} \pm 1, 2, 3 \ldots$.

Based on the structural diagram *2K-H* (Fig. 3a) the demonstrational prototype of the precessional reducer *2K-H* was designed and manufactured. Housing made

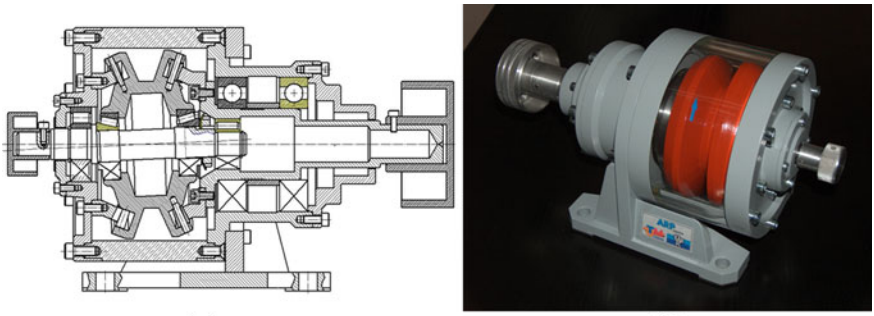

Fig. 4 The first (1988) demonstrational model of precessional reducer 2K-H

of transparent material allows viewing sphere-spatial specific motion (precessional) of the satellite block, the process of toothed wheel gearing with the toothed crowns of the satellite block (Fig. 4a, b).

Precessional transmission (Fig. 3d) shows that the central wheel *b* is linked to the casing, and the central wheel *c*—to the driven shaft *V*. Satellite gear *g*, mounted between the central gears *a* and *b*, gearing simultaneously with the teeth of the fixed *b* and movable *c* central wheels, conveys the driven shaft *V* a reduced motion of rotation. The number of teeth conducting the load simultaneously in the gearing is $z = (z_4 - 1)/2$ for the number of teeth z_4 with couples. The remained teeth contact between each other with passive flanks.

It is necessary to specify a number of features of precessional transmissions *2K-H*, which gives them higher performance compared to similar planetary transmission with cylindrical wheels:

- Precessional transmissions do not require compliance of equal distance between the axes, which fact broadens their optimum design field;
- Kinematics of precessional transmissions does not limit the choice of teeth modules of the gear torque or rollers location pitch, which increases the possibilities of generation of tooth numbers torque and gear ratio interval;
- Characteristics of the designed precessional gearings, unlike traditional involute gears, enlarge considerably kinematical possibilities and performances of precessional transmissions.

Advantages of planetary precessional transmission 2K-H:

- Increased bearing capacity due to the multiplicity of gearing;
- wide range of speed reduction $i = \pm 10 \ldots 3{,}600$ fully guaranteed by the involvement of a satellite with two central wheels;
- 2K-H gearing provides self-locking and one-way or opposite rotation of the drive and driven shafts;
- operates as reducer, multiplier (special constructions) and differential.

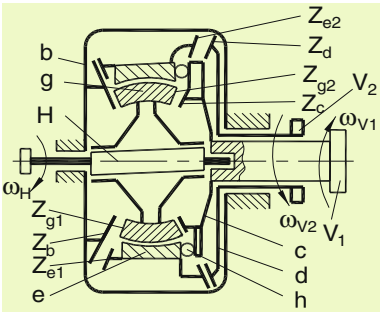

Fig. 5 Kinematical diagrams of complex precessional transmissions

Complex planetary precessional transmission. If specific areas, where you need a very high transmission ratio, a complex structural diagram is proposed, which is a planetary transmission precession 2K-H in two steps. Arrangement of the wheels in the bi-planetary combined transmission version *2K-H* (according to *V.N. Kudreavtzev's* classification) ensures maximum kinematical effect under reduced dimensions and low mass (Fig. 5a) (Bostan 2011). To this end, satellite *g* is installed on a reclined crank *H*, and the satellite *e* is installed on the outer spherical surface of the first satellite. Both satellites are equipped with two serrated crowns, which gear simultaneously with the fixed wheel *b* and with movable wheels *c* and *d*. Wheel carrier *H* rotates and conveys precessional motion to satellite *g*, and to central wheel *C* and the driven shaft V_1—reduced rotational motion. Rotational motion *a* of the wheel *c* turns into precessional motion of the satellite *e* through the rolling bodies, installed between the front inclined part of wheel *c* and the front part of satellite *e* gears with the teeth of fixed *b* and movable *d* wheels, sending to the last wheel and shaft V_2 rotational motion with the degree of reduction:

$$i = \frac{z_{g_1} z_c z_{e_1} z_d}{z_b z_{g_2}(z_b z_{e_2} - z_{e_1} z_d) - z_{g_1} z_c(z_b z_{e_2} - z_{e_1} z_d)} = 12,960,000. \quad (7)$$

This transmission, with the number of teeth $z_b = 59$, $z_{e2} = z_{g2} = 61$, $z_{e1} = z_d = z_{g1}$ $z_c = 60$, for example, will allow obtaining the gear ratio $i = 12{,}960{,}000$.

On the basis of the structural diagram (Fig. 5) an industrial prototype of the driving device for gas pipelines fittings was elaborated, designed and manufactured (Fig. 6a, b). Drive mechanism involves a bi-planetary precessional transmission *2K-H*, in combination with a transmission with one-step cylindrical gear wheels, and fulfils gear ratio $i = 20{,}000$ and torque moment $T = 30{,}000$ Nm.

Advantages of complex planetary precessional transmissions 2K-H:

- high kinematical effect, estimated with motion gear ratio over $i = 1{,}000{,}000$;
- compactness, reduced dimensions and mass.

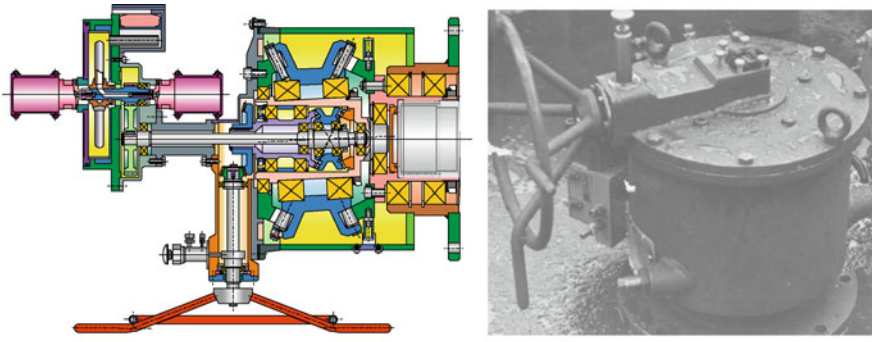

Fig. 6 The first (1991) planetary precessional reducer 2K-H in two steps ($T = 30{,}000$ Nm, $i = 20{,}000$)

3 Generation Technologies

3.1 General Remarks

Development of mechanical transmission with gear, different from the classical one, requires complex research in various fields. This finding refers to planetary precessional transmission with multicouple gear, which is characterized by essential constructive-kinematical features. In solving complex problems related to "*gear synthesis—profile research—fabrication*" an important role belongs to developing efficient methods of teeth manufacturing, which would ensure maximum productivity, reduced cost and quality.

Manufacture of precessional gear wheels with convex-concave and variable tooth profile cannot be achieved by existing generation technologies, but through fundamentally new technology. Generation technology of precessional wheel teeth must ensure continuity of motion transformation function with the following conditions: non-standard and variable tooth profile, and satellite carrying out sphere-spatial motion with a fixed point. To achieve the above, a new procedure for teeth processing is proposed by self-generating method with precessional tool against rotating blank.

To develop the theoretical basis for generating tooth profile by running the precessional tool it is necessary to determine the character of continuous contact of the tool cutting edge and profile of the processed wheel tooth for a complete "tool-blank" precessional cycle. In this connection a mathematical model of tooth self-generating method by running the precessional tool was elaborated, which fully reflects the actual interaction of teeth in precessional transmission. For this purpose the following was described:

- kinematical connection of the precessional tool with the blank that ensures continuity of motion transformation function in the linkage "tool-blank";

- path of motion of the tool centre in the fixed system of coordinates;
- path of motion of the tool centre in the movable system of coordinates, connected with the rotating blank;
- the generating contour of the tool in the movable system of coordinate and the system envelope of generating surfaces of the tool for a cycle of precession;
- projection of tool contour envelope in the plane system of coordinates.

3.2 *Technological System for Teeth Generation by Sphere-Spatial Motion of Tool as Truncated Cone*

3.2.1 Kinematics of Gear Generation System

To achieve teeth generation method a tool carrier device was developed, which diagram is shown in Fig. 7. In the designed device the node, which involves the tool in sphere-spatial motion, is stopped from rotating around the common axis of the main shaft-blank—a kinematic joint. Rotation of blank 3 and main shaft 1is coordinated by the division kinematic chain of machine tool. Kinematic joint of tool with the body must be built so as to ensure continuity of the transmission function of rotation motion, i.e. $\omega_1/\omega_3 = const$. Continuity of transmission function of rotation motion is determined by path of motion of point C, belonging to the movable system of coordinates. To research the kinematics of the device that involves the tool in precessional motion: Imaginary satellite gear (profile generating

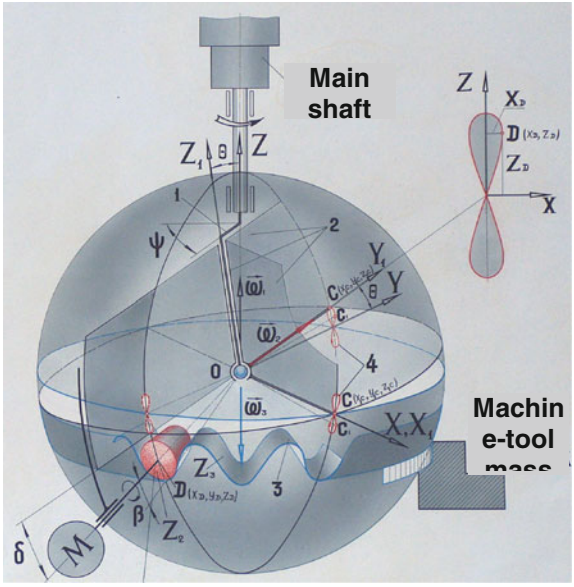

Fig. 7 Principled spatial diagram of teeth processing method by precessional tool running

tool) 2 with an imaginary number of teeth Z_2 (determined by the machine-tool kinematics) gears with the blank 3, fixed on machine-tool table, with the number of teeth $Z_2 = Z_2 \pm 1$. At a turning of the main shaft 1 the blank rotates at angle ψ_3, that corresponds to the angle between the difference of the wheel teeth:

$$\psi_3 = \frac{2\pi}{Z_3}(Z_2 - Z_3). \tag{8}$$

To define the position function of the given device $\psi_3 = f(\psi)$ it is necessary to determine beforehand the equations of the tool motion in the fixed $OXYZ$ and movable $OX_1Y_1Z_1$ systems of coordinates. The link between the mentioned systems of coordinates is determined by the Euler angles. Sphere-spatial motion of tool (imaginary wheel) at uniform rotation of the main shaft 1 ω_1 is described by the system of equations

$$\psi = \omega_1 t,\ \theta = const.,\ \varphi = \varphi(t), \tag{9}$$

Design of the working device for teeth generating technology should provide limitation of tool rotation around the main shaft of the tool-machine by a certain technical solution, for example by kinematical coupling "bolt-gutter".

In this case the coordinates of the bolt contact point C (Fig. 8) with the groove in the movable system of coordinates OX1Y1Z1 will be:

$$X_{1C} = 0,\ Y_{1C} = R_c,\ Z_{1C} = 0, \tag{10}$$

where R_c is the radius of point C location.

At sphere-spatial motion of tool 2, the motion of point C located in plane OZX is limited by the groove walls, i.e. the condition is realised for each value of ψ:

$$X_C = 0. \tag{11}$$

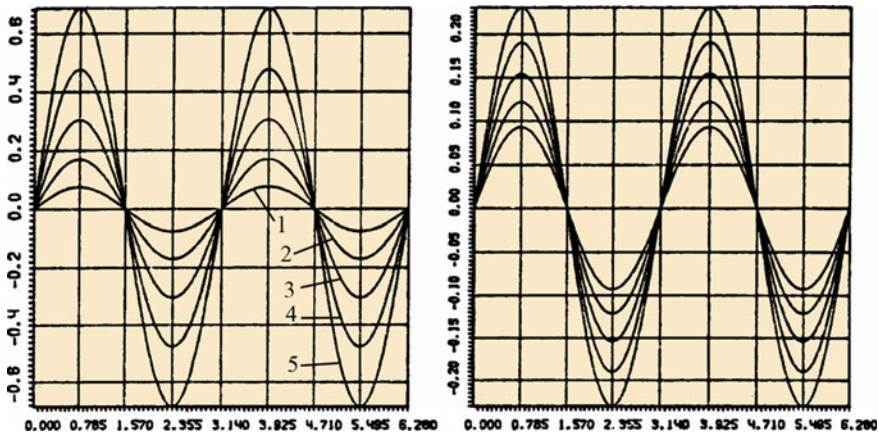

Fig. 8 Dependence of tool position error on the angle of rotation ψ of the main shaft for various angles of nutation θ

Using the transition matrix of the movable system of coordinates $OX_1Y_1Z_1$ connected with the tool and the bolt limiting its rotation around the shaft Z in the fixed system of coordinates, condition $X_c = 0$ o can be written in the form:

$$X_C = \left\| \begin{matrix} X_{1c} \\ Y_{1c} \\ Z_{1c} \end{matrix} \right\| = 0. \tag{12}$$

Or in extended form

$$X_c = a_{11}X_{1c} + a_{12}Y_{1c} + a_{13}Z_{1c} = 0$$

By replacing a_{11}, a_{12} *and* a_{13} in (11) we obtain:

$$X_c = X_{1c}(\cos\psi \sin\varphi - \sin\psi \sin\varphi \cos\theta) - Y_{1c}(\cos\psi \sin\varphi + \sin\psi \cos\varphi \cos\theta) + Z_{1c} \sin\psi \sin\theta = 0 \tag{13}$$

For the contact point of the bolt with the groove coordinates (1.5) we have:

$$X_c = -R_c(\cos\psi \sin\phi + \sin\psi \cos\phi \cos\theta) = 0. \tag{14}$$

Thus,

$$(\cos\psi \sin\varphi + \sin\psi \cos\varphi \cos\theta) = 0. \tag{15}$$

By solving Eq. (15) we determine the linkage equation between the angle of tool self-rotation 2 and the angle of rotation of the main shaft:

$$\varphi = -arctg(\cos\theta tg\psi). \tag{16}$$

In such case the equations of tool 2 precessional motion take the form:

$$\psi = \omega_1 t,\ \theta = \text{const}.\ \varphi = \text{minus};\ \text{arctg}(\cos\theta \cdot \text{tg}\psi). \tag{17}$$

To establish the dependence of the angle of rotation of blank ψ_3 on the angle of rotation of the main shaft ψ we describe the blank motion composed of the involved rotational motion with the crank of the main shaft ψ_{3e} and the relative motion of rotation with regard to the crank of the main shaft ψ_{3r}.

In the compound motion of blank $\psi_{3e} = \psi$, and ψ_{3r} represents a certain function $f(\varphi)$ of the angle of rotation of tool φ, that is:

$$\psi_3 = \psi + f(\phi). \tag{18}$$

For ideal precession of the drive mechanism of machine/tool function $f(\varphi)$ will take the form:

$$\psi_3 = \psi + \frac{Z_2}{Z_1}\phi. \tag{19}$$

By considering Eq. (16) we obtain the position function of the kinematical linkage mechanism of the device:

$$\psi_3 = \psi - \frac{Z_2}{Z_1} arctg(\cos\theta tg\psi). \tag{20}$$

Momentary gear ratio of the kinematical linkage mechanism of the device is obtained deriving (20) after ψ:

$$i_{31} = \frac{d\psi_3}{d\psi} = \frac{\omega_3}{\omega_1} = 1 - \frac{Z_2}{Z_3} \cdot \frac{\cos\theta}{\cos^2\psi + \cos^2\theta \sin^2\psi}. \tag{21}$$

Average gear ratio for a rotation of the main shaft will be

$$i_{31}^{med} = \frac{1}{2\pi}\int_0^{2\pi} i\psi d\psi = \frac{1}{2\pi}\left[\psi - \frac{z_2}{z_3} arctg(\cos\theta tg\psi)\right]\Big|_0^{2\pi} = -\frac{Z_2 - Z_3}{Z_3}. \tag{22}$$

Analysis of dependence (22) demonstrates that for the ratio of teeth $z_2 < z_3$ the direction of main shaft rotation of gear cutting machine and blank (imaginary wheel) coinsides, and for the ratio of teeth $z_2 > z_3$ is different. Division kinematical chain of machine tool must provide the following kinematical link: at full rotation of the main shaft the blank (imaginary wheel) should rotate under angle $\psi_3 = 2\pi(Z_2 - Z_3)/Z_3$. This kinematical link defines the average gear ratio of the manufactured gear. Given the fact that the kinematical link "tool—blank" is done by the machine—tool dividing chain under condition $\omega_1/\omega_2 = const.$, the angular velocity variation caused by the kinematic link mechanism (neasurică) of the tool with the frame will transpose on the tooth profile, therefore, it will introduce a diagram error $\Delta\psi_3$ in the tooth profile. The diagream error $\Delta\psi_3$ can be identified by angular positioning error of the blank ψ_3 relative to position ψ_3^{med} of the same blank, which conditionally would rotate uniformly with the gear ratio $i_{31}^{med} = -(Z_2 - Z_3)/Z_3$. in this case the diagram error will be:

$$\Delta\psi_3 = \psi_3 - i_{31}^{med} = \frac{Z_2}{Z_3}[\psi - arctg(\cos\theta tg\psi]. \tag{23}$$

So, the kinematical link of the tool with the frame introduces some diagram error in the tooth profile.

Figure 8 shows the graph of diagram error of tool position error ψ_3 at one rotation of the main shaft and motion of point D in OZY plan. If point C makes a motion in OZY plane the error is transmitted intact to the tool, and the last generates the tooth profile with the same error. To ensure continuity to motion processing function it is necessary to modify the tooth profile by diagram error value $\Delta\psi_3$ by communicating additional motion to the tool.

Correctness of additional motion of the tool was established using a computer calculation program. It was found that generation precision of the manufactured wheel teeth 3 depends on the continuity of its angular speed $\dot{\varphi}$ of the tool 2.

Function analysis (19) shows that for $\varphi = -\psi$ the instantaneous transmission ratio $i_{31} = const$. For condition $\varphi = -\psi$ from Eq. (19) we have:

$$\psi_3 = \psi - \frac{Z_2}{Z_3}\varphi = \frac{Z_2 - Z_3}{Z_3}\psi = \frac{Z_2 - Z_3}{Z_3}\omega_1 t.$$

From this analysis we find that any technical solution to eliminate the influence of diagram error of tooth profile precision generation with precessional tool would be 3D profiling of the contact surfaces of the groove of kinematical link mechanism, which supports the bolt (delimiter of rotation). The bolt contact with the shaped surfaces of groove transmits also the reaction torque from the node, on which the tool is installed to the frame. To achieve the proposed technical solution to exclude the error of 3D profiling of supporting surface of the link channel with the bolt it is necessary to describe the profile of contact surfaces with parametric equations. In this case we take an arbitrary point C on the tool axis with coordinates X_{1c}, Y_{1c}, Z_{1c} (Fig. 7), and identify the path of motion in the fixed system of coordinates $OXYZ$ to satisfy the condition $i_{31} = const$. Using the matrix form for the transition from the coordinate system $OX_1Y_1Z_1$ to the fixed system $OXYZ$ we get:

$$\begin{Vmatrix} X_c \\ Y_c \\ Z_c \end{Vmatrix} = A \begin{Vmatrix} X_{1c} \\ Y_{1c} \\ Z_{1c} \end{Vmatrix} \tag{24}$$

or by components:

$$\begin{aligned} X_c &= a_{11}X_{1c} + a_{12}Y_{1c} + a_{13}Z_{1c}; \\ Y_c &= a_{21}X_{1c} + a_{22}Y_{1c} + a_{23}Z_{1c}; \\ X_c &= a_{31}X_{1c} + a_{32}Y_{1c} + a_{33}Z_{1c}. \end{aligned} \tag{25}$$

where $a_{i,j}$, $i,j = 1\ldots3$ are cosines of angles between the axes of coordinates.

Considering that instantaneous gear ratio $i_{31} = const$. when $\varphi = -\psi$ then Eq. (25) are transcribed as:

$$\begin{aligned} X_C &= X_{1C}(\cos^2\psi + \cos\theta\sin^2\psi) + Y_{1C}(1 - \cos\theta)\cos\psi\sin\psi + Z_{1C}\sin\theta\sin\psi; \\ Y_C &= Y_{1C}(1 - \cos\theta)\cos\psi\sin\psi + Y_{1C}(\sin^2\psi + \cos\theta\cos^2\psi) - Z_{1C}\sin\theta\cos\psi; \\ Z_{1C} &= Z_{1C}\sin\theta\sin\psi + Y_{1C}\sin\theta\cos\psi + Z_{1C}\cos\theta. \end{aligned} \tag{26}$$

For the case when point "C" is placed on axis OY_1 its position is defined by coordinates $X_{1C} = 0, Y_{1C} = R_c$, $Z_{1C} = 0$, and Eq. (26) take the form:

$$\begin{aligned} X_C &= R_C(1 - \cos\theta)\cos\psi\sin\psi; \\ Y_C &= R_C\left(\sin^2\psi + \cos\theta\cos^2\psi\right); \\ Z_C &= R_C\sin\theta\sin\psi. \end{aligned} \tag{27}$$

Equation (27) represent parametrical equations of groove lateral surfaces, by which the limiting bolt of tool rotational motion around the fixed axis OZ, form a kinematical coupling, and provides the condition $i_{31} = const$. Thus, the shape of groove lateral surfaces by which the bolt forms the kinematical coupling of tool with the casing, described by parametrical Eq. (27), excludes the influence of diagram errors on tooth profile generated with precessional tool.

3.2.2 Analytical Description of the Precessional Tool Path of Motion

According to the principle of teeth generation by proposed method the tool should copy with certain accuracy the shape and path of motion of the pin tooth in the real gearing (involving the central wheel with teeth—satellite gear with pin teeth). In this connection it was necessary to research the tool path of motion with the angle of position to the blank $\delta \geq 0$. For this purpose, a point D was identified on the tool axis (Fig. 9) with coordinates X_{1D}, Y_{1D}, Z_{1D} in the movable system of coordinates $OX_1Y_1Z_1$ and parametrical equations of its motion in the movable system of coordinates were described. For i_{31}-*const*. after a number of transformations we obtain:

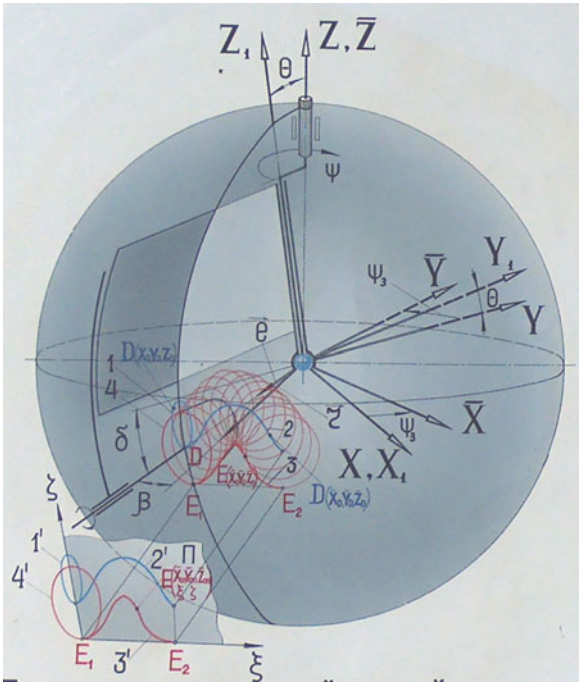

Fig. 9 Determination of the tool surface family envelope

$$\begin{aligned} X_D &= \alpha_{11}X_{1D} + \alpha_{12}Y_{1D} + \alpha_{13}Z_{1D}; \\ Z_D &= \alpha_{21}X_{1D} + \alpha_{22}Y_{1D} + \alpha_{23}Z_{1D}; \\ Z_D &= \alpha_{31}X_{1D} + \alpha_{23}Y_{1D} + \alpha_{33}Z_{1D}. \end{aligned} \tag{28}$$

With condition $\varphi = -\psi$ and constant instantaneous gear ratio i_{31}-*const* we have:

$$\begin{aligned} X_D &= X_{1D}(\cos^2\varphi + \cos\Theta\sin^2\varphi) + Y_{1D}(1-\cos\Theta)\cos\varphi\sin\varphi + Z_{1D}\sin\Theta\sin\varphi; \\ Y_D &= X_{1D}(1-\cos\Theta)\sin\varphi\cos\varphi + Y_{1D}(\sin^2\varphi + \cos\Theta\cos^2\varphi) - Z_{1D}\cos\varphi\sin\Theta; \\ Z_D &= X_{1D}\sin\Theta\sin\varphi + Y_{1D}\sin\Theta\cos\varphi + Z_{1D}\cos\Theta. \end{aligned} \tag{29}$$

For $\delta = 0$ tool coordinates will take the form:

$$X_{1D} = 0, Y_{1D} = -R_u, Z_{1D} = 0. \tag{30}$$

In this case the equations of tool motion depending on the angle of rotation ψ of the main shaft will be:

$$\begin{aligned} X_D &= -R_u(1-\cos\Theta)\cos\varphi\sin\varphi, \\ Y_D &= -R_u(\sin^2\varphi + \cos\Theta\cos\varphi), \\ Z_D &= -R_u\sin\Theta\cos\varphi. \end{aligned} \tag{31}$$

In the case of toothed wheels with angle $\delta > 0$ the tool should be located under the same angle. Then point D will have the following coordinates:

$$\begin{aligned} X_{1D} &= 0, Y_{1D} = -R\cos d, \\ Z_{1D} &= -R\sin d, \end{aligned} \tag{32}$$

And the equations of the path of motion of tool in the fixed system of coordinates OXYZ have the form:

$$\begin{aligned} X_D &= -R_u\cos\delta(1-\cos\Theta)\cos\varphi\sin\varphi - R_u\sin\delta\sin\Theta\sin\varphi; \\ Y_D &= -R_u\cos\delta(\sin^2\varphi + \cos\Theta\cos\varphi) + R_u\sin\delta\sin\Theta\cos\varphi; \\ Z_D &= -R_u\cos\delta\sin\Theta\cos\varphi - R_u\sin\delta\cos\Theta. \end{aligned} \tag{33}$$

Exact performance of the tool path of motion according to Eq. (33) was taken into account in the process of elaboration of the tool-carrier device, shown in Fig. 7.

3.2.3 Determination of Family Envelope of Tool Generating Contour

Tooth profile of the processed wheel represents the family envelope of tool generating contour in its relative motion with the tooth. The envelope is determined from the equations of the working surface of the generating tool and parameters of relative motion at folding.

To simplify the process of envelope determination it is necessary to pass to the coordinates of tool centre D in the movable system of coordinates (Fig. 9), linked with the blank 3:

$$\begin{aligned}\overline{X}_D &= X_D \cos\psi_3 + Y_D \sin\psi_3;\\ \overline{Y}_D &= -X_D \sin\psi_3 + Y_D \cos\psi_3;\\ \overline{Z}_D &= Z_D.\end{aligned} \tag{34}$$

where $\overline{X_D}, \overline{Y_D}, \overline{Z_D}$ are the coordinates of the tool centre in the movable system of coordinates; $\psi_3 = \psi/i$ is the blank angle of rotation; i—gear ratio of the kinematical chain "main shaft—blank". Equation (34) define the path of motion of the tool centre, evolving on the sphere. Further, the envelope equations on the sphere were defined (curve 3, Fig. 9).

Further, we find the tool 1 conical working surface (with geometrical shape as frustum) in the movable system of coordinates, applying the condition known from the differential geometry:

$$\overline{re} = r\cos\beta, \text{ or } X\cdot\bar{X}_D + Y\cdot\bar{Y}_D + Z\cdot\bar{Z}_D = R\cdot r\cos\beta, \tag{35}$$

where $\bar{e}$ is the unit vector oriented to the cone axis; β—taper angle of tool.

Wrapping Eq. 5 on the sphere is obtained as result of solving jointly the equations, which describe the family wrapping of tool 1 working surfaces:

$$\begin{aligned}\Phi(X,Y,Z,\psi) &= X\bar{X}_D + Y\bar{Y}_D + Z\bar{Z}_D - Rr\cos\beta = 0,\\ \frac{d\Phi}{d\psi} &= (X,Y.Z,\psi) = 0\end{aligned} \tag{36}$$

And the equation of spherical surface:

$$X^2 + Y^2 + Z^2 - R^2 = 0. \tag{37}$$

Therefore we find:

$$\begin{aligned}\frac{d\Phi}{d\psi} &= X\frac{\partial\bar{X}_D}{\partial\psi} + Y\frac{\partial\bar{Y}_D}{\partial\psi} + Z\frac{\partial\bar{Z}_D}{\partial\psi} = 0,\\ \frac{\partial\bar{X}_D}{\partial\psi} &= \frac{\partial X_D}{\partial\varphi}\cos\psi_3 - \frac{X_D}{u}\sin\psi_3 + \frac{\partial Y_D}{\partial\psi}\sin\psi_3 + \frac{Y_D}{u}\cos\psi_3,\\ \frac{\partial Y_D}{\partial\psi} &= -\frac{\partial X_D}{\partial\psi}\sin\psi_3 - \frac{X_D}{u}\cos\psi_3 + \frac{\partial Y_D}{\partial\psi}\cos\psi_3 - \frac{Y_D}{u}\sin\psi_3,\\ \frac{\partial\bar{Z}_D}{\partial\psi} &= \frac{\partial Z_D}{\partial\psi}.\end{aligned} \tag{38}$$

$$\begin{aligned}
\frac{\partial X_D}{\partial \psi} &= -R\cos\delta(1-\cos\Theta)\cos^2\psi - R\sin\delta\sin\Theta\cos\psi \\
\frac{\partial Y_D}{\partial \varphi} &= -R\cos\delta(1-\cos\Theta)\sin^2\psi - R\sin\delta\sin\Theta\sin\psi, \\
\frac{\partial Z_D}{\partial \psi} &= -R\cos\delta\sin\Theta\sin\psi.
\end{aligned} \tag{39}$$

After introducing (38), (39) into (36) and (37) we obtain:

$$\begin{aligned}
X_o &= \frac{-(ab+de) \pm \sqrt{(ab+de)^2 + (1+a^2+d^2)(R^2-b^2-l^2)}}{1+a^2+d^2}; \\
Y_o &= aX_o + b; \\
Z_o &= dX_o + e,
\end{aligned} \tag{40}$$

where:

$$\begin{aligned}
a &= \frac{X_c\frac{\bar\delta Z_D}{\partial\psi} - Z_C\frac{\bar\delta X_D}{\partial\psi}}{Z_c\frac{\bar\delta Y_D}{\partial\psi} - Z_C\frac{\bar\delta Z_D}{\partial\psi}}, \quad a = \frac{R^2\cos\beta\frac{\bar\delta Z_D}{\partial\psi}}{Z_D\frac{\bar\delta Y_D}{\partial\psi} - Y_C\frac{\bar\delta Z_D}{\partial\psi}}, \\
d &= -\frac{(X_D - aY_D)}{\bar Z_D}, \quad e = \frac{R^2\cos\beta - bY_D}{\bar Z_D}.
\end{aligned} \tag{41}$$

Equation (40) determine the envelope on the sphere (curvature 3, Fig. 9). To define the envelope of teeth profile in cross section it is necessary to project it in plane Π, perpendicular on two generators, which cross two minimum successive points of profile on the sphere, i.e. points E_1 and E_2 and the centre of precession "O". Coordinates of points E_1 and E_2 are determined from the relations:

$$\begin{aligned}
X_{E_1} &= X_1 = X_o|_{\psi=0} = 0, \\
Y_{E_1} &= Y_1 = Y_o|_{\psi=0} = -R\cos(\delta+\Theta+\beta), \\
Z_{E_1} &= Z_1 = Z_o|_{\psi=0} = -R\sin(\alpha+\Theta+\delta), \\
X_{E_2} &= X_2 = X_o|_{\psi=\frac{2\pi z_2}{z_1}}, Y_{E_2} = Y_2 = Y_o|_{\psi=\frac{2\pi z_2}{z_1}}, Z_{E_2} = Y_2 = Y_o|_{\psi=\frac{2\pi z_2}{z_1}}.
\end{aligned} \tag{42}$$

Via points E_1 and E_2 is drawn a plane, perpendicular on generators OE_1 *and* OE_2. The equation of this plane is determined from the condition:

$$\left[\overline{E_1E_2}\cdot\overline{E_1E}\right][OE_1\cdot OE_2] = 0 \tag{43}$$

where E is an arbitrary point on plane. Equation (43) is represented as:

$$\begin{vmatrix} \bar i & \bar j & \bar k \\ X_2-X_1 & Y_2-Y_1 & Z_2-Z_1 \\ X-X_1 & Y-Y_1 & Z-Z_1 \end{vmatrix} \begin{vmatrix} i & j & k \\ X_1 & Y_1 & Z_1 \\ X_2 & Z_2 & Z_2 \end{vmatrix} = 0, \tag{44}$$

or

$$A_1X + B_1Y + C_1Z + D = 0, \tag{45}$$

where:

$$\begin{aligned} A_1 &= (Z_2 - Z_1)(X_2Z_1 - X_1Z_2) - (Y_2 - Y_1)(X_1Y_2 - X_2Y_1);\\ B_1 &= (X_2 - X_1)(X_1Y_2 - X_2Y_1) - (Z_2 - Z_1)(Y_1Z_2 - Y_2Z_1);\\ C_1 &= (Y_2 - Y_1)(Y_1Z_2 - Y_2Z_1) - (X_2 - X_1)(Z_1X_2 - X_1Z_2);\\ D_1 &= -A_1X_1 - B_1Y_1 - C_1Z_1. \end{aligned} \tag{46}$$

Envelope of teeth profile in cross section was determined by designing the envelope from the sphere on a plane perpendicular on two generators that cross via two minimum successive points of the profile on the sphere. In this case envelope equations of tooth profile in plane will be:

$$X_{0_P} = \frac{D_1X_0}{A_1X_0 + B_1Y_0 + C_1Z_0};\ Y_{0_P} = X\frac{Y_0}{X_0};\ Z_{0_P} = X\frac{Z_0}{X_0}\ , \tag{47}$$

where X_0, Y_0, Z_0; X_1, Y_1, Z_1; X_2, Y_2, Z_2 are the coordinates of the centre of precession O and minimum points on the tooth profile.

Envelope equations of the described coordinates X, Y, Z in the system of coordinates $OXYZ$ are transcribed as equations with two coordinates ξ and ζ in the system of coordinates $E_1\xi\zeta$ (Fig. 9) linked to the described plane with equations

$$\begin{aligned} E_1E_2 &= \sqrt{(X_2 - X_1)^2+(Y_2 - Y_1)^2+(Z_2 - Z_1)^2};\\ E_1E &= \sqrt{(X - X_1)^2+(Y - Y_1)^2+(Z - Z_1)^2} = \sqrt{\xi^2 + \zeta^2};\\ E_2E &= \sqrt{(X - X_2)^2+(Y - Y_2)^2+(Z - Z_2)^2} = \sqrt{(E_1E_2 - \xi)^2 + \zeta^2}. \end{aligned} \tag{48}$$

We obtain the envelope equations in two coordinates ξ and ζ in the system of coordinates $E_1\xi\zeta$, which represent teeth profile generated by precessional tool from Eq. (48):

$$\begin{aligned} \xi &= \frac{(E_1E_2) + (X - X_1)^2+(Y - Y_1)^2+(Z - Z_1)^2-(X - X_2)^2+(Y - Y_2)^2+(Z - Z_2)^2}{2E_1E_2};\\ \zeta &= \sqrt{(X - X_1)^2+(Y - Y_1)^2+(Z - Z_1)^2-\xi^2}. \end{aligned} \tag{49}$$

Figure 10 shows the profilograms of teeth profile generation with precessional tool performed in CAD/CAM/CAE/CATIA V5R7. On the profilograms curve 1 (Fig. 10*a*) describes the path of motion of the tool centre in the fixed $OXYZ$ system of coordinates, and curve 2—the path of motion of the tool centre in the movable system of coordinates $O\bar{X}\bar{Y}\bar{Z}$, curve 3—family wrapping of precessional tool surfaces (tooth profile), curve 4—generating tool contour.

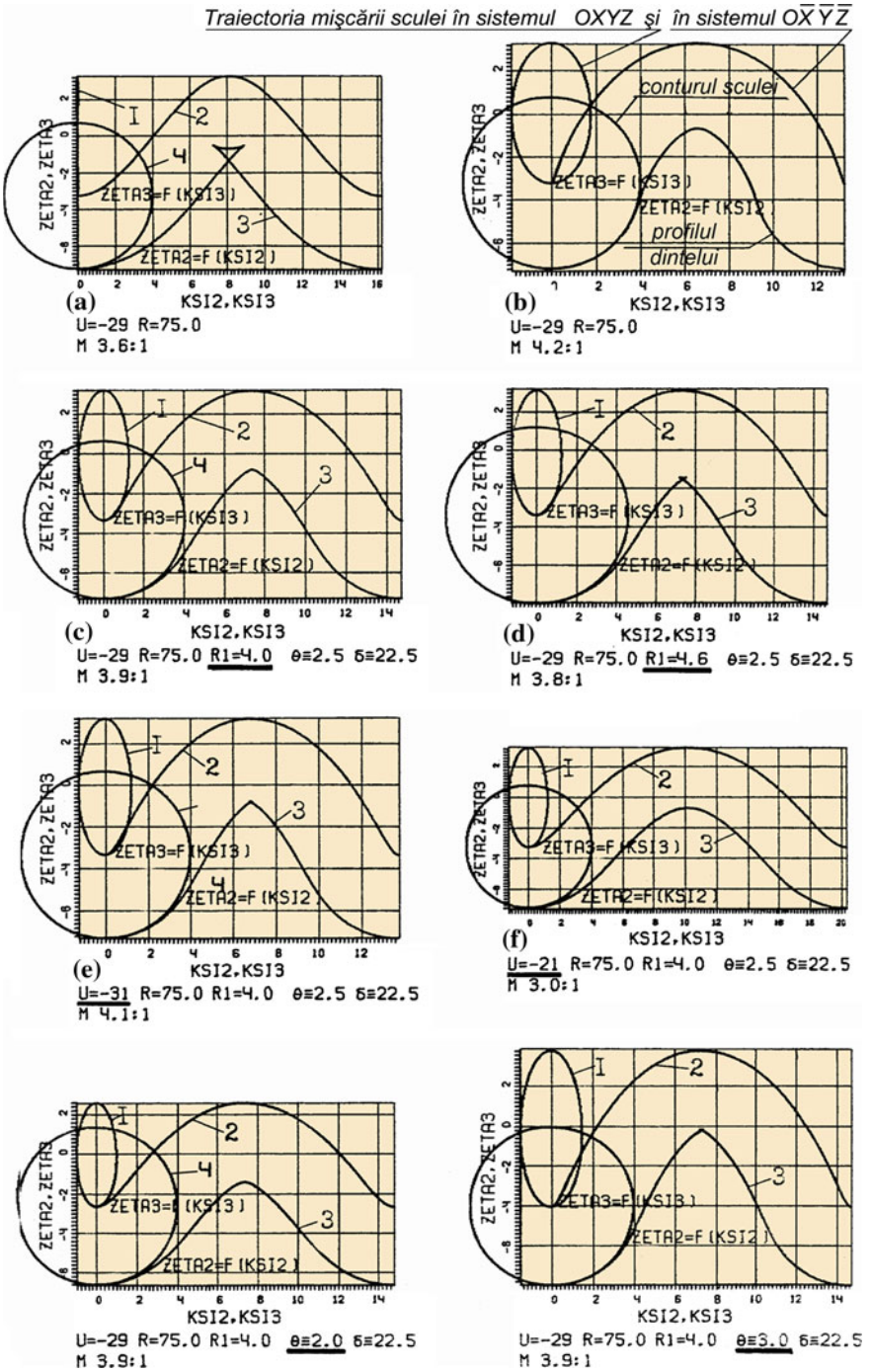

Fig. 10 Profilograms of teeth profile generation with cone-shape precessional tool: *1*, *2* path of motion of tool *centre* in the fixed OXYZ and movable OX'Y'Z' systems of coordinates; *3* teeth profile; *4* generating tool contour

Profilogram analysis (Fig. 10) demonstrates the degree and direction of influence on generated tooth profile of the position angle of tool δ (conical axoid angle) with regard to the axis of rotation of the blank, tool radius R and gear ratio i of the kinematical linkage "main shaft—blank".

3.2.4 Technological Equipment for Generating Teeth with Sfero-Space Motion of Truncated Cone Shaped Tool

The profile of central wheel tooth of precessional gear is variable depending on the values of conical axoid angle δ, taper angle of the rollers β, the nutation angle θ, the number of teeth of gears Z_1, Z_2 and the correlation between them. Fabrication of these profiles using traditional methods is practically impossible, because for each correlation value of all parameters δ, β, θ and Z tooth profile changes shape, which requires the design and manufacture of the tool with the respective profile.

Therefore a new generating technology was proposed, which carries out a set of profiles of the teeth, using a tool with the same geometrical parameters. The method consists of the following: a series of motions coordinated between them against the rotating blank is communicated to the tool (milling cutter or grinding wheel with truncated cone-shaped geometry). The kinematic link of the blank with the tool provides rotation of one-toothed blank in a closed cycle of the motion communicated to the tool. The tool is given such a shape and motion that allows the processing of any possible profile of the set, including longitudinal and profile modification. The described surface on the peripheral side of the tool against the rotating blank reproduces a certain conceivable body, called the *imaginary wheel* (generators).

Using the kinematic chain of gear cutting machine-tool running, gear blank and the tool are brought in a coordinated motion—running motion, which reproduces the imaginary wheel gearing with the blank. Part of metal is removed at each elementary change of tool position in space in relation to the blank. Therefore the working surface of the wheel teeth processed is obtained as envelope of a consecutive series of positions of rotating tool profile generator contour against the blank.

A tool holder device was developed to realize the demanded motions of the tool (Fig. 11a), which can be adjusted to gear cutting machines models *5K32P53*, *5330P*, *53A50*, *5A60*, *5342*, with accuracy class *GOST 6-77*.

To compensate error diagram of the satellite at its sphere-spatial rotation, a kinematical joint connecting the cross-rail with the body is introduced into the teeth grinder, ensuring continuity of the transformation function of rotational motion $\omega_1/\omega_3 = const.$ in the kinematic chain "main shaft—tool—blank". In other words, at teeth processing by proposed method, their profile is corrected by an amount equal to the kinematical diagram error introduced by the sphere-spatial motion of tool with regard to the casing (bed).

It was defined that in real precessional transmissions *2K-H* the link of precessional satellite with the body introduces an error in the driven shaft position.

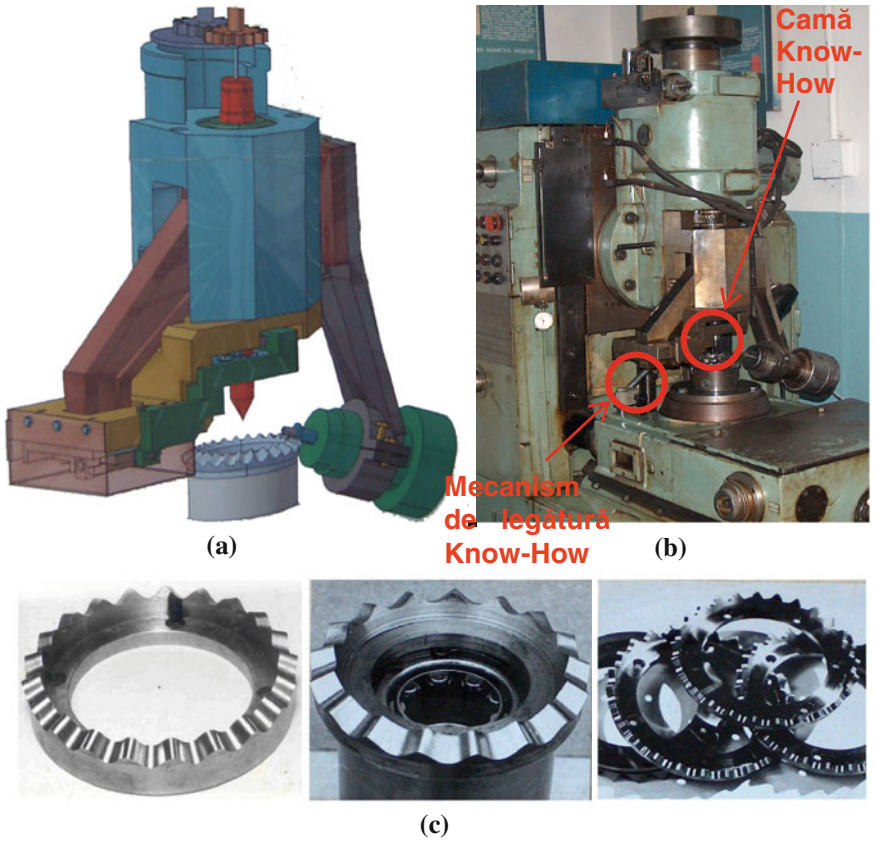

Fig. 11 Generation device for gears with non-standard profile (**a**), machine-tool with fabricated device (**b**) and samples of fabricated gears (**c**)

This fact provokes non-uniformity of its rotation at uniform turning of the drive shaft. Drawback is eliminated by transposition of driven shaft position error on the processed tooth profile. Diagram error elimination is achieved through the construction of cross-rail connection joint to the body, which through a cam installed on the crank shaft communicate auxiliary motion to the tool. The joint ensures continuity to the transformation function of rotational motion along the linkage *shaft-crank-tool-blank*. At tooth processing by proposed method their profile is correlated to value of the shift angle of driven shaft introduced by precessional satellite link in the real transmission.

In the developed tool-carrier device the point of intersection of the fixed axis OZ with the movable axis OZ_1 of the crank (centre of precession) is on the axis of rotation of the gear cutting machine table. To research the features of interaction between the tool and the wheel processed tooth ($\delta > 0$), which axis coincides with axis OZ of the device crank-shaft:

Figure 11, *a* shows the 3D computer model of the processing device for gear wheels with non-standard profile, designed in *AutoDeskInventor* and simulated in *MotionInventor*. Figure 11, *b* shows the picture of gear cutting machine-tool endowed with the device for profile generation by precessional tool. Figure 11, *c* presents samples of gear wheels with non/standard profile, worked out on this machine-tool.

4 Conclusions

Among the characteristics of the estimated results of research in the field of new and efficient drive development we can enumerate the following:

- the elaborated precessional gears ensure: high bearing capacity; high kinematical efficiency; high kinematical accuracy; low noise level and vibrations;
- generation procedure for variable convex-concave teeth profiles provide high efficiency and processing accuracy.

Structural optimization of the precessional transmissions will allow synthesis of new diagrams of precessional transmissions with constant and variable transmission ratio and elaboration of new diagrams of precessional transmissions for specific running conditions.

References

Bostan I et al (2011) Anthology of inventions, vol 1. Planetary precessional transmissions (in Romanian). Bons Offices SRL, pp 542,594

A Unique Concept (2012) http://www.ohiobelting.com/pdfs/cyclogen.pdf

Kaabushiki K (1977) Mechanical power transmission equipment and parts namely gears, gearings. Hitachi Ltd. http://trade.mar.cx/symmarc

Tzejtlin NI, Tzukerman EM (1969) Wave transmissions. Moskva

Krasnoshhekov NN, Fedeakin RV, Chesnokov V (1976) Novikov theory of gearing. Nauka p 173

New Tendencies in the Design of the Modern Aerospace Transmissions

Nicoleta Ene and Florin Dimofte

Abstract The modern aerospace transmissions require an increased power density while their weight, fabrication and maintenance costs should be as low as possible. In addition, the future helicopter transmissions should generate less noise and vibration then the actual transmissions. The fluid film bearings, and particularly the wave bearings, could help approaching these goals. In this paper, the aspects implied by using these bearings to support transmission rotating parts are discussed from two points of view: (1) the capacity of the wave bearings to support the bearing sleeve distortions under similar loads as rolling element bearings: and (2) the capacity of the wave bearings to attenuate the noise/vibration generated by the gear mesh compared to the rolling element bearings due to the increased damping properties of the wave bearings.

Keywords Fluid film bearings · Wave bearings · Gears · Transmission · Noise

1 Introduction

In the last years, the aerospace transmissions, turbofan (turbo-shaft) or helicopter transmissions, require larger and larger loads. In the same time, the transmission components must be as light as possible. Therefore the metallic parts have to be very thin but to carry high loads. Particularly, the gear mesh forces can deform the gears due to the small thickness of the gears walls. Another problem encountered when designing high power density transmissions, especially for helicopter

N. Ene (✉) · F. Dimofte
The University of Toledo, Toledo, OH, USA
e-mail: nicoleta.m.ene@gmail.com

F. Dimofte
e-mail: florin.dimofte@gmail.com

G. Dobre (ed.), *Power Transmissions*,
Mechanisms and Machine Science 13, DOI: 10.1007/978-94-007-6558-0_3,

applications, is the transmission noise and vibration. The helicopter transmissions should be as quiet as possible due to their close proximity to the crew and passenger cabin. In addition, the fabrication and maintenance costs should be maintained very low.

In recent years, efforts have been made to find new design methods to approach all the above requests. One of the new tendencies is to replace the rolling element bearings, traditionally used to support the transmission rotating components, with fluid film bearings. The fluid film bearings can provide similar load capacities as the rolling element bearings, but in a smaller volume helping to reduce the transmission weight. The fluid film bearings are simple with less precision parts than rolling element bearings. In addition, the fluid film bearings could provide significant damping that can modify the transmission dynamics and reduce the noise and vibrations generated by the transmission.

A planetary-geared transmission with fluid film bearings for a turbo-fan engine is presented for example in Fig. 1. A fluid film bearing having the ratio between the length and diameter between 1 and 2 supports the planet gears. The specific load (the load divided by the projected surface of the bearing) of such a bearing could be very significant. In particular conditions, it can be up to 18 MPa (2,600 PSI). In these extreme-loading conditions, the bearing minimum film thickness is very small (only few microns). In addition, the bearing should run thermally stable. Therefore, the increase of the oil temperature through the fluid film (ΔT) must be lower than 30 °C (54 °F). To assure the ΔT limit, the oil should be circulated through the bearing at a specific flow.

Recent investigations revealed that a particular type of fluid film bearings—the wave bearing could be a promising alternative to the rolling element bearings in aerospace transmissions. Some aspects of using the wave bearings in aerospace transmissions are presented next.

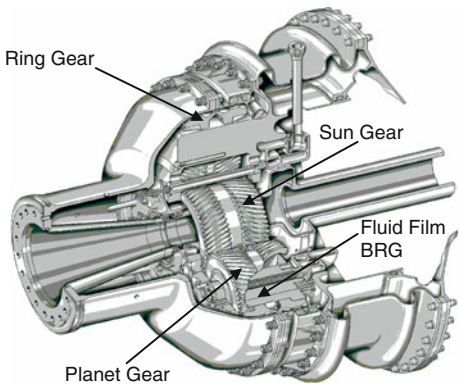

Fig. 1 Geared transmission for a turbo-fan engine

2 Wave Bearing Concept

The wave bearing was introduced by Dimofte (1995a, b), as an alternative to the plain (circular) journal bearing. Unlike the plain bearing, the wave bearing has a slight continuous variation of its profile. The variation is such that a continuous waved profile is circumscribed onto the non-rotating bearing surface. To exemplify the concept, a comparison between a wave bearing having circumscribed a three–wave profile and a plain journal bearing is presented in Fig. 1. The wave amplitude and the clearance are greatly exaggerated for clarity (Fig. 2).

The performance of the wave bearing depends on the number of the waves, the wave amplitude ratio, and the position of the waves with respect to the load. The wave amplitude ratio is defined as the ratio between the wave amplitude and clearance.

The wave bearing has an improved stability compared to the plain journal bearing due to better defined rotor positioning. In addition, because the geometry of the wave bearing is very close to the geometry of the plain circular bearing, the load capacity of the wave bearing is close to that of the plain journal bearing and superior to the load capacity of other types of journal fluid bearings such as fixed or tilting pad bearings, grooved bearings, etc.

3 Wave Bearings in the Planetary Stages of a Turboprop Transmission

The possibility to apply the wave bearings in a two-stage planetary turboprop transmission (Fig. 3) used to reduce the turbo-shaft speed (24,733 rpm) to the propeller speed (1,997 rpm) was analyzed. The first planetary stage is a star stage. The carrier is stationary (the gears are stars rotating only around their axis), the input is through the sun, and the output is from the ring. For the second step the ring is stationary, the input is through the sun, and the output is from the carrier.

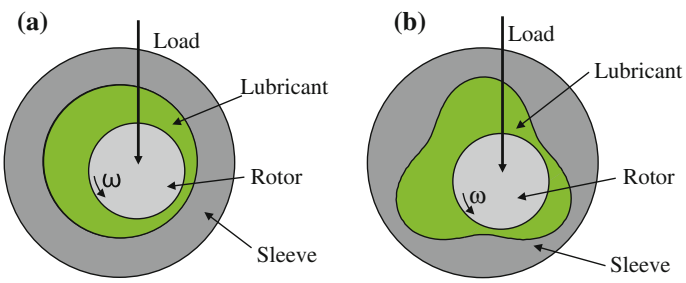

Fig. 2 Comparison between the plain journal bearing and the wave bearing. **a** Plain journal bearing. **b** Wave journal bearing

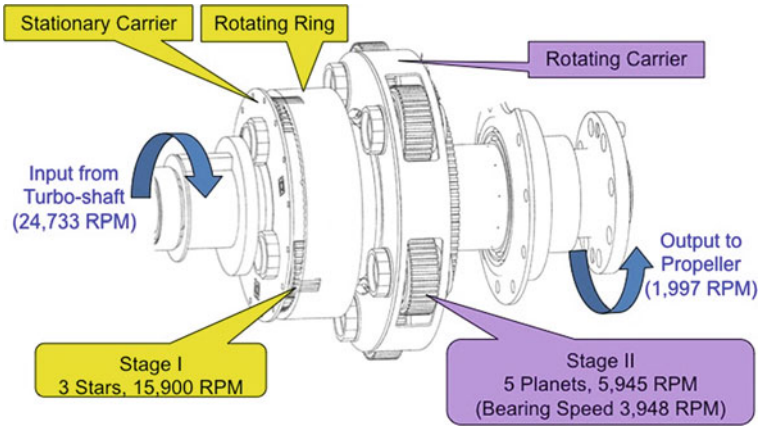

Fig. 3 Double-stage planetary transmission

The planets rotate around their axis and also with the carrier. An additional centrifugal force is applied to the planet due to its rotation with the carrier. The wave bearings are used to support the star/planet gears. In this case, the wave bearing sleeve is the inner diameter of the gear. Different loading regimes were considered for each stage.

The numerical simulations showed that at high loaded regimes the elastic deformations have an important effect on the wave bearing performance by increasing the bearing minimum film thickness and, consequently the safety operation limit. More details about this analysis can be found in Ene and Dimofte (2012a).

4 Attenuation of the Gear Mesh Noise/Vibration by the Wave Bearings Compared to Rolling Elements

One of the major problems in helicopter transmissions is the transmission noise/vibration. The primary source of the noise and vibration is the dynamic force of the gear mesh. The dynamic forces generate torsional, axial, and transverse vibrations of the gear shaft (Townsend 1991). The vibrations are transferred to the bearings that support the shaft, generating lateral and vertical displacements at the support bearing locations. The vibration and noise then travels primarily by structural paths into the helicopter cabin. Measurements performed in helicopters cabins showed that the gear generated noise can be over 100 dB in a helicopter cabin (Lenski 1995). In addition, the noise predominant frequencies are in the most sensitive regions of hearing spectrum, contributing to crew and passenger fatigue and hearing loss (Hansen et al. 2002).

The capacity of the wave bearings to attenuate the gear mesh noise and vibration compared to the rolling element bearings was analyzed. Tests were performed on the Gear Noise Rig located at NASA Glenn. The rig is driven by a 150 kW (200 hp) DC electric motor (1,750 rpm max speed) with a poly-v belt speed-increaser drive to supply input shaft speeds. The motor connects to the test gearbox through shafts, a torque meter and vibration isolating couplings. The output connects through shafting to an eddy current dynamometer, which supplies a resisting torque. The dynamometer has a maximum speed of 6,000 rpm. More details about the test rig can be found in Oswald et al. (1994) (Fig. 4).

A simple spur gearbox that can accommodate both rolling element bearings and wave bearings to support the shafts was used to experimentally investigate the attenuation effects on the gear mesh noise and vibration of the wave journal bearings compared to rolling element bearings. The baseline configuration employs two deep groove ball bearings (bearings no 1 and 4 in Fig. 5) supporting the coupling end of each shaft and two roller bearings (bearings no 2 and 3 in Fig. 5) at the stub (unconnected) end of the shafts. Four wave bearings with a very small wave amplitude ratio replace the ball and roller bearings in the gearbox wave bearing configuration.

The gear mesh noise was measured with a microphone suspended above the gearbox outside the acoustic near field zone and precisely positioned with a laser beam device. A hyper-cardioid sensitivity pattern was chosen for the microphone to reduce the response from sources other than the test gearbox. Two accelerometers were mounted on each bearing support to measure the vibration in vertical and horizontal directions, respectively (Fig. 5). Speed, torque, wave bearing oil supply pressure, temperature, and flow were measured and recorded.

Because the gear noise is accompanied by noise from other internal or external sources, not associated with the mesh frequencies, a method was developed to

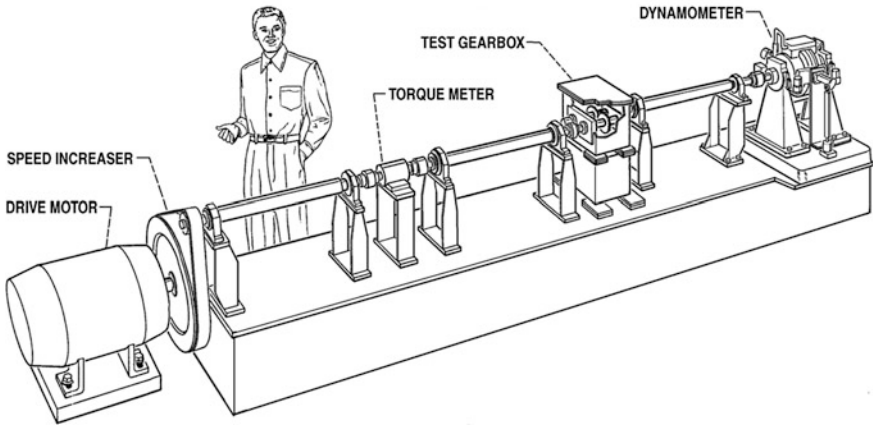

Fig. 4 Gear noise test rig

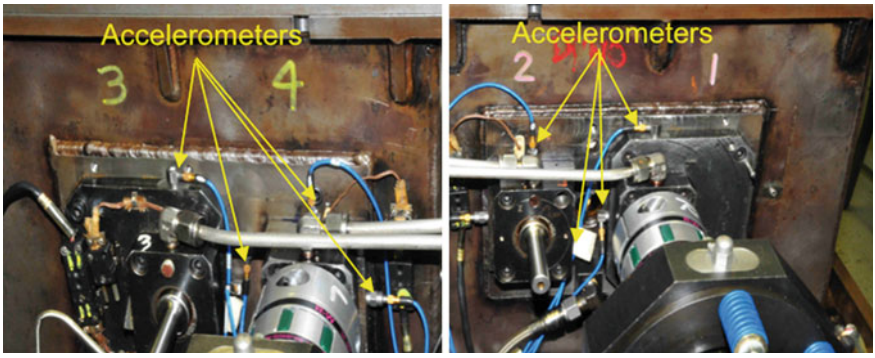

Fig. 5 Side views of the gearbox: input side (*right*) and output side (*left*)

extract from the original signal only the mesh harmonics components (Ene and Dimofte 2012b).

Tests were conducted at three torque levels, 34, 68 and 79 Nm. These represent 62.5, 125 and 146 % of the design level of the profile modifications on the test gears. The lubricant used for experiments was the synthetic mineral turbine oil Mil-L-23699. During all the measurements, the input oil temperature was maintained approximately constant, close to 70 °C. The oil supply pressure was 0.35 MPa.

The experiments showed that at speeds up to 3,400 rpm the wave bearings can attenuate the gear mesh vibration by up to 15 dB compared to rolling element bearings. As an example, the vibration reductions in vertical and horizontal directions measured with the accelerometers located on bearing at the coupling end of the input shaft are presented in Fig. 6.

Better results were obtained for the gear mesh noise measurements. The gear mesh noise reductions of wave bearings compared to rolling element bearings recorded with the microphone at torques of 34, 68, and 79 Nm are presented Fig. 7. It can be seen from Fig. 7 that for almost all of the speeds the noise generated by the gear mesh is smaller when the gearbox shaft is supported by the wave bearings instead of rolling element bearings. The greatest noise reduction was obtained at torques of 34 and 68 Nm.

A theoretical study was also performed to better understand the dynamic behavior of the wave bearings. The analysis was performed for a constant torque of 32 Nm. The theoretical analysis indicated that all the dynamic stiffness coefficients (K_{xx}, K_{xy}, K_{yx}, K_{yy}) and three of the dynamic damping coefficients (B_{xy}, B_{yx}, B_{yy}) are almost constant or have only a small variation with respect to speed (Fig. 8). The only dynamic coefficient that has an important variation with speed is the direct damping coefficient, B_{xx} (Fig. 8). The value of the direct damping coefficient decreases very fast as the speed increases. For example, the value of the direct damping coefficient at 6,000 rpm is almost half of its value at 2,000 rpm.

A direct consequence of the fast decrease of the direct damping coefficient with speed is the reduced capacity of the tested wave bearing to damp the vibration at

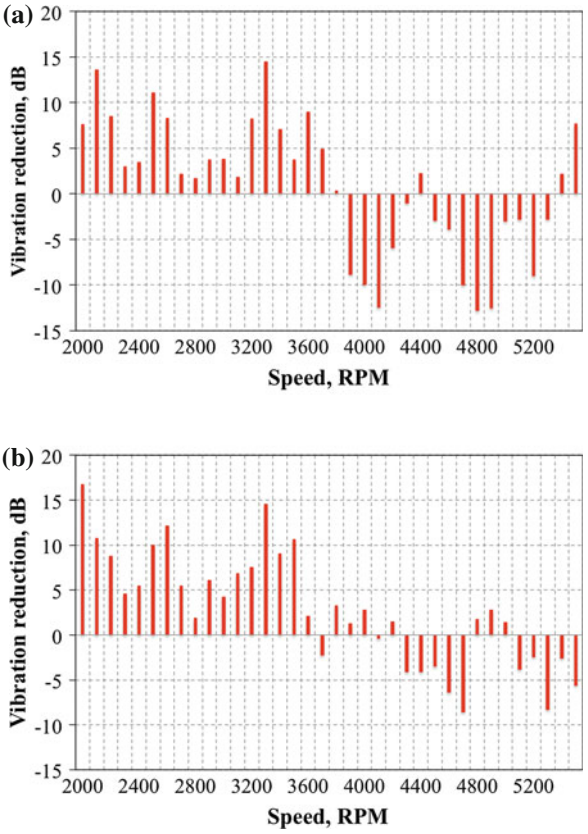

Fig. 6 Vibration reduction on bearing no 4 for a torque of 34 Nm. **a** Vertical direction. **b** Horizontal direction

high speeds. Therefore to improve the capacity of the wave bearing to attenuate noise and vibration, especially for speeds between 3,800 and 6,000 rpm, a solution to increase the value of the direct damping coefficient must be found.

Because the wave amplitude ratio has a strong influence on the wave bearing performance (Ene et al. 2008), the influence of the wave amplitude ratio on the direct damping coefficient was next analyzed. The variation of the direct damping coefficient with the wave amplitude ratio for different speeds is presented in Fig. 9.

For all the wave amplitude ratios greater than 0, the direct damping coefficients are greater than those corresponding to a zero wave amplitude ratio (the wave amplitude ratio of the wave bearings used in experiments was almost zero). The most significant increase is for the wave amplitude ratio equal to 0.2 (Fig. 9). For speeds lower than 4,000 rpm, an increase of the wave amplitude ratio from 0 to 0.2 induces an increase of the direct damping coefficient with more than 70 %. For speeds between 4,000 and 6,000 rpm, the increase is smaller, but still significant (greater than 50 %). Therefore an increase of the wave amplitude ratio to 0.2 could increase the wave bearing capacity to reduce the noise and vibration level of the test gearbox at any speed and torque.

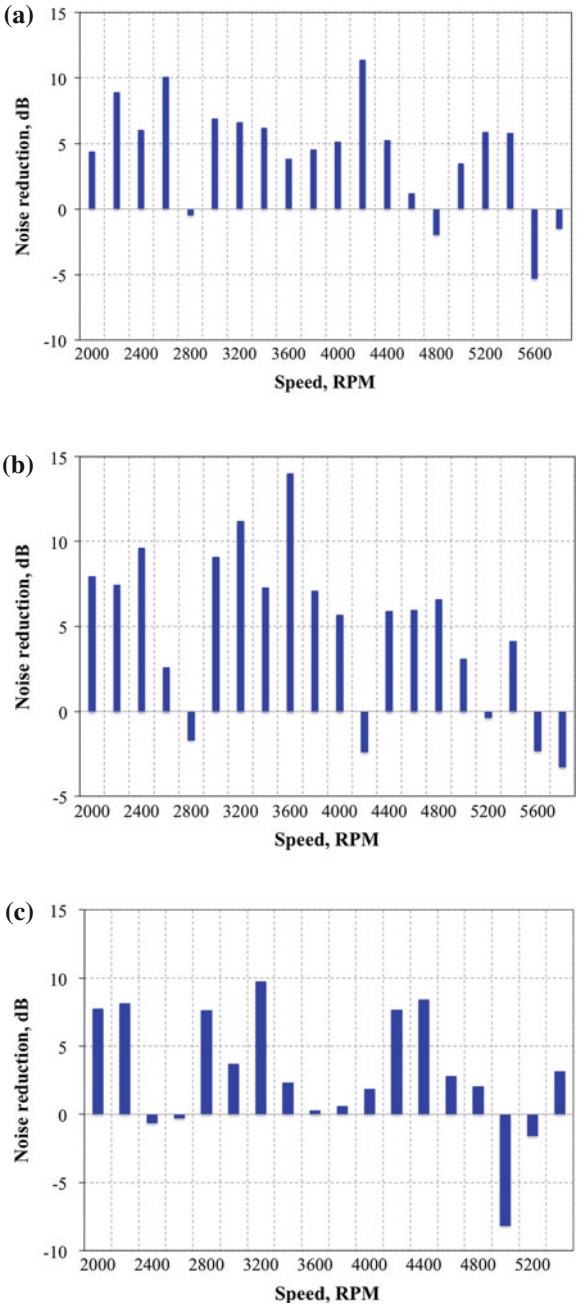

Fig. 7 Gear mesh noise reduction for different torques. **a** 34 Nm. **b** 68 Nm. **c** 79 Nm

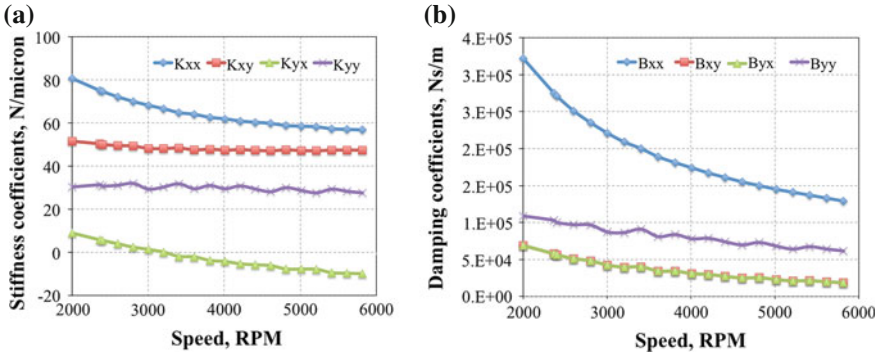

Fig. 8 Variation of the dynamic coefficients with speed. **a** Stiffness coefficients. **b** Damping coefficients

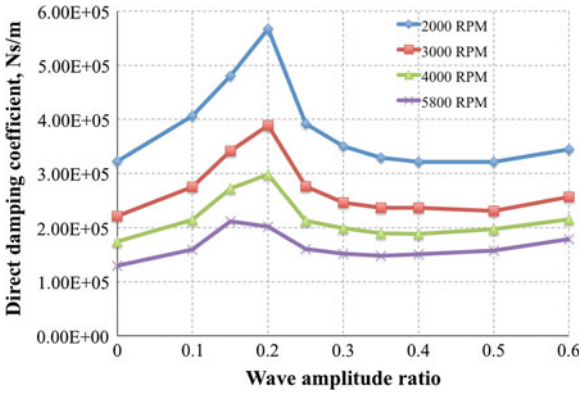

Fig. 9 Variation of the direct damping coefficient with wave amplitude ratio for different gearbox speeds

5 Concluding Remarks

The aerospace transmissions of the new generation are strongly required to be lighter, cheaper, and noiseless than the actual generation.

Using fluid film bearings, particularly wave bearings, to support transmission rotating parts can help achieve the desired goals.

Lighter and greater power density transmissions imply thinner parts that can experience large elastic deformation under the heavy loading conditions. The wave bearings can properly support the elastic parts and increase the safety operation margin of the transmissions.

The experiments showed that the wave bearings can attenuate the gear mesh noise and vibration with up to 15 dB compared to the rolling element bearings. Using the wave bearings in the new generation of the helicopter transmissions can significantly reduce the noise/vibration generated by these transmissions.

References

Dimofte F (1995a) Wave journal bearing with compressible lubricant—Part I: the wave bearing concept and a comparison to the plain circular bearing. STLE Tribol Trans 38(1):153–160

Dimofte F (1995b) Wave journal bearing with compressible lubricant—Part II: a comparison of the wave bearing with a groove bearing and a lobe bearing. STLE Tribol Trans 38(2):364–372

Ene NM, Dimofte F (2012a) The influence of the sleeve elastic deformations on the wave bearing performance in heavy loaded transmissions. Proceedings of the 4th international conference on power transmissions, Sinaia, Romania

Ene NM, Dimofte F (2012b) Effect of fluid film wave bearings on attenuation of gear mesh noise and vibration. Tribol Int 53:108–114

Ene NM, Dimofte F, Keith TG (2008) A stability analysis for a hydrodynamic three-wave journal bearing. Tribol Int 41(5):434–442

Hansen B, Salerno M, Winkelman L (2002) Isotropic superfinishing of S-76C+ main transmission gears, AGMA 06FTM02

Lenski Jr JW (1995) Advanced rotorcraft transmission program (ART) NASA-CR-195461, ARL-CR-224

Oswald FB, Townsendt DP, Valco MJ, Spencer RH, Drago RJ, Lenski Jr JW (1994) Influence of gear design parameters on gearbox radiated noise, NASA TM 106511

Townsend DP (1991) Dudley's gear handbook, McGraw Hill

An Overview of the Development of Gears

Jože Hlebanja and Gorazd Hlebanja

Abstract Power transmission has been a challenge during human history. Men used gears to accomplish this task already at the emergence of our civilisation. Gears were simple wooden aids at first, but the evidences of complex mechanical devices of antiquity exist. Water and animal powered devices were used during the middle ages, whereas the renaissance and subsequent development of science discovered steam engines. The combustion engine, the turbines, and electricity imposed new impact to the mechanical transmissions which developed up to contemporary highly efficient devices embedded into aircrafts, vehicles, machine tools, etc. The question is if there is still possible to improve gears, which are substantial part of these transmissions, in any way.

Keywords Gears · Power transmission · Standardisation · History of gears

1 Emergence of Gears

Gears are important parts of machines, which, when working in tandem, transmit power and movement from the energy source to the user of the job performed. Machines are devices which can do useful work, and are composed of functionally connected moveable and fixed parts. To accomplish a task, a machine must have a source of energy, whereby gears are vital machine elements. According to current historical evidence, machines emergence might be attributed to ancient Egypt because of human need, as people living by the Nile had to irrigate soil to produce

J. Hlebanja · G. Hlebanja (✉)
University of Ljubljana, Ljubljana, Slovenia
e-mail: gorazd.hlebanja@fs.uni-lj.si

J. Hlebanja
e-mail: joze.hlebanja@siol.net

G. Dobre (ed.), *Power Transmissions*,
Mechanisms and Machine Science 13, DOI: 10.1007/978-94-007-6558-0_4,

needed food. This was performed by using primitive machines, Fig. 1, which used simple wooden gears to transmit power and rotation. Since then, gears have been used and perfected in all periods of human civilization for exploiting natural energy resources to perform work for the benefit of humans. At first, the ancient population probably irrigated land by manually drawing water from the river and then watering the fields. Based on observation, they realised that they could increase capacity by tying a greater number of containers to a rope. On this basis, a paternoster-like device was gradually developed, which consists of a rope formed into a ring, with buckets (containers) attached at regular intervals, hung onto a wheel. They probably first rotated the wheel manually and thus lifted the water from the river, poured it into a trough and irrigated the fields. The hard manual operation was strenuous and ineffective, so later a whim was developed to replace human power with that of draught animals. The whim is composed of a horizontal gear wheel attached to a rotary vertical pillar, which the animal pulls and spins around its vertical axis, while the gear drives the paternoster via its tandem gear and a horizontal shaft, roughly as shown in Fig. 1.

It is obvious that this primitive device could have been produced at the time with simple tools, when humans began to use domesticated animals as a source of energy for their benefit. These and similar devices used the oldest wooden gears we know as a result of human creative capacity.

Figure 2 shows that gear teeth were simple round pegs fixed in the gear wheel. The whim gear rotated slowly with a pace of the draught animals, while the speed of the paternoster wheel depended on the transmission ratio of the gears. The precision of the rotation transmission was insignificant, and uninterrupted rotation of the whim, continuously fed the soil. Through the centuries, pumping water by whim with simple gears was perfected and spread to the fields of the great rivers like the Euphrates and Tigris in Mesopotamia, the Indus and Ganges in India, and the Yellow River and Yangtze in China.

Antiquity time was of the utmost importance for the development of geared devices and machines. Many machines with gears were described and passed on to

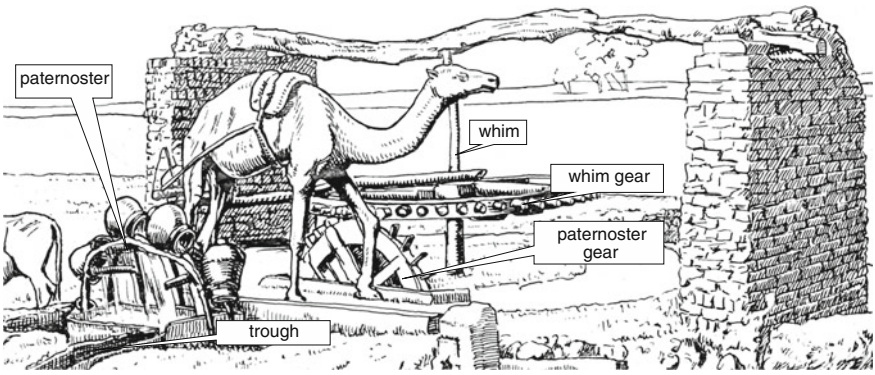

Fig. 1 Illustration of a sakia in Luxor (Matschoß 1940)

Fig. 2 Gearing of a sakia

succeeding generations by great scholars of that era, including the Greek philosopher Aristotle (384–322 BC), a student of Plato and the teacher of Alexander the Great, who in his works described machines such as the pulley, crankshaft, rollers and also irrigation devices with gears.

Archimedes of Syracuse (287–212B C) was a mathematician, physicist and engineer, who knew the principle of leverage and cranes, as well as worm gears. Thus, Fig. 3 illustrates a winch made of a gear train and a worm for the handle. He is famous for saying: "Give me a place to stand on, and I will move the Earth", while the Archimedean principle is taught already in primary schools. Ancient reports have revealed that Archimedes moved a ship weighing 4,200 tonnes out to sea using a system of levers, pulleys and gear trains.

Philo of Byzantium (~ 230 BC) was a Greek engineer and mechanic famous for a chain drive and water lifting device consisting of a gear and a rack employing also hydraulic principles.

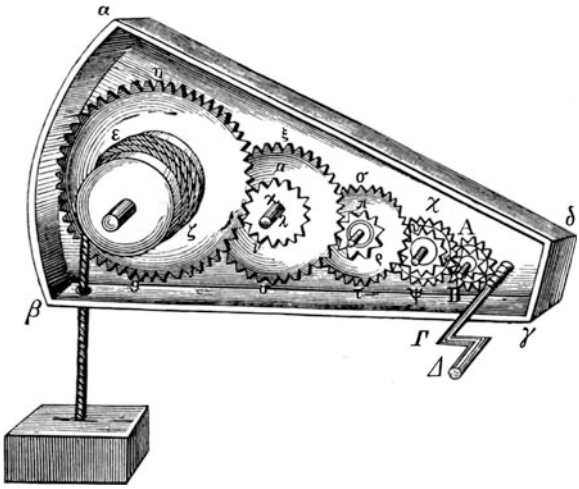

Fig. 3 Archimedes' winch consisting of a gear train and a worm ended handle (Matschoß 1940)

Fig. 4 The Antikythera mechanism—model of a front part (*left*); original archeological artefact (*right*) (The Antikythera Mechanism Research Project 2012)

The Antikythera mechanism was recovered in 1900–1901 from the Antikythera wreck. Its significance and complexity were not understood until decades later. The construction has been dated to the early 1st century BC. This precious example of antique genius complexity grade was so high that artefacts of similar complexity and workmanship did not reappear for a millennium and half, when mechanical astronomical clocks were built in Europe (Fig. 4).

The true function of the Antikythera mechanism was not understood until recently, when scientists disclosed its structure and written material by contemporary methods, which include surface imaging, digital radiography (2D&3D) and Computer tomography. The device is remarkable for the level of miniaturization and for the complexity of its parts and has more than 30 gears, although some scientists suggested as many as 72 gears, with teeth formed through equilateral triangles. The mechanism calculated the position of the Sun and Moon or other astronomical information such as the locations of planets, so it can be treated as an ancient analogue mechanical computer. Since the purpose was to position astronomical bodies with respect to the celestial sphere, with reference to the observer's position on the surface of the Earth, the device was based on the geocentric model (Wikipedia, "Antikythera Mechanism" 2012).

2 Gears in Roman Times

The underlying mechanism of the sakia type irrigation device was used by many generations throughout Antiquity and the Middle Ages, with the gear teeth being perfected, while expanding the use of whim as a source of energy for various tasks. By expanding their rule over a large part of Europe, the Romans also spread knowledge inherited from the Greeks and Egyptians. Instead of a whim, the Romans also used the water energy of rivers or streams by a water wheel on a horizontal shaft, which drove the conical millstones on a vertical shaft by a gear pair, as illustrated in Fig. 5a, as an example of Vitruvius' (c. 80–70 BC to c. 15 BC) (Wikipedia, "Vitruvius" 2012) engineering work. Vitruvius also designed a hodometer, consisting of a set of gears and worms, which dropped a small ball into the box for each passed mile. Vitruvius himself said that his knowledge derived from famous old Greek sources (Matschoß 1940).

The power from the energy source—a whim or a water wheel—was transmitted by wooden gears, similar to those shown in Fig. 6 for over 2,000 years without major changes. Manufacturers of such gears were always master carpenters. They shaped the water wheels and the geared wheels based on experience. According to historical sources, such gears on country mills and saws would have lasted for several decades. The Romans also used water power for sawing. The Roman sawmill at Hierapolis in Asia Minor from 3rd century incorporated a crank and connecting rod mechanism, which was used for saws cutting marble (Wikipedia, "List of ancient watermills" 2012), as illustrated in Fig. 5b.

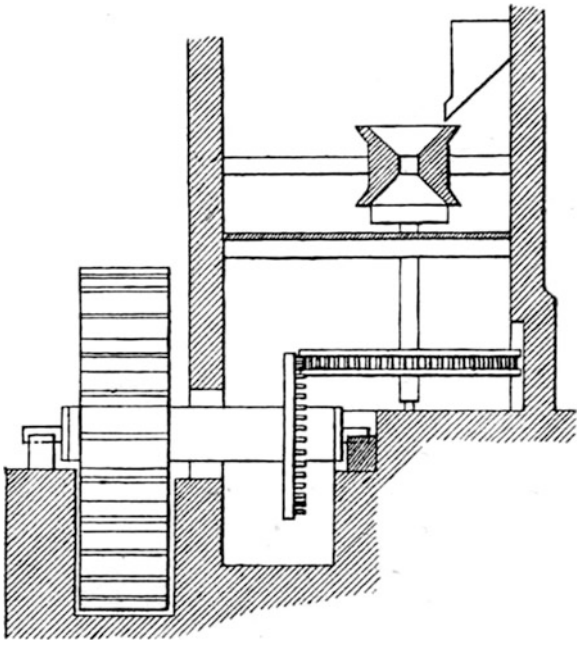

Fig. 5a Roman water mill, according to Vitruvius (Matschoß 1940)

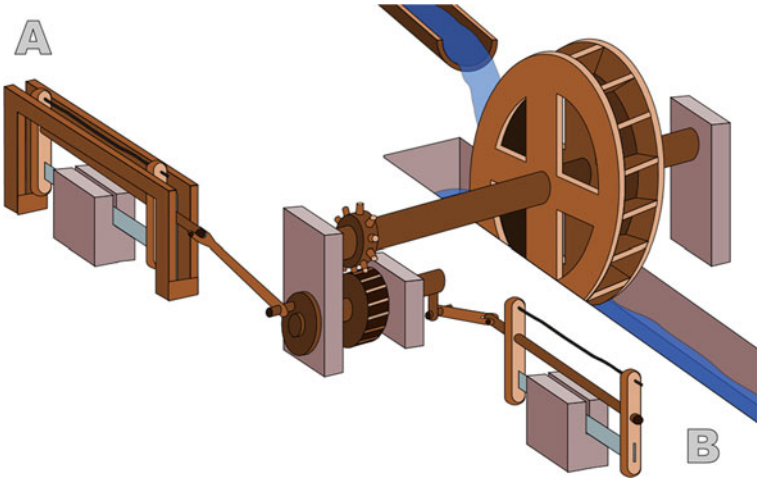

Fig. 5b Sketch of a water-powered sawmill (Wikipedia, "List of ancient watermills" 2012)

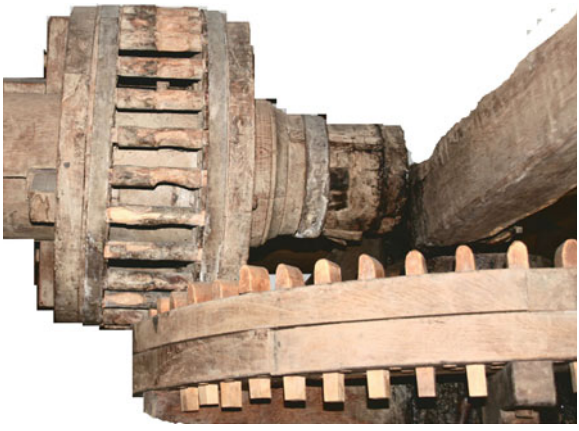

Fig. 6 Design and appearance of wooden gears after many years of in operation

Water-driven mills and saws with wooden gears could have been found along the rivers and streams all over Europe until the beginning of the twentieth century.

Heron of Alexandria (c.10–70 AD) was an ancient Greek mathematician and engineer active in his native city of Alexandria, Roman Egypt. He is considered the greatest experimenter of antiquity (Wikipedia, "Heron of Alexandria" 2012). His numerous works start with an aeolipile, a jet engine which spins when heated. A vending machine, distributing a dose of holy water after insertion of a coin, a wind-wheel, a force pump, the Heron's fountain and a syringe-like device are also attributed to Heron. Several variants of gear train arrangements for lifting heavy loads; e.g. such as illustrated in Fig. 7, are his inventions as well.

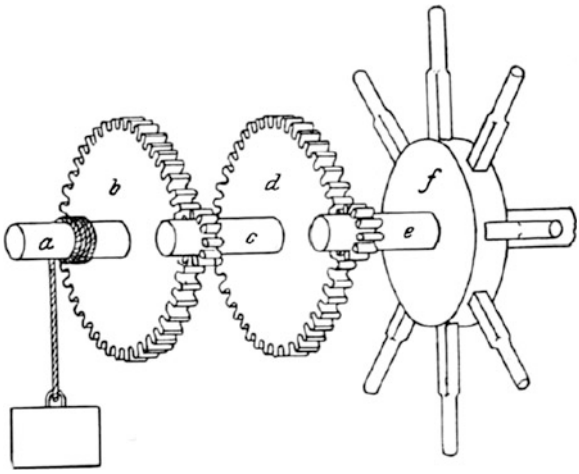

Fig. 7 A winch consisting of gear trains for lifting heavy loads (Matschoß 1940)

3 The Situation in the Middle Ages

In the late Middle Ages, from the 13th century on, mining became fairly widespread. Agricola (1556) extensively described development of mining methods, metallurgical processes, geology, mineralogy and according law from the earliest times to the 16th century in his work *De Re Metallica*. The mechanical principles of winding, ventilating, and pumping machinery described in the book are very old. The block and pulley, the windlass, the water-wheel, the transmission of power through shafts and gear-wheels, chain-pumps, piston-pumps with valves, were all known to the Greeks and Romans. Devices, used for lifting ore ranged from simple man-powered windlasses to rather complex, in both direction operating water-wheels. Horse operated whims were also often, with the same working principle as ancient sakia as illustrated in Fig. 8.

Specialty of the machine from Fig. 8 is the usage of a brake. A miner in the shaft pushed the vertical beam down and thus lifted the braking beam up by reverting the oscillating beam and stopped the braking wheel. This machine could have lifted ore 240 feet and up to four horses could have rotated the whim, depending on the actual depth and loads. Nevertheless, water power was the limiting factor of the mine shaft depth. This did not change until discovery of the steam engine which offered a new, powerful source of energy. Parallel to mining, craftsmanship was also thriving. Able self-taught masters honed their skills and learned how to make complex wooden gear wheels by hand, while in the meanwhile, with the advancement of metallurgy, they also began to manufacture cast iron gears. Despite the fairly widespread use of gears to transmit movement and energy, manufacturing was still based on previous experience. The whims were also widely used in agriculture, e.g. for threshing.

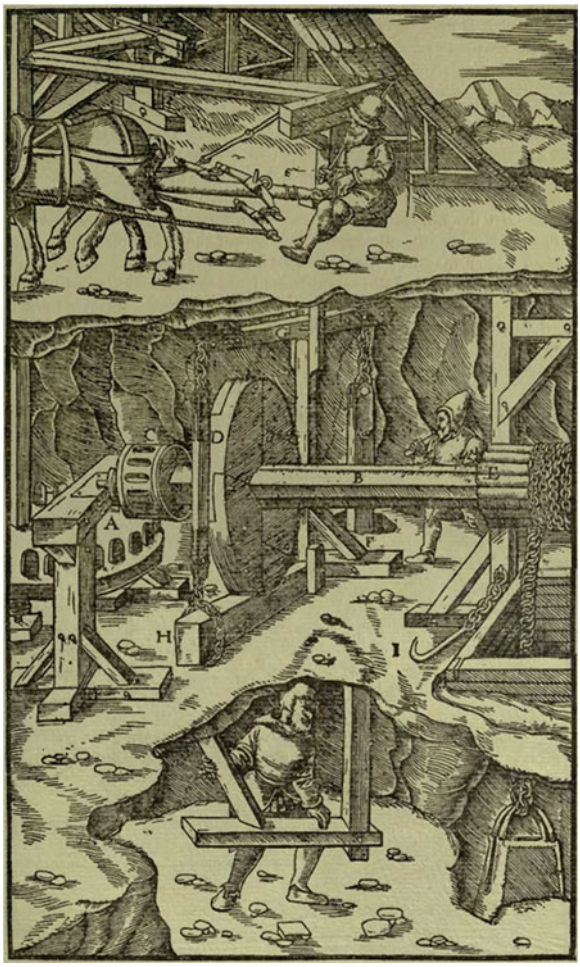

Fig. 8 A whim based lifting machine. *A*—toothed drum which is on the upright axle; *B*—horizontal axle; *C*—drum which is made of rundles; *D*—braking wheel; *E*—drum made of hubs; *F*—brake; *G*—oscillating beam; *H*—short beam; *I*—hook. (Agricola 1556)

4 Mechanical Clocks

Sun dials and water clocks were introduced to Europe by the Romans and also perfected by Arabs. The rare "horologes" during the Middle Ages were water-powered. The word clock (from the Latin word clocca, "bell"), which gradually supersedes "horologe", suggests that it was the sound of bells which also characterized the prototype mechanical clocks that appeared during the 13th century in Europe (Dohrn-Van Rossum 1996). These devices were often without hands, indicating time only by bells, telling people to attend service. Churches and monasteries needed to know the precise time to perform their duties, so the first mechanical clocks were developed by monks in monasteries. The first mechanical clock with hands in Germany dated to 1304 and was situated in the Benedictine monastery of Erfur (Matschoß 1940). It was driven by a weight and regulated by a

simple step regulator. In that period, similar clocks appeared in Italy, France and England, e.g. Canterbury Cathedral installed a 'great horologe' in 1292. The complexity of the geared mechanism of such clocks is represented in Fig. 9 showing the clock mechanism of the Überlingen cathedral tower near Bodensee (Matschoß 1940).

The gears were from iron, and the wheels were forged and geared manually, shaped by an experienced master. The clocks of the period were powered by weights and the introduction of springs in the 15th century was highly advantageous. Christiaan Huygens used a pendulum for clocks in 1656 (Encyclopædia Britannica Online, "pendulum" 2012), which increased accuracy of mechanical clocks. With an increased demand for clocks, the reputation of the clock-making profession grew, and the number of clockmakers' guilds and masters increased, which led to the accelerated development of clocks, their miniaturisation and increased precision.

5 Gears During the 15th and 16th Century

Leonardo da Vinci (1452–1519) was the most famous engineer of all time. He left the legacy of his ideas of gear transmission in the form of sketches, some of which are shown on Fig. 10. Leonardo was directly involved with the technological

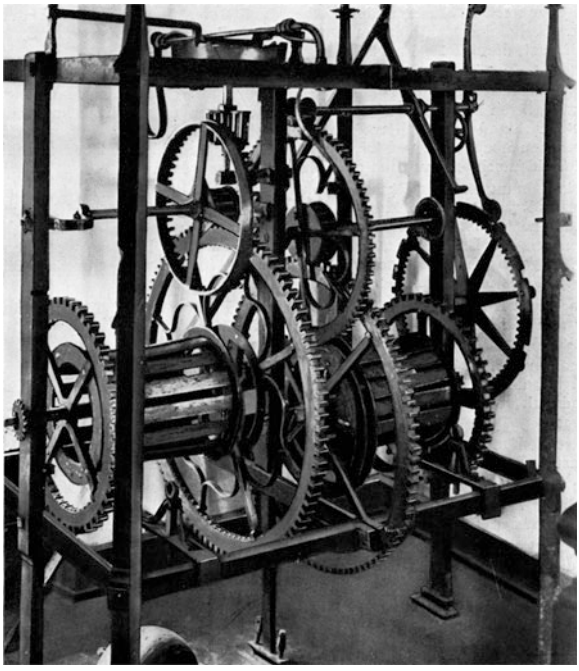

Fig. 9 Überlingen clock mechanism, 1540 (Matschoß 1940)

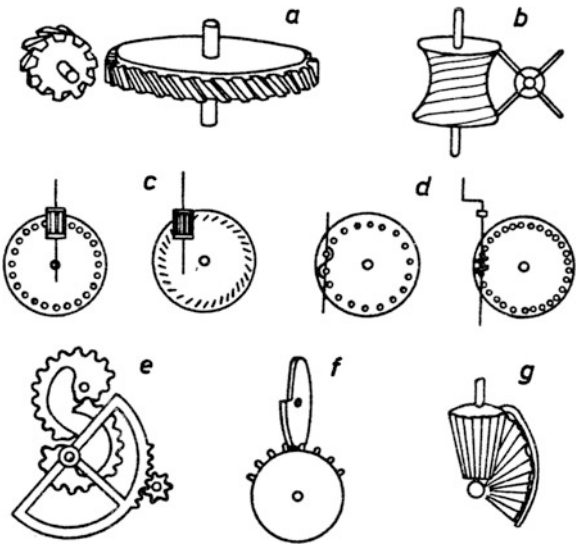

Fig. 10 Leonardo's sketches of gears (Matschoß 1940)

issues of his time, and sought to find answers to questions with a pencil in his hand, drawing solutions to an issue, which could not all have been realised at the time. In any case, his sketches present solutions and reflect the technology of the time. Although Leonardo left a multitude of sketches on transmitting power and movement from one shaft to another, he did not study teeth flanks, so he did not contribute to the advancement of teeth theory.

Already mentioned Georgius Agricola (1494–1555) described iron gears in his most known work De Re Metallica. Since iron is more durable material, this also signifies the discovery of new, improved teeth flanks.

6 Early Development of Modern Gears

Contemporary gears for the uniform transmission of power and movement are based on the application of mathematical curves discovered by scientists in the 16th and 17th centuries, in the design of teeth flanks. One of such pioneers was Galileo Galilei (1564–1642), who, after having finished his studies in medicine, devoted his research to geometry and the mathematics of plane curves. In his 1598 treatise, he was the first to name and mathematically define curves generated by a point on a circle rolled along a straight line or along another circle of a cycloid. In addition to other laws of nature and physics, his discoveries include the law of oscillation of the pendulum (1583) and free fall. He also improved the telescope (1609). Galileo was a professor of geometry, mechanics and astronomy at the University of Padua until 1610. In 1633 he was sentenced to the house arrest due to spreading and teaching heliocentric system and during this time he wrote works on

new disciplines, now known as kinematics and strength of materials (Encyclopædia Britannica Online, "Galileo" 2012).

The first record on the use of cyclic curves for practical purposes is related to French architect and engineer Girard Desargues (1591–1661), who is considered the predecessor of descriptive geometry and is known in particular for his work on conic sections (curves obtained by intersecting a cone with a plane). Desargues is also known for constructing a system for raising water, which he installed near Paris, using the principle of the epicycloidal wheel (Encyclopædia Britannica Online, "Girard Desargues" 2012).

Some of Desargues' work is known only from the records made by his student Philippe de la Hire (1640–1718), French physicist, astronomer, mathematician and engineer, who learned from Desargues all that was known about cycloids at the time. A treaty on epicycloides and their usage in mechanics was published in his 1694 book entitled Mémoires de mathématique et de physique. Philip de La Hire was the first to describe the use of epicycloids for gears that ensured a uniform transmission of rotation (Complete Dictionary of Scientific Biography, "La Hire, Philippe De" 2008a). Such a gear with a one-sided epicycloidal gearing with eight teeth is shown in Fig. 11a, while Fig. 11b shows a pin gearing, for which de la Hire designed the correct shape of the tooth flank by generating an equidistant curve for the involute. Until recently, such gearing was used in raising mechanisms for small floodgates in water-powered sawmills. De la Hire explored the use of cycloids for the shape of teeth flanks of particular gears, while in 1733 in his work "Sur la figure des dents des roués et des ailes des pignons pour rendre les horologes plus parfaits" Charles Etienne Louis Camus (1699–1768), a mathematician and professor from Paris (Complete Dictionary of Scientific Biography,

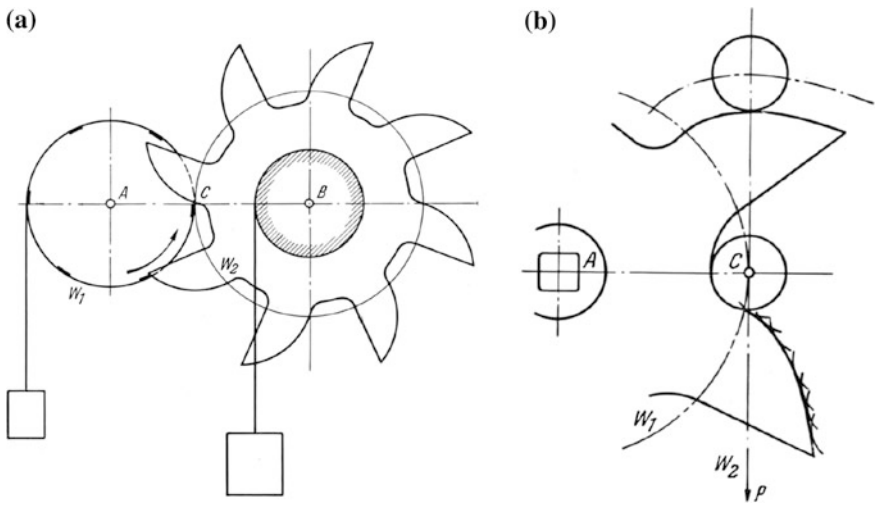

Fig. 11 Single sided pin gearing (*left*); pin-gear rack driven by a single sided gearing with an equidistant involute flank (*right*)

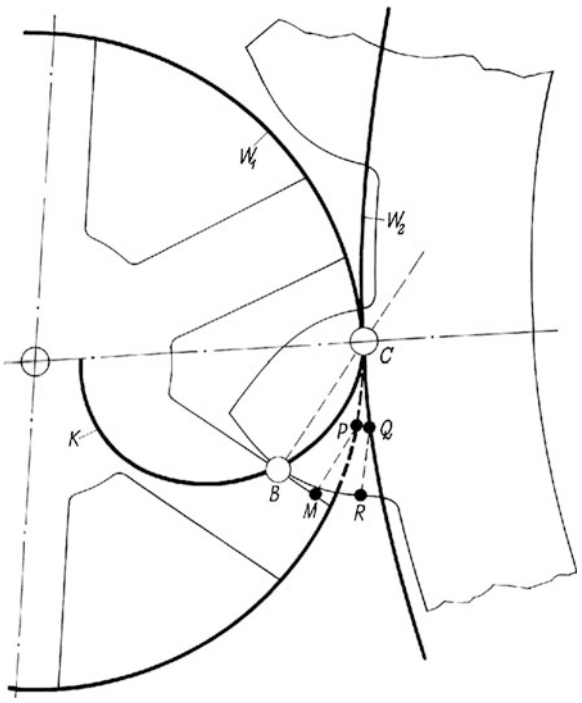

Fig. 12 Illustration of Camus' gearing principle from 1733

"Camus, Charles-Étienne-Louis" 2008b), discovered the conditions that have to be fulfilled for a pair of gears. This condition is defined by the following: if, in uniform rotation, power is to be transmitted via a pair of teeth, then the normal to the teeth flanks at the contact point P (on the path of contact) must pass through the pitch point C (Matschoß 1940), as shown in Fig. 12, which is exactly the law of gearing known today.

This can be illustrated by a pair of cycloid gears with a rolling circle whose point P generates a hypocycloid on the pinion with a straight tooth flank, while the gear tooth flanks have the shape of an epicycloid. The teeth flanks come into contact on the path of contact where both flanks have a common tangent and normal, the latter passing through the pitch point C.

Independently of de la Hire and Camus, Leonhard Euler (1707 Basel–1783 St. Petersburg) sought the most advantageous shape of gear teeth flanks, and according to Jacobi, (The Euler Archive 2012) in 1752 he was the first to publish a treatise on the usefulness of the involute for the shape of gear teeth flanks (Euler 1760). His concept of involute gearing shown in Fig. 13a is in common use today. Euler also discovered that the uniform transmission of power by gear teeth flanks always involves friction, which causes loss of energy. He also showed how to graphically determine the radii of curvature, which is presented for a pair of cycloid gears in Fig. 13b. During the rotation of the gears, the normal to teeth flanks at contact point must always pass through the pitch point C, which is why

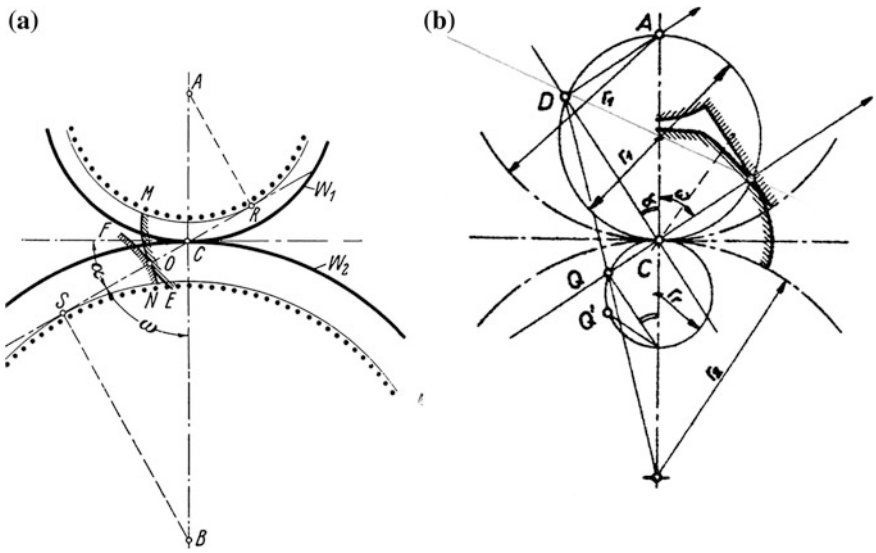

Fig. 13 Euler's involute gearing (**a**); curvature centres of teeth flanks at the contact point in the case of a cycloid pair of teeth (**b**)

the instantaneous centre of rotation is at point D, while at the same time the gear also rotates around axis O_1, which is why the curvature centre of the tooth flanks must be at contact point P, i.e., the intersection Q of the normal to the teeth flanks at the contact point and the connecting line DO_1. Since the diameter of the rolling circle is equal to half of the pitch diameter of the big gear, the tooth flank of the big gear in this illustration has the shape of a straight line with the curvature centre in infinity. Euler and Savary together devised an analytical method for determining the curvature centres of gear teeth flanks.

Christiaan Huygens (1629–1695) also had a major impact on the accelerated development of gears, when he made the pendulum clock in 1656/57. The Huygens clock, which he patented in 1657, was very precise for its time, and with later improvements it could also display minutes as well as hours. Gears were used to transmit movement from the escapement mechanism to the handles, and weights for driving the pendulum. In the following years, Huygens also made a clock whose gear mechanism was driven by a spiral spring made of steel.

Discoveries by Galileo (doctrine of cycloids and the law of the pendulum, 1583), de la Hire (normal to the tooth flank, 1694), Camus (law of gearing, 1733) and Euler (involute gearing, 1752), can be treated as the basis for the development of contemporary gears. The era of the early development ended when the first steam engine was successfully constructed at the beginning of the 17th century. This was an exceptional milestone for humanity, as it was now possible to translate heat energy into mechanical operation based on natural laws, and marked the time when machines began to perform physical tasks previously done by people and animals.

7 James Watt's Epic Achievement

James Watt (1736–1819) is considered the inventor of the steam engine. The first actual steam engines were simple piston engines used for drawing water from the mines, and on the basis of which a double-action rotary shaft engine was developed in 1781. In 1770, Watt introduced a unit for power based on horse power 'HP' (1HP = 75 kpm/s), and the watt unit for measuring power was named after him (1 W = J/s). He invented a centrifugal speed governor for his machines, which had 'rapid' velocity for the time—40 movements per minute—which later decreased to 30 movements per minute. Although the crank shaft was already known in Roman times, the patent was granted to Watt's opponent. Watt overcame this obstacle with planetary gears, as shown by Fig. 14, where a planetary gear is rigidly attached to the connecting rod of the tandem, while the sun gear is attached to the driven shaft. (Encyclopædia Britannica Online, "James Watt" 2012).

The new steam machine immediately became very popular, and in 1784 the Abion milling company ordered a Watt steam machine with a rotary shaft and gears. The machine, with a power of 20 PS to drive 20 mill stones was built in four years, and in 1788 there was a ceremony to mark the beginning of operations. The gears had cycloid teeth flanks, and were made by hand from forged iron. Watt and Rennie assessed in 1783 that teeth in corresponding gears were submitted to bending, so they their calculations were adjusted accordingly. After the first successes, the development of the steam engine blossomed both in terms of construction and use. The first railways were laid on land, and the first steam ships started sailing the sea.

The successful introduction of the Watt steam engine in the 18th century was followed by new successes by inventors in 19th century, dealing with electric power. Thus the Belgian Zenobe Gramme (1826–1901) in 1870 invented the first

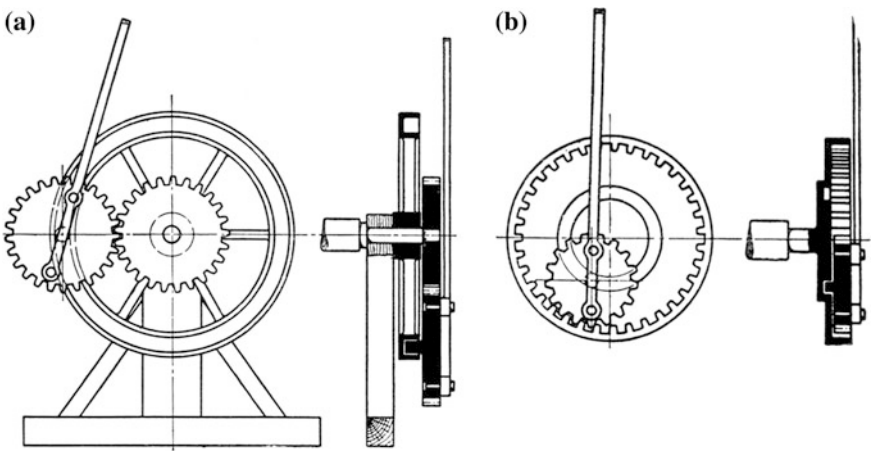

Fig. 14 Watt's planetary gears for the transmission of the piston movement into shank rotation **a** for outer teeth **b** inner teeth

electrical generator producing direct current. Nikola Tesla (1856–1943) in 1885 discovered the rotating magnetic field of alternating current. As result of Tesla's work, the Niagara power-plant producing 2.4 MW of electric energy from AC generator was connected to grid in 1895.

On the other hand, in 1861, Nikolaus August Otto (1831–1891) patented the first internal combustion engine running on petrol, in 1892 Rudolf Diesel (1858–1913) patented the internal combustion engine running on gas, while Karel Benz (1844–1929) and Gottlieb Daimler patented an engine-driven automobile almost at the same time, at about 1887. These inventions demanded a much higher quality and loading capacity of gear transmissions. In addition to the already mentioned inventions, we should stress the discovery of the high-pressure steam turbine developed by the Swede Gustav de Laval (1819–1913) in 1887, and the low-pressure turbine designed by Charles Algernon Parsons (1854–1931) the same year.

The enthusiasm over new sources of power and possibilities for mechanical operation gave birth to ambitious goals, which included a rack railway to the Jungfrau in Switzerland. In 1894, the entrepreneur Adolf Guyer-Zeller (1839–1899) was granted a license for the construction of the 9.34 km rack railway from the Kleine Scheidegg station at 2.061 m to the Jungfraujoch summit station at 3.454 m.

The construction of the railway with the gauge of 1 m began in 1896, and was built in four stages. It was inaugurated in 1912. The difference in height between the upper and lower station was 1.393 m, the average operational speed was 12.5 km/h, the average gradient 15 % and maximum gradient 25 % (Jungfrau Railway 2012). Figure 15 shows the view of the electrical AC locomotive of 50 Hz (Fig. 15a) and a detailed view of the rack gear (Fig. 15b). The successful project was remarkable at the time.

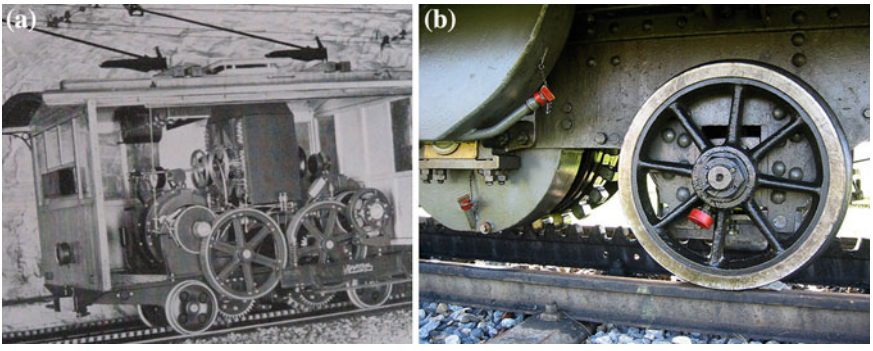

Fig. 15 **a** Jungfrau locomotive; **b** gear drive

8 Gears in the 19th Century

The eighteenth century laid the foundations and laws for designing teeth flanks, which were followed by more elaborate designs considering particular machine parts for power transmission. Together with the development of energy machines came the development of processing machinery, which had specific issues regarding speed, i.e. significantly lower operational features, which were overcome by gearboxes. Production demands for gears and higher quality standards rose accordingly, but the manufacturers had limited knowledge. Due to the need for much greater loads and speeds, the gears had to be made of more durable materials, which posed the problem of manufacturing the demanding design of teeth flanks. This led to calls for uniform manufacturing guidelines.

Robert Willis (*1800–1875*) was a professor at Cambridge, who in 1841 published the book, entitled Principles of Mechanisms, where he compiled the lectures for his students and knowledge about gears which could be used in practice. At the time, gears were mostly made from cast iron, which made correcting casting-related mistakes a great problem. In 1836, Willis presented his idea on the unification of the shape of gear teeth with the gear train composed of three gears. His suggestion implies that the gears have to be interchangeable, which means same pitches and same teeth sizes and an arbitrary number of gear teeth, ranging between $z = 12$ and $z = \infty$. He expressed the listed requirements with a 'module', which he designated with the letter M and defined as the quotient of the pitch t and the number π ($M = t/\pi$). He also defined pitch circles with a given number of teeth and pitch t, whose diameter was expressed with the product of the module and the number of teeth, $d_0 = M\pi$. He chose a uniform height of the teeth, which was equal to the module ($h = M$). Sometime later (1873), Paul Hoppe (Seherr-Thoss (Graf von) and Fronius 1965), similarly as Willis before him (Fig. 16a), expressed the unification of teeth sizes with the threesome involute gear train (Fig. 16b).

Willis also studied the effect of the contact angle on the shape of teeth. He found that 15° is the appropriate value when the number of teeth is limited (undercutting when $z < 15$). The shape of gears was determined by the number of teeth z, module M and pressure angle.

Franz Reuleaux (*1829–1905*) was one of the professors who were strongly involved in the development of gears. He studied the effect of the contact path on the shape of gear teeth flanks and the flank load carrying capacity. On the basis of his research, he discovered that involute gears are the most advantageous. He became famous for his textbook Construkteur (Reuleaux 1861), which focused on the topics of design in mechanical engineering and the kinematics of gear pairs.

In the period until the end of the 19th century, the development of the tooth flank profile shape was more or less completed, the law of gearing, which uniformly defined the relations between the contacting teeth flanks and the path of contact, was affirmed. Based on the above, the involute gearing prevailed as the most advantageous shape of teeth flanks.

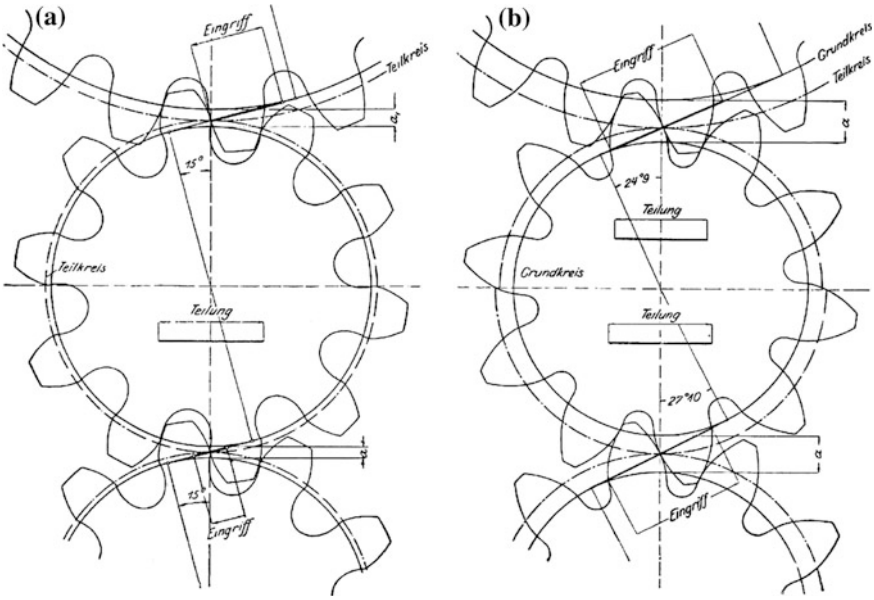

Fig. 16 Threesome gear train **a** after Willis; **b** after Hoppe

9 Manufacturing Gears by Rolling

In his book New General Theory of the Teeth of Wheels (1852), Edward Sang (1805–1890) defined a rack as a gear with an infinite radius whose pitch circle is a straight line. In 1861, Carl Hermann Wiebe (1818–1881) defined a rack for involute teeth flanks where the common normal passes through the convergence point of two involutes, always through the same point on the line connecting the axes of base circles, which also means that all contact points represent the path of contact and that the rack teeth flanks are straight (Matschoß 1925).

The basis for manufacturing cylindrical gears by rolling with a spiral milling cutter was first constructed and patented in 1856 by Christian Schile of Oldham. Schile was the first to carry out the coordinated movement (rotation) of the workpiece (gear) and worm milling cutter, but this system did not last as a manufacturing machine. The latter was constructed on the basis of an American patent first in 1887 by George Grant (1849–1917) and in 1894 by Julius Eduard Reinecker (1832–1895) from Chemnitz. The Reinecker Company was the first German factory that produced machine tools for manufacturing gears by rolling with a worm milling cutter (Matschoß 1940).

Hermann Pfauter (1854–1914) from Chemnitz substantially improved Reinecker's system of manufacturing gears with a worm milling cutter and patented the improvement in 1900, receiving the patent entitled "Pfauterverfahren".

He, too, founded a factory of machine tools for serrating gears by rolling with a worm milling cutter (Hermann Pfauter Werkzeugmaschinenfabrik 1976).

Parallel to the development of gear manufacturing with a milling cutter, a gear shaper system with a straight rack tool and the Fellows gear shaper system with a circular rack tool were also developed. The gear shaper system with a straight rack was realised by Reinecker and in 1908 by Max Maag (1883–1960); while the gear shaper system with a circular rack was realised in 1896 by Edwin Fellows (1865–1945) (Litvin 1997).

10 Before World War II

At the turn of the century, the use of involute gearing was already established in general engineering, while cycloidal gears were mostly used in fine mechanics. Moreover, also known were effective methods for manufacturing gears either by rolling with a milling cutter or by a straight or a circular shaping (Fellows). The development of gears was closely connected to the development of energy machines at the time, which was based on emerging higher education courses in applied sciences in developed European countries that also comprised machine elements, design, and technical drawing. The knowledgeable graduates intensely worked on developing energy and processing machines, whose power, rotational speeds and consequently complexity of gear arrangements grew rapidly. In general, the speed of energy supplying machines did not correspond to the needs of processing machines, which was resolved by gear transmissions.

Among the major sources of power were the quickly developing electric motors, which drove processing machines via added or built-in gears. In this respect, Werner von Siemens (1816–1892), who built the first electric railway in 1879 (Siemens 2012), deserves special credit. Parsons' (1854–1931) low pressure steam turbine (1884) was also gaining importance (Encyclopædia Britannica Online, "Sir Charles Algernon Parsons" 2012). Thus power of anew installed devices scaled rapidly as well as the demand for appropriate gears. In power plants, Steam piston engines were replaced by steam turbines, which also began driving large freight, passenger and military ships. Steam turbines of high power outputs (from 30.000 to 70.000 HP) and rotational speeds between 4,000 to 5,000 RPM were used to run propellers on big ships. Rotational speeds of the ship propeller should be substantially smaller, depending on the type of propeller, which was overcome with high performance turbine gear transmissions.

Manufacturers of all types of vehicles became new customers of specially designed gears. The field developed quickly, so a new plant for manufacturing high performance gears according to the MAAG system was built in Friedrichshafen to satisfy the demand of the automobile and aviation industry.

Other new specialty fields imposed new requirements for gearings, which included highly loaded but slower running gears used in transport devices and lifts,

quietly operating gears used in the textile industry, high performance printing machines and particularly demanding high precision gears for machine tools.

In all periods of development, gears with small teeth of small modules and dimensions were developed for precision instruments in fine mechanics, for which appropriate manufacturing technology was needed. The development went toward smaller friction, and, accordingly, involute gears were mostly used, while cycloid gears were used for watch industry.

Euler already determined involute as the most favourable design for teeth flanks; however, the shape could be accurately manufactured by rolling with suitable cutting tools. This was the reason why in 1927 (DIN 867) tools for manufacturing involute gears were standardised along with the module values, pressure angles, and uniform addendum size equalling the module. Gear manufacturing by rolling enabled the rack profile shifting, which furthermore enabled the improved kinematic characteristics of gears. Materials for gears changed from cast iron at the turn of the century to alloy steels, which were already on the market in the 1930s. High-quality and stronger steel was made in electric arc furnaces. With tempering and surface heat treatment, gear teeth flanks became more durable, gears became smaller and achieved greater load-bearing capacity. Besides steel, brass and plastic materials were used for gears in fine mechanics. Improved tools and new machinery shortened production time. Moreover, new machines and cutting tools also perfected treatment processes, such as grinding, honing and lapping, achieving smoother teeth flank surface.

Dimensioning of gears also greatly improved in the first half of the twentieth century. In this respect, Stephen P. Timoshenko (1878–1972) in 1925 based on the theory of elasticity (Timoshenko and Goodier 1934) improved theoretical foundations of gear teeth root strength dimensioning, whereas Robert V. Baud (1894–1970) in 1925 elaborated the stress state of gear teeth by the principles of photoelasticity, which was proved by Timoshenko (Linke 2010). Both highlighted that the basic factor influencing the root strength of a tooth was stress concentration on the fillet, that is a rounding between the dedendum and root circle, needs to be considered.

Wear of gear flanks was recognised even before the end of the nineteenth century on the gears made of grey cast iron. When the wear and pitting continued on steel gears, it was realised that this was due to flank load. Hertzian pressure, which became a measure of the tooth flank load, was formulated by Heinrich R. Hertz (1857–1894) in 1881. Major researchers in the field of gearings studied the application of the Hertzian equation for designing teeth flank, including: August Föppl (1854–1924), who presented Hertz's theory for the first time to a wide circle of engineers in Munich in 1897 (Linke 2010), Earle Buckingham (1887–1978), who studied Hertzian equation regarding the influence of load on flank wear considering the material and the pressure angle and presented his findings to AGMA in 1926; and Gustav Niemann (1899–1982) who in 1938 studied the rolling strength based on to Hertz's theory depending on the surface state, hardness and loading (Seherr-Thoss (Graf von) and Fronius 1965).

With the development of working and energy supplying machines, the mechanical loads and working speeds increased and thereby also the heat produced due to friction, which could have caused severe damage due to the scuffing of teeth flanks. In 1931, Hermann Hofer (1891–1963), who was head of gear development at the ZF factory, suggested that the measure of scuffing risk should be the limit value $A = P\ n_1/b$, with P being the tangential force on the teeth, n_1 rotational speed of the pinion and b the tooth width. With numerous tests on gears of various intended functions and loads (automobile industry—gear-boxes), Hofer obtained a partial limit value A' for each test, and then calculated the average limit value $A = 70{,}000$. This means that particular gear pairs are scuffing resistant during operation if their resistance $S_a = 70{,}000/A' < 1$ (Seherr-Thoss (Graf von) and Fronius 1965).

John O. Almen (1886–1973) was employed at GM's (General Motors) research laboratory and defined the measure of scuffing risk load as the product $PV_{max} < P\,V$, with P being the Hertzian pressure, V the sliding speed of one flank along another at a contact point and PV_{max} experimentally obtained value (Seherr-Thoss (Graf von) and Fronius 1965).

Dutch researcher H. Blok chose flash temperature $T_{fl,max}$ at the most exposed point of contact for the measure of scuffing risk. Blok presented his "flash temperature" concept and equation in 1937. T_{fl} is a consequence of friction and the sliding speed of the contact surfaces. During operation, the teeth are scuffing safe if Blok's flash temperature is lower than the permissible one determined by tests (Blok 1937).

On the basis of these important development milestones we can see that the development of geometric characteristic and the manufacturing of gears from the turn of the century to World War II reached a high level of industrial production in all industrially developed countries. Many new shapes were possible and could have been manufactured by advanced machinery; however, according to the current needs in terms of production and operating features, involute gears were the most appropriate. The production of gear increased along with the growing needs and the expansion of the engineering field.

Several gear types were developed depending on the position of the shafts and transmission rates, e.g. cylindrical, helical, bevel and worm gears. During decades, the cutting technology greatly improved and was supplemented by fine machining for lower surface roughness and heat treatment. New materials, particularly alloy steel, made possible less weight and better durability, and special materials enabled production of gears operating in special atmospheric and temperature conditions. Due to higher complexity and demands, gear manufacturing faced requirements towards smaller tolerances, consequently corresponding machine tools and cutters were developed, as well as necessary measurement equipment. Standards defining gear qualities for various applications were enforced. Unfortunately this also enabled more lethal war machinery helping effective ruination of previous achievements and welfare of our civilisation during WW II. The corresponding knowledge retained and the development soon continued with an accelerated pace in the new millennium. Some notable scientists, who contributed

to new achievements and disseminated their knowledge, are professors H. Winter and B.-R. Höhn from TU Munich, F.L. Litvin from the University of Illinois at Chicago, and D.W. Dudley from California.

11 Recent Development

From the ruins of World War II rose the European Community/the European Union, whose history began in 1950 with the European Coal and Steel Community, which brought together six European countries (European Union, "ECSC Treaty" 2012). The number rose to nine members with the Treaty of Rome. There was a strong need for renovation and consequently for research and development. In 1947, the International Organisation for Standardisation, ISO, was founded in London. The organization says that *ISO* is not an acronym for its full name in either official language; rather, it adopted *iso*, based on the Greek word *isos* (ἴσος, meaning *equal*), as the universal short form of its name (ISO "Discover ISO" 2012). ISO became a network of the national standards institutes of 162 countries, one member per country, with a Central Secretariat in Geneva, Switzerland, that coordinates the system. And within its framework, ISO committee TC60 for gears was founded. The ISO committee coordinates development of recommendations and standards in the field of gears, and its members come from research institutions or gear manufacturers in their countries, where all gear-related activities are conducted. Besides international, there are several national organisations dealing with gears, e.g. AGMA in the USA, BGA in the UK, VDI in Germany, I.E.T. in France, JSME in Japan, and CMSE in China. The International Federation of Theory of Machines and Mechanisms (IFTOMM) was founded in the town of Zakopane, Poland, in 1969, initiated by professor Artabolevky (IFTOMM, "Historical Background," 2012). Its members largely focused on gear researching. Foundation of the theory on elasto-hydrodynamic lubrication is among the most important development of this later period. Regarding production, automated manufacturing of the highest-quality gears is the most prominent. The belief that involute gears are the best solution is still persisting, and a lot of research work has been and is conducted in this context. Despite the engineering industry at the turn of the third millennium can offer almost perfect involute gears, they might not be appropriate for all tasks faced by the industry today.

The perfect, optimal shape of involute gears transmits power by the convex–convex contact. However, the intrinsic property of the involute gear is their curvature radius function in the dedendum part when approaching the base circle. Values in general are small and limit to zero at the base circle and therefore high contact loads in this area. Additionally, for gears with low number of teeth the dedendum flank is comparatively short thus invoking excessive sliding and friction losses. Yet another problem is undercutting of the dedendum area. This was why numerous gear developers sought new solutions to make the teeth flanks of the driving and the driven gears fit together better. In view of this requirement, the

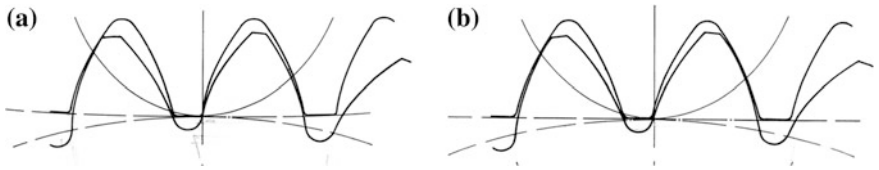

Fig. 17 VBB gearing (Vickers—Bostock—Bramley), **a** gear pair = $30/z_2 = 180$; **b** $z_1 = 30/z_2 = :$ (rack)

concave-convex pair seems an obvious solution, which was precisely what researchers and inventors suggested. Let us mention only a few, the most characteristic ones, in this paper. In 1921, Francis John Bostock (1881–1943) and Swinfen Bramley-Moore filed a patent for the V.B.B. gearing (Fig. 17), which was bought by Vickers shipbuilding company after successful tests in 1924 (Seherr-Thoss (Graf von) and Fronius 1965). The V.B.B. gearing is based on a mathematically defined curved contact path. The tests showed that flank stiffness increased three to four times. With the V.B.B. gearing, Vickers manufactured a large number of turbine gearboxes for powers ranging between 450 and 19.000 HP and rotational speeds between 5.9 and 44.2 m/s. Despite its great initial success, V.B.B. gearing did not survive in practice. H.W. Harisson reported that the reason for this was that it was too noisy during operation and the susceptibility to changes in the distance between axes.

Ernest Wildhaber, a development engineer at Gleason, worked along the same lines. In 1923, he designed and in 1926, he patented a concave-convex gear pair whose flanks are in the form of arcs with the curvature centre near the rolling circles. In 1955, M. L. Novikov designed identical pair of profiles, which he patented in 1956. WN gearing has the point contact of teeth flanks and can operate only as helical gearing. The Wildhaber tooth flank profile is in normal section to the helix, while the Novikov gear profile in Fig. 18 is shown in the front view (in the direction of the gear axis).

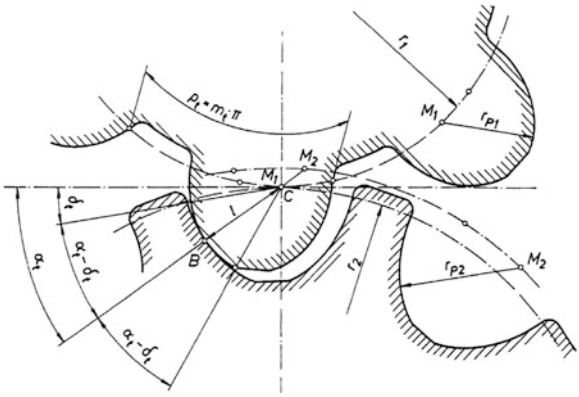

Fig. 18 Wildhaber-Novikov gears

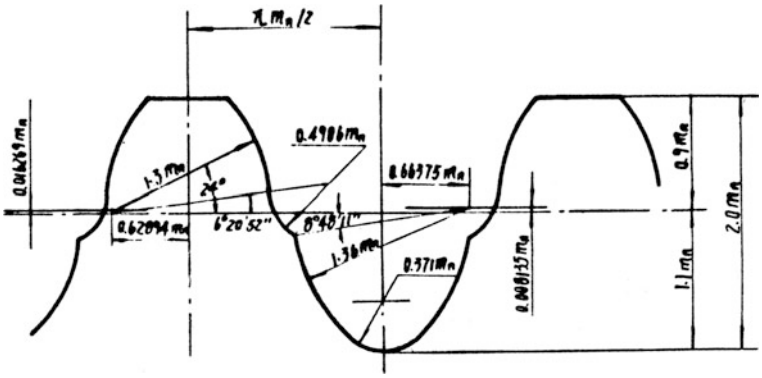

Fig. 19 Rack for WN gear with double teeth contact

Extensive research was carried out on the load-bearing capacity of WN gears. And researchers largely agree (Niemann 1961) that untempered WN gears have approximately three times higher flank strength as the same size involute gears, while surface-hardened or tempered involute gears are superior to WN gears. Wildhaber failed in researching his gear to such extent that would enable users to learn their qualities, so they were never included in production. On the contrary, Soviet engineers did study Novikov gears and use them widely in oil pumps, compressors, tractors, construction machines, etc. The Russians developed the Novikov gear with double contact, as represented on a rack in Fig. 19, which is defined by the Russian standard GOST 17744–72. The Chinese, who follow advancements achieved in Russia, also use WN double-contact gears to a great extent, prescribed by the Chinese standard JB 2940–81.

Another attempt is that of Hawkins, who in 2005 patented non-involute gears with conformal contact. In 2009 G. Hlebanja and J. Hlebanja proposed a new version of WN gears, UPT (uniform power transmission) gears illustrated in Fig. 20. According to this proposal, the tooth flank profile is comprised of three circular arcs, with the first arc forming the addendum; the second forming the dedendum; the third arc forming the intermediate section, which prevents the flanks from touching as they rotate around the kinematic pole C. The advantage of this solution is a simple flank geometry, which is easier in terms of tools, while the relative rotation of one gear vis-à-vis its pair is similar to the movement of the shaft in the bearing. The essential element of the UPT gears is the absence of a pitch line and the gear-teeth contact in the transverse plane. In addition, there is no sliding between the teeth flanks in the transverse plane. Power is mainly transmitted by the rolling of the teeth flanks at both contact points, with the simultaneous sliding of the teeth flanks around the pitch point C. The contact load is divided into two contact points. Better lubrication conditions can be expected as a result of the thicker oil-film thickness and lower heat generation. And the most important features of the UPT gears are non-intermittent sliding and power transmission. These features indicate that UPT gears can be used with heavy loads

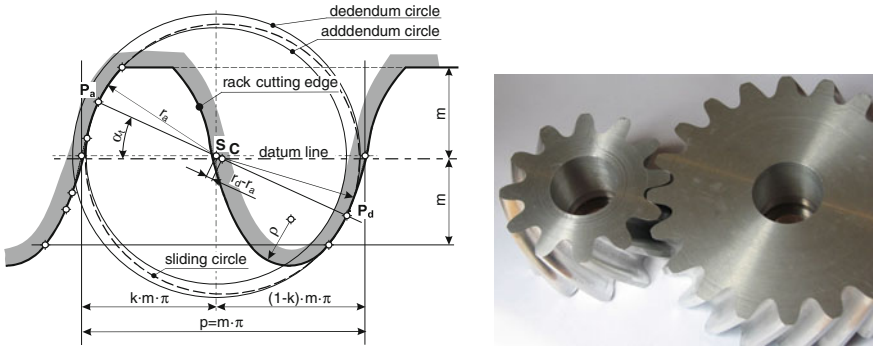

Fig. 20 UPT gears proposed by Hlebanja; rack profile (*left*); UPT gear pair with $m_n = 5$ mm; $z_1 = 12$, $z_2 = 20$

in non-stop operating condition, for example, in the power transmission of wind turbines, gear units for refinery services, and similar applications.

In the latest period of the development of gear, the belief that involute gears are the best shape persisted, and therefore remained the focus of research. Consequently, at the turn of the second millennium, the engineering industry can manufacture almost perfect involute gears, which sometimes face new problems, deriving from new applications. Therefore, the authors believe that non-involute geometry can be advantageous in this respect. Recently, G. Hlebanja and J. Hlebanja (2010) presented a new method of designing gears based on the basic rack tooth profile, as shown by Fig. 21. The basic rack tooth profile is defined by a mathematical function and according to the fundamental law of gearing for each point P_i of the base rack profile a single point U_i on the path of contact can be assigned and based on that a unique point G_i on the gear tooth flank. The basic rack profile is defined as an analytic curve, Eq. (1).

$$y_{Pi} = a_p(1 - (1 - x_{Pi})^n) \tag{1}$$

where (x_{Pi}, y_{Pi}) are Cartesian coordinates originating in the pitch point C, a_p parameter designating a size factor, and n is the exponent. Both, a_p and n, have decisive influence on expected characteristics of the designed gears. Eq. (1) defines the addendum part of the rack profile and the half symmetric counterpart defines its dedendum part. The path of contact is unique for a given module regardless of the number of teeth. The mating gears exhibit convex-concave contact in the vicinity of the contact start and contact end. Another advantage is minimal teeth number of S-gears, which can be as low as four. The S-gear tooth flank profile assures higher comparative curvature radii, and thus lower contact load and higher relative velocities of the contact surfaces which imply better lubrication. Due to their S-shape, the velocity characteristics of mating gears are improved, especially in both external areas with high relative velocities and low sliding velocity. The meshing start zone in involute gears represents potential danger of micro-pitting, whereas S-gears exhibit advantage in this context due to the ticker oil film in this

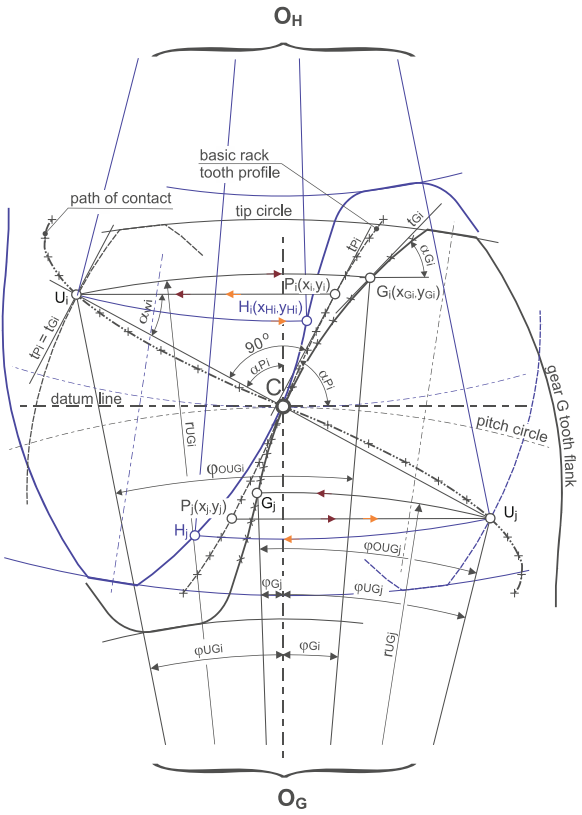

Fig. 21 Generation of a gear tooth flank from the basic profile of S rack

area, which diminishes possibility of damage. Another important feature of the S-gears is more evenly distributed contact point density, which causes lower sliding and less power losses. The dedendum flank of pinion is not substantially smaller as that of gear addendum even for low number of teeth. This is why authors believe this gear type can be a successful substitute for involute gears for diverse applications, like gear-boxes for wind power-plants on the large scale and miniature plastic gears for domestic appliances.

12 Conclusion

Millennia ago, humans invented machines driven by animals which could perform useful work for them. Energy is transmitted by the movement of gears to those elements which perform the given task. In all periods, from the first irrigation devices along the Nile to this day, gears have been essential composite parts of machines, transmitting energy from the source to the user. For millennia, wood was the only material available for making gears, and humans or animals the only sources of energy. This machine system was still used in agriculture in the first half

of the twentieth century. The first iron gears date back to when the steam engine became the source of power, while the use of involute machines date back to Euler. Machines for manufacturing gears followed industrial needs of the 19th century and were further developed with the accelerated pace in the 20th century. In-depth scientific work and standardisation followed after World War I. After WW II, Wildhaber-Novikov gears were developed, which are widely used in Russia and China, while involute gears are preferred in the West. In spite of that many efforts have been made to design even better geometry. S-gears can be regarded in this way, with some features, which can cope with arising problems with new industrial applications with standardised involute gears.

One of the great names of gear science is Darle W. Dudley, who presented the development of gears at a conference on gears in 1988 in Zhengzhou in China, concluding his presentation with a centennial forecast. The set targets have already been achieved and even exceeded in the 25 years since. Today, we can also concur that the difference in the rotational speed of energy and working machines is not overcome. This cannot be always solved by direct driving electro-motors, which means that gears and the development of the field will still be needed.

It is also important to mention the Balkan Association of Power Transmissions, which started under the initiative of professor Arnaudow from Sofia to promote research in this field. BAPT presidency is currently held by professor Dobre, who also organises the 4th International conference on power transmissions in Sinaia.

References

Agricola G (1556) De Re Metallica. Agricola G (1912) The mining magazine (trans: Hoover HC, Hoover LC). London

Blok H (1937) Measurement of temperature flashes on gear teeth under extreme pressure conditions. In: Proceedings of general discussion lubrication 2, Institution of Mechanical Engineers, p 14–20

Complete Dictionary of Scientific Biography (2008a) "La Hire, Philippe De," from Encyclopedia.com. http://www.encyclopedia.com/doc/1G2-2830902429.html. Accessed 7 Apr 2012

Complete Dictionary of Scientific Biography (2008b) "Camus, Charles-Étienne-Louis," from Encyclopedia.com: http://www.encyclopedia.com/doc/1G2-2830900770.html. Accessed 7 Apr 2012

de la Hire P (1694) Mémoires de mathématique et de physique. Impr. Royale, Paris

DIN 867 (1927) Bezugsprofile für Evolventenverz. An Stirnrädern (Zylinderr.) für allgem. Maschinenbau und den Schwermaschinenbau

Dohrn-Van Rossum G (1996) History of the hour: clocks and modern temporal orders. (trans: Dunlap T). The University of Chicago Press, Chicago. ISBN 0226155102

Dudley WD (1988) Gear technology—past, present, and future. In: Proceedings of international conference on gearing, 5–10 Nov 1988, Zhengzhou, China

Encyclopædia Britannica Online, s.v. "James Watt". http://www.britannica.com/EBchecked/topic/637673/James-Watt. Accessed 15 Apr 2012

Encyclopædia Britannica Online, s.v. "pendulum". http://www.britannica.com/EBchecked/topic/449736/pendulum. Accessed 27 Mar 2012

Encyclopædia Britannica Online, s.v. "Sir Charles Algernon Parsons". http://www.britannica.com/EBchecked/topic/444719/Sir-Charles-Algernon-Parsons. Accessed 7 May 2012

Encyclopædia Britannica Online, s.v. "Girard Desargues". http://www.britannica.com/EBchecked/topic/158756/Girard-Desargues. Accessed 6 Apr 2012
Encyclopædia Britannica Online, s.v. "Galileo". http://www.britannica.com/EBchecked/topic/224058/Galileo. Accessed 6 Apr 2012
Euler L (1760) Novi Commentarii academiae scientiarum Petropolitanae 5, 1760, pp 299–316
European Union, s.v. "Treaty establishing the European Coal and Steel Community, ECSC Treaty". http://europa.eu/legislation_summaries/institutional_affairs/treaties/treaties_ecsc_en.htm. Accessed 7 May 2012
Hawkins RM (2005) Non-involute gears with conformal contact. US Patent No. 6,837,123, dated 4 Jan 2005
Hermann Pfauter Werkzeugmaschinenfabrik (1976), Ludwigsburg (Hrsg.): *Pfauter-Wälzfräsen Teil 1. 2. Auflage*. Springer, Berlin 1976, ISBN 3-540-07446-5
Hertz H (1881) Über die Berührung fester elastischer Körper. Journal für die reine und angewandte Mathematik 92:156–171
Hlebanja G, Hlebanja J (2009) Uniform power transmission gears. J Mech Eng 55(7/8):472–483
Hlebanja J, Hlebanja G (2010) Spur gears with a curved path of contact for small gearing dimensions. VDI Berichte 2108:1281
ISO, "Discover ISO". http://www.iso.org/iso/about/discover-iso_isos-name.htm. Accessed 7 May 2012
Jungfrau Railway http://www.jungfrau.ch/en/quick-navigation/top-of-europe/jungfrau-railways/. Accessed 15 Apr 2012
Linke H (2010) Stirnradverzahnung, 2., vollständig überarbeitete Auflage. Hanser
Litvin FL (1997) Development of gear technology and theory of gearing. NASA Lewis Research Center, Cleveland
Matschoß C (1925) Männer der Technik: Ein biographisches Handbuch. VDI, Berlin
Matschoß C (1940) Geschichte des Zahnrades. VDI, Berlin
Niemann G (1961) Novikov gear system and other special gear systems for high load carrying capacity. VDI Berichte, p 47
Novikov ML (1956) U.S.S.R., Patent no. 109,750, 1956
Reuleaux F (1861) Der Constructeur. Vieweg, Braunschweig
Sang E (1852) A new general theory of the teeth of wheels. A&C Black, Edinburgh
Seherr-Thoss (Graf von) HC, Fronius S (1965) Die Entwicklung der Zahnrad-technik: Zahnformen und Tragfähigkeitsberechnung. Springer, Berlin
Siemens, s.v. "Siemens history, Transportation". http://www.siemens.com/history/en/innovations/transportation.htm. Accessed 7 May 2012
The Antikythera Mechanism Research Project (AMRP). http://www.antikythera-mechanism.gr. Accessed 23 Mar 2012
The Euler Archive, s.v. "E249—De aptissima figura rotarum dentibus tribuenda". http://www.eulerarchive.com/. Accessed 15 Apr 2012
Timoshenko SP, Goodier JN (1951) Theory of elasticity, 2nd edn. McGraw-Hill, New York
IFTOMM, v.s. "Historical Background". http://www.iftomm.org/index.php?option=com_content&view=article&id=8&catid=7&Itemid=112. Accessed 7 May 2012
Wikipedia, s.v. "Antikythera mechanism". http://en.wikipedia.org/wiki/Antikythera_mechanism. Accessed 23 Mar 2012
Wikipedia, s.v. "Vitruvius". http://en.wikipedia.org/wiki/Vitruvius. Accessed 23 Mar 2012
Wikipedia, s.v. "Heron of Alexandria". http://en.wikipedia.org/wiki/Heron_of_Alexandria. Accessed 23 Mar 2012
Wikipedia, s.v. "List of ancient watermills". http://en.wikipedia.org/wiki/List_of_ancient_watermills. Accessed 23 Mar 2012
Wildhaber E (1926) Helical gearing. US patent no. 1 601 750, issued 5 Oct 1926
Willis R (1841) Principles of mechanism. University Press, Cambridge

Recent Development of Non-Involute Cylindrical Gears

Gorazd Hlebanja and Jože Hlebanja

Abstract The paper represents an overview over the development of gears aiming to improve contact circumstances during meshing. It is well known fact that classical involute gears form a convex–convex contact during meshing and that the curvature radius value is very low in the vicinity of the basic circle. Corresponding research was focused in development of gears with convex-concave contact. Therefore, a gradual development of gears with a curved path of contact is presented below. Furthermore, attempts to extend these concepts to various gear types and applications are also presented in the paper.

Keywords Gears · Power transmission · Non-involute gears · Curved path of contact · S-gears

1 Introduction

Gears are necessary in accurate power and rotation transmission from a motor (power supply) to a work machine. Uncountable work machines have been invented; however, they govern numerous processes with various rotational speeds. Also numerous power machines have been developed with ever increasing speed. Increasing input speed and variety of output speeds of pairs power-work machines imply more sophisticated geared transmissions each new generation.

Requirements, to which power-transmissions should comply and which imply their functionality, are becoming higher every day, so wide spread scientific

G. Hlebanja (✉) · J. Hlebanja
University of Ljubljana, Ljubljana, Slovenia
e-mail: gorazd.hlebanja@fs.uni-lj.si

J. Hlebanja
e-mail: joze.hlebanja@siol.net

G. Dobre (ed.), *Power Transmissions*,
Mechanisms and Machine Science 13, DOI: 10.1007/978-94-007-6558-0_5,

research is necessary and resulting progress notable. In this respect are many research institutions, which have human resources and specialized equipment, also financially funded by manufacturers and sometimes even by governmental sources.

We should also point out some basic development and economic trends:

- working power of energy supplying machines and demands for working machines are increasing;
- rotational speed and variety of speeds of such machine pairs are increasing;
- capacity of working machines and automation production are higher;
- power flow is increasing;
- higher loads and more demanding working circumstances of such gears;
- gears endurance for the entire life cycle is becoming a law;
- requirements towards lower vibrations and less noise and uniform running are becoming higher;
- production capacities all over the world are high, prices of gear transmissions are lowering.

All above directs to the search of new ways to improve competitive abilities of gear manufacturers.

2 Basic Principles

The basic principles of contemporary gearings were discovered in 1733 by Charles-Étienne Louis Camus (1699–1768), a mathematician and professor from Paris (Complete Dictionary of Scientific Biography, "Camus, Charles-Étienne-Louis," 2008) and independently by famous Leonhard Euler in 1752. Camus defined the conditions that have to be fulfilled for a pair of gears in his work "Sur la figure des dents des roués et des ailes des pignons pour rendre les horologes plus parfaits". This condition is defined by the following: if, in uniform rotation, power is to be transmitted via a pair of teeth, then the normal to the teeth flanks at the contact point P on the path of contact must pass through the pitch point C (Matschoß 1940), as illustrated in Fig. 1, which is exactly the law of gearing known today.

Leonhard Euler (1707 Basel–1783 St. Petersburg) sought the most advantageous shape of gear teeth flanks, and according to Jacobi, (The Euler Archive 2012) in 1752 he was the first to publish a treatise on the usefulness of the involute for the shape of gear teeth flanks (Euler 1760). His concept of involute gearing is in common use today. He also showed how to graphically determine the radii of curvature as represented in Fig. 2.

Cycloids, involutes and rolling curves can be used to form gear teeth according to the law of gearing.

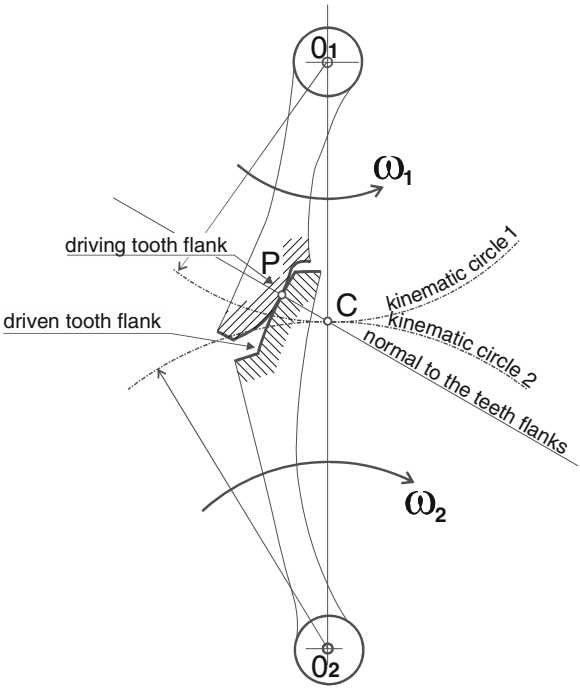

Fig. 1 The law of gearing

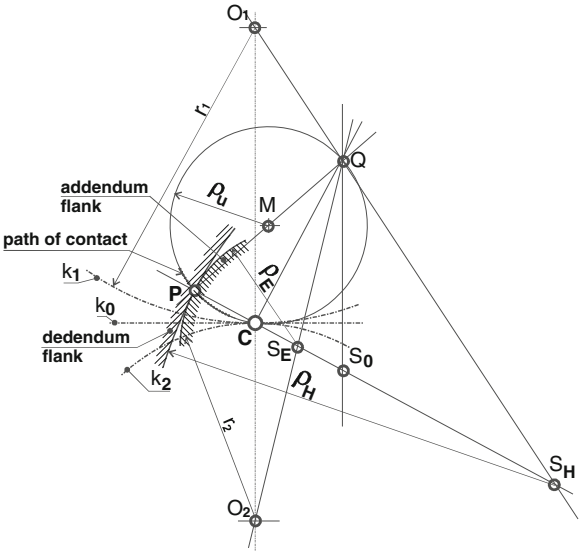

Fig. 2 Graphical determination of the radius of curvature after Euler-Savary

3 Curved Path of Contact

Gradual development evolved in the perfect, optimal shape of involute gears which transmit power by the convex–convex contact. However, the intrinsic property of the involute gear is their curvature radius function in the dedendum part when approaching the base circle. Values in general are small and limit to zero at the base circle and therefore imply high contact loads in this area. Additionally, for gears with low number of teeth the dedendum flank is comparatively short thus invoking excessive sliding and friction losses. Yet another problem is undercutting of the dedendum area. This was why numerous gear developers sought new solutions to make the teeth flanks of the driving and the driven gears fit together better. In view of this requirement, the concave-convex pair seems an obvious solution, which was precisely what researchers and inventors suggested. However, this paper is focused on gradual development of S-gear shape.

The aim was to define tooth flanks of adequate characteristics. This was achieved by the curved path of contact which implies a concave-convex fit of the meshing gear teeth flanks. The path of contact is a sequence of contact points of the meshing gear pair, which transmits rotation, and each contact point should comply with the law of gearing at the same time. The path of contact should warrant sufficiently high contact ratio. The contact load in the kinematic pole C depends on the pressure angle α_C. The starting pressure angle α_A should be also limited. The sector defined by points A, C, 1 (Fig. 3) represents the zone of possible paths of contact. The condition for manufacturing gears of the same module with arbitrary number of teeth by the same tool profile is the half-symmetrical path of contact.

Gears are designed according to their root strength and flank durability. The path of contact shape and the root fillet influence the root thickness. However, the flank shape essentially influences its durability. The most important factors influencing flank durability are the reduced radius of curvature and sliding. The higher radii imply lower Hertzian pressure. The sliding circumstances are essentially improved in the case of convex-concave contact. The research showed that

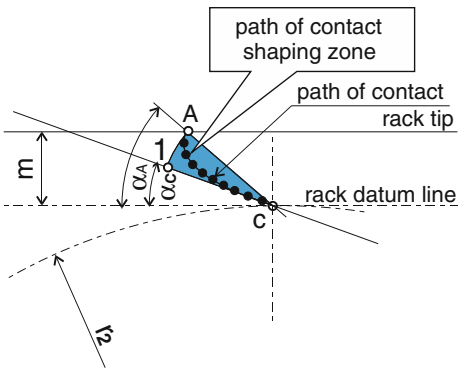

Fig. 3 Path of contact shaping zone (Hlebanja 1976)

areas of the path of contact with a higher curvature imply lower sliding and higher reduced radii of curvature. Due to necessity of the stronger oil film in the meshing start zone the path of contact curvature in that area should be higher and the path of contact gets a distinctive S-form.

This tooth flank form was used in grooved roller gear for rolling mills. It was installed in Sisak rolling mill. It transmitted 1500 kW at 80 up to 160 RPM. Material was alloy steel 30CrMoV9. The tooth profile is illustrated in Fig. 4. Initially the involute gearing was installed, which suffered severe scuffing in the gear teeth dedendum and addendum areas. S-formed gearing was an essential improvement. This gear form was also reported in Niemann and Winter (1989).

4 S-Shaped Path of Contact

Subsequent research was oriented to define the S-gear path of contact in such a way to ensure smaller flank pressure, better lubrication and less sliding and which would be linear or almost linear in the vicinity of the kinematic pole C. Figure 5

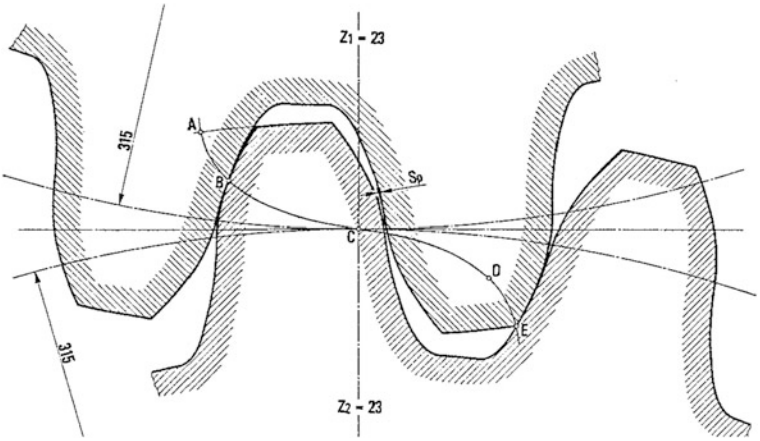

Fig. 4 Industrial implementation (Hlebanja 1976)

Fig. 5 Path of contact with gradually increasing curvature

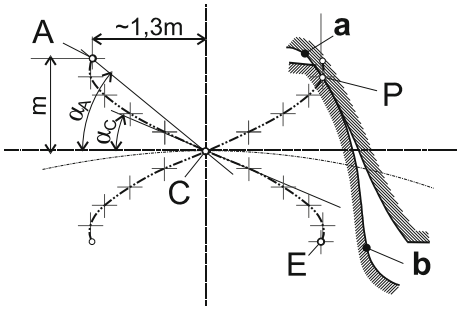

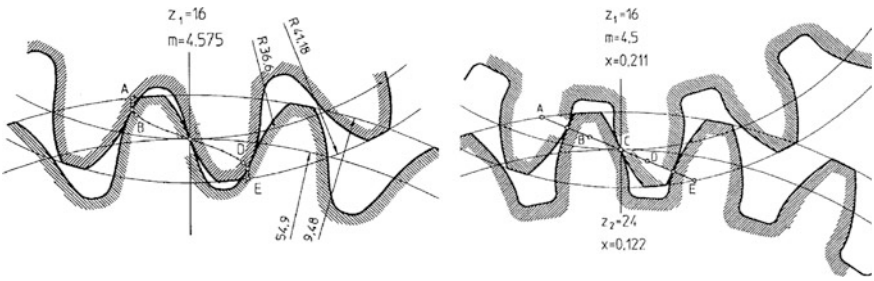

Fig. 6 Gear pairs for comparison: (*left*) S-gears, (*right*) E-gears

represents such a path of contact, with the basic characteristic of gradual increase of curvature towards the meshing start and end and corresponding gear and pinion flanks.

Furthermore, the research was conducted in order to compare S- and E-gears. First, typical characteristics have been calculated for both gear types and later experiments on the FZG-machine were carried out. Both gear pairs are illustrated in Fig. 6.

Therefore, S- and E- gears are to be compared regarding damages, which might appear during operation: (a) fracture due to overloading; (b) damages of tooth flanks due to pitting; (c) cold and hot scuffing; and (d) wear of tooth flanks.

Regarding endurance against tooth fracture, the measure of such endurance is the tooth root stress, which further depends on the tooth root thickness and fillet radius. It was demonstrated in this particular case that the S-gear teeth are stronger in the root, as well as their fillet radius is larger, which also imply that S-type teeth are stronger for approximately 20 %.

The contact load of teeth flanks is evaluated by Hertzian pressure σ_{H}. For cylindrical surfaces we have:

$$\sigma_H = \sqrt{\frac{F \cdot E}{2\pi(1-\nu^2)\,l} \cdot \frac{1}{\rho_{red}}} = 0,418\sqrt{w \cdot E'} \cdot \sqrt{\frac{1}{\rho_{red}}} \tag{1}$$

However, Hertzian pressure may not exceed maximal allowable limit σ_{Hdop}. The contact force F, the tooth width l and the reduced radius of curvature ρ_{red} are those design parameters which decisively influence gear durability. Calculated values for σ_{H} are represented for both, i.e. S- and E-gears on Fig. 7. It should be pointed out that the Hertzian pressure and pressure angle α_{C} in the kinematic pole C are equal for both gear types.

The measure of endurance against damages of tooth flanks is oil film thickness h_0, which is defined by the Dowson-Higginson's (1977) equation:

$$h_0 = 1,6 \cdot \alpha^{0,6} \cdot \eta_0^{0,7} \cdot E^{0,03} \cdot w^{-0,13} \cdot \rho_{red}^{0,43} \cdot u^{0,7} \tag{2}$$

Factors in the above Eq. (2) are: α—the pressure coefficient of oil; η_0—dynamic viscosity; E—module of elasticity; w—line load of teeth, i.e. F/l; ρ_{red}—reduced

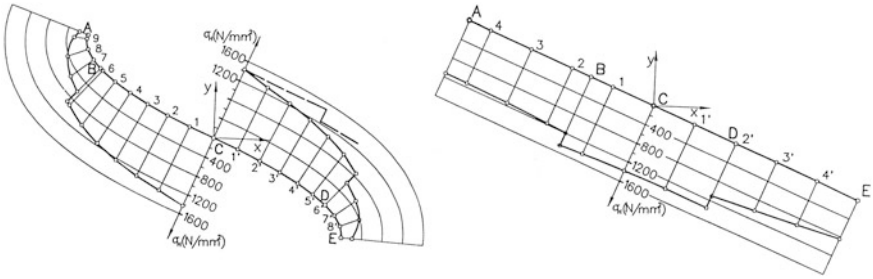

Fig. 7 Hertzian pressure (*left*) S-gears, (*right*) E-gears

radius of curvature; and u—sum of relative velocities. Having equal loads of S- and E-gears, equal lubrication means, the same rotational speeds and equal gear materials, the only remaining parameters influencing the oil film thickness are the reduced radius of curvature ρ_{red} and the sum of relative velocities u. Both have better characteristics for S-gears (i.e. higher relative velocities, higher reduced radii of curvature) and therefore imply better lubrication and thicker oil film. Figure 8 represents velocity circumstances in the vicinity of the meshing start.

Another important issue is a temperature characteristic of a meshing gear pair. Blok's temperature concept (Blok 1963), represented in Eq. 3 is adopted here.

$$\vartheta_{fl} = 0,62\mu w^{0,75}\left(\frac{E\prime}{\rho_{red}}\right)^{0,25}\frac{|v_{rS} - v_{rP}|}{\sqrt{B_{MS}v_{rS}} + \sqrt{B_{MP}v_{rP}}} \tag{3}$$

Symbols in the equation are: ϑ_{fl}—"flash" temperature; μ—friction coefficient; w—contact load (line load); ρ_{red}—reduced radii of curvature; v_{rS}, v_{rP}—relative velocities of the flanks in contact; B_{MS}, B_{MP}—property of material; $B_M = \lambda\ \rho\ c$, where λ stands for thermal conductivity, ρ for material density and c for specific heat. The friction coefficient is given by (Niemann and Winter 1989)

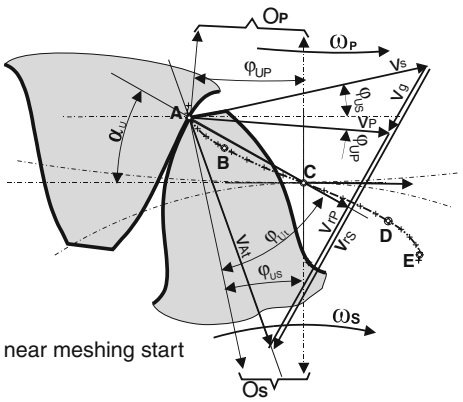

Fig. 8 Velocities in the vicinity of the meshing start $u = v_{rP} + v_{rS}$

$$\mu = 0,12 \cdot \left(\frac{w \cdot R_a}{\eta \cdot u \cdot \rho_{red}} \right)^{0,25} \quad (4)$$

where additional factors are u—sum of the relative velocities and R_a—average surface roughness. Figure 9 illustrates behaviour of the flash temperature along the path of contact.

5 Experiments

Experiments have been conducted in order to examine endurance against:

- Pitting of tooth flanks
- Scuffing of tooth flanks
- Surface heating, wear and efficiency.

Experimental work has been carried out on a FZG testing machine, so values for the module and the centre distance were adapted accordingly. The selected material was alloy steel 42CrMo4, which was heat treated to 28–30 HRC prior to toothing. Experimental lots comprised (a) hardened and tempered gears "V" and (b) hardened, tempered and plasma nitrided gears "NV". Technical data of gears are collected in Table 1.

Experimental results with regard to pitting are summarised in Woehler diagrams, Fig. 10. Results indicated that the load capacity for hardened and tempered S-gears was slightly increased, whereas for hardened, tempered and nitrided S-gears the load capacity was bigger as that for E-gears. However, more experiments would have been necessary.

Hardened, tempered and nitrided S- and E-gears have been tested with regard to scuffing. Experiments were conducted according to the load levels prescribed by DIN 51354. E-gears exhibited scuffing damages of the addendum part of the flanks already at the load level 11, whereas S- gears did not have damages even at the level 12. Oil ISO VG 100 without additives was used in both cases. Lubrication

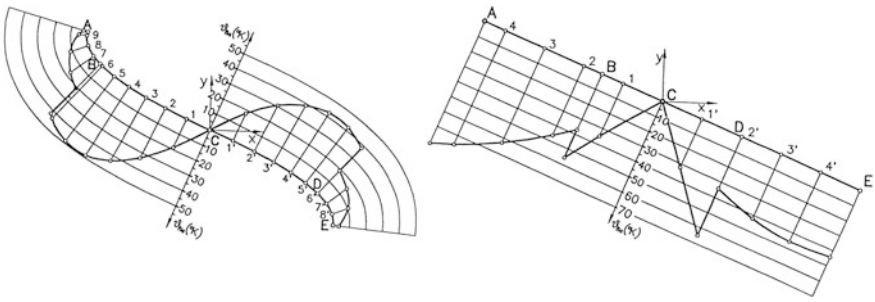

Fig. 9 Flash temperatures along the path of contact (*left*) S-gears, (*right*) E-gears

Table 1 Data of the gears used in experiments

	Designation	S-gears		E-gears	
Module	m_n [mm]	4,575		4,5	
Number of teeth	z	16	24	16	24
Coefficient of the profile shift	x	–	–	+0,233	+0,12
Kinematic circle diameter	d_w[mm]	73,2	109,8	73,2	109,8
Pressure angle in C	α_C [^{0}]	22		22,438	
Face width	b [mm]	20		20	
Centre distance	a [mm]	91,5		91,5	
Rotational speed	n [min^{-1}]	2100	1400	2100	1400

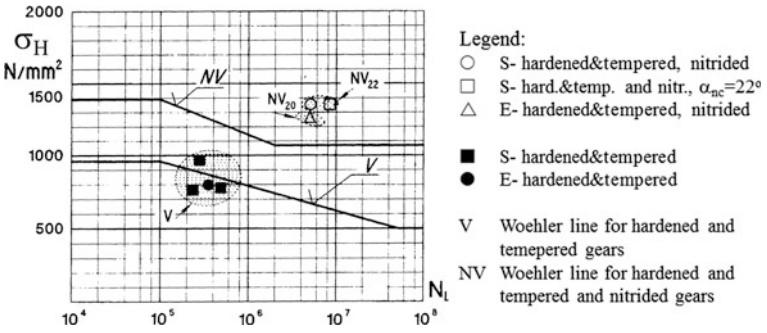

Fig. 10 Woehler diagrams of the pitting experiments

procedure was with gears dipped into the oil. The oil temperature in the casing was 90 °C in both cases. Each loading level lasted for 15 min. The oil temperature in the casing during this time increased due to friction losses of the operating gears. Measurement of temperatures clearly indicated that oil in the casing was less heated in the case of S-gears, which implies that losses in this case were lower. The difference in the temperature increase between S- and E-gear type was approximately 10 %.

Wear of gear tooth flanks was determined during the pitting tests by weighting gear pairs in a precision balance. Weighting was conducted before and after experiments for both gear types. The experiment on the FZG loading level 9 lasted 4×10^6 rotations of the pinion. Results are summarised in Table 2. It can be concluded that the wear of S-gears is approximately half of that in E-gears, which can be attributed to the ticker oil film. More information can be found in Hlebanja and Okorn 1999.

Design work with the S-type path of contact, which was first used for spur gears, continued in the direction of other gear types in order to explore their usability (Hlebanja and Hlebanja 2005):

Table 2 Wear measured by a balance

Gear type	Load level according to DIN 51354	Wear [mg]		
		Pinion	Gear	Sum
S-	9	17	16	33
S-	9	15	8	23
E-	9	41	21	62

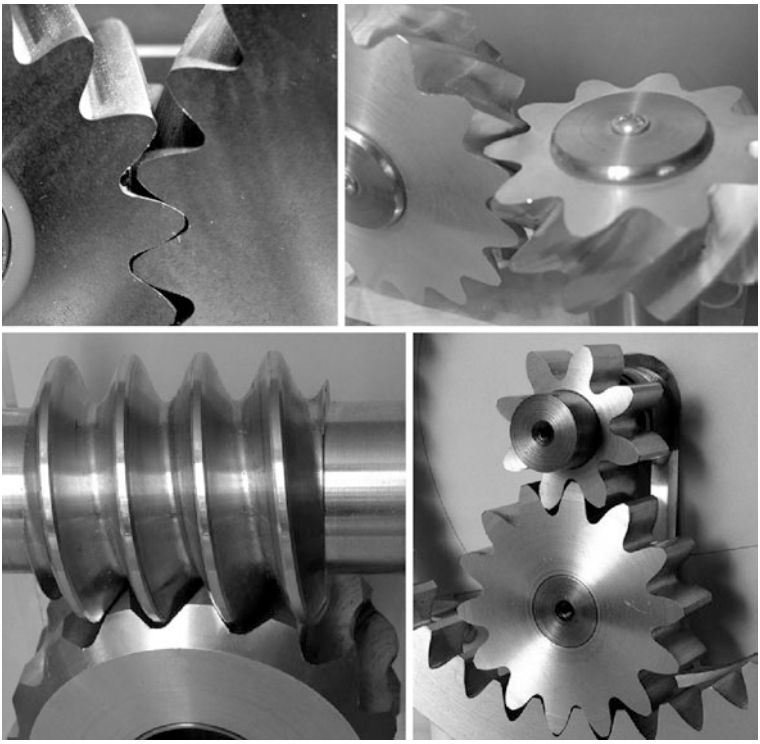

Fig. 11 Working models for various S-type gearings **a** helical; **b** crossed helical; **c** ZS worm drive;**d** planetary arrangement

- Helical gears
- Crossed helical gears
- ZS worm drives
- Internal S-gears for planetary gear trains.

Working prototypes or models were produced for the each type, as revealed from Fig. 11.

6 Recent Development

Another proposal are cylindrical worm-gearings with a progressively curved shape of teeth flanks, the so called parabolic worm gear drives (Hlebanja et al. 2009), Fig. 12. The proposed approach in cylindrical worm gearings design is based on the mathematically defined worm tooth profile in the worm axial plane, wherefrom the worm gear tooth profile derives and profiles in any parallel plane can be calculated and in this way teeth flanks are defined. The primary feature of the proposed teeth flanks is their progressive curvature and continual concave-convex contact. Worm and worm gear meshing of such an arrangement generates better lubricating oil film, resulting in better EHD lubrication conditions, therefore reduced energy losses and lower wear damages are anticipated. An experimental worm-gearing loaded under working conditions verified theoretical considerations. Computer simulation also confirmed contact theory of the proposed gearing.

G. and J. Hlebanja (2009) proposed a new version of WN gears, UPT (uniform power transmission) gears illustrated in Fig. 13. According to this proposal, the tooth flank profile is comprised of three circular arcs, with the first arc forming

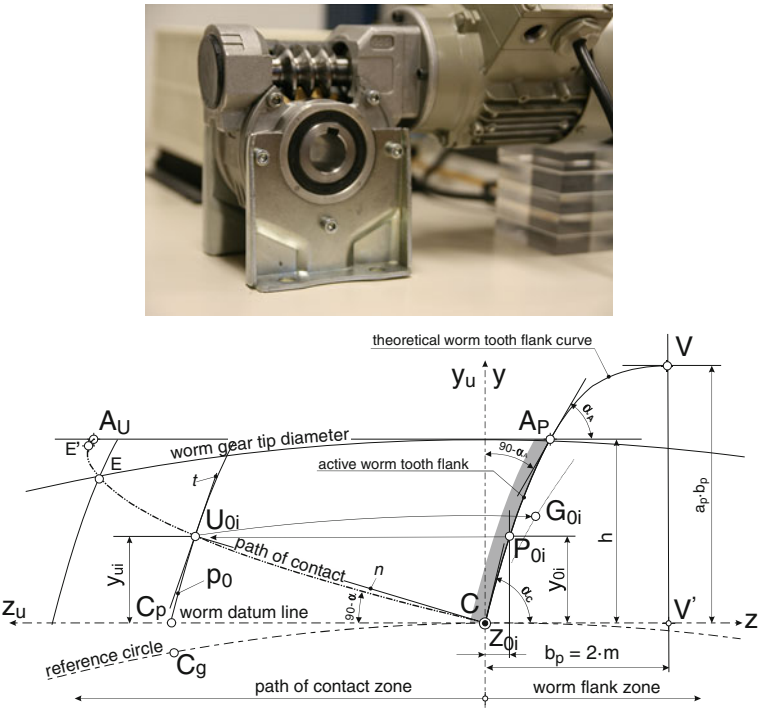

Fig. 12 Parabolic worm-gearing; industrial housing after an observation window had been cut off (*above*); worm tooth basic profile and the corresponding path of contact in the axial section (*below*)

the addendum; the second forming the dedendum; the third arc forming the intermediate section, which prevents the flanks from touching as they rotate around the kinematic pole C. The advantage of this solution is a simple flank geometry, which is easier in terms of tools, while the relative rotation of one gear vis-à-vis its pair is similar to the movement of the shaft in the bearing. The essential element of the UPT gears is the absence of a pitch line and the gear-teeth contact in the transverse plane. In addition, there is no sliding between the teeth flanks in the transverse plane. Power is mainly transmitted by the rolling of the teeth flanks at both contact points, with the simultaneous sliding of the teeth flanks around the pitch point C. The contact load is divided into two contact points. Better lubrication conditions can be expected as a result of the thicker oil-film thickness and lower heat generation. And the most important features of the UPT gears are non-intermittent sliding and power transmission. These features indicate that UPT gears can be used with heavy loads in non-stop operating condition, for example, in the power transmission of wind turbines, gear units for refinery services, and similar applications.

Hlebanja and Hlebanja (2010); Hlebanja (2011) developed S-gear concept from the S-shaped path of contact to the S-shaped rack profile. This method of designing gears based on the definition of the basic rack tooth profile. It is defined by a mathematical function and according to the fundamental law of gearing for each point P_i of the base rack profile a single point U_i on the path of contact can be assigned and based on that a unique point G_i on the gear tooth flank. The basic rack profile is defined as an analytic curve, Eq. (5).

$$y_{Pi} = a_p(1 - (1 - x_{Pi})^n) \tag{5}$$

In this way we have a clearly defined cutting tool and arbitrary gears defined through this rack profile by proper coordinate transformations. The size factor a_p and the exponent n can also be optimised in order to achieve required results, e.g. ticker root, or the size of convex-concave area, as it can be seen from Fig. 14. The

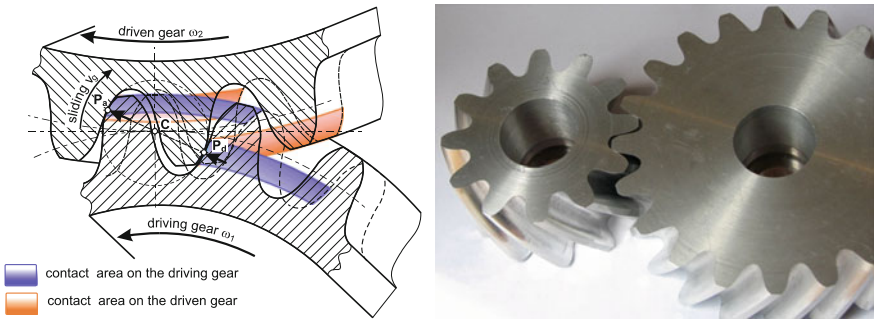

Fig. 13 UPT gears proposed by Hlebanja; contact areas (*left*); UPT gear pair with $m_n = 5$ mm; $z_1 = 12$, $z_2 = 20$

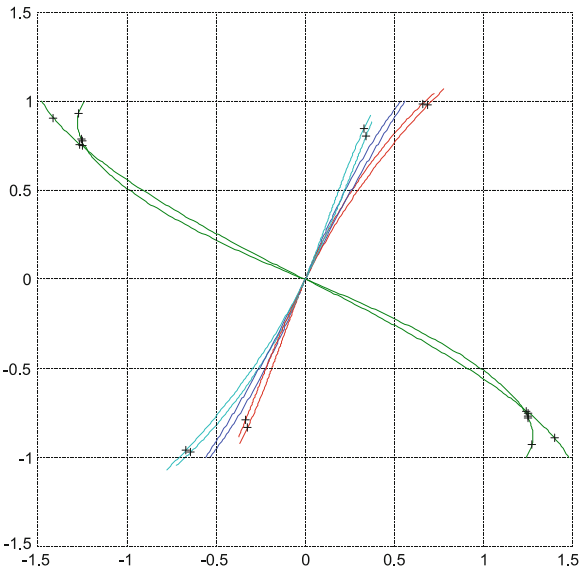

Fig. 14 Influences of parameter changes on gear and path of contact shapes

diagram shows how the change of vital parameters influences the path of contact, gear and pinion tooth flank shape and the rack profile.

The crucial characteristics of the S-gear concept are summarised in the following paragraph. The mating gears exhibit convex-concave contact in the vicinity of the contact start and contact end. The minimal teeth number of S-gears can be as low as four. The S-gear tooth flank profile assures higher comparative curvature radii, and thus lower contact load and higher relative velocities of the contact surfaces which imply better lubrication. Due to their S-shape, the velocity characteristics of mating gears are improved, especially in both external areas with high relative velocities and low sliding velocity. The meshing start zone in involute gears represents potential danger of micro-pitting, whereas S-gears exhibit advantage in this context due to the ticker oil film in this area, which diminishes possibility of damage. Another important feature of the S-gears is more evenly distributed contact point density, which causes lower sliding and less power losses. The dedendum flank of pinion is not substantially smaller as that of gear addendum even for low number of teeth.

7 Conclusion

Let us summarise this paper with some advantages of the S-gears and dissimilarities from the E-gears.

The list of improvements over the E-gears starts with a higher root strength of the S-gears due to thicker teeth in the root and bigger fillet radius. A higher

strength of flanks can be attributed to the S gears, which is due to the convex-concave contact, implying lower Hertzian stress. Thicker oil film implies less wear, lower losses and better efficiency. Due to convex-concave contact and high relative velocities in the meshing start area the thicker oil film forms there, preventing scuffing and makes tip relief in S-gears unnecessary. For many common applications nitriding may be sufficient procedure, which makes special heat treatment and subsequent grinding unnecessary. S-gear gaps are thinner, which implies less cut material. The contact point density of the S-gears is more evenly distributed, which causes lower sliding and less power losses.

However, the acting force varies in accordance with pressure angle deviations along the curved path of contact, which is dissimilar to the involute case. The centre distance depends on the number of teeth and the module. The profile corrections are limited in comparison to the E-gears. And due to the curved path of contact there is some sensitivity to centre distance deviations. However, quite many industrial applications incorporating gears with the curved path of contact ran successfully for many years. An attempt has been made to construct the path of contact with a small linear part in the vicinity of the kinematic pole C. And even for the path of contact without such a linear segment it can be observed, that its mid-part near C is almost linear.

We can also state that the S-gears are new, without routine production experience and standards and with little practical experience. However, already mentioned advantages make authors believe that this gear type can be a successful substitute for involute gears for diverse applications, like gear-boxes for wind power-plants on the large scale and miniature plastic gears for domestic appliances.

References

Blok H (1963) The flash temperature concept. Wear 6 (Nov): 483–494

Complete Dictionary of Scientific Biography (2008) Camus, Charles-Étienne-Louis, from Encyclopedia.com: http://www.encyclopedia.com/doc/1G2-2830900770.html, accessed 7.4.2012

Dowson D, Higginson GR (1977) Elasto-Hydrodynamic Lubrication. Pergamon Press, SI Edition

Euler L (1760) Novi Commentarii academiae scientiarum Petropolitanae 5, 1760, pp 299–316

Hlebanja J (1976) Konkav-konvexe Verzahnung Ermitlung der Zahnflanken und einige Grenzfälle. Antriebstechnik 15 Nr. 6, p 324–329

Hlebanja J, Okorn I (1999) Charakteristische Eigenschaften von Zahnrädern mit stetig gekrümmter Eingriffslinie. Antriebstechnik, Jg. 38, Nr. 12, p 55–58

Hlebanja, J, Hlebanja G (2005) Anwendbarkeit der S-Verzahnung im Getriebebau : Nichtevolventische Verzahnungen weiterentwickelt. Antriebstechnik, Jg. 44, Nr. 2, p 34–38

Hlebanja G, Hlebanja J, Čarman M (2009) Cylindrical wormgearings with progressively curved shape of teeth flanks. J Mech Eng 55(1):5–14

Hlebanja G, Hlebanja J (2009) Uniform power transmission gears. J Mech Eng 55(7/8):472–483

Hlebanja J, Hlebanja G (2010) Spur gears with a curved path of contact for small gearing dimensions. International Conference on Gears, Garching near Munich, Germany, Oct. 4th–6th 2010: Europe invites the world, (VDI-Berichte 2108). Düsseldorf: VDI-Verlag, p 1281–1294

Hlebanja G (2011) Specially shaped spur gears: a step towards use in miniature mechatronic applications. Balkan J Mech Transm, vol 1, Iss. 2, p 25–31

Matschoß C (1940) Geschichte des Zahnrades. VDI Verlag, Berlin 1940

Niemann G, Winter H (1989) Maschinenelemente. Springer, Band II

The Euler Archive s.v. E249—De aptissima figura rotarum dentibus tribuenda, http://www.eulerarchive.com/, accessed 15.4.2012

Future Transmissions for Wind Turbines

Bernd-Robert Höhn

Abstract Most transmissions for wind turbines are set up by multiple consecutively arranged planetary gear sets and/or normal gear sets. Therefore these transmissions have a constant ratio. In order to feed the electricity produced by the wind turbines into the grid, an electric conversion to a constant frequency of 50 Hz is necessary. FZG developed a new concept for transmissions of wind turbines based on a planetary gear. By superposition of a small electric engine the transmission ratio is continuously variable. This makes an electric conversion unnecessary and thereby increases the efficiency of the wind turbine.

Keywords Next generation for transmissions for wind turbines · Optimization of efficiency and durability

1 Introduction

The use of wind for energy production has a long history. In Europe since more than 800 years the wind energy will be used for production of mechanical energy. The first use of wind power will be used directly for mills, saws and waterpumps. Beginning of the 18th century first experiments for generating electric power are known. But these experiments have not brought the brake-through for the wind power. In the beginning 8th decade of the 20th century a revival of wind power began. The world wide discussion about energy-waste and the forecast of ending of oil reserves in the world and the accompanying discussion about the CO_2-emission and climate changes (increase of average temperature of the world) started the development of regenerative energy production more and more. The

B.-R. Höhn (✉)
FZG, Technische Universität München, München, Germany
e-mail: fzg@fzg.mw.tum.de

G. Dobre (ed.), *Power Transmissions*,
Mechanisms and Machine Science 13, DOI: 10.1007/978-94-007-6558-0_6,

use the water power was one solution for generating electric power without increase of the CO_2-emissions. Extreme big water energy-production started with the Yangste-dam in China and the Iquacu-dam in South America. In Germany the wind power becomes an acceptable part of electric energy production. In 2009 more than 7 % of German electric energy consumption is produced with wind turbines. A main reason is caused by the politics which installed a new law, which the grid owner has to buy the electric power from wind turbines to a high price above the market price. The consumer has to pay for it. Though an indirect subvention of wind power (and other regenerative energy production like photo voltaic) is installed in Germany. Subvention for photo voltaic has reached a value of more than 2 billion € per year!!! This subvention of regenerative energy leads to the very high installed wind power in Germany.

And how is the situation in wind turbine market worldwide? In Europe the increase of installing wind power has stopped through the financial crisis in 2009 and beginning 2010. The banks have stopped the financing especially for wind parks in the sea. Different is the situation in China and India. Their national industry has to fulfill the big demand for wind turbines.

2 State of the Art

The next figures (Fig. 1) show the state of art of wind turbines. Two technical solutions are in the market. With and without transmissions. In the market till 1 MW the multipol low speed generators without transmissions have a market share up to 20 %. As higher the power per unit (for offshore >5 MW is planned) as

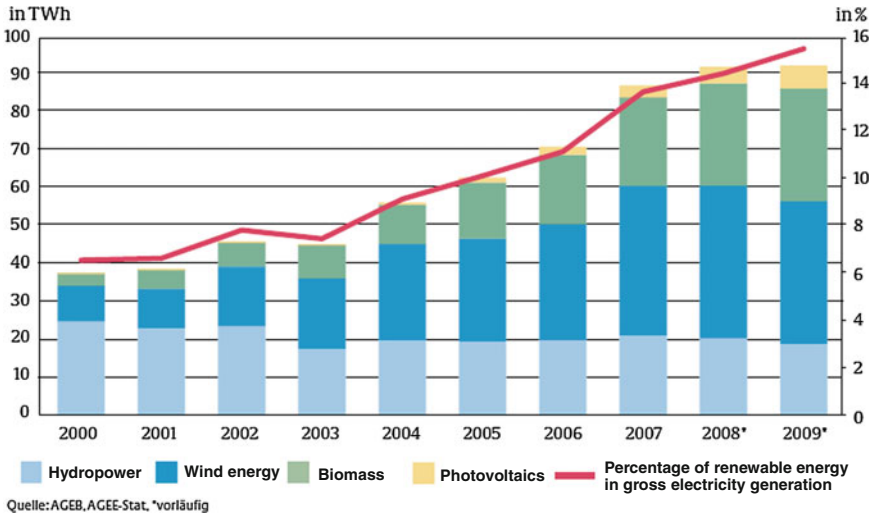

Fig. 1 Electric energy out of regenerative energy sources (2010)

Fig. 2 Hansen

lower is the speed of the rotor shaft and the need for transmissions is absolutely necessary regarding the weight of the gondola. As higher the speed of the generator as lower is the weight (2008). Though trans-mission ratio up to I = 100 is normal for wind power >2 MW. Figure 2 shows the principle of Hansen for up to 5 MW. One planetary set after the rotor and two normal gear sets for increasing speed up to 100 times rotor speed. The generator shaft is parallel to the rotor shaft. Same principle you can see by Winergy Fig. 3. Rotor is connected to the carrier of the planetary gear set, the sun is connected to the output shaft and the ring gear is fixed to the housing. With this principle you have the highest ratio in a planetary gear set. ZF will start with a similar design with Vestas in 2012.

Figure 4 shows the design of Renk. They have designed a double planet with a higher ratio between ring gear (connected to the rotor = inputshaft) and sun. They offer this principle as Multibrid for a medium speed generator (about 200 min^{-1}) with higher pole numbers and additional with another normal gear set for total ratios of about i = 100.

Figure 5 shows the principle from Bosch-Rexroth. They have a power split for the rotor power to two coupled planetary sets. The torque is divided to two planetary gear sets though the diameter of the ring gear are smaller for the same power compared to the principles of Hansen or Winergy. But the design is more complicated. More parts give more risks, a problem for guaranty wishes for a safe run for 20 years.

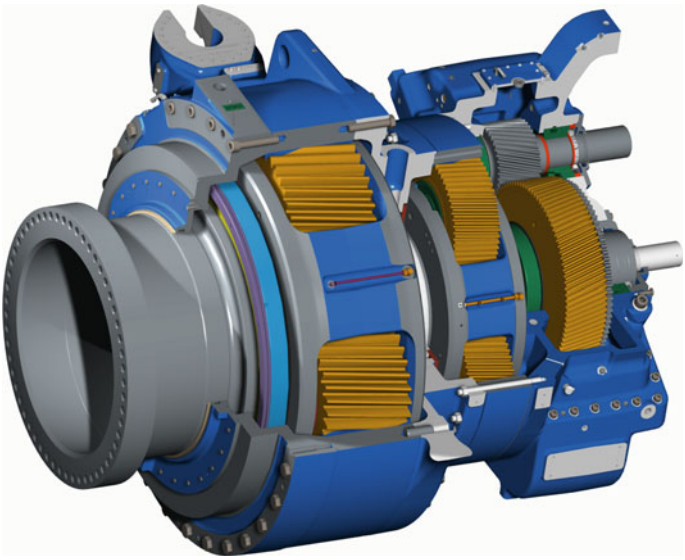

Fig. 3 Winergy

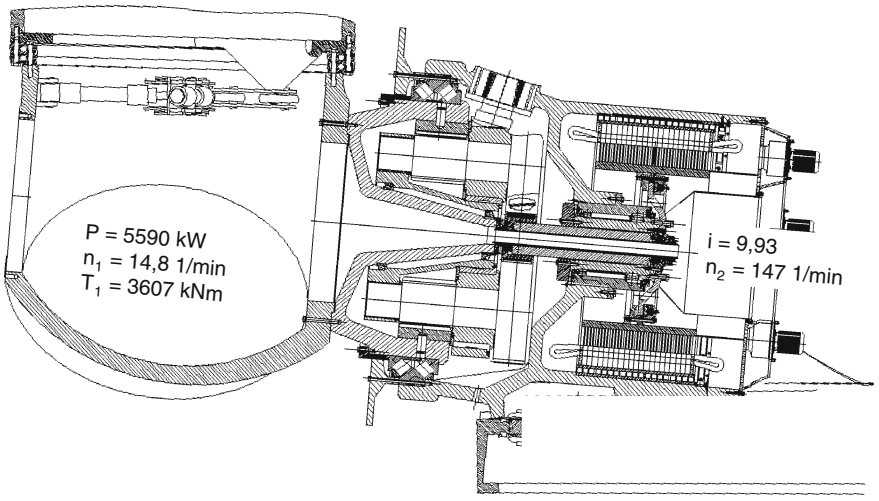

Fig. 4 Renk Multibrid

Figure 6 shows the Maag DPPV gear design. This design also distributes the input power of the rotor to the planet carrier of the first stage and the ring gear of the second stage. The output shaft is connected to the sun wheel of the first stage.

Figure 7 shows the new patent for the Bard V MW gear design (GDC solution). The power split of the first two stages of this design is very similar to the Maag

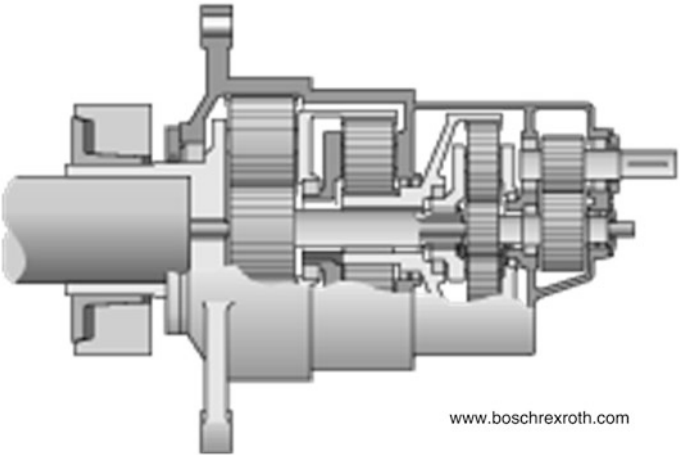

Fig. 5 Bosch Rexroth Redulus

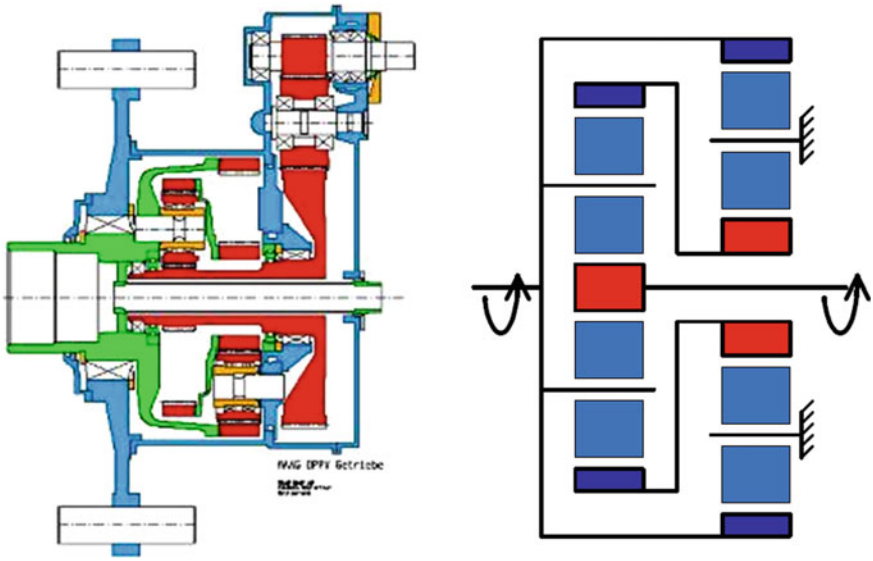

Fig. 6 Maag DPPV

DPPV. A high number of planets is used in order to increase the maximum torque and at the same time reduce the bearing reaction. The patent-registered flex-pin-system by GDC is used to provide a good load sharing between the planet wheels.

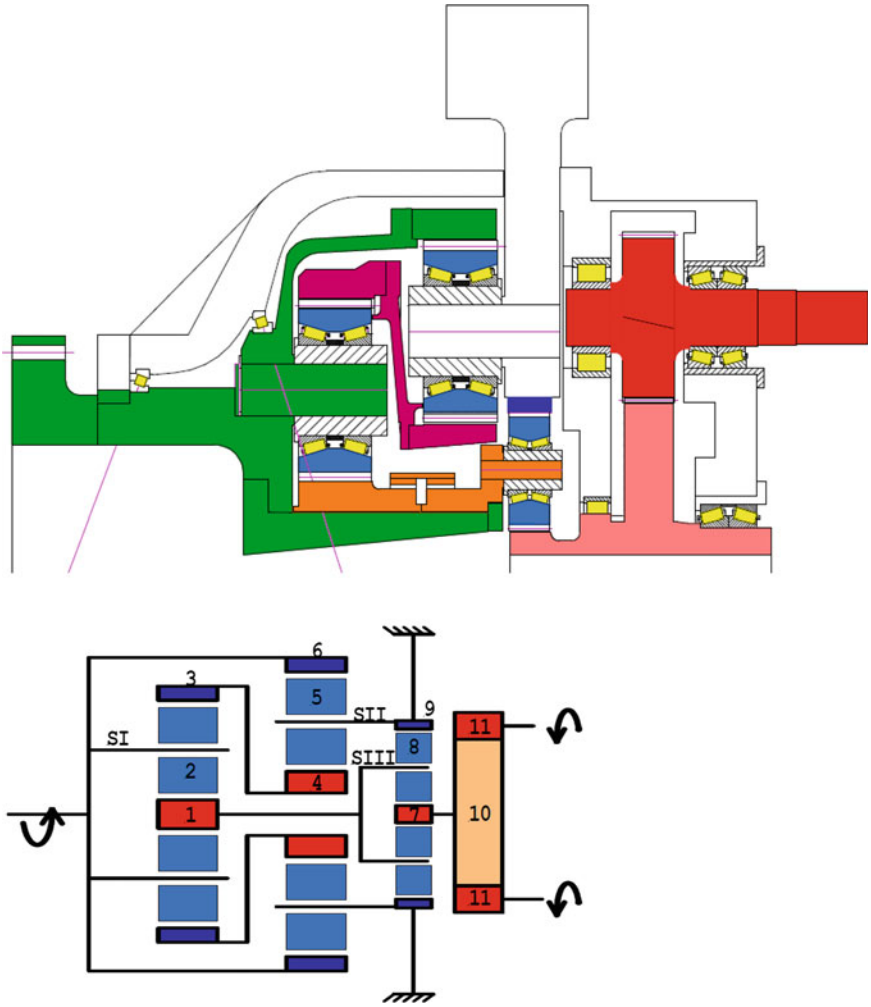

Fig. 7 Bard V MW new patent (GDC solution)

3 Future Trends

Voith windrive. Caused by the actual financial and guaranty problems the European wind turbine firms are not intensively engaged in research and in developing the next generation of wind turbines. Only Voith as a newcomer introduces a new concept, the windrive in 2008. Figure 8 shows the principle with a CVT, an hydrodynamic converter (Voith is the worldwide known specialist for such couplings and torque converter). This CVT combined with two planetary gear sets they offer a really new concept. The generator is a synchronous generator which acts with constant speed. Though the electric power is produced with a

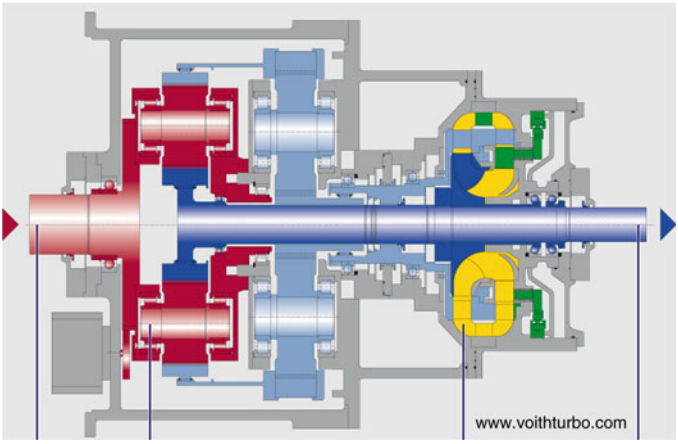

Fig. 8 Voith windrive

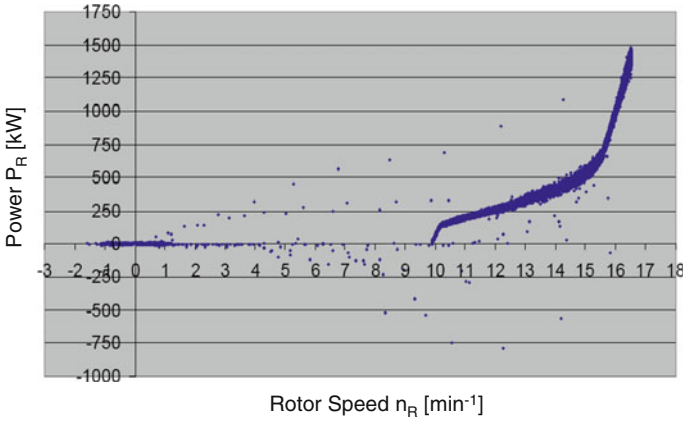

Fig. 9 Measured load spectrum

constant frequency of 50 Hz and give the power direct to the grid without electric conversion as it is normal for all existing wind turbines with a fixed ratio. The rotor produces mechanical energy by different rotor speed between 12 and 16 min^{-1}. If you have fixed ratio the generator turns between 1,200 and 1,600 min^{-1} for a 2.5 MW example. Figure 9 shows a measured load spectrum of such a wind turbine. It is different from the aerodynamic potential curve for a given rotor. The dynamic potential for such a wind turbine shows Fig. 10. With a pitch-control the maximum power is only possible by a windspeed >15 m/s. With the Voith windrive the generator turns with 1,500 min^{-1} for given rotor speed between 12 and 16 min^{-1}. The disadvantage in gear box efficiency could be overtaken through the better total efficiency. For established systems the overall efficiency is

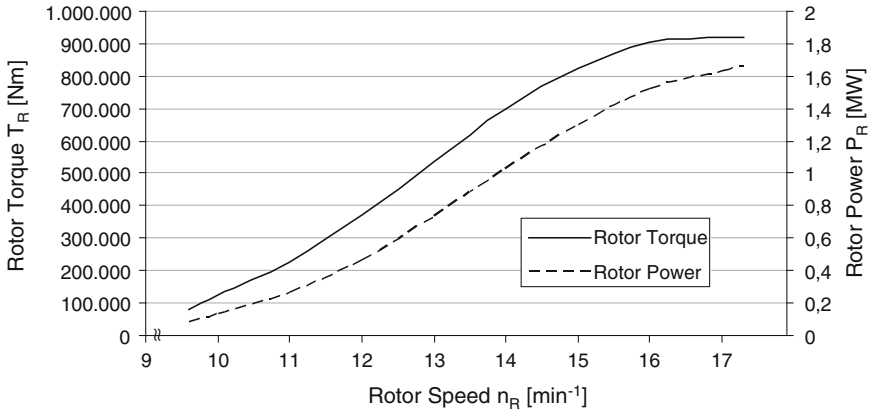

Fig. 10 Dynamic potential

$$\eta_{ges} = \eta_{transmission} \cdot \eta_{Gen} \cdot \eta_{el} \tag{1}$$

and for the Voith Windrive:

$$\eta_{Ges} = \eta_{transmission} \cdot \eta_{Gen} \tag{2}$$

Details of the efficiency for all components are kept very secret and confidential from the firms, therefore a detailed comparison is not possible. But let give an approximation and an example:

a) Conventional system:	
Transmission	$\eta_{transmission} = 0{,}96$
Asynchron generator	$\eta_{Gen} = 0{,}95$
Electric conversion	$\eta_{El} = 0{,}94$
With Eq. 1	$\eta_{Ges} = 0{,}857$
b) Voith windrive:	
Transmission	$\eta_{transmission} = 0{,}93$
Synchronous generator	$\eta_{Gen} = 0{,}96$
With Eq. 2	$\eta_{Ges} = 0{,}893$

That means this system has a better efficiency and a better energy production factor which can be calculated in € or $ or Rupie or Yen or…..

FZG-Concept. Engaged through the Voith idea and an old Siemens patent application of 1992 (2010), FZG designed a new planetary gear set with a superposition of a small electric power to synchronous generator with constant speed for a rotor range speed between 12 an 16 min^{-1} (Fig. 9). The targets for the future wind turbines are defined in Fig. 11. Figure 12 shows the wind turbine drive train for such a constant generator speed. That means for such superposition a

normal planetary gear set is used. If the electric engine runs as a motor you have a power addition in the planetary gear. Rotor power PR and P_{EM} drive the generator PG and the electric power for the motor M comes from the generator.

Only P_G–P_M goes to the grid. If the electric motor runs as a generator you have power split in the planetary gear box and both electric engines P_M and P_G give their power to the grid. The task for FZG was to find out, what power size of P_M is necessary for a wind turbine of PG = 1.5 MW (only as example, without problems scalable) and the given load spectrum, see Fig. 9. For characteristic curve A out of calculated power-windspeed-diagram and in Fig. 10 for the given measured load spectrum for a wind turbine. For this calculation the Willis—equation and the derived formulas from Mueller (1998) are used. Especially for the measured load spectrums you can see, that below of rotor speed $n = 10\ min^{-1}$ no electric power will be produced and for example $n_{Rot} = 12\ min^{-1}$ only 15 % of the maximum (and given) power of the wind turbine (here 1.5 MW) will be produced. Figure 13 shows the difference of the new concept and common. Basic concept once more. The result of these calculation done with Mueller formulas show Fig. 14. The electric demand for motor power P_{EM} is for characteristic A $P_E = 242$ KW and for

Fig. 11 Targets

Targets:

- Transformation of the wind speed dependend rotor speed in a constant generator speed of 1500 min^{-1}
- Application of cost-saving synchronous generators
- Easy drive train concept
- Less power electronics

Fig. 12 Wind turbine drive train

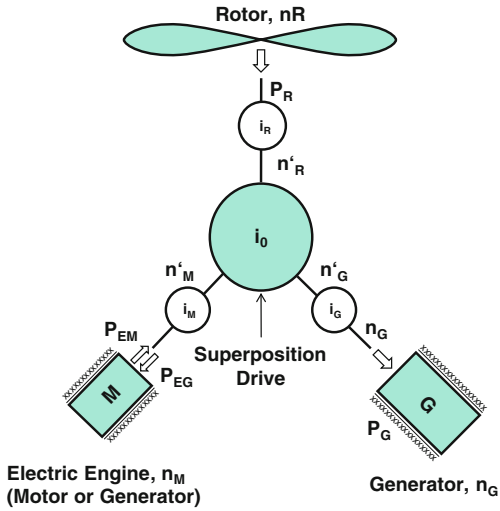

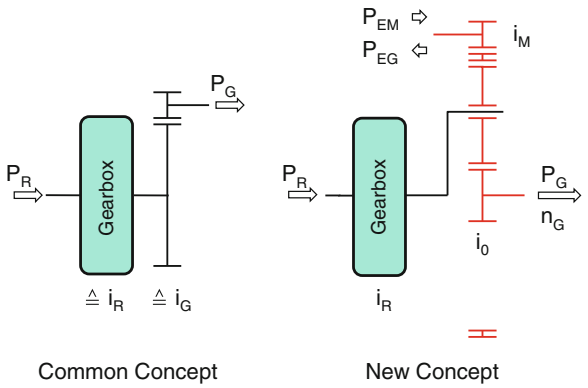

Fig. 13 Common and new concept

characteristic B only P_{EM} 100 = KW. Figure 15 show the power ratio between P_{EM} and P_{Rotor}. You see that the power ratio is still increasing when rotor speed decreases. The absolute value is decreasing (see Fig. 14) which the rotor power decreases very much. If you use the motor P_E as generator (power split) and motor (power addition) the maximum power of that unit decreases to P_E = 84 KW—Fig. 16. That means for the additional installed power of P_{EM} only 7 % of the maximum power of the rotor is necessary. This engine has to run as motor and generator and needs adequate power electronics. For such dimension—84 KW against 1.5 MW by normal wind turbines—the power electronics is much cheaper. The synchronous generator delivers the electric power direct to the grid. How can be the design of such a concept. FZG made two examples.

First we use a first planetary gear set for increasing speed like in the principle of Hansen, Winergy, Eikhoff or other, Fig. 17. The two normal gear stages are exchanged from a so called "plus-planetary gear set" (1998) which has a high gear ratio, when you fix one ring gear. This fixed ring gear of the "plus-planetary set" is connected to the motor P_{EM} and works as motor for rotor speed lower than

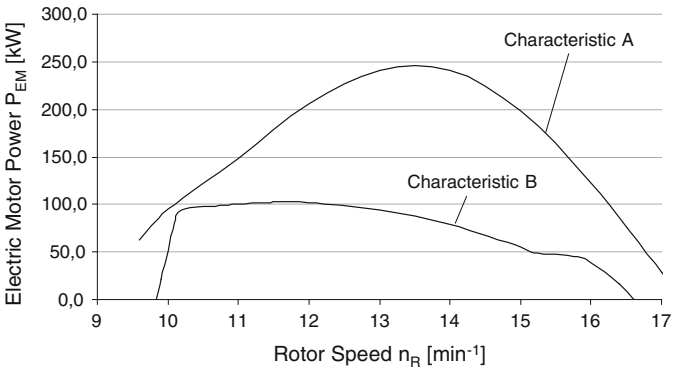

Fig. 14 Required electric power

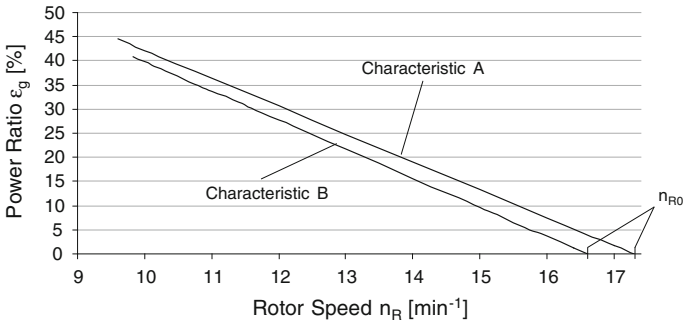

Fig. 15 Power ratio

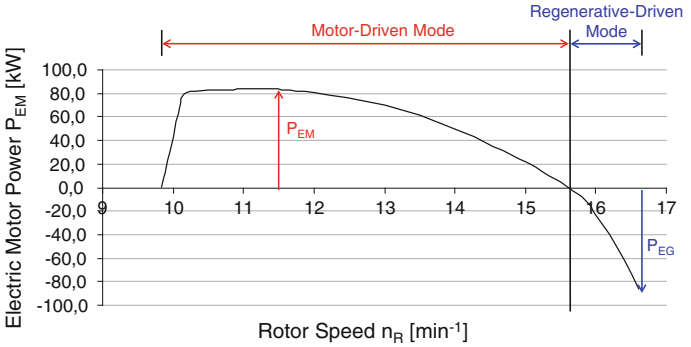

Fig. 16 Power of superposition motor

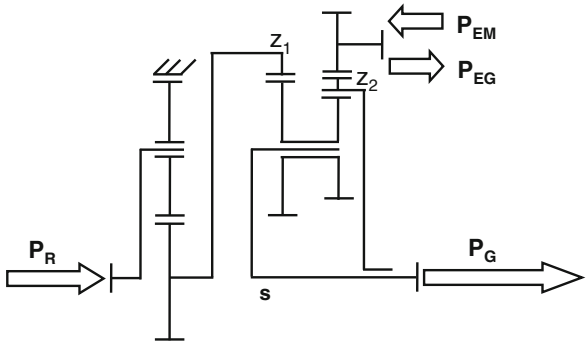

Fig. 17 Wind turbine drive train (1st example)

$n_{Rot} = 15.5\ min^{-1}$ and as generator between $n_{Rot} = 15.5$ till $16.5\ min^{-1}$ (Fig. 16).

Second example shows Fig. 18. Here the "plus-planetary gear" (no. I) is used as a first step with speed increase of about i = 25 and a normal "minus-planetary

set" (no. II) is used for superposition of P_{EM}. The advantage is the lower torque in the ring gear of II (Fig. 18) the disadvantage is the lower efficiency of the "plus-planetary gear set" used by high tooth power in the "plus-planetary gear set".

These disadvantages can be reduced dramatically to the low loss tooth geometry which is developed from FZG with several research projects since 2003. Figure 19 shows the comparison with normal tooth geometry. The plus gear box has an efficiency of $\eta = 0{,}89$ for the speed increaser of i = 25 and with low loss geometry from FZG $\eta = 0{,}96$. This value is necessary that the total efficiency will become higher than normal design (see Eq. 2). If you calculate the total efficiency like the example (see Eqs. 1 and 2), you will get

$\eta_G = 0{,}95$	Plus + minus planetary gear set of Fig. 18 inclusive bearing losses
$\eta_{Syn} = 0{,}96$	
$\eta_{ges} = 0{,}91$	much better than η_{ges} normal = 0,866

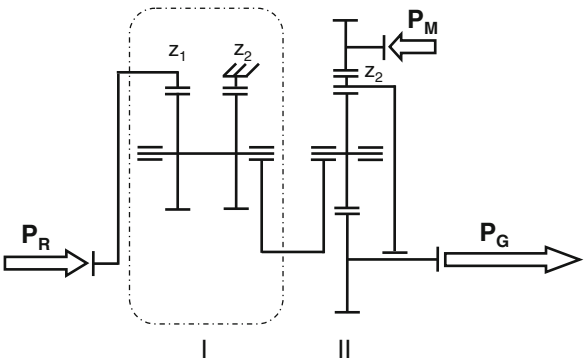

Fig. 18 Wind turbine drive train (2nd example)

Fig. 19 Comparison of load depended losses

Efficiency Factor for Standard Tooth Geometry [1], [2]:

$$\eta_{12} = 0.9975 \bullet 0.9981 = 0.9956$$

$$\eta_{1S} = (i_{12}/\eta_{12} - 1)/(i_{12} - 1) =$$

$$(0.962 / 0.9956 - 1)/(0.962 - 1) = 0.8881$$

Efficiency Factor for low-loss-Tooth Geometry:

$$\eta_{12\_opt} = 0.9993 \bullet 0.9991 = 0.9984$$

$$\eta_{1S} = (i_{12}/\eta_{12} - 1)/(i_{12} - 1) =$$

$$(0.962 / 0.9984 - 1)/(0.962 - 1) = 0.9594$$

4 Conclusions

The FZG-concept shows the possibility with an electric superposition for a rotor speed of about 12–16 min^{-1} a constant generator speed of 1,500 min^{-1}. The superposition power is only 7 % of the rotor power. A cheap power electronic can be used. The overall efficiency of such a concept can be higher than normal conventional wind turbine with a transmission with a fixed ratio. The FZG will become the partner for future wind turbine concepts for concept design and total calculation for gears and bearings.

References

1. Energie in Deutschland www.bmwi.de. August 2010
2. Weiss T, Pinnekamp B (2008) Concept for a multi megawatt wind turbine—gear and field experience, AGMA fall technical meeting
3. Hehenberger G (2010) Energiegewinnungsanlagen und Verfahren zum Betreiben dieser, WO 2010/063052 A2
4. Müller HW (1998) Die Umlaufgetriebe, Springer Verlag, ISBN 3-540-63227-1

Grinding Burn on Gears: Correlation Between Flank-Load-Carrying Capacity and Material Characteristics

Bernd-Robert Höhn, Karsten Stahl, Peter Oster, Thomas Tobie, Simon Schwienbacher and Peter Koller

Abstract A high geometric accuracy of case-hardened gears requires a grinding process after heat treatment. In appropriate grinding conditions can induce surface tempering, alter hardness and lead to an unfavorable residual stress state. This effect is commonly known as grinding burn. The influence of grinding burn on the flank-load-carrying capacity was systematically investigated within a research project. This paper summarizes the main results. Different methods for analyzing the surface and the near subsurface characteristics are presented. Based on the results of experimental testing and the analysis of surface and near subsurface, the paper summarizes the correlation between grinding burn and flank-load-carrying capacity.

1 Introduction

A typical heat treating process for highly loaded gears is case hardening. The intention of this heat treatment is to trim the material characteristics to the present loading. However, the heat treatment may lead to some geometric distortion. In order to remove this distortion and to achieve quality and performance requirements gears normally have to be ground after hardening. The grinding operation has a mechanical and a thermal influence on microstructure, hardness and residual stresses. The superposition of both, thermal and mechanical influence, makes it

B.-R. Höhn (✉) · K. Stahl · P. Oster · T. Tobie · P. Koller
FZG, Technische Universität München, Munich, Germany
e-mail: fzg@fzg.mw.tum.de

P. Koller
e-mail: koller@fzg.mw.tum.de

S. Schwienbacher
Alupress, Brixen, Italy
e-mail: Simon.Schwienbacher@alupress.it

G. Dobre (ed.), *Power Transmissions*,
Mechanisms and Machine Science 13, DOI: 10.1007/978-94-007-6558-0_7,

difficult to predict the changing of surface and near subsurface characteristics during the grinding operation. An unfavorable residual stress state, surface tempering and an altered hardness after the grinding operation are commonly known as grinding burn. Within a FVA research project (Schwienbacher and Wolter 2007) gears with different grades of defined grinding burn were manufactured and afterwards tested using the FZG back-to-back test rig. The results show that an inappropriate grinding operation has a detrimental effect on the flank-load-carrying capacity. Dependent on the intensity and the magnitude of grinding burn a decrease in flank-load-carrying capacity is obvious.

2 Experimental Test Series

The experimental tests were carried out with two different gear geometries sized $m_n = 3$ mm ($a = 75.6$ mm, $z_1/z_2 = 23/25$) and $m_n = 5$ mm ($a = 91.5$ mm, $z_1/z_2 = 17/18$). For the production of these test gears, the case hardening steels 16MnCr5 and 18CrNiMo7-6 were used. All test gears of the same geometry were milled the same way and heat treated in one lot. By appropriate grinding processes after heat treatment test series with different grades of defined grinding burn on the flanks of the test pinions were produced. Besides generating grinding, profile grinding was used for some test series.

3 Indicating Grinding Burn

The tooth flanks of all test pinions were examined by surface temper etch inspection according to ISO 14104 (1997) and assigned to the corresponding test series (grinding burn grades). Furthermore, the produced grinding burn grades of the different test series were characterized and documented extensively before and after the gear running tests, using non-destructive an additional destructive test methods.

3.1 Surface Temper Etch Inspection

A standard testing method for indicating grinding burn is surface temper etch inspection according to ISO 14104 (1997). After cleaning, the gears are etched in nitric acid. Following the etching, the gears are rinsed in water and bleached in hydrochloric acid. After a further rinsing, the gears get neutralized in an alkaline solution and dipped into oil in order to prevent corrosion. Areas which are not influenced by the grinding process show a light grey or brown color. Influenced areas show a dark grey or black color. Figure 1 shows tooth flanks, which were

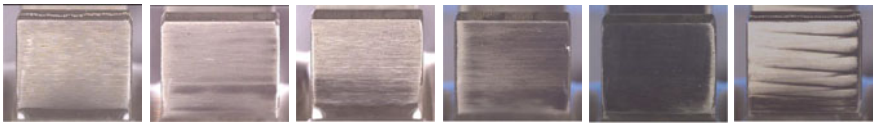

Fig. 1 Tooth flanks after the etching process with different grades of grinding burn

treated with different grinding parameters. The flank with temper class FA0 does not show any dark colored areas. Therefore, an influence by grinding burn can be excluded. The test series FB1, FB2 and FB3 show lightly tempered areas. They vary in the dimension of the tempered area. The intensity is equal. Test series FD3 shows heavy tempering on 100 % of the active tooth flank. The tempered area is darker than that of class B. Test series FE3 shows the most intense effect of grinding burn. The heat generated during grinding led to a re-hardening of the tooth flank. The re-hardened area is white colored after etching. Nearby the re-hardened area, the material is heavy tempered. According to ISO 14104 (1997) the classification of grinding burn was done in the following way:

Class:	A	No tempering
	B	Light tempering
	D	Heavy tempering
	E	Rehardening, severe overheating
Level:		Maximum percentage of surface area affected
	1	10 %
	2	25 %
	3	Unrestricted.

3.2 Destructive Analysis

3.2.1 Metallographic Analysis

The metallographic analysis was generally focused on the dedendum area in the mid of the tooth width. In case of specimen with local grinding burn, the affected area was examined.

The etched microsections of the different test series are shown in Fig. 2. The different stages of tempering can be noticed obviously. Unlike specimen FA0 without grinding burn, the other microsections show tempered areas. Dependent on the temper class the dimension and the colour of the tempered areas vary. The microsection of FE3 shows white re-hardened zones, which are not connected completely (compare Fig. 1). Nearby the re-hardened zones the microstructure is dark coloured and shows a severe tempering.

For all examined microsections, a measurement of hardness with HV1 according to DIN EN ISO 6507-1 (2006) was done. To get reliable results, with

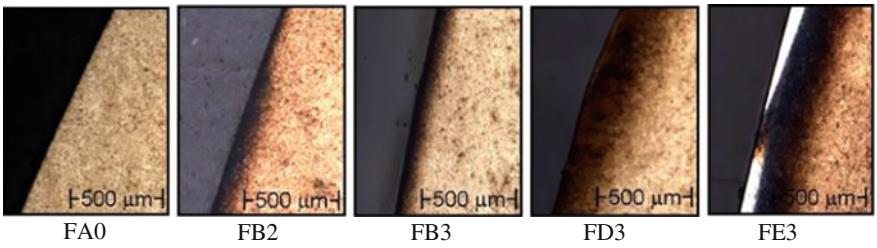

Fig. 2 Metallographic specimen with different grades of grinding burn

this method the hardness cannot be measured in an area nearer than 0.1 mm to the rim. Hence a decrease in hardness cannot be determined for specimens with light tempering (class B). According to Fig. 2 the tempered area is limited to a depth <0.1 mm. In contrast, specimens with heavy and severe tempering (class D and E) show a decrease in hardness in a depth >0.1 mm. The decrease in hardness is about 70–100 HV1. The re-hardened area of class E also cannot be captured by conventional measurement of hardness with HV1. In order to measure the surface hardness, another method called "ESATEST" was used (see 3.3.1). The values of surface hardness and the hardness at the depth 0.1 mm are shown in Fig. 3.

3.2.2 X-ray-Diffraction Analysis

The distribution of residual stresses and retained austenite was detected by x-ray-diffraction analysis. The examined area was either the centre of the active flank or the area showing grinding burn. X-ray-diffraction analysis is based on the diffraction of x-rays at the crystal lattice. With help of Bragg reflexion, the distortion of the crystal lattice can be captured and the present residual stresses can be calculated. X-ray-diffraction analysis only offers information about a small depth.

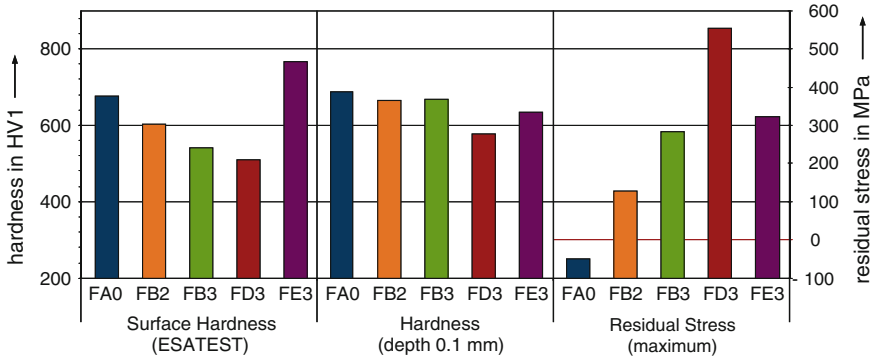

Fig. 3 Exemplary results of ESATEST, hardness testing and X-ray diffraction analysis

To get the distribution of residual stresses and retained austenite over the near subsurface, the surface has to be removed step by step by electroerosion.

Specimens without grinding burn (class A) showed residual compressive stresses over the whole examined depth of 0.64 mm. With increasing grinding burn residual tensile stresses were found in the near subsurface. Temper class B (light tempering) showed residual tensile stresses with maxima in the range of 200–300 N/mm^2. Maxima of residual tensile stresses of temper class D (heavy tempering) can reach 450 up to 650 N/mm^2. The maxima of residual tensile stresses for temper class B and D were detected in a depth of about 0.05–0.1 mm below the surface. Specimens with severe tempering and re-hardened areas (class E) showed residual compressive stresses with a high scatter. Nearby the re-hardened areas the residual compressive stresses changed into residual tensile stresses. The maxima of residual stresses for each test series are shown in Fig. 3.

3.3 Non-Destructive Analysis

3.3.1 Surface Hardness (ESATEST)

Surface hardness measurement by ESATEST can be considered as a quasi-non-destructive measurement. A diamond, coated with a conductive layer, is applied with an increasing load on the specimen. The measured resistance gives information about the penetration. With help of comparative measurement, it is possible to quantify the surface hardness. Measuring surface hardness by ESATEST leads to a microscopic small indentation. An influence on tooth load carrying capacity caused by these indentations could not be noticed during the research project (Schwienbacher und Wolter 2007).

Specimens without grinding burn (Temper Class A) showed a surface hardness of about 680–700 HV-ESATEST. The more the tooth flanks were influenced by the grinding process, the more the surface hardness decreased. Temper Class B showed a surface hardness of about 570–630 HV-ESATEST at the influenced area. The greatest decrease of surface hardness was located for temper class D with heavy tempering. Its hardness was about 510–550 HV-ESATEST. Temper class E showed a surface hardness of about 770–810 HV-ESATEST in the re-hardened area. The results of surface hardness measurement are summarized in Fig. 3.

Comparing measured hardness and results of the surface temper etch inspection a good correlation can be seen. Flanks with a consistent condition showed a comparable hardness. Flanks with local temper burn showed a changing hardness over the flank.

3.3.2 3MA Testing

3MA is an acronym for "Mikromagnetischer Multiparameter Mikrostruktur- und Spannungs-Analysator". The 3MA-apparatus was developed by the IZFP-Saarbrücken (Fraunhofer Institute for Non-Destructive Testing). It is based on measuring different micromagnetic parameters. Because of physical and material-based interrelations, micromagnetic parameters can be used for indicating grinding burn and determining material characteristics of the surface and the near subsurface.

The used 3MA-technique records 41 different micromagnetic parameters. One of these micromagnetic parameters is barkhausen noise. Which parameters are important and are used to define a material characteristic is determined by regression analysis. Some micromagnetic parameters can be redundant. Its different behaviour toward disturbances makes it possible to eliminate or reduce the influence of those disturbances.

In order to get quantitative results by 3MA Testing the 3MA analyser has to be calibrated with specimens which have a well-known surface and subsurface condition. This calibration is based on a multiple regression analysis [see Eq. (1)].

$$y = b_0 + b_1 \cdot x_1 + b_2 \cdot x_2 + b_3 \cdot x_3 + \ldots + b_k \cdot x_k \quad (1)$$

The variable y is a characteristic of surface or the near subsurface like hardness or residual stress. The variables x_1, x_2, x_3, …, x_k are micromagnetic parameters. b_0, b_1, b_2, …, b_k are the coefficients of the regression analysis.

Figure 4 shows results of 3MA Testing after calibration. A good correlation between the characteristics detected by ESATEST, metallography and x-ray-diffraction analysis and the results of 3MA testing can be seen.

3MA Testing is an adequate method for a comprehensive, non-destructive inspection of gear flanks before, during and after the test run. After a calibration, the 3MA-system can be used for the quantitative determination of the hardness distribution and the distribution of residual stresses over the depth. These results are elementary for detecting correlations between the flank-load-carrying capacity and material characteristics.

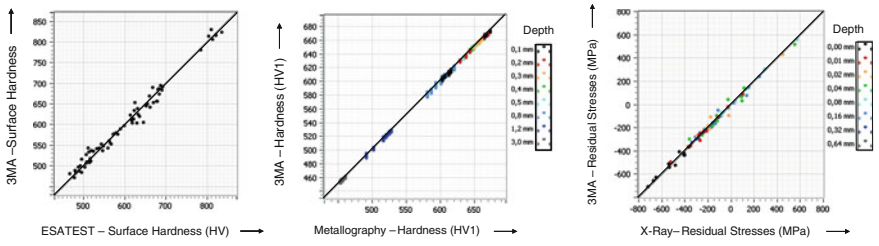

Fig. 4 Correlation between 3MA Testing and ESATEST, metallography and x-ray-diffraction analysis

3.3.3 Barkhausen Noise Measurement

Based on the amplitude of the barkhausen noise the influence of the grinding process can be indicated qualitatively. By measuring only one micromagnetic characteristic a quantitative information concerning the surface and near subsurface condition is not possible. Barkhausen noise measurement is a non-destructive method for indicating grinding burn which is occasionally used by industry.

During the measurement, an alternating magnetic field is induced by field coils and a magnet yoke. The occurring barkhausen effect, i.e. changes or rotation of ferromagnetic domains, is detected by a hall-element. As a function of the magnetic field intensity the barkhausen noise level M_{MAX} is detected.

The barkhausen noise level is dependent on hardness and residual stresses. Therefore, barkhausen noise measurement is an option for detecting grinding burn.

Figure 5 shows the mean values of measured barkhausen noise levels for the examined gears with different grades of temper burn. A good correlation between the etchings and barkhausen noise measurement can be seen. Specimen FA0 shows a barkhausen noise level MP < 50. Specimens with temper class FB and FD show a barkhausen noise level MP > 50 in the tempered area. For specimen FE3 the re-hardened tooth flank obviously leads to a reduced barkhausen noise level. Therefore, it can be seen that the analysis of the surface and the near subsurface of specimen with re-hardened areas is limited.

The combined use of different methods for indicating grinding burn made a detailed description of every test series possible. Every method has its own

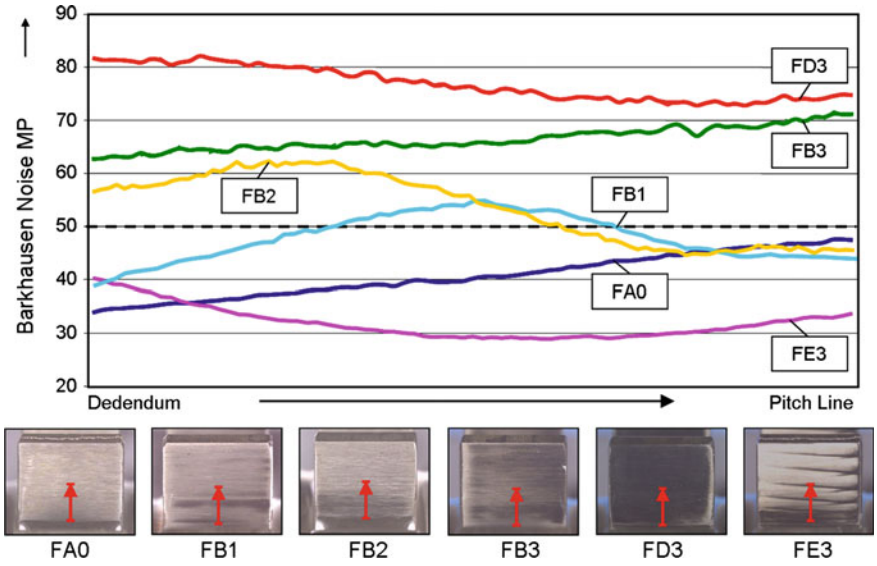

Fig. 5 Measured Barkhausen Noise (mean values) for different grades of grinding burn; correlating etchings

benefits but also some disadvantages. A detailed evaluation, based on the results from the research project and a rating by industrial partners is given by Schwienbacher and Wolter (2007).

4 Running Tests

The gear running tests were carried out under defined testing conditions in a standard FZG back-to-back test rig with centre distance a = 91.5 mm (gear geometry II) as well as in a FZG back-to-back test rig with variable centre distance (three-axis test rig, here a = 75.6 mm, gear geometry I).

For each test series a number of repeated test runs in the range of infinite and finite life were done. The limiting number of load cycles was $100 \cdot 10^6$. Based on these results, S–N-curves with a failure probability of 50 % and the allowable stress number regarding pitting damages σ_{Hlim} acc. to DIN 3990 (1987) were determined for each test series.

Compared to the reference test series without grinding burn effects all other test series, except FB1, show a variable reduction of the flank-load-carrying capacity depending on the grinding burn grade. In Fig. 6 the experimentally determined values of the endurance limit regarding pitting damages based on S–N-curves are summarized for each test series.

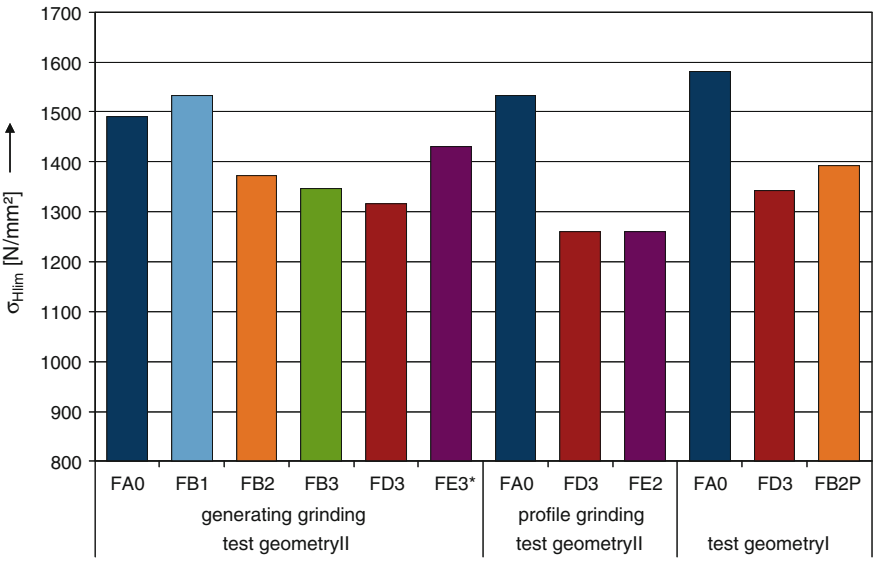

Fig. 6 Experimentally determined values of the endurance limit regarding pitting damages (* partly strong micropitting)

The test series FB1 with light grinding burn on max 10 % of the active flank area shows no reduction of flank-load-carrying capacity in comparison to the reference state (FA0). In contrast to the other test series no tensile residual stresses were measured at the influenced flank area of this test series.

With increasing flank area influenced by grinding burn (25 and 100 %) the supporting effect of non-damaged adjacent areas diminishes. Therefore, the corresponding test series show a significant reduction of the endurance limit regarding pitting damages in comparison to the reference state without grinding burn. The grade of grinding burn correlates with the reduction of the flank-load-carrying capacity for these test series. For example the endurance limit of test series with heavy tempering (class D) decreases more than the endurance limit of test series with light tempering (class B).

The test series with rehardening (FE3) shows the least reduction of endurance limit in comparison to the reference state without grinding burn, but during the running tests additionally also micropitting in the dedendum flank area of some teeth was observed.

Profile ground test series with grinding burn damages showed the most considerable reduction of the endurance limit. A deeper effect of grinding burn (in comparison to the test series produced by generating grinding with similar visual appearance after the etching process) was supposed for this fact.

Compared to the main geometry II ($m_n = 5$ mm, 18CrNiMo7-6), the test series with gear geometry I ($m_n = 3$ mm, 16MnCr5), showed the same decrease of flank-load-carrying capacity induced by grinding burn effects. These investigations were done with a reduced number of trials.

5 Correlations Between Flank-Load-Carrying Capacity and Single Material Characteristics

The reduction of flank-load carrying capacity can be correlated with the results of the analysis of grinding burn (surface temper etch inspection, destructive and non-destructive analysis). Figure 7 faces exemplarily the ratio $\sigma_{Hlim,\ exp}/\sigma_{Hlim,\ exp,\ reference}$ with the change of surface hardness due to grinding burn. Regarding Barkhausen noise, the hardness distribution or the residual stress distribution similar correlations were found.

The results of analysis of surface and subsurface condition can be used for predicting the resulting flank-load-carrying capacity. For this purpose, Schwienbacher (2008) defined the so-called surface zone factor Z_S and proposed to upgrade the calculation method according to DIN 3990 (1987)/ISO 6336 (2003). Z_S takes account of the reduction of the endurance limit (pitting) due to grinding burn effects. It can be determined based on the results of surface temper etch inspection, by knowing the reduction of surface hardness or by knowing the entire

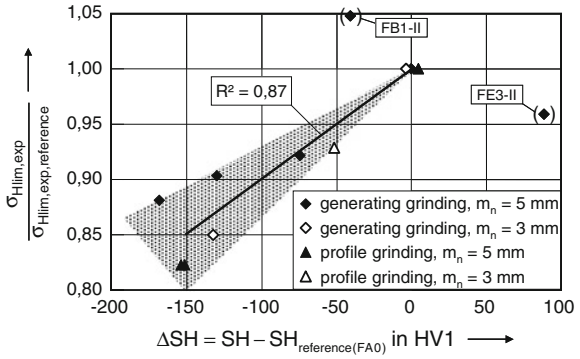

Fig. 7 Correlation between the endurance limit and the change of surface hardness (SH) in relation to the reference (FA0)

condition of the near subsurface (hardness distribution, residual stresses). Z_S is described comprehensively by Schwienbacher (2008).

6 Conclusions

An inappropriate grinding of case hardened gears may lead to grinding burn damages. This effect may diminish the flank-load-carrying capacity significantly. It is possible to characterize the relevant material condition of surface and near subsurface by using different inspection methods. With help of the results of this characterization the flank-load-carrying capacity of gears showing grinding burn effects can be estimated. For this purpose the surface zone factor Z_S has been defined based on extensive experimental and theoretical investigations. The here in described methods for analyzing gears are different possibilities for indicating grinding burn. Every method has its own benefits but also its disadvantages. For getting a detailed description of the condition of surface and near subsurface after grinding a combination of different testing methods is generally the best way.

Acknowledgments The present paper is a short excerpt from the project "Randzonentragfähigkeit—Zahnflanke—Ermittlung und Charakterisierung von Randzonen-Kennwerten und –eigenschaften und deren Einfluss auf die Flankentragfähigkeit einsatzgehärteter, geschliffener Zahnräder" which was founded by the **AVIF** (Arbeitsgemeinschaft der Eisen und Metall verarbeitenden Industrie e.V. [**AVIF-Nr. A200**] and the **FVA**—Forschungsvereinigung Antriebstechnik e.V. (**FVA 453 Ia + Ib**).

References

DIN 3990 Teil 1-5 (1987) Tragfähigkeitsberechnung von Stirnrädern, Beuth-Verlag

DIN EN ISO 6507-1 (2006) Metallische Werkstoffe—Härteprüfung nach Vickers—Teil 1: Prüfverfahren

ISO 14104 (1997) Gears—Surface temper etch inspection after grinding

ISO 6336-5 (2003) Calculation of load capacity of spur and helical gears—part 5: strength and quality of materials

SCHWIENBACHER S (2008) Einfluss von Schleifbrand auf die Flankentragfähigkeit einsatzgehärteter Zahnräder. Dissertation TU München

SCHWIENBACHER S, WOLTER B (2007) Ermittlung und Charakterisierung von Randzonen-Kennwerten und –eigenschaften und deren Einfluss auf die Flankentragfähigkeit einsatzgehärteter, geschliffener Zahnräder. Forschungsvorhaben Nr. 453 Ia + Ib, Abschlussbericht, Forschungsheft Nr. 830 der Forschungsvereinigung Antriebstechnik e.V

Recent Developments in Automotive Differential Design

Athanassios Mihailidis and Ioannis Nerantzis

Abstract The current paper consists of two main parts: In the first, the evolution of passenger car differentials during the past twenty years of automotive design is presented. A short description on the features and principle of operation of each device is given. In the second part, a recent advance in differential design is presented. It is a newly developed differential, designed to actively control the distribution of the driving torque to the wheels. The new device incorporates an electric machine, which can operate either as a motor or generator and affects torque distribution to the vehicles driving wheels. The driving behavior of a vehicle equipped with the new differential was simulated in ADAMS/Car. Comparative results were obtained using the following three types of differentials: an open differential, a limited slip differential and the new actively controlled device. Acceleration tests on road surface with different friction coefficient on each side of the vehicle for each differential type verified the accuracy of the simulation and verified that driving stability can be enhanced by actively controlled differentials.

Keywords Differential · Torque vectoring · Torque sensing · Active yaw

1 Introduction

The development and use of differential mechanisms starts form the ancient times and evolves in our days to the most complex driveline systems. Historical evidence for the existence of an early differential device is the Antikythera mechanism (de Price 1974). The device is dated back to 80 BC and it derives from many

A. Mihailidis (✉) · I. Nerantzis
Aristotle University of Thessaloniki, Thessaloniki, Greece
e-mail: amih@auth.gr

I. Nerantzis
e-mail: nerantzis@meng.auth.gr

G. Dobre (ed.), *Power Transmissions*,
Mechanisms and Machine Science 13, DOI: 10.1007/978-94-007-6558-0_8,

analyses that it contained a differential gear, which is interpreted as a mechanism with two degrees of freedom. Since the first automobiles were built, the implementation of a differential device on the drive axle became an urgent necessity. Historically, the invention of the differential is attributed to Onésiphore Pecueur, who patented in 1828 a steam vehicle that included a differential gear on the driving axle (Nunney 1998).

In the following, the development of automotive differentials during the past twenty years is presented. According to their special design features, they can be categorized into six categories:

- Bevel gear differentials
- Crossed helical spur gear differentials
- Parallel axes spur gear differentials
- Parallel axes internal spur gear differentials
- Gearless differentials with CAM curved surfaces
- Gearless differentials with friction clutches.

Torque is applied to the driving wheels through a differential gearbox that allows the driving wheels of a vehicle to rotate at unequal rates while cornering. The most common type is the open differential, which distributes the driving torque equally to both driving wheels. It operates satisfactory when the wheels operate below the traction limit. When the traction limit of one wheel is exceeded, it slips and the torque on both wheels is reduced. A solution to this problem is the use of a limited slip differential (LSD) that limits the torque difference by introducing friction between the halfshafts and the differential's body in terms of mechanical or hydrodynamic clutches. This design solves the problem of acceleration on road surfaces with different friction coefficient on each side (split μ), where the traction of one wheel is limited. However, these types of differentials affect cornering ability towards under-steering. In this paper the evolution of the differential design is outlined at first. Then, a newly developed differential is presented that allows for enhancement of handling performance by actively controlling the torque distribution to the driving wheels.

2 Recent Differential Designs

2.1 Bevel Gear Differentials

The most common design of a vehicle's differential is the bevel gear differential. In 1989 Tochigi Fuji Sangyo (Hagiwara and Teraoka 1989) presented a differential in which slip limiting control is done by an electric motor (Fig. 1).

Figure 2 shows a design of Honda (Shibahata 1990) where a hydraulic continuously variable transmission system is used in parallel with a differential to control torque distribution.

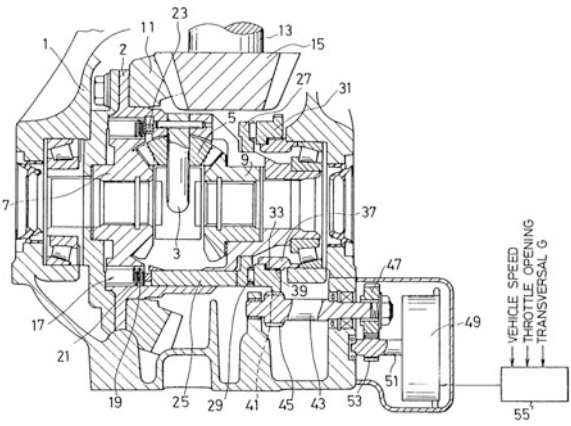

Fig. 1 Limited slip bevel gear differential (Hagiwara and Teraoka 1989)

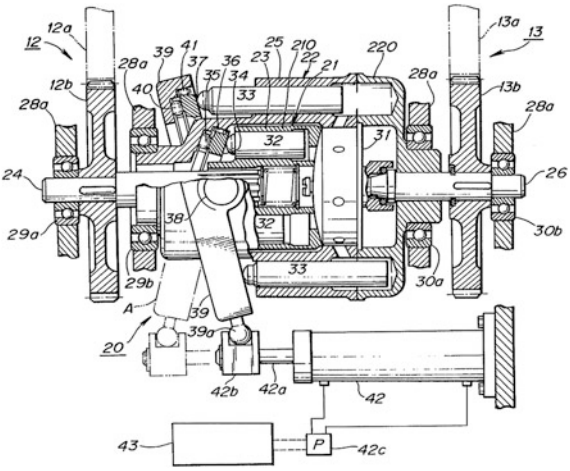

Fig. 2 Hydraulic CVT system used to control the torque distribution (Shibahata 1990)

The Active Yaw Control system introduced by Mitsubishi was developed during the 1990s. As seen in Fig. 3, it consists of a bevel gear differential, two multiple disk clutches and three gear pairs, which enable the alteration of speed of the clutch disks. This combination makes possible the distribution of torque to the driving wheels independently of their speed (Sawase and Sano 1999). In such systems the meaning of slip limiting is often confusing and therefore they are called torque proportioning or torque vectoring systems. In the last decade the term "torque vectoring" is used to describe the controllable torque distribution to the driving wheels of road vehicles. This is achieved with differentials similar to the two previously described in combination with an electronic system that monitors and logs the dynamic status of the vehicle and determines the desired torque for each wheel. Park and Kroppe (2004) describe a torque vectoring system which

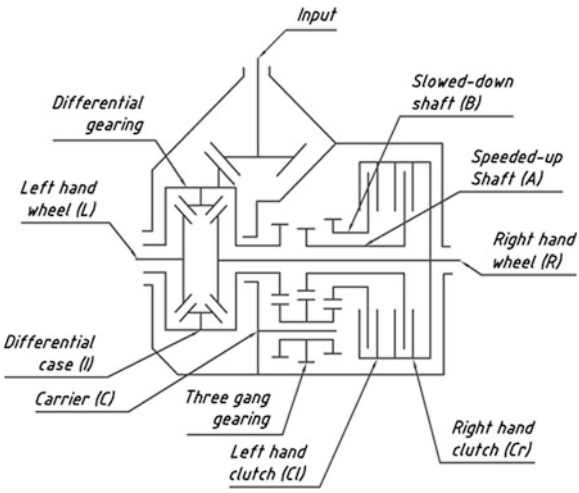

Fig. 3 Active Yaw Control differential (Sawase and Sano 1999)

includes a bevel gear differential. Other systems use a hydraulically actuated clutch to control torque proportioning of a bevel gear differential (Piyabongkarn et al. 2006a, b).

2.2 Crossed Helical Spur Gear Differentials

In such differentials the motion between the sun gears is transmitted with two sets of intermediate planets. The planet sets have opposite verse of rotation while their axes are crossed. During the 1950s Vernon Gleason sets the main design features of a crossed helical spur gear differential that evolved to the widely known Torsen type I differential. The mass production of this type of differential starts in the 1980s. Gleason Corporation, that produced the differential for the first time, published in 1988 the specifications of the Torsen type I differential (Chocholek 1988). A detailed analysis of the operation principles and the properties of Torsen type I differentials was presented by Shih and Bowerman (2002). One of the latest advances in the gear characteristics of such differentials was presented by Torvec Inc. (Gleasman et al. 2008). The differential is shown in Fig. 4.

2.3 Parallel Axes Spur Gear Differentials

This category includes differentials with spur gears, in which each sun gear engages with a separate set of planets and the two sets of planets are engaged together. The planet carrier receives torque from the vehicles engine. When either sun gear rotates clockwise in relation to the carrier the planets meshing with it

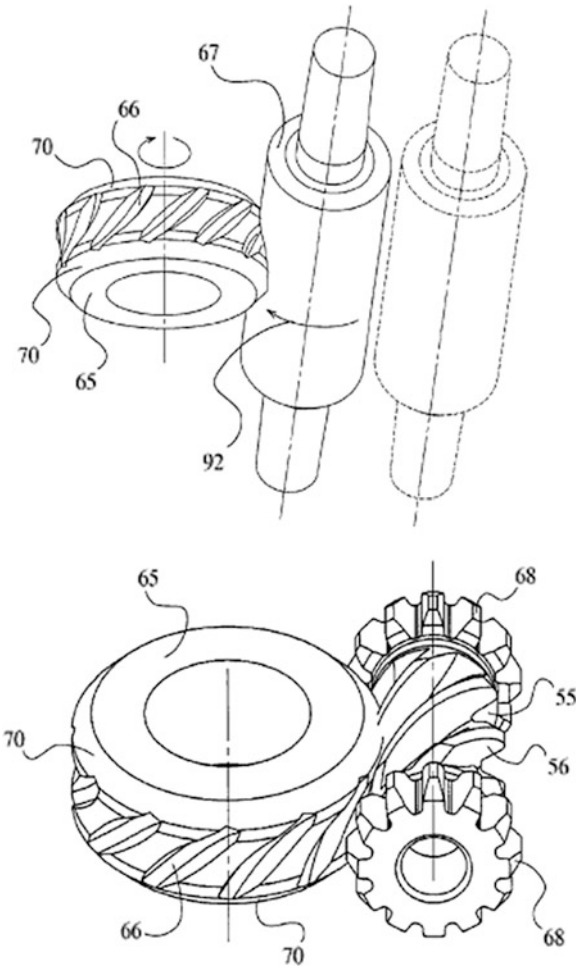

Fig. 4 Torvec differential (Gleasman et al. 2008)

rotate counterclockwise. Then, the other set of planets rotates clockwise and the second sun rotates counterclockwise. With the carrier motion superimposed to the previous motions the resulting motion is that of a differential. The Torsen type II differential is the most common design in this category.

Figure 5 shows a variation in which the two planet sets are mounted on different axial distances from the corresponding sun gears. The slip limitation can be adjusted by altering the preloading of springs (Ceccano and Novelli 1990).

In 1992, Zexel Gleason announces the invention shown in Fig. 6. The main difference is that two planets from separate sets engage at two separate regions at both ends of their length (Tseng 1992).

Mohan and Sharma (2006) presented a differential with parallel axes capable of controllable torque distribution in combination with a four wheel steering system.

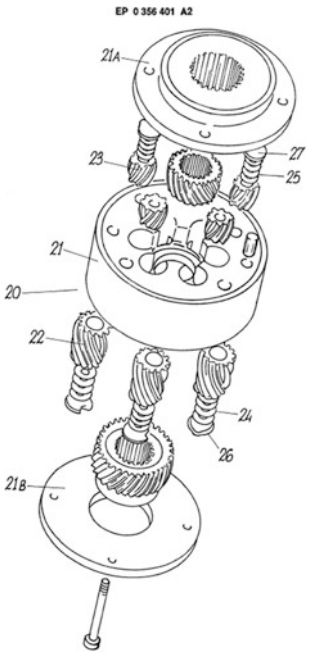

Fig. 5 Parallel axes spur gear differential (Ceccano and Novelli 1990)

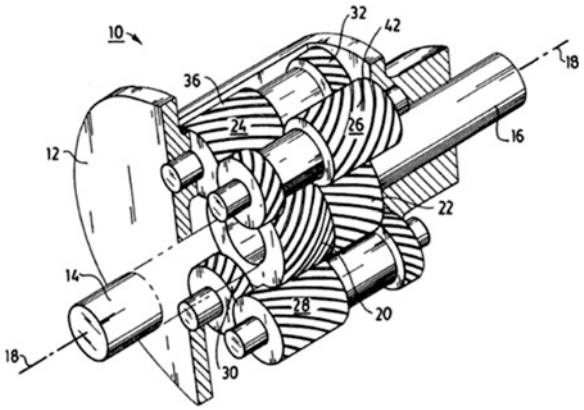

Fig. 6 Parallel axes spur gear differential (Tseng 1992)

2.4 Parallel Axes Internal Spur Gear Differentials

These differentials are actually planetary gear systems where the drive axles and engine shaft are connected with the internal and external sun gears and the carrier respectively.

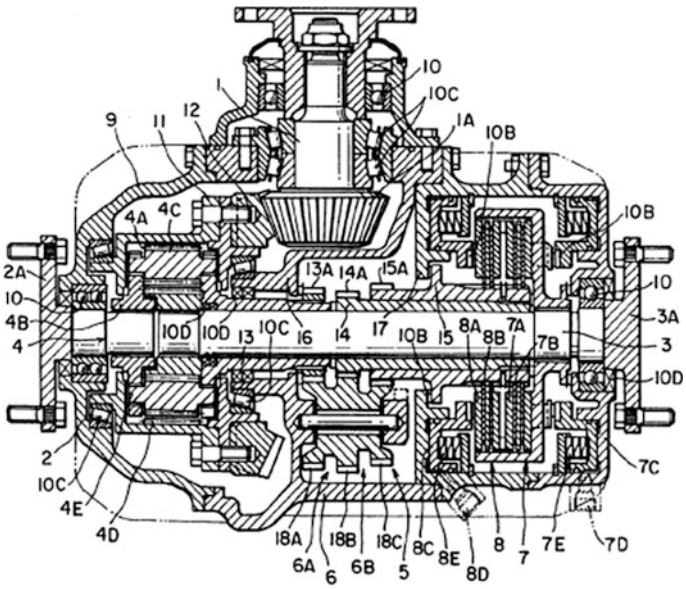

Fig. 7 Mitrsubishi active yaw control differential (Sawase and Niwa 1993)

In 1993, the differential shown in Fig. 7 was presented, which consists of a planetary system, two disk clutches and three gear pairs that alter the speed of the clutch shafts (Sawase and Niwa 1993). This differential and the further evolved versions as well comprise basic parts of the Super AYC (active yaw control) system developed by Mitsubishi. They allow torque distribution independently of the relative speed of the driving wheels to the differential shell (Ushiroda et al. 2003).

Honda Motor presented in 1994 a series of devices one of which is shown in Fig. 8. Although the planetary systems are connected in various ways, they all have a common feature: A hydraulic pump and motor pair that is electronically controlled to determine the torque distribution independent of the relative wheel speed to the differential shell (Shibahata and Tokushima 1994).

Analyses of torque vectoring systems consisting of parallel axes internal spur gear differentials can be found in literature (Wheals et al. 2004, 2005, 2006).

Figure 9 shows a differential that consists of a helical spur gear planetary system where the planets are floating and their face surface and the cylindrical surface of the teeth tips are sliding on the planet carrier (Yoshiyama and Hasegawa 2004). The carrier is connected to the input shaft while the ring and sun gears are connected with the output shafts. The torque is distributed unequally and this is the reason why this device is used as a central differential in four wheel drive vehicles. Further development of this main idea lead to the differential known commercially as Torsen type 3 of Zexel Gleason.

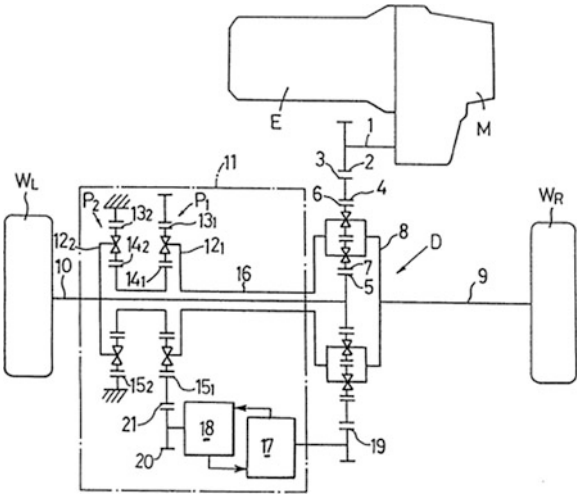

Fig. 8 Honda active yaw control differential (Shibahata and Tokushima 1994)

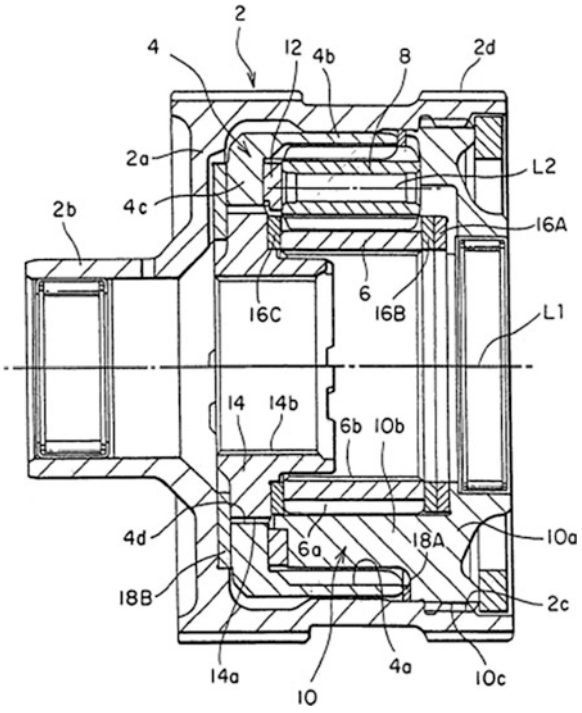

Fig. 9 Planetary gear train used as a differential (Yoshiyama and Hasegawa 2004)

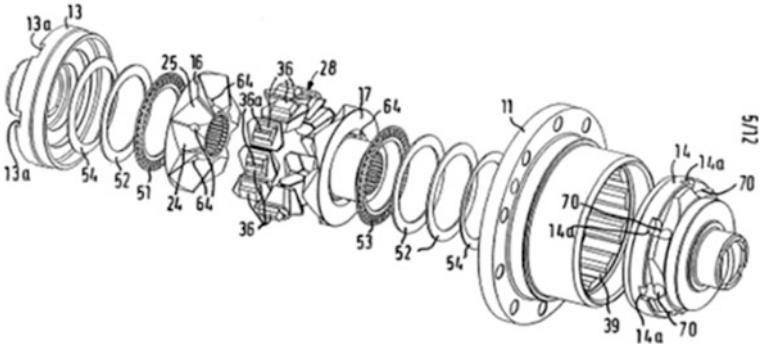

Fig. 10 Gearless differential (Young et al. 1995)

2.5 Gearless Differentials with CAM Curved Surfaces

In the 1990s many variations of differentials with sliding elements were designed. Figure 10 shows a representative example of such differentials (Young et al. 1995). The ends of each sliding element are inclined and have triangular shape. The disks that are in contact with the elements are formed similarly to bevel gears though their flanks are planar. Behind each disk surface treated rings are placed in order to increase friction with the shell.

The differential shown in Fig. 11 consists of two cylinders with circumferential grooves (Mimura 1999). The shell has corresponding straight grooves. In the intermediate space spherical rolling elements are placed. Cages formed from metal sheets hold the rolling elements and swing axially. They connect the cylinders imposing them to rotate in opposite directions. The shell is connected to the input and the two cylinders the output shafts of the differential.

One of the most recent gearless differential designs with CAM surfaces is shown in Fig. 12. It is patented by Eaton Corp. (Radzevich 2011) and it is known with the commercial name Detroit Locker.

2.6 Gearless Differentials with Friction Clutches

Haldex Traction Corp. presented in 1998 the first version of a joint for drive axle connections with a multiple disk clutch that is activated by an electromagnetic brake (Severinsson 1998). It substitutes the central differential in four wheel drive vehicles as it allows torque transfer to the two drive axels independently of their relative speed. In the following year, the evolution of this invention was presented. The device is known by the name Haldex (Lundstroem 1999). It consists of a multiple disk clutch and a unit that contains three rotating disks with properly

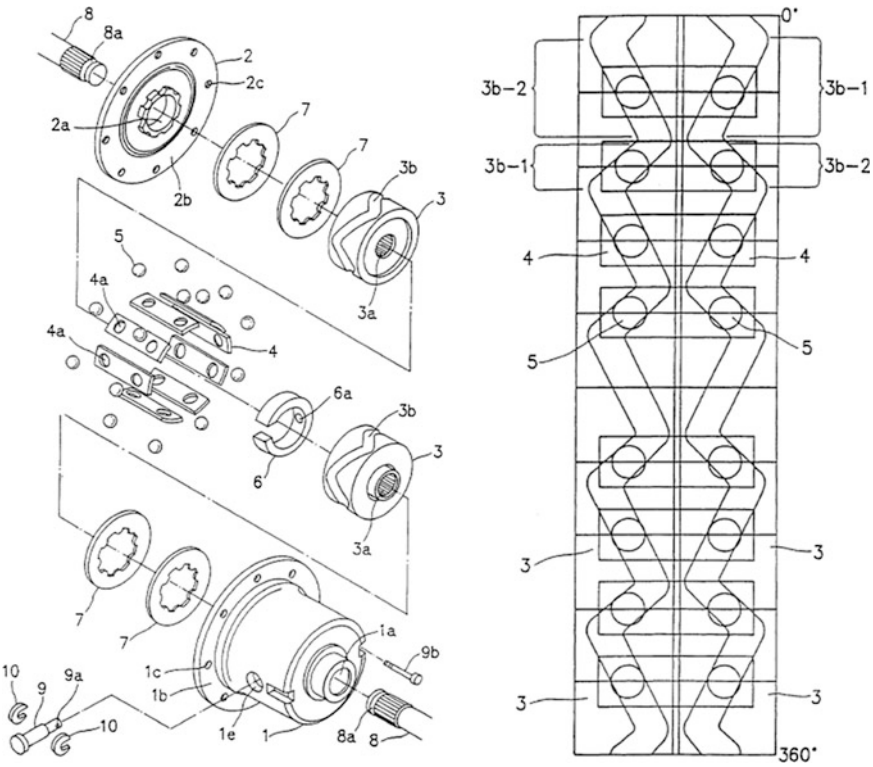

Fig. 11 Rolling elements differential (Mimura 1999)

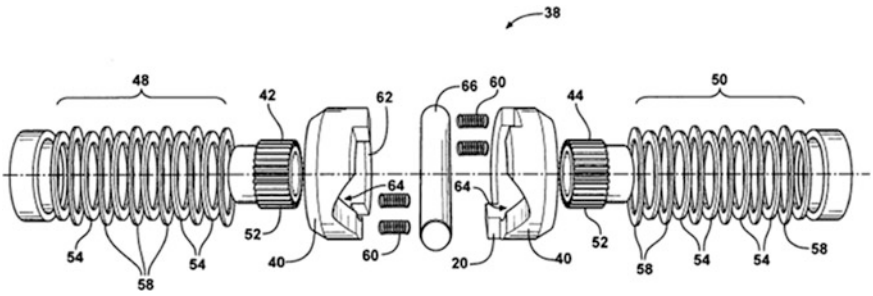

Fig. 12 Eaton gearless differential (Detroit Locker) (Radzevich 2011)

located holes (Fig. 13). A hydraulic system pressurizes oil through these holes generating an axial thrust that compresses the clutch. Another design, which substitutes the central differential, is described by Gassmann and Barlage (2004).

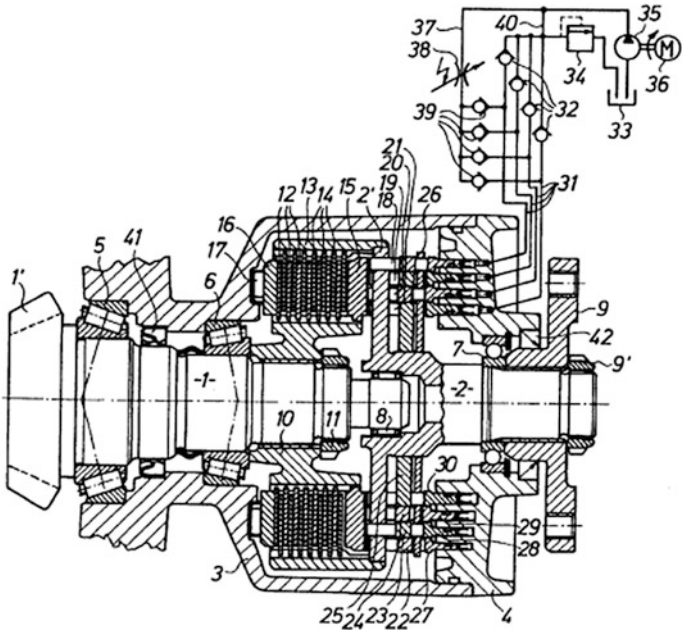

Fig. 13 Haldex joint (Lundstroem 1999)

3 New Differential

In the following, a new differential featuring controllable torque distribution that has been recently developed by the authors is presented. It consists of two identical planetary gear systems, an inversion mechanism and an electric machine with the ability to operate both as a motor and as a generator (Mihailidis and Nerantzis 2010).

The schematic view of Fig. 14 shows the principle of operation. The ring gears 3, 3′ are both connected to the input shaft 7 and thus always have equal speed. The sun gears 1, 1′ are interconnected through the inversion mechanism that consists of shafts C, C′, E, and E′ and gears 4, 4′, 5, 6, 5′ and 6′. As the vehicle enters a turn the carriers B, B′ of the two planetary systems, which are connected to the driving wheels, rotate at different speeds. The inversion mechanism forces the two sun gears to rotate in opposite directions allowing the carriers to have different speeds. The torque distribution is controlled by the electric machine that is connected to one of the inversion mechanism shafts. By breaking or assisting the motion of the shaft higher torque is transmitted to the internal or the external wheel respectively. An electronic system, which controls the direction and magnitude of the torque applied by the electric machine, is needed to determine the torque distribution.

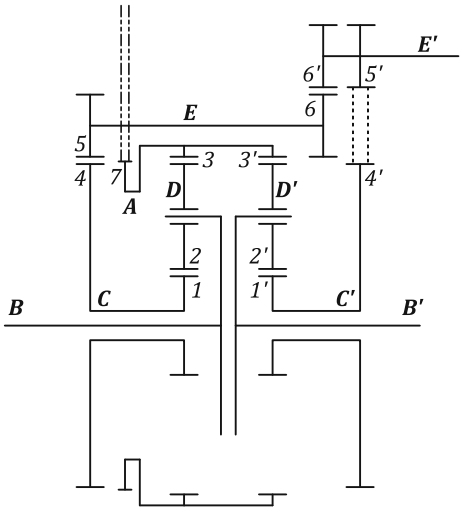

Fig. 14 Schematic view of the new differential

4 Simulation

In order to evaluate the handling performance of the new differential, the first Formula SAE race car of the Aristotle University Race Team (Mihailidis et al. 2009) was modeled in the ADAMS/Car environment. It is a rear wheel drive car with front and rear double wishbone suspensions. The following three types of differentials were modeled and compared: (a) An open differential where both halfshafts apply equal torques to the wheels. (b) A viscous differential (LSD) in which the differential torque is determined from a map of halfshaft rotational speed difference and applied friction torque. (c) The third is a model using a torque distribution strategy to exemplify the capabilities of the new differential.

The simulation scenario is acceleration on split μ surface, where the right wheels are driven on a surface with $\mu = 0.5$ while for the left wheels on a surface with $\mu = 1$. The initial speed is 10 km/h, the steering wheel is locked at 0° and the throttle position is set to 100 %. Under this conditions the new differential emulates a viscous one.

Figure 15 shows the differential torque over time. A positive value means that the left wheel receives more torque than the right. Therefore, the vehicle deflects to the right as shown in Fig. 16. Finally, Fig. 17 shows that the acceleration performance of the new differential, when emulating a viscous unit, is superior compared to the performance of an open differential. In the latter case at approx. 4 s. slip occurs and the acceleration drops.

An experimental layout of the device has already been designed and built and experiments concerning the effect of the new differential on the driving behavior are currently carried out. Figure 18 shows the experimental differential. An electronic system that determines the torque distribution was also designed and built for the purposes of experimentation. Some early tests proved that the new

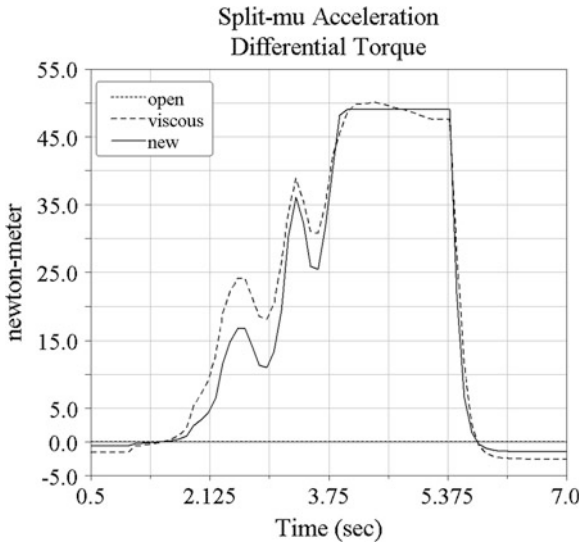

Fig. 15 Split μ test—differential torque

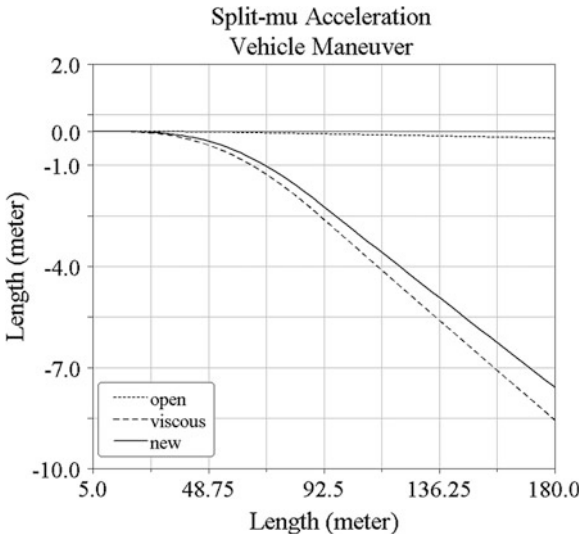

Fig. 16 Split μ test—vehicle maneuver

differential affects vehicle driving behavior selectively either towards understeer or oversteer depending on the torque applied to the inversion mechanism by the electric machine.

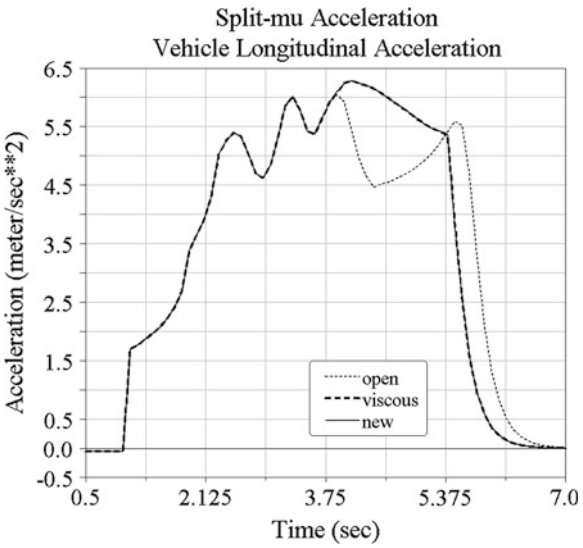

Fig. 17 Split μ test—vehicle longitudinal acceleration

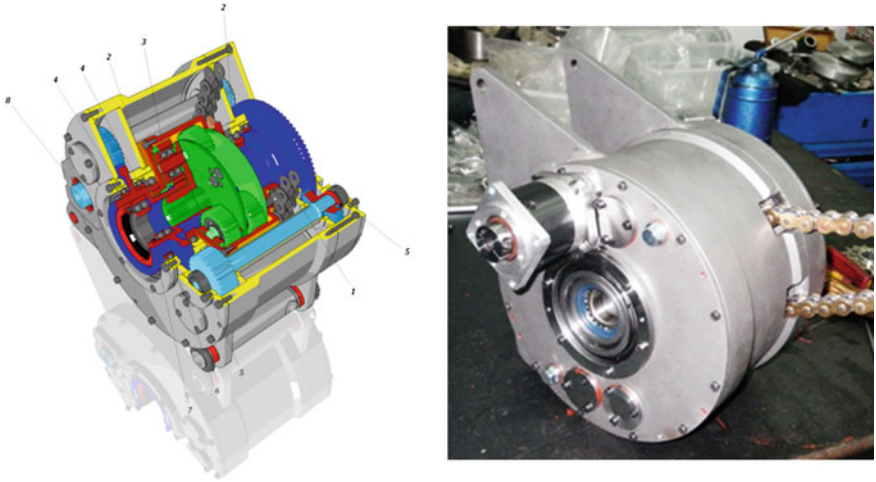

Fig. 18 Experimental differential

5 Conclusion

This paper presents the design of the differential mechanism as it has evolved during the last twenty years. Open differentials have the drawback that they fail to transmit the required torque and introduce driving instability on sloppy roads. Locked differentials, and to a lesser extent limited slip differentials, influence the driving behavior towards under-steering. Therefore, the most challenging design

requirement is to build a differential with adjustable torque distribution. A recently developed such device is also presented in this paper. First test runs show promising results.

References

Ceccano L, Novelli M (1990) A differential mechanism with limited sliding. EP0356401A2
Chocholek SE (1988) The development of a differential for the improvement of traction control. C368/88 © IMechE, Gleason Corporation, pp 75–82
Gassmann T, Barlage JA (2004) Electronic torque manager. SAE Trans 113(6):589–593 (2004–01-0866)
Gleasman KE, Gleasman JY, Suwijn PW (2008) Full traction differential with hybrid gearing. US2008103008A1
Hagiwara M, Teraoka M (1989) Locking differential gear assembly. US4805486A
Lundstroem B (1999) Device for transmitting torque between two rotatable shafts. US5979631A
Mihailidis A, Nerantzis I (2010) Differential device with controllable torque distribution. EP 10191000.8
Mihailidis A, Samaras Z, Nerantzis I et al (2009) The design of a formula student race car: a case study. Proc Inst Mech Eng Part D J Automobile Eng 223(6):805–818
Mimura K (1999) Balls and cam type differential gear. US5904073A
Mohan SK, Sharma A (2006) Torque vectoring axle and four-wheel steering: a simulation study of two yaw moment generation mechanisms. SAE Trans 115(6):780–789 (2006–01-0819)
Nunney MJ (1998) Automotive technology. Warrendale, SAE International
Park J, Kroppe WJ (2004) Dana torque vectoring differential dynamic trak. SAE Trans 113(6):1057–1062 (2004–01-2053)
Piyabongkarn D, Grogg J, Yuan Q, Lew J (2006) Dynamic modeling of torque-biasing devices for vehicle yaw control. SAE technical papers (2006-01-1963)
Piyabongkarn D, Lew J, Grogg J, Kyle R (2006b) Stability-enhanced traction and yaw control using electronic limited slip differential. SAE Trans 115(6):931–941 (2006–01-1016)
de Price DSJ (1974) Gears from the Greeks: the Antikythera mechanism—a calendar computer from ca. 80 BC. Trans Am Philos Soc New Series 64(7):1–70
Radzevich SP (2011) Locking differential having improved torque capacity. WO2011012968A1
Sawase K, Niwa T (1993) Vehicular left/right drive force adjusting apparatus. EP0575151A1
Sawase K, Sano Y (1999) Application of active yaw control to vehicle dynamics by utilizing driving/breaking force. JSAE Review 20:289–295
Severinsson L (1998) A torque transmitting device. WO9826950A1
Shibahata Y (1990) Torque distribution control using continuously variable transmission in parallel with differential. GB2224790A
Shibahata Y, Tokushima S (1994) Torque distributor mechanism for a differential. DE4408587A1
Shih S, Bowerman W (2002) An evaluation of torque bias and efficiency of Torsen differential. SAE Trans 111(6):1495–1505 (2002–01-1046)
Tseng GB (1992) Parallel-axis combination gear differential. US5122101A
Ushiroda Y, Sawase K, Takahashi N et al (2003) Development of super AYC. Technical review, pp 73–76
Wheals JC, Baker H, Ramsey K, Turner W (2004) Torque vectoring AWD driveline: design, simulation, capabilities and control. SAE Trans 113(6):557–576 (2004–01-0863)
Wheals JC, Deane M, Drury S et al (2005) Torque vectoring driveline: SUV-based demonstrator and practical actuation technologies. SAE Trans 114(6):631–648 (2005–01-0553)

Wheals JC, Deane M, Drury S et al (2006) Design and simulation of a torque vectoring™ rear axel. SAE Trans 115(6):767–779 (2006–01-0818)

Yoshiyama T, Hasegawa Y (2004) Differential gearing for vehicle including planetary gear mechanism and method of manufacturing. EP1473489A1

Young AJ, Spooner J, Chippendale JP (1995) A differential mechanism. WO9500777A1

Load Capacity of Worm Gears

Vojislav Miltenović, Milan Banić and Aleksandar Miltenović

Abstract Worm gearing has very wide use in power transmission in movement and the correct work of the complete machine system depends on it. Latest research in this area shows that there may be a large number of limited states in its work which are identified on the basis of the state of working surface. This paper considers these limited states and gives a critique of load capacity calculation.

Keywords Worm gear · Load capacity · Limited state

1 Introduction

Worm gears have very wide use in transmission gear and movement because they have several advantages in comparison to other types of gears. The basic characteristics of worm gears are:

- Possibility of achieving huge gear ratio of one worm gear pair. If revolution is reduced, gear ratio is in $5 \leq u \leq 70$ (for small power it is possible to achieve gear ratio of up to $u \leq 1000$).
- Considerably smaller internal dynamic forces and sound, by absorbing vibrations.
- Efficiency of worm gearing is relatively high because of huge sliding between sides in contact of gear and worm gear.

V. Miltenović (✉) · M. Banić · A. Miltenović
Mechanical Engineering Faculty, University of Niš, Niš, Serbia
e-mail: vojamiltenovic@yahoo.com

M. Banić
e-mail: banicmilan@hotmail.com

A. Miltenović
e-mail: amiltenovic@yahoo.com

G. Dobre (ed.), *Power Transmissions*,
Mechanisms and Machine Science 13, DOI: 10.1007/978-94-007-6558-0_9,

- They can be produced as self-stopping transmission gearing, which enables them to have a wide use.
- Power input and output are possible on the both sides of a worm transmission gear.

2 Limited States of Worm Gears

In modern construction solutions it is common to use worm gear made of tin bronze and worm made of hardened and whetted steel (Fig. 1). Worm gears have following limited states:

- Destruction of tooth side under pitting,
- Tooth side wear,
- Tooth breakage,
- Worming, mining changing temperature stability of gear transmission,
- Scuffing,
- Worm shaft deflection.

2.1 Pitting Resistance

Pitting is actually the destruction of tooth surface (shaped like small holes and dimples, Fig. 2) as an effect of huge surface pressures and dynamic stress wear.

One can see the difference between the initial and advance stage of pitting. The initial stage of pitting is the effect of the first phase of working of transmission gears. It has a positive effect because it leads to equal load distribution of stress

Fig. 1 Standard worm gear

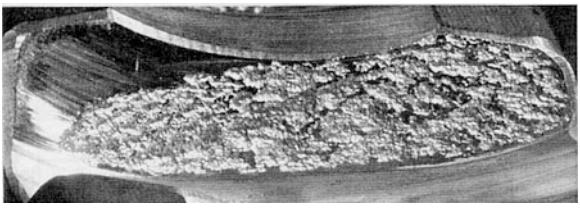

Fig. 2 Damage of tooth surface with pitting Bernhard (1996)

and better contact pattern. When working conditions are unchanged, this type of pitting is smaller during a period of time, that is, the damaging process is digressive. Medium and highly loaded worm gear pairs can be attacked by advance pitting and it is a huge problem. This pitting has progressive character, so that destroyed surfaces (Fig. 2) are larger and at the same time the contact pattern is smaller. The effect is a continuous spreading of damaged surface and change in the shape of tooth surface. This leads to sudden tooth surface wear, and then tooth breakage.

While maintaining the working capability of worm gear as limited destruction, it is taken that the destruction is 30–50 % of tooth surface due to pitting (Fig. 2). In that case, the correct work of transmission gear is no longer possible.

The process of pitting develops in 4 phases:

- dynamic stress wearing;
- beginning of initial crack;
- crack largening;
- destruction of tooth surface or pitting.

The following can occur as possible causes of pitting:

- existence of hard bodies (contaminants) in oil;
- micro welding of tooth surface tips of prominence in contact;
- cavitations;
- tense forces between oil and metal in the period of sudden unload of pressured surfaces;
- chemical activity/load-crack-corrosion;
- abstracting acid from lubricant.

2.2 Wear Load Capacity

During the period of wearing mining continually wearing material tooth width is smaller. In the first phase, wearing has a positive effect because it leads to rubbing of material and accommodation between shapes of tooth surfaces and later stopping any further wear. However, in the cases of huge intensity rubbing, wearing resistance can be a criterion of working period. Wearing basically depends on working criteria. Changing of shaft rotation conditions and regime of work, as well

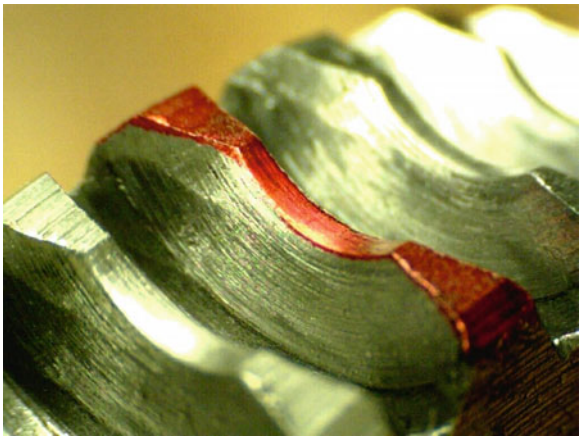

Fig. 3 Wear damage of tooth surface, Miltenović (2011)

as terming off and on transmission gear, lead to increased effect of wearing (Fig. 3). Using hard and quality worm tooth sides (Case carburising, whetting, polishing) can result in decreased wearing.

Wearing depends on lubricants as well. When using mineral oils, oil viscosity has an important effect on wearing. Oils with smaller viscosity result in larger wearing in comparison to oils with huge viscosity, so it can be said that there is a proportional relation between intensity of wearing and ISO-VG class.

2.3 Root-Strength of Teeth

Worm gear pairs have dangerous working loads only in tooth root of worm gear, considering that they are less resistant and less durable in comparison to worm teeth. In the root tooth of a worm gear, there is a complicated load, and the dominant stresses are shear and bending.

Worm gear tooth breakage is very rare. Most often causes are striking overloads when loads appear that are larger than the static strength of material. Wear is also a considerable effect that causes tooth breakage, and wearing diminishes its cross-section. Monitoring of working capability in comparison to tooth breakage is important in due course, and observing critical width of wear layer which prevents appearance of cracks on tooth.

2.4 Thermal Stability

When designing a gearbox, one should also consider the heat generated inside the gearbox (efficiency of gearing, friction of bearings, and friction in sealing). This parameter is not so important in spur or bevel but it is in worm gearing. As worm

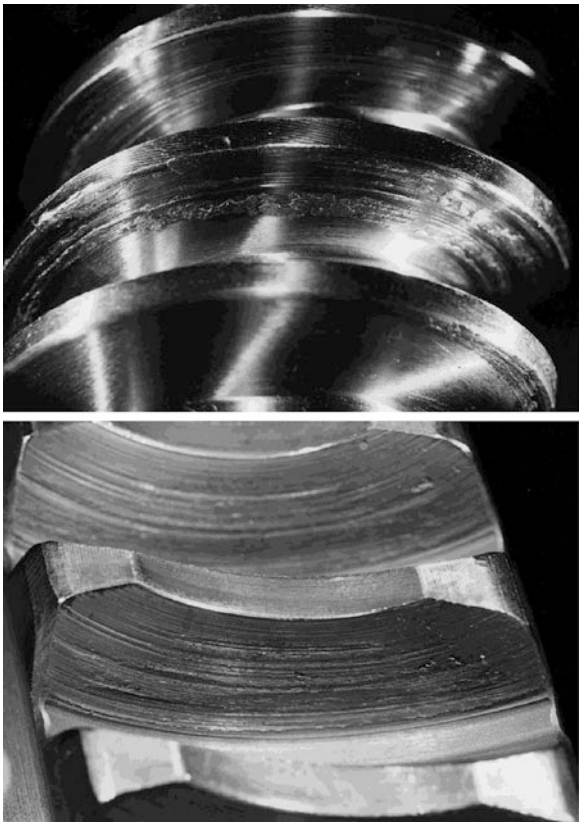

Fig. 4 Scuffing at worm of through hardened steel and at wheel of globular cast iron, Steingröver (1995)

gearing efficiency is lower considerably than that of spur or bevel gearing, considerably more heat is generated in the gearing and has to be removed. Therefore, thermal safety has great importance for a correct design to ensure gearbox function within the permitted temperature range of oil. Thermal design/safety tends to be one of the limiting factors when designing transmissions.

2.5 Scuffing

Scuffing appears as an effect of local overload of tooth side or inefficient lubrication meaning lubricating with oil with non-becomingly lubricated characteristics and mostly in conditions of huge sliding velocity between tooth sides in contact. Hardened tooth side of worm with inadequate picture of caring mining interrupted geometry between sides in touch are also condition lead to destruction due to scuffing. Typical shapes of destruction due to scuffing are shown in Fig. 4. If there is destruction due to scuffing and combination of material steel/cast iron this

process leads to total destruction and it cannot be stopped. However, destruction due to scuffing can be stopped after short time using the combination of material steel/bronze and it can lead to uninterrupted running.

2.6 Worm Shaft Deflection

Worm shaft is loaded by radial, axial and tangential force, which leads to considerable bending of shaft, considering relatively large distance between bearings. Due to bending, deflection of shaft appears which can lead to interference in contact. Tangential force depends on friction on the teeth sides, so in cases of insufficient lubricating friction force grows which has for effect considerable deflection of worm shaft. In conditions of changing loads and revolution per minute this can lead to smaller contact between tooth sides and local overload of same, and the effect can be deflection of worm shaft.

Monitoring of work correctness is based on control of contact line between tooth surface and monitoring of transmission gear thermal stability.

3 Relation Between Limited States

There is mutual relation between certain worm transmission gears. For example, the development of pitting can be stopped by increased wearing of tooth sides. If there is critical wearing at worm gear pair than pitting has a secondary mining. But if critical damage is caused by pitting than wearing is not an important criterion for calculation.

There is a mutual dependency between wearing and tooth breaking in root. Wearing diminishes width of worm gear tooth, which should be taken in consideration while maintaining work ability in comparison to tooth breakage in root.

3.1 Wearing and Pitting Process

Fig. 5 shows wearing and pitting process by synthetic oils as lubricants in the period of time where we can see three phases.

- Phase I—phase of initial pitting. In this phase until number of load circles is N_{LI} small initial damage appears from pitting and there is almost no wearing.
- Phase II—phase of developed pitting. In this phase damage caused by pitting increases almost linearly. At the end of this phase after number of circles is N_{LII} ($N_{LII} = 3–5 \times N_{LI}$) pitting intensity is maximal. Wearing in this phase in minor.

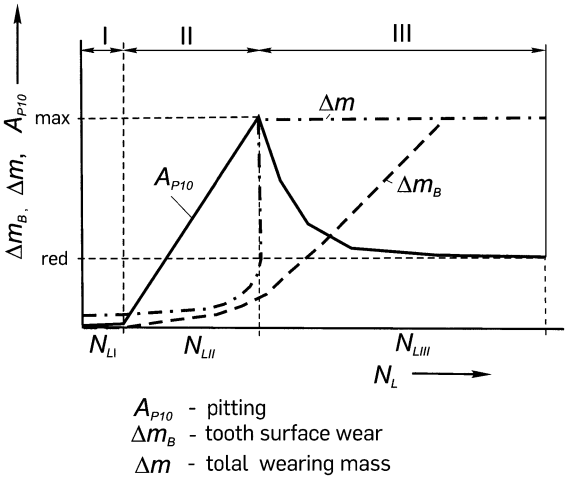

Fig. 5 Trend of wearing and pitting process

- Phase III—phase of wearing. In this phase we have sudden increase of wearing and in the same time reduction of pitting size. By increasing the load surface tooth side wearing size is smaller and in further work period it is almost constant. Surface destroyed by pitting becomes smaller at approximately $A_{\mathrm{P10\ red}} = 3\text{–}30\ \%$, whole amount of worn material from tooth sides for both types destruction is almost constant.

Most common load limitations of worm transmission gears are connected to pitting and wearing of tooth sides of worm gear. Phases of developing destruction point show that they are mutually dependent.

3.2 Contact Pattern and Load Capacity

Lubrication between tooth flanks and contact pattern have a decisive influence on lifetime of worm gears. During the work the slight wear of tooth flanks of worm gear occurs. Wear zone is the contact pattern (Fig. 6). Contact pattern has a huge impact on the successful fulfilment of work functions, efficiency and lifetime of transmissions.

During run-in period, there is only a partial contact (Fig. 7), which leads to intense wear of tooth flanks. When the full contact pattern is achived, Hertzian surface pressures are reduced so then the steady state operation occurs, followed by minimal wear due to mixed friction.

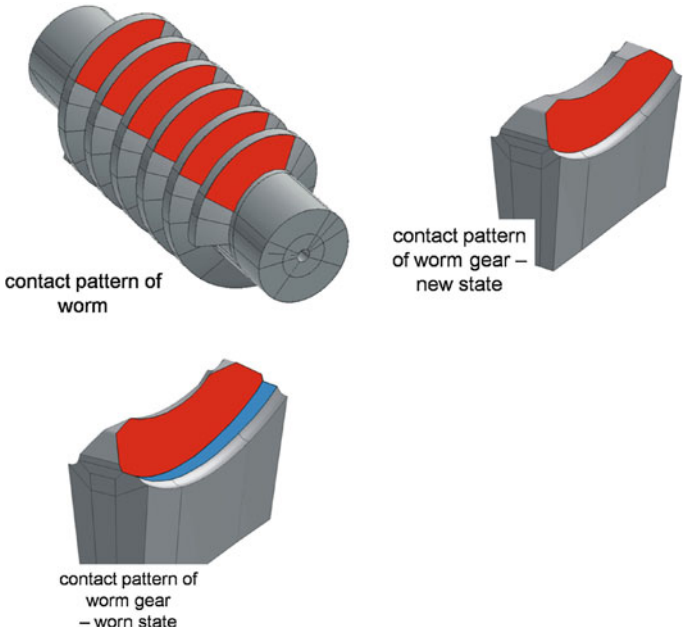

Fig. 6 Contact pattern on worm and worm gear

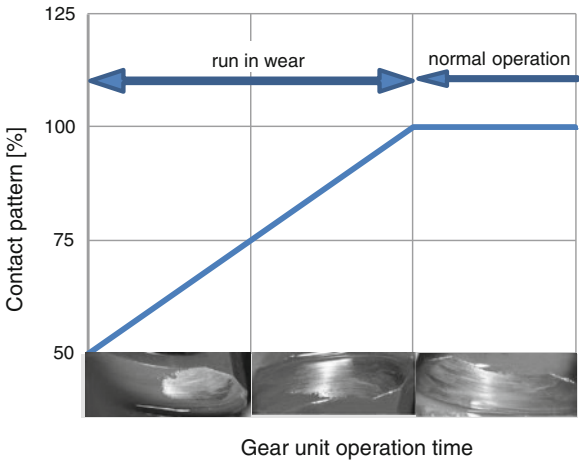

Fig. 7 Development of contact pattern during operational time

Experimental studies show that there is direct dependence between the contact pattern, load and wear (Fig. 8). Minimal wear corresponds to full contact pattern and moderate loads. Decrease of contact pattern leads to increase of wear.

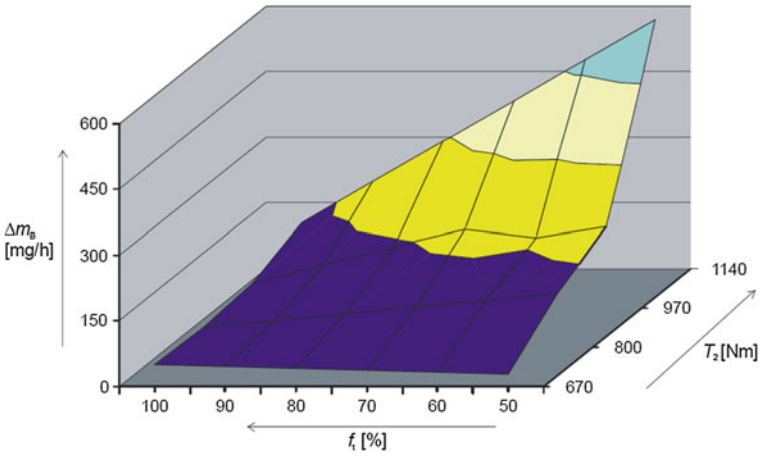

Fig. 8 Relationship between wear and contact pattern, Höhn et al. (2010)

4 Load Capacity of Worm Gears

Initial work on the coupling worm pairs were made by Stribeck (1897/98) and Erbst (1901). Notable research in this area was conducted by Niemann, Weber and Maushake (1956) also. Calculations of geometry and contact lines are given in the works of Wilkesmann (1974) and Predki (1982). They give an accurate analytical procedure for determining the equivalent radius of curvature.

Calculation of load capacity of worm pairs is today based on DIN 3996 (8/2005), where dimensionless physical characteristic values are defined. These characteristic values mainly depend on the geometry of the gearing and cannot be measured directly. They are characteristic value for mean Hertzian pressure p_m*, mean lubricant gap thickness h* and mean sliding path s*. Characteristic value p_m* and h* are defined by Predki (1982), and s* by Neupert (1990). Such defined parameters are part of DIN 3996 and allow not only the calculation of load capacity and efficiency, but also a direct comparison of different worm gear geometry.

According to DIN 3996, the ratio between limiting value of contact stress σ_{Hkr} and mean contact stress σ_{Hm} represents a pitting safety:

$$S_H = \frac{\sigma_{Hkr}}{\sigma_{Hm}} \geq S_{H\min} = 1. \tag{1}$$

The wear safety S_W is calculated from the permissible wear $\delta_{W\lim n}$ and abrasive wear in the normal section δ_{Wn} according to Eq. (2).

$$S_W = \frac{\delta_{W\lim n}}{\delta_{Wn}} \geq S_{W\lim} = 1,1. \tag{2}$$

Abrasive wear in the normal section δ_{Wn} is the function of:

- combination of materials used,
- oil type and structure,
- lubrication film thickness,
- load cycle,
- loading intensity.

The wear in the normal section δ_{Wn} is the result of product of wear intensity J_W and wear distance s_{Wm}.

$$\delta_{Wn} = J_W \cdot s_{Wm}. \tag{3}$$

Boundary value for flank-removal δ_{Wlimn} can be determined on different approaches. The wear limits can be defined by the geometric boundaries and by experiment determined boundaries.

According to DIN 3996 one of the criteria is to avoid the appearance of a pointed tip tooth. In this case is given a boundary value of pointed tip tooth for wear. Permissible wear in the normal section $\delta_{W\text{limn}}$ must not exceed the thickness of the tooth in the normal section.

Safety for root-strength of teeth S_F is calculated according to (4):

$$S_F = \frac{\tau_{Fkr}}{\tau_F} \geq S_{F\,\text{lim}} = 1,1. \tag{4}$$

where:

$\tau_{F\text{kr}}$ permissible shear stress,
τ_F shear stress

Temperature safety S_T is calculated according to (5):

$$S_F = \frac{\vartheta_{S\,\text{lim}}}{\vartheta_S} \geq S_{S\,\text{lim}} = 1,1. \tag{5}$$

where

$\vartheta_{S\text{lim}}$ boundary value of oil temperature
ϑ_S oil temperature

Worm deflection safety S_F is calculated according to (6):

$$S_\delta = \frac{\delta_{\text{lim}}}{\delta_m} \geq S_{\delta\text{min}} = 1. \tag{6}$$

where

δ_m worm shaft deflection,
δ_{lim} permissible worm shaft deflection

Table 1 Transmission gear data

Geometrical size	Values
Cental distance a (mm)	100 (63, 160, 315)
Transmission ratio i	20,5 (10, 30, 40)
Modul m (mm)	4 (2.5, 6.3, 12.5)
Diameter quotient q	9 (10.6)
Number of teeth z_1	2 (1, 4)
Number of teeth z_2	41 (30)
Wheel material	CuSn12-C-GZ
Worm material	16MnCr5
Input speed (min^{-1})	200–2000
Synthetic oil (Polyglykol)	$v_{40} = 460$ mm^2/s; $v_{100} = 82$ mm^2/s

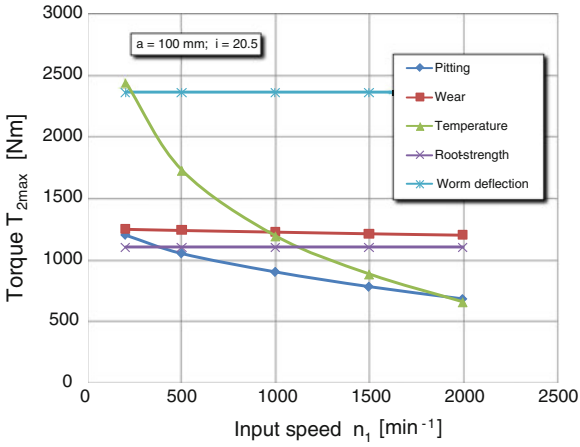

Fig. 9 Comparison of worm gear load capacity for difference values of input speed n_1

Analysis of worm gear load capacity is made for family of gear drives with characteristics given in Table 1. Calculation of load capacity for worm gear according to DIN 3996 is done through 5 criteria:

- Pitting resistance,
- Wear load capacity,
- Root-strength of teeth,
- Thermal stability, and
- Worm shaft deflection.

The calculation was performed for various numbers of input speed, gear ratio and the center distance. For each calculation the maximum output torque $T_{2\ max}$ was obtained for the required safety. Calculation results of load capacity are shown in Figs. 9, 10 and 11.

Balanced load capacity is calculated for the selected gear drive ($a = 100$ mm, $i = 20.5$) with different input speed $n_1 = 200$–2000 min^{-1} (Fig. 9). This is the optimal case, which should be used in practical construction solutions.

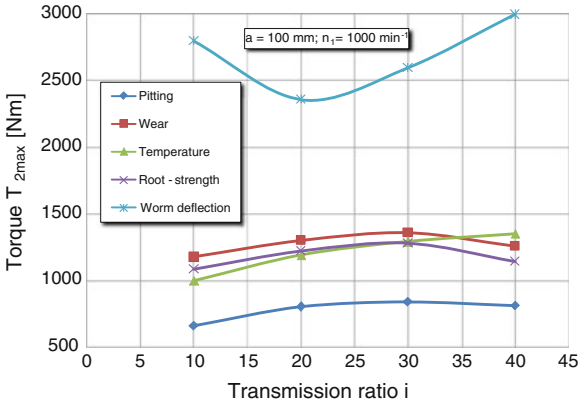

Fig. 10 Comparison of worm gear load capacity for difference values of transmission ratio *i*

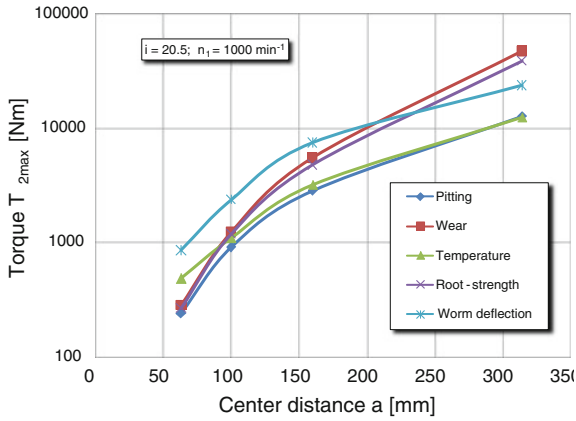

Fig. 11 Comparison of worm gear load capacity for difference values of central distance *a*

Load capacity for variation of gear ratio *i* for constant values of center distance and input speed ($a = 100$ mm; $n_1 = 1000$ min^{-1}) is limited by pitting safety (Fig. 10).

Other criteria have balanced values.

In case of change of center distance variation and for constant value of gear ratio and the input speed ($i = 20.5$; $n_1 = 1000$ min^{-1}). Maximal load capacity is limited by pitting and sump temperatures (Fig. 11).

5 Conclusion

Based on this display one can draw the following conclusions:

1. Conducted analysis of limited states show that most common load limitations of worm gear pair are connected to pitting and tooth side wearing of worm gear. It should be taken in consideration mutual dependents between certain types of destruction and conditions of exploitations.

2. Load capacity and efficiency of worm gear mainly depends on contact pattern of the tooth flanks. Selecting the optimal contact pattern reduce wear and increase efficiency.
3. Shown boundaries of load capacity have for a goal to define the structural solutions of optimal load capacity of worm gear. Conducted calculation analysis of worm gear load capacity selected for different criteria shows that it is possible to obtain a uniform load on all criteria by appropriate selection of the most influential parameters.

References

Bernhard R (1996) Untersuchungen zur Grübchen-bildung bei Zylinder-Schneckengetrieben. Dissertation. TU München

DIN 3996 (8/2005) Tragfähigkeitsberechnung von Zylinder- Schneckengetrieben mit sich rechtwinklig kreuzenden Achsen

ERNST A (1901) Eingriffsverhältnisse der Schneckengetriebe. Springer, Berlin

Höhn B-R, michaelis K, weisel CH (2010) Load capacity and efficiency of crossed helical worm gears, International Conference on Gears—Gears 2010. VDI Berichte 2108.2 Munich, pp 1221–1232

Miltenović A (2011) Verschleißtragfähigkeits-berechnung von Schraubradgetrieben mit Schraubrädern aus Sintermetall. Dissertation, Ruhr-Universität Bochum

Neupert K (1990) Versuche zum Einfluss der Baugröße auf Wirkungsgrad und Flankentragfähigkeit von Schneckengetrieben unter Berücksichtigung der Schmierstoffviskosität. Abschlußbericht, Frankfurt Forschungsvereinigung Antriebstechnik e.V. Heft 312

Predki W (1982) Hertzsche Drücke, Schmierspalthöhen und Wirkungsgrade von Schneckengetrieben. Dissertation, Universität Bochum

Steingröver K (1995) Untersuchungen zu Verschleiß, Verlustgrad und Fressen bei Zylinder-Schneckengetrieben. Dissertation, TU München

Stribeck R (1897/98) Versuche mit Schneckengetrieben. Z. VDI 41/42

Weber C, Maushake W (1956) Untersuchung von Zylinderschnecken-getrieben mit rechtwinklig sich kreuzenden Achsen. Verlag Vieweg, Braunschweig

Wilkesmann H (1974) Berechnung von Schneckengetrieben mit unterschiedlichen Zahnprofilformen. Dissertation, TU München

Gear System Reliability-Based Design of Gear Drive Units

Milosav Ognjanović and Miloš Ristić

Abstract In the field of Engineering Design various methods are established for technical systems development. Gear transmission units are really a complex structure with various indicators of their behavior, such as the level of reliability, vibration and sound level, etc. This article contains the application of property-based design approach to gear unit reliability system structuring, and then the application of elementary reliability as a design constraint in design parameters definition. A specific way for elementary reliability and system reliability is introduced. Robust and axiomatic design of gear unit components is adapted for design parameters definition.

Keywords Gear · Reliability · Design · Property · Robust · Axiomatic

List of Symbols

R	Reliability
F_p	Unreliability
p	Statistic weight
P_F	Failure probability
σ_H	Herzian (flank) stress of the gear teeth
n_Σ	Total stress cycle number in exploitation
η, β	Waybill's function parameters
T	Torque
d	Diameter
σ_{Hdes}	Design available flank (Herzian) stress
m	Gear module
C	Bearing dynamic caring capacity

M. Ognjanović (✉) · M. Ristić
Faculty of Mechanical Engineering, University of Belgrade, Belgrade, Serbia
e-mail: mognjanovic@mas.bg.ac.rs

G. Dobre (ed.), *Power Transmissions*,
Mechanisms and Machine Science 13, DOI: 10.1007/978-94-007-6558-0_10,

1 Introduction

Property-based design and product development is a specific approach that provides the possibility to obtain a mature product in the first attempt. In general, technical systems (products) are the relations established between the function structure, the organ (machine parts) structure and the system behavior. The main task of the design process is to provide for the system behavior in order to satisfy necessary functional requirements (user needs). In the product design process, it is necessary to start with functional requirements and finish with the product behavior. Product behavior is the result of product components' properties and characteristics. For this purpose, in Fig. 1 the V-model (VDI 2206) of design process is adapted by Kruhmer et al. (2011). The recognised procedure that starts with functional requirements and finishes with overall system behavior is divided into 20 steps of actions. The first 10 steps contain the deduction function requirements to the level of the parts and assembly properties. Then, there follow the design synthesis and analysis in order to define the design structure and system integration with the aim to fulfil the desired systems behavior.

In Fig. 2 is presented the definition of the main terms used in Fig. 1 and relations between the characteristics and properties at the parts and assembly level. Also, this presentation explains the basis of the approach presented in this article.

Reliability in the sense as shown in Figs. 1 and 2 can be a user need (functional requirement), an assembly or a part property and a product behavior indicator (parameter). The machine part property elementary reliability can be used as the design constraint in defining the design parameters of the part, assembly and complete design structure. The objective of this article is to apply the presented

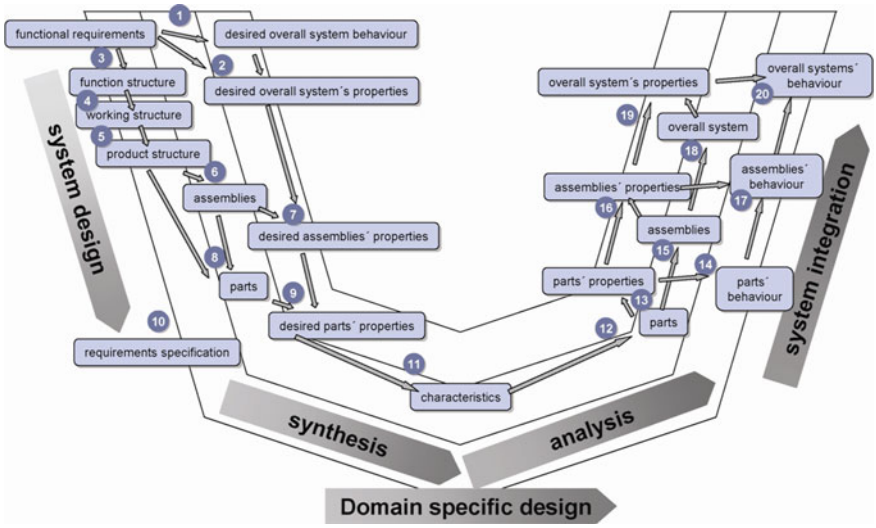

Fig. 1 Model for the property-based product development (Kruhmer et al. 2011)

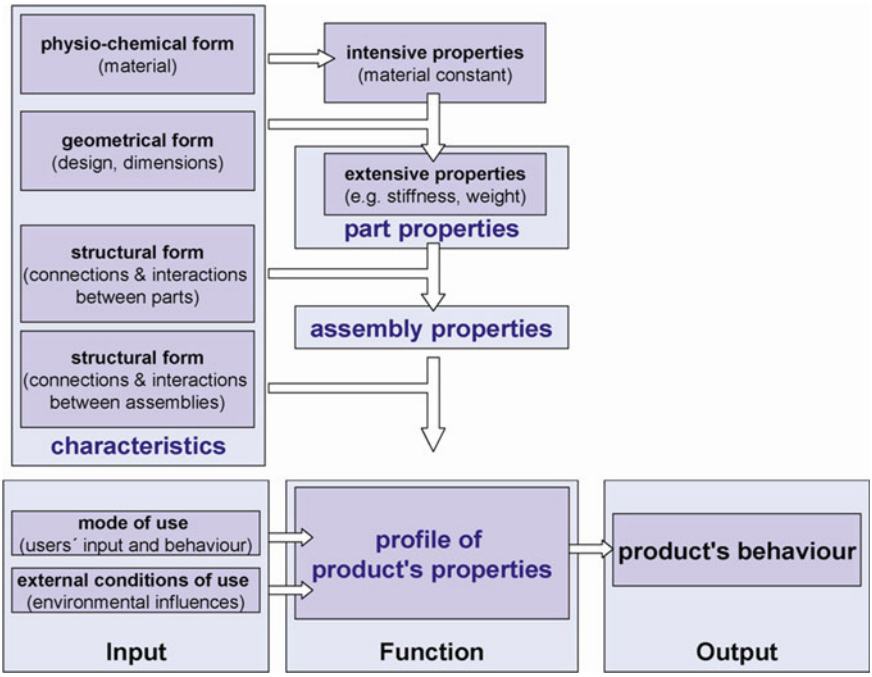

Fig. 2 Definition of the product's behavior based on characteristics and properties (Kruhmer et al. 2011)

methodology for introduction of the system reliability of gear transmission units, which will present the basis for design parameters definition. Gear unit behavior provided by this methodology should be indicated by reliability that is desired before the design process has started.

Reliability system of mechanical structures has been studied in numerous works and reliability system models provided by these studies produced results that did not match those identified in exploitation. Besides, the models mentioned are not oriented to design necessity. They are predominantly developed for the maintenance of the systems. These problems were the reason why reliability systems weren't developed for gear drive units. The objective of the article is application of presented property-based approach in order to establish a specific methodology for the gear drive units' development. Reliability is defined in specific way suitable for design purposes i.e. property-based design.

2 Elementary Reliability as Design Property

Elementary reliability R is defined at the level of machine part or assembly and connected to a certain failure of this component. In contrast to reliability there stands unreliability $F_p = 1 - R$ that presents the complex probability. This is a

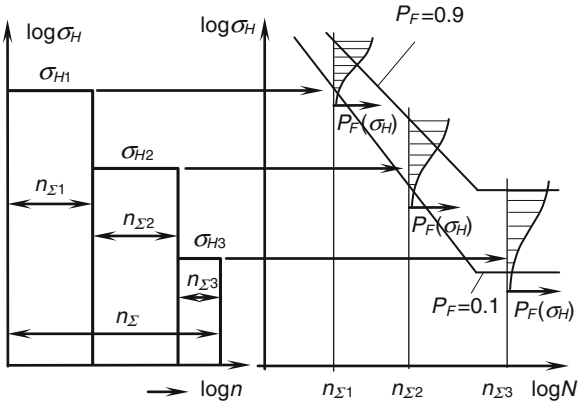

Fig. 3 Relation between service stress varying and gear wear probability

combination of service conditions probability p and failure probability P_F under these service conditions, i.e. $F_p = p\ P_F$. If during service life the gear pair is exposed to the flank stress σ_{H1} with $n_{\Sigma1}$ cycles and to stress σ_{H2} with $n_{\Sigma2}$ cycles and to σ_{H3} with $n_{\Sigma3}$ cycles (Fig. 4), gear wear unreliability can be calculated as

$$F_p = \sum_{i=1}^{3} p_i P_{Fi}; \quad p_i = \frac{n_{\Sigma i}}{n_\Sigma}; \quad P_{Fi} = 1 - e^{-\left(\frac{\sigma_{Hi}}{\eta_i}\right)^{\beta_i}} \tag{1}$$

Teeth wear (failure) probability P_{Fi} is presented by Weibull's functions, where the parameters of those functions η_i and β_i are defined for every σ_{Hi} and $n_{\Sigma i}$ (see Fig. 3). For this purpose, it is necessary to have the area of failure probability for a certain gear pair, which can be obtained by extensive gear wear testing.

Gear pair can be damaged by wear of the teeth flanks or by teeth fracture. For both damages, unreliability (elementary reliability) can be defined and calculated. The question raised is how to define total reliability of the gear pair. It is necessary to consider the next fasts: (a) If one gear is damaged, it is necessary to remove both—complete gear pair; (b) Gear pair has to be removed when the first damage arises—wear or fracture. These are the reasons why total reliability of the gear pair is equal to lesser reliability connected to wear or fracture. In the dominant number of cases gear wear reliability is lesser and this is the total reliability of gear pair.

Planetary gear set structure contains three types of gears, central pinion, satellite gears and inside toothed ring (Fig. 4). In the two types of teeth connections, Herzian flank stress is much higher in the mesh 1 than in the mesh 2. Stress cycles number of the central pinion teeth is also high because the speed is higher and three connections in the course of one revolution. Gear satellites are with much lower number of revolutions and in the two connections acting with different flanks, left and right. If the hardness of all flanks is the same, wear will be extremely different (Fig. 4). This difference is possible to reduce by the choice of corresponding design parameters. Complete planetary gear set has to be removed without any damage of the teeth. Total reliability of planetary gear set is equal to minimal reliability in relation to any damage. This is, first of all, reliability of the central pinion teeth wear.

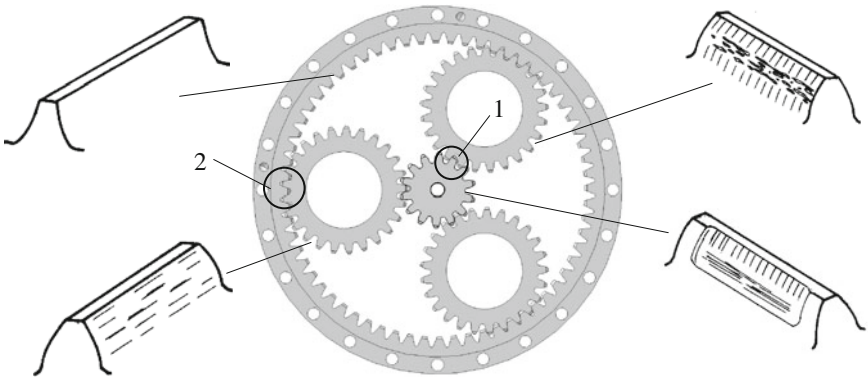

Fig. 4 Relation of teeth wears in planetary gear set

3 Gear System Reliability

Before deducing functional requirements, it is necessary to deduce design structure into components suitable for hierarchy processing of requirement indicator. In Fig. 5a gear transmission unit for bucket wheel traction of bucket wheel excavator is presented. For hierarchy processing (deduction) of total gear unit reliability, gear unit is structured into three sub-units i.e. transmission steps. The first stage (1) contains bevel gear pair together with planetary set for auxiliary drive. The second (2) and third (3) stages are planetary sets connected between each other. Physically, decomposition is realised by dismounting the middle screw bolted joint.

In Fig. 5b is presented the structure of elementary reliability for all three stages of the gear drive unit i.e. reliability three. The second II and third III stages include reliability of planetary gear set—PGS, reliabilities of the two bearings supporting planetary carriers—Bg and reliability of the bearings supporting satellite gears—BS. These three bearings SB are equal and have to be removed when the first of them fails. This is the reason why the reliability SB is equal to one of the three equal reliabilities of the three satellite gears. Presentation in Fig. 5b contains reliabilities of the three sealing sets Se, one at the III-stage i.e. at the output shaft, one at the input shaft and one at auxiliary traction shaft (stage-I).

The first stage of the sub-system is presented in Fig. 6. This is the gear system which consists of bevel gear pair and planetary gear set settled inside the bevel gear. The bevel gear pair transmits torque from the main traction motor to the second stage of planetary gear set. In the course of this operation inside the planetary gear set is fixed by the shaft for auxiliary drive. When the mine traction motor (shaft with the bevel gear) is fixed, auxiliary drive is acting via planetary gear set and bevel gear presents the inside toothed ring of this planetary set. Bevel gear and inside toothed ring of planetary set is the same machine part. Failure of the bevel gear pair (R_{BG}), or failure of the planetary gear set (R_{PG}), requires the replacement of both, bevel gear pair and planetary gear set. This is why the

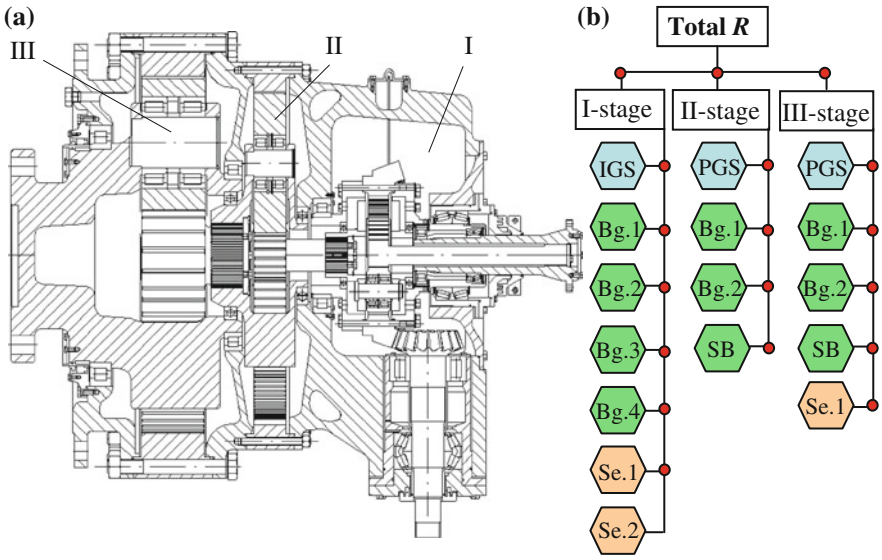

Fig. 5 Planetary gear drive unit of the wheel of bucket wheel excavator. **a** Gear drive drawing. **b** Structure of elementary reliability—reliability tree

reliability of all gears in I-stage assembly R_g (Fig. 6) is equal to minimal reliability of R_{BG} and R_{PG}. This planetary gear set contains four bearings B-1, B-2, B-3 and B-4, and each of them in the reliability three in Fig. 6b is presented by a single elementary reliability. Also, satellite gears are supported by bearings and elementary reliability of one of them Sb is included in the reliability system. The reason for this was explained above. The satellite carrier can be damaged in the spleen connections and elementary reliability is presented by SC. Elementary reliabilities of gears, bearings of planetary gear set and satellite carrier, multiplied between each other, all present the reliability of input gear set IGS (R_{IGS}). The system of reliability of the I-stage gear unit is completed by elementary reliabilities of bearings Bg-1, Bg-2, Bg-3, Bg-4 and reliabilities of seals Se-1 and Se-2. These bearings are supporting bevel gear pair and the whole assembly of bevel gear pair and planetary gear set inside the bevel gear hub.

4 Gear Unit Design

Design parameters of gear unit components provide fulfilment of the overall design behavior. Design robustness based on axiomatic rules is suitable approach for design parameters definition. Necessary properties of components are constraints in this process. Axiomatic approach contains two axioms, the axiom of

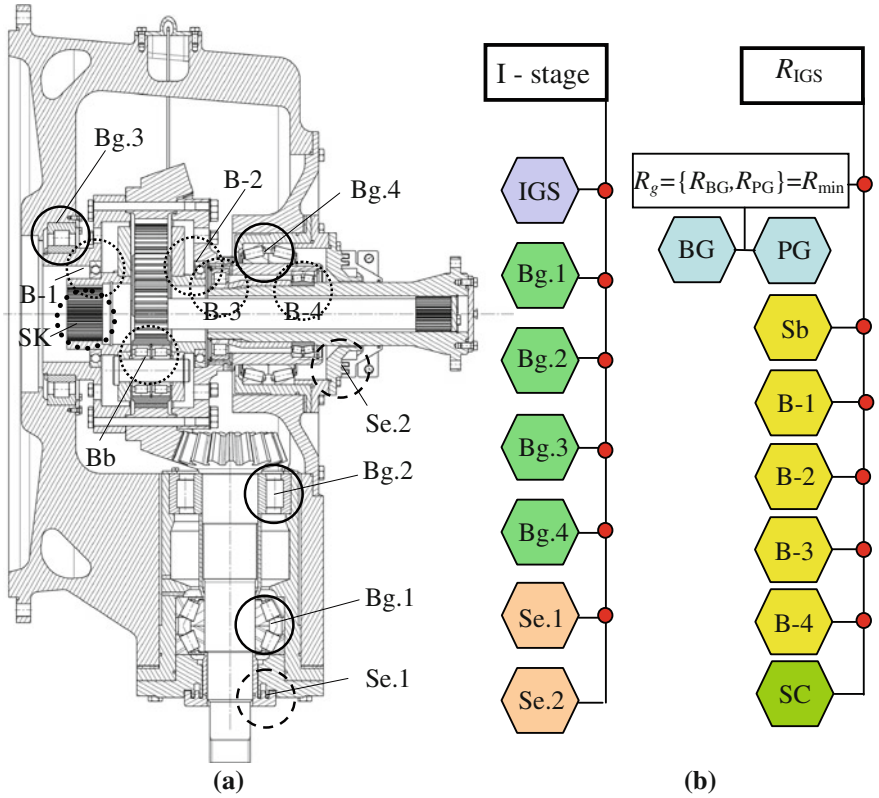

Fig. 6 First stage of the gear drive unit presented in Fig. 5. **a** Design structure. **b** Structure of reliability system

independency and the axiom of information minimum. Transformation matrix $[A]^{-1}$ (Fig. 7) defines the relations in design component, which are constrained by numerous limitations, such as safety or reliability, stiffness, standards, rules, etc.

In Fig. 8, the example is presented. The assembly of the gear, shaft and bearing is defined by a great collection of design parameters, especially dimensions. The calculation of dimensions is reduced to the three dimensions, gear diameter d, gear width b and shaft diameter d_{sh}. In this way, the axiom of information minimum is fulfilled. Other dimensions are in relation with those calculated. Matrix [G] (Fig. 8) is the shape vector which defines transformation of parameters in all shape dimensions. This is the shape parameterization, where varying of the shape parameters varies the complete shape and dimensions. In Fig. 8 are presented the two shapes of the same assembly obtained in this way. Similar approach is incorporated in CAD tools for the shape modeling.

The structure of the matrix [A], according to Suh (Armen et al. 2007), can be uncoupled, coupled and decoupled. The ideal situation is with uncoupled matrix, where one DP is responsible for one FR. Real situation is more complex. In order

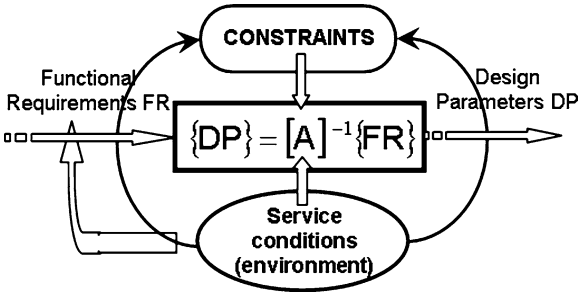

Fig. 7 Relations in axiomatic approach

to obtain the decoupled matrix of transformation, the matrix $[A]^{-1}$ is presented in the form of matrix [C] in the following form.

$$\begin{Bmatrix} d \\ d_{sh} \\ C \\ SE \end{Bmatrix} = \begin{bmatrix} c_{11} & 0 & 0 & 0 \\ 0 & c_{22} & 0 & 0 \\ 0 & 0 & c_{33} & 0 \\ 0 & 0 & 0 & c_{44} \end{bmatrix} \begin{Bmatrix} T^{1/3} \\ T \\ T \\ 1 \end{Bmatrix} \tag{2}$$

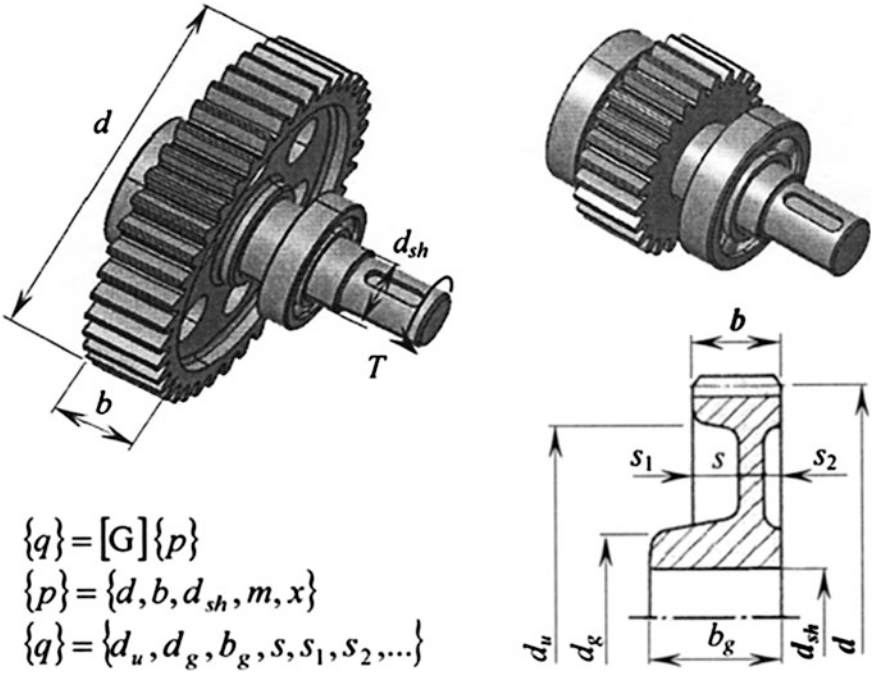

Fig. 8 Example of DP minimization and variation

The axiom of independency is conditionally fulfilled. The members of matrix [C] and design parameters d, d_{sh}, carrying capacity of the bearings C and seal type indicator SE have to be calculated successively. The member c_{11} is in relation with elementary reliability R_1 against wear failure of gear pair, $c_{11} = f(R_1)$.

$$d = k_{11}\sqrt[3]{\frac{T}{\varphi\sigma_{Hdes}^2}} = c_{11}(\sigma_{Hdes})T_{\max}^{1/3} \tag{3}$$

After the calculation of gear diameter d, it is possible to calculate the shaft diameter because the shaft loads depend of the gear diameter, i.e. $c_{22} = f(d, R_2)$, and also of the shaft reliability R_2. The next step is calculation of bearing carrying capacity using matrix member c_{33} which is in relation with the both diameters d and d_{sh}, the total number of bearing revolutions along the service life n_Σ, and of bearing reliability R_3, i.e. $c_{33} = f(d, d_{sh}, n_\Sigma, R_3)$. Lastly, the matrix member c_{44} is in relation to the shaft diameter d_{sh}, to the total number of the shaft revolutions n_Σ and to seal reliability R_4, i.e. $c_{44} = f(d_{sh}, n_\Sigma, R_4)$. The main feature of robustness is covered by reliability.

5 Conclusion

The presented methodology shows a few new approaches to design of technical (mechanical) systems applied for gear transmission units design. Some of the new approaches and applications are as follows:

- Property-based product development is presented and applied for gear units design. Gear unit reliability is treated as a functional requirement at the beginning of the development process, as a structural component property in order to design parameters definition, and as an indicator of product behavior at the end of the process.
- The new and specific way of gear units reliability structuring is presented. Reliability is connected to possible failures at the elementary level, at the assembly level, and at the system level. Structuring of the system reliability is also specific.
- Axiomatic approach and robust design methodology are also adapted for application in gear transmission units design.

Acknowledgments This article is a contribution to the Ministry of Education and Science of Serbia funded project TR 035006.

References

Armen Z, James K, Lusine B (2007) Modeling and analysis of system robustness. J Eng Des 18:243–263

Kruhmer H, Meerkamm H, Wartzack S (2011) Monitoring a property based product development. In: e-Proceedings of the 17th international conference on engineering design 2009 (ICED′11), Copenhagen

On Fundamentals of the Scientific Theory of Gearing

Stephen P. Radzevich

Abstract Fundamentals of scientific theory of gearing are briefly disclosed in the paper. The undertaken research is based on an extensive application of the DG/K-based method of surface generation. Criteria a scientific theory of gearing must meet with are formulated in the paper. It is postulated that the given kinematics of a gear pair (namely, a given configuration of the rotation vectors of the driving and of the driven members) along with the power being transmitting is the principal start point, which the scientific theory of gearing can be derived from. Starting from that, analytical expressions for the gear and for the pinion teeth flanks are derived. Spatial gearing of this kind is geometrically accurate. It is featuring line contact of the interacting teeth flanks. All known kinds of gearing are covered by the developed theory of gearing. Moreover, the proposed theory is a powerful tool for the development of gearing of novel kinds with a prescribed performance.

Keywords Gear · Pinion · Synthesis · Indicatrix of conformity · R-gearing

List of Symbols

G and P	Teeth flanks of the gear and of the pinion
$Cnf\,(G/P)$	Indicatrix of conformity of the gear tooth flank, G, and of the pinion tooth flank, P
$\boldsymbol{\omega}_g$ and $\boldsymbol{\omega}_p$	Rotation vectors of the gear and of the pinion
$\boldsymbol{\omega}_{pl}$	Vector of instant rotation of the pinion in relation to the gear
C	Center-distance of a gear pair
Σ	An angle between the rotation vectors $\boldsymbol{\omega}_g$ and $\boldsymbol{\omega}_p$
O_g and O_p	Axis of rotation of the gear and of the pinion
P_{ln}	Axis of instant rotation of the gear in relation to the pinion
Γ_b and γ_b	Base cone angle of the gear and of the pinion

S. P. Radzevich (✉)
Mechanical Engineering, Manufacturing Engineering, Principal Gear Engineer, Johnson Controls, Inc, Plymouth, MI, USA
e-mail: Radzevich@usa.com

G. Dobre (ed.), *Power Transmissions*,
Mechanisms and Machine Science 13, DOI: 10.1007/978-94-007-6558-0_11,

$\phi_{n.\omega}$	Normal pressure angle
A_g and A_p	Apexes of the gear and of the pinion
A_{pa}	Apex of the plane of action.

1 Introduction

Beginning of the developments in the realm of theory of gearing can be traced back for centuries ago. A profound overview of the accomplishments in the field can be found out in Radzevich (2012). All the significant achievements in the field of gearing attained by Leonardo and by the later researchers are covered by the performed retrospective analysis.

It is shown in the performed analysis that for a long while only particular problems those pertain to gearing were under consideration. Starting from the famous monograph by Olivier (1842) more general problems in the field of gearing were involved into the research. The monograph by Theodore Olivier (1842) is the first book ever entitled as "Theory of Gearing".

However, no *scientific* theory of gearing is developed so far. A profound scientific theory of gearing is proposed by Radzevich (2012).

The developed *Theory of Gearing* is based on the fundamental postulate[1]:

Postulate: *All the design parameters of an optimal gear pair for a particular application can be derived from a given configuration of the rotation vectors of the driving of the driven shafts, and on the power being transmitting by the gear pair.*

Fundamentals of the developed *Theory of Gearing* are briefly outlined below. Any and all possile kinds of gearing, both already known as well as not known yet can be derived from the proposed *Theory of Gearing* following formal routine.

2 Principal Features of the Proposed Scientific Theory of Geairng

The developed scientific *Theory of Gearing* is based on rotations of the driving and of the driven shafts, and on power being transmitting by the gear pair. This is the least possible amount of the input information based on which design parameters of an optimal gear pair can be calculated.

[1] It is instructive to point out here on the similarity between the proposed ***scientific*** *Theory of Gearing*, and between *Euclidian geometry*. *Euclidian geometry* is entirely derived from the postulated set of five axioms. Any and all scinetific theories should posses this property. The proposed ***scientific*** *Theory of Gearing* meets this requirement as it is entirely derived from the fundamental postulate.

Principal features of the developed scientific *Theory of Gearing* are briefly outlined below.

2.1 Kinematics of a Gear Pair

Kinematics of a gear pair to be designed can be specified in terms of rotation vectors $\boldsymbol{\omega}_p$ of the driving shaft (commonly, of the pinion), and $\boldsymbol{\omega}_g$ of the driven shaft (commonly, of the gear) as it is schematically shown in Fig. 1. In general case the rotation vectors $\boldsymbol{\omega}_g$ and $\boldsymbol{\omega}_p$ are apart of one another at a center-distance, C. The rotation vectors $\boldsymbol{\omega}_g$ and $\boldsymbol{\omega}_p$ make an angle, which is commonly denoted by Σ, $[\Sigma = \angle(\boldsymbol{\omega}_g,\ \boldsymbol{\omega}_p)]$.

For a given configuration of the rotation vectors $\boldsymbol{\omega}_g$ and $\boldsymbol{\omega}_p$ a rotation vector of instant rotation $\boldsymbol{\omega}_{pl}$ is calculated ($\boldsymbol{\omega}_{pl} = \boldsymbol{\omega}_p - \boldsymbol{\omega}_g$). Axis P_{ln} of the instant rotation of the pinion about the gear is along the rotation vector $\boldsymbol{\omega}_{pl}$ (Fig. 2). It is convenient to apply the rotation vectors $\boldsymbol{\omega}_g$, $\boldsymbol{\omega}_p$ and $\boldsymbol{\omega}_{pl}$ at the points A_g, A_p and A_{pa} of intersection of the straight line along C with the axis of rotation of the gear, O_g of the pinion, O_p, and the axis of instant rotation, P_{ln}. The points A_g, A_p and A_{pa} are apexes of base cones of the gear, of the pinion, and of the plane of action accordingly.

Total number of possible kinds of vector diagrams of gear pairs is limited just to 11 vector diagrams. The vector diagrams of gear pairs are classified. All possible kinds of gearing (external gearing, internal gearing, as well as gear-to-rack meshes) are covered by these 11 kinds of vectors diagrams.

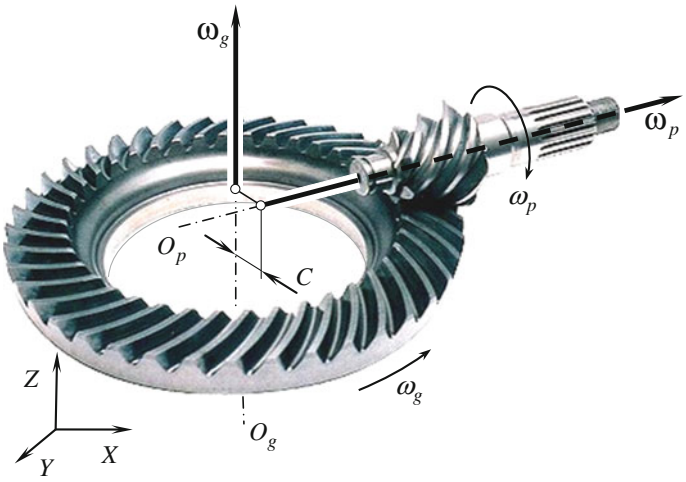

Fig. 1 On the concept of vector representation of kinematics of a gear pair

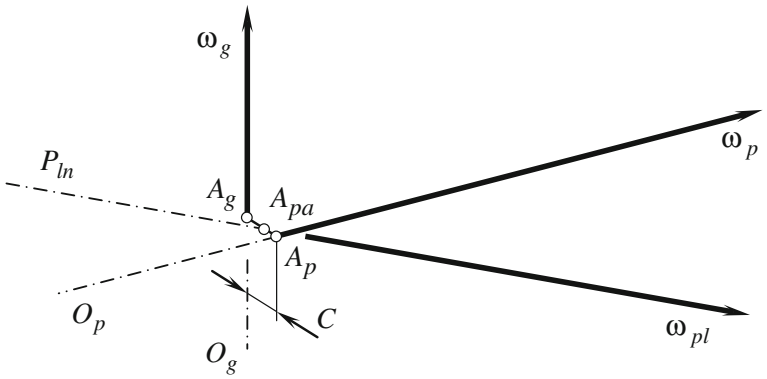

Fig. 2 An example of the vector diagram of a gear pair

2.2 Generation of Teeth Flanks of the Gear and of the Pinion

Base cones of the gear and of the pinion together with the plane of action are employed for the purposes of generation of lateral surfaces of the gear tooth, and of the pinion tooth.

Plane of action, *PA* (Fig. 3), is a plane through the vector of instant rotation, $\boldsymbol{\omega}_{pl}$. The plane of action makes normal pressure angle, $\phi_{n.\omega}$, with the straight line segment $A_g A_p$.

Base cone of the gear can be generated as an envelope to successive positions of the plane of action in rotation of the *PA* about the gear axis of rotation, O_g. Base cone of the gear is designated as Γ_b.

Base cone of the pinion is determined in a way similar to that above the base cone of the gear is determined. It is generated as an envelope to successive positions of the plane of action in rotation of the *PA* about the pinion axis of rotation, O_p. Base cone of the pinion is designated as γ_b.

When the gears rotate the plane of action is in permanent tangency to both the base cones. The plane of action is unwrapping from the base cone of the driving member, and it is wrapping on the base cone of the driven member.

Teeth flanks of the gear and of the pinion are generated by a line of contact, *LC*. Prior to generate the teeth flanks a line of contact, *LC* having reasonable geometry must be chosen. A planar curve that is entirely located within the plane of action, *PA*, can be employed as the line of contact, *LC*, between the gear tooth flank, *G*, and between the pinion tooth flank, *P*. The planar line of contact, *LC*, is associated with the plane of action, and it is traveling together with the *PA* when the gears rotate.

Tooth flank of the gear, *G*, is represented by a family of consecutive positions of the line of contact when the *LC* is moving in relation to a reference system

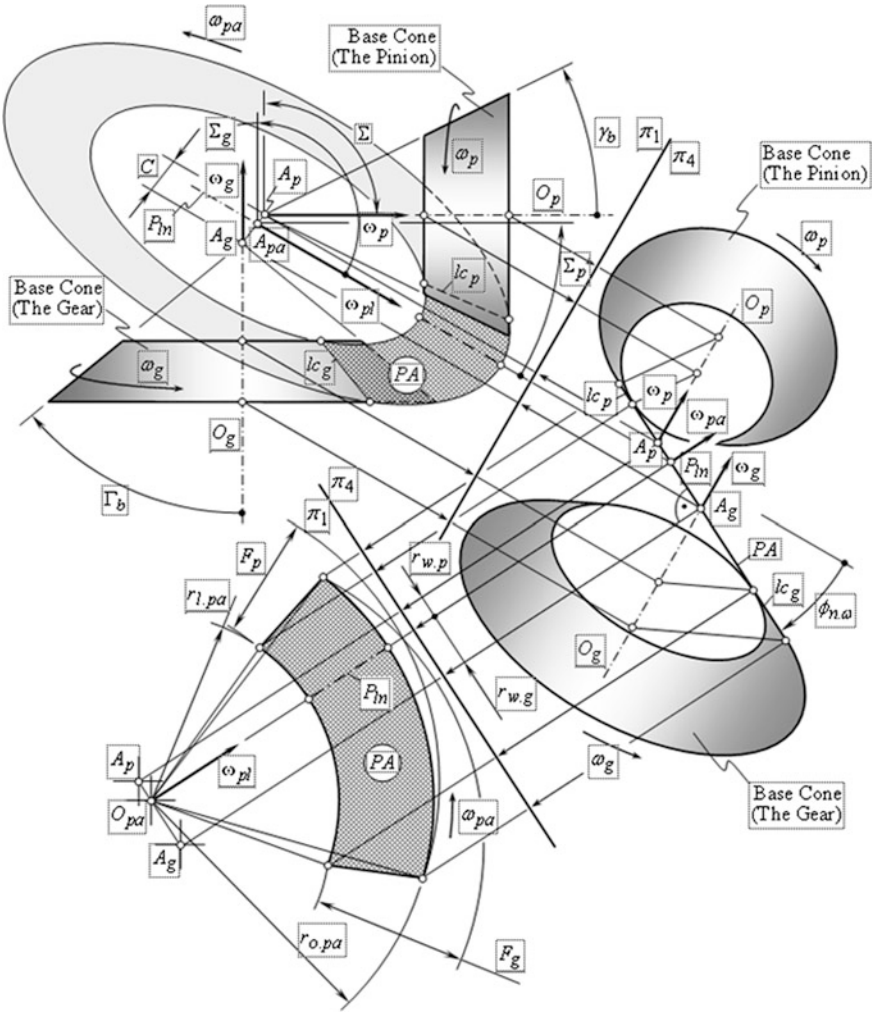

Fig. 3 Base cones and the plane of action, *PA*, in an orthogonal crossed-axis gear pair

$X_gY_gZ_g$ associated with the gear. In this case the generated tooth flank, G, is represented in the reference system $X_gY_gZ_g$.

Similarly, tooth flank of the pinion, P, is represented by a family of consecutive positions of the line of contact when the LC is moving in relation to a reference system $X_pY_pZ_p$ associated with the pinion. In this case the generated tooth flank, P, is represented in the reference system $X_pY_pZ_p$.

The generated in this way teeth flanks G and P of the gear and of the pinion are a kind of conjugate surfaces.

Crossed-axis gearing (further, *CA*–gearing) featuring teeth flanks of the just disclosed geometry is a novel kind of gearing. This kind of *CA*–gearing is referred

to as $R-$gearing.[2] $R-$gearing is the only kind of geometrically accurate $CA-$gearing with line contact of the teeth flanks of the gear, G, and of the pinion, P, which is capable of transmitting a smooth rotation from the driving shaft to the driven shaft. $CA-$gearing of no other kind is capable of doing that.

In a degenerate case, namely when center-distance, C, reduces to zero ($C = 0$) the crossed-axis $R-$gearing is simplified to an intersected-axis conical involute gearing. Intersected-axis gearing (further, $IA-$gearing) of this particular kind features teeth flanks in the form of involute surfaces developed from the corresponding base cones.[3] $IA-$gearing of this kind may feature various geometries in lengthwise direction of the gear teeth.

In another degenerate case, namely when the angle Σ is equal $\Sigma = \pi n$ (here n is an integer number, $n = 0,\ 1,\ 2,\ \ldots$), the crossed-axis $R-$gearing is simplified to a parallel-axis cylindrical involute gearing. Parallel-axis gearing (further, $PA-$gearing) of this particular kind features teeth flanks in the form of involute surfaces constructed on base cylinders.[4] Again, $PA-$gearing of this kind may feature various geometries in lengthwise direction of the gear teeth.

Optimal geometry of the teeth flanks G and P in lengthwise direction of the gear tooth is another problem to be solved.

2.3 Optimal Geometry of the Teeth Flanks in Lengthwise Direction

Teeth flanks in $R-$gearing are specified in terms of geometry of the line of contact of a reasonable geometry. Optimal geometry of the line of contact, LC, is remained undetermined yet.

For the purposes of determining of optimal geometry of the line of contact in lengthwise direction of the teeth flanks of the gear and of the pinion an analytical description of the contact geometry of the teeth flanks G and P is employed. This approach is adopted from the $DG/K-$based method of surface generation. Details on the $DG/K-$ based method of surface generation can be found out in Radzevich (1991, 2001, 2008, 2010, as well as from many other sources).

In the $DG/K-$ based method of surface generation indicatrix of conformity, $Cnf_R(G/P)$, of the contacting teeth flanks of the gear, G, and of the pinion, P, is employed. An example of the indicatrix of conformity $Cnf_R(G/P)$ for the case of line contact of the teeth flanks G and P is schematically illustrated in Fig. 4.

---

[2] The development of $R-$gearing is credited to Radzevich.

[3] It is worthy to point out here that geometrically accurate intersected-axis gearing with line contact between teeth flanks of the gear and of the pinion could be known (?) to George Grant: on July 1889 a US Patent No. 407.437 on a gear cutting machine has been issued on his name. This issue needs into be investigated more in detail.

[4] The development of involute gearing is credited to Leonhard Euler (1781).

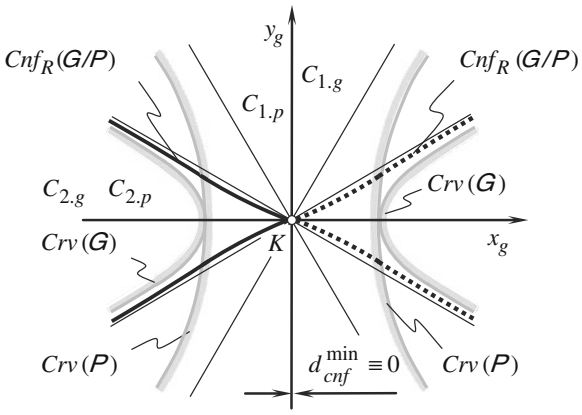

Fig. 4 An example of the indicatrix of conformity $Cnf_R(G/P)$ for the teeth flanks G and P in an intersected-axis $R-$gearing

Indicatrix of conformity, $Cnf_R(G/P)$, of the teeth flanks G and P of the gear and of the pinion is a planar centro-symmetrical curve of the fourth order. In a particular case this characteristic curve may also feature mirror symmetry.

Indicatrix of conformity is constructed in a common tangent plane through a point, K, within the line of contact, LC. Indicatrix of conformity, $Cnf_R(G/P)$, is commonly represented in a local Cartesian reference system with the origin at the point K. In general case of $R-$gearing it features minimum diameter, $d_{cnf}^{\min}$, of zero value ($d_{cnf}^{\min} \equiv 0$.)

Due to lack of space optimal geometry of the line of contact, LC, is not discussed in detail in the paper. The interested reader may wish to go to the monograph by Radzevich (2012) for details on this particular issue.

2.4 Working Portion of the Line of Contact

In order to transmit a given power it is always desired to design and to implement gearboxes of the smallest possible size. From this prospective active portion of the line of contact, LC, should begin from the apex A_{pa} of the plane of action, PA. Evidently, line of contact of such geometry is far from to be practical as maximum contact and bending strength is restricted by physical properties of the material the gear and of the pinion are made of.

Calculation of the design parameters of the favorable portion of the line of contact is base on the assumption that the power being transmitting by a gear pair is equally sharing within active portion of the gear pair face width. With that said, under torque of constant value the smaller diameter of a gear/pinion the large force and vice versa. Therefore practical value of the smallest feasible diameter of the gear/pinion is limited by the yield contact and bending stress in the gear tooth.

Due to lack of space calculation of parameters of the working portion of the line of contact, LC, in $R-$gearing is not discussed in detail in the paper. The interested reader may wish to go to the monograph by Radzevich (2012) for details in this concern.

2.5 Approximate Gearing

Without going into details it should be mentioned here that all kinds of crossed-axis gearing those used in the nowadays practice are the examples of approximate gearing. Generally speaking approximate gearing of all kinds feature point contact between teeth flanks of the gear and of the pinion. No one of all kinds of approximate gearing is capable of transmitting the rotation smoothly. For more details on approximate gearing the interested reader may wish to go to the monograph by Radzevich (2012).

3 Conclusion

Principal features of the newly developed *scientific Theory of Gearing* are outlined in the paper. The proposed *Theory of Gearing* is based on the fundamental postulate in accordance to which all the design parameters of an optimal gear pair for a particular application can be derived from a given configuration of the rotation vectors of the driving of the driven shafts, and on the power being transmitting by the gear pair. All known designs of gearing as well as all kinds of gearing to be developed in the future are covered by the proposed *Theory of Gearing*. It is shown that all kinds of crossed-axis gearing, as well as intersected-axis gearing those used in the nowadays practice are examples of approximate gearing. Approximate gearing is not geometrically accurate in nature. This could be the root cause for an excessive vibration generation and noise excitation when the gear pair is operating.

References

Olivier T (1842) Théorie Géométrique des Engrenages destinés, Bachelier, Paris 1842, p 118
Radzevich SP (1991) Differential-geometric method of surface generation. Doctoral thesis, Tula, TulPI, 1991, p 300 (In Russian)
RADZEVICH SP (2001) Fundamentals of surface generation. Kiev, Rastan, p 292 (In Russian)
Radzevich SP (2008) Kinematic geometry of surface machining. CRC Press, Boca Raton, p 508
Radzevich SP (2010) Gear cutting tools: fundamentals of design and computation. CRC Press, Boca Raton, p 754
Radzevich SP (2012) Theory of gearing: kinematics, geometry, and synthesis. CRC Press, Boca Raton, p 856

Towards Optimum Involute Gear Design by Combining Addendum and Thickness Modifications

Vasilios Spitas and Christos Spitas

Abstract Involute gear sets are being produced through a variety of cutting tools and generation methods in a number of pressure angle and whole depth systems with 20–2.25 m being the most common. Positive addendum modifications (profile shifts) are also common particularly because the resulting teeth are stronger, although at the expense of the contact ratio, scoring resistance and pitting resistance. This paper discusses the effect of combined addendum modifications and changes in nominal tooth thickness of meshing gears on the minimization of the root bending stress. The tooth mesh-strength problem is treated as non-dimensional, which substantially reduces computational time as well as the total number of design variables. Instead of modeling the loaded gear tooth and running a numerical method (i.e. FEM) to calculate the maximum root stress at every iterative step of the optimization procedure, the stress is calculated by interpolation of tabulated values, which were calculated previously for different combinations of the design parameters. Significant stress reduction was achieved in this way as was confirmed experimentally with photoelasticity.

Keywords Spur gears · Root stress · BEM · Optimization · Photoelasticity

List of Symbols

α_o Pressure angle
a_{12} Center distance
b Tooth width
c_c Cutter radius coefficient

V. Spitas (✉)
National Technical of Athens, Athens, Greece
e-mail: vspitas@central.ntua.gr

C. Spitas
Delft University of Technology, Delft, The Netherlands
e-mail: c.spitas@tudelft.nl

G. Dobre (ed.), *Power Transmissions*,
Mechanisms and Machine Science 13, DOI: 10.1007/978-94-007-6558-0_12,

c_f Dedendum coefficient
c_k Addendum coefficient
c_s Thickness coefficient factor
ε Contact ratio
P_N Normal force
r_b Operating pitch radius
r_g Involute base radius
r_k Outside radius
σ Critical bending stress
s_o Tooth thickness at pitch circle
t_g Base pitch
x Addendum modification coefficient
z Number of teeth

1 Introduction

Gear optimisation has always been a difficult task, mainly due to the complex kinematics and the continuously changing load in terms both of point of application, direction and magnitude. Despite the advancement of novel computational techniques gear optimisation was mainly limited to specific gear pairs (Yeh et al. 2001; Litvin et al. 2000) mostly due to the multitude of the gear design parameters (Ciavarella and Demelio 1999). Some researchers deal with this fact by using empirical formulas (Pedrero et al. 1999), or by introducing simplified models (Andrews 1991; Rogers et al 1990). A different approach was followed by Spitas et al. (2006) and Spitas and Spitas (2006) where non-dimensional teeth were considered and the Highest Point of Single Tooth Contact (HPSTC) was defined with respect to the geometry of the tooth in question and the contact ratio of the pair instead of the standard design parameters of the meshing gear, thus reducing the total number of parameters. Each gear was modeled and consequently loaded at different points corresponding to different values of the contact ratio and numerical analysis followed to calculate the maximum root stress. The resultant values were tabulated in a "stress table" characterizing a given number of teeth, which were used in an optimization algorithm, where all the required intermediate values were quickly calculated by interpolation of the tabulated ones.

The benefits of this modeling technique include improved accuracy and significantly smaller calculation times as opposed to the standard techniques employed. Also, due to the 'stress table' concept the method can be readily synthesized in a modular way in any problem requiring the calculation of the maximum fillet stress. The optimum design was verified using two-dimensional photoelasticity on PCB plastic gear-tooth models.

2 Basic Geometrical Modelling

In a pair of spur gears let gear 1 be the pinion and gear 2 the wheel. The law of gearing (Townsend 1992) requires that these gears should have the same nominal pressure angle α_o and the same module m in order to mesh properly. In the general case the gears are considered to be non-dimensional (i.e. with $m = 1, b = 1$) and incorporate addendum modifications x_1, x_2 respectively. Their pitch thickness is given by the following relationship:

$$s_{oi} = c_{si}\pi + 2x_i \tan\alpha_o \tag{1}$$

where c_{si} is the thickness coefficient of gear i,$(i = 1, 2)$, which in the general case is $c_{s1} \neq 0.5 \neq c_{s2}$. The center distance O_1O_2 of the non-dimensional gear set is calculated using the following formula:

$$a_{12} = \frac{z_1 + z_2}{2} + (x_1 + x_2) \tag{2}$$

The actual operating pitch circle r_{bi} of gear i, $(i = 1, 2)$ should verify the law of gearing and therefore be equal to:

$$r_{bi} = \frac{z_i}{z_1 + z_2}\, a_{12u} \tag{3}$$

Gears 1 and 2 are revolving about their centers O_1 and O_2 respectively and meshing along the path of contact AB as illustrated in Fig. 1. During meshing there are two pairs of gear teeth in contact along the segments AA' and BB', thus sharing the total normal load, while there is only a single such pair when tooth contact takes place along the region $A'B'$, carrying the total normal load. Point B' is the Highest Point of Single Tooth Contact (HPSTC) for gear 1 and its position, defining the radius $r_{B'}$, is (Spitas et al. 2006; Spitas and Costopoulos 2001):

$$r_{B'} = O_1B' = \sqrt{r_{k1}^2 + (\varepsilon - 1)t_g\left[(\varepsilon - 1)t_g - 2\sqrt{r_{k1}^2 - r_{g1}^2}\right]} \tag{4}$$

From the above equation it is evident that the position of the HPSTC of a gear depends only on its geometry and on the contact ratio of the pair, in which all the characteristics of the mating gear are incorporated in a condensed form.

Stresses can also be calculated in non-dimensional teeth $\sigma_u(z, x, c_s, \varepsilon)$ with unit loading $P_{Nu} = 1$ and related to the actual stress σ using the following equation:

$$\sigma = \sigma_u \frac{P_N}{bm} \tag{5}$$

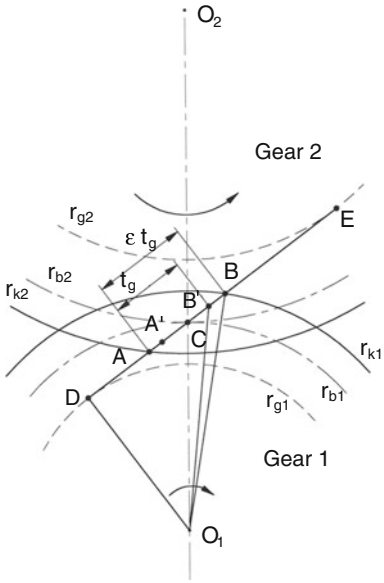

Fig. 1 Path of contact

3 Constrained Optimisation of Gear Teeth

The static analysis results obtained by loading the aforementioned non-dimensional gear sets with various addendum modification coefficients and tooth thickness coefficients were tabulated in 'stress tables' (Spitas et al. 2006; Spitas and Spitas 2006). In order to calculate an intermediate stress value σ corresponding to a given number of teeth (z) and set of parameters z, x, c_s, ε not necessarily included in the stress table, linear interpolation was used as described in (Spitas et al. 2006).

Analytical optimization methods are not suitable for gear stress optimization problems due to the complex implicit functions that relate the main geometrical variables to the resulting stresses. An efficient method of solving such intricate problems is the Complex algorithm (Box 1965), which calculates the minimum of a function of n variables f(**x**), where $\mathbf{x} = (x_1, x_2, \ldots, x_n)^T$ is the variable vector.

The independent variables of a stress optimization problem considering non-dimensional gears are the following:

Addendum modifications: x_1 for gear 1 x_2 for gear 2
Thickness coefficients: c_{s1} for gear 1 c_{s2} for gear 2.

The objective function without any constraints is defined as $\min f(x_1, x_2, c_{s1}, c_{s2}) = \max(\sigma_1, \sigma_2)$, where σ_1, σ_2 are the maximum tensile stresses developed at the fillets of the conjugate gears 1 and 2 respectively when loaded at their corresponding HPSTC. Also, the optimization must be constrained because the optimum teeth should still fulfill certain operational criteria. There are 7 different constraints described below and in order to include them in the optimization

procedure the following form of the objective function is adopted using weighted residuals:

$$\min f(x_1, x_2, c_{s1}, c_{s2}) = \max(\sigma_1, \sigma_2) + \sum_{i=1}^{7} w_i c_i \tag{6}$$

The penalty functions c_i and the weighting coefficients w_i employed in Eq. (6) are defined below.

Constraint 1: Allowable addendum modification: The addendum modification coefficient for gear i is restricted between two values $x_{i\min}$ and $x_{i\max}$ depending on the number of teeth z. These values are dictated by common gear practice and manufacture. The penalty functions are defined therefore:

If $x_i < x_{i\min}$ or $x_i > x_{i\max}$, $i = 1, 2$ then $w_1 c_1 = 1000$, $\sigma_1 = \sigma_2 = 1000$
If $x_{i\min} \leq x_i \leq x_{i\max}$, for every $i = 1, 2$ then $w_1 c_1 = 0$.

Constraint 2: Allowable thickness coefficients: For technical reasons the cutting tool producing the gears (rack cutter, pinion cutter or hob) cannot have infinitely thick or infinitely thin teeth and this imposes a constraint on the resulting thickness of the produced gear. Therefore the thickness coefficient should range between the values $c_{s\min}$ and $c_{s\max}$, which are the limit values specified in the stress tables.

If $c_{si} < c_{simin}$ or $c_{si} > c_{simax}$, $i = 1, 2$ then $w_2 c_2 = 1000$, $\sigma_1 = \sigma_2 = 1000$
If $c_{simin} \leq c_{si} \leq c_{simax}$, for every $i = 1, 2$ then $w_2 c_2 = 0$.

Constraint 3: Minimum radial clearance: In order to ensure that the conjugate gears operate without the risk of seizure, there should be a minimum allowable radial clearance $c_{rmin}m$,, where $c_{rmin} = 0.25$. For the dimensionless gear i it is calculated from the equation:

$c_{ri} = a_{12} - r_{kiu} - r_{fiu} = c_f - c_k = c_r$, where $r_{uki} = \frac{z_i}{2} + x_i + c_k$ and $r_{ufi} = \frac{z_i}{2} + x_i - c_f$ are the tip and root radius of the non-dimensional gear i and $c_k = 1.0$, $c_f = 1.25$ are the addendum and dedendum coefficients respectively. The penalty functions are formulated as follows:

If $c_r < 0.25$ then $c_3 = 0.25 - c_r$ and $w_3 = 10$

Here the penalty function c_3 has been chosen to be a function of the radial clearance in order to help the convergence of the solution at points where the non-dimensional coefficient c_r approaches its nominal value of 0.25. The value of the weighting coefficient was chosen equal to 10 in order to improve the convergence of the algorithm.

If $c_r \geq 0.25$ then $w_3 c_3 = 0$.

Constraint 4: If the tip radius r_{ki} of gear i revolving about O_i exceeds a maximum value r_{kimax} so that the intersection of the tip circle of the gear with the common path of contact at point U defines on the mating gear j a radius which is lower than its form radius r_{js}, then interference occurs, since the tooth part below

the form radius has a trochoidal and not an involute form. Consequently, it should always be $r_{ki} \leq r_{kimax}$, where $r_{kimax} = O_iU$. In terms of the corresponding dimensionless gears this results in the following penalty function:

If $r_{kiu} > r_{kimax}, i = 1, 2$ then $c_4 = \max(r_{k1u} - r_{k1max}, r_{k2u} - r_{k2max})$ and $w_4 = 5$.
If $r_{kiu} \geq r_{kimax}$ for every $i = 1, 2$ then $w_4c_4 = 0$.

Constraint 5: Minimum tip thickness: In common gear practice the tip thickness is never below 0.2 times the module or tip fracture would occur. In a non-dimensional gear the tip thickness should always be $s_{ku} \geq 0.2$.

If $s_{kui} < 0.25$, $i = 1, 2$ then $c_5 = \min(s_{k1}, s_{k2})$ and $w_5 = 10$
If $s_{ki} \geq 0.25$ for every $i = 1, 2$ then $w_5c_5 = 0$.

Constraint 6: Allowable contact ratio: In order to ensure smooth and unproblematic running the contact ratio of a gear pair should exceed 1.2. A usual upper limit is 1.8, which in 20° standard or shifted spur gears is never surpassed. Similarly to the constraints 1 and 2 the contact ratio εof the pair should lie in the range defined in the stress tables, therefore big penalties are applied at the boundaries:

If $\varepsilon < \varepsilon_{min}$ or $\varepsilon > \varepsilon_{max}$ then $w_6c_6 = 1000$, $\sigma_1 = \sigma_2 = 1000$
If $\varepsilon_{min} \leq \varepsilon \leq \varepsilon_{max}$ then $w_6c_6 = 0$.

Constraint 7: Allowable backlash: The backlash of a gear pair (B) should always be positive and usually optimized designs require that this is kept minimum since the thicker the working teeth are, the less the root stress is. Although zero backslash is never actually desirable for power transmissions, the presence of a minimum backlash does not seriously reduce the tooth thickness, hence the root stresses, and therefore in order to simplify the calculations the optimum backlash can be considered zero. This can be expressed in terms of a penalty function, suitably big beyond the permissible boundaries, as:

$$c_7 = B \text{ and } w_7 = 100.$$

After the formulation of the objective function, the algorithm described in Fig. 2 is executed.

4 Results and Discussion

Various combinations of a 20° involute pinion with 12 teeth meshing with gears having 15, 18, 22, 28 and 50 teeth were modeled and examined. The stress tables were first constructed for all the above-described numbers of teeth and for the optimization algorithm the following parameter values were used: $\varepsilon = 10^{-4}$ (tolerance), $\alpha = 1.2$ (reflection coefficient), $\beta = 1.0$ (expansion coefficient), $\gamma = 2.0$ (contraction coefficient). The parameter values were chosen so as to provide quick convergence and stability of the algorithm.

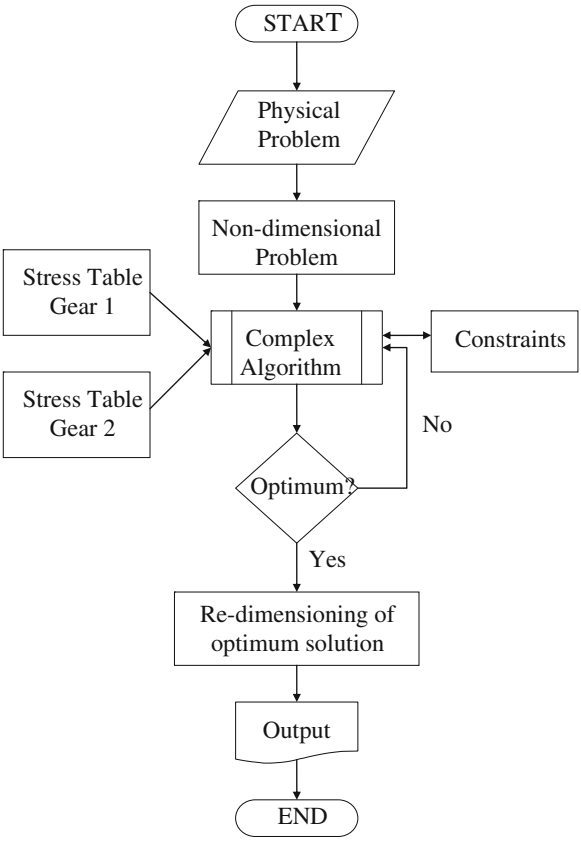

Fig. 2 The optimization algorithm

In Fig. 3 the values of the maximum root stress for the non-dimensional pinion with 12 teeth and its conjugate gears with 18–50 teeth are plotted. In this figure it can be observed that the maximum pinion stress (gear 1) is always greater than the maximum stress on the mating wheel (gear 2) in the case of standard gears while

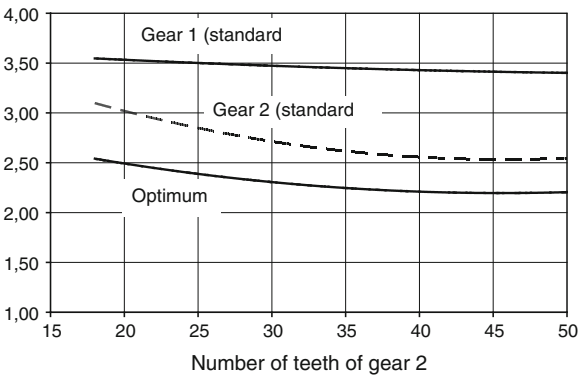

Fig. 3 Non-dimensional root stress for $z_1 = 12$ pinion teeth

Fig. 4 Photoelastic fringe patterns on sample gear-tooth models

these stresses are equal in the case of optimized gears. The total computational time was 12 s on a 2.4 GHz Intel Quad-Core system. The optimization algorithm used a complex of 1,000 vectors and reached the optimum solution after 29 iterations performing over 40,000 stress calculations. By following the standard methodology performing full gear modeling (run time 0.2 s), mesh generation (run time 0.1 s) and BEA (run time 6 s) at each iterative step, this would result in a total run time of nearly 70 h.

The optimum design has been experimentally verified using two-dimensional photoelasticity (Spitas et al. 2006). The optimum gear tooth of a 28-tooth pinion / 50-tooth wheel system is illustrated in Fig. 4. The photoelastic specimen was cut from a 10 mm PSM-1 sheet from Vishay Inc. and placed on a special fixture on a planar polariscope where it was loaded at its HPSTC with progressively increasing normal load until a 3rd order isochromatic fringe appeared at the root fillet. Similar tests on other plastic models indicated that the numerical results are in good agreement with photoelastic investigations (Spitas et al. 2006). The experimental results are in excellent agreement with the numerical predictions (maximum deviation of 3.6 %) and the new design offers a decrease of the maximum fillet stress ranging from 13.5 to 36.5 % depending on the geometrical characteristics of the gear pair.

5 Conclusion

Non-dimensional gear tooth modelling in terms of the number of teeth, the profile shift and the tooth thickness coefficient was employed for gear stress optimization with the Complex algorithm. The non-dimensional models were used in order to decrease the total number of the optimization parameters by introducing the

contact ratio of the pair as the parameter defining completely the point of loading. This reduction in the number of parameters enabled the tabulation of the maximum root stress developed on each non-dimensional gear with a given number of teeth for different values of addendum modification, pitch thickness and contact ratio using numerical analysis. Throughout the optimization procedure, the stress values for different combinations of the geometrical parameters of the conjugate gears of the pair were calculated from interpolation of the tabulated values at high speed and with satisfactory accuracy. In this way, the run time decreased dramatically without any effect on the accuracy.

References

Andrews J (1991) A finite element analysis of bending stresses included in external and internal involute spur gears. Strain Anal Eng Des 26(3):153–163

Box M (1965) The complex algorithm, Computers 8:42

Ciavarella M, Demelio G (1999) Numerical methods for the optimization of specific sliding, stress concentration and fatigue life of gears. Int J Fatigue 21:465–474

Litvin F, Qiming L, Kapelevich A (2000) Asymmetric modified spur gear drives: reduction of noise, localization of contact, simulation of meshing and stress analysis. Comput Methods Appl Mech Eng 188:363–390

Pedrero J, Rueda A, Fuentes A (1999) Determination of the ISO tooth form factor for involute spur and helical gears. Mech Mach Theory 34:89–103

Rogers C, Mabie H, Reinholtz C (1990) Design of spur gears generated with pinion cutters. Mech Mach Theory 25(6):623–634

Spitas V, Costopoulos T (2001) New concepts in numerical modeling and calculation of the maximum root stress in spur gears versus standard methods. A comparative study. In: Proceedings 1st national conference on recent advances in Mechnical Engineering, Patras, No. ANG1/P106

Spitas V, Spitas C (2006) Optimising involute gear design for maximum bending strength and equivalent pitting resistance. Proc IMechE Part C: J Mech Eng Sci 221:479–488

Spitas V, Costopoulos T, Spitas C (2006) Optimum gear tooth geometry for minimum fillet stress using BEM and experimental verification with photoelasticity. J Mech Des 128(5):1159–1164

Townsend D (1992) Dudley's gear handbook. Mc-Graw Hill, New York

Yeh T, Yang D, Tong S (2001) Design of new tooth profiles for high-load capacity gears. Mech Mach Theory 36:1105–1120

Dynamical Simulation and Calculation of the Load Factor of Spur Gears with Indexing Errors and Profile Modifications for Optimal Gear Design

C. Spitas, V. Spitas and M. Rajabalinejad

Abstract The exact geometry of tooth meshing is incorporated into a dynamical non-linear model of the considered gear system, in consideration of the effect of pitch errors, tooth separation, DOF-coupling, and profile modifications. Various possible combinations of error distributions and profile corrections are applied to the gear model, which is simulated dynamically to calculate the load factor.

Keywords Gear vibration · Indexing errors · Profile modifications · Dynamic load factor · Dynamical simulation

List of symbols

θ_i	Angular position of gear i (additional subscripts: n, ref defined in the text)
$\mathbf{s}_i$	Deflection vector of DOF i
θ_s	Slip angle
δ_k	Angular interference of tooth pair k
i_{12}	Transmission ratio
I_{12}	Directional index (equal to 1 for external gears, -1 for internal gears)
$\mathbf{r}_i$, $\mathbf{r}_{i,k}$	Position vector of a contact point in relation to centre of gear i (the optional k index refers to a specific tooth pair)
$\mathbf{f}_i$	Vector function of tooth profile of gear i
$\mathbf{a}_{12}$	Centre distance vector
$\mathbf{R}$	Generic rotary translation matrix

C. Spitas (✉) · M. Rajabalinejad
Section Product Engineering, Delft University of Technology, Delft,
The Netherland
e-mail: c.spitas@tudelft.nl

V. Spitas
Laboratory of Machine Elements, National Technical University of Athens,
Athens, Greece

G. Dobre (ed.), *Power Transmissions*,
Mechanisms and Machine Science 13, DOI: 10.1007/978-94-007-6558-0_13,

$\hat{\mathbf{x}}_i$	Unitary vector along the x_i direction, where i=1, 2, 3 (in Cartesian coordinates)
$\mathbf{n}_k$	Normal unitary vector at contact point of tooth pair k
$\mathbf{m}_k$	Unitary vector along the direction of instant sliding velocity of tooth pair k
$\sigma^{(j)}$, σ_o, σ_{or}	Anticipated indexing error of tooth j, maximum anticipated indexing error, maximum real indexing error
$U\sigma$, $L\sigma$	Upper and lower tolerance for the maximum indexing error σ_o
m,m_r	Prescribed modification (equal to maximum slip angle θ_s), actual modification
Um, Lm	Upper and lower tolerance for the modification m
k_k	Instant stiffness of individual tooth pair k
c_{hyst}	Damping coefficient due to tooth material hysterisis
f_k	Instant friction coefficient of individual tooth pair k
$F_{k,elast}$	Elastic component of the contact force of tooth pair k
$\mathbf{F}_{k,hyst}$	Hysteretic component of the contact force of tooth pair k
$\mathbf{F}_{k,frict}$	Frictional component of the contact force of tooth pair k
$\mathbf{M}_i$	Mass matrix of rotating element i
$\mathbf{C}_i$	Damping coefficient for bending of shaft i due to hysterisis
$\mathbf{K}_i$	Lumped bending stiffness matrix of DOF i (shaft with elastic supports: bearings/ housing)
J_i	Mass moment of inertia of rotating element i
D_i	Damping coefficient related to rotation of DOF i (i.e. windage)
E_{i-j}	Damping coefficient for torsion of shaft segment $i-j$ due to hysterisis
G_{i-j}	Torsional stiffness of shaft segment $i-j$.

1 Introduction

Gears with indexing errors are known to undergo impact loading ranging from mild to quite severe, depending on the extent and distribution of the errors. The most unfavourable scenario is the linear (saw-tooth) distribution of indexing errors, which is the result of the accumulation of small consecutive indexing errors in conventional or CNC machine tools when there is either a mismatch between the linear motion of the machine bed and the indexing rotation of the work-piece chuck (Townsend 1992) or due to deflections from the cutting forces.

The established remedy to lessen the impacts and overloads caused by indexing errors is by applying modifications on the tooth profiles. Tip relief, root relief, or a combination of both, are all accepted ways of modification, with tip relief being the simplest and most popular (Munro et al. 1988). The selection and dimensioning of these profile modifications, also termed ‘corrections’ has been documented in

various guidelines and standards as in AGMA (1976, 1965), Maag Taschenbuch et al. (1985), Dudley (1984), and Niemann and Winter (1983). These guidelines consider the statically loaded gear pair and introduce a profile modification equal to the maximum indexing error. In vibration-critical applications the calculated profile modification is increased to anticipate the cumulative effect of elastic deflections due to tooth bending. These deflections are normally calculated from statical analysis, however more accurate predictions can be made by dynamical simulation.

The objective of these modifications is to eliminate the possibility of detrimental tip contact during tooth engagement, which is affected by material removal. It should be noted that these corrections are, strictly speaking, errors in themselves and that their introduction is clearly a compromise. In fact, it has been observed that excessive corrections can lead to increased transmission errors (TE), deterioration of the vibratory response and to even worse overloads.

In this paper a methodology is proposed for conducting this sensitivity analysis, using 'sensitivity charts' derived from dynamical simulation. Common linear single-DOF models are not detailed enough and coupled multi-DOF models either consider an abstracted gear mesh geometry, or are not built to take into account combined indexing errors and profile modifications. On the other hand, accurate geometrical models such as in Litvin 1994 have still not made the transition from quasi-statical to truly dynamical analysis (Seol and Kim 1998), so their results can only be indicative of what might be expected under real dynamic conditions.

In this paper the mesh analysis model by Spitas et al. 2002 is used, allowing detailed calculation of the operating transmission errors as a function of the actual tooth form, including corrections. No simplifying assumptions are made in developing this theory and it is possible to model individual errors and complex error distributions. The mesh analysis results are then fed into a detailed dynamical model comprising 3 DOFs/ gear, which takes into account torsional-bending vibration coupling, friction and tooth separation. Tooth interference is calculated individually for each pair in real time to avoid simplifying assumptions and achieve realistic modelling of the dynamical response of gears with errors.

This model is used to simulate the dynamical response of a single-stage spur gear speed reducer and a range of combinations of indexing error distributions and corrective profile modifications is considered. These results are used to predict the dynamic load factor in each case, which is used as a performance index.

2 Modelling Of Gear Meshing Geometry

2.1 Formulation of the Meshing Equations

Let us assume a pair of gears and their respective teeth 1 and 2 in contact as shown in Fig. 1. If tooth 1 is regarded as the reference and conjugate gear action is assumed, then tooth 2 should be at a nominal angular position θ_{2n}, such that:

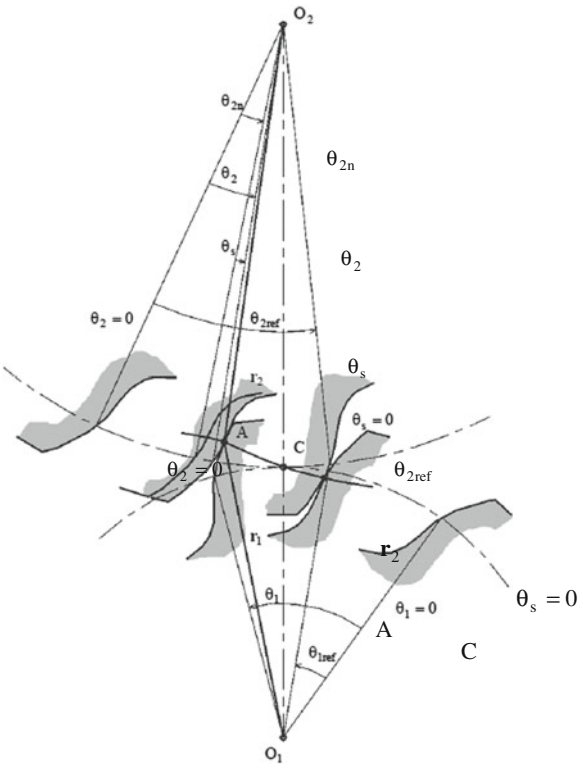

Fig. 1 Gear contact geometry

$$\theta_1 - \theta_{1\text{ref}} = -\mathrm{I}_{12}\mathrm{i}_{12}(\theta_{2\text{n}} - \theta_{2\text{ref}}) \tag{1}$$

where $\theta_{1\text{ref}}$ and $\theta_{2\text{ref}}$ are tooth reference positions.

In fact, no conjugacy requirement will be made in this analysis, so the actual position θ_2 of tooth 2 will deviate from the nominal $\theta_{2\text{n}}$ by an angle θ_{s}, which expresses the relative slip of the operating pitch circles of both gears (slip angle).

$$\theta_2 - \theta_{2\text{n}} = \theta_{\text{s}} \tag{2}$$

The working part of each tooth profile is assumed to be a C^1 continuous curve, so any contact point A should simultaneously satisfy the following two equations:

$$\mathbf{r}_1 - \mathbf{r}_2 = \mathbf{a}_{12} \tag{3}$$

$$\frac{\partial \mathbf{r}_1}{\partial \mathrm{r}_1} \times \frac{\partial \mathbf{r}_2}{\partial \mathrm{r}_2} = 0 \tag{4}$$

where $\mathbf{r}_1 = \overrightarrow{\mathrm{O_1A}}$ and $\mathbf{r}_2 = \overrightarrow{\mathrm{O_2A}}$ in the global coordinate system.

At this point the generic rotary translation matrix is introduced:

$$\mathbf{R}_j = \begin{bmatrix} \cos\theta_j & -\sin\theta_j & 0 \\ \sin\theta_j & \cos\theta_j & 0 \\ 0 & 0 & 1 \end{bmatrix} \tag{5}$$

where θ_j is any arbitrary rotation angle about the axis of rotation of the gear. If the profile of a tooth of gear 1 at an arbitrary reference position $\theta_1 = 0$ is described by a parametric vector function $\mathbf{f}_1$, then the following equations are true:

$$\mathbf{r}_1 = \mathbf{f}_1 \tag{6}$$

$$r_1 = \|\mathbf{f}_1\| \tag{7}$$

where r_1 serves as the profile function parameter and the operator $\|\cdot\|$ denotes the Euclidian norm. The same tooth profile at any other rotation angle can be expressed as:

$$\mathbf{r}_1 = \mathbf{R}_1\mathbf{f}_1 \tag{8}$$

Similar definitions apply to the teeth of gear 2. In this case r_2 is the profile function parameter so that in general:

$$\mathbf{r}_2 = \mathbf{R}_2\mathbf{f}_2 \tag{9}$$

Introducing the slip angle θ_s and considering Eqs. (2, 5) it is easy to derive the following expression:

$$\mathbf{R}_2 = \mathbf{R}_{2n}\mathbf{R}_s \tag{10}$$

so that Eq. (9) becomes:

$$\mathbf{r}_2 = \mathbf{R}_{2n}\mathbf{R}_s\mathbf{f}_2 \tag{11}$$

Finally, substituting Eqs. (8, 11) into Eqs. (3–4), it is possible to arrive at a different form of the equations of meshing as follows:

$$\mathbf{R}_1\mathbf{f}_1 - \mathbf{R}_{2n}\mathbf{R}_s\mathbf{f}_2 = \mathbf{a}_{12} \tag{12}$$

$$\mathbf{R}_1\frac{\partial\mathbf{f}_1}{\partial r_1} \times \mathbf{R}_{2n}\mathbf{R}_s\frac{\partial\mathbf{f}_2}{\partial r_2} = \mathbf{R}_1\frac{d\mathbf{f}_1}{dr_1} \times \mathbf{R}_{2n}\mathbf{R}_s\frac{d\mathbf{f}_2}{dr_2} = 0 \tag{13}$$

These are the general equations that relate the positions of teeth 1, 2 to their shapes. Obviously, if the tooth shapes are known in the form of functions $\mathbf{f}_1$ and $\mathbf{f}_2$ and, then the path of contact and the TE, if any, can be uniquely calculated.

2.2 Solution of the Meshing Equations

Here the slip angle θ_s will be calculated as a function of the reference gear position θ_1 for known tooth profile functions $\mathbf{f}_1(r_1)$ and $\mathbf{f}_2(r_2)$.

By solving Eq. (12) in terms of r_2 we obtain:

$$r_2 = \|\mathbf{R}_1\mathbf{f}_1 - \mathbf{a}_{12}\| = U_1(\theta_1, r_1) \tag{14}$$

It can be observed (Fig. 1) that vectors $\mathbf{f}_2$ and $\mathbf{R}_2\mathbf{f}_2 = \mathbf{R}_{2n}\mathbf{R}_s\mathbf{f}_2$ form by default an angle equal to $\theta_2 = \theta_{2n} + \theta_s$, therefore:

$$\theta_2 = \pm\cos^{-1}\left\{\frac{\mathbf{R}_2\mathbf{f}_2 \cdot \mathbf{f}_2}{\|\mathbf{R}_2\mathbf{f}_2\|\,\|\mathbf{f}_2\|}\right\}$$

$$\theta_{2n} + \theta_s = \pm\cos^{-1}\left\{\frac{[\mathbf{R}_1\mathbf{f}_1 - \mathbf{a}_{12}] \cdot \mathbf{f}_2}{\|\mathbf{R}_1\mathbf{f}_1 - \mathbf{a}_{12}\|\,\|\mathbf{f}_2\|}\right\}$$

Finally by inserting Eq. (14) we obtain:

$$\theta_s = -\theta_{2n} \pm \cos^{-1}\left\{\frac{1}{r_2^2}[\mathbf{R}_1\mathbf{f}_1 - \mathbf{a}_{12}] \cdot \mathbf{f}_2\right\} = U_2(\theta_1, r_1, r_2) \tag{15}$$

Since vectors $\frac{d\mathbf{f}_1}{dr_1}$ and $\frac{d\mathbf{f}_2}{dr_2}$ lie on the same plane, which is normal to the axis of revolution, a scalar equivalent of Eq. (13) can be obtained:

$$\left(\mathbf{R}_1\frac{d\mathbf{f}_1}{dr_1} \times \mathbf{R}_{2n}\mathbf{R}_s\frac{d\mathbf{f}_2}{dr_2}\right) \cdot \hat{\mathbf{x}}_3 = U_3(\theta_1, r_1, r_2, \theta_s) = 0 \tag{16}$$

where $\hat{\mathbf{x}}_3$ is the unitary vector along the x_3-axis (axis of revolution).

Substituting Eqs. (14–15) into Eq. (16) we obtain a scalar equation involving r_1 only, with θ_1 being the independent parameter:

$$U_3(\theta_1, r_1, U_1(\theta_1, r_1), U_2(\theta_1, r_1, U_1(\theta_1, r_1))) = 0 \tag{17}$$

Equation (17) can be solved in terms of r_1 and subsequently Eqs. (14–15) can be solved explicitly in terms of r_2 and θ_s respectively, thus forming a parametric solution to the tooth meshing problem, with the reference gear position θ_1 as the independent parameter.

2.3 Implementation of Pitch Errors and Profile Corrections

Considering the above analysis, it is possible to obtain the appropriate function of θ_s for modified profiles or profiles with errors. From the meshing analysis standpoint, these two variants are treated in exactly the same way and profile modifications can be regarded as 'deliberate' errors. Implementing pitch errors and/ or profile corrections requires the input of the modified profile functions $\mathbf{f}_1$ and $\mathbf{f}_2$.

3 Dynamical Modelling

3.1 Contact Forces

Gear teeth are subjected to (a) elastic, (b) internal friction (hysteretic) and (c) frictional contact forces and deform as cantilever beams of varying cross-section with elastic foundation (Cornell 1981); local Hertzian contact pressure displacements are also taken into account (Timoshenko and Goodier 1970). The hysteretic friction component is negligible for the usual gear materials (i.e. steel), but it plays a significant role in assuring the stability of time-domain simulations of the dynamical response.

The force components at a given contact point, designated by index k, are calculated as functions of the interference δ_k from the Eqs. (18–20). By default they are considered to act on the teeth of the reference gear (gear 1) and are illustrated in Fig. 2.

$$\mathbf{F}_{k,elast} = -|\delta_k| k_k \mathbf{n}_k \tag{18}$$

$$\mathbf{F}_{k,hyst} = c_{hyst} \frac{d|\delta_k|}{dt} \mathbf{n}_k \tag{19}$$

$$\mathbf{F}_{k,frict} = |\delta_k| f_k k_k \mathbf{m}_k \tag{20}$$

where $\mathbf{n}_k$ is the unitary normal vector to the tooth profile at the contact point (pointing outwards) and $\mathbf{m}_k$ is the unitary vector in the direction of the sliding velocity. By default it is $\mathbf{m}_k \perp \mathbf{n}_k$.

Equation (19) represents the basic linear viscoelastic model (Voigt–Kelvin model) of the inelastic damping forces (Dowling 1998). There is currently no general agreement regarding the calculation of the damping coefficients and usually the linear damping model is considered primarily for convenience (Casuba

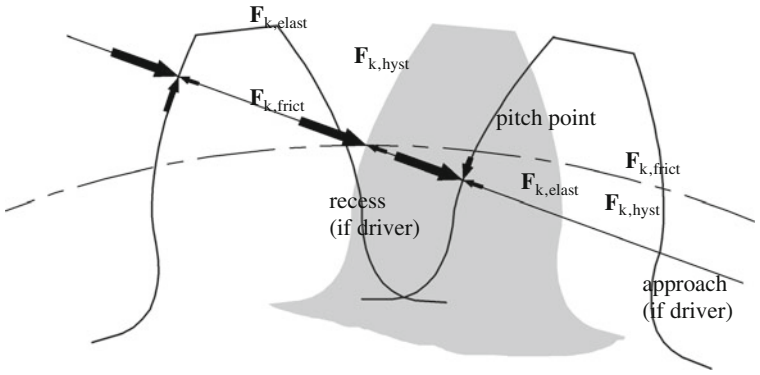

Fig. 2 Tooth contact forces on a single tooth free body

and Evans 1981). The popular practice of estimating a fairly realistic constant value of $\zeta = 0.1$ for the non-dimensional damping coefficient (Casuba and Evans 1981) has been adopted. The stiffness coefficient k_k is generally a function of tooth position and can be calculated from (a) analytical/ empirical formulae (Cornell 1981; Timoshenko and Goodier 1970), (b) Finite/Boundary Element Analysis (Tsai 1997; Muthukumar; Raghavan 1987) or (c) a hybrid method combining the first two (Andersson and Vedmar 2003). Here the formulae of (Cornell 1981; Timoshenko and Goodier 1970) were used. These offer good calculation speed and comparisons with Finite Element Results have shown good correlation.

3.2 Gearbox Model

The layout studied in this paper is shown in Fig. 3. The motor element (0) provides the power at a controlled speed through shaft I to gear 1 (DOF 1) and then, through the tooth mesh (III) to gear 2 (DOF 2). The power is then transmitted through shaft II to the break element (DOF 3), where a controlled torque is applied. The 'analysis plane' and its universal coordinate system are also defined, with axis x_3 being the axis of revolution.

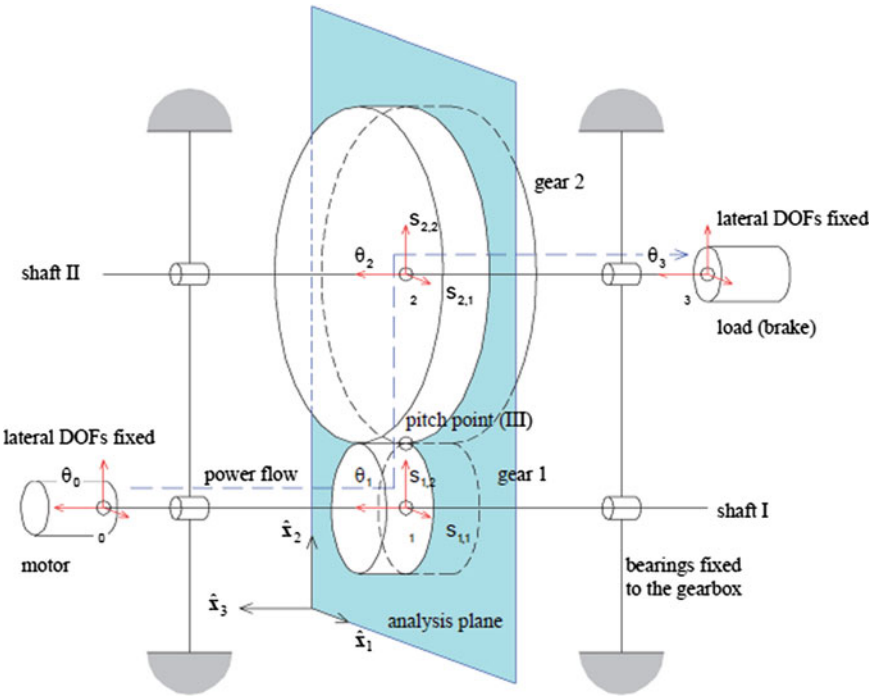

Fig. 3 Simulated single-stage gear speed reducer layout and DOF definition

The free DOFs are identified in Fig. 3. Spur gear shafts are seldom placed in cantilever arrangements, so bending of the shafts is not considered to affect the parallelism of gears (1) and (2) significantly and hence the rotations of the gear centres about the axes x_1 and x_2 and the corresponding DOFs can be neglected. This brings along the additional advantage of allowing each shaft- bearing system to be modelled as a lump element of combined stiffness.

With respect to the free DOFs the dynamical equations are as follows.

$$J_1 \frac{d^2}{dt^2}\theta_1 + D_1 \frac{d}{dt}\theta_1 - \hat{\mathbf{x}}_3 \cdot \sum_k \left[\mathbf{r}_{1,k} \times \left(\mathbf{F}_{k,elast} + \mathbf{F}_{k,hyst} + \mathbf{F}_{k,frict}\right)\right] - E_{0-1}\left(\frac{d}{dt}\theta_0 - \frac{d}{dt}\theta_1\right) - G_{0-1}(\theta_0 - \theta_1) = 0 \tag{21}$$

$$\mathbf{M}_1 \frac{\mathrm{d}^2}{\mathrm{dt}^2}\mathbf{s}_1 - \sum_{\mathrm{k}} \left(\mathbf{F}_{\mathrm{k,elast}} + \mathbf{F}_{\mathrm{k,hyst}} + \mathbf{F}_{\mathrm{k,frict}}\right) + \mathbf{C}_1 \frac{\mathrm{d}}{\mathrm{dt}}\mathbf{s}_1 + \mathbf{K}_1\mathbf{s}_1 = 0 \tag{22}$$

$$J_2 \frac{d^2}{dt^2}\theta_2 + D_2 \frac{d}{dt}\theta_2 + \hat{\mathbf{x}}_3 \cdot \sum_k \left[\mathbf{r}_{2,k} \times \left(\mathbf{F}_{k,elast} + \mathbf{F}_{k,hyst} + \mathbf{F}_{k,frict}\right)\right] + E_{2-3}\left(\frac{d}{dt}\theta_2 - \frac{d}{dt}\theta_3\right) + G_{2-3}(\theta_2 - \theta_3) = 0 \tag{23}$$

$$\mathbf{M}_2 \frac{\mathrm{d}^2}{\mathrm{dt}^2}\mathbf{s}_2 + \sum_{\mathrm{k}} \left(\mathbf{F}_{\mathrm{k,elast}} + \mathbf{F}_{\mathrm{k,hyst}} + \mathbf{F}_{\mathrm{k,frict}}\right) + \mathbf{C}_2 \frac{\mathrm{d}}{\mathrm{dt}}\mathbf{s}_2 + \mathbf{K}_2\mathbf{s}_2 = 0 \tag{24}$$

$$\mathrm{J}_3 \frac{\mathrm{d}^2}{\mathrm{dt}^2}\theta_3 + \mathrm{D}_3 \frac{\mathrm{d}}{\mathrm{dt}}\theta_3 - \mathrm{E}_{2-3}\left(\frac{\mathrm{d}}{\mathrm{dt}}\theta_2 - \frac{\mathrm{d}}{\mathrm{dt}}\theta_3\right) - \mathrm{G}_{2-3}(\theta_2 - \theta_3) - \mathrm{T}_\mathrm{B} = 0 \tag{25}$$

where:

$$\mathrm{s_i} = \left[\mathrm{s_{i,1}} \quad \mathrm{s_{i,2}} \quad \mathrm{s_{i,3}}\right]^\mathrm{T},\ \mathbf{M_i} = \begin{bmatrix} \mathrm{M_{i,1}} & & \\ & \mathrm{M_{i,2}} & \\ & & \mathrm{M_{i,3}} \end{bmatrix}$$

$$\mathbf{C_i} = \begin{bmatrix} \mathrm{C_{i,1}} & & \\ & \mathrm{C_{i,2}} & \\ & & \mathrm{C_{i,3}} \end{bmatrix},\ \mathbf{K_i} = \begin{bmatrix} \mathrm{K_{i,1}} & & \\ & \mathrm{K_{i,2}} & \\ & & \mathrm{K_{i,3}} \end{bmatrix},\ \mathrm{i} = 1, 2$$

In essence, they resemble a typical system of dynamical equations for the rotor system (compacted in vector form) with the addition of the gear mesh force/ torque components. The exact tooth contact geometry and the resulting DOF coupling is represented implicitly in Eqs. (18–20), i.e. the stand-alone calculation of the contact force components.

Spur gears do not generate axial force components; therefore the components of the vector Eqs. (22, 24) along the x_3-axis are zero, so Eqs. (21–25) define a system of 7 2nd-order ordinary differential equations. The contact force components

calculated from the gear meshing analysis render these equations non-linear, allowing the following phenomena to be simulated:

- tooth separation
- backlash
- dynamic centre-distance variations.

The dynamical equations can be solved using standard time-domain numerical integration methods.

4 Simulation Results

For the purpose of demonstrating the method the specific gearbox layout shown in Table 1 will be used.

Gear 1 is assumed errorless and indexing errors on gear 2 are assumed to follow a linear law, where the indexing error for each working surface $j = 1, 2, \ldots, N_2$ is given by the formula:

$$\sigma^{(j)} = \sigma_o \frac{j - 1}{N_2 - 1} \tag{26}$$

Table 1 Definition of simulated gear pair

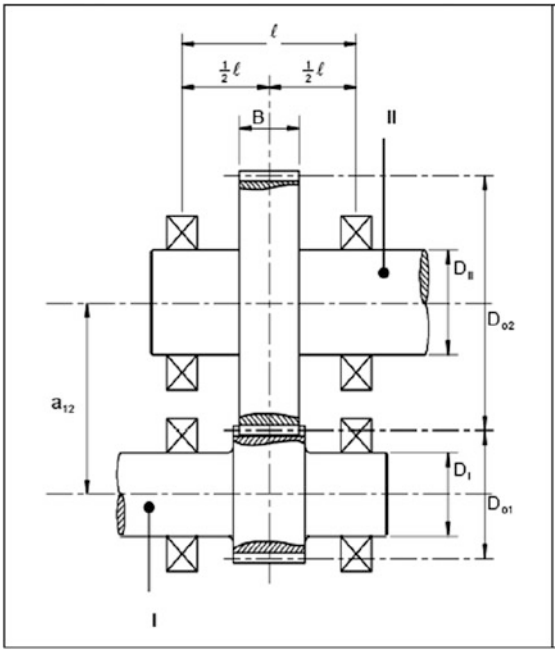

basic gear dimensions	
pressure angle	20°
module	2.5 mm
gear 1 (pinion):	
number of teeth N_1	25
pitch Ø D_{o1}	62.5 mm
gear 2 (wheel):	
number of teeth N_2	50
pitch Ø D_{o2}	125 mm
gear width B	25 mm
gear & shaft material	
Young's modulus	210 GPa
Poisson's ratio	0.3
density	8.3 Kg/cm^3
gearbox/ shaft dimensions	
centre dist. a_{12}	93.75 mm
shaft Ø D_I	30 mm
shaft Ø D_{II}	40 mm
length ℓ	50 mm
lubricant	SAE 75W-90

This is by far one of the most problematic distributions of indexing errors, as it produces a 'dropped tooth', which causes severe mesh excitation at the rotating shaft frequency and its harmonics (AGMA 1976). To consider the combined effect of errors in both gears, σ_o can be set equal to the sum of the maximum indexing errors of both gears. This in fact gives a more pessimistic prediction than if the errors were considered separately, so the results can be considered to include a safety margin. The choice of concentrating indexing errors on gear 2 is made to minimise the number of independent parameters and allow for an easier visualisation and ultimately a more versatile method. Clearly, the employed TCA model can handle much more complicated distributions and combinations, if needed.

The following test cases are examined for various σ_o values and profile corrections: Table 2.

Specialised in-house developed code was used to simulate the dynamic responses for the various test cases in the time domain, considering input speed = 100 rad/s (954.9 rpm) and output torque = 10 Nm. Both the torsional and the lateral vibration components are checked.

From the simulated vibration response the load factor is calculated as follows:

$$\text{load factor} = \frac{\text{maximum force}}{\text{nominal force}} \tag{27}$$

where the nominal force is calculated for static loading with nominal output torque.

The calculated load factor is shown in Fig. 4 for all test cases. Loci of minimum vibration are clearly identifiable by the dashed line (opt-line) and its surrounding dotted band-region (opt-region).

The effectiveness of the modification in terms of absolute vibration levels is believed to depend quite heavily on other parameters not varied in this study, such as mass, stiffness and damping of the gearbox elements (AGMA 1976), but for the purposes of comparison between alternative modification schemes on the same gearbox all these factors are essentially constant.

The 'opt-line' in Fig. 4 delimits two regions, corresponding to two antagonistic trends: To the left the indexing errors are larger than the modifications and some impact is expected to occur during tooth engagement, hence increased vibration levels are expected. There, the indexing errors are predominant. To the right the modification is larger than the indexing errors, so smooth engagement is assured. However, the increased modification sacrifices contact ratio and essentially acts as an error in itself; gradually, this leads to increased vibration levels, with the TE due to profile modification becoming the primary source of excitation.

Finally, the opt-line itself and its surrounding band-like region, termed here the 'opt-region', represent what may be considered optimal or near-optimal conditions. Any gear set with such distributions of errors and profile modifications will operate with minimal vibration.

Table 2 Definition of simulated test cases used in the construction of the sensitivity chart

Indexing error (in μrad)	Profile correction (in μrad)											
	0	2.5	5	7.5	10	15	20	25	50	75	100	125
0	0 N											
5	5 N	5C2.5	5C5		5C10	5C15		5C25	5C50	5C75		
10	10 N	10C2.5	10C5		10C10			10C25	10C50		10C100	10C125
15	15 N			15C7.5	15C10	15C15		15C25	15C50			15C125
20	20 N				20C10		20C20		20C50		20C100	
25	25 N				25C10			25C25		25C75		25C125

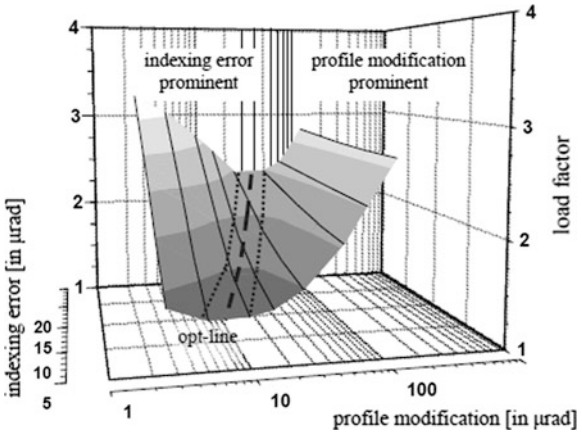

Fig. 4 3-D plot of the load factor as a function of indexing error and profile modification

5 Conclusion

The exact geometry of tooth meshing was used as a starting point for a comprehensive dynamical modelling of gear systems, incorporating the effect of pitch errors, tooth separation, DOF coupling, and profile modifications producing a fundamentally non-linear model. Various possible combinations of error distributions and profile corrections were applied to the gear model, which was simulated dynamically to calculate the load factor. The results show clear competing influences of the maximum indexing error and of the profile modification, as well as the existence of an 'optimal region'. This can be a helpful guideline in gear design.

References

AGMA 109.16 (1965) Profile and longitudinal corrections on involute gears. AGMA, 1965

AGMA 170.01 (1976) Design guide for vehicle spur and helical gears. AGMA, 1976

Andersson A, Vedmar L (2003) A dynamic model to determine vibrations in involute helical gears. J Sound Vib 206:195–212

Casuba R, Evans JW (1981) An extended model for determining dynamic loads in spur gearing. ASME J Mech Des 103:398–409

Cornell RW (1981) Compliance and stress sensitivity of spur gear teeth. ASME J Mech Des 103:447–459

Dowling NE (1998) Mechanical behavior of materials, 2nd edn. Prentice Hall, Englewood Cliffs

Dudley DW (1984) Handbook of practical gear design. McGraw-Hill, New York

Litvin FL (1994) Gear geometry and applied theory. Prentice-Hall, Englewood Cliffs

Maag Taschenbuch, Maag Zahnräder AG (1985) Zürich

Munro RG (1988) Data item on profile and lead correction. BGA Technical Publications, Leicester

Muthukumar R, Raghavan MR (1987) Estimation of gear tooth deflection by the finite element method. Mech Mach Theory 22:177–181

Niemann G, Winter H (1983) Maschinenelemente Band II. Springer, Berlin
Seol IH, Kim DH (1998) The kinematic and dynamic analysis of crowned spur gear drive. Comput Methods Appl Mech Eng 167:109–118
Spitas CA, Costopoulos ThN, Spitas VA (2002) Calculation of transmission errors, actual path of contact and actual contact ratio of non-conjugate gears. VDI-Berichte 1665:981–994
Timoshenko S, Goodier J (1970) Theory of elasticity, 3rd edn. McGraw-Hill, New York
Townsend DP (1992) Dudley's gear handbook. The design, manufacture and application of gears (2nd edn). McGraw-Hill, New York
Tsai M-H, Tsai Y-C (1997) A method for calculating static transmission errors of plastic spur gears using FEM evaluation. Finite Elem Anal Des 27:345–357

Part II
Theory, Design and Experimental Researches on Power Transmissions

Regarding the Effect of the Rack-Cutter Fillet on the Undercutting of Gears

Ognyan Alipiev, Sergey Antonov and Tanya Grozeva

Abstract In this work a generalized approach for defining the phenomenon "undercutting of involute teeth" is proposed, where besides the traditional boundary case, called "undercutting—type I", additionally two more boundary cases, called "undercutting—type II" and "undercutting—type III" are included. According to this approach the nontraditional cutting—type II and type III is caused by the rack-cutter fillet, when the trajectories of some points cross respectively: (1) the radial line of the gear (the line connecting the gear centre and the starting point of the involute profile); (2) the involute profile of the cut teeth. The parametric equations of the so called "boundary fillets" of the type II and type III of the rack-cutter are specified and in an evident state the additional boundary condition for avoiding the under-cutting of teeth is drawn up. The maximum value of the radius of the rack-cutter fillet at which the cut teeth are not undercut, is specified.

Keywords Gear · Involute profile · Undercutting of teeth · Rack-cutter fillet

1 Introduction

In the traditional theory of involute meshing (Litvin 1968; Bolotovskii 1986; GOST 16532–70 1970; Colbourne 1987; Alipiev 2011) the condition that defines the nonundercutting of teeth is defined with the examination of the meshing of the

O. Alipiev (✉) · S. Antonov · T. Grozeva
University of Ruse, Ruse, Bulgaria
e-mail: oalipiev@uni-ruse.bg

S. Antonov
e-mail: santonov@uni-ruse.bg

T. Grozeva
e-mail: tgrozeva@uni-ruse.bg

G. Dobre (ed.), *Power Transmissions*,
Mechanisms and Machine Science 13, DOI: 10.1007/978-94-007-6558-0_14,

rectilinear profile of the rack-cutter with an involute profile of the manufactured gear. In this case the undercutting of teeth, called by the authors "*undercutting—type I*", is avoided when the trajectories of all points of the rectilinear profile of the rack-cutter cross the line of action. When using the traditional approach the influence of the rack-cutter fillet on the teeth undercutting is not taken into account and the obtained results are correct only in cases when the radius of the rack-cutter fillet is not too large. When this radius exceeds a specified value (Alipiev 2011) it might turn out that the traditional condition for nonundercutting is satisfied but in reality the involute gear teeth are undercut. For that reason, in the present work a new generalized method for defining the undercutting of gears is proposed, where together with the traditional boundary case (undercutting—type I), two more boundary cases defined as "*undercutting—type II*" and "*undercutting—type III*" are taken into consideration. In these two additional cases the undercutting is done by the rack-cutter fillet and not by its rectilinear profile. Under this the undercutting—type II is characterized by the decrease of the tooth thickness at their bottom without cutting the involute profile, while by undercutting—type III, a part of the initial area of the involute profile is cut.

2 Undercutting of Teeth at Meshing of an Involute Gear with the Rack—Cutter

2.1 Undercutting—Type I (Traditional Case)

The undercutting of teeth—type I of the involute gear is obtained when at its meshing with the rack-cutter (Fig. 1a), points of the rectilinear profile KE of the tooth cutter are situated under the line of action AB. Then the trajectories of these points (lines parallel to the line n–n) do not cross the line of action AB (they cross its extension), as a consequence of which the basic theorem of meshing is not satisfied when realizing the contact between the pair profiles. In this case the rectilinear area $K^{*}E$ of the rack-cutter becomes a non-operating area that penetrates into the bottom of the processed tooth and cuts a part of an involute profile.

In order to avoid the undercutting—type I it is necessary that the tip line g–g of the rack-cutter cuts the line of action AB (Fig. 1b). Otherwise, when the crossing point L lies outside the line of action on the extension of the line PA (Fig. 1a), the cut teeth are undercut. This means that the condition for nonundercutting—type I generally can be expressed by the inequality

$$\overline{PA} \geq \overline{PL}, \tag{1}$$

and taking into account the specified distances marked on Fig. 1, *the traditional condition for undercutting—type I* finally is written in the following way (Litvin 1968).

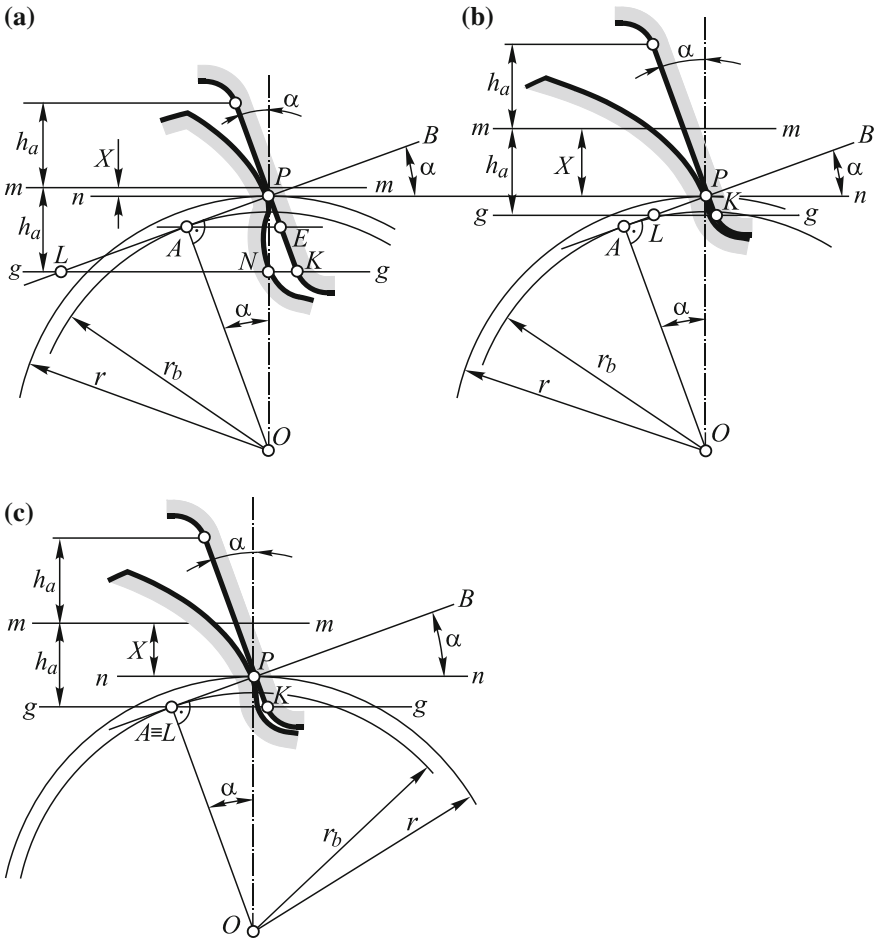

Fig. 1 Conditions of nonundercutting—type I **a** $X < X_{\min}$; **b** $X > X_{\min}$; **c** $X = X_{\min}$

$$x \geq h_a^* - 0,5z\sin^2\alpha. \tag{2}$$

In the inequality (2) $x = X/m$ is a shift (modification) coefficient of the rack-cutter, $h_a^* = h_a/m$—a coefficient of the height of the addendum, z—teeth number of the gear, α—pressure (profile) angle of the rack-cutter, m—a module of the gear. The smallest displacement $X_{\min}$ of the rack-cutter, eliminating the undercutting—type I, is defined by the equation

$$X_{\min} = x_{\min}m = (h_a^* - 0,5z\sin^2\alpha)m. \tag{3}$$

This displacement corresponds to the so called *boundary case—type I* (Fig. 1c), where the tip line g–g passes through the boundary point A (the point where the line of action contacts the base circle of a radius r_b).

2.2 Undercutting—Type II and Type III

As already mentioned, the undercutting—type I and type II are caused by the rack-cutter fillet AF (Fig. 2) in the process of teeth cutting. When this fillet is a circle of a small radius ρ_1 (Fig. 2a) the cut teeth are not undercut. Then the fillet fa of the gear teeth does not cross the radial line, passed from the centre O to the starting point a of the involute profile ae (at $X = X_{min}$ point a lies on the base circle of a radius r_b).

At comparatively larger radius ρ_2 of the fillet AF (Fig. 2b), an undercutting—type II is obtained, where the fillet fa of the cut tooth crosses (cuts) the radial line Oa, but does not cross the involute profile ae. This means that in the presence of undercutting—type II the tooth thickness at the bottom decreases without cutting an involute profile in the vicinity of its starting point a.

When the radius ρ_3 (Fig. 2c) of the rack-cutter fillet increases considerably, the fillet fq of the gear crosses the radial line Oa, as well as the involute profile. In this case besides the decrease of the tooth thickness at the bottom, the area aq of the involute profile ae is also cut.

The essence of the undercutting—type II and type III is explained on Fig. 3, where the undercutting—type I is avoided by a positive displacement of the rack-cutter at a distance $X_{\min}$. At this boundary displacement, the tip line g–g of the rack-cutter crosses the line of action AB in its starting point A.

In order to define the maximum radius of the rack-cutter fillet AF, corresponding to the boundary case where there is no undercutting—type II, on Fig. 3a additionally is drawn the curve q_{II}, called a *boundary fillet—type II*. It is obtained as an envelope of the relative positions that take the radial line l (the line aO) of the gear in the plane of the rack-cutter, when realizing the meshing between the rectilinear profile AE of the rack of the involute profile ae of the gear. In other words the profiles l and q_{II} are also *conjugated profiles* at rolling without sliding of

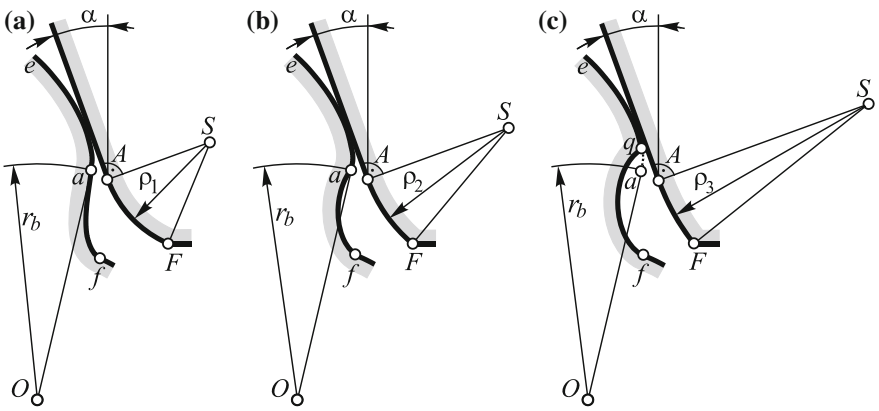

Fig. 2 Types of undercutting of the rack-cutter fillet **a** nonundercutting profile; **b** undercutting—type II; **c** undercutting—type III

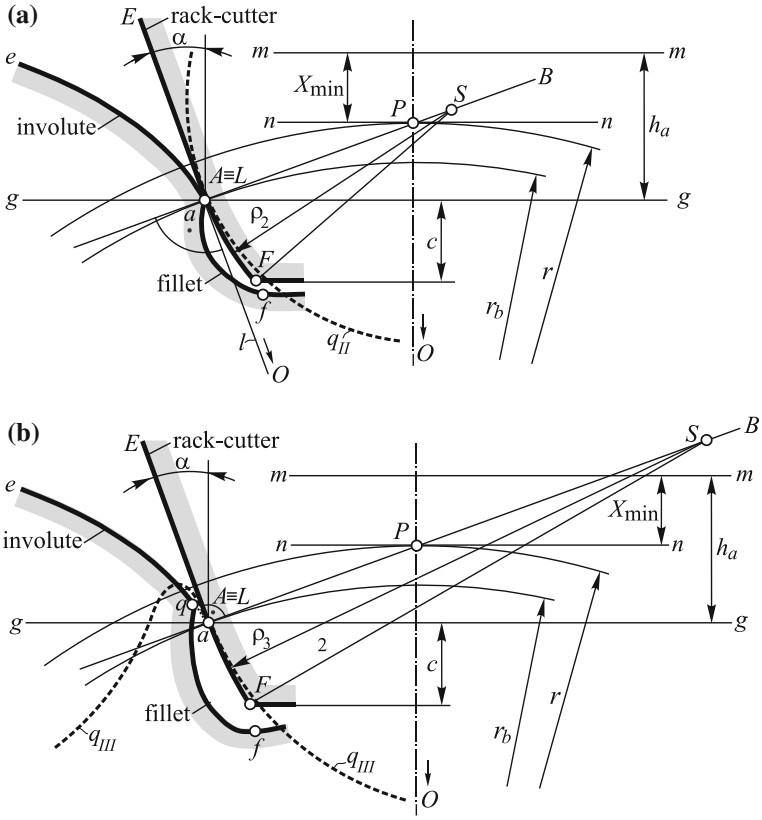

Fig. 3 Undercutting of teeth by rack-cutter fillet **a** type II; **b** type III

the centroid line *n–n* of the a rack-cutter on the reference circle of the gear of a radius *r*. Knowing the curve q_{II} allows us to define the following boundary condition: *the undercutting—type II is avoided if the real rack-cutter fillet AF is placed internally regarding the boundary fillet* q_{II} *(in the material of the cutter).* On Fig. 3a the curve *AF* is placed externally regarding the curve q_{II}, as a result of which gear teeth are undercut—type II.

Analogously the condition for nonundercutting—type III is defined by drawing a curve q_{III} (Fig. 3b), called a *boundary fillet—type III*. In this case the curve q_{III} is obtained as a trajectory (drawn in the plane of the rack-cutter) of the point *a* from the plane of the reference circle of a radius *r*, rolling without sliding on a reference circle on the line *n–n.* As point *a* lies on the internal side of the reference circle, the drawn trajectory represents a *shortened epicycloid*. The same curve q_{III}, connected without moving with the rack-cutter, can be considered also as a conjugated curve of the starting point *a* of the involute profile. This means that if the real rack-cutter fillet coincides with q_{III}, at each moment it will contact with point *A* and will not cut the involute profile *aq*. Therefore *the undercutting—type III is avoided if the*

real rack-cutter fillet AF is placed internally regarding the boundary fillet q_{III}. In the case shown on Fig. 3b this condition is not satisfied and as a result the gear teeth are undercut—type III.

2.3 Equations of Boundary Fillet Curves

2.3.1 Boundary Fillet—Type II

The equations of this curve are obtained using the theory of plane meshing (Litvin 1968; Litvin and Fuentes 2004), where one of the two meshed profiles appears and the other one is obtained as an envelope of the relative positions which the specified profile occupies in the plane of the searched profile. In this case (Fig. 4) the specified profile is the radial line l of the gear and the searched profile is the boundary fillet q_{II} of the rack-cutter.

In order to solve the problem of the geometrical synthesis two mobile coordinate systems are introduced: $X_lO_lY_l$—connected with the gear (the specified profile l); $X_{II}OY_{II}$—connected with the rack-cutter (the searched profile q_{II}). As the axis OX_{II} (the centroid line) of the rack-cutter rolls without sliding on the reference circle (of a radius r) of the gear, the displacement s of $X_{II}OY_{II}$ is synchronized with the rotation of $X_lO_lY_l$ at an angle φ, where $s = r\,\varphi$. The place of the contact points of profiles l and q_{II} in the motionless plane, designed with K, A, etc. is defined as from the pitch point P perpendicular lines to the respective positions which the radial line l takes, are dropped. In fact the equations of the curve q_{II} are derived by defining the place of the same contact points in the rectilinear moving coordinate system $X_{II}OY_{II}$.

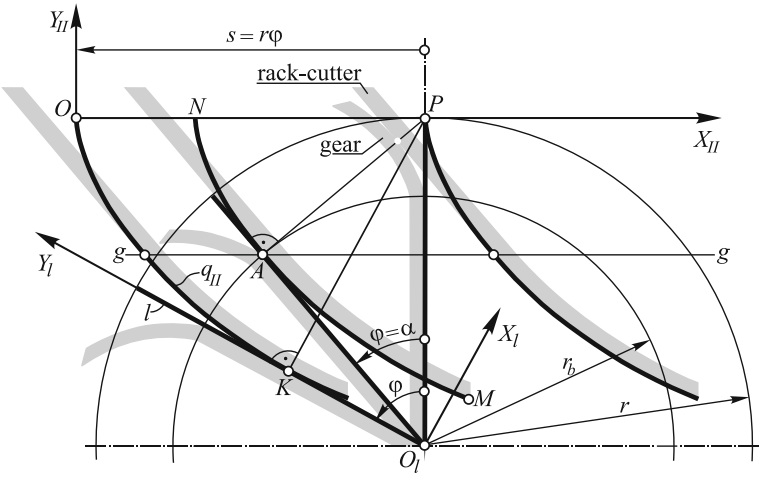

Fig. 4 A boundary fillet of the rack-cutter—type II

After executing the respective transformations and conversions (Litvin 1968), the parametric equations of the boundary fillet—type II are finally written as follows:

$$\begin{aligned} X_{II} &= r(\varphi - \cos\varphi \ \sin\varphi) = X_{II}(\varphi), \\ Y_{II} &= -r \ \sin^2\varphi \ = Y_{II}(\varphi), \end{aligned} \tag{4}$$

where φ is the angular parameter of the curve, and r—the radius of the reference circle of the gear, calculated by the equation

$$r = m\,z/2. \tag{5}$$

The obtained curve q_{II} is divided by point A to two areas: AN and AM. On Fig. 4 it is seen that only the area AM appears as the real boundary rack-cutter fillet. This means that when drawing the real curve q_{II}, the parameter φ gets an initial value of $\varphi = \alpha$ (point A) and increases in the direction from point A to point M.

From the differential geometry it is known that the radius of a curvature ρ on each curve, specified as $X = X(\varphi)$, $Y = Y(\varphi)$, is defined from the equation

$$\rho = \frac{(\dot{X}^2 + \dot{Y}^2)^{3/2}}{(\dot{X}\ddot{Y} - \ddot{X}\dot{Y})} = \rho(\varphi), \tag{6}$$

where $\dot{X}$, $\dot{Y}$, $\ddot{X}$, $\ddot{Y}$ are the first and second derivatives to the parameter φ.

Taking into account that

$$\dot{X}_{II} = 2r\sin^2\varphi,\ \ddot{X}_{II} = 4r\sin\varphi\cos\varphi,\ \dot{Y}_{II} = -2r\sin\varphi\cos\varphi,\ \ddot{Y}_{II} = -2r\cos 2\varphi \tag{7}$$

for the equation of the radius of the curvature of the curve q_{II}, it is finally obtained

$$\rho_{II} = 2\,r\,\sin\varphi = m\,z\,\sin\varphi. \tag{8}$$

2.3.2 Boundary Fillet—type III

It is obtained as a trajectory of the point A of the coordinate system $X_AO_AY_A$ connected with the gear (Fig. 5), drawn in a coordinate system $X_{III}OY_{III}$, connected with the rack-cutter. The obtained trajectory q_{III}, as it was already explained, represents a shortened cycloid, whose parametric equations can be written as follows

$$\begin{aligned} X_{III} &= r\varphi - r_b\sin\varphi = X_{III}(\varphi), \\ Y_{III} &= -r + r_b\cos\varphi = Y_{III}(\varphi), \end{aligned} \tag{9}$$

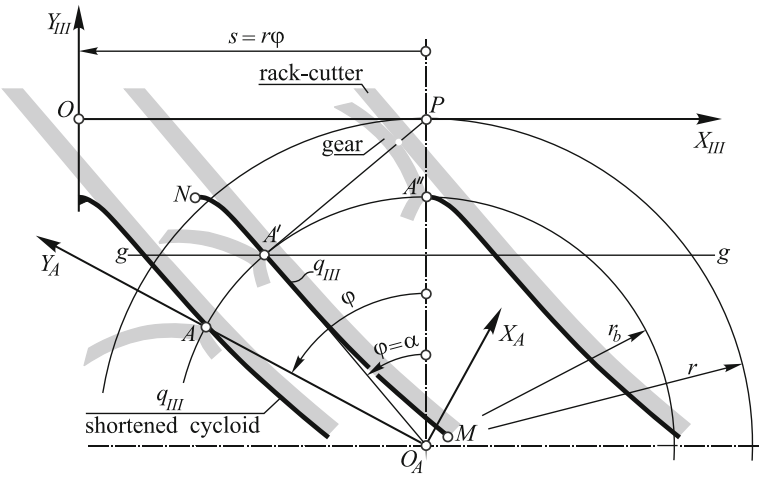

Fig. 5 A boundary fillet of the rack-cutter—type III

where r_b is the radius of the base circle, defined by the formula

$$r_b = r\cos\alpha = 0,5mz\cos\alpha. \tag{10}$$

In the initial position of the coordinate systems, when at $\varphi = 0$, point A coincides with point A'', and at $\varphi = \alpha$—with point A'. In that case, point A' appears as an inflection point, which divides the curve q_{III} in two parts:—a concave area NA' and a convex area $A'M$. In this case it should be taken into account that only area $A'M$ is the real rack-cutter fillet—type III .

The equation of the radius of the curvature of the curve q_{III} is obtained in analogous way as the curve q_{II}, with the use of the Eq. (6). In this case the first and second derivatives of X_{III} and Y_{III} to φ are defined from equations

$$\dot{X}_{III} = r - r_b\cos\varphi\,\ddot{X}_{III} = r_b\sin\varphi,\ \dot{Y}_{III} = -r_b\sin\varphi,\ \ddot{Y}_{III} = -r_b\cos\varphi, \tag{11}$$

and the radius of the curvature $\rho_{III} = \rho_{III}(\varphi)$ of the curve q_{III} is obtained by the formula

$$\rho_{III} = \frac{(r^2 - 2\,r\,r_b\cos\varphi + r_b^2)^{3/2}}{r_b^2 - r\,r_b\cos\varphi} = \frac{mz(1 - 2\cos\alpha\cos\varphi + \cos^2\alpha)^{3/2}}{2\cos\alpha(\cos\alpha - \cos\varphi)}. \tag{12}$$

2.4 Conditions of Nonundercutting—Type II

In order to clarify the causes by reason of which the rack-cutter fillet undercuts the gear teeth, on Fig. 6 both boundary curves q_{II} and q_{III} are drawn simultaneously in the current position where their common contact point coincides with the starting

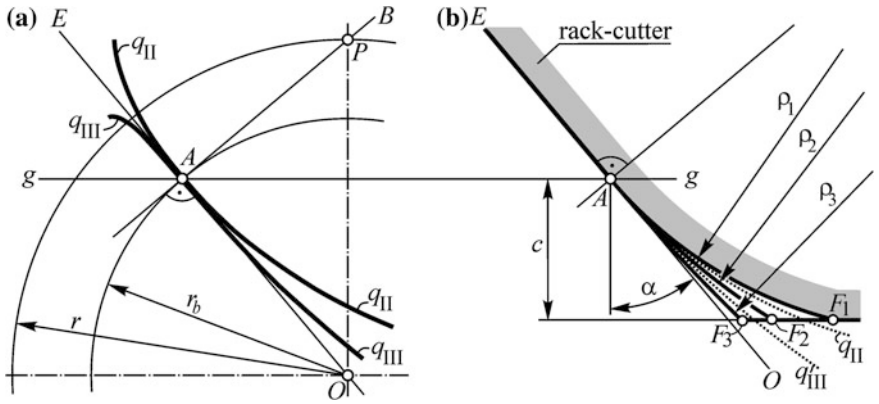

Fig. 6 Radius of the rack-cutter fillet

point A of the line of action AB (the position where $\varphi = \alpha$). In this position the radial line OAE (Fig. 6a), representing simultaneously a rectilinear profile of the rack-cutter, crosses the curve q_{III} in its inflection point, where in this case coincides with point A and appears as a contact point of OAE with the curve q_{II}.

From Fig. 6b it becomes clear that if the rack-cutter fillet is an arc of a circle of a small radius ρ_1 there exists no undercutting—type II and type III, because in this case the arc AF_1 lies on the internal side of curves q_{II} and q_{III}. When the rack-cutter fillet is positioned between both curves q_{II} and q_{III} (the arc AF_2 of a radius $\rho_2 > \rho_1$) an undercutting—type II appears, and when the rack-cutter fillet is placed between the curve q_{III} and the line OE (the arc AF_3 of a radius $\rho_3 > \rho_2$) besides an undercutting—type II, an undercutting—type III is derived.

In the case where the rack-cutter fillet is profiled on an arc from a circle, the following boundary condition is defined: *the undercutting—type II is avoided if the radius of the fillet is smaller or equal to the radius of the curve $\rho_{II,A}$ of the boundary fillet q_{II} in point A*. Since in point A of the curve q_{II} the value of the angular parameter is $\varphi = \alpha$, for the radius of the curve $\rho_{II,A}$ in this point according to the Eq. (8), it is obtained

$$\rho_{II,A} = mz \sin\alpha. \tag{13}$$

Then the condition for the nonundercutting—type II, defined by the inequality $\rho \leq \rho_{II,A}$, is written finally as follows

$$\rho^* \leq z \sin\alpha, \tag{14}$$

where $\rho^* = \rho/m$ is a coefficient of the radius of the circle, on which the rack-cutter fillet is profiled. The condition (14) shows that the undercutting—type II depends only on the teeth number z of the gear and the profile angle α of the rack-cutter.

In Table 1 the maximum values of the dimensionless coefficient $\rho^*_{\max}$, are shown, corresponding to profile angles used in practice for different number of cut teeth. In order to avoid the undercutting—type II it is enough for the radius ρ, on

Table 1 Maximum coefficient fillet radius of the rack-cutter— $\rho^*_{max} = z \sin\alpha$

Number of teeth z	Profile angle of the rack-cuter—α							
	14°30′	15°	17°30′	20°	22°30′	25°	28°	30°
5	1.252	1.294	1.504	1.710	1.913	2.113	2.347	2.5
10	2.504	2.588	3.007	3.420	3.827	4.226	4.695	5.0
20	5.008	5.176	6.014	6.840	7.654	8.452	9.389	10.0
40	10.015	10.353	12.028	13.681	15.307	16.905	18.779	20.0
80	20.030	20.706	24.056	27.362	30.615	33.809	37.558	40.0
160	40.061	41.411	48.113	54.723	61.229	67.619	75.115	80.0

which the rack-cutter fillet is profiled, to be smaller or equal to the respective value ρ^*_{max}, multiplied by the module m of the gear ($\rho \leq \rho^*_{max}\, m$). From Table 1 it is seen that ρ^*_{max} increases when the pressure angle α and teeth number z are increased. Besides, from the specified values it becomes clear that if a standard rack-cutter is used, for which $\alpha = 20°$ and $\rho^* = 0.38$, the cut teeth are not undercut—type II and type III (at $z = 5$ and $\alpha = 20° \rightarrow \rho^*{}_{max} = 1.71$).

Here it is important to note that if the cut teeth are not undercut—type II, they are also not undercut—type III. Therefore the satisfying of the boundary condition (14) guarantees the nonundercutting of teeth of type II, as well as of type III.

3 Conclusion

The carried out investigations connected to the undercutting of teeth of involute gears when cut by the rack-cutter, result in the following conclusions:

1. The undercutting of teeth is done from the rectilinear profile of the rack-cutter (traditional case—type I), as well as by the fillet, on which are cut the teeth of its cutting teeth crests (the non-traditional case) are cut.
2. The undercutting of teeth, caused by the rack-cutter fillet is found in two variants, defined in the present work as "undercutting—type II" and "undercutting—type III".
3. In the presence of the undercutting—type II the teeth thickness in their bottom is decreased without cutting their involute profile, and in the presence of undercutting—type III a part of the involute profile is additionally cut.
4. The condition for nonundercutting—type II is defined uniquely by two independent parameters: the number z of the cut teeth and the profile angle α of the rack-cutter.
5. In order to avoid the undercutting of the involute teeth, it is necessary to satisfy the traditional condition (2) as well as the boundary condition (14).

References

Alipiev OL (2011) Geometric design of involute spur gear drives with sym-metric and asymmetric teeth using the Realized Potential Method. Mech Mach Theory 46(1):10–32

Bolotovskii IA et al. (1986) Reference book in geometric calculation of involute and worm gearings, Mashinostroyenie, Moscow, (in Russian)

Colbourne JR (1987) The Geometry of Involute Gears. Springer–Verlag, New York

GOST 16532–70 (1970) Cylindrical involute external gear pairs—calculation of geometry, Moscow

Litvin FL (1968) Theory of gearing. In: Nauka (ed) Moscow, (in Russian)

Litvin F, Fuentes A (2004) Gear Geometry and Applied Theory. Cambridge University Press, Cambridge

Influence of Uncertainties on PD Tuning

Gabriele Barbaraci and Gabriele Virzi' Mariotti

Abstract The aim of this work is to present a method for tuning the parameters of PD controller under the influences of the uncertainties, in order to stabilize the position of a rotor supported by active magnetic bearings (AMBs). The uncertainties are relative to mass, transverse and polar moment of inertia of the rotor. The introduction of the uncertainties is due to an incomplete modeled dynamic of the system or in the case the system being subjected to a parametric variation. The presence of the uncertainties produces a set of differences among the values of the output. Poles displacement method is used to reach the asymptotically stability condition characterized by a periodic oscillation during the transient response as a consequence of the impulse input. In this way we carried out some particular condition under graphical representation which helps making a prevision when the phenomena of instability occurs. In the present approach the poles displacement is obtained by imposing respectively the condition on the real part, which must be negative, and in the discriminant of a second degree equation, which must be less than zero, both depend on the uncertainties and the angular speed of the rotor. All calculations are performed through a 4-axis AMB rigid rotor to validate the PD controller method rule introduced in this work.

Keywords Uncertainties · Active magnetic bearing · PD controller · Shaft

List of Symbols

Ω	Angular velocity
$f_{mag\_to\_g}\ (t)$	Vector of force components acting on center of mass of shaft

G. Barbaraci (✉) · G. Virzi' Mariotti
Dipartimento di Ingegneria Chimica, Gestionale, Informatica e Meccanica,
University of Palermo, Palermo, Italy
e-mail: gabriele.barbaraci@unipa.it

G. Virzi' Mariotti
e-mail: gabriele.virzimariotti@unipa.it

G. Dobre (ed.), *Power Transmissions*,
Mechanisms and Machine Science 13, DOI: 10.1007/978-94-007-6558-0_15,

i_c(t)	Vector of current components
q_g(t)	Vector of center of mass displacements
q_b(t)	Vector of bearing section displacements
q_{sensor}(t)	Vector of displacement captured by sensors
$x(t)$	State vector
$y(t)$	Output vector
A	Dynamic matrix
B	Input-state matrix
C	State-output matrix
$B_{\Theta mag}$	Transformation matrix of magnetic bearing force
B_{mag}	Transformation coordinates matrix of magnetic bearing force on center of mass of rotor
$B_{\Theta disp}$	Transformation matrix of magnetic bearing Section's displacement
B_{sensor}	Transformation coordinates of displacements of sensor and center of mass of shaft
G	Gyroscopic matrix
K_I	Current gains matrix
K_s	Displacement gains matrix
M	Mass matrix
P_m	Maximum percentage of mass uncertainty
P_{I_T}	Maximum percentage of transverse inertia uncertainty
P_{I_P}	Maximum percentage of polar inertia uncertainty
Δ_{m}	Normalized mass uncertainty
Δ_{G}	Normalized polar inertia uncertainty
α	Slope of magnets

1 Introduction

AMB uses electromagnets to attract the ferromagnetic cape winding the rotor which is free to rotate without physical contact with the bearing. This operation, called active magnetic levitation, is unstable unless of a certain control's algorithm performed respecting the imposed constraining. In order to achieve a stable levitation, an active feedback control of the current in the magnetic coils is needed. As it might be expected, a variety of control schemes are used and a variety of studies have been done for AMB control. The dynamic system however depends above all on the rotor's angular speed, as the case for any rotor dynamic system because of the gyroscopic effect. The gyroscopic effect leads the system into instability phenomena which must be considered to achieve stable levitation. The rotor motion is given by complex variables, and it is decomposed into translation motion of the controlled sections by coordinates of transformation which considers the displacements of the center of mass and the rotation of the rotor around it.

Moreover the transformation coordinates (Schweitzer et al. 2003), allows relating the displacements captured by the sensors and the displacements of the section located on the middle plane of the bearings location. For each rotor's section the control law is designed independently and as a function of angular velocity and uncertainties. The condition, which describes the asymptotically stability condition of the rotating machinery, is related to the sign of the real part of four eigenvalues two of which have the real part as a function of angular speed and gyroscopic uncertainty. The periodic oscillation is reached by imposing a proportional gain which leads the discriminant to be negative. Both real and imaginary part of eigenvalues, are also function of uncertainties. The introduction of uncertainties modifies the analysis to reach the desired goal, because a tridimensional representation of the parameter must be considered in order to choose the derivative and proportional gain and to analyze the characteristics of a rotating machinery such as the Campbell diagram which is affected by the uncertainties. All the imposed conditions produce a set of inequalities which must be respected in order to stabilize the position of the rotor. Once the parameters of the controller are fixed, the impulse response study is performed to show the different dynamic behavior of the system according with the uncertainties. Based on the computer simulations it has been demonstrated that the tuning of the PD controller with uncertainties can stabilize the system for different values of angular speed according the limits established by the uncertainties.

2 Mathematical Model of Rigid Rotor

The particular configuration of the rotor shown in this work considers a rotor with four degree of freedom with eight poles for each active magnetic bearing, having a slope of 45° with regard to the horizontal direction so that the force's resultant supports the rotor along the x and y direction, as Fig. 1 shows:

The system is subjected to a state of uncertainty about its mass, cross and polar moment of inertia dictated by the parameters δ_m, δ_{I_P} and δ_{I_T} in the range respectively P_m, P_{I_T} and P_{I_P}. The motion equation is referred to the center of gravity and has the following expression, (Schweitzer et al. 2003):

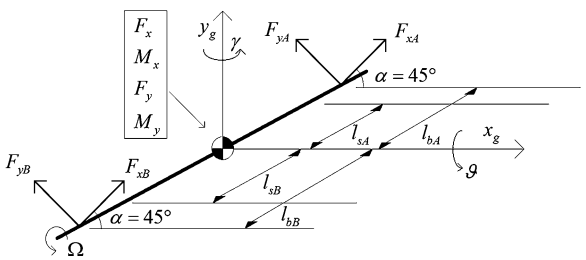

Fig. 1 Schematic view of 4-axis rotating shaft supported by two radial active magnetic bearings with sensors

$$M\frac{d^2q_g(t)}{dt^2}+\Omega G\frac{dq_g(t)}{dt}=B_{\Theta mag}B_{mag}f(i_c(t),q_b(t)) \tag{1}$$

where

$$M=\begin{vmatrix} m & 0 & 0 & 0\\ 0 & I_T & 0 & 0\\ 0 & 0 & m & 0\\ 0 & 0 & 0 & I_T \end{vmatrix},\ G=\begin{vmatrix} 0 & 0 & 0 & 0\\ 0 & 0 & 0 & -I_P\\ 0 & 0 & 0 & 0\\ 0 & I_P & 0 & 0 \end{vmatrix},$$

$$B_{mag}=\begin{vmatrix} 1 & 0 & 1 & 0\\ -l_{bA} & 0 & l_{bB} & 0\\ 0 & 1 & 0 & 1\\ 0 & l_{bA} & 0 & -l_{bB} \end{vmatrix},f(i_c(t),q_b(t))=\begin{vmatrix} F_{xA}(i_{cxA}(t),x_{bA}(t))\\ F_{yA}(i_{cyA}(t),y_{bA}(t))\\ F_{xB}(i_{cxB}(t),x_{bB}(t))\\ F_{yB}(i_{cyB}(t),y_{bB}(t)) \end{vmatrix},$$

$$B_{\Theta mag}=\begin{vmatrix} \cos(\alpha) & 0 & -\sin(\alpha) & 0\\ 0 & \cos(\alpha) & 0 & \sin(\alpha)\\ \sin(\alpha) & 0 & \cos(\alpha) & 0\\ 0 & -\sin(\alpha) & 0 & \cos(\alpha) \end{vmatrix},$$

$$q_g(t)=|\,x_g(t)\quad \gamma(t)\quad y_g(t)\quad \vartheta(t)\,|^T.\left\{\begin{array}{l} m=\bar{m}(1+P_m\delta_m)\\ I_T=\bar{I}_T(1+P_{I_T}\delta_{I_T})\\ I_P=\bar{I}_P(1+P_{I_P}\delta_{I_P})\\ \delta_{m,I_T,I_P}\in[-1,1], P_{m,I_T,I_P}=20\% \end{array}\right\}$$

The last expression leads to structured uncertainties matrix such as:

$$\Delta_M=\begin{vmatrix} P_m\delta_m & 0 & 0 & 0\\ 0 & P_{I_T}\delta_{I_T} & 0 & 0\\ 0 & 0 & P_m\delta_m & 0\\ 0 & 0 & 0 & P_{I_T}\delta_{I_T} \end{vmatrix},\Delta_G=\begin{vmatrix} 0 & 0 & 0 & 0\\ 0 & P_{I_P}\delta_{I_P} & 0 & 0\\ 0 & 0 & 0 & 0\\ 0 & 0 & 0 & P_{I_P}\delta_{I_P} \end{vmatrix}$$

respectively the mass and gyroscopic structured uncertainties matrices, (Wu and Lin 2005).

By introducing a transformation of coordinates (Genta 2005) (2) which has a great consideration the relation of the displacements between the section relative to bearing location and the sensors, the system is analyzed according the equation of motion (3)

$$\begin{array}{l} q_b(t)=B_{\Theta disp}B_{mag}^T q_g(t)\\ q_{sensor}(t)=(B_{\Theta disp}B_{sensor})q_g(t)\\ q_{sensor}(t)=(B_{\Theta disp}B_{sensor})(B_{\Theta disp}B_{mag}^T)^{-1}q_b(t)\\ f_{mag\_to\_g}(t)=B_{\Theta mag}B_{mag}f(i_c(t),q_b(t)) \end{array} \tag{2}$$

$$M\frac{d^2q_b(t)}{dt^2}+\Omega G\frac{dq_b(t)}{dt}=f(i_c(t),q_b(t)) \tag{3}$$

where

$$B_{\Theta disp} = \begin{vmatrix} \cos(\alpha) & \sin(\alpha) & 0 & 0 \\ -\sin(\alpha) & \cos(\alpha) & 0 & 0 \\ 0 & 0 & \cos(\alpha) & \sin(\alpha) \\ 0 & 0 & -\sin(\alpha) & \cos(\alpha) \end{vmatrix},$$

$$B_{sensor} = \begin{vmatrix} 1 & -l_{sA} & 0 & 0 \\ 0 & 0 & 1 & l_{sA} \\ 1 & l_{sB} & 0 & 0 \\ 0 & 0 & 1 & -l_{sB} \end{vmatrix},$$

$$q_b(t) = |\, x_{bA}(t) \quad y_{bA}(t) \quad x_{bB}(t) \quad y_{bB}(t) \,|^T$$
$$q_{sensor}(t) = |\, x_{sA}(t) \quad y_{sA}(t) \quad x_{sB}(t) \quad y_{sB}(t) \,|^T$$

where

$$M_t = \bar{M}_b + M_b(\Delta_M) \in \Re^{4\times 4}$$
$$G_t = \bar{G}_b + G_b(\Delta_G) \in \Re^{4\times 4}$$

or rather the sum of the nominal value and the uncertainties contributes (Schweitzer and Maslen 2009).

The magnetic forces produced by active magnetic bearings are linearized by Taylor series expansion which leads to the expression of the force (4):

$$f(i_c(t), q_b(t)) \approx K_s q_b(t) + K_I i_c(t) \tag{4}$$

where

$$K_s = \begin{vmatrix} k_x & 0 & 0 & 0 \\ 0 & k_x & 0 & 0 \\ 0 & 0 & k_x & 0 \\ 0 & 0 & 0 & k_x \end{vmatrix}, K_I = \begin{vmatrix} k_I & 0 & 0 & 0 \\ 0 & k_I & 0 & 0 \\ 0 & 0 & k_I & 0 \\ 0 & 0 & 0 & k_I \end{vmatrix}, i_c(t) = \begin{vmatrix} i_{cxA}(t) \\ i_{cyA}(t) \\ i_{cxB}(t) \\ i_{cyB}(t) \end{vmatrix}$$

By complex notation, that is obtained multiplying the second and fourth row for the imaginary unit the Eq. (3), we obtain the (5) (Barbaraci and Virzì Mariotti 2009)

$$M_J \frac{d^2 r_b(t)}{dt^2} + j\Omega G_J \frac{dr_b(t)}{dt} = f(i_{cJ}(t), r_b(t)) \tag{5}$$

where

$$f(i_{cJ}(t), r_b(t)) \approx K_{XJ} r_b(t) + K_{IJ} i_{cJ}(t) \tag{6}$$

and

$$
\begin{aligned}
M_J &= \begin{vmatrix} m_{J11} + m_{J11\delta} & m_{J12} + m_{J12\delta} \\ m_{J21} + m_{J21\delta} & m_{J22} + m_{J22\delta} \end{vmatrix}; \\
G_J &= \begin{vmatrix} g_{J11} + g_{J11\delta} & g_{J12} + g_{J12\delta} \\ g_{J21} + g_{J21\delta} & g_{J22} + g_{J22\delta} \end{vmatrix}; \\
K_{XJ} &= \begin{vmatrix} k_x & 0 \\ 0 & k_x \end{vmatrix}; K_{IJ} = \begin{vmatrix} k_i & 0 \\ 0 & k_i \end{vmatrix}; \\
r_b(t) &= \begin{vmatrix} x_{bA}(t) + jy_{bA}(t) \\ x_{bB}(t) + jy_{bB}(t) \end{vmatrix}; i_{cJ}(t) = \begin{vmatrix} i_{cxA}(t) + jy_{cyA}(t) \\ i_{cxB}(t) + ji_{cyB}(t) \end{vmatrix}
\end{aligned} \tag{7}
$$

3 Analysis of Stability Conditions

Introducing the state space representation (8)

$$
\begin{cases} \dot{x}(t) = Ax(t) + Bu(t) \\ y(t) = Cx(t) \end{cases} \tag{8}
$$

where

$$
\begin{cases} A = \begin{vmatrix} 0 & I \\ M_J^{-1}K_{XJ} & -M_J^{-1} \end{vmatrix} \in \Re^{4\times4}, B = \begin{vmatrix} 0 \\ M_J^{-1}K_{IJ} \end{vmatrix} \in \Re^{4\times2} \\ C = \begin{vmatrix} \left(B_{\Theta disp}B_{sensor}\right)\left(B_{\Theta disp}B_{mag}^T\right) & 0 \end{vmatrix} \in \Re^{4\times2} \\ x(t) = \begin{vmatrix} r_b(t) \\ \dot{r}_b(t) \end{vmatrix} \in \Re^{4\times1}, y(t) \in \Re^{2\times1}, i_{cJ}(t) \in \Re^{2\times1} \end{cases} \tag{9}
$$

we see that the system is unstable without a controller, as Figs. 2 and 3 show:

Figures 2 and 3 are carried out as a function of the uncertainties at zero angular speed relative to the transfer function (10):

$$
W(s, \Delta_M, \Delta_G) = \frac{\prod_{l=1}^{h}(s + z_1(\delta_m, \delta_{I_T}\delta_{I_P}))}{\prod_{r=1}^{n}(s + p_r(\delta_m, \delta_{I_T}\delta_{I_P}))} \tag{10}
$$

Variation of the uncertainties, in terms of combination of three uncertainties, produces the displacements of poles and zero along real and imaginary axis on both Gauss plane and throughout we concluded the system is unstable. In terms of frequency domain the influence of the uncertainties is revealed by the Bode plot as shown in the Figs. 4 and 5:

Figure 4 shows that differences between the nominal values and the perturbed plant are more evident by the increasing with frequency in the magnitude while the difference is not emphasized in the phase. From the Fig. 5 the influence of the

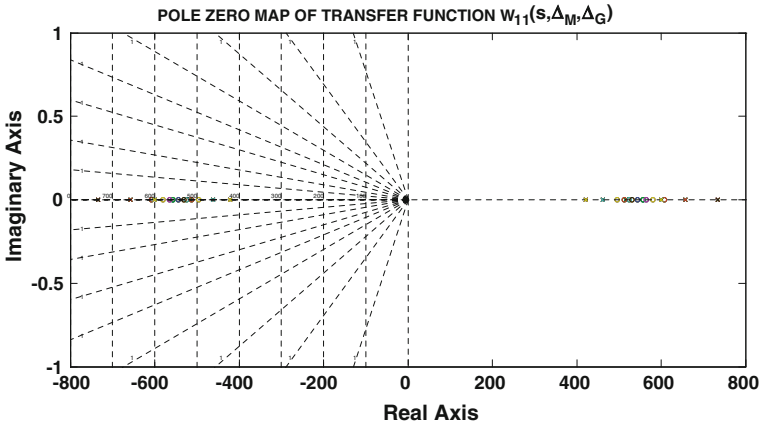

Fig. 2 Distribution of poles and zeros of $W_{11}(s, \Delta_M, \Delta_G)$ in the complex plane

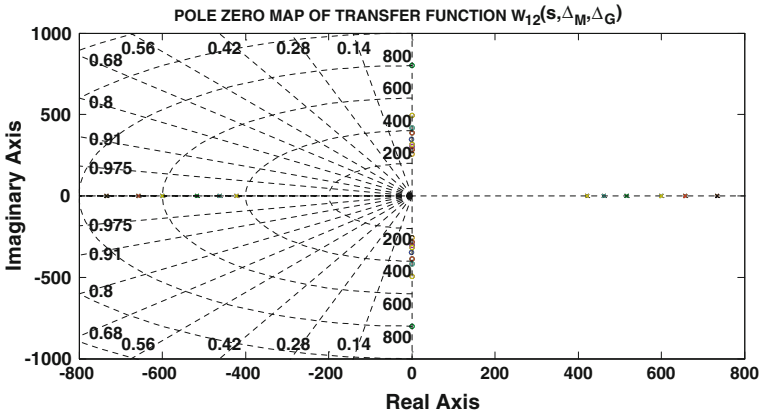

Fig. 3 Distribution of poles and zeros of $W_{12}(s, \Delta_M, \Delta_G)$ in the complex plane

uncertainties is relevant in the both magnitude and phase diagram. The same figure shows that the magnitude is characterized by attenuation relative to a different value of the frequency according with the number of uncertainties permutation (Zhoa et al. 2002), (Knospe and Fittro 1997), (Bugajski et al. 1993). The same characteristic affects the phase diagram on the same fig., where the changing in phase is relative to different value respect the nominal system.

The stable active magnetic levitation in absence of gravity is reached by PD controller obtained by moving the poles in the left half plane according with the structure of the eigenvalues obtained by state feedback.

By assuming a negative feedback, the control signal assumes the expression (11):

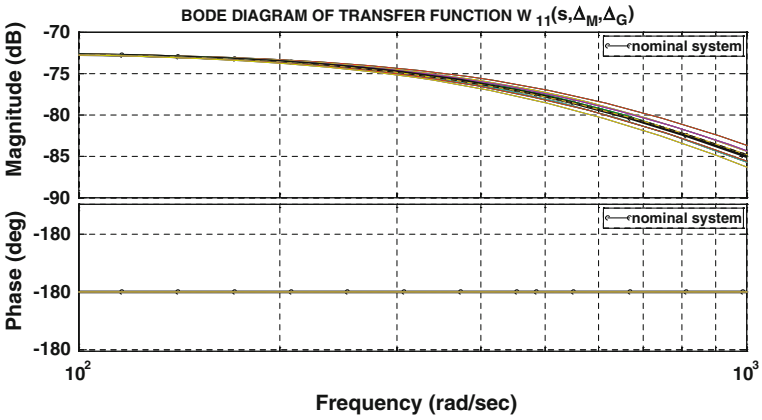

Fig. 4 Frequency response of $W_{11}(s, \Delta_M, \Delta_G)$

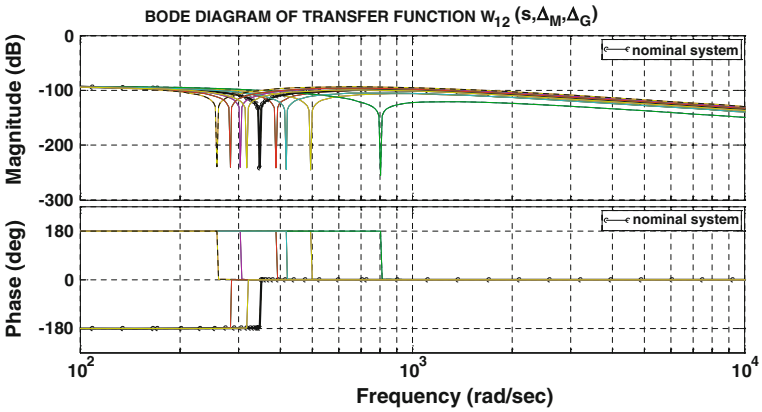

Fig. 5 Frequency response of $W_{12}(s, \Delta_M, \Delta_G)$

$$i_{cJ}(t) = -K_{PJ} r_b(t) - K_{DJ} \dot{r}_b(t) \tag{11}$$

where

$$K_{PJ} = \begin{vmatrix} k_p & 0 \\ 0 & k_p \end{vmatrix}; K_{DJ} = \begin{vmatrix} k_d & 0 \\ 0 & k_d \end{vmatrix}$$

That are the proportional and derivative gain matrices respectively, so the structure of the Eq. (5) is modified and becomes (12) (Genta 2005):

$$M_J \ddot{r}_b(t) + |j\Omega G_J + K_{IJ} K_{DJ}| \dot{r}_b(t) + |K_{IJ} K_{PJ} - K_{XJ}| r_b(t) = 0^{2\times 1} \tag{12}$$

The eigenvalues of (12) are shown in the system (13):

$$\left\{ \begin{array}{l} \lambda_{12} = k_d k_t \pm f\left(k_d, k_i, k_x, k_p, m_{1r}, m_{1r\delta}\right) \\ \lambda_{3,4} = k_d k_i - 2 \cdot \Omega \cdot (g_{12} + g_{12\delta}) \pm f\left(k_d, k_i, k_x, k_p, m_{1r}, m_{1r\delta}, g_{12}, g_{12\delta}\right) \end{array} \right\} \quad (13)$$

where

$\left\{m_{pr}, m_{pr\delta}\right\} \in M_J$ and $\left\{g_{pr}, g_{pr\delta}\right\} \in G_J \, \forall p, r = 1, \ldots 2$

By analysis of λ_{12} and assuming that k_d must be positive, as a first condition on it to stabilize λ_{12}, we verify under what condition of uncertainties the denominator of all eigenvalues are positive.

By trial calculation we carried out the conclusion (14)

$$\begin{array}{c} \sum_{r=1}^{2} (m_{1r} + m_{1r\delta}) \Leftrightarrow \delta_m > -5 \, \forall \delta_{I_T} \\ \sum_{r=1}^{2} (-1)^{1+j} (m_{1r} + m_{1r\delta}) > 0 \Leftrightarrow \delta_{I_T} > -5 \, \forall \delta_m \end{array} \quad (14)$$

This means that we can use the entire range of the uncertainties to build our analysis. The asymptotically stability condition for the $\lambda_{3,4}$ is shown in (15); it is also depending on the angular speed:

$$k_d > \frac{3.5593 \cdot 10^{-26} (5.32007 \cdot 10^{-23} \Omega + 1.06401 \cdot 10^{23} \delta_{I_p} \Omega)}{k_i} \quad (15)$$

Given the inequality (15) we have seen that asymptotically stability condition is verified by choosing a value of derivative gain more than the quantity established by the its right hand. Left and right of the Fig. 6 are carried out by choosing two different value of derivative gain in particular, we have chosen the derivative gain $k_d = 1$ *A s/m*, Fig. 4a, and we have seen that the real part of eigenvalues $\lambda_{3,4}$ is negative in a certain range of angular speed. For each value of angular speed there is a different range of stability condition dictated by the state of the gyroscopic uncertainty. In particular we see that an increasing of δ_{I_p} such as the angular speed leads the system to the instability phenomena. Figure 4b shows that the instability phenomena due to the increasing of the angular speed can be avoided by an increasing of the derivative gain in such way to recover the negative sign of the real part of eigenvalues $\lambda_{3,4}$. Once obtained the negative real part of $\lambda_{3,4}$, automatically is verified $\Re\left(\lambda_{1,2}\right) < 0$ since it's verified for positive value of derivative gain.

The periodic oscillation is performed by studying where the sign of the terms under square root of (15) is negative. The study of the sign under the square root returned the conditions (16) and (17) for the eigenvalues λ_{124} and $\lambda_{3,4}$ respectively:

$$k_p|_{\lambda(1,2)} > \frac{1.28099 k_d^2 k_i^2 + 3.45868 k_x + 0.69173 k_x \delta_m}{3.45868 k_i + 0.69173 k_i \delta_m} \quad (16)$$

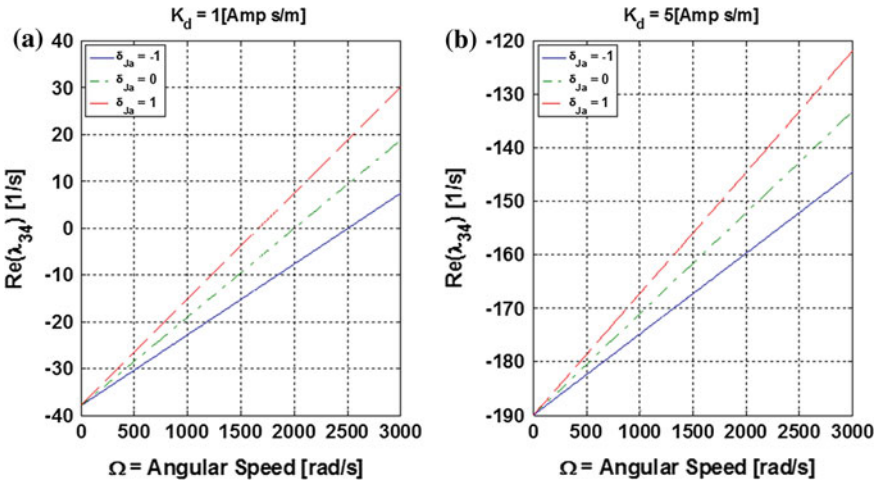

Fig. 6 Real part of eigenvalues $\lambda_{3,4}$

$$k_p|_{\lambda(3,4)} > \frac{\left(\begin{array}{r} 1.36 \cdot 10^5 + 1.02628 \cdot 10^3 k_d^2 + 2.73 \cdot 10^4 \delta_{I_T} - (1.02 k_d + 0.204 k_d \delta_{I_P})\Omega + \\ \left(2.54 + 1.01\delta_{I_P} + 10.1\delta_{I_P}^2\right) \cdot 10^{-4}\Omega^2 \end{array}\right)}{36 + 7.21\delta_{I_T}} \tag{17}$$

We see that expression (16) does not depend on angular speed, and once fixed k_x and k_i, respectively the displacement and current gain, it became a function of mass uncertainty δ_m and derivative gain k_d while the relation (17) is a function of $k_d, \delta_m, \delta_{I_P}, \delta_{I_T}$ and Ω.

In order to provide the value of k_p, which leads the system to assume a periodic oscillation during the transient response, we solved the inequalities (16) and (17) to capture a value of k_p from the graphical representation shown in Figs. 7 and 8:

Figure 7 shows that the periodic oscillation condition for eigenvalues $\lambda_{1,2}$ is reached for values of k_p which lay over the surface according to the relation (16). The same figure represents the lower limit to reach the periodic oscillation under one the solution becomes real and nothing can be said about the asymptotically stability condition, so that a further discussion about the sign between two real number must be introduced. Once the value of δ_m is fixed we see that k_p decreases by decreasing the value of k_d to reach the periodic oscillation. By fixing k_d the proportional gain k_p decreases by increasing the mass uncertainty:

Figure 8 shows the graphical representation of the function $k_p(\delta_{I_T} = 0, \delta_{I_P})$ *and* $k_p(\delta_{I_T}, \delta_{I_P} = 0)$ respectively on the left and on the right. From the figure on the left we see that periodic oscillation condition is reached for value of k_p which

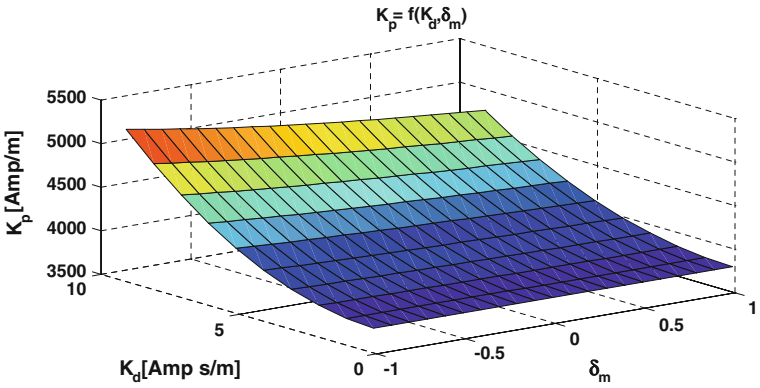

Fig. 7 Surface describing the lower limit to reach the periodic oscillation for the eigenvalues $\lambda_{1,2}$

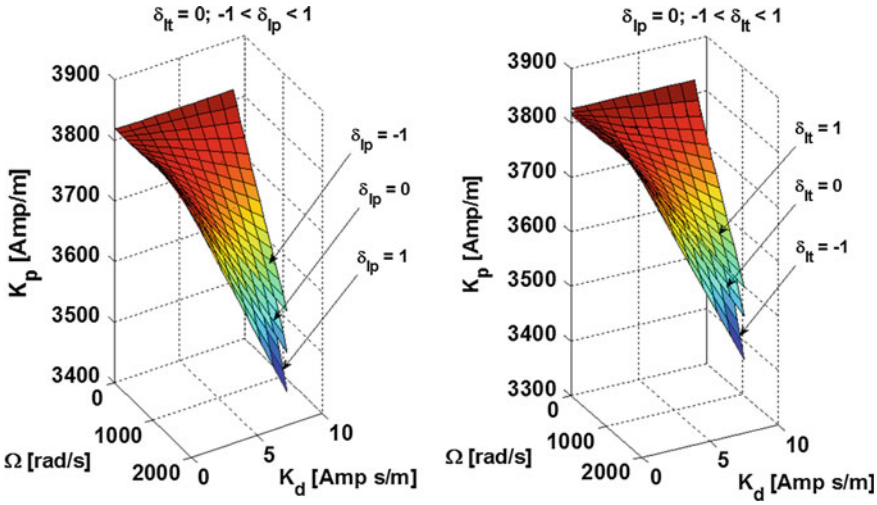

Fig. 8 Surfaces describing the lower limit to reach the periodic oscillation for the eigenvalues $\lambda_{3,4}$ varying with uncertainties

decreases by increasing Ω and δ_{I_P}, and it increases by increasing the derivative gain k_d. From the figure on the right we see that k_p maintained the same behavior with respect the variable k_d and Ω, but in this case k_p increased by increasing the δ_{I_P}. According to the previous results we have decided to focus on the Fig. 7 to tune k_p value because it represents the most restrictive condition since the inequality (16) is verified for higher values than the inequality (17).

4 Campbell Diagram

The effect of the uncertainties is revealed also by computing 3D Campbell Diagram. In order to have more visibility of the graphical representation we carry out only the positive values of the frequency to study the characteristics of the diagram. A plane that has a slope of 45° is the equivalent synchronous line straight line in 2D Campbell diagram. All the imaginary parts of the eigenvalues of the system are shown in the Fig. 9a and b. They give two different distribution of the imaginary part of the eigenvalues referring to the system shown before. The different distribution is due to the presence of the uncertainties. Figure 9a shows the imaginary part of $\lambda_{1,2}$ (violet surface) with the imaginary part of $\lambda_{3,4}$ varying with transverse moment of inertia. The particular the graph 9a about $\Im(\lambda_{3,4})$ is sketched in the Fig. 10a and b:

Figure 10a shows that the variation of δ_{I_T} produces a different distribution of imaginary part of eigenvalues $\lambda_{3,4}$ so that a plane having a slope of 45 degrees compared to the horizontal plane produces three different intersections with the imaginary part of $\lambda_{3,4}$ having relevant differences once we consider the variation of δ_{I_P}in Fig. 10b. These multiple intersections are relative to different values of critical speed, as Fig. 11 shows. Figure 12 shows the variation of $\Im(\lambda_{3,4}) = f\left(\delta_{I_P}|_{-1,0,1}, \delta_{I_T}, \Omega\right)$. The same figure is relative to the Fig. 9b of the 3D Campbell diagram and it shows that influence of δ_{I_P}on critical speed is smaller than that produced by δ_{I_T} of an order of magnitude.

The intersection of $\Im(\lambda_{3,4}) = f\left(\delta_{I_P}|_{-1,0,1}, \delta_{I_T}, \Omega\right)$ with a plane of 45° returns as the eigenfrequencies are changing varying with $\delta_{I_P}|_{-1,0,1}, \delta_{I_T}, \Omega$ as shown in the Fig. 13:

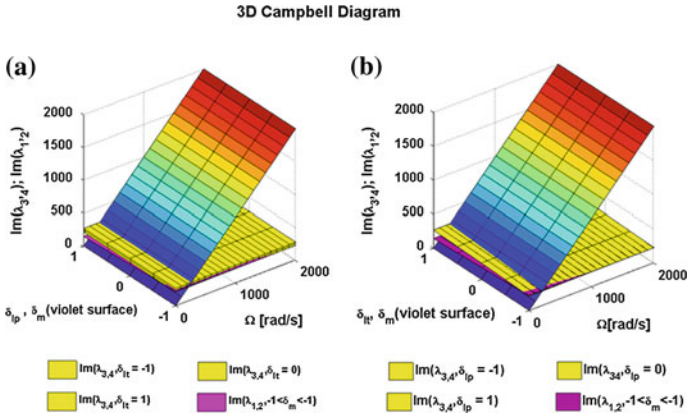

Fig. 9 Campbell diagram in 3D space according with uncertainties δ_{I_P} and δ_{I_T}

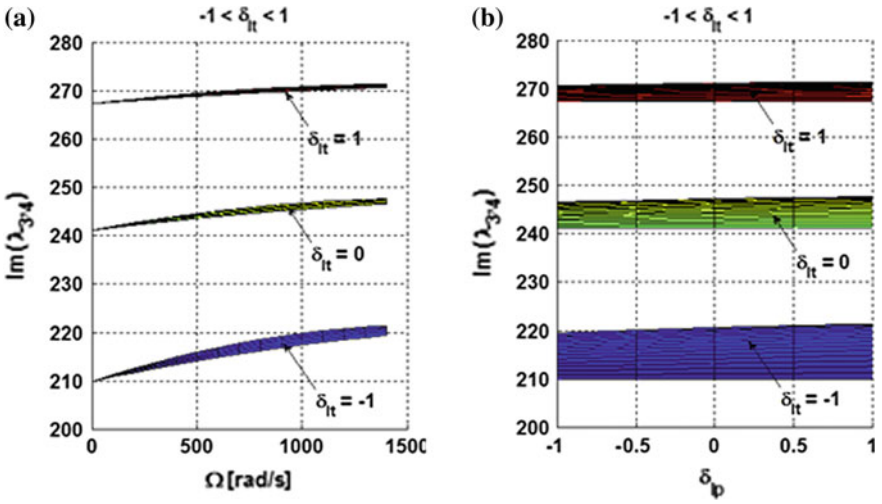

Fig. 10 Eigenfrequencies of $\Im(\lambda_{3,4}) = f\left(\delta_{I_T}|_{-1,0,1}, \delta_{I_P}, \Omega\right)$ relative to Campbell diagram

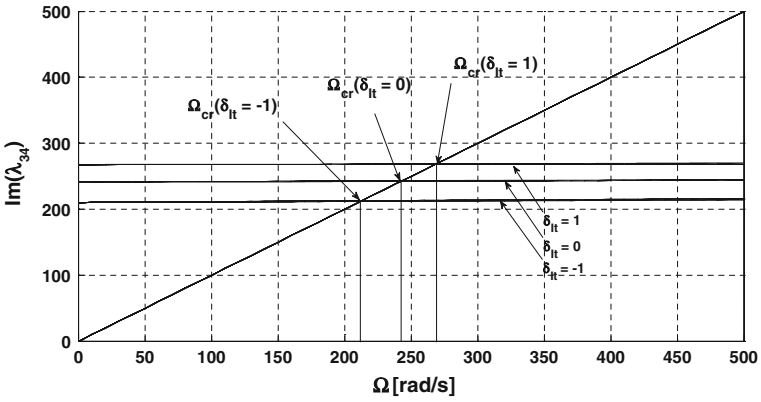

Fig. 11 Intersection of $\Im(\lambda_{3,4}) = f\left(\delta_{I_T}|_{-1,0,1}, \delta_{I_P}, \Omega\right)$ with a plane of 45°

Figure 13 shows that the eigenfrequencies increased by an increasing of δ_{I_T} more fast than an increasing of δ_{I_P}, by maintaining constant the angular speed. The values of the critical speeds are distributed on (δ_{I_T}, Ω) plane and they increase by increasing of δ_{I_T} along an approximated line of second degree.

Figure 14 shows the variation of the eigenvalues $\Im(\lambda_{1,2}) = f(\delta_m, \Omega)$ which is sketched in both Figs. 9a and b. In that same figure we see that the eigenfrequencies decrease by increasing of δ_m, on the contrary the critical speed decreases.

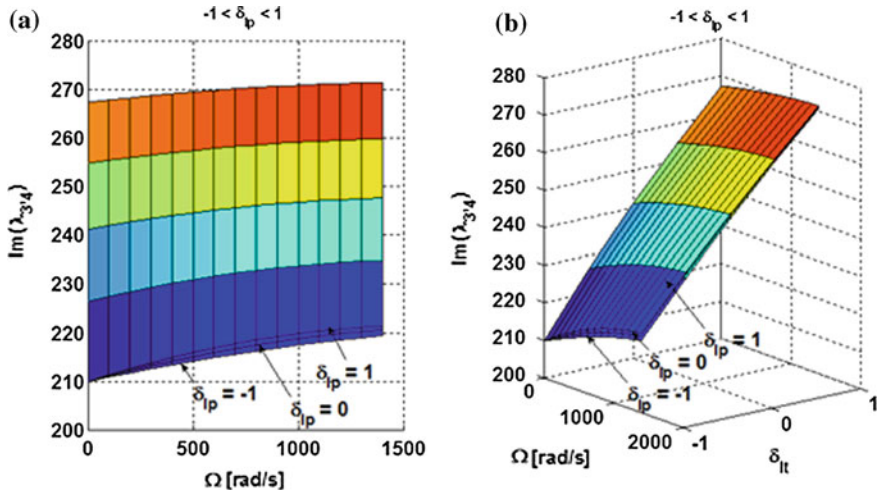

Fig. 12 Eigenfrequencies belonging to of $\Im(\lambda_{3,4})$ relative to Campbell diagram

Fig. 13 Intersection of $\Im(\lambda_{3,4})$ surfaces with a plane of 45°

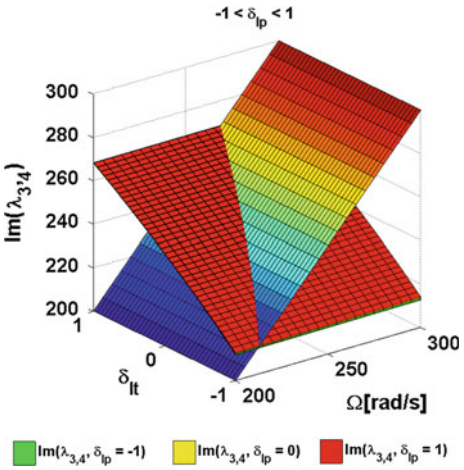

5 Simulations for Rotary Motion

In order to simulate the stabilized system we choose the data shown in the Table 1

We see that the transfer function matrix is symmetric, so that we have studied only one element of the entire transfer function matrix. Moreover there is no cancellation between poles and zeros on each transfer function which characterizes the system so we have realized that the system is on internal and external asymptotically stable. To give more information about the reached stability we have shown the distribution of the poles and zeros of $W_{11}(s, \Delta_M, \Delta_G)$ as in the Fig. 15;

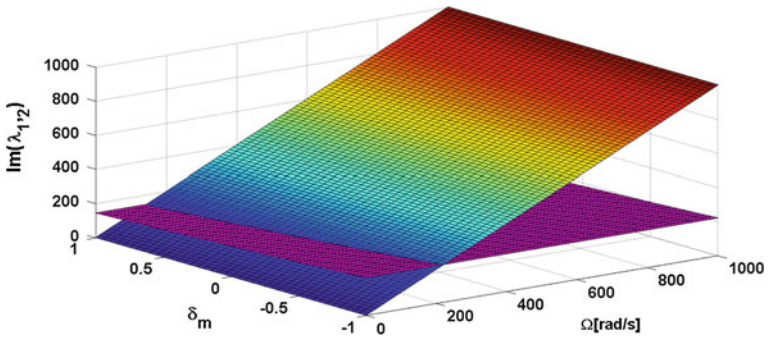

Fig. 14 Intersection of $\Im(\lambda_{1,2})$ surface with a plane of 45°

Table 1 Data for simulation of active magnetic suspended rotor

Name	Symbol	Value
Mass of the rotor	m	1.35 *kg*
Cross moment of inertia	I_T	0.00722 *kg* m^2
Polar moment of inertia	I_P	0.000406 *kg* m^2
Current gain	k_i	38 *N/A*
Displacement gain	k_x	14,4000 *N/m*
Proportional gain	k_p	5,400 *A/m*
Derivative gain	k_d	$1 \div 5$ *A s/m*

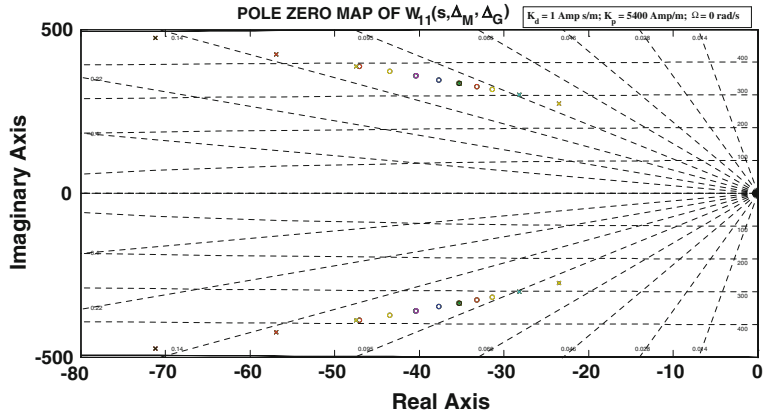

Fig. 15 Distribution of poles and zeros of $W_{11}(s, \Delta_M, \Delta_G)$ in the complex plane

As we can see from the Fig. 15 the system is stabilized according with the data shown in the upper right corner of the same figure. This stability is compromised when the angular speed increases until the value of $\Omega = 2{,}000$ *rad/s* as Fig. 16 shows as a confirmation of the Fig. 6a:

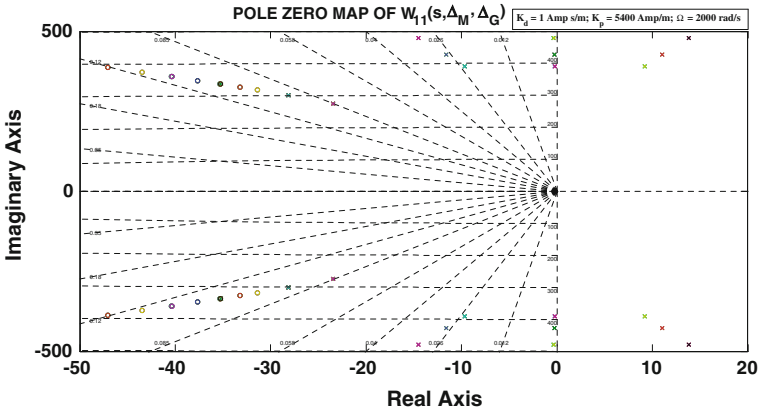

Fig. 16 Distribution of poles and zeros of $W_{11}(s, \Delta_M, \Delta_G)$ in the complex plane

In order to recover the stability condition of the system we increase the derivative gain $k_d = 5\ A\ s/m$ according to the Fig. 6b whose poles-zeros map I shown on the Fig. 17. In order to perform the simulations we calculate the impulse response of the state space equations of the controlled system shown in (15)

$$\begin{cases} \left\{ s^2 M_j + s\left[j\Omega G_j + K_{I_j} K_{D_j} \right] + \left[K_{I_j} K_{P_j} - K_{X_j} \right] \right\} r_b(s) = \left[\delta(t)|_{t=0} \quad 0 \right]^T \\ \dot{r}_b(t)|_{t=0^-} = 0^{2\times 1} \\ r_b(t)|_{t=0^-} = 0^{2\times 1} \end{cases} \tag{15}$$

According to Dirac's impulse located in the origin of temporal frame, we calculate the output displacements of the two section stabilized by PD controller tuned as a function of uncertainties $(\delta_m, \delta_{I_P}, \delta_{I_T})$. Due to the symmetry of the

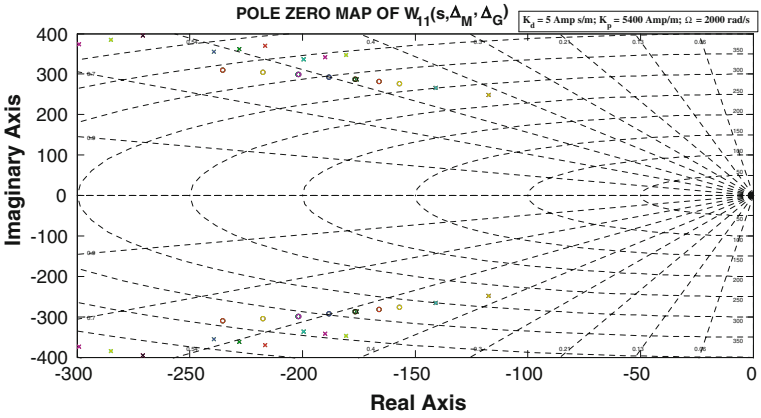

Fig. 17 Distribution of poles and zeros of $W_{11}(s, \Delta_M, \Delta_G)$ in the complex plane

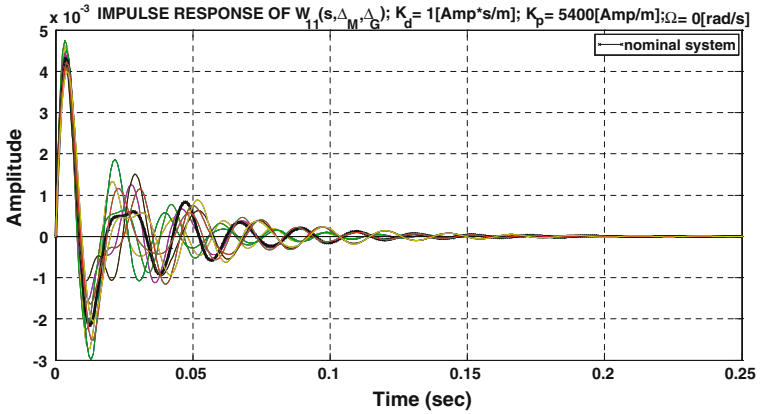

Fig. 18 Impulse response varying the permutation of the uncertainties

system only one output is shown on each simulation according (16) once known the state vector $x(t) = |\, r_b(t) \quad \dot{r}_b(t)\,|^T$.(Barbaraci et al. 2010)

$$y(t) = \left| \left(B_{\Theta disp} B_{sensor}\right) \left(B_{\Theta disp} B_{mag}^T\right)^{-1} \quad 0 \right| x(t). \tag{16}$$

The simulations were performed with the same conditions expressed by poles-zeros map distribution in terms of k_d, k_p and Ω (see Figs. 15, 16 and 17) as Figs. 18, 19 and 20 show.

Previous figures show the recovering of stability condition according to the information provided by Fig. 6. The uncertainties affect the dynamic behavior in terms of time response and settling time which values are different from those produced by nominal plant. Figure 18 shows the system is subjected to a periodic

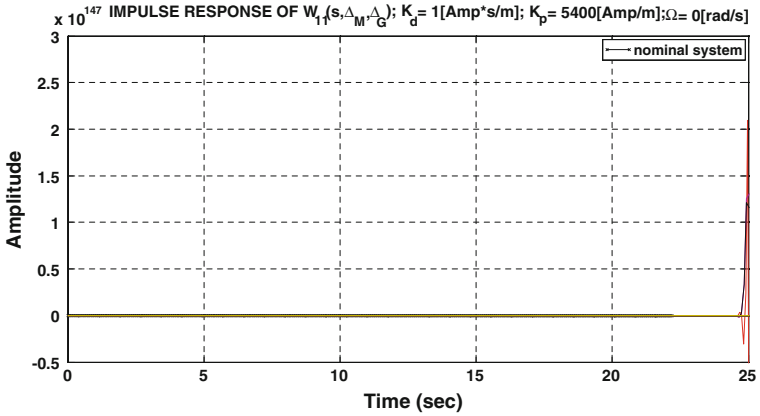

Fig. 19 Impulse response varying the permutation of the uncertainties

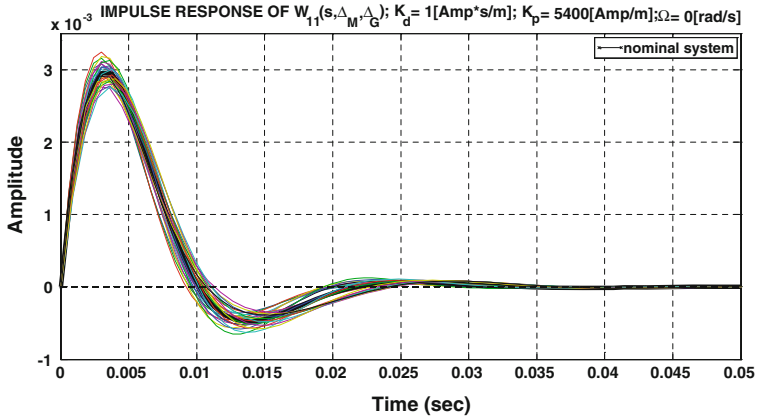

Fig. 20 Impulse response varying the permutation of the uncertainties

oscillation during the transient response which frequency is different according the permutation of the uncertainties. In the Fig. 19 the instability is due to the increasing of the angular speed since characterizes the real part of the eigenvalues $\lambda_{3,4}$. Figure 20 shows the effect of an increasing of the derivative gain which produces an increasing of the dumping effect in such way to recover the negative sign lost by the increasing of angular speed. The increasing of derivative gain leads the system to recover the stability condition. This last is characterized by a periodic oscillation also characterized by different values of rise time and settling time according to different trajectory of the response during the time.

6 Conclusion

A technique for PD tuning is introduced by considering the uncertainties on the physical properties of a rotating shaft magnetically suspended by active magnetic bearings. The uncertainties are introduced to model the apparent exogenous excitation in terms of centrifugal force produced by an unknown value of centripetal acceleration. The influence of uncertainties is revealed by stabilizing the position of the rotor. This is made by moving the real part of eigenvalues obtained by state space form of differential equation describing the lateral motion of the rotor. The influence of uncertainties is also shown in the Campbell diagram from where different values of critical speed were carried out according the state of the uncertainties relative to the physical parameter of the rotor. The negative real part of eigenvalues is obtained by choosing the value of the uncertainty from where depends the value of the current and stiffness gain in order to achieve the asymptotically stability condition of the suspended sections. The study of the real part of eigenvalues reveals the relation between the gyroscopic effect and the stability of the rotor magnetically suspended.

References

Barbaraci G, Virzì Mariotti G (2009) Controllo Sub-ottimo per un Albero Rotante in Levitazione Magnetica Attiva, XXXVIII Convegno nazionale AIAS, 9–11 Settembre, Torino

Barbaraci G, Pesch AH, Sawicki JT (2010) Experimental investigation of minimum power consumption optimal control for variable speed AMB rotor. In Proceedings of the ASME 2010 International Mechanical Engineering Congress & Exposition IMECE2010 (pp 1–10). Vancouver, British Columbia

Bugajski D, Enns D, Tannenbaum A (1993) Synthesis methods for robust nonlinear control, American Control Conference, pp 531–535

Genta G (2005) Dynamics of Rotating Systems, Mechanical Engineering Series. Springer editions, Torino

Knospe CR, Fittro RL (1997) Control of a High Speed Machining Spindle via μ-Synthesis, Proceedings of the 1997 IEEE International Conference on Control Applications, Hartford

Schweitzer G, Maslen EH (2009) Magnetic Bearings: Theory, Design and Application to Rotating Machinery. Springer, Zurich

Schweitzer G, Bleuler H, Traxler A (2003) Active magnetic bearings—basics, properties and applications. vdf Hochschulverlag AG, ETH Zürich, 1994 (sold out). Author's Reprint, Zurich

Wu JD, Lin JH (2005) Implementation of an active vibration controller for gear-set shaft using μ-analysis. J Sound Vib 281:1037–1055

Zhoa L, Zhang K, Zhu R, Zhao H (2002), Experimental research on a momentum wheel suspended by active magnetic bearings, Proceedings of the 8th ISMB, Mito

Comparative Experimental Study on Noise and Vibration Level of Gearbox with Worm Face-Gear with Reverse Tapered Pinion

Bogdan Bucur and Vasile Boloş

Abstract This paper presents some comparative aspects obtained on an experimental basis, on the determination of noise and vibration level in the operation of a gearbox with worm face-gear with reverse tapered pinion for a pair materials of steel-bronze, steel-gray cast iron and steel-polyamides, oil lubricated T90EP2, with 1:47 transmission ratio. The worm face-gear with reverse tapered is less known and attempts should be carried out to reveal how they conduct the operation and how performance is achieved.In the experiments we used an Archimedes worm with nitrided steel sides finished by fine turning. The conjugate tooth of wheels was obtained by hob-cutter milling. The noise and vibration level measurements were made on a scale of 10 levels in the range 0–115.77 Nm on a bench equipped with electromagnetic powder brake, separate flank the 10° and then 30° for each couple of material. Gearbox which has the gear structure is made of cast iron casing.

Keywords Gearbox · Worm-face gear · Reverse tapered · Vibration · Noise

List of Symbols

A	Axial distance
i	Transmission ratio
m	Module
α_1	Bearing flank
α_2	Support flank
δ_1	Tapered worm
δ_2	Tapered worm wheel
Ra	Roughness

B. Bucur (✉) · V. Boloş
Petru Maior University of Tîrgu-Mureş, Tîrgu-Mureş, România
e-mail: bbogdan@upm.ro

V. Boloş
e-mail: vbolos@upm.ro

G. Dobre (ed.), *Power Transmissions*,
Mechanisms and Machine Science 13, DOI: 10.1007/978-94-007-6558-0_16,

E Modulus of elasticity
σ_r Normal stress
HB Brinell Hardness.

1 Introduction

The family of worm-face gears also includes the worm-face gear with reverse tapered pinion. Patented by A.K. Georgiev (Georgiev 1966) this worm gear is composed of a tapered pinion, which engages with a wheel gear having a conical surface on its inner side. This type of gears has some functional advantages such as: high contact ratio, about 10–12 % of the number of teeth in gear wheel being simultaneously engaged with the surfaces of the worm drive screw, good lubrication conditions due to the relative speed vector position to the contact line of teeth.

These elements represent premises of a good load bearing capacity in conditions of reduced size, respectively of a low noise operation.

Added to all these advantages is the fact that in contrast to conventional worm gear the worm wheel can be made also of hard materials (heat-treated steel), thus the conditions of a correct hydrodynamics are fulfilled.

The specialized literature makes few references to the gears even though they may be used, in good conditions, for equipping speed reducers, which can function well under difficult operating conditions.

In the papers: Abadjiev (2009), Bodzas and Dudas (2010), Kuznetzov et al. (2007), Mudrik and Rieciciarova (2008), Popova and Goldfarb (2006), Popova (2007), Rieciciarova (2007), Rieciciarova and Duris (2010), Trubachev and Kuniver (2007), www.mechanik.udmnet.ru (2009), are presented some results obtained in the experimental testing of worm face-gears with normal tapered execution of the combination steel/steel that steel/plastic in the thermal limits and performance. In these papers are given and details of construction of test stands used.

In this paper we present comparative experimental results obtained from testing three speed reducers equipped with this type of gear in three different combinations of materials: hardened steel/bronze, hardened steel/cast iron, hardened steel/polyamide (Fig. 1), Bucur and Bolos (2011b).

The study of scientific literature carried out showed clearly that there are no experiment showing the results regarding the behavior of worm face-gears with reverse tapered pinion. Thus, the results presented below cannot be reported for other research.

The entire field regarding reverse tapered worms has been studied and researced to a little extent.

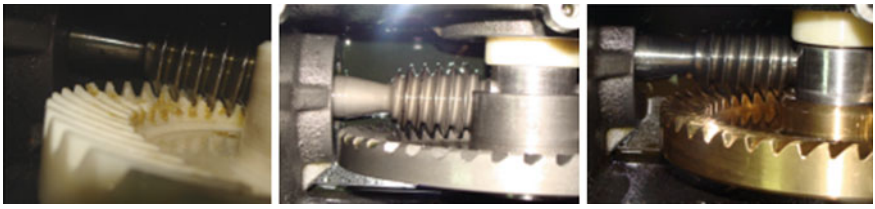

Fig. 1 Worm face-gear with reverse tapered pinion

2 Construction of the Gearboxes and the Experimental Stand

The gearboxes that have been tested include in their structure a worm gear with reverse tapered having the following geometric characteristics: A = 58 mm axial distance, transmission ratio i = 1:47, m = 2.5 mm module, bearing flank angle α_1 = 10°, support flank angle α_2 = 30°, tapered worm $\delta_1 = -5°$, tapered worm wheel $\delta_2 = -8°$.

The gearbox construction (Fig. 2) is detailed in Bolos et al. (2005) and the experimental stand is presented in Bucur and Bolos (2011a). For the lubricating of the gearbox using T90EP2 oil, quality features to STAS 8960-85. The casing of gearbox is made of cast iron casting, constructive solution recommended for good damping properties of shock and vibration.

The bearings supporting of the worm and the shaft of worm wheel, using radial-axial ball bearings.

The tapered worm (Fig. 3) of Archimedes type is made of alloy steel 41MoCr11 SR EN 10084-2008 hardened by nitriding at 960HV (Fig. 4), with the

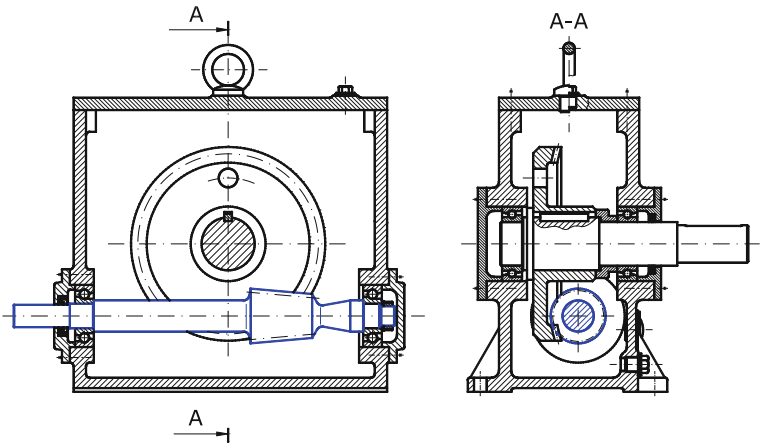

Fig. 2 The gearbox for testing

Fig. 3 Tapered worm (pinion)

Fig. 4 Worm hardness measurement

flank roughness of Ra = 6.3 μm. According to the GOST 22850-77, the worm type corresponds to SOA.

Reverse tapered worm wheel (Fig. 5) was made by gear hobbing with hob worm-thread milling cutter, on the gear cutting machine FD 500 type UM Cugir, by using the method of axial advance (Fig. 6).

For the experimental comparative study three types of materials have been used. Table 1 shows their main mechanical characteristics.

3 Experiment Implementation

Reducers tested were mounted on the support stand being subjected to identical experimental tests. Resistant torque control was performed with an electromagnetic brake type with powder FRAT 3500 in 10 successive steps of loading (about 15 min to stabilize the temperature for each step), following a series of values series specific to the numbers R10a.

Fig. 5 The worm wheel with reverse tapered

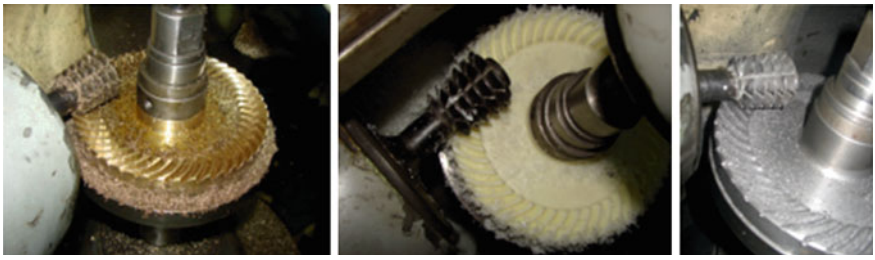

Fig. 6 Toothing of worm wheel

Table 1 The mechanical characteristics of worms wheel's material

Material type	E [N/mm^2]	σ_r [N/mm^2]	[HB]
Polyamide (Ertacetal C)	3,100	68	140
Cast iron (EN – GJS – HB250)	1.15–1.6 × 10^5	210–250	200
Bronze (CuSn12)	1.15 × 10^5	300–450	95

Electromagnetic powder brake, type FRAT 3500 allows for adjustment when loading and displaying the output shaft of the gearbox. Depending on the current can amount to precision torque output shaft of gear, with standard diagram. Electromagnetic brake adjustment is performed by potentiometer on the control panel, the control panel mounted on the chassis, through changes induced in current amperage.

Determining the level of vibration was performed with a digital type vibrometer VIB-10/VIB-11, whose capture piezo-electric sensor was fixed to the gearbox carcass (Fig. 7a) and for determining the noise level it was used an sound level meter, Voltcraft SL-50 digital type, placed at the distance of 0.5 m from the gearbox (Fig. 7b).

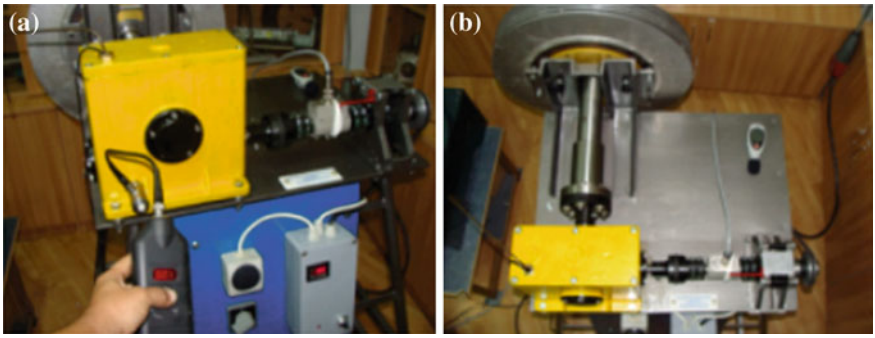

Fig. 7 The experimental stand

4 Experimental Data Results

The experiment has taken into account that the worm load bearing flanks have different values so that the tests were done for each gear in both directions of engagement (one direction bearing 10° engaging the other bearing 30°).

Tables 2 and 3 shows the average measured values corresponding to each load increase.

The measured average values of noise levels are graphically compared (Figs. 8 and 9) for the three types of gears.

The vibration level, compared to the three types of gear, shown in Figs. 10 and 11, duly bearing engagement with the flank 10° and 30°.

Table 2 The experimental data, noise level

Load increase [Nm]	Noise level [dB]					
	Hardened steel/ polyamide		Hardened steel/cast iron		Hardened steel/bronze	
	Flank 10°	Flank 30°	Flank 10°	Flank 30°	Flank 10°	Flank 30°
0.00	78.90	80.10	74.30	86.05	77.60	80.10
7.70	78.25	81.00	75.80	84.82	77.85	81.00
9.73	80.45	79.55	76.32	84.77	78.70	79.55
14.07	85.25	78.10	75.88	84.20	78.68	78.10
19.09	82.30	77.20	76.45	84.75	78.85	77.20
23.36	79.85	76.40	76.70	85.87	78.10	76.40
34.88	81.95	76.75	78.03	86.90	77.78	76.75
56.25	79.10	78.18	80.25	87.90	78.88	78.18
83.82	80.42	79.15	79.15	88.61	81.45	79.15
115.77	81.13	78.10	78.58	87.87	82.33	78.10

Table 3 The experimental data, vibration level

Load increase [Nm]	Vibration level [mm/s]					
	Hardened steel/ polyamide		Hardened steel/cast iron		Hardened steel/bronze	
	Flank 10°	Flank 30°	Flank 10°	Flank 30°	Flank 10°	Flank 30°
0.00	1.55	1.50	1.60	3.25	1.65	1.50
7.70	1.50	1.55	1.75	2.95	1.70	1.80
9.73	1.62	1.40	1.75	3.95	1.75	1.45
14.07	1.65	1.38	1.70	4.05	1.80	1.40
19.09	1.65	1.20	1.65	3.55	1.80	1.25
23.36	1.66	1.22	1.85	3.20	1.80	1.25
34.88	1.68	1.25	1.95	3.10	1.80	1.30
56.25	1.85	1.25	2.15	3.25	2.00	1.30
83.82	1.90	1.48	2.00	3.00	2.00	1.55
115.77	1.95	1.50	1.75	3.75	2.10	1.50

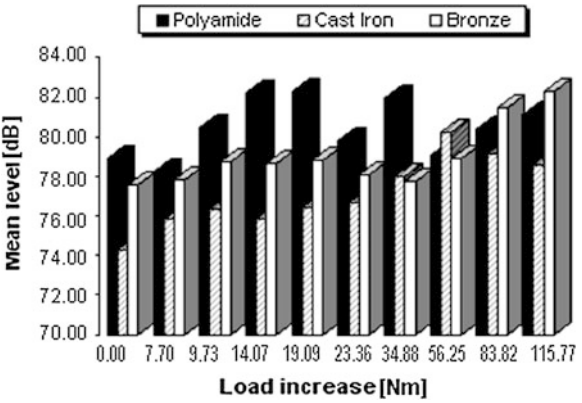

Fig. 8 Graphical comparison of noise level, flank 10°

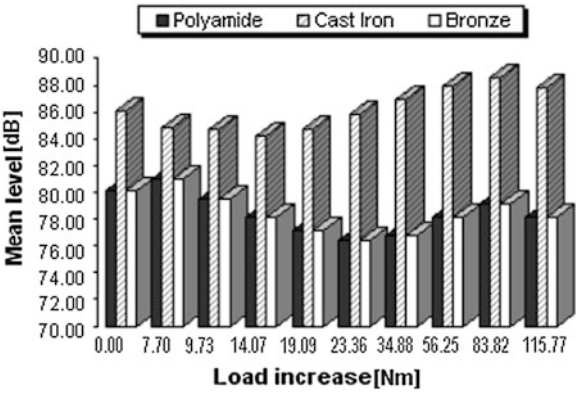

Fig. 9 Graphical comparison of noise level, flank 30°

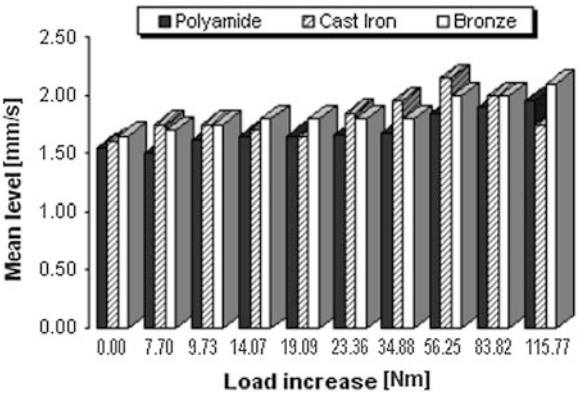

Fig. 10 Graphical comparison of vibration level, flank 10°

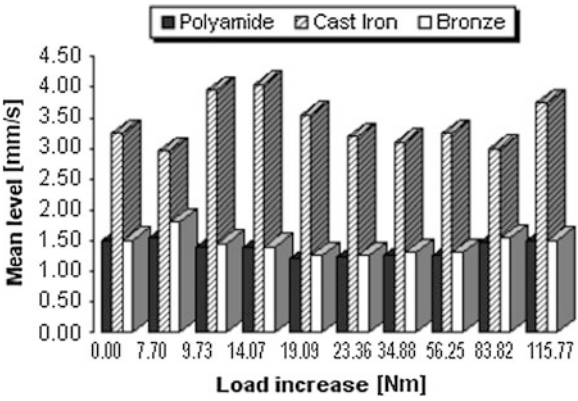

Fig. 11 Graphical comparison of vibration level, flank 30°

5 Conclusions

Following the experiment several important conclusions can be drawn:

- the gearbox equipped with worm face-gear with reverse tapered pinion is comparable to the normal operation of reduction gears for general use;
- the gearbox that uses steel-polyamide, has a high degree of quietness compared to other types of gears;
- reducers with use different combinations of materials: steel-cast iron and steel-bronze, have a certain behavior in terms of noise, vibrations respectively, which is approximately identical;
- to obtain highly reliable results, in terms of noise and vibration level, the experiment needs to be repeated with a larger lot of gears in each category, to exclude the effect of accidental parameters;
- it is also required achievement of an experiment that uses steel–steel material couple which allegedly has a much enlarged lift and noise levels higher steel-iron combinations, steel-bronze and steel- polyamide;

- the costs of implementing the worm face-gear with reverse tapered pinion are substantially higher than the general purpose worm gear.

References

Abadjiev V (2009) Synthesis design and manufacture of high reduction hyperboloid gears: brief review of researches institute of mechanics—BAS, international conference general machine design, 15–16 Oct 2009, University of Ruse, pp 25–29

Bodzas S, Dudas I (2010) Modern quality assurance of spiroid worm. In: Proceeding of factory automation 2010 15–16 April 2010 Kecskemet, Hungary, pp 139–144

Boloş, V, Boloş C, Bucur B (2005). Gearbox with reversed tapered spiroid gearsets, interdisciplinarity in engineering. In: Proceedings of the scientific conference with international participation "inter-Ing 2005", ISBN 973-8084-81-4, Tg Mures, 6–7 Nov 2005, vol I. Petru Maior University of Tg-Mureş, Romania, pp 59–66

Bucur B, Boloş V (2011a) Experimental study of the thermal limit for the gearbox worm face-gear with reverse tapered pinion. In: Gyenge CS (ed) Proceeding of the 9th international conference MTeM 2011, Technical University, ISBN 978-606-8372-02-0, Cluj-Napoca, Oct 2011, Cluj-Napoca, Romania, pp 53–56

Bucur B, Boloş V (2011b). Experimental research on noise and vibration level of gearbox using worm face-gear with reverse tapered pinion, Scientific Bulloetin of the Petru Maior University of Tirgu-Mures, vol 8 (XXV) no.2, 2011, Romania, pp 147–150

Georgiev AK (1966) Ortogonal worm-bevel gearing. Brevet SUA, nr. 3289489

Gost XXX 22850-77 Peredach spiroideniie-Termini, Opredelenia i Oboznachenia

Kuznetzov AS, Treteakova MS, Domnin NN (2007) Issledovanie staticheskoi prochnosti zatzepleaiuschihsia spiroidnoi o peredach reductora ZRA. Vestnik Ijevskovo gosudartsveno tehnichskovo universiteta 33(1):135–138

Mehanik Nauchno-proivodstvenoe Predpriatie, Katalog productzii, Privodi truboprovodnoi armaturi. www.mechanik.udmnet.ru 2009

Mudrik J, Rieciciarova E (2008) Load application of the spiroid gears using dynamic dynanomater, ADEKO, Faculty of technical science Novi Sad, 18 May 2008, 48th anniversary of the faculty, pp 83–86

Popova EI (2007) Nagruzochnaia sposobnosti peredach s metalloplastmassovimi kolesami, Vestnik Ijevskovo gosudartsveno tehnichskovo universiteta, vol 33, No.1, 2007, pp 154–156

Popova EI, Goldfarb VI (2006) Investigation of spiroid gears with plastic gearwheels. J Mech Eng Des 9(1):38–43

Rieciciarova E (2007) Contribution to influence loading of efficiency and operation temperature of spiroid gears, J Eng Ann Faculty Eng Hunedoara, Tome V (year 2007), fascicole 2, pp 185–188

Rieciciarova E, Duris E (2010) Dynamic measurement over-all efficiency of spiroid gears, 7th international DAAAM Baltic conference "industrial engineering" 22–24 April 2010. Tallin, Estonia

Trubachev ES, Kuniver AS (2007) Ispitania malogabaritnih spiroidnih reductorov. Vestnik Ijevskovo gosudartsveno tehnichskovo universiteta 33(1):175–179

CAD/CAE Approach of the Strain and Stress Static Analysis for Spur Gear Pairs

Sorin Cananau and George Dobre

Abstract In the last years there is an increasing demand for the efficiency, compact size, low noise level and reliability of gear transmission. This imposed that gear designers use adequate software for design and verify the product development. The paper aims to evaluate the use of different software for design and test the spur gear transmissions. An algorithm from the concept and geometric profiles of the teeth and linked parts to the models obtained using Finite Element Analysis (FEA) which aims to test and verify the comportment of the involved structures in the meshing process is presented. The paper aims also to demonstrate that ISO or other standards cannot conduct a reliable analysis of the root tooth bending and teeth contact stress. The proposed algorithm shows that o lot of software can be used but also the necessity to generate specific codes to interlink the steps in the algorithm. Also the paper put in discussion the use of 2D and 3D models in the transmission design process. One feature of the algorithm is the necessity of the 3D model in the process. The use of FEM as a numerical method to evaluate the behavior under static load conditions is also one of the necessity in the modern conditions of product development and the paper aimed to demonstrate that feature. Finally the presented FEM software shows a complete suitability for the calculation of spur gears transmission and not only.

Keywords Spur gears · FEA static analysis · Strain · Stress

S. Cananau (✉) · G. Dobre
University Politehnica of Bucharest, Bucharest, Romania
e-mail: s_cananau@yahoo.com

G. Dobre
e-mail: G.Dobre@gmail.com

G. Dobre (ed.), *Power Transmissions*,
Mechanisms and Machine Science 13, DOI: 10.1007/978-94-007-6558-0_17,

1 Introduction

The increasing demand for power transmission with a uniform functioning, a low level of vibrations and noise of different technical systems leaded to a more precise analysis of the characteristics of gear systems incorporated in these systems. The demands of the industry conduct to a rapidly growing field of office-automation; usually equipment is marked by the demand of noise reduction of incorporated gear pairs that affect in an important way environment. The last environment legislation in the UE and other important industrial countries shows the significance of improving the power efficiency and reduction of noise level in gear transmission systems.

The activity of designing highly loaded spur gears for power transmission systems is a difficult task in order to produce in the same time a reliable mechanical product and a system with a low noise level; this activity requires methods that are to be implemented and also to provide information on the two important stress: bending stress and contact strain and stress in the meshing process but also information concerning the torque influence on the structure shift-gear elasticity, information concerning transmission errors and others. The structural integrity of high speed reduction gear systems requires a proper assessment of the tooth contact and fillet stresses. In calculating these stresses, it is important to consider gears as "structures" rather than as pairs of teeth in mesh. Therefore in this paper we will consider a structure composed from teeth with a defined profile and the part of the gear corresponding to the shaft or the rim of the wheel gear.

Another important problem regards the results of the strain and stress analysis as consequence of the 2D or 3D involved models.

Early studies concern stress and deformation on gears (Tobe et al. 1973) but also mathematical programming methods for design of elastic bodies in contact was developed (Conry and Serireg 1971; Baronet and Tordion 1973). Very soon solutions which takes into account integrated elastic deformation of loaded teeth are developed (Li and Zhao 1984). The design of gears using Loaded Tooth Contact Analysis (LTCA) as a modern method was first developed by Litvin (Litvin et al. 1996). 2D and 3D mathematical models developed for solving with FEM tools as numerical method are presented in many papers (Brauer 2004). This method became one of the most important tool used for static and dynamic analysis of spur (and helical) gears.

In the same time many contributions based on experimental studies on tooth surface contact strength and root bending strength were developed (Rademacher 1967; Niemann and Reister 1966). Kalkert (1963), Feltkamp and Rademacher (1968), Umezawa (1972), Cananau (1999) also investigated static behavior and the effects of gear machining errors on tooth contact for spur and helical gears by experiments. Thus, the analytical solution for the bending deformation of loaded

tooth is rarely reported recently. But in most cases, the pre-processing and computing is very time-consuming, and it is hard to find a suitable analytical solution for comparison. So, a high-precision analytical solution on bending deformation of loaded tooth is still of great significance.

The paper tries to emphasize the importance of the 3D model in some analysis as the hertz contact between teeth in mesh. Also, the paper will show the importance in gathering information of numerical methods in the analysis of static behavior of gears in mesh. The finite element method is capable of providing this information, but the preprocessing, processing and postprocessing activities time needed to create such a model is large. In order to reduce the modeling time, a preprocessor method that creates the geometry with optimal design is needed for a next finite element. As new contributions, the paper finds if a certain algorithm of tasks (modeling and analysis) is suitable for spur meshing gears analysis. The root bending stress and surface contact stress are important parts in any standard for calculation of load capacity for mechanical transmissions with gears. The ISO standard 6336 standard give analytical expressions to calculate the load capacity. The factors involved in these relations, as application factor, face load and transverse load factors, dynamic factor, are introduced to consider different effects on the experience and experimental results.

To get the correct values of these factors is very difficult and the standards cannot precisely calculate the root bending stress and contact stress. In our case we discuss of specific standard. The paper proposes a suitable algorithm for CAD and CAE activities and an sample list of software for the development of gears design. In the same time, the paper introduces the idea of a necessity for a code based on mathematical and numerical model in order to obtain results regarding the surface contact stress. Only with a method and an algorithm which combine FEA commercial codes and specific written codes a designer could obtain a precise analysis for the behavior of a gear transmission under load, in static conditions. In Fig. 1 we synthesize this algorithm.

2 Gear 2D Structure

2.1 Gear 2D Structure and Substructures

A gear wheel is carried out from linked substructures (teeth with defined profile) which have identical geometry and material properties and are connected to each other in the circumferential direction. A gear wheel is considered a rotationally periodic structure.

According to this concept, each tooth will have an identical behavior on the same load applied (load applied in the same conditions, on the same line contact along the width of the tooth).

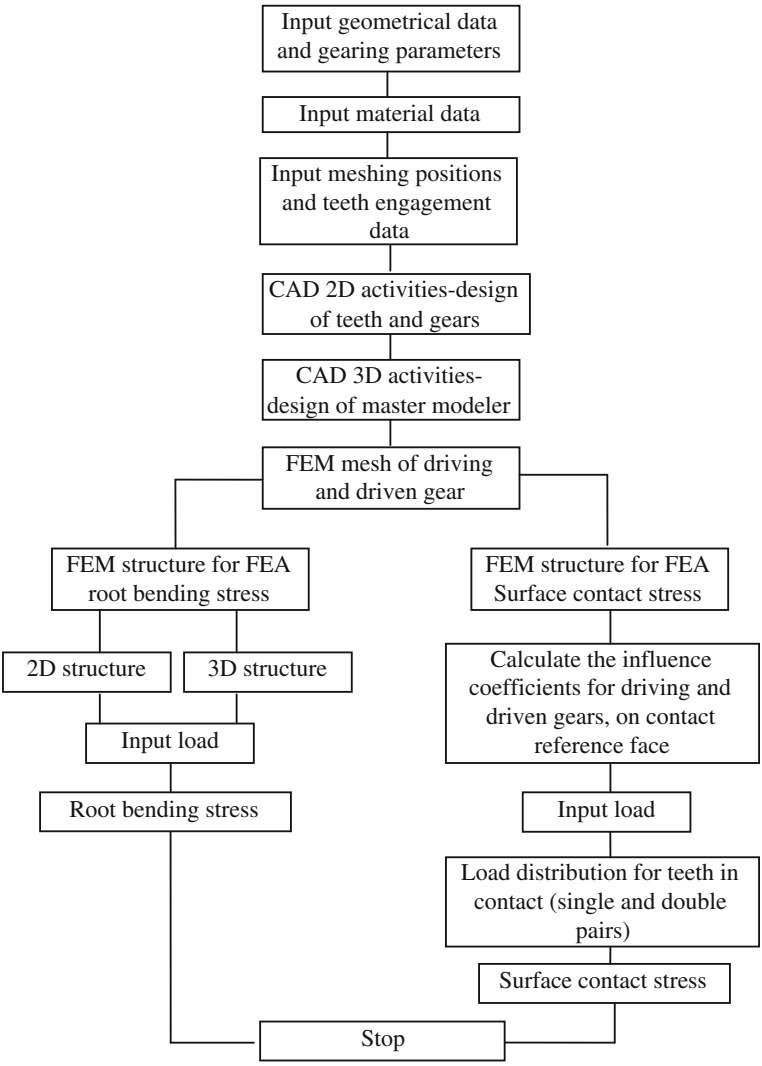

Fig. 1 Flowchart of the gear CAD/CAE design activities

2.2 Parametric Description

In terms of computational geometry gear tooth surface is an involute surface. Into a left-handed Cartesian Coordinates system X_0 Y_0 Z_0 it can be analytically described in terms of Gaussian parameters θ and ψ (Radzevich 2002):

$$r_0(\theta, \Psi) = \begin{bmatrix} r_{b,0} \sin\theta - \Psi \cos\theta \\ r_{b,0} \cos\theta - \Psi \sin\theta \\ p \cdot \theta \\ 1 \end{bmatrix}, \quad (1)$$

in which: $r_{b,0}$ is the gear base radius; p—a screw parameter of the gear tooth functional surface. This is the base for the gear tooth surface machined by generation with an auxiliary rack. For the spur gear there is a logical simplification. The generation of the profile was divided in three parts: the addendum part, the involute part and the fillet tooth generated by the rack cutter (gear hob). The parameters for the CAD model of the gear pairs are given in Table 1.

The generation of the surface of an involute gear hob is determined pursuant to the use of a routine written in Matlab cod. The functions of the profile modeling for addendum of the tooth (Fig. 2a), left involute profile, (Fig. 2b), the right profile of the tooth. (Fig. 3a) and fillet of the tooth profile (Fig. 3b) are represented.

Figure 4a, b give the CAD structure for the gear wheel and, respectively, one of its sector considered in the present analysis.

2.3 3D Geometric Model

The activity of designing highly loaded spur gears for power transmission systems that are in the same time a reliable mechanical and a low noise level products requires analysis methods that can easily be implemented and also provide information on surface contact and bending stresses, along with transmission errors. The finite element method is capable of providing this information, but the preprocessing, processing and postprocessing activity time needed to create such a model is large. In order to reduce the modeling time, a preprocessor method that creates the geometry needed for a finite element analysis may be used. There are many CAD software such as that provided by DSS SolidWorks, DSS CATIA, ProEngineering, Autodesk INVENTOR etalt. Some of these software can generate models of three-dimensional gears easily. But the problem is to have a strong CAD

Table 1 Parameters of the CAD gear model

Parameters	Units	Data
Number of teeth, z_1/z_2	–	21/31
Center distance, a	mm	130
Pressure angle, α_0	deg	20
Module, m	mm	5
Diametral pitch, p_e	mm	15.7079
Working face width, b	mm	40
Elasticity modulus, E	N/mm^2	$2.07 \cdot 10^5$
Poisson's ratio, v	–	0.32

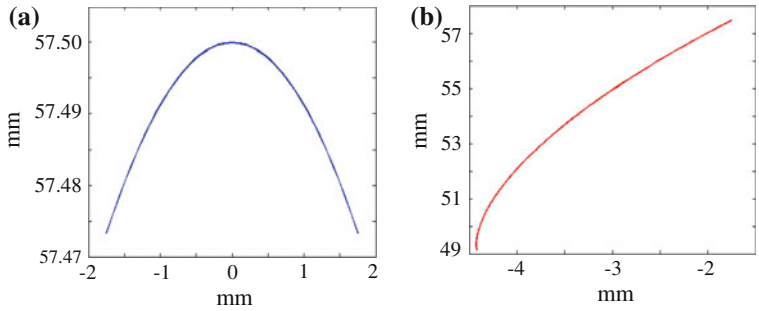

Fig. 2 Tooth profile generation. **a** Addendum profile. **b** Left involute profile

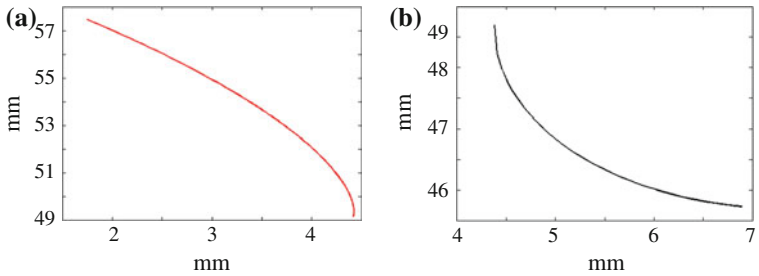

Fig. 3 Tooth profile generation, **a** Right involute profile. **b** Fillet of the tooth profile

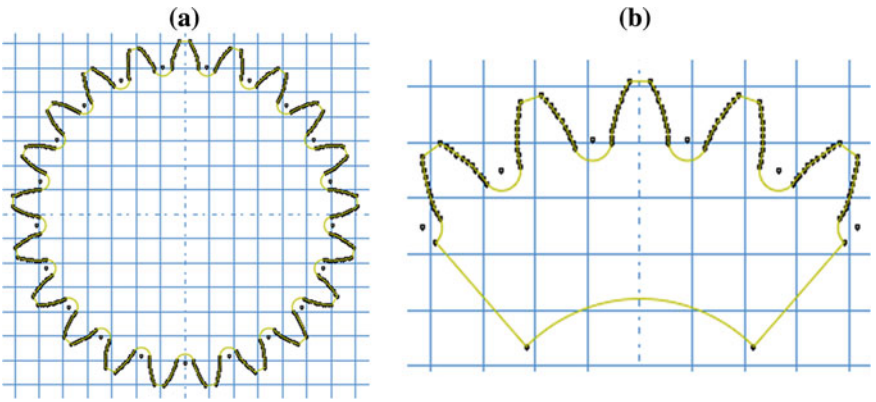

Fig. 4 2D gear structures of the entire spur gear wheel (**a**) and a of a sector used in the paper analysis (**b**)

description in order to submit this model to a Finite Element Analysis. Some of this software has own codes for FEM. In other situations is preferred the solution of transferring the CAD model to a very strong cod FEM.

The algorithm depends on the analysis needs, the experience of the team and, not at least, software and hardware possibilities of the working team. An algorithm which use the SolidWorks (for CAD model) and ABAQUS (for FEM analysis) software could be described in few words: in SolidWorks, the geometry is saved as a file and then it can be transferred from SolidWorks to ABAQUS. In the new software one can click File > Import > IGES > and check No disfeaturing and Merge coincident key points. After that the mesh is generated in accordance with the analysis purpose, the tests for evaluating the convergence of the solution with different mesh and the analysis process and post process.

For a suitable analysis it is more convenient to use a 3D model in the gear analysis because of tooth height, tooth thickness and tooth face width of a gear in three mutually perpendicular directions are comparable with each other. More than this using a 3D model is the only way to superpose the effects of various loads and stresses in the gear substructure.

In this paper we are going to take into account the effect of the bending stress of a tooth and the effect due to the local contact along meshing line (Hertz contact). In order to consider the effect of adjacent teeth five teeth model was taken into account for the load distribution (the real meshing contact) but in order to magnify the effects here the contact was considered for a single pair teeth.

The 2D model in a IGES structure form for the selected pitch diameter and number of teeth is saved. The profile developed in Matlab code was perform as a gear profile in SolidWorks (Fig. 2) and then was prepared for static stress and deflection analysis in a 3D model as is shown in Fig. 5. The number of contact lines in a parametric way, but also the geometric characteristics of the tooth as standard gear, circular or involute crowned tooth can be set when the process is developed in a 3D model.

The root bending stress, contact compressive stress and gear tooth deflection are calculated with load application at the points located along to five contact lines, uniform distributed along the active involute profile of a tooth. These lines are chosen from the root of the tooth to the upper bound, with a constant distribution.

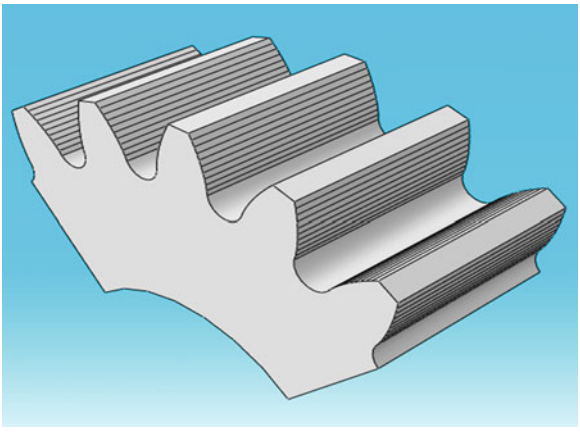

Fig. 5 The generation of 3D gear structure

2.4 FEM Structure

As we stated the most powerful numerical method of determining accurate stress and deflection information is the Finite Element Method. The loads acting on the mating gears will act along the pressure line, which can be resolved into both tangential and radial components using the pressure angle.

The gear tooth contact stresses, tooth bending stresses and gear tooth deflection of single tooth contact of spur gear are analyzed using FEM into a frame of ABAQUS model. A thick full rim with five teeth FE model is used for stress analysis. The finer mesh size is selected to ensure line contact and uniform distribution of load over flank.

The element of the type eight-noded hexahedral is chosen. This is used for the 3D modeling of solid structures. The element is defined by eight nodes having three degrees of freedom at each node, translations in the nodal x, y, and z directions.

The material is assumed to be isotropic and homogeneous. The type of contact was surface to surface. The contact pair consists of a target surface and a contact surface. The contact surface moves into the target surface; nodes at the side portions and the bottom portion of rim of the gear are fixed during gear analysis to avoid misalignment and to localize the load distribution (Fig. 6).

3 ISO Standard for Load Capacity of Spur Gears

The ISO standard 6336-2:2006 (Part2) and 6336-3:2006 (Part3) gives the following expersions for the root bending stress (1) and the surface contact stress (2):

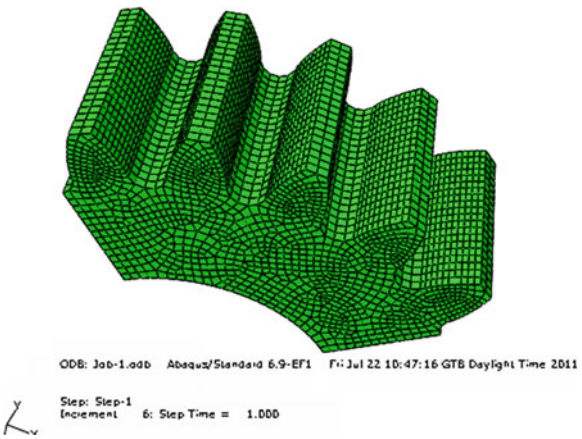

Fig. 6 FEM structure of the gear in ABAQUS model

$$\sigma_F = \frac{F_t}{bm_n} Y_{Fa} Y_{Sa} Y_\varepsilon Y_\beta K_A K_V K_{F\beta} K_{F\alpha}. \quad (2)$$

$$\sigma_H = Z_D Z_H Z_E Z_\varepsilon Z_\beta \sqrt{\frac{F_t}{d_1 b} \frac{U+1}{U}} \sqrt{K_A K_V K_{H\beta} K_{H\alpha}} \quad (3)$$

The Eq. (2) is the formula ISO 6336-3 for root bending stress calculation of the point at 30° angle tangency on the root fillet. The meanings and values of the nomenclature is given in the next table (Table 2).

The Eq. (3) is the formula ISO 6336-2 for surface contact stress for a pair of spur and helical gearswith a contact ratio between $1 < \varepsilon < 2$. In Table 3 are shown the meanings and values of the nomenclature.

4 Results, Comparisons and Discussions

Concerning CAD/CAE approach of the strain and stress static analysis there are some observations: a model of a meshing gears loaded by an equivalent torque will conduct to results which are closer to the real behavior of the structure. That means we have in this model a superposition of the two stresses: bending stress and contact stress. But, if we need to compare separate stresses with ISO standard calculation results, we have to use special techniques to separate the two stresses.

The first stress taken into account is the bending stress. For this analysis we also two investigate two aspects. First of all is the behavior of the tooth using a 2D model and, second, the behavior of the tooth under load for a model closer to reality, for a 3D model. Also, in both cases we imposed the load conditions as is stated in ISO standard.

The result for the 2D model, concerning the strain state, is shown in Fig. 7. Also, results concerning the state of stress and displacement are shown in Table 4. In the process of meshing, the maximum displacement is 1.554 mm, which corresponds of the position at the top of the teeth of the main gears. The displacement decreases from the top of the tooth to the root of the teeth.

Table 2 Factors in root bending stress calculation formula, Eq. 2

Nomenclature	Symbol	Value
Application factor	K_A	1.0
Dynamic factor	K_V	1.0
Face load factor	K_{Fb}	1.0
Stress correction factor	Y_{Sa}	1.5
Contact ratio factor	Y_ε	0.75
Transverse load factor	K_{Fa}	1.0
Form factor	Y_{Fa}	2.73
Helix factor	Y_b	1.0

Table 3 Factors in surface contact stress calculation formula, Eq. 3

Nomenclature	Symbol	Value
Zone factor	Z_H	2.5
Elasticity factor	Z_E	189.8
Contact ratio factor	Z_ε	0.9115
Helix angle factor	Z_b	1.0
Application factor	K_A	1.0
Dynamic factor	K_V	1.0
Face load factor	K_{Hb}	1.2
Transverse load factor	K_{Ha}	1.0

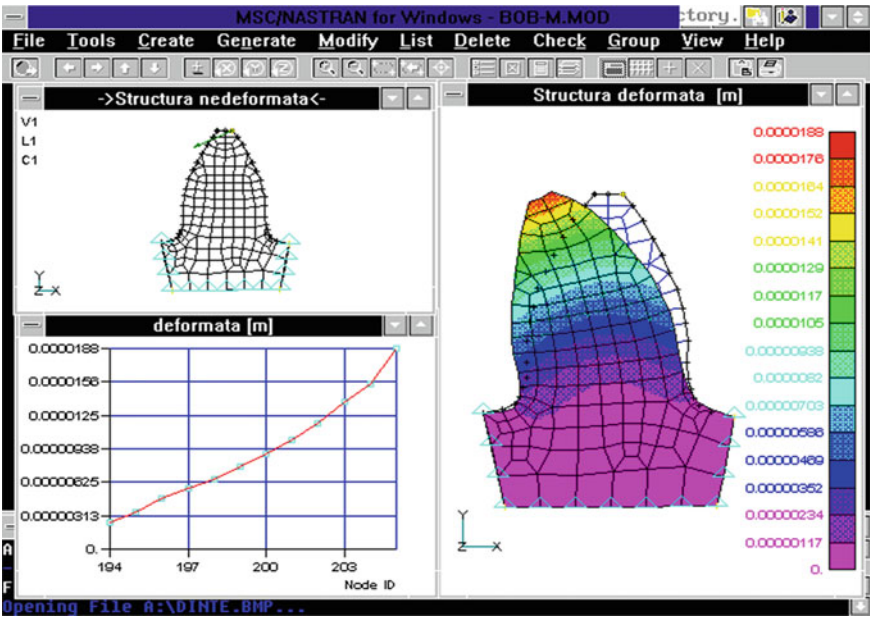

Fig. 7 Bending state of strain for 2D model, single pair in contact

Table 4 Equivalent stress and displacement in meshing process

Mesh position	Maximum equivalent stress (MPa)	Maximum displacement (mm)
Line 1	144.2	1.261
Line 2	148.5	1.312
Line 3	153.1	1.391
Line 4	157.4	1.442
Line 5	163.8	1.554

Table 4 shows the value of the maximum equivalent stress and displacement at different locations in the meshing process (Abaqus).

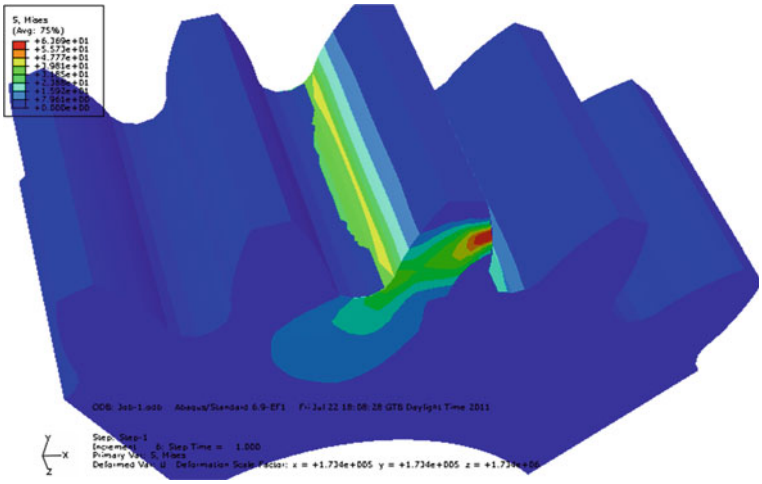

Fig. 8 Von Misses stresses for 3D bending model with 40 % of nominal load

From the Table 4, it can see that the maximum displacement and equivalent stress occurs at the point of the upper bound in the meshing of the single gear.

But the 3D model is closer to real process. For the bending stress we performed the state of stress in a series of analysis imposing an increasing load. In Fig. 8 we can observe the development of bending stress at the root of the tooth for 40 % of the nominal load. We can see the non uniform distribution of the stress along the flank line in the root region.

Regarding the effect of the bending stress the maximum principal stress at the root on the tensile side of tooth is used for evaluating the tooth bending strength of a gear. The Von Misses stress at the critical contact points was found out. Theoretical values of these stresses are compared with the ISO results calculation.

More than that we perform a parallel analysis using a second software to compare and verify the results.

In Fig. 9 are shown the results for this analysis. We can see that FEM software indicate the non-uniform distribution of bending stress during the ISO results is a constant value, and did not take into account the distribution of the stress along the

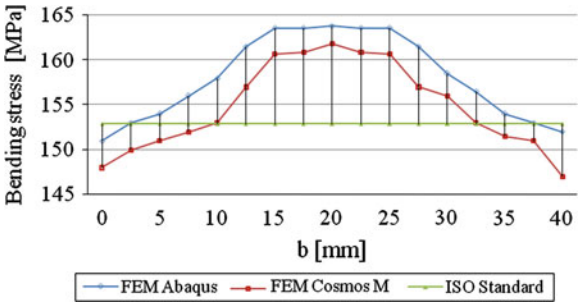

Fig. 9 Root bending stress comparison for ISO standard and FEM software

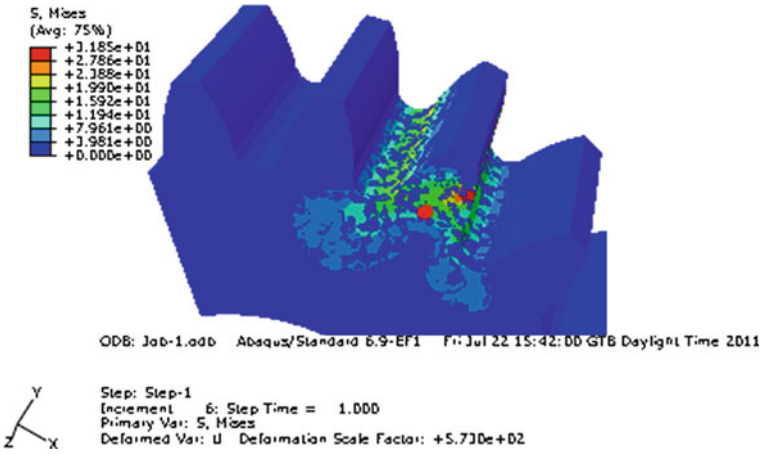

Fig. 10 Von Misses stresses for 3D bending model with 100 % of nominal load

tooth width. The error Cosmos M regards to ISO calculation is 5.82 % and Abaqus regards to ISO calculation is 7.12 %.

The development of the state of stress for 100 % of nominal load is given in Fig. 10 it shows large stresses at the root of the tooth, these being practically equal to the tensile stresses which are the main causes of crack failure.

Contact failure in gears is currently predicted by comparing the calculated Hertz stress to experimentally determine allowable values for the given material. The details of the subsurface stress field usually are ignored. This approach is used because the contact stress field is complex and its interaction with subsurface discontinuities is difficult to predict. However, all of this information can be obtained from the ABAQUS model. For the corresponding model of gear mesh (with consequent values for 2D and 3D model) we impose an equivalent load to a value of 362 Nm torque.

On the basis of elastic contact theory we assume that a pair of teeth in contact represents an elastic bodies contact and is handled as contact of many pairs of points on corresponding contact surfaces, supposed in contact along lines of the width of teeth. The mathematical model used to solve the contact problem assume that all the contact forces shared in the contact points are along the direction of the load F_{tot}. As consequence, the external load P is equal to the sum of all contact force F_i. The displacements due to elastic deformations can be found using eq. under the condition of knowing the clearance Δ_j and the influence coefficients α_{ij}, for the force applied in i point with an elastic influence in a j point. The mathematical programming method can be used in correlation with a FEM model from which we can find the values of influence coefficients. The relations for the mathematical model in a discrete form is given in the Eqs. (4) and (5) (Cananau 1999). In Fig. 11 we can show at a large scale the state of stress for the contact model.

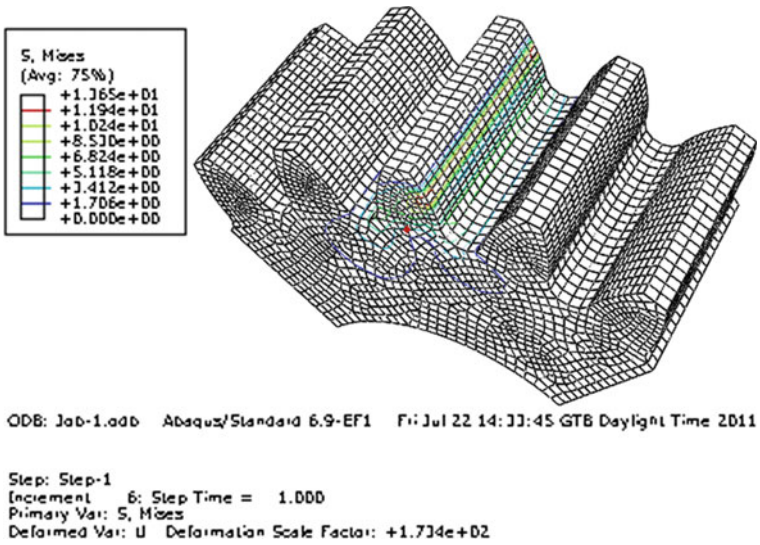

Fig. 11 Von Misses stresses for 3D contact model

$$F_{tot} = \sum_{i=1}^{n} F_i \tag{4}$$

$$s_j = \sum_{i=1}^{n} \alpha_{ij} F_i + \Delta_j, \quad \text{where } s_j = const. \tag{5}$$

For the 3D model, the state of von Misses contact stress for local contact along the contact line, the maximum values for the von Misses stress are less than 1,100 MPa.

The advantage of virtual testing and simulation process is the information we can get for the meshing process. In this activity we can develop special codes linked with the FEA/FEM commercial codes in order to obtain the load distribution along tooth width in the real meshing process. For the 3D studied model we can obtain the load (pressure) distribution along meshing line for a single and double pairs of teeth in contact. Also in a 3D representation we can get the information regarding the load distribution along the contact lines on the tooth width.

In Fig. 12 we get this information for the model already studied. Some aspects as the effect of load distribution at the end of the tooth could be found only using numerical methods and are not taken into account in actual standards calculations.

For two contact load cases and single pair tooth contact we studied the loaded tooth contact. The developed analysis is applied for the line along the tooth width and corresponding to the C (rolling) contact point. It is found that the contact stress contour lines present symmetry versus the initial contact line and also versus the middle plan of the gear (on the width). Also we found that the load contact

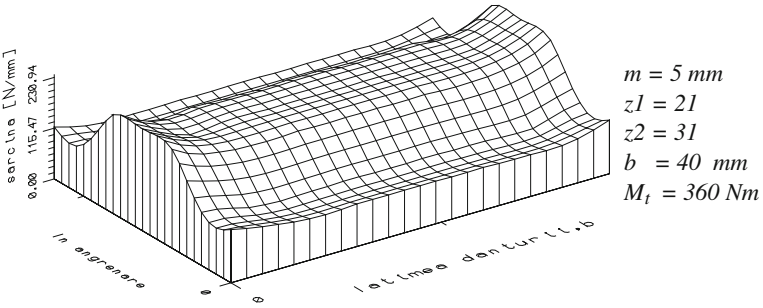

Fig. 12 Load contact distribution along mehing line and tooth width

distribution is changed from the first case, Fig. 12, to the pattern as is shown in Fig. 13, due to gear involute profile error. In Fig. 14, due to tooth direction the load distribution is modified along the tooth width.

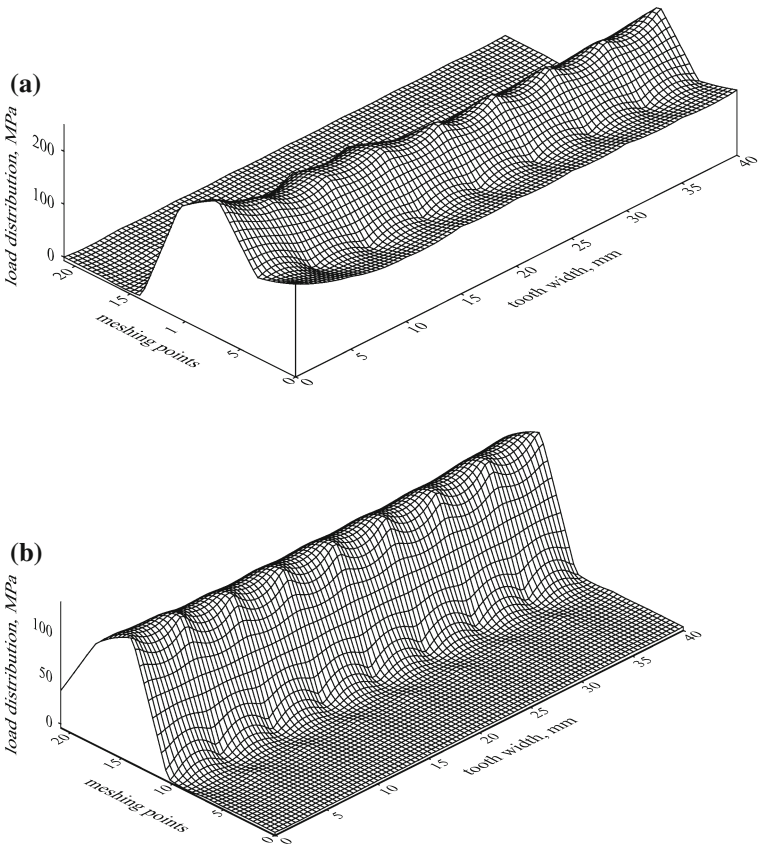

Fig. 13 Load contact distribution along mehing line and gears profile errors: **a** involute addendum profile error, **b** involute dedendum profile error

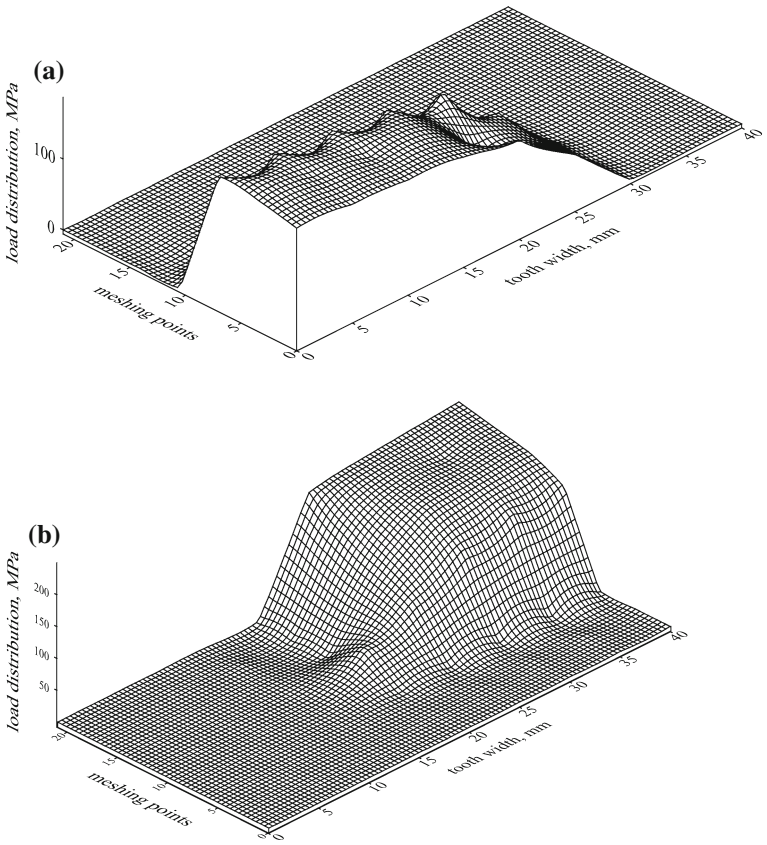

Fig. 14 Load contact distribution along mehing line and tooth width tooth direction errors: **a** right flank error, **b** left flank error

In Fig. 15 there are presented the contour lines along of tooth contact stress. In the first case presented in Fig. 15a, there is a contact distribution pattern corresponding to the reciprocating two lines in contact (along tooth width) at C point (along meshing line) for 40 % of nominal load. In Fig. 15b, the same pattern is shown for 100 % of nominal load. There is interesting that the symmetry of the contact lines stress can be observed for both cases and the hertz contact stress for the model of two cylinders in contact is involved.

In Fig. 16 there are presented the contour lines along of tooth contact stress for different points along meshing line and for flank surfaces with profile involute errors. In Fig. 16a, is shown the pattern tooth contact stress for corresponding surfaces with involute dedendum profile error and in Fig. 16b, the pattern for surfaces contact stress taking into account an involute addendum profile error.

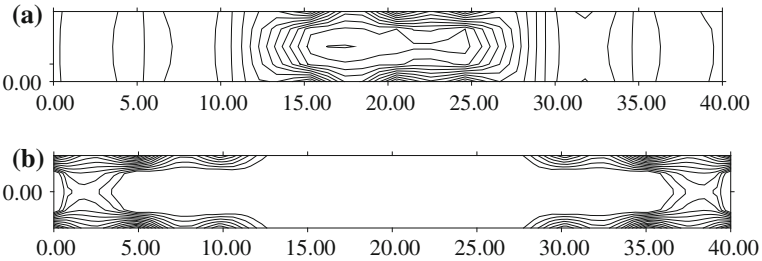

Fig. 15 Contour lines along of tooth contact stress for pure rolling position **a** −40 % of nominal load **b** −100 % of nominal load

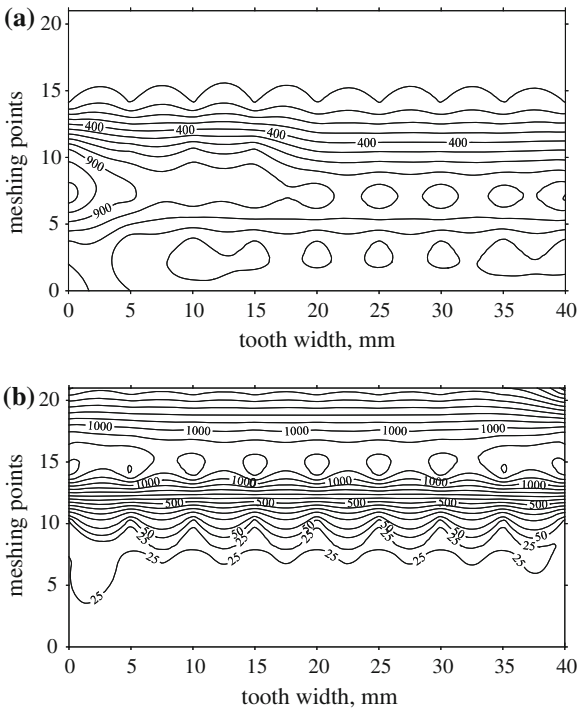

Fig. 16 Contour lines along of tooth contact stress for corresponding surfaces with gears profile errors: **a** involute dedendum profile error, **b** involute addendum profile error

5 Conclusions

In a modern and actual designing process of the transmissions with gears it makes necessary that gear designers have information regarding the behavior of the elastic structures under load. That means the designers must know the root bending stress and the surface contact stress. The ISO and other standards cannot give precise information and cannot conduct to a precise analysis of this stress.

For accomplish this information task is necessary to adopt and to have the knowledge to use a lot of software for gear calculation, CAD activity and, the most important, CAE analysis. This analysis involves in the same time the knowledge regarding commercials codes with finite elements but also responsive FEM programs which are also developed for personal computers.

An example of the capabilities and an algorithm of the "course" we have to taken in order to achieve relevant information in the designing process of gear transmission was shown in the paper.

References

Baronet CN, Tordion GV (1973) Exact stress distribution in standard teeth and geometry factors. J Eng Ind Trans ASME, 1159–1163

Brauer A (2004) A general element model of involute gears. Finite Elem Anal Des 40(13–14):1857–1872

Cananau S (1999) Non uniform load distribution along width tooth line for spur gears. PhD Thesis, Univ.Politehnica Buc

Conry TF, Serireg A (1971) A mathematical programming method for design of elastic bodies in contact. J Appl Mech Trans ASME 6:387–392

Feltkamp F, Rademacher J (1968) Fertigungsgenauigkeit und Laufverhalten von Zahnradgetrieben. Ind. Anz. 90:1769–1775

Kalkert W (1963) Untersuchungen über den Einfluss der Fertigungsgenauigkeit auf den Zahnkraftverlauf und die Flankentragfahigkeit ungeharteter Stirnrader, Ind. Anz. 85 175–353, 513

Li R-Z, Zhao Q-H (1984) Gear strength design data. Mechanical Industry Press, Beijing

Litvin FL, Chen J-S, Lu J, Handschuh RF (1996) Application of finite element analysis for determination of load share, real contact ratio, precision of motion, and stress analysis. J Mech Des 118:561–567

Niemann G, Reister D (1966) Einseitiges Breitentragen bei geradverzahnten Stirnrädern. Konstruktion 18:95–101

Rademacher J (1967) Ermittlung von Lastverteilungsfaktorenfü r Stirnradgetrieben. Ind Anz 89:331–337

Radzevich SP (2002) About hob idle distance in gear hobbing gear operation. ASME J Mech Des 125(3):632–639

Tobe T, Kato M, Inone K (1973) Effects on the inclination of the root on the deflection of gear teeth. Trans Jpn Soc Mech Engres 39:3473–3480

Umezawa K (1972) The meshing test on helical gear under load transmission—1st. report. The approximate formula for deflections of gear tooth, Bulletin of the JSME 15(90), 1632–1639

On the Efficiency of a Planetary Speed Increaser Usable in Small Hydros

Oliver Climescu, Codruţa Jaliu and Radu Săulescu

Abstract The paper focuses on the efficiency determination for a planetary speed increaser with deformable element, usable in micro hydro power plants. The proper selection of a suitable speed increaser between the turbine and generator is needed in order to allow a good and economical operation of these power generating units. Firstly, the generator and the turbine are tested on experimental rigs in order to find out the mechanical characteristics. Then, the synthesis of the planetary speed increaser is performed. The paper presents also the experimental efficiency determination of the speed increaser for different loads and speed regimes, by using an electrical generator with known characteristics as a braking load. The validation of the theoretical results with the experimental investigations guarantees a good functioning of the physical prototype of the planetary speed increaser in certain operating conditions.

Keywords Speed increaser · Efficiency · Planetary · Micro-hydro · Deformable

List of Symbols

η	Efficiency (%)
i	Multiplication ratio (-)
n	Rotational speed (rpm)
ω	Angular speed (rad/s)
T	Torque (Nm)
P	Power (W)

O. Climescu (✉) · C. Jaliu · R. Săulescu
Transilvania University of Braşov, Braşov, Romania
e-mail: climescu.oliver@unitbv.ro

C. Jaliu
e-mail: cjaliu@unitbv.ro

R. Săulescu
e-mail: rsaulescu@unitbv.ro

G. Dobre (ed.), *Power Transmissions*,
Mechanisms and Machine Science 13, DOI: 10.1007/978-94-007-6558-0_18,

1 Introduction

Micro hydropower plants can be designed to match many different working conditions. These plants are generally placed in rural locations to generate electrical energy for off-grid users or in locations where the connection to an electrical grid is not a viable solution, as mentioned by Harvey (2005). The main hydrological characteristics of a certain location (the available water head and flow), the type of the desired electrical generator (and its operating speed) and the required electrical power defines the type of the hydraulic turbine, that will be used in the given operating conditions, as shown in literature (Pelikan et al. 2004; Von Schon 2007).

Generally, the optimum running speed for the hydraulic turbines is less than 600–700 rpm, while the off-shelf generators require much higher operating speeds, above 2,000 rpm as mentioned in literature (Harvey 2005). In order to eliminate the discrepancy between the optimum speed regimes and to allow for both components (turbine and generator) to run at maximum efficiency, a speed increasing transmission is required, which transmits the mechanical energy from the turbine to the generator, and, in the same time, it modifies the parameters.

From the hydro energetic potential point of view, Brasov area is characterized by short rivers, with medium and high heads, medium and low values of the water flows due to the low quantity of precipitation (average value 637 mm/year), and high fluctuations of flow (30–40 % of the flow comes from the annual snow melting). Based on the measurements of flow and head performed on some of the rivers from this region, it was decided to design an off-grid small hydropower plant for a rural community to be implemented on Poarta River, near Bran. The chosen location is characterized by a mean value of the water flow $Q_m = 0.585$ m^3/s and a head H = 1,285 m, as presented by Jaliu et al. (2010). Therefore, a Turgo turbine, with a maximum power of 1 kW at 4,000 rpm (values given by the manufacturer, http://www.lpelectric.ro/ro/products/hydro/turbine_ro.html) (Fig. 1) was purchased to be installed on Poarta river. By taking into account the site hydrological parameters, the turbine reaches its highest efficiency at a particular speed regime that is much lower than the generator optimum speed. Therefore, the use of a speed increaser is needed between the hydraulic turbine and the electrical generator. However, the use of a mechanical transmission to get the necessary speed

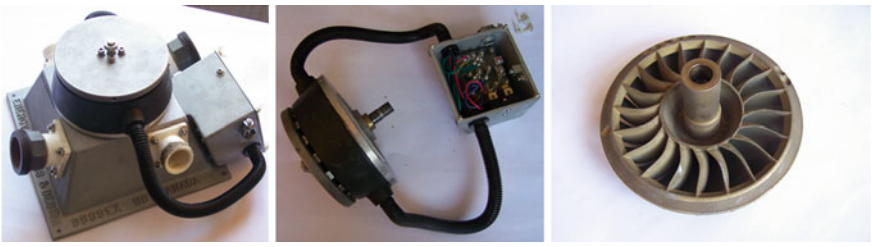

Fig. 1 The turgo turbine

multiplication involves several disadvantages that refer to the overall efficiency, dimensions and cost of the micro hydro plant.

Under these considerations, the paper presents the synthesis and experimental validation of the theoretical characteristics of a speed increaser to be assembled between the Turgo turbine and generator in order to ensure their operation at higher performances. The concept of the speed increaser is proposed by the authors in (Diaconescu et al. 2010).

Thus, firstly, the generator and turbine were tested on experimental stands for different speed regimes, in order to identify the efficiency—speed characteristic. Then, based on the testing results, the synthesis of the proposed planetary speed increaser is performed in order to get the required efficiency and multiplication ratio. The prototype of the speed increaser is manufactured and implemented into the Turgo assembly. The assembly consisting of the developed speed increaser and the electrical generator (as braking load) is tested on the experimental test rig from Electroprecizia Sacele factory in order to validate the theoretical results.

The validation of the theoretical results by testing the components separately in special test facilities, guarantees the good functioning of the physical prototype of small hydropower plant in real operating conditions.

2 The Turbine and Generator Characteristics

The turbines and generators are characterized by a power—speed characteristic and efficiency—speed characteristic. The first step in the establishment of the generator and turbine characteristics is to find out their input and output parameters: flow, discharge, torque, angular speed and voltage. Therefore, the Turgo turbine and the electrical generator were tested for different speeds and nozzles on experimental test rigs in Transilvania University of Brasov laboratories (Fig. 2a); in the generators case, the measured values were validated on the rig in Electroprecizia factory (Fig. 2b). The results allow the calculation of the input and output powers, and, of their efficiency, respectively. The diagrams obtained by

Fig. 2 Establishment of the turbine (**a**) and generator (**b**) parameters on testing rigs

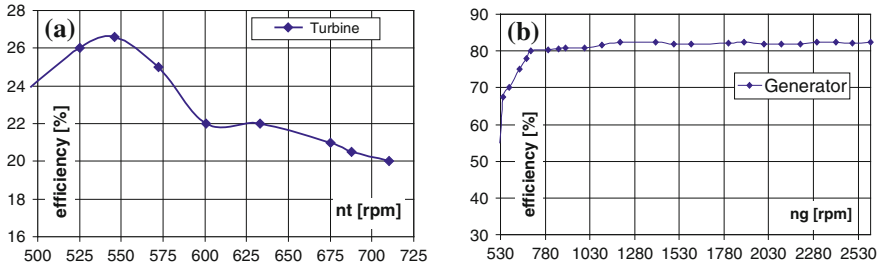

Fig. 3 The diagrams representing the variation of turbine (**a**) and generator (**b**) efficiency as function of rotational speed

Fig. 4 The speed increaser block diagram

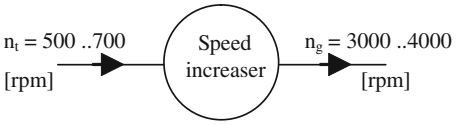

measurements processing are represented in Fig. 3. The diagrams allow the establishment of the turbine and generator efficiency variations, and, also, highlight the fact that the turbine has better performances at lower speed regimes while the generator performances are better for higher speeds (Jaliu et al. 2010). Thus, in order to increase the performances of the whole micro-hydro plant, the turbine speeds have to be lower, and the generator has to work at higher speeds. Therefore, a speed increaser has to be placed between the turbine and the generator (see Fig. 4).

The conclusions of the experiments are materialized in the speed increaser block diagram (Fig. 4), which allows the establishment of the speed increaser multiplication ratio for optimum speeds of the turbine and generator.

3 Speed Increaser Synthesis

In small hydropower plants three basic types of speed increasing transmissions are generally used: belt transmissions, parallel-shaft and planetary gearboxes, each with its advantages and disadvantages. Thus, belt transmissions are characterized by friction losses and overall dimensions increasing with their transmission ratio. The transmission ratio of the parallel shaft gearboxes can be increased by multiple stages placed in series, but this layout increases the overall dimensions, weights and decreases the system efficiency. The planetary gearboxes have many advantages compared to the other speed increasers: they are relatively light and compact, the input and output shafts are coaxial, reducing thus the overall dimensions, as presented by Raghavan (2010).

New solutions of planetary speed increasers for renewable energy systems were developed in the previous papers (Jaliu et al. 2009, 2010), in which the concept was generated based on a conceptual design algorithm. The innovative planetary transmission with deformable element (Fig. 6a) is under certification, and consists of a chain planetary set and a Schmidt coupling with three parallel connecting rods (4) (Diaconescu et al. 2010).

The main requirements used in the speed increaser dimensional synthesis are to multiply the input (turbine) speed between 4–6 times with a good as possible efficiency, and to ensure the turbine and generator optimum operation. Therefore, numerical simulations of the multiplication ratio (i) and efficiency (η) for different combinations of teeth numbers were made in order to identify the optimum combinations of the sprockets teeth numbers. The relations used in the synthesis are presented by Diaconescu and Duditza (1994a, b) and Neagoe et al. (2008).

Part of the simulation results is presented in Fig. 5. The diagram presented in the paper is obtained for $z_2 = 34$ teeth of the satellite gear, which ensures an optimal ratio between the values of radial dimensions and efficiency; the results are obtained by imposing the theoretical values of the chain transmission internal efficiency [$\eta_{23}^H = 0.95$], as given by American Chain Association (2005), of the linkage efficiency [$\eta_{12}^H = 0.995$] and the radial dimension of the planetary increaser ($\Phi = 160$ mm, given by the turbine dimensions and power). By using the results of the numerical simulations (Fig. 5) it can be stated that the efficiency maximum value for this configuration and for a multiplication ratio in the 4–6 range is 0.7 ± 8 %. Similar multiplication ratios ($|i| = 4\ldots6$) and efficiencies can be obtained for several combinations of teeth numbers, like: $z_2 = 34/z_3 = 40$ teeth, $z_2 = 34/z_3 = 41$ teeth and $z_2 = 34/z_3 = 42$ teeth (see Fig. 5); the variant with higher efficiency and the radial dimension closer to the turbine diameter is selected among these dimensional combinations. The winning variant is characterized by the following parameters: the teeth numbers $z_2 = 34$ and $z_3 = 41$, a multiplication ratio of −4.857 and an average efficiency of 67.93 %. The constructive scheme of the optimum speed increaser (Fig. 6b1 and b2), accomplished with the aim of modern CAD/CAE software (AutoDesk Inventor, Dassault

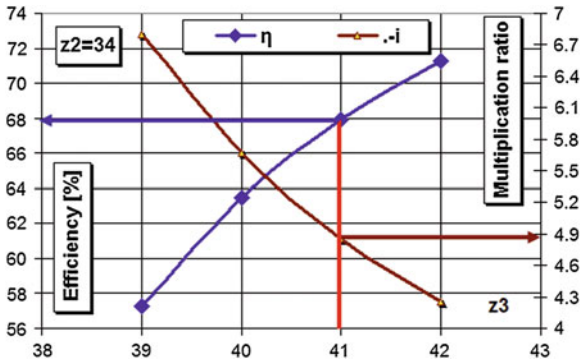

Fig. 5 Diagram of the speed increaser multiplication ratio (i) and efficiency (η) versus the teeth number of the sun gear z_3, for $z_2 = 34$ teeth

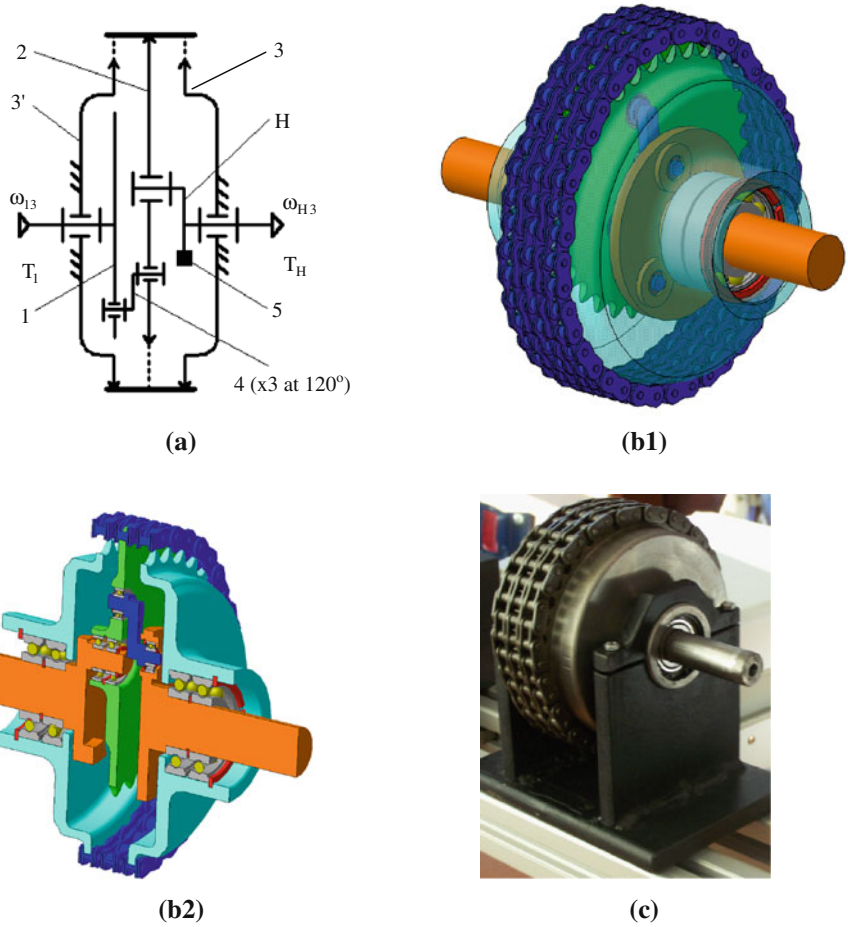

Fig. 6 The speed increaser concept (**a**), virtual model (**b**1, **b**2), and physical prototype (**c**) (*1* input central element—its axis of rotation coincides to the carrier H axis of rotation; *2* the satellite gear, belonging to the chain transmission; *3* (*3′*) the fixed sun gear, belonging to the chain transmission; *4* three connecting rods)

Systemes CATIA) has an eccentricity of 15.326 mm and needs a counterweight to balance the inertial force of the satellite gear.

According to the relations presented in literature (Diaconescu and Duditza 1994a, b), the speed increaser kinematic and dynamic parameters are systematized below:

$$i_0 = i_{13}^H = \frac{z_3}{z_2} = \frac{41}{34}; i = i_{H1}^3 = \frac{\omega_{H3}}{\omega_{13}} = \frac{1}{i_{1H}^3} = \frac{1}{1 - i_0} = -4.857 \quad (1)$$

$$\eta_0 = \eta_{13}^H = \eta_{12}^H \cdot \eta_{23}^H = 0.995 \cdot 0.95 = 0.9452 \quad (2)$$

$$\eta = \eta_{1H}^3 = \frac{-\omega_{H3} T_H}{\omega_{13} T_1} = \frac{1 - i_0 \eta_0^{-1}}{1 - i_0} = 0.6793 \tag{3}$$

$$\omega_{H3} = \frac{\omega_{13}}{\mathrm{i}} = -4.857\omega_{13};\ \varepsilon_{H3} = \frac{\varepsilon_{13}}{i} = -4.857\varepsilon_{13} \tag{4}$$

$$T_H = T_1 \cdot i_{1H}^3 \cdot \eta_{1H}^3 = -T_1 \cdot 0.2058 \cdot 0.6793 = -0.1398 \cdot T_1 \tag{5}$$

Further, the transmission physical prototype (Fig. 6c) is assembled between the Turgo turbine and generator, in order to verify the characteristics of the speed increaser, experimentally.

4 Experimental Investigation

The speed increaser efficiency is determined experimentally on a special test rig at Electroprecizia factory (see Fig. 7) that drives the system formed of the speed increaser and the electric generator used as a brake/load (Fig. 7a). The system

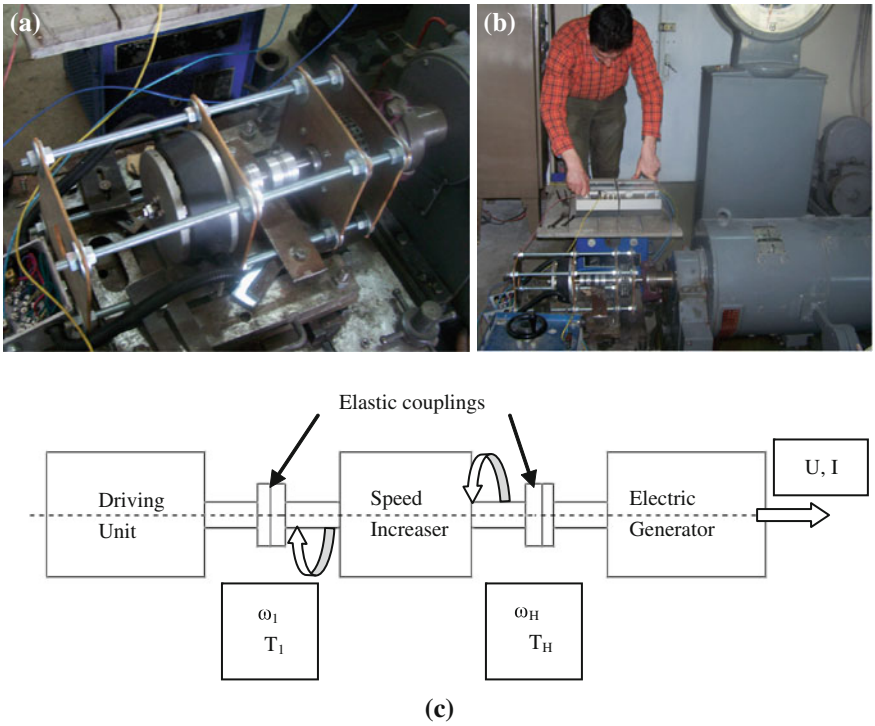

Fig. 7 The experiment presentation: the speed increaser—electric generator system (**a**), installing the system on the test rig (**b**), and the scheme of the test rig (**c**)

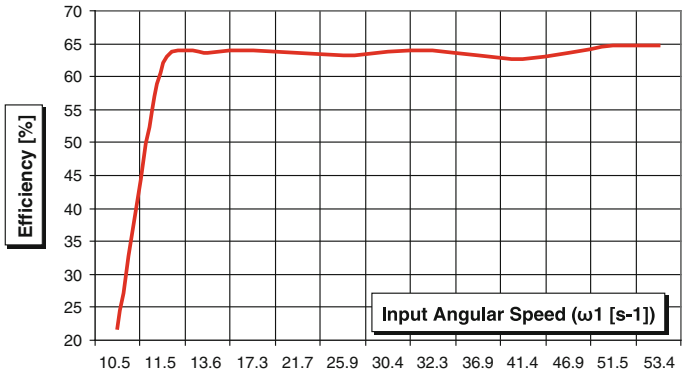

Fig. 8 The variation of the transmission efficiency versus input speed

efficiency (Fig. 7b) is obtained by measuring the system input and output power parameters (Fig. 7c): the angular speed (ω_1) and the torque (T_1) developed by the electric motor, the voltage (U) and the intensity (I) of the generated current, respectively.

The turbine mechanical power and the electric power developed by the generator can be calculated using relations (6):

$$P_{mec1} = T_1 \cdot \omega_1,\ P_{el} = I \cdot U\ (W) \tag{6}$$

The speed increaser output power and efficiency can be calculated based on the efficiency of the electric generator (see Fig. 3, $\eta_g = 82\ \%$):

$$P_{mec2} = \frac{P_{el}}{\eta_g}\ (W). \tag{7}$$

$$\eta = \frac{P_{mec2}}{P_{mec1}} = \frac{U \cdot I}{T_1 \cdot \omega_1 \cdot \eta_g}\ (\%) \tag{8}$$

The results of the experimental investigations are summarized in Fig. 8, which presents the variation of the transmission efficiency as function of the input angular speed. By analyzing the results, it can be stated that the tested planetary speed increaser with deformable element has a stable efficiency above a certain rotational speed (approx. 130 rot/min), which corresponds to the domain in which the turbine speed is, in the steady state regime, as stated by Pelikan. The difference between the transmission theoretical (67.93 %) and experimental efficiencies (64.25 %) is given by the power losses generated by the used bearings, elastic couplings and to the manufacturing errors.

5 Conclusions

- The Turgo turbine and the electric generator were tested on experimental rigs to obtain the efficiency—speed characteristic; the results highlight the fact that the generator has better performances at higher speeds, while the turbine performances are better for lower values of the angular speed. This behavior justifies the use of a speed increaser between the turbine and the generator, which has to increase the turbine speed in the range 4…6.
- The presented speed increaser, consisting of a planetary transmission with deformable element and a Schmidt coupling with three parallel connecting rods is an innovative solution and it is under certification.
- The diagrams and results of the speed increaser synthesis form a data base that can be used in the selection and dimensioning of a planetary transmission for a small hydropower plant or a wind turbine.
- The presented planetary transmission increases the input speed 4.857 times and decreases the input moment 7.153 times, that means a theoretical efficiency of 67.93 % for an angular speed of $\omega_1 > 12.6\ s^{-1}$; experimentally, it can be obtained an average efficiency of approx. 64 % that means an error of approx. 6 %, which is acceptable in the micro hydro domain. The manufacturing costs of the speed increaser are increasing with the decrease of the efficiency error.
- The results of the experimental investigations promise a good working of the speed increaser with a constant, as high as possible efficiency for a wide range of input angular speed (from 150 to 500 rpm).
- The use of a speed increaser between the turbine and the generator allows the good functioning of the two components at higher efficiencies, increasing, thus, the quality of the small hydropower plant.
- The next step in the development process is the implementation of the speed increaser in a stand-alone micro hydro plant, equipped with the Turgo turbine, in order to validate the theoretical and experimental results.

Acknowledgments This paper is supported by the Sectoral Operational Programme Human Resources Development (SOP HRD), ID59321 financed from the European Social Fund and by the Romanian Government.

References

American Chain Association (2005) Standard handbook of chains: chains for power transmission and material handling, 2nd edn. Dekker Mechanical Engineering

Diaconescu DV, Duditza FL (1994a) Efficiency calculation of the planetary transmissions. PII. Calculation examples, S. 61–63. (German)

Diaconescu DV, Duditza FL (1994b) Efficiency calculation of the planetary transmissions. PI. Development of a new method, S. 70–74 (German)

Diaconescu D, Jaliu C, Neagoe M, Munteanu O, Săulescu R, Climescu O, Tohăneanu D (2010) Planetary chain transmission. Patent solicitation no. A/00084/10.02.2010

Harvey A (2005) Micro-hydro design manual. TDG Publishing House

Jaliu C, Saulescu R, Diaconescu D, Neagoe M (2009) Conceptual design of a chain speed increaser for small hydropower stations. In: Proceedings of the ASME 2009 international design engineering technical conference and computers and information in engineering conference IDETC/CIE 2009, 30 Aug 2009, San Diego, California, USA, ISBN: 987-0-7918-3856-3

Jaliu C, Visa I, Diaconescu D, Saulescu R, Neagoe M, Climescu O (2010) Dynamic model of a small hydropower plant. In: OPTIM 2010, proceedings of the 12th international conference on optimization of electrical and electronic equipment, 20–21 May 2010, Braşov, Romania, pp 1216–1223

Neagoe M, Diaconescu DV, Jaliu C, Pascale L, Saulescu L, Sisca S (2008) On a new cycloid planetary gear used to fit mechatronic systems of RES. In: OPTIM 2008, proceedings of the 11th international conference on optimization of electrical and electronic equipment, vol II-B. Renewable energy conversion and control, 22–23 May 2008, Braşov, pp 439–449, IEEE Catalogue 08EX1996. ISBN 987-973-131-028-2

Pelikan B et al (2004) Guide on how to develop a small hydropower plant. ESHA, Brussels

Raghavan M (2010) The analysis of planetary gear trains. Trans ASME, J Mech Robot 2:021005-1–021005-5

Von Schon HAEC (2007) Hydro-electric practice—a practical manual of the development of water, its conversion to electric energy, and its distant transmission. France Press

Surface and Kinematical Joint Formation from Standpoint of Task Based Conceptual Design Method

Hrayr Darbinyan

Abstract Descriptive and synthesis methods of a novel presented task based conceptual design method are allowing to review from different point the formation of surfaces and kinematical joints. Kinematical joints are considered from the standpoint of surface formation by means of model and executive kinematical chains. Surfaces reproduced by technological machines are considered as special types of kinematical joints where two links are contacting each other over demanded surfaces. Such approach allows creating homogenous (including only low class joints) kinematical chains and involving further demanded function for synthesis of so-called "technological machines". Several examples are reviewed to confirm the theoretical approaches presented in the paper.

Keywords Kinematical joint · Function · Link · Synthesis · Surface

List of Symbols

X	Link
γ	Virtual kinematic joint
F	Function
M	Mechanical structure (mechanism, chain, object)
c	Kinematical joint
m	Model
F	Function
(X)	Link, repeated in equation

H. Darbinyan (✉)
Olympia Tools International Inc., Industry, USA
e-mail: hvdarbin@yahoo.com

H. Darbinyan
Shanghai Kunjek Handtools & Hardware Co. Ltd, Shanghai, China

G. Dobre (ed.), *Power Transmissions*,
Mechanisms and Machine Science 13, DOI: 10.1007/978-94-007-6558-0_19,

1 Introduction

The novel methods (Darbinyan 2011) of task based conceptual design are allowing to review from a single standpoint issues of surface formation by technological machines and formation of contact surfaces in kinematical joints.

It is useful to consider the category of a kinematical joint for description and study of surfaces generated by technological machines. Also such approach will contribute into attempt to generalize the category of a kinematical joint by the case of formation of a technological surface, considering the contacting surfaces as virtual case of a kinematical joint.

Mathematical and methodical background for description of a surface generated by a technological machine can be found in Reshetov and Portman (1985) where the end of a radius vector is pointing the surface to be reproduced and is described as a product of 4×4 matrices. This study aims analyzes of accuracy of surface formation and doesn't contain resources for involvement more functions necessary for turning a surface generating open chain into a full function mechanism. On the other hand the surface description method per (Reshetov and Portman 1985) is not including directly the links of the mechanical system thus limiting the scope of the method to consideration of a single function of surface accuracy and making difficult consideration of other functions connected with links and mechanical chains.

In the current study geometrical reproduction of a surface is also challenged as a key function, anyhow the synthesis methods of the novel method are able to expand this key function based mechanism into more complicated configurations with essential involvement of the whole spectrum of demanded functions.

Any kinematical joint mandatory implies reproduction of a surface by means of contacting elements of the joint; similarly any work tool driven by proper kinematics will move over a work piece surface and will generate it. It's quite logical to think that the kinematical surface generated by consecutive positions of the work tool and the work piece surface will act like a kinematical joint.

This obvious judgment is getting quite definite methodical advantages when seen from the standpoint of novel method of conceptual design and namely from the point of model mechanism and executive chain generation, creation of homogenous mechanical entity and setting the possibility of further function involvement once the key function of surface generation is satisfied.

The novel synthesis methods (application of standard set of synthesis tools, using virtual chains with further substitution with physical ones, direct dependence between a function and set of movable links implementing this function) can be useful for examination and study of functional of kinematical joints and surface generation mechanisms in particular.

Current study aims to consider the surface included between the mechanism of a surface generating technological machine and frame a special type of kinematical joint thus consider the whole generalized mechanical system (GMS) a single closed loop homogeneous chain suitable for synthesis and analyzes of given mechanism.

A special case of not continuous but discrete character surface generation (gemstone faceting machine) will also be considered from the same methodical standpoint.

2 Tasks and Objectives

The objective of the current study is to develop a homogenous mechanical entity (Generalized Mechanical System—GMS) included between work piece and work tool. Normally this GMS is an open chain and it is closed by a contact of the work tool on the work piece over so-called processed surface.

Another objective is to consider the work tool—work piece contact surface as a special kind kinematical joint, thus turn GMS into closed loop including exclusively low class (revolute and prismatic) kinematical joints with a single virtual joint on the contact surface.

Further objective is to establish the frame inside the homogeneous GMS, dividing it into two methodically important parts.

First chain starting from frame and ending on work tool surface for formation of work piece in most simplest (less links) and function vise efficient way.

And the second chain starting from the frame and ending also on the same point of the work piece is for set of executive links as conceptual structure for the further surface generation mechanism.

Next objective is to describe the homogenous chain and confirm it is suitable for application of standard synthesis tools.

And the last objective is to describe the case of discrete surface formation on an example of faceting machine.

Three examples for Slab Saw, Chamfering Machine and Faceting Machine will be considered to confirm the validity of this theory.

3 Surface Formation and Kinematical Joint

On Fig. 1a work piece X_1 and work tool X_2 are contacting through virtual kinematic joint γ, some kinematic chain c is providing this contact (Fig. 1b) and the combined graph (Fig. 1c) is including the both chains (Fig. 1c).

A work tool will contact the work piece to produce the demanded surface (let' say that's a virtual kinematic joint) and it needs another physical executive mechanical chain for providing the necessary movements over the work piece surface. The first contacting chain and second physical chain together are composing a closed loop which includes regular kinematical joints and one virtual joint for work piece—work tool contact.

To get a homogenous mechanical structure including exclusively low class joints need to do the following transformations with X_1, X_2c and γ.

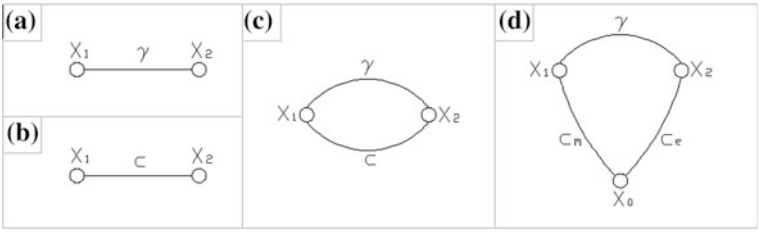

Fig. 1 Graphs for virtual joint (**a**), executive chain (**b**), combined graph (**c**), general graph (**d**)

- For X_1 a set of simplest movements should be arranged to provide in a most simple and function vise effective way a chain for demanded surface reproduction. This chain connected with work piece coordinate system will present the **model** of surface generation.
- For X_2 an open homogenous chain should be generated for describing the contacting work surface of the work tool. This is possible to do by application of surface liquefaction tool described in Darbinyan (2012). Large variety of options are available for fulfilling this task, anyhow the preferable solution should sound with the structure already built for work piece surface (surface model formation). This chain can be called executive movement's chain.
- For c an open homogenous chain should be generated duplicating (but not the same) all the movements of the model chain for X_1.
- After transformations above are done the virtual joint of γ can be described by consecutive positions of work tool over work piece with consideration of functional movements and relations between functional parameters due to kinematical and geometrical contact conditions.

Both model and executive chains are starting from immovable link (frame) and are forming virtual joint γ in the contact point (Fig. 1d). Descriptions of models in Fig. 1 are presented in matrix expressions (1–4).

$$J = J[X_1 \quad c \quad X_2] \tag{1}$$

$$C = C[X_1 \quad c \quad X_2] \tag{2}$$

$$M = M\begin{bmatrix} X_1 & \gamma & X_2 \\ (X_1) & c & (X_2) \end{bmatrix} \tag{3}$$

$$G = G\begin{bmatrix} X_0 & c_m & X_1 \\ (X_0) & c_e & X_2 \\ (X_0) & \gamma & (X_2) \end{bmatrix} \tag{4}$$

The homogenous structure generated in above described way has the ability of further transformation (expanding, squeezing, adding parallel chains-by application synthesis tools according Darbinyan 2011) accompanied by insertion of further (after satisfaction of task of surface generation) synthesis tasks and functions.

At this level it includes two basic chains (model and executive) which are the base of mechanism development subject to key function (technological surface generation).

The homogeneous field of parameters opens wide possibilities for analyzes and synthesis as for the main function as well for further functions and features of the mechanism.

3.1 Kinematical Joint Sphere to Sphere

Kinematical joint **sphere to sphere** (**SS**) is used for showing formation of a virtual joint. We consider one sphere as a work piece and the other one as a work tool which may reproduce the work piece as a result of definite executive movements. Such approach implies presence of a kinematical chain necessary for directing the movement of the work tool sphere around the work piece sphere. One sphere surface in this case is not a counterpart of the kinematical joint but a result of consecutive positions of the other sphere driven by some surface reproduction mechanism (Fig. 2). Matrix (5) shows the contents of GMS (generalized mechanical system) for SS kinematical joint.

$$M = M\begin{bmatrix} X_0 & \alpha & X_1 & \beta & X_2 & r_1 & . & . & . & . & . & . & X_3 \\ (X_0) & \alpha_f & X_4 & \beta_f & X_5 & (r_1 + r_2) & X_6 & \alpha_T & X_7 & \beta_T & X_8 & r_T & X_9 \\ (X_3) & . & . & . & . & \gamma & . & . & . & . & . & . & (X_9) \end{bmatrix} \tag{5}$$

- First row in the matrix (5), ended by link X_3 is for work piece surface reproduction chain (model chain).
- Second row is for kinematic chain driving the work tool over work piece surface. Second row has two parts. The first part ended by X_6 is for executive mechanism, and the second part ended by X_9 is for work tool surface description by a mechanical chain created using the solid liquefying tool according Darbinyan (2012).
- The third row is description of virtual kinematical joint γ between last links of the chains for work piece sphere and work tool sphere.

In spite the fact of using joint SS joint per kinematical chain need (a regular task) this GMS is useful from standpoint of spherical (in general of any surface) surface generation by another spherical surface according consecutive position generation method and may serve as model for further development of such reproduction mechanism.

The described chain is not the only one for sphere reproduction. It is showing the elements of novel methodical approach and may have many options for

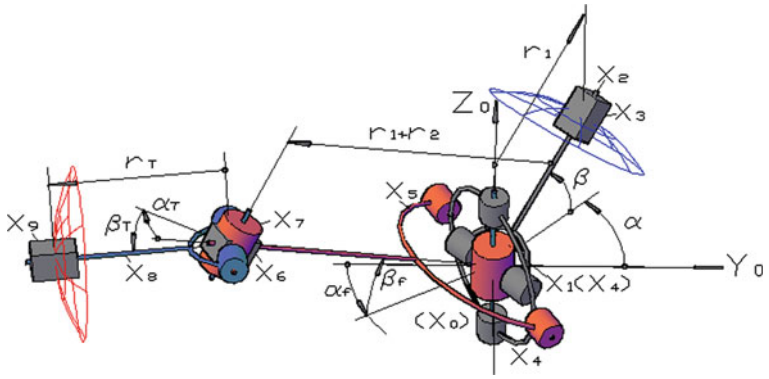

Fig. 2 GMS for kinematical joint sphere to sphere

implementation of executive chain, which starts on the frame and is ending on the sphere surface of the work piece.

4 Surface and Kinematical Joint Formation Examples

4.1 Slab Saw Example

The other example is for Slab Saw where the plane (cut or slice surface on a Slab Block) should be generated by other plane of the work tool—of a Diamond Slab Saw. In a similar way we build two chains of GMS, first for cut surface (plane) model anchored to Slab Block [first row in (6)] and second one including a set of functional movements for cutting surface (plane) of the Slab Saw (Fig. 3).

$$M = M\begin{bmatrix} X_0 & z & X_1 & x & X_2 & y & . & . & X_3 \\ (X_0) & A & X_4 & y_f & X_5 & (x_f, \alpha_T) & X_6 & R_T & X_7 \\ (X_4) & . & . & . & \gamma & . & . & . & (X_7) \end{bmatrix} \tag{6}$$

The third row in (6) is for virtual kinematic joint. This GMS can serve as base for one scenario of Slab Saw mechanism development according specific demands and requirements of this kind of machines (Darbinyan and Darbinyan 2007). A sample of further function may serve the tile thickness adjustment function that can be presented as additional parallel chain between links X_0 and X_1: $Fa = [X_0 F_a X_1]$c, where Fa is challenged function for tile thickness adjustment and is inserted as unknown joint between links X_0 and X_1.

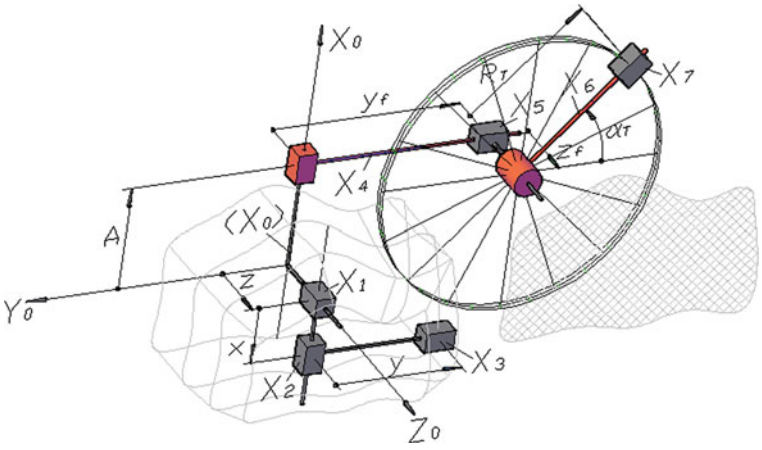

Fig. 3 GMS for slab saw

4.2 Chamfering Machine Example

In the GMS for Gear Chamfering Mechanism (Fig. 4) a model is linked to the work piece gear, the executive chain is starting from the same coordinate system connected to work gear and the chain for a work tool with point, linear or surface formation element. This tool will go around the work piece and generate the needed surface of chafer along toothed pattern. The mentioned kinematic chains with appropriate descriptive matrices are shown in Fig. 4 and in (7).

Large number of parameters is reduced due to geometrical and kinematical relations specific for higher class kinematical joints and due to producing solids using the solidifying synthesis tool described (Darbinyan 2012). As a result we will get surfaces *Sw* for work piece gear and surface S_T for work tool gear, which will produce demanded surface of chamfer due to inter generation.

In the homogenous mechanical chain (GMS) reproduction of any kinematical joint of GMS is equally successful by means of remained links of the system, and

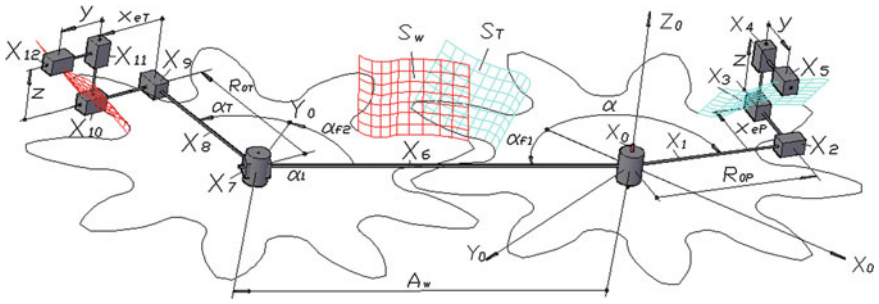

Fig. 4 GMS for gamma surface for gear chamfering mechanism

there is no difference which kinematical joint is being reproduced—revolute joint, prismatic joint or virtual "γ" joint.

$$M = M\begin{bmatrix} X_0 & \alpha & X_1 & R_{0P} & X_2 & x_{eP} & X_3 & z & X_4 & y & . & . & . & . & X_5 \\ (X_0) & \alpha_{f1} & X_6 & A_w & X_7 & (\alpha_{f2}+\alpha_T) & X_8 & R_{0T} & X_9 & x_{eT} & X_{10} & z & X_{11} & y & X_{12} \\ (X_5) & . & . & . & . & . & \gamma & . & . & . & . & . & . & . & (X_{12}) \end{bmatrix} \tag{7}$$

Simplification of GMS, further reduction of DOF, consideration of exploitation and maintenance features of work tool are implying further synthesis procedure of gear chamfering mechanism and are unveiled in Darbinyan and Darbinyan (2007).

4.3 Faceting Machine Example

The faceting machines are used for shaping gemstones of different standard shapes (emerald cut, diamond cut, marquise, drop, etc) (Faceting Machine 2012). First we develop the surface formation model as a set of minimum necessary set of movement elements anchored to coordinate system of the emerald cut gem stone. This model will include formation of just one face from total 25 (simplified case) faces, and the model needs to include functional movements for accessing all the demanded faces. Then we build a parallel duplicating chain of executive movement elements which includes a plane as processing element (a rotating disc-plane is shown by two prismatic joints, instead of rotating and prismatic ones, for matching with plane formation mechanism of the model) and will duplicate the functional possibilities of the first chain (Fig. 5).

Analogously the first row in (8) is for model formation, second one for executive mechanism and movements for Diamond Disc plane formation, and the third one for **plane to plane** (PP) virtual joint.

Obviously both GMS for Slab Saw and for Faceting Machine are providing the same **plane to plane** (PP) virtual kinematical joint. Anyhow both chains as for

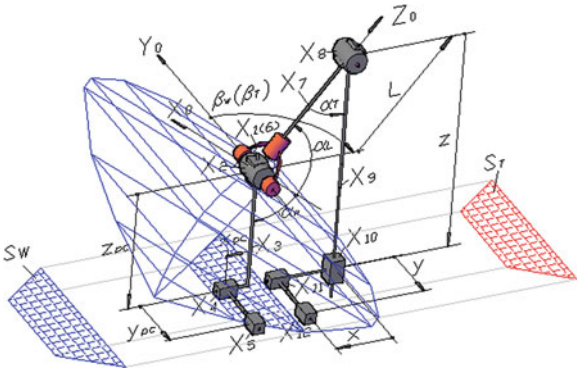

Fig. 5 GMS for faceting machine

model as well for parallel executive chains are totally different due to different and specific functional requirements of different mechanisms.

$$M = M\begin{bmatrix} X_0 & \beta_w & X_1 & \alpha_w & X_2 & z_{pc} & X_3 & x_{pc} & X_4 & y_{pc} & . & . & . & . & X_5 \\ (X_0) & \beta_T & X_6 & \alpha_L & X_7 & L & X_8 & \alpha_T & X_9 & z & X_{10} & y & X_{11} & x & X_{12} \\ (X_5) & . & . & . & . & . & . & \gamma & . & . & . & . & . & . & (X_{12}) \end{bmatrix} \tag{8}$$

A gemstone is formed by variety of planes that implies special predefined order of locking (freezing) of some degrees of freedom (DOF). Those requirements are composing set future functions for Faceting Machine mechanism further synthesis.

Set of parameters β and α (indexes are omitted, so far this set exists in both chains for model and executive chain) are describing 24 faces of the emerald cut according combinations in matrix (9)

$$\begin{bmatrix} \beta_1\alpha_1 & \beta_1\alpha_2 & \beta_1\alpha_3 & \beta_1\alpha_4 & \beta_1\alpha_5 & \beta_1\alpha_6 \\ \beta_2\alpha_1 & \beta_2\alpha_2 & \beta_2\alpha_3 & \beta_2\alpha_4 & \beta_2\alpha_5 & \beta_2\alpha_6 \\ \beta_3\alpha_1 & \beta_3\alpha_2 & \beta_3\alpha_3 & \beta_3\alpha_4 & \beta_3\alpha_5 & \beta_3\alpha_6 \\ \beta_4\alpha_1 & \beta_4\alpha_2 & \beta_4\alpha_3 & \beta_4\alpha_4 & \beta_4\alpha_5 & \beta_4\alpha_6 \end{bmatrix} \tag{9}$$

Combinations (9) inserted into (8) will describe 24 surfaces (planes) of emerald cut gemstone. One special surface is for the table (base) of gemstone described by (8) when $\alpha_w = 0$ for model chain and when $\alpha_T = 90^\circ$ for executive chain.

Further synthesis of mechanism for Faceting Machine may include functions for accurate adjustments for all three functional movements (α_T, β_T, L) needed for gemstone surface reproduction.

Several kinematical diagrams of gear chamfering (for example Nalyan et al. 1986) and slab saw (Darbinyan and Darbinyan 2007) machines were invented and the kinematical diagram of a Faceting Machine (2012) was reinvented using the methodical recommendations of surface formation described in this paper.

This study is considered as contribution into and expansion of task based conceptual design method presented in Darbinyan (2011).

5 Conclusions

1. Creation of a homogenous mechanical chain (including exclusively low class kinematical joints) is unveiling the surface formation resources of technological machines and is including a virtual kinematical joint of work tool and work piece contact.
2. Formation of a homogeneous mechanical chain is done by and allows application of a standard set of synthesis tools described in Darbinyan (2011, 2012). This chain includes three major segments (model chain, executive chain and virtual joint) all described by the same mathematical and physical models.

3. The generalized mechanical system (GMS) for a kinematical joint can be described as a complicated shape generation mechanism. The GMS consists of two parts—the model part and the parallel chain for executive mechanism.
4. The generalized mechanical system (GMS) presented as a homogenous mechanical chain contains resources for further (once the key feature of surface generation is satisfied) development of the mechanism per given functions.
5. Developed approach for kinematical joint generalization and description provides wide range for composing chains for model and executive mechanisms to satisfy as key function of surface generation as well other essential (in some cases more essential than surface generation is) functions.

References

Darbinyan HV (2011) Task based conceptual design method. In: Proceedings of 13th world congress in mechanism and machine science, A23–559

Darbinyan HV (2012) Task based conceptual design method for gear chamfering mechanisms. In: Proceedings of 4th international conference on power transmissions

Darbinyan HV, Darbinyan VH (2007) Slab saw. Republic of Armenia Patent 2005. http://aipa.am/patents/view_item.php?id=2005A2AM20070009&language=en (accessed on 15 May 2012)

Faceting Machine (2012) http://www.ultratec-facet.com/?gclid=CIP70sPAgbACFcRU4godFB2gTw (accessed on 15 May 2012)

Nalyan GH, Baghdasaryan ZS, Darbinyan HV (1986) A method for machining gear chamfer. USSR Patent 1389952

Reshetov DN, Portman VT (1985) Accuracy of machine cutting tools. Mashinostroyenie

Task Based Conceptual Design Method for Gear Chamfering Mechanisms

Hrayr Darbinyan

Abstract A novel conceptual design method is based on establishment of direct dependence between the features of the mechanism and the mechanical chains. The design method is further extended for the case of gear chamfering mechanism by enlarging the standard synthesis tool set by movement solidifying and liquefying tools. A description method is developed for compact presentation of mechanisms and functions. The key feature of accuracy of chamfer surface is described by open kinematical chain constructed by standard tool set. Methodically identical conceptual design cycle is developed and applied for various stages of concept design.

Keywords Conceptual · Design · Description · Gear · Chamfering

List of Symbols

X	Link or body
M	Mechanism or sub chain
c	Relation between two links
r	Radius vector
(X)	Link or body already mentioned in the matrix. A repeated symbol for x
φ	Orientation angle of chamfering triangle
z	Movement along the vertical page of chamfering triangle
R	Movement along normal page of chamfering triangle

H. Darbinyan (✉)
Olympia Tools International Inc., Industry, USA
e-mail: hvdarbin@yahoo.com

H. Darbinyan
Shanghai SANTO Handtools & Hardware Co. Ltd, Shanghai, China

G. Dobre (ed.), *Power Transmissions*,
Mechanisms and Machine Science 13, DOI: 10.1007/978-94-007-6558-0_20,

1 Introduction

Chamfering along the teeth of gears allows to reduce the stress concentration, removes sharp edges, prevents the sharp corners from damage and improves the cosmetic appearance of the toothed gears. Most of examples chamfering techniques have not been developed independently but were used as modifications of existing methods of gear processing technology and most of them are lacking in accuracy and efficiency for gear chamfering. An exception is for chamfer deformers in the shape of gears which are efficient and accurate and are used in car production. Conceptual design methods are based on combinational scanning the possible solutions of demanded structure from large variety of options. A cumbersome search and synthesis engine is practically not efficient and another methodically different search engine afterwards should be used to satisfy additional constraints and limitations (Chen and Pai 2005; Freudenstein and Maki 1979; Yan 1991).

A novel task based conceptual design method (Darbinyan 2011) uses a standpoint of direct dependence between mechanical chain and function and allows to arrange the entire design process is as a set of repeatable identical actions. The method is effective both for synthesizing and analyzing the mechanical object. The objectives of current study are:

- Enlarge the set of a synthesis tool developed earlier for the case of surface reproduction mechanisms like gear chamfering mechanisms are.
- Develop appropriate descriptive method to manage large amount of data generated by synthesis and analyses tools.
- Apply the enlarged set of tools and descriptive means to synthesize and design novel gear chamfering mechanisms.

2 Task Based Conceptual Design Method for Gear Chamfering Mechanisms

2.1 New Enlarged Set of Tools and Design Cycle

The following function targeted tool set was suggested:

- Add a link with new degree of freedom (granting DOF to a link),
- Add a physical or virtual chain with definite functional meaning,
- Condition links and chains by drives.

Tools are applied consecutively and in a cyclic manner. Application of a tool is satisfying one or more functions, and functions are driving themselves the order and number of tools applied. Requirement of geometrical accuracy of chamfer surface is emphasizing on consecutive application of Grant DOF tool that result in

construction of open kinematical chain with an end point tracking the surface of chamfer.

The set of three tools mentioned above will be updated by two more tools specifically developed for the case of gear chamfering mechanisms Those new two tool are relating to surface and solid generation by means of movable links, when a surface is tracked kinematically as a geometrical set of consecutive positions of a movable link. So any solid can be considered as result of "solidification" of some movements necessary to shape it and in reverse "liquefaction" of the solid will reveal the set of movements and mechanism for implementation of those movements behind the solid.

The same five component tool set, used to serve challenged, resolved and challenging functions are applicable for different stages of conceptual design like analyzes of existing and creating of novel mechanisms, synthesizing models and are used in a repeatable (cyclic) manner.

2.2 Descriptive Means for Mechanisms

A matrix presentation for both mechanical and functional entities is developed to facilitate the arrangement of concept design actions where for mechanical entity on the first row is showing main open chain of the mechanism, while the next rows are showing the parallel chains. Each row of the matrix is a product of links and movement parameters. The links and movement parameters themselves are 4×4 sized matrices. Parallel chains are arranged on lower rows and are linked with upper ones by links symbols of which are taken in parenthesis.

3 Analyzes and Synthesis Models

3.1 Point Ended Model

Point ended model (PEM) (Fig. 1) is developed by consecutive application of the tool Grant DOF and aims to **analyze** the existing methods of gear chamfering mechanisms from stand point of **geometrical accuracy** of chamfer surface. The

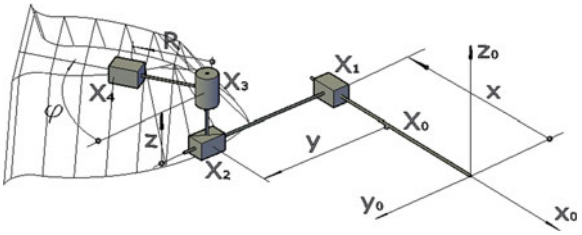

Fig. 1 Point ended model (*PEM*)

model has minimum set of movements to provide surface of chamfer along the toothed pattern including the profiles of the teeth and the bottom between the profiles.

Open chain includes links and movement parameters:

$$P = P[X_0 \quad x \quad X_1 \quad y \quad X_2 \quad z \quad \varphi \quad X_3 \quad R \quad X_4] \tag{1}$$

where movement parameters X and Y are for tracking the toothed pattern while z and R are for creating a chamfering triangle which is perpendicular to toothed pattern by means of orientation angle φ. z is axial page and R the normal page of chamfering triangle.

Both links X_0, X_1, X_2, X_3, X_4 and movement parameters x, y, z, R, φ are presented by 4×4 square matrices $A_i(x_j)$. The chamfer surface can be traced by the end of radius vector (2). Expression (2) is extracted from (1) by missing the unit matrices for links. In the formula e_4 is a unit vector.

$$r_0 = A_1(x) \quad A_2(y) \quad A_3(z) \quad A_4(\varphi) \quad A_2(R) \quad e_4 \tag{2}$$

Future challenges and unsolved functions (cutting process, shape of tool, adjustment, versatility, drives, etc.) are out of discussion now and are passed to next step of concept.

3.2 Linear Edged Model

Linear edged model (LEM) (Fig. 2) is developed on base of PEM to address future mechanism's ability to cut or plastically deform chip over chamfer surface.

PEM will turn into LEM by granting DOF by adding one more link carrying the Linear Edge. Link X_5 with additional parameter $-\varphi$ is needed to restore the original position of cutting edge thus provide the accuracy of generation chamfer generating lines to be equally distanced from original toothed pattern. Geometrical accuracy of chamfer surface is provided by the same contents of necessary movements included in PEM (1):

$$L = L[X_0 \quad x \quad X_1 \quad y \quad X_2 \quad z \quad \varphi \quad X_3 \quad R \quad X_4 \quad -\varphi \quad X_5] \tag{3}$$

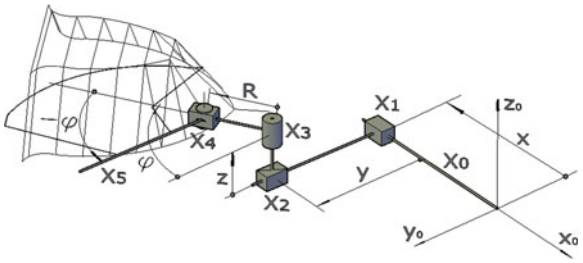

Fig. 2 Linear edged model (*LEM*)

Versatility of LEM (freedom to chose shape, size and angle of chamfer and chamfering location on toothed pattern) of LEM is defined by presence in (3) of movements parameters z, R, φ.

3.3 Analyzes of Cutter Bit Method

The traditional gear teeth rounding technology is used for chamfering purpose. Granting DOFs for functional and tool set up movements and liquefying tools solid body into moveable links will get an open chain of Generalized Mechanical Structure (GMS) (Fig. 3) for this method of gear chamfering.

$$B = B[X_0 \quad 1/z \quad X_1 \quad L \quad X_2 \quad H \quad X_3 \quad x \quad \varphi \quad X_4 \quad R \quad X_5] \tag{4}$$

This method is not able provide accurate chamfering because the chamfer surface is presented as a portion of revolved work surface of the Bit Cutter:

$$S = S[X_3 \quad x \quad \varphi \quad X_4 \quad R \quad X_5] \tag{5}$$

Omitting links in (4) will get the radius vector tracking the chamfer surface. In (6) e_4 is unit vector:

$$r_0 = A_4(1/z) \quad A_1(L) \quad A_3(H) \quad A_1(x) \quad A_4(\varphi) \quad A_2(R) \quad e_4 \tag{6}$$

The same limited space according (5) is indicating on tool's short life and GMS according (4) is indicating on tooth by tooth low efficiency chamfering.

3.4 Analysis of Plastic Deformer Method

This gear chamfering method is using double beveled gears for deforming the sharp edges of the toothed pattern into a surface of chamfer.

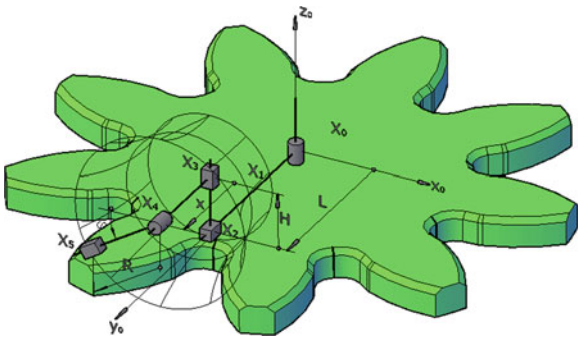

Fig. 3 GMS for bit cutter

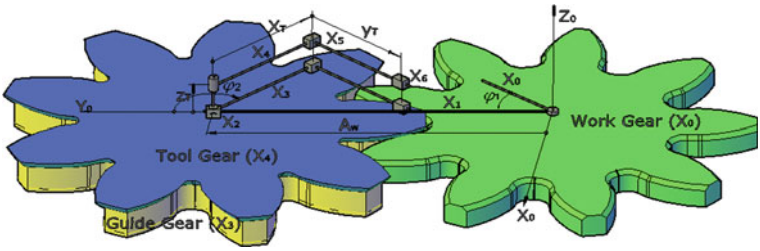

Fig. 4 GMS for plastic deformer

GMS (Fig. 4) for this method is developed by separating the mechanical chain for reproduction of the toothed pattern and reveal the solidified chain inside the double beveled gear to describe the formation of surface of chamfer.

$$M = M[X_0 \quad \varphi_1 \quad X_1 \quad A_w \quad X_2 \quad \varphi_2 \quad X_3 \quad z_T \quad X_4 \quad x_T \quad X_5 \quad y_T \quad X_6 \quad c \quad (X_0)] \tag{7}$$

where sub chain: $T = T[X_3 \quad z_T \quad X_4 \quad x_T \quad X_5 \quad y_T \quad X_6]$ is for formation the tool surface is for formation the tool surface.

And sub chain: $R = R[X_0 \quad \varphi_1 \quad X_1 \quad A_w \quad X_2 \quad \varphi_2 \quad X_3]$ is for reproduction of toothed pattern.

GMS has the necessary parameters for accurate and efficient formation of chamfer surface for the same time concentration of three solidified parameters in tool surface is making the tool manufacturing complicated and is defining the chamfering process as plastic deformation against cutting process that can be performed by Linear Cutting Edge. On the other hand the method has low versatility for the same reason of concentration of tool formation parameters.

4 Synthesis of Novel Gear Chamfering Mechanisms

4.1 Generalized Mechanical Structure

GMS (Fig. 5) is the next stage of synthesis that uses the advantageous features (accuracy, simplicity of tool and versatility) of LEM and is developed by two next steps:

1. Add a parallel chain between links Guide Gear (X_7) and Tool Gear (X_{10}) to simplify the structure and reduce DOF:

$$S = S[(\overline{X_7}) \quad z \quad \varphi \quad X_{15} \quad R \quad X_{16} \quad -\varphi \quad (\overline{X_{10}})] \tag{8}$$

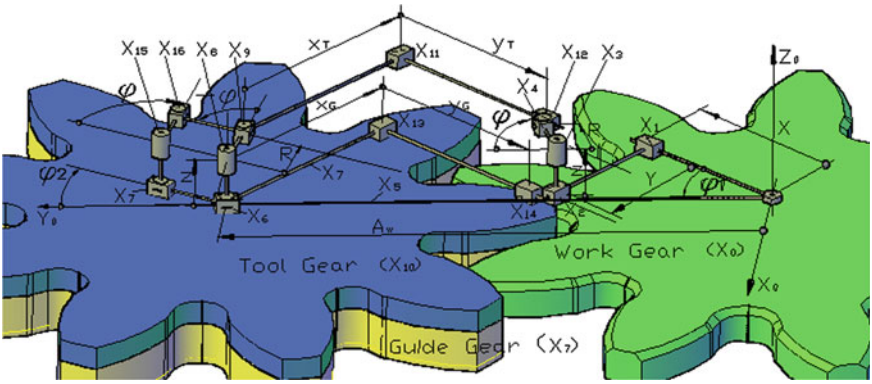

Fig. 5 Generalized mechanical structure (*GMS*)

2. Substitute LEM theoretical mechanism for reproduction of toothed pattern:

$$R = R[X_0 \quad x \quad X_1 \quad y \quad X_2] \tag{9}$$

by a mechanism of two coupled gears, so far toothed patterns of engaged gears are reproducing each other:

$$E = E[(\overline{X_0}) \quad \varphi_1 \quad X_5 \quad A_w \quad X_6 \quad \varphi_2 \quad X_7] \tag{10}$$

As a result GMS for gear chamfering mechanisms (Fig. 6) is developed:

$$M = M\begin{bmatrix} \overline{X_0} & z & \varphi & X_3 & R & X_4 & c & X_{12} & . & . & . & . & . & . \\ (\overline{X_0}) & \varphi_1 & X_5 & A_w & X_6 & \varphi_2 & X_7 & z & \varphi & X_8 & R & X_9 & -\varphi & \overline{X_{10}} \\ . & . & . & . & . & . & (\overline{X_7}) & c & . & . & . & . & . & \overline{X_0} \\ . & . & . & . & . & . & (\overline{X_7}) & z & \varphi & X_{15} & R & X_{16} & -\varphi & (\overline{X_{10}}) \end{bmatrix} \tag{11}$$

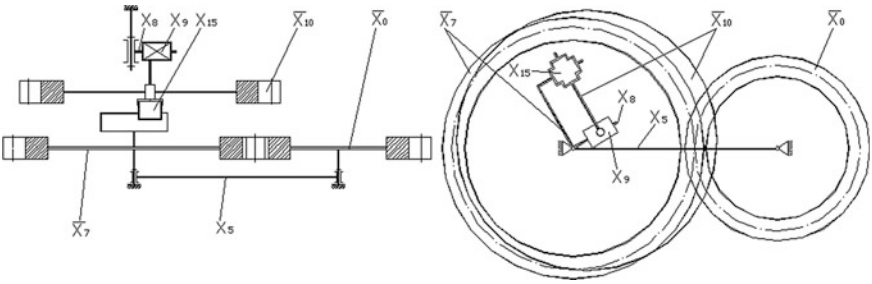

Fig. 6 Novel mechanism #1

Symbol c is for virtual kinematical joint between Guide Gear (X_7) and Work Gear (X_0). Link $\overline{X_{10}}$ is solidified combination of links X_{10}, X_{11} and X_{12}. The body of Tool Gear (X_7) is extruded solid of Linear Edge (12):

$$T = T[X_{10} \quad x_T \quad X_{11} \quad y_T \quad X_{12}] \tag{12}$$

GMS provides a $T = T[X_{10} \quad x_T \quad X_{11} \quad y_T \quad X_{12}]$ simple shape for cutting tool which is a toothed wheel of standard geometry with sharp toothed edge.

Note First row of the matrix (11) *is showing Point Ended Model* (*PEM*).

4.2 Movement Inversions

For turning GMS into novel gear chamfering mechanisms need to inverse movements of movable links and condition the movements by drives from immovable links. For both novel mechanisms link X_5 is stopped and Guide Gear X_7 and Work Gear X_0 rotate around fix axis like regular coupled gears. Conditioning by drive Link X_8 from Frame X_5 chamfering will have kinematically defined base X_8 for Links X_7 (Guide Gear) and X_{10} (Tool Gear) being parallel to each other and performing synchronized rotation staying parallel to each other as bars of parallelogram mechanism:

$$P = P[X_6 \quad X_8 \quad X_9 \quad X_{16} \quad X_{15} \quad (X_6)] \tag{13}$$

Links X_7 and X_{10} rotate synchronously and they act as clutch with shifted axis of rotation. Also in both cases the drives for z, R, φ are applied from frame which is traditional approach for machine tools. Depending on way of implementation of inner chain $I = I[(\overline{X_7}) \quad z \quad \varphi \quad X_{15} \quad R \quad X_{16} \quad -\varphi \quad (\overline{X_{10}})]$ between Links X_7 and X_{10} gear chamfering two mechanisms are created.

4.3 Synthesis of Gear Chamfering Mechanism #1

The first mechanism (Fig. 6) is generated by donating prismatic joints to two ends of link X_{16} with 90° cross position of axis. Link X_{16} ("stone") provides synchronous rotation of Guide Gear and Tool Gear. The mechanism is described by (14):

$$M = M\begin{bmatrix} X_0 & \varphi_1 & X_5 & \varphi_2 & \overline{X_7} & c & (X_0) & . & . & . \\ (X_5) & \varphi & X_8 & R & X_9 & z & -\varphi & \overline{X_{10}} & c & (X_0) \\ (\overline{X_{10}}) & R & X_{15} & z & (\overline{X_7}) & . & . & . & . & . \end{bmatrix} \tag{14}$$

Equation of chamfer hypotenuse $H = H(z, R)$ can be chosen either by external parallel chains (including cams for example) or by connecting z and R movements through CNC system with no limitation for shape of chamfer hypotenuse.

4.4 Synthesis of Gear Chamfering Mechanism #2 (Nalian and Darbinyan 1983)

For the second mechanism (Fig. 7) movements z and R are connected through angle of chamfer α ($tg\alpha = z/R$) so only one drive is needed for movement R more drive is needed for movement z. Solidifying chain of movements $K = K[X_7 \quad z \quad \varphi \quad X_8 \quad R \quad X_9]$ from (11) into two conical surfaces-external X_{K10} (belonging to Tool Gear X_{10}) and internal X_{K7} (belonging to Guide Gear X_7) will get conical pin/cup joint. Totally three pairs of conical joints are needed to provide cinematically definite position of Guide Gear X_7 and the Tool Gear X_{10}.

$$M = M\begin{bmatrix} (\overline{X_0}) & z & \varphi & X_3 & R & X_4 & c & X_{12} & \cdot & \cdot & \cdot & \cdot & \cdot & \cdot \\ (\overline{X_0}) & \varphi_1 & X_5 & A_w & X_6 & \varphi_2 & X_7 & z & \varphi & X_8 & R & X_9 & -\varphi & \overline{X_{10}} \\ \cdot & \cdot & \cdot & \cdot & \cdot & \cdot & (\overline{X_7}) & c & \cdot & \cdot & \cdot & \cdot & \cdot & \overline{X_0} \\ \cdot & \cdot & \cdot & \cdot & \cdot & \cdot & (X_{7K1}) & c_1 & \cdot & \cdot & \cdot & \cdot & \cdot & (X_{10K1}) \\ \cdot & \cdot & \cdot & \cdot & \cdot & \cdot & (X_{7K2}) & c_2 & \cdot & \cdot & \cdot & \cdot & \cdot & (X_{10K2}) \\ \cdot & \cdot & \cdot & \cdot & \cdot & \cdot & (X_{7K3}) & c_3 & \cdot & \cdot & \cdot & \cdot & \cdot & (X_{10K3}) \end{bmatrix} \tag{15}$$

Second gear chamfering mechanism and appropriate description matrix are shown in Fig. 7 and in (15). Conceptual design is resulting in diagrams of mechanisms #1 and #2 which contain improved features of chamfering process and can serve as base for further design of chamfering machines.

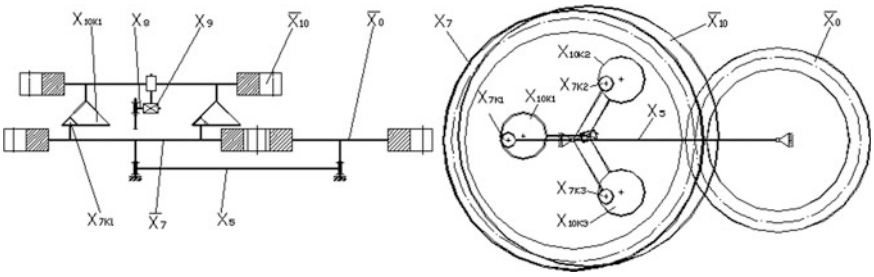

Fig. 7 Novel mechanism #2

5 Conclusions

1. Task based conceptual design method for gear chamfering mechanisms allows to organize the concept process in a systematic way with involvement of limited number of synthesis and analyzes tools.
2. Movement Liquefying and Solidifying synthesis and analyzes tools are specifically developed for the case of surface reproduction mechanisms. Liquefying allows to reveal mechanism behind solidified surface work surface of a link or body and Solidifying is for constructing solids and surfaces based on movement of links.
3. Suggested matrix presentation of mechanism or mechanical chain is contributing in concept structural design formalization task and allows to describe mechanical structures in a compact and informative way.
4. Developed Generalized Mechanical Structure (GMS) can be squeezed down to simple design models carrying just one basic feature of the mechanism and oppositely be expanded to finalized mechanism capable to perform all the features and functions of gear chamfering mechanism.
5. The method of linking the mechanical structure helps to reveal mechanical chains responsible for definite functions.
6. Tracking the chamfer surface by the last point of mechanical chain gets special status of joint and is described by same mathematical way as the regular joints. Breaking the chain at any joint will create an open chain having necessary set of movements for reproduction of contact surface of that joint.
7. The tool set and methodic of synthesis confirmed their validity for concept design for gear chamfering mechanisms. The paper shows concept design just for two of several patented gear chamfering mechanisms.

References

Chen D-Z, Pai W-M (2005) A methodology for conceptual design of mechanisms by parsing design specifications. J Mech Des 127(6):1039–1044

Darbinyan HV (2011) Task based conceptual design method. In: Proceedings of 13th World Congress in Mechanism and Machine Science, A23–559

Freudenstein F, Maki ER (1979) The creation of mechanisms according kinematic structure and function. Environ Plann B 6(4):375–391

Nalian GH, Darbinyan HV (1983) Method for chamfering teeth of toothed wheels. USSR Patent 1122458

Yan H-S (1991) A methodology for creative mechanism design. Mech Mach Theory 27(3):235–242

Theoretical Investigation of the Energy Efficiency of Planetary Gear Trains

Antoaneta Dobreva

Abstract The paper presents an investigation in the area of planetary gear trains. Based upon previous investigations of the author, methodology for the determination of geometrical boundaries for planetary gear trains is systemized. Precise analytical relationships are analyzed. The objectives of the presented investigation are: to summarize and improve the existing methodology for the determination of the geometry boundaries of internal gear trains; to analyze the influence of the tribological parameters upon the functional capacity of such gear trains, to define and precise the influence of the geometry in internal meshing upon the energy efficiency in such transmission elements and to indicate the approach for finding optimal design solutions considering the energy efficiency of gear trains. The results of the investigation of internal gear trains with small difference between the teeth number of the pinion and the teeth number of the ring (from 1 to 10) give the options for a quick and precise determination of the optimal addendum modification coefficients for the pinion and the ring considering the criteria contact strength and energy efficiency of the gear meshing. Conclusion and recommendations concerning the energy efficiency of planetary gear trains are suggested by the author.

Keywords Internal meshing · Geometry boundaries · Energy efficiency · Friction · Heating

List of Symbols

a	Centre distance
d_{a1}	Addendum diameter of pinion
d_{a2}	Addendum diameter of ring
d_{b1}	Base diameter of pinion
d_{b2}	Base diameter of ring
d_{f1}	Root diameter of pinion

A. Dobreva (✉)
University of Ruse, Ruse, Bulgaria
e-mail: adobreva@uni-ruse.bg

G. Dobre (ed.), *Power Transmissions*,
Mechanisms and Machine Science 13, DOI: 10.1007/978-94-007-6558-0_21,

h_a^*	Coefficient of the addendum of the tooth depth
m	Module
m_n	Normal module
u	Gear ratio of pair
W	Ratio characterizing special kind of interference
x_0	Addendum modification coefficient of cutter
x_1	Addendum modification coefficient of pinion
z_0	Teeth number of cutter
z_1	Teeth number of pinion
z_2	Teeth number of ring
α_0	Angle of the standard basic tooth profile
α_{at1}	Profile angle of tooth at addendum pinion circle
α_{at2}	Profile angle of tooth at addendum ring circle
α_{w0min}	Minimal pressure angle during tooth generation
α_{wt}	Pressure angle of meshing
θ_{1D}	Angle decribing inteference, Eq. (5)
θ_{2D}	Angle decribing inteference, Eq. (6)
μ	Coefficient of friction
ν	Angle decribing inteference, Eq. (8)
ψ	Angle decribing inteference, Eq. (7).

1 Introduction

For certain design layouts of gear trains and transmissions it is possible to realize great values of gear ratios in cases when some of the gear stages have internal meshing and especially those internal gear trains with small difference between the teeth number of the pinion and the teeth number of the ring (from 1 to 10).

It is well known that a scientific team with leader Assoc. Prof. E. Angelova and Prof. P. Nenov from the University of Ruse elaborates software programs for geometrical and strength calculation of gear trains with the help of geometry and power blocking contours as described by Angelova et al. (2010, 2011).

For different kinds of internal gear trains, there are graphical presentations of the geometry boundaries, represented in DIN 3993. For certain gear trains with great values of gear ratios and in some cases with internal meshing with small difference between the teeth number of the pinion and the teeth number of the ring, those graphical presentations of the geometry boundaries can not always be applied.

The objectives of the presented investigation are: to summarize and improve the existing methodology for the determination of the geometry boundaries of internal gear trains; to analyze the influence of the tribological parameters upon the functional capacity of such gear trains, to define and precise the influence of the geometry in internal meshing upon the energy efficiency in such transmission

elements and to indicate the approach for finding optimal design solutions considering the energy efficiency of gear trains.

2 Methodology for Determination of Geometry Boundaries for Internal Gear Trains

The theoretical research of planetary gear trains with special applications is based upon the systemized and additionally elaborated methodology for the determination of the geometry boundaries of internal gear pairs, which is described in details by Dobreva (2011).

The geometry boundaries of the internal meshing have to fulfill the following conditions: avoiding the cutter interference of the gear pair; additional specific condition for the internal meshing, non-admission of meshing interference in the area outside the plane of action; ensuring a minimal allowable contact ration and providing a sufficient length of the space width at the root diameter of the ring with internal teeth.

The solutions of those several conditions for the geometry boundaries of the internal meshing are presented usually in a graphical form and they are used as general bases for the geometrical design of cylindrical internal involute gear pairs.

The geometry conditions, which the internal gear pair has to fulfill, are to be defined through the following approach:

2.1 Avoiding Cutter Interference

The first geometry boundary condition is defined according to DIN 3960 in Eq. (1):

$$x_{1\min} = \frac{(inv\alpha_{w0\min} - inv\alpha_0).(z_1 + z_0)}{2.tg\alpha_0} - x_0. \quad (1)$$

The meaning of the parameters, used in Eq. (1) is as follows: $x_{\mathbf{1min}}$—minimal permissible addendum modification coefficient of the pinion; $\alpha_{\mathbf{0}}$—angle of the standard basic tooth profile; $z_{\mathbf{0}}$—teeth number of the cutter; $z_{\mathbf{1}}$—teeth number of the pinion; $x_{\mathbf{0}}$—addendum modification coefficient of the cutter. One of the parameters from Eq. (1) is described through the following equation:

$$\alpha_{\mathbf{w0min}} = \text{arctg}\{z_{\mathbf{0}}/(z_{\mathbf{1}} + z_{\mathbf{0}}).\text{tg}[\arccos(m.z_{\mathbf{0}}.\cos\alpha_{\mathbf{0}}/(m.z_{\mathbf{0}} + 2h_{\mathbf{a}} * + 2x_{\mathbf{0}})]\}. \quad (2)$$

The additional parameters, used in Eq. (2) are: m—module of the gear pair; $h_{\mathbf{a}}$*—coefficient of the addendum of the tooth depth.

The graphical solution of the Eqs. (1) and (2) are presented through the line 1, shown on Fig. 1.

2.2 Additional Specific Condition for Internal Meshing

A very important additional specific condition for the internal meshing is describing the boundary case, when the addendum (tip) circle of the ring is crossing the approach contact of the active part of the path of meshing contact at the base diameter of the pinion.

The geometry relationships for this case are defined precisely by Linke (2010) as a special type of interference by internal meshing. In order to satisfy this condition, it is necessary according to the literature source mentioned, the following inequality to be fulfilled:

$$|d_{a2}| \geq \sqrt{d_{b2}^2 + \left(2|a| \sin \alpha_{wt} + \sqrt{d_{f1}^2 - d_{b1}^2}\right)^2}. \tag{3}$$

The following parameters are applied in Eq. (3): d_{a2}—addendum diameter of the ring with internal teeth; d_{b2}—base diameter of the ring with internal teeth; a—centre distance; α_{wt}—pressure angle of the meshing; d_{f1}—root diameter of the pinion; d_{b1}—base diameter of the pinion.

The graphical solution of inequality (3) is based upon several other well known geometry relationships of the internal meshing. It is visualized on Fig. 1, line 2.

2.3 Interference Outside the Plane of Action

The non-admission of meshing interference in the area outside the plane of action is especially important for internal meshing in cases when the difference between the teeth numbers of the pinion z_1 and of the ring z_2 is small, for example: between one and 10. For that kind of eccentric planetary gear trains, an impact between the addendum parts of the pinion and of the ring is possible to occur in the area outside the plane of action.

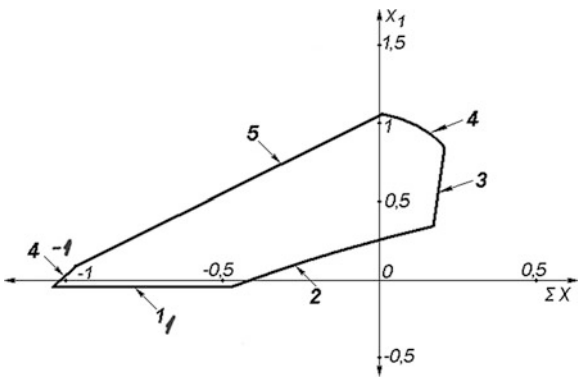

Fig. 1 Geometry boundaries of internal gear pair as a function of addendum modification coefficient of pinion x_1 and of the sum modification x_Σ in accordance to DIN 3993

In order to avoid that type of interference, the following inequality has to be fulfilled mentioned in literature (Linke 2010):

$$W = \frac{\theta_{1D} + \psi}{u.(\theta_{2D} - v)} \geq 1. \tag{4}$$

The designations used in (4) are cooresponding to those applied by Linke (2010): W—the ratio, which is characterizing this kind of interference; u—gear ratio of the gear pair ($u = |z_2|/z_1$). The angles θ_{1D}, θ_{2D}, ψ and v are to be calculated according to the relationships in Eqs. (5), (6), (7) and (8):

$$\theta_{1D} = \arccos \frac{d_{a_2}^2 - d_{a_1}^2 - 4a^2}{4d_{a_1}.|a|} \tag{5}$$

$$\theta_{2D} = \arccos \frac{d_{a2}^2 - d_{a1}^2 + 4a^2}{4|d_{a2}|.|a|} \tag{6}$$

$$\psi = inv\alpha_{at1} - inv\alpha_{wt} \tag{7}$$

$$v = inv\alpha_{wt} - inv_{at2}. \tag{8}$$

The angles, which are included in the Eqs. (7) and (8), are calculated through the addendum and base diameters as shown in the Eqs. (9) and (10):

$$\alpha_{at1} = \arccos \frac{d_{b_1}}{d_{a_1}} \tag{9}$$

$$\alpha_{at2} = \arccos \frac{d_{b_2}}{d_{a_2}}. \tag{10}$$

The geometry parameters from Eqs. (4) to (10) are presented precisely in a graphical way by Linke (2010).

2.4 Influence of the Contact Ratio

The necessary condition to be fulfilled concerning the contact ratio is well known. The following relationship has to be satisfied: $\varepsilon_\alpha \geq 1.1$.

2.5 Space Width at the Root Circle of the Ring

The space width at the root circle of the ring with internal teeth is recommended to be assumed at least equal to 0, 2. m_n. It is calculated according to DIN 3960. The graphical solution of that relationship is presented through line 5 on Fig. 1.

The solutions of the relationships, described briefly in that part of the paper, are shown in a graphical way on Fig. 1. Each one point from the area inside the contour is representing a solution of a given problem considering only the geometrical point of view.

3 Investigation of Tribological Parameters of Internal Gear Trains

Based upon a contract between the University of Ruse and a Bulgarian enterprise, it was necessary to develop several versions for eccentric planetary gear trains with small difference between the teeth number of the pinion and the teeth number of the ring. The activities of the contract included the theoretical analyses of those developed versions and a carried out comparison between the preliminary design layouts of the elaborated gear trains.

According to the results of the implemented research the best possible verions for eccentric planetary gear trains are those with difference between the teeth number of the pinion and the ring equal to two or four teeth. In both cases, the ring of the planetary gear train was designed with 110 teeth.

The geometry boundaries for eccentric planetary gear trains have been solved according to the methodology, presented in the second part of this paper. The graphical solutions for those two possible gear ratios are shwon on Fig. 2.

Based upon methods, described in details by Linke (2010) and Dobreva (2011), a tribological investigation is carried out concerning the energy efficiency of variety of possible planetary gear trains with a teeth difference between z_1 and z_2, equal to two and four.

The results of the theoretical analyses of the energy efficiency of the investigated planetary gear trains are shown on Fig. 3. The values of the zone factor Z_H, which takes into account the flank curvatures at the pitch point and transforms the tangential load at the reference cylinder to tangential load at the pitch cylinder, are calculated according to ISO 6336-2: 2006(E). The obtained results for Z_H and for the transverse contact ratio are shown in a graphical way as a function of the sum modification x_{Σ} for the eccentric planetary gear train with the following teeth numbers: $z_1 = 106$ and $z_2 = 110$.

As a second stage, an analysis is carried out concerning the influence of the contact stresses upon the energy efficiency. The following conclusion is deduced: the influence of the contact stresses upon the energy efficiency for that kind of planetary gear trains is considerably greater in comparison with the influence of the bending stresses at the root diameters of the pinion and the ring.

The geometry of the internal meshing influences mainly the relative and the specific sliding along the path of the path of contact and respectively the efficiency coefficient in gear meshing.

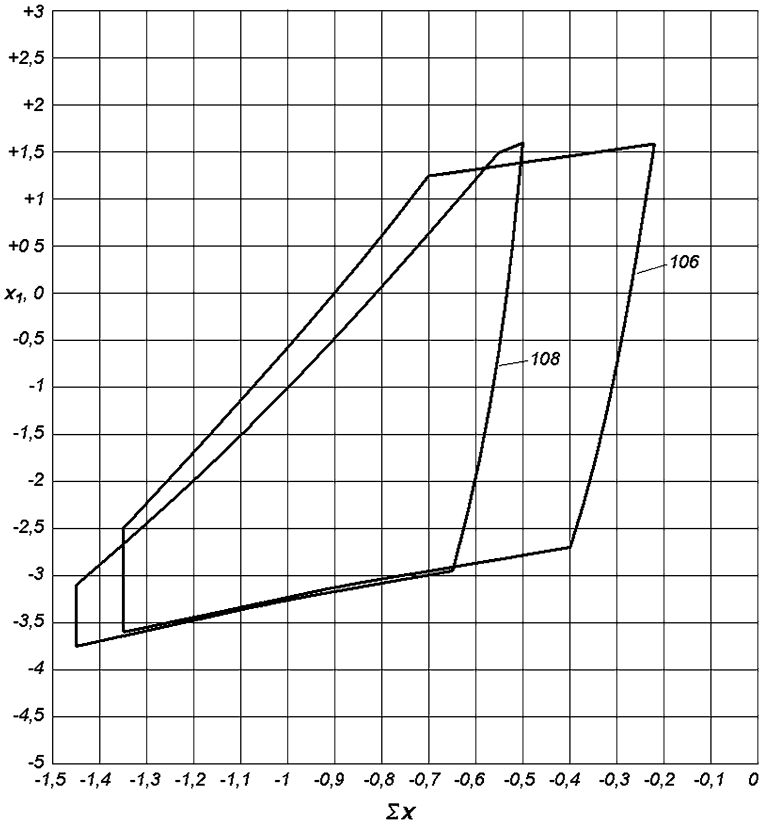

Fig. 2 Geometry boundaries for eccentric planetary gear trains ($z_1 = 106$ and $z_2 = 110$; $z_1 = 108$ and $z_2 = 110$)

Based upon the implemented theoretical research, the author recommends that the planetary gear train with a difference between z_1 and z_2, equal to 4, i.e. $z_1 = 106$ and $z_2 = 110$ has to be produced for the needs of the Bulgarian enterprise for gear trains and reducers taking into account certain technological considerations. Concerning the energy efficiency, the best solution would be the specific gear pair with the following parameters: a sum modification $\Sigma x = -0, 9$ and an addendum modification coefficient for the pinion $x_1 = -1$. The selected geometry for the gear pair has the following advantages: the contact strength is secured with a sufficient safety coefficient and the value of the contact ratio ensures a minimal friction coefficient along the active path of meshing contact.

With the exception of the pitch point, the teeth profiles in meshing area are moving relatively to each other through out the length of the path of contact. The relative movement between the pinion and the ring and the sliding cause increasing the temperatures in the lubrication film. This process changes the thickness and the loading capacity of the lubrication film and it has a considetable

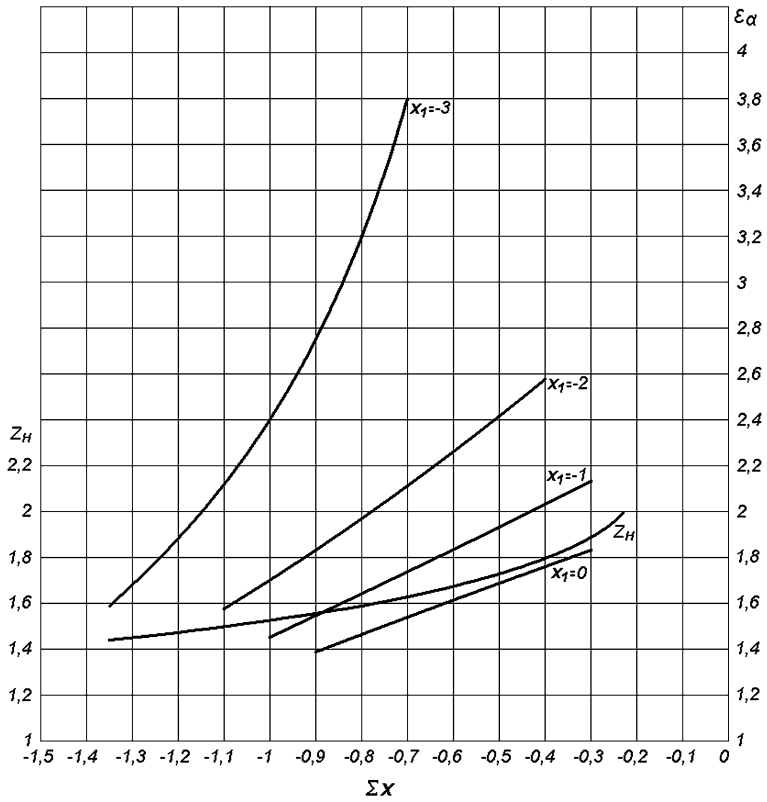

Fig. 3 Tribological parameters for eccentric planetary gear trains as a function of sum modification x_{Σ}

influence upon the magnitude of the friction forces in the meshing. The value of the temperature in the meshing contact depends considerably from the friction coefficient μ, which is changing with the magnitude of the sliding.

Besides, the high surface temperatures of the gears lead to reducing the strength of the lubrication film and therefore to a secondary increasing of the friction in the meshing area. This process, based upon the mutual dependance between temperature and friction causes pitting, breakage of teeth and other damages.

For planetary and eccentic gear trains, which ensure great gear ratios, the relative sliding achieves great values and therefore, the strength calculations according to the criteria contact strength and bending is not enough for ensuring the normal functioning of that kind of internal gear trains.

It is also necessary a calculation of the heating temeperatures to be carried out, because it is possible that internal gear trains which are calculated in a perfect way according to the main criteria: contact strength (pitting) and bending and also possessing meshing geometry entirely corresponding with the geometry boundaries of the described methodology can be overheated. Therefore, that type of

internal gear trains may loose their functional capacity earlier in comparison with the envisaged preliminary calculated durability. A precise methdology for calculation of the heating parameters concerning planetary and eccentric gear trains is described by Dobreva and Dobrev (1993).

4 Conclusions

The presented investigation of internal and planetary gear trains gives the reasons to deduce the follwoing conclisions:

1. The results of the investigation of internal gear trains with small difference between the teeth number of the pinion and the teeth number of the ring (from 1 to 10) give the options for a quick and precise determination of the optimal addendum modification coefficients for the pinion and the ring considering the criteria contact strength and energy efficiency of the gear meshing.
2. Based upon precisely defined geometry boundaries for internal gear trains with small difference between the teeth number of the pinion and the teeth number of the ring, the value of the contact ratio is an important indicator for the selection of a gear pair considering the optimal operational parameters of the gear trains.
3. For planetary and eccentric gear trains ensuring great gear ratios, it is necessary to implement calculation of the heating parameters as well.

Acknowledgments The work has been funded through the Fund of Scientific research at the University of Ruse.

References

Angelova E, Ronkova V, Nenov P (2010) Increasing load capacity of cylindrical gear by optimizing their geometric parameters, "INMATEH—Agricultural Engineering", May-August, 31(2), National Institute of Research-Development for Machines and Installations Designed to Agriculture and Food Industry-INMA Bucharest, ISSN:2068-2239, ISSN:2068-4215, pp 40–46

Angelova E, Ronkova V, Tiufektchian A (2011) Computer-aided design of involute cylindrical gear drives for portable electric tools. In: 2nd internacional scientific and practical conference "technology, materials, transport and logistics: development prospects" TMTL'11, Yalta (Crimea), Ukraine, The Scientific Journal 12(166) ISSN 1998-7927, pp 14–18

DIN 3960. Begriffe und Bestimmungsgroessen fuer Stirnraeder (Zylinderraeder) und Stirnpaare (Zylinderpaare) mit Evolventenverzahning

DIN 3993. Geometrische Auslegung von zylindrischen Innenradpaaren

Dobreva A (2011) Improving tribological characteristics of gear trains with internal meshing. In: Proceedings of scientific conference of University of Ruse, vol 50. Book 4, ISSN:1311-3321, pp 175–180

Dobreva A, Dobrev V (1993) Improving the tribological characteristics of heavy loaded gear boxes. In; Proceedings of the first balkan conference on tribology “Balkantrib’93”, vol 2.3. Sofia, pp 166–170
ISO 6336 (2006)(E) Calculation of load capacity of spur and helical gears
Linke H (2010) Stirnradverzahnung. Hanser Verlag, ISBN 978-3-446-41464-8

The Influence of the Sleeve Elastic Deformations on the Wave Bearing Performance in Heavy Loaded Transmissions

Nicoleta M. Ene and Florin Dimofte

Abstract The purpose of this paper is to study the influence of the elastic deformations of the planet/star gear on the performance of a wave bearing supporting an elastic planet/star gear. An iterative algorithm that takes into consideration the responses of both the wave bearing and gear was developed. The turbulence effects and the influence of the temperature on the oil viscosity were also introduced in the computations. The numerical simulations showed that the elastic sleeve deformations have an important effect on the bearing performance by increasing the minimum film thickness and the safety limit margins.

Keywords Wave bearings · Gears · Transmissions

List of Symbols

C	Bearing clearance, m
F_f	Friction force, N
F_r	Gear radial load, N
F_t	Gear tangential load, N
h	Fluid film thickness, m
k_θ, k_z	Correction coefficients for turbulent flow
L	Bearing length, m
M	Gear moment, Nm
p	Pressure, N/m^2
q	Total flow, m^2/s
P_j	Bearing pressure force at location θ_j, N
R	Bearing radius, m

N. M. Ene (✉) · F. Dimofte
The University of Toledo, OH, USA
e-mail: nicoleta.m.ene@gmail.com

F. Dimofte
e-mail: florin.dimofte@gmail.com

G. Dobre (ed.), *Power Transmissions*,
Mechanisms and Machine Science 13, DOI: 10.1007/978-94-007-6558-0_22,

r_n Gear neutral circle radius, m
r_p Pitch radius, m
z Axial coordinate, m
α Pressure angle, rad
θ Circumferential coordinate, rad
μ Lubricant viscosity, Ns/m^2
ω Angular velocity, rad/s

1 Introduction

Aerospace transmissions require higher and higher power density to reduce the weight and to increase the power. The metallic parts have to be very thin, but to carry very high loads. Due to the small thickness of the gear walls, the forces applied on the gear mesh can deform the gear. Therefore, a study of the influence of the gear deformations on the performance of the bearing that supports an elastic gear is of practical importance.

In this paper, a special type of fluid film bearings, called wave bearings, is used to support the planetary gears of a two-stage turboprop transmission.

2 Wave Bearing

The wave bearing was introduced by Dimofte (1995a, b) as an alternative to the plain journal bearing. Unlike the plain circular bearing, the wave bearing has a slight, continuous variation of its profile. The variation is such that a continuous waved profile is circumscribed onto the non-rotating bearing surface. For example, a wave bearing having three-wave profile on its non-rotating rotor is presented in Fig. 1. In Fig. 2, the wave amplitude is greatly exaggerated to exemplify the concept. The wave amplitude is usually a fraction (up to 0.5) of the clearance. The radial clearance is defined as the difference between the sleeve radius and radius of the mean circle of the waves. The ratio between the wave amplitude and clearance is usually called wave amplitude ratio. The wave amplitude ratio is a very important parameter of the bearing because the performance of the wave bearing is strongly influenced by it (Ene et al. 2008). The performance of a wave bearing also depends on the number of the waves, and on the position of the waves relative to the direction of the load. In the present study, the wave bearing sleeve is incorporated in the planet/star gears and the gears rotate around the bearing rotor.

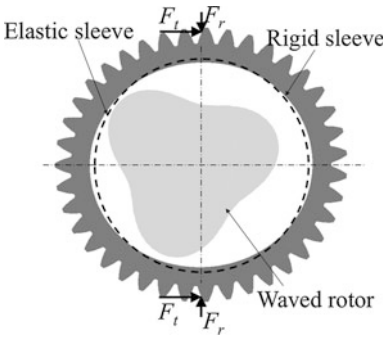

Fig. 1 Wave bearing supporting an elastic planet/star gear

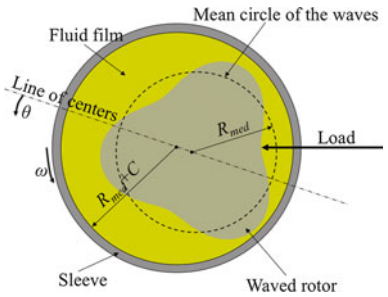

Fig. 2 Wave journal bearing with stationary rotor and rotational sleeve

3 Theoretical Analysis

For each planet/star gear, the tooth load can be resolved into a radial load–F_r and a tangential load–F_t, (Fig. 3).

The radial and tangential loads act on the pitch circle and are related by the following relation:

$$F_r = F_t \tan \alpha \tag{1}$$

where α is the pressure angle (Fig. 3). The radial and tangential loads are transmitted to the neutral circle of the bearing sleeve where the moment M is generated:

$$M = F_t(r_p - r_n) \tag{2}$$

In Eq. (2) r_p is the pitch radius and r_n is the neutral circle radius (see Fig. 3).

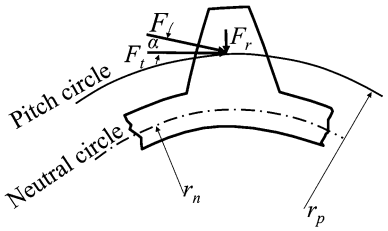

Fig. 3 Gear tooth loads

If the bearing sleeve is relatively thin, then its elastic deformation under the tooth load can be in the order of bearing's clearance and should be taken in consideration in the analyze of the bearing performance. Liu et al. (1976) proposed analytical equations to calculate the gear deformations when rolling element bearings support the gear. These equations can be adapted for wave bearings by replacing the rolling element contact loads with wave bearing pressure forces calculated in n locations along the fluid film circumference (Fig. 4). In these conditions, the radial deformation δ_{ri} at the location θ_i (Fig. 4) is given by:

$$\delta_{ri} = W_G(\theta_i) - \sum_{j=1}^{n} W_s(\varphi) P_j \tag{3}$$

where:

$$\varphi = \begin{cases} \theta_i - \theta_j & \theta_i \geq \theta_j \\ \theta_i - \theta_j + 2\pi & \theta_i < \theta_j \end{cases}$$

$$\begin{aligned} W_G(\theta_i) = {} & F_r[W_s(2\pi - \theta_i) + W_s(k\pi - \theta_i)] \\ & + F_t[W_t(2\pi - \theta_i) - W_t(k\pi - \theta_i)] + M[W_m(2\pi - \theta_i) - W_m(k\pi - \theta_i)] \end{aligned}$$

$$W_s(\varphi) = \frac{r_n^3}{4\pi EI}\left\{(\pi - \varphi)sin\,\varphi + \frac{1}{2}\left[(\varphi - \pi)^2 - \frac{\pi^2}{3} - \frac{3}{2}\right]cos\,\varphi - 2\right\}$$

$$W_t(\varphi) = \frac{r_n^3}{2\pi EI}\left\{(\varphi - \pi)cos\,\varphi + \frac{1}{4}\left[(\varphi - \pi)^2 - \frac{\pi^2}{3} - \frac{11}{2}\right]sin\,\varphi - \varphi\right\}$$

$$W_m(\varphi) = \frac{r_n^2}{2\pi EI}\left[(\varphi - \pi)cos\,\varphi + \frac{3}{2}sin\,\varphi - \varphi\right]$$

$$k = \begin{cases} 1 & 0 \leq \theta_i \leq \pi \\ 3 & \pi < \theta_i \leq 2\pi \end{cases}$$

where F_r, F_t and M are the tooth loads at the neutral circle location (Fig. 3), P_j is the wave bearing pressure force at location θ_j, EI is the flexural rigidity and r_n is the neutral radius.

The pressure distribution inside the bearing can be obtained by integrating the Reynolds equation:

$$\frac{1}{R^2}\frac{\partial}{\partial\theta}\left(\frac{h^3}{k_\theta \mu}\frac{\partial p}{\partial\theta}\right) + \frac{\partial}{\partial z}\left(\frac{h^3}{k_z \mu}\frac{\partial p}{\partial z}\right) = \frac{\omega}{2}\frac{\partial h}{\partial\theta} \tag{4}$$

where p is the pressure, h–the fluid film thickness, R–the radius of the mean circle of the waves of the shaft, ω–the rotational velocity, θ–the angular coordinate (Fig. 1), z–the axial coordinate, μ–the lubricant viscosity, and k_θ and k_z correction

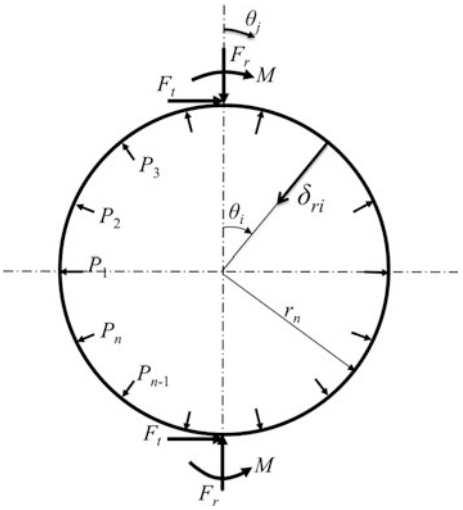

Fig. 4 Gear loads, bearing pressure forces, sleeve/gear deformations

coefficients for modeling the turbulent flow. At the equilibrium, the resultant of the bearing pressure forces must be equal to the resultant of the gear loads:

$$\int_{-\frac{L}{2}}^{\frac{L}{2}} \int_{0}^{2\pi} R \begin{bmatrix} p\cos\theta \\ p\sin\theta \end{bmatrix} = \begin{bmatrix} 0 \\ 2F_t \end{bmatrix} \tag{5}$$

The correction coefficients for turbulent flow are calculated using Constantinescu's model of turbulence (Frêne and Constantinescu 1975). According to Constantinescu, the correction coefficients are given by:

$$\begin{aligned} k_\theta &= 12 + 0.0136 Re_{eff}^{0.9} \\ k_z &= 12 + 0.0044 Re_{eff}^{0.9} \end{aligned} \tag{6}$$

where the effective Reynolds number is calculated with:

$$Re_{eff} = \begin{cases} 0 & Re_m < Re_{cr} \\ \left(\frac{Re_m}{Re_{cr}} - 1\right)\frac{\rho\omega Rh}{\mu} & Re_{cr} \le Re_m \le 2Re_{cr} \\ \frac{\rho\omega Rh}{\mu} & Re_m > 2Re_{cr} \end{cases}$$

$$Re_m = \frac{2\rho q}{\mu},$$

$$Re_{cr} = min\left(41.2\sqrt{\frac{R}{h}}, 2000\right) \tag{7}$$

and q is the total flow.

Due to computational time considerations, a constant mean temperature was assumed over the entire film. It was also assumed that the total heat generated in the fluid film is removed exclusively through fluid transport (convection). The heat removed from the fluid through conduction to the bearing walls is neglected. Also, the conduction within the fluid itself is neglected. With these assumptions, the lubricant temperature increase (the difference between the temperature of the lubricant entering the film and the constant mean temperature of the film) is given by:

$$\Delta T = \frac{F_f R\omega}{\rho c_v Q_{lat}} \tag{8}$$

where c_v is the lubricant specific heat, Q_{lat} is the rate of lateral flow and F_f is the friction force. The friction force is obtained by integrating the friction stresses on the bearing surfaces.

An iterative algorithm was developed to determine the elastic sleeve deformations for a given position of the sleeve characterized by an eccentricity e and an attitude angle ϕ. It was assumed that the sleeve deformations are initially zero. In the first step, a pressure distribution is obtained by solving the Reynolds equation, Eq. 4, for laminar flow. The correction coefficients for turbulent flow corresponding to the new pressure distribution are then calculated with Eq. 6. Also, the new mean film temperature (Eq. 8) and the new lubricant properties are determined. Then the Reynolds equation (Eq. 4) is solved again for the new turbulence correction coefficients and the new mean film temperature. The iterative process is repeated until the relative errors for the turbulence correction coefficients are smaller than prescribed values. Next, the elastic deformations of the sleeve corresponding to the new pressure distribution are computed with Eq. 3 and the new fluid film thickness distribution is obtained. The algorithm is repeated from step 1 for the new film thickness distribution until the convergence is attained.

The above algorithm is successively repeated for different bearing eccentricities and attitude angles until the equilibrium position is obtained (i.e. Eq. 5 are satisfied). A bisection algorithm was used for this purpose.

A finite difference scheme combined with a Gauss–Seidel method is used to solve the Reynolds equation. The axial ends of the bearing are assumed to be exposed to atmospheric pressure. The pressure in the region of supply pockets is supposed constant and equal to the supply pressure. The Reynolds boundary conditions are considered for the cavitation regions.

4 Numerical Results

A transmission designed for a turbo prop application was considered for the numerical analysis. Two steps are used to reduce the turbo shaft speed to the propeller speed. The first step of the transmission is a star step: the carrier is stationary, the input is through the sun, and the output is from the ring. The second

stage is a planetary stage: the input is through the sun, the ring is stationary, and the output is from the carrier. The most important geometrical parameters of the star/planet gears and of the wave bearings that support the transmission shafts are presented in Tables 1 and 2, respectively. The speeds of the wave bearings in the star and planetary stages are 15,960 and 3,948 rpm, respectively.

Two running regimes were analyzed for each transmission step:

- The star step:
  - a low loaded regime (816 N load, 15,960 rpm rotational speed)
  - a heavy loaded regime (7,107 N load, 15,960 rpm rotational speed)
- The planetary step:
  - a low loaded regime (1,760 N load, 3,952 rpm rotational speed)
  - a heavy loaded regime (5,940 N, 3,952 rpm rotational speed)

For all the above regimes, the oil (Mil-L-23699) is supplied to the bearing through three supply pockets situated at 120° one from each other. The oil supply pressure is 5.5 bars at 120 °C. For each running regime, two different situations were considered: (1) the sleeve is rigid; (2) the sleeve is elastic and the elastic deformations of the sleeve were taken into consideration.

The rotor—sleeve/gear inner diameter profiles with and without taking into consideration the sleeve elastic deformations and the pressure distributions for the elastic cases are presented for all the above regimes in Figs. 5, 6, 7, 8. In Figs. 5, 6, 7, 8, the bearing clearance, wave amplitude, and sleeve/gear deformations were greatly exaggerated compared to the rotor or sleeve diameters to visualize the effect. It can be seen from Figs. 5 and 7 that the sleeve/gear deformations are very small (less than 10 %) at low loads. Therefore, at low loads the sleeve/gear elastic deformations do not have an important effect on the wave bearing performance.

At high loads, the elastic deformations of the gear/sleeve have important values (Figs. 6 and 8). In these cases, the minimum film thicknesses of the bearings with elastic sleeves are almost or more than double the minimum film thickness corresponding to the rigid cases. A direct consequence of the minimum film thickness increase is the increase of the safety operation margin. It can be also seen from Figs. 6 and 8 that at heavy loaded regimes, the bearing load is supported by two peaks of pressure. Fresh oil that cools the film is supplied between them.

Table 1 Geometrical characteristics of the planet/star gears

Major tooth diameter, mm	69.85
Pitch tooth diameter, mm	66.675
Minor tooth diameter, mm	62.686
Tooth width diameter, mm	20.828
Gear width, mm	21
Tooth pressure angle, deg	22.5
Number of teeth	42

Table 2 The geometrical characteristics of the wave bearings

	Stage I (star)	Stage II (planet)
Diameter, mm	45	45
Length, mm	21	26
Clearance, microns	16	11
Wave amplitude ratio	0.3	0.3

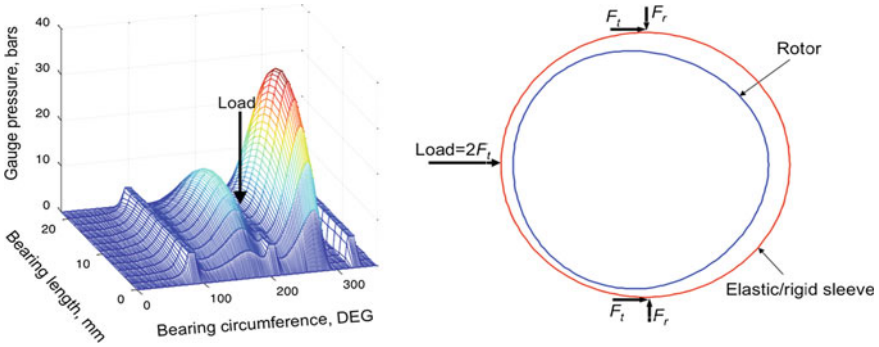

Fig. 5 Pressure distribution and sleeve deformation for star gear (15,960 rpm, 816 N)

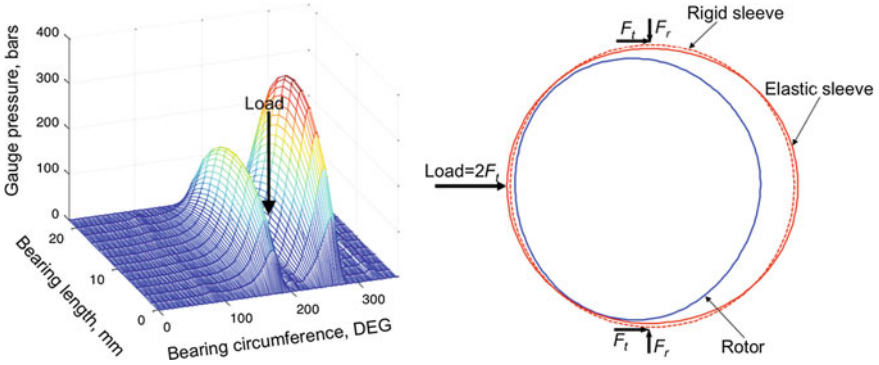

Fig. 6 Pressure distribution and sleeve deformation for high loaded star gear (15,960 rpm, 7,107 N)

Therefore, the sleeve elastic deformations significantly influence the bearing performance under heavy loads.

A summary of the results for the minimum film thicknesses corresponding to the rigid and elastic cases is presented in Table 3.

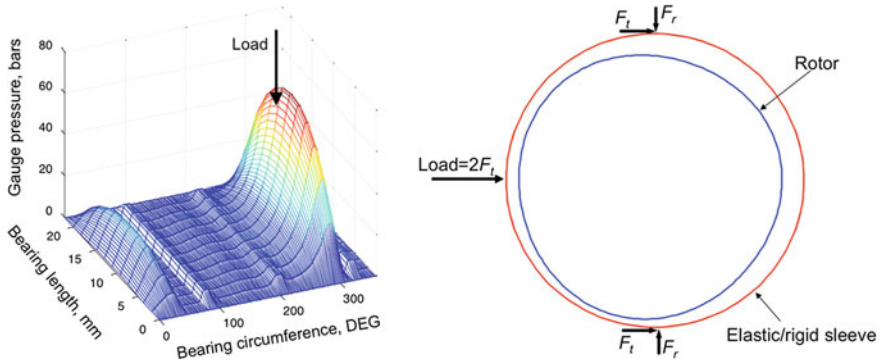

Fig. 7 Pressure distribution and sleeve deformation for low loaded planet gear (3,952 rpm, 1,760 N)

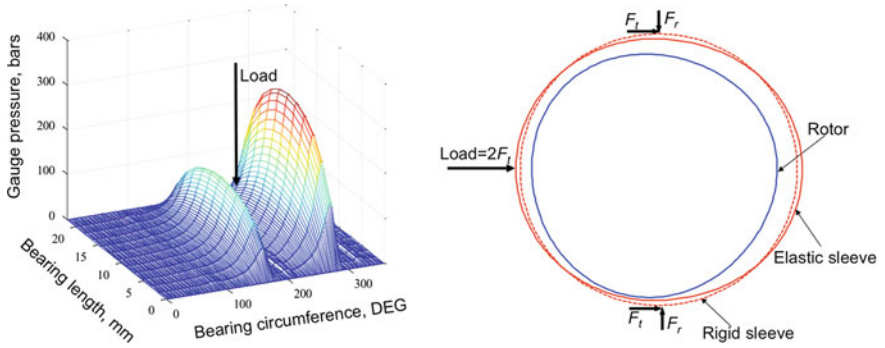

Fig. 8 Pressure distribution and sleeve deformation for heavy loaded planet gear (3,952 rpm, 5,940 N)

Table 3 Minimum film thickness. Comparison between elastic and rigid gear/sleeve

	Speed, rpm	Load, N	h_{min}, microns elastic sleeve	h_{min}, microns rigid sleeve	Δh, %
Star stage	15,960	816	16	15.6	2.45
	15,960	7,107	2.97	1.43	108.3
Planet stage	3,952	1,707	5.58	5.10	9.4
	3,952	5,948	2.2	1.14	93

5 Conclusions

The influence of the elastic deformations on the performance of a wave journal bearing supporting an elastic gear was studied. Low and high loaded running regimes for a star and a planetary stage of a turbo prop transmission were considered. The turbulence effects and the effect of the oil inlet temperature were

introduced in the computations. The numerical simulations showed that at high loaded regimes the elastic deformations have an important effect on the wave bearing performance by increasing the bearing minimum film thickness and safety operation limit.

References

Dimofte F (1995a) Wave journal bearing with compressible lubricant—part I: the wave bearing concept and a comparison to the plain circular bearing. STLE Tribol Trans 38(1):153–160

Dimofte F (1995b) Wave journal bearing with compressible lubricant—part II: a comparison of the wave bearing with a groove bearing and a lobe bearing. STLE Tribol Trans 38(2):364–372

Ene NM, Dimofte F, Keith TG (2008) A stability analysis for a hydrodynamic three-wave journal bearing. Tribol Int 41(5):434–442

Frene J, Constantinescu VN (1975) Operating characteristics of journal bearings in the transition region. In: Proceedings of the 2nd leeds-lyon symposium on tribology, pp 121–124

Liu JY, Chiu YP (1976) Analysis of a planet bearing in a gear transmission system. J Lubr Technol 70–76

Contribution to the Development of Cylindrical Gears

Gorazd Hlebanja and Jože Hlebanja

Abstract Authors propose S-gears as an improvement with regard to involute gears. The tooth flank profile of the former is based on the basic rack profile, defined as an analytic curve and implies the shape of a tooth flank which is the matter of discussion in the paper. An important feature of S-gears is the convex-concave contact of a pinion and a gear in the meshing start and meshing end areas which provides better characteristic as in E-gears. Therefore, the mechanism of sliding, the oil film build-up and power losses will be demonstrated. In this context several important features, e.g. curvatures, Hertzian stresses, temperatures, oil film thickness, velocity circumstances will be also discussed. The S-type gears can be used in all scales from small to large and in planetary gear trains as well.

Keywords Cylindrical gears · Non-involute gear geometry · Gear contact · Meshing circumstances

List of Symbols

P_i	Point on the rack profile
G_i	Point on a gear tooth flank
U_i	Point on the path of contact
x, y	Cartesian coordinates
a_p	Size factor
n	Exponent
t_{Pi}, t_{Gi}	Tangents in point P_i, G_i
α_C	Pressure angle
α_{Gi}	Inclination angle in G_i

G. Hlebanja (✉) · J. Hlebanja
University of Ljubljana, Ljubljana, Slovenia
e-mail: gorazd.hlebanja@fs.uni-lj.si

J. Hlebanja
e-mail: joze.hlebanja@siol.net

G. Dobre (ed.), *Power Transmissions*,
Mechanisms and Machine Science 13, DOI: 10.1007/978-94-007-6558-0_23,

ρ_{Gi}	Radius of curvature in G_i
m	Module
ρ_1, ρ_1	Radii of curvature—gear 1, gear 2
ρ_{red}	Reduced radius of curvature
F_t	Tangential force
F_b	Contact force
α_U	Incidence angle
b	Gear width
E	Modulus of elasticity
v	Poisson's ratio
σ_H	Hertzian stress
$\mathbf{v_p}$, $\mathbf{v_s}$	Absolute velocity—gear, pinion
$\mathbf{v_{rP}}$, $\mathbf{v_{rS}}$	Relative velocity—gear, pinion
$\mathbf{v_{At}}$	Tangential velocity along the path of contact
$\mathbf{v_g}$	Sliding velocity
$\mathbf{v_t}$	Tangential velocity
φ_{UP}, φ_{US}	Angular position—gear, pinion
ω_P, ω_S	Angular velocity—gear, pinion
$\vartheta_{fl}\vartheta_M$	Flash, mass temperature
μ	Friction coefficient
w_{tb}	Line load
E'	Reduced Young's modulus
v	Poisson's ratio
λ	Thermal conductivity
ρ	Density
c	Specific heat
h_0	Minimal oil film thickness
u	Average contact velocity
η_0	Dynamic viscosity (atm. circumstances)
α	Pressure viscosity coefficient
κ	Ellipcity parameter (a, b—ellipse semi-axes)

1 Introduction

Gears are frequent choice for power transmission from fast power sources to working machines. Transmitted power levels can vary from low in miniature mechanisms to very high in contemporary wind power plants. Power ranges can exceed 5 MW in the latter.

Transmission gears from the engine to the drive wheels are also of great importance in the automotive and truck industry. The overwhelming majority of gears used in practice are involute. User requirements are increasing, therefore the

gears should provide more accurate transfer of motion, better endurance, higher efficiency and the lowest dimensions, which are nowadays the major trends in gear development, which should be followed by both, the researchers and gear manufacturers, as reported by Blickle (2010), Hirt (2010), Joachum et al. (2010).

The involute gear shape has been in use from the time of Euler and is based on the mathematical form of the involute function. The involute tooth flank can be put through the kinematic velocity pole which furthermore resides on the kinematic circle and divides the tooth flank to the addendum and dedendum part.

The active length of the tooth dedendum of the involute gear is relatively short; the corresponding curvature radius in the direction of involute starting point is decreasing to zero. Very high contact loads and sliding arise in this area due to power transmission from a pinion to a gear, which cause energy losses because of friction and consequently severe damages of teeth flanks in form of wear, micro and macro pitting as stated by Butterfield (2010) and Lütig (2007) in his dissertation. S-gears exhibit more appropriate shape of tooth flank profile, with higher loading capacity and lower energy losses in power transmission.

S-gears are illustrated in Fig. 1. The tooth flank profile is based on the basic rack profile as proposed by Hlebanja (2010). The rack profile is defined as an analytic curve, Eq. (1), for which the derivatives are also defined.

$$y_{Pi} = a_p(1 - (1 - x_{Pi})^n) \tag{1}$$

where (x_{Pi}, y_{Pi}) are Cartesian coordinates originating in the pitch point C, a_p parameter designating a size factor (in this case with the value $a_p = 1{,}30{,}267$), and n is the exponent ($n = 1{,}9$). Both, a_p and n, have decisive influence on expected

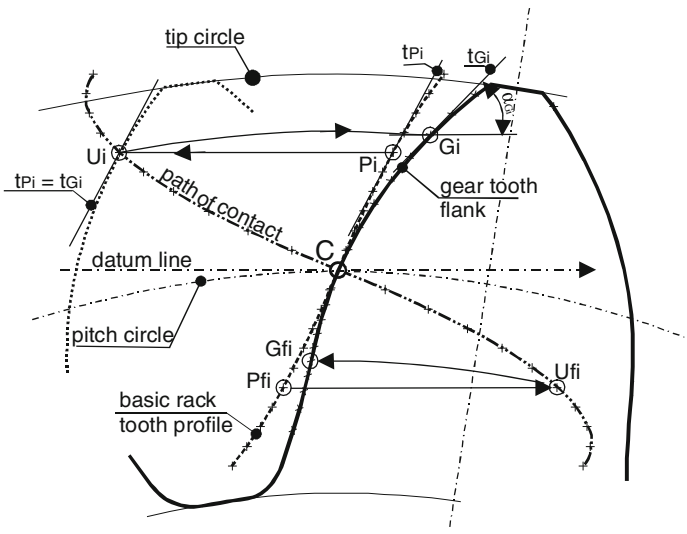

Fig. 1 S-gear tooth flank profile creation

characteristics of the designed gears. Equation (1) defines the addendum part of the rack profile and the half symmetric counterpart defines its dedendum part.

Furthermore, the tangent t_{Pi} is defined for any point P_i on the rack profile. Point U_i on the path of contact is defined based on t_{Pi}. U_i can be regarded as a rack's cutting edge generating a gear tooth flank profile point G_i.

The rack tooth flank distance from the velocity pole C in point U_i is P_iU_i, which is exactly the arc U_iG_i length on the reference circle for which the emerging gear point G_i rotates around its axis. The transformations from P_i to U_i and from U_i to G_i are unique and reversible, that is bijective. The path of contact is characterized by its half symmetry. Properties of S-gears can be illustrated by mating gear and pinion shown in Fig. 2. The dedendum of one gear is in contact with the addendum of the other gear during mating which corresponds to a half of the path of contact, which is unique for a given module regardless of the number of teeth. An important feature of S-gears is a convex-concave contact of a pinion and a gear in the meshing start and end areas (in vicinity of points A and E). Another advantage is minimal teeth number of S-gears, which can be as low as four.

S-type rack differs from involute rack by parabolic shaped flanks. With the defined rack the same manufacturing technology can be employed in S-gears as in involute case, however always with appropriate cutting profiles.

Regarding the geometric shape S-gears are usable for small and micro gears in miniature applications (Hlebanja 2011) as well as for large gears, suitable for high power transmission.

Details of geometric definitions and manufacturing principles of S-gears have been disclosed in several recent papers (e.g. Hlebanja 2010, 2011). Therefore, several important characteristics of S-gears will be revealed and discussed in the continuation, which prove their advantages, not only in spur gears, but also in

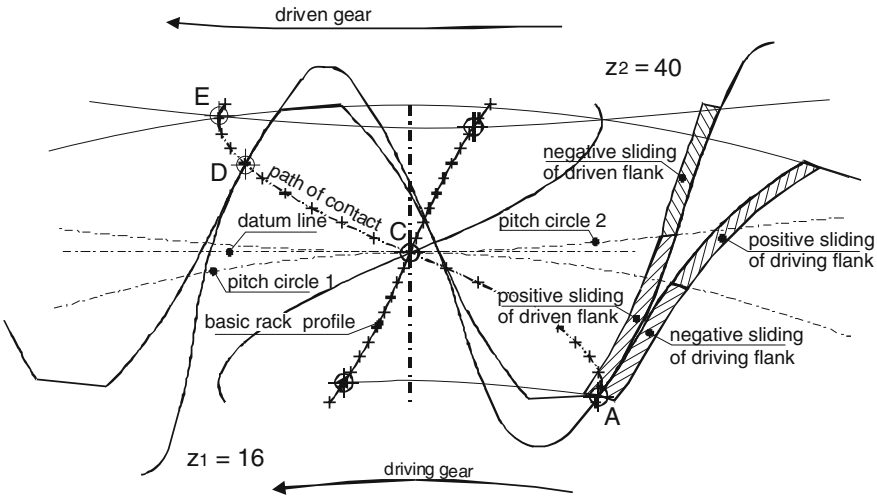

Fig. 2 Meshing circumstances and sliding zones

helical and skew gears as well. S-gear geometry is also appropriate in internal gears, thus enabling design of planetary gear trains.

2 Important Characteristics

2.1 Tooth Flank Curvature

The tooth flank profile is defined continuously for any point, based on the previously explained transformations from the rack profile to the path of contact and at last to the gear tooth flank. Its curvature is mathematically defined by an expression containing first and second derivative. Knowing tooth profile inclination angle for any point of the profile implies tangent and thus first and second derivative in that point (Hlebanja 2010). The curvature is therefore given by a simple Eq. (2)

$$\rho_{Gi} = \frac{1}{\cos \alpha_{Gi}} \cdot m. \tag{2}$$

Characteristic of the meshing gears is that both gears dedendum flanks are partly concave, the rest being convex, whereas both addendum flanks are convex. Both flanks are convex around the pitch point, with relative high radii of curvature. Another important observation is that a concave-convex contact appears in the vicinity of meshing start and meshing end areas, which implies better loading circumstances there.

In order to evaluate tooth flank durability in a contact point the reduced radii of curvature ρ_{red} are necessary

$$\rho_{red} = \frac{\rho_1 \rho_2}{\rho_1 \pm \rho_2} \tag{3}$$

If the contact between two flanks is convex–convex, both factors of the denominator should be summed, otherwise (convex-concave case) they should be subtracted.

Distribution of the reduced radii of curvature over the path of contact diagrammatically represented in Fig. 3, reveals some interesting facts. First, comparatively high values of ρ_{red} are in the zones AB and DE are due to convex-concave contact, indicating that the contact load is smaller and lubrication conditions are better; quite so two pairs of teeth are in contact in AB and DE. ρ_{red} changes are small and have a local maximum in the pitch point in the zone of the single pair contact BCD, which indicates evenly distributed power transmission. The actual curve depends on geometrical data (number of teeth, module) of a gear pair and the value in C equals that in involute gear shape.

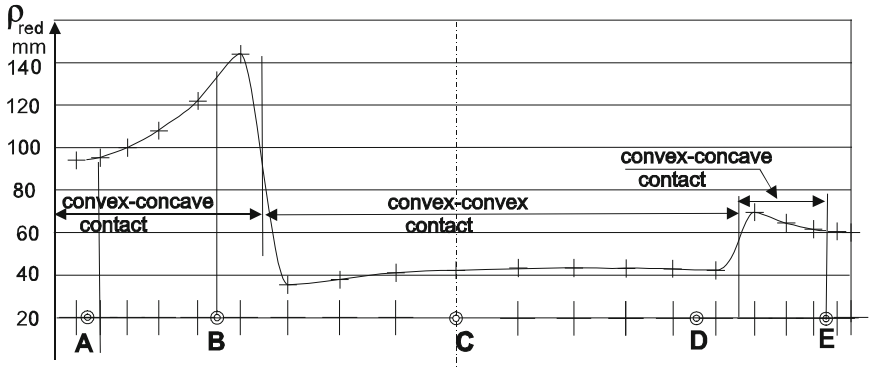

Fig. 3 Reduced radii of curvature along the path of contact $m = 30$ mm, $z_1 = 42$ and $z_2 = 12$

2.2 Contact Force and Hertzian Pressure

The dedendum part of a tooth flank is the most loaded area in power transmission from a gear to a pinion, due to negative sliding in that area. This is why this loading state is of particular importance and discussed in the following paragraphs. Contact load in a particular time instant appears in the contact spot on the path of contact and is influenced by the contact force F_b, which is acting rectangular to the teeth flanks in the direction of the kinematic pole C. The situation is illustrated in Fig. 4 particularly for contact point B. The contact force magnitude along the path of contact is variable conforming to the incidence angle α_U changes, as indicated in Fig. 5, and defined by following equation

$$F_b = \frac{F_t}{\cos \alpha_U} \tag{4}$$

Hertzian pressure as a common measure of contact load of mating teeth flanks is expressed by

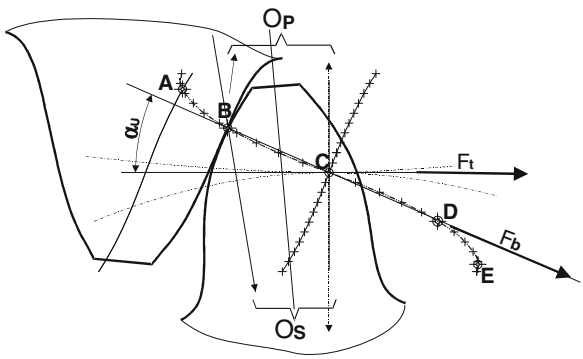

Fig. 4 Forces resulting on teeth flanks

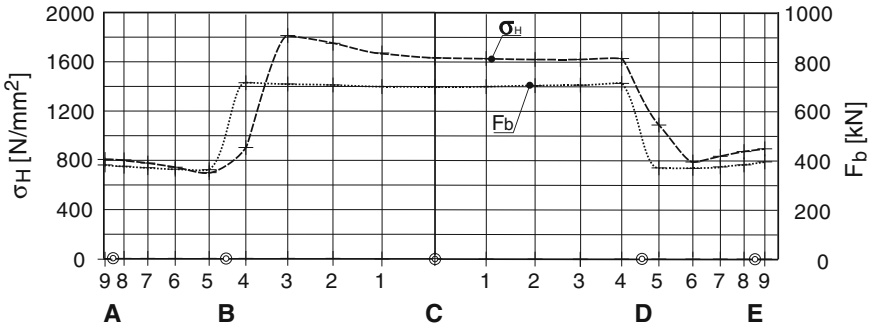

Fig. 5 Hertzian pressure and contact force along the path of contact $m = 30$ mm; $b \approx 6{,}7\ m = 200$ mm; $E = 2{,}06 \times 10^6$ N/mm^2; $\nu = 0{,}3$

$$\sigma_H = \sqrt{\frac{F_b E}{2\pi b \rho_{red}(1-\nu^2)}} \leq \sigma_{Hdop}. \tag{5}$$

However, Hertzian pressure may not exceed maximal allowable limit σ_{Hdop}. The contact force F_b, tooth width b and reduced radius of curvature ρ_{red} in Eq. (5) are those design parameters which decisively influence gear durability. The tangential force F_t, transmitted from the driving to the driven gear, is distributed among two gear pairs in the zones of double contact AB and DE. This is also true for F_b, which is clearly indicated in the diagram, Fig. 5.

2.3 Velocity Circumstances

Velocity circumstances in the gear tooth contact points, appearing along the path of contact, decisively influence oil film thickness. They depend on the tooth flank geometry derived from the path of contact, whereas each point on the tooth flank profile features a unique curvature radius. Absolute velocities, relative velocities of teeth flanks, and the contact point movement velocity in the tangential direction to the path of contact can be distinguished with regard to the tangential direction to the teeth flanks in the contact point. Two critical states are illustrated in Fig. 6, namely first in the vicinity of the meshing start and then in the vicinity of the meshing end. The absolute velocity of the pinion tooth flank is represented by the vector $\mathbf{v_s}$, and the absolute velocity of the gear by $\mathbf{v_P}$. The relative velocities $\mathbf{v_{rS}}$ and $\mathbf{v_{rP}}$ act tangentially to corresponding teeth flanks, whereas $\mathbf{v_{At}}$ is the velocity of the contact point in the direction of tangent to the path of contact. Thus, expressions for $\mathbf{v_s}$ and $\mathbf{v_P}$ are

$$\vec{v}_S = \vec{\omega}_S \times \vec{r}_S \ \text{ and } \ \vec{v}_P = \vec{\omega}_P \times \vec{r}_P \tag{6}$$

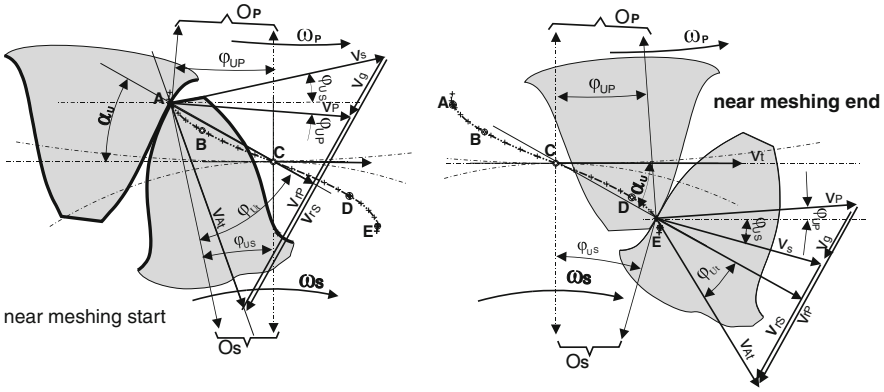

Fig. 6 Velocity circumstances for S-gears *left*—in the meshing start area; *right*—in the meshing end area

Velocity components in the direction of teeth flank surfaces influence the oil film formation; the corresponding velocity of the pinion $\mathbf{v_{rS}}$ and the gear $\mathbf{v_{rP}}$ are

$$\vec{v}_{rS} = \vec{v}_S - \vec{v}_{At} \text{ and } \vec{v}_{rP} = \vec{v}_P - \vec{v}_{At} \tag{7}$$

The sliding velocity $\mathbf{v_g}$ is defined as the difference of absolute velocities of teeth flanks in the contact point or as the difference of both relative velocities.

$$\vec{v}_g = \vec{v}_S - \vec{v}_P \text{ and } \vec{v}_g = \vec{v}_{rS} - \vec{v}_{rP} \tag{8}$$

Values of both relative velocities can be calculated from geometric relations.

$$\begin{aligned} v_{rP} &= v_P \sin(\alpha_{Ui} - \varphi_{UP}) + v_t \cos\alpha_{Ui} \tan\varphi_{Ui} \\ v_{rS} &= v_S \sin(\alpha_{Ui} - \varphi_{US}) + v_t \cos\alpha_{Ui} \tan\varphi_{Ui} \end{aligned} \tag{9}$$

The diagram Fig. 7 illustrates functional dependence of relative velocities of the path of contact and these particular calculations assume the tangential velocity amounting to 2,26 m/s.

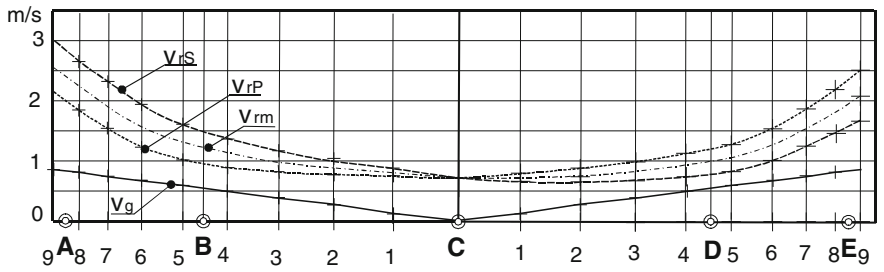

Fig. 7 Diagram of the relative velocities along the path of contact v_{rm} is aritmetic average of v_{rS} and v_{rP}

2.4 Temperatures of Teeth Flanks in a Contact Spot

The contact temperature is a function of the gear bulk material temperature ϑ_M and the flash temperature ϑ_{fl}. The first is a a steady temperature during operation, and the latter is an instantaneous temperature of the contact appearing due to local friction heat and reaches its maximal value at the gear meshing point—contact; afterwards it diminishes. The apparent time of the contact depends on angular velocities of gears, on actual geometry and surface parameters, it is exceedingly short in general and thus its temperature contribution is named flash temperature. The flash temperature is an important influencing factor in emergence of scuffing and to great extent also of micro-pitting. If angular velocities are rather low then no high temperature shocks should be expected. The flash temperature functional dependence on the path of contact is illustrated in diagram, Fig. 8. The Block's expression for the line contact (Blok 1963 and Theyse 1967) was employed in calculations:

$$\vartheta_{fl} = 0,62\mu(w_{tb})^{0,75}\left(\frac{E'}{\rho_{red}}\right)^{0,25}\frac{v_g}{\sqrt{B_{MS}v_{rS}}+\sqrt{B_{MP}v_{rP}}} \tag{10}$$

where $E' = E/(1\text{-}\nu^2)$ and $\sqrt{B_{MS,P}} = \sqrt{\lambda\rho c} = 12,5\left[\mathrm{N/mms^{0,5}K}\right]$. The heat contact coefficient is material property—the above value is for steel. The other values are $\lambda = 47,5[\mathrm{W/(mK)}]$, $\rho = 7800\,[\mathrm{kg/m^3}]$, $c = 440\,[\mathrm{J/(kgK)}]$. An average value for the friction coefficient results from data (Nieman and Winter 1989) and amounts to 0,08. All other variables are varying along the path of contact and represented in preceding figures. The diagram represented in Fig. 8 indicates that thermal load of the teeth flanks in the zones of double contact is comparable smaller as in the zone of single contact. This is due to lower teeth load and higher reduced radii of curvature, whereas in the single contact zone the flash temperature diminishes towards C, where its value is 0, which is due to lowering of the sliding velocity.

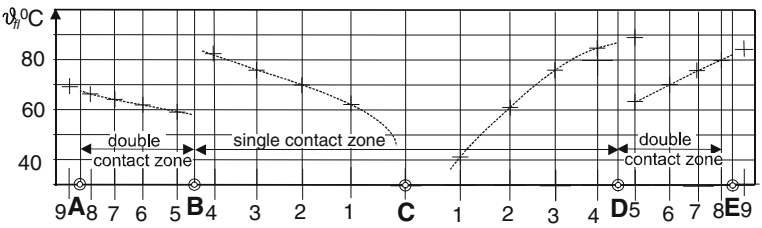

Fig. 8 Flash temperature along the path of contact (the bulk temperature should be added to the above values)

2.5 Oil Film Thickness

Micro-pitting is fatigue damage of gear teeth flanks where the contact area is surface-hardened and ground. Emerging micro-damages, lowering transmission accuracy, evolve into gearing failures. The main cause of micro-pitting is attributed to insufficient lubrication of the contact surfaces due to slow sliding speeds and high contact loads—i.e. slow running gears is mixed lubrication (Stachowiak and Batchelor 2006, p. 311). Therefore, the oil film thickness between the meshing gear flanks is one of crucial parameters in this context and it should be higher as roughness. The oil film thickness is influenced by: load, contacting teeth flank surfaces velocities, sliding velocities, temperature, surface roughness, oil characteristics, material properties, and tooth shape which actually transmits the load. Another important factor is friction heat governing oil temperature which affects its viscosity. Dimensioning of gears with regard to micro-pitting is based on oil film thickness based on elasto-hydrodynamic lubrication theory. Due to EHL importance, research led to many improvements. However, most of them derive from Dawson's and Higginson's (1977) work. Following equation (Stachowiak and Batchelor 2006) was used for a general elliptic type of contact in order to get basic relations:

$$\frac{h_0}{\rho_{red}} = 3,63\left(\frac{u\,\eta_0}{E'\,\rho_{red}}\right)^{0,68}(\alpha E')^{0,49}\left(\frac{F_b}{E'\rho_{red}^2}\right)^{-0,073}\left(1 - 0,61e^{-0,68\kappa}\right). \quad (11)$$

Since the contact surfaces, dealt with here, are cylindrical their contact is the line contact. Therefore, the longer ellipse axis limits to infinity, so the ellipticity parameter value is 0. Assuming equilibrium bulk thermal circumstances and given material, Eq. (11) can be rearranged to

$$h_0 = \left[3,63\eta_0^{0,68}\alpha^{0,49}E'^{-0,117}\right]u^{0,68}\rho'^{0,466}W^{-0,073}. \quad (12)$$

Variables in Eq. (12) are the average contact velocity, the reduced radius of curvature and the contact force, whereas the values in brackets are constant for given conditions. The oil viscosity parameters in calculations are from Stachowiak and Batchelor (2006, p. 21). Heavy industrial oil was selected having high dynamic viscosity and the pressure viscosity coefficient values collected in Table 1. The reduced elasticity module for steel amounts to 206×10^9 N/m^2.

Knowing above data and functional values for the average velocity (Fig. 7), the contact force (Fig. 5) and the reduced radius of curvature along the path of contact (Fig. 3), a diagram, Fig. 9, can be drawn. The curve in the diagram has been

Table 1 Viscosity parameters for a heavy industrial oil

ϑ	30 °C	60 °C
$\eta 0$	153×10^{-3} Pa	34×10^{-3} Pa
α	$23,7 \times 10^{-9}$ m^2/N	$20,5 \times 10^{-9}$ m^2/N

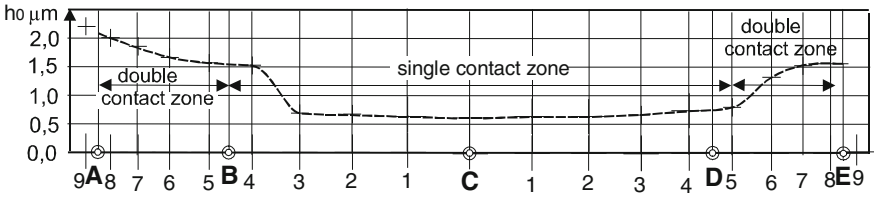

Fig. 9 Oil film thickness course along the path of contact

calculated for operating conditions with the temperature 30 °C. The oil film thickness lowers for about 33.6 % when the temperature is 60 °C. Thus, the minimal oil thickness in the kinematic pole C is 0.21 µm. This is the same value as the value in C for involute gears with the same module and the same gear ratio. Oil film thickness enlarges considerably in double contact zones near both end contact zones.

Considering, that the potential danger of micro-pitting exist in the zone of meshing start for involute gears (Höhn et al. 2003), S-gears exhibit advantage in this context due to the tick oil film in this area, which diminishes possibility of damage.

3 Conclusion

Solutions for preventing or diminishing micro-pitting occurence are prevailingly searched for in the direction of better lubrication means, in high quality surface treatment (super-finishing), in gear tooth flank profile change in meshing start area, and finally in better materials. This proposal introduces a new gear tooth flank profile—S-gear tooth flank profile, which assures higher comparative curvature radii, and thus lower contact load and higher relative velocities of the contact surfaces which implies better lubrication.

Not only that the curvature radii are higher, the mating gears exhibit convex-concave contact in the vicinity of the contact start and contact end, whereas slowly varying curvature is characteristic for the central area.

Due to their S-shape, the velocity characteristics of mating gears are improved, especially in both external areas with high relative velocities and low sliding velocity.

The meshing start zone in involute gears represents potential danger of micro-pitting, whereas S-gears exhibit advantage in this context due to the tick oil film in this area, which diminishes possibility of damage.

S-gears can be used in a large and small scale application and planetary gear trains. Comparatively smaller outer diameter of internal S-gears also implies smaller weight.

It is true that special tools are necessary to produce S-gears, however with contemporary CNC machine tools and technologies this does not denote much of an obstacle.

References

Blickle R (2010) SEW: crisis scenarios are driving forces for innovation and progress. In: International conference on gears, Munich, 4–6 Oct 2010

Blok H (1963) The flash temperature concept. Wear 6:483–494

Butterfield S (2010) Wind turbine micro-pitting workshop. Technical report NREL/TR 500-46572, February 2010

Dowson D, Higginson GR (1977) Elasto-hydrodynamic lubrication. SI Edition. Pergamon Press, Oxford

Hirt M (2010) What are the influences of the global financial and economic crisis on the transmission and gear market worldwide. In: International conference on gears, Munich, 4–6 Oct 2010

Hlebanja J, Hlebanja G (2010) Spur gears with a curved path of contact for small gearing dimensions. VDI Berichte 2108:1281

Hlebanja G (2011) Specially shaped spur gears: a step towards use in miniature mechatronic applications. In: 7th International science conference on research and development of mechanical elements and systems—IRMES 2011, April 27–28. Zlatibor, Serbia. Proceedings. Niš: Mechanical Engineering Faculty, pp 475–480

Höhn BR, Oster P, Steingröver G (2003) The new micro-pitting short test 1. In: International conference power transmissions'03, Varna, Bulgaria, 11–12 Sept 2003

Joachum F-J, Börner F-J, Kurz N (2010) How to minimize power losses, transmissions, axles and steering systems. VDI-Berichte 2108:111

Lütig G (2007) Großgetriebe-Graufleckigkeit, Dissertation. Universität Bochum, Bochum

Nieman G, Winter H (1989) Maschinenelemente, Band II: Getriebe allgemein, Zahn-rad-getriebe Grundlagen, Stirnrad Getriebe. ISBN 3-540-11149-2, Springer Berlin, Heidelberg, New York

Stachowiak GW, Batchelor AW (2006) Engineering tribology. Elsevier Butterworth-Heinemann, Oxford

Theyse FH (1967) Die Blitztemperaturhypothese nach Blok und ihre praktische Anwendung bei Zahnrädern. Schmiertechnik 14:22–29

Transfer of Motion by Closed Contour: Basis of Cvt

Konstantin Ivanov and Elena Yaroslavceva

Abstract Continuously variable transmission contains the closed gear differential and the controlled device. The elementary toothed continuously variable transmission has form of the gear closed differential with two degrees of freedom. The gear differential with the closed contour of toothed wheels creates additional constraint and supports a transition regime of motion from a start-up to bi-mobile regime with independent stepless regulating. It is necessary to prove that closed gear differential in itself carry out a function of a controlling device. The equations of interconnection of power, kinematic and geometrical parameters of transmission in statics, kinematics and dynamics are searched out. The synthesis of transmission consists in determination of teeth wheels numbers on a condition of overcoming the given maximum moment of resistance.

Keywords Transmission · Closed contour · Equilibrium · Stepless regulating

List of Symbols

Symbol	Description
CVT	Continuously variable transmission
H	Carrier
F	Force
R	Reaction
M	Moment
s	Displacement
v	Speed

K. Ivanov (✉)
Almatinsky University of Power Engineering and Telecommunications,
Almaty, Kazakhstan
e-mail: ivanovgreek@mail.ru

E. Yaroslavceva
Saint-Petersburg University of Technology and Design,
Saint-Petersburg, Russia
e-mail: yaroslavceva_elena@rambler.rud

G. Dobre (ed.), *Power Transmissions*,
Mechanisms and Machine Science 13, DOI: 10.1007/978-94-007-6558-0_24,

φ	Instant angle of turn
ω	Angular speed
a, b, c, d, l, e	Sizes of links
r	Radius of link

1 Introduction

At last time a continuously variable transmission (CVT) which contains the closed gear differential mechanism with two degrees of freedom and the controlling device has been extended and patented. The controlling device imposes an additional constraint leading to definability of motion and self-regulating. Transmission has only one input (one engine) and meets the requirement of theoretical mechanics and theory of mechanisms and machines on Levitskiy and Markeev (1979, 1990): number of initial links (or input links) of a mechanism should be equal to number of degrees of freedom.

In designs of Volkov (2004) and Crockett (1990) the engine transmits a motion to fluid converter which drive two links of gear differential with two degrees of freedom (Fig. 1). The fluid converter creates an additional hydrodynamics constraint which realizes a self-regulating. An output link of the differential has definability of motion with stepless self-regulating.

However the closed contour of the gear differential mechanism in itself is capable to impose additional constraint on motion of links. This property is used in the patent of Harries. The transmission has self-regulation in operating regime

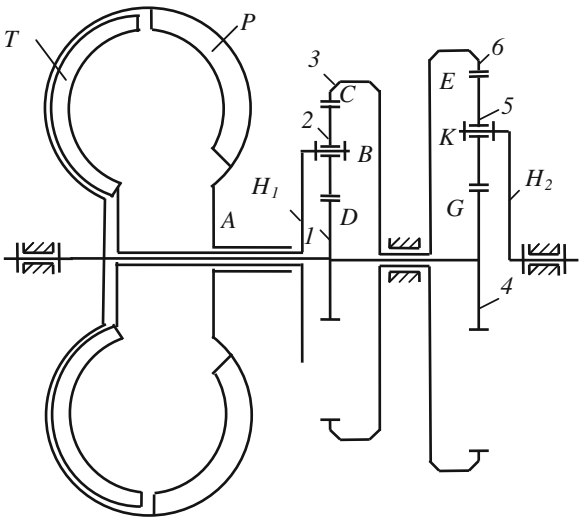

Fig. 1 Continuously variable transmission with the hydraulic converter *P*—pump; *T*—turbine

with two degrees of freedom. However in this transmission the brake of one of wheels carries out an additional constraint for the start.

The elementary designs of transmission in form gear differential mechanism on patents of Ivanov and Yaroslavtseva (1996, 2010) create additional constraint by way of self-braking and inertial properties of the mechanism.

In all patented designs of continuously variable transmission the closed contour is used. However the theoretical description of interacting parameters of transmission of Volkov (2004), Crockett (1990) and Harries (1991) is executed without taking into account presence of two degrees of freedom. In patents of Ivanov and Yaroslavtseva (1996, 2010) an interacting of parameters of gear differential is presented on the basis of a principle of virtual works. However in them there is no theoretical substantiation of a technique of research.

Earlier in theoretical works of Ivanov (2007, 2010) the opportunity of transfer motion in a gear differential by means of the closed contour has been researched. The analytical description of transfer motion in the gear mechanism with two degrees of freedom has been executed on the basis of a principle of virtual works. It has been shown, that the closed contour imposes additional constraint on motion of links that leads to definability of motion of the kinematic chain with two degrees of freedom at presence only one input. However in these works there is no theoretical substantiation of an opportunity of use of a principle of virtual works.

The purpose of the present work is to prove theoretically a definability of motion of gear differential with two degrees of freedom at presence only one input and to create analytical dependences of interconnection parameters of motion of gear continuous variable transmission with stepless self-regulation.

The research is executed on the basis of laws of theoretical mechanics and theory of mechanisms and machines.

2 Transfer of Motion in the Closed Differential with Two Degrees of Freedom

Subject of research is the closed toothed differential mechanism with two degrees of freedom which represents a continuously variable transmission. The toothed continuously variable transmission (Fig. 2) has form of the closed differential mechanism.

Toothed wheels 4–1, 2, 3–6, 5 form the closed contour. On the input carrier H_1 the external active motive moment M_{H1} acts. On an output link H_2 the external active moment of resistance M_{H2} acts. In engagement of wheels we shall consider only horizontal components of reactions as vertical components are perceived by a frame.

Forces and displacements (speeds) are parallel a horizontal axis Ox.

Let's accept following designations: r_{H1}, r_{H2}—radiuses of input and output carriers, r_i $(i = 1, 2 \ldots 6)$—radiuses of toothed wheels, M_{H1}, M_{H2}—moments on

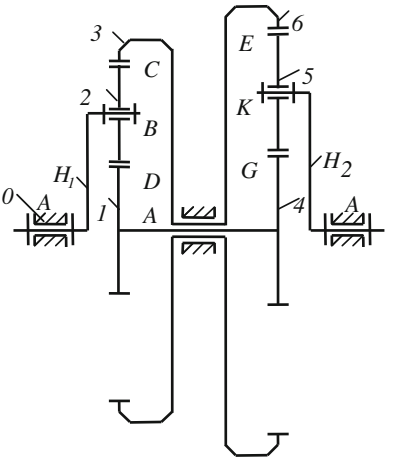

Fig. 2 Toothed continuously variable transmission *0*—frame; H_1—input carrier; *2*—input satellite; *1–4*—block of central toothed wheels with external teeth; *3–6*—block of central toothed wheels (ring wheels) with internal teeth; *5*—output satellite; H_2—output carrier

input and output carriers, M_i $(i = 1, 2...6)$—moments on toothed wheels, $F_{H1} = M_{H1}/r_{H1}$—input motive force, $R_{H2} = M_{H2}/r_{H2}$—output force of resistance, $R_{12} = M_1/r_1$, $R_{32} = M_3/r_3$, $R_{45} = M_4/r_4$, $R_{65} = M_6/r_6$—reactions in kinematic pairs.

3 Interconnection of Parameters of the Kinematic Chain in a Condition with One Degree of Freedom

The beginning of motion of the kinematic chain (or start) occurs in a condition to one degree of freedom. Start is a transition of the kinematic chain from a condition with one degree of freedom in a condition with two degrees of freedom under act of the input motive (driving) moment. On start the motion of an input link H_1 under act of the input driving moment M_{H1} at a motionless output link H_2 occurs. Input motive force $F_{H1} = M_{H1}/r_{H1}$ is transferred on link 2 of the closed contour from an input link H_1. Output force of resistance $R_{H2} = M_{H2}/r_{H2}$ is transferred on link 5 of the closed contour from output link H_2.

The closed contour (in difference from open chain) transmits an active input force on output link in a condition with one degree of freedom.

Transfer of an input motive force F_{H1} on an output link H_2 by means of the closed contour occurs as follows.

Force F_{H1} creates on a link of 2 reactions $R_{32} = F_{H1}/2$, $R_{12} = F_{H1}/2$.

These reactions are transferred to blocks of wheels 1–4 and 3–6 and will be converted to the reactions acting on the output satellite 5 $R_{45} = R_{12}r_1/r_4$, $R_{65} = R_{32}r_3/r_6$.

The sum of the reactions acting on satellite 5 is equal to reaction transferred by the output satellite 5 on the output carrier H_2

$$R_{5H2} = R_{45} + R_{65}. R_{5H2} = F_{H1}(r_1/r_4 + r_3/r_6)/2.$$

Thus, the input motive force F_{H1} is transferred to the output carrier H_2 in the form of the reaction R_{5H2} overcoming the output force of resistance R_{H2}. $R_{H2} = R_{5H2}$. Or

$$R_{H2} = F_{H1}(r_1/r_4 + r_3/r_6)/2. \quad (1)$$

Let's substitute the values of the forces, expressed through the moments in this formula, and we shall gain an output moment of resistance which is overcome by the input driving moment

$$M_{H2} = M_{H1}\frac{r_{H2}}{2r_{H1}}\left(\frac{r_1}{r_4} + \frac{r_3}{r_6}\right). \quad (2)$$

As a result all kinematic chain comes to motion only under act of one input motive force (moment) and passes from a condition with one degree of freedom in a condition with two degrees of freedom. Reactions R_{45}, R_{65} on a link 5 create also the internal driving unbalanced moment $M_5 = (R_{45} - R_{65})r_5 = 0.5F_{H1}(r_1/r_4 - r_3/r_6)r_5$. Or

$$M_5 = 0.5M_{H1}\frac{r_5}{r_{H1}}\left(\frac{r_1}{r_4} - \frac{r_3}{r_6}\right). \quad (3)$$

On conditions of statics the start occurs at accomplishment of conditions of statics (1) and (3). The unbalanced moment M_5 on a link 5 calls a transition dynamic regime of motion of the kinematic chain with acceleration.

In a transition regime of motion the increase in the input driving moment M_{H1} (and force F_{H1}) by formula (1) will lead to increase in the force R_{5H2} transferred to a motionless output link H_2, up to the value overcoming output starting force of resistance R_{H2} and an output moment of resistance M_{H2}. From the formula (2) we shall gain the demanded starting value of the input driving moment necessary for overcoming of a starting moment of resistance M_{H2S}

$$M_{H1S} = 2M_{H2S}\frac{r_{H1}}{r_{H2}}\left(\frac{r_4 r_6}{r_1 r_6 + r_3 r_4}\right). \quad (4)$$

If $M_{H1S} = kt$, (k—the set factor of change of the input driving moment on start in N/s) from (4) it is possible to find a time t_S necessary for overcoming of a starting moment of resistance

$$t_S = 2M_{H2S}\frac{r_{H1}}{kr_{H2}}\left(\frac{r_4 r_6}{r_1 r_6 + r_3 r_4}\right). \quad (5)$$

The equation of motion of the kinematic chain in a transition regime is reduced to the equation of motion of a link 5 and looks like $M_5 = J_5\frac{d\omega_5}{dt}$ or in view of (3)

$$0.5kt\frac{r_5}{r_{H1}}\left(\frac{r_1}{r_4} - \frac{r_3}{r_6}\right) = J_5\frac{d\omega_5}{dt}. \quad (6)$$

Here ω_5—angular speed of a link 5, J_5—a moment of inertia of a link 5.

Solving the differential equation of motion (6), we shall find angular speed ω_5 of a link 5 in the end of a transition period. The beginning of motion of a link 5 occurs from a motionless condition $\omega_{50} = 0$. Then we shall gain value of angular speed after a time t_S

$$\omega_5 = \frac{kt_S^2}{2J_5}\frac{r_5}{r_{H1}}\left(\frac{r_1}{r_4} - \frac{r_3}{r_6}\right). \tag{7}$$

4 Interconnection of Parameters of the Kinematic Chain in Condition with Two Degrees of Freedom

Further motion of the kinematic chain in a condition with two degrees of freedom occurs. A subject of research basic new, therefore it is necessary to use basic new approach to research of interconnection of its parameters.

We shall consider all over again equilibrium of the kinematic chain with two degrees of freedom on conditions of statics. Equilibrium occurs at equality of the moments of superposed forces

$$M_{H2} = M_{H1}. \tag{8}$$

We shall consider equilibrium of the closed contour under act of the superimposed forces $F_{H1} = M_{H1}/r_{H1}$ and $R_{H2} = M_{H2}/r_{H2}$. From the input satellite 2 on intermediate links 1–4 and 3–6 reactions $R_{21} = F_{H1}/2$, $R_{23} = F_{H1}/2$ are transferred. From the output satellite 5 on intermediate links 1–4 and 3–6 reactions $R_{54} = R_{H2}/2$, $R_{56} = R_{H2}/2$ are transferred. Let's express force of resistance R_{H2} through motive force F_{H1}. From the formula (8) follows $R_{H2} = F_{H1}r_{H1}/r_{H2}$. Then $R_{54} = F_{H1}r_{H1}/2r_{H2}$, $R_{56} = F_{H1}r_{H1}/2r_{H2}$.

As a result the link 1–4 will appear under act of the unbalanced moment

$$M_{1-4} = R_{21}r_1 - R_{54}r_4 = \frac{F_{H1}}{2}\left(\frac{r_{H2}r_1 - r_{H1}r_4}{r_{H2}}\right). \tag{9}$$

The link 3–6 will appear under act of the unbalanced moment

$$M_{3-6} = R_{23}r_3 - R_{56}r_6 = \frac{F_{H1}}{2}\left(\frac{r_{H2}r_3 - r_{H1}r_6}{r_{H2}}\right). \tag{10}$$

Let's substitute in formulas (9), (10) values $r_{H1} = (r_1 + r_3)/2$, $r_{H2} = (r_4 + r_6)/2$ we shall gain $M_{1-4} = \frac{F_{H1}}{2}\left(\frac{r_1r_6 - r_3r_4}{r_4 + r_6}\right)$, $M_{3-6} = \frac{F_{H1}}{2}\left(\frac{r_3r_4 - r_1r_6}{r_4 + r_6}\right)$. From here follows

$$M_{1-4} = -M_{3-6}. \tag{11}$$

Thus, internal forces are led to unbalanced forces and moments on links 1–4 and 3–6. The condition of equilibrium of internal forces by a principle of virtual works in view of a time is expressed as

$$M_{1-4}\omega_1 + M_{3-6}\omega_3 = 0. \tag{12}$$

As $M_{1-4} = -M_{3-6}\ \omega_1 = \omega_3$. In this case angular speeds of all links are equal, and the kinematic chain is twirled as a single whole without internal mobility of links.

Thus, the kinematic chain is in the equilibrium representing a special case when there is no motion of links inside of a contour. Thus equilibrium is carried out both on conditions of statics, and by a principle of virtual works.

Further we shall consider a common case of motion. It is possible to assume, that in common case at presence of two degrees of freedom in the kinematic chain with the closed mobile contour equilibrium by a principle of virtual works also will occur.

Theorem *If the kinematic chain with two degrees of freedom with the closed four-bar contour moves under action of the arbitrary driving moment and the arbitrary moment of resistance for these external moments of forces the condition of equilibrium by a principle of virtual works is carried out.*

We shall use power instead of work in view of a time. Analytical form of the theorem:

$$M_{H1}\omega_{H1} + M_{H2}\omega_{H2} = 0. \tag{13}$$

For the demonstration of the theorem we shall use the main property of closed four-bar contour, leading definability of the interconnected parameters. The main property closed four-bar contour is: all internal reactions in a contour can be expressed through superposed forces. (For comparison we shall note: it is impossible to express all internal reactions through the superposed forces applied to two links of a contour if the contour contains, for example, five mobile links).

Let's make for each satellite an equilibrium equation by a principle of virtual works. Each satellite represents scleronomous (hardening) mechanical system as all the forces acting on the satellite are known. Therefore the valid displacements of points of the satellite can be accepted for possible (1). We shall gain

$$R_{12}s_D + R_{32}s_C = F_{H1}s_B, \tag{14}$$

$$R_{45}s_G + R_{65}s_E = F_{H2}s_K. \tag{15}$$

Here $s_i\ (i = D,\ C,\ B,\ G,\ E,\ K)$—the valid linear displacements $s_i\ (i = D,\ C,\ B,\ G,\ E,\ K)$ of points of satellites. Let's express linear displacements s_i points of satellites through instant angles of turn of links and radiuses$s_D = \varphi_1 r_1,\ s_C = \varphi_3 r_3,\ s_B = \varphi_{H1} r_{H1},\ s_G = \varphi_4 r_4,\ s_E = \varphi_6 r_6,\ s_K = \varphi_{H2} r_{H2}$ $\varphi_1,\ \varphi_3,\ \varphi_{H2},\ \varphi_4,\ \varphi_6,\ \varphi_{H2}$—instant angles of turn of toothed wheels and carriers.

The moments on links: $R_{12}r_1 = M_1$, $R_{32}r_3 = M_3$, $F_{H1}r_{H1} = M_{H1}$, $R_{45}r_4 = M_4$, $R_{65}\ r_6 = M_6$, $F_{H2}r_{H2} = M_{H2}$.

In view of a time from the Eqs. (14) and (15) we shall gain

$$M_1\omega_1 + M_3\omega_3 = M_{H1}\omega_{H1}, \tag{16}$$

$$M_4\omega_4 + M_6\omega_6 = M_{H2}\omega_{H2}. \tag{17}$$

As satellites are a links of the mechanism, we shall sum the made expressions for satellites. We shall gain a condition of interacting of parameters of all mechanism as a whole

$$M_1\omega_1 + M_3\omega_3 + M_4\omega_4 + M_6\omega_6 = M_{H1}\omega_{H1} + M_{H2}\omega_{H2}. \tag{18}$$

In the left side of an equation the sum of powers (works) of internal forces of a contour takes place. In the right side of an equation the sum of powers (works) of superposed forces of a contour takes place. All internal forces are single-valued functions of external forces. As constraints are ideal and stationary then work of constraint reactions is equal to null (1)

$$M_1\omega_1 + M_3\omega_3 + M_4\omega_4 + M_6\omega_6 = 0. \tag{19}$$

Let's substitute this value in the Eq. (18), we shall gain

$$M_{H1}\omega_{H1} + M_{H2}\omega_{H2} = 0. \tag{20}$$

Thus, for the external moments of forces the condition of equilibrium by a principle of virtual works, as was to be shown is carried out. In the Eq. (20) one of the external moments should be a moment of resistance, differently the condition of equilibrium of the kinematic chain in the form of equality of works of motive forces and forces of resistance will not be carried out. The kinematic link to which the driving moment is applied will be an input link. The link to which the moment of resistance M_{H2} is applied will be an output link. Work (or power) a moment of resistance is negative. Then the Eq. (20) will become

$$M_{H1}\omega_{H1} = M_{H2}\omega_{H2}. \tag{21}$$

For the resolution of the Eq. (21) it should contain one unknown parameter. It is logical to consider: the external moments M_{H1}, M_{H2} and input angular speed ω_{H1} are given. Then output angular speed ω_{H2} will be determined from expression (21). Angular speeds of initial links will be known. Angular speeds of all links of a contour will be accordingly known. Transition of one of initial links in a condition of an output link leads to reception of number of input links per unit less numbers of degrees of freedom of all kinematic chain. However the Eq. (21) characterizes the additional constraint providing conservation of definability of motion of the consider kinematic chain. As a result the Eq. (21) means, that statically and kinematically definable mobile contour is in equilibrium under act of arbitrary superposed forces (moments). Thus, the patented opportunity of transfer of motion

from an input link to an output link through closed four-bar contour (3, 4 and 5) has gained the theoretical acknowledging.

Consequence 1. The kinematic chain with the closed contour provides stepless regulating of transfer, that is possesses effect of force adaptation.

From the formula (21) it is possible to determine value of output angular speed.

$$\omega_{H2} = M_{H1}\omega_{H1}/M_{H2}. \tag{22}$$

According to the formula (22) at a constant input power $P_{H1} = M_{H1}\omega_{H1}$ the output angular speed ω_{H2} is in return proportional dependence on a variable output moment of resistance M_{H2}. This dependence expresses effect of force adaptation of an output link to a variable load.

Consequence 2. In the closed contour circulation of energy takes place.

The Eq. (19) contains positive and negative members and characterizes equilibrium of works (powers) on intermediate links of a contour.

As $\omega_1 = \omega_4,\ \omega_3 = \omega_6,\ M_1 > M_4,\ M_6 > M_3$, from the Eq. (19) we shall gain

$$(M_1 - M_4)\omega_1 - (M_6 - M_3)\omega_3 = 0. \tag{23}$$

Let's designate $(M_1 - M_4) = M_{1-4},\ M_6 - M_3 = M_{6-3}$—The moments on intermediate links 1–4 and 3–6. Then the equilibrium of works (powers) on intermediate links of a contour will become $M_{1-4}\omega_1 = M_{6-3}\omega_3$.

The Eq. (23) reflects unknown earlier the phenomenon of circulation of energy inside of a contour during its motion.

5 Kinematics of the Mechanism

We shall determine transfer ratios of links of transfer through numbers of t of wheels $z_i\ i = 1,\ 2,\ \ldots 6$.

The interconnection of angular speeds of transfer is determined by formulas

$$\frac{\omega_1 - \omega_{H1}}{\omega_3 - \omega_{H1}} = u_{13}^{(H1)}, \tag{24}$$

where $u_{13}^{(H1)} = -z_3/z_1$.

$$\frac{\omega_1 - \omega_{H2}}{\omega_3 - \omega_{H2}} = u_{46}^{(H2)}, \tag{25}$$

where $u_{46}^{(H2)} = -z_6/z_4$. From (24)

$$\omega_1 = u_{13}^{(H1)}(\omega_3 - \omega_{H1}) + \omega_{H1}. \tag{26}$$

From (25)

$$\omega_1 = u_{46}^{(H2)}(\omega_3 - \omega_{H2}) + \omega_{H2}. \tag{27}$$

Let's subtract (27) of (26), we shall get

$$u_{13}^{(H1)}(\omega_3 - \omega_{H1}) + \omega_{H1} - u_{46}^{(H2)}(\omega_3 - \omega_{H2}) - \omega_{H2} = 0.$$

From here

$$\left(u_{13}^{(H1)} - u_{46}^{(H2)}\right)\omega_3 - u_{13}^{(H1)}\omega_{H1} + u_{46}^{(H2)}\omega_{H2} = \omega_{H2} - \omega_{H1},$$

$$\omega_3 = \frac{\omega_{H2}\left(1 - u_{46}^{(H2)}\right) - \omega_{H1}\left(1 - u_{13}^{(H1)}\right)}{u_{13}^{(H1)} - u_{46}^{(H2)}}. \tag{28}$$

Formulas (22), (28), (26) determine sequence of acts by definition angular speeds of links of transfer. Let's determine the starting transfer ratio. The starting transfer ratio represents the transfer ratio of the closed differential at the stopped output carrier H_2 from the input carrier H_1 to the output satellite 5: $u_{H1-5} = \omega_{H1}/\omega_5$.

Let's divide numerator and a denominator of expression (24) on ω_3. We shall designate $\omega_1/\omega_3 = u_{13} = -z_6/z_4$, $\omega_{H1}/\omega_3 = u_{H1-3}$, $u_{13}^{(H1)} = -z_3/z_1$.

We shall receive $\frac{u_{13}-u_{H1-3}}{1-u_{H1-3}} = u_{13}^{(H1)}$. From here

$$u_{H1-3} = \frac{u_{13}^{(H1)} - u_{13}}{u_{13}^{(H1)} - 1}. \tag{29}$$

As $u_{H1-3} = u_{H1-6}$ and $u_{H1-5} = u_{H1-6}u_{65}$, where $u_{65} = z_5/z_6$. Then $u_{H1-5} = \frac{u_{13}^{(H1)}-u_{13}}{u_{13}^{(H1)}-1}u_{65}$.

Let's substitute numbers of teeth; we shall gain the starting transfer ratio

$$u_{H1-5} = \frac{z_3z_4 - z_6z_1}{z_3z_4 + z_1z_4} \cdot \frac{z_5}{z_6}. \tag{30}$$

6 Force Analysis of the Mechanism

The force analysis of the mechanism can be reduced to definition of the internal moments M_i ($i = 1, 3, 4, 6$) through reactions in kinematic pairs on the set external moments M_{H1}, M_{H2}.

$$M_1 = R_{21}r_1 = 0.5M_{H1}r_1/r_{H1},\ M_3 = R_{23}r_3 = 0.5M_{H1}r_3/r_{H1},$$

$$M_4 = R_{54}r_4 = 0.5M_{H2}r_4/r_{H2},\ M_6 = R_{56}r_6 = 0.5M_{H2}r_6/r_{H2}. \tag{31}$$

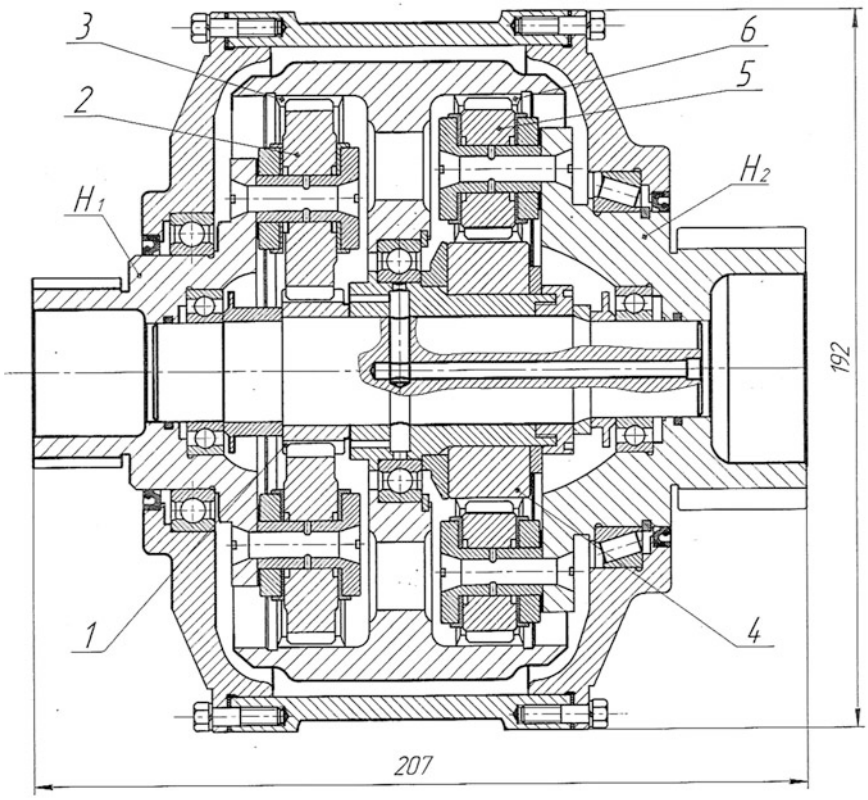

Fig. 3 Continuously variable transmission. Assembly drawing

The developed assembly drawing of the continuously variable transmission presented on Fig. 3.

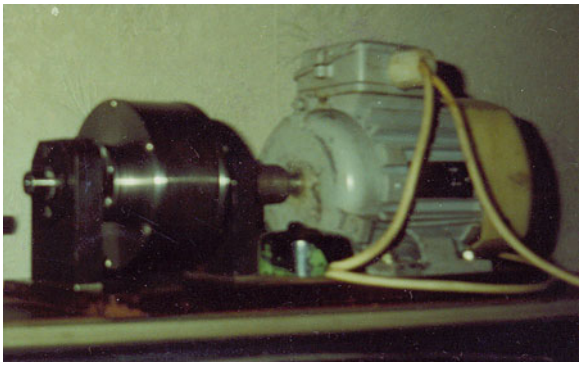

Fig. 4 Gear continuously variable transmission. Acting example

The acting example of transmission is presented on Fig. 4. It confirms presence of effect of force adaptation in the mechanism with the closed contour.

7 Conclusion

The creation of gear continuously variable transmission in the form of the toothed closed differential mechanism with two degrees of freedom is theoretically proved.

It is proved, that the mobile closed mechanical contour of transmission creates additional constraint and provides the transition regime of motion translating the mechanism of transfer from a one-mobile condition at start-up in bi-mobile condition in operating regime of motion. It is proved, that in operating regime of motion the equilibrium by a principle of virtual works, providing stepless regulating of transmission takes place.

The equations of interconnection of force parameters, kinematic parameters and geometrical parameters of transmission in kinematics and dynamics are developed. These equations are mustered by numerical instances, confirmed by skilled acting specimens and the developed computer animation model. The assembly drawing of the gear continuously variable transmission is presented.

The found regularities allow synthesizing gear continuously variable transmission on the given operational parameters of motion, to execute the kinematic and dynamic analysis of transmission and to determine design data of transmission.

Gear continuously variable transmission in the form of the gear closed differential mechanism with constant engagement of wheels is the elementary transmission of such type and it has the reliability matching reliability of a gear mechanism. The specified properties allow using the transmission both in easy local drives of manipulators, and in heavy drives of transport machines, including in the motor-wheels.

The gear closed differential mechanism of transmission possesses effect of force adaptation to variable technological loading. Force adaptation allows creating the easy and hard loaded adaptive drives of machines with the variable transfer ratio depending on technological resistance (for velocipede, motorcycle, car, drilling rig, bulldozer, lorry, etc.).

References

Crockett SJ (1990) Shiftless continuously-aligning transmission. Patent of USA 4,932,928, Cl F16H 47/08, US Cl 475/51; 475/47, p 9

Harries J (1991) Power transmission system comprising two sets of epicyclic gears. Patent of Great Britain GB2238090 (A), p 11

Ivanov KS (1996) Transfer with automatically adjustable speed. The preliminary patent of republic Kazakhstan 3208 from 15 Mar 1996, p 12

Ivanov KS (2007) Gear Automatic adaptive variator with constant engagement of gears. In: Proceedings of the 12th world congress in mechanism and machine science, vol 2. Besancon, France, pp 182–188

Ivanov KS (2010) The simplest automatic transfer box. WCE 2010. World Congress on Engineering 2010 (ICME). London, UK, pp 1179–1184

Ivanov KS, Yaroslavtseva EK (2010) Way of automatic and continuous change of a twisting moment and speed of twirl of the output shaft depending on a tractive resistance and the device for its realization. The description of the invention to the patent application of Russia RU 2007139258/11 (042965), the solution on output of the patent from 25 Mar 2010, p 28

Levitskiy NI (1979) Theory of mechanisms and machines, Science. Moscow, p 576

Markeev AP (1990) Theoretical mechanics, Science. Moscow, p 414

Volkov IV (2004) Way's of automatic and continuous change of a twisting moment and speed of twirl of the output shaft depending on a tractive resistance and the device for its realization. The description of the invention to the patent of Russia RU 2,234,626 from 27 Mar 2004, p 26

Synthesis of the Two-Stream Transmissions

Alexander Kraynev, Konstantin Salamandra and Madhusudan Raghavan

Abstract One of the modern trends in transmissions design is the increase in the number speed ratios. By means of generalized structures method, the gear transmission types (layshaft and planetary) were analyzed with a view to increasing the number of speed ratios. The analysis showed that the speed ratio increase in the layshaft and planetary transmissions lead to significant complication and an increase in the number of clutches. The two-stream transmissions allow obtaining greater number of speeds with fewer clutches. The two-stream transmissions synthesis method is proposed. Examples of 8 and 12-speed transmissions synthesis are presented.

Keywords Gears · Gearbox · Transmission · Analysis and synthesis

List of Symbols

N	Total number of speeds in the transmission
I	Input member
O	Output member
GB	Internal gearbox with own speeds
N_{GB}	Number of speeds in the internal gearbox GB
i_{GB}	Gear ratio of the internal gearbox GB
m, n	Differential members
i_{nO}^{m}	Differential gear ratio of member n to output member O, assuming member m is stopped

A. Kraynev (✉) · K. Salamandra
Institute of Machines Science of the Russian Academy of Sciences, Moscow, Russia
e-mail: ksalamandra@yandex.ru

M. Raghavan
General Motors R&D Center, Warren, MI, USA
e-mail: madhu.raghavan@gm.com

G. Dobre (ed.), *Power Transmissions*,
Mechanisms and Machine Science 13, DOI: 10.1007/978-94-007-6558-0_25,

i^{n}_{mO} Differential gear ratio of member m to output member O, assuming member n is stopped
i^{m}_{In} Differential gear ratio of input member I to member n, assuming member m is stopped
i^{n}_{Im} Differential gear ratio of input member I to member m, assuming member n is stopped
l_1, l_2 Amount of modes when differential works together with GB1 and GB2 respectively
l_D Amount of modes when differential works independently

1 Introduction

In theory, increasing the number of speed ratios in a transmission results in better characteristics of operation and fuel consumption in a vehicle. The transmissions with 3–4 forward speeds were replaced by transmissions with 5 and 6 speeds. The next generation of vehicles could feature transmissions with 7 and 8 speeds. The increased number of speeds is aimed at reducing the step size between gear ratios and improving the shift quality of the transmission by making the speed interchanges substantially imperceptible to the operator. The increase in speed ratios results in design complexity, growth of overall dimensions, weight and cost of such transmissions.

Automotive transmissions generally consist of layshaft and planetary gears.

Every speed in a layshaft transmissions results from the conversion of the rotating movement on one or two sets of intermeshing gears. Selectively engageable torque-transmitting mechanisms (different types of clutches or synchronizers) are engaged to transfer torque to establish the various gear ratios. For simplicity, we will henceforth refer to all possible kinds of controllable torque-transmitting mechanisms as clutches.

Dual-clutch transmissions consist of two layshaft gearboxes and two clutches that alternately connect the engine shaft with the corresponding gearbox. These transmissions permit a significant reduction in shift time because the next speed ratio can be engaged and pre-selected ahead of time (Matthes 2005; Wheals et al. 2007).

The number of speeds in the layshaft transmission is defined by the number of sets of intermeshing gears. Therefore for speed ratio increases, it is necessary to add the required number of new gear sets and an adequate number of clutches to engage the intermeshing gears. The power stream in all layshaft transmissions passes through one branch only.

The planetary gears have bigger load capability (by reason of incorporating several satellite gears). The power stream as a rule is divided into two or more parallel branches because of the links between the planetary gear sets. Therefore

the load in each corresponding branch is lower. The number of speeds achieved depends on the number and type of used planetary mechanisms.

The synthesis methods with specified parameters (e.g., type of planetary mechanisms, velocity and acceleration of members, number of speeds, etc.) allow the creation, description, and assessment of all possible variants of the planetary transmission design. But known synthesis methods are complicated in practice, limited by type and number of planetary mechanisms, number of degrees of freedom etc. [for example see Kosov (2005) and Raghavan et al. (2007)].

Many modern planetary transmission designs were obtained by combination of known gear sets: Ravigneaux gear set, Simpson gear set and etc. Transmission designs obtained by using these gear sets result in desired speed ratios and good characteristics of weight and overall dimensions (Klaus 2001; Haupt 2004; Kondo et al. 2007). Attempts to unify the advantages of layshaft and planetary transmissions with a view to increasing speed ratios led to two-stream transmissions creation for examples see Hall (1998), Gitt and Schnitzer (2006).

Two-stream transmissions work in two modes: one-stream and two-stream. In the one-stream mode the power stream from engine passes through one branch of the transmission as in dual-clutch transmissions. In two-stream mode the power stream divides into two branches and passes through in parallel as in planetary transmissions. The main purpose of this paper is to study features of the double-stream transmissions and the methods their analysis and synthesis.

Transmission complexity can be defined in different ways. One of the most complex transmission components are clutches because they require special calculations, materials, conditions control, management programs etc. Here we presumed: the fewer clutches in transmission the better such transmission.

The method of generalized structures shown by Volkov and Kraynev (1968) was used for simplification and comparative analysis of the various designs under consideration.

2 Analysis of Layshaft Transmissions

Amongst layshaft gear sets, the most common are cylindrical (Fig. 1a) and conical (Fig. 1b) gear sets. These gears have one degree of freedom.

The gears on Fig. 1a and on Fig. 1b as well as other gears with two members and one degree of freedom can be defined by generalized structure G (Fig. 1c). Several G-gears connected consequentially with clutches that manage corresponding G-gears and provide several various speeds are defined as internal gearboxes GB. Then the dual-clutch transmission may be represented by the structure shown on Fig. 2.

The closed loop of the dual-clutch transmission never works because it does not have a mechanism that sums up power streams from the both branches. The branches work alternatively by switching on corresponding clutches c1 and c2.

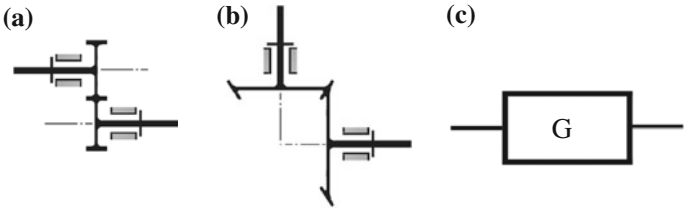

Fig. 1 Structures of the layshaft gears. **a** Cylindrical gear set. **b** Conical gear set. **c** Generalized structure of the gear with one degree of freedom

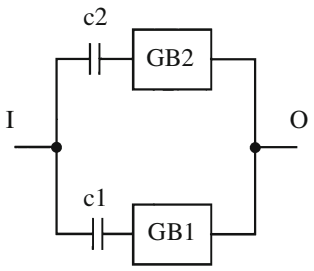

Fig. 2 Generalized structure of the dual-clutch transmission c1 and c2—clutches that switch on corresponding internal gearboxes

The power passes over from I to O always by one stream either through GB1 or GB2.

N in either dual-clutch transmission is defined by formula (1).

$$N = N_{GB1} + N_{GB2} \tag{1}$$

Total number of clutches that provide N speeds in the dual-clutch transmissions always is $N + 2$. Every additional speed is obtained by means of a clutch addition in one of the internal gearboxes with respective gear set.

3 Analysis Planetary Transmissions

Complex mechanisms that have two degrees of freedom can be made of mechanisms with three members, where each member's motion is determined by the motion of the other two members as defined by the generalized structure shown on Fig. 3e. That is, the D-mechanism defines planetary gear (Fig. 3a–d) and any other gearbox that consists of three members. Hereafter, in this paper, we will refer to all D-mechanism type systems as differentials.

Differentials connect with other mechanisms, drives, transmission units and fixed members only by means of three members 1, 2 and 3 (Fig. 3e).

Differentials have three work conditions:

1. Reduction or multiplication gear when one member has been stopped.

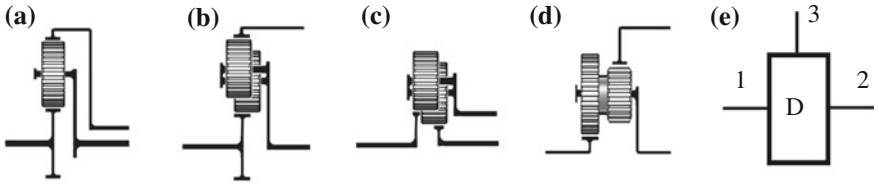

Fig. 3 Structures of planetary gear sets. **a** Simple planetary gear set. **b** Planetary gear set with two intermeshed satellites and one sun gear. **c** Planetary gear set with two intermeshed satellites and two sun gears. **d** Planetary gear set with double-pinion satellites. **e** Generalized structure of the mechanism with two degrees of freedom

2. Blocked and rotates in direct gear when two members have been connected with driver.
3. Summing or distributing gear in dependence of connection it members in the transmission.

Therefore the differential can be depicted by only two structures (Fig. 4) that differ one from another by the placement of input and output members. And these members define the differential as summing (Fig. 4a) or distributing (Fig. 4b) mechanism. The clutches shown on Fig. 4 are appropriately selected for the differential's work condition above. Two clutches can't engage together. The regime 3 occurs if all clutches are disengaged.

As mentioned by Kudryavcev and Kirdyashev (1977), the total number of speed ratios (in a planetary transmission that consist of simple planetary gears) depends on the transmission's degrees of freedom and number of clutches. For example, in the transmission with 2 degrees of freedom, each additional speed is obtained by means of a clutch addition (as in dual-clutch transmissions). If we are to increase number of clutches from 4 to 5 in a transmission with 3 degrees of freedom, a transmission with 7–10 speeds may be obtained theoretically. However the designs may be hard to identify in practice due to the structural complexity and permutations involved. To achieve designs with more than 10 speed ratios it may easiest to add planetary gear sets to existing 7- and 8-speed concepts.

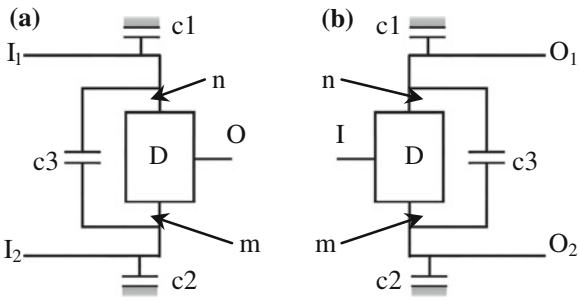

Fig. 4 Differential's structures. **a** Differential that sums power streams. **b** Differential that distributes power streams. c1 and c2—clutches that stop members m and n respectively; c3—clutch that connects members m and n together and blocks differential for direct gear

4 Two-stream Structure Synthesis

Differential's structures (Fig. 4) define two possible two-stream transmissions structures (Fig. 5). The clutches shown on the Fig. 5 define work modes of the two-stream transmissions.

If one of the clutches c1, c2 or c3 engages the one-stream mode occurs. If clutches c4, c5 or neither engages the two-stream mode occurs. If clutches c3 and c4 (c3 and c5 or c4 and c5) engage simultaneously the independent differential's direct gear occurs. If clutches c1 and c4 (c2 and c5) engage simultaneously the independent differential's reduction gear occurs.

5 Two-stream Transmission's Work Modes and Total Number of Gear Ratios

Total number of speeds in either two-stream transmissions calculates by formula (2).

$$N = N_{GB1} \cdot N_{GB2} + l_1 \cdot N_{GB1} + l_2 \cdot N_{GB2} + l_D \\ l_1 \leq 3,\ l_2 \leq 3,\ l_D \leq 3 \tag{2}$$

As seen from (2), the increase in number of speeds in the two-stream transmissions can be made with less number of clutches. If for example one extra gear ratio will be added to GB1 then total number of transmission speed ratios will increase as $N_{GB2} + l_1$. It is a good result when compared with layshaft and planetary transmissions.

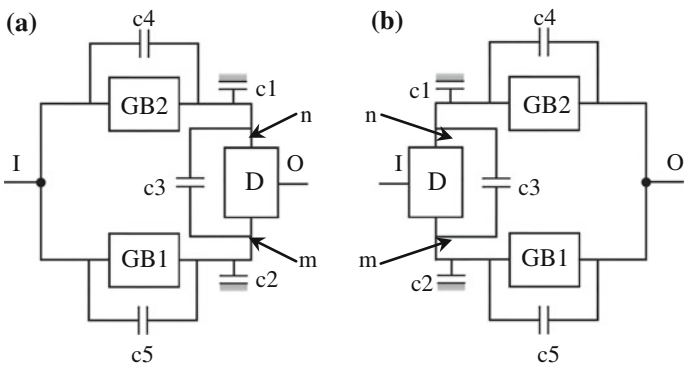

Fig. 5 Two-stream transmissions structures with differential that sums power streams (**a**), and with differential that distribute power streams (**b**). c1 and c2—clutches that stop members m and n respectively; c3—clutch that connects members m and n together and blocks differential; c4 and c5—clutches that provide differential's independent work modes

Table 1 Two-stream transmission's work modes in dependence on switching clutches, and gear ratios calculation's formulae

Transmission mode	Differential condition	Speed	Switched on clutches	Gear ratio calculation's formula	
				For Fig. 6a	For Fig. 6b
One-stream	Blocked	1.	c3, GB1	i_{GB1}	i_{GB1}
		2.	c3, GB2	i_{GB2}	i_{GB2}
	Reduction gear	3.	c1, GB1	$\frac{i_{GB1}}{i^{n}_{Om}}$	$i_{GB1} \cdot i^{n}_{Im}$
		4.	c2, GB2	$\frac{i_{GB2}}{i^{m}_{On}}$	$i_{GB2} \cdot i^{m}_{In}$
Independent differential		5.	c2, c4	i^{m}_{nO}	i^{m}_{In}
		6.	c1, c5	i^{n}_{mO}	i^{n}_{Im}
	Blocked	7.	c3, c4 or c3, c5	1	1
	Blocked		c4, c5	1	1
Two-stream	Adder	8.	GB1, GB2	$\frac{1}{\frac{i^{n}_{Om}}{i_{GB1}} + \frac{i^{m}_{On}}{i_{GB2}}}$	$i_{GB1} \cdot i^{n}_{Im} + i_{GB2} \cdot i^{m}_{In}$
		9.	c4, GB1	$\frac{1}{\frac{i^{n}_{Om}}{i_{GB1}} + i^{m}_{On}}$	$i_{GB1} \cdot i^{n}_{Im} + i^{m}_{In}$
		10.	c5, GB2	$\frac{1}{i^{n}_{Om} + \frac{i^{m}_{On}}{i_{GB2}}}$	$i^{n}_{Im} + i_{GB2} \cdot i^{m}_{In}$

There is a two-stream transmission structure with the maximum number of clutches in Fig. 5 that is represented by parameter values $l_1 = l_2 = l_D = 3$.

By means of the formulae and structures represented above the two-stream transmission's analysis and synthesis can be carried out (Table 1).

6 Two-stream Transmissions Synthesis

The two-stream transmissions designs are obtaining by substituting the kinematic structures of the appropriate mechanisms instead of the generalized structures. For example, 8-speed two-stream transmission synthesis of the concept in Fig. 5a may be carried out according to the following conditions:

1. internal gearboxes GB1 and GB2 have equal speeds $N_{GB1} = N_{GB2} = 2$;
2. reverse gear is in the internal gearbox GB1;
3. the differential hasn't independent modes $l_D = 0$;
4. the differential can't be blocked (clutch c3 on Fig. 5a should absent);
5. all used mechanisms have negative gear ratio and the rotation direction of the input member I coincides with direction of the output member O.

The mechanisms Gm and Gn are necessary for performing the item (5) of the specification.

The design of the 8-speed two-stream transmission is obtained by Kraynev et al. (2011) from structure on Fig. 6 and shown on Fig. 7.

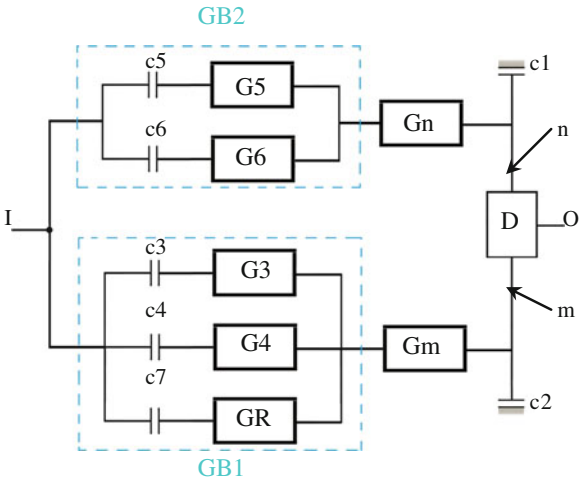

Fig. 6 The structure of the 8-speed two-stream transmission with summing differential c1 and c2—clutches that stop members m and n respectively; G3, G4, G5 and G6—layshaft gears that perform forward ratios; GR—layshaft gear that performs reverse ratio; c3, c4, c5, c6 and c7—clutches that connect G3, G4, G5, G6 and GR respectively with input member

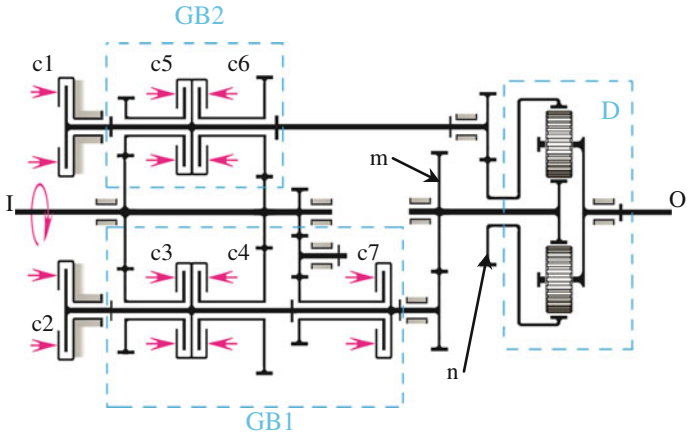

Fig. 7 The design of the 8-speed two-stream transmission with summing differential c1 and c2—clutches that stop members m and n respectively; c3, c4, c5 and c6—clutches of the forward speed ratios; c7—clutch of the reverse speed ratio

The gear ratios values of the transmission Fig. 7 are calculated according to the method shown by Salamandra (2009) (Table 2).

12-speed two-stream transmission synthesis of the concept in Fig. 5b may be carried out according to the following limitations:

1. internal gearboxes GB1 and GB2 have equal speeds $N_{GB1} = N_{GB2} = 2$;

Table 2 The gear ratios values of the transmission Fig. 7

Speed	Gear ratio	Gear ratio step	Clutches condition						
			c1	c2	c3	c4	c5	c6	c7
1.	4.533		×		×				
2.	2.973	1.525		×			×		
3.	2.103	1.414	×			×			
4.	1.796	1.171			×		×		
5.	1.232	1.458				×	×		
6.	0.963	1.279		×				×	
7.	0.794	1.213			×			×	
8.	0.660	1.203				×		×	
R	−3.753		×						×

2. reverse gear is in the internal gearbox GB1;
3. the differential hasn't independent modes $l_D = 0$;
4. all used mechanisms have negative gear ratio and the rotation direction of the input member I doesn't coincide with direction of the output member O.

The design of the 12-speed two-stream transmission is obtained by Kraynev et al. (2010) from structure on Fig. 8 and shown on Fig. 9 (Table 3).

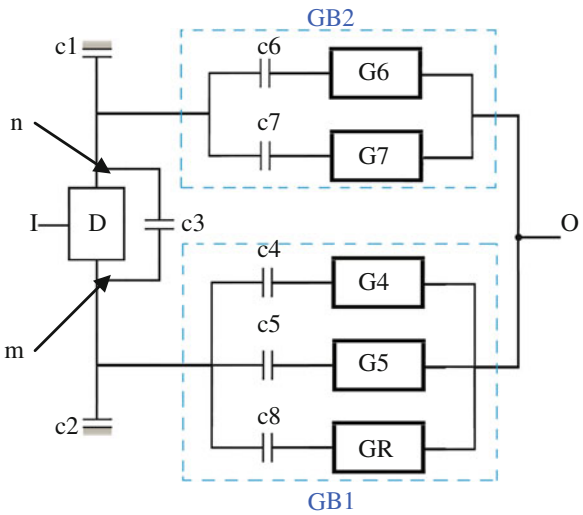

Fig. 8 The structure of the 12-speed two-stream transmission with distributing differential c1 and c2—clutches that stop members m and n respectively; c3—clutch that connects members m and n together and blocks differential; G4, G5, G6 and G7—layshaft gears that perform forward ratios; GR—layshaft gear that performs reverse ratio; c4, c5, c6, c7 and c8—clutches that connect G4, G5, G6, G7 and GR respectively with input member

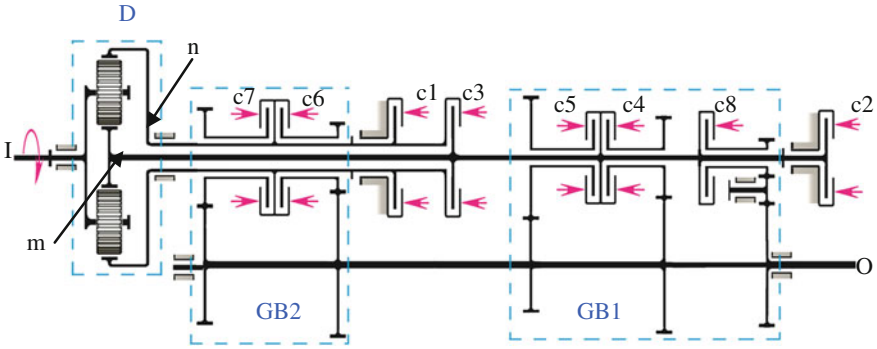

Fig. 9 The design of the 12-speed two-stream transmission with distributing differential c1 and c2—clutches that stop members m and n respectively; c3—clutch that connects members m and n together and blocks differential; c4, c5, c6 and c7—clutches of the forward speed ratios; c8—clutch of the reverse speed ratio

Table 3 The gear ratios values of the transmission Fig. 9

Gear	Gear ratio	Gear ratio step	Clutches condition							
			c1	c2	c3	c4	c5	c6	c7	c8
1.	2.997				×			×		
2.	2.333	1.285				×		×		
3.	2.128	1.096					×	×		
4.	1.798	1.184		×				×		
5.	1.339	1.343			×	×				
6.	1.121	1.194				×			×	
7.	0.977	1.147			×				×	
8.	0.916	1.067					×		×	
9.	0.826	1.109			×		×			
10.	0.586	1.410		×					×	
11.	0.535	1.095	×			×				
12.	0.330	1.621	×				×			
R1	−3.0				×					×
R2	−1.2		×							×

7 Conclusion

Layshaft, planetary and two-stream transmissions have been studied. The increase in the number of speed ratios in purely layshaft or planetary transmissions may result in certain design compromises. By way of comparison, transmissions obtained by adding 1 clutch to existing designs (plus the requisite gearing) result in 1 additional speed ratio in layshaft designs, 1–4 additional speeds in planetary designs and as many as 2–8 additional speeds in two-stream designs.

Each mechanism in a two-stream transmission takes part in both modes (one-stream and two-stream) therefore the speed ratios can be significantly increased. Two possible two-stream transmission configurations were analyzed by varying the location of the "differential" in the power flow. The transmission structures and speed ratios were obtained in generic form. Two-stream transmission analysis and synthesis was then carried out for a specific application and two samples transmission design with number of speed ratios greater than 8 were presented.

Using the described here methods for analysis and synthesis of the multi-stream transmissions it is supposed carry out the research generic characteristics and number of speeds of the three-stream transmissions that have two differentials.

In addition the prospective way may be applying specified methodology and multi-stream transmissions in the field of electro-mechanical (hybrid) powertrains.

References

Gitt C, Schnitzer D (2006) Automated transmission for a motor vehicle and method for operating the same. WO Patent 2006/032312, 30 Mar 2006

Hall A (1998) Multi-speed power transmission. US Patent 5823051, 20 Oct 1998

Haupt J (2004) Automatic gearbox. US Patent 6729990, 4 May 2004

Klaus R (2001) Planetary speed change transmission. US Patent 6302820, 16 Oct 2001

Kondo M, Hasegava Y, Takanami Y, Arai K, Tanaka M, Kinoshita M, Ootsuki T, Yamaguchi T, Fukatsu A (2007) Toyota AA80E 8-speed automatic transmission with novel powertrain control system. SAE Paper No 2007-01-1311

Kosov VP (2005) Sintez kinematicheskih shem planetarnih korobok peredach transportnih mashin (synthesis of the planetary gearboxes for transport vehicles). UrO RAN, Ekaterinburg

Kraynev AF, Astashev VK, Salamandra KB, Oreshkin VE (2010) Transmission. RU Patent 2391588, 10 June 2010

Kraynev AF, Astashev VK, Salamandra KB, Raghavan M (2011) Multi-speed transmission. US Patent application 2011/0245014, 6 Oct 2011

Kudryavcev VN, Kirdyashev YuN (1977) Planetarnie peredachi (spravochnik) [Planetary Gears (Handbook)]. Mashinostroenie, Leningrad

Matthes B (2005) Dual clutch transmissions: lessons learned and future potential. SAE Paper No 2005-01-1021

Raghavan M, Bucknor N, Maguire J, Hendrickson J, Singh T (2007) The algebraic design of transmissions and EVTs. SAE Paper No 2007-01-1458

Salamandra KB (2009) The parametric synthesis method for the two-stream multi-speed gearboxes. In: Handbook. Engineering Journal, vol 9. Mashinostroenie, Moscow, pp 12–18

Volkov DP, Kraynev AF (1968) Planetarnie, volnovie i kombinirovannie peredachi stroitelnih i dorojnih mashin (planetary, wave and combined gears for the constructional and road vehicles). Mashinostroenie, Moscow

Wheals JC, Turner A, Ramsay K, O'neil A, Bennet J, Fang H (2007) Double clutch transmission (DCT) using multiplexed linear actuation technology and dry clutches for high efficiency and low cost. SAE Paper No 2007-01-1096

Experimental Analysis of a Kinetic Energy Recovery System Intended for Small and Medium Passenger Cars

Tiberiu Laurian, Victor G. Marian and Tudor Prisecaru

Abstract This article presents experimental tests on kinetic energy recovery system (KERS) intended for small and medium passenger cars. The test rig is composed of an electric motor, a two stage timing belt drive and a high speed flywheel. The evolution of the rotation speed was measured using a speed sensor mounted on the flywheel. The flywheel rotation speed was measured during the first minute of deceleration and the total friction torque was obtained. The measurements were taken for three different maximal speeds of the flywheel. The friction torque on the deep groove ball bearings was computed and hence the percentage of the total friction torque was obtained. It is found that the flywheel presents low friction torque and it is capable to maintain the stored energy for a sufficient period of time in order to give it back to the wheels or to slowly store it to an electrical storage system.

Keywords Belt multiplier · High-speed flywheel · Kinetic energy recovery system · Vehicle braking

List of Symbols

E	Stored energy of the flywheel
I	Moment of inertia of the flywheel

T. Laurian (✉) · V. G. Marian
Department of Machine Elements and Tribology, Faculty of Mechanical Engineering and Mechatronics, University Politehnica of Bucharest, splaiul Independenţei 313, sector 6 060042 Bucharest, Romania
e-mail: tlaurian@omtr.pub.ro

V. G. Marian
e-mail: victormarian@omtr.pub.ro

T. Prisecaru
Department of Heat Engineering, Engines, Thermal and Cooling Equipments, Faculty of Mechanical Engineering and Mechatronics, University Politehnica of Bucharest, splaiul Independenţei 313, sector 6 060042 Bucharest, Romania

G. Dobre (ed.), *Power Transmissions*,
Mechanisms and Machine Science 13, DOI: 10.1007/978-94-007-6558-0_26,

M	Torque on the flywheel shaft
n	Rotation speed of the flywheel
t	Time
ω	Angular rotation speed of the flywheel
M_{bb}	Frictional torque of the deep groove ball bearings
M_{rr}	Rolling frictional moment of the deep groove ball bearings
M_{sl}	Sliding frictional moment of the deep groove ball bearings
M_{seal}	Frictional moment of the seals of the deep groove ball bearings
M_{drag}	Frictional moment of drag losses, churning, splashing, etc. of the deep groove ball bearings

1 Introduction

Reducing fuel and energy consumption for terrestrial vehicles became a very strong issue, especially because of global warming and fuel price. A lot of energy is lost when a car slows down or stops because its kinetic energy is significantly diminished and the difference of energy is transformed into heat by the vehicle brakes. One way to recover much of the wasted energy is to use regenerative braking. With regenerative braking, the consumption of terrestrial vehicles could be significantly reduced (Qin et al. 2007; Xiao et al. 2008; Boretti 2011; Kobayashi et al. 2009; Clarke et al. 2010; Zhang et al. 2008; Peng et al. 2008; Ahn et al. 2009; Jang et al. 2001).

Along with other engineering solutions, such as fuel cut mechanisms, stop-start, downsizing and turbocharging, regenerative braking represents a strategy for low fuel consumption and low CO_2 emissions. Braking energy recovery feature is attractive for mitigating urban air pollution and it is especially useful for city vehicles. Regenerative braking systems allow the vehicle to recapture, store and reuse a part of the kinetic energy that would otherwise be lost as heat during braking. The regenerative and conventional braking can be employed together when additional braking torque is needed.

Usually, urban driving involves frequent starts and stops which may represent an opportunity to recover much of the, otherwise lost, braking energy. This braking energy may be recovered through kinetic energy recovery systems (KERS).

In the case of flywheel based KERS, besides the actual flywheel, an additional energy storage system may be required to store and deliver the braking energy. This can be an electrical battery connected to an electrical motor/generator.

Integration of flywheel energy storage system in a vehicle can be accomplished in two ways: electrical integration or mechanical integration. In the first method, the flywheel is connected to an electric motor/generator which is electrically connected to another motor/generator that is coupled to the powertrain. In the

second method the flywheel is connected to the driveshaft through a transmission and one or several clutches. The first method offers more flexibility in locating the flywheel system in the vehicle, but has the disadvantage of low efficiency because of the important energy loss in the two motors/generators. The big advantage of the second method is the large power that can be transferred mechanically from wheels to flywheel, but the disadvantage is the presence of a clutch which may be a limiting factor both from the efficiency and durability points of view.

An important issue in regenerative braking is the transfer and storage of the braking energy which is captured in a short amount of time. High speed flywheels have the ability of charging in a short amount of time and are clean for the environment (Lindley 2010; Douglas 2009; Ashley 1993; Liu 2007; Hebner et al. 2002; Gulia 1988; Strößenreuther 1996).

The present article describes experimental tests on a low cost kinetic energy recovery system (KERS) intended for small and medium passenger cars.

2 Description of the Test Rig Components

2.1 The High Speed Flywheel

A solution for a flywheel using permanent magnetic bearings was designed and is presented in Fig. 1.

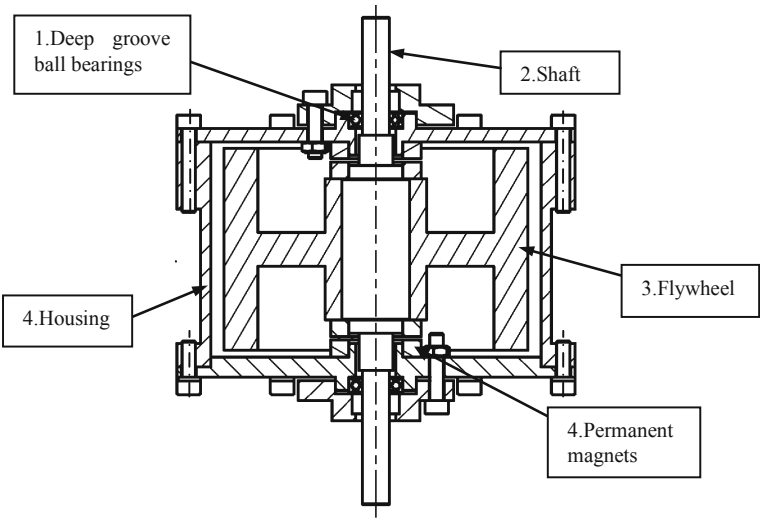

Fig. 1 Section of a flywheel supported on permanent magnetic bearings

The flywheel is supported on the radial direction by two deep grove ball bearings and in axial direction by two pairs of permanent magnetic rings made of Neodym.

The construction has the following advantages:

- bearings friction torque reduction
- bearings lifespan increase
- increase of flywheel maximal speed by eliminating the axial force on the bearings

The mass of the flywheel is 1.5 kg and the maximum supported torque of 3 Nm is limited by a roller clutch. The calculated moment of inertia of the flywheel is 0.0021 kg m^2.

Using the formula:

$$M = I\dot{\omega} \tag{1}$$

we obtain as result a flywheel acceleration from 0 to 18,000 rot/min in 1.3 s.

We can remark the extremely short charging time of the flywheel which makes flywheels suitable for recovering the braking energy of vehicles.

The energy stored in the flywheel can hence be computed:

$$E = \frac{I\omega^2}{2} = 3,729J \tag{2}$$

A vehicle weighing 1,000 kg at a speed of 40 km/h has a kinetic energy of about 61 kJ, so we can store this energy either using 4 flywheels rotating at 40,000 rpm, either increasing the mass moment of inertia of the flywheel.

2.2 The Speed Multiplier

The speed multiplier consists of a two stage timing belt drive having a total ratio of 12. The multiplier is shown in Fig. 2.

The first stage of the multiplier consists of a type H timing belt with a ratio $i_{12} = 4$, while the second stage consists of a type L timing belt with a ratio $i_{34} = 3$. The nominal torque is 36 Nm for the input and 3 Nm for the output. The maximum output speed is 18,000 rpm.

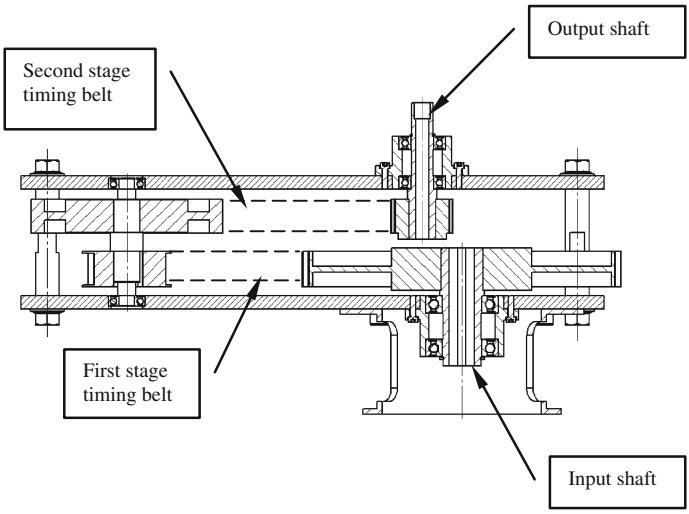

Fig. 2 Cross-section of the multiplier

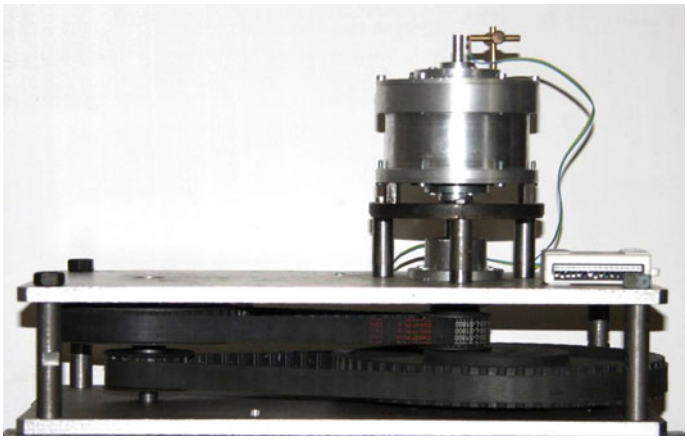

Fig. 3 Photo of the experimental set-up

3 Experimental Analysis

3.1 Experimental Setup

A photo of the test rig and its components is presented in Fig. 3. The energy source is a three phase asynchronous electric motor, which is directly coupled to the input shaft of the speed multiplier. The multiplier is a two stage toothed belt transmission with a total ratio $i_m = 12$. The flywheel assembly is linked to the speed

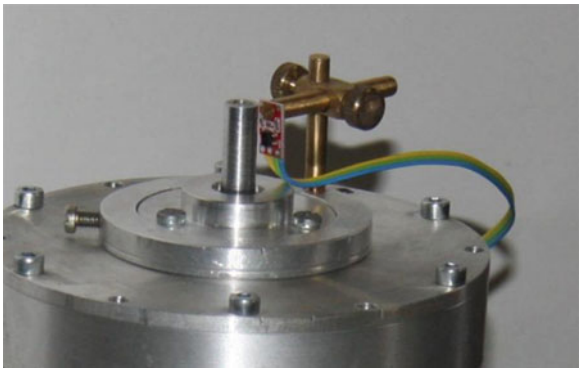

Fig. 4 Detail view of the speed sensor mounted on the flywheel

multiplier by a roller clutch (one-way coupling) so that the flywheel is allowed to rotate freely when the energy input (here the electric motor) stops.

One speed sensor, mounted on the flywheel shaft, is used to measure the flywheel speed variation during acceleration and after the input energy removal (Fig. 4). It is an infrared light sensor which emits and detects the infrared light reflected by an object. Data are collected by a National Instruments data acquisition device (USB-6008) which is controlled through a program written in MATLAB. The obtained results, which consist of two different signals for the reflected and not reflected infrared light, were processed using a FORTRAN program in order to obtain the rotation frequency of the flywheel shaft.

The acquired speed data offers information about the kinetic energy transferred from the input source to the flywheel, on one hand, and the energy loss due to flywheel bearings friction, on the other hand. Actually, the energy loss at the flywheel site is accounted for three main reasons: the bearings friction, the flywheel-air fluid friction and the roller clutch friction.

3.2 Experimental Results

The variation of the rotation speed function of time for three different tests is presented in Fig. 5. We can notice that we have two functioning phases for the flywheel system:

- the acceleration phase where the flywheel is driven by the electrical motor. We can remark that during this phase the rotation speed sharply increases
- the deceleration phase where the flywheel decelerates constantly. We can remark that the deceleration occurs at a much lower rate than the acceleration. The deceleration is due to the friction torque of the ball bearing and to the friction between the flywheel and the surrounding air. It can be noticed that the deceleration rate is larger for higher flywheel speeds

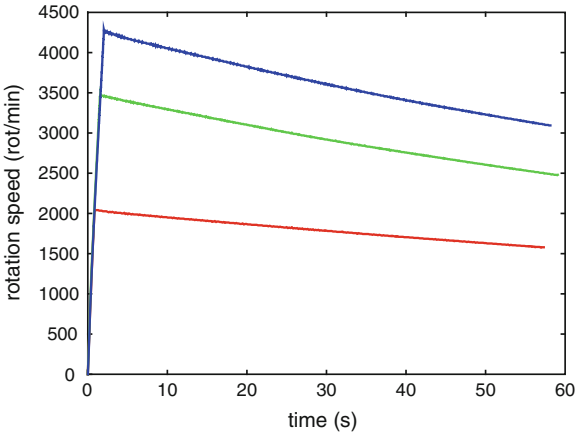

Fig. 5 Variation of the rotation speed function of time for three tests at different maximum speeds (*red line*—2,043 rot/min, *green line*—3,518 rot/min, *blue line*—4,349 rot/min)

The experimental curves were fitted using the least-squares algorithm by the following functions:

$$n_1(t) = 0.02073\ t^2 - 9.2985\ t + 2043.53$$
$$n_2(t) = 0.06956\ t^2 - 21.5297\ t + 3518.05$$
$$n_3(t) = 0.08729\ t^2 - 26.2158\ t + 4349.94$$

The origin of time for each curve is taken at the maximal value of the rotation speed.by using the relation:

$$M = I\frac{d\omega}{dt} = I\frac{2\pi}{60}\frac{dn}{dt} = 2.2 \cdot 10^{-4}\frac{dn}{dt} \tag{3}$$

we can compute the friction torque (in Nmm) for the three analyzed cases:

$$M_1(t) = 0.009121\ t - 2.0456$$
$$M_2(t) = 0.03061\ t - 4.7365$$
$$M_3(t) = 0.0384\ t - 5.7675$$

We can remark that the friction torque is higher for higher rotation speeds. The values of rotation speed and friction torque at initial deceleration point and after one minute are presented in Table 1.

Table 1 Values of rotation speed and friction torque at initial deceleration point and after one minute

Time(s)	M_1 (Nmm)	n_1 (rot/min)	M_2 (Nmm)	n_2 (rot/min)	M_3 (Nmm)	n_3 (rot/min)
0	−2.046	2,043	−4.736	3,518	−5.767	4,349
60	−1.498	1,560	−2.9	2,477	−3.434	3,091

The friction torque of the deep groove ball bearings was calculated using the new model for calculation of the frictional moment. It enables a more accurate computation of the frictional moment generated in SKF rolling bearings according to equation:

$$M_{bb} = M_{rr} + M_{sl} + M_{seal} + M_{drag} \quad (4)$$

For a rotation speed of 4,000 rpm friction torque of the two deep groove ball bearings computed with the specialized SKF software is 0.746 Nmm. The total friction torque on the flywheel shaft computed using the fitted function is 5.23 Nmm. In conclusion the deep groove ball bearings have 14 % of the total friction torque of the system.

4 Conclusions

It is shown that the flywheel represents a reliable and cheap method for storing the braking energy of a vehicle. The flywheel rotation speed decreased by approximately 25 % during 60 s. This time could be the time that the car stays during a red light or at a car queue. Also the friction torque decreases with the rotation speed. The deep groove ball bearings have 14 % of the total friction torque of the system.

Acknowledgments Financial support for the study described in this article was provided by the Sectoral Operational Programme Human Resources Development 2007–2013 of the Romanian Ministry of Labour, Family, and Social Protection POSDRU/89/1.5/S/62557.

References

Ahn J, Jung K, Kim D, Jin H, Kim H, Hwang S (2009) Analysis of a regenerative braking system for hybrid electric vehicles using an electro-mechanical brake. Int J Automot Technol 10:229–234

Ashley S (1993) Flywheels put a new spin on electric vehicles. Mech Eng-CIME Am Soc Mech Eng 115:42–51

Boretti AA (2011) Improvements of vehicle fuel economy using mechanical regenerative braking. Int J Veh Des 55(1):35–48

Clarke P, Muneer T, Cullinane K (2010) Cutting vehicle emissions with regenerative braking. Transp Res Part D: Transp Environ 15:160–167

Douglas E (2009) New generation flywheels. Power Engin 113(5):14

GULIA, N.V. (1988). Der "Energiekonserve" auf der Spur. MIR, Moskau, VEB Verlag Technik, Berlin, Moskau, Berlin

Hebner R, Beno J, Walls A (2002) Flywheel batteries come around again. IEEE Spectr 39(4):46–51

Jang S, Yeo H, Kim C, Kim H (2001) A study on regenerative braking for a parallel hybrid electric vehicle. J Mech Sci Technol 15(11):1490–1498

Kobayashi S, Plotkin S, Ribeiro SK (2009) Energy efficiency technologies for road vehicles. Energ Effi 2(2):125–137

Lindley D (2010) The energy storage problem. Nature 463(7277):18–20

Liu H, Jiang J (2007) Flywheel energy storage–an upswing technology for energy sustainability. Energy Buildings 39(5):599–604

Peng D, Zhang Y, Yin CL, Zhang JW (2008) Combined control of a regenerative braking and antilock braking system for hybrid electric vehicles. Int J Automot Technol 9(6):749–757

Qin D, Ye M, Liu Z (2007) Regenerative braking control strategy in mild hybrid electric vehicles equipped with automatic manual transmission. Front Mech Eng China 2(3):364–369

Strößenreuther F (1996) Machbarstudie und Konzept einer stationären Schwungradanlage zur dezentralen, verbrauchorientierten Energiespeicherung. Diplomarbeit, Fakultät für Maschinenwesen, Institut für Dampf- und Gasturbinen der RWTH Aachen, Aachen, 1996

Xiao W, Wang F, Zhuo B (2008) Regenerative braking algorithm for an ISG HEV based on regenerative torque optimization. J Shanghai Jiaotong Univ (Sci) 13(2):193–200

Zhang Y, Mao X, Li L, Zhuo B (2008) Control of energy regeneration for electric vehicle. J Shanghai Jiaotong Univ (Sci) 13(4):430–435

Mathematical Simulation in Center of Gravity Position and Effect of Weight for a Biped Robot

Csaba Zoltan Mate, Erzsebet Faluvegi and Luciana Cristea

Abstract This paper deals with the kinematics solution of biped robots. It debates the direct and inverse kinematics problems of Leg's 5-dof biped robot, with which a leg can accumulate a position by multiple angle combinations. The symbolic solution for kinematics equations of biped robots is of great importance for the efficient controllability of these robots, describes explicitly in trigonometric form the biped robots' sole's position and orientation according to the joint coordinates. Paper aims to present special issues concerning the analysis of mobile robots with kinematic motion effects on the stability study. In the analysis, the authors used inverse kinematics, which enables rapid modeling and identifying solutions as regards the stability of bipedal robots. The symbolic solution for kinematics equations of biped robots is of great importance for the efficient controllability of these robots. The following article focuses on the biped robot center of gravity simulation and control handle with the aid of mathematical modeling methods (in MATLAB).

Keywords Mechatronics · Stability · Biped robot · Kinematics · Simulation

C. Z. Mate (✉) · E. Faluvegi · L. Cristea
Product Design, Mechatronics, and Environment Department,
Transilvania University of Braşov, Braşov, Romania
e-mail: mcsabazoltan@yahoo.com

E. Faluvegi
e-mail: faluvegi.erzsebet@gmail.com

L. Cristea
e-mail: lcristea@unitbv.ro

G. Dobre (ed.), *Power Transmissions*,
Mechanisms and Machine Science 13, DOI: 10.1007/978-94-007-6558-0_27,

1 Introduction

For a biped robot the sole position and orientation is known, defined within the domain of exterior coordinates if a $\vec{q}$ vector is given with join coordinates. In the case of a robot with n freedom degree, the vector of joint variables is the following:

$$\vec{q} = [q_1, q_2, \ldots, q_{n-1}, q_n]^T \tag{1}$$

and the vector of unknown exterior coordinates is the following:

$$x_q = [x_{q1}, x_{q2}, \ldots, x_{qk-1}, x_{qn}]^T \tag{2}$$

The equation below is the only solution for the so called direct kinematics problem:

$$x_q = f(\vec{q}). \tag{3}$$

If we know sum of the joint's setup and from this we define the coordinate system's position, according to the sole's centre point, as well as its orientation, thus we solved the direct kinematics problem. Inverse kinematics problem means that if the sole's expected position and orientation (within the exterior coordinates) is known, and then with which joint setups can we obtain this. In other words we can say that we are looking for an optimal solution:

$$\vec{q} = f^{-1}(x_q). \tag{4}$$

This task is more complex, and for the direct kinematics problem, since it is not linear, we have to solve equations containing trigonometric functions.

2 The Symbolic Solution for the Direct Kinematics Task

The symbolic solution for kinematics equations of biped robots is of great importance for the efficient controllability of these robots. In the world of low-cost computers, the real-time motion control is an increasingly important requirement. In order to achieve this feature, the lowest computational demand requesting method has to be used. The use of symbolic solution, opposing to numerical methods, is important because accelerates the manipulator trajectory control signals needed to be determined according to the track.

The symbolic form of the kinematics equations describes explicitly in trigonometric form the biped robots sole's position and orientation according to the joint coordinates. In this case, the equation in the range of real numbers can be solved with the minimal possible operations.

3 Kinematic Modeling

Direct kinematics problem is to define all relationships that end-effector position (foot of biped robot) based on joint coordinates practically it ensures internal coordinates conversion (joint) Coordinate external (operational).

Biped robot kinematics equations are (Fig. 1):

$$T_{16} = \begin{bmatrix} cq_1 \cdot cq_5 \cdot cq_2 - sq_1 \cdot sq_5 & -cq_1 \cdot sq_5 \cdot cq_2 - sq_1 \cdot cq_5 \\ sq_1 \cdot cq_5 \cdot cq_2 + cq_1 \cdot sq_5 & -sq_1 \cdot sq_5 \cdot cq_2 + cq_1 \cdot cq_5 \\ cq_5 \cdot sq_2 & -sq_5 \cdot sq_2 \\ 0 & 0 \end{bmatrix}$$
$$\begin{matrix} cq_1 \cdot sq_2 \\ sq_1 \cdot sq_2 \\ cq_2 \\ 0 \end{matrix} \tag{5}$$
$$\begin{bmatrix} cq_1 \cdot (l2 + l3 \cdot cq_2 + l4 \cdot cq_3 + cq_2 \cdot (l5 + l6 \cdot cq_5)) - l6 \cdot sq_1 \cdot sq_5 \\ sq_1 \cdot (l2 + l3 \cdot cq_2 + l4 \cdot cq_3 + cq_2 \cdot (l5 + l6 \cdot cq_5)) + l6 \cdot cq_1 \cdot sq_5 \\ lz2 + l3 \cdot \sin(q_2) + l4 \cdot sq_{23} + l5 \cdot sq_2 + l6 \cdot cq_5 \cdot sq_{234} \\ 1 \end{bmatrix}$$

where: $cq_2 = \cos(q2 + q3 + q4)$, $sq_{234} = \sin(q2 + q3 + q4)$, $cq_1 = \cos(q1)$, $sq_1 = \sin(q1)$, $cq_5 = \cos(q5)$, $sq_5 = \sin(q5)$, $cq_3 = \cos(q2 + q3)$, $sq_{23} = \sin(q2 + q3)$, $l2 = l \times 2$, $l3 = l \times 3$, $l4 = l \times 4$, $l5 = l \times 5$ and $l6 = l \times 6$.

Convert coordinate joint operational details is done by solving the direct kinematics problem and coordinate joint operational coordinate conversion is done by solving the inverse kinematics problem.

Inverse kinematics problem allows the calculation coordinates of the joints, which provide end-effector in the desired position and orientation, given the absolute coordinates (operational). When the problem is the inverse kinematics absolute coordinates (operational). When the problem is the inverse kinematics absolute coordinates (operational).

When the problem is the inverse kinematics solution, it is the inverse geometrical model. If we cannot find an analytical solution for inverse kinematics problem (which happens quite frequently) we resort to numerical methods, but whose weakness is the sheer volume of calculations. The most common method is Newton–Raphson method. Among these features is remarkable for the way it offers and Khalil Pieper and Paul's method. Pieper and Khalil's method allows solving inverse kinematics problem regardless of the values of the robot geometrical.

4 Inverse Kinematics Problem Solving Opportunities

In other word we can say that we are searching for the equations solution, where $\vec{q}$ the searched joint is coordinates vector, and x_q is the known external coordinate's vector:

$$\vec{q} = f^{-1}(x_q). \tag{6}$$

The solution for the inverse kinematics problem, generally speaking is unclear. In the case of the so-called cinematically redundant robots (Zoltán et al. 2002; Christine et al. 2004; Jimmy 2010), where the mobility number is greater than the dimension of the external coordinates, an infinite number of vector $\vec{q}$ can be found, which satisfies the $f(f(\vec{q}) = x_q)$ equation.

In the case of the cinematically non-redundant robots only a finite number of solutions exist. Easy to imagine, for example, we can approach the same point with the same hand-coordination with raised and lowered elbow position as well.

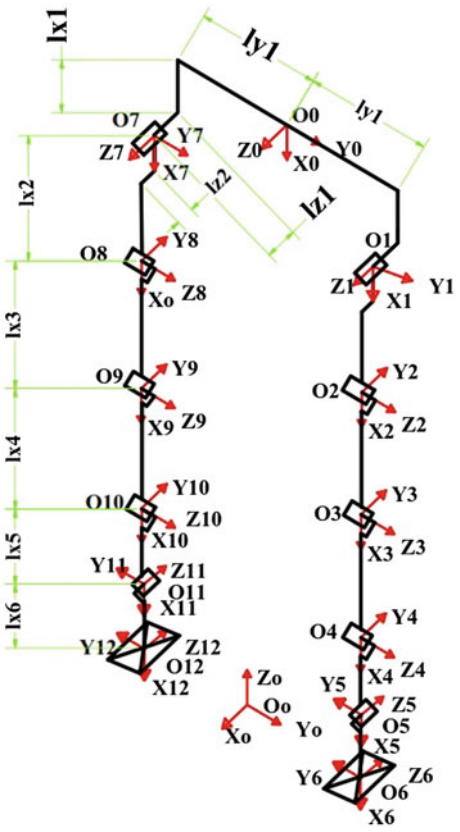

Fig. 1 Kinematic model

Furthermore the possibilities for solving the inverse problem are discussed only for non-redundant manipulators.

During the solution of the problem, non-linear equations have to be solved. For the determination of the roots, two modes of approach are found in the literature: a general numerical solution method is applied (e.g., Newton's method) and other techniques the given biped robot in closed form searches for symbolic solutions.

5 Centre of Gravity

During walking, the feet are subjected to the action of forces (Mate and Cristea 2011; Christine et al. 2004; Jimmy 2010; Nakamura et al. 2007) and moments of inertia and gravity forces. Balancing the forces of gravity is to reduce the mechanical work consumed for drive motor. The position of equilibrium of a system subject to stationary and links under the action of forces is given, is called stable equilibrium, if for a sufficiently small arbitrary variation of the coordinates of its points and arbitrary speeds sufficiently small print of these points, the system will move all the time remaining in the vicinity of equilibrium position. To

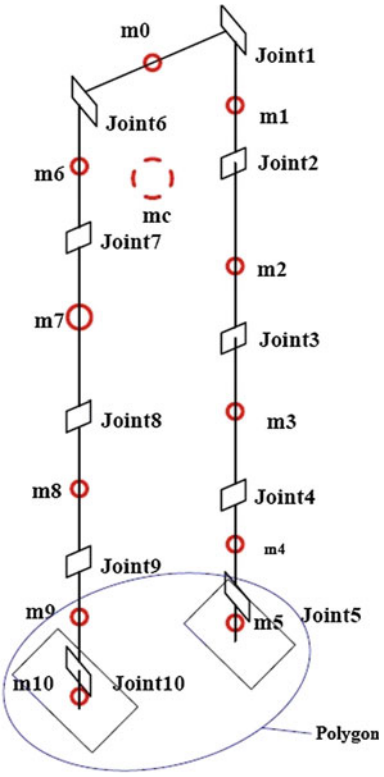

Fig. 2 Robot model and polygon by two leg (mc—weight center)

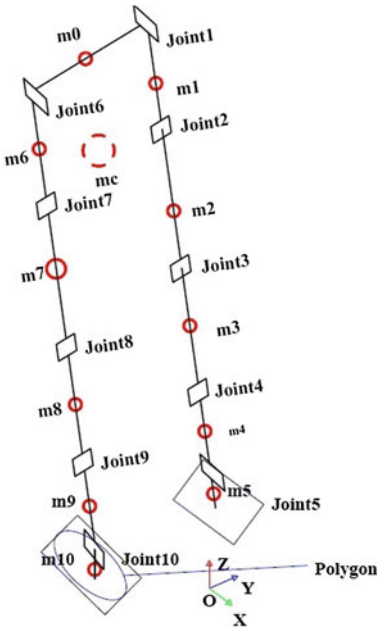

Fig. 3 Robot model and polygon by one leg

determine the center of gravity G of a facility plan is sufficient to determine the position vector r_g thereof with the relationship:

$$\vec{r}_g = \frac{\sum_{i=0}^{10} m_i \cdot r_i}{\sum_{i=0}^{10} m_i}. \tag{7}$$

$$\vec{r}_g = x_g \cdot \vec{i} + y_g \cdot \vec{j} + z_g \cdot \vec{k}. \tag{8}$$

where: m_i is the mass of the *i* element; r_i is the position vector of center of gravity of element *i*.

During walking robot must be stable. This means that its centre of gravity must fall within the polygon (Fig. 2) which consists of the two legs of the robot. If the left leg is raised then the centre of gravity must fall within the polygon of the right leg (Fig. 3). If the projection centre of gravity doesn't fall within the polygon, the robot is unstable. Then it is necessary to tilt (Fig. 3) robot to the right. We know direct and inverse kinematics of the robot and in this way we can calculate the coordinates of the joints. After calculating the joint coordinates it must be checked if the centre of gravity falls within the polygon or, if other compensation is needed for the robot to tilt to the right until the centre of gravity projection falls within the polygon. Easier to solve the problem can be done with an algorithm based on

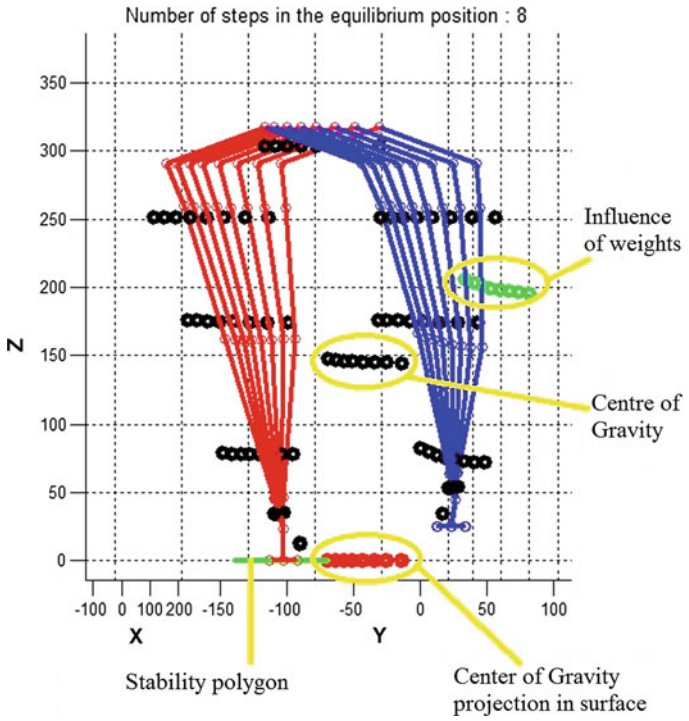

Fig. 4 The influence of weights in a ham

direct and inverse kinematics, with which to verify and ensure the necessary compensation to realize that the position of gravity centre projection of the robot is falling inside the stability polygon.

Bipedal walking is difficult when viewed as a general dynamic system. The dynamics are high degree-of-freedom, nonlinear, under-actuated, naturally unstable, and discretely change from step to step. These combined characteristics place bipedal walking control outside the realm of traditional book control techniques. It is in part due to these difficulties that a large number of different control methods have been developed, and no single method has proven advantageous over the others.

During walking, the feet are subjected to the action of forces (Mate and Cristea 2011; Christine et al. 2004; Jimmy 2010; Nakamura et al. 2007) and moments of inertia and gravity forces. Balancing the forces of gravity is to reduce the mechanical work consumed for drive motor. The position of equilibrium (Fig. 4) of a system subject to stationary and links under the action of forces is given, is called stable equilibrium, if for a sufficiently small arbitrary variation of the coordinates of its points and arbitrary speeds sufficiently small print of these points, the system will move all the time remaining in the vicinity of equilibrium position (Fig. 5).

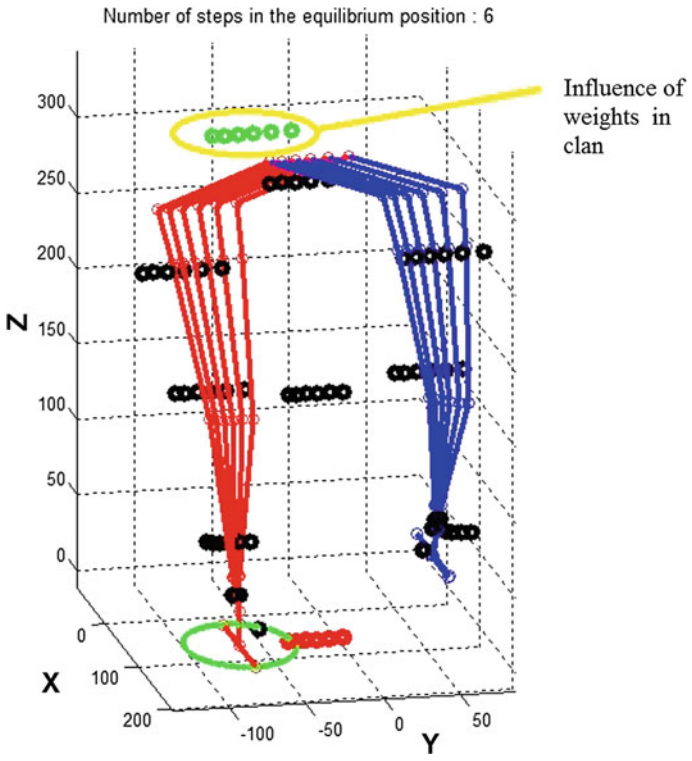

Fig. 5 The influence of weights in a clan

This means that its centre of gravity must fall within the polygon (Fig. 4) which consists of the two legs of the robot. We know direct and inverse kinematics of the robot and in this way we can calculate the coordinates of the joints.

The step (Fig. 4) to raise the left leg or right leg and remains below the leg centre of gravity must fall within the polygon of the remains below the leg. If the projection centre of gravity doesn't fall within the polygon, the robot is unstable. In Fig. 4, is presented an eight -step motion control of the Humanoid robot until a stable position. The only engines give last joints position so you avoid the potential for rollover. The Inverse kinematics solution controlled in path and a direct kinematics is controlled a center of gravity and stability control. So dynamic motion control of the robot is standing into leg keep up without having to disrupt (Fig. 6).

Mathematical analyzes were performed on a humanoid robot, we put some weights in a hips, thighs, shin such part of it in the right sides of the left. Some positions of legs examining a center of gravity by a biped robot It examined how many steps the equilibrium and the following conclusions. When the weights get as close are symmetrical the shaft is to the XZ plane parallel is level, which at passing the $O_0X_0Y_0Z_0$ point (Fig. 1), the robot quickly in all the equilibrium

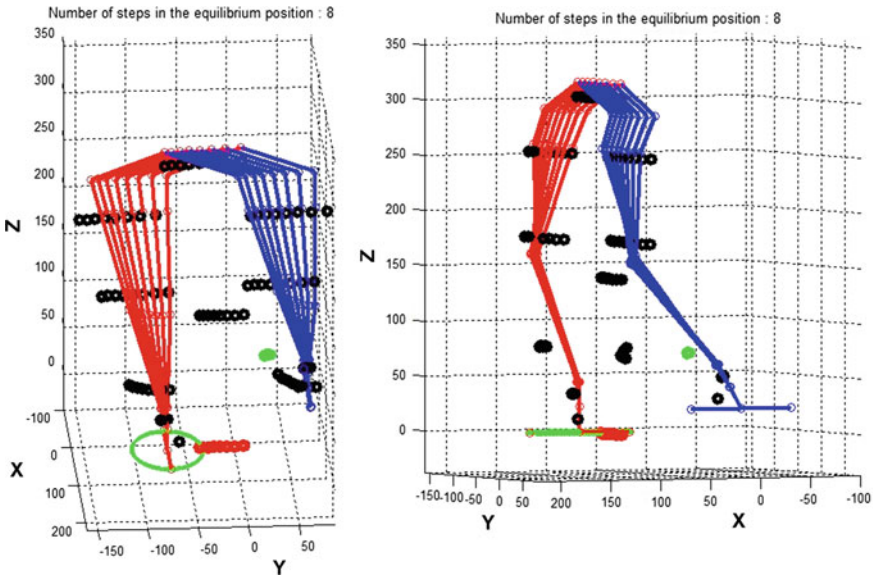

Fig. 6 The influence of weights in a shin

position of the other one can observe food was when the weight of the ground space is then also coming soon to reach the stability position.

6 Conclusions

The method described in this paper is well suited to obtain symbolical inverse functions for the practical relevant redundant kinematics with parallel and/or perpendicular joint axes. The symbolic solution is derived in a closed form and contains the parameters of the additional geometrical constraints. They allow a simple selection of the solution sets, which describe the different possible biped robot poses. The optimization of these poses to the given biped robots task may be fulfilled through any criterion, including nonanalytic. If a biped robot's inverse kinematics problem is symbolic solved well, then this helps a lot on the stability, because the well positioned ligament's overall center of weight has to fall in the given sole's polygon, so that the robot wouldn't tumble over.

Acknowledgments This paper is supported by the sectional Operational Programmer Human Resources Development (SOP HRD), ID59321 financed from the European Social Fund and by the Romanian Government References.

References

Christine A, Philippe P, Bernard E (2004) Artificial locomotion control: from human to robots. Robot Auton Syst 47:203–223

Mate CZ, Cristea L (2011) Aspecte of biped robot stabilization. Comput Sci Inf Technol Optim Robots Manipulators 8:164–169

Jimmy O (2010) A hybrid CPG_ZMP control system for stable walking of a simulated flexiblespine humanoid robot. Neural Netw 23:452–460

Zoltán V (2002) Automatizált eszközök, Budapesti Műszaki Főiskola, Budapest, Június

Nakamura Y, Mori T, Sato M, Ishii S (2007) Reinforcement learning for a biped robot based on a CPG-actor-critic method. Neural Netw 20:723–735

Irregular Speed of Rotation in the Hooke's Joint: Visualization and Study of its Influence on the Value of the Forces into the Pivot and on the Strength of the Forks

Peter Nenov, Trifon Trifonov, Dimiter Velchev and Viarka Ronkova

Abstract This study presents a simplified version for load determination in the limit positions of the forks and the dependencies to specify the forces in the hinges of the forks at a set angle. It is proven that not always maximum stress values are caused when operating in two limit positions, and this contradicts the existing design recommendations in the literature. Difficult to observe special features of the Hooke's joint operation under the conditions of variable values of the transmission ratio are illustrated.

Keywords Hooke's joint' · Kinematics · Power analysis · Strength calculation · Visualization

List of Symbols

φ_1	The angle between the fork of the driving shaft and plane II
φ_2	The angle between the fork of the driven shaft and the plane perpendicular to plane II and passing through the shaft 2
a	Radius of the circle described by the fork hinges
γ	The angle between the intersecting driving and driven shafts

P. Nenov (✉) · T. Trifonov · D. Velchev · V. Ronkova
University of Ruse, Ruse, Bulgaria
e-mail: pnenov@gmail.com

T. Trifonov
e-mail: trifonow@yahoo.com

D. Velchev
e-mail: dvelchev@uni-ruse.bg

V. Ronkova
e-mail: vronkova@uni-ruse.bg

G. Dobre (ed.), *Power Transmissions*,
Mechanisms and Machine Science 13, DOI: 10.1007/978-94-007-6558-0_28,

$F_tF_aF_r$ Tangential and axial components of the reactions in hinges (the marks * at the top show the projections of the forces)
T, P Torque and power transmitted by the shafts
α, β The angles between the forces $F_{t1} - F_{r1}$, and $F_{t2} - F_{r2}$

1 Introduction: Determination of the Rotation Variability Through Analysis of the Angles of Forks Rotation

A simple universal joint (known also as Hooke's joint) consists of a pair of hinges connected at 90° to each other. The axis of each hinge is perpendicular to the axis of the shaft to which it connects. The axes of shafts and hinges cross each other at a point (Fig. 1). This allows the use of universal joints for transmitting torques between intersecting shafts at angles of 30° up to 45° and for compensating significant variations.The problem with them is the irregular speed of rotation of the driving shaft. A brief description of the classic approach for finding the relationship between the angular velocities of both shafts of Hooke's joint is given below. A random position of rotation is selected, and the elements of the joint are examined in three planes of projection - plane I, perpendicular to the drive shaft;—plane II—defined by the axes of both shafts;—plane III—perpendicular to the axis of the driven shaft. By rotating and overlaying plane I and plane III on plane II [see Fig. 1, Reshetov 1989)] also from the animations in Fig. 2 (visualizing the kinematics and facilitating the extension of our conclusions) and from $\Delta\, O'''A'''B'''$ can be seen that $tg\varphi_2 = \overline{A'''B'''}/O'''B'''$. Differentiating with respect to time t and its angles φ_1, φ_2 and taking into consideration that $d\varphi_1/dt = \omega_1$ and $d\varphi_2/dt = \omega_2$ we obtain (Nenov et al. 2010):

$$\mathrm{tg}\varphi_2 = \mathrm{tg}\varphi_1/\cos\gamma,$$

$$\omega_2 = \omega_1 \cos\gamma/\,(1 - \sin^2\gamma\ \cos^2\varphi_1) \tag{1}$$

and

$$\omega_{2\max} = \omega_1/\cos\gamma,\ (\varphi_1 = 0), \tag{2}$$

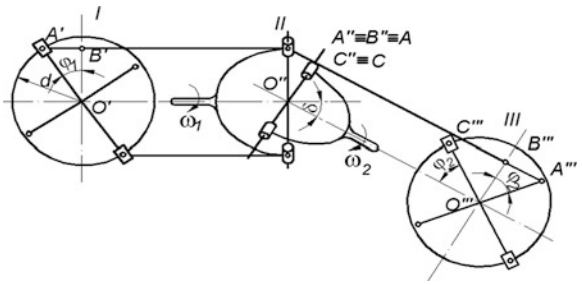

Fig. 1 Hooke's joint

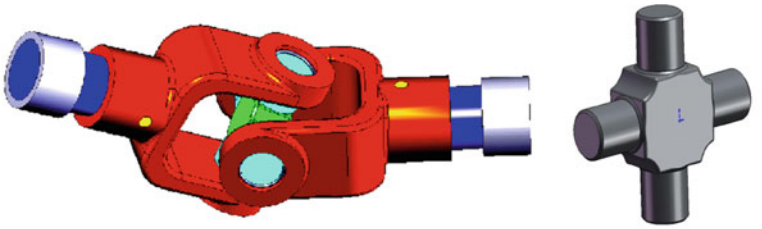

3D-images of the universal joint and his components (a vie presentation)

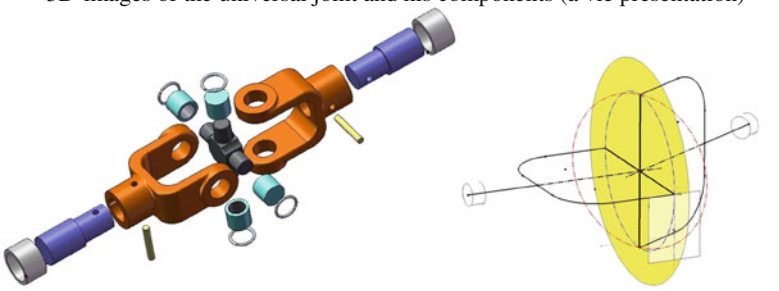

Elements of the Hook's joint and particularities. How is the cross moving

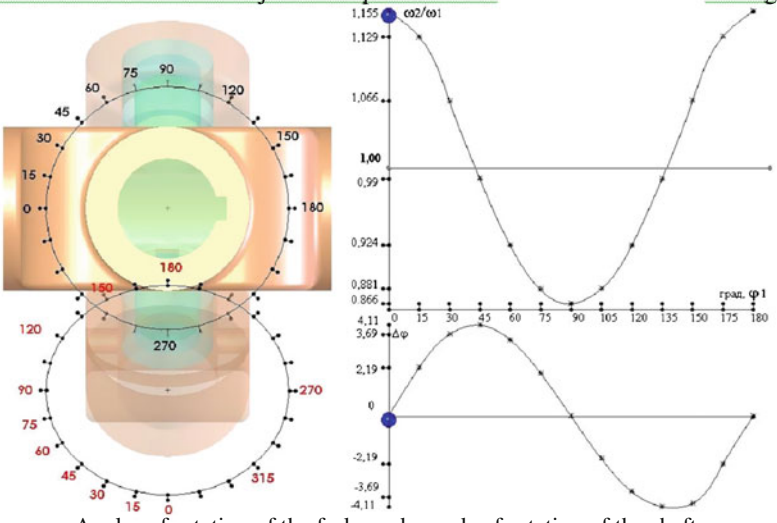

Angles of rotation of the forks and speeds of rotation of the shafts

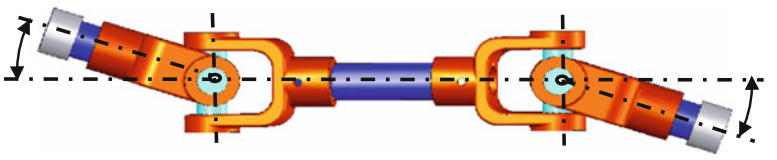

Universal double joint – conditions for synchronization the speeds of rotation

Fig. 2 Extracts of animations for the universal joint

resp.

$$\omega_{2\min} = \omega_1 \cos\gamma, \varphi_1 = 90^\circ. \tag{3}$$

2 Direct Determination of the Extreme Values of Forces and Variation Through Power Analysis

2.1 Extreme Values of the Forces in the Hinges

Significant forces with periodic variations exist in the universal joint. Their extreme values and components are particularly interesting. These can be defined by equilibration the forks and the cross.

The cross that can be only subjected to forces lying in its plane is under the action of both forks. The torque T_1 is transmitted from the driving fork to the cross by means of the couple $F_{t1} = T_1/(2a)$.

At $\varphi_1 = 0$ no other forces or torque are acting on the driving fork, and the driving fork is not under the action of a bending moment, i.e. $M_1 = 0$. From the condition for equilibrium of the cross-connection follows that $(2a)F_{t1} = (2a)F_r$, where F_r is the couple of forces with which the driven fork counteracts the F_{t1} forces. The couple F_r acts in a plane perpendicular to the axis of the driving shaft (I plane of projection). The torque T_2 creates a couple in a plane perpendicular to the axis of the driven shaft (III plane of projection). The forces F_r decompose into components. First component F_{t2} corresponds to the moment T_2. The second one, F_{a2} lies in the plane of the driven fork.

From the above description and Fig. 3 follows that

$$\begin{aligned} F_{t2} &= F_r \cos\gamma = F_{t1} \cos\gamma \\ \text{and } F_{a2} &= F_r \sin\gamma = F_{t1} \sin\gamma \end{aligned} \tag{4}$$

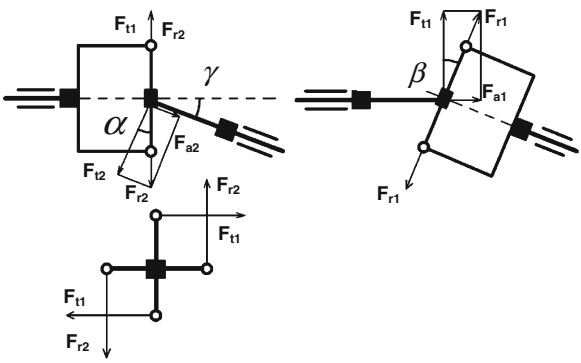

Fig. 3 Determination of the extreme forces in Hooke's joint in its two limit positions ($\phi_1 = 0;\ 90^\circ$)

From the equation of the driven fork the equilibration comes out that

$$\begin{aligned} T_2 &= 2a\,F_{t2} = 2a\,F_{t1}\cos\gamma = T_1\cos\gamma \\ \text{and } M_2 &= 2a\,F_{a2} = 2a\,F_{t1}\sin\gamma = T_1\sin\gamma. \end{aligned} \tag{5}$$

When $\varphi_1 = 90^\circ$ (Fig. 3) the plane of the cross is perpendicular to the axis of the driven shaft and this shaft is subjected only to torsion:

$$F_{t2} = F_r = F_{t1}/\cos\gamma\; T_2 = 2a\,F_{t2} = 2a\,F_{t1}/\cos\gamma = T_1/\cos\gamma\,. \tag{6}$$

The driving shaft is subjected to combined torsion including bending:

$$F_{a1} = F_{t1}tg\gamma\; M_1 = 2a\,F_{a1} = 2a\,F_{t1}tg\gamma = T_1tg\gamma. \tag{7}$$

2.2 Extreme Values of the Rotation Non-uniformity

The obtained values of the forces F_{a1}, F_{t1}, F_{a2} and F_{t_2} can be used for a strength test of the shafts and the endangered sections of the cross and the forks. Details of these calculations are given in the (Handbook of Agricultural Machines 1967; Nenov et al. 2007).

The analysis of forces and moments (Fig. 3) we have made, apart from being simple and clear, allows additionally an easier and direct determination (compared with the method of Reshetov) of the extreme values of the speed of rotation. The logic of the summary is that if losses in the bearings of the universal joint are ignored, then may be accepted that the input shaft power (P_1) is the same as the output shaft power (P_1), i.e.

Respectively

$$P_1 = P_2 \text{ and } T_1\omega_1 = T_2\omega_2. \tag{8}$$

When the forks are arranged in the first specific position $(\varphi_1 = 0)$, then torques T_1; $T_2 = T_1\cos\gamma$ and as the angular velocity of the first fork is ω_1, we got $T_1\omega_1 = T_2\omega_2 = T_1\cos\gamma\;\omega_2$, or $\omega_2 = \omega_1/\cos\gamma = \omega_{2\max}$ (it confirms conclusion 2).

In the second specific position $(\varphi_1 = 90^\circ)$ the torques are T_1 ; $T_2 = T_1/\cos\gamma$ and from $T_1\omega_1 = T_2\omega_2 = \omega_2T_1/\cos\gamma$ is evident that $\omega_2 = \omega_1\cos\gamma = \omega_{2\min}$ (it confirms conclusion 3).

3 Power Components of Load at Any Given Angle of Rotation of Fork 1

The direction of the resultant force F_{r1} is always parallel to the arm $\overline{OB}$. In the intermediate position it will be parallel to $\overline{OB_1}$.Their projections F^*_{r1} and $\overline{OB}^*$ on H**P** should also be parallel: $F^*_{r1}||\overline{OB}^*$. From Fig. 4 $\overline{MM}^* \perp \overline{OA_o}^*$ and $F^*_{t1} \perp \overline{OA_1}^*$.

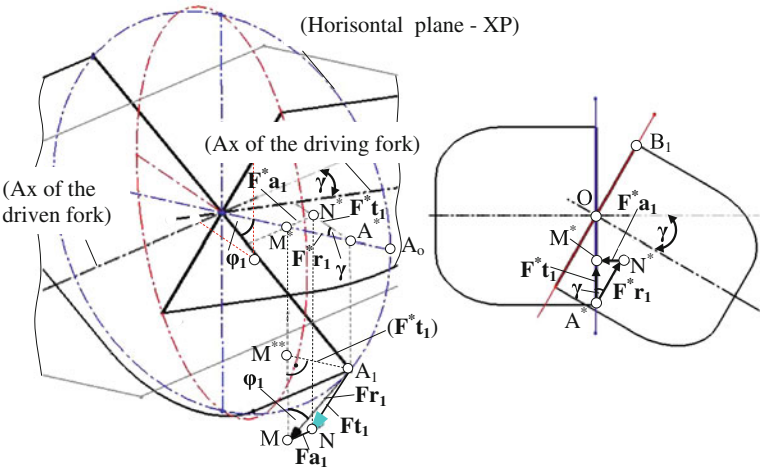

Fig. 4 Forces in the pivot of the ax of the spider jointed it with fork1, and their projections in the plane of the booth shafts

Therefore angle ϕ_1 is equal to the angle (M * MA1) as angles with mutually perpendicular arms.

If a straight line $||F^*_{t1}$ is drawn through point A_{11}, it will cross $\overline{MM^*}$ at point M^{**}. Then $\overline{M^{**}A_1} = F^*_{t1}$ and A_1MM^{**} is equal to ϕ_1, as they are angles with mutually parallel arms $\left(\overline{OA_o}||\overline{M^{**}A_1}\right.$ and of $\left.\overline{OA_1} - \text{a mutual arm}\right)$

From $\Delta MM^{**}A_1$ comes out that

$$F^*_{t1} = F_{t1} \sin \phi_1. \tag{9}$$

Because F^*_{a1} and F_{a1} are parallel to the axis of *Fork 1* the angle $M^*N^*A^*$ is equal to $(90^\circ - \gamma)$ or angle $N^*A^*M^*$ is equal to angle γ. From $\Delta\, N^*M^*A^*$ follows that $F^*_{t1}/F^*_{r1} = \cos\gamma$. Substituting F^*_{t1} with its value from (9), then for F^*_{r1} we get

$$F^*_{r1} = F_{t1} \sin \phi_1 / \cos\gamma. \tag{10}$$

From the same triangle $F^*_{a1} = F^*_{t1} \sin\gamma = F_{t1} \sin\varphi_1\, tg\gamma$ and as $F^*_{a1}||F_{a1}$, the magnitude of the axis component is

$$F_{a1} = F^*_{a1} = F_{t1} \sin\varphi_1\, tg\gamma. \tag{11}$$

In Hooke's joints are acting significant forces with periodic variations.

The schemes and analyzes represented here allow us to determine the forces in the hinges of the first fork as well as the torque on the first shaft for any random position of the angle of rotation φ_1 using the following formulas:

Forces and moments applied to the driving fork and driving shaft

$$T_1, \varphi_1, F_{t1} = T_1/(2a), F_{a1} = F_{t1} \sin\varphi_1 \, tg\gamma, F_{r1} = \sqrt{F_{t1}^2 + F_{a1}^2}, M_1 = F_{a1}.2a$$

The forces and moments applied to the second fork and the second shaft can be calculated without any additional graphic diagrams, using only still available results. Besides, the requirement on equality of the reactions in both fork hinges should be taken into account, as well as its compulsory positioning in the plane of the cross-connection of the hinge.

Forces and moments applied to the driving fork and driven shaft

$$\varphi_2 = aTrctg(tg\varphi_1/\cos\gamma),\ \omega_2 = \omega_1 \cos\gamma/(1 - \sin^2\gamma \cos^2\varphi_1),\ F_{r2} = F_{r1}$$
$$T_2 = T_1\ \omega_1/\omega_2,\ F_{t2} = F_{t1}\ \omega_1/\omega_2,\ F_{r1} = \sqrt{F_{t1}^2 + F_{a1}^2}, F_{a2} = \sqrt{F_{r2}^2 - F_{t2}^2}$$
$$M_2 = F_{a2}.2a$$

Table 1 and Fig. 5 display the forces in the joints of both forks, for seven angles.

Table 1 Forces acting on the hinges of booth forks, at $\varphi_1 = 0 \div 90°$

#	φ_1 (degrees)	φ_2 (degrees)	ω_1 (1/ min)	$\frac{\omega_2}{\omega_1}$ (1/ min)	F_{t1} (N)	$\frac{F_{a1}}{F_{t1}}$ (–)	$\frac{F_{r2}}{F_{t1}}$ (–)	$\frac{F_{a2}}{F_{t1}}$ (–)
1	**0**	**0**	**1**	$(1/\cos\gamma)$	**1**	**0**	$(\cos\gamma)$	$(\sin\gamma)$
				1.155			0.867	0.500
2	15	17.192		1.129		0.149	0.886	0.488
3	30	33.690		1.066		0.289	0.938	0.451
4	45	49.107		0.990		0.408	1.010	0.382
5	60	63.435		0.924		0.500	1.082	0.280
6	75	76.936		0.881		0.558	1.135	0.148
7	**90**	**90**		0.867		0.577	1.155	**0**
				$(\cos\gamma)$		$(tg\gamma)$	$(1/\cos\gamma)$	

Example: *Input* T_1, $2a$ $\gamma = 30°$ n_1 $\omega_1 = \pi\, n_1/30$

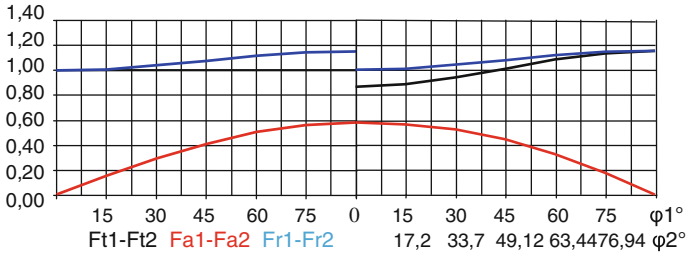

Fig. 5 Loading the forks caused by turning within the range $\varphi_1 = 0 \div 90°$. **a** Driving fork (fork 1) **b** driven fork (fork 2) (The load within the other intervals can be determined through mirror projecting)

4 Stress Determination in the Bound Positions and at Any Given Angle of the Fork Rotation

4.1 Model, Forks Fixing and Load Distribution

The strength analysis of the forks is performed by means of the software package [COSMOS-Works Designer, 2007]. Seven positions of both forks according to the pre-set angle of rotation of the driving *Fork 1* - φ_1 are being examined:

The torque transmitted to the driving *Fork 1* is assumed for T_1 = 170 Nm. Driving *Fork 1* and driven *Fork 2* have the same form and sizes. A discretized model is shown in Fig. 6. The real sizes and shapes of the forks (Nenov et al. 2007; Solid Works 2006) and second-order tetrahedral finite elements with intermediate units (Kurowski 2004) are used. The nominal dimension of KE is 10 mm, but at the areas of stress concentration a local improvement of the net has been

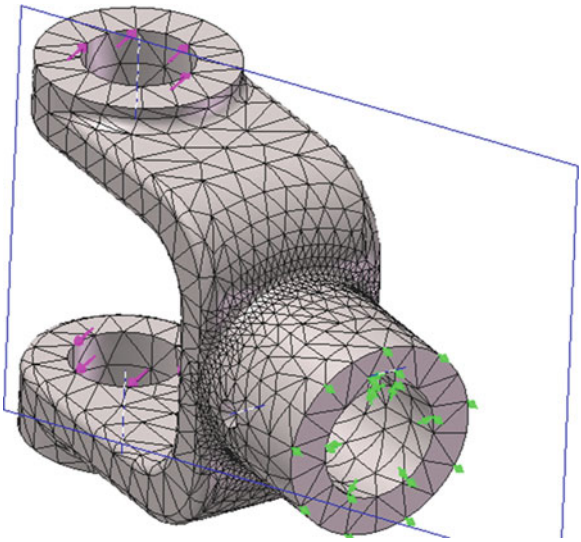

Fig. 6 Discretized model of the forks

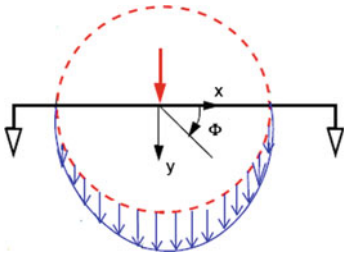

Fig. 7 Load distribution at the holes of the joints: f(fi) = F.Sin(fi)

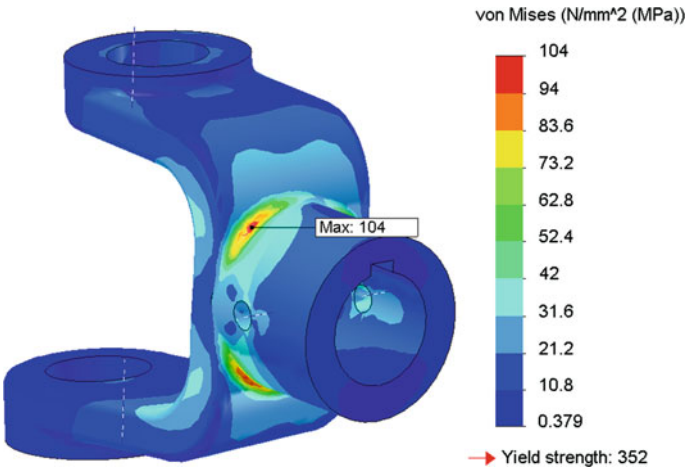

Fig. 8 Stressed state of Fork 1, $\varphi_1 = 90°$

Table 2 Fork 1 - External loading and maximum stresses, (MPa)

$\phi_1,^\circ$	0	15	30	45	60	75	90
F_{r1}, N	2,073	2,096	2,158	2,239	2,318	2,374	2,394
$\alpha,^\circ$	0	8.50	16.10	22.21	26.57	29.15	30
$\sigma_{\max}$	85.0	85.1	95.9	98.6	99.3	100	104

performed, thus KE dimension of 2 mm. The final section is rigidly fixed. This does not satisfy the real boundary conditions, but our analysis refers mainly to the stress on the fork, not in the bearing housings and keyhole. In this case the Saint-Venant's principle can be used, as the areas under consideration are located far away from the attachment points. The load is applied to the bearings by using a special distribution function f(fi), (Fig. 7). For each case the surfaces under imposed load are different and created by the intersection of the cylindrical hinge hole with a plane passing through its axis and perpendicular to the direction of the acting force $F_{r1}(F_{r2})$ (Fig. 8).

4.2 Stresses in the Limit at a Given Positions of the Forks

According to the calculations, maximum stress values in the forks occur not always when operating in both limit positions (see Table 2, $\sigma_{\max}$ at $\varphi_1 = 60°$), that may contradict the existing recommendations.

Table 3 Fork 2—External loading—values and visualizing the stresses (MPa)

ϕ_1,°	0	15	30	45	60	75	90
F_{r2}, N	2,073	2,096	2,158	2,239	2,318	2,374	2,394
β,°	30	28.88	25.66	20.70	14.48	7.44	0
σ_{max}	90.4	92.4	96.2	98.1	101	97.4	98.2
Position & appearance of zones of high stresses	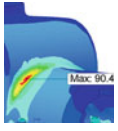	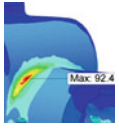	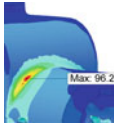	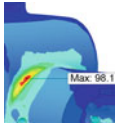	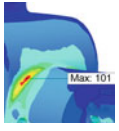	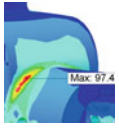	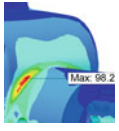

5 Conclusion

- A simplified option of load determination in the limit positions of the forks is proposed.
- Dependency-related determinations of the forces acting on the hinges of both forks at each set angle of rotation are derived.
- It is proven through computation that not always maximum stress values occur at forks when working in the two limit positions (Table 3, σ_{max} when $\phi_1 = 60°$), which contradicts the current design recommendations in the literature.
- Difficult to observe features in Hooke's joint operation are illustrated by overcoming the standard limitations of the 3D-animation systems under the conditions of variable values of the transmission ratios.

References

Reshetov DN (1989) Machine elements, M., Machinary
Nenov P, Angelova E, Dobreva A, Dobrev V (2010) Machine elements with almanac. University of Ruse, Ruse, p 311
Handbook of Agricultural Machines (1967) In: Kleckin M (ed) Machinary
Nenov P, et al. (2007) Design of machine elements, S., Technika, 2002, 2007
COSMOS-Works Designer (2007) Training manual, 2006, Dass.Systemes, SAE I
Kurowski P (2004) Finite element analysis for design engineers. SAE International, Pennsylvania
Solid Works (2006) Книга за потребителя, С., Техно.Логика ЕООД

Geometrical Blocking Contours as an Instrument for High-Technology Design of Geometry of Involute External and Internal Gear Drives

Peter Nenov, Bojidar Kaloyanov and Emilia Angelova

Abstract In our practice The GBC from the type "profile shifts coefficients-centre distance" are new instrument and style for more effective design of involute cylindrical gear drive with high level of their parameters for quality. The final results of the design procedures depend strongly from the correctly finding of the area of all possible decisions. It's very useful this area to be completed with some basic geometrical and kinematic parameters for quality, such as contact ratio, thickness at the top of the teeth, velocity of sliding on the working profiles and others. The new high-technologic design strategy concerns especially the design process of the gear drives, jointed really or conditionally for receiving some additional advantages.

Keywords Design · Involute gear drives · Geometrical blocking contours · Joint gear drives · Optimizing of gearing

List of Symbols

many The same, as in the standards

P. Nenov (✉) · B. Kaloyanov · E. Angelova
University of Ruse, Ruse, Bulgaria
e-mail: pnenov@gmail.com

B. Kaloyanov
e-mail: kaloyanovi@yahoo.com

E. Angelova
e-mail: ang@uni-ruse.bg

G. Dobre (ed.), *Power Transmissions*,
Mechanisms and Machine Science 13, DOI: 10.1007/978-94-007-6558-0_29,

1 Introduction: Interconnected Gearings

The design of different gear transmissions, gearboxes, speed reducers, etc., is hampered by the fact that some of their gears are interconnected. The connection may be real or conditional (Nenov 2002). Figure 1a shows a version of a machine-tool unit-head, in which the internal gear ring participates directly and at the same time in the operation of several internal gearing. For example, in the family of planetary speed reducers K-H-V (Fig. 1b) each product includes only one internal gear, operating completely independently of the other representatives from this type. But for technologic and economic reasons it is expedient that the internal gear rings of all reducers of the family are identical and they have the same module, number of teeth, profile shifts coefficient, etc. This makes the ring a conditional joining component, invariable to the whole family.

The example of Fig. 1c refers to 2 K-H gear reducer, whose branches include one external and one internal gear mesh. Or the both gearings have the same centre distances and the satellite gears are common for the external and the internal meshes i.e., they are practically real connecting components. In other constructions from the previous type, developed as a family of reducers having different gear ratios of each member, a conditional (indirect) joins presents, also. They are imposed by additional requirements, for example for fixed parameters of the ring gear with internal teeth (Fig. 1d). It is especially important in the given case that the application of a ring gear with constant parameters assures higher economic manufacturing indexes. In the same time such requirement significantly complicates the design of the family of speed reducers.

In the engineering practice the design of gear drives for: Norton's gearboxes of machine-tools, gearboxes of motor vehicle and different families of cylindrical speed reducers is based on the idea for their "equal centre distance".

Our software systems, creating Geometric Blocking Contours (GBC)—type 'xi-aw' for external spur and helical gear drives are well known [Fig. 2; see also Nenov et al. (1988), (2010)]. They provide effective solutions for an independent gear give, as well for interconnected gears. This paper is focused on developing a

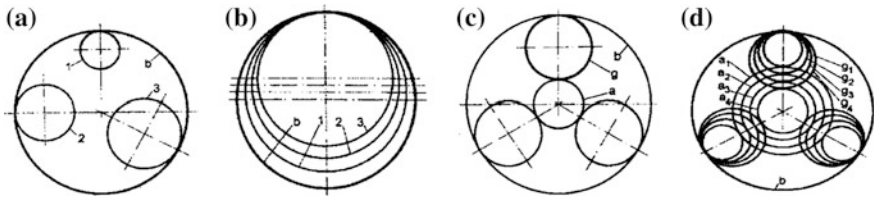

Fig. 1 Gear trains with real and conditional connecting units: **a** A machine-tools unit-head (the real connecting unit is the gear with internal teeth-"b"); **b** A family of planetary gearings K-H-V (conditional connecting component is a gear with internal teeth "b"); **c** Planetary gear 2K-H with *three streams* (with a real connecting unit—satellite pinion "g", integrated in the external and internal gearing); **d** A family of planetary gears 2K-H (the real connection units—pinions "g" and the conditional connecting component—ring gear "b")

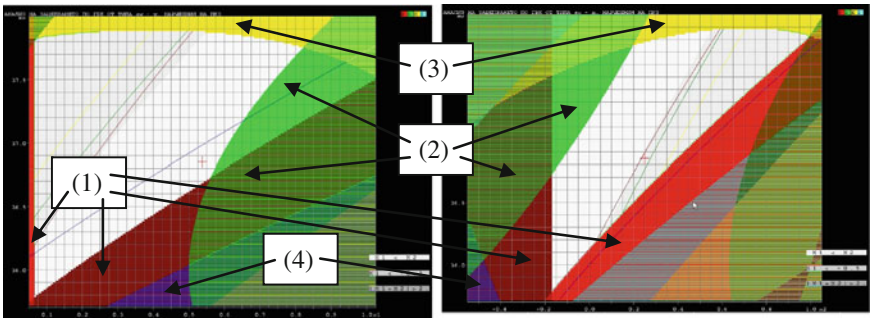

(a) First projection (x1-aw) **(b)** Second projection (x2-aw)

(c) Colors of limitations:

Undercut-**red(1)**; Pointing-**green(2)**; Overlapping-**yellow(3)**; Interference-**blue(4)**

Fig. 2 Geometric blocking contours of a cylindrical external gear (z1, 2 = 16, 20)

similar system for internal gearing. The clarification of the characteristics and capabilities of the system is supported with examples, solving the problems of specific types of schemes.

2 Parameters of Gear Meshing Quality

The geometric blocking contours created by the new author's system are based on the main restrictive conditions, resulting from the quality requirements for internal gearing. Detailed descriptions are given in the handbooks and standards on Geometry of involute internal gearing. The version presented here is oriented to design gear drives without modification of the initial contour.

By developing the program system several requirements are taken into consideration. They can be defined, as follows:

1. The teeth of the pinion should not be undercut at the fillet or root;
2. The teeth of the pinion should not be cut at their top;
3. Provide for radial clearance in the gearing;
4. Provide for necessary contact ratios;
5. Provide for a sufficient thickness at the top of the teeth;
6. Lack of interference at the top of gear teeth, in the time of action;
7. Lack of interference at the top of the teeth, in case of radial assembly;

8a. Lack of interference at the top of the internal gear's teeth, during the cutting process by gear shaper cutter;

8b. Lack of cut-off the teeth of the gear with internal teeth during the gear-cutting process.

Table 1 shows the summarized requirements of meshing quality (GOST 16530-70; GOST 16532-70) in order to clarify the information that is synthesized in the

Table 1 Provide for quality parameters of internal gearing (excerpt)

1. Requirement of avoid the undercutting: $x_{1\min} = h_l^* - h_a^* - z_1 \sin^2 \alpha + 2\cos\beta$
   At $x_1 \le x_{1\min}$ there are undercutting in the base of the external toothing
2. Requirement of avoid cutting of the teeth of the pinion in their top:

2.1. $h_1 = (d_{a1} - d_{f1})/2 \le (2h_a^* + c^*)m$; or

2.2. $\rho_{j1} = (d_1/2)\sin\alpha_t + (h_{l0}^* - h_a^* - c^* + x_1)m/\sin\alpha_t > \rho_{a1} = (d_{a1}/2)\sin\alpha_{a1}$,
   where h_{l0}^* have to be given or assigned as $h_{l0}^* = 2h_a^* + c^*$, or

2.3. $h_{j1} = \left(0.5d_{a1} - \sqrt{\rho_{j1}^2 + 0.25d_{b1}^2}\right) \ge 0$

3. Checking up the radial clearance in the gear drive
   $c_1 = a_w - 0.5(d_{a2} + d_{f1}) \quad c_1 > [c_1] \quad c_2 = a_w - 0.5(d_{a1} + d_{f2}) \quad c_2 > [c_2]$
4. Finding the transverse (ε_α), overlap (ε_β) and total (ε_γ) contact ratios:

4.1. $\varepsilon_\alpha = [z_1 tg\alpha_{a1} - z_2 tg\alpha_{a2} + (z_2 - z_1)tg\alpha_{tw}]/2\pi \; \varepsilon_\alpha^n = [z_1(tg\alpha_{a1} - tg\alpha_{l1})]/2\pi$

4.2. $\varepsilon_\beta = bw\sin\beta/(\pi m)$

4.3. $\varepsilon_\gamma = \varepsilon_\alpha + \varepsilon_\beta$

5. Control on the thickness of the teeth at their outside diameters

5.1. $s_{na1} = d_{a1}\left(\frac{\pi/2 + 2x_1 tg\alpha}{z_1} + inv\alpha_t - inv\alpha_{a1}\right)\cos\beta_{a1} \; \beta_{a1} = arctg(d_{a1}tg\beta/d_1)$

5.2. $s_{na2} = d_{a2}\left(\frac{\pi/2 - 2x_2 tg\alpha}{z_2} - inv\alpha_t + inv\alpha_{a2}\right)\cos\beta_{a2} \; \beta_{a2} = arctg(d_{a2}tg\beta/d_2)$

6. Inspection for interference at the top of gear teeth, in the time of action;

6.1. When $\delta = \frac{z_1}{z_2}\mu_{\max} - \arcsin\left(\frac{d_{a1}}{d_{a2}}\sin\mu_{\max}\right) + \gamma_{12} > 0$, there is no interference
   Here $\gamma_{12} = inv\alpha_{a1}\; z_1/z_2 - inv\alpha_{a2} + (1 - z_1/z_2)\; inv\alpha_{tw}$
   and $\mu_{\max} = \arccos\left(d_{a2}^2 - d_{a1}^2 - 4a_w^2/(4a_w d_{a1})\right)$

7. Inspection for lack of interference at the top, in case of radial assembly;

7.1. Condition for lack of interference: $d_{a2}/d_{a1} \ge 1$

7.2. Additional condition for lack of interference
   $\mu' = \arccos\sqrt{\frac{(d_{a2}/d_{a1})^2 - 1}{(z_2/z_1)^2 - 1}} > \mu_{\max} = \arccos\left(\frac{d_{a2}^2 - d_{a1}^2 - 4a^2 w}{4a_w d_{a1}}\right)$

7.3. Condition for lack of interference when $\mu \le \mu_{\max}$
   $\delta = \mu_{\max} z_1/z_2 - \arcsin(\sin\mu_{\max} d_{a1}/d_{a2}) + \gamma_{12} \ge 0$

7.4. Condition for lack of interference, when $\delta < 0$:

Combinations of 4 value of the auxiliary angle $\mu_{1\div4} = \psi_{a1} + \pi n/z_1$,
calculated for $\psi_{a1} = \frac{\pi}{2z_1} + \frac{2x_1 tg\alpha}{z_1} + inv\alpha_t - inv\alpha_{a1}$ and 4 integer values of n:
   $n_2 = \mathrm{int}[z_1(\mu\prime - \psi_{a1})/\pi)]; \; n_1 = n_2 - 1; \; n_3 = n_2 + 1; \; n_4 = n_2 + 2$

8a. Lack of interference at the top of the internal gear's teeth, during the cutting process by gear shaper cutter: $\rho_{l2} > \rho_{p2}$, where

$\rho_{l2} = 0.5d_{a0}\sin\alpha_{a0} + a_{w02}\sin\alpha_{tw02}$ and $\rho_{p2} = 0.5d_{b1}tg\alpha_{a1} + a_w\sin\alpha_{tw}$.

8b. Lack of cut-off the teeth of the gear with internal teeth during the gear-cutting process. Calcul
   $\mu'_{02} = \arccos\sqrt{[(d_{a2}/d_{a0})^2 - 1]/[(z_2/z_0)^2 - 1]}$
where $\gamma_{02} = inv\alpha_{a0}\, z_0/z_2 - inv\alpha_{a2} + inv\alpha_{tw02}(z_2 - z_0)/z_2$
   and $a_{w02} = (z_2 - z_0)m\cos\alpha_t/(2\cos\beta\cos\alpha_{tw02})$
When $\delta_{02} = z_0\mu'_{02}/z_2 - \arcsin d_{a0}\sin\mu'_{02}/d_{a2} + \gamma_{02} < 0$ "there is no cut-off"

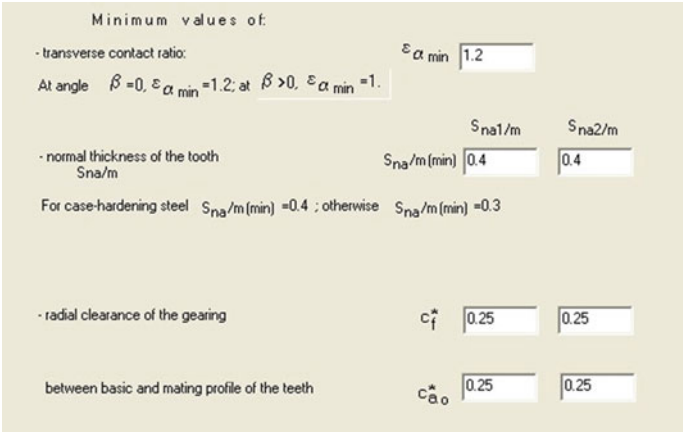

Fig. 3 Excerpt from the input information of the system

automatically developed contour of the given gear. However, if additional data is needed, it can be provided through new modular units supplementing the system's project tasks (GOST 19274-73; Bolotovskii et al. 1986).

The great number of the parameters for quality of the gearing and the relatively complicated mathematical description of a part of them make it difficult to determine directly the limit for vary with the basic meshing parameters and the relevant areas of solutions tolerance. Therefore, a pure mathematical summarizing variant seems to be unreasonably complicated to develop, control the results, and expand the possibly changes of the solution requirements. The possibilities of making the follow-up processing and easy use of the results, are also essential. The data for contours plotting is developed through programme modules that provide for checking by a particular parameter of meshing quality.

A great number of gearings are checked by the set dialogue figures of limitations (Fig. 3) that are formed with a certain module and within an interval, focused on covering good project's solutions.

Limitation data input for the minimum transverse contact ratio $\varepsilon_{\alpha\,\min}$, the thickness at the top of the teeth $(S_{na\,\min})$ and for radial clearance factor c*o.

In the cases, when verification task are performing only, the results of the follow-up checks on different criteria are compared with the limit values, in a table format as current data. The approximation to the final solutions looks for an optimal values, and requires complex assessment of the results of the meshing quality checks. And it is even more difficult to find good solutions for the interconnected gears. That's why a higher efficiency for assessing the results has been asked by using their graphical layout. The strength of such analysis comes from the visual connection between the calculated and the admissible (blocking) values for a grate number of important indicators.

3 Creation of GBC for Internal Gearing

The module units used for the quality checks of a gear drive meshings with a completely familiar geometry are in the basis of the automatically developed contour. The GBC is creating and developing on the check results of all possible gears, formed for a sequence of centre distances and admissible for the initial basic parameters. A package of profile shifts coefficients x_1, resp. x_2 is generating at a small step, till achieving sufficient remoteness from their zero values in positive and negative directions. The generating scheme we preferred has elements of wastefulness, in terms of the volume of calculations, and its rationality could be disputed. But with the present parameters of the computing equipment the detected defect slows down the calculation process insignificant. And in the same time this is strongly balanced by the simplicity of the algorithm provided. Generally, the creation of contours according to this scheme is reduced to calculation and analysis of all gearing quality parameters (Table 1) with following visualization through the GBC (Fig. 4):

Input: α, β, z_1, z_2, m, distance packet $a_w(i)$, matrix with factors $x_{1/2}(i, j)$.

$$\begin{aligned} \alpha_t &= arctg(tg\alpha/\cos\beta) \\ \alpha_{tw}(i) &= ar\cos[(z_2 - z_1)m\cos\alpha_t/(2\cos\beta\, a_w(i)] \end{aligned} \tag{1}$$

$$x_\Sigma(i) = (inv\alpha_{tw}(i) - inv\alpha_t)(z_2 - z_1)/(2tg\alpha);\ x_2(i, j) = x_\Sigma(i) + x_1(i, j)$$

The new automatically generated geometric blocking contours for internal gearings looks like those for external, because of the good results obtained up to now. The other reason is connected with providing conformability with the GBC

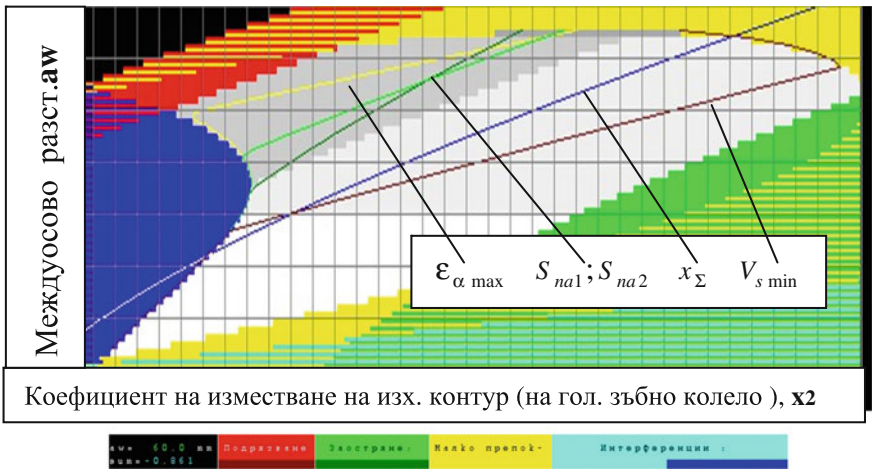

Fig. 4 Second projection (x2-aw) of GBC of internal gearing. *x2* profile shifts coefficient, *aw* centre distance [basic parameters of the gearing: m = 2 mm, z1 = 48, z2 (*ring gear*) = 96]

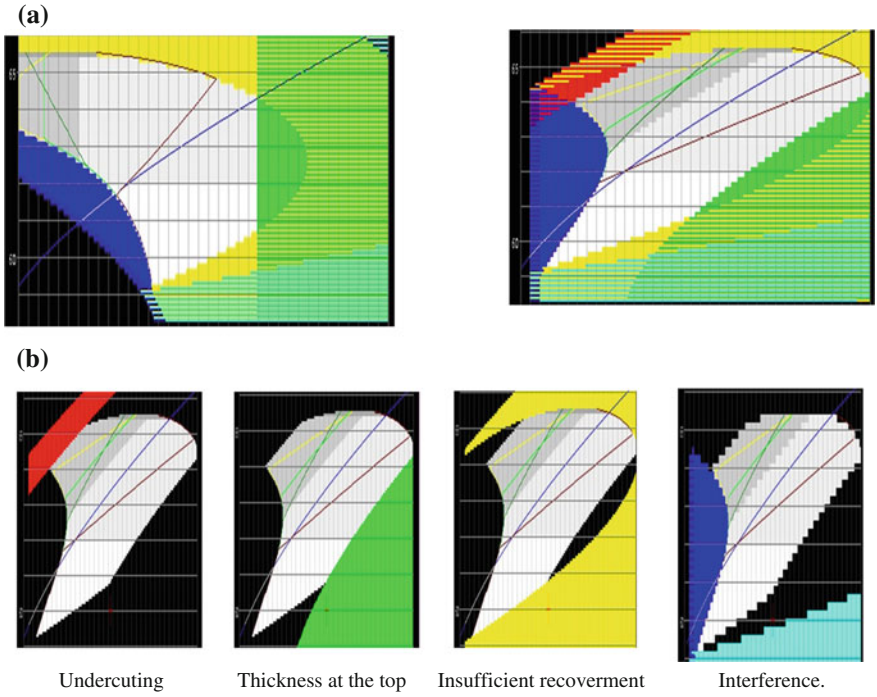

Fig. 5 GBC of internal gearing—projections and analysis, according to the gearing quality parameters (*GQP*). **a** First (x1-aw) and second (x2-aw) projection of GBC of a gearing with c z1, 2 = 48, 96. **b** Information from the second projection for the limits of the basic quality parameters

of interconnected gearings (which are still in process of development) where one gear runs at the same time in internal and in external meshing.

It is assumed that everywhere (see Fig. 2) the red areas (1) are indicating undercut, those in green (2)—pointing, the yellow ones (3)—insufficient overlapping factor, the blue areas (4)—interference and/or tooth cut-off respectively. The lighter color nuances mean disturbed parameters of gearing quality for small gears, and the deeper color nuances—for big gears.

In the new structure of GBC there is an additional curve with information about the total (summarized) shifts coefficient x_Σ (*see formula* 1) as a function of the centre distance a_w. Having in mind that: $x_\Sigma = x_2 - x_1$ (internal gearing) and $x_\Sigma = x_2 + x_1$ (external gearing), the data for x_Σ available in the coordinate system with abscissa x_1, respectively x_2 make obvious and the total shifts coefficient, which is helpful for the final estimation of her quality parameters.

Important information is brought with the curve $\varepsilon_{\alpha\,\max}$, that indicates the area of maximum values of the transverse contact ratio for each centre distance in the range of possible solutions (see the grey–white sections of the contour—Figs. 4, 5; data

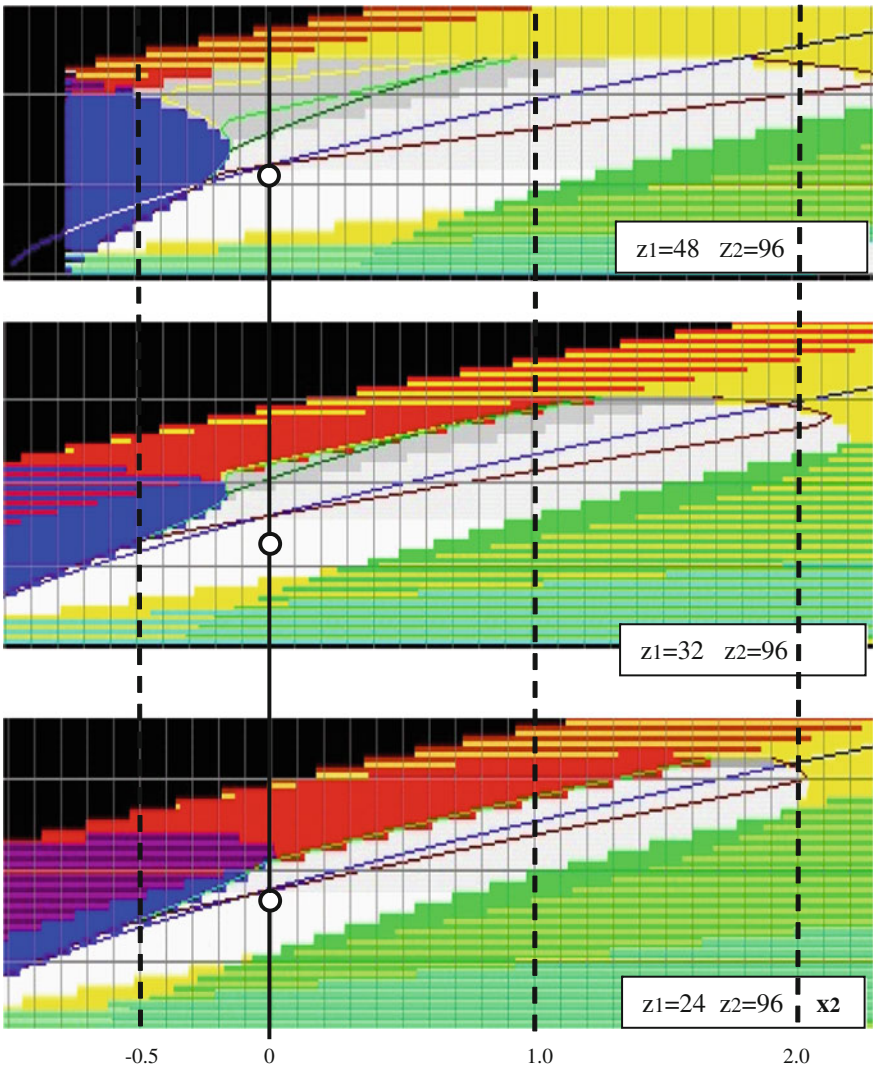

Fig. 6 Second projection of GBC of really joined internal gearings (an aggregate gear-head for metal-cutting machine tool; u1 = 2.00 u2 = 3.00 u1 = 4.00)

for the parameter's values, displayed through the curves, appears at the lower part of the screen when moving the mouse or cursor).

The third curve displays the areas, where the thicknesses at top of the teeth of the both gears are approximate the same or are as closer as possible (see Table 1, p. 5). The fourth curve represents the areas within the range of possible solutions of GBC, where **the maximum speeds of sliding over the working profiles of the booth gear have a minimum value**:

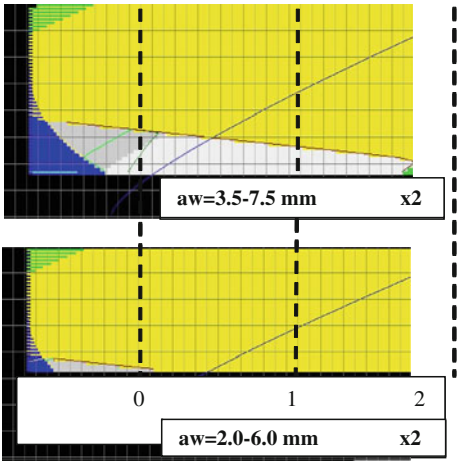

Fig. 7 Second projections of GBC of conditionally connected gearing from a family reducers K-H-V (z2 = 100; z1, 2 = 97, 98)

$$V_{s\min}[a_w(i),\ x_1/x_2(i,j)] = \min\{[\max[V_{sa1}(i,j),\ V_{sa2}(i,j)]\}, \tag{2}$$

where

$$V_{sa1}(i,j) = \omega_2[tg\alpha_{a1}(i,j) - tg\alpha_{tw}(i)](z_2/z_1 - 1)d_{b1}/2,$$
$$V_{sa2}(i,j) = \omega_2[tg\alpha_{tw}(i) - tg\alpha_{a2}(i,j)](z_2/z_1 - 1)d_{b2}/2,$$
$$\textit{and} \quad d_{a1}(i,j), \alpha_{a1}(i,j),\ \textit{pend}\ d_{a2}(i,j), \alpha_{a2}(i,j)\ u\ \alpha_{tw}(i),$$

[see (GOST 16530-70, GOST 16532-70; GOST 19274-73)].

Figure 6 presents GBC of gearings with a really joining gear ring "b" (Fig. 1a). The gear ring "b" is a really joined element in the gear trains on Fig. 1c, d also.

By examining the contours comes out that:

- The profile shifts coefficient **x2** of the gear ring b could not be greater than 2.0, according to the lowest contour;
- The high values of the transverse contact ratio are in the upper part of the contours; in the same time the profile shifts coefficient x2 have to be bigger than (−0.2), because in the left positions of the contour the value of ε_α are too small;
- Values of x2 higher than 0.7 do not increase the contact ratio (see upper contour);
- The thickness of the teeth at the outside circles are almost equal at x2 $\approx$ 0.6.

Figure 7 displays the second projections of GBC of interconnected K-H-V gearings (see Fig. 1b).

Appropriate values of the profile shifts coefficient x2 of the joining gear are in the range (−0.5 $\div$ 0) while greater center distances are preferable, because of the high load of the bearings; (the third gearing of the family—see Fig. 1b—requires certain changes of the tooth proportions).

The raising of the contours by curves, presenting the examining parameters, together with their values within the whole range of the admissible decisions,

makes them more clear and usefull. The including into the creating contours some other data, concerning the power abilities of the designed gear trains extend the opportunities for optimization on the base of complex criteria.

4 Conclusion

The presented GBC type "x-aw", for internal gearings, offer new design opportunities for finding the total range of the admissible solutions, from the point of view "parameters of quality". The GBC form a suitable basis calculation and optimizing of internal gearings on the ground of complex criteria. They could help designer in efficient projecting of joined internal gear drives.

References

Bolotovskii IA, Bezroukov BE et al (1986) Reference book by geometric calculation of invlolute and worm gear drives. M Machinary

GOST 19274-73. Cylindrical involute gear drives with internal gearig. Calculation of geometric parameters. Rassion State Standard

GOST 16530-70, GOST 16532-70. Gear drives. Russian State Standard

Nenov P (2002) Parametric optimizing of cylindrical gear drives. Sofia, Tehnica (Bulgarian), p 152

Nenov P, Angelova E, Dobreva A, Dobrev V (2010) Machine elements with almanac. UR, Ruse (Bulgarian), p 311

Nenov P, Tjufectchj A, Kaloyanov B, Angelova E (1988) Program system for geometric calculation of involute gear drives with internal gearing, by PC. In: Proceedings of RPTU. Riga, Russia (Russian), p 210–211

Bearings Failure of Gear Drive Unit Caused by Gear Resonance

Milosav Ognjanović, Miloš Ristić and Sanja Vasin

Abstract Gear transmission units could work properly in the resonance conditions but they cause very unfavorable effects on other components and the environment. It is necessary to identify the resonance range, and afterwards to harmonize design parameters with operating conditions, so as to avoid primary and secondary resonance. This article presents the procedures for gear resonance identification and its influence on rapid failure of bearings and other gears of bucket wheel excavator drive's gearbox, entitled SRs-1301. Thereafter follows the correction of design parameters of critical gear pair in order to avoid its resonance and excitation of natural frequency of gearbox housing. Besides the analysis of dynamic behavior of gears, this article provides FEM analysis of stiffness of gearbox components and modal analysis of gearbox housing. Applying new parameters, calm work of gearbox is obtained, and life cycle of bearings suits service load.

Keywords Gear transmissions · Gear resonance · Bucket wheel excavators

List of Symbols

T	Torque
n	Speed of rotation (revolutions per minute – RPM)
K_v	Dynamical factor
K_A	Application factor
v_s	Velocity of teeth collision

M. Ognjanović (✉) · M. Ristić · S. Vasin
Faculty of Mechanical Engineering, University of Belgrade, Belgrade, Serbia
e-mail: mognjanovic@mas.bg.ac.rs

M. Ristić
e-mail: mristic@mas.bg.ac.rs

S. Vasin
e-mail: vasinsanja@gmail.com

G. Dobre (ed.), *Power Transmissions*,
Mechanisms and Machine Science 13, DOI: 10.1007/978-94-007-6558-0_30,

f	Teeth mesh frequency
f_r	Frequency of resonance (natural frequency)
c_{th}	Theoretical average specific teeth stiffness
c_γ	Average specific teeth stiffness
c'	Real average specific teeth stiffness
c	Total average teeth stiffness
z_n	Equivalent number of teeth
x	Offset factor
β_{1-2}	Helical angle
ε_α	Contact ratio
b	Face width
J	Moment of inertia
m_r	Reduced mass
m_e	Equivalent mass

1 Introduction

Gear teeth meshing process is distinguished by many phenomena (Ognjanovic and Agemi 2010). Resonance is among the most important of them. So far, researches in the field of gear dynamics have been mainly oriented to sub-critical range of teeth mesh frequency. The aim of these researches is to determine the influence of transmission errors on dynamic characteristics (Velex et al. 2011). Researches of gears behavior in the range of resonance are not frequent. The operation of gears in resonance frequency range is possible, but undesirable. Additionally, variable stiffness of gear teeth in mesh produces nonlinear vibrations of gears. This nonlinearity is one of the most common topics in the gear resonance field (Liu and Parker 2008; Faggioni et al. 2011). The influence of friction and sliding between tooth flanks on above mentioned nonlinearity is very significant for the behavior of gears in resonance (He et al. 2008), but stiffness of supports, bearings and shafts too (Kang et al. 2011). Identification of different types of resonance (Shuting 2008; Rama Rao et al. 2011) has major importance for recognition of resonance effects. These effects are important for determining the consequences (Ognjanovic et al. 2010) and coordinating the design parameters (Ognjanovic and Benur 2011).

This article analyses the effects of gear resonance on other components of gearbox and possibility to design parameters harmonization in order to eliminate undesirable effects. The case study refers to the input gearbox at bucket wheel of bucket wheel excavator SRs-1301.

2 Problem Identification

The traction gearbox at bucket wheel of bucket wheel excavator SRs-1301 has five stage transmissions with fixed shaft axes. At the second stage, there is a pair of spiral bevel gears, and all other stages consist of helical gears. The output shaft is connected with bucket wheel shaft by means of a flange. The bucket wheel shaft is one of the supports of the gearbox. There is a 3D model of gears of the input gearbox at bucket wheel of bucket wheel excavator, presented in Fig. 1. The gearbox is driven by electromotor with the power of 400 kW and $n = 1{,}480$ rpm. Nominal torque at the input shaft is $T_1 = 2{,}581$ Nm.

In the course of exploitation, the bearings of the second shaft were prone rapidly to failure. At once, there was even the failure of the teeth of spiral bevel gears that were torn apart. It was determined by calculation that all of the gears and bearings shouldn't fail due to the service loads, even if they were intensively overloaded. Figure 2 shows the assembly of the second shaft and bearings. The damage occurred previously at spherical roller bearings. Due to bearings worn out, internal clearance was extremely enlarged. Axial displacement of the shaft became huge. All these facts indicated large axial forces with variable direction.

Axial forces applied to the second shaft for a given rotation direction are directed opposite to each other (Fig. 3a), and their subtraction is directed to axial bearing at the left support. Due to resonance of helical gear pair, displacements of these gears are in anti phase. Teeth collide with each other very intensive, vibrations are intensive as well, and axial force is with alternated direction (Fig. 3b). Spherical roller bearings are very sensitive to axial loads, and they fail quickly. Fast failure of bearings is aided by axial supporting of the outer ring, which enforces bearing to accept axial force oriented to spiral bevel gear. When axial clearance in spherical roller bearings becomes higher than lateral clearance

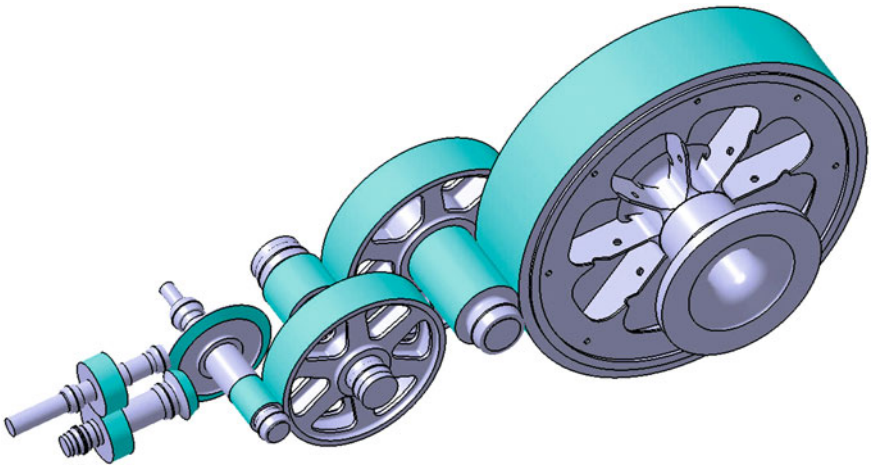

Fig. 1 3D model of the bucket wheel of bucket wheel excavator

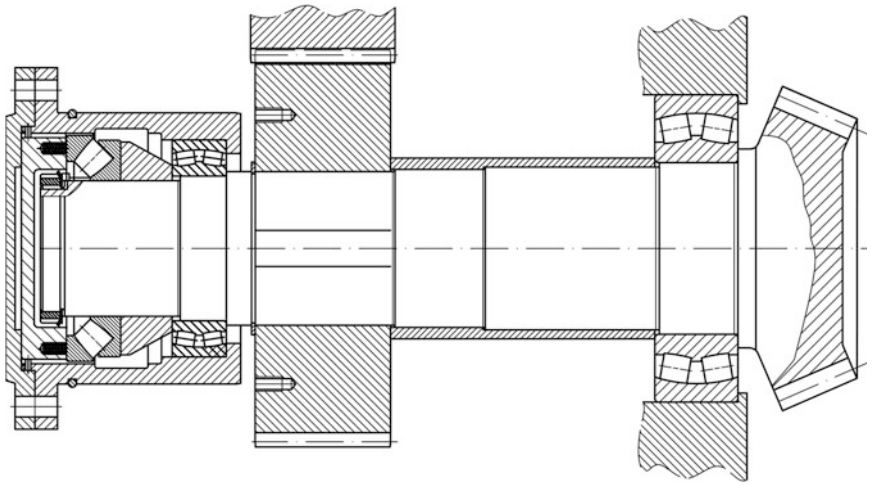

Fig. 2 Assembly of the second shaft

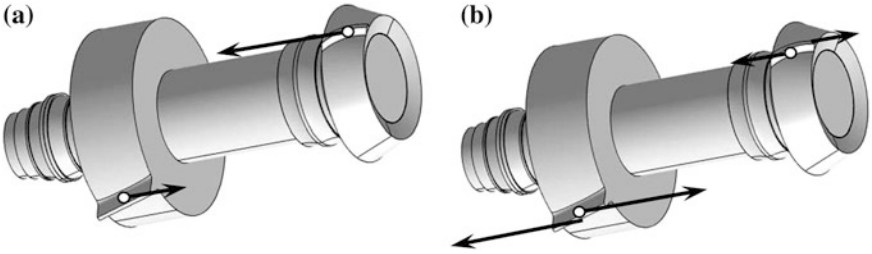

Fig. 3 Axial forces at second shaft: **a** at stationary work, **b** at resonance

between teeth of spiral bevel gears, axial resonance force from helical gears becomes accepted by bevel gears. Because of spiral shape of the teeth, axial resonant force from helical gear pair acts on the teeth of bevel gear pair in alternative directions, leading to their failure.

Causes of the failure of bearings could be also additional loads induced by elastic deformations of shaft, bearing supports, housing walls or by natural frequencies of housing. These reasons led to systematic analysis of these components by FEM. Figure 4 presents a 3D model of shaft meshed by tetrahedron elements, with extremely enlarged deformations. Figure 6 shows deformations of bearing nave. Stresses and displacements of all components are determined assuming the forces on gears that correspond to nominal power increased by the magnitude of short- time overload (application factor $K_A = 1.75$). Shaft deformations are very small (highest displacement is 12 μm), so it could be assumed that those deformations didn't affect self-adaptive bearings. The way of supporting of the bearing nave contributes to unequal displacement, which reflects to unequal distribution of

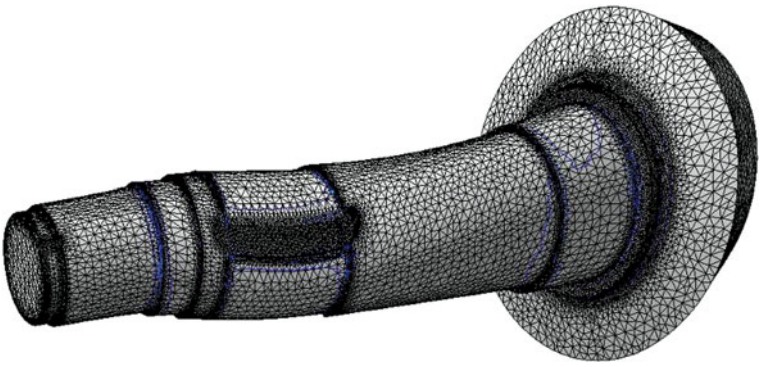

Fig. 4 Elastic deformation of shaft caused by forces on gears

radial force on two bearings in this support. Analyzing the stiffness and natural frequencies of housing by means of FEM, it is determined that housing is rigid enough and is not the cause of bearing failure (Figs. 5 and 6).

3 Gear Drive Resonance Identification

Gear teeth meshing is a dynamical process which generates dynamical excitation forces, such as elastic variable forces and collision forces (Fig. 7), but also forces due to sliding and rolling of tooth flanks. When constant load is applied, variation of gear teeth number in mesh leads to variation of displacement, and consequently to variation of teeth stiffness in the course of teeth meshing process. Speaking of helical gears, these effects are reduced by magnitude and steadiness of variation. Elastic excitation forces change proportionally to variation of the stiffness of meshed teeth. Above listed changes relate to gears with no geometrical deviation. Since deviation of shape and pitch cannot be fully avoided, these deviations contribute to additional increase of amplitude and change of shape of "stiffness variation-elastic force" function. Another significant excitation during the teeth meshing is collision of teeth. Due to elastic deformation of teeth caused by load they transmit, the position of teeth changes, so the contact starts by collision. The collision speed is proportional to the teeth deformation and the speed of rotation n. The difference in pitch of meshed teeth could increase collision speed, which is taken into account by means of dynamical factor K_v. The value of this factor increases proportionally to the increase of gear teeth mesh frequency f. Depending of the ratio between f and resonance frequency f_r it's been distinguished sub-critical, critical and super-critical range of teeth mesh frequency. When teeth mesh frequencies become equal to natural frequency, there comes to a resonance, which drastically increases the K_v factor. According to standards for gear calculations

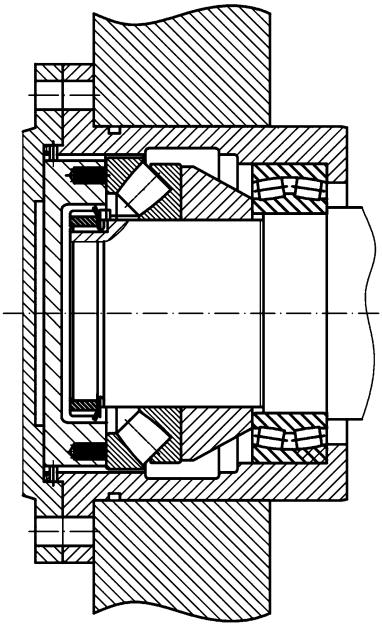

Fig. 5 Supporting of nave and bearing

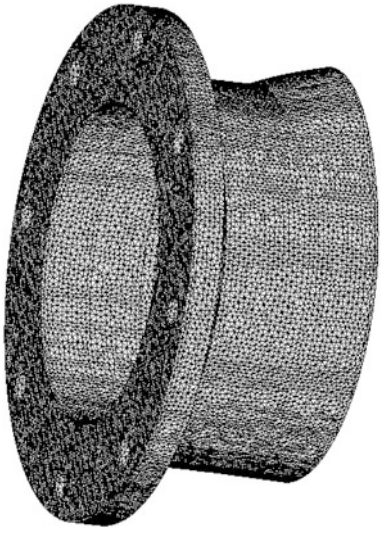

Fig. 6 Supporting nave deformation

ISO 6336 and DIN 3990, dynamical factor is determined in a different way for every of these three ranges.

Gears are specific for their characteristic to work in resonance, unlike the other mechanical structures whose amplitudes increase so much in resonance that could lead to failure in a short time. That is possible since teeth could absorb free

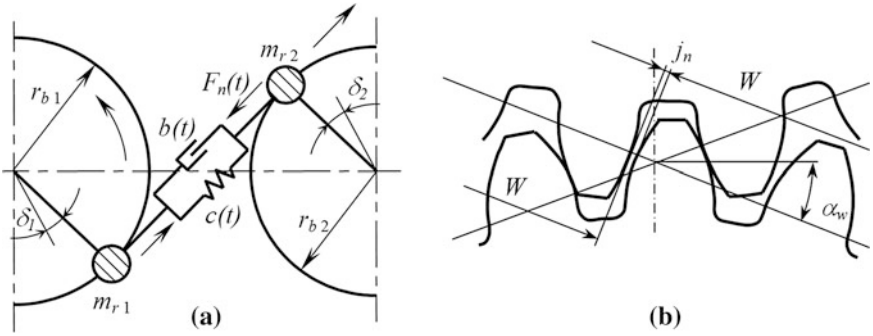

Fig. 7 Gear vibrations; **a** model of vibration, **b** lateral clearance out of resonance

vibrations in resonance during their interaction. That's how both flanks are making alternating (reverse) contacts (Fig. 7b). One of the signs that gears are in resonance is the trace of carrying, which could be seen on both flanks of a tooth. Figure 7b presents the lateral clearance between teeth. In resonance, due to anti phase displacement of gears, teeth alternately collate by left and right flank, generating intensive alternate forces (Fig. 3b). Regarding the wear analysis of left and right tooth flank, it is determined that resonances are present at first and second stage of transmission (Fig. 1).

Basic parameters for calculating the resonance frequencies of meshed gears are teeth in mesh stiffness and value of the reduced mass. According to DIN 3990 for helical gear pair at first stage of transmission, theoretical teeth stiffness is:

$$\frac{1}{c_{th}} = 0.04723 + \frac{0.15551}{z_{n1}} + \frac{0.25791}{z_{n2}} - 0.00635x_1 - 0.11654\frac{x_1}{z_{n1}} - 0.00193x_2 - 0.24188\frac{x_2}{z_{n2}} + 0.00529x_1^2 + 0.00182x_2^2 \quad (1)$$

Equivalent numbers of teeth and offset factors of these gears are $z_{n1} = 56$, $z_{n2} = 63.4$, $x_1 = x_2 = -0.198$. For these values, theoretical specific teeth stiffness is $c_{th} = 17.49$ N/μm, mm. The influence of elastic displacements in teeth contact is included multiplying by 0.8, and influence of helical angle multiplying by cos β, so real specific teeth stiffness of full cross-section (without gear hub holes—full hub) is $c' = 0,8 \cdot c_{th} \cdot \cos\beta_{1-2} = 0,8 \cdot 17,49 \cdot \cos 11^0 = 13,73$ N/μm·mm. Average specific stiffness of mashed teeth is $c_\gamma = c'(0,75\varepsilon_\alpha + 0,25)$ for $\varepsilon_\alpha = 1.88$, $c_\gamma = 22.79$ N/μm, mm. Total average stiffness of gear teeth in mesh is $c = c_\gamma b$, for face width $b = 150$ mm, it is $c = 3{,}418$ N/μm.

Rotation mass of the first gear is mass of the gear itself together with shaft, rotation mass of input clutch with rotor of electromotor, all of them with total moment of inertia $J_\mathrm{I} = 3.761$ kg m^2. The second shaft with gears 2 and 3 has the moment of inertia $J_\mathrm{II} = 5.147$ kg m^2. According to calculation of gear geometry, the radii of basic circle of gears 1 and 2 are $r_{b1} = 177$ mm and $r_{b1} = 200$ mm, so

reduced masses at the contact line direction (Fig. 7a) and equivalent mass are $m_{r1} = J_I/r_{b1}^2 = 3.761/0.177^2 = 120$ kg, $m_{r2} = J_{II}/r_{b2}^2 = 5.147/0.2^2 = 128$ kg

$$m_e = \frac{m_{r1}m_{r2}}{m_{r1} + m_{r2}} = \frac{120 \cdot 128}{120 + 128} = 62\,\text{kg}. \tag{2}$$

Natural frequency of the first pair of gears is

$$f_{rI} = \frac{1}{2\pi}\sqrt{\frac{c}{m_e}} = \frac{1}{2\pi}\sqrt{\frac{3,418 \times 10^6}{62}} = 1,181\,\text{Hz}. \tag{3}$$

The gear teeth mesh frequency is $f_I = n_1 z_1/60 = 1{,}480 \times 53/60 = 1{,}307$ Hz. The ratio between this exciting and natural frequency $f_I/f_{rI} = 1{,}307/1{,}181 = 1.1$ is in the range 0.85–1.15, which indicates the full resonance of helical gear pair. For bevel gear pair, applying the same procedure, natural frequency is obtained:

$$f_{rII} = \frac{1}{2\pi}\sqrt{\frac{c}{m_e}} = \frac{1}{2\pi}\sqrt{\frac{1,562 \times 10^6}{99}} = 632\,\text{Hz} \tag{4}$$

and frequency of gear teeth meshing $f_{II} = n_3 z_3/60 = 1{,}305 \times 23/60 = 500$ Hz. The ratio between exciting and natural frequency $f_{II}/f_{rII} = 500/632 = 0.792$ is close to resonance, since it is close to the lower limit of 0.85–1.15.

In resonance, the intensity of force at the tooth flank increases extremely, which is taken into account in calculation of forces and stresses by dynamical factor K_v. It is not only about the increased magnitude of this force. Due to contact interruption and anti-phase frequency, it comes to high intensity collision between teeth flanks. The frequency of collision is two times higher than the frequency of gear teeth meshing, since during the interruption of contact it comes to collision with both, left and right flank (Fig. 7b). This process realizes very high level of vibration, since it brings very intensive disturbance energy.

4 Gear Drive Design Parameters Harmonization

Resonance of the gear pair 1–2 could be avoided if a significantly big difference were made between frequency of gear teeth meshing and natural frequency of this gear pair. Natural frequency depends on gear teeth stiffness in mesh and magnitude of rotation masses. These magnitudes could not be significantly changed at the present design solution of this gearbox. The frequency of gear teeth meshing depends on rotation speed and of gear teeth number. The rotation speed also couldn't be changed. There is only one possibility left, and that is to change the gear teeth number (z) and gear modulus (m), so the gear pair center distance and gear transmission ratio remain unchanged. Increasing gear modulus from 7 to 12 mm and proportionally decreasing the of gear teeth number and helix angle from 11 to 8.1°, the gear pair center distance of 400 mm remains constant. For

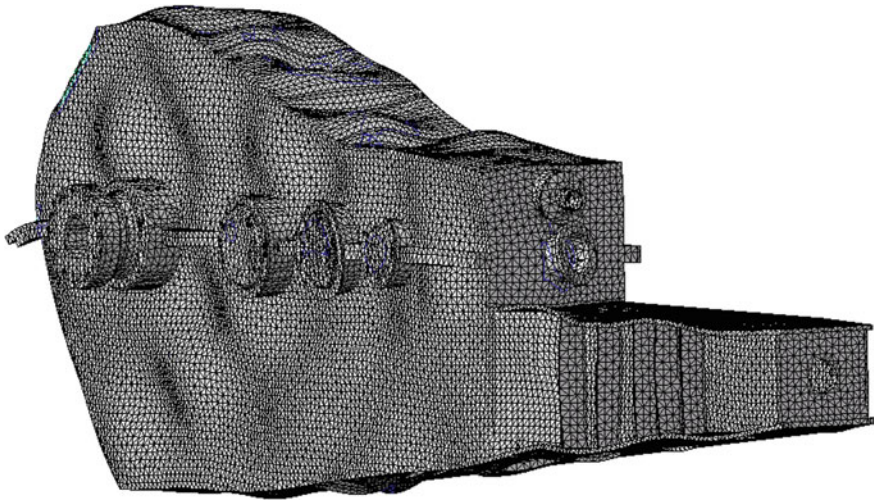

Fig. 8 Modal shape of natural vibrations with 1,300 Hz

these changed parameters, following the same procedure, it is calculated natural frequency of $f_{rI} = 1{,}199$ Hz and gear teeth mesh frequency $f_I = 749$ Hz. The ratio between these frequencies is $f_I/f_{rI} = 749/1{,}199 = 0.62$, which indicates that new parameters led helical pair out of resonance and led it into sub-critical service condition.

The original gear teeth mesh frequency of helical gear pair $f_I = 1{,}307$ Hz is not only close to natural frequency of rotation masses, but also to natural frequency of housing, which is 1,300 Hz (Fig. 8). This match of frequencies refers to increased level of noise, emitted by housing. By decreasing the gear teeth mesh frequency to 749 Hz, this phenomenon is eliminated, gearbox is led into smooth service conditions and service life of spherical roller bearings is extended.

5 Conclusions

Presented research involves the modeling of parts of input gearbox and assembling them together, development and analysis of dynamic model of meshed gears, analysis of displacements and stresses at relevant parts of gearbox by means of FEM and modal analysis of housing and other parts of gearbox. The most important results and observations are:

- Resonance of gears at the first stage of transmission is identified as a cause of failure of bearings at the second shaft. Resonance generated alternated forces of high intensity, which led to progressive failure of spherical roller bearings on this shaft.

- Changing design parameters of helical gear pair at the first stage of transmission, resonance and dynamical loads generated by resonance were eliminated. Also, matching of gear teeth mesh frequency with natural frequency of housing is eliminated and smooth work of gearbox is provided.

Acknowledgments This article is a contribution to the Ministry of Education and Science of Serbia funded project TR 035006.

References

Faggioni M, Samani F, Bertacchi G, Pellicano F (2011) Dynamic optimization of spur gears. Mech Mach Theor 46:544–557

He S, Rook T, Singh R (2008) Construction of semianalytical solutions to spur gear dynamics given periodic mesh stiffness and sliding friction functions. J Mech Des 130:122601-1–122601-9

Kang CH, Hsu WC, Lee EK, Shiau TN (2011) Dynamic analysis of gear-rotor system with viscoelastic supports under residual shaft bow effect. Mech Mach Theor 46:264–275

Liu G, Parker R (2008) Dynamic modeling and analysis of tooth profile modification for multimesh gear vibration. J Mech Des 130:121402-1–121402-13

Ognjanovic M, Agemi F (2010) Gear vibrations in supercritical mesh-frequency range caused by teeth impacts. J Mech Eng 56(10):653–662

Ognjanovic M, Benur M (2011) Experimental research for robust design of power transmission components. Meccanica 46(4):699–710

Ognjanovic M, Simonovic A, Ristivojevic M, Lazovic T (2010) Research of rail traction shafts and axles fractures towards impact of service conditions and fatigue damage accumulation. Eng Fail Anal 17(7–8):1560–1571

Rama Rao GV, Sreekala R, Gopala Krishan R, Sathish Kumar K, Muthunani K, Lakshmanan N (2011) Coasting down signal analysis as a tool for detection of proximity of resonances and a case study. Eng Fail Anal 18:340–353

Shuting L (2008) Experimental investigation and FEM analysis of resonance frequency behavior of three-dimensional, thin-walled spur gears with a power-circulating test rig. Mech Mach Theor 43:934–963

Velex P, Bruyere J, Houser DR (2011) Some analytical results on transmission errors in narrow-faced spur and helical gears: influence of profile modifications. J Mech Des 133:031010-1–031010-11

The Transmission Coefficient of Hydrostatic Drives

Mircea Rădulescu

Abstract This paper presents some theoretical considerations regarding the calculus of the transmission coefficient of the pressure energy in hydrostatic mechanisms. After defining all categories of transmission and efficiency coefficients, we present the laws of calculus for various combinations of hydraulic components and formulae of their resultant transmission coefficients. Beginning with the mathematical model of hydrostatic machines, presented in a generalized original form, we obtain the calculus formulae for overall transmission coefficients of a simple hydraulic circuit. These formulae can be useful in scientific researches, designing the equipment for the hydraulic drives and also in the didactic activity with students.

1 Introduction

For the purpose of improving the technical—economical performances of hydrostatic drives, in the designing stage, it is necessary for us to dispose of an improved mathematical model, which to allow obtaining beforehand some energetic characteristics accurate enough. The transmission of pressure energy is refers to all processes that occur in hydraulic mechanisms while the source transfers energy to the receiver. The transmission coefficient is a basic indicator of the pressure energy and it is defined as the ratio between the amount of the output and input respectively, of the same size that interferes in the description of a non-steady or transitory hydro-mechanical process. Except for papers (Blackburn 1962; Buculei and Radulescu 1993; Prokes 1977), we haven't found any detailed approaches on this subject in literature.

M. Rădulescu (✉)
University of Craiova, Craiova, Romania
e-mail: radulescumrc@yahoo.com

G. Dobre (ed.), *Power Transmissions*,
Mechanisms and Machine Science 13, DOI: 10.1007/978-94-007-6558-0_31,

For hydromechanical steady processes, instead of the term "transmission coefficient", we use "efficiency", with a similar definition (Buculei and Radulescu 1993; Prokes 1977). A few methods for the calculation of the energetical characteristics of hydrostatic machines in steady states processes are known:

- the method of the general note of losses, which has a general aspect but it does not allow the calculation of the losses in the nodes (centers) of the machines (Thoma 1970);
- the calculation method of the losses in separated nodes (centers) of the hydrostatic machines, which is not universal, but gives the possibility of obtaining some values of the parameters in nodes on the basis of which the constructive optimization of the machines would be possible;
- the energetic method introduces the concept of energetic efficiency of a machine, a complex universal criterion which takes into consideration the level of utilization of the machine;
- the dimensional analysis theory (Blackburn 1962) which has the disadvantage that leads to incomplete calculus relations, which will be experimentally finalized;
- the experimental method which is a safe and relatively precise method but has the disadvantage that it can not be used in the designing stage.

2 The Transmission Coefficient and Efficiency

We consider a parameter λ which characterizes a certain element of the hydraulic circuit, for example, a generator or an engine. The *transmission coefficient* of the parameter λ is defined by the ratio of the amount of parameter λ_e available at the output terminal and the amount of parameter λ_i at the input terminal:

$$H_\lambda = \frac{\lambda_e}{\lambda_i} = 1 - \frac{\Delta\lambda}{\lambda_i};\ \Delta\lambda = \lambda_i - \lambda_e > 0 \quad (H_\lambda \leq 1) \tag{1}$$

using the following graphical representation:

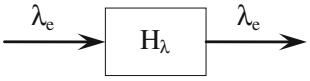

()

The relations describing the transmission coefficient H is thus similar in form to commonly used expressions for efficiency, η. Since the term of "efficiency" is used only in steady states transmission processes, it is safer to stick to the single term "transmission coefficient", which is used to describe only transient states and non-steady motion of the machinery (Prokes 1977).

Further will be introduced some generalized parameters which characterize the machines as components of hydraulic drives (generator—pump or motor):

- *displacement*:

$$q = \begin{cases} x[m],\ stroke\ length\ of\ the\ piston,\ for\ linear\ hydraulic\ machines\ (L.M.) \\ \varphi[rad],\ angle\ of\ rotation,\ for\ rotative\ hydraulic\ machines\ (R.M.) \end{cases} \quad (2)$$

- *effort*:

$$\phi = \begin{cases} F[N],\ the\ force\ reduced\ to\ the\ geometrical\ axis\ of\ the\ piston\ -\ for\ L.M. \\ M[Nm],\ torque\ reduced\ to\ the\ geometrical\ axis\ of\ the\ machine\ -\ for\ R.M. \end{cases} \quad (3)$$

- *velocity*:

$$w = \begin{cases} v = \dot{q}[m/s],\ linear\ velocity\ of\ the\ piston\ -\ for\ L.M. \\ \omega = \dot{\varphi}[rad/s],\ angular\ velocity\ (motion\ frequency)\ -\ for\ R.M. \end{cases} \quad (4)$$

- *mass*:

$$\mathfrak{M} = \begin{cases} m[kg],\ the\ mass\ reduced\ to\ the\ axis\ of\ the\ piston\ -\ for\ L.M. \\ J[Nm^2s],\ the\ moment\ of\ gyration\ reduced\ to\ the\ axis \\ of\ the\ machine\ -\ for\ R.M. \end{cases} \quad (5)$$

- *geometric capacity*:

$$K = \begin{cases} A_1[m^3/m = m^2],\ the\ piston\ area\ of\ the\ active\ chamber\ -\ for\ L.M. \\ q/2\pi[m^3/rad];\ q = V_g,\ the\ displacement\ volume\ -\ for\ R.M. \end{cases} \quad (6)$$

Particularly, in view of Eq. (1), for hydraulic drives, we obtain the types of transmission coefficients and efficiencies presented in Table 1. In problems of circuit analysis, the hydraulic components of the same or different types appear frequently and are variously connected. Starting with Eq. (1) we will deduce the set of rules for the hydraulic components connected in series, in parallel, in downstream and upstream node and outer feedback, these being presented in

Table 1 Types of transmission coefficient/efficiency for simple elements

Transmission coefficient, H_λ	Parameter, λ	Efficiency, η_λ
$H_V(t) = \frac{V_e(t)}{V_i(t)} = 1 - \frac{\Delta V(t)}{V_i(t)}$ (I.1)	Volume $(\lambda \to V)$	$\eta_V = 1 - \frac{\Delta V}{V_i}$ (I.1′)
$H_Q(t) = \frac{Q_e(t)}{Q_i(t)} = 1 - \frac{\Delta Q(t)}{Q_i(t)}$ (I.2)	Flow $(\lambda \to Q)$	$\eta_Q = 1 - \frac{\Delta Q}{Q_i}$ (I.2′)
$H_p(t) = \frac{p_e(t)}{p_i(t)} = 1 - \frac{\Delta p(t)}{P_i(t)}$ (I.3)	Pressure $(\lambda \to p)$/water head $(\lambda \to h)$	$\eta_h = 1 - \frac{\Delta h}{h_i}$ (I.3′)
$H_\phi(t) = \frac{\phi_e(t)}{\phi_i(t)} = 1 - \frac{\Delta \phi(t)}{\phi_i(t)}$ (I.4)	Generalized force (effort) $(\lambda \to \phi)$	$\eta_m = 1 - \frac{\Delta \phi}{\phi_i}$ (I.4′)
$H_w(t) = \frac{w_e(t)}{w_i(t)} = 1 - \frac{\Delta w(t)}{w_i(t)}$ (I.5)	Velocity $(\lambda \to w)$	$\eta_w = 1 - \frac{\Delta w}{w_i}$ (I.5′)
$H_q(t) = \frac{q_e(t)}{q_i(t)} = 1 - \frac{\Delta q(t)}{q_i(t)}$ (I.6)	Displacement $(\lambda \to q)$	$\eta_q = 1 - \frac{\Delta q}{q_i}$ (I.6′)
$H_W(t) = \frac{W_{pe}(t)}{W_{p_i}(t)} = 1 - \frac{\Delta W_p(t)}{W_{p_i}(t)}$ (I.7)	Pressure energy $\left(\lambda \to W_p\right)$	$\eta_W = 1 - \frac{\Delta W_p}{W_{p_i}}$ (I.7′)
$H_P(t) = \frac{P_e(t)}{P_i(t)} = 1 - \frac{\Delta P(t)}{P_i(t)}$ (I.8)	Power $(\lambda \to P)$	$\eta_P = 1 - \frac{\Delta P}{P_i}$ (I.8′)

Table 2, obtained as a generalization for the formulae given in the literature (Buculei and Radulescu 1993; Prokes 1977).

3 The Overall Transmission Coefficient for Interlinking Components

As an example, beginning with Eq. (1), (I.1)–(I.3) and (I.8), the three elementary types of hydraulic resistances (R_H, L_H, C_H) (Radulescu 2010), have been analyzed, taking into consideration the hydraulic characteristic $\Delta p = \Delta p(Q)$, on the basis of which the dependencies $H_\lambda = H_\lambda(Q; p)$. The results are given in the first part of Table 3, both for the transient/non-steady state and the efficiency (for the steady state). We have noted $R_H = \kappa R*$ the value of the resistance to motion in the non-steady/transient state, which significantly differs from the one established for the steady-state flows, noted with $R*$. The notation κ is a dimensionless adjustment coefficient, which is computed using formulae indicated in Buculei and Radulescu (1993), Radulescu (2010). In all the relations in the table, the value of R_H—resistance—must be linear or linearized. In the final part of the Table 3, we have studied the combination of resistances linked in series, for a pipe with leakage loss, with concentrated parameters, regarding the calculation of the transmission coefficient of power (non-steady/transient state).

The values of the simple hydraulic resistances can be computed using practical formulas presented in a synthetic form in Radulescu (2010), for cylindrical pipes and narrow slots with various shapes of the cross section profile, as well as for common types of hydrostatic motors. These formulas have been theoretically deduced taking into consideration the electrohydraulic analogy (Buculei and Radulescu 1993; Radulescu 2010). The elementary study of the combinations of different types of resistances is made in the following stages:

Table 2 The formulae for the overall efficiency of the most common system components

Type	Scheme of connection	Preliminary calculus formulae	Overall transmission coefficient
Series	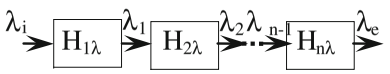	$H_{1\lambda} = \frac{\lambda_1}{\lambda_i}$ $H_{k\lambda} = \frac{\lambda_k}{\lambda_{k-1}}$ $H_{n\lambda} = \frac{\lambda_e}{\lambda_{n-1}}$ $Q_1 = Q_2 = \ldots Q_{n-1} = Q_n$ $H_{1\lambda} = H_{2\lambda} = \cdots = H_{n\lambda}$	$H_\lambda = \prod_{k=1}^{n} H_{k\lambda}$ $\lambda = p$ or $\lambda = P$
Parallel	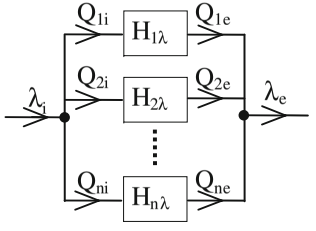	$Q_i = \sum_{k=1}^{n} Q_{ki};$ $Q_e = \sum_{k=1}^{n} Q_{ke}$ $H_{Q_k} = \frac{Q_{ki}}{Q_i}$	$H_\lambda = \sum_{k=1}^{n} K_{Q_k} H_{k\lambda}$ $\lambda = Q$ or $\lambda = P$
Upstream node	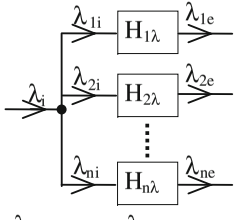	$K_k = \frac{\lambda_{ki}}{\lambda_i}$ $\lambda_i = \sum_{k=1}^{n} \lambda_{ki}$	$\lambda_{ke} = K_k H_{k\lambda} \lambda_i$ $\lambda = Q$ or $\lambda = P$
Down-stream node	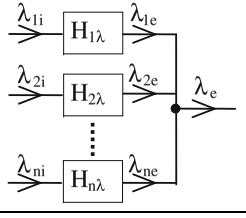	$\lambda_e = \sum_{k=1}^{n} \lambda_{ke}$	$\lambda_e = \sum_{k=1}^{n} H_{k\lambda} \lambda_{ki}$ $\lambda = Q$ or $\lambda = P$

(continued)

Table 2 (continued)

Type	Scheme of connection	Preliminary calculus formulae	Overall transmission coefficient
Outer feedback	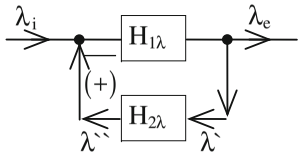	$K_2 = \frac{\lambda'}{\lambda_e};\ \mathrm{H}_{2\lambda} = \frac{\lambda''}{\lambda'}$ $\mathrm{H}_\lambda = \mathrm{H}_{1\lambda} - \mathrm{H}_{1\lambda}\frac{\lambda''}{\lambda_i}$ $\lambda'' = \mathrm{H}_{2\lambda}K_2\lambda_e$	$\mathrm{H}_\lambda = \frac{\mathrm{H}_{1\lambda}}{1(\pm)K_2\mathrm{H}_{1\lambda}\mathrm{H}_{2\lambda}}$

Table 3 The transmission coefficient for commonly used individual hydraulic resistances and their series connections

Type of resistance	Relations between pressure drops and flow ratio	Transient/non-steady state The transmission coefficient (H_λ)
Resistance to motion $R_H = R = Z^{-1}\left[Ns/m^5\right]$ (Z—hydraulic transmittance)	$\Delta p = R_H Q^n$ $\Delta p = p_i - p_e > 0$ $(1 \le n \le 2)$ $R_H = \kappa R^* \quad (\kappa \ge 1)$	$H_p(t) = \frac{p_e}{p_i} = 1 - R_H p_i^{-1} Q^n(t)$ $(\kappa > 1)$
Resistance to acceleration $H = L_H = M^{-1}\left[\mathrm{Ns^2/m^5}\right]$ (M—hydraulic mobility)	$\Delta p = L_H \overset{o}{Q} \quad Q = Q(t)$	$H_p(t) = \frac{p_e}{p_i} = 1 - L_H p_i^{-1} \overset{o}{Q}(t)$
Resistance to deformation $D_H = C_H^{-1} = D\left[\mathrm{N/m^5}\right]$ ($C_\mathrm{H} = C$—hydraulic capacity)	$\Delta p = D_H \Delta V;$ $\Delta V = \int_0^t \Delta Q(u)\mathrm{d}u$	$H_V(t) = \frac{V_e}{V_i} = 1 - B_e^{-1}\Delta p(t)$
R—H—D—G combination of resistances linked in series, for a pipe with leakage loss, with concentrated parameters	$\Delta p = R_H Q + L_H \overset{o}{Q} + D_H \int_0^t Q du$ $R_H = \begin{cases} R_L; & n = 1 \\ 2R_N Q_0; & 1 < n \le 2 \end{cases};$ $Q = Q(t);\ Q_e = Q_i - \Delta Q_s;$ $\Delta Q_s = p_i Z_s \ge 0$ $\overline{\Delta p} = R_H \overline{Q} + sL_H \overline{Q} + \frac{D_H}{s}\overline{Q}$ $Z_s = R_s^{-1}; P_s = Z_s p_i^2$ $P_e = P_i + R_H Q^{n+1} + L_H Q_i \overset{o}{Q}_i +$ $+ D_H^{-1} p_i \overset{o}{p}_i + Z_s p_i^2; G = R_s^{-1}$	$H_P = 1 - \frac{1}{P_i} R_H Q_i^{n+1} + Z_s p_i^2$ $+ L_H Q_i \overset{o}{Q}_i + D_H^{-1} p_t \overset{o}{p}_t$ $\left.\frac{dH_P}{dQ}\right\|_{Q_{opt}} = 0,\ H_P(Q_{opt}) = H_{1P_1 max} Q_{opt} = \sqrt[n+1]{\frac{p_i}{R_H}\left(\frac{p_i}{R_s} + \frac{\overset{o}{p}_i}{D_H}\right)}$ $\left.\frac{dH_P}{dp_i}\right\|_{p_{i_{opt}}} = 0,\ H_P(p_{i_{opt}}) = H_{2P max} p_{i_{opt}} = \sqrt{R_s Q_i \left(R_H Q_i^n + L_H \overset{o}{Q}_i\right)}$

1. After finding the dependence $\Delta p(Q)$ for each type of resistance, the total pressure loss is calculated and the Laplace transform is applied, obtaining:

$$\overline{\Delta p}_t(s) = Z_H(s)\overline{Q}(s);\ s = \alpha + j\omega;\ \left(j = \sqrt{-1}\right) \tag{7}$$

2. With $\alpha = 0,\ s = j\omega$ relation (8) becomes:

$$\underline{\Delta p_t}(j\omega) = \underline{Z}_H(j\omega)\underline{Q}(j\omega) \tag{8}$$

where:

$$\underline{Z}_H = R_H + jX_H,\ \underline{Z}_H = \sqrt{R_H^2 + X_H^2}\ \left[\mathrm{Ns/m^5}\right] \tag{9}$$

is the complex impedance associated to the series connection $(R_H L_H C_H)$ and:

$$X_H = X_L - X_C;\ X_L = \omega L_H;\ X_C = \omega^{-1} C_H^{-1} \tag{10}$$

is the hydraulic reactance (Radulescu 2001).

3. The phase angle between $\underline{\Delta p}(j\omega)$ and $\underline{\Delta Q}(j\omega)$ is:

$$\varphi = arctg\left(\frac{X_L - X_C}{R_H}\right)\ [-] \tag{11}$$

4. Given the total pressure loss:

$$\Delta p_t(t) = R_H Q(t) + L_H \overset{o}{Q}(t) + C_H^{-1}\int_0^t Q(u)\mathrm{d}u \tag{12}$$

and the flow loss due to leakages:

$$\Delta Q_s(t) = Z_s p_i(t)\ \left[\mathrm{m^3/s}\right] \tag{13}$$

we can write the loss of power between the input and output combination:

$$\Delta P(t) = P_i(t) - P_e(t) = \Delta p_t Q_i + p_i \Delta Q_s \tag{14}$$

5. The transmission coefficient of power is obtained by replacing (14) in (I.8), given the function:

$$\mathrm{H}_P = \mathrm{H}_P(p_i;\ Q_i) \tag{15}$$

which can be regarded as a special case of general dependence:

$$H_\lambda = H_\lambda(x_k);\ k = \overline{1 \div n} \tag{16}$$

where x_k are the n variables on which the transmission coefficient H_λ depends.

6. If in relation (16) the maximum conditions are imposed:

$$\frac{\partial H_\lambda}{\partial x_k} = 0;\ \frac{\partial^2 H_\lambda}{\partial^2 x_k} < 0 \tag{17}$$

we can determine the optimal values of the variables x_k, which are noted $(x_k)_{opt}$ and replaced in (16), achieving the maximum values of this coefficient:

$$(H_\lambda)_{\max} = H_\lambda\left[(x_k)_{opt}\right] \tag{18}$$

In the final part of Table 3, we have determined by calculation, the dependence

$$H_P = H_P(p;\ Q) \tag{19}$$

for the combination of hydraulic resistances linked in series, with concentrated parameters, with leakage loss. Then, applying the first conditions (17) we have obtained theoretical formulae for the optimum pressure and flow calculation and as a result, formulae for the calculation of the maximum values for the transmission coefficient:

$$H_{2P_{\max}} = H_P\left(p_{i_{opt}}\right);\ H_{1P_{\max}} = H_P\left(Q_{opt}\right) \tag{20}$$

4 The Transmission Coefficients of the Commonly Used Hydrostatic Components

4.1 Energy Losses in Hydrostatic Machines

Beginning from the Navier-Stokes equations, we can deduce the formula for the flow that travels through a narrow slot with mobile walls, for the stationary laminar motion of the Newtonian viscous liquids (Buculei and Radulescu 1993; Radulescu 2001, 2010) and the formula for the resultant friction force in the slot:

$$Q_l = a_1 v_r + Z_L \Delta p;\ F_f = a_1 \Delta p + a_2 v_r \tag{21}$$

where $\Delta p = p_i - p_e \geq 0$ is the pressure drop between the slot ends and $Z_L = K_Q \delta^3/\mu = R_L^{-1}$ is the linear transmittance of the narrow slot, where $\delta = J/2 = j$ is the radial clearance between the fixed and the mobile walls of the slot, μ the dynamic viscosity and K_Q a structural coefficient, which reflects the size and configuration of the flow course of the liquid inside the slot.

For some common types of slots this last coefficient can be computed with some simple equations, such as:

$$K_Q = \begin{cases} b/12L, \ for\ plane - parallel\ slots\ (P.P.S.); \\ \pi(d_1 + d_2)/24L, \ for\ narrow\ concentric\ ring\ slots\ (C.R.S.); \\ \pi(d_1 + d_2)(1 + 3e/2\delta)/24L, \ for\ narrow\ non - concentric\ ring\ slots\ (C.N.S.); \\ \pi/6 \ln(D/d), \ for\ plane\ slots\ with\ rotational\ symetry\ (P.R.S.); \\ \pi/6(ctg\alpha + ctg\beta), \ for\ narrow\ tapered\ slots\ (N.T.S.); \\ \pi/6 \ln[tg(\theta_2/2)/tg(\theta_1/2)], \ for\ narrow\ spheric\ slots\ (N.S.S.) \end{cases} \tag{22}$$

$$a_1 = \begin{cases} bh/2 \\ \pi d\delta/2 \end{cases}; a_2 = K_F \frac{\mu}{\delta}; \ K_F = \begin{cases} bl, for\ P.P.S. \\ \pi dL, for\ C.R.S. \end{cases} \tag{23}$$

where K_F reflects the size and configuration of the solid surfaces in motion.

For linear hydrostatic machines we can compute the volumetric and mechanic losses by applying Eq. (21), and for rotary machines, considering the generalized parameters, with (2–6), if $v_r = \lambda(q)w$ (Buculei and Radulescu 1993), we can deduce the following formulae:

$$Q^* = \alpha^* w + Z^* \Delta p^*; \ \phi^* = \gamma^* w + \delta^* \Delta p^* \tag{24}$$

where $\alpha^* = a_1 \lambda_{med}$, γ^* and δ^* are the losses gradients and Z^* is the equivalent transmittance of a parallel connection of linear resistances.

For deducing the mathematical model of hydrostatic machines we take into consideration Eqs. (21) or (24).

In the structure of the simplified mathematical model of the hydrostatic machines, the formulas for the flow losses, the mechanic losses respectively, become:

$$\Delta Q = \alpha w + \beta p; \ \Delta \phi = \gamma w + \delta p \tag{25}$$

In Fig. 1 is given the balance of power losses and in Fig. 2 are given the diagrams of losses for rotary hydrostatic machines (Buculei and Radulescu 1993), depending on the angular velocity, for different constant values of pressure (p varies as a parameter), for flow losses (a) and for torque losses (b).

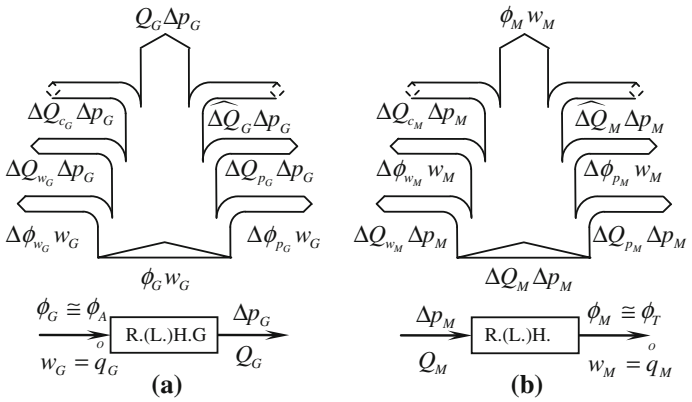

Fig. 1 Balance of power losses

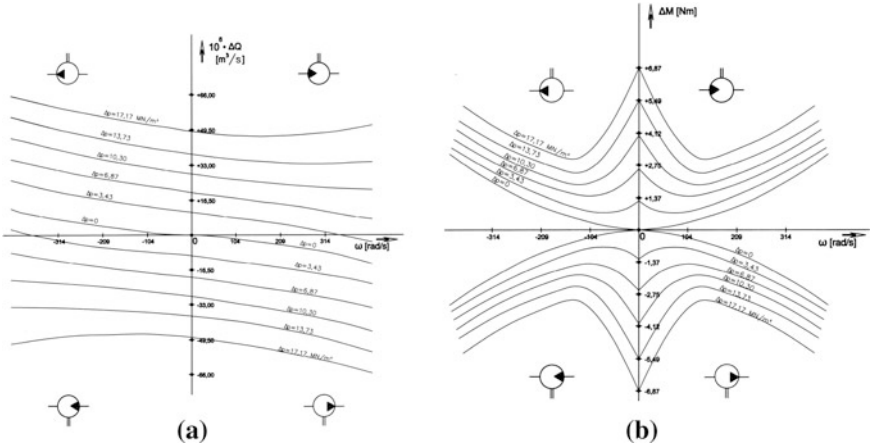

Fig. 2 Diagrams of losses for rotary hydrostatic machines **a** flow losses, **b** torque losses

4.2 The Mathematical Model of Hydrostatic Machines

These equations are non-linear and can be generalized and applied both for pumps and motors. Usually, we use a simplified form, which is obtained by ignoring the flow equation which corresponds to the low pressure part of the two machines.

Further we present the simplified mathematical model for hydrostatic machines, beginning with the formula obtained in Buculei and Radulescu (1993), Radulescu (2001), which, considering the generalized parameters introduced by Eqs. (2–6), we will write in a generalized (united) form, applicable both for linear-motion and rotary-motion machines

4.2.1 The Flow Equations

The actual flow rate of hydraulic machines can be computed using the generalized formula:

$$Q_{ef} = Q_t \mp \left(\Delta Q + \widehat{\Delta Q}\right);\ Q_t = Kw;\ \Delta Q = \Delta Q_w + \Delta Q_p + \Delta Q_c \tag{26}$$

with the (−) sign for a generator machine (G—pump) and (+) sign for a motor machine (M—engine).

In Eq. (26) is the theoretical flow rate of the machine, $\widehat{\Delta Q}$ is the flow pulsation and ΔQ, the total flow loss, with its components, $\Delta Q_w = \alpha w$—the flow loss proportionally to the generalized velocity and $\Delta Q_p = \beta p$—the flow loss proportionally to pressure (where $\alpha = (\partial(\Delta Q)/\partial w)|_p$ and $\beta = (\partial(\Delta Q)/\partial p)|_w$ are the gradient of the flow losses depending on the velocity and pressure) and ΔQ_c is the flow loss due to the compressibility of the fluid. Returning to (26) we obtain the flow equation:

$$Q_{ef} = Kw \mp \left[\left.\frac{\partial(\Delta Q)}{\partial w}\right|_p w + \left.\frac{\partial(\Delta Q)}{\partial p}\right|_w p + \frac{1}{B}\left(V_0 + \int_0^q K(u)du\right)\overset{o}{p} + \widehat{\Delta Q}\right] \tag{27}$$

In the case of rotary hydraulic machines, Eq. (21) becomes:

$$Q_{ef} = \frac{V_g}{2\pi}\omega \mp \left[\left.\frac{\partial(\Delta Q)}{\partial \omega}\right|_p \omega + \left.\frac{\partial(\Delta Q)}{\partial p}\right|_\omega p + \frac{1}{B}\left(V_0 + \int_0^\varphi K(u)du\right)\overset{o}{p} + \widehat{\Delta Q}\right] \tag{28}$$

4.2.2 The Equation of Motion for Machines

The equation of motion that describes hydrostatic machines can be generalized with formula:

$$\frac{1}{2}\mathfrak{M}'_{red}(q)w^2 + \mathfrak{M}_{red}(q)\overset{o}{w} = \phi * \Delta p - \Delta\phi - \widehat{\Delta\phi} \tag{29}$$

where $\mathfrak{M}_{red} = \mathfrak{M}_{red}(q)$ is the generalized mass of the rotary devices of G and the engine M which entrains it, reduced to the geometrical axis of the hydrostatic machine.

$$\phi* = \begin{cases} +\phi_A - \textit{acting effort for } (G) \\ -\phi_T - \textit{load effort for } (M) \end{cases};\ \Delta p = \begin{cases} p_e - p_i > 0,\ \textit{pressure jump for } (G) \\ p_i - p_e > 0,\ \textit{pressure drop for } (M) \end{cases} \tag{30}$$

$\widehat{\Delta\phi}$ is the fluctuation of the effort parameter due to pulsation and $\Delta\phi$, the overall effort loss, with two components:

$$\Delta\phi = \Delta\phi_w + \Delta\phi_p;\ \Delta\phi_w = \gamma w;\ \Delta\phi_p = \delta\Delta p \tag{31}$$

which represent the effort loss proportionally to the generalized velocity and to the pressure respectively where $\gamma = (\partial(\Delta\phi)/\partial w)|_p$ and $\delta = (\partial(\Delta\phi)/\partial p)|_w$ are the gradient of effort losses due to coulombian, respectively newtonian frictions.

Replacing (31) in (29) we obtain the motion equation in a generalized form.

$$\frac{1}{2}\mathfrak{M}'_{red}(q)w^2 + \mathfrak{M}_{red}(q)\overset{o}{w} = \phi * \mp K\Delta p - \left[\left.\frac{\partial(\Delta\phi)}{\partial w}\right|_p w + \left.\frac{\partial(\Delta\phi)}{\partial p}\right|_w + \widehat{\Delta\phi}\right] \tag{32}$$

In the case of hydraulic rotary machines, Eq. (32) can be written as:

$$\frac{1}{2}J'_{red}(\varphi)\omega^2 + J_{red}(\varphi)\overset{o}{\omega} = \pm M * \mp K\Delta p - \left[\left.\frac{\partial(\Delta M)}{\partial\omega}\right|_p \omega + \left.\frac{\partial(\Delta M)}{\partial p}\right|_\omega \Delta p + \widehat{\Delta M}\right] \tag{33}$$

where $M*$ corresponds to ϕ^* and $\widehat{\Delta M}$ corresponds to $\widehat{\Delta\phi}$.

Equations (27) and (32) describe the non-linear generalized simplified mathematical model of hydrostatic machines and Eqs. (28) and (33) correspond to the particular case of hydrostatic rotary machines.

In the steady states $\left(\overset{o}{w} = \overset{o}{p} = 0\right)$, those equations become:

$$Q_{eff} = Kw \mp (\alpha w + \beta p);\ \phi_{eff} = K\Delta p \pm (\gamma w + \delta\Delta p) \tag{34}$$

$$Q_{eff} = \frac{V_g}{2\pi}\omega \mp (\alpha\omega + \beta p);\ M_{eff} = \frac{V_g}{2\pi}\Delta p \pm (\gamma\omega + \delta\Delta p) \tag{35}$$

The major difficulties arising from the application of these mathematical models are due to the uncertainty of numerical values for the gradients α, β, γ, δ.

Further we will try to obtain calculus relations for the transmission coefficients of rotary hydrostatic machines, beginning from the mathematical model shown above, this model being deduced taking into consideration (Radulescu 2001). In the Table 4 are also given the transmission coefficients for hydraulic lines with distributed parameters, taking into consideration their mathematical model deduced in Buculei and Radulescu (1993), Radulescu (2001).

5 Application in the Case of a Hydrostatic Transmission

Finally, we present an example of the theoretical calculus of the overall transmission coefficient of the simple hydrostatic transmission in a closed-loop circuit (Fig. 3). The base structure of a circuit with rotary machines consists in a hydrostatic generator (RHG), a hydrostatic motor (RHM), and the two main pipes which connect the two machines. The technological object (T.O.) is driven by the hydraulic motor and the pump drive is made by the acting (prime) motor (A.M.).

Table 4 The overall transmission coefficient for hydraulic components

Type	Mathematical model, notation	The transmission coefficient (H_λ)
Hydraulic generator (HG)	$Q_{e_G} = K_G(q)w - \Delta Q_s - \Delta Q_c;\ \Delta Q_s = \alpha_G w_G + \beta_G p_G = Z_s \Delta p_G$ $V_{i_G} = V_{0i_G} + \int_0^q K_G(u)\mathrm{d}u;\ \Delta Q_c = \frac{1}{B}(V_G - V_{i_G})$ $\frac{1}{2}\mathfrak{M}'_{red_G} w_G^2 + \mathfrak{M}^o_{red_G} G = \phi_A(q,\ w_G,\ t) - K_G \Delta p_G - \Delta\phi_G$ $\Delta\phi_G = \gamma_G w_G + \delta_G \Delta p_G;\ \Delta p_G = p_e - p_i \cong p_e > 0\ (p_i \cong 0)$	$H_Q = 1 - \dfrac{\Delta Q_s}{Q_{t_G}}$ $H_Q = 1 - \dfrac{Z_s \Delta p_G}{K_G(q) w_G}$
Hydrostatic motor (HM)	$Q_{i_M} = K_M(q)w_M + \Delta Q_s + \Delta Q_c$ $\Delta Q_s = \alpha_M w_M + \beta_M p_M = Z_s \Delta p_M$ $V_{i_M} = V_{0i_M} + \int_0^q K_M(u)du;\ \Delta Q_c = \frac{1}{B}\left(V_{0i_M} + \int_0^q K_M(u)du\right)$ $\frac{1}{2}\mathfrak{M}_{red_M}(q) w_M^2 + \mathfrak{M}_{red_M}(q)^o_{,M} = K_M(q)\Delta p_M - \Delta\phi_M - \phi_T$ $\Delta\phi_M = \gamma_M w_M + \delta_M \Delta p_M;\ \Delta p_M = p_i - p_e \cong p_i > 0\ (p_e \cong 0)$ $R = R_M;\ L = L_M;\ C = C_M;\ Z = Z_S; R_S = Z_S^{-1} -$ leakage resist	$H_Q(s) = \dfrac{Q_t(s)}{Q_i(s)};\ H_p(s) = \dfrac{p_e(s)}{p_i(s)}$ $H_Q = 1 - LCs^2 - (RC + LZ)s - RZ$ $H_p = \dfrac{1}{1 + LCs^2 + (RC + LZ)s + RZ}$ $H_P(s) = H_Q(s) \cdot H_p(s)$ $H_P = \dfrac{1 - LCs^2 - (RC + LZ)s - RZ}{1 + LCs^2 + (RC + LZ)s + RZ}$
Hydraulic line with distributed parameters	$\frac{\partial^2(\Delta p)}{\partial x^2} = L\prime C\prime \frac{\partial^2(\Delta p)}{\partial t^2} + (R\prime C\prime + G\prime L\prime)\frac{\partial(\Delta p)}{\partial t} + R\prime G\prime \Delta p$ $\frac{\partial^2(\Delta Q)}{\partial x^2} = L\prime C\prime \frac{\partial^2(\Delta Q)}{\partial t^2} + (R\prime C\prime + G\prime L\prime)\frac{\partial(\Delta Q)}{\partial t} + R\prime G\prime \Delta Q \frac{d^2(\overline{\Delta p})}{dx^2} - \gamma(s)\overline{\Delta p} = 0;\ \frac{d^2(\overline{\Delta Q})}{dx^2} - \gamma(s)\overline{\Delta Q} = 0$ After solving the dif. eq. we obtain the matric relation $\begin{bmatrix} \overline{\Delta p_e}(s) \\ \overline{\Delta Q_e}(s) \end{bmatrix} = \begin{bmatrix} ch(\gamma l) & Z_c sh(\gamma l) \\ Z_c^{-1} & ch(\gamma l) \end{bmatrix} \begin{bmatrix} \overline{\Delta p_i}(s) \\ \overline{\Delta Q_i}(s) \end{bmatrix}$ $Z_c(s) = \sqrt{\frac{R\prime + Ls}{G\prime + Cs}}; \gamma(s) = \sqrt{(R\prime + Ls)(G\prime + Cs)}$ $R\prime = \frac{dR_H(x)}{dx}; L\prime = \frac{dL_H(x)}{dx}; C\prime = \frac{dC_H(x)}{dx}; G\prime = \frac{dG_H(x)}{dx}$	$H_Q(s) = \frac{\Delta Q_e}{\Delta Q_i} = \frac{1}{\frac{R_d}{Z_c} sh(\gamma l) + ch(\gamma l)}$ $H_p(s) = \frac{\Delta p_e}{\Delta p_i} = \frac{1}{\frac{Z_c}{R_d} sh(\gamma l) + ch(\gamma l)}$ $H_P(s) = H_Q \cdot H_p = \frac{1}{1 + \frac{1}{2} \rightarrow}$ $\frac{1}{\rightarrow \left(\frac{R_d}{Z_c} + \frac{Z_c}{R_d}\right) sh(2\gamma l) + 2sh^2(\gamma l)}$ R_d—dynamic resistance of the load

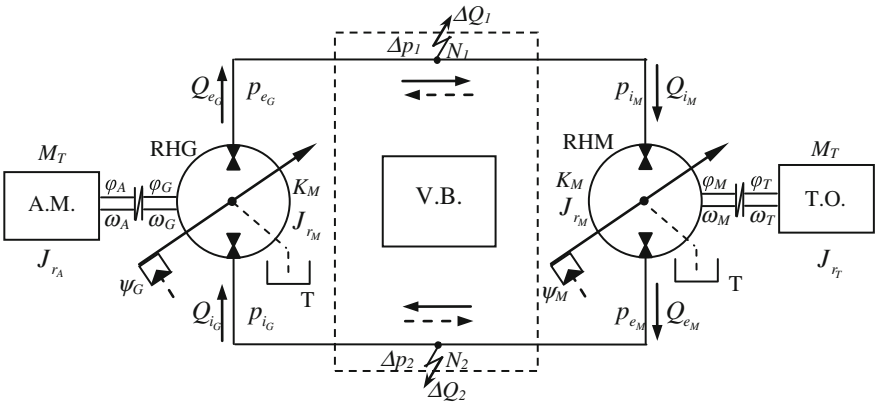

Fig. 3 Overall transmission coefficient of the simple hydrostatic transmission in a closed-loop circuit

In the figure the common valve block (V.B.) is indicated by a point broken line and contains, for example, a priming pump, relief valves, coolers, filters, oil tanks etc.

The overall transmission coefficient of power can be deduced from the mathematical model of the transmission or considering the partial results presented in Table 4. Having a limited space for this paper, we have chosen the second variant, obtaining the transmission coefficient of power (H_P) of each circuit elements as a product of the transmission coefficient of flow (H_Q) and pressure (H_p), finally obtaining the overall transmission coefficient:

5.1 The Overall Transmission Coefficient of the Hydrostatic Generator

$$H_Q = 1 - \frac{\Delta Q_s}{Q_{t_G}} = 1 - \frac{Z_s \Delta p_G}{K_G(\varphi)\omega_G} \tag{36}$$

5.2 The Overall Transmission Coefficient of the Primary Hydraulic Line

$$H_{Q_{c1}}(s) = \left(\frac{R_{d_1}}{Z_{c_1}} sh(\gamma l_1) + ch(\gamma l_1)\right)^{-1};\ H_{p_{c1}}(s) = \left(\frac{Z_{c_1}}{R_{d_1}} sh(\gamma l_1) + ch(\gamma l_1)\right)^{-1} \tag{37}$$

$$H_{P_{c1}}(s) = H_{Q_{c1}}(s)H_{p_{c1}}(s) = \left(1 + \frac{1}{2}\left(\frac{R_{d_1}}{Z_{c_1}} + \frac{Z_{c_1}}{R_{d_1}}\right)sh(2\gamma l_1) + 2sh^2(\gamma l_1)\right)^{-1} \quad (38)$$

5.3 The Overall Transmission Coefficient of the Hydraulic Motor

$$H_Q(s) = Q_t(s)/Q_i(s) = 1 - L_M C_M s^2 - (R_M C_M + L_M Z_s)s - R_M Z_s \quad (39)$$

$$H_p(s) = p_e(s)/p_i(s) = \left(1 + L_M C_M s^2 + (R_M C_M + L_M Z_s)s + R_M Z_s\right)^{-1} \quad (40)$$

$$H_{P_M} = H_Q(s)H_p(s) = \frac{1 - L_M C_M s^2 - (R_M C_M + L_M Z_s)s - R_M Z_s}{1 + L_M C_M s^2 + (R_M C_M + L_M Z_s)s + R_M Z_s} \quad (41)$$

5.4 The Overall Transmission Coefficient of the Secondary Hydraulic Line

$$H_{Q_{c2}}(s) = \left(\frac{R_{d_2}}{Z_{c_2}}sh(\gamma l_2) + ch(\gamma l_2)\right)^{-1};\ H_{p_{c2}}(s) = \left(\frac{Z_{c_2}}{R_{d_2}}sh(\gamma l_2) + ch(\gamma l_2)\right)^{-1} \quad (42)$$

$$H_{P_{c2}}(s) = H_{Q_{c2}}(s)H_{p_{c2}}(s) = \left(1 + \frac{1}{2}\left(\frac{R_{d_2}}{Z_{c_2}} + \frac{Z_{c_2}}{R_{d_2}}\right)sh(2\gamma l_2) + 2sh^2(\gamma l_2)\right)^{-1} \quad (43)$$

5.5 The Overall Transmission Coefficient of the Hydrostatic Transmission

$$\mathrm{H}(s) = H_{P_G}(s)H_{P_{c1}}(s)H_{P_M}(s)H_{P_{c2}}(s) \quad (44)$$

$$\mathrm{H}(s) = \frac{1 - \frac{Z_s \Delta p_G}{K_G(\varphi)\omega_G}}{1 + \frac{1}{2}\left(\frac{R_{d_1}}{Z_{c_1}} + \frac{Z_{c_1}}{R_{d_1}}\right)sh(2\gamma l_1) + 2sh^2(\gamma l_1)} \frac{\frac{1 - L_M C_M s^2 - (R_M C_M + L_M Z_s)s - R_M Z_s}{1 + L_M C_M s^2 + (R_M C_M + L_M Z_s)s + R_M Z_s}}{1 + \frac{1}{2}\left(\frac{R_{d_2}}{Z_{c_2}} + \frac{Z_{c_2}}{R_{d_2}}\right)sh(2\gamma l_2) + 2sh^2(\gamma l_2)} \quad (45)$$

For finding the value of overall power transmission coefficient of the hydrostatic transmission in real time, we apply the inverse Laplace transform in Eq. (45).

6 Conclusions

The overall transmission coefficient of a hydrostatic mechanism is a very complex parameter which depends on many other operational parameters (like T, p, n etc.). For this reason, an exact analytical evaluation of the time dependent transmission coefficient of the hydrostatic mechanisms is laborious and very difficult to make.

The transitory character of the hydraulic liquid motion through narrow slots with mobile walls from inside the machines as well as the major difficulties with interfere in the accurate calculation of the geometrical elements of the slots do not allow the theoretical computation. On the other hand, it is necessary to study in detail the influence of temperature and pressure on the physical–mechanical properties (ρ, v, B etc.) of the hydraulic medium, having into consideration the operating conditions of the hydrostatic transmission. Therefore, it is necessary to improve the mathematical models of the hydraulic circuit elements and to use cautiously some correction coefficients for the calculation of non-steady and transient states losses.

The generalized mathematical model and calculation formulae presented in this paper offer the opportunity to theoretically calculate the overall transmission coefficient of power (H_P), but the results we obtain offer only preliminary approximate values. Some of the formulae deduced here for the transmission coefficients H_λ of some circuit elements are consistent with those shown in Prokes (1977). However, these formulae can be useful in scientific researches, designing the hydraulic drives and also for students and candidates for a doctor's degree.

References

Blackburn JF (1962) Fluid power control. Krauskopf Verlag

Buculei M, Radulescu M (1993) Hydraulic drives and automations. University of Craiova

Prokes J (1977) Hydraulic mechanisms in automation. Elsevrier Scientific Publishing Company, Amsterdam-Oxford, New Jork

Radulescu M (2001) About the dynamic model of hydrostatic transmission. In: First international SMAT conference, Craiova, 2001

Radulescu M (2010) Systematization of the resistance theory in hydraulic drives/mechanisms. "Mecatronica", 1:38–49

Thoma J (1970) Modern oilhydraulic engineering. Trade&Technical Press, Morden

Design of Loboid Gear Pairs Using Involute Discretization

Vasilios Spitas and Christos Spitas

Abstract Loboid gears are used in rotary pump applications mainly in positive displacement pneumatic compressors (i.e. Roots blowers) in which high volumetric capacity and smooth running are of major importance. This paper approaches the problem of numerically defining the meshing surfaces of such loboid gears using the newly developed theory of involute discretization. According to this approach, every gear tooth of any form can be discretized in infinitesimal involute segments therefore rendering the determination of the path of contact and the geometry of the meshing teeth of the conjugate gears easy and straightforward, using the well-known properties of the involute. The achieved savings in programming time and effort are considerable compared to the standard Theory of Gearing and other form-specific gear tooth geometrical formulae.

Keywords Involute · Discretization · Loboid gears · Cycloidal gears · Roots blowers

List of Symbols

r_o	Rolling circle
r_g	Base circle
a_o	Pressure angle
r_{gG}	Local base circle of infinitesimal involute at G
a_{oG}	Local pressure angle of infinitesimal involute at G
ρ	Radius of circular addendum
N	Number of teeth

V. Spitas (✉)
National Technical of Athens, Athens, Greece
e-mail: vspitas@central.ntua.gr

C. Spitas
Technical University of Delft, Delft, The Netherlands
e-mail: c.spitas@tudelft.nl

G. Dobre (ed.), *Power Transmissions*,
Mechanisms and Machine Science 13, DOI: 10.1007/978-94-007-6558-0_32,

1 Introduction

A common solution for positive-displacement (PD) gear-pump design is the use of loboid gears (Townsend 1992). Their important advantage is that they offer high volumetric displacement capacity and high volumetric efficiency with low noise and vibration due to the closed form of their path of contact. Therefore, they have dominated the field of low and medium pressure PD pneumatic pump designs. Due to their large diameters and the low number of teeth (usually two or three) these gears are not suitable to be machined with the usual gear generation processes (i.e. hobbing), since this would require expensive hob cutters and enormously rigid hobbing machines to withstand the high cutting forces associated with the removal of so much material. In order to overcome this discrepancy the trend in modern gear cutting technology is to rough and finish machine these loboid gears in CNC machining centers, either with three or more axes (Yang and Blanche 1990; Yao et al. 2005). Cutting and subsequent grinding after thermal treatment give the most accurate and silent gears, whereas more productive manufacturing methods such as rolling produce gears with form and pitch errors and therefore noise.

The CNC machining center cutting of these gears requires accurate modeling of the working gear tooth flanks since it is a non-generating method as opposed to hobbing or rack cutting. Therefore, extensive tooth modeling is required and most often CAD/CAM software is used. Litvin and Feng (1996), Vecchiato et al. (2001), Demenego et al. (2002) have used the Theory of Gearing (Litvin and Fuentes 2004) to address the problem of the calculation of loboid gear tooth geometry, while other existing works have developed geometry-specific methods (Yang and Blanche 1990; Ye et al. 2006; Shin and Kwon 2006; Stryczek 1990, 1993; Sung and Tsai 1997). The basic characteristic of these theories is that they offer implicit solutions requiring elaborate numerical methods to solve the complex differential equations and therefore they are characterized by increased computational time requirements. Moreover, due to the closed shape of the path of contact of the loboid gears, singular points are encountered requiring special treatment (Hwang and Hsieh Hwang and Hsieh 2007; Dizioglu 1986).

This paper is based on a new concept in gear flank modeling using the principle of involute discretisation of the tooth flanks (Spitas et al. 2007). According to this principle the gear tooth flank is discretised not in straight linear segments but in involute segments instead. Therefore, it is possible to obtain a closed non-implicit solution for the calculation of the conjugate profile at only a fraction of the time needed by the standard conventional methods. The basic advantage of the proposed new technique is that it offers a substantial reduction of the computational time needed for calculating conjugate tooth profiles (Spitas et al. 2007) since it does not have to solve any equations as in the standard theory of gearing. This improvement is particularly useful in gear optimization algorithms where the computation of the conjugate profile must be repeated a number of times at each iterative step. The method is proven to provide good results on closed paths of contact like those of loboid gear pairs as it was for gears with an open path of contact.

2 Theory of Involute Discretisation

Consider a two-dimensional gear tooth for which the working tooth profile $y_G = G(x)$ and the rolling circle of the gear r_o are given (Fig. 1). The problem of conjugate tooth geometry is to determine the path of contact $y_P = P(x)$, the geometry of the generating rack $y_R = R(x)$ and the geometry of the conjugate gear $y_W = W(x)$. Let us also consider a random point $G(x_G, y_G)$ on the working gear tooth profile $y_G = G(x)$ and the Oxy Cartesian coordinate system, where O is the center of rotation of the gear and Oy coincides with the tooth centerline. At point G the tooth profile is approximated with an involute segment with corresponding local pressure angle equal to a_{oG}, such that the local involute has the same tangent with the actual profile at that point. The normal (ε_1) to the profile at point G has inclination equal to $-1/(dG/dx)$ and equation (after Spitas et al. 2007):

$$y = G(x_G) + \frac{x_G - x}{dG/dx|_{(x_G, y_G)}} \tag{1}$$

From the center O of the gear, line (ε_2) normal to (ε_1) is drawn, so that it intersects with it at point $A(x_A, y_A)$. Since (ε_2) is parallel to the tangent to the profile at point G, its inclination is $dG/dx|_{(x_G, y_G)}$ and its equation:

$$y = x\frac{dG}{dx} \tag{2}$$

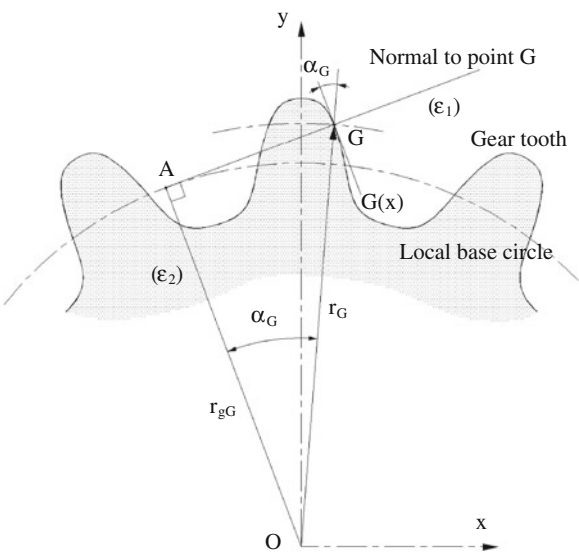

Fig. 1 Local involute and local pressure angle

Point $A(x_A, y_A)$ should verify Eqs. (1) and (2) simultaneously, thus:

$$x_A = \frac{G(x_G) + x_G/(dG/dx)}{dG/dx + 1/(dG/dx)}, \quad y_A = x_A(dG/dx) \tag{3}$$

The radius of the local base circle r_{gG} corresponding to the local involute at G is:

$$r_{gG} = \frac{x_G + G(x_G)dG/dx}{\sqrt{1 + (dG/dx)^2}} \tag{4}$$

The local pressure angle corresponding to the local involute at G is:

$$\alpha_{oG} = \cos^{-1}\left(r_{gG}/r_o\right) \tag{5}$$

Expressions (4) and (5) are independent of the coordinate system used. Therefore, the above equations will remain the same if the coordinate system is such that axis Oy passes through the point where the rolling circle intersects with the tooth flank. It is proven (Spitas et al. 2007) that the corresponding point of the path of contact has the coordinates:

$$x_P = r_{gG}\left[\sqrt{\frac{r_G^2 - r_{gG}^2}{r_o^2}} - \sqrt{1 - \left(\frac{r_{gG}}{r_o}\right)^2}\right], \quad y_P = \left(\sqrt{\left(\frac{r_o}{r_{gG}}\right)^2 - 1}\right) x_P \tag{6}$$

The conjugate rack profile $y_R = R(x)$ and the tooth profile of the conjugate gear (wheel) $y_W = W(x)$ are determined from the calculated path of contact according to the well-known calculation methods.

The method of involute discretisation although it uses local (infinitesimal) involutes to discretise the actual tooth flank is precise and not approximate. The theory does not demand that the tooth flank is divided into fixed finite involute segments, in which case the density of the nodes would affect the precision of the method, but the coordinates and the tangent at each flank point $(x, y, dx/dy)$ are sufficient to define the corresponding point of the path of contact in a unique way.

3 Modeling of Loboid Gears

3.1 Cycloidal Loboid Rotors

Consider the two-lobed rotor illustrated in Fig. 2. This is composed of two epicycloidal curves (BC and AD) and two hypocycloidal curves (AB and CD). Point B is the point of intersection of the hypocycloidal and the epicycloidal curve and also the rolling point, because $r_g = r_o$ so the Law of Gearing (Buckingham 1988)

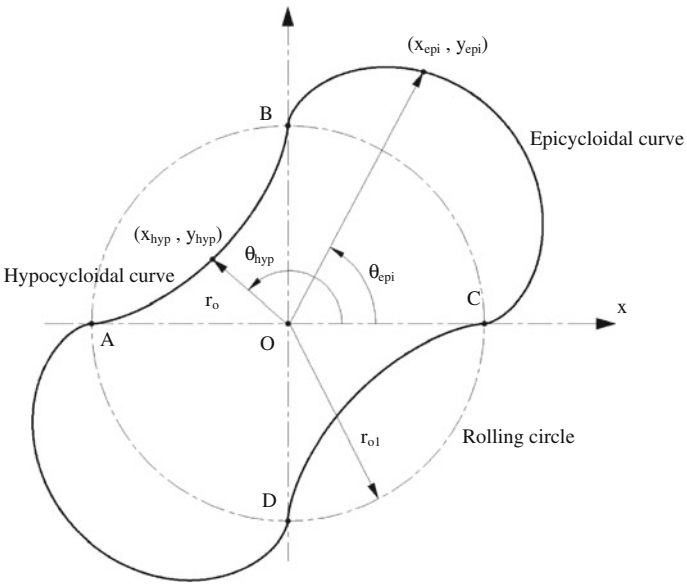

Fig. 2 Geometry of a cycloidal two-lobed rotor

is satisfied. The epicycloidal part begins at point B and ends at point C. It is calculated by the standard equations (Buckingham 1988):

$$x_e = -r_1 \sin\left(\frac{\varphi\, r_{g1}}{r_1}\right)\cos\varphi + C\sin\varphi \quad y_e = r_1 \sin\left(\frac{\varphi\, r_{g1}}{r_1}\right)\sin\varphi + C\cos\varphi \quad (7)$$

where $C = r_1 + r_{g1} - r_1\cos\left(\varphi r_{g1}/r_1\right)$, $r_1 = r_{o1}/4 = r_{g1}/4$, $\varphi = \{0, \pi/N\}$ and N is the number of teeth (lobes). The hypocycloidal part begins at point B and ends at point A and its geometry is given by the following equations (Buckingham 1988):

$$\begin{aligned} x_h &= r_1 \sin\left(-\tfrac{\varphi\, r_{g1}}{r_1}\right)\cos\varphi + C\sin\varphi \\ y_h &= -r_1 \sin\left(-\tfrac{\varphi\, r_{g1}}{r_1}\right)\sin\varphi + C\cos\varphi \end{aligned} \quad (8)$$

where
$C = -r_1 + r_{g1} + r_1\cos\left(\varphi r_{g1}/r_1\right)$, $r_1 = r_{o1}/4 = r_{g1}/4$ and $\varphi = \{\pi/N, 2\pi/N\}$

After calculating the two curves (Eqs. 7 and 8) composing one tooth, the flanks of the other teeth are calculated by rotating the previous by $i\frac{2\pi}{N}$, where $i = 0 \div N$ using the following equation:

$$x' = x\cos\left(i\frac{2\pi}{N}\right) - y\sin\left(i\frac{2\pi}{N}\right), \quad y' = x\sin\left(i\frac{2\pi}{N}\right) + y\cos\left(i\frac{2\pi}{N}\right) \quad (9)$$

3.2 Circular Addendum Loboid Rotors

A two-lobed circular addendum rotor is illustrated in Fig. 3. The geometry of this rotor is suggested by Litvin and Feng (1996). The addendum of each lobe is a circular arc of radius ρ and center (x_{ad}, y_{ad}). The dedendum is generated by the addendum of the mating rotor, during meshing.

To model the addendum, point A is calculated. As illustrated in Fig. 3 the coordinates of point A are:

$$x_A = r_o \cos\frac{\pi}{2N} \quad y_A = r_o \sin\frac{\pi}{2N} \tag{10}$$

Angle θ_1 is calculated from the relation:

$$\theta_1 = \cos^{-1}\frac{y_A}{\rho} = \cos^{-1}\left(\frac{r_o}{\rho}\sin\frac{\pi}{2N}\right) \tag{11}$$

The coordinates of the center of the circle (addendum), point B are calculated:

$$x_B = \rho \sin\left(\cos^{-1}\left(\frac{r_o}{\rho}\sin\frac{\pi}{2N}\right)\right) + r_o\cos\frac{\pi}{2N}, \quad y_B = 0 \tag{12}$$

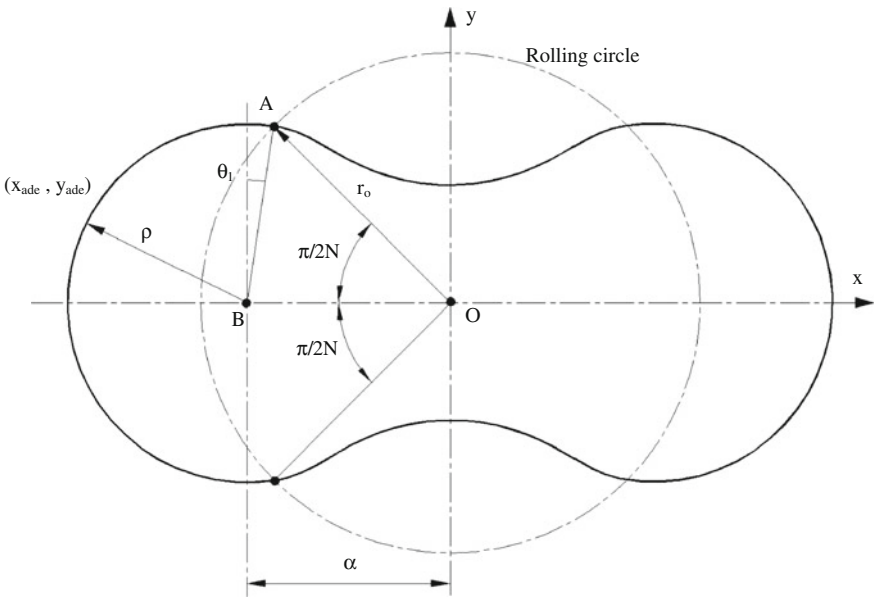

Fig. 3 Geometry of a circular addendum two-lobed rotor

and the addendum is calculated by the following equations:

$$x_{ad} = \rho \cos\theta + x_B, \quad y_{ad} = \rho \sin\theta, \quad \theta = \left\{ \frac{\pi}{2N} - \theta_1, \frac{3\pi}{2N} + \theta_1 \right\} \tag{13}$$

To calculate the dedendum, the resulting path of contact corresponding to the meshing action of the addendum is calculated and then the flank of the conjugate gear, using the equations of the proposed theory Eqs. (4) and (5). Then the flank is rotated about point A by $i(2\pi/N)$ rad for $i = 1 \div N$ to produce the rest of the gear teeth using the following set of equations:

$$\begin{aligned} x_{de} &= (x - x_A)\cos\left(i\tfrac{2\pi}{N}\right) - (y - y_A)\sin\left(i\tfrac{2\pi}{N}\right) \\ y_{de} &= (x - x_A)\sin\left(i\tfrac{2\pi}{N}\right) + (y - y_A)\cos\left(i\tfrac{2\pi}{N}\right) \end{aligned} \tag{14}$$

4 Results and Discussion

The above presented non-involute spur gear tooth geometries were generated using a specially developed computer program in C++ based on the proposed theory. The input for the algorithm is the following:

- Number of teeth of the generating gear N_1 and the generated gear N_2. If a rack is to be designed then the number of teeth is fixed to two by default.
- The coordinates of the given tooth flank (for 1 tooth) as (x, y) values with respect to the center of the gear or the coordinates of the path of contact with respect to the rolling point (pitch point). The given tooth coordinates should be specified whether they belong to gear 1, gear 2 or to the generating rack.
- The coordinates of the center point of gear 1 or gear 2 or the coordinates of the rolling point (pitch point).

The program then uses a B-spline approximation to connect the given points and calculate the tangent and the normal vector at each point. Then for each point on the flank the corresponding mating point on the generating rack and the path of contact are calculated using Eqs. (4–5) and the corresponding point on the mating gear is derived from the rack geometry using the Theory of Gearing. The rest of the teeth of both the generating and the generated gear are plotted by arraying the basic tooth form in a circular pattern around its center of rotation N_1 and N_2 times respectively. This approach offers good accuracy and faster computing time compared to the standard Theory of Gearing (Spitas et al. 2007).

The output from the computational program was imported to the AutoCAD 2002 environment using an AutoLISP interface program. Inside the CAD environment the gears and the racks are designed as pairs in mesh at the rolling point of the gear set. Also the path of contact can be automatically drawn.

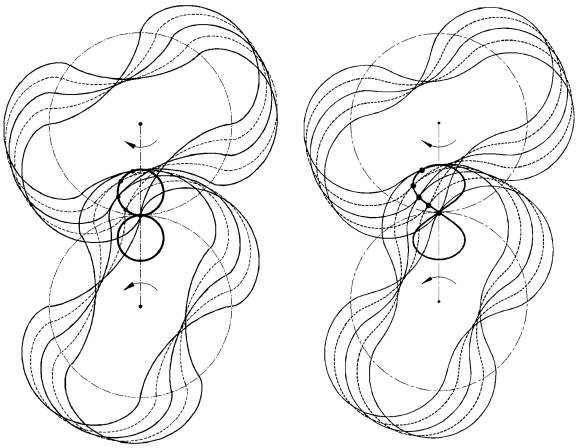

Fig. 4 Path of contact of a cycloidal (*left*) and a circular addendum (*right*) two-lobed gear pair in mesh

The first step of the present theory for the computation of the mating gear is the determination of the corresponding path of contact. Although the path of contact of the examined gears is closed (Buckingham 1988) and therefore the rolling point (pitch point) is a singular point for the kinematics of the mechanism (i.e., the path of contact crosses it two times per revolution) the proposed theory did not encounter any problem and calculated the closed path of contact with good accuracy. The corresponding path of contact for two-lobed rotors one with cycloidal and the other with circular arc addendum teeth in mesh is illustrated in Fig. 4. The path of contact is computed as an intermediate step of the Involute Discretisation algorithm and has a distinct "8" shape for the circular addendum gears as opposed to the two circles in contact at the rolling point of the cycloidal rotors.

5 Conclusion

In this paper the theory of involute discretisation for calculating conjugate tooth profiles of gears was applied on closed path of contact non- involute gears used in loboid gear pumps and Roots blowers of either cycloidal or circular addendum form. By discretising the gear tooth profile into infinitesimal local involutes the corresponding point on the mating wheel/rack and the relevant point on the path of contact are calculated using simple, closed analytical formulae instead of having to solve complex equations which often exhibit branching points.

In the examples presented it was demonstrated that the theory works satisfactorily without any special adaptation in the case of cycloidal power transmission gearing, two-lobed or three lobed Roots blowers either with cycloidal or with circular addendum teeth. Due to the concept of involute discretisation, branching and singular points did not pose any problem for the method. The basic algorithm

was implemented in a computer program in C++ integrated with a CAD environment through an Auto LISP interface batch program for generating the mating gear pairs.

References

Buckingham E (1988) Analytical mechanics of gears. Dover Publications Inc., New York

Demenego A, Vecchiato D, Litvin F, Nervegna N, Mancó S (2002) Design and simulation of meshing of a cycloidal pump. Mech Mach Theor 37(3):311–332

Dizioglu B (1986) On the real singularities points of cycloids, epicycloids and hypocycloids. Mech Mach Theor 21(3):223–224

Hwang Y-W, Hsieh C-F (2007) Determination of surface singularities of a cycloidal gear drive with inner meshing. Math Comput Model 45(3–4):340–354

Litvin F, Feng P (1996) Computerized design and generation of cycloidal gearings. Mech Mach Theor 31(7):891–911

Litvin F, Fuentes A (2004) Gear geometry and applied theory, 2nd edn. Cambridge University Press, Cambridge

Shin J-H, Kwon S-M (2006) On the lobe profile design in a cycloid reducer using instant velocity center. Mech Mach Theor 41(5):596–616

Spitas V, Costopoulos T, Spitas C (2007) Fast modeling of conjugate gear tooth profiles using discrete presentation by involute segments. Mech Mach Theor 42(6):751–762

Stryczek J (1990) Design of cycloidal gears in hydraulic machines. Mech Mach Theor 25(6):597–610

Stryczek J (1993) Characteristic parameters of hydraulic displacement machines with cycloidal gearing. Mech Mach Theor 28(1):97–112

Sung LM, Tsai YC (1997) A study on the mathematical models and contact ratios of extended cycloid and cycloid bevel gear sets. Mech Mach Theor 32(1):39–50

Townsend D (1992) Dudley's gear handbook. Mc-Graw Hill, New York

Vecchiato D, Demenego A, Argyris J, Litvin F (2001) Geometry of a cycloidal pump. Comput Methods Appl Mech Eng 190(18–19):2309–2330

Yang D, Blanche J (1990) Design and application guidelines for cycloid drives with machining tolerances. Mech Mach Theor 25(5):487–501

Yao L, Ye Z, Dai JS, Cai H (2005) Geometric analysis and tooth profiling of a three-lobe helical rotor of the roots blower. Mater Process Technol 170(1–2):259–267

Ye Z, Zhang W, Huang Q, Chen C (2006) Simple explicit formulae for calculating limit dimensions to avoid undercutting in the rotor of a cycloid rotor pump. Mech Mach Theor 41(4):405–414

Cams-Software Program to Design and Synthesis of Cams Mechanisms

Ljupco Trajcevski and Tale Geramitchioski

Abstract In this paper algorithms are developed and implemented in a software program for kinematic and dynamic analysis of two characteristic cams mechanisms with rotating cam profile and translating follower. The follower configuration is: Flat-Face follower and Roller follower. The name of the software package is CAMS and it is written in a programming language DELPHI v.5.0. This software provides us the possibility with the first profiled profile that is based on the previous given movement trajectory of the follower member of the mechanism, which indicates the performance of all kinematics and dynamic analysis of the cams mechanisms. After the performed calculations, the program provides an entirely graphical visualization of input and output components and complete animation of the cam mechanisms.

Keywords Cams · Mechanisms · Flat-flower follower · Roller follower

1 Introduction

The transformation of one of the simple motions, such as rotation, into any other motions is often conveniently accomplished by means of a cam mechanism. A cam mechanism usually consists of two moving elements, the cam and the follower, mounted on a fixed frame. Cam devices are versatile, and almost any arbitrarily-specified motion can be obtained. In some instances, they offer the simplest and most compact way to transform motions.

L. Trajcevski (✉) · T. Geramitchioski
University St. Kliment Ohridski Bitola, Bitola 7000, Republic of Macedonia
e-mail: trajcevski@uklo.edu.mk

T. Geramitchioski
e-mail: geramitcioski@uklo.edu.mk

G. Dobre (ed.), *Power Transmissions*,
Mechanisms and Machine Science 13, DOI: 10.1007/978-94-007-6558-0_33,

A cam may be defined as a machine element having a curved outline or a curved groove, which, by its oscillation or rotation motion, gives a predetermined specified motion to another element called the follower. The cam has a very important function in the operation of many classes of machines, especially those of the automatic type, such as printing presses, shoe machinery, textile machinery, gear-cutting machines, and screw machines. In any class of machinery in which automatic control and accurate timing are paramount, the cam is an indispensable part of mechanism. The possible applications of cams are unlimited, and their shapes occur in great variety.

Cam analysis and synthesis fundamentals are well documented in the literature. Classical graphical techniques, specialized coordinate system, digital computer processing, numerical techniques etc. have all enjoyed favor in cam design.

While each of researcher's analytical techniques has their supporters, it is the author's intent to show their extremely important individual efforts. Combining their contributions takes advantage of the mathematics of kinematics to develop a consistent, common, design process well adapted for computer programming.

2 Software Package: Cams

The software package CAMS is written in Visual Delphi version 4.0. In addition, block diagrams are given for kinematic and dynamic analysis of mechanisms such as cams and synthesis of shore known law of motion of roller follower. Before you start the program that should be performed numerically solving certain mathematical problems, as a first step, it is good to study numerical methods to be used. Next step is the organization of programs, the formation of its structure which is a direct function of the type of calculations to be carried out. For this purpose it is necessary to systematically define the tasks that are set before the program, which is a good theoretical knowledge of the problem to be solved.

Tasks set before the program can be systematized as follows:

–It is necessary to allow the assignment of this road you need to perform translator roller follower; Assignment of geometrical characteristics of cam mechanisms; Calculation of the stiffness kinematic members who are taken for elastic; Calculation of the first, second and third transfer function;

Interpolation of all functions in exactly certain points; Solving nonlinear differential equation with time dependent coefficients before changing; Numerical differentiation; Visual presentation of results in the form of diagrams and their animation. The given review may conclude that it is necessary to perform numerous and complex mathematical calculations. Schematic representation of the main menu of the CAMS software package is displayed Fig. 1.

The structure of each program that will solve the problem, made the five modules that have separate tasks that must communicate with each other. These modules are:

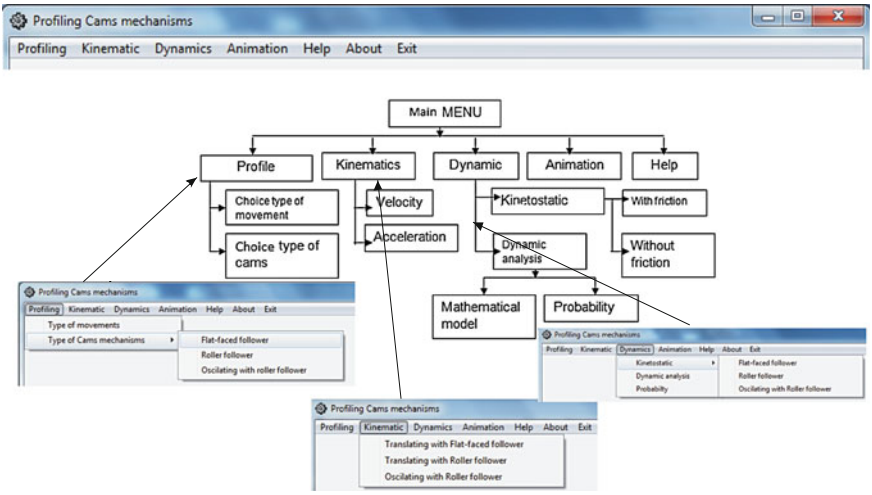

Fig. 1 Schematic representation of the main menu-CAMS

- Module PROFILE;
- Module KINEMATIC;
- Module KINETOSTATIC;
- Module DYNAMIC;
- Module ANIMATION;

One of the most important tasks when we design the cams mechanisms is the choice of the motion law of the executive member. Basic criteria for selection that step of the cam design are:

- Consent of the law of motion with the requirements in the technological process;
- Minimum consumption of energy for propulsion of the mechanism and
- Simple preparation of cam plate.

As a means of avoiding infinite jerk (the change of acceleration which is determined by the third derivative of displacement) and its harmful impact on cam transmitter, developed a system of cams structures (Kloomok and Muffley) using three analytical functions:

- Cycloid and half-cycloid
- Harmonic and half-harmonic
- Polynomial of eighth order

All these curves are defined derivatives in all points between and acceleration is changing gradually and jerk is final. The choice of profile that fits the requirements is carried out according to the criteria:

- Gives acceleration to zero at both ends. Therefore it may be linked to dwell on both ends. Because it is pressure angle of a relatively large and unnecessary acceleration returns to zero two cycloid should not be linked together.
- Harmonic law gives the smallest peaks of acceleration and angle of pressure is also the most in terms of the above three types of functions. Therefore better acceleration when both ends of which starts and finishes to match the final acceleration of the adjacent profile. Because the acceleration in the mid-point is equal to zero, half-harmonic can be associated with half-cycloid or semi polynomial.
- Polynomial of eighth order has not symmetric curve acceleration and gives the peaks of acceleration and angle of pressure by value between cycloid and harmonic.

Module PROFILE—This module define the geometrical parameters and kinematic reviewed the mechanism and to calculate the first, second and third transmission function.

Also this module aims to project the profile of cams mechanisms depending on the selected type of mechanisms already known to the law of movement of roller translator follower. This module perform analytical calculations for the design of cam profile.

In determining the bend radius of the profile are constructed by using diagrams and M.Kloomok and R.V.Muffley rather transcendent function is solved in the program. To find the angle of pressure used diagram that found in the literature depending on the chosen law of motion but it is solved analytically.

This module consists of several sub-module as sub-module numeric differentiation. If the law of motion is given as a consecutive numerical values can be calculated velocities and accelerations required to perform numerical differentiation. If the law of motion is given in explicit form, speed and acceleration are calculated with appropriate mathematical expressions. After calculating the data is writing in file depending on the type of cams mechanisms.

Block diagram and graphic from profile of cams mechanisms are shown in Fig. 2.

Module KINEMATIC—This module performs the calculation of velocity and acceleration at characteristic points of the cams mechanisms. As input data used by the module PROFILE.

Depending on the selected type of mechanism are obtained velocities and accelerations in Diagrammatic form with the possibility of accurately reading the same. These results are recorded in the file. Block diagram of this module is given in Fig. 3.

Module KINETOSTATIK—This module uses the results of the module and the module KINEMATIC PROFILES. The results of these modules together with the fact that there is friction is input in this module.

Depending on the selected type of mechanisms are calculated kinematic sizes or reactions to touch in Higher kinematic pair and the reaction in the lower kinematic pair. Before calculating the magnitudes kinematic is calculated on inertial forces, the force in spring and inertial point if it exists.

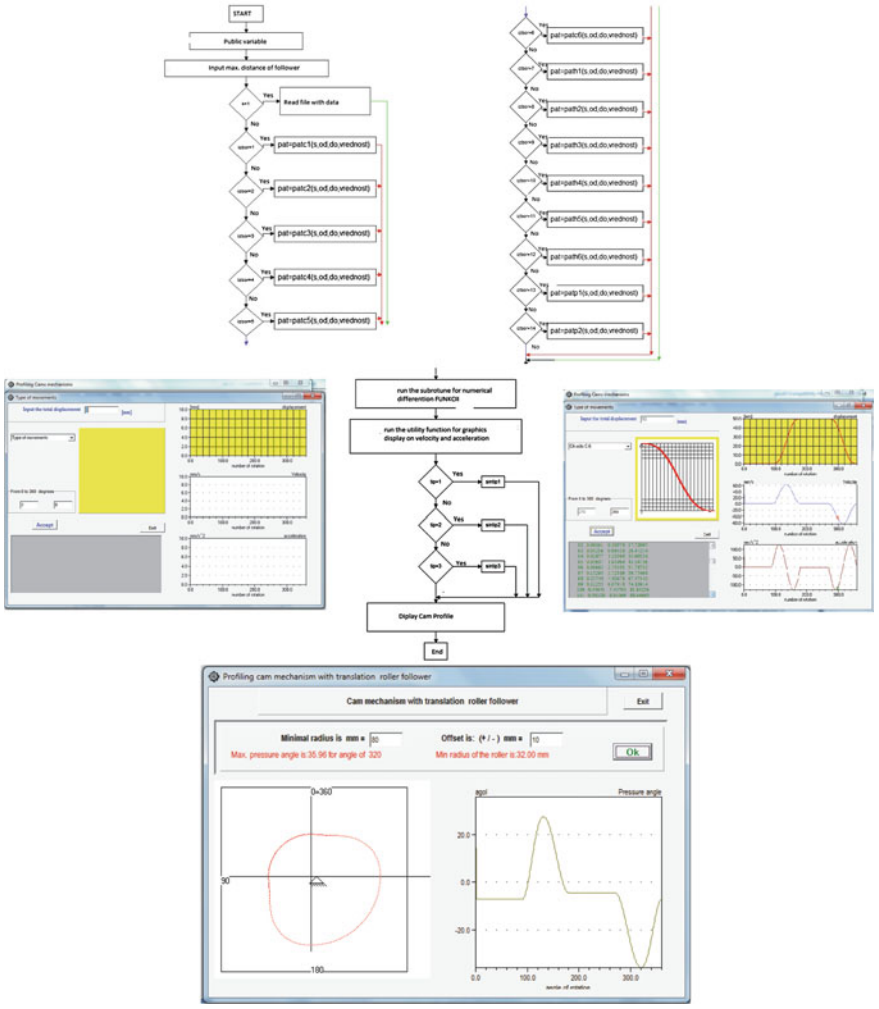

Fig. 2 Block diagram on the module PROFILE

The calculation of kinematic magnitudes is based on analytical expressions. Block diagram is given in Fig. 4.

Module DYNAMIC—This module solves mathematical model cams mechanisms by solving the nonlinear equation. Nonlinear nature of the differential equation to solve. difficult analytical equation that applies numerical solution. To permanently store the same accuracy of results is necessary to introduce adaptive step and every step to analyze the stability of the numerical solution. To solve the system differential equations using Runge–Kutta method of 4 order. After the calculation results are displayed in the form of a diagram. Block diagram is shown in Fig. 5.

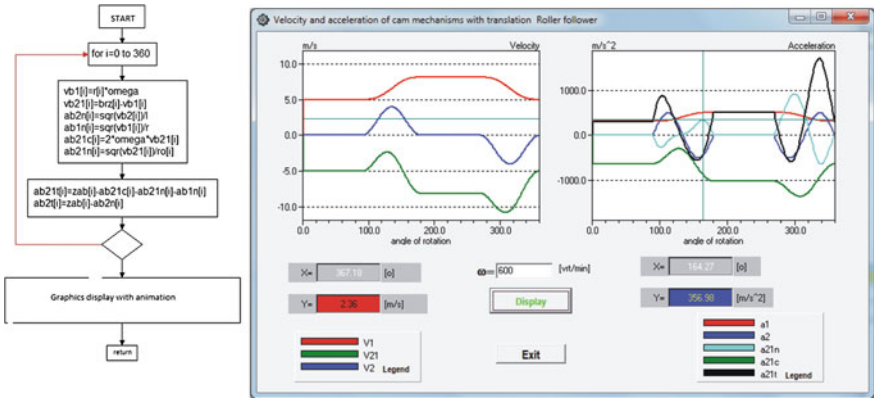

Fig. 3 Block diagram on the module KINEMATIC

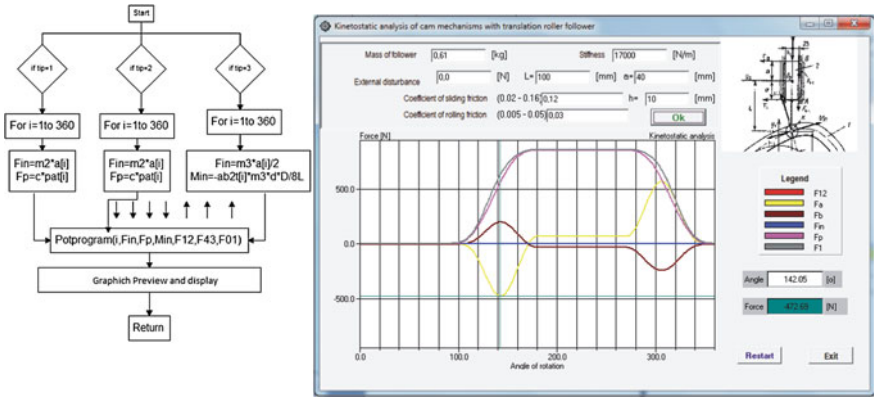

Fig. 4 Block diagram on the module KINETOSTATIC

Module ANIMATION—The task of this module is based on calculations in all previous modules to give a visual presentation of final results with the possibility of animation. The module is designed so that the display of results diagram be animated for better visual appearance, and visualization the way we want to have cam mechanisms. Charts are presented depending on the angle of rotation of the cam profile, because thus get a clear picture of the movement in a cycle of his work. For the best effect in visualization of the results are used by the company utility subprogram Software Development Lohninger. Graphic presentation is given in Fig. 6.

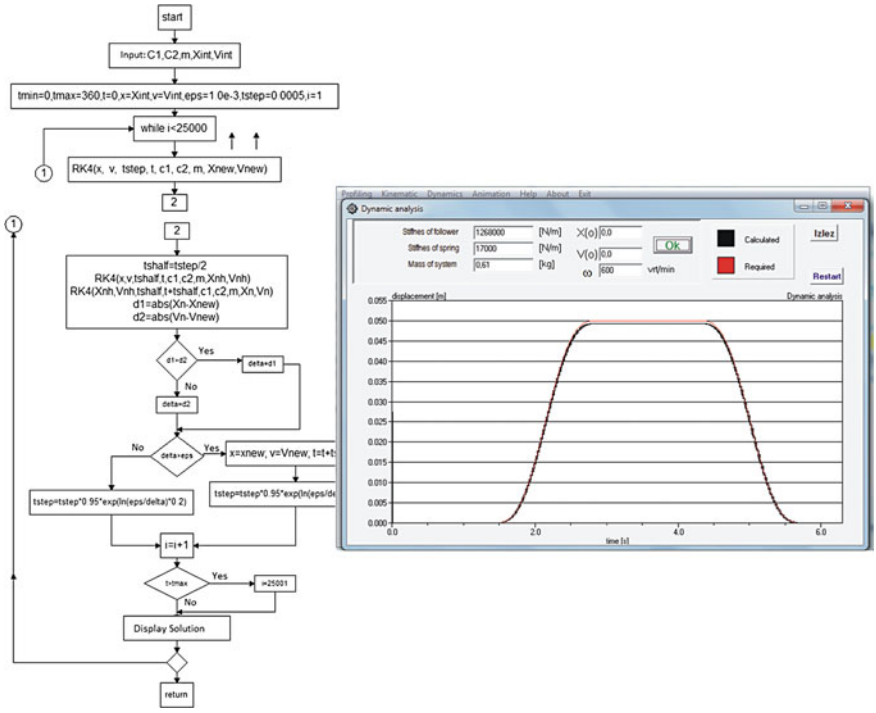

Fig. 5 Block diagram on the module DYNAMIC

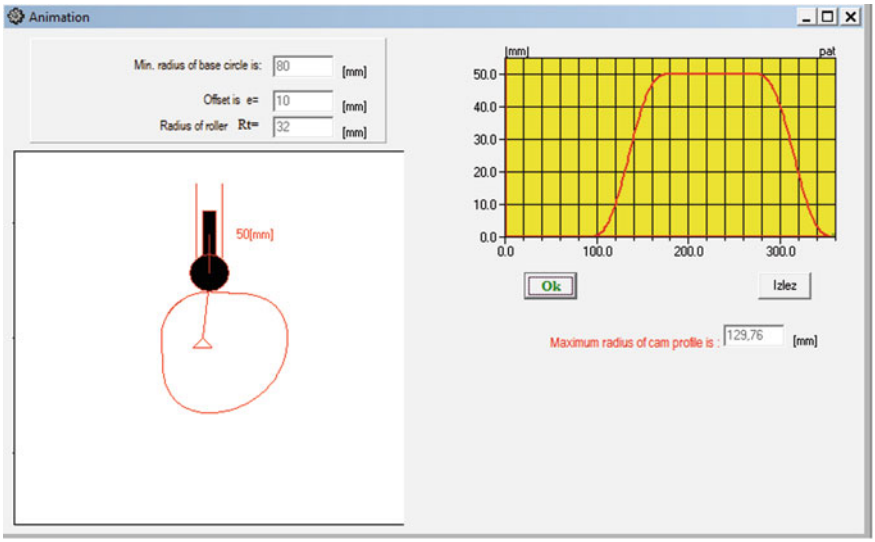

Fig. 6 Display the animation form from module ANIMATION

3 Conclusion

This research is a theoretical study on the synthesis of the cams mechanisms. Developed programs it is a new design strategy, based on a choice of the law of motion of the executive member using three analytical functions (Kloomok and Muffley).This software CAMS is a powerful tool to design the cam shapes and analysis the kinematic, kinetostatic and dynamic of cams mechanisms.

References

Geramitcioski T, Vilos I, Trajcevski LJ (2000) Applied numerical method for evaluating probability of CAM profile, Design 2000, Dubrovnik, 25–27 May 2000, pp 295–300

Geramitcioski T, Vilos I, Trajcevski LJ (2000) CAD and shape optimization of the CAM profile, Design 2000, Dubrovnik, 25–27 May 2000, pp 301–306

Geramitcioski T, Trajcevski LJ (2000) "Software package for kinematics and dynamics analysis and synthesis of CAM mechanisms with roller translator follower". In: The 7th international conference research and development of mechanical elements and systems IRMES' 2011, Zlatibor, 27–28 Apr 2011, Serbia, pp 127–132

Hamilton NM (1973) Mechanisms and dynamics of machinery. Wiley, New York

Smith DJ (1999) Gear noise and vibration. Cambridge University, England

New Algorithm for Variable Speed Gear Generation Process

Marius Vasie, Domenico Mundo and Laurenţia Andrei

Abstract The paper is focused on the generation process of a particular type of noncircular gears, i.e. the variable speed gears. A curiosity in the old gear industry, the noncircular gears have become a challenge and an opportunity for the computer graphics and technology. In the attempt of generalizing the gear generation process, the Gielis supershape is proposed for the gear pitch curve. Limited to proper variation ranges, the supershape defining parameters generate symmetric-asymmetric, convex-concave, close-open pitch curves. Based on the rolling method, using either a rack cutter or a shaper, the further gear generation is simulated in AutoCAD environment, importing Matlab data. Original algorithms are created to configure the main stages of the variable speed gear generation process: (1) the pitch curve modeling and analysis, (2) the selection of the proper cutting tool and kinematics, (3) the simulation of the tooth generation.

Keywords Noncircular gear · Variable speed gear · Noncircular pitch curve · Supershape · Gear generation

List of Symbols

r_i, θ_i	Polar coordinates for the driving ($i = 1$) and driven ($i = 2$) gears
m_{12}	Gear instantaneous transmission ratio
D	Center distance
ω_{ij}	Angular speed for gear blank ($ij = rr$) or shaper ($ij = cr$)

M. Vasie (✉) · L. Andrei
University Dunarea de Jos of Galati, Galati, Romania
e-mail: v_marius_gl@yahoo.com

L. Andrei
e-mail: landrei@ugal.ro

D. Mundo
University of Calabria, Cosenza, Italy
e-mail: d.mundo@unical.it

G. Dobre (ed.), *Power Transmissions*,
Mechanisms and Machine Science 13, DOI: 10.1007/978-94-007-6558-0_34,

v_{ij}	Velocity of translational motion for gear blank ($ij = rr$) or rack cutter ($ij = ct$)
x_{rt}, y_{rt}, y_{ct}	Displacements of gear blank (rt) and rack cutter (ct)
γ_r, γ_c	Rotational angles of gear blank (r) and shaper (c)
m	Gear modulus
z_i	Number of teeth for the driving ($i = 1$) and driven ($i = 2$) gears

1 Introduction

Noncircular gears are a special category of geared transmissions that can be used in those applications that require a variable output motion. Noncircular gears are similar to cams, chains and sprockets or linkages, but from other points of view, they are better (compact sized, there is no gross separation or decoupling between elements, possibility of rotation in both directions, large variety of shapes) as mentioned by Dooner and Seireg (1995).

The first manufacture attempts were made with tools that used master noncircular racks, methods that proved to be complex and inefficient. After the enveloping method was proposed by Litvin (1994), noncircular gears could be manufactured like any other gear, performing a pure rolling of the tool's centrode over the gear's centrode. In the design of noncircular gears, some scientists focused on the synthesis of the centrodes, some concentrated on profile generation, while others found various applications for this type of gears. Yang and Tong (1998) generated identical noncircular centrodes, using a monotonically increasing function for the driving pitch curve. In order to generate teeth for a planetary gear train, Mundo (2006) used a numerical approach, by integrating a differential equation describing the contact point displacement along the line of action, during meshing. Instead of deducing and solving complicated meshing equations specific to enveloping method, Li et al. (2007) proposed a method for generating noncircular gears' teeth based on the real shaping process. Jing (2009) introduced a pressure angle function to characterize the mathematical model for the geometry and geometric characteristics of noncircular gears' tooth profiles.

The authors develop a general procedure for the variable speed gear generation, based on the simulation of the gear cutting process by rolling method. The Gielis supershape (Gielis et al. 2003) is used for the modeling of gear pitch curve and requires optimal selection of its six defining parameters, in order to lead to potential gear pitch curves. Once the pitch curve is modeled, the generation of the gear teeth follows the traditional algorithm of the noncircular gear cutting process, simulating the rolling between the gear blank and the selected tool, i.e. a rack cutter or a shaper, for convex or convex-concave pitch curves, respectively.

2 Gear Pitch Curve Modeling Process

The noncircular gear generation procedure starts with the design of conjugate pitch curves that perform assigned transmission function or correspond to predesigned geometries. The modeling of mating pitch curves manipulates two essential data, i.e. the constant center distance and the pure rolling motion. As regards to the hypothesis of desired noncircular driving pitch curve, several designs have been reported: elliptical shapes (Litvin and Fuentes 2004; Bair et al. 2009), N-lobe and polinomial smooth profiles (Yang and Tong 1998; Figliolini and Angeles 2005), deformed limacon shapes (Dawei and Tingzhi 2011) and curves aproximated by Fourier series (Tsay and Fong 2005) or generated with monotonically increasing functions.

The authors also developed the modeling process of mating pitch curves, starting from a desired driving pitch curve. The significant steps considered for the modeling process are as follows (Fig. 1):

Step 1. Driving pitch curve modeling and analysis. In the attempt of generalizing the noncircular gear design, the authors propose the Gielis' superformula (Andrei and Vasie 2010) for the driving noncircular pitch curve polar expression:

$$r_1(\theta_1) = \left[\left|\frac{1}{a}\cdot\cos\frac{n\theta_1}{4}\right|^{n_2} + \left|\frac{1}{b}\cdot\sin\frac{n\theta_1}{4}\right|^{n_3}\right]^{-\frac{1}{n_1}} \tag{1}$$

where a, b are the semilengths of the major axes, n–a real number that determines the number of lobes of the shape; n_1, n_2 and n_3–real numbers that leads to pinched, bloated or polygonal, symmetric or asymetric forms.

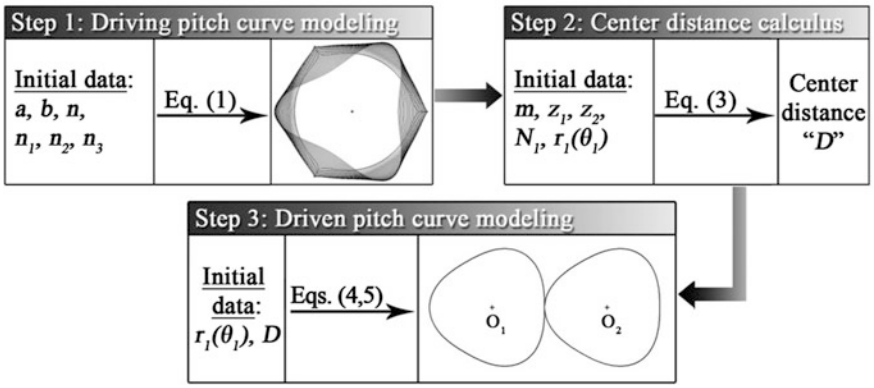

Fig. 1 Algorithm of mating pitch curves design

Analyzing the supershape family, a proper selection for the defining parameters is imposed in order to generate adequate pitch curves that would not lead to further undercutting.

Step 2. Determination of constant center distance. Considering the general case, in which the driving pitch curve performs N_I revolutions for one revolution of the driven pitch curve, in order to get a closed form curve for the driven centrode, the following condition must be considered (Litvin 1994):

$$\frac{2\pi}{N_1} = \int_0^{2\pi} \frac{1}{m_{12}(\theta_1)} d\theta_1 = \int_0^{2\pi} \frac{r_1(\theta_1)}{r_2(\theta_2)} d\theta_1 = \int_0^{2\pi} \frac{r_1(\theta_1)}{D - r_1(\theta_1)} d\theta_1 \tag{2}$$

Equation (2) enables the center distance D to be determined through numerical integration and iterative procedure. The accuracy for the above calculus is considered as:

$$\Delta = \frac{2\pi}{N_1} - \int_0^{2\pi} \frac{r_1(\theta_1)}{D - r_1(\theta_1)} d\theta_1 \leq 10^{-6} \tag{3}$$

Step 3. Driven pitch curve modeling. Based on the driven pitch curve and the constant center distance, the driven pitch curve is represented by:

$$r_2(\theta_2(\theta_1)) = D - r_1(\theta_1) \tag{4}$$

$$\theta_2(\theta_1) = \int_0^{\theta_1} \frac{1}{m_{12}} d\theta_1 = \int_0^{\theta_1} \frac{r_1(\theta_1)}{D - r_1(\theta_1)} d\theta_1 \tag{5}$$

Using Gielis' superformula for the pitch curve definition, six defining parameters are influencing the shapes of the mating pitch curves. A brief analysis on the influence the supershape parameters have on the pitch curve geometry and gear ratio is presented in Figs. 2, 3, and 4. The pitch curves are scaled in order to correspond to a gear with modulus 2 mm and number of teeth 36. It can be noticed that:

- as the number of lobes (n) is increased (Fig. 2), the pitch curves change from eccentric circular shapes ($n = 1$) to elliptical ($n = 2$) and rounded polygonal shapes ($n = 3$), while the gear ratio keeps constantly its amplitude but gets periodical variation;
- as the exponent n_1 is increased (Fig. 3), the shape changes from convex–concave to convex shapes and the amplitude of the gear ratio is reduced; an increase of 500 % of the n_1 value leads to a reduction of 88 % of the gear ratio amplitude;

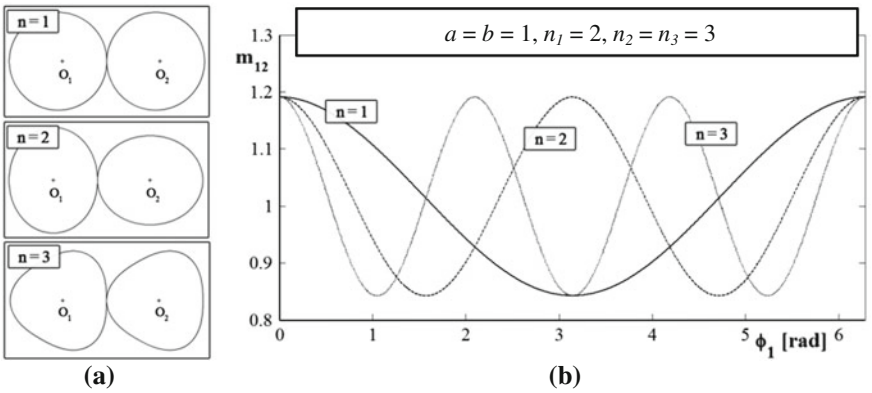

Fig. 2 Influence of parameter n on pitch curve geometry (**a**) and on gear ratio (**b**)

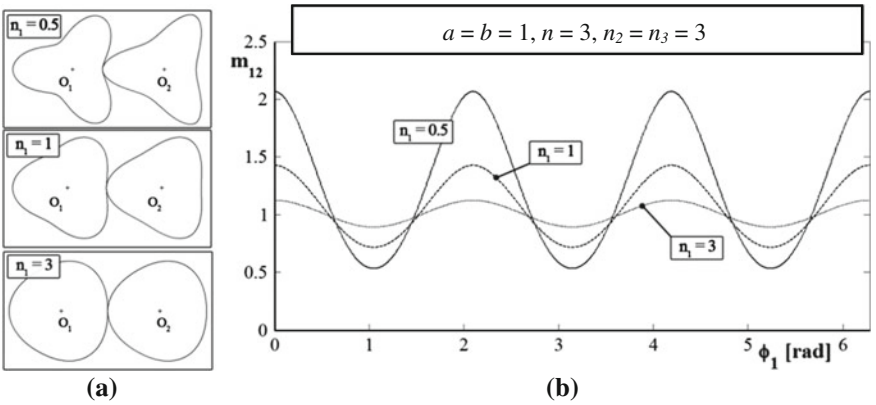

Fig. 3 Influence of parameter n_1 on pitch curve geometry (**a**) and on gear ratio (**b**)

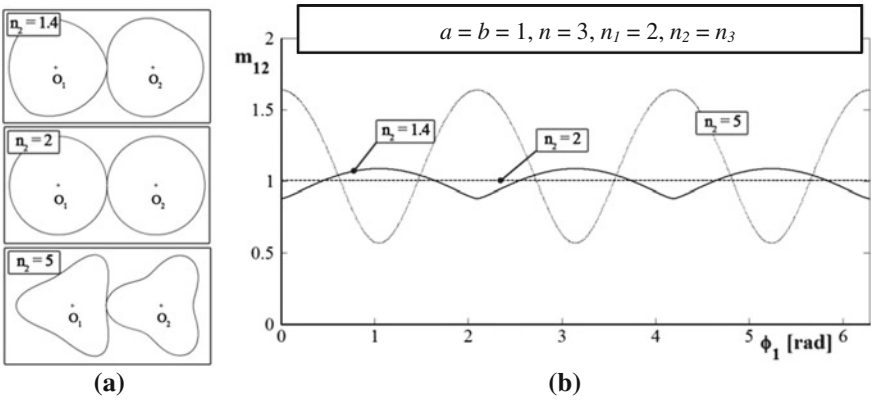

Fig. 4 Influence of parameter n_2 on pitch curve geometry (**a**) and on gear ratio (**b**)

- as the exponent n_2 is increased (Fig. 4), the shape is changed from convex-concave ($n_2 < 2$) to circular shapes ($n_2 = 2$) and back to convex–concave shapes ($n_2 > 2$). The gear ratio variation is slightly reduced as the pitch curves get close to circular shapes (no variation for m_{12}, as known) and increased by high values of n_2;

If one of the major axis length is increased, the elliptical shapes are generated and an increase of their eccentricity is reported.

3 Generation of Variable Speed Gear

The noncircular gears are usually manufactured by a rack cutter, a shaper, a hob, or by wire EDM. Considering the tooth generation by rolling method, the rack cutter and the shaper are the most common tools dedicated to convex and convex-concave pitch curves, respectively. As the authors are using Gielis' supershape for the driving pitch curve, the choice of the cutting tools and kinematics is directly influenced by the supershape defining parameters. The simulation of the gear generation is developed in AutoCAD environment, using imported Matlab data.

3.1 Generation by a Rack Cutter

To enable noncircular gear generation by a rack cutter, an analysis on pitch curve convexity is firstly developed. Therefore, the selection of the supershape defining parameter is focused on the variation/sign of pitch curvature radius, calculated by:

$$\rho(\theta) = \frac{\left[r^2(\theta) + \left(\frac{dr(\theta)}{d\theta}\right)^2\right]^{\frac{3}{2}}}{r^2(\theta) + 2\left(\frac{dr(\theta)}{d\theta}\right)^2 - r(\theta)\frac{d^2r(\theta)}{d\theta^2}} \tag{6}$$

As long as $\rho > 0$, the convexity of the pitch curve recommends the gear generation by a rack cutter. The simulation of the gear generation is based on the following coordinate systems (Fig. 5):

- a fixed system, $O_fX_fY_f$, with the origin O_f in the initial position of the contact point, T_0, and with the Y_f axis along the common tangent, and
- two movable coordinate systems, $O_1X_1Y_1$ and $O_cX_cY_c$ rigidly attached to the noncircular gear blank and to the rack cutter, respectively.

The rack cutter, defined by a standard geometry, is translated with velocity v_{ct}, along the common tangent (t) to the centrodes. The current position is defined by:

$$y_{ct}(\theta_1) = -s(\theta_1) \pm r(\theta_1) \cdot \cos\mu(\theta_1) \tag{7}$$

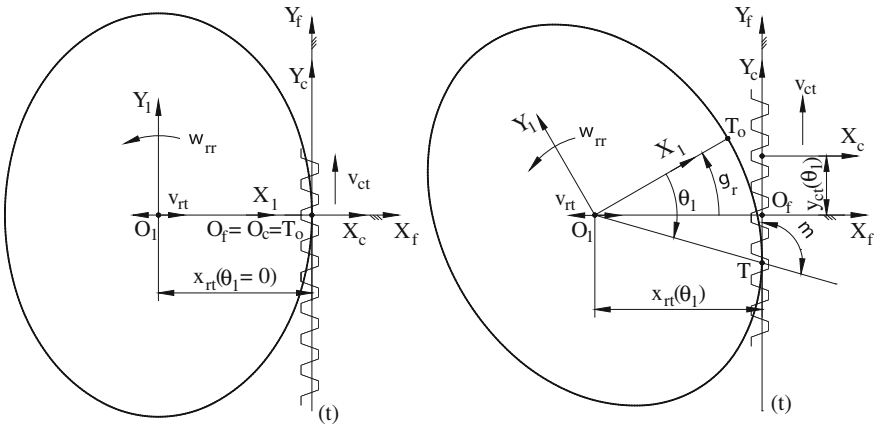

Fig. 5 Kinematics of noncircular gear generation process by rack cutter

where $\mu(\theta_1)$ defines the orientation of the tangent (t) to the gear centrode, at contact point T,

$$\mu(\theta_1) = arctg \frac{r(\theta_1)}{\frac{dr(\theta_1)}{d\theta_1}} \tag{8}$$

$s(\theta_1)$ is the rolling distance, respectively the length of the arc T_0T:

$$s(\theta_1) = T_0T = TO_c = \int_{-\theta_1}^{0} \frac{r(\theta_1)}{\sin \mu(\theta_1)} d\theta_1 \tag{9}$$

The gear is rotated about its center of rotation O_1, with the angular velocity ω_{rr}, and is translated along the perpendicular to (t) direction, with velocity v_{rt}. The current position is defined by:

$$\gamma_r(\theta_1) = \theta_1 + \mu(\theta_1) - \pi/2 \tag{10}$$

$$x_{rt}(\theta_1) = -r(\theta_1) \cdot \sin \mu(\theta_1) \tag{11}$$

3.2 Generation by Shaper Cutter

For convex-concave noncircular gears, the generation of the gear teeth is developed by simulating the manufacture using a shaper cutter. The range of the supershape defining parameters variation that leads to lobed pitch curves is further

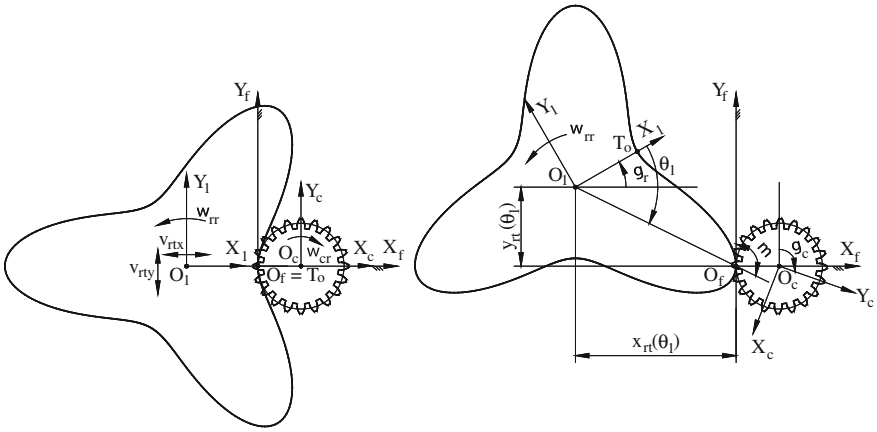

Fig. 6 Kinematics of noncircular gear generation process by shaper

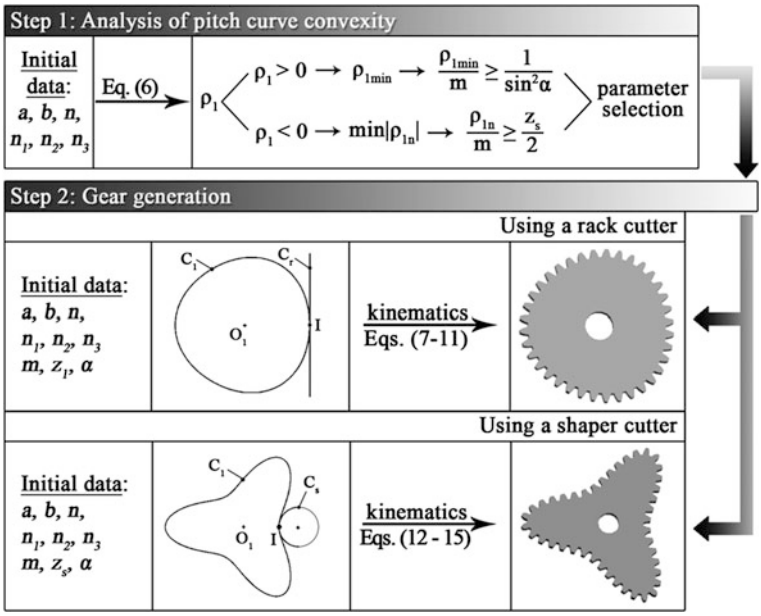

Fig. 7 Algorithm of variable speed gear generation

limited in order to avoid undercutting. Therefore, a new requirement is analyzed, i.e. the minimum curvature radius at concave sectors should be larger than the shaper pitch radius. The simulation of the gear generation by a shaper is based on the following coordinate systems (Fig. 6): a fixed system, $O_fX_fY_f$, with the origin

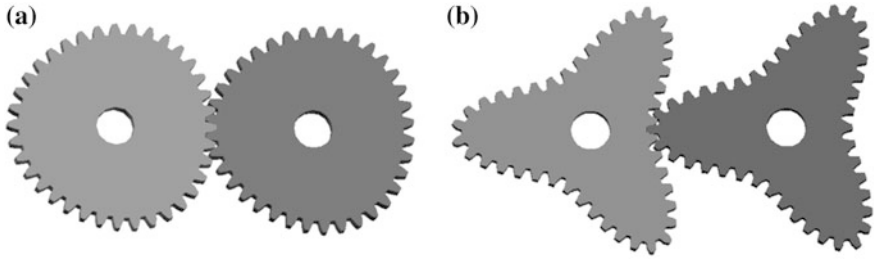

Fig. 8 Variable speed gears generated by rack cutter (**a**) and shaper cutter (**b**)

in the initial contact point, T_0 and two movable coordinate systems, $O_1X_1Y_1$ and $O_sX_sY_s$, rigidly attached to the noncircular blank and shaper, respectively.

The shaper, defined by a standard geometry of m modulus, pressure angle $\alpha = 20^\circ$ and z_s number of teeth, is rotated about its center of rotation O_c, by:

$$\gamma_s(\theta_1) = \frac{s(\theta_1)}{R_s} \tag{12}$$

The gear is rotated about its center, O_1, and translated along the common tangent (t) and along the perpendicular to (t) direction. The current position is defined by:

$$\gamma_r(\theta_1) = \theta_1 + \mu(\theta_1) - \pi/2 \tag{13}$$

$$x_{rt}(\theta_1) = r(\theta_1) \cdot \sin \mu(\theta_1) \tag{14}$$

$$y_{rt}(\theta_1) = r(\theta_1) \cdot \cos \mu(\theta_1) \tag{15}$$

Figure 7 illustrates the algorithm developed for the gear generation, based on the driving pitch curve defined by Gielis superformula and gears "manufactured" by a rack cutter and a shaper, as pitch curve shapes required. Pairs of variable speed gears are presented in Fig. 8.

4 Conclusions

The latest developments in computer graphics and manufacture technologies have enabled new approaches to noncircular gear design and generation. As a special type of noncircular gears, the variable speed gears are the main objective of the paper. Based on the hypothesis of the predesigned driving pitch curve, modeled by Gielis' superformula, algorithms for mating pitch curves generation and tooth manufacture simulation are developed by the interference Matlab-AutoLISP applications. The generalization of the gear generation process is based on the

proper selection of the supershape defining parameters that lead to suitable pitch curves and avoid undercutting during the applied process of gear generation.

Acknowledgments The work of Marius Vasie was supported by Project SOP HRD—EFICIENT 61445/2009.

References

Andrei L, Vasie M (2010) Using supershape in noncircular centrode modeling process. In: Annals of "Dunarea de Jos" University of Galati, Mathematics, Phisics, Theoretical Mechanics, Fascicle II, Year II (XXXIII), no. 2, pp. 259–266

Bair B-W et al. (2009) Tooth profile generation and analysis of oval gears with circular-arc teeth. In: Mechanism and machine theory, vol 44. pp. 1306–1317

Dawei L, Tingzhi R (2011) Study on deformed limacon gear and motion optimization of its serial mechanism. J Mech Des 133: 061004-1–061004-8

Dooner D, Seireg A (1995) The kinematic geometry of gearing. Wiley, New York

Figliolini G, Angeles J (2005) Synthesis of the base curves for N-lobed elliptical gears. J Mech Des 127:997–1005

Gielis J, Beirinckx B, Bastiaens E (2003) Superquadrics with rational and irrational symmetry.In: Symposium on solid modeling and applications

Jing L (2009) A pressure angle function method for describing tooth profiles of planar gears. J Mech Des 131:051005-1–8

Li J-G et al (2007) Numerical computing method of noncircular gear tooth profiles generated by shaper cutters. Int J Adv Manufact Technol 33:1098–1105

Litvin FL (1994) Gear geometry and applied theory. Prentice Hall, New Jersey

Litvin FL, Fuentes A (2004) Gear geometry and applied theory, 2nd edn. Cambridge University Press, Cambridge

Mundo D (2006) Geometric design of a planetary gear train with non-circular gears. Mech Mach Theory 41:456–472

Tsay M-F, Fong Z-H (2005) Study on the generalized mathematical model of noncircular gears. Math Comput Model 41:555–569

Yang DCH, Tong S-H (1998) Generation of identical noncircular pitch curves. J Mech Des 120:337–341

Part III
Product Development, Manufacturing and Metrology

Single-Row Planetary Gearbox Gearings Optimization Using Genetic Algorithms

Ovidiu Buiga and Simion Haragâş

Abstract Nowadays huge amounts or positions on market may be lost due to a slow accommodation at the changing conditions of production. This moment is favorable to the application of optimal solutions obtained thought optimal design. Considering these, the main goal of this paper lies in emphasizing once again the advantages of optimal design of all sorts of products as compared to the classical design. In this particular case we deal with the optimal design with genetic algorithms (GAs) of the gearings corresponding to a single-row planetary gearbox.

Keywords Optimal design · Planetary gearbox · Genetic algorithm

List of Symbols

a_w	Standardised centre distance, mm
$b_{1,2,3}$	Face widths of the single-row planetary gearbox wheels (mm)
c_{sa}	Clearance coefficient
$d_{a1,2,3}$	Tip diameters of the single-row planetary gearbox wheels (mm)
$d_{w1,2,3}$	Pitch diameters of the single-row planetary gearbox wheels (mm)
$d_{f1,2,3}$	Root diameters of the single-row planetary gearbox wheels (mm)
$F(x)$	Objective function
$g_i(x)$	Constraints
i_T	Overall transmission ratio
m	Module (mm)
n_w	Number of planetary pinions
$s_{a1,2,3}$	Outside cylinder circular tooth thickness corresponding to single-row planetary gearbox wheels (mm)

O. Buiga (✉) · S. Haragâş
Technical University of Cluj-Napoca, Cluj-Napoca, Romania
e-mail: Ovidiu.Buiga@omt.utcluj.ro

S. Haragâş
e-mail: Simion.Haragas@omt.utcluj.ro

G. Dobre (ed.), *Power Transmissions*,
Mechanisms and Machine Science 13, DOI: 10.1007/978-94-007-6558-0_35,

S	Thickness of the planetary pinions (mm)
x	Design variable vector
$x_{1,2,3}$	Tooth addendum coefficients of single-row planetary gearbox wheels
$z_{1,2,3}$	Numbers of teeth on central pinion, on planetary pinions and on stationary central wheel
$\varepsilon_{\alpha e,i}$	Radial contact ratio of the external toothing of the wheels 1 and 2, and of the internal toothing of the wheels 2 and 3
ρ	Density of gear material (kg/mm^3)
$\rho_{a1,2,3}$	Curvature profile radii for the single-row planetary gearbox wheels (mm)
ρ_{A1}, ρ_{E2}	Curvature profile radii in the first and the last point of contact for external toothing of wheels 1 and 2 (mm)
ρ_{A2}, ρ_{E3}	Curvature profile radii in the first and the last point of contact for internal toothing of wheels 2 and 3 (mm)
$\rho_{N1,2,3}$	Curvature profile radii in the measurement points of span in radial direction, for the single-row planetary gearbox wheels (mm)
σ_H	Hertzian contact stress (MPa)
σ_{Hp}	Allowable Hertzian contact stress (MPa)
$\sigma_{F1,2}$	Bending stress on the teeth of the central pinion 1 and on the planetary pinions 2 (MPa)
σ_{FP}	Allowable bending stress (MPa)

1 Introduction

Nowadays gears are used on a daily basis and can be found in most people's everyday life from clocks to cars rolling mills to marine engines. Gears are the most common means of transmitting power in mechanical engineering and they do several important jobs, the most important being that they provide a gear reduction. This is vital to ensure that even though there is enough power there is also enough torque. Gear design is a very complex task which arises from strong and often intractable connections between the design variables describing its subsystems. Also it is known that gear design (involving computations based on tooth bending stress, Hertzian contact pressure, interference etc.) is an iterative process in which it is necessary to make some tentative choices and to determine which parts of the design are critical. Furthermore complex shape and geometry of gears lead to a large number of design variables which could be integer (e.g. number of teeth), discrete (e.g. module), and real (e.g. gears width). So, in order to solve such complex design problem *optimal design methodology* (*conceiving and solving an optimization program based on the mathematical model of a real engineering problem*, Tudose et al. 2006) seems to be the proper one. Considering these, in this particular case we deal with the *optimal design* of the gearing corresponding to a

single-row planetary gearbox (i.e. are gears that have gear wheels with moving axes Grote and Antonsson 2009). In the last decades many researchers have reported solution on this problem of gear optimization. Aberšek et al. (1996) described an expert system to design and manufacture a gearbox. Deb and Jain (2003) used a non-dominated sorting genetic algorithm (NSGA-II) in order to solve a multi-objective optimization of a multi-speed gearbox. Del Castillo (2002) presented two procedures to obtain the analytical expression for the efficiency of any planetary gear train. Salgado and Alonso (2009) optimised a planetary gear trains (PGTs) used in mechanical spindle speeders by minimising the volume and the kinetic energy. Li et al. (1996) carried out a study for minimising the centre distance of a helical gear using American Gear Manufacturers Association (AGMA) procedures. Yokota et al. (1998) solved an optimal weight design problem of a gear with an improved Genetic Algorithm (GA). In the following sections a detailed discussion about the optimal design of the gearing is presented. The industrial relevance of the exercise is ensured by the consideration of all design constraints typically encountered in practice–we bound the design space by a total of 27 constraints categorized into 10 groups.

2 A Single-Row Planetary Gearbox Gearing Optimal Design Problem

Consider the following design problem. The gearing corresponding to a single-row planetary gearbox (see Fig. 1) is to be designed for minimum mass and a service life of 8000 h, given an input speed of 925 rpm, a power of 2.9 kW and an overall transmission ratio of 7.6. The gears are based on ISO 53 basic rack profile, and are made from quenched and tempered 42CrMo4. In the next section the design variables (or the genes) of the optimization problem are presented.

2.1 The Genes Describing the Gearing of the Single-Row Planetary Gearbox

The gearing of the single-row planetary gearbox which we are considering in this work (see Fig. 1) is described by a total of *seven* genes. The genes are:

- ***Gene* 1**: z_1 *representing the number of teeth on the central pinion* 1. *Integer values*: {21, 22, 23, 24};
- ***Gene* 2:** n_w *is the number of the planetary pinions. Integer values*: {2, 3, 4, 5};
- ***Gene 3:*** a_w *representing the center distance of planetary gears. Standardized, discrete, real values, in the range of:* {56,…, 315};
- ***Gene* 4:** x_1 *is the tooth addendum coefficient of central pinion* 1. *Standardized, discrete, real values, in the range of* : {–0.5,…, 1};

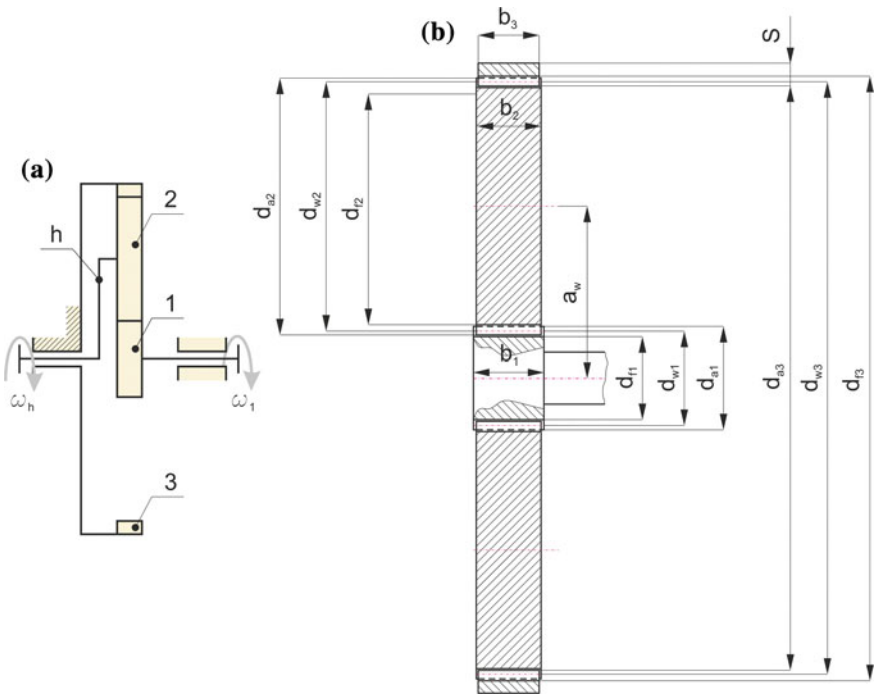

Fig. 1 Single-row planetary gearbox gearing

- ***Gene* 5:** ψ_a *is the ratio between the central pinion* 1 *width and center distance. Real values in the range of*: [0.2,…, 0.8];
- ***Gene* 6:** Δu *representing the elative error of the gear ratio. Real values in the range of*: [–0.04,…, +0.04];
- ***Gene* 7:** *rd* representing the round direction. Integer values: {0, 1}.

In the following are presented some remarks regarding the calculation of the tooth matching number of the stationary central wheel 3. From Grote and Antonsson (2009) it is known that z_3 should be calculated by taking into consideration three conditions: *coaxiality*, *mounting*, *and adjacency*, and also according to the set of transmission ratio. Taking into consideration these, the expression for calculation of z_3 is:

$$z_3 = \text{round}[z_1(i_T - 1)] \tag{1}$$

The authors of this paper propose a new form for the Eq.1, which is:

$$z_3 = \begin{cases} z_3^{'} - r \ \text{ if } \ (r \neq 0) \wedge (rd = 0) \\ z_3^{'} + n_w - r \ \text{ if } \ (r \neq 0) \wedge (rd = 1) \end{cases} \tag{2}$$

where: $z_3^{'} = \text{round}[i_T z_1(1 + \Delta u) - 1]$, $r = z_1 + z_3^{'} - n_w \ \text{round}\left(\frac{Z_1 + Z_3^{'}}{n_w}\right)$.

By using this equation we succeeded to avoid losing some important values for z_3. In order to exemplify this we present a brief example. Consider the same data as in our optimal design problem. From Eq. 1 we could determine for z_3 a set of 19 values. By using the Eq. 2 the number of possible values for z_3 becomes 34, resulting a set of 15 new possible values.

2.2 Objective Function

The objective of our optimal design is to minimize the mass of the single-row planetary gearings. The mass is represented in Eq. 3.

$$\text{Obj: } F(x) = \frac{1}{4}\pi\rho\left[d_{w1}^2 b_1 + n_w d_{w2}^2 b_2 + \left(d_{f3} + 2S\right)^2 b_3 - d_{w3}^2 b_3\right] \rightarrow \min \quad (3)$$

where: $\rho = 7.85 \cdot 10^{-6}$, $b_1 = 1.1b_2$, $b_2 = \Delta + \Psi_a a_w$, $\Delta = 5$, $b_3 = \Psi_a a_w$, $S = 2.2m + 0.05b_3$.

2.3 Constraints

There are a total of 27 *constraints*, which were structured into 10 *groups* (e.g. the same constraint applied to central pinion 1, to planetary pinions 2 and to stationary central wheel 3 constitutes one group; though it is implemented as two separate constraints in our optimization program). As it will become apparent these constraints are all of the inequality type, involving geometrical or structural considerations. The solutions of the optimization problem have to satisfy the following list of constraints (note that all values of these constraints have to be negative or at last 0) which should be viewed with reference to the sketch presented in Fig. 1.

CG1. *The adjacency, mounting and coaxiality conditions should be satisfied.*

$$g_1(x) = 2a_w \sin\frac{\pi}{n_w} \geq d_{a2} \quad (4)$$

$$g_2(x) = \frac{z_1 + z_2}{n_w} = \text{an integer} \quad (5)$$

$$g_3(x) = |z_1 + 2z_2 - z_3| \leq 2 \quad (6)$$

CG2. *The Hertzian contact pressure on external toothing of the wheels* 1 *and* 2 *must not exceed a specified value.*

$$g_4(x) = \sigma_H \leq \sigma_{HP} \quad (7)$$

CG3. *The bending stress on the teeth of the central pinion* 1 *and on the planetary pinions* 2 *must not exceed a specified value.*

$$g_{5,6}(x) = \sigma_{F1,2} \leq \sigma_{FP} \tag{8}$$

CG4. *The teeth on central pinion* 1 *and on the planetary pinions* 2 *must not be undercut.*

$$g_{7,8}(x) = \left(14 - z_{1,2}\right) \leq 17x_{1,2} \tag{9}$$

CG5. *The top land of the teeth on gears of the single-row planetary gearbox must not vanish.*

$$g_{9,\,10,\,11}(x) = c_{sa}m \leq s_{a1,\,2,\,3} \tag{10}$$

CG6. *The contact ratio of the external toothing of the wheels* 1 *and* 2*, and of the internal toothing of the wheels* 2 *and* 3 *must be greater than a specified value.*

$$g_{12,\,13}(x) = \varepsilon_{\alpha i,e} \leq \varepsilon_{\alpha} \tag{11}$$

CG7. *The addendum coefficients of the planetary pinions* 2 *and of the stationary central wheel* 3 *should be in the range* $[-0.5,\ 1]$.

$$g_{14,\,15}(x) = \left|x_{2,3} - 0.25\right| \leq 0.75 \tag{12}$$

CG8. *Constraints necessary to avoid the interference of the internal toothing of wheels* 2 *and* 3.

$$g_{16}(x) = d_{b3}^2 + 4a_w \sin^2 \alpha_w \leq d_{a3}^2 \tag{13}$$

$$g_{17,\,18}(x) = z_2\phi_{2i,\,3e} \leq z_3\phi_{3i,\,2e} \tag{14}$$

CG9. *Measurability constraints for all the wheels of the single-row planetary gearbox.*

$$g_{19}(x) = \rho_{A1} \leq \rho_{N1} \tag{15}$$

$$g_{20}(x) = \rho_{N1} \leq \rho_{a1} \tag{16}$$

$$g_{21}(x) = \rho_{E2} \leq \rho_{N2} \tag{17}$$

$$g_{22}(x) = \rho_{N2} \leq \rho_{a2} \tag{18}$$

$$g_{23}(x) = \rho_{A2} \leq \rho_{N2} \tag{19}$$

$$g_{24}(x) = \rho_{N3} \leq \rho_{E3} \tag{20}$$

$$g_{25}(x) = \rho_{a3} \leq \rho_{N3} \tag{21}$$

CG10. *The numbers of teeth on the gears of external and internal gearings must be relative primes.*

$$g_{26,\,27}(x) = \begin{cases} -1 & (z_{1,\,2},\ z_{2,\,3}) = 1 \\ 1 & (z_{1,\,2},\ z_{2,\,3}) \neq 1 \end{cases} \tag{22}$$

2.4 Results

For solving the optimal design problem of the gearings corresponding to a single-row planetary gearbox a GA was used with a *crossover rate* of 0.75 and a *mutation rate* of 0.01. After optimization the values of the optimal design problem genes are presented in Table 1.

With these values (presented in Table 1) the mass of the gearings was 7.463 kg. This solution was very near to *eight* additional constraint boundaries which are highlighted with red points in Fig. 2. The blue points represent the values of the other remaining 20 constraints.

In Table 2, the main characteristics of the gearings (*classical* and *optimal* solutions) are presented side-by-side.

A comparison of the *optimal* and *classical* design solutions is shown in Fig. 3 (also in Fig. 3c is presented an overlap image of these two variants).

Table 1 The values of the optimization problem genes

No	Genes symbol	Genes values
1	z_1	24
2	n_w	2
3	a_w(mm)	90
4	x_1	1
5	Ψ_a	0.285
6	Δu	–0.0268
7	rd	1

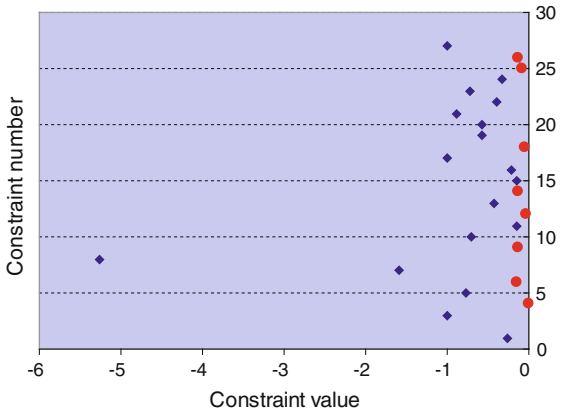

Fig. 2 Constraints values for the optimal dsign solution

Table 2 Classical and optimal design solutions

No	Symbol	Classical solution	Optimal solution
1	a_w(mm)	90	90
2	m(mm)	2	2.25
3	z_1	24	21
4	z_2	65	58
5	z_3	154	137
6	b_1(mm)	30	31
7	b_2(mm)	27	28
8	b_3(mm)	25	26
9	d_{f1}(mm)	47	43.875
10	d_{f2}(mm)	123.081	124.978
11	d_{f3}(mm)	313.163	316.331
12	d_{w1}(mm)	48.539	47.848
13	d_{w2}(mm)	131.460	132.151
14	d_{w3}(mm)	311.46	312.151
15	d_{a1}(mm)	55.918	53.896
16	d_{a2}(mm)	132	135
17	d_{a3}(mm)	304.081	306.103
18	$F(x)$ (kg)	*7.463*	*8.181*

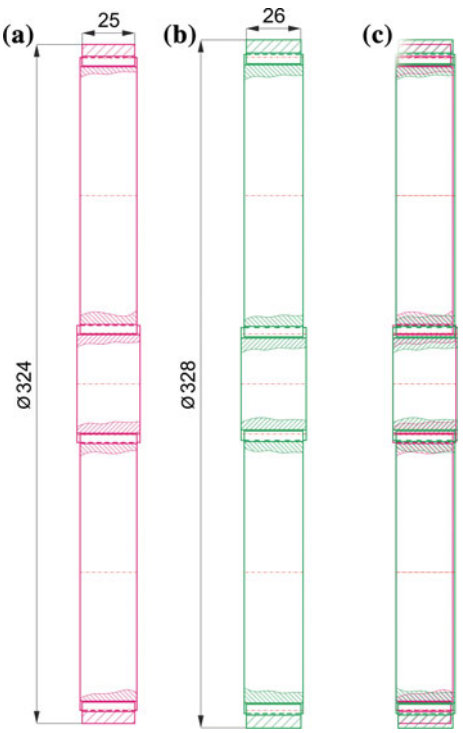

Fig. 3 *Optimal* and *classical* design solutions

Table 3 Two interesting solutions

z_1	n_w	a_w (mm)	x_1	Ψ_a	Δu	rd	$F(x)$ (kg)
23	2	*63*	1	*0.7906*	0.0312	1	*7.5988*
21	2	*100*	0.9528	*0.2047*	−0.0098	0	*7.6118*

In Table 3 are presented two interesting solutions which are very close to the optimal one.

3 Conclusions

In this paper an optimal design for the gearings corresponding to a single-row planetary gearbox was presented. The objective of this optimal design was the minimization of the gearings mass. The classical method offers a mass of 8.181 kg while after the optimization the gearings weighted 7.463 kg, i.e. a 8.77 % reduction. The optimization of the gearings presented in this paper represents only the starting point for a more complex optimal design of an entire single-row planetary gearbox (complete with the sizing and selection of shafts, bearings, housing etc.). Also, other interesting objective functions could also be considered–manufacturing cost representing a potential example.

Acknowledgments This paper was supported by the project "Development and support of multidisciplinary postdoctoral programmes in major technical areas of national strategy of Research–Development–Innovation" 4D-POSTDOC, contract no. POSDRU/89/1.5/S/52603, project co-funded by the European Social Fund through Sectoral Operational Programme Human Resources Development 2007–2013.

References

Abersek B, Flasker J, Balic J (1996) Expert system for designing and manufacturing of a gear box. Expert Syst Appl 11(3):397–405

Deb K, Jain S (2003) Multi-speed gearbox design using multi-objective evolutionary algorithms. ASME J Mech Des 125:609–619

del Castillo JM (2002) The analytical expression of the efficiency of planetary gear trains. Mech Mach Theory 37:197–214

Grote KH, Antonsson EK (2009) Springer handbook of mechanical engineering 2009. Springer, Berlin

Li X, Symmons GR, Cockerhan G (1996) Optimal design of involute profile helical gears. Mech Mach Theory 31(6):717–728

Salgado DR, Alonso FJ (2009) Optimal mechanical spindle speeder gearbox design for high-speed machining. In. Int J Adv Manuf Technol 40(7–8):637–647

Tudose L, Pop D, Haragâş S, Nistor G, Jucan D, Pustan M (2006) Optimal design of complex systems, Mediamira, Cluj-Napoca, (in Romanian), Mediamira, ISBN 973-713-076-6, Cluj-Napoca, 2006

Yokota T, Taguchi T, Gen M (1998) A solution method for optimal weight design problem of the gear using genetic algorithms. Comput Ind Eng 35:523–526

Application of MEMS Technique for Micro Gear Metrology

Syuhei Kurokawa, Yoji Umezaki, Morihisa Hoga, Ryohei Ishimaru, Osamu Ohnishi and Toshiro Doi

Abstract We try to measure direct transmission of rotational motion between a gear pair, which is called transmission error, without knowing the tooth flank accuracy of each gear. In transmission error measurement, the rotational angle of the shaft of each gear is measured with a pair of rotary encoders. For micro gear engagement, the center distance between a pair of gears is very small, so the rotary encoders have to be small as well as micro gears. A grating disk with a small diameter for a micro rotary encoder must be designed and manufactured. In machining process, one of the MEMS technique is applied. Patterning accuracy is examined in detail.

Keywords Micro gear · Metrology · Nano-manufacturing · MEMS · Micro rotary encoder

S. Kurokawa (✉) · Y. Umezaki · O. Ohnishi · T. Doi
Kyushu University, Fukuoka, Japan
e-mail: kurobe-@mech.kyushu-u.ac.jp

Y. Umezaki
e-mail: umezaki@mech.kyushu-u.ac.jp

O. Ohnishi
e-mail: ohnishi@mech.kyushu-u.ac.jp

T. Doi
e-mail: doi-t@mech.kyushu-u.ac.jp

M. Hoga
Dai Nippon Printing Co, Kashiwa, Japan
e-mail: houga_m@mail.micro.dnp.co.jp

R. Ishimaru
Kurume National College of Technology, Kurume, Japan
e-mail: ishimaru@kurume-nct.ac.jp

G. Dobre (ed.), *Power Transmissions*,
Mechanisms and Machine Science 13, DOI: 10.1007/978-94-007-6558-0_36,

List of Symbols

A_1	Rotational angle of a driving gear
A_2	Rotational angle of a driven gear
TE_p	Transmission error based on a driver
z_1	Number of teeth of a driving gear
z_2	Number of teeth of a driven gear

1 Introduction

It is very important to measure machined parts to check the manufacturing accuracy. Nowadays, micro machine elements can be manufactured with the MEMS (Bhushan 2004; Johnstone and Parameswaran 2004). Those which have concave parts such as micro gear surfaces (Horiuchi et al. 2006) should be also measured, but at this moment, it is not possible because their overhanging part becomes the obstacle against measurement. For example, a conventional contact type stylus is too large comparing to concave spaces of micro machine parts so that it cannot reach deeply inside into a concave space (Fujio et al. 1994; Gao et al. 2004; Okuyama et al. 1994). A conventional detecting unit for AFM also has the same problem.

On the other hand, non-contact type probe such as a laser light beam would be an alternative tool, however, it is blocked off or reflects with a very small angle, so unfortunately the beam cannot come back to a detector in consequence.

To overcome those difficulties, it might be applicable to utilize a small tipped stylus in a special shape which is preferable for measurement of concave shapes. Another possibility evaluating gear accuracy is to measure direct transmission of rotational motion between a gear pair, which is called transmission error, without knowing the tooth flank accuracy of each gear. In transmission error measurement, the rotational angle of the shaft of each gear is measured with a pair of rotary encoders (Kurokawa et al. 2009). For micro gear engagement, the center distance between a pair of gears is very small, so the rotary encoders have to be small as well as micro gears. Unfortunately, a commercial high precision rotary encoder with a diameter smaller than 1 mm does not exist. A grating disk with a small diameter for a micro rotary encoder must be designed and manufactured. In machining process, one of the MEMS technique is applied, i.e., the photolithography which utilizes the combination of the electron beam exposure and the etching process of a silicon chip.

The number of gratings is an important parameter for the resolution of a rotary encoder. To achieve high resolution, many gratings must be manufactured in small diameter region. Using photo-lithography technique, radial gratings are patterned onto the silicon disk. The number of designed grating is 10,000, and an inner half pitch of the grating disk is corresponding to about 50 nm. Patterning accuracy is

examined in detail. Measurement ideas and strategy as a micro rotary encoder will be also described briefly.

2 Evaluation of Gear Accuracy by Transmission Error Measurement

Transmission error of single flank engagement is defined as the deviation from the geometrically ideal rotation of a driven gear. When the input rotational speed is constant, transmission error can be regarded as the variation of output rotational motion. In the ideal engagement, we write as follows:

$$A_1 : A_2 = z_2 : z_1 \text{ or } A_2 \cdot \frac{z_2}{z_1} - A_1 = 0 \tag{1}$$

Transmission error (TE) is therefore defined by the following equation.

$$TE_p = A_2 \cdot \frac{z_2}{z_1} - A_1 \tag{2}$$

TE_p is transmission error based on a driver in units of rotational angle.

It is therefore necessary to detect rotational angles of both driver and follower according to Eq. (2). The easiest way is to implement a pair of rotary encoders. For conventional-sized gears, a typical transmission error measuring system is like in Fig. 1 (Kurokawa et al. 2009).

A pair of rotary encoders is installed at the end of each shaft and they are connected through interpolating units to a personal computer. Sinusoidal waves from each rotary encoder are divided electrically and transformed into a series of

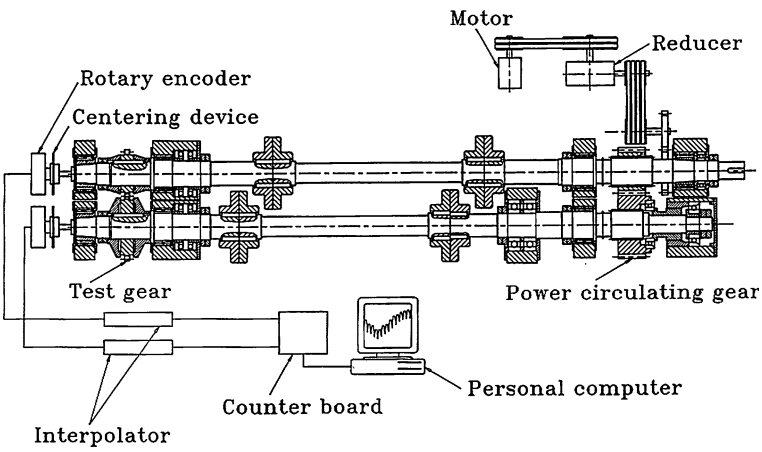

Fig. 1 Typical illustration of transmission error measurement system

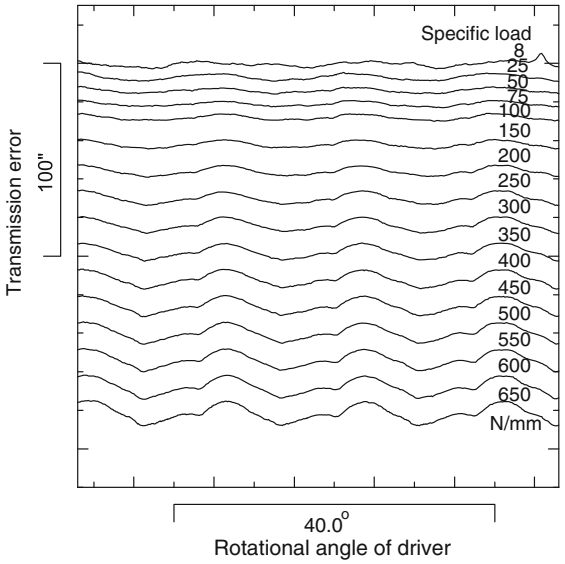

Fig. 2 Measured transmission error of a helical gear pair with sub-micro radian resolution under several stages of applied load

pulses. The counter board detects the rotational angle of each shaft by counting those output pulses.

By using a high resolution encoder, which has the number of output sinusoidal waves per revolution of 225,000, detailed transmission error variation can be observed. For example, Fig. 2 shows measured TE for a non-modified helical gear pair under 16 different stages of applied load. According to the load increase, the periodic wave appears clearly. At the middle range load of 350 N/mm and higher load, it can be observed that there is local delay near the transit period from triple-tooth contact to double-tooth contact in every one pitch. The delay gets larger according to the load increase.

To examine the influence of the measurement resolution, TE under the specific load of 245 N/mm for the same gear pair is shown magnified in Fig. 3. Quantisation error is hardly seen in Fig. 3. Maximum peak-to-valley value of quantisation error of this encoder is below 0.3″ (1.4 μrad). The local delay near the transit period from triple-tooth contact to double-tooth contact can be observed in the magnified figure. From the fact that peak-to-valley value of this TE curve is about 8″, this measuring system has sufficient accuracy to investigate TE in detail.

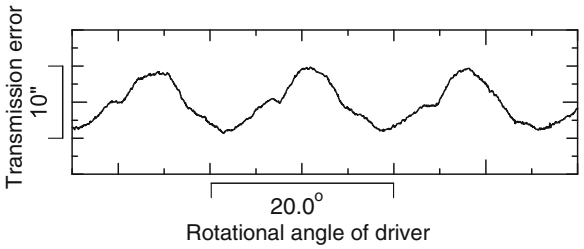

Fig. 3 Magnified transmission error for the helical gear pair with sub-micro radian resolution under the specific load of 245 N/mm

The target of next measurement here is supposed to be a micro gear pair whose reference diameter is smaller than 1 mm. For such a micro gear pair engagement, the center distance will be smaller than about 1 mm. Therefore the diameter of a designed grating disk of a micro rotary encoder should be also smaller than the center distance. The smaller the grating disk diameter becomes, the wider the application for micro gear measurement extends. The authors here try to manufacture the grating disk whose diameter is smaller than 1 mm.

3 Design of a Grating Disk

The designed grating disk pattern is shown in Fig. 4. All essential features are arranged within the field of 1 mm squared. The outer diameter is 950 μm, and the inner diameter is 320 μm.

Each of the radial gratings has the same shape of the trapezoid, and its length is 315 μm in the radial direction. At the center of the grating disk, the cross-shaped mark is drawn to be recognized easily. This center mark will be useful to adjust the eccentricity between the center of rotation and the center of the grating disk when the disk is mounted on a rotational shaft. The width of each radial grating depends

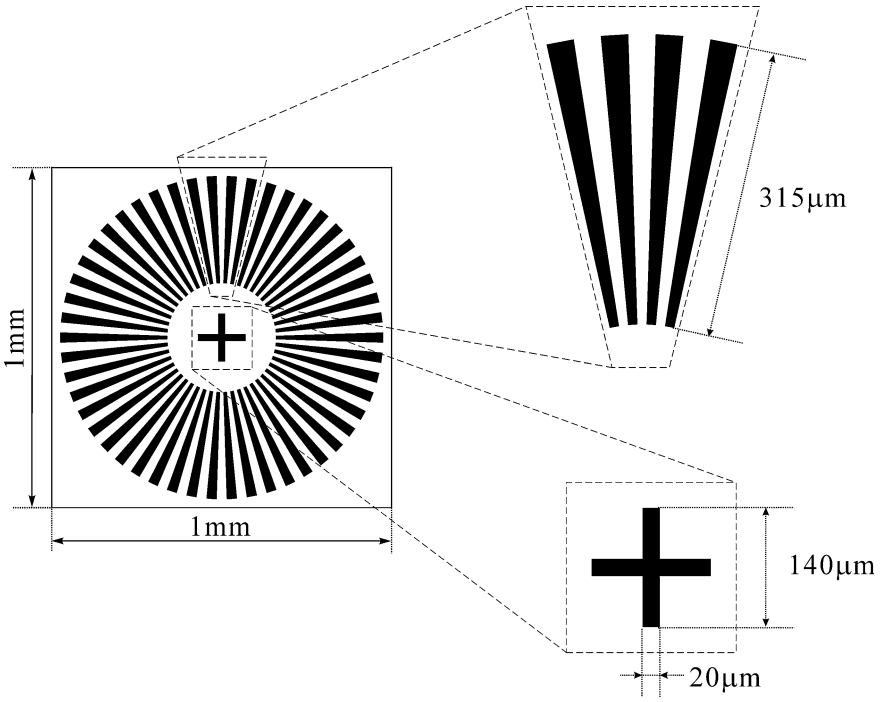

Fig. 4 Example of designed grating disk pattern

on the number of gratings on a disk, which decide the resolution of the rotary encoder. That means it will be more difficult to manufacture the grating patterns as the disk diameter gets smaller. In the case of 10,000 gratings, the width at the inner end is only about 50 nm. In such a resolution grating disk, the line width becomes very narrow due to the tiny disk diameter.

To manufacture such a tiny radial grating pattern, the nano-manufacturing technique is essential. To achieve both the narrow width of the gratings and homogeneity of it, it is utilized here the combination of electron beam (EB) lithography and etching technique of silicon substrate.

4 Nano-Manufacturing Process for Grating Disk

Figure 5 shows the illustration of the whole procedure of EB lithography and dry etching.

Material substrate is silicon (Si), on which EB resist is directly pasted by spin coating. Hard mask is not necessary this time because the depth of etched grooves in the following etching process is specified to be shallow (about 30 nm). The desired pattern is drawn by electron beam on the EB resist, and EB resist is exposed by electron beam energy. After development procedure, the exposed area is removed, and the desired pattern of EB resist is formed by the difference of solubility of exposed and unexposed resist parts. By use of the remained resist as a mask, Si substrate is etched, and finally, the EB resist is stripped by O_2 plasma ashing.

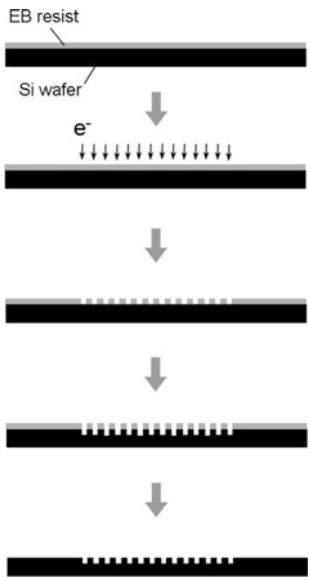

Fig. 5 Procedure of EB exposure and dry etching process

The workpiece wafer is 152 mm (6 inches) in diameter and the thickness of Si substrate is about 500 μm. The thickness of spin-coated EB resist (ZEP520A, ZEON corp.) is about 50 nm. EB exposure was carried out using a high-resolution electron beam lithography system. The system is based on an electron gun as exposure system (JBX-9300FS, JOEL Ltd.). The EB resist of the black drawn area in Fig. 5 was exposed. Development after EB exposure was carried out by use of the developing solution (ZED-N50, ZEON corp.) with a rotary spray, and developing time was about 60 s. After development, a rinse procedure was carried out for about 60 s by use of the rinse agent (ZMD-B). The dry etching was carried out using a dry etcher with a reactive ion etching (RIE) by utilizing inductive coupled plasma (ICP). In the RIE process, the hydrogen bromide (HBr) gas was used in etching Si substrate and the depth of etched grooves was intended to be about 30 nm.

5 Results and Discussion

5.1 Results in Nano-Manufacturing

The whole etched image of the radial patterns was captured by the confocal laser scanning microscope (CLSM) (LEXT OLS3500, Olympus corp.) and is shown in Fig. 6.

The whole shape of a grating disk pattern seems to be successfully etched, but any radial gratings cannot be seen due to the limitation of low resolution of CLSM. The scanning electron microscope (SEM) was therefore used to observe the details. Figure 7 shows the SEM image of the outer end of the part of radial gratings, and the inner end are shown in Fig. 8. The etched line width at the outer end is about 150 nm and at the inner end is about 50 nm as intended. It has been

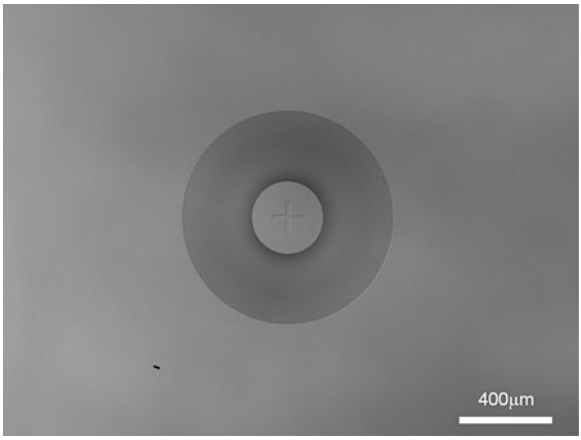

Fig. 6 Confocal laser scanning microscope image of the whole grating disk with 10,000 gratings

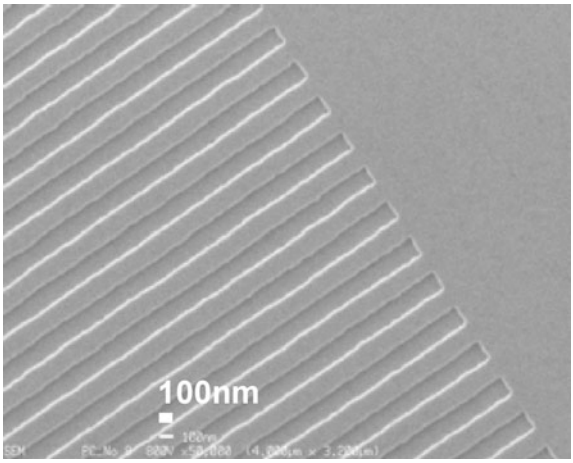

Fig. 7 SEM image of the outer end of gratings

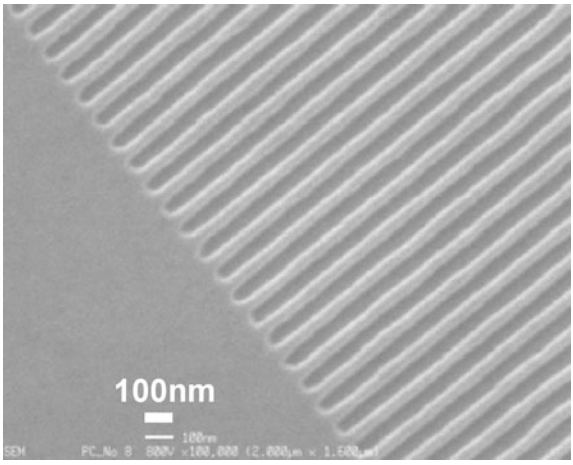

Fig. 8 SEM image of the inner end of gratings

manufactured also almost homogeneously with enough pitch accuracy. From those results, a grating disk up to 50 nm line widths can be manufactured successfully and accurately. The accuracy of these repeated grating patterns affects the accuracy of the rotary encoder directly. The next step is to detect the output signals with the etched grating disk. Contact methods and non-contact detection will be considered.

5.2 Measurement Ideas and Strategy

The first approach is to use a contact type stylus with controlled tip radius. An AFM stylus with dynamic mode will be useful in this case. If the grating disk

rotates while the AFM stylus taps the surface at the same position without scanning motion, the detected height variation will be regarded as the output signal of a rotational angle of the grating disk. To achieve high resolution, it is necessary that the local peak becomes the smooth mountain shape and its height changes gradually according to the position. The number of height division in each local peak improves the resolution. For example, in the case of the grating disk with the number of gratings of 10,000, if the number of height division in each local peak is 16 (4 bits), the corresponding angular resolution becomes about 8″, that is quite enough for measurement of micro gear engagement. Since an AFM stylus vibrates at high resonance frequency (up to 300 kHz) in dynamic mode measurement, signal detection can be realised under the rotational frequency within allowable limit. If multi-probing system with multi-AMF styli is adopted, the opposite reading cancels out the influence of disk eccentricity, and self-calibration will be also possible.

The second approach is non-contact detection. Normal light detection cannot be utilised because of the limitation of a light wavelength. The authors believe one of the effective detections will be the use of the evanescent light. If the sinusoidal output signal is obtained, the conventional signal processing is applicable to improve the resolution.

It is important to mention that a rotary encoder has the advantage against the temperature change comparing to a linear encoder. The diameter of a rotary encoder increases according to the rise in temperature, but the number of gratings, so the detected rotational angle does not change while the length of a linear encoder changes proportional to the temperature increase. The robustness will be remarkable especially in micro and nano-scales.

6 Conclusions

For micro gear measurement, a grating disk for a micro rotary encoder was designed and manufactured with EB-lithography and MEMS techniques aiming for practical application of micro gear measurement. The grating patterns, of which line width is up to 50 nm, were successfully manufactured homogeneously and accurately on the Si substrate. The developed disk is expected to be useful for measurement of micro gears from effective approach: angle measurement. Nano-imprinting techniques could be also applicable for mass production of grating disks. Since traceability for angle is already established, calibration procedures of these tools are also significant issues.

References

Bhushan B (ed) (2004) Handbook of Nanotechnology. Springer, Berlin

Fujio H, Kubo A, Saitoh Y, Suzuki M, Tochimoto S, Hanaki H, Honda T (1994) Laser holographic measurement of tooth flank form of cylindrical involute gear. ASME J Mech Des 116:721–729

Gao W, Furukawa M, Kiyono S, Yamazaki H (2004) Cutting error measurement of flexspline gears of harmonic speed reducers using laser probes. Precis Eng 28:358–363

Horiuchi T, Furuuchi Y, Nakamura R, Hirota K (2006) Micro-gear fabrication using optical projection lithography on copper-clad plastic substrates and electroplating of nickel. Microelectron Eng 83:1316–1320

Johnstone RW, Parameswaran M (2004) An introduction to surface-micromachining. Kluwer Academic Publishers, Berlin

Kurokawa S, Ariura Y, Matsukawa Y, Doi T (2009) Evaluation of gear engagement accuracy by transmission error with sub-micro radian resolution. Int J Surf Sci Eng 3(3):160–177

Okuyama E, Kiyono S, Moritoki H (1994) Investigation of an optical noncontact gear geometry measurement system: measurement of pitch errors and tooth profiles. Precis Eng 16(2):117–123

Evaluation and Choice of Conceptual Solutions for a Universal Geared Engine Reducer

Siniša Kuzmanović, Radivoje Mitrović, Milan Rackov and Đorđe Miltenović

Abstract This paper deals with the issues of evaluation and choice of conceptual solution for a universal motor gear reducer, usually carried out during its development. It is a known fact that reducers could be delivered with a motor installed or in the so-called motorless version. In case of the delivery version with the motor, they could be equipped either with special reducer electric motors or with standard (IEC) motors. In case of a reducer intended for the special motor, in motorless version it has to be equipped with IEC motor adapter, for the customer's option to use standard motors, plus it should have a classic input shaft. In case of a reducer delivered with IEC motor, its motor might be connected indirectly, using IEC motor adaptor, or directly onto the reducer, without the use of adaptor. In both cases the reducer has to be delivered with a classic input shaft. This paper conducts the evaluation of some particular solutions by leading reducer manufacturers, with the intention to point out the most satisfactory conceptual solution.

Keywords Choice · Evaluation · Conception · Universal · Gear motor · Reducer

S. Kuzmanović (✉) · M. Rackov
Faculty of Technical Sciences, University of Novi Sad, Novi Sad, Serbia
e-mail: kuzman@uns.ac.rs

M. Rackov
e-mail: racmil@uns.ac.rs

R. Mitrović
Mechanical Engineering Faculty, University of Beograd, Beograd, Serbia
e-mail: radivoje.mitrovic@mas.bg.ac.rs

Đ. Miltenović
Textille College, Leskovac, Serbia
e-mail: milten2004@yahoo.com

G. Dobre (ed.), *Power Transmissions*,
Mechanisms and Machine Science 13, DOI: 10.1007/978-94-007-6558-0_37,

1 Introduction

By the term "universal reducer" we consider all of reducers whose attributes, such as their shape, connection dimensions and features, as well as mounting positions, are suited for the most common demands of production line (Kuzmanović 2009). As a consequence of such universality, they are somewhat more complex, having more parts and demanding larger extent of machining, all of which is needed to fulfill almost all demands of installation; regardless of that, in smaller production series, they are also cheaper then the so-called "special reducers", designed for precisely specified purposes and without nonessential parts or machining.

Of course, for large production series (term "large series" mainly depends on the size of reducer) the use of universal reducers is not justified in most cases, mostly because of their high price and relatively great mass, so as a rule in these cases only special reducers are used, for example in civil engineering and agricultural machines, machine tools, or similar. Manufacturers of universal reducers always try to provide some extra advantages for their reducers in order to compete more successfully against the manufacturers of special reducers; when there are no market demands for additional production of universal reducers they also come with special reducers of their own, or switch their production to manufacturing some items for them as subcontractors, for example the gears.

Universal reducers today have the greatest use in mechanical engineering, thanks to less complicated manufacturing, low price, great factor of efficiency and the easier maintenance. They are produced in numerous variants, depending on:

- the type of connection with driving machine, mostly an electric motor,
- the type of connection with working machine,
- installation mode,
- mounting position,
- number of levels, and
- special demands (installation of one-way clutch, installation of safety clutch and today very commonly used regulated drive for motor reducers, usually frequency regulators for the number of revolutions, etc.).

Universal gear reducers are produced as single, double, triple or multi-stage reducers. Some manufacturers do not produce single-stage reducers, because of low market demand for them; a similar case is for multi-stage reducers, so they are usually produced as a combination of lower-stage ones. There are manufacturers oriented towards the production of multi-stage reducers, which are installed in special casings for such reducers, but this is a rather rare case.

Universal reducers could be produced as motor reducers, with special reducer motor and/or standard IEC motor, or as motorless reducers with classic input shaft and/or adaptor for IEC motors. The use of motorless reducers with classic input shaft is extremely rare today for the reasons of somewhat complex construction and more difficult installation. That is because this design requires additional clutch (for connecting motor to the reducer) and more space for installation

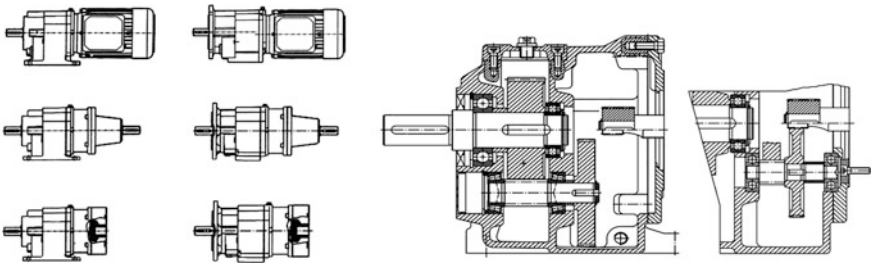

Fig. 1 Characteristic solutions for motor reducer marked SK with special (reducer-type) motor, for motorless reducer and for IEC motor adaptor (*NORD*)

(for the size of this clutch), but there are also problems with centering of input reducer shaft and the electric motor shaft. Reducer manufacturers have sometimes such designs in their catalogues (because of occasional market demands and ever-present competition), but this is hardly a rule.

2 Characteristic Conceptual Solutions of Motor Reducers

Classic conceptual solutions of motor reducers with a special reducer electric motor, in motorless variant with an adaptor for IEC motors and classic input shaft are presented in the offers of numerous manufacturers, with NORD company given as the characteristic representative (Fig. 1).

Company PUJOL produces motor-reducers with standard IEC motors, with motor connected to reducer via IEC motor adaptor (Kuzmanović and Rackov 2009a, b); however, at special customer request, PUJOL allows them to do it themselves, with reducers delivered with classic input shaft (Fig. 2).

Company ROSSI also produces motor-reducers with standard IEC motors, offering them also with classic input shaft (Fig. 3). They do not deliver motorless reducers with special adaptor for IEC motors, since they already offer motor-reducers with such motors; however, in their catalogues they instruct customers on how to install IEC motors on their reducers.

The same company, ROSSI, has similar reducers (ES) in their product line, also delivered only with standard IEC motors (Fig. 4), but they make them also in the version with IEC motor adapters, while motorless variants are not offered.

Reducer designers are always faced with the dilemma—which concept to adopt?

The analysis of concrete solutions indicates that the first concept, motor-reducer with special motor, is the most favorable one, since its use could achieve the greatest transmission ratios, greatest carrying capacity and provide the cheapest manufacturing (Kuzmanović et al. 2009). This solution is most suitable for reducer manufacturers who have an electric motor factory of their own.

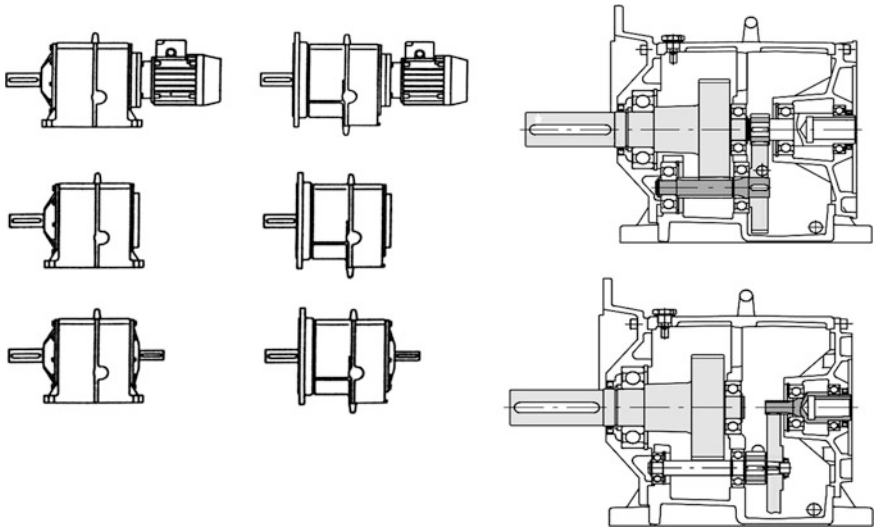

Fig. 2 Characteristic solutions for motor-reducer with IEC motor and for motorless reducer (*PUJOL*)

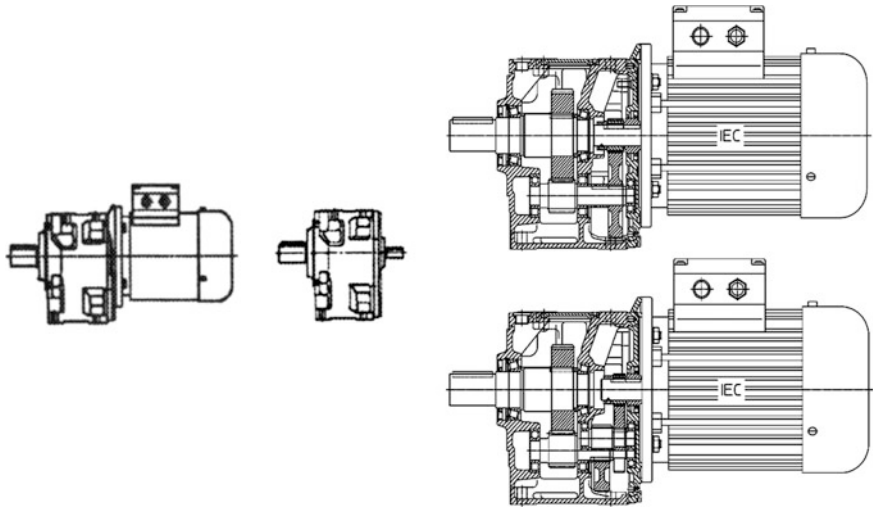

Fig. 3 Characteristic solutions for motor-reducers with IEC motor and for reducer with free input shaft (*ROSSI*)

Smaller manufacturers are forced to avoid the use of a large number of various motors (with different diameters of flanges and shafts), so they employ only the standard motors. Manufacturers who connect motors via IEC motor adapters also reduce the number of various motors, but they increase the number of required adapters, which leads to the additional burden to production. By the use of IEC

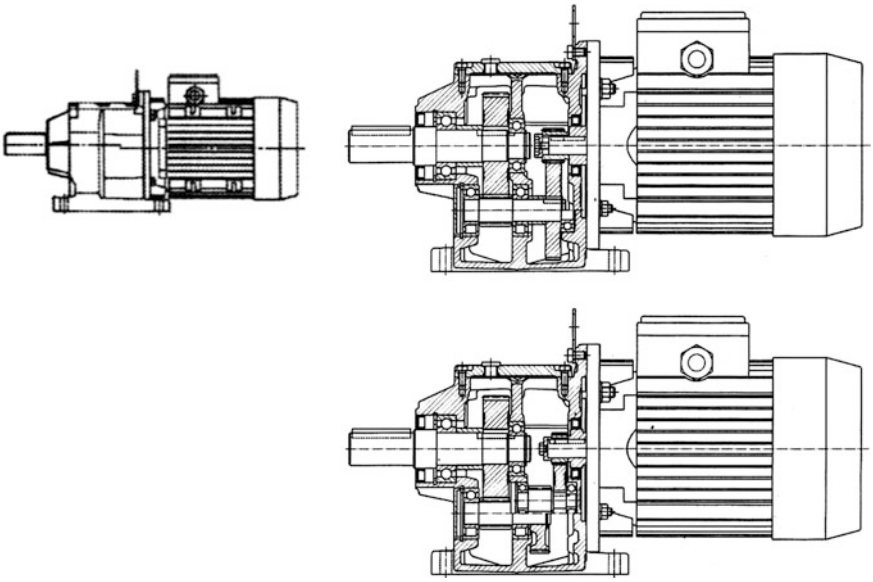

Fig. 4 Characteristic solutions of motor-reducers with IEC motor (*ROSSI*)

motor adapters they also decrease the number of various gears needed, which is definitely a great advantage. Beside that, manufacturers who use standard IEC motors do not have the need to offer IEC motor adapters separately, which also represents a certain benefit.

The purpose of this analysis is to also determine the justifiability of the employment of special reducer motors, used by almost all of large reducer manufacturers (Table 1). Based on the data from Table 1, it is noticeable that transmission ratios at two-stage reducers are rather uniform, although it is also evident that carrying capacities of reducers with IEC motors are somewhat lesser. At three-stage reducers this difference is more visible. Accordingly, transmission rations and carrying capacities are smaller. Exceptions are the transmission ratios at

Table 1 Technical characteristics of universal gear reducers of different manufacturers

Manufacturer		NORD	PUJOL	PUJOL	ROSSI	ROSSI
Model	Designation	SK	IPCM	SP	R	MR
Axis height	h, mm	140	142[a]	160[b]	132	140
Transmission ratio	i_{2x}	26.86	45.2	48.1	31.9	22.5
Torque	T_{2x}, Nm	820	265	705	267	597
Transmission ratio	i_{3x}	395.46	–	467.4	96.4	194
Torque	T_{3x}, Nm	850	–	700	335	496

[a] Only double-stage reducers are made in this axis height

[b] This is the minimal axle height. It is slightly larger than the observed, but it is taken into consideration because of the value of axis height in triple-stage variant

manufacturer PUJOL models, where the use of the adapter for IEC motors achieves all advantages of special reducer motors. Other manufacturers, who connect IEC motors directly to first gear wheel in order to maintain relatively high transmission rations, were forced to lower the carrying capacity of their reducers.

The fact that the carrying capacity of a reducer is considerably higher, if this model is intended for installation with special reducer electric motor, leads to the conclusion that its high usage is fully justifiable (Kuzmanović et al. 2008). However, the question arises about the advantages of IEC motors utilization, who can use them and why use them at all?

The main advantage of their utilization is in reduction of the number of different electric motors required to have in factory storage (various motors in the same power class are used with different flanges), although it is otherwise necessary to keep a considerably larger number of IEC motor adapters in warehouse. (However, adapters are much cheaper than electric motors and—if needed—their manufacture is less demanding, faster and easier.) Another advantage is that, quite opposite to reducers with special reducer-motor, there is no requirement to offer them in motorless version with adapter for the IEC motor (Kuzmanović et al. 2010). There is also the benefit in the reduction in number of different first gear wheel variations—when used at special reducer motors, these gears have to be manufactured with different shaft openings to enable the use of every type of motor intended to connect with the particular reducer.

To conclude, the utilization of standard IEC motors decreases the number of electric motors required to keep in storage, these motors are easier and faster to obtain, there is also a lesser number of reducer variants in manufacturer's offer (also needed to keep in warehouse), specially if there is an intention to avoid the offer of motorless reducers with classic input shaft, as practiced by manufacturer ROSSI.

3 Evaluation Procedure

A more complete evaluation of conceptual solution could be achieved in many ways by using a simple comparison of particular quality parameters, such as transmission ratio (i), nominal torque (T_N), mass (m) and similar, or with the introduction of so-called "complex indexes": the proportion between transmission ratio and mass (i/m), or between nominal torque and mass (T_N/m). To obtain even more complete evaluation, it is necessary to introduce more complex indexes, such as the quotient of transmission ratio multiplied by nominal torque and the mass ($i \cdot T_N/m$), etc. Special care should be paid to the fact that only the reducers with the same axis height could be evaluated this way. So, the axis height (h) should also be taken into consideration to enable more accurate evaluation, i.e., to introduce the indexes ($i \cdot T_N/h$) or ($i \cdot T_N/m \cdot h$), where the values of these parameters should be as high as possible.

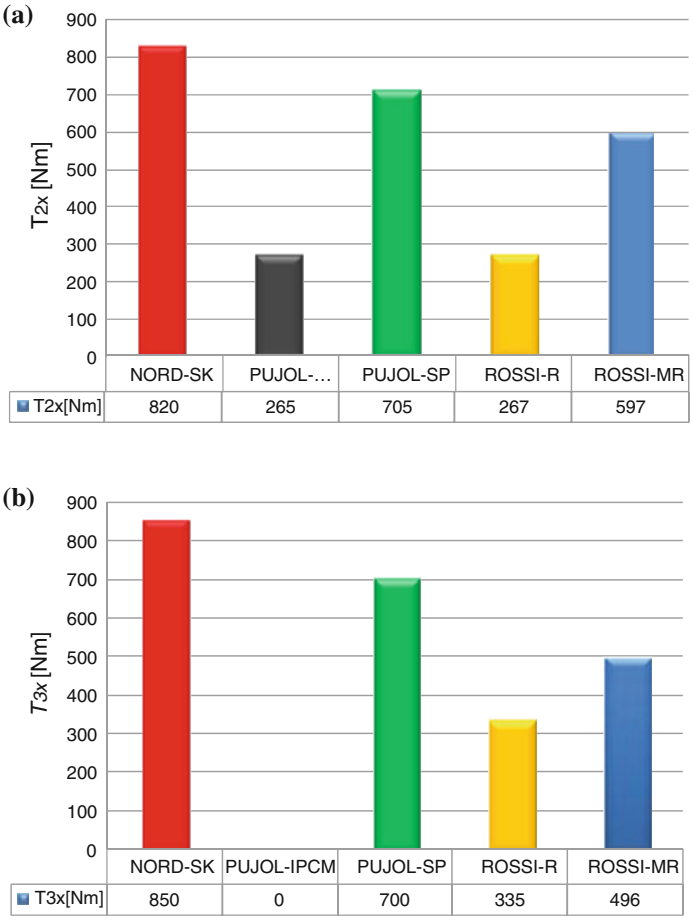

Fig. 5 Comparison of nominal torque values T_N for universal gear reducers and axis height $h \approx 140$ mm. **a** Double-stage, **b** triple-stage

Naturally, to conduct a completely high-quality evaluation, it is necessary to employ the same materials for the manufacture of casings (grey iron, for example), because if different materials are used, the obtained values are not comparable (although some obtained evaluations could tell a lot about the benefits of particular solutions). Consideration should also be given to the manufacturers practices—some of them go for large carrying capacities and lesser transmission rations, others are oriented towards lesser carrying capacities with high transmission ratios. Likewise, some manufacturers offers two gear sets applicable for the same reducer casing (or different casings with the same axis height), covering this way both solutions (lesser carrying capacity—high transmission ratio and large carrying

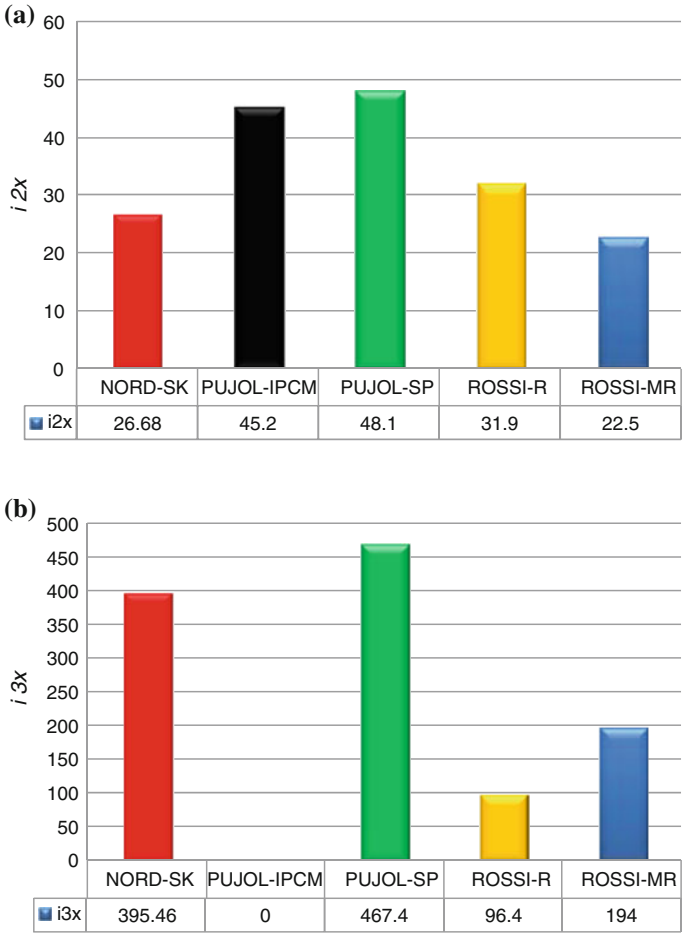

Fig. 6 Comparison of transmission ratio values i for universal gear reducers and axis height $h \approx 140$ mm. **a** Double-stage, **b** triple-stage

capacity—lesser transmission ratio) for the purpose of being more competitive to the other manufactures. Such an approach gives the manufacturers a considerable advantage on the market, but with the penalty of having somewhat more complex product line and storage situation (Rackov and Kuzmanović 2011). The approximate evaluation of reducer concept solutions are of no benefit if they are not compared with the market competition, taking into consideration each transmission ratio achieved for the particular axis height.

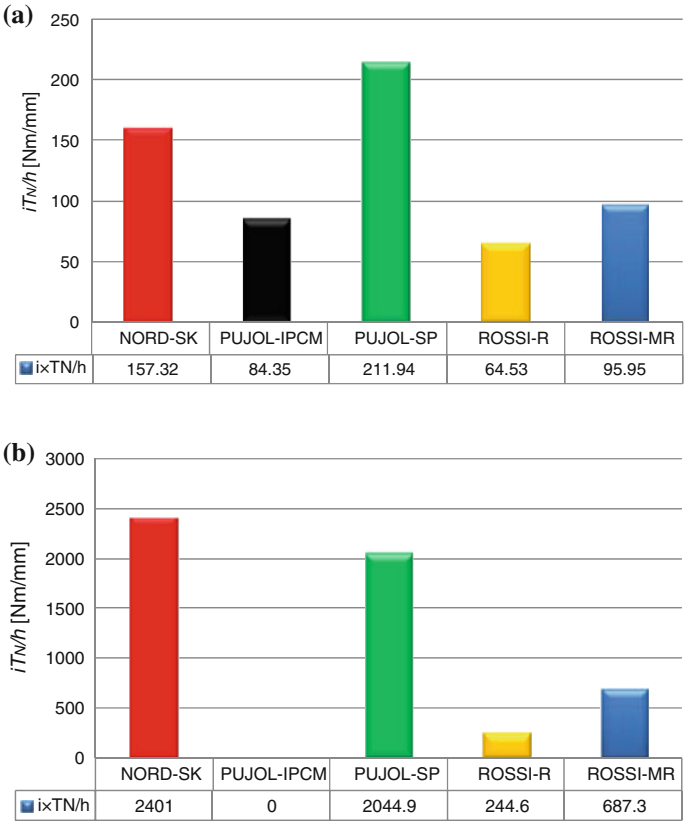

Fig. 7 Comparison of complex index $i{\cdot}T_N/h$ for universal gear reducers and axis height $h \approx 140$ mm. **a** Double-stage, **b** triple-stage

4 Evaluation of Characteristic Solutions

This paper will provide the evaluation of technical characteristics of two- and three-stage universal gear reducers of the abovementioned reducer manufacturers.

Based on the given technical solutions for the reducer axis height of 140 mm, it could be observed that manufacturer NORD has the largest values of torques (T_N) in double-stage and triple-stage variants (Fig. 5); however, this is not the case with the transmission ratio (i) values (Fig. 6).

Manufacturer PUJOL has the greatest transmission ratio values, although in the triple-stage variant only one value is considered, so the results are not fully comparable.

With the introduction of the complex index $i{\cdot}T_N/h$ into the survey, it is possible to notice that PUJOL has the most suitable conceptual solution in double-stage

variant, whereas the solution used by NORD is the best in triple-stage variant. The solution by PUJOL is also high-ranked between the triple-stage variants; however, it could not be fully taken into consideration because it has considerably larger reducer size. Nevertheless, the evaluation for PUJOL conceptual solution is made for the same axis height, so its complex index demonstrates that this manufacturer has a respectably good solution.

Naturally, many representative indexes might be obtained by taking into consideration the mass of reducers and (specially) their prices, showing the worthiness of a particular solution. Other factors, like storage costs and reducer delivery time could also influence the final conclusion.

This kind of evaluation is something principally conducted by the reducer designers (manufacturers). The reducer customers may draw completely different conclusions; judging by the stresses in reducer material, they can make a decision on which one is more reliable or has better quality (Fig. 7).

5 Conclusion

Based on conducted analysis, the main feasible conclusion is that motor-reducers with special reducer electric motors have the best technical characteristics. However, reducers manufactured with the standard IEC motors, connected to them via IEC motor adapters, may have almost the same technical characteristics, because the inner shaft of an IEC motor adapter could be machined to the identical diameter as found at special reducer electric motors.

Of course, the IEC motor adapter (always used in this solution) would have the negative impact on reducer mass and length, leading to more expensive manufacturing process; on the plus side, there is a reduction in the number of different electric motors (with similarly different flange diameters inside the same size class) needed to keep in warehouse. Another advantage of the manufacture of such reducers (with IEC motor adapters) is the lack of the requirement for a separate production of the direct connection with a special motor, making their manufacture somewhat easier.

This leads to the conclusion that the concept used by company PUJOL is exceptionally good. The solution used by company ROSSI is somewhat inferior, because of lesser carrying capacities or transmission ratios, and also because the first gear wheel is placed directly on the shaft of standard IEC electric motor, having much larger output diameter compared to the reducer electric motor.

However, even this solution is not to be disregarded, because it avoids the use of IEC motor adapter, since these reducers are already offered with such motors, special savings are achieved in cases when motorless reducers are not offered at all and having classic input shaft. These savings have significant impact on production costs, surely compensating for somewhat lower technical characteristics of such reducers. The mufacturers that use such a concept would confirm that view.

References

Kuzmanović S (2009) Universal gear reducers with cylindrical gears. University of Novi Sad, Faculty of Technical Sciences, Novi Sad, p 231

Kuzmanović S, Rackov M (2009) Development tendencies of universal gear reducers. In: Proceedings of the 3rd international conference pover transmissions 09, Kallithea, 1–2 October 2009, pp 145–148

Kuzmanović S, Rackov M (2009) Usual possible ways of increasing of speed rations values of universal gear reducers, Acta technica napocensis, Technical University of Cluj-Napoka, Romania, Applied mathematics and mechanics, vol 3(52), pp 221–226

Kuzmanovic S, Tudose L, Rackov M (2008) Testing of universal gear reducers during the exploitation. J Mech Eng Des, Novi Sad, ISSN 1450-5401, pp 45–52

Kuzmanović S, Vereš M, Rackov M (2009) Analysis of characteristical mounting ways of gear wheels in universal gear reducers, Zeszyty Naukowe Politechniki Poznanskiej Budowa maszyn i zarzadzanie produkcja, Wydawnictwo Politechniki Poznanskej, Poznan 2009, No 11, pp 81–91

Kuzmanović S, Ianici S, Rackov M (2010) Analysis of typical method of connection of electric motor and gear unit in the frame of universal motor gear reducers.In: Proceedings of the machine design 2010, ISSN 1821-1259. Faculty of Technical Sciences, Novi Sad, pp 141–146

Rackov M, Kuzmanović S (2009) Analysis of the most common failures of gears in universal gear reducers. J Eng Ann Fac Eng Hunedoara, Tome VII, Fascicule 4, ISSN 1584-2665, University “Politechnica” Timişoara, Faculty of Engineering, Hunedoara, Romania, pp 67–74

Design Optimization of High Ratio Planetary Systems

Athanassios Mihailidis and Cristina Pupaza

Abstract The study deals with the optimization of the rim thickness of the ring of a high-ratio planetary system with straight gears. In order to reduce the weight and to increase the maximum transmittable torque a new design strategy is applied. The geometry of the gears was generated using a numerical procedure which takes into account the geometrically correct form of the flank. The mesh on the active flanks, as well as in the area of the tooth foot was fine, allowing the accurate calculation of both flank pressure and foot stress. The model also included the support conditions between the ring gear and the housing. Improved solutions were found.

Keywords Optimization · Rim · Thickness · Torque · Gears

List of Symbols

DOE Design of experiments
GDO Goal driven optimization
FZG Forschungsstelle für Zahnräder und Getriebebau/Research Centre for Gears and Transmissions

1 Introduction

The Planetary gear transmissions are widely used in machine design due to the internal power splitting and the resulting high load carrying capacity. Aiming to increase the load carrying capacity a lot of work employing the Finite Element

A. Mihailidis (✉)
Aristotle University, Thessaloniki, Greece
e-mail: amih@auth.gr

C. Pupaza
University Politehnica, Bucharest, Romania
e-mail: cristinapupaza@yahoo.co.uk

G. Dobre (ed.), *Power Transmissions*,
Mechanisms and Machine Science 13, DOI: 10.1007/978-94-007-6558-0_38,

Analysis (FEA) has been reported in recent literature. Most of these studies address two major issues: the geometry of the tooth root fillet (Hebbal et al. 2009) and the rim thickness (Nan and Zang 2008). Novel gear root fillets were designed (Kapelevich and Shekhtman 2003) in order to minimize the stress and improve the strength of the gear. The influence of the rim thickness on the load carrying capacity has been extensively studied, but only for external gears (Winter and Podlesnik 1984). Later, the rim thickness of internal gears was considered for stress calculation (Jahn 1997); (Linke et al. 2005). In order to avoid modeling difficulties, most authors either consider a simplified tooth profile, or they employ a rather coarse mesh. The drawback of these simplifications is that the stress field in the foot fillet area and the pressure on the mating flanks cannot be concurrently studied. Furthermore, no multi-optimization procedure has been applied, although FEA is extensively used. On the other hand, stress calculations of the planetary systems are conducted using formulae developed by the known DIN3990:1987 and ISO 6336:1996 standards.

The current study presents a combination of multi-criteria optimization techniques employed in order to reduce the weight and to increase the maximum transmissible torque of a simple high-ratio planetary system with straight gears. The geometry of the gears was generated using a numerical procedure which takes into account the manufacturing process. The model of the planetary system also included the support conditions between the ring gear and the housing.

2 The Planetary System

The high-ratio planetary system used in this study is part of the pre-loading system developed for the FZG test rig (Mihailidis and Neranzis 2009). It consists of a sun gear, 3 planetary gears attached to a carrier and a ring gear (Fig. 1). All the

Fig. 1 3D model of the planetary system

Table 1 Dimensions of the gears

Gear dimensions	z [-]	m [mm]	x [-]	β [°]	b [mm]	d [mm]
Sun	+11	1.25	+0.5	0	20	13.75
Planet	+48		+0.30			60
Ring	-109		+0.437			136.25

Table 2 Material properties of the gearings

Density [kg/m^3]	7850
Poisson ratio	0.3
Young module [GPa]	300
Allowable contact stress [MPa]	1,500
Allowable tooth-root stress [MPa]	1,000

gearings were assumed error-free. The carrier was not considered in the model. Due to the relatively small dimensions, the sun gear was considered that it is manufactured from a solid disc. This is reasonable for high transmission ratio gear trains and it also simplifies the analysis. Table 1 contains the main gear dimensions, where symbols are according to ISO 6336:1996 standard. All the gears are made from case hardened steel. The material properties are shown in Table 2.

3 Finite Element Model

In a non-linear analysis the mesh is particularly important to obtain accurate results and fast convergence. On the other hand, during the optimization cycle the model is remeshed several times without user intervention. Therefore mesh controls were combined to obtain a smoothed and good quality mesh: mapped mesh between contacting flanks—to avoid oscillating contact pressure and the element size was set lower than 0.08 mm. An appropriate sphere of influence was defined in the neighborhood of the contact regions. The target was to keep the mesh configuration constant throughout the optimization cycle (Fig. 2).

Because the ring gear is not fixed in the housing, equally spaced spring elements were included in the model. The stiffness of the springs was set to 200 N/mm, a mean value found in the literature for this type of planetary systems.

The model was checked using calculation of the gearings according with the ISO 6336:1996 standard. The error was less than 5.5 % and this was caused by the mesh size. In this particular case the element size has to be tuned both with the contact problem, and with the multiple non-linear loops required by the optimization procedure. On the other hand, we have to take into account that the analytical calculations of the foot stress are based on the rack tooth profile. Figure 3 shows a detail with the maximum equivalent stress plot for one of the design variants.

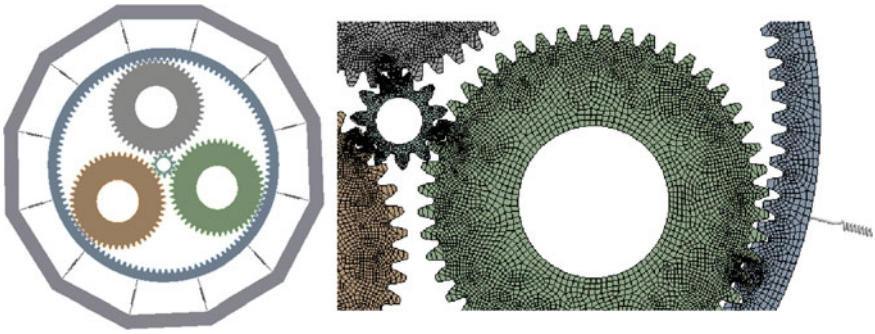

Fig. 2 Finite element model of the planetary system

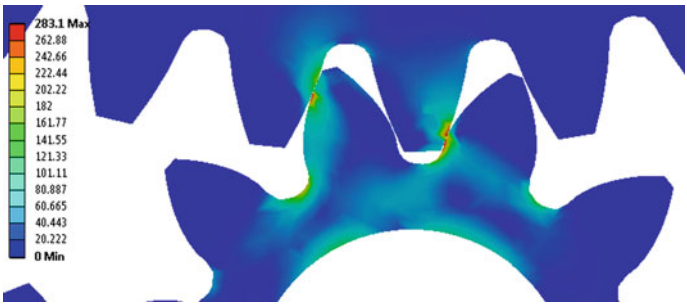

Fig. 3 Maximum equivalent stress plot. Detail

4 The Optimization Procedure

The optimization goals were to minimize the total weight for a given power rating and to determine the minimum rim thickness of the ring gear and of the planets. Another target was to find the maximum value of the input torque the assembly can withstand for a given weight. The assumption was made that the initial transmittable torque was known and for all calculations the safety factor was set to 1, with respect to the allowable stress.

The initial conditions were: the planetary system should withstand a moment of $T = 343.75$ Nmm applied on the sun, the maximum Hertzian pressure σ_H should not exceed 1,500 MPa and the maximum von Mises stress at the tooth foot σ_F was set to 1,000 MPa.

The design variables were: the external diameter of the ring gear, the internal diameters of the planets and the output torque. The objective functions were considered the maximum equivalent (von Mises) stress in the contact region of the gears, the maximum equivalent (von Mises) stress at the tooth root and the total weight.

Figure 4 shows the main steps of the optimization procedure. An initial static analysis was performed, than the relationships between the objectives and the

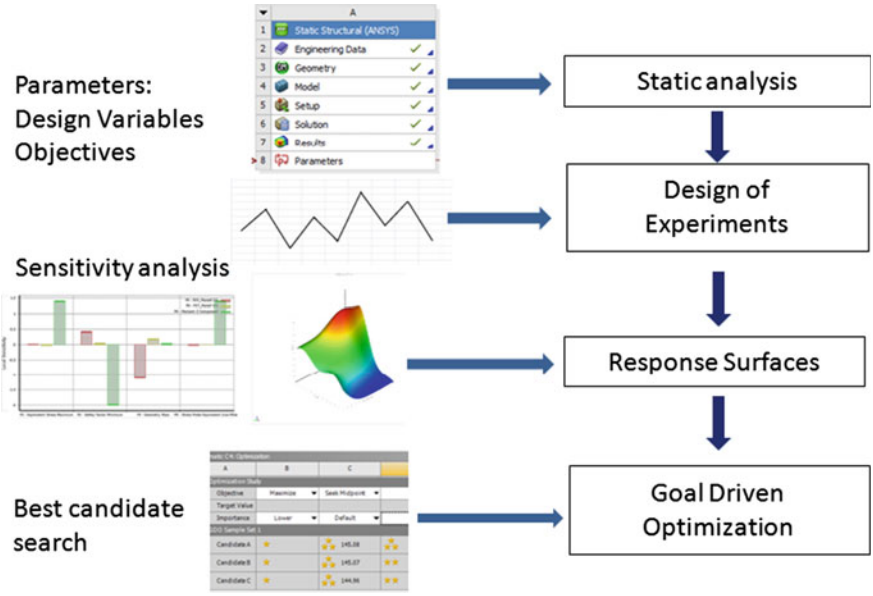

Fig. 4 The optimization procedure

design variables were identified using DOE combined with Response Surfaces techniques.

The DOE was used to generate the sample data and to fit an appropriate model for each of the output variables. Once the approximation was done the Response Surfaces were built and the behavior of the model was estimated using them instead of looping through the FE model.

The main advantage of the procedure is that finding the approximation functions takes fractions of seconds, but a static analysis takes at least several minutes.

This leads to an important reduction of the computation time. On the other hand multi criteria objectives were imposed. The last step was a constrained, multi-objective optimization.

Each step of the optimization procedure has its own options and characteristics. The static analysis is a non-linear analysis on a parameterized model. The DOE stage uses an optimal space filling strategy, which creates an optimal filling of the design space with a relatively small number of points, while keeping the discrepancy as low as possible. The samples were generated using Central Composite Design strategy and the number of cycles was 20. It is an efficient scheme when a complex Meta Model is used, like Kriging models are. Therefore, according to the DOE step, the Kriging option was used when building the Response Surfaces. This interpolation method is accurate and it provides information regarding the goodness of fit, or the maximum relative residual.

The GDO was primary performed using the screening method in order to obtain a draft solution. After this step a genetic algorithm was chosen to refine the search of

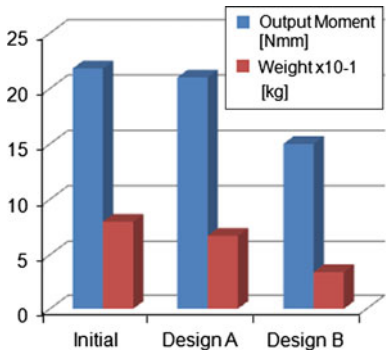

Fig. 5 Maximum output moment and total weight of the chosen design variants

the optimum design set. The algorithm incorporates filters, and yields to the global Pareto front. The best candidate was identified among 10,000 sampled points.

5 Optimization Results

The design parameters were varied continuously over imposed ranges and the output parameters of the planetary system were examined over these ranges. Two variants were identified as preferred design solutions.

The external diameter of the ring was decreased from 150 to 143 mm (design variant A) and the internal diameters of the planets were increased from an initial value of 27–50 mm (design variant B). Therefore the total weight of the planetary system was found 16 % lower for design variant A and 57 % for design variant B. Multicriteria optimization is always a trade-off between the desired objectives. In fact it is a trade-off between different targets. In our case: the minimum weight, the maximum allowable stress and the maximum transmissible torque.

The maximum output torque remained nearly at the initial value for variant A, but decreased for variant B. Figure 5 shows a comparison of the weight and the maximum output torque for the initial design and the preferred design variants.

6 Conclusion

This research is a theoretical study on the multicriteria design optimization of the high-ratio planetary systems. Improved solutions were found with a limited number of performed simulations. It is a new design strategy, based on a geometrically correct form of the flank. Because the solution is not unique, a “trade off” between parameters was carried out and improved design variants for the rim thickness of the ring gear and for the internal diameters of the planet gears were found. The total weight of the assembly was also reduced. Work is in progress to take into account

other parameters, too. However, this attempt proved that there are powerful simulation tools that can be applied for high-ratio power transmissions.

This optimization strategy can be applied in the early stage of the design. The procedure enforces traditional design of planetary-systems. Business today is racing to improve product quality, to innovate and to minimize the costs of the products. Multicriteria optimization is a powerful tool to address these challenges.

References

Hebbal MS, Math VB, Sheeparamatti BG (2009) A study on reducing the root fillet stress in spur gear using internal stress relieving feature of different shapes. Int J Recent Trends Eng 1(5):163–165

Jahn C (1997) Theoretische und Experimentelle Untersuchungen zur Zahnfußtragfähigkeit von Innenverzahnungen. Dissertation, TU Dresden

Kapelevich AL, Shekhtman YV (2003) Direct gear design: bending stress minimization. Gear Technology http://www.onestepmolding.com/tfpo.pdf. Accessed on 15 Jan 2012

Linke H, Trempler U, Baumann F (2005) Analysis on the stress of toothings of planetary gearings, VDI Berichte 1904 Band I, pp 345–355

Mihailidis A, Neranzis I (2009) New system for testing gears under variable torque and speed. Recent Pat Mech Eng 2(3):179–192

Nan G, Zhang J (2008) Finite element analysis of internal gear in high-speed planetary gear units, vol 14(1). Transactions of Tianjin University, Tianjin University, Springer, Berlin, pp 11–15

Winter H, Podlesnik B Zahnfedersteifigkeit von Stirnradpaaren, Teil 1 Antriebstechnik 22 (1983), 39–42, Teil 2 Antriebstechnik 22 (1983) 51–58, Teil 3 Antriebstechnik 23 (1984), pp 43–49

The Numerical Calculus of Hobs Used to Cut W–N Gears

Gheorghe Miloiu

Abstract After a short introduction showing the evolution of Wildhaber–Novikov (W–N) gears, the evolution of the study of hob geometry is presented, with special focus on the author's contribution in the field. Then a general method of study of the hob geometry is exposed. The calculus model takes into account the hob with non-zero rake angle, a wide range of re-sharpenings, a generation by relief grinding, which can easily be customized for the type of abrasive tool chosen, to obtain the profile of the abrasive tool and the hob profile for various re-sharpenings. The hob profile deviation is then evaluated in an axial plane. To reduce the cumulated profile error on re-sharpening, the setting parameters on relieving are modified. The algorithm is developed on matrix basis. In the next part of the paper the customizing of the general method is presented, for the case of hobs designed to cut gears with arc-of-circle profile (reference profile with two arcs of circle). This part includes numerical results presented in tables and diagrams, for hobs in the modulus range 4–20, three values of the rake angle (0°, 3°, 6°), three values of the relief for each modulus and three values of the position angle of the generation rack (around the value of the angle of the basic helix) and five values of the re-sharpening angle (0°, $\pm 3^{\circ}$, $\pm 6^{\circ}$). The calculi carried out have been the basis for the manufacturing and inspection of four sizes of hobs—for the moduli 4, 10, 14 and 20. Several details of the manufacturing of hobs for W–N gears are presented in the end of the paper.

Keywords W–N gears · Hobs · Hob geometry · Hob sharpening · Grind relieving of hobs

List of Symbols

m_n	Normal modulus
γ	Hob rake angle
r	Profile radius

G. Miloiu (✉)
S.C. Confind Campina, Campina, Romania
e-mail: gmiloiu@confind.ro

G. Dobre (ed.), *Power Transmissions*,
Mechanisms and Machine Science 13, DOI: 10.1007/978-94-007-6558-0_39,

$K_{\Delta;}$ H_{Δ}	Relieving depth; arhimedic parameter
C; Γ	Curve; characteristic curve
Π; Σ	Plan, surface
S; index	Reference system; tool
δ; Δ	Deviation; cumulated error
Q	Diametrical hob coefficient
U	The parameter of the basic profile
p	Linear parameter by which the profile describes the basic rack
μ	The parameter of the generation of the surface of the abrasive tool relieving the hob
ν	The parameter of the relative motion rack—worm
w	The angular parameter of the hob rake surface
ξ	The position angle of the hob rake surface
ψ	The setting parameters of the abrasive tool used for relieving
τ	The angular parameter of the abrasive tool used for relieving
t	The parameter of the hob rake surface
θ	The position angle of the basic rack
T_{ab}	Square matrix representing the transfer from the reference system b to the reference system a
X_c	Column matrix representing the vector radius of the current point from the system C, with the components x_c, y_c, z_c
$DX_{c(u)}$	The derivative of the matrix X_c with respect to the parameter u
N_c	Column matrix representing the normal vector attached to the current point C, with the components n_{xc}, n_{yc}, n_{zc}
,	The symbol for the dot product of two vectors. Ex.: A,B is the dot product of the vectors A and B (column matrix)
.	The symbol of the vectorial product of two vectors. Ex.: A.B is the vectorial product of the vectors A and B (column matrix)
,.	The symbol for the mixed product of three vectors. Ex.: A, (B.C) is the mixed product of the vectors A, B, C (column matrix)
	Matriceal product: no sign is applied. Ex.: AB is the product of the matrices A and B, which can be only done when A has as many columns as B has lines

1 The Evolution of W–N Gears (In Brief)

W–N gears have arc-of-circle profile and they have been first proposed by Wildhaber (1923) and Novikov (1956). These gears have been studied in various centres from Russia: Novikov (1956–1958), Fedeakin and Cesnokov a.o.(1958) a.o,; Romania: Miloiu (1964, 1965, 1975, 1980, 1990), China (1981–1988), Japan (1999–2001), USA: Litvin (1985–2009).

In the 70s the W–N gears have won in the competition with involute gears made of non-hardened steel: general use gearboxes—in Russia, special gearboxes in the oil industry—in Russia and China, heavy gearboxes for high capacity belt conveyors—in Romania.

After 1985 the situation has changed. The technological progress—heat treatment for hardening plus finishing by grinding at gears with big diameter—has been used on involute gears, not on W–N gears (Miloiu 1997). Under these conditions the area of application for W–N gears has been restricted to the gearboxes for pump jacks, where non-hardened gears, finished only by hobbing, are still used. Research has followed the same route. Watching the trend in three top international congresses one can notice that in 1988 (China 1988) 8 studies were presented, and in 1999 (Paris 1999) and 2001 (Fukuoka 2001) only one, respectively three studies on the W–N gears.

A proper answer to the question "What is the future of W–N gears?" can only be given if high accuracy W–N gears hardened and ground will be manufactured (Miloiu 1997). Profiled grinding machines are now offering a technological possibility which has not been capitalized yet.

2 The Evolution of Hob Geometry Research

Three papers appeared in the 7th decade of the 20th century have opened the door for the research of hob geometry using the methods of differential geometry: Litvin (1968, which in time has become the monumental work from 2004 to 2009), Liukshin (1968) and Lashnev (1971). Next are the contributions of: Miloiu (1975), Bocian (1976) and Gyenge (1979), which present thorough theories of hobs with arbitrary reference profile and applications for hobs to cut W–N gears, respectively for hobs designed to cu worm wheels for globoidal gears and Duplex worm (ZA) gears.

The paper (Miloiu 1975) was materialized in the manufacturing of several (W–N) hobs of high accuracy with the moduli 4; 10; 14 and 20, verified based on a method published eventually (Miloiu 1990).

In the years 1976–1978 Bocian and Miloiu have published several papers regarding the geometry of the sharpening (rake) surface of the hobs. In the years 1979–1987, Miloiu and Visa have refined the sharpening of hobs, establishing the precision thresholds of the mechanical systems for profiling of the special hob sharpening machines: Klingelnberg, Kapp, MODUL, 3A 622.

The current paper provides a short look over the author's papers in the field of accuracy hobs, published since 1975, but within an environment of small circulation and without an overall view. In two recent studies, Hiltcher a.o. (2006) and Radzevich (2007) step up the research on the hobs to make located, numerical controlled contact in helical worms, respectively the geometric optimization of hobs processing involute cylindrical gears.

3 General Method for the Study of Hob Geometry

The study steps can be visualised on the scheme in Fig. 1 (Miloiu 1975). Given the basic rack of the gear for which the hob is calculated (Block B1), the hob envelope worm is generated for the reference position of the rack (Block 2). Eventually the rake surface of the hob is defined (Block 3).

Crossing the surface from the blocks 2 and 3, the reference cutting edge of the hob is obtained (Block 4). In the Block 5 the normal to the reference cutting edge is established. By imposing the relieving motion and a certain relative position between the abrasive relieving tool and the hob (Block B6), the reference edge generates the surface of the abrasive tool (Block B7).

Using the abrasive tool obtained, the hob clearance surface relieved is generated (Block B8). The next two steps define the actual cutting edge (the Block B9) and evaluate the hob profile deviation (Block B10) for certain re-sharpenings: the links AB and CD. The deviation is evaluated in axial plan.

Passing step by step through B2–B10, for the whole hob re-sharpening interval, the cumulated profile error is established, respectively the interval within which the actual axial profile fits. To reduce the cumulated profile error, the setting parameters for relieving and the link EF are modified.

The basic rack (*Block B*1). It is defined by the vector radius $X_c = X_c$ (u, p) and the normal $N_c = N_c$ (u).

The generation of the hob enveloping worm (*Block B*2). The equations of the envelope worm have the form: $X_M = X_M$ (u, *v*, ΔR), where ΔR is the displacement of the rack from the reference position: $\Delta R = H_A \cdot \xi$. To write X_M, the cinematic method for the study of mutually enveloping surfaces (Lashnev 1971; Litvin 2009) is used. The matrix for transfer from the reference system related to the rack S_c to the system related to the envelope worm S_M (Fig. 2), T_{MC}, the reverse thereof—T_{CM}, and the relative speed between Σ_M and Σ_C, V_{MC}, are respectively:

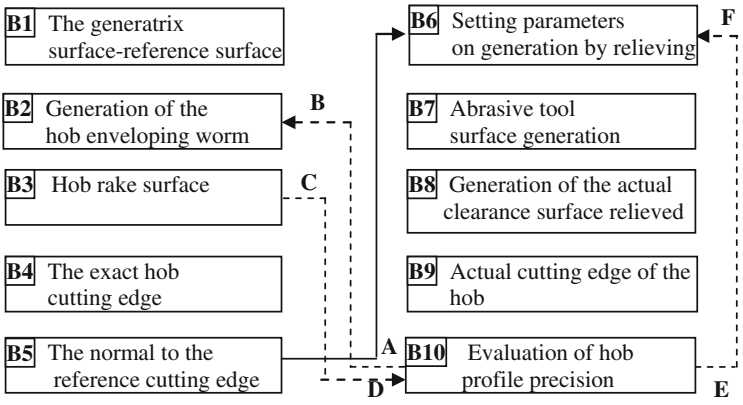

Fig. 1 The layout for the study of the geometry of hobs designed for gear cutting

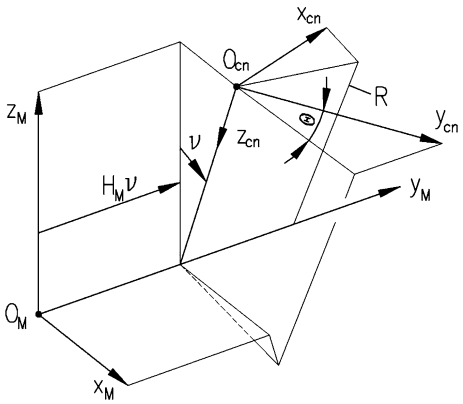

Fig. 2 The systems of coordinate axes at the generation of the hob enveloping worm Σ_M

$$T_{MC} = \begin{bmatrix} -\cos v \sin\theta & \cos v \cos\theta & -\sin v & R \sin v \\ \cos\theta & \sin\theta & 0 & H_M v \\ -\sin v \sin\theta & -\sin v \cos\theta & -\cos v & R \cos v \\ 0 & 0 & 0 & 1 \end{bmatrix} \tag{1}$$

$$T_{CM} = \begin{bmatrix} -\cos v\ \sin\theta & \cos\theta & -\sin v\ \sin\theta & -H_M v \cos\theta \\ \cos v\ \cos\theta & \sin\theta & \sin v\ \cos\theta & -H_M v \sin\theta \\ -\sin v & 0 & -\cos v & R \\ 0 & 0 & 0 & 1 \end{bmatrix} \tag{2}$$

$$V_{MC} = T_{CM} \frac{\partial T_{MC}}{\partial v} X_C = \begin{bmatrix} z_{cn} \sin\theta - R \sin\theta + H_M \cos\theta \\ z_{cn} \cos\theta + R \cos\theta + H_M \sin\theta \\ -(Kx_{cn} \sin\theta - y_{cn} \cos\theta)[1 - \cos v(\cos v - \sin v)] + z_{cn} \sin v(\cos v - \cos\theta) \\ +R \sin v(\cos v + \cos\theta) \\ 0 \end{bmatrix}. \tag{3}$$

From:

$$N_C(u), V_{MC}(u, v, p) = f(u, v, p) = 0 \tag{4}$$

results a relation between the parameters u, v and p:

$$p = f(u, v) \tag{5}$$

and from:

$$X_M = T_{MC} X_C \tag{6}$$

we get the equations of the family of envelope worms:

$$X_M = \begin{bmatrix} -(Kx_{cn}\sin\theta - y_{cn}\cos\theta)\cos v - (z_{cn} - R)\sin v \\ Kx_{cn}\cos\theta + y_{cn}\sin\theta + H_M v \\ (kx_{cn}\sin\theta - y_{cn}\cos\theta)\sin v - (z_{cn} - R)\cos v \\ 0 \end{bmatrix} \tag{7}$$

The rake surface (*Block B*3). The equations of the surface Σ_γ (Fig. 3) are:

$$X_\gamma = \begin{bmatrix} t\sin(\gamma + w + \xi) - R_\gamma\cos(\gamma + w + \xi) \\ -H_\gamma w \\ t\cos(\gamma + w + \xi) + R_\gamma\sin(\gamma + w + \xi) \\ 1 \end{bmatrix}, \tag{8}$$

where: $H_\gamma = R_o/\ \mathrm{tg}\ \theta_o$, $R_\gamma = R_o.\sin\gamma$.

The actual cutting edge (*Block B*4). The edge C_a is obtained by crossing Σ_M with Σ_γ, which is analitically equivalent to:

$$\left.\begin{array}{l} w = y_M(u, v, \Delta R)\,/\,(-H_\gamma); \\ t = [z_M(u, v, \Delta R) - R_\gamma.\sin(\gamma + w + \xi)]\,/\cos(\gamma + w + \xi) \\ x_M(u, v, \Delta R) - t\ .\sin(\gamma + w + \xi) + R_\gamma.\cos(\gamma + w + \xi) = 0 \end{array}\right\}. \tag{9}$$

Considering these relations, the edge C_a is:

$$X_a = X_a(u, \xi). \tag{10}$$

For $\xi = \xi_0 = 0$, (10) defines C_{ao} (of reference).

The normal to reference cutting edge (*Block B*5). The vector normal on C_{ao} (C_{ao} is on the surface relieved Σ_α), $X_a = X_a\ (u_i, \xi)$ is defined by the product:

$$N_a = D\ X_{a(u)} \cdot D\ X_{\alpha(\xi)}. \tag{11}$$

In which DXa(u) is the derivative along the curve Cao (ξ = constant), and DX$\alpha(\xi)$ is the derivative along the relieving directrix. DXa(u) and DX$\alpha(\xi)$ are obtained by the finite difference method.

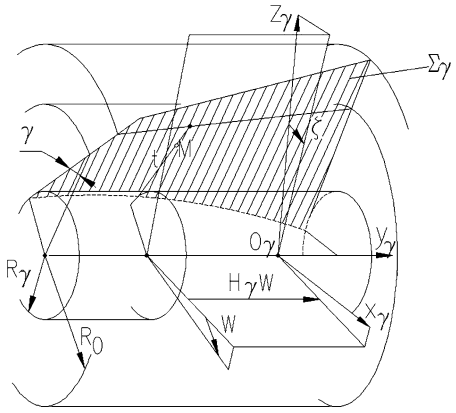

Fig. 3 The generation of the hob rake surface (sharpening surface)

The setting parameters on generating by relieving the hob clearance surface (*Block B*6). The values of the setting parameters Ψ_1, Ψ_2, Ψ_3, d_0 (Figs. 4 and 5) are given in the Table 1, corresponding to the relieving with the three types of abrasive tools known: cylindrical, disc, straight. The following symbols are used in this table: R_0—the reference radius of the hob; θ_0—the angle of the reference helix of the hob; R_S—the abrasive disc radius; h_1—the depth of the dedendum of the generatrix rack tooth, d_0—the reference distance between the origins of the coordinate systems related to the hob (S_a) and to the abrasive tool (S_S).

The abrasive tool surface generation (*Block B*7). The surface relieved Σ_α, in the relative motion V_r given by the law of motion between Σ_s si Σ_α, generates a surface Σ_v in the reference system S_s, the cinematic relation being:

$$N_S,\ V_r = 0 \tag{12}$$

The revolution surface Σ_s of the abrasive tool is determined as a surface tangent to Σ_v, enforcing the normal N_v on Σ_v to pass through the tool axis, that is:

$$j_s,\ (X_s.\ N_v) = 0, \tag{13}$$

where j_s is the matrix of the versor of the axis of the abrasive tool in relation to the reference system S_s, and N_v—the matrix of the common normal of the mating surfaces.

The family of surfaces Σ_α in the system S_s will be defined by the equations:

$$X'_\alpha(u, \xi, \mu) = \begin{bmatrix} x'_\alpha(u, \xi, \mu) \\ y'_\alpha(u, \xi, \mu) \\ z'_\alpha(u, \xi, \mu) \\ 1 \end{bmatrix} \tag{14}$$

The monoparametric meridian curve (u) of the surface Σ_s is determined eliminating from X'_α two parameters, by means of the relations (12) and (13).

From the above mentioned results that in general the characteristic curve Γ_s between Σ_s and Σ_α does not coincide with the cutting edge, having in common only one point. In consequence, the method described can not produce any theoretically exact edge.

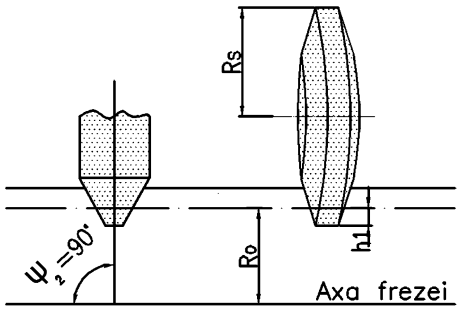

Fig. 4 The reference positions for relieving cylinder and disc abrasive tools

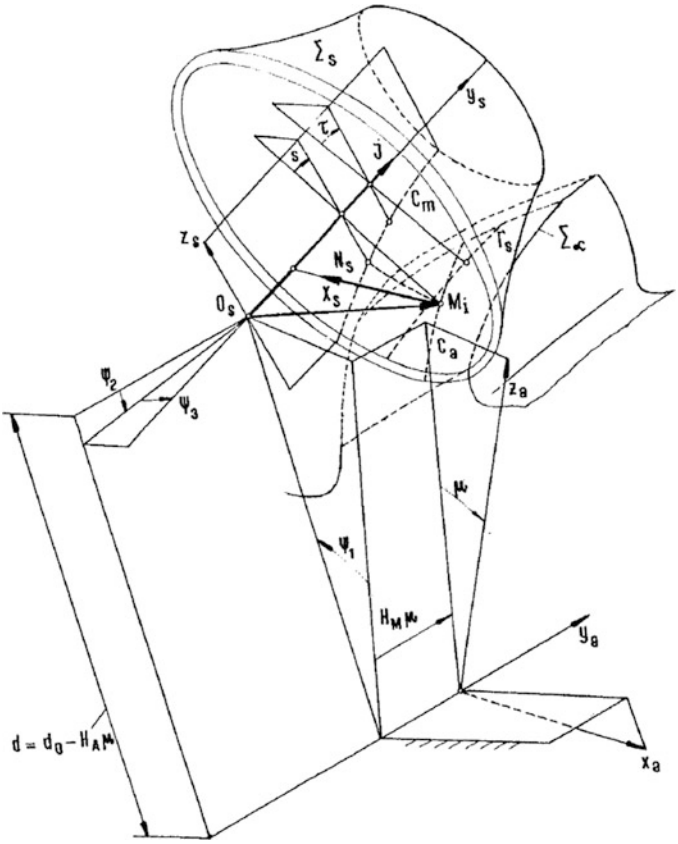

Fig. 5 The scheme of generation of the abrasive tool Σ_s by the reference cutting edge of the hob C_a and the generation of the surface relieved Σ_α by Σ_s

Table 1 Setting parameters for relieving

Abrasive tool	Fig	ψ_1	ψ_2	ψ_3	d
Cylinder	4	0	$\pi/2$	0	$R_0 + \mu H_\Delta$
Disc	4	0	0	$\theta \approx \theta_0$	$R_0 + R_S + \mu H_\Delta - h_1$
Straight	5	$\psi 1$	$\psi 2$	$\psi 3$	$d_0 + \mu H_\Delta$

In case an exact edge is imposed, the parameter ζ being constant, the calculus process becomes over defined through the Eqs. (12) and (13). This is why the problem is solved by means of a compromise. Adopting the parameter ζ, only the Eqs. (13) is considered, replacing N_v with N_s, a vector resulting from the vectorial product of the relative speed vector and the vector tangent to the cutting edge, $DX_{a(u)}$, (the Block B5). Considering Fig. 5, from where result the transfer matrices T_{as} and T_{sa} and the verso of the axis of the abrasive tool j_s, we can write the following form for (13), the cinematic relation between Σ_α and Σ_s:

$$F(u, \mu) = x_s n_{S3} - z_s n_{S1} = 0, \tag{15}$$

where (x_s, y_s, z_s) are the components for X_s, and (n_{S1}, n_{S2}, n_{S3}) are the components for N_s.

The median curve of the abrasive tool, C_m, has the position vector of a current point X_m and the normal N_m :

$$X_m = \begin{bmatrix} 0 \\ y_s \\ x_s \cos s - z_s \sin s \\ 1 \end{bmatrix} \qquad N_m = \begin{bmatrix} 0 \\ n_{s2} \\ n_{s1} \cos s - n_{s3} \sin s \\ 1 \end{bmatrix} \tag{16}$$

where s is:

$$s = \text{arc tg}\,(x_s / z_s) \tag{17}$$

The generation of the actually relieved clearance surface (*Block B*8). Imposing the generation way from Fig. 5, the tool Σ_s generates by relieving the clearance surface o the hob Σ_α. Since the characteristic Γ_s and the profile C_m change their position and form depending on the parameter ξ, profile error occur at the abrasive tool and at the hob.

Introducing the rotation parameter τ, the surface Σ_s and the corresponding normal are written:

$$X_S = X_S(u, \tau, \xi_o; N_S = N_S(u, \tau, \xi_o) \tag{18}$$

Taking into account T_{sa} and T_{as} (Fig. 5) and (18), the relative speed abrasive tool—hob is:

$$V_{as} = (T_{sa}\, T_{as})\, X_s \tag{19}$$

From the condition of meshing of the surfaces Σ_s and Σ_α results a relation between the parameters, such as: $\mu = f(\tau)$. The surface relieved Σ_α results:

$$X_\alpha = T_{as} X_s = X_\alpha(u, \tau, v, \xi) \tag{20}$$

The actual cutting edge (*Block B*9). Crossing Σ_α (20) with Σ_γ (8), we obtain the actual cutting edge C^*_r:

$$X_r = X_r(u, \xi) \tag{21}$$

The evaluation of the precision of the actual profile (*Block* 10). The actual edge C^*_r (21) deviates from the exact edge C_a (10).

The evaluation of the deviation is done in the axial plan of the hob, for discrete values of the parameter ξ (re-sharpening). The axial profiles obtained through the helicoidal projection of the edges C_r and C_a, C^*_r and C^*_a, Fig. 6, have the equations:

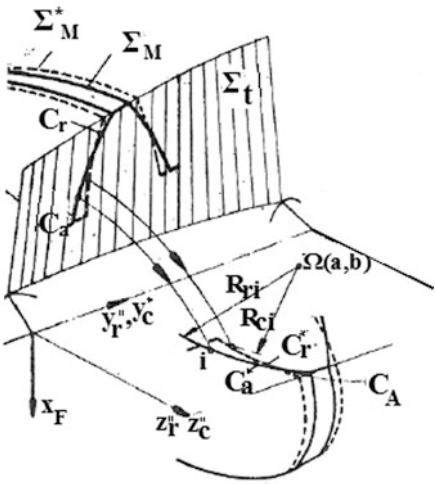

Fig. 6 The evaluation of hob precision

$$X_r^* = \begin{bmatrix} 0 \\ y_r - H_M \cdot arctg(x_r/z_r) \\ \sqrt{x_r{}^2 + z_r{}^2} \\ 1 \end{bmatrix}; \; X_a^* = \begin{bmatrix} 0 \\ y_a - H_M \cdot arctg(x_a/z_a) \\ \sqrt{x_a{}^2 + z_a{}^2} \\ 1 \end{bmatrix} \tag{22}$$

The profile deviation is considered perpendicular to the exact profile

4 The Customizing of the General Theory to Hobs for W–N Gears. Numerical Results

The basic rack is defined by the vectors (Fig. 7):

$$X_C = \begin{bmatrix} K\{(r_1k_1 + r_2k_2)\cos_u + (x_A - u\ \sin\ \chi)k_2 + [ak_1 - (b + \pi/2)]k_3 + (r_3 \sin u - \pi/2)k_4 - \pi/2 \\ 0 \\ -(r_1k_1 + r_2k_3)\sin u - (z_A - u\ \cos\ \chi)k_2 + ck_3 + [h_2 - r_3(1 - \cos u)k_4 \\ 1 \end{bmatrix} \tag{23}$$

$$N_C = \begin{bmatrix} -(r_1k_1 + r_2k_3)\cos\ u + k_2 \cos\ \chi - k_4 + \sin u \\ 0 \\ K[-(r_1k_1 + r_2k_3)\sin u - k_2\ \sin\ \chi)k_2 + k_4r_3 \cos u) \\ 0 \end{bmatrix} \tag{24}$$

in which K = ± 1: K = + 1 corresponds to the left flank of the rack, and K = −1 to the right flank.

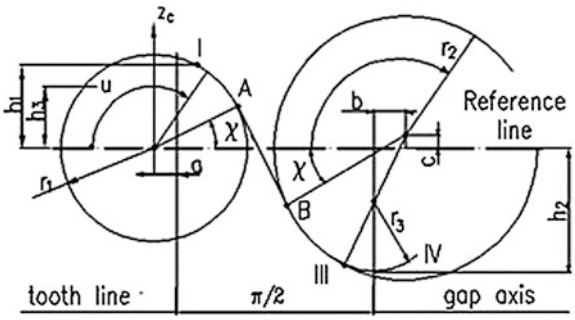

Fig. 7 The definition of the basic rack (type GOST—15023)

For the numerical definition of a point from the surface X_c, a discrete value of the parameter u is considered, contained within the limits $u_1 \leq u \leq u_2$:

$$u_1 = u_{min} - (1 + k_1 + k_2 + k_3 + k_4).\Delta u;$$
$$u_2 = u_{max} - (1 + k_1 + k_2 + k_3 + k_4).\Delta u,$$

where u_{max} and u_{min} are extended with 10 % on the branch r_1 and with about 15 % on the branch r_3; the pitch Δu (15 points on the branches I and III, 5 points on the branches II and IV—Fig. 7):

$$\Delta u = (u_{max} - u_{min}) / (15k_1 + 5k_2 + 15k_3 + 5k_4)$$

Several numerical results are eventually given for the hob with the following parameters:

(normal) modulus	$m_n = 14$
diametral coefficient	$Q = 10; Q = 2R_o/m_n$
number of grooves	$z_F = 8$
relief	$K_\Delta = 12; 14; 16$
rake angle	$\gamma = 0° ; 3° ; 6°$
position angle	$\theta = 4.5° ; 5° ; 5.5°$
re-sharpening interval	$\mathfrak{Z} = 0° ; \pm 3° ; \pm 6°.$

The checking (axial) profile of the hob (the envelope worm) is presented in Table 2; the coordinates are given in 5 points on the branches I and III, respectively two points on the branch II.

Table 3 shows the coordinates of the profile of the cylinder type abrasive tool. Since $\theta \neq \theta_o$ ($\theta_o = 5.71°$), one profile results for the grinding tool used at the right flank and another one for the tool used for the left flank. The difference $\Delta\theta = 0.21°$ being quite small, the profile differences are very small. On re-sharpening the hob the profile deviations presented in Fig. 8 appear (evaluated on the abrasive tool). It is found that these deviations increase with the increase of the rake angle γ, for the same hob re-sharpening interval.

The influence of the basic rack position θ over the profile deviation is presented in Fig. 9, for two values of the relief K_Δ and three values of the rake angle γ of the

Table 2 The checking (axial) profile the W–N hob

Branch and profile point		HOB: $m_n = 14$; $Q = 10$; $Z_F = 8$; $K_\Delta = 14$; $\theta = 5{,}5^0$					
		$\xi = 0^o$		$\xi = 3^o$		$\xi = 6^o$	
		Z	$Y_{D(+)}$; $Y_{S(-)}$	Z	$Y_{D(+)}$; $Y_{S(-)}$	Z	$Y_{D(+)}$; $Y_{(s)}$
r_2	1	82,60	16,88	83,53	16,88	84,47	16,88
	4	80,72	15,00	81,65	15,00	82,59	15,01
	7	78,58	13,43	79,51	13,43	80,45	13,43
	10	76,22	12,20	77,16	12,20	78,09	12,21
	13	73,71	11,34	74,64	11,35	75,58	11,35
–	2	70,89	10,83	71,81	10,82	72,75	10,82
	5	67,67	10,35	68,58	10,34	69,49	10,34
r_1	4	65,12	9,76	66,04	9,75	66,97	9,75
	7	62,72	8,78	63,65	8,77	64,58	8,77
	10	60,51	7,42	61,44	7,42	62,37	7,41
	13	58,55	5,73	59,48	5,72	60,42	5,72

hob. In all cases, the profile deviations are smaller for $\gamma = 0$, and for θ angles close to the angle of the reference helix ($\theta_o = 5.71°$). As regards K_Δ, the deviations increase with bigger K_Δ reliefs (Fig. 10).

The influence of hob re-sharpening on the profile deviation is shown in Fig. 10. It is found that: at re-sharpening behind the reference rake surface ($\xi < 0$) the profile errors are positive, and at re-sharpening in front of the reference surface ($\xi > 0$)—they are negative; the profile deviations on re-sharpening are smaller for $\gamma = 0$ than for $\gamma = 6°$ or 3° Fig. 11

From the Table 4, in which the profile deviations calculated and those admissible (DIN 3968) are presented, results that: 1. For the hobs with $\gamma = 0$ and re-sharpening $\xi = \pm 3°$, the theoretical profile precision fits within class A at m = 4–14, but not also at m = 20; 2. For $\gamma = 3°$ and $\xi = \pm 3°$,—class A at m = 4–10; 3. For $\gamma = 6°$, class A can not be obtained at any moduli; 4. For $\gamma = 3°$ at m = 14 and 20, and at $\gamma = 6°$ for all the moduli, the theoretical profile precision corresponding to class A is obtained only for re-sharpening within narrower than six degrees.

5 Researches on the Geometry of Hob Re-Sharpening

Using in principle the study method described in Chap. 3, for the study of the precision in relieving hobs, in the papers (Miloiu et al. 1980) and (Miloiu 1987) a general method for the study of the geometry of the sharpening (rake) surface of hobs with helicoidal grooves and of the abrasive (straight) tool used for sharpening is presented.

The exact geometry of the abrasive tool has been studied in the paper Bocian and Miloiu (1977). There are several papers in which results of the numerical

Table 3 The profile of cylinder abrasive tool for relieving the W–N hob

Profile point		HOB: mn = 14; Q = 10; $Z_F = 8$; $K_\Delta = 14$; $\theta = 5{,}5°$			
		Right		Left	
		Y_1	Z_1	Y_1	Z_1
r_2	1	15,80	13,16	−15,72	12,73
	2	15,08	12,50	−15,02	12,11
	3	14,40	11,81	−14,35	11,45
	4	13,76	11,10	−13,72	10,77
	5	13,17	10,36	−13,13	10,07
	6	12,61	9,61	−1,58	9,34
	7	12,10	8,83	−12,08	8,59
	8	11,62	8,03	−11,61	7,81
	9	11,20	7,22	−11,18	7,02
	10	10,81	6,39	−10,80	6,21
	11	10,47	5,54	−10,46	5,38
	12	10,17	4,69	−10,17	4,54
	13	9,92	3,82	−9,92	3,69
	14	9,71	2,94	−9,71	2,83
	15	9,55	2,05	−9,55	1,96
Straight	1	9,55	2,05	−9,55	1,96
	2	9,39	0,99	−9,39	0,91
	3	9,23	0,06	−9,23	−0,13
	4	9,07	−1,11	−9,07	−1,16
	5	8,91	−2,15	−8,91	−2,19
r_1	1	8,91	−2,15	−8,91	−2,19
	2	8,76	−2,96	−8,76	−3,00
	3	8,58	−3,76	−8,57	−3,79
	4	8,35	−4,53	−8,34	−4,56
	5	8,07	−5,30	−8,07	−5,32
	6	7,76	−6,04	−7,75	−6,06
	7	7,41	−6,77	−7,40	−6,78
	8	7,02	−7,48	−7,00	−7,49
	9	6,59	−8,17	−6,57	−8,18
	10	6,12	−8,33	−6,10	−8,84
	11	5,61	−9,48	−5,59	−9,49
	12	5,07	−10,10	−5,05	−10,11
	13	4,49	−10,70	−4,48	−10,71
	14	3,88	−11,27	−3,86	−11,29
	15	3,23	−11,82	−3,21	−11,85

research on the effectiveness of the profiling systems of hob sharpening machines (Fig. 10) have been presented: Bocian et al. (1977a, b, 1978), Miloiu and Visa (1983a, b, 1984a, b, 1985, 1987), Visa and Miloiu (1980a, b, 1983b, 1984).

In the Table 5 (Miloiu and Visa 1984b) several numerical results are presented, which allow the comparison of three systems being used for the profiling of the

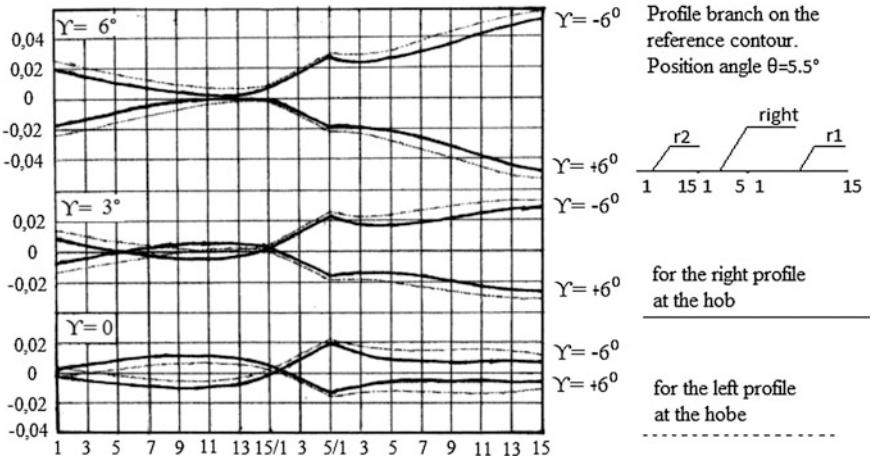

Fig. 8 Profile deviation at the cylinder type abrasive tool used to relief hobs $\chi = \pm 6°$ against the profile corresponding to re-sharpening $\chi = 0°$

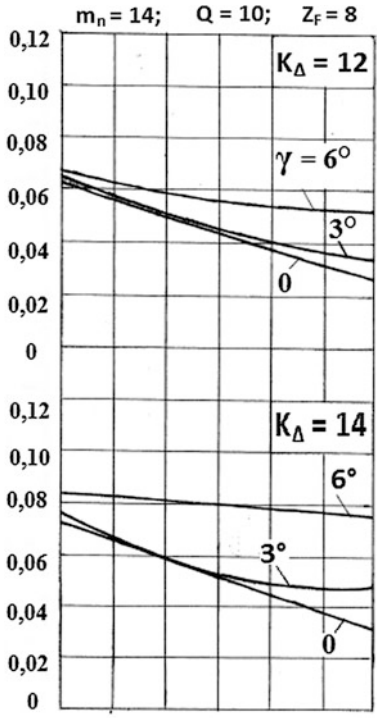

Fig. 9 The influence of the angle θ on the profile deviation

abrasive disc, between them and in relation to the tolerances admitted by the norms. Findings: (1) the smallest deviations are obtained at the elliptical profiling with three optimising parameters and at profiling by a trigonometric function;

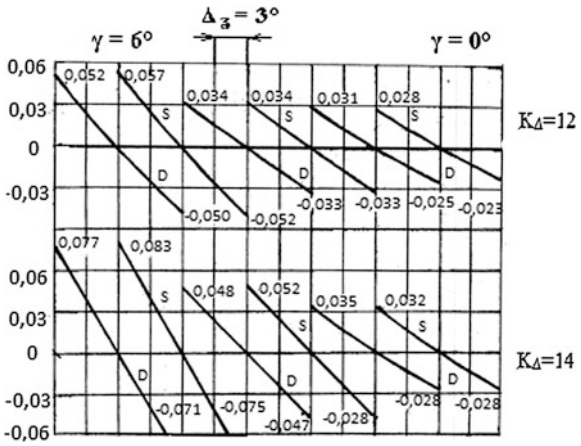

Fig. 10 The influence of re-sharpening on the profile deviation at the W–N hob: $m_n = 14$ $Q = 10$; $z_F = 8$; $\theta = 5.5°$; $K_\Delta = 12$; 14

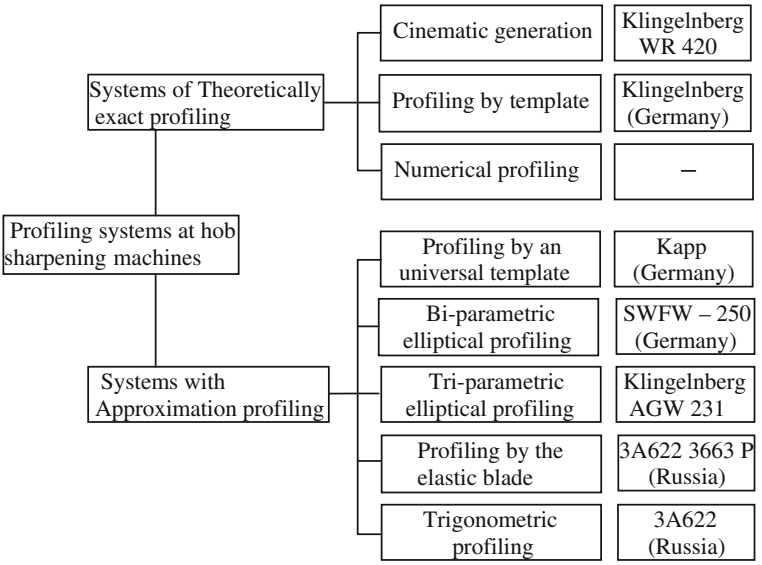

Fig. 11 The classification of the systems used to dress the sharpening disc for hobs with helicoidal grooves

(2) the profiling deviations of the system with elastic blade are 2–3 times bigger than those of the other two systems; (3) the profiling deviations increase with the angle of the sharpening helix and with the depth of the surface profiled.

Table 4 Fitting within class A, DIN 3968, of the theoretical profile errors of hobs used to cut W–N gears

Hob mn/ Q/K_{Δ}	γ degrees	Profile deviation μm at $\xi = \pm 3°$	Profile tolerance μm	Deviation/ tolerance %	The re-sharpening interval for class A	
					Degrees	mm
4/72/7	0	3,2	10	32	18,8	14,8
	3	7,3		73	8,2	6,5
	6	13,1		131	4,6	3,65
6/18/9	0	5	12	42	14,4	13,6
	3	10,8		90	6,7	6,3
	6	14		117	5,1	4,85
8/15/10	0	6,4	16	40	15	15,8
	3	13,4		84	7,2	7,6
	6	23,2		145	4,1	4,3
10/13,5/12	0	6,5	16	40,5	14,8	17,6
	3	13,8		86,5	6,9	8,2
	6	24		150	4	4,75
14/10/14	0	15	20	75	8	9,8
	3	25		125	4,8	5,9
	6	39		195	3,1	3,8
20/8,5/18	0	30	25	120	5	7,5
	3	45		180	3,3	4,9
	6	64		256	2,35	3,5

Table 5 The precision of sharpening disc profiling

Hobs		Profiling system	Disc and generation way		Optimising parameters, mm			Profile deviation, mm		
D m z_F	θ_0 p_E T		D_S	$\alpha = \eta$	I	II	III	Δ_{cf}	F^*_{fN}	Δ_{cf}/F_{fN} (%)
66,5	*6°19′38″*	Elliptical tri-parametric	200	15°	36,33	8,12	7,92	12,3	32	38
6	*1530*									
1	*20*	With elastic blade	200	20°	6,89	6,85	–	28	32	73
		Trigonometric profile	200	20°	–	–	–	17	32	53
175	*39°3′43″*	Elliptical tri-parametric	190	30°	42,01	−9,94	17,31	23,5	40	59
8	*600*									
16	*24*	With elastic blade	190	20°	14,44	16,84	–	21,4	40	178
		Trigonometric profile	190	20°	–	–	–	23	40	57

Fig. 12 Range of hobs used to cut W–N gears made by NEPTUN Campina

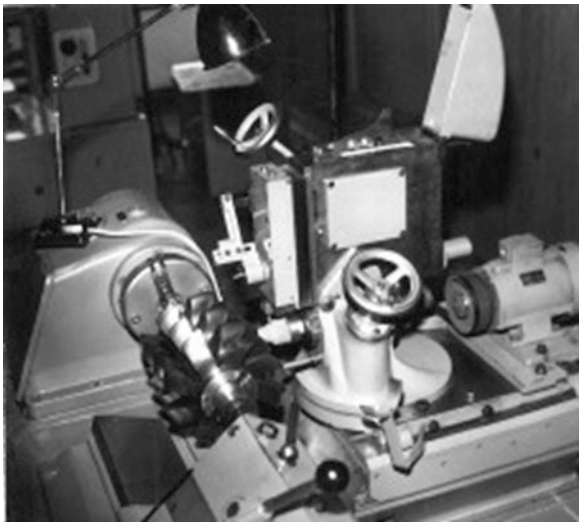

Fig. 13 Hob relieving on the machine HSF—33A—Klingelnberg

Fig. 14 Hob inspection on the device PWF 250—Klingelnberg

6 Technological Aspects

The author has made at the gearbox factory NEPTUN Campina hobs with the moduli $m_n = 4$; 10; 14 and 20 (Fig. 12). Profile sharpening, relieving and inspection have been done on Klingelnberg machines—see Figs. 13 and 14. Based on the coordinate profile (envelope worm) measuring settings have been done at the relieving machine; finally the hobs fitted within the precision class A to DIN 3968.

References

Bocian I (1976) The geometrical study of double-enveloping worm gears for increasing their Loading Capacity (in Romanian). Phd Thesis. Politechnic Institut of Cluj Napoca, p 178

Bocian I, Miloiu G (1977) Numerical approximation method for a given surface with a helical surface (in Romanian). News in design, technology and use of cutting devices, University of Brasov, pp 39–42

Bocian I, Visa F, Miloiu G (1977a) About eliptical approximation of the abrasive profile for hobbing cutters sharpening, hobbing cutters with helical channels (in Romanian).News in design, technology and use of cutting devices, University of Brasov, Brasov, pp 31–37

Bocian I, Visa F, Miloiu G (1977b) Numerical study of the cutting disc geometry used for sharpening the hobbing cutters with channels (in Romanian).News in design, technology and use of cutting devices, University of Brasov, Brasov, pp 23–29

Bocian I, Visa F, Miloiu G (1978) Problemes geometriques de l'affutage des fraises-meres à canaux en helicoïde. Word Symposium on gears and gear transmisions-IFToMM-JUDEKO, Dubrovnik-Kapari, vol C, pp 27–41

Fedeakin RV, Cesnokov VA (1958) Novikova helical gears. Vestnik mas-hinostroyenia (in Russian). vol 4, pp 3–11
Fukuoka (2001) JSME International Conference on Motion and Power Transmissions, 430 Fukuoka, Japan
GOST 18692 (1973) Finishing assembly single-start hobbing cutters for screw wheels Novikov's with double line of action (in Russian)
Gyenge C (1979) Contributions to the improved of high precision hobs used to cut Duplex worm gear (in Romanian). Phd Thesis, Politechnic Institut of Cluj Napoca, p 184
Hiltcher Y, Guingand M, de Vaujany JP (2006) Numerical simulation and optimization of worm gear cutting. Mech Mach Theory 41:1090–1110
Lashnev SI (1971) Processing tools gears with rack type (in Russian). Moscov, Izd.Mashinostroyenie, p 212
Litvin FL, Fuentes A (2009) Gear geometry and applied theory (in Romanian), Cambridge University press, Cambridge, p 1038
Liukshin VS (1968) Teoria vintovih poverhnostei, Mashinostroenie (Theory of helical surfaces, Mechanical Engineering), Moskva
Maros D (1971) Loi fundamentale de l'angrènement avec application au calcul cinématique de l'engrènement des flancs hélicoïdaux (in Romanian). Société d'Etudes de l'Industrie de l'Engrenage 62:3–75
Miloiu G (1964) Some basic problems concerning the accuracy of the Novikov –type helical gears (in Romanian). Constructia de masini (Machinery) 12:659–666
Miloiu G (1965) Checking the dimensions of Novikov gears (in Czech). Strojirenstvi (Machinery) 6:455–458
Miloiu G (1975) Contributions to the theoretical and experimental study of circular arch profile gears (in Romanian). Phd Thesis, University of Brasov, p 214
Miloiu G (1987) Algorithm for optimizing the geometry of hobs and estimate the errors of the generated gear wheel. Brasov University Bulletin, Serial A, vol XXIX, pp 121–132
Miloiu G (1990) Profile checking of hobbing cutters for non-involute gears. Revue Roumaine des Sciences Techniques, Ed Acad Romane 35(3)249–261
Miloiu G (1997) W-N gears: Romanian research and applications. MTM'97 –International Conference on Mechanical Transmissions and Mechanism,Tianjin, China, pp 533–538
Miloiu G, Visa F (1983) About the efficiency of profiling using elastic blades devices for hobbing cutters with wore beginnings (in Romanian). News in design, technology and use of cutting devices, University of Brasov, Brasov, pp 35–40
Miloiu G, Visa F (1984a) Sharpening of hobbing cutters standard STAS 3092/3-76 using machine type 3A 622-USSR (in Romanian). Constructia de masini (Machinery) (5):323–334
Miloiu G, Visa F (1984b) Profiling systems for the abrasion disc at hobbing cutters sharpening machines (in Romanian). Symposium of Fabrication of Machine Tools, I.M. Cugir, I:137–146 (12–13.07.1984)
Miloiu G, Visa F (1985) Researches regarding precision limits of the 3A622-USSR type machine for sharpening hobbing cutters used for processing worm gears (in Romanian). Constructia de masini (Machinery), (1):44–53
Miloiu G, Visa F (1987) Numerical researches on abrasive disk relieving devices at hob sharpening machines model 3A622, vol XXIX. Brasov University Bulletin, Brasov, Serial A, pp 133–145
Miloiu G, Dudita F, Diaconescu D (1980) Modern mechanical transmissions (in Romanian), II-nd edn. Tehnica, Bucuresti, p 552
Novikov ML (1956) U.S.S.R., Patent No. 109, 750
Radzevich SP (2007) On the accuracy of precision involute hobs: an analytical approach. J Manuf Process 9(2):121–135

Visa F, Miloiu G (1980a) Researches regarding the profiling with elastic blade devices for hobbing cutters sharpening (in Romanian). News in design, technology and use of cutting devices, University of Brasov, Brasov, pp 222–227

Visa F, Miloiu G (1980b) Geometrical problems encounted at using the abrasion disc, two parameters optimum eliptic form, used for sharpening the hobbing cutters (in Romanian). News in design, technology and use of cutting devices, University of Brasov, pp 210–221

Visa F, Miloiu G (1983) Numerical researches regarding elastical blade profiling devices efficiency used for sharpening machines for hobbing cutters. News in design, technology and use of cutting devices, University of Brasov, Brasov, pp 27–34

Visa F, Miloiu G (1984) Profiling systems for the abrasion disc at hobbing cutters sharppening machines (in Romanian), Symposium of fabrication of machine tools, I.M.Cugir, vol I, pp 147–153 (12–13.07.1984)

Wildhaber E (1923) Helical gearing. US patent no. 1 601 750

The Optimization of the Straight Bevel Gears Used in the Mechanical Transmissions of a PV Tracker

Gheorghe Moldovean, Bianca Butuc and Radu Velicu

Abstract In the context of nowadays economical development of the world, energy saving and obtaining energy from renewable sources are priority targets of many governments. As such, using tracking devices to optimise the energetic efficiency of the photovoltaic conversion systems represents a viable method from the economical and technical point of view. The efficiency and the durability of the tracking systems of photovoltaic platforms depend on the characteristics of their mechanical transmissions. Therefore, the straight bevel gears, as component parts of the mechanical transmissions of different tracking systems, must be designed considering the functional and constructive features of the tracking systems. This paper presents a calculus program, developed to generate the optimum constructive solution of a straight bevel gear of a particularly azimuthal tracking system; the calculus program is developed based on the indications and relations presented in the ISO 10300-1, 2, 3 standards.

Keywords Straight bevel gear · Optimization criteria · PV trackers

1 Introduction

The constructive optimization of a product is the process based on which the best solution for a particular product is determined. This optimization is based on the objectives to be achieved, on the restrictions and on variables that can be modified.

G. Moldovean (✉) · B. Butuc · R. Velicu
Transilvania University of Brasov, Brasov, Romania
e-mail: ghmoldovean@unitbv.ro

B. Butuc
e-mail: bia_butuc@yahoo.com

R. Velicu
e-mail: rvelicu@unitbv.ro

G. Dobre (ed.), *Power Transmissions*,
Mechanisms and Machine Science 13, DOI: 10.1007/978-94-007-6558-0_40,

A product having all the objectives optimized is not a realistic one due to the conflicting nature of the objectives to be optimized (Deaky 2009).

The objectives to be achieved in the designing process must be specified based on the product feasibility research. The non feasible solutions are not taken into consideration due to **the constraints**. Considering both the objectives and the constraints, the technical problem is identified and solved. Many possible solutions are generated in this way. They are analyzed considering the optimization criteria and are grouped in three categories of solutions: the accepted solutions, the rejected solutions and the ones that have to be modified. At the end of the process, the optimum solution is determined.

The designer has to decide on the optimum solution considering his experience. The researchers proposed different techniques for solving the multi-criteria optimization (known as multi-objectives optimization). The optimization algorithms are based on non linear techniques. The multi-criteria optimization are based on different algorithms: evolutive algorithms (Ghosh and Dehuri 2004), genetic algorithms (Tudose and Dumitru 2002), artificial intelligence (fuzzy-logical or neuronal) (Milčić and Miltenović 1999), algorithms based on intervals and criteria marks (Bobancu and Cioc 2003; Ichida and Fujii 1990). The optimization of the bevel gears is specified in literature by Rey (2004).

2 Criteria for the Optimizations of the Straight Bevel Gears

Based on the required input data such as torque transmission, operating speed, gear ratio and operating conditions, sizing relations for straight bevel gears are fulfilled by many values of the parameters included. Considering different ranges of these values, the number of the possible solutions decreases, but remains high enough. Therefore, the optimum constructive solution—that considers the specific constructive, technological and functional characteristics of the bevel gear—is determined considering one of the optimization methods presented in the branch literature.

In order to determine the optimum solution for the straight bevel gear this paper is proposing an optimization method based on certainty decisions. This method is also used and presented in several papers, such as (Deaky 2009) for cylindrical gears, and in (Velicu 1999) for planetary mechanisms. Using this method the best solution is selected considering all the quantities and quality criteria. The calculus program is using a method based on decisions made in certainty conditions (Velicu 1999).

The influence criteria that allow taking the proper decision have to consider the bevel gear characteristics, their application in the tracking system of the photovoltaic platforms and their target efficiency. For each criterion, the designer has to

decide on the mark assign N_i of a specific solution i ($i \in [1 \ldots k]$, k—number of possible solutions), considering the following conditions (Velicu 1999):

- The mark scale has to be the same for each criterion;
- The marks have to be as higher as the compliance is higher.

The goal function is given by the following relation (Velicu 1999)

$$F_i = \sum_{j=1}^{n} a_j N_{ji} \tag{1}$$

where a_j is the importance coefficient of the criterion j; n—the total number of the criteria; N_{ji}—the score for j criterion of i the solution.

The importance of the criterion is imposing the value of the a_j coefficient of each criterion. Thus, the value of the a_j coefficient has to be as high as more important the criterion is. The ranking of the k solutions is given by ordering the values of the goal function (1).

The **optimization criteria** imposed to the straight bevel gears are set in order to obtain a reduced overall size, a reduced precision of execution and high efficiency. When these conditions are fulfilled, the obtained bevel gear is characterized by low execution price and low energy losses. The proposed optimization criteria and the mathematical relations used to determine the score of each criterion are presented in Table 1.

The criterion of the **length of the exterior generator of the pitch cone, C_{Re}** considers the influence of the length of the exterior generator of the pitch cone, R_e, on the overall size of the bevel gear, aiming to minimize it.

The criterion of the **technological accuracy C_{trpr}** considers the influence of the technological accuracy on the execution cost, aiming to maximize the accuracy grade T_{rpr}.

Table 1 Mathematical model of optimization criteria

No.	Criterion	Mark
1.	Length of the exterior generator of the pitch cone, C_{Re}	$N_{C\,\mathrm{Rei}} = 10\frac{R_{e\max} - R_{ei}}{R_{e\max} - R_{e\min}};\ 0 \le N_{C\mathrm{Rei}} \le 10;$ $R_{e\max} = \max(R_{ei})_{i=1\ldots k};\ R_{e\min} = \min(R_{ei})_{i=1\ldots k};$
2.	Technological accuracy, C_{Trpr}	$N_{C\,Trpri} = 10\frac{Trpr_i - Trpr_{\min}}{Trpr_{\max} - Trpr_{\min}};\ 0 \le N_{C\,Trpri} \le 10;$ $Trpr_{\max} = \max(Trpr_i)_{i=1\ldots k};\ Trpr_{\min} = \min(Trpr_i)_{i=1\ldots k};$
3.	Gear efficiency, $C\eta$	$N_{C\eta i} = 10\frac{\eta_i - \eta_{\min}}{\eta_{\max} - \eta_{\min}};\ 0 \le N_{C\eta i} \le 10:$ $\eta_{\max} = \max(\eta_i)_{i=1\ldots k};\ \eta_{\min} = \min(\eta_i)_{i=1\ldots k};$
4.	Contact ratio, $C_{\varepsilon\upsilon\alpha}$	$N_{C\varepsilon\upsilon\alpha i} = 10\frac{\varepsilon_{\upsilon\alpha i} - \varepsilon_{\upsilon\alpha\min}}{\varepsilon_{\upsilon\alpha\max} - \varepsilon_{\upsilon\alpha\min}};\ 0 \le N_{C\varepsilon\upsilon\alpha i} \le 10:$ $\varepsilon_{\upsilon\alpha\max} = \max(\varepsilon_{\upsilon\alpha i})_{i=1\ldots k};\ \varepsilon_{\upsilon\alpha\min} = \min(\varepsilon_{\upsilon\alpha i})_{i=1\ldots k};$
5.	Precision of gear ratio $C_{\Delta u}$	$N_{C\Delta ui} = 10\frac{\Delta u_{\max} - \Delta u_i}{\Delta u_{\max} - \Delta u_{\min}};\ 0 \le N_{C\Delta ui} \le 10;$ $\Delta u_{\max} = \max(\Delta u_i)_{i=1\ldots k};\Delta u_{\min} = \min(\Delta u_i)_{i=1\ldots k};$
6.	Gear width, C_b	$N_{Cbi} = 10\frac{b_{\max} - b_i}{b_{\max} - b_{\min}};\ 0 \le N_{Cbi} \le 10;$ $b_{\max} = \max(b_i)_{i=1\ldots k};\ b_{\min} = \min(b_i)_{i=1\ldots k};$

The criterion of the **gear efficiency** $C\eta$ considers the mechanical energy losses due to the sliding friction, aiming to maximize the straight bevel gear efficiency.

The criterion of the **contact ratio** $C_{\varepsilon v}$ considers the influence of the contact ratio on the capacity of gear to transmit the load.

The criterion of the **gear ratio** $C_{\Delta u}$ aims to minimize the relative deviation Δu between the gear ratio imposed by specification u_{dat} and the real gear ratio. This deviation is determined by the following relation $\Delta u = |(u_{dat} - u)/u_{dat}|$.

The criterion of the **face width** C_b considers the influence of the straight bevel wheels face width on the axial overall size and on the volume of the material necessary, aiming to minimize the width of the bevel wheel b.

Based on the branch literature (Moldovean et al. 2002; Velicu et al. 2004), the following restrictions are imposed tot the straight bevel gears:

- Avoiding teeth profile interference;
- Achieving a minimum contact ratio $\varepsilon_{v\alpha\min} = 1.1$;
- Avoiding teeth sharpening $s_{ahm1} \geq s_{am\min}$ §i $s_{ahm2} \geq s_{am\min}$ ($s_{am\text{-}\min} = 0.25\ mm$—for wheels made from through hardened wrought steel; $s_{am\text{-}\min} = 0.4\ mm$—for wheels made from hardened wrought, nitriding or case hardened wrought steels);
- Choosing a minimum module considering the treatment of the steel ($m_{m\min} \geq 1.5$ mm, for wheels made from through hardened wrought steel, respectively $m_{m\min} \geq 2.0$ mm, for wheels made from hardened wrought, nitriding or case hardened wrought steels);
- Minimizing the effective contact stresses for fatigue stress, respectively the tooth root stress for static and fatigue bending, in order to be smaller than the allowable stresses, $\sigma_H \leq \sigma_{HP}$; $\sigma_{F1} \leq \sigma_{FP1}$, $\sigma_{F2} \leq \sigma_{FP2}$, respectively $\sigma_{F1St} \leq \sigma_{FP1St}$ §i $\sigma_{F2St} \leq \sigma_{FP2St}$.

3 Calculus Program for Multicriteria Optimization of the Straight Bevel Gears

The strength or the geometrical calculus of the straight bevel gear, based on ISO 10300-1 (2001), ISO 10300-2 (2001) and ISO 10300-3 (2001), are time consuming. To obtain the optimum solutions of straight bevel gears considering the criteria presented above, a specific programme calculus is developed and presented.

The main menu of the programme developed, is presented in Fig. 1. The main menu of the programme is divided in: *Input data*, *Optimization criteria* and *Results*.

The optimization programme is presented as an application example for a straight bevel gear used as a component in the mechanical transmission of a tracking system for photovoltaic platforms. The general scheme of this mechanical

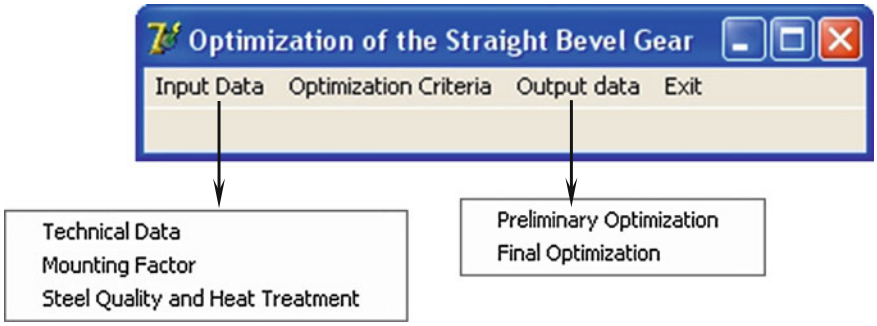

Fig. 1 The main menu of the programme

transmission, also presented in (Butuc et al. 2010; Moldovean et al. 2011, 2011), is design for a photovoltaic platform of 8 polycrystalline modules. The platforms dimensions are $H = 1{,}660$ mm şi $V = 990$ mm and the total weight (the modules and the frame) is $G = 1{,}820$ N. The main components of the mechanical transmission are presented in Fig. 2.

The input technical data, presented in Fig. 3, are: the maximum value of the torque at pinion, determined for the altitudinal tracking situation characterized by a trapezoidal pressure wind distribution and a medium pressure coefficient of $c_p = 1.2$ (Moldovean et al. 2011); the total running hours for a lifetime of 25 years; the gear ratio deviation $\Delta u = \pm 3$ %; the dynamic factor is $K_A = 1$ due to overvaluation of the wind load.

The elements that are modified in order to determine the optimum solution are the number of the teeth z_1 of the pinion, profile shift coefficient x_{hm1}, the thickness modification coefficient x_{sm1} and the width coefficient ψ_R.

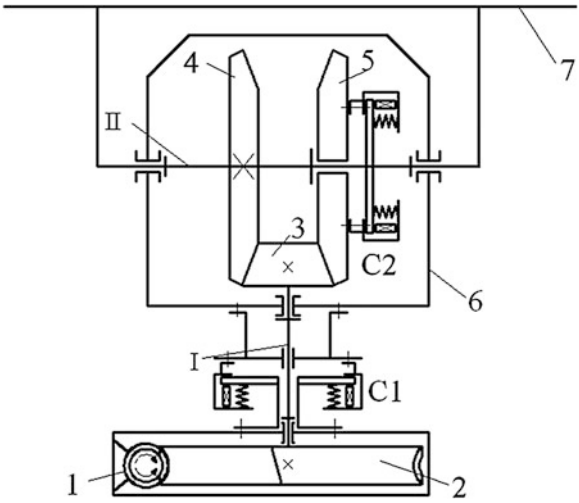

Fig. 2 The conceptual scheme of the photovoltaic platform: *1* worm; *2* worm wheel; *3* bevel pinion; *4*, *5* bevel wheels; *6* housing; *7* photovoltaic platform; *C1*, *C2* clutches

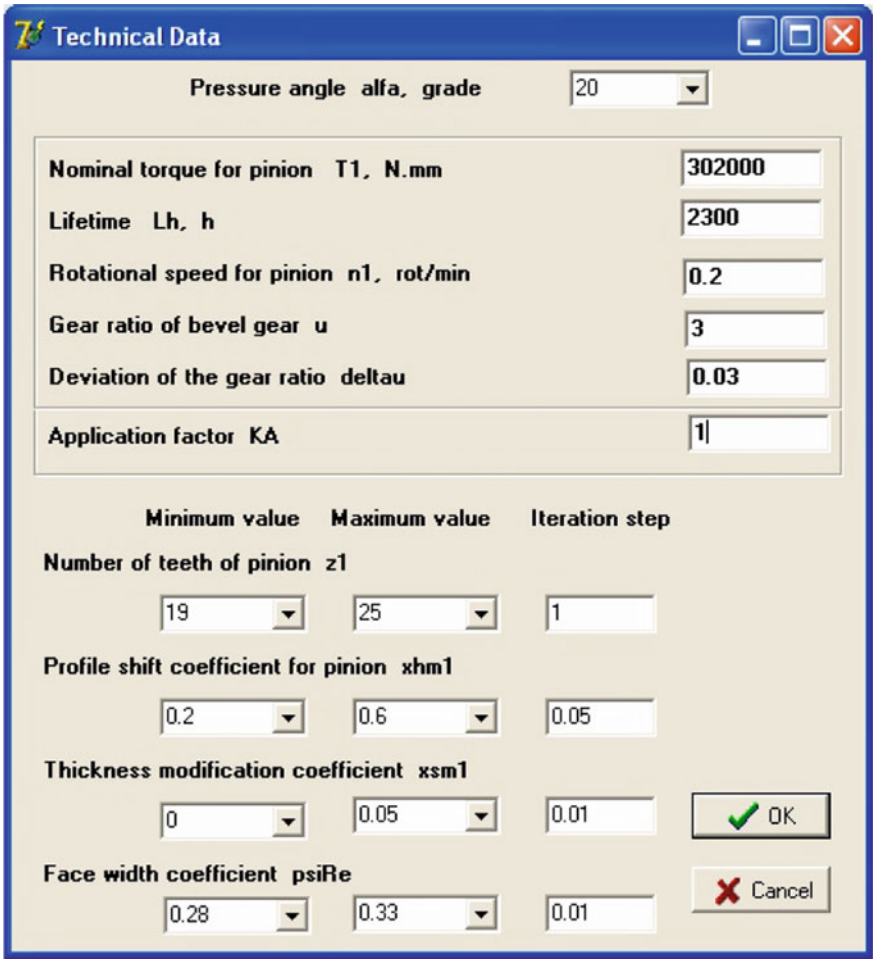

Fig. 3 Technical data window

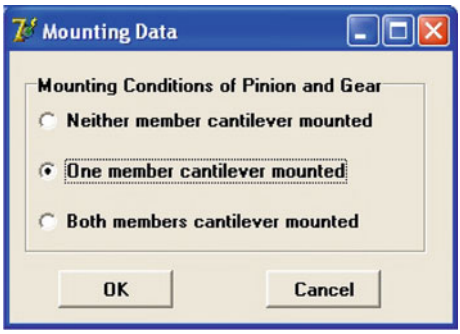

Fig. 4 Wheels mounting position

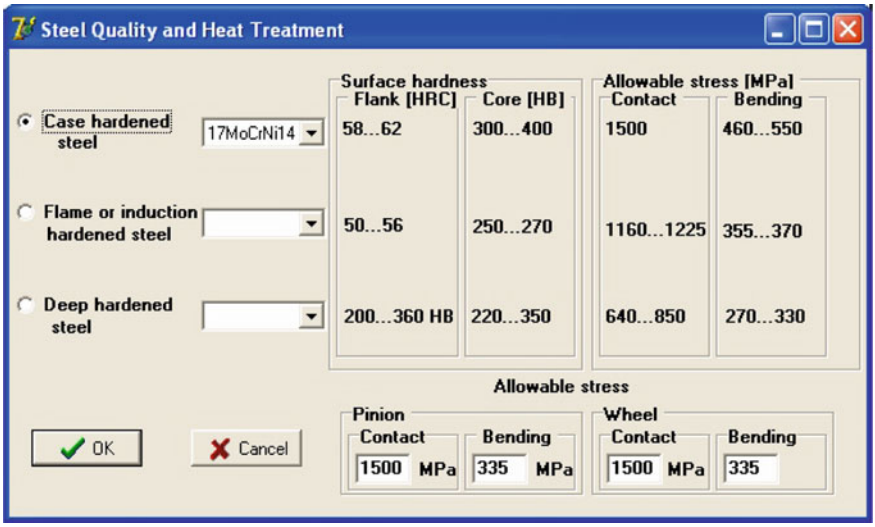

Fig. 5 Steel quality and heat treatment user interface window

For the determination of the face load factor it is necessary to define the position of pinion and wheel in accordance to the shaft bearings. By choosing *Mounting conditions of pinion and gear* a user interface window is opened, as presented in Fig. 4. The user has to select one of the possible mounting solutions.

By choosing *Steel Quality and Heat Treatment*, the user interface window, presented in Fig. 5, is opened. The user has to select the type of the steel and the treatment, the surface and core hardness after the treatment, the allowable stresses

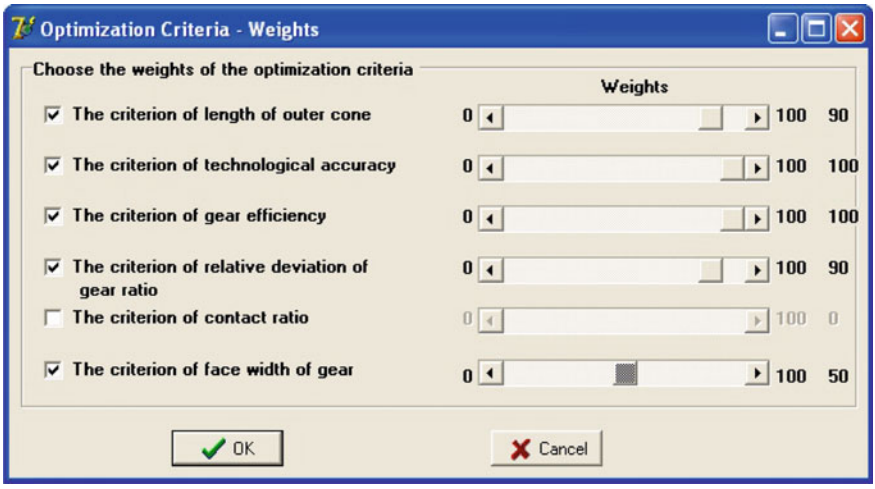

Fig. 6 The weights of the optimization criteria

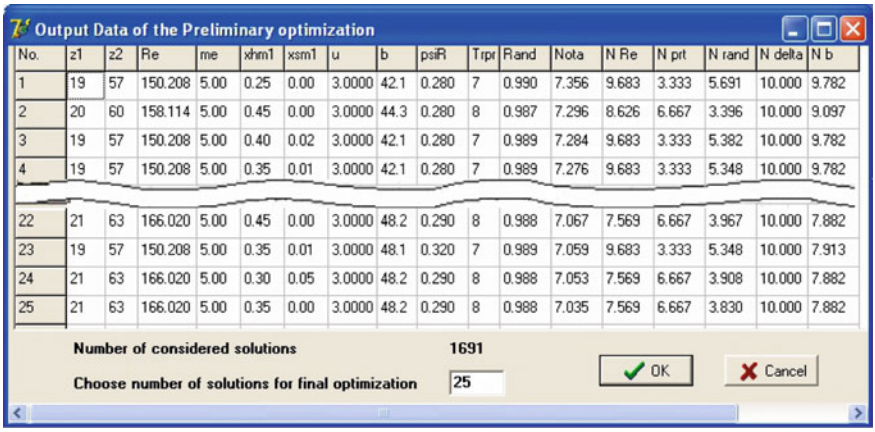

No.	z1	z2	Re	me	xhm1	xsm1	u	b	psiR	Trpr	Rand	Nota	N Re	N prt	N rand	N delta	N b
1	19	57	150.208	5.00	0.25	0.00	3.0000	42.1	0.280	7	0.990	7.356	9.683	3.333	5.691	10.000	9.782
2	20	60	158.114	5.00	0.45	0.00	3.0000	44.3	0.280	8	0.987	7.296	8.626	6.667	3.396	10.000	9.097
3	19	57	150.208	5.00	0.40	0.02	3.0000	42.1	0.280	7	0.989	7.284	9.683	3.333	5.382	10.000	9.782
4	19	57	150.208	5.00	0.35	0.01	3.0000	42.1	0.280	7	0.989	7.276	9.683	3.333	5.348	10.000	9.782
22	21	63	166.020	5.00	0.45	0.00	3.0000	48.2	0.290	8	0.988	7.067	7.569	6.667	3.967	10.000	7.882
23	19	57	150.208	5.00	0.35	0.01	3.0000	48.1	0.320	7	0.989	7.059	9.683	3.333	5.348	10.000	7.913
24	21	63	166.020	5.00	0.30	0.05	3.0000	48.2	0.290	8	0.988	7.053	7.569	6.667	3.908	10.000	7.882
25	21	63	166.020	5.00	0.35	0.00	3.0000	48.2	0.290	8	0.988	7.035	7.569	6.667	3.830	10.000	7.882

Fig. 7 The results of the preliminary optimization

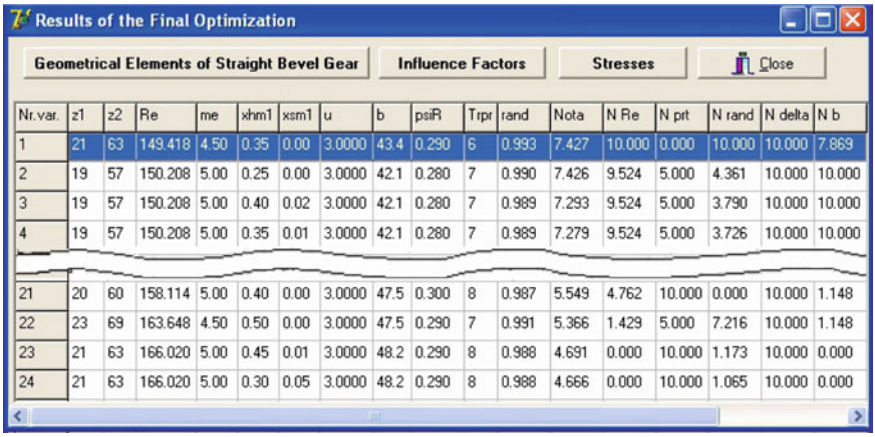

Nr.var.	z1	z2	Re	me	xhm1	xsm1	u	b	psiR	Trpr	rand	Nota	N Re	N prt	N rand	N delta	N b
1	21	63	149.418	4.50	0.35	0.00	3.0000	43.4	0.290	6	0.993	7.427	10.000	0.000	10.000	10.000	7.869
2	19	57	150.208	5.00	0.25	0.00	3.0000	42.1	0.280	7	0.990	7.426	9.524	5.000	4.361	10.000	10.000
3	19	57	150.208	5.00	0.40	0.02	3.0000	42.1	0.280	7	0.989	7.293	9.524	5.000	3.790	10.000	10.000
4	19	57	150.208	5.00	0.35	0.01	3.0000	42.1	0.280	7	0.989	7.279	9.524	5.000	3.726	10.000	10.000
21	20	60	158.114	5.00	0.40	0.00	3.0000	47.5	0.300	8	0.987	5.549	4.762	10.000	0.000	10.000	1.148
22	23	69	163.648	4.50	0.50	0.00	3.0000	47.5	0.290	7	0.991	5.366	1.429	5.000	7.216	10.000	1.148
23	21	63	166.020	5.00	0.45	0.01	3.0000	48.2	0.290	8	0.988	4.691	0.000	10.000	1.173	10.000	0.000
24	21	63	166.020	5.00	0.30	0.05	3.0000	48.2	0.290	8	0.988	4.666	0.000	10.000	1.065	10.000	0.000

Fig. 8 The results of the final optimization

for contact and bending for the pinion and the wheel. The allowable bending stress is determined considering that the wheel teeth are subjected to the alternate-symmetrical cycle, and therefore, in accordance tot ISO 6336-5 the allowable tension must be reduced by 30 %.

After the input data are set, the optimization criteria and their weights are selected, as presented din Fig. 6. In this specific case, only 5 criteria of 6 have been selected as the contact gear ratio criterion is excluded, due to the low functioning speed.

The technological accuracy and the gear efficiency criteria were considered the most important, thus the corresponding weights for these criteria are set to 100 %. For the length of the exterior generator of the pitch cone and precision of the gear

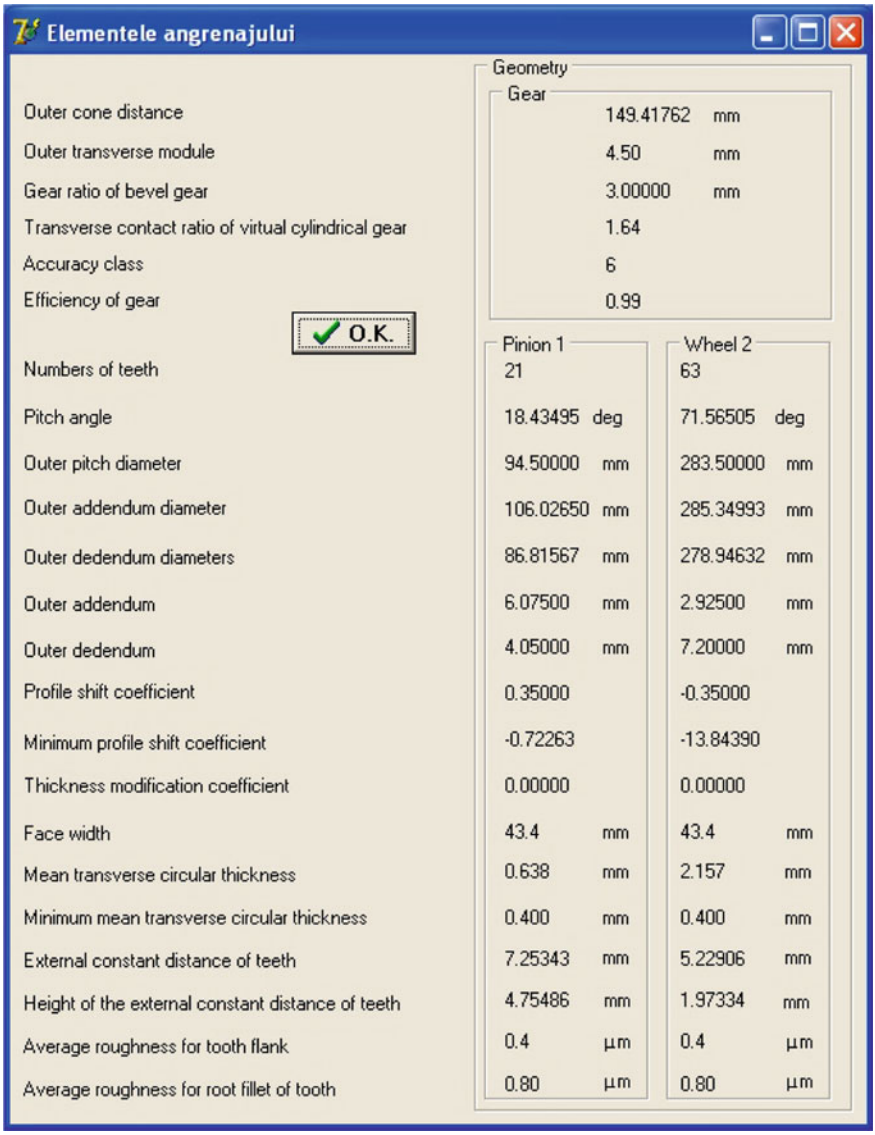

Fig. 9 The geometrical elements of the straight bevel gear

ratio criteria the weight was set at 90 %, while for gear width criteria was considered 50 %. Considering the weight values, the importance coefficients are determined $a_{1...6}$ ($a_5 = 0$), see relation (1).

Some results of the preliminary optimization for the analysed case are presented in Fig. 7. It can be noticed that are 1,691 solutions that fulfil the imposed restrictions and that the best solution mark is 7.356. For this particularly case of straight bevel

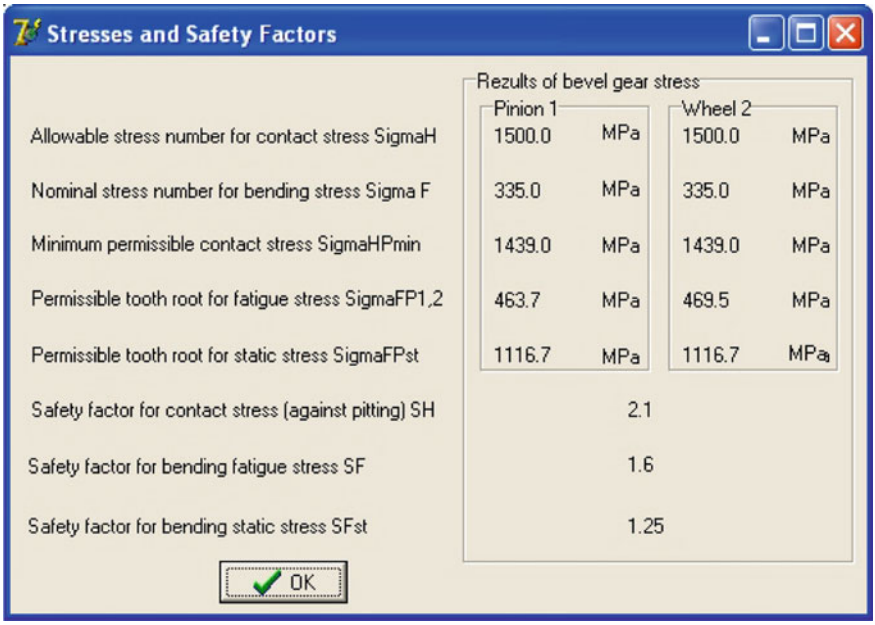

Fig. 10 The stresses and the safety coefficients of the straight bevel gear

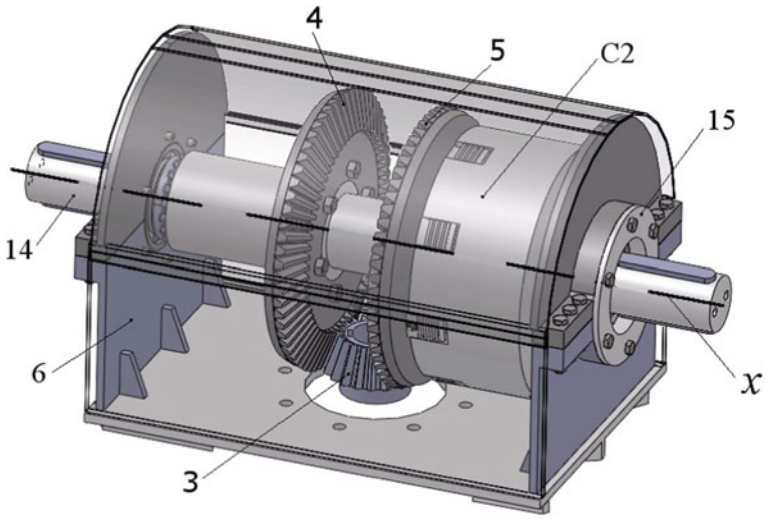

Fig. 11 The constructive solution of the *x* axis—the altitudinal movement

gear were considered 25 variants, reorder in accordance with their marks as presented in Fig. 8 (Butucet al. 2011). The first optimum solution obtained after the preliminary optimization is the second optimum final solution. The first optimum

final solution is the sixth solution of the preliminary optimization. All the others solutions are different due to the modification of the minimum mark of each criterion as the number of the solution were reduced.

The main advantages of the first solution, in comparison with the second one, are the reduced overall size (characterised by the shortest length of the generator of the cone pitch and by the smallest gear module), the highest efficiency ($\eta = 99.3$ %) and a gear ratio equal to the one imposed by specifications. The disadvantage of this solution is given by the technological accuracy 6, compared to the second optimum solution characterised by a technological accuracy of 7.

By selecting the row corresponding to the optimal solution, all the geometrical elements of the gear, the calculus factors and the allowable stresses for bending and contact are calculated again. The results are presented in Figs. 9 and 10.

Figure 11 presents the virtual model of the altitudinal axis of the tracking system consisted of the double straight bevel gear 3-4-5, the clutch C2, the shaft 14 and the housing 6. This assembly was also presented in Butuc et al. 2010 and Moldovean et al. 2010).

4 Conclusions

The conclusions of the analysis of the safety coefficients are:

- The highest value of the safety coefficient is obtained for contact, therefore the contact stress is less important;
- The lowest value of safety coefficient is obtained for the static bending stress, therefore this is the most important stress; considering that the effective static bending stress is determined for a wind speed of 30 m/s (110 km/h), the safety coefficient of $S_{Fst} = 1.25$ ensures an adequate strength for the designed photovoltaic platform.

References

Bobancu S, Cioc V (2003) Secţiunea I: Calculul armoniei proporţiilor şi culorilor. Secţiunea II: Prelevare şi prelucrare de imagine. Seria "Inovare Inginerească în design", Braşov, Editura Universităţii Transilvania

Butuc B, Moldovean G, Velicu R (2011) Implementation of gear transmissions in photovoltaic solar tracking systems. Balkan J Mech Transm 1(1):22–27

Butuc B, Lateş M, Moldovean G (2010) FEM analysis of the bevel gear housing of an azimuthal tracked PV platform. In: Annals of the Oradea University, Fascicle of Management and Technological Engineering, vol 9(19), issue 2

Deaky BA (2009) Analiza şi optimizarea multicriterială a angrenajelor cilindrice exterioare. Teză de doctorat, Universitatea Transilvania din Braşov

Ghosh A, Dehuri S (2004) Evolutionary algorithms for multi-criterion optimization: a survey. Int J Comput Inf Sci 2(1):38–57

Ichida K, Fujii Y (1990) Multicriterion optimization using interval analysis. Computing 44(1):47–57
ISO 10300-1 (2001) Calculation of load capacity of bevel Gears. Introduction and general influence factors. International standard
ISO 10300-2 (2001) Calculation of load capacity of bevel Gears. Calculation of surface durability (pitting). International standard
ISO 10300-3 (2001) Calculation of load capacity of bevel Gears. Calculation of tooth root strength. International standard
Milčić D, Miltenović V (1999) Application of artificial intelligence methods in gear transmitters. Conceptual design. Facta Universitas, University of Niš, Series "Mechanical Engineering", vol 1, issue 6, pp 721–734
Moldovean G et al (2002) Angrenaje cilindrice şi conice. Metodici de proiectare. Brasov, Editura Lux Libris
Moldovean G, Butuc BR, Velicu R (2010) Dual axis tracking system with a single motor. In: New trends in mechanism science. Analysis and design, series: mechanisms and machine science, vol 5, pp 649–656
Moldovean G, Butuc B, Velicu R, Gavrila CC (2011) Mechanical efficiency of straight bevel gears used in photovoltaic trackers depending on geometrical parameters. In: The 13th world congress in mechanism and machine science, Guanajuato, México, A9-387, pp 1–10
Moldovean G, Velicu R, Butuc B (2011) On the influence of geometry over the transverse load factor for bending stress of the straight bevel gears applied to a PV tracking system. In: The 7th international conference research and development of mechanical elements and systems, IRMES, Zlatibor, Serbia, pp 515–520
Moldovean G, Butuc B, Velicu R (2011) Shafts design of a gear based azimuthal tracked photovoltaic platform. Environ Eng Manage J 10(9): 1291–1298 (Iaşi, Romania)
Rey GG (2004) An optimized approach to straight bevel gear design. Gear Solutions 40–47
Tudose L, Dumitru P (2002) Proiectare optimală cu algoritmi genetici. Cluj-Napoca, Editura Mediamira
Velicu R (1999) Cercetări asupra transmisiilor planetare de putere. Teză de doctorat. Universitatea Transilvania din Braşov
Velicu D, Moldovean G, Velicu R (2004) Proiectarea angrenajelor conice si hipoide. Editura Universitatii Transilvania din Brasov

Pareto Approach in Multi-Objective Optimal Design of Single-Row Cylindrical Rolling Bearings

Lucian Tudose, Gyorgy Kulcsar and Cristina Stănescu

Abstract Even if it seems simple, the design of the rolling bearings is a difficult task for mechanical engineering. Their specific structure and the involved tribological phenomena in their operation lead to many and complex calculations of rolling bearings. Consequently, to find the optimal design of the rolling bearings the Multi-Objective Optimization should be used. In this paper, two objective functions (the basic dynamic radial load rating of the bearing and the minimum thickness of the elastohydrodynamic film between rollers and raceways) are optimized using multi-objective Evolutionary Algorithms (EAs) in order to obtain the optimal design of a single-row cylindrical roller bearing. Three design variables (the complex factor γ, the roller diameter, and the roller length) were used to fully, completely, and uniquely describe the bearing geometry and to construct the objective functions and the constraints. To solve this optimal design problem the authors used Cambrian optimization platform.

Keywords Rolling bearings · Multi-objective optimization · Pareto set · Evolutionary algorithms

List of Symbols

B	Bearing width, $B = 100$ mm
C_r	Bearing dynamic radial load rating, N
d	Bore diameter of the bearing, $d = 460$ mm
D	Outer diameter of the bearing, $D = 680$ mm
D_{pw}	Pitch diameter, mm

L. Tudose (✉) · G. Kulcsar · C. Stănescu
Technical University of Cluj-Napoca, Cluj-Napoca, Romania
e-mail: Lucian.Tudose@omt.utcluj.ro

G. Kulcsar
e-mail: kulcsar_gyorgy@yahoo.com

C. Stănescu
e-mail: Cristina.Stanescu@omt.utcluj.ro

G. Dobre (ed.), *Power Transmissions*,
Mechanisms and Machine Science 13, DOI: 10.1007/978-94-007-6558-0_41,

D_{we} Roller diameter, mm
F_r Bearing radial load, N
G Material parameter
h_{min_i} Minimum lubricant film thickness in inner ring raceway-roller line contact, μm
h_{min_o} Minimum lubricant film thickness in outer ring raceway-roller line contact, μm
i Number of roller rows
I Maximum interference, mm
L_w Roller length, mm
L_{we} Effective roller length, mm
Q Radial load acting on the most loaded roller, N
R_r Reduced curvature radius of the contact, mm
U Speed parameter
W' Load parameter
Z Numbers of rollers
α Nominal contact angle, rad
γ Complex factor
δ_c Tenon thickness, mm
δ_{cmin} Minimum tenon thickness, mm
δ_i Inner ring thickness, mm
δ_{imin} Inner ring minimum thickness, mm
δ_o Outer ring thickness, mm

1 Introduction

Because rolling bearings decisively influence the operating accuracy and all sorts of costs of the machines in which they operate, to develop an optimal design of them it becomes very important and this will certainly have a big impact on both their and machine performance and life. Two aspects are the most important here: the basic rating life of the rolling bearing and rolling bearing lubrication, respectively. Since bearing basic rating life impact is clear, recall that the lubricant in rolling bearings mainly serves to avoid or least reduce metal-to-metal contact between the rolling and sliding contact surfaces and to remove the contaminants and the heat between them. If a sufficiently thick lubricant film cannot be formed between the rolling elements and raceways, metal-to-metal contacts occur, and that will dramatically reduce the life of the bearing. Because rolling bearings have a specific design and there are many tribological phenomena involved during their operation, a single objective is not enough for constructing an optimization problem which accurately models the complex reality of rolling bearing operation.

Many scientific papers have been reported on optimization of different machine elements, but there are very few papers available focused on the optimization of the rolling bearings. Chakrabotrhy et al. (2003) describes the optimization of a ball bearing having five design parameters (diameter of the ball, number of balls, pitch diameter, curvature radius coefficient of the outer raceway groove, and curvature radius coefficient of the inner raceway groove) using genetic algorithms. The objective of the problem was the fatigue life which is maximized. Limitation of this work was the use of a single objective function and some constraints were clearly unrealistic. Rao and Tiwari (2007) also have developed a mono objective optimal design methodology of ball bearing using genetic algorithms. The objective function was the lifetime which is maximized, considering a set of constraints. The genes of the problem were: bearing pitch diameter, the rolling element diameter, number of rolling elements and inner and outer race groove curvature radii. The fatigue life obtained after optimization was compared to bearing fatigue life calculated with the bearing capacity extracted from catalogues. Gupta and Tiwari (2006) described a multi-objective optimization problem. The used tree objectives were: the dynamic capacity, the static capacity and the elastohydrodynamic minimum film thickness. They were optimized separately, pairwise and simultaneously using the well known multi-objective optimization algorithm NSGA II (non-dominated sorting based genetic algorithm). The limitation of this approach was the use of non-conflicting objectives and only of geometrical constraints. After the authors of this paper knowledge, in the open literature, there are no papers available in which cylindrical roller bearing optimization is presented. In a recently published book (Rao and Savsani 2012) solely the previously mentioned paper is presented, and that indicates that a scientific study in this area becomes very important.

The cylindrical roller bearings are best suited of all bearings where there are particularly heavy radial loads combined with high speeds, especially if there is a limited amount of axial displacement of the shaft (as a result of thermal elongation) with respect to the bearing housing. The single-row cylindrical roller bearings have the advantage of a simple installation, especially in the case when an interference fit is required for both rings, because they are separable and thus the ring with cage and roller assembly can be mounted independently of the other ring. Cylindrical roller bearings are produced in many design, the main difference between them consist in the configuration of the flanges. The well-known cylindrical bearings designs are: NU, N, NJ, and NUP, but also there are available specials designs (e.g., NUB, NF, NJP NP, etc.). This paper is focused on the optimization of a single-row cylindrical roller bearing with NP special design. The authors' experience in the field of machine element optimal deign showed that the Evolutionary Algorithms (EAs) are the most suitable to accomplish this task.

2 Multi-Objective Evolutionary Algorithms

The problem of multi-objective optimization can be represented as (Fig. 1):

In case of MOO, optimization means finding a solution having values, for all objective functions, that satisfy the decision maker. Because there are many and more likely conflicting objectives to be optimized simultaneously, there is no longer a single optimal solution but rather a whole set of possible solutions of equivalent quality. Generally speaking, in MOOPs two different solutions are related to each other in two possible ways (Fig. 2a): either one dominates the other or none of them is dominated.

The optimal solution of a MOO is not a single solution but a set of solutions composed of all the potential solutions such that the components of the objectives vector cannot be simultaneously improved. The set of Pareto solutions consists of good solutions, where none can be said to be better than the others (i.e. the set of non-dominated solutions). The authors considered that the most convenient way to obtain the Pareto set and the Pareto front is via EAs. The Fig. 2b shows a structure of a simple evolutionary algorithm. Further information reader can find in Yu and Gen (2010) and Sivanandam and Deepa (2008), respectively.

3 Multi-Objective Optimization of the Cylindrical Roller Bearing Np1092

In this paper, two objective functions, namely, the basic dynamic radial load rating C_r of a single-row cylindrical roller bearing and the minimum thickness h_{min} of the lubricant elastohydrodynamic film along the line contact between rollers and raceways were set in order to obtain the optimal design of bearing NP1092.

3.1 Geometry of the Cylindrical Roller Bearing NP 1092

The geometry of a cylindrical roller bearing is presented in Fig. 3.

$$\text{design vector } \bar{x} = (x_1, x_2, \ldots, x_P)$$

$$\text{objective functions} \begin{cases} f_1(\bar{x}) \rightarrow \textbf{min } or \textbf{ max} \\ f_2(\bar{x}) \rightarrow \textbf{min } or \textbf{ max} \\ \ldots\ldots\ldots\ldots\ldots\ldots\ldots\ldots \\ f_M(\bar{x}) \rightarrow \textbf{min } or \textbf{ max} \end{cases} \qquad \text{constraints} \begin{cases} g_1(\bar{x}) \lhd 0 \\ g_2(\bar{x}) \lhd 0 \\ \ldots\ldots\ldots \\ g_Q(\bar{x}) \lhd 0 \end{cases}$$

$$\text{"}\lhd\text{" means "}\leq\text{", "}<\text{", "}\geq\text{", "}>\text{", or "}=\text{"}$$

Fig. 1 Multi-objective optimization problem

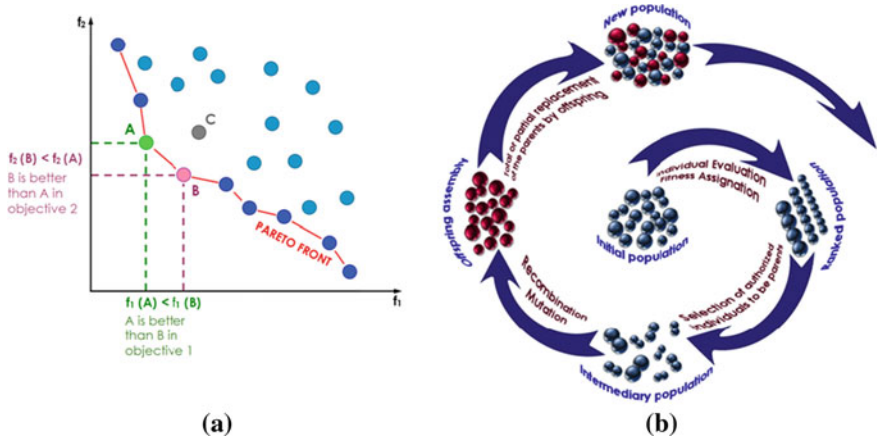

Fig. 2 **a** Pareto front (Either *A* or *B* dominates *C*, *A* and *B* do not dominate each other). **b** Simple evolutionary algorithm

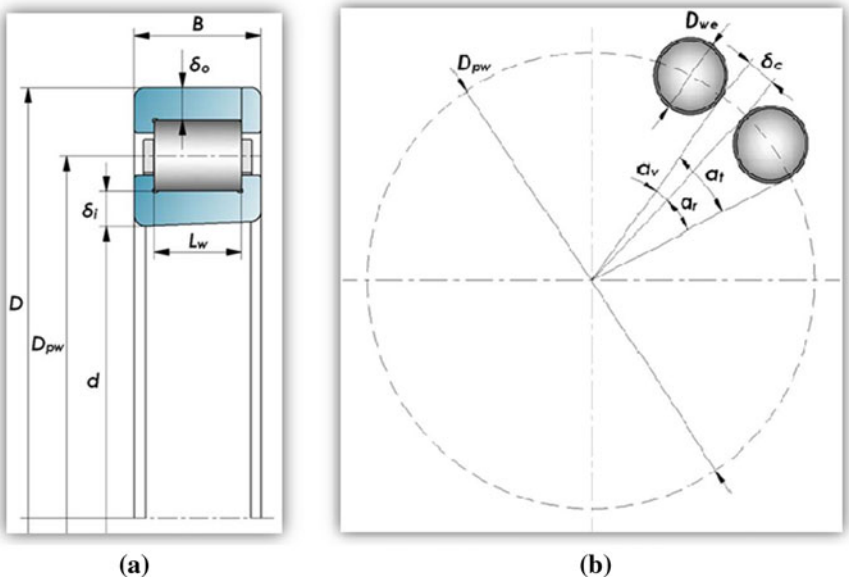

Fig. 3 **a** Geometry of the cylindrical roller bearing NP1092. **b** Rollers distribution along the pitch circle

The well-known complex factor γ is given by:

$$\gamma = \frac{D_{we} \cdot \cos \alpha}{D_{pw}} = \frac{D_{we}}{D_{pw}} \tag{1}$$

The exact value of the tenon space thickness (Fig. 3b) can be calculated using the following equation:

$$\delta_c = \frac{D_{we}}{\gamma}\sin\left[\frac{\pi}{Z} - \arccos\left(1 - \frac{1}{2}\gamma^2\right)\right] \tag{2}$$

but, it is more convenient to be approximate by:

$$\delta_c \approx \frac{D_{we}}{\gamma}\cdot\left(\frac{\pi}{Z} - \gamma\right) \tag{3}$$

In order to reduce the number of design variables the number of roller Z was calculated using the equation:

$$Z = \text{floor}\left(\frac{\pi}{\gamma}\cdot\frac{D_{we}}{D_{we} + \delta_{c\min}}\right) \tag{4}$$

3.2 Design Variables

The bearing internal geometry was uniquely described by means of three genes which are presented together with their range, type, and precision in Table 1.

3.3 Objective Functions

The first objective function is the basic dynamic radial load rating (according to ISO 281:2007 and Harris and Kotzalas 2007) and it should be maximized:

$$C_r(\gamma,\ D_{we},\ L_{we}) = f_{Cr}(\gamma)\cdot L_{we}^{\frac{7}{9}}\cdot D_{we}^{\frac{29}{27}} \quad \rightarrow \quad \mathbf{max} \tag{5}$$

where:

$$f_{Cr}(\gamma) = 189.70078\cdot\gamma^{\frac{2}{9}}\cdot(1-\gamma)^{\frac{29}{27}}\cdot(1+\gamma)^{-\frac{1}{4}} \cdot\left[1 + 1.19303\cdot\left(\frac{1-\gamma}{1+\gamma}\right)^{\frac{143}{24}}\right]^{-\frac{2}{9}}\cdot\left[\text{floor}\left(\frac{2.70827}{\gamma}\right)\right]^{\frac{3}{4}} \tag{6}$$

Table 1 The design parameters

No	Gene	Symbol	Range	Type	Precision
1	Complex factor	γ	0…0.3	Real	10^{-6}
2	Roller diameter	D_{we}	1…100 mm	Integer	10^{0}
3	Roller length	L_w	5…200 mm	Integer	10^{0}

According to Dowson and Higginson (1966) the minimum lubricant film thickness h_{min} in the area of a rolling line contact is:

$$h_{\min} = 2.65 \cdot U^{0.7} \cdot G^{0.54} \cdot W'^{-0.13} \cdot R_r \tag{7}$$

The second objective function was considered the minimum value from h_{min_i} and h_{min_o} (minimum lubricant film thickness in inner/outer ring raceway/roller contact) and it also should be maximized:

$$h_{\min}(\gamma,\ D_{we},\ L_{we}) = f_{h\_\min}(\gamma) \cdot L_{we}^{0.02889} \cdot D_{we}^{0.99037} \rightarrow \mathbf{max} \tag{8}$$

where,

$$\begin{aligned} f_{h\_\min}(\gamma) = {} & 3.264924 \cdot 10^{-3} \cdot \gamma^{-0.72889} \cdot \left[1 + 1.19303 \cdot \left(\frac{1-\gamma}{1+\gamma}\right)^{\frac{143}{24}}\right]^{0.02889} \\ & \cdot (1-\gamma)^{0.56037} \cdot (1+\gamma)^{0.4625} \cdot \left[\text{floor}\left(\frac{2.70827}{\gamma}\right)\right]^{0.0325} \cdot \min\left[\left(\frac{1-\gamma}{1+\gamma}\right)^{0.43},\ 0.61557\right] \end{aligned} \tag{9}$$

In the above calculation the authors have considered the actual bearing radial load as a fraction p_c of the basic dynamic radial load rating:

$$F_r = p_c \cdot C_r \tag{10}$$

It was assumed that $p_c = 0.15$ means the frontier between a loaded and a very loaded bearing. In the following this value was used and the radial load acting on the most loaded roller is given by the equation:

$$Q = \frac{5 \cdot \frac{F_r}{i}}{Z \cdot \cos\alpha} = \frac{5 \cdot p_C \cdot C_r}{Z} \tag{11}$$

3.4 Constraints

The constraints of an optimization problem reduce the parameter space to the feasible parameter space. This section summarizes the eight constraints of the multi-objective optimization problem.

C1. The roller diameter D_{we} must be greater than or equal to a required value, D_{we_min}:

$$D_{we} \geq D_{we\_\min} = 0.225 \cdot (D - d) \tag{12}$$

C2. The roller diameter D_{we} must be less than or equal to an imposed value, D_{we_max}:

$$D_{we} \leq D_{we\_\max} = 0.275 \cdot (D - d) \tag{13}$$

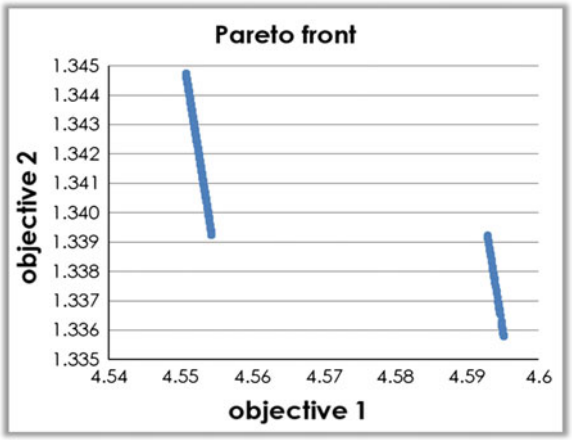

Fig. 4 Pareto front

C3. Difference between inner and outer ring thickness has to be greater than or equal to a minimum value:

$$\delta_i - \delta_o \geq \delta_{io\_\min} = 2\,\text{mm} \tag{14}$$

C4. Difference between inner and outer ring thickness has to be less than or equal to a maximum imposed value:

$$\delta_i - \delta_o \leq \delta_{io\_\max} = 5\,\text{mm} \tag{15}$$

C5. Circumferential distance (tenon thickness) δ_c between rollers, measured on the pitch circle, has to be greater than or equal to a minimum value, δ_{c_min}:

$$\delta_c \geq \delta_{c\_\min} = 0.16 \cdot D_{we} \tag{16}$$

C6. Circumferential distance (tenon thickness) δ_c between rollers, measured on the pitch circle, has to be less than or equal to a maximum value, δ_{c_max}:

$$\delta_c \leq \delta_{c\_\max} = 0.25 \cdot D_{we} \tag{17}$$

C7. Roller length L_w has to be less than or equal to a maximum imposed value, L_{w_max}:

$$L_w \leq L_{w\_\max} = 0.69 \cdot B \tag{18}$$

C8. The maximum hoop stress σ_{hoop} along inner ring cross-section must be less than or equal to the allowable hoop stress (for a maximum value, $I = 0.3$ mm, of the interference):

$$\sigma_{hoop} \leq \sigma_{hoop\_all} = 150\,\text{MPa} \tag{19}$$

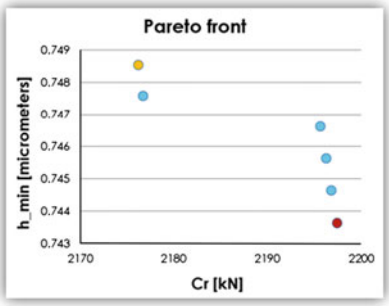

(a)

D_{pw} [mm]	D_{we} [mm]	Z	C_r [kN]	h_{min} [μm]
575	60	25	2176.269	0.74854
574	60	25	2176.816	0.74756
575	59	26	2195.744	0.74660
574	59	26	2196.307	0.74561
573	59	26	2196.869	0.74462
572	59	26	2197.432	0.74364

(b)

Fig. 5 **a** Solutions from Pareto front. **b** Design variables and objective functions

Fig. 6 Chosen solution

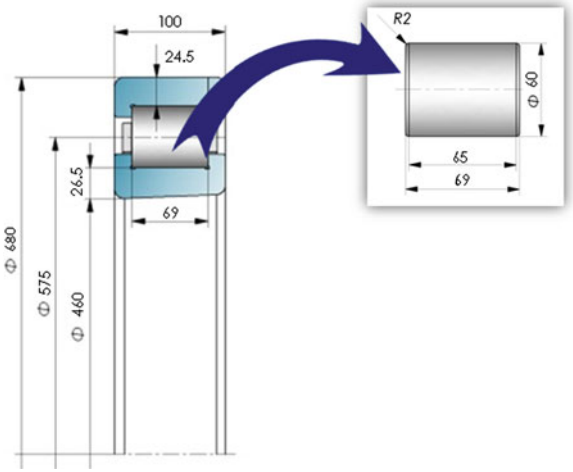

4 Result and Conclusions

The main difference between the previous works presented in Sect. 1 and this paper is the inclusion of multiple and conflicting objectives for the optimization and the use of an important strength of materials constraint in addition to the realistic geometric ones. Also, this approach uses a minimum number of design variables to describe uniquely the internal geometry of the rolling bearing.

In order to solve this optimization problem the Cambrian platform, developed within Optimal Design Center of the Technical University of Cluj-Napoca, Romania, was used (reader is advised to refer to Tudose and Ştefanache 2007). Since Cambrian deals only with function minimization, as objective functions were used the inverse of the objective functions described in Sect. 3.3. Figure 4 was obtained after the algorithm convergence.

Figure 5 shows a set of solutions selected from the above mentioned Pareto front for which D_{we} is integer. The first solution represents the best solution for the second objective h_{min} and the last solution represents the best solution for the first objective C_r.

Because, for all selected solutions (Fig. 5b), the second objective function has values close to each other, the design solution can be considered the solution with the maximum basic radial load rating C_r (the last solution). Using the design variables belonging to this solution the entire geometry of the single-row cylindrical roller bearing NP1092 can be now easily described (Fig. 6). We should remark also here that all the optimal found solutions correspond to a remarkably large dynamic radial load rating and a sufficiently thick lubricant film.

Acknowledgments This paper was co-supported by the RKB Group, the Swiss bearing manufacturer and the project "Doctoral studies in engineering sciences for developing the knowledge based society-SIDOC" contract no. POSDRU/88/1.5/S/60078, project co-funded from European Social Fund through Sectorial Operational Program Human Resources 2007–2013. The authors greatly appreciate and wish to thank all the RKB staff for their great assistance during this project.

References

Chakrabotrhy I, Vinay K, Nair SB, Tiwari R (2003) Rolling element bearing design through genetic algorithms. Eng Optimisation 35(6):649–659

Dowson D, Higginson GR (1966) Elasto-hydrodynamic lubrication. Pergamon Press, Oxford

Gupta S, Tiwari R, Nair SB (2006) Multi-objective design optimisation of rolling bearings using genetic, Mechanism and Machine Theory

Harris TA, Kotzalas MN (2007) Essential concepts of bearing technology, rolling bearing analysis, 5th edn. Taylor and Francis, London

Rao BR, Tiwari R (2007) Optimum design of rolling element bearings using genetic algorithms. Mech Mach Theory 42(2):233–250

Rao VR, Savsani JV (2012) Mechanical design optimization using advanced optimization techniques. Springer, London

Sivanandam SN, Deepa SN (2008) Introduction to genetic algorithms. Springer, Berlin Heidelberg

Tudose L, Ştefanache C (2007) Cambrian application package for mono and multi-objective. In: The 1st international conference advanced engineering in mechanical systems, ADEMS'07, Cluj-Napoca, in Acta Technica Napocensis, series: applied mathematics and mechanics, Nr. 50, vol 2, pp 367–374, 7–8 June

Yu X, Gen M (2010) Introduction to evolutionary algorithms. Springer, London

On Evaluation Methods in Product Development. Application on Mechanical Transmissions

Mihai Robert Vladu, George Dobre and Radu Florin Mirica

Abstract Successful companies design and produce products which satisfy optimally the needs and desires of the customer. For this goal new concept ideas need to be generated, optimised and the optimal of them to be selected for production. A literature review considering the state of the art of the systematic approach of product development and of the evaluation methods is realized. Two evaluation methods are considered. One is the classical evaluation method (Pahl et al. 2007) and the second is the fuzzy logic evaluation method proposed by authors. A comparison of the two methods is realized and the principal advantages and disadvantages using a case of study of four variants for a mechanical transmission between a turbine and an electrical generator.

Keywords Evaluation · Fuzzy logic evaluation method · Product development · Optimal solution · Mechanical transmission

1 Introduction

In order to satisfy the customer needs and wants, the necessity to achieve low-cost and high-quality products is vital for the companies' future. In these conditions, the companies must provide the ability to continuously adapt to the changes of the market. Thus, it is necessary that the product development process to be

M. R. Vladu (✉) · G. Dobre · R. F. Mirica
University Politehnica of Bucharest, Bucharest, Romania
e-mail: mvladu@omtr.pub.ro

G. Dobre
e-mail: G.Dobre@gmail.com

R. F. Mirica
e-mail: mirica@meca.omtr.pub.ro

G. Dobre (ed.), *Power Transmissions*,
Mechanisms and Machine Science 13, DOI: 10.1007/978-94-007-6558-0_42,

continuously improved and allowing to the companies the possibility to adapt to customer needs and to fully satisfy them.

The product development process represents an important stage from the life cycle of a product. It starts with the requirement list of the product, conceptual design and it ends with the product final documentation (the product is ready to be manufactured).

In the literature the systematic approach of product development manifests a great interest (Cross 2008; Dieter 2000; Ehrlenspiel 2007; Kahn 2005; Pahl et al. 2007; Ulrich and Eppinger 2010), although the approach of product development process differs regarding diverse references and authors. Thus, an important idea is expressed by Pahl et al. (2007), which consider that "the systematic approach to engineering design has been brought to a level that provides a basis for successful product development".

The conceptual design constitutes a fundamental part of the product development process. A stage of the conceptual design is the complex process of finding, selecting and evaluating of the product solution variants. This process has as scope the establishment of the product optimal solution and it bases on the qualitative and quantitative characteristics of the product, which resulted from the requirement list. The paper is concentrated only on the evaluation methods and the previous steps of finding and selecting of the solution variants will not be presented.

Approach of the evaluation process has begun in the first part of the twentieth century in Germany, where Erkens (1928) makes reference to modern systematic design including constant testing and evaluation. Kesselring (1942) referred to technical and economical principles of evaluation of form variant in the systematic design which could be considered even actually: minimum production costs; minimum space requirement; minimum weight; minimum losses; optimum handling. Wögerbauer (1943) demonstrated that the design solutions could be improved by test and evaluation realized considering the cost as main criterion. In the second part of the twentieth century, Rodenacker (1970) emphasized original design considerations including the evaluation of all parameters of the technical system based on the following criteria: quantity, quality and cost. A historical evolution of the technical and economic evaluation has been approached by Pahl et al. (2007) starting from the first edition of their book edited in 1977 in German language. The authors propose modern ideas and procedures of evaluation during the systematical design or product development.

Recently new approaches on the evaluation methods have been made by the authors. These has emphasized the beneficial effect of the optimal product solution evaluation in the case of conceptual or embodiment design with applications in the power transmission field (Dobre et al. 2011; Mirica et al. 2011). The newest researches in this area indicate the fact that the application of the fuzzy logic in the evaluation methods has the advantage over classical approaches that uncertain, imprecise and vague information in the product development process (Vladu et al. 2012a, b) can be described realistically. Thus, due to the fuzzy approach the subjectivity of the human experts in the field is diminished and the inexperienced

users in the approached field could find easier the optimal product solution. The fuzzy logic evaluation method makes possible to find out the weak spot at each the design concept variant and to choose the most satisfactory one.

The paper's aim is the analysis of the evaluation methods of solution variants existing after the design step (as part of product development). The two analyzed methods are the classical evaluation method (Pahl et al. 2007) and fuzzy logic evaluation method proposed by authors. The main objective of this analysis is to compare the two evaluation methods and to observe the advantages and disadvantages of these. A case of study of an evaluation of the solution variants for a mechanical transmission will be presented.

2 Evaluation Methods in Product Development

2.1 The Classical Evaluation Method

One of the most known and actual or now already classical evaluation methods used in the product development process for the analysis and comparison of the different design solution variants of a product has been proposed by Pahl et al. (2007). The method combines two types of approaches recommended: cost-benefit-analysis (Zangemeister 1970) and technical and economic evaluation (VDI Ricthlinie 2225, 1997, derived from Kesselring 1951). In a short description, the evaluation method determined the optimal solution of a product considering the different technical and economic criteria which are resulted from the requirement list and general constraints. The technical and economical criteria are arranged on different levels of dependence (the complexity is decreasing from the first level to the last one) under the form of a tree network (such an example will be presented in the case of study). Thus, the criteria with the lowest complexity form the evaluation criteria.

Each criterion is quantitative appreciated using two weighting factors. The node weighting factor (n) indicate the relative contribution of the criterion to the associated sub-group with respect to the superior criterion and the level weighting factor (l) indicate the relative importance of a criterion at a particular level with respect to the criterion from the first level. A weighting factor is a real, positive number ranging from 0 to 1 (or can be from 0 to 100) having the advantage to reflect in the same time percentage. The node weighting factor is established by the human experts and the level weighting factors is calculated with the help of the node weighting factor (details are presented in Dobre et al. 2011).

For each solution variant two overall values (unweighted and weighted) are calculated using the Eqs. (1) and (2). Excepting the situations when two or more solution variants have the overall values very close, the optimal solution is the solution variant with the highest overall values.

$$\Sigma v = \sum_{i=1}^{n} v_i, \tag{1}$$

$$\Sigma lv = \sum_{i=1}^{n} l_i v_i, \tag{2}$$

where: Σv is the unweighted overall value of the solution variant; v_i—assessing value of the evaluation criterion i; Σlv—weighted overall value of the solution variant; l_i—level weighting factor of the evaluation criterion i.

In the known literature these values were not connected with the fuzzy logic analysis possibilities. This aim is focused further.

2.2 Fuzzy Logic Evaluation Method

The fuzzy logic theory (Zadeh 1965) has the possibility to deal with the inexact and vague information that appears in the evaluation process like the uncertain assessing values and weighting factors because of the subjective character of this assessing.

Starting from this idea, Vladu et al. (2012a, b) proposed a fuzzy logic evaluation method as an instrument for the establishment of the optimal solution. The principle of the evaluation criteria necessary for product characterization is the same with the one used in Pahl et al. (2007): it is based on the tree network scheme describing the hierarchical dependence of different criteria from superior to inferior levels (a representation will be give later in Fig. 5) and the node weighting factors.

These evaluation methods define differently the solution evaluation values. Therefore they have been named differently to avoid confusion. Pahl et al. (2007) calculates unweighted (1) and weighted (2) overall values. But in the fuzzy logic method one based on fuzzy logic system determines the assessing weighting global values.

The application of the fuzzy logic evaluation method to a solution variant is very simple due the fuzzy logic program: it creates the fuzzy logic systems to calculate the assessing weighting global value. The fuzzy logic system as group of items is represented by input and output variables, membership functions attached to each variable and the fuzzy rule base (if–then rules). Now it is not detailed in the present paper (see for details, for example, Vladu et al. 2012a, b). The fuzzy logic system used in the present paper has a fuzzy rule base that is automatically generated through a method developed by authors. The method takes into account the node weighting factors of the criteria.

The capacity of fuzzy logic to formulate and calculate usefully the inexact and vague information at the evaluation process has the effect to diminish the subjective character of the assessing values and the weighting factors.

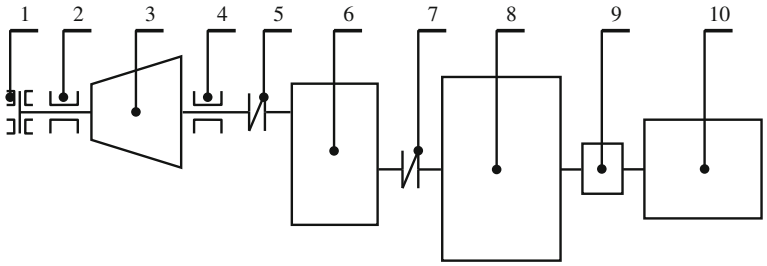

Fig. 1 Configuration scheme of the solution variant *1* (high speed gearbox and planetary gearbox). *1*, *2*, *4* bearings; *3* turbine; *5*, *7* elastic couplings; *6* high speed gearbox; *8* planetary gearbox; *9* gear coupling; *10* electric generator

3 The Case of Study For Power Transmission

3.1 The Variants for Optimal Selection

The case of study wants to emphasize a detailed analysis on the evaluation methods considering the advantages and disadvantages of the two mentioned evaluation methods. Thus, an evaluation example of the solution variants for a mechanical transmission between a turbine and an electrical generator is presented as a case of study.

Starting from the design data of the mechanical transmission (turbine power, turbine rotation speed, generator rotation speed and the transmission ratio) four solution variants have been established for further evaluation (Figs. 1, 2, 3, 4). The design details of the four solution variants will not be specified in the presented paper.

The four solution variants of the mechanical transmission are:

- variant V_1: high speed gearbox and a planetary gearbox (Fig. 1);
- variant V_2: belt transmission and planetary gearbox (Fig. 2);

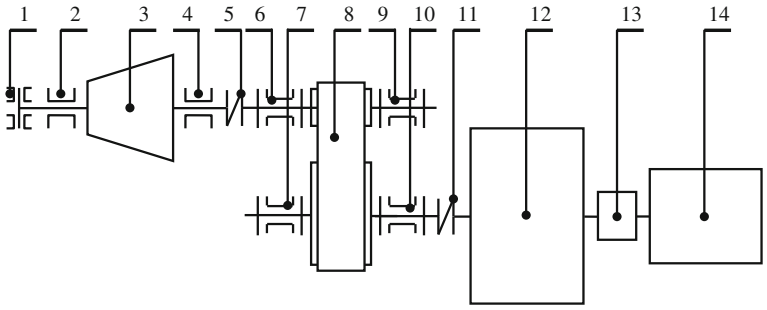

Fig. 2 Configuration scheme of the solution variant *2* (belt transmission and planetary gearbox). *1*, *2*, *4*, *6*, *7*, *9*, *10* bearings; *3* turbine; *5*, *11* elastic couplings; *8* belt; *12* planetary gearbox; *13* gear coupling; *14* electric generator

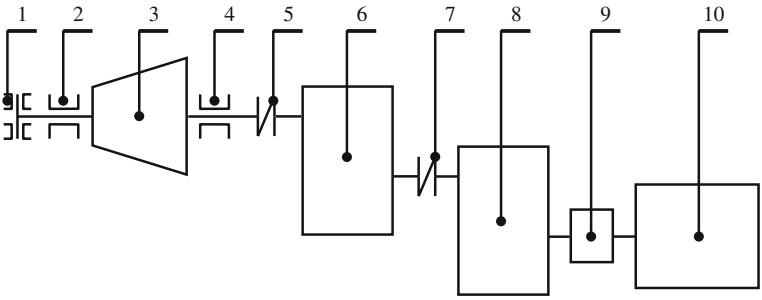

Fig. 3 Configuration scheme of the solution variant *3* (two high speed gearboxes). *1*, *2*, *4* bearings; *3* turbine; *5*, *7* elastic couplings; *6*, *8* high speed gearboxes; *9* gear coupling; *10* electric generator

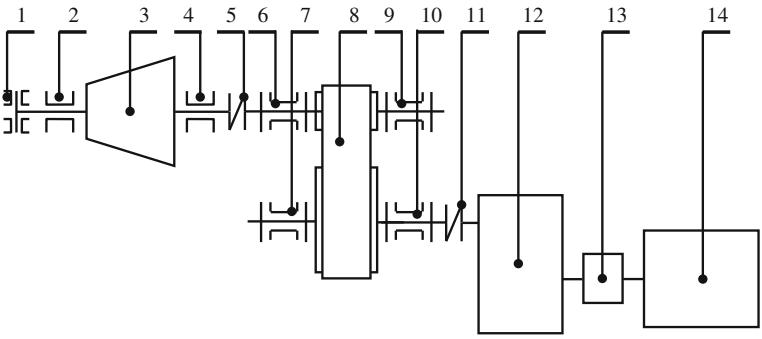

Fig. 4 Configuration scheme of the solution variant *4* (belt transmission and high speed gearbox). *1*, *2*, *4*, *6*, *7*, *9*, *10* bearings; *3* turbine; *5*, *11* elastic couplings; *8* belt; *12* high speed gearbox; *13* gear coupling; *14* electric generator

- variant V_3: two high speed gearboxes (Fig. 3);
- variant V_4: belt transmission and high speed gearbox (Fig. 4).

3.2 Application of the Classical Method

3.2.1 Performance Criteria at Three Level Network

The first part of the evaluation process for both analysis methods is likely the same. A network tree of technical and economical criteria is defined here (Fig. 5). The criteria are arranged hierarchically on four levels of dependence and decreasing complexity (number considered sufficient for a plenty characterization of product qualities). The general (or global) quantifying criterion (reliable and

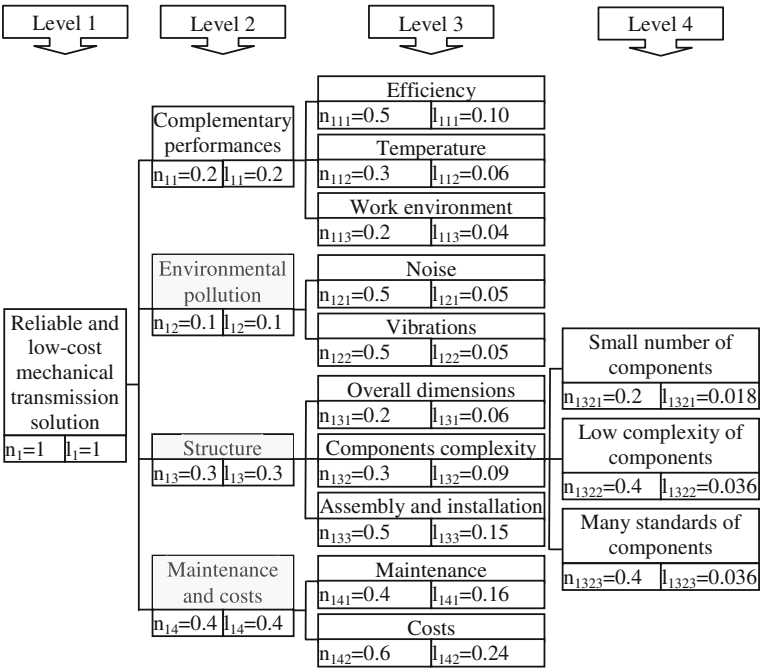

Fig. 5 Evaluation network of criteria to quantify transmissions solutions

low-cost mechanical transmission solution) is defined on the level 1; the criteria associated to the global criterion are defined into other three levels, that describe better the performances from superior to inferior level. The criteria with the lowest complexity (from levels 3 and 4) detailing better the product performances form the evaluation criteria: thus, twelve evaluation criteria are obtained for the evaluation of the four studied solution variants.

As can be observed, two weighting factors (node and level) are shown for each criterion. The node weighting factors has been established by the human experts and has a subjective character. The level weighting factor of each criterion is determinate by the product between the values of the node weighting factor of the considered criterion and of the level weighting factor of the superior associated criterion (for example: $l_{1321} = n_{1321} \cdot l_{132} = 0.2 \cdot 0.09 = 0.018$). This weighting factor is used further in the classical evaluation method. The fuzzy logic evaluation method takes into consideration only the node weighting factors.

3.2.2 Results of Using the Classical Method

Table 1 gives the evaluation results after the classical evaluation method (Pahl et al. 2007). Each evaluation criterion was appreciated using assessing values, v, on a scale of values chosen from 0 to 10 (describing at increased number

Table 1 Evaluation of the four solution variants of mechanical transmission (after Pahl et al. 2007)

Evaluation criteria			Variant V_1		Variant V_2		Variant V_3		Variant V_4	
i	Denomination	l_i	v_{i1}	$l_i v_{i1}$	v_{i2}	$l_i v_{i2}$	v_{i3}	$l_i v_{i3}$	v_{i4}	$l_i v_{i4}$
1	Efficiency	0.10	10	1	8	0.8	8	0.8	7	0.7
2	Temperature	0.06	5	0.3	9	0.54	5	0.3	9	0.54
3	Work environment	0.04	10	0.4	8	0.32	10	0.4	8	0.32
4	Noise	0.05	9	0.45	10	0.5	8	0.4	8	0.4
5	Vibrations	0.05	9	0.45	10	0.5	8	0.4	8	0.4
6	Overall dimensions	0.06	6	0.36	10	0.6	4	0.24	8	0.48
7	Small number of components	0.018	10	0.18	6	0.108	10	0.18	6	0.108
8	Low complexity of components	0.036	10	0.36	6	0.216	10	0.36	6	0.216
9	Many standard of components	0.036	10	0.36	6	0.216	10	0.36	6	0.216
10	Assembly and installation	0.15	8	1.2	10	1.5	8	1.2	9	1.35
11	Maintenance	0.16	4	0.64	7	1.12	6	0.96	8	1.28
12	Costs	0.24	6	1.44	4	0.96	10	2.4	8	1.92
Σl		**1**								
			$\Sigma v_1 = 97$		**$\Sigma v_2 = 94$**		**$\Sigma v_3 = 97$**		**$\Sigma v_4 = 91$**	
			$\Sigma lv_1 = 7.14$		**$\Sigma lv_2 = 7.38$**		**$\Sigma lv_3 = 8.00$**		**$\Sigma lv_4 = 7.93$**	

Note *i* index of criterion; *j* index of solution; *l* level weighting factor
v assessment value on the scale 0…10; *lv* weighted evaluation value; *Σv* unweighted overall evaluation value; *Σlv* weighted overall evaluation value

a higher degree of characterization accuracy). The unweighted, Σv, and weighted, Σlv, overall evaluation values are calculated for each solution variant.

The values calculated after the proposed method based on FL analysis are given only in the comparison analyses following emphasizing the so called weak spots.

Table 1 shows that the variant V_3 has the highest overall evaluation values: $\Sigma v = 97$ and $\Sigma lv = 8.00$; thus this solution could represent the optimal one.

But an interesting observation can be made: the difference between the weighted overall evaluation values of the variants V_3 [$\Sigma lv = 8.00$] and V_4 [$\Sigma lv = 7.93$] is not very significant. In order to establish the optimal solution from these variants a further analysis is necessary to identify the weak spots of each solution variants. The definition of this quantity will result from the further analysis about the considerations from Pahl et al. (2007).

For this the following representations of the so-called value profile of each solution variant are drawn in Fig. 6.

In these representations, the bar for each criterion has the length corresponding to the assessment values, v, and the thicknesses—to the level weighting factor values, l. Thus, the area of a bar indicates the weighted value, lv, of the evaluation criterion and the cross-hatched line the overall weighted value, Σlv, of a solution variant.

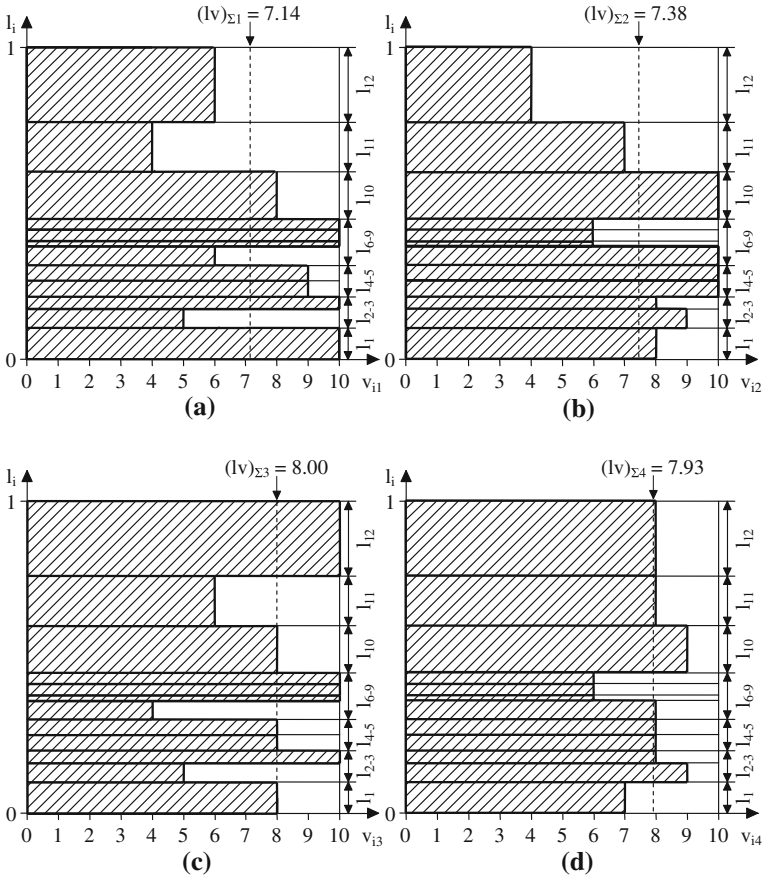

Fig. 6 Value profile representations for the variants V_1 (**a**), V_2 (**b**), V_3 (**c**) and V_4 (**d**) to analyze the weak spots (the notations are given in the note from Table 1)

3.2.3 Weak Spots in Each Variants

The weak spots of a solution variant in this analysis are the evaluation criteria having the bar thickness greater as approximate (not calculated) average level weighting factor value (that is of great importance relative to others criteria), but the length lower as the calculated average assessment value; for example, the criteria 11 and 12 are the weak spots according to this point of view for the variant V_1 (Fig. 6a).

As a conclusion: the solution variants V_3 and V_4 are better then V_1 and V_2 considering also the value profiles analysis beside the weighted overall evaluation values.

The further problem: what is the optimal version between V_3 and V_4? The weighted overall value of the solution variant V_3 is little bit higher than the one for

the variant V_4 and their difference is insignificant; that is the solution V_3 could be better as V_4. However, V_4 has a balanced value profile with no serious weak spots in regard to V_3, see Fig. 6c and d. In conclusion, the solution variant V_4 is the optimal solution of the mechanical transmission considering the weak spots analysis. Another conclusion results: for the optimal solution is not important to have a high overall value, but a balanced value profile with no serious weak spots.

An analysis of the other two variants, V_1 and V_2, from the point of view of weak spots shows that V_2 is better then the solution variant V_1 because it has fewer weak spots; at the same time the weighted overall value of the solution variant V_2 is higher, that is V_2 is a better solution as V_1 from the two analysis points of view.

3.3 Results of Using the Fuzzy Logic Evaluation Method

An own fuzzy logic program is used to evaluate the solution variants. As it was mentioned before (Sect. 3.2), the program is based on the network tree and the node weighting factors of criteria shown in Fig. 5.

Figure 7 shows the graphical user interface for all of analyzed variants. Twelve evaluation criteria with the assessing values, v, are written in the left side. The assessing weighting global parameter of the analyzed variant and some buttons are given in the right side.

The solution variant V_4 has the highest assessing weighting global value, 8.08, when the other variants (V_1…V_3) have in order the following values: 7.42, 7.76 and, respectively 8.04. From this analysis, the optimal variant is V_4.

3.4 Comparison Between the Results of the Classical and Fuzzy Methods

Table 2 synthesizes the results of the both methods indicating the variants in order of the performances of characterizing values (from higher to lower) for each method of analysis. The results emphasize the same conclusion: the variant V_4 is the optimal solution, it having the high values of weighted overall and assessing weighting global.

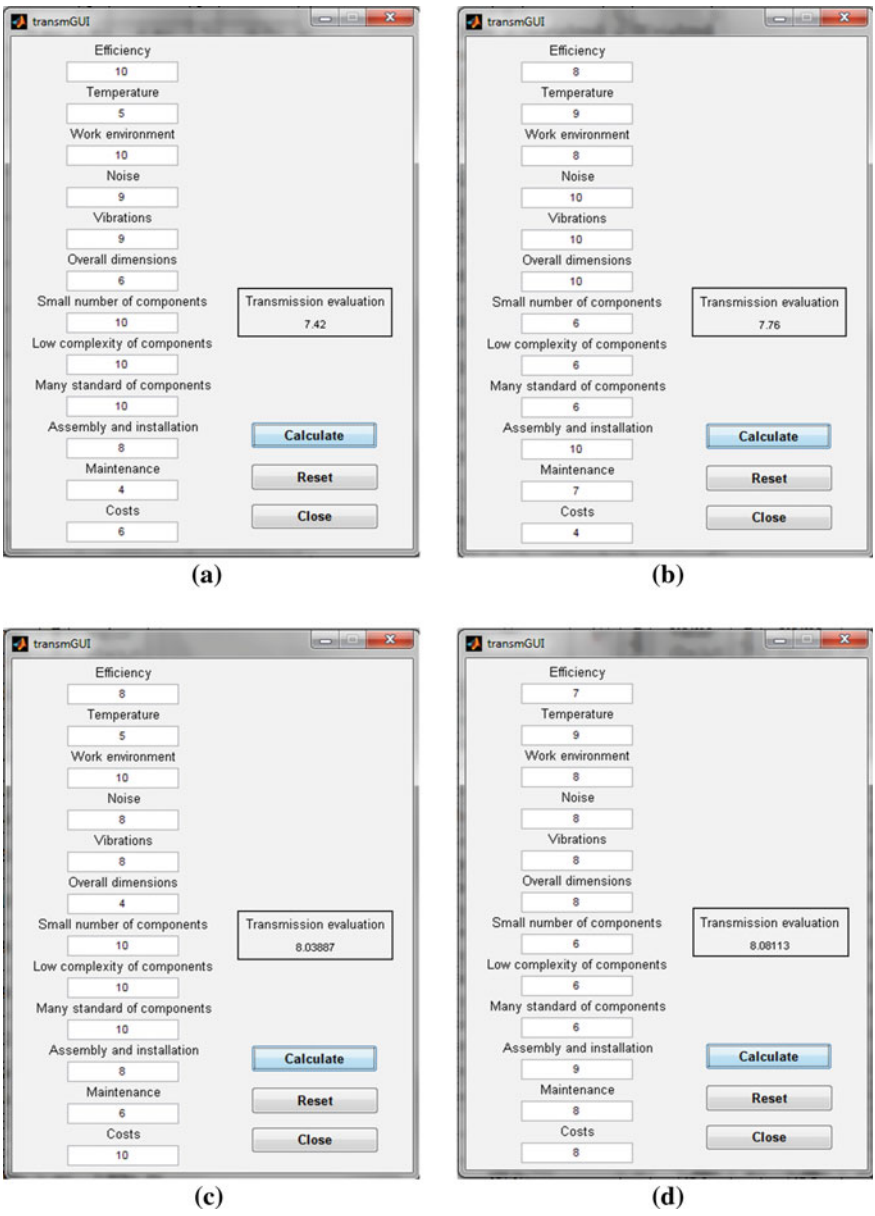

Fig. 7 Graphical user interfaces in the fuzzy logic program for variants V_1 (**a**), V_2 (**b**), V_3 (**c**) and V_4 (**d**)

Table 2 Results of the evaluation of the four solution variants of mechanical transmission using the classical evaluation method (after Pahl et al. 2007) and fuzzy logic evaluation method

Evaluation methods		Order of classification of variants according the performance analyzing criteria			
		1	2	3	4
Evaluation after Pahl et al. (2007)	Without weak spots	V_3, $(lv)_{\Sigma 3} = 8$	V_4, $(lv)_{\Sigma 4} = 7.93$	V_2, $(lv)_{\Sigma 2} = 7.38$	V_1, $(lv)_{\Sigma 1} = 7.14$
	With weak spots	V_4, $(lv)_{\Sigma 4} = 7.93$	V_3, $(lv)_{\Sigma 3} = 8$	V_2, $(lv)_{\Sigma 2} = 7.38$	V_1, $(lv)_{\Sigma 1} = 7.14$
Fuzzy logic evaluation method		V_4	V_3	V_2	V_1
		Assessing weighting global value			
		8.08	8.04	7.76	7.42

4 Conclusions

The evaluation of the four solution variants using the two methods has emphasized that the optimal solution was the same.

Application of the two evaluation methods to select the optimal one of four variants shows that the all are nearly equally optimal. One more analysis is needed to differentia out the most satisfying one for the end user. It is the weak spot analysis.

The evaluation without weak spot analysis by Pahl et al. (2007) is adequate to achieve simple evaluation (with few criteria) and it is efficient when the optimal solution stand out clearly and not vaguely. In some situation, the evaluation becomes very difficult, especially when the number of evaluation criteria is high and the value profiles of the solutions are not balanced. Thus, a disadvantage of their approach is the need of the human evaluation experts to make the final optimality assessment.

Fuzzy logic has the inherent property of giving one clear cut crisp final optimal answer even when all design information is inexact and decision variable are qualitative and imprecise and vague and subjective as is the normal case in real design work.

The fuzzy logic evaluation method can be formulated basing it directly on the desires of the customer. In this method the weighting factors and weak spots are naturally taken care of without need of tedious expert's evaluations. Also the designer need not be hi level expert since the goal is all the time directed to satisfy the end customers giving a trade off results which is clear and crisp and cannot be changed unless customer desires are changed.

Thus the fuzzy logic program is used easily by inexperienced users and ensures desirable designs with weak spots ironed out.

Acknowledgments The work has been funded by the Sectoral Operational Programme Human Resources Development 2007–2013 of the Romanian Ministry of Labour, Family and Social Protection through the Financial Agreement POSDRU/88/1.5/S/60203.

References

Cross N (2008) Engineering design methods: strategies for product design, 4th edn. Wiley, Chichester. ISBN 978 0 470 51926 4

Dieter GE (2000) Engineering design, 3rd edn., Mechanical engineering seriesMcGraw-Hill International Editions, New York. ISBN 10: 0073661368/0-07-366136-8, ISBN 13: 9780073661360

Dobre G, Vladu MR, Mirica RF (2011) On the evaluation process in product development, with applications to screw-nut transmission solutions. Balkan J Mech Transm 1(1):32–42

Ehrlenspiel K (2007) Integrierte Produktentwicklung. Denkabläufe, Methodeneinsatz, Zusammenarbeit. Carl Hanser Verlag, Munchen-Wien, ISBN-10:3-446-40733-2, ISBN-13: 978-3-446-40733-6

Erkens A (1928) Beiträge zur Konstruktionserziehung. VDI 72, pp 17–21

Kahn BK (2005) The PDMA handbook of new product development, 2nd edn. Wiley, Hoboken. ISBN 0-471-48524-1

Kesselring F (1942) Die starke Konstruktion. VDI-Z 86, pp 321–330, pp 749–752

Kesselring F (1951) Bewertung von Konstruktionen, ein Mittel zur Steuerung von Konstruktionsarbeit. VDI-Verlag, Dusseldorf

Mirica RF, Dobre G, Vladu MR (2011) Innovative solutions for screw-nut transmissions as application case using requirements lists. Acta Tech Napocensis 54:95–104

Pahl G, Beitz W, Feldhusen J, Grote KH (2007) Engineering design: a systematic approach, 3rd edn. Springer London Limited, Berlin. ISBN 10: 1846283183

Rodenacker WG (1970) Methodisches Konstruieren. Konstruktionsbücher, Band 27, Springer, Berlin

Ulrich TK, Eppinger DS (2010) Product design and development, 5th edn. McGraw Hill, New York. ISBN 0-07-123273-7

VDI-Richtlinie 2225 (1997) Technisch-wirtschaftliches Konstruieren. Dusseldorf, VDI-Verlag

Vladu MR, Dobre G, Mirica RF (2012a) Application of the fuzzy logic in the evaluation of solution variants in the product development process. U P B Sci Bull 75(1):207–222 ISSN 1454-234x

Vladu MR, Dobre G, Mirica RF (2012b) On the evaluation of solutions in product development based on fuzzy logic approach. Appl Soft Comput, Revise Resubmit

Wögerbauer H (1943) Die Technik des Konstruierens, 2nd edn. München, Oldenbourg

Zadeh LA (1965) Fuzzy sets. Inf Control 8:338–353

Zangemeister C (1970) Nutzwertanalyse in der Systemtechnik. München, Wittenmannsche Buvhhandlung

A Fundamental Study on the Improvement for Chipping Characteristics in Gear Hobbing with Carbide Tipped Hob

Ryohei Ishimaru, Isao Sakuragi and Naoshi Izumi

Abstract In gear hobbing, it is important that improving productivity for gear manufacturing is increased by using carbide tipped hob with heatproof. However, damage might occur in the tool at the early stage when the cutting condition is mistaken, and the tool life be shortened extremely. Therefore, when carbide tipped hob is applied for gear cutting, it is important to understand the characteristic of it enough, and to understand the condition for the tool life. In this study, the factor of the damage of the carbide tool is systematically examined. The chipping factor of the carbide tool, i.e. carbide material, cutting velocity, feed, grinding condition for tool face, is investigated by using modified machining center and fly tool.

Keywords Gear · Hobbing · Carbide tipped hob · Fly tool · Tool life

1 Introduction

In gear hobbing, there are many tools that can be used effectively as mentioned by Ariura et al. (1989), Sakuragi et al. (2001) and Umezaki et al. (2008). Particurarly, High Speed Steel (HSS) hob is one of the most useful tools. However, the improvement of productivity by HSS gear hobbing is reaching critical limit, because the hardness of HSS hob decreases rapidly when in the high temperature of 600C or more. Therefore, it is important that improving productivity for gear

R. Ishimaru (✉) · I. Sakuragi · N. Izumi
Kurume National College of Technology, Fukuoka, Japan
e-mail: ishimaru@kurume-nct.ac.jp

I. Sakuragi
e-mail: sakuragi@kurume-nct.ac.jp

N. Izumi
e-mail: izumi@kurume-nct.ac.jp

G. Dobre (ed.), *Power Transmissions*,
Mechanisms and Machine Science 13, DOI: 10.1007/978-94-007-6558-0_43,

manufacturing is increased by using carbide tipped hob with heatproof. However, damage might occur in the tool at the early stage when the cutting condition is mistaken, and the tool life be shortened extremely. Therefore, when carbide tipped hob is applied for gear cutting, it is important to understand the characteristic of it enough, and to understand the condition for the tool life as mentiond by Sakuragi et al. (1994). Furthermore, the cutting mechanics in gear hobbing is very complex as mentioned by Umezaki et al. (2001, 2008) and Ishimaru et al. (2011). Also it is difficult to examine all the cutting situations at the same time.

In this study, the aim is to find experimental relationship between selected production variables. Thus Fly tool which simulate one cutting edge of the hob is used to investigate the hobbing conditions. The aim is to maximise the practical utility of machineing by finding out conditions which give long life when inexpensive tooling is desired.

2 Experimental Appratus and Method

2.1 Machining Center

The cutting mechanics of hobbing is very complex. Each cutting edge cuts various shapes of work while one rotation of hob. In this study, machining center and fly tool are used in order to investigate the mechanism of one cutting edge. The cutting condition and method can be variously set. Figure 1 shows the machining center, which has the over arm supporting the tool holder. Fly tool is attached at the tool holder.

Fig. 1 Machining center modified for fly tool test

Table 1 Specifications of fly tool and work

Carbide fly tool	
Outside dia.	80 mm
Rake angle	0 deg.
Relief angle	6 deg.
Work	
Outside dia.	205.6 mm
Width	100 mm
Material	SCr420
Hardness	HB180

2.2 Fly Tool and Work

The specifications of fly tool and work are given in Table 1. The dimensions of carbide fly tool are given in Fig. 2.

2.3 Grinding Machine and Grinding Wheel

In order to re-grind the rake face of fly tool, the tool grinding machine is used with #200 resinoid diamond wheel. Their diameter is 125 mm, and grinding speed is 1,500 m/min.

Fig. 2 Dimensions of fly tool

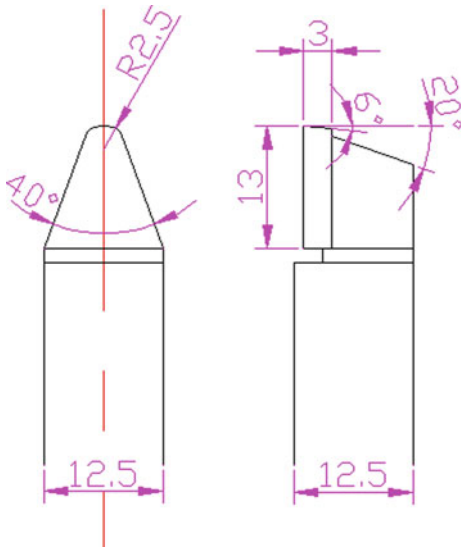

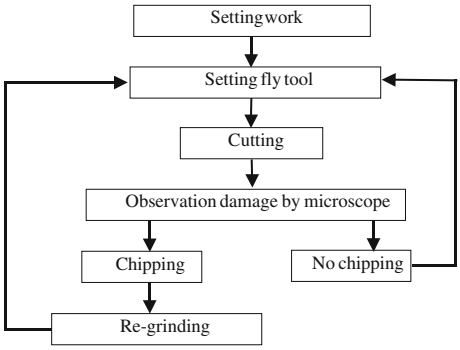

Fig. 3 Procedure of experiment

2.4 Experimental Method

In this study, the tool life is evaluated by generation of chipping. The procedure of experiment is shown in Fig. 3. After the cutting for the outside of work, the damage of the tool is observed with microscope. While no chipping occurs, the experiment is continued. If a chipping appeared, then the chipping is ground off by grinding wheel in order to continue the test by other experimental conditions.

3 Experimental Results and Discussions

3.1 Influence of Cutting Condition on Tool Life

In this section, the influence of tool material and cutting condition on tool life is investigated. The performance of tool material is evaluated by cutting length until a chipping occurred. Also, a similar experiment is executed about the cutting speed, feed rate, and cutting method.

3.1.1 Carbide Material

Figure 4 shows the tool life of four kinds of fly tools with a different carbide material. The work material is SCr420 with its hardness HB180, cutting speed is 300 m/min, feed is 0.38 mm/rev, depth of cut is 0.75 mm, and cutting method is up cutting. As a result of experiment, carbide material P20 is the most excellent. P20 has a lot of additives, i.e. TiC, TaC, Nb, and is superior to heat resistance compared with the other kinds of material. It is considered that the occurrence of chipping for P20 is restrained by its higher heat resistance. Figure 5 shows the appearances of chipping both P20 and K20 material.

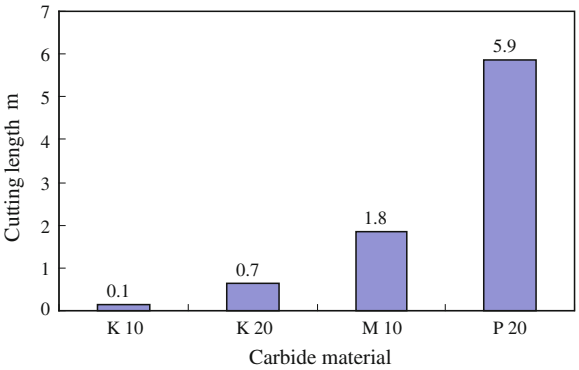

Fig. 4 Influence of carbide material on tool life (V = 300 m/min, f = 0.38 mm/rev h = 0.75 mm, up cutting)

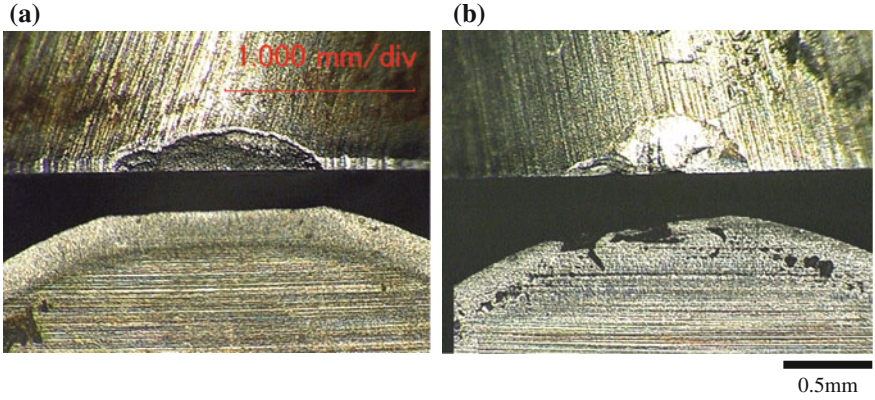

Fig. 5 Appearances of chipping (*upper* relief face, *lower* rake face) (**a**) P20, $\ell = 5.9$ m (**b**) K20, $\ell = 0.7$ m

3.1.2 Cutting Speed

The relationship between tool life and cutting speed is given in Fig. 6. The work material is SCr420, fly tool is P20, feed is 0.38 mm/rev, depth of cut is 0.75 mm, and cutting method is up cutting. It is found that the tool life becomes longer as cutting speed becomes faster. Because it is considered that for cutting temperature to become higher, when machine speed is faster, the cutting force decreases by work material's softening by that. However, it is necessary to select the carbide tool having higher heat resistance because heat crack can be easily occurred at higher temperature condition. Figure 7 shows the appearances of chipping when the cutting speed is 200 and 300 m/min.

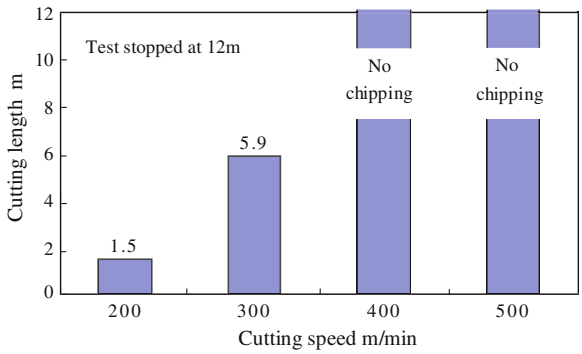

Fig. 6 Influence of cutting speed on tool life (P20, f = 0.38 mm/rev h = 0.75 mm, up cutting)

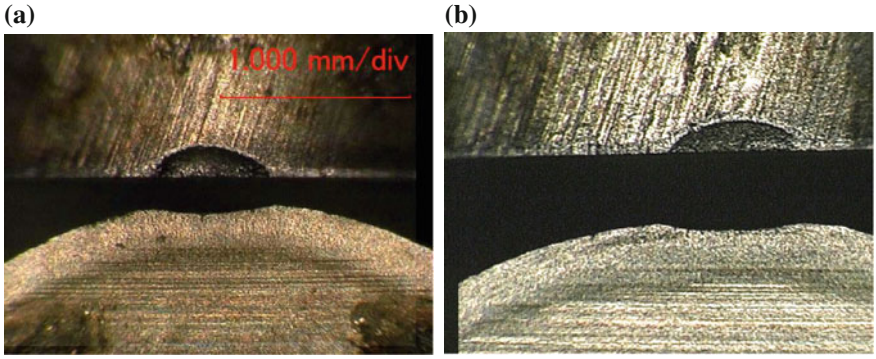

Fig. 7 Appearances of chipping (*upper* relief face, *lower* rake face) (**a**) V = 200 m/min, ℓ = 1.5 m (**b**) V = 300 m/min, ℓ = 5.9 m

3.1.3 Feed Rate

The relationship between tool life and feed is given in Fig. 8. The work material is SCr420, fly tool is P20, cutting speed is 500 m/min, depth of cut is 0.75 mm, and cutting method is up cutting. It is found that the tool life shortens when feed is small. Figure 9 shows the appearances of chipping when feed is 0.1 and 0.38 mm/rev.

3.1.4 Cutting Method

The experimental result when making the cutting method a down cutting is shown on Table 2. It is found that the tool life remarkably improves by changing cutting method to down cutting from up cutting. It is considered that the reason is the difference of contact angle θ, which is formed between work and the edge of fly

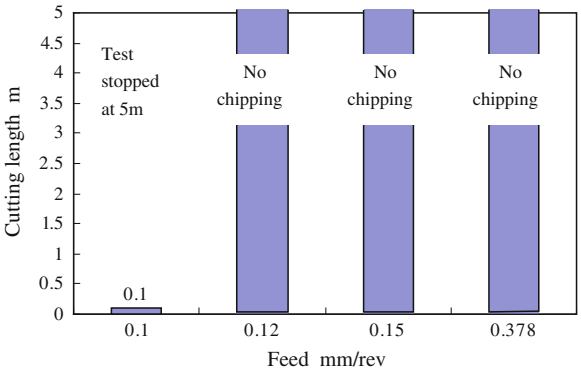

Fig. 8 Influence of feed on tool life (P20, V = 500 m/min, h = 0.75 mm, up cutting)

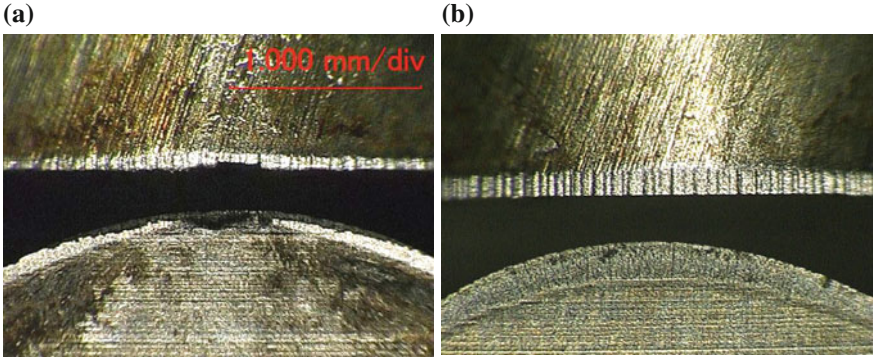

Fig. 9 Appearances of chipping (*upper* relief face, *lower* rake face) (**a**) f = 0.1 mm/rev, ℓ = 0.1 m (**b**) f = 0.38 mm/rev, ℓ = 5.0 m

Table 2 Influence of cutting method on tool life

	V = 200 m/min f = 0.38 mm/rev h = 0.75 mm	V = 300 m/min f = 0.38 mm/rev h = 0.75 mm	V = 500 m/min f = 0.1 mm/rev h = 0.75 mm
Up cutting	Cutting length = 1.5 m	Cutting length = 5.9 m	Cutting length = 0.1 m
Down cutting	Over 12 m no chipping	Over 12 m no chipping	Over 12 m no chipping

tool. Figure 10 compared the cutting shape of cut method. Since up cutting and down cutting exist together in hobbing, it is necessary to consider up cutting, which makes tool life short.

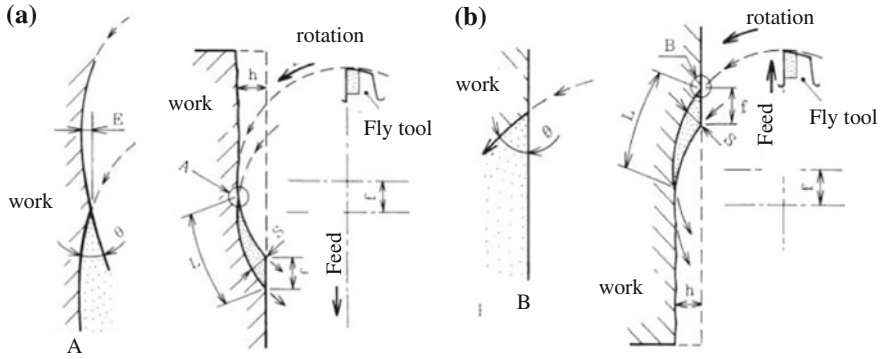

Fig. 10 Difference of cutting shape caused by up cutting and down cutting (**a**) up cutting (**b**) down cutting

3.2 Influence of Grinding Tool Face on Tool Life

It is considered that tool life is influenced from not only the characteristic of cutting condition and tool material but also states of the method of grinding the tool face. In this section, the influence of grinding wheel on tool life is investigated.

3.2.1 Resinoid Diamond Wheel

A resinoid diamond wheel is often used for the grinding wheel which re-grinds a tool rake face. It is necessary to dress the grinding wheel when its performance decreases. It is important dressing interval for using grinding wheel. The influence of the grinding performance decrease of the wheel on the tool life is examined. The wheel used is that decreases the grinding performance by repeating a lot of grinding (old wheel), and that does just dressing (fresh wheel), Then the fly tool is re-ground using them. The result is shown in Fig. 11. The work material is SCr420, fly tool is P20, cutting speed is 200 m/min, feed is 0.38 mm/rev, depth of cut is 0.75 mm, and cutting method is up cutting. The experiment has two types of depth of re-grinding; they are 10 and 100 μm. It is found that the tool life re-ground by fresh wheel is longer than that by old wheel. Yoshikawa et al. (1987) and Sakagami (1987) were reported that the compressive residual stress will be left on the surface of the tool in grinding by diamond grain, then, the tool life becomes long by the compressive residual stress. It is considered that the compressive residual stress exists more on the tool rake face re-ground by fresh wheel.

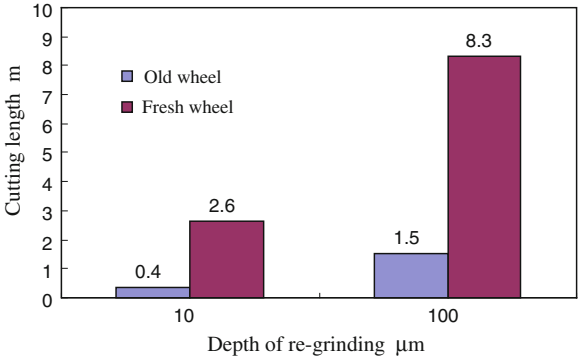

Fig. 11 The influence of grinding performance decrease of wheel on the tool life (P20, V = 200 m/min, f = 0.38 mm/rev, h = 0.75 mm, up cutting, resinoid diamond wheel)

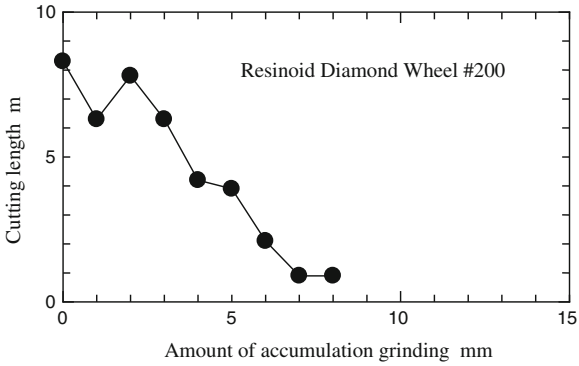

Fig. 12 Relationship between tool life and amount of accumulation grinding (P20, V = 200 m/min, f = 0.38 mm, h = 0.75 mm, up cutting)

3.2.2 Dressing Interval for Resinoid Diamond Wheel

It is important to clear the dressing interval for grinding wheel. Since, in hobbing, it is necessary to re-grind a lot of edges of hob similarly. The experiment is done in order to clarify the dressing interval. Tool face is re-ground by resinoid diamond wheel. The work is cut by fly tool, which re-ground every 1,000 μm accumulation grinding. Figure 12 shows the results of experiment. The work material is SCr420, fly tool is P20, cutting speed is 200 m/min, feed is 0.38 mm/rev, depth of cut is 0.75 mm, and cutting method is up cutting. It is found that the tool life is half at 4 mm of accumulation re-grinding, one eight at 6 mm, compared from first re-grinding. Accumulation re-grinding of 4 mm corresponds to the re-grinding of about 40 times for the amount of the cut of 100 μm.

4 Conclusions

This paper gives experimental results showing how the chipping factor of the carbide tool deprnds on carbide material, cutting velocity, feed rate, and so on.

1. The authors recommend for carbide tool, P20 has high enough heat resistance cutting speed can prevent an initial chipping.
2. The tool life is much longer at down cutting compared with up cutting. However, both up cutting and down cutting are by necessity used in hobbing. To obtain long total tool life with a machining needed some part of up cutting and down cutting, it is necessary to focus on improving the up cutting which shortens more effectivity the tool life than the down cutting.
3. In case of using resinoid diamond wheel, it is found that the tool life using tool grinding by re-ground with fresh wheel is longer than that with old wheel. The tool life is half at 4 mm of accumulation re-grinding compared from fresh wheel.

References

Ariura Y, Umezaki Y, Nara H (1989) Finish hobbing of medium-hardness gears with cermet tipped hobs. In: Proceedings of the 1989 international power transmission and gearing conference, pp 691–696

Ishimaru R, Sakuragi I, Izumi N (2011) A fundamental study on the improvement for chipping characteristics in gear hobbing. Jpn Soc Mech Eng (Preprint). No.11-1, S112012

Sakagami K (1987) A study for bending and compressive fatigue characteristics of carbide steel. Academic dissertation, pp 16–22

Sakuragi I, Yonekura M, Hiroo Y, Nagano K (1994) A fundamental study of the carbide hob—for the carbide material of the carbide hob -. Mem Kurume National Coll Technol 9(2):1–14

Sakuragi I, Hiroo Y, Yonekura M (2001) Study on practical application of carbide hobbing—full depth cutting of hardened gear teeth-. In: Proceedings of international conference on motion and power transmissions, vol 1, pp 321–326

Umezaki Y, Ariura Y, Matsumoto H, Yoshimura K, Kimura D (2001) Transient phenomenon of chip generations and movements in hobbing. In: Proceedings of international conference on motion and power transmissions, vol 1, pp 327–332

Umezaki Y, Ariura Y, Suzuki T, Ishimaru R (2008) High-speed finishing of hard gear teeth with cBN-tipped hob. Int J Autom Technol 2(5):348–353

Yoshikawa A, Suzuki I, Suzuki K, Tsujigo Y, Yamamoto Y, (1987) Diamond tool, Nikkei Gizyutsu Tosho, p 475

Modelling of Trochoidal Gearing at the Gerotor Pump

Lozica Ivanović, Danica Josifović and Andreja Ilić

Abstract In this paper, generating and analyzing of meshing of the gear pair profiles with internal trochoidal gearing is considered. Firstly, parameter and vector equations of the conjugated tooth profiles are defined. The forces and torques which are acting on the gear pair of the gerotor pump are also considered in this paper. The problem of the contact forces determination is complex because the pumps with trochoidal gearing loading are transmitting simultaneous at the more contact points. The fluid pressure forces which are acting on the tooth gear flanks, and which are depended of the numerous influential parameters are also given. From this reason, one simply physical model and corresponding analytical method are applied. The aim of this analysis is to determine the load distribution at the trochoidal pumps with fixed axes of shafts. The calculation of the contact stresses and the choice of construction solution with the minimum contact tooth loading can be done on the basis of the obtained results.

Keywords Trochoidal gearing · Gerotor pumps · Contact force · Load distribution · Contact stresses

List of Symbols

$O_a x_1 y_1$	Coordinate system attached to the generating point
$O_t x_t y_t$	Coordinate system attached to the internal gear
$O_a x_a y_a$	Coordinate system attached to the external gear
$O_f x_f y_f$	Fixed coordinate system

L. Ivanović (✉) · D. Josifović · A. Ilić
University of Kragujevac, Mechanical Engineering, Sestre Janjić 6 34000 Kragujevac, Serbia
e-mail: lozica@kg.ac.rs

D. Josifović
e-mail: danaj@kg.ac.rs

A. Ilić
e-mail: gilic9@sbb.rs

G. Dobre (ed.), *Power Transmissions*,
Mechanisms and Machine Science 13, DOI: 10.1007/978-94-007-6558-0_44,

O_t, O_a	Center of the internal gear and the external gear, respectively
C	Pitch point
D	Generating point
P	Contact point
z	Teeth number of the external gear
$z - 1$	Teeth number of the internal gear
e	Center distance between the internal and external gear (eccentricity)
r_t	Radius of the internal gear pitch circle
r_a	Radius of the external gear pitch circle
d	Distance between the generating point D and the center of the external gear
r_c	Radius of the equidistant
c	Equidistant coefficient
b	Gear width
K_i	Chamber
r_s	Radius of the external gear root circle
Δp	Pressure drop
k	Constant
w_i	Deformation in the contact point P_i
a_{ni}	Contact half-width
w_{ni}	Normal component of deformation w_i
F_p	Fluid pressure force
F_l	Reaction of support
F_n	Normal force
M_p	Torque of fluid pressure
M_l	Drive torque
M_t	Torque of fluid pressure with respect to the center of the internal gear
M_a	Torque of fluid pressure with respect to the center of the external gear
M_{nt}	Torque due to normal force with respect to the center of the internal gear
E	Young's modulus
ϕ	Generating rotation angle
λ	Trochoid coefficient
δ	Leaning angle
ϕ_t	Rotation angle of the internal gear about its own axis
ϕ_a	Rotation angle of the external gear about its own axis
ψ	Referent angle of rotation
τ_i	Angle between the axis x_a and the axis x_i
ω_t	Angular frequency of the internal gear about its own axis
ω_a	Angular frequency of the external gear about its own axis
α_{P_i}	Angle between the line O_tP_i and the normal CP_i
α_{ni}	Angle between the axis x_f and the normal CP_i
ξ	Angle of displacement
ν	Poisson's ratio

1 Introduction

Geometry of the trochoids and their coupled envelopes is defined and analyzed to details in the literature. Analytical model to calculate the force at each contact point by neglecting friction and by that, maximum contact stress in the gear teeth was obtained by Colbourne (1974). Unified and compact equation for describing the geometry, the geometric properties of the different types of trochoid and the geometric properties of a conjugate envelope is presented in the literature (Shung and Pennock 1994). Modification of epitrochoidal profiles of rotary pumps analyzed Robinson and Lyon (1976). They showed that equidistant of basic conjugated curves satisfies fundamental law of gearing and that it can be applied for definition of gearing profile. Detailed analysis of geometric, kinematic and functional characteristics of rotating machines with gerotor mechanisms is shown by Maiti and Sinha (1990, 1988). They developed analytical method for contact stresses calculation that can be applied for epitrochoidal hydraulic pumps and engines. Relationships that show the influence of the trochoid ratio, the pin size ratio and the radius of the generating pin on the curvature of the epitrochoidal gerotor is derived by Beard et al. (1992). Envelope's relation to surface family by considering envelopes formed by several branches for cycloidal pumps and conventional worm gear drives is investigated by Litvin and Feng (1996). General method showing the analytical condition for avoiding undercutting using the concept of the limit curve is found by Mimmi and Pennacchi (2000). Computer program for tooth contact analysis, tooth interference and rapid wearing through modification of the rotor profile geometry of a cycloidal pump whose one pair of teeth is in mesh at every instant, as mentioned Demenego et al. (2002). General procedure for the computerized design of gerotor lubricating pumps for internal combustion engines is presented in the literature (Mancò et al. 2000). A kinematic analysis of the trochoidal gearing in the gerotor is presented in the literature (Ivanović and Josifović 2006). Developed a simple analytical model of a trochoidal pump assuming frictionless contact between teeth is given in the literature (Gamez-Montero et al. 2006). The authors have compared analytical and finite element analysis results of the maximal contact stresses with experimental results obtained by the photo elasticity method. The methodology for the selection of the optimal shape profile of teeth for lubrication pumps is described in the literature (Ivanović 2007).

On the base of the theoretical considerations in the area of trochoidal gearing the main aim of this paper is development of the analytical model to analysis of influence geometrical parameters on the contact forces and stresses by gerotor pump. This paper deals with the gearing of the trochoidal pump gearing pair where the outer gear has one more tooth than the inner one. The inner gear profile is described by peritrochoid equidistant while the profile of the outer gear is described by a circular arc with r_c radius. For trochoidal gearing, meshing of all teeth is obtained, at the same time, with theoretical profiles of gearing. This is the reason that general equations of profile point coordinates need to be established, so

that they could be applied for all teeth. Towards derivation of coordinates equations for any P_i contact point, it was needed to generalize the geometric relations between the rotation angles of the elements of the trochoidal gearing couple. A kinematic pair model with the fixed gear shaft axes was adopted, whereby the drive shaft is connected to the inner gear. Further on, forces and torques that act on the gearing pair of the rotary trochoidal pump are discussed. A modified analytical method presented by Colbourne (1976) and Maiti (1991) is applied for the analysis of forces and torques.

2 Analysis of a Load of the Trochoidal Pumps with Fixed Axes of Shafts

In this section is given the analytical method for calculation of the instantaneous torque and contact forces in trochoidal pumps with fixed axes of shafts, where the driving shaft is connected to the inner gear.

The basic geometric relations for the generation of peritrochoid, which is adopted for defining the basic profile at the observed gear pump, are shown in Fig. 1.

The position vector of the P_i contact point in the coordinate system of the trochoid can be written in the form of the following matrix relation:

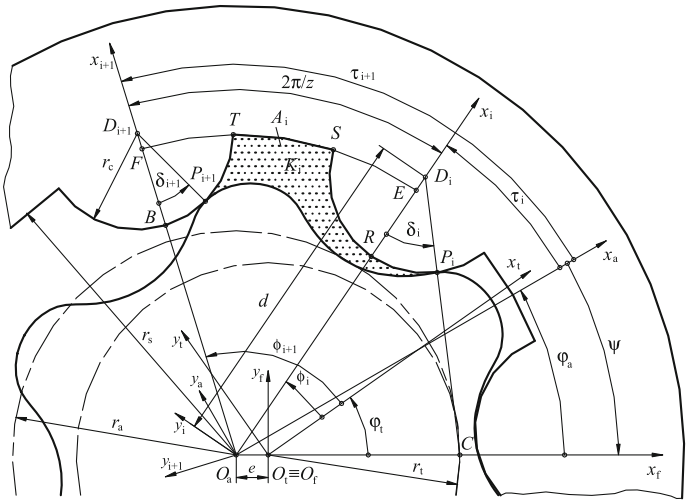

Fig. 1 Schematic presentation of the gearing pair of the trochoidal pump with the basic geometric variables for the P_i contact point and for the P_{i+1} contact point

$$r_{P_i}^{(t)} = \begin{bmatrix} e[\cos z\phi_i + \lambda z \cos\phi_i - c\cos(\phi_i + \delta_i)] \\ e[\sin z\phi_i + \lambda z \sin\phi_i - c\sin(\phi_i + \delta_i)] \\ 1 \end{bmatrix} \quad (1)$$

Parameters used in Eq. (1) are explained in details in the literature (Ivanović et al. 2010).

After defining the gearing geometry of the gerotor pump gearing pair and after establishing a basic kinematic model, calculation of forces and torques, which act on the gears, can be done.

2.1 Fluid Pressure Force and Torques

The fluid pressure force which separates the suction inlet chambers from the pressure outlet chambers is a continuous force that can be represented by the equivalent concentrated pressure force $\boldsymbol{F}_p$. The direction of vector $\boldsymbol{F}_p$ coincides with the centerline of the line segment **AB** that connects two contact points at the separation borderline between the suction inlet chambers and the pressure outlet chambers zones, as shown in Fig. 2. In accordance with this, the equivalent pressure force in the pump can be expressed in the following vector form:

$$\boldsymbol{F}_p^{(f)} = -\Delta p b \boldsymbol{k}_f \times \boldsymbol{AB}^{(f)}. \quad (2)$$

The torque of the equivalent pressure force in respect to the instantaneous rotation center C, is expressed by the multiplication of vectors as:

$$\boldsymbol{M}_p^{(f)} = \boldsymbol{CS}^{(f)} \times \boldsymbol{F}_p^{(f)}, \quad (3)$$

where S is the middle point of the vector $\boldsymbol{AB}$ (Fig. 2).

Consequently the equivalent pressure force, Eq. (2), could be expressed in the following form:

$$\boldsymbol{F}_p^{(f)} = \Delta p b \left[\left(y_{\boldsymbol{CB}}^{(f)} - y_{\boldsymbol{CA}}^{(f)} \right) \boldsymbol{i}_f - \left(x_{\boldsymbol{CB}}^{(f)} - x_{\boldsymbol{CA}}^{(f)} \right) \boldsymbol{j}_f \right]. \quad (4)$$

As a result, the torque of the equivalent pressure force in the pump in condensed form is defined as:

$$\boldsymbol{M}_p^{(f)} = \frac{\Delta p b}{2} \left(|\boldsymbol{CA}|^2 - |\boldsymbol{CB}|^2 \right) \boldsymbol{k}_f. \quad (5)$$

The resultant of all contact forces that act on the inner gear can be calculated as sum of vectors

$$\boldsymbol{F}_n = \sum_{i=1}^{z} \boldsymbol{F}_{ni}, \quad (6)$$

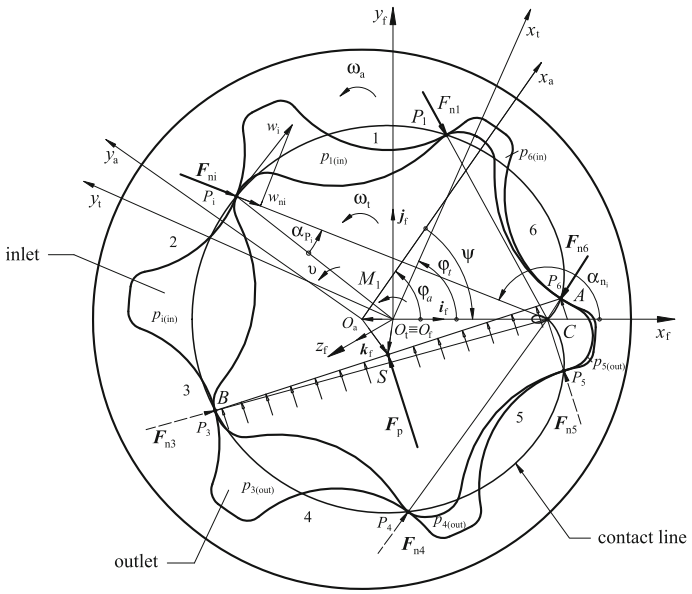

Fig. 2 The fluid pressure force and the contact forces acting on the inner gear

that acts in the kinematic pole C.

For the considered pump model, the equilibrium equation of forces could be written in the vectorial form as,

$$\boldsymbol{F}_{\mathrm{p}} + \boldsymbol{F}_{\mathrm{n}} + \boldsymbol{F}_{\mathrm{l}} = 0. \tag{7}$$

Equilibrium equations of the torque in respect to point O_{t} could be written as

$$\boldsymbol{M}_{\mathrm{F_p(O_t)}} + \boldsymbol{M}_{\mathrm{F_n(O_t)}} + \boldsymbol{M}_{\mathrm{l}} = 0, \tag{8}$$

or in respect to point O_{a} as,

$$\boldsymbol{M}_{\mathrm{F_p(O_a)}} + \boldsymbol{M}_{\mathrm{F_n(O_a)}} = 0. \tag{9}$$

The torques from the previous equations could be expressed by the multiplication of vectors in the form as:

$$\boldsymbol{O_tS} \times \boldsymbol{F}_{\mathrm{p}} + \boldsymbol{O_tC} \times \boldsymbol{F}_{\mathrm{n}} + \boldsymbol{M}_{\mathrm{l}} = 0 \tag{10}$$

and

$$\boldsymbol{O_aS} \times \boldsymbol{F}_{\mathrm{p}} + \boldsymbol{O_aC} \times \boldsymbol{F}_{\mathrm{n}} = 0. \tag{11}$$

Based on the Eqs. (10) and (11), the equivalent contact force torque in respect to point O_{a} could be expressed in the scalar form as

$$M_{\mathrm{F_n(O_a)}}^{(\mathrm{f})} = \frac{\Delta p b}{2}\left\{ \left[r_{\mathrm{B}}^{(\mathrm{f})}\right]^2 - \left[r_{\mathrm{A}}^{(\mathrm{f})}\right]^2 + 2e\left[x_{\mathrm{B}}^{(\mathrm{f})} - x_{\mathrm{A}}^{(\mathrm{f})}\right]\right\}. \tag{12}$$

The equivalent pressure force torque, in respect to point O_t, could be written in the scalar form as

$$M_{\mathrm{F_p(O_t)}}^{(\mathrm{f})} = \frac{\Delta p b}{2}\left\{ \left[r_{\mathrm{A}}^{(\mathrm{f})}\right]^2 - \left[r_{\mathrm{B}}^{(\mathrm{f})}\right]^2\right\}. \tag{13}$$

Vector of the fluid pressure force $\boldsymbol{F}_{\mathrm{p}}$ is the only one completely defined in the Eq. (7) and for further calculation it is convenient to express the Eq. (8) in the following scalar form

$$M_1 = -M_{\mathrm{F_p(O_t)}} + M_{\mathrm{F_p(O_a)}}\frac{z-1}{z}. \tag{14}$$

For the calculation of the contact forces it is necessary to determine the equivalent contact force torque with respect to the center of the interior gear O_t.

2.2 Contact Forces

During the gear rotation, the total load caused by momentum on the gear shaft is transferred by simultaneous meshing of the gear pair teeth. The normal force F_{ni} that acts on the meshed teeth causes local tooth deformation and displacement of the contact point for the value w_{ni} in the direction of the force action. It also causes an angular displacement ξ which is assumed to be equal for all contact points, for selected angular position. If the deformation w_{ni} at the contact point P_{i} is greater than zero it is confirmed that contact is created at that point. If the deformation w_{ni} at the contact point P_{i} is negative or equal zero, the contact is not created and this contact point do not participate in the load distribution. Based on Fig. 2, the total torque about the gear center is equal to the sum of torques of normal forces that act at individual teeth pairs,

$$M_{\mathrm{F_n(O_t)}} = \sum_{i=p}^{q} M_{\mathrm{F_{ni}(O_t)}} = k\,\xi \sum_{i=p}^{q} e^2(z-1)^2 \sin^2\alpha_{\mathrm{ni}}, \tag{15}$$

where p and q are the ordinal numbers used to identify the first and the last teeth of the external gear that are transmitting the load and k is the tooth stiffness that is considered to be constant The final form of the contact force F_{ni} is obtained:

$$F_{\mathrm{ni}} = M_{\mathrm{F_n(O_t)}}\frac{\sin\alpha_{\mathrm{nj}}}{\sum\limits_{\mathrm{j}=p}^{q} e(z-1)\sin^2\alpha_{\mathrm{nj}}} \tag{16}$$

After the procedure of the gear pair identification that transmits the load and the calculation of the contact forces is possible to calculate the contact stresses.

2.3 Contact Stresses

The analytical calculation of contact stresses at elastic bodies in contacts is based upon the results of mathematical theory developed by Hertz. In these problems it is assumed that acting load is static. It is also assumed that the materials of the bodies are homogeneous and isotropic. The friction is neglected in considered problems. As the consequence of the contact force influence at the teeth comes to the appearance of elastic deformation. Different models for the calculation of the elastic deformation exists in literature, but the best results of calculation of the teeth elastic deformation w_{ni} and the contact half-width a_{ni} are obtained by the model that is developed by Weber, as concluded in the literature (Cornell 1981). The assumption that both bodies in the contact are made of the same material, so as that they have the same Young's modulus and Poisson's ratio, is introduced. If the contact force and the contact half-width are known, maximum contact stress can be calculated in the following Hertzian formula:

$$\sigma_{\mathrm{ni}} = \frac{2F_{\mathrm{ni}}}{\pi a_{\mathrm{ni}} b}. \tag{17}$$

Upon identification of the teeth pairs that transmit the load, is coming to the calculation of the torques and contact forces. Geometrical parameters of the gear set are: $z = 6$, $e = 3.56$ mm, $b = 16.46$ mm, $\lambda_{(1)} = 1.375, \lambda_{(2)} = 1.575, c_{(1)} = 2.75, c_{(21)} = 3.95$. Other characteristics are: $\Delta p = 0.6$ MPa, $n_{\mathrm{t}} = 1500$ rpm, $\omega_{\mathrm{t}} = 2\pi n_{\mathrm{t}} = 50\mathrm{ps}^{-1}$, $E = 2 \cdot 10^5$ MPa, $v = 0.3$. The graphical representation of the analytically calculated contact forces, for the single phase of rotation ($\varphi_{\mathrm{a}} = 2\pi/z$), is presented in Fig. 3 and contact stresses is presented in Fig. 4.

Maximum contact force occurs at the beginning of the first phase at the tooth whose adjacent chamber starts its expansion phase. For example, in the Fig. 3 at the beginning of the first phase, maximum contact force acts on the tooth no. 1, and at the beginning of the second phase, maximum contact force acts on the tooth no. 6. It is concluded that, during gears rotation, contact forces and deformation equal zero for certain angular position (Fig. 3). Figure 3 shows that teeth denoted as 4 and 5 do not get in contact during one operating cycle.

Maximum contact stress (Fig. 4) is appeared at the beginning position, not on the teeth that transmits the maximum contact force, but on the teeth where the contact is in the area with the minimal equivalent radius of curvature of the meshing profile.

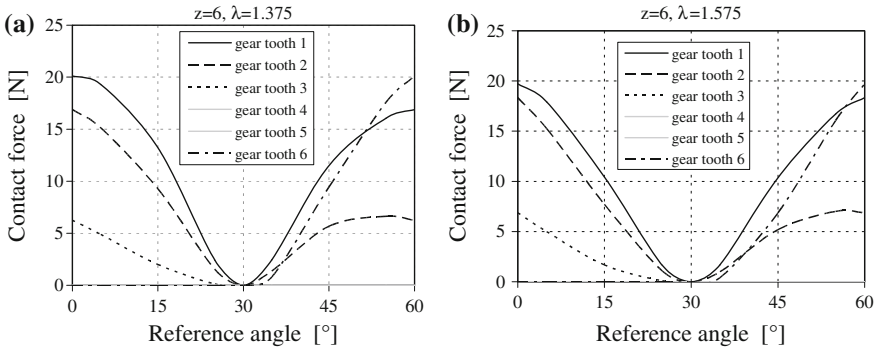

Fig. 3 Results of analytical calculation of contact forces: **a** $\lambda = 1.375$. **b** $\lambda = 1.575$

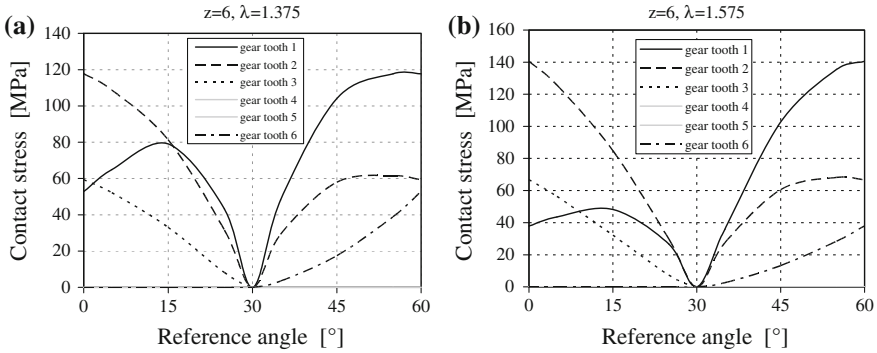

Fig. 4 Results of analytical calculation of contact stresses: **a** $\lambda = 1.375$. **b** $\lambda = 1.575$

3 Conclusion

This paper shows the analysis of the general geometrical and kinematical model of the trochoidal gearing applicable to all teeth of trochiodal pump at any moment of meshing. Application of the analytical model identifies the teeth that are getting in contact during a single phase of the pump working process. The results of the analytical calculation indicate that in the pumps with the same working volume and the same number of teeth, the more contact stresses are appeared at the gear set with the greater value of trochoid coefficient λ.

Further investigations will be focussed to the development of the model for identification of the optimal geometrical parameters of the trochoidal teeth, from the aspect of maximal contact stress reduction and consideration of constrains related to functionality and practical applicability.

Acknowledgments The work has been funded through the Financial Agreement by Serbian Ministry of Education and Science, project TR35033.

References

Beard JE, Yannitell DW, Pennock GR (1992) The effects of the generating pin size and placement on the curvature and displacement of epitrochoidal gerotors. Mech Mach Theory 27(4):373–389

Colbourne JR (1974) The geometry of trochoid envelopes and their application in rotary pumps. Mech Mach Theory 9:421–435

Colbourne JR (1976) Reduction of the contact stress in internal gear pump. J Eng Ind, Trans. ASME, Nov., 98(4):1296–1300

Cornell RW (1981) Compliance and stress sensitivity of spur gear teeth. ASME J Mech Des 103(2):447–459

Demenego A, Vecchiato D, Litvin FL, Nervegna N, Manco S (2002) Design and simulation of meshing of a cycloidal pump. Mech Mach Theory 37:311–332

Gamez-Montero PJ, Castilla R, Khamashta M, Codina E (2006) Contact problems of a trochoidal-gear pump. Int J Mech Sci 48(1):1471–1480

Ivanović L (2007) Identification of the optimal shape of trochoid gear profile of rotational pump elements. PhD dissertation, The Faculty of Mechanical Engineering in Kragujevac, Kragujevac (In Serbian)

Ivanović L, Josifović D (2006) Specific sliding of trochoidal gearing profile in the gerotor pumps. FME Trans 34(3):121–127

Ivanović L, Devedžić G, Mirić N, Ćuković S (2010) Analysis of forces and moments in the gerotor pumps. In: Proceedings of institution of mechanical engineers, part C: journal of mechanical engineering science, vol 224(10), pp 2257–2269. doi:10.1243/09544062JMES2041

Litvin FL, Feng P (1996) Computerized design and generation of cycloidal gearings. Mech Mach Theory 31(7):891–911

Maiti R (1991) Active contact stresses at epitrochoid generated rotor-stator set of fixed axis or equivalent system ROPIMA type hydrostatic units. J Eng Ind 113:465–473

Maiti R, Sinha GL (1988) Kinematics of active contact in modified epitrochoid generated rotary piston machines. Mech Mach Theory 23(1):39–45

Maiti R, Sinha GL (1990) Limits on modification of epitrochoid used in rotary piston machines and the effects of modification on geometric volume displacement and ripple. Ingenieur-Archiv 60:183–194

Mancò G, Mancò S, Rundo M, Nervegna N (2000) Computerized generation of novel gearings for internal combustion engines lubricating pumps. Int J Fluid Power 1(1):49–58

Mimmi G, Pennacchi P (2000) Non-undercutting conditions in internal gears. Mech Mach Theory 35:477–490

Robinson FJ, Lyon JR (1976) An analysis of epitrochoidal profiles with constant difference modification suitable for rotary expanders and pumps. J Eng Ind, Trans ASME 98:161–165

Shung JB, Pennock GR (1994) Geometry for trochoidal-type machines with conjugate envelopes. Mech Mach Theory 29(1):25–42

New Worm Technologies Manufacturing on the NC Lathe

Alexandru Pozdirca, Andrei Oltean and Cristian-Sorin Albu

Abstract The paper presents a new method of worms processing on NC lathes, using end mills. The authors denote ZPA this new type of worm. It presents the enveloping calculus for determining the contact line between the tool and the flank of the worm and also the calculus for determining the axial profile obtained for the worm. As an example, the paper indicates the deviation of the axial profile of ZPA against to the ZA profile. Due to the manufacturing possibilities offered by an Okuma Multus NC lathe, the paper indicates milling settings in order to process an Archimedes worm using end mills. The main advantages of this new worm generation method are: (1) use of standard end mills with reduced costs; (2) short processing time of worm.

Keywords Cylindrical worm · NC lathe · Technology · ZPA

1 Introduction

According to DIN 3975 standard, the cylindrical worms are classified as:

- ZA—worm gear with straight-line tooth profile in axial section.
- ZN—worm with a straight-line tooth profile in normal tooth section.

A. Pozdirca (✉)
"Petru Maior" University, Tirgu Mures, Romania
e-mail: apoz@upm.ro

A. Oltean · C.-S. Albu
Technical University of Cluj-Napoca, Cluj-Napoca, Romania
e-mail: olteandrei@yahoo.com

C.-S. Albu
e-mail: cris_s_a@yahoo.com

G. Dobre (ed.), *Power Transmissions*,
Mechanisms and Machine Science 13, DOI: 10.1007/978-94-007-6558-0_45,

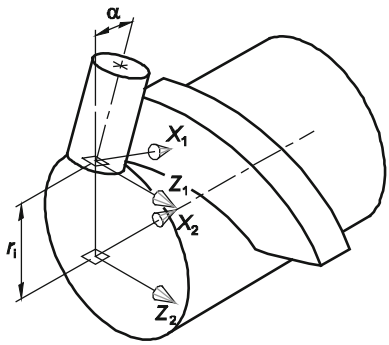

Fig. 1 Position of the tool relative to the processed worm

- ZE—worm with a straight-line tooth profile in a plane tangent to the main cylinder.
- ZK—profile formed by a cone ground using a wheel and/or shank tool.
- ZC—concave tooth profile.

The geometry and generation of each listed worm type are well known in literature (Litvin and Fuentes 2004; Dudas 2000). The worms ZA, ZN and ZE can be generated using a lathe tool and the resulted flank of worm is a ruled surface. The worms ZK are generated using conical tools with straight-line generatix; the resulted flank of the worm is a non-ruled surface. The worm ZC is similar with ZK2; the generating surface is a revolution surface with circular arc as axial profile.

The paper proposes a new type of worm's generation, using standard cylindrical milling tools. This approach can be done self-contained or by comparison with one of the know worms. The authors propose ZPA to denote this new type of worm. This paper focuses on comparing the deviation of the ZPA's axial profile against the ZA worm profile.

Let there be a frontal—cylindrical tool set for processing ZA worm (called Archimedes). We associate to the tool and to the worm the systems as in Fig. 1. The tool position relative to worm is determined by two parameters: α and r_i. We seek to determine the contact curve between the tool and the worm, the axial profile of the generated worm and also the deviation in comparison with the Archimedes nominal profile.

2 Contact Curve Tool-Worm

In order to determine the contact curve between a cylindrical tool and the generated worm, we write the parametrical equations of the cylindrical surfaces of the tool, in own system, and also of the unit normal, as follows:

$$\begin{cases} x_1 = r_s \cos u \\ y_1 = v \\ z_1 = r_s \sin u \end{cases} \tag{1}$$

$$\begin{cases} n_{x1} = \cos u \\ n_{y1} = 0 \\ n_{z1} = \sin u \end{cases} \tag{2}$$

We apply a transformation of the coordinates in order to rapport the tool surface to the system of the worm:

$$\mathbf{r}_2 = \mathbf{M}_{2,1} \cdot \mathbf{r}_1 \tag{3}$$

As a result of the reference to the worm system, the equations of the tool surface and the projections of the unit normal, become:

$$\begin{cases} x_2(u,v) = r_s \cos u \cos \alpha + v \sin \alpha \\ y_2(u,v) = -r_s \cos u \sin \alpha + v \cos \alpha + r_i \\ z_2(u,v) = r_s \sin u \end{cases} \tag{4}$$

$$\begin{cases} n_{x2} = \cos \alpha \cos u \\ n_{y2} = -\sin \alpha \cos u \\ n_{z2} = \sin u \end{cases} \tag{5}$$

In the contact points between the tool and the worm, the following condition must be respected (Maros 1985; Pozdirca 2010):

$$-n_{y2} z_2 + n_{z2} y_2 + h n_{x2} = 0 \tag{6}$$

in which h represents the helical parameter of the worm. Replacing the relations (4) and (5) in relation (6) we obtain a connection between the u and v parameters as follows:

$$\tan u = \frac{-h \cos \alpha}{v \cos \alpha + r_i} \tag{7}$$

The contact curve between the a cylindrical tool and the worm is obtained by giving values to the v parameter; for each value of the v parameter we determine, using the relation (7), a corresponding value for parameter u. The pair of values, u and v, replaced in relation (5), will give the position of a contact point in the worm system.

3 The Axial Profile of the Worm

For each P point of the contact curve between the tool—worm, we make a rotation movement, with a γ angle, around the X_2 axis in order to bring it to the axial plan X_2Y_2 (Fig. 2).

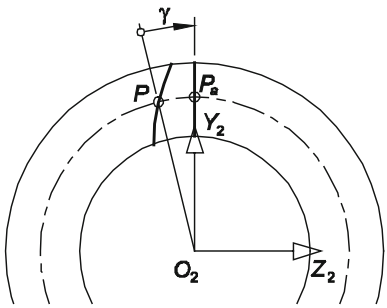

Fig. 2 Determining the axial profile

Corresponding to this rotation, in order to keep the point on the flank, the point must go forward on the X_2 axis, with a value equal to the helical parameter h. As a result, the coordinates of the points of the axial profile P_a will be determined as follows (Pozdirca 2010):

$$\begin{cases} x_a = x_2 - h \cdot \gamma \\ y_a = \sqrt{y_2^2 + z_2^2}, \text{ where } \tan\gamma = \dfrac{z_2}{y_2} \\ z_a = 0 \end{cases} \tag{8}$$

4 Deviations from the Archimedes Profile

The axial profile of the worm, generated by the cylindrical cutter is different from the Archimedes one, even if the inclination angle is equal to 20°.

Table 1 presents the deviation of the determined axial profile against the right line of the Archimedes profile, interacting on the exterior diameter (Fig. 3). The values are determinate for a worm with the following characteristics:

- Axial module, $m_a = 10$ mm
- Diametric coefficient, $q = 7.6$
- Helical parameter, $h = 7.6$
- The ray of the cylindrical cutter, $r_s = 5$ mm.

The deviations from the table are measured for different diameters of the worm. As compared to the Archimedes worm, the one generated by the cylindrical cutter

Table 1 Deviations of the axial profile

a mm	$\alpha = 20°$	$\alpha = 20.35°$
0	0.000	0.000
5	−0.022	0.011
10	−0.053	0.013
15	−0.098	0.000
19	−0.152	−0.027

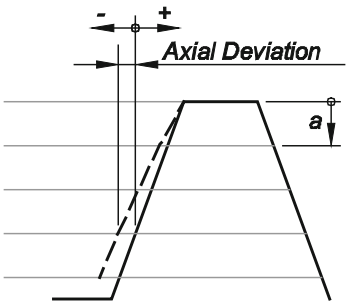

Fig. 3 Deviations of determined axial profile against to the archimedes profile

shows a convex flank, a fact which can lead to a better localization of the contact, on the height of the tooth.

5 Correcting the Errors

The correction of the errors must take into consideration the possibilities offered by the use of the equipment with numerical control. We consider a NC lathe with 5 controlled axes (Okuma 2005): X, Y, Z, B, and C (Fig. 4).

The control of the Z axis allows the translation of the axial profile along the axis of the worm. The control of the B axis allows the correction of the α angle. The control of the Y axis allows the realization of an eccentricity between the axis of the tool and the axis of the worm. To be mentioned that, in Fig. 1, the axis of the tool and of the worm are concurrent—resulting an eccentricity equal to zero.

Through applying the corrections on the axis Z, B and Y, we seek the reduction of the deviation of the axial profile as compared to the Achimedes one, chose as a reference. For the worm and the chosen tool, Table 1 presents the deviations of the

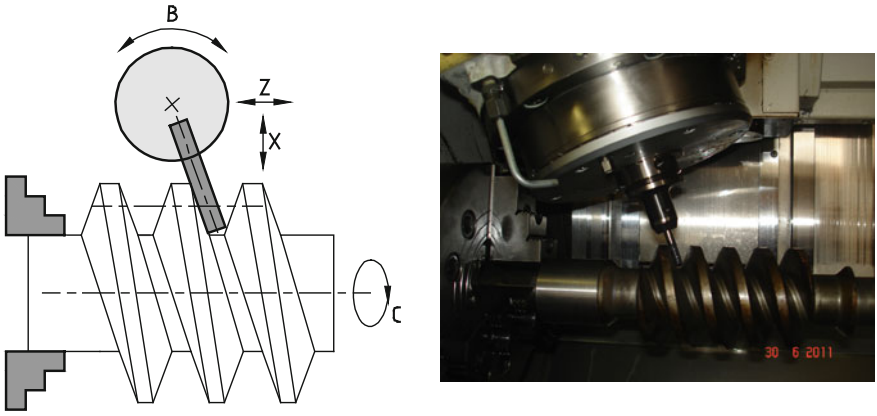

Fig. 4 The axis of the OKUMA Multus B300 lathe

axial profile, along the axis of the worm, when correcting the inclination of the cutter from 20° to 20.35°. We can observe the reduction of the maximum deviations to the level of 0.027 mm. The sign of the deviation indicates if the point of the real profile is on the left (minus) or on the right (plus), reported to the nominal profile. The search of the optimal corrections was accelerated through implementing a program in AutoLISP, which displays the graphical result in AutoCAD (Pozdirca 2010).

6 Technological Aspects

Level of 0.02 mm of the error, measured in the axial profile, can be practical acceptable. For processing the worm shown in paragraph 3, we propose a technological itinerary which assumes the processing of the worm, after treatment, with the utilization of three milling tools, made out of metallic carbide.

The first cutter is dedicated to roughing the worm (Fig. 5, steps A). The second cutter is dedicated to process the base of the flank and the third cutter is dedicated to finishing the flank (Fig. 5, steps B and C).

According to the durability calculus, a set of cutters can process approximately 100 worms, until the cutters need to be re-sharpened. The cutters used can be

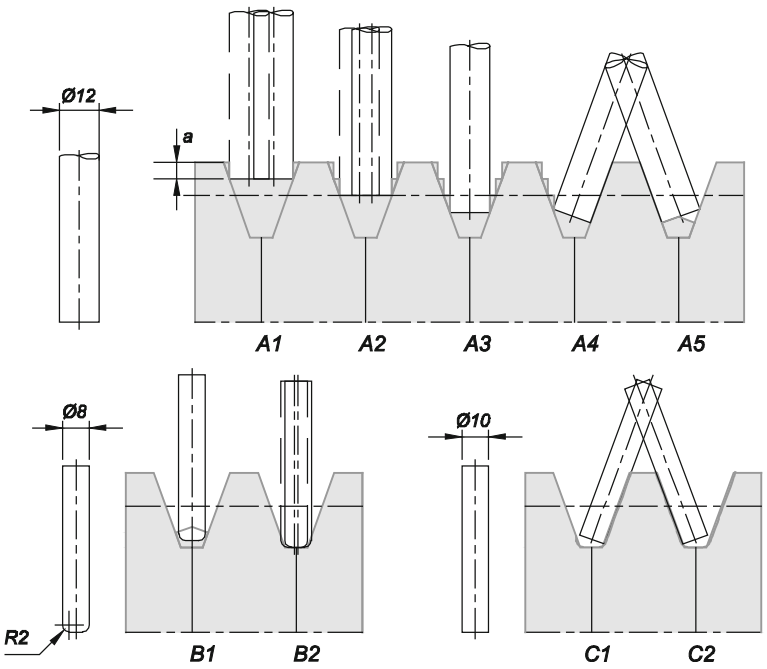

Fig. 5 Steps of worm processing

Table 2 Data sheet of the processing of the worm

No.	Operation	Tool	Settings	Time
1	Thinning A1, A2, A3	Diameter: Ø12	Cutting speed: 120 m/min	9
		Length: 16/73	Speed: 3,200 rot/min	
		Tool type: 2897A.012	Feed per tooth: 0.08 mm	
		Taper: 6563.12080	Feed speed: 1,024 mm/min	
2	Semi finishing A4, A5	Diameter: Ø12	Cutting speed: 140 m/min	2.5
		Length: 16/73	Speed: 3,800 rot/min	
		Tool type: 2897A.012	Feed per tooth: 0.10 mm	
		Taper: 6563.12080	Feed speed: 1,520 mm/min	
3	Thinning B1	Diameter: Ø8R2	Cutting speed: 80 m/min	6
		Length: 19/63	Speed: 3,200 rot/min	
		Tool type: 2673A.008020	Feed per tooth: 0.03 mm	
		Taper: 6563.08065	Feed speed: 400 mm/min	
4	Semi finishing B2	Diameter: Ø8; R2	Cutting speed: 100 m/min	5
		Length: 19/63	Speed: 4,000 rot/min	
		Tool type: 2673A.008020	Feed per tooth: 0.04 mm	
		Taper: 6563.08065	Feed speed: 640 mm/min	
5	Flank finishing C1, C2	Diameter: Ø8	Cutting speed: 90 m/min	4
		Length: 16/68	Speed: 3,400 rot/min	
		Tool type: 2887A.008	Feed per tooth: 0.028 mm	
		Taper: 6563.08065	Feed speed: 760 mm/min	
			Base time [*min*]	*26.5*

situated in the family of the tools with a relatively low price, making this process an efficient one, from both the point of view of the tools used, but also from the point of view of the processing time, reported to the obtained quality and precision.

Table 2 represents the splinting regime and the integral processing times (roughing and finishing) of the worm presented in paragraph 4, using solid carbide end mills (Emuge 2012). The processing was made out of tempering steel, with a hardness of 46 HRC, for a length of the worm of 130 mm. As it can be observed in the table no. 2, the total processing time was of 26.5 min.

7 Conclusions

The Archimedes worms can be processed on recent NC lathes, with 4 or 5 controlled axes, using cylindro-frontal standard milling tools in some phases of roughing and finishing. The processing can be done in treated steel, and the surface roughness can be $R_a = 0.8$ μm.

In order to reduce the deviation as compared with a nominal profile, when finishing the flank of the worm, it must to correct the position of the tool, controlling on the NC lathe the axis B, Z and Y.

Searching of the right correction can be optimizing using CAD applications. The authors have developed an application in AutoCAD environment in order to optimize the corrections, and evaluate the errors. This method use simple tools and the processing time is reduce. All these considerations make the presented technology very interesting from a practical point of view.

The idea of this method can be used in order to process other different worm than Archimedes. In fact, the worm generated with this method can be considerate a new type of non-ruled worm. The authors propose to denote ZPA this new type of worm.

References

DIN 3975 (2002). Definitions and parameters on cylindrical worm gear pairs with rectangular crossing shafts—part 1: worm and worm wheel, July 2002

Dudas I (2000) The theory and practice of worm gears drives. Penton Press, Kogan Page Ltd., London

Emuge (2012) FRANKEN milling technology, tool catalogue 240. FRANKEN GmbH&Co. www.emuge-franken.de

Litvin FL, Fuentes A (2004) Gear geometry and applied theory, 2nd edn. Cambridge University Press, Cambridge

Okuma (2005) OKUMA Multus B300, OSP-P200LL, Programming manual, Pub. No. 5238-E-R5 (LE33-013-R01a), 1st edn., May 2005

Pozdirca A (2010) Curves and surfaces calculation and representation. “Petru Maior” University of Tirgu Mures, pp 166–175

Pelecudi C, Maros D (1985) Mecanisme, Editura Didactică şi Pedagogică, Bucureşti, pp 164–176

Part IV
Load Capacity, Structure and Components

Methodological Approach to Recovery of the Cracks on the Turbine-Shaft at Hydroelectric Power Plant Djerdap II

Vujadin Aleksić, Brane Vistać and Ljubica Milović

Abstract In present paper, the methodological approach to analysis of the causes of failures and recovery of the damages has been presented using the example of the damage of the turbine-shafts construction. This approach can be applied to various types of similar constructions, and its application in preventive maintenance would contribute to extension of the operating life of the turbine shafts.

Keywords Turbine shaft · Testing · Crack · Analysis · Recovery

1 Introduction

At HE Djerdap II, during the period from 1985 to 1987, 8 capsule-type aggregates of PL-15/826-G-750 type manufactured by LMZ (USSR) had been put into operation. Their parameters are available at http://www.djerdap.rs: max. head—12.75 m, calculation head—7.45 m, min. head—5 m, turbine power at calculation head—28 MW, diameter of runner wheel—7,500 mm, number of revolutions—62.5 min^{-1}, number of runner wheel blades—4 pcs.

Later on, from 1998 to 2000, another two aggregates of the same type, manufactured by UCM Resica (Romania) under the licence of LMZ, were put into operation. Cross-section of the power station with the aggregate and shaft under consideration and the space where recovery was conducted is given in Fig. 1.

V. Aleksić (✉) · B. Vistać
IMS Institute, Belgrade, Serbia
e-mail: vujadin.aleksic@institutims.rs

L. Milović
Technology and Metallurgy, University of Belgrade, Belgrade, Serbia
e-mail: acibulj@tmf.bg.ac.rs

G. Dobre (ed.), *Power Transmissions*,
Mechanisms and Machine Science 13, DOI: 10.1007/978-94-007-6558-0_46,

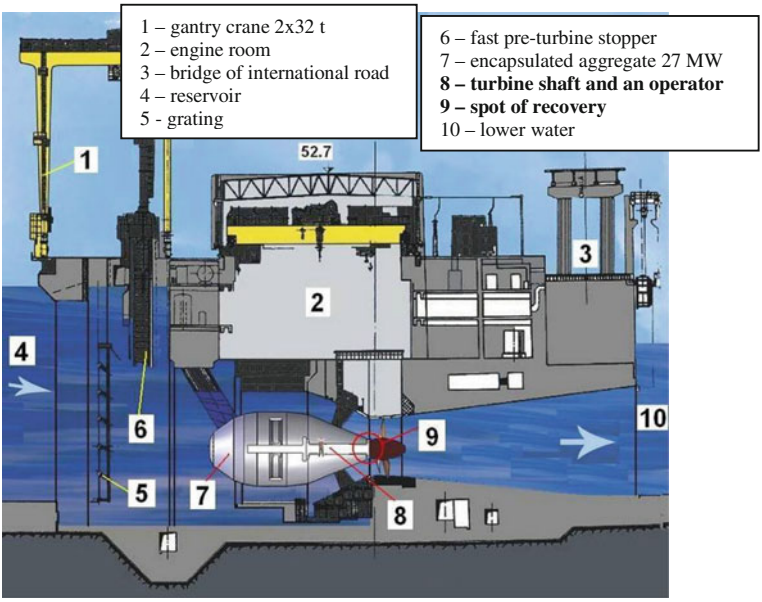

Fig. 1 Cross-section of the power station

2 About Shafts

The hollow shafts at hydroelectric power plants are vital parts connecting turbine with generator, thus enabling transformation of hydro- into electric power.

Turbine shafts of the aggregates at HE DJERDAP II are made from three parts, Fig. 2, either by welding of the flanges and cylindrical part of the shaft or by forging in one piece.

The properties of the material for manufacture of the turbine shafts according to Documentation (1984) are given in Tables 1 and 2.

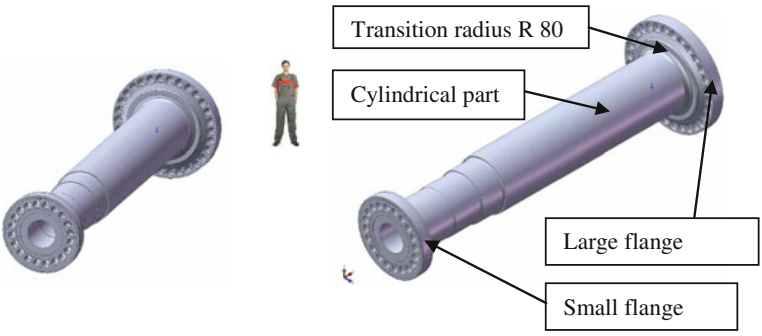

Fig. 2 The appearance of the hollow shaft of the turbine PL—15/826-G-750 at HE Djerdap II

Table 1 Chemical composition of the material for manufacture of the shafts

Steel designation		Chemical composition in mass %							
Basic designation	GOST or TU	C	Si	Mn	P-max	S-max	Cr	Ni	Cu
20GS 20GSL	977	0.16 – 0.22	0.60 – 0.80	1.00 – 1.30	0.030	0.030	<0.30	<0.30	<0.30

Table 2 Mechanical properties of the material for manufacture of the shafts

Steel designation		Mechanical properties in normalized and tempered state				
Basic designation	GOST or TU	Yield limit Re min (N/mm^2)	Tensile strength Rm min (N/mm^2)	Elongation A min (%)	Shrinkage Z min (%)	Toughness KCU min (J/cm^2)
20GS 20GSL	TU 108-11-358-78	275	470	16	–	39

Before exploitation, the flange zone toward the hub RK and transition radius R80, affected by water leaking through the shaft gasket, was protected by WRS (water-resistant system) according to TU AKZS-200. Total depth of the system was 400 μm. Preparation of the surfaces for application of the first, ground coating consisted of degreasing only, as these were previously subjected to fine finishing, temporarily protected with mineral grease with no traces of corrosion, although TU predicts sand blasting up to the Sa level of 2.5 according to SIS 05 59 00/1967. The shafts were exposed to the process of crack initiation and crack propagation, the extent of which depended only on the quality of initial anti-corrosive protection.

3 Testing of the Shafts

Before assembling, all the shafts were subjected to testing using the method of non-destructive testing in situ, disregarding the reports from the factory, and as applicable—without repair—installed under supervision of the experts authorized by the manufacturer of the equipment.

During exploitation, the zones of transition radius were not tested—not even visually: ACP was not renewed, either.

After 25 years of operation of the aggregate, in order to establish the state of the turbine shafts, the welded joints and shaft base metal were thoroughly tested using the non-destructive methods: visual testing (VT), penetrant testing (PT), magnetic-particle testing (MT) and ultrasonic testing (UT).

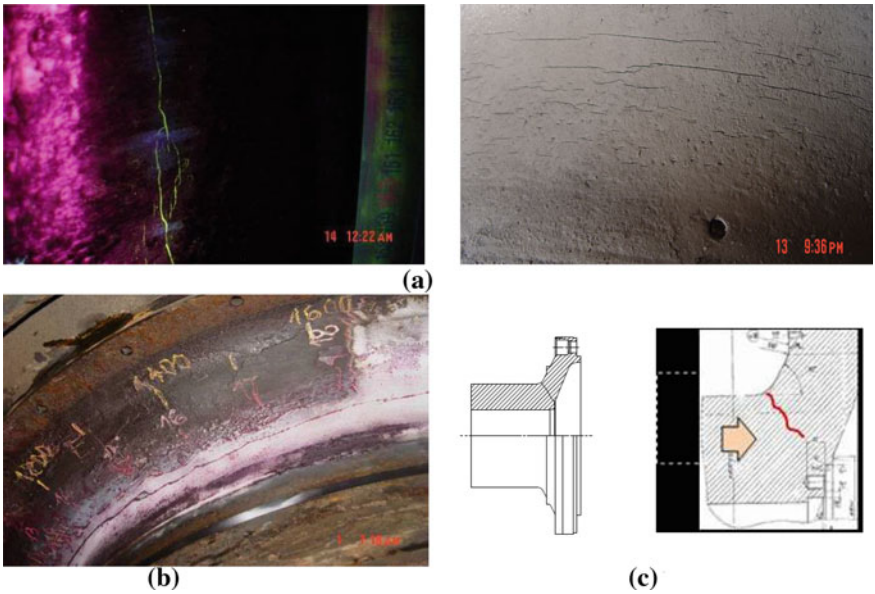

Fig. 3 Characteristic defects of testing using the NDT methods on the radius R80. **a** MT. **b** VT i PT. **c** UT

On all shafts, surface cracks of various lengths and depths were detected, from initial cracks to those 20 mm deep, on the whole periphery of the shaft and extending to the width of up to 200 mm in the zone of the transition radius, R80, between the cylindrical part and large flange of the shaft. On the shaft A6, a through-crack 2,100 mm long was detected, through which the oil from the regulating system leaked.

In Fig. 3, characteristic findings of testing using VT, MT, PT and UT methods have been presented, as shown in the NDT Reports (2007).

After that, two shafts (A6 and A7) were replaced by the new ones, while the rest of them were planned to be subjected to recovery of the cracks based on testing and analysis that were conducted and according to the Technology (2009) of the IMS Institute from Belgrade.

After disassembling of the shaft A6, the large flange was cut off and the material from the spot of leakage was used to make specimens for testing using the methods of destructive testing (DT) to establish the cause of the through-crack nucleation on the turbine shaft.

On the surface of the through-crack on the shaft A6, Fig. 4, characteristic spots were observed indicting fatigue character of crack initiation induced by the effect of corrosive medium.

The results of testing using the DT methods are presented in Table 3.

Dissipation of the results in terms of the mean values is obvious in all investigations. The results of micro-structural testing indicate that metallurgical quality

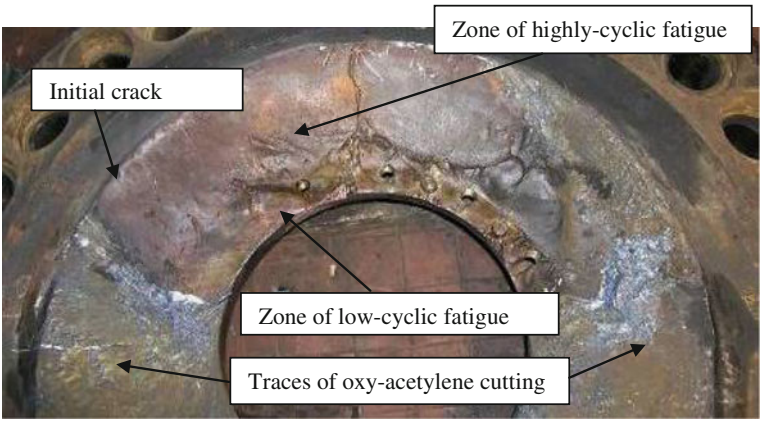

Fig. 4 Large flange of the turbine shaft A6 at HE Djerdap II after cutting

of the castings made of 20GSL steel does not meet the requirement for a long-term, many-a-year operation of a turbine-shaft for hydro-generators under conditions of its exploitation.

Based on the test results, in spite of lower values of elongation and tensile strength, the cause of fracture was not searched for in quality of the shaft material.

4 The Analysis of the Causes of Leakage and Calculation

The turbine shaft is exposed to tensile stress due to the effect of hydraulic force on turbine runner wheel. Oil pressure in a servomotor of the runner wheel on the closing stroke and axial hydraulic force load the flange to bend. The weight of the turbine runner wheel and the weight of the very shaft, too, expose the shaft to cyclic bending. Due to power transmission, the shaft is deflection-loaded as well. The loadings to which the turbine shafts are exposed are shown in Fig. 5 and Table 4.

Characteristic dimensions of the shaft flange, used for calculation by applying the finite element method (FEM), are presented in Figs. 6 and 7.

The calculation was made using both FEM and usual method based on the formulae of the manufacturer, and the results of the calculations have been presented in Fig. 8 and Table 5.

The analysis of loading and calculations have shown that cyclic tensile stresses to which the shaft was exposed and corrosive medium (leakage of water through the gasket and inadequately applied and non-renewed ACP) led to the phenomenon of corrosive fatigue on transition radius. As far as stress concentration is concerned, fatigue corrosive damages behave as initial cracks, which led to their propagation during exploitation and later on to their coalescence resulting in predominant cracks.

Table 3 Survey of the results of testing according to the DT report (2008)

Testing	Standard/requirement	Result	Note
Chemical composition	Values from Tables 2 and 3 GOST 977/88	Tested sample meets the requirements of GOST 977/88 related to chemical composition for steel castings 20GSL	XRF device, OES method
Tensile properties	SRPS EN 10002-1 GOST 1497/84 to obtain the data comparable with GOST 977/88/ GOST 977/88	Tested sample of steel casting does not meet the requirements for tensile properties specified by standard GOST 977/88, as the values of tensile strength and elongation are somewhat lower than issued	Testing was conducted according to the standard SRPS and GOST, in different directions in relation to the shaft axis
Impact energy	SRPS EN 10045-1 GOST 9454-78/ GOST 977/88	Large dissipation of the results; the results obtained by testing according to the requirement issued in GOST 9454-78, at temperatures of -10. 0, +10 and +20 °C, are higher than minimum prescribed values of impact energy, at room temperature, for steel casting 20GSL according to GOST 977-88	
Microstructure	Documentation of the customer	Presence of dendritic structure indicates the possibility of incomplete or inadequate heat treatment of the shaft flange, as well as possible cause of large dissipation of the results of all mechanical tests	
Permanent dynamic strength	GOST 25.502/79/ Documentation of the customer	Large dissipation of the results due to inhomogeneous microstructure, with permanent dynamic strength R_{din} of the material of the shaft flange of 137 MPa	
Parameters of fracture mechanics	ASTM E…/	Crack-growth rate was unstable for both tested samples, which confirms that the rate of growth of fatigue crack cannot be accurately determined due to inhomogeneity of microstructure	Testing was conducted in different directions in relation to the shaft axis

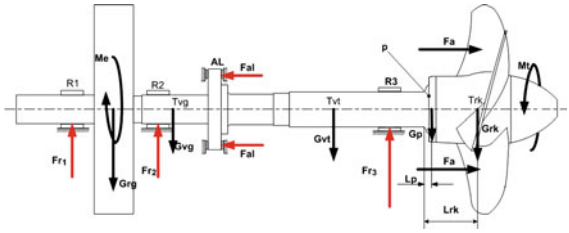

R1, R2 and R3–radial bearings;
AL – axial bearing;
rg – rotor-generator;
vg –generator shaft;
vt –turbine shaft;
rk – runner wheel;
p – large flange;
T – centre of gravity.

Fig. 5 Loadings relevant for calculation of the zone of transition radius

Table 4 Data for calculation of critical cross-section of the shaft according to calculation (1984)

Loadings and distances of the centre of gravity		Note
Axial hydraulic force, F_a	$5{,}5426 \times 10^6$ N	Re. Fig. 5
Torque, M_t	$4{,}278 \times 10^6$ Nm	
Weight of runner wheel, G_{rk}	941,760 N	
Distance between the centre of gravity RK and critical cross-section, l_{rk}	2,050 mm	
Weight of the flange with bolts up to critical cross-section, G_p	98,100 N	
Distance between the centre of gravity of the flange and critical cross-section, l_p	350 mm	

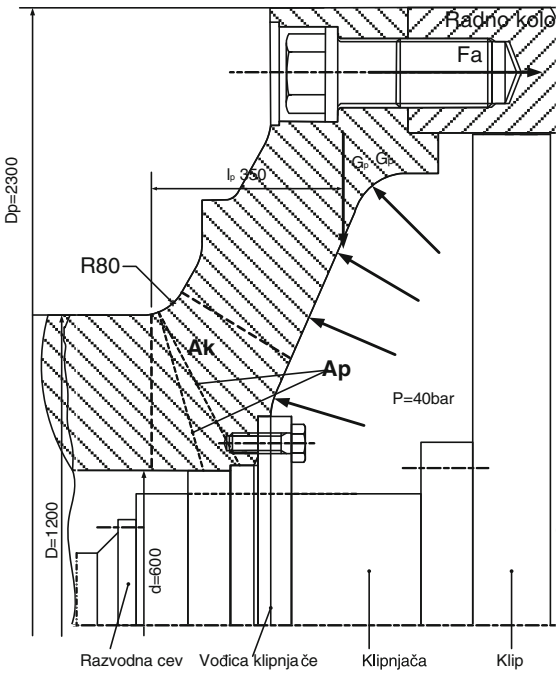

Fig. 6 Critical cross-section zone

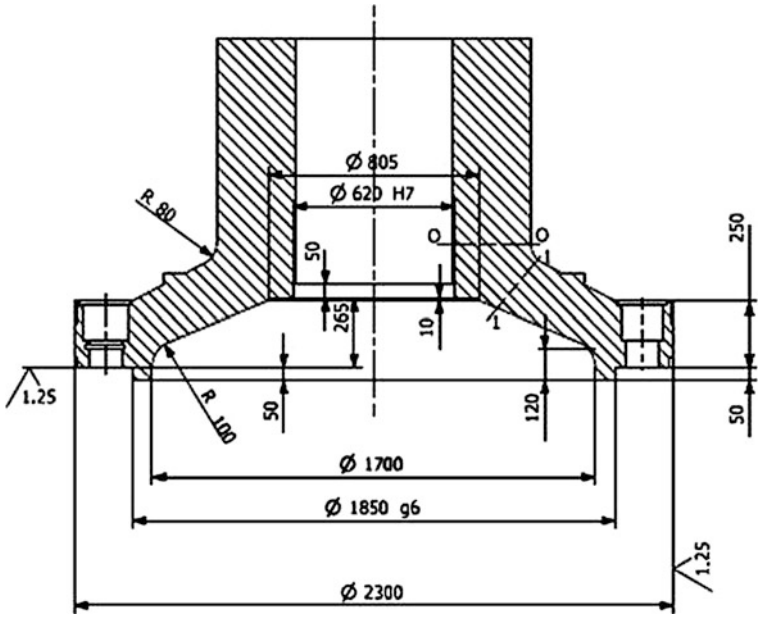

Fig. 7 Critical cross-sections according to Calculation (1984)

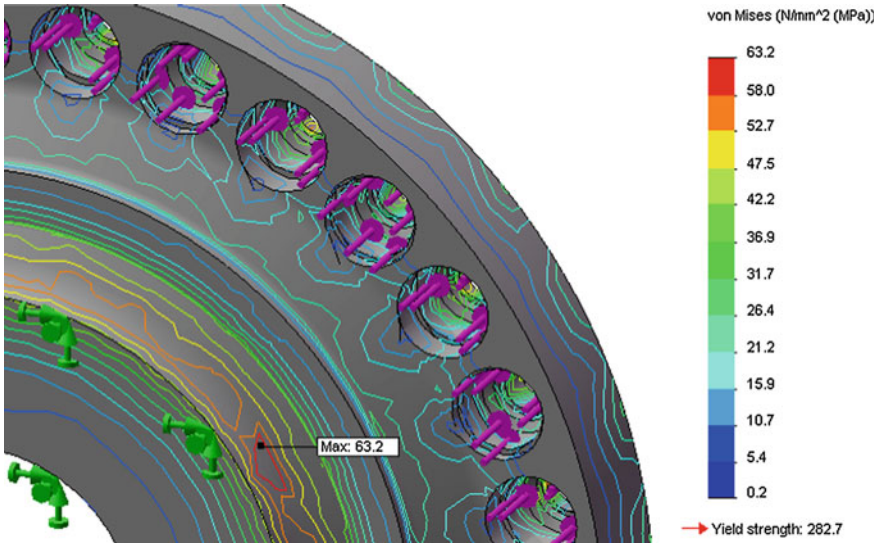

Fig. 8 Confirmation, FEM, of the critical cross-section of the flange

Table 5 The results of the calculation of critical cross-section of the shaft

Stresses and degree of safety at critical cross-section		Note
Tensile stress induced by axial hzdraulic force, σ_z	14.3 MPa	Re. Fig. 8
Bending stress induced by axial force and pressure force in servomotor RK, σ_s	22.52 MPa	
Deflection stress, τ_u	20.85 MPa	
Equivalent static stress at critical cross-section, σ_e	55.60 MPa	
Cyclic stress, σ_c	24.46 MPa	
Degree of safety to corrosive fatigue, n_σ	0.96	Anticipated 1.5

Predominant cracks grew within a larger period of time, under conditions of high-cyclic fatigue in a corrosive medium of leaking water, which can explain the products of corrosion present on the fracture surface, Fig. 4. The surfaces of this part of fracture are relatively smooth, with distinct corrosion.

When the surface of the shaft cross-section in this zone of the crack growth fell bellow critical value, very soon a through-crack was initiated under conditions of low-cyclic fatigue and the oil from the axial hole penetrated, which can explain the absence of corrosion even after a year of presence on the surfaces of this part of fracture. These surfaces are relief surfaces, without products of corrosion, created a few hours before the aggregate was stopped; they differ very much from the described surfaces ascribed to the effect of highly cyclic fatigue, Fig. 4.

5 Techno-Economic Analysis

Replacement of the shafts by the new ones would cost US$ 800,000 or US$ 1,400,000, respectively, depending on the country of origin (Romania or Russia). These are the expenses for disassembling, manufacture and assembling (9–14 months), including the losses in production of electric power which, based on the price of US$ 0.02 at the threshold of a power station, amounts to approx. US$ 3,800,000 annually (7,000 h) per aggregate.

Finding out that the phenomenon of cracks is affected by corrosion and fatigue, and not by quality of the material, makes it easier to decide to repair the shafts and thus extend their life of exploitation until the planned revitalization of the aggregate. By removal of the cracks without welding and prevention of the effects of corrosion, good prospects for safe operation of the aggregate until the above-mentioned revitalization would be achieved. Nevertheless, it has been decided that the defective parts after grinding should be welded, too, in order to avoid the stress concentrators and decrease of the cross-sections.

6 Recovery and Working out Procedure

Based on the theoretical considerations, testing results, analysis of initiation of a through-crack, calculations and Report on WPQ (Welding Procedure Qualification) (2009), Technology (2009) for recovery of the defects on the shafts of the aggregate at HE DJERDAP II without their disassembling was elaborated, Fig. 9a and b, with preparation and sequence of realization of operations.

The preparation for repair-welding included the following: disassembling of the gaskets, lifting of the shafts with repair hydraulic crane, removal of the segments of a radial bearing R3, partial unloading of the radius zone by pushing the wedges under the runner wheel blades, enclosure of the radial bearing R3, complete sealing of the oil bath with silicone putty, assembling of the rope for rotation of the runner wheel using the crane of 2,500 + 500 kN, removal of all inflammable objects and materials from the zone of operation, fire prevention in the zone of operation, supply of fresh air into zone of operation, discharge of polluted air and gases from the zone of operation and installation of proper platforms for easier approach to transition radius.

The recovery of the cracks on the shaft, the procedure for repair with coated electrode providing weld of austenitic type was chosen. For the shafts with detected cracks, the following was necessary: removal of impermissible defects by grinding, MT, hard-surfacing of ground spots and zone of the whole radius according to the qualified welding technology, treatment of hard-faced spots with control of homogeneity and surface shape, cold/hardening of the transition-radius surface with top-rounded pneumatic hammer, preparation of the transition-radius surface and ACP.

After recovery and satisfying results obtained by PT, Fig. 10, a wider zone of the shaft along the shaft was treated with fan-shaped emery cloth, first with rough one and then with a fine one, Fig. 11, before ACP.

From September 2009 to January 2012, the shafts A3, A4, A8, A9 and A10 were recovered.

(a) **(b)**

Fig. 9 Presentation of limited space for the shaft recovery. **a** Shaft prepared for recovery. **b** Position of the welding operator during recovery

Fig. 10 PT after recovery

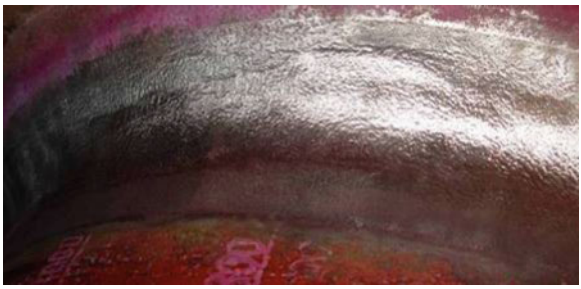

Fig. 11 The polished surface

7 Testing and Periodical Examination

First test to prove the success of recovery was the possibility to mount the gasket. Should any considerable deformation caused by welding be present, centring of the gasket would have been hindered.

Second test was registration of vibrations when putting the aggregate into operation and during the operation. No change was registered in terms of the state before recovery of the shaft.

After 14 days of operation and stoppage of the aggregate, a wide zone of the transition radius of the first recovered shaft was subjected to penetrant testing. The result was satisfactory.

The shafts recovered have been subjected to testing every 6 months, and the results have shown that until now there is no change in terms of the state after completion of recovery.

8 Conclusion

Among the causes of these failures, omissions of the designers—errors in loading analysis, modelling, response analysis and inadequate exploitation and maintenance—are highly ranked.

In this case, the methodological approach and selected procedure for recovery of the shafts prove to be entirely correct, both from technical/quality and economic point of view.

The process of recovery lasts approx. 24 days without disassembling of the shaft.

Acknowledgment Present paper is the result of realization of the project TR 35011, financed by the Ministry of Education and Sciences of the Republic of Serbia.

References

http://www.djerdap.rs. Assesed on 07 Mar 2012
Calculation (1984) of the turbine shaft, LMZ, Sankt Petersburg
Documentation (1984) of the manufacturer of the turbine shafts, LMZ Sankt Petersburg
Reports on NDT (2007) of the transition radius, R80, of the turbine shaft at HE Djerdap II. Institute for Material Testing, Belgrade
Report on DT (2008) of the sample of a large flange of the turbine shaft A6 at HE Djerdap II. Institute for Material Testing, Belgrade
Report on WPQ (2009) Institute for Material Testing. Belgrade
Technology (2009) for repair procedure on the transition radius, R80, of the turbine shaft at HE Djerdap II. Institute for Material Testing, Belgrade

Some Practical Problems of Distribution and Equalization of Internal Loads in Planetary Gear Trains

Kiril Arnaudov, Dimitar Karaivanov and Lubomir Dimitrov

Abstract The reasons for the uneven distribution of load between the planets in planetary gear trains and the methods for its experimental determination are discussed. An analysis of influencing factors is made up. Below are ways for solving of various problems in the design of one extreme responsible gear train from the mechanism of lifting 200-tons load.

1 Introduction

Planetary gear trains, which are most often with more than one planet, are statically undetermined systems. Inevitable manufacturing deviations within the tolerances prescribed in combination with the statically indetermination lead to uneven distribution of load between planets, i.e. between the internal power paths. This reduces the beneficial effect of using the principle of multi-threading in planetary gear trains. Therefore the problem of uneven distribution of the load between planets and its alignment is an important issue of planetary gear trains. It is not by chance a subject of many scientific studies (see References).

K. Arnaudov (✉)
Bulgarian Academy of Sciences, Sofia, Bulgaria
e-mail: k_arnaudov@abv.bg

D. Karaivanov
University of Chemical Technology and Metallurgy, Sofia, Bulgaria
e-mail: dipekabg@yahoo.com

L. Dimitrov
Technical University of Sofia, Sofia, Bulgaria
e-mail: Lubomir_dimitrov@tu-sofia.bg

G. Dobre (ed.), *Power Transmissions*,
Mechanisms and Machine Science 13, DOI: 10.1007/978-94-007-6558-0_47,

2 Influencing Factors

For solving successfully the problem of uneven distribution of load between planets it is necessary to identify the influencing working process factors. These factors can be arranged in the following condensed and simplified manner:

Negative factors:

These are factors causing the uneven distribution of load between planets (Fig. 1):

Gear wheels	run-out (eccentricity) f_e of all gears; unequal thickness s_2 of the teeth of planets;
Carrier	Tangential misalignment of the planets axes (planets centerlines), respectively different central angle ψ between them; misalignment f_{1S} between bore of sun gear bearing and carrier bearings sites;
Planet bearings	non-equal radial clearances Δj_2.

Positive factors:

These are factors leading to the load equalization between planets:

- Deflection of all elements of the gear train: gear meshings, bearings, planet pins, shaft of the sun gear, ring gear (in case that the deformations do not lead to non-uniform distribution of load over the gear face width).
- Bearing clearance of the central elements (sun gear and carrier).

Neutral factors:

These factors do not influence to the uneven distribution of load between planets. Such factor is the radial deviation f_{rS} of the location of the planet centerlines, i.e. of the center distance from its nominal value (in identical angles of meshing—the external and internal meshing).

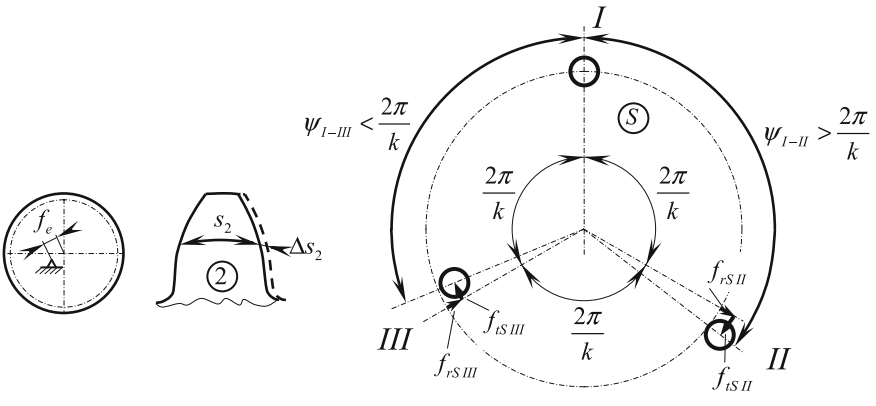

Fig. 1 Negative factors of the gear wheel and the carrier

Other factors:

These are factors that generally affect the equalization process—loading torque T and angular velocity ω of the gear train at the input shaft or at the output shaft.

3 Ways and Methods for Solving the Problem

There are the following measures that can be taken for solving this problem:

Active (technological) measures	high manufacturing accuracy;
Passive (constructive) measures	use of kinematic equalizing devices (floating elements);
	purposed deflection (compliance).

The best technological approach is to achieve the highest technically possible and economically acceptable accuracy. This measure (active measure) affects causes but not just the consequences of the uneven distribution of load between planets. Apart from the economic factor there are limitations for achievable accuracy, so that full alignment of sharing the load between planets is generally impossible.

There are numerous patented kinematic aligning devices (floating elements) (Arnaudov 1968, 1990). However, very a few of them have practical application. Such devices are mainly used in high-power gear trains and not in widely used comparatively low-power industrial gear trains. The reason for this is that on one hand the use of these devices makes the gear train more expensive, and on the other hand in some cases this increases the train overall dimensions.

For industrial gear trains functioning in the range of normal speeds along with the economically acceptable accuracy, a prescribed deflection is required. It is difficult to affect the deflection of the planet pins and especially of the teeth meshing stiffness. The deflection of the ring gear requires some space. The deflection of the shaft of the sun gear appears to be the most appropriate element for regulating the deflection. There are two options for bearing the sun gear—in the carrier (most often) and in the housing (less frequently). In both cases the loading of the gear elements and lines of force flow are different and thus is the influence of the deflections of separate elements on the distribution of the load (Fig. 2). In both cases the influence of the deflection of the shaft on the sun gear can be described easily and is easily attainable.

The solution of this problem is examined below by using a “purposed deflection” to the shaft of the sun gear beard in the carrier.

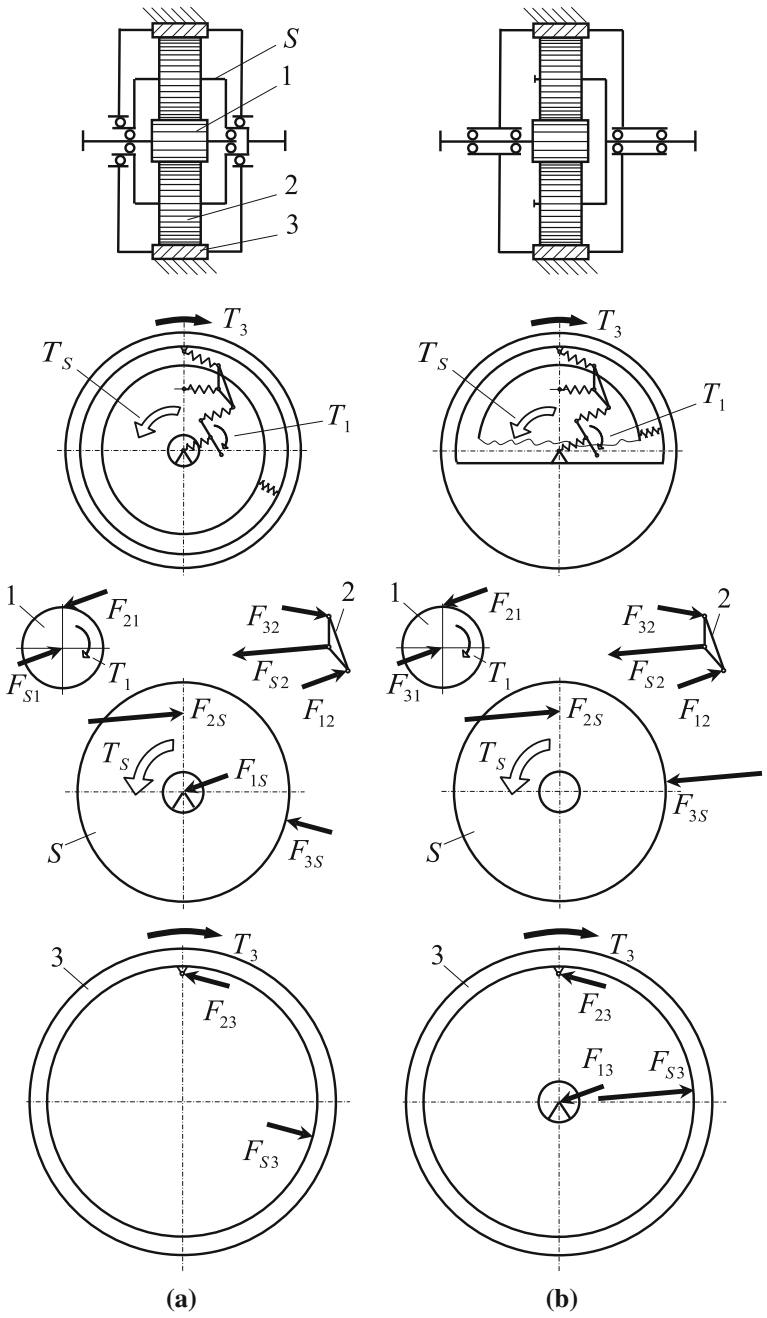

Fig. 2 Different load of the elements of the gear train depending on the location of the bearing of the sun gear, leading to different impacts of different deflections **a** bearing in the carrier, **b** bearing in the housing

4 Ways for the Experimental Determination of the Load Distribution Between Planets

There are basically two ways for identification of the load in each power paths in the planetary gear train, i.e. the planets

- measuring the stress indirectly from the deformation;
- measuring directly the deformation;

of the examined object. Studies have shown an appropriate measurements the following objects:

- the outer side of the ring gear;
- the teeth of the ring gear;
- the planet pins.

Figures 3 and 4 illustrate these possibilities. Their comment is as follows.

The ability to measure the deformation and in this way to determine indirectly the stress on the outer side of the ring gear (and hence the load in this place) is very limited. On the other hand the influence of load in the other meshing in a planet gear train can not be always excluded. The biggest disadvantage of this method is that we can register the load in separate moments but not the load on different planets (i.e. on the each separate power paths) as a continuous function of rotation.

Basically it would be proper to register the real loading on the gear teeth, which actually is interesting. This can be done relatively comfortable at an available fixed ring gear. This method has similar disadvantages as the above mentioned. It is also difficult to put strain gauges to all teeth. Therefore in this measurement method only moment values of load on an individual tooth can be measured and not on all them.

The determination of load distribution by stress or by deformation of the planet pins has important advantage. By its use the distribution of load as a continuous function of position (rotation) can be found. Unfortunately this measuring method has some disadvantages. The planet pins are subjected not only to a load due to the external load of the gear train but also by internal dynamic forces from the two meshings gears to this planet—external and internal. Strictly speaking here in a correlation are three factors used in calculation of the gear teeth stress—mesh load

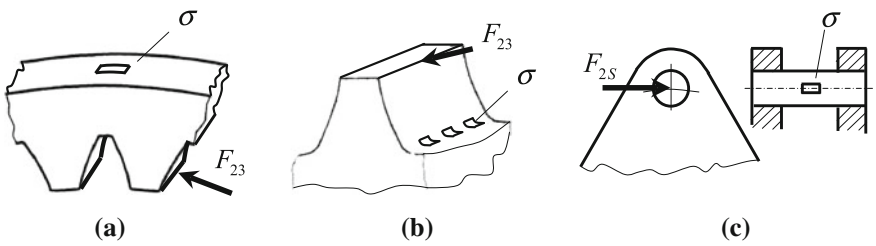

Fig. 3 Experimental methods for determining the load distribution between the planets, using stress state: **a** outside of the ring gear, **b** teeth of the ring gear, **c** the planet pins

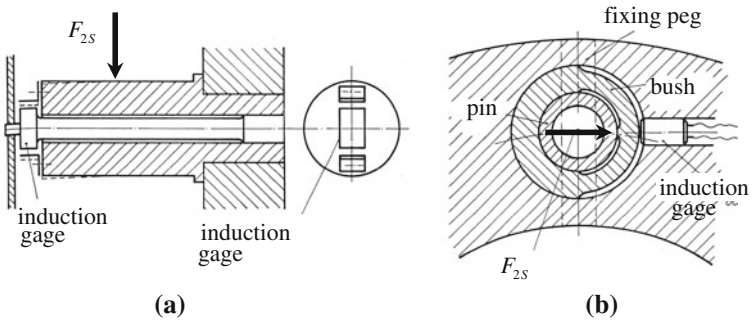

Fig. 4 Experimental methods for determination of load distribution between planets, using the deformations in: **a** planet pins, **b** additional deflective busing

factor K_γ, dynamic factor K_v and transverse load factor K_β. Some researchers mention the mutual interrelation among these factors. For example K_γ and K_v (Terplán et al. 1987; Vonderschmidt 1982; Wagner 1984; Winkelmann 1984) or K_γ and K_β (Terplán et al. 1987). As a fact all three factors take account of the load simultaneously therefore in experimental examination their complex effect is registered.

Next paragraph deals with the recording of load distribution between satellites by following the load in planet pins.

5 Calibration of Planet Pins

This is a very important and delicate problem in practice. The difficulty lies in the fact that it is better to calibrate the planet pins in integrated state in the gear train but not out of it.

One original and already tested solution of this problem is shown in Fig. 5. A so-called "calibration sun gear" is applied in this case. The specific here is that it has partial toothing as shown in (Fig. 5a). Thus, the planets come consequentially one by one in mesh with this sun gear and always only one planet can be loaded (Fig. 5b). By this a calibration line is obtained and it has spontaneous dispersing.

6 Distribution of Internal Loads

Figure 6 illustrates the change of the load on an individual planet pin. This figure also shows how in principle the load spectra of a individual tooth of the sun wheel 1, the planets 2, and the ring gear 3 can be determined. From these spectra the equivalent load on each tooth which is authoritative for their reliable strength

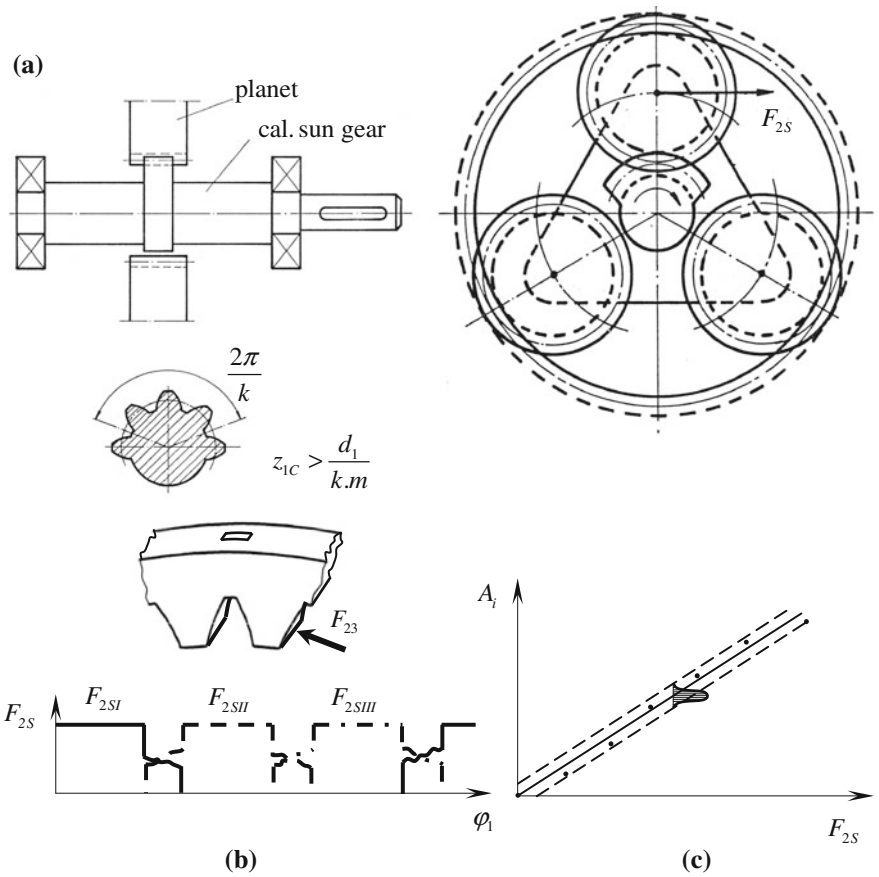

Fig. 5 Obtaining of calibration lines of each planet pins using calibration sun gear **a** calibrating sun gear, **b** consequently load the planet pins, **c** calibration line of one planet pin

calculations can be obtained. It is understood that the teeth of each gear have different spectrum of load. For each gear the applied load is consider to be the largest of the equivalent loads from all its teeth.

The described method of processing the results, although being possible, is not known of having found application in understandable reasons. In practice, the maximum load of the teeth F_{t-max} has been taken, obtained at one of the planets, to be placed in relation to the average load of the teeth F_{t-m}. Thus gets mesh load factor K_γ according to ISO 6336,[1] DIN 3990.[2] and ANSI/AGMA6123-B06.[3]

[1] ISO 6336 Calculation of load capacity of spur and helical gears.

[2] DIN 3990 Tragfähigkeitsberechnung von Stirnrädern.

[3] ANSI/AGMA 6123-B06 Design manual for enclosed epicyclic gear drives.

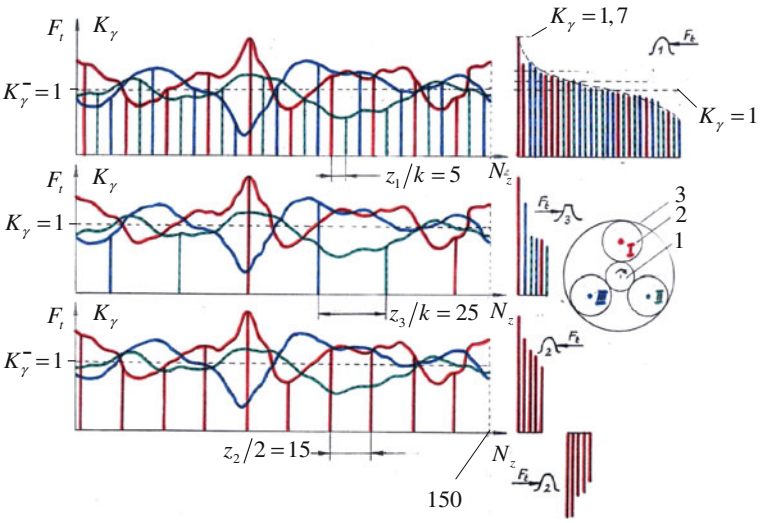

Fig. 6 Ghange of the load on each planet pin at k = 3 and setting the load spectra of the each teeth of the sun gear 1, the planets 2 and the ring gear 3 of specific gear ($z_1 = 15$; $z_2 = 30$; $z_3 = 75$) with a kinematic cycle of 150 rotations of the sun gear

$$K_\gamma = \frac{F_{t\max}}{F_{tm}} \tag{1}$$

One understands that in situation a conscious mistake is made but it is favor of security.

7 Effective Measures Applied to a Particular Gear Train

An example below illustrates the application of described above principles. It concerns an extremely important planetary gear train for lifting of 200 tons load (Arnaudov et al. 2008). The scheme of this train is shown in Fig. 7. This gear train had to replace another failed gear train.

It is a specific feature of this train that it has two-engine drive. There is a planetary gear which provides two speed ratios. As shown in Fig. 8 the sun gear is not located in the middle of its shaft. The uneven distribution of the loads bends the shaft because the sun wheel is tilted (with the same diameter of the shaft on both sides). This tilt leads to non-uniform distribution of the load over the gear face width and respectively to a high value of transverse load factor K_β. Providing of parallel displacement of the sun wheel at bending of its shaft is a really small problem but with very unpleasant consequences. It is known from statistics that non-uniform distribution of load over the gear face width is one of the most

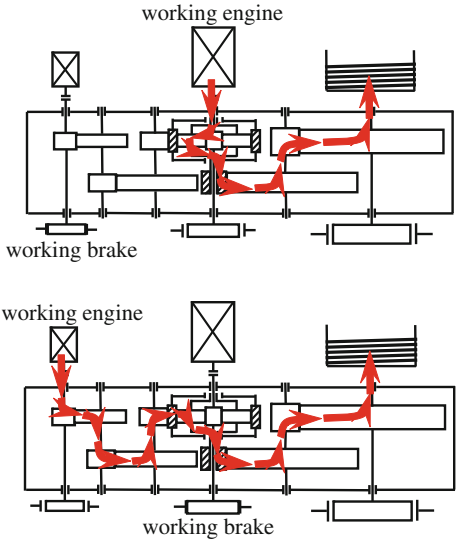

Fig. 7 Gear train of a mechanism for lifting of 200 ton load with two lifting speeds

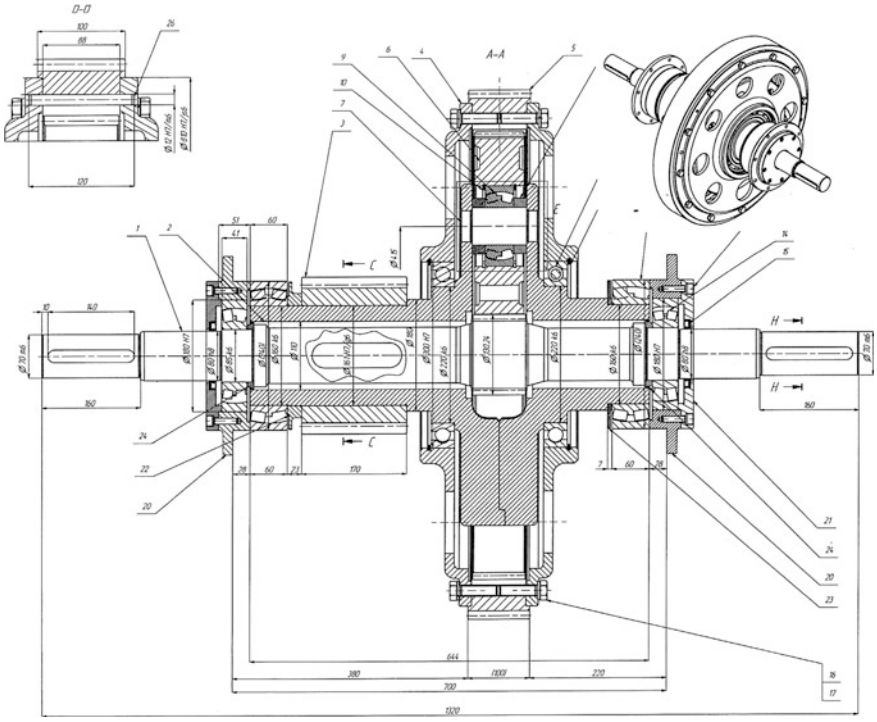

Fig. 8 Planetary stage from the gear train shown in Fig. 7

common reasons for the gears to be out of order (Allianz-Handbuch der Schadenverhütung 1984).

This problem has been solved as follows. As shown in Fig. 9 an inversion is carried out where the sun wheel becomes immovable but their bearing seats remain free. This bearing seats are loaded with bearing reactions F_A and F_C calculated as follows:

$$\left.\begin{aligned} F_A &= F\frac{c+\frac{b}{2}}{l} \\ F_C &= F\frac{a+\frac{b}{2}}{l} \end{aligned}\right\} \quad \frac{F_A}{F_C} = \frac{c+\frac{b}{2}}{a+\frac{b}{2}} < 1 \tag{2}$$

The deflections which occur on both consoles as a result of the bearing reactions F_A and F_C are:

$$f_A = \frac{F_A.a^3}{3E.J_A} = \frac{F_A.a^3}{3E\frac{\pi.d_A^4}{64}} \approx 7\frac{F_A.a^3}{d_A^4} \tag{3}$$

$$f_C \approx 7\frac{F_C.c^3}{d_C^4} \tag{4}$$

Both deflections f_A and f_C have to have the same value (Fig. 9) in order to achive a parallel displacement of the sun gear. After the equalization of (3) and (4) the relation between the diameters of the shaft d_A and d_C is obtained on both sides of the sun gear (5):

$$\frac{d_A}{d_C} = \sqrt[4]{\frac{\left(c+\frac{b}{2}\right)a^3}{\left(a+\frac{b}{2}\right)c^3}} \tag{5}$$

Since $c/a > 1$, it follows that d_A diameter must be bigger than d_C. The diameter d_A, which is at the side of the input torque, is determined by the requirement of sufficient strength under the action of torsional and bending loads of the shaft. The deformation itself and hence the deflection of the shaft is determined using the equivalent diameter d_{eq}, calculated by the following formula (Iosilevich 1988):

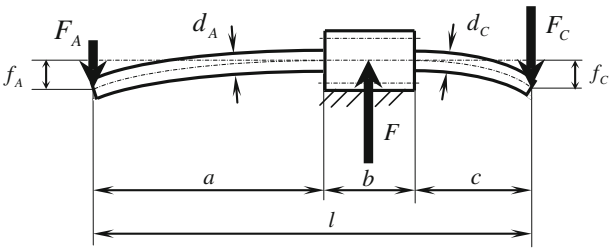

Fig. 9 Determination of diameters d_A and d_C of the sun gear shaft in order to ensure its parallel displacement at shaft deflection due to uneven distribution of load between planets

$$d_{eq} = \frac{d_f}{\sqrt[4]{\left(\frac{d_f}{d_A}\right)^4 \frac{a}{l} + \left(\frac{d_f}{d_f}\right)^4 \frac{b}{l} + \left(\frac{d_f}{d_C}\right)^4 \frac{c}{l}}} < d_f \tag{6}$$

where d_f is the root diameter of the sun gear tooth, which on the other site is the maximum diameter of the shaft.

To ensure maximum safety of this extremely responsible planetary gear train were applied a

number of appropriate measures taken in this case:

1. The number of planets has been increased from 2 to 3. This measure increases the load capacity theoretically with 50 %;
2. The accuracy of manufacturing was technically as high as possible and economically affordable;
3. By appropriate shift modifications of the gear teeth their maximum load capacity was provided;
4. The maximum flexibility of the shaft of the sun gear was reached but within the shaft allowable strength;
5. Bearings with high radial clearance for the shaft of the sun gear were used and by this a sufficient radial floating was provided;
6. Load capacity, both of the gear wheels and of other elements of the train were carried out with higher mesh load factor $K_\gamma = 2$.

As a result of the above suggested measures the gear train works completely sufficiently.

8 Conclusion

In the calculation, design, and testing of gear trains many problems, such as follow, have to be solved.

- First, providing of sufficient equalization of the load between planets, respectively providing low value of mesh load factor $K\gamma$;
- Second, avoiding of tilting the sun wheel at bending of the shaft due to the uneven distribution of load of the planets, respectively providing low value of transverse load factor K_β.

Especially important, when testing the planetary gear trains, is the determination of the actual distribution of load between planets. Usually there is a problem with calibration of the measuring objects and determination of a calibration line. The choice of measuring object and measurement method is essential.

References

Allianz-Handbuch der Schadenverhütung (1984) VDI, Düsseldorf

Arnaudov K (1990) Theoretical-experimental study of the internal load shearing in planetary gear trains. Hability-working Institute of Mechanics, Bulgarian Academy of Sciences, Sofia. (in Bulgarian)

Arnaudow K (1968) Untersuchung des Lastausgleiches in Planetengetrieben. Dissertation, Technische Universität Dresden

Arnaudov K, Kolev E, Liubenov L (2008) Construction of a special reducer with 2 speeds. In: Proceedings of the 4th conference machinery and machine elements, Sofia, pp 47–57, ISSN 1314-040X. (in Bulgarian)

Iosilevich GB (1988) Machine elements. Mashinostroenie, Moscow (in Russian)

Terplán Z, Dobroszöni (1987) Development of calculations of planetary gear trains. In: Proceedings of international symposium "planetary gear trains"[microfishe], Pernik (Bulgaria). (in Russian)

Vonderschmidt RW (1982) Zahnkräfte in geradverzahnten Planetenradgetrieben. Dissertation, Ruhr-Universität, Bochum

Wagner HT (1984) Versuche zur Lastaufteilung und zum Breitentragen in geradverzahnten Planetenradgetrieben. Dissertation, Ruhr-Universität, Bochum

Winkelmann L (1984) Lastverteilung in Planetenradgetrieben. Dissertation, Ruhr-Universität, Bochum

Development of Planetary Precessional Transmission with Multicouple Gear

Ion Bostan and Valeriu Dulgheru

Abstract Some problems of mechanical transmissions can be solved with special effects by developing new types of transmissions based on planetary precessional transmissions with multiple gear, that were developed by the authors. Absolute multiplicity of precessional gear (up to 100 % pairs of teeth simultaneously involved in gearing, compared to 5–7 %—in classical gearings) provides increased lifting capacity and small mass and dimensions. The article presents the analysis of the main structures of precessional transmissions, the theoretical aspects of gearing and design methodology.

Keywords Precessional transmission · Gear · Tooth profile

List of Symbols

i	Gear ratio
ψ	Semi product angle of rotation
$\Delta\psi_3$	Diagram error
δ	Pitch angle of the roller axis
θ	Nutation angle
β	Roller taper angle
z	Number of teeth
α	Gearing angle

I. Bostan (✉) · V. Dulgheru
Technical University of Moldova, Chişinău, Moldova
e-mail: bostan@adm.utm.md

V. Dulgheru
e-mail: dulgheru@mail.utm.md

G. Dobre (ed.), *Power Transmissions*,
Mechanisms and Machine Science 13, DOI: 10.1007/978-94-007-6558-0_48,

1 Introduction

Diversity of requirements forwarded by the beneficiaries of mechanical transmissions consists, in particular, in increasing reliability, efficiency and load-carrying capacity, and in reducing the mass and dimensions. It becomes more and more difficult to satisfy the mentioned demands by partial updating of traditional transmissions (Muns 2008; Böge 2004). The target problem can be solved with special effects by developing new types of multipliers based on precessional planetary transmissions with multiple gear, that were developed by the authors.

The advantages of the precessional planetary transmissions (Bostan 2011) lead to important economic advantage in using such drives. Some of the advantages are:

- *high efficiency*, rating 96 %, is due to the gearing use with convex-concave teeth profile;
- *wide range of transmission ratio* is from ±8.5 to ±3,599 in the drive with only one stage;
- *high load-carrying capacity* is achieved by meshing with about 100 % teeth couples simultaneously engaged compared to 5–7 %—in classical gearings;
- *compactness and reduced weight*—the specific weight of drives ranges from 0.022 to 0.05 kg/Nm.
- *high kinematic accuracy*;
- *high rating life*;
- *low level of noise and vibration* from 50 to 60 dB;
- *low moment of inertia* due to the peculiarities of the spherical motion of the planet pinion.

The engineering methods based on computer permitted to develop a new type of precessional transmissions with multi-couple meshed teeth, which, from the technological point of view, can be manufactured by means of a new method of processing conical teeth with convex-concave profile.

It appeared the necessity of elaboration of new profiles adequate to the sphero-spatial motion of the gears which would ensure high performances to the precessional transmission. Considering the necessity of achieving the transfer function continuity and gear multiplicity some objectives were taken into account. One of them is the integrated methods of design, modelling and simulation using powerful means of creation and management of parametrical models of the mechanical assemblies on the basis of CAD-CAE platforms. Also, it was necessary to develop new conceptual diagrams of precessional transmissions that function under multiplier regime.

2 Study of Performances and Selection of Kinematical Structure

The majority of precessional planetary transmissions diagrams developed previously operate efficiently in reducer's regime (Bostan 2011). Depending on the structural diagram, precessional transmissions fall into two main types—*K-H-V* and 2*K-H*, from which a wide range of constructive solutions with wide kinematical and functional options that operate in multiplier regime. The kinematical diagram of the precessional transmission *K-H-V* (Fig. 1a), comprises five basic elements: planet career *H*, satellite gear *g*, two central wheels *b* with the same number of teeth, controlling mechanism *W* and the body (frame). The roller rim of the satellite gear *g* gears internally with the sun wheels *b*, and their teeth generators cross in a point, so-called the centre of precession. The satellite gear *g* is mounted on the planet (wheel) career *H,* designed in the form of a sloped crank, which axis forms some angle with the central wheel axis θ (nutation angle).

Revolving, the sloped crank *H* transmits sphero-spatial motion to the satellite wheel regarding the ball hinge installed in the centre of precession. For the transmission with the controlling mechanism designed as clutch coupling (Fig. 1a), the gear ratio (gear reduction rate) varies in the limits:

$$i_{HV}^{g} = -\frac{z_g \cos\theta - z_b}{z_b};\ i_{HV}^{g} = -\frac{z_g \cos\theta - z_b}{z_b \cos\theta}, \tag{1}$$

reaching the extreme values of 4 times for each revolution of the crank *H*. If necessary this shortcoming can be eliminated using as a controlling mechanism the constant cardan joint (Hooke's joint), the ball synchronous couplings, etc.

$$i_{HVmed}^{g} = -\frac{z_g - z_b}{z_b}. \tag{2}$$

For $z_g = z_b + 1$, $i_{HV}^{g} = -\frac{1}{z_b}$, the driving and driven shafts have opposite directions.

For $z_g = z_b - 1$, $i_{HV}^{g} = \frac{1}{z_b}$, the shafts revolve in the same direction.

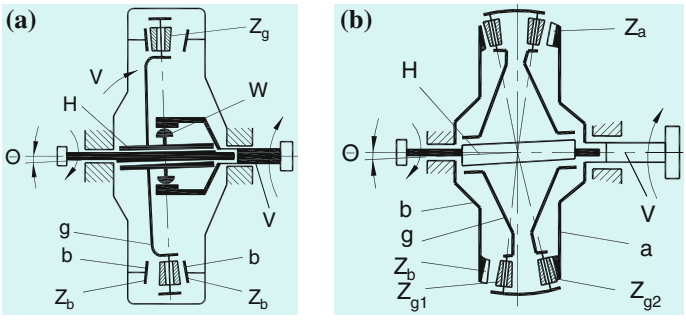

Fig. 1 Conceptual diagrams of precesional transmissions

This kinematical diagram of the precessional transmission ensures a range of gear ratios $i = 8\ldots60$, but in the multiplication regime it operates efficiently only for the range of gear ratios $i = 8\ldots25$. As well, in the controlling mechanism W, that operates with pitch angles of the semi couplings up to 3^{o}, power losses occur reducing the efficiency of the multiplier on the whole.

The precessional transmission $2K$-H has higher performances, including the kinetostatic one as well (Figs. 1b, 2). The transmission comprises a satellite gear g with two crown gears Z_{g1} and Z_{g2}, that gears with the unshiftable b and movable a central wheels.

$$i = -\frac{z_{g_1} z_a}{z_b z_{g_2} - z_{g_1} z_a}. \tag{3}$$

The analysis of this relation demonstrates that precessional transmissions **2*K*-*H*** provide the fulfilment of a large range of transmission ratios $\boldsymbol{i = \pm}$ (**12**…**3599**) (Bostan 2011). But in multiplier regime the transmission operates efficiently only in the limits $\boldsymbol{i = \pm}$ (**12**…**30**). The process of self-braking (self-stopping) occurs at bigger transmission ratios. It is necessary to point out the series of peculiarities of the precessional transmissions **2*K*-*H*** that ensure higher performances compared to similar planetary transmissions with cylindrical gears: precessional transmissions do not demand conditions of distance equality between the axis. This factor widens the area of their optimal design; precessional transmission kinematics does not limit the selection of the gear couples modules or of the rollers placement pitch. This factor increases the possibilities of shaping teeth pairs and of the transmission ratios interval; the peculiarities of the designed precessional gears allow increasing in the number of teeth that transmit the load simultaneously and this fact reduces significantly the dimensions and mass for the same loads compared to the traditional involute gearings.

Based on the carried out analysis a constructive diagram of the precessional planetary transmission was designed, taken as the base of precessional multipliers design. The precessional planetary transmission (Fig. 2) comprises the crank shaft 1 on which the satellite block 2, and the fixed and the movable wheels 3 (the movable wheel is connected to the shaft 5) are installed. The satellite block 2 has two crown gears (6 and 7) with the teeth executed as conical rollers mounted on the axle with the possibility of revolving around them. The transmission operates in the multiplier mode, as follows: at the rotation of the input shaft 5 with the gear 4, due to the difference in the number of geared teeth ($Z_4 = Z_7 - 1$, $Z_3 = Z_6 - 1$), the satellite block 2 will perform a spherical-spatial motion around the point—centre of precession (the point of intersection of the crown gear roller axes and of the crank shaft axes 1), producing a complete precessional cycle at the rotation of the gear 4 at an angle equal to the angular pitch. Due to its mounting on the sloped side of the crank shaft 1, the precessional motion of the satellite block 2 is transformed into rotational motion of the crank shaft 1 that will produce a complete rotation during a complete precessional cycle of the satellite block.

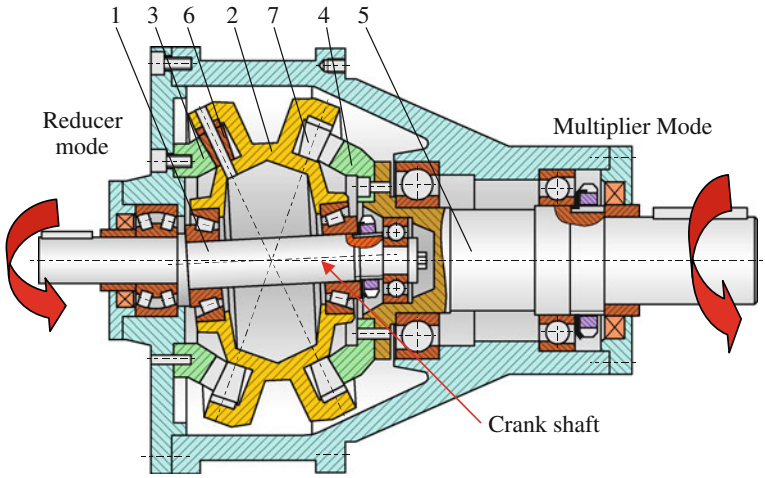

Fig. 2 Constructive diagram of the planetary precessional transmission 2*K-H*

3 Analytic Description of Teeth Profile and Justification of Precessional Gear Parameters Selection

3.1 Analyse of "satellite-driven shaft" *link*

Teeth profiles have an important role in the efficient transformation of motion in the precessional transmissions that operate as multiplier. Multiple precessional gear theory, previously developed, did not take into consideration the influence of the diagram error of the linking mechanism in the processing device for gear wheel on the teeth profile. Functioning under the multiplication regime, these errors have major influence, which can lead to instant blocking of gear and to power losses. With this purpose, a thorough analysis was conducted on the motion development mechanism under multiplication, and on the teeth profile error generating source. On the basis of fundamental theory of multiple precessional gear, previously developed, a new gear with modified teeth profile and the technology for its industrial manufacturing was proposed and patented (Bostan 2011).

Cinematically, the link between the semi product and the tool, in which one of them (the tool) makes spherical-spatial motion being, at the same time, limited from rotating around the axis of the main shaft of the teething machine tool, is similar to the "*satellite-driven shaft*" link from the precessional planetary transmission of the K-H-V type. The kinematical link between the tool and the stationary part of the device represents a Hooke articulation that generates the variability of transfer function in the kinematical link "*tool-semi product*". This variation will influence the teeth profile. Thus, the connection of tool with the housing registers a certain scheme error $\Delta\psi_3$ (to understand the deviation of the

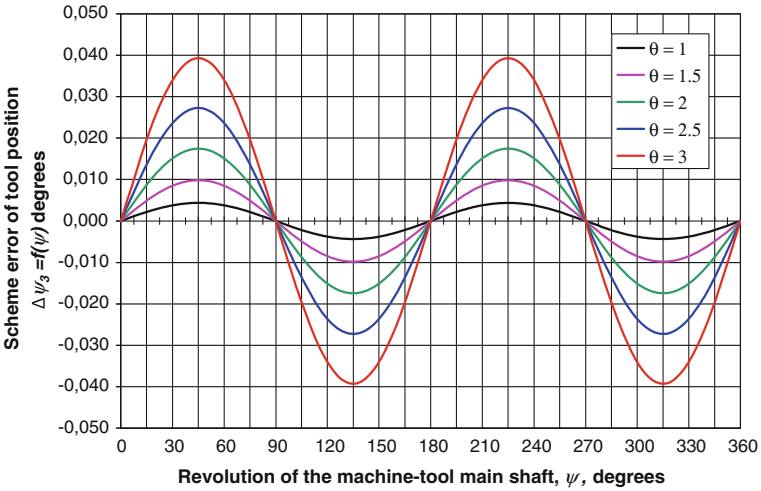

Fig. 3 Dependence of the scheme error of tool position $\Delta\psi_3$ at a revolution of the machine-tool main shaft ψ

semi product angle of rotation $\boldsymbol{\psi_3}$ from the angle of rotation of the semi product itself ψ_3^m at its uniform rotation):

$$i_{31}^m = -\frac{z_2 - z_3}{z_3}; \Delta\psi_3 = \psi_3 - i_{31}^m = \frac{z_2}{z_3}(\psi - arctg(\cos\theta \cdot tg\psi)). \quad (4)$$

Figure 3 shows the dependence of the tool position diagram error $\boldsymbol{\Delta\psi_3}$ at a revolution of the machine tool main shaft $\boldsymbol{\psi}$. This error is transmitted to the tool that shapes the teeth profile with the same error. To ensure continuity of the transfer function and to improve the performances of precessional transmission it is necessary to modify teeth profile with the diagram error value $\boldsymbol{\Delta\psi_3}$ by communicating supplementary motion to the tool. In this case the momentary transmission ratio of the manufactured gear will be constant.

3.2 Description of Teeth Profile Designed on Sphere

Usually, in theoretical mechanics the position of the body making spherical-spatial motion is described by Euler angles. The mobile coordinate system $\boldsymbol{OX_1Y_1Z_1}$ is connected rigidly with the satellite wheel, which origin coincides with the centre of precession $\boldsymbol{0}$ (Fig. 4.) and performs spherical-spatial motion together with the satellite wheel relative to the motionless coordinate system $\boldsymbol{OXYZ}$.

The elaboration of the mathematic model of the modified teeth profile is based integrally on the mathematic model of teeth profile, previously developed by the authors. With this purpose it is necessary to present the detailed description of

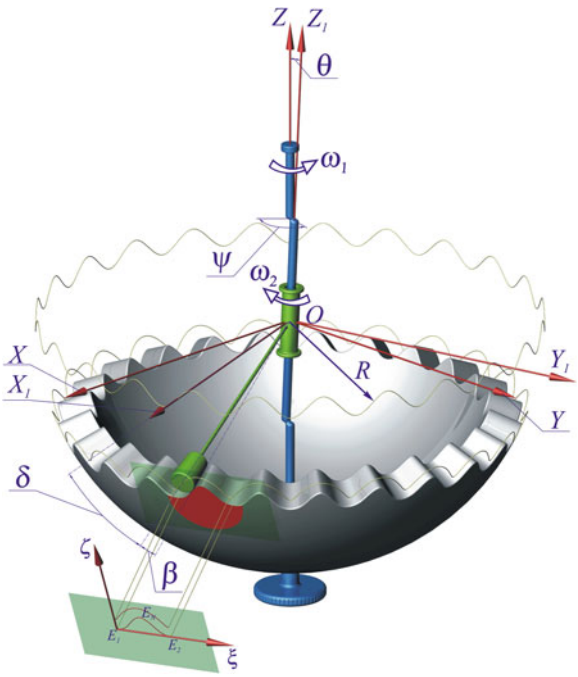

Fig. 4 Tooth profile in normal section

teeth profile without modification and, then, to present of the description of modified profile peculiarities.

An arbitrary point $\boldsymbol{D}$ of the tool axis describes a trajectory relative to the fixed system according to the equations:

$$\begin{aligned} X_D^m &= -\sin\delta\sin\left[Y_C^m\sin\theta + Z_C^m(1-\cos\theta)\cos\psi\right];\\ Y_D^m &= -Y_C^m\cos\delta + Z_C^m\sin\delta\left[\cos^2\psi + \cos\theta\sin^2\psi\right];\\ Z_D^m &= -Y_C^m\sin\delta\left(\cos^2\psi + \cos\theta\sin^2\psi\right) - Z_C^m\cos\delta. \end{aligned} \tag{5}$$

Index $\boldsymbol{m}$ means "*modified*".

The motion of point $\boldsymbol{D^m}$ compared to the movable system connected rigidly to the semi product is described by formulas:

$$\begin{aligned} X_{1D}^m &= X_D^m\cos\frac{\psi}{Z_1} - Y_D^m\sin\frac{\psi}{Z_1};\\ Y_{1D}^m &= X_D^m\sin\frac{\psi}{Z_1} + Y_D^m\cos\frac{\psi}{Z_1};\\ Z_{1D}^m &= Z_D^m. \end{aligned} \tag{6}$$

The projections of point $\boldsymbol{D^m}$ velocities is expressed by formulas:

$$
\begin{aligned}
\overset{\bullet}{X}{}^m_D &= -\sin\delta\cos\psi\left[Y^m_C\sin\theta + Z^m_C(1-\cos\theta)\cos\psi\right]\overset{\bullet}{\psi} - \\
&\quad -\sin\delta\sin\psi\left[\overset{\bullet}{Y}{}^m_C\sin\theta + \overset{\bullet}{Z}{}^m_C(1-\cos\theta)\cos\psi - Z^m_C(1-\cos\theta)\sin\psi\cdot\overset{\bullet}{\psi}\right]; \\
\overset{\bullet}{Y}{}^m_D &= -\overset{\bullet}{Y}{}^m_C\cos\delta + \overset{\bullet}{Z}{}^m_C\sin\delta\left[\cos^2\psi + \cos\theta\sin^2\psi\right] + \\
&\quad + Z^m_C\sin\delta[-2\cos\psi\sin\psi + 2\cos\theta\sin\psi\cos\psi]\overset{\bullet}{\psi}; \\
\overset{\bullet}{X}{}^m_{1D} &= \overset{\bullet}{X}{}^m_D\cos\frac{\psi}{Z_1} - \frac{\overset{\bullet}{\psi}}{Z_1}X^m_D\sin\frac{\psi}{Z_1} - \overset{\bullet}{Y}{}^m_D\sin\frac{\psi}{Z_1} - \frac{\overset{\bullet}{\psi}}{Z_1}Y^m_D\cos\frac{\psi}{Z_1}; \\
\overset{\bullet}{Y}{}^m_{1D} &= \overset{\bullet}{X}{}^m_D\sin\frac{\psi}{Z_1} + \frac{\overset{\bullet}{\psi}}{Z_1}X^m_D\cos\frac{\psi}{Z_1} + \overset{\bullet}{Y}{}^m_D\cos\frac{\psi}{Z_1} - \frac{\overset{\bullet}{\psi}}{Z_1}Y^m_D\sin\frac{\psi}{Z_1}.
\end{aligned}
\tag{7}
$$

The coordinates of point $\boldsymbol{E^m}$ on the sphere is calculated by formulas:

$$
\begin{aligned}
X^m_{1E} &= k^m_2 Z^m_{1E} + d^m_2; \\
Y^m_{1E} &= k^m_1 Z^m_{1E} - d^m_1; \\
Z^m_{1E} &= \frac{(k^m_1 d^m_1 - k^m_2 d^m_2) - \sqrt{(k^m_1 d^m_1 - k^m_2 d^m_2)^2 + (k^{m2}_1 + k^{m2}_2 + 1)\cdot(R^2_D - d^{m2}_1 - d^{m2}_2)}}{k^{m2}_1 + k^{m2}_2 + 1},
\end{aligned}
\tag{8}
$$

where:

$$
k^m_1 = \frac{X^m_{1D}\left(X^m_{1D}\overset{\bullet}{X}{}^m_{1D} + Y^m_{1D}\overset{\bullet}{Y}{}^m_{1D}\right) + Z^{m2}_{1D}\overset{\bullet}{X}{}^m_{1D}}{Z^m_{1D}\left(X^m_{1D}\overset{\bullet}{Y}{}^m_{1D} - Y^m_{1D}\overset{\bullet}{X}{}^m_{1D}\right)}; k^m_2 = -\frac{\left(k^m_1 Y^m_{1D} + Z^m_{1D}\right)}{X^m_{1D}};
$$

$$
d^m_1 = \frac{R^2_D\cos\beta\,\overset{\bullet}{X}{}^m_{1D}}{\left(X^m_{1D}\overset{\bullet}{Y}{}^m_{1D} - \overset{\bullet}{X}{}^m_{1D}Y^m_{1D}\right)}; d^m_2 = \frac{\left(R^2_D\cos\beta + d^m_1 Y^m_{1D}\right)}{X^m_{1D}}.
$$

According to the obtained analytical relations a soft for the calculation and generation of teeth was developed in CATIA V5R7 modelling system that allowed obtaining the modified trajectories of points E^m_e and E^m_i on the spherical front surfaces, both exterior and interior ones, by which the teeth surface was generated (Fig. 5).

Description of modified teeth profile projected on a transversal surface. Projection of point E^m on the tooth transversal plane has the following coordinates:

$$
X^{//m}_E = \varepsilon^m\cdot X^m_{1E},\ Y^{//m}_E = \varepsilon^m\cdot Y^{//m}_{1E},\ Z^{//m}_E = \varepsilon^m\cdot Z^{//m}_{1E},
\tag{9}
$$

where $\varepsilon^m = -\frac{D}{AX^m_{1E}+BY^m_{1E}+CZ^m_{1E}}$.

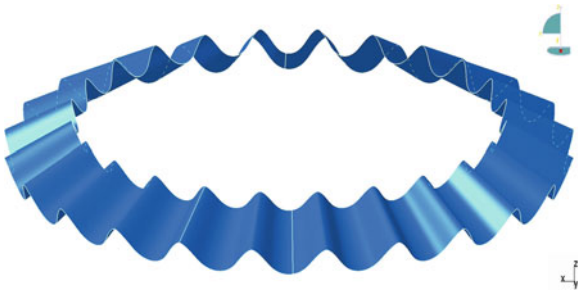

Fig. 5 Teeth generating surface

The modified teeth profile in plane is described by the equations:

$$\begin{aligned}\xi^m &= X_E''^m \cos\frac{\pi}{Z_1} + \left[R_D \cos(\delta+\theta+\beta) + Y_E''^m\right] \sin\frac{\pi}{Z_1};\\ \zeta^m &= X_E''^m \sin\gamma \sin\frac{\pi}{Z_1} - \left[R_D \cos(\delta+\theta+\beta) + Y_E''^m\right] \sin\gamma \cos\frac{\pi}{Z_1} + \\ &+ \left[R_D \sin(\delta+\theta+\beta) + Z_E''^m\right] \cos\gamma.\end{aligned} \tag{10}$$

A wide range of modified teeth profiles with different geometrical parameters were generated in MathCAD 2001 Professional software (Fig. 6). The solid model of a gear wheel is shown in Fig. 7

Based on the carried out research it was established that from the point of view of decreasing energy losses in gearing, in the multiplication mode of operation, the gearing angle should be $\alpha > 45^0$, and the nutation angle (the pitch angle of the crank shaft) should be—$\theta \leq 2{,}5^0$. This is dictated by the reverse principle of movement in the multipliers compared to the reducers: the axial component of the normal force in gear must be maximal to drive the crank shaft in the rotation movement through the satellite wheel.

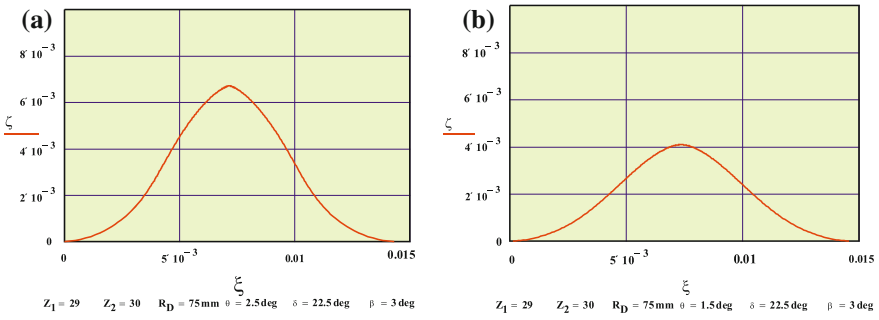

Fig. 6 Teeth profiles for reducers (**a**) and multipliers (**b**)

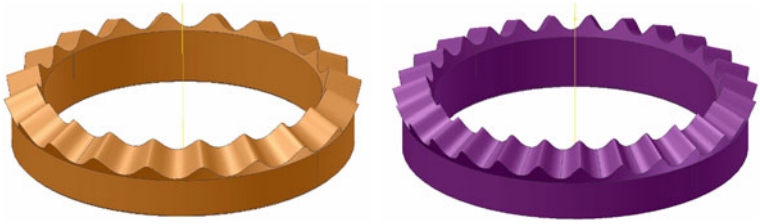

Fig. 7 The solid model of a gear wheels

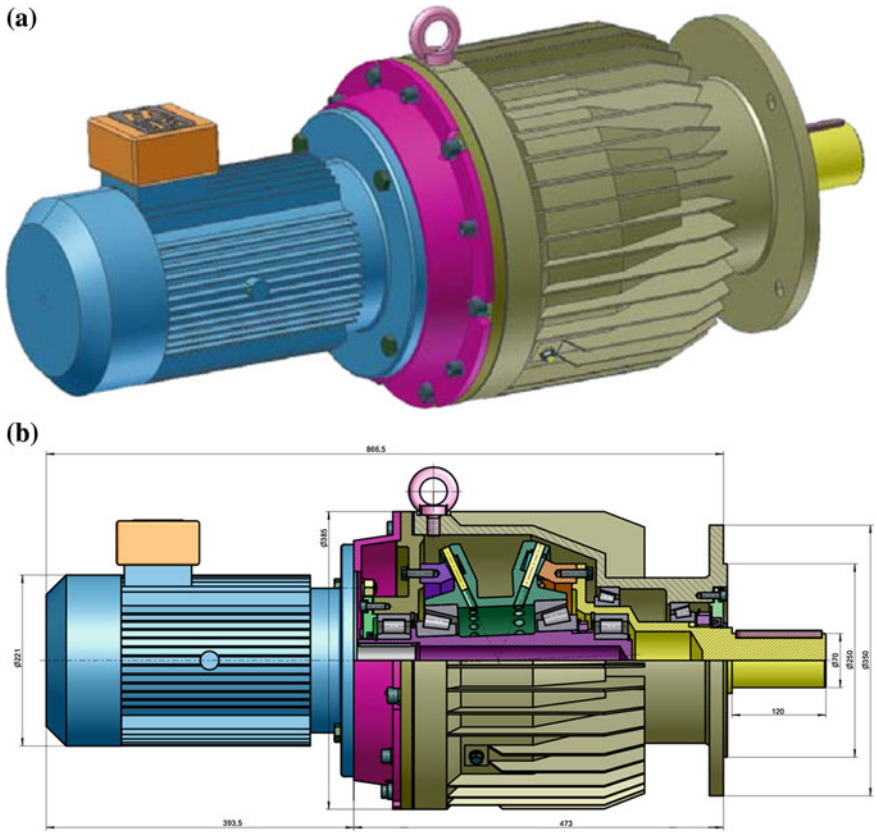

Fig. 8 Planetary precessional transmission: **a**—general view; **b**—section view

3.3 Design of Precessional Transmission Structure

On the basis of the undertaken study, diagram 2K-H (Fig. 1a) was selected for the development of planetary precessional transmission. As a result of analysis of a wide range of tooth profiles with different geometrical parameters of gear by using the mathematical modelling package MathCAD 2001 Professional, the optimum tooth profiles were selected with account of their functioning in real conditions. Also, in MathCAD 2001 Professional software the calculation of geometrical parameters of precessional gear was done. The structure of planetary precessional reducer were designed in SolidWorks software. The planetary precessional reducer is connected by flange with an electric motor, which allows obtaining a compact module, coaxial with the working mashine. The structure from Fig. 8 is proposed for planetary precessional reducer functioning in conditions of lower temperatures. To simulate the multiplier assembly and functioning, the dynamic computerised model of the precessional reducer was developed in AutoDesk Motion Inventor. The planetary precessional transmission has reduced dimensions and mass, high lifting capacity and multiplication ratio up to $i = 144$ (based on a two stage diagram) with satisfactory mechanical efficiency.

4 Conclusions

Among the characteristics of the estimated results of the research in the field of new and efficient drive development we can enumerate the followings:

- the precessional drives elaborated ensure: high load-carrying capacity; high mechanical efficiency; high kinematic accuracy; low noise level and vibrations;
- costs of drives becomes more attractive as the costs of other equivalent drives.

The structural optimization of the precessional transmissions will allow synthesis of new schematics of precessional transmissions with constant and variable transmission ratio and elaboration of new schematics of precessional transmissions for specific running conditions.

References

Muhs D, Wittel H, Jannasch D, Voßiek J (ed) (2008) Roloff/matek maschinenelemente. Vieweg and Sohn Verlag/GWV-Fachverlage GmbH, Wiesbaden, Vol 2. pp 752–755

Böge A (ed) (2004) Vieweg handbuch maschinenbau-technik. Vieweg, Sohn Verlag/GWV-Fachverlage GmbH, Wiesbaden, p I150

Bostan I et al (2011) Anthology of inventions. Planetary precessional transmissions (in Romanian). Bons Offices SRL, vol 1. p 594

Mathematical Model of the Bevel Gears Flanks Considering the Cutting Machine Type

Erzsebet Faluvegi, Csaba Zoltan Mate and Luciana Cristea

Abstract This paper presents the mathematical equations of the bevel gears with straight octoid II teething made by Heidenreich-Harbeck gear cutting machine. The generation of the bevel gear flanks bases on the face gear flanks. During the manufacture two teeth of the imaginary face gear are used as cutting tools. The flanks of the face gear are determined using vector algebra. The determination if the surface equations of the bevel gears flanks bases on envelope surfaces. To obtain the flanks of the bevel gear coordinate transformations are used which are expressed by homogenous matrixes. These transformations present the relative motion between the imaginary face gear and the bevel gear during the engagement. Thus, the calculated equations results a point cloud which forms the surfaces of the left and right flanks of the bevel gear made in Matlab software. The obtained surfaces are idealistic flanks of the bevel gear without any post processing.

Keywords Octoid II teething · Flanks surfaces · Face gear · Bevel gear · Coordinate transformation

List of Symbols

φ_b	Dedendum angle
φ_a	Addendum angle
$\vec{\sigma}_1$, $\vec{\sigma}_2$	Tangential vectors, unit vectors
$\vec{\sigma}_{1x}$, $\vec{\sigma}_{1y}$, $\vec{\sigma}_{1z}$	The components of the $\vec{\sigma}_1$ vector
$\vec{u}_1$, $\vec{u}_2$	Tangential vectors of the right flank, unit vectors

E. Faluvegi (✉) · C. Z. Mate · L. Cristea
Transilvania University of Braşov, Brasov, Romania
e-mail: faluvegi.erzsebet@gmail.com

C. Z. Mate
e-mail: mcsabazoltan@yahoo.com

L. Cristea
e-mail: lcristea@unitbv.ro

G. Dobre (ed.), *Power Transmissions*,
Mechanisms and Machine Science 13, DOI: 10.1007/978-94-007-6558-0_49,

R_0, R_i	Exterior and interior radius of the face gear
$\overrightarrow{n}_\Sigma$	The normal vector of the flanks
Ψ, υ_k	Angles of the flanks
$\overrightarrow{v}$, $\overrightarrow{w}$	Unit vectors
u, ξ	Variable parameters
φ_1, φ_2	The rotation angle of the face gear and the bevel gear
m	Module
δ	Pitch angle
z	Number of teeth
$\propto$	Pressure angle
b	Teeth length

1 Introduction

The manufacturing of the bevel gears are realized using the face gear, presented in Hollanda (1982, 1996), having a straight trapezoidal profile. Thus, the line of contact has the shape of the number eight and the gears are called bevel gears with octoid teeth. Technical literature as Hollanda (1982, 1996), mentions two kinds of bevel gears with straight teeth. The difference manifests in the method of generating the gears, effective the angle between the face gear shaft and the direction line of the cutting tool. These bevel gears are called octoid I and octoid II teething. In Fig. 1 is presented the generation method of the octoid II teething.

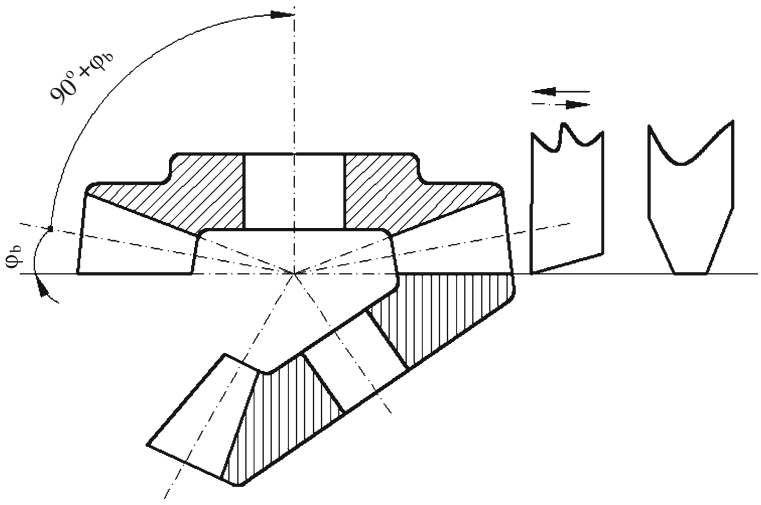

Fig. 1 The generation method of the octoid II teething, mentioned by Hollanda (2004)

This method is simplified compared to the manufacturing the octoid I teething which flanks are presented in Faluvegi (Faluvegi et al. 2011). Manufacturers have resorted to eliminating the additional movement of control from the gear cutting machines guides. Thus, the rolling takes place between the rolling cone of the face gear and the pitch cone of the bevel gear.

These gears are made by Heidenreich-Harbeck cutting machine using two cutting tools of the imaginary face gear. Both of the tools execute a linear alternating motion which is in phase opposition. The direction of the motion is oriented to the top of the pitch cone of the bevel gear. Thus, the cutting edges wrap one tooth of the bevel gear.

The aim of this paper is to determine the mathematical equations of the bevel gear flanks with straight octoid II teething made by Heidenreich-Harbeck gear cutting machine. The determined surfaces are calculated using Matlab software. The obtained surfaces are idealistic flanks without any post processing.

2 The Flanks of the Face Gear

The octoid II teething is generated by Heidenrech-Harbeck gear cutting machine.

Figure 2 presents the geometric elements which help to model the mathematical surfaces of the face gear flanks.

Using vector algebra the equations of the face gear flanks are determined. To calculate these equations, some parameters and variables are introduced.

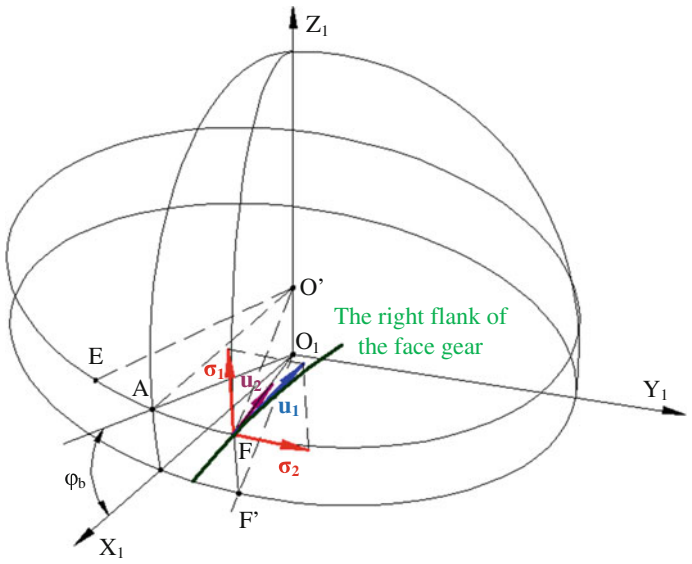

Fig. 2 The *right flank* of the face gear

The $O_1X_1Y_1Z_1$ is the coordinate system fixed with the face gear, which is the reference system where the surfaces are determined. X_1Z_1 is the symmetry plane of the face gear tooth. O_1A radius coincides with the pitch cone generator of the bevel gear that engages with. The pith cone angle is δ_2. The pitch cone centre of the face gear is in O_1 and the generators O_1E, O_1A and O_1F form an angle of φ_b with the basic plan $O_1X_1Y_1$.

The $\vec{\sigma}_1$ tangent vector consists of two vectors $\vec{\sigma}_{1xy}$ and $\vec{\sigma}_{1z}$ which are identified in $O_1O'FF'$ plan (Fig. 3).

The $\vec{\sigma}_{1xy}$ vector has two components: $\vec{\sigma}_{1x}$ and $\vec{\sigma}_{1y}$ in $O'EF$ plan (Fig. 4).

Thus, the tangent vector has the following mathematical form:

$$\begin{aligned}\vec{\sigma}_1 &= \sigma_{1x}\cdot\vec{i} + \sigma_{1y}\cdot\vec{j} + \sigma_{1z}\cdot\vec{k} \\ &= -\sin\varphi_b\cdot\cos\psi\cdot\vec{i} - \sin\varphi_b\cdot\sin\psi\cdot\vec{j} + \cos\varphi_b\cdot\vec{k}\end{aligned} \tag{1}$$

The $\vec{\sigma}_2$ vector is:

$$\vec{\sigma}_2 = -\sin\psi\cdot\vec{i} + \cos\psi\cdot\vec{j} \tag{2}$$

These are unit vectors which are perpendiculars, thus they build a coordinate system. In this system the $\vec{u}_1$ vector is determined (Fig. 5):

$$[\vec{u}_1] = \begin{bmatrix} -\sin\varphi_b\cdot\cos\psi\cdot\cos\alpha - \sin\psi\cdot\sin\alpha \\ -\sin\varphi_b\cdot\sin\psi\cdot\cos\alpha + \cos\psi\cdot\sin\alpha \\ \cos\varphi_b\cdot\cos\alpha \end{bmatrix} \tag{3}$$

The $\vec{u}_2$ vector is the unit vector of the O_1F:

$$\vec{u}_2 = \cos\varphi_b\cdot\cos\psi\cdot\vec{i} + \cos\varphi_b\cdot\sin\psi\cdot\vec{j} + \sin\varphi_b\cdot\vec{k} \tag{4}$$

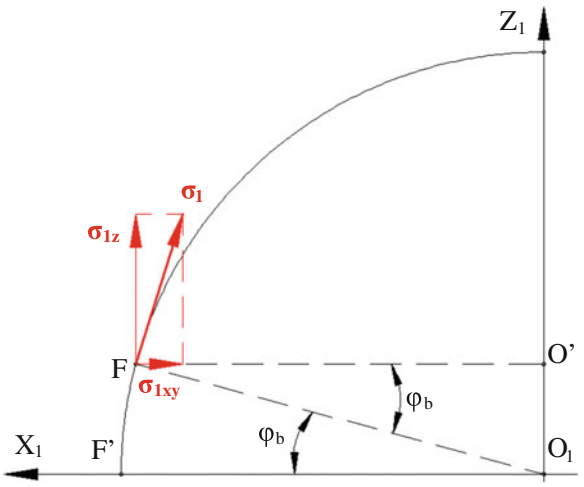

Fig. 3 Decomposing of the $\vec{\sigma}_1$ vector

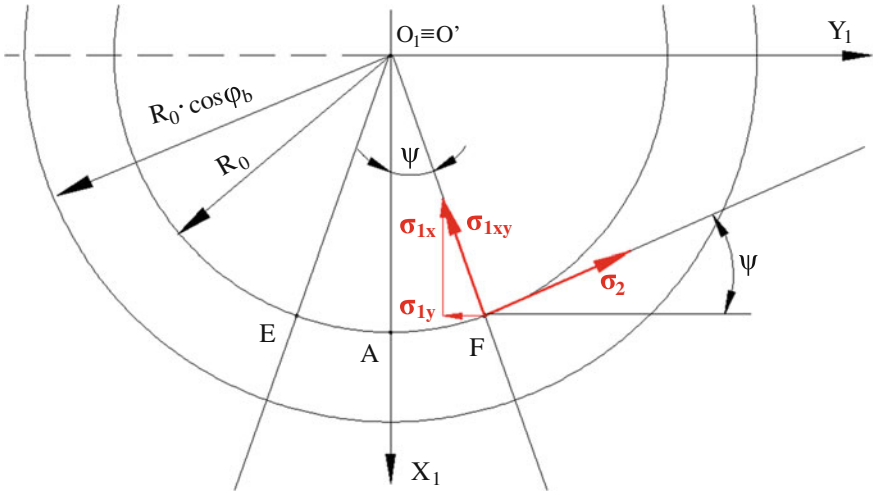

Fig. 4 Decomposing of the $\vec{\sigma}_{1xy}$ vector

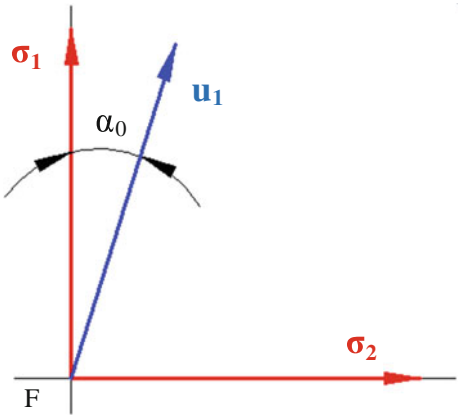

Fig. 5 Determinig the $\vec{u}_1$ vector

The normal vector of the right flank in matrix form is:

$$\vec{n}_\Sigma = \vec{u}_1 \times \vec{u}_2 = \begin{bmatrix} \sin\varphi_b \cdot \cos\psi \cdot \sin\alpha - \sin\psi \cdot \cos\alpha \\ \sin\varphi_b \cdot \sin\psi \cdot \sin\alpha + \cos\psi \cdot \cos\alpha \\ -\cos\varphi_b \cdot \sin\alpha \end{bmatrix} \tag{5}$$

In Fig. 6 is presented the υ_k angle:
The υ_k angle is determined using mathematical equations:

$$K\_\text{point} = \text{plan}(OX_0Y_0) \cap \text{plan } n_\Sigma \cap \text{circlewith } R_0 \text{ radius} \tag{6}$$

thus

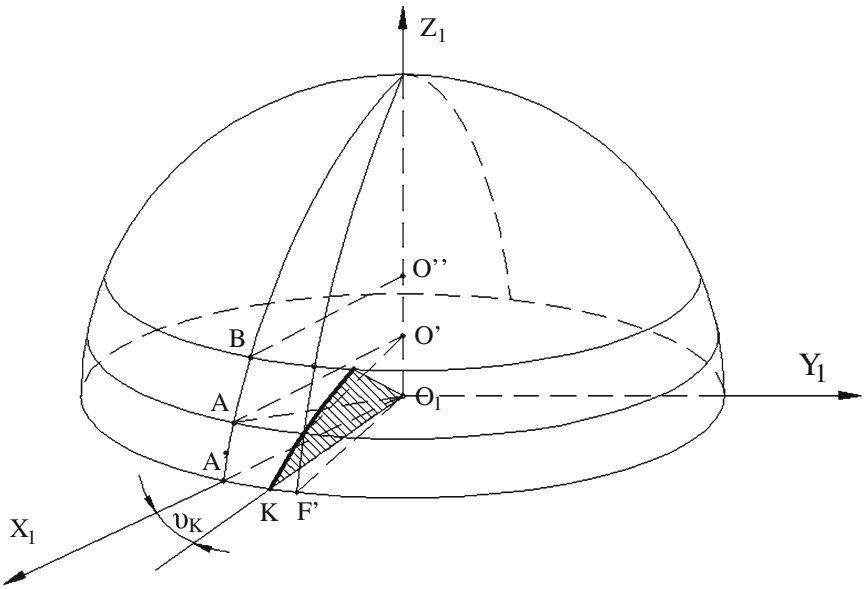

Fig. 6 Determining the υ_k angle

Fig. 7 The *right flank* representation

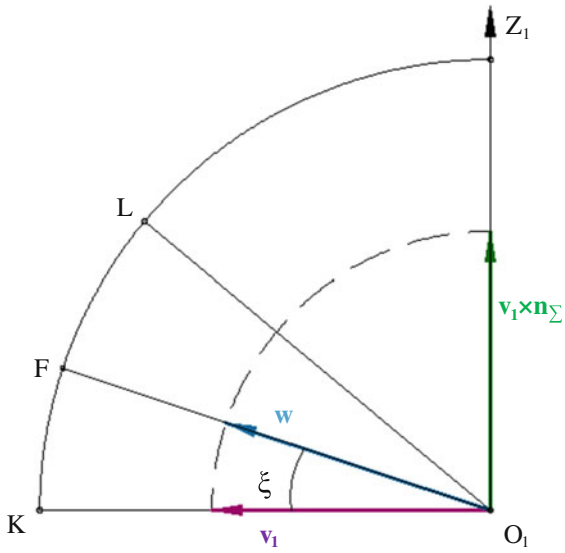

$$\tan \upsilon_k = -\frac{n_{\Sigma x}}{n_{\Sigma y}} = \frac{\sin\psi \cdot \cos\alpha - \sin\varphi_b \cdot \cos\psi \cdot \sin\alpha}{\cos\psi \cdot \cos\alpha + \sin\varphi_b \cdot \sin\psi \cdot \sin\alpha} \tag{6'}$$

Figure 7 presents the right flank surface, where $\overrightarrow{v}_1$, $\overrightarrow{v}_1 \times \overrightarrow{n}_\Sigma$ are unit vectors and form a coordinate system:

So,

$$\overrightarrow{v}_1 = \begin{bmatrix} \cos\upsilon_k \\ \sin\upsilon_k \\ 0 \end{bmatrix} \tag{7}$$

$$\overrightarrow{w} = \overrightarrow{v}_1 \cdot \cos\xi + \overrightarrow{v}_1 \times \overrightarrow{n}_\Sigma \cdot \sin\xi \tag{8}$$

Thus, the right flank of the face gear is:

$$\overrightarrow{r}(u,\xi) = u \cdot \left(\overrightarrow{v}_1 \cdot \cos\xi + \overrightarrow{v}_1 \times \overrightarrow{n}_\Sigma \cdot \sin\xi\right) \tag{9}$$

Resolving the (10) the surface equations of the right flank are obtained:

$$\begin{cases} x_1(u,\xi) = u \cdot (\cos\upsilon_k \cdot \cos\xi - \sin\upsilon_k \cdot \cos\varphi_b \cdot \sin\alpha \cdot \sin\xi) \\ y_1(u,\xi) = u \cdot (\sin\upsilon_k \cdot \cos\xi + \cos\upsilon_k \cdot \cos\varphi_b \cdot \sin\alpha \cdot \sin\xi) \\ z_1(u,\xi) = u \cdot [\sin\upsilon_k \cdot (\sin\psi \cdot \cos\alpha - \sin\varphi_b \cdot \cos\psi \cdot \sin\alpha) \\ \qquad + \cos\upsilon_k \cdot (\cos\psi \cdot \cos\alpha + \sin\varphi_b \cdot \sin\psi \cdot \sin\alpha)] \cdot \sin\xi \end{cases} \tag{10}$$

and for the left flank

$$\begin{cases} x_1(u,\xi) = u \cdot (\cos\upsilon_k \cdot \cos\xi - \sin\upsilon_k \cdot \cos\varphi_b \cdot \sin\alpha \cdot \sin\xi) \\ y_1(u,\xi) = u \cdot (-\sin\upsilon_k \cdot \cos\xi - \cos\upsilon_k \cdot \cos\varphi_b \cdot \sin\alpha \cdot \sin\xi) \\ z_1(u,\xi) = u \cdot [\sin\upsilon_k \cdot (\sin\psi \cdot \cos\alpha - \sin\varphi_b \cdot \cos\psi \cdot \sin\alpha) \\ \qquad + \cos\upsilon_k \cdot (\cos\psi \cdot \cos\alpha + \sin\varphi_b \cdot \sin\psi \cdot \sin\alpha)] \cdot \sin\xi \end{cases} \tag{11}$$

The parameter limits are:

$$\begin{cases} u \in (R_i, R_0) \\ \xi \in (0, \varphi_a + \varphi_b) \end{cases} \tag{12}$$

Figure 8 presents the flanks of the face gear with octoid II teething obtained in Matlab software:

3 The Flanks of the Bevel Gear

In the paper of Faluvegi et al. (Faluvegi et al. 2011) are presented the relative motions between the face gear and the bevel gear during engagement. Assigning these relative motions by the homogenous matrix the equation of the surface family in the bevel gears system is obtained.

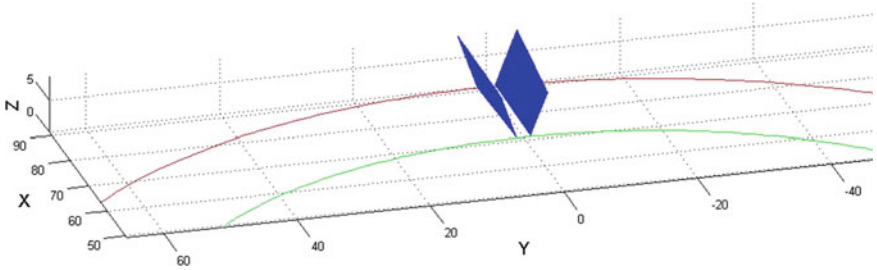

Fig. 8 The flanks of the face gear with octoid II teething

Obtaining the equations of the flanks surfaces a relation between the u, v, φ_1 and φ_2 parameters are determined. Using the engagement equation shown by Litvin and Fuentes (Litvin and Fuentes 2004), the rotation angle of the face gear φ_1 is determined according to u and v. During the engagement the angular velocity of the bevel gear is equal with the angular velocity of the face gear. So the rotation angle of the bevel gear φ_2 is determined according to φ_1. Replacing the obtained equations for the parameters the equations of the bevel gear flanks are determined:

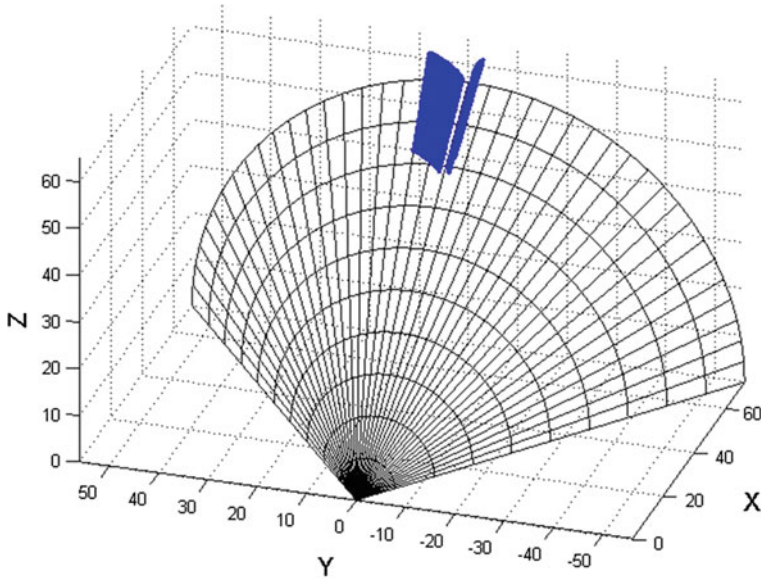

Fig. 9 The bevel gear flanks with octoid II teething

$$\begin{pmatrix} X_2(u,\xi,\varphi_1,\varphi_2) \\ Y_2(u,\xi,\varphi_1,\varphi_2) \\ Z_2(u,\xi,\varphi_1,\varphi_2) \\ 1 \end{pmatrix} = \begin{pmatrix} X_2(u,\xi,\varphi_1(u,\xi),\varphi_2(\varphi_1(u,\xi))) \\ Y_2(u,\xi,\varphi_1(u,\xi),\varphi_2(\varphi_1(u,\xi))) \\ Z_2(u,\xi,\varphi_1(u,\xi),\varphi_2(\varphi_1(u,\xi))) \\ 1 \end{pmatrix} = \begin{pmatrix} X_2(u,\xi) \\ Y_2(u,\xi) \\ Z_2(u,\xi) \\ 1 \end{pmatrix} \tag{13}$$

The flanks presented in Fig. 9 are calculated using the following initial parameters: m = 4 mm; $\delta = 37{,}875°$; z = 28; $\alpha = 20°$; b = 20 mm. The flanks are calculated in Matlab software made by the authors.

4 Conclusions

The aim of this paper is to determine the mathematical equations of the bevel gears flanks with straight octoid II teething. The obtained surfaces are idealistic flanks without any post processing. Knowing this the precision of the gear cutting machine can be determined by overlapping the measured surfaces with the theoretical flanks.

Acknowledgments This paper is supported by the Sectoral Operational Programme Human Resources Development (SOP HRD), ID59321 financed from the European Social Fund and by the Romanian Government References. The authors express their deep gratitude to Dionisie Hollanda, professor at the Sapientia Univetsity, Târgu Mureş.

References

Faluvegi E, Mate CZ, Coblis CI, Cristea L (2011) Measuring and analyzing the bevel gears with Ocotid I teething, International proceedings of computer science and information technology, ICMERA 2011, pp 104–109

Hollanda D (1982) Aschiere si Scule Aschietoare, Institutul de Invatamant Superior din Targu Mures

Hollanda D (1996) Bazele Aschierii si Generarii Suprafetelor, Universitatea Petru Maior Targu Mures

Litvin FL, Fuentes A (2004) Gear geometry and applied theory, Cambridge University Press, Cambridge

Motor Drives of Modern Drilling and Servicing Rigs for Oil and Gas Wells

Aurelian Iamandei and Gheorghe Miloiu

Abstract This paper provides a synthetic view on the most recent achievements in the field of drilling and servicing rig drives for oil and gas wells. This field is featuring powers of hundreds and thousands of kilowatts and speeds of 150–250 rpm for drilling and 30–200 rpm at servicing rigs. In the first part the paper presents achievements in the field of rotary tables—the central piece of equipment of the drilling rigs. In the second part of the paper recent achievements in the field of hydraulic motor driveheads (HMD) are presented. Details are given regarding a recent product of S.C. CONFIND: the cement plug drilling installation with HMD of 80 tons and thermic motor of 160 HP. In the last part of the paper the newest international achievements in the field of power swivels are described: Top Drive (TD) and Direct Drive (DD), using slow speed hydraulic and electric motors.

Keywords Rotary tables · Power swivels · Top drive · Direct drive

1 Introduction

With the increase of the consumption of fuel obtained from oil the interest in the discovery and exploitation of oil reserves has grown as well. This infernal race sustained by the need for getting faster to the precious resource to gain money more and faster has also generated a technological leap regarding the drilling methods.

The history of oil equipment for well drilling is not very old (about 130 years), starting from the old black oil pits manually exploited until today, when snap drilling speeds of about 40–80 m/h (depending on the rocks drilled) have been reached.

A. Iamandei (✉) · G. Miloiu
CONFIND Campina, Campina, Romania
e-mail: Iamandei_aurelian@yahoo.com

G. Miloiu
e-mail: gmiloiu@confind.ro

G. Dobre (ed.), *Power Transmissions*,
Mechanisms and Machine Science 13, DOI: 10.1007/978-94-007-6558-0_50,

Table 1 Well equipments and works

Equipment	Works on fixed installations		Works on mobile installations	
	Drilling	Interventions, repairs	Drilling	Interventions, repairs
Rotary table and hydraulic drive	x	–	x	x
Hydraulic motor drivehead	–	x	–	x
Top drive/direct drive	x	–	x	x

To make a well a series of units are necessary, able to perform two main movements:

– the rotation movement of the drill bit;
– the feed movement of the drill bit.

Starting from the 80s the commitments of the oil equipment manufacturers have focussed on increasing the performances of the cinematic driving chains of the main units, to increase the technological parameters of the drill bit, considering the new developments in the production of drill bits.

A synthetic view on the well equipment and works is presented in Table 1.

The main works performed at wells are related to the well drilling and construction, respectively to interventions and repairs to be performed through the well exploitation.

The installations performing the various works of well drilling or repairs can be fixed or mobile. Taking into account the character of the works done during well drilling or well repairs and the time needed to make a well construction work, in comparison to the time needed for a well repair, it was found that the fixed rigs are especially fit for drilling works, but they are clumsy as regards well intervention or repair works, while the mobile rigs have a high degree of transportability and setting on location. Regarding the main subassemblies included, the fixed rigs and the mobile ones do not have major differences regarding the components—the differences are in the construction thereof.

The main units of well drilling or repairs rigs are presented in Table 2.

Recent achievements regarding the well drilling and servicing equipments are eventually presented in this paper. Examples are given from the international manufacture and from Romania.

2 Rotary Table: The Central Piece of Equipment of Drilling Rigs

The rotary tables are designed to rotate the drilling string. The input shaft of the table is driven by a diesel-hydraulic, diesel-electric or electrical drive-head. Rotary tables meet the requirements of API Spec. 7 K. The constructive size of the rotary table is coded by the diameter of the table opening.

Table 2 Main assemblies of a drilling rig/workover rig

Rig type	Fixed (drilling)	Mobile (repairs)
Force motor group	x	x
Hoisting system (draw work, crown block, traveling block)	x	x
Rotary table	x	Optional
Swivel hydraulic	x	Optional
Swivel hydraulic motor drive head	–	x
Top drive (TD)	x	–
Direct drive (DD)	x	–
Mast	x	–
Substructure	x	Optional
Mud preparation and claning system	x	Optional
Mud circulation system	x	Optional
Working platform	–	x

Table 3 presents the characteristics of several fixed tables (American Block 2011), at which the clearance diameter is of 17 ½–60 ½ in, the static load is from max. 275 tf (300 ts) up to 1,135 tf (1250 ts), the maximum speed 500 rpm, the transmission ratio is ranging from 3.16 to 4.76, the table weight from 2,707 to 17,236 kg.

The design of a Romanian rotary table is presented in Fig. 1 (the size 17 ½). Basically, the rotary table includes a housing, a bevel gear, bearings, sealings and a bevel gear wheel blocking system. The bevel pinion is composed of the pinion 1 and the shaft 2, and the bevel wheel includes the crown 3 and the body 4.

The bevel pinion is supported on the bearings 5 and 6 into the case 7, and the bevel gear wheel is supported on two radial-axial bearings (angular contact thrust ball bearings, single directions) 8 and 9; the first one takes the axial load created by the weight of the drilling string, the second is closing the assembly. The sealing of the space of bearings and gears is done with high labyrinths. The housing 10 and the case 7 make the fabricated construction 11. To perform operations at the well without rotating the table, this is provided with a locking system consisting in a latch driven from outside, 12.

High performance bevel gears only are used at the rotary tables: spiral bevel gears, hardened (57–62 HRC) and ground with high accuracy. The bevel gears for rotary tables are machined by the HPG process (machining after quenching, with interchangeable CBN tips), developed three decades ago (Bosch 1979). Gears with the maximum diameter of the gear of 1,600 mm (which can be extended to max. 2,000 mm), max. permissible total width of 300 mm, permissible tooth number 6–120, can be machined on the machines AMK 1602 and AMK 1603. These are high power gears, for up to 4,500 kW (Klingelnberg 1980).

Table 3 Technical features of "American Block" rotary tables

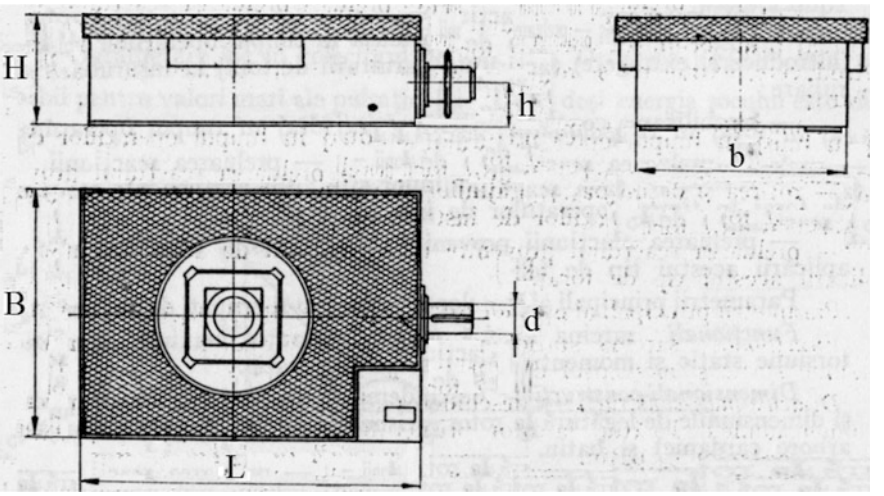

Size		RK-175S	RK-175	RK-205	RK-275	RK-375	RK-495	RK-605
Static load capacity, tonnes		272	272	318	454	560	726	1135
Maximum table speed, rpm		500	500	500	500	650	800	150
Maximum table opening dia., mm		445	445	521	699	953	1,257	1,537
Gear ratio		3.78	3.78	3.79	3.16	3.60	3.93	4.76
Dimensions mm	L	1,689	1,755	1,612	2,133	2,184	2,590	
	B	1,219	1,219	1,377	1,600	1,797	2,184	2,184
	H	523	523	559	705	711	819	921
	b	956	956	1,123	1,219	1,442	1,600	1,905
	d	108	108	114	125	125	125	
	h	254	254	280	330	330	368	
Weight less master bushings, kg		2,707	2,780	3,322	5,306	6,712	11,700	17,236

Table 4 The main technical characteristics of some hydraulic motor driveheads

Characteristics	U.M.	Logan 85	Logan 120	UPET CHM 50	UPET CHM 80	Sunnda PW 150
Maximum working load	tf	77.1	108.8	50	80	136
Equivalent load	tf	40.8	59	28	70	
Maximum speed	rpm	155	150	140	107	210
Motor power	HP	83	240		110	150
	rpm	2,000	2,000		110	
Maximum torque	Nm	5,350	10,980	4,040	8,330	14,920
Torque at maximum speed	Nm	3,380	7,100	2,020	4,165	
Weight	kg	527	907	728	960	

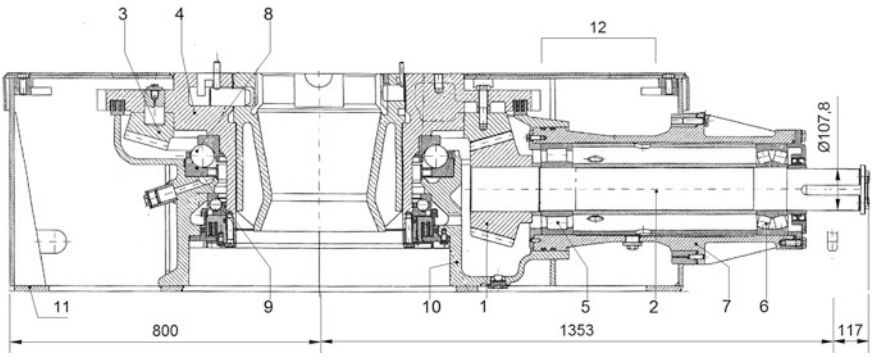

Fig. 1 Rotary table (Cristea a.o. 1985)

3 Hydraulic Motor Drive Head

The hydraulic head with hydrostatic drive (HMD), Fig. 2, is suspended in the rig hook and takes the role of the hydraulic head of the rotary table. The hydraulic drive ensures the transmission of the torque to the working string, the change of the rotation direction, the speed and torque variation.

The functions of the hydraulic motor head are the following:

– to support the drilling string and to make it rotate.
– to direct the under-pressure drilling fluid to the fixed loader through flexible hose to the drilling string.

The hydraulic head is composed of two kinds of parts: the first group is formed of motionless parts suspended in the hook, and the second group is formed of parts in rotation movement. The motionless parts include the hydraulic head body 1, in which the main bearing 2 is supported, and the bails 3, articulated into the body by means of the bolts 4 at the upper part. The body is closed with the cover 5, which is provided with a sealing system for the oil pan of the body; over this is assembled the lantern 6, which has at the upper part the fixing flange of the gooseneck coupling 7 achieving the connection to the rotary hose. At the lower part of the hydraulic body is also attached the hydraulic head driving system, consisting in a two step gearbox 8, onto which two hydraulic motors 9 are mounted.

The rotating parts include the shaft 10, supported on the main bearing 2, which is provided with the clearance hole for the drilling fluid, having at the lower part a conical thread for assembling with the safety valve 11. The connection between the upper part of the shaft and the gooseneck coupling is ensured by the assembly of the washing pipe 12. To secure the safety valve from the shaft against unscrewing during the left–right rotation, the shaft is provided with a safety sleeve 13.

There is a big number of constructive variants for the hydraulic motor drive-heads, forming generally standard series, covering a wide field of drilling depths.

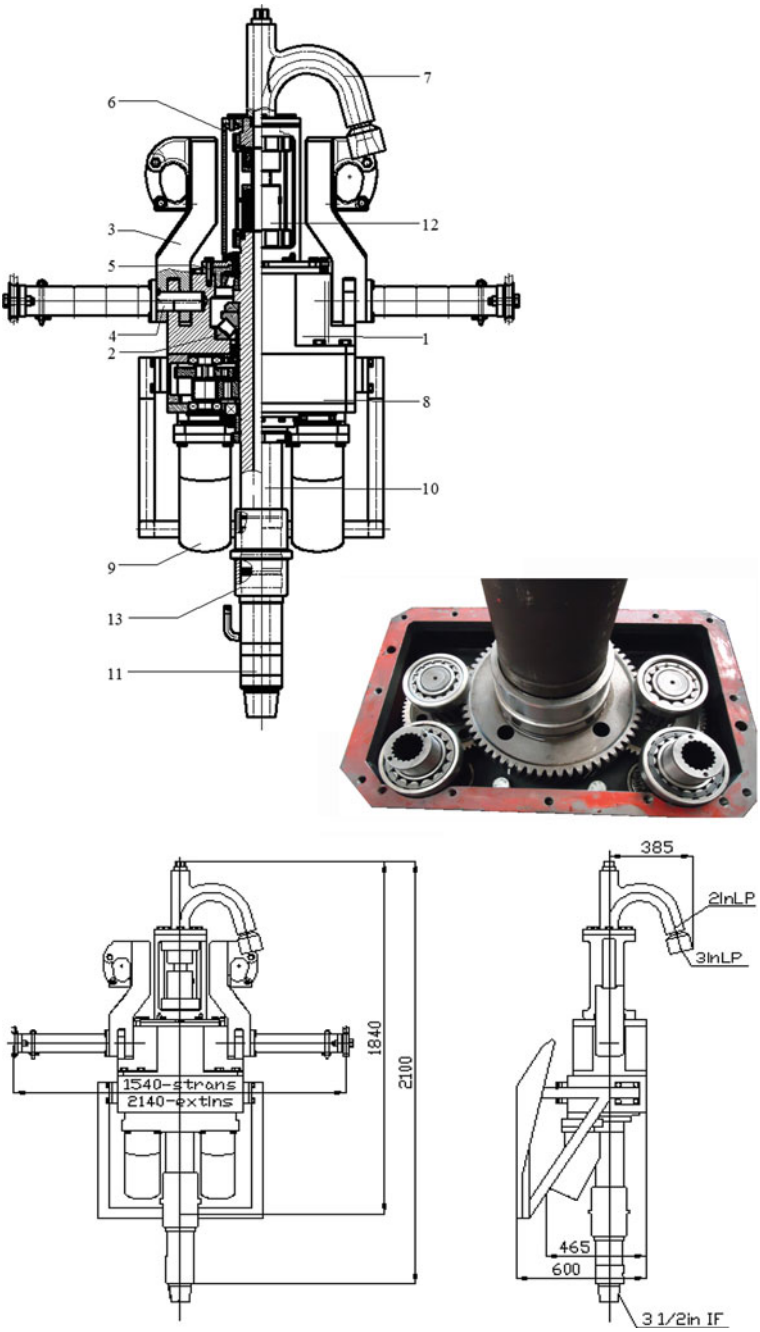

Fig. 2 Construction of hydraulic motor drive head CHM80 confind type (Confind 2011) and (Iamandei and Miloiu 2011)

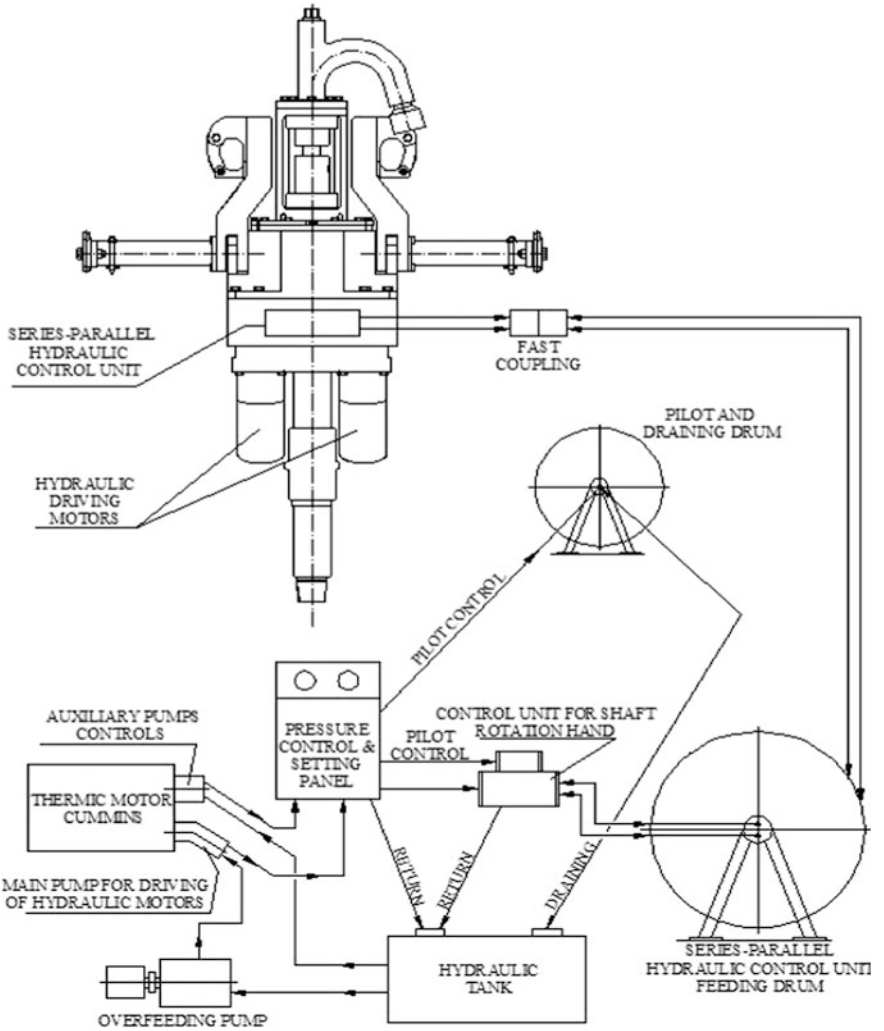

Fig. 3 Hydraulic block diagram of the CONFIND 80 tf drilling unit type IDFC80

On designing the assembly of a hydraulic motor head, there is a tendency to obtain as low an own weight as possible, to attenuate the danger of bending the driving rod when this is introduced into its guide, a height as short as possible, in order to occupy as reduced as possible a part of the cinematic space of the mast, to locate the mass centre in a position as low as possible in relation to the bail joint points, thus leading to a better stability during drilling.

Using the HMD from Fig. 2, in 2010, CONFIND has developed an instalation for drilling cement plugs (but for other operations as well), by the scheme from Fig. 3 and with the characteristics shown in Table 5. This installation is characterized by:

Table 5 The technical characteristics of the cement plug drilling installation IFDC 80 (Confind 2011)

Characteristics	U.M.	Values
Maximum load: static/dynamic	tf	100/80
Equivalent load (100 rpm, 3,000 h)	tf	70
Maximum speed/maximum torque	rpm/Nm	160/90
Maximum torque/minimum speed	Nm/rpm	9,200/510
Shaft rotation direction	–	Left/right
Hydraulic motor driving	–	Series/parallel
Thermic motor:	-HP/rpm	CUMMINS QSB 4.5
Power/maximum speed		160/2,500
Maximum torque/max. speed	32 Nm/rpm	624/1,500
Maximum hydraulic pressure	bar	290
Maximum circulation pressure	bar	350
Transport skid overall dimensions	m	5.46 × 2 × 2
Oil tank capacity	l	500

– a new system of clamping the HMD with independent bails has been adopted, which results in saving the space from the cinematic chain of the mast;
– the gearbox is provided with gears of high bearing capacity, finished at high accuracy;
– the most stressed parts are forged: the shaft, the bails, the gears, the head body;
– new sealing case has been designed, able to seal with very good results up to 350 bar.

The automation degree has been increased by introducing hydraulic pre-controls (Table 4).

Other concerns can be noticed regarding the improvement of the bubbling lubrication system, by creating an oil circulation through the channels built inside the body, and also the usage of some new materials for the wear elements (such as the sealing gasket).

The bails of the hydraulic head are made of alloy steel, forged and heat treated, the radii of the contact surfaces having standardised values according to API 8A/8C.

The gooseneck coupling of the hydraulic head is used to link to the hose, generally having an interior thread connection. The stuffing box for the washing pipe, with lateral insertion and extraction, has become quite common at almost all the hydraulic heads. Worth being noted at these designs is the fact that the gaskets have an individual seat with sealing effect caused by the pressure created by the drilling fluid.

The upper nut and the lower nut have threads allowing the fast screwing/unscrewing, either by introducing some stems into the radial holes for rotation or by hitting into the protuberances provided at the exterior.

The last designs appeared allow the replacement of the assembly without dismounting the gooseneck coupling or the hose. The system does not need any setting during operation, and the washing pipe, which has the outer surface hardened, is self-aligning.

Table 6 Trends in construction of hydraulic power swivels (HMD) and solution for CHM80

Trends in construction HMD	Solutions for CHM 80
Minimum weight	Body + handle + gears of alloy stell, forged and final head treated
As low possible-height (to not take too much kinematic space inside the mast)	
Mass center location in the lowest position, beside the handle joint (for stability)	Insured—by designing
Function direction: left/right	Movable—coupling between spindle and kelly valve
Maintenance, troubleshooting	Easy replacement of wear parts

The shaft of the hydraulic head has the shape of a revolution body, having at the middle a shoulder meant to support onto the main bearing. At the lower extremity, the shaft is provided with a spigot thread for screwing the safety valve.

The two step gearbox has a robust and compact design; the hydraulic motors with inclined body and axial pistons and the distributor for series–parallel switching of the position of the functioning position of the hydraulic motors are attached to its housing.

The hydraulic motor head is provided with a system for taking over the reactive torque, consisting in two arms guided on two cables.

Confind hydraulic motor driveheads (HMD) it aligns itself to the newest trends in the field, systematized in Table 6.

S.C. CONFIND S.R.L. is currently manufacturing a first batch of drilling installations of 80 tf by own design, with characteristics superior to many hydraulic heads produced both in the country and abroad.

4 Top Drive

The TOP DRIVE (TD) is a multifunctional unit carrying out the rotation movement of the drilling string directly, without the need for a driving rod, also ensuring the mechanization of some operations at the wellhead—Fig. 4. All the same, TD delivers technological parameters (speed, torque) superior to those provided by the Rotary Table (RT).

Taking into account the kinematics presented in Fig. 5, they can see the major difference between the complexity of the cinematic chain of drive (consisting in mechanical transmissions) of a RT with centralized system and the cinematic chain of a Top Drive—see Fig. 6.

In principle, the main advantages of driving the drilling string by means of TD against the RT drive are the following:

(1) Simpler cinematic chain;
(2) Superior technological parameters (torque—speed);
(3) Efficiency increased by some 20–30 %, due to the simpler cinematic chain.

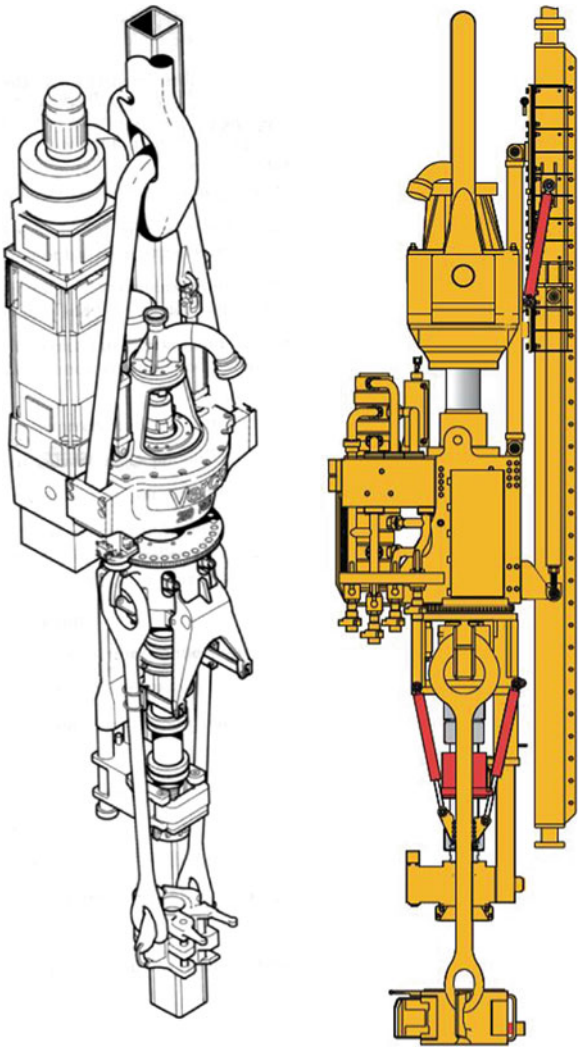

Fig. 4 TOP DRIVE general assembly electrical actuated (VARCO 2000), hydraulic actuated, TESCO 2011)

(4) Shorter drilling time, because of eliminating the driving rod;
(5) Shorter drilling time, because of drilling at entire pitch (of three pieces);
(6) The possibility of fitting the TD with some wellhead automation mechanisms, such as for:

handling the links, handling the elevators, screwing-unscrewing, fastening-loosening the tubular material;

(7) The possibility to manipulate the rod joints;
(8) The possibility to move the TD along at least one axis for accurate alignment at the wellhead, etc.

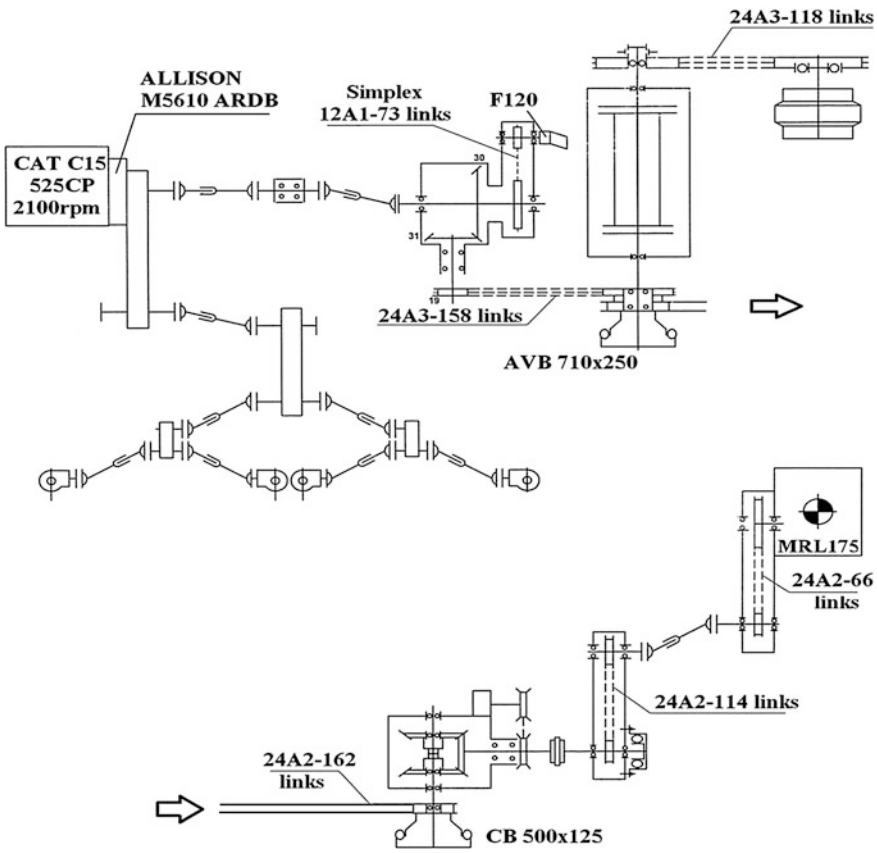

Fig. 5 Power drive kinematics of the rotary table, in centralised drive system (UPET 2010)

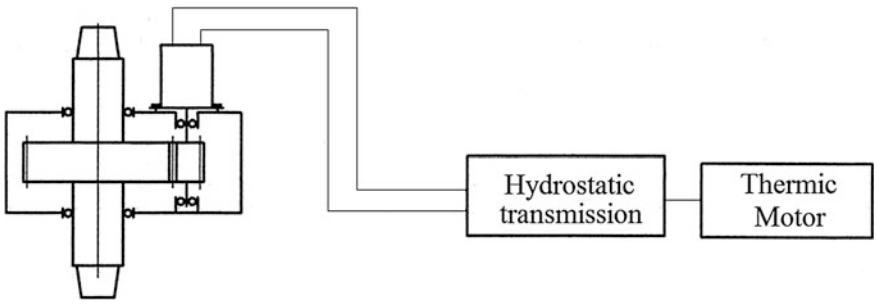

Fig. 6 Hydraulic drive kinematics of TOP DRIVE (or hydraulic motor drive head)

Taking advantage of the technical developments of the hydraulic and electrical drives and having as a basis the hydraulic motor heads (HMD), the product TOP DRIVE has been imposed as a concept in the late 80s.

Table 7 The functions or operations performed by TD's and HMD's

Function/operation	HMD	TD
String rotation	Yes	Yes
Screwing of upper string	No	Yes
Screwing of lower string	Yes	Yes
Fastening of top/bottom string	No	Yes
Loosening of top/bottom string	No	Yes
Handling of links	No	Yes
Fitted with automatic elevator	No	Yes
Handling of bridge joints	No	Yes
Torsion torque	0…1,000 daNm	0…8,000 daNm
Speed	0…160 rpm	0…200 rpm
Hydraulic/mechanic IBOP	No	Yes

Big companies (VARCO, TESCO) have invested in this concept, and in the mid 90s the product TOP DRIVE has been launched on the market, to become today customary in the drilling process—Fig. 4.

The "heart" of any TD is an HMD. In the meantime, HMD's have been developed both for the well repair industry and for installations of small capacity for water and geological drilling. Not having the possibility to transmit to the drilling string any adequate speeds and torques, and especially the lack of mechanizations, the HMD's have not been used in the oil industry for drilling big depth wells. However, the HMD has been the basis for designing the TD. A comparison of technological parameters can not be done, since the load range is shared between HMD's and TD's. Thus, HMD's have been produced until a 200 tf hook load, while TD's have been built for over 200 tf. There are no significant differences from the point of view of the operational phylosophy, the cinematic chain being identical, but the powers transmitted differ. Differences also appear regarding the auxiliary functions and operations performed—see Table 7.

The parameters of some TOP DRIVES of Tesco, Varco and Sunnda are given in Table 8. In the Eastern European, TD are manufactured in Russia (Promtechinvest 2010). In Romania has recently appeared the first study (Stan and Avram 2010).

5 Direct Drive

Taking into account the success achieved by TD, more and more companies producing oilfield equipment have drawn out their own projects for the manufacturing of some TD's. Taking advantage of the development of slow electric and hydraulic motors, delivering high torques at low speed, some companies have developed the Direct Drive (DD—see Fig. 7). The major difference between TD and DD is that at DD's the driving of the drilling string is done directly from the motor shaft. The motor shaft is built so that it can allow the passage through its interior of a coupling transmitting to the drilling string the torque; the load of the

Table 8 The technical parameters of TD's

Parameter	UM	TESCO 500/65 HCI 1205	NorDrill ND500/650	Sunnda TD 500 AC	CANRIG 1250 AC
Load	tf	650	650	500	500
Maximum fastening torque	daNm	7,158	8,025	6,006	6,970
Maximum loosening torque	daNm	8,053	10,200	9,002	12,880
Maximum torque/speed	daN/rpm	7,150/120	8025/60	–	6,970/120
Maximum speed	rpm	210	200	200	265
Weight	kg	8,770	10,250	–	13,200
Length	m	6.1	7.1	7.2	8.3
Elevator handling	–	Yes	Yes	Yes	Yes
TD handling	–	Yes	No	No	No
Tongs rotation	–	Yes/unlimited	Yes/24 steps	–	Yes/unlimited

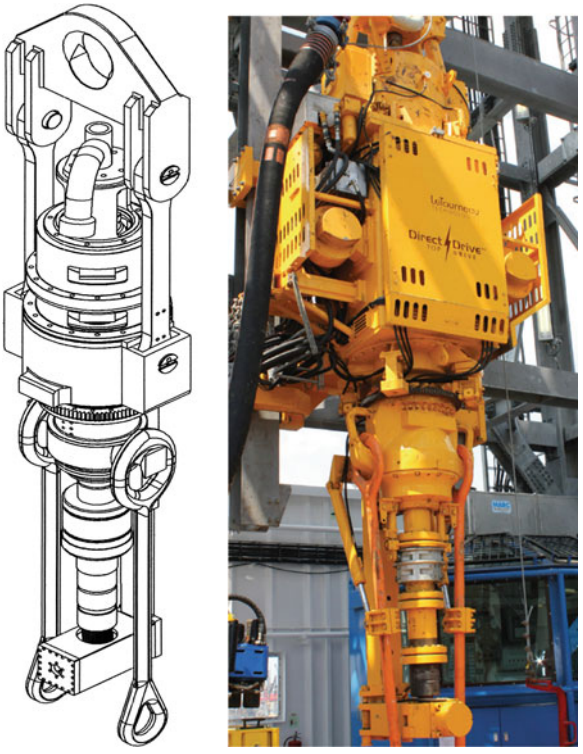

Fig. 7 Direct drive (fluid design solution, Le Tourneau—LTI 2011)

drilling string is suspended like in the case of TD in swivel. The parameters of a DD are given in Table 9.

Table 9 The technical parameters of DD

Parameter	UM	LE- TOURNEAU AC	Fluid design solution hydraulic
Load	tf	500	250
Maximum fastening torque	daNm	10,845	3,400
Maximum loosening torque	daNm	10,845	3,300
Maximum torque/speed	daN/rpm	5,900/115	3,000/100
Maximum speed	rpm	115	200
Weight	kg	16,236	–
Length	m	7.25	–
Elevator handling	–	Yes	Yes
TD handling	–	Yes	Yes
Tongs rotation	–	Yes/unlimited	Yes/unlimited

Fig. 8 Hydraulic traction motor (Dynex/Rivert 2011)

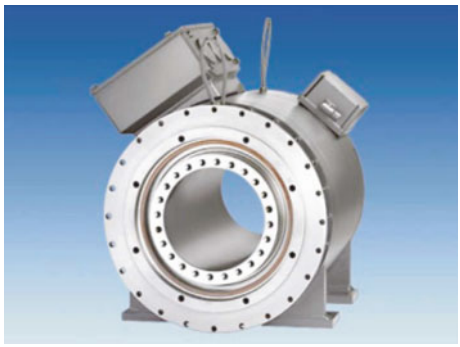

Fig. 9 Electrical traction motor (Siemens 2009)

The traction motors of Direct Drive are of two types:

– hydraulic traction motors (HTM)—Fig. 8;
– electrical traction motors (ETM)—Figs. 9, 10, 11.

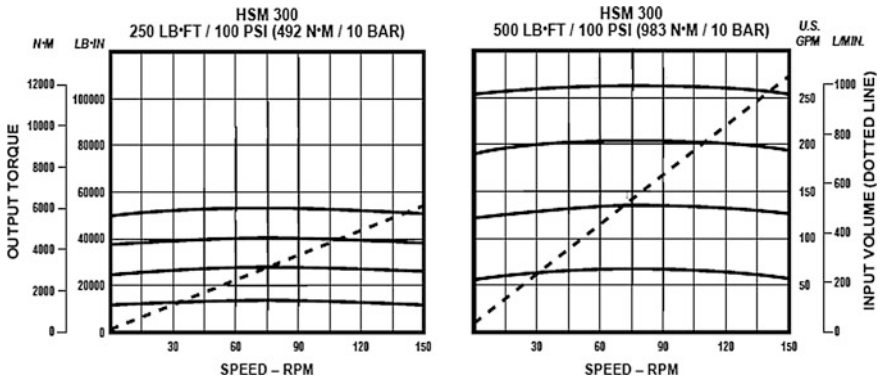

Fig. 10 The working curves of the hydraulic motor (Dynex/Rivert 2011)

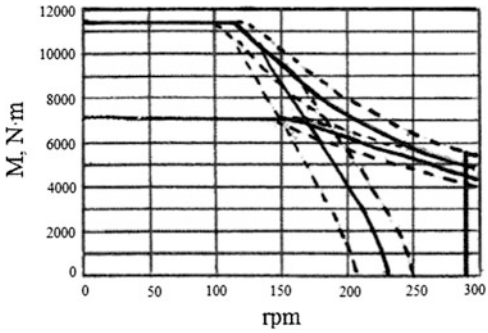

Fig. 11 The working curves of the electric motor (Siemens 2009)

6 Conclusion

The Rotary Table remains the central unit of the fixed drilling rigs, and the Hydraulic Motor Drivehead (HMD)—the main piece of equipment of the mobile installations.

The developments achieved in the field of slow motors have determined great improvements at HMD's, respectively at TD's and Direct Drives.

References

American Block (2011) Rotary tables. Houston, Texas, USA

Bosch M (1979) Neue Tehnologie zum Hersteller spiralverzahnter Grosse-kegelrader imm Zyklo-Palloid-Verfahren. Antriebstechnick, nr.10, 3S

Confind-Servicing rigs for oil and gas wells AM 12/40 si AM 12/50 (2011) Campina, Romania. www.confind.ro

Cristea V s.a (1985) Boring rigs and equipment for drilling wells (in Romanian) Ed. Tehnica, Bucharest

Dynex/Rivert Inc (2011) www. Dynexhydraulics. com
Lamandei A, Miloiu G (2011) Gear rig with hydro drive 80 tf (in Romanian) Petroleum Industry Review, pp 26–28
Klingelnberg (1980) Generating machines for large cyclo-palloid spiral bevel gears. Models AMK 1602 and AMK 1603
LTI Drilling system (2011) www.lti-drilling.com
Promtechinvest (2010) Top drives. Sankt Petersburg, Russia
Stan M, Avram L (2010) Dynamic system composed top drive and drill pipe. Bull Oil and Gas University Ploiesti vol. LXII, Nr.1, pp 79–86
Siemens Germany (2009) www.siemens.com
Sunnda Drilling equipment (2011) www.sunnda.com
TESCO CORPORATION (2011) www.Tesco Corp.com
UPET (2010) Oil and gas equipment. Targoviste, Romania. www.upetgroup.ro
VARCO Systems (2000) TDS-10SA Top drive drilling system. Orange, California, USA

Testing of the Electromotor Power Transmitter Properties

Lozica Ivanović, Danica Josifović, Dobrivoje Ćatić and Andreja Ilić

Abstract The requirements set, which modern gear power transmitter have to fulfill, are quite complex. The modern gear power transmitters are working on higher and very fluctuating load level, while need to be even more smaller, efficient, quieter, easier to produce and finally they have to cost less. Although the latest development made in the analysis and simulation of power transmitter, experimental testing is still essential. This paper presents the experimental method of measurement and assessment of working properties of electromotor power transmitter. The testing method presented in this paper is specific application-oriented full-scale testing with simulation of working conditions. Testing of the characteristic properties values was conducted on a three stage electromotor power transmitter and on the production series of five pieces. The paper presents two kinds of examination, the method of serial examination and the method of occasional (reduced—standard) testing. Experimentally determined characteristics and performances of power transmitters in working conditions represented real result of its design and used manufacturing processes. The obtained results are used as essential data for design modifications and its proper qualification, so as developing completely new designs. Also, results obtained by the same methodology represented the current technical condition of the examined power transmitter and could be used as condition diagnosis of the power transmitter elements without the need of their disassembly. The needs for standardizing of the testing methods are pointed out.

L. Ivanović (✉) · D. Josifović · D. Ćatić · A. Ilić
Faculty of Mechanical Engineering, University of Kragujevac, Sestre Janjić 6 34000 Kragujevac, Serbia
e-mail: lozica@kg.ac.rs

D. Josifović
e-mail: danaj@kg.ac.rs

D. Ćatić
e-mail: caticd@kg.ac.rs

A. Ilić
e-mail: gilic9@sbb.rs

G. Dobre (ed.), *Power Transmissions*,
Mechanisms and Machine Science 13, DOI: 10.1007/978-94-007-6558-0_51,

Keywords Electromotor power transmitter · Noise · Vibration · Torque · Thermal loading

List of symbols

P	Power
T	Torque
n	Output number of rotation
n_m	Number of electromotor rotation
U	Electrical voltage
f	Frequency of alternated current
u	Speed ratio
I	Current
T	Temperature
T_1, T_2, T_3	Temperature of oil, housing of the transmitter and housing of the electromotor, respectively.

1 Introduction

1.1 General Characteristics of Power Transmitter and its Properties Testing

Power transmitters are the crucial elements of power transmission drives of most mechanical systems. They can be used in a wide diapason of speeds and loads, thus ensuring high kinematic accuracy, working continuance, and reliability needed in different exploitative conditions. Their main function is to transmit movement and torque from one shaft to another using a so called form connection which is in this case represented by the teeth grasp of the gears at suitable level of noise, vibration and temperature. In addition, a certain transformation of rotation number and torque is conducted. Basic advantages of the gear power transmitters, in comparison with other transmitters, are: simple acting, accurate kinematical transmitting relation, small dimensions and a high degree of efficiency. The disadvantages of gear power transmitters are: great rigidity in transmitting power, vibration and noise intensity. Power transmitters and the electromotor power transmitters, after their manufacture, pass testing procedure concerning their safety and working reliability in exploitative conditions. It is essential to declare the quality of power transmitters before they are utilized and, by that, to ensure problem free functioning of systems, as shown in literature (Josifović 2000; Rešetov 1979; Trbojević et al. 1988 and Chase 2005).

1.2 Testing Methodology and Object

To fulfill requirements of methodology testing identification, literature survey was undertaken with the observation to finalize features of testing devices and specification of methodology. An apparently simplest testing approach is to set the test power transmitter between a motor and a brake. The used motor has to provide the power level for testing and the brake has to transform it to heat that is often difficult to dissipate. A more efficient testing approach can be done by closed power circuit, which can be either mechanical or electrical. Very important characteristic of testing methodology is permitting the determination of the degree of efficiency of the power transmitter directly by measuring the rotational speed and torque of the power motor. In the view of considering the high efficiency of modern power transmitters it is difficult to obtain the power loss of power transmitters with acceptable accuracy by measuring the input and output power. Flexible and advanced testing approach can be obtained by hydraulic torque applying device in order to regulate the test load by controlling the hydraulic pressure, but with decreasing the complexity of testing devices system and coasts. More advantages can be obtained be the digital control of load applying, as mentioned in literature (Höhn 2000; Kollmann 2000; Meltzer 2000 and Smith 2003).

For the experimental determination of the electromotor power transmitter working characteristics presented in this paper the open power circuit testing mode is chosen. This was done to its simple construction, precise load simulation, low cast and no need for high energy efficiency in testing. Figure 1 represents scheme of used testing device system. The tested motor power transmitter was set to a testing device, ensuring the axis alignment of shafts to 0.1 mm and crossing angle of shaft's axis up to 1^{o}. Testing of the motor power transmitter was conducted according to the so-called indirect testing method, which means that two motor transmitters are mutually connected by the shaft with torque measuring device (rigid connection). The connection between the motor-reductor and multiplier-generator ensure that the output number of rotation from the redactor, in fact, is the input number of rotations in multiplier. This paper deals with the testing methodology of electromotor power transmitter which is based on the standard and recommendations by AGMA and VDI. The testing presented in this paper experimentally determined the following parameters: torque on output shaft, speed ratio, thermal loading, oil and housing temperature, degree of efficiency, noise and vibration control. The used testing methodology has to be able to indirectly identify early formation of failure modes. There are many gear power transmitter failure modes that may occur in exploitation. Tooth breakage, pitting and micro-pitting as well as excessive wear or even scuffing are the most commonly met at the gears as elements of power transmitters. Besides the load parameters carrying capacity, there are also other important parameters like dynamic power efficiency and behavior of power transmitters in dynamic load conditions that need to be

experimentally investigated, but they are not in the focus of this paper as mentioned in literature (Chase 2005; Litvin and Fuentes 2004 and Davis 2005).

2 Testing Procedures and Results

For measurement and examination of the characteristics of motor transmitter, for the purposes of testing presented in this paper, the motor power transmitter with technical characteristics is shown in Fig. 2.

2.1 Transmitter Control to Noise and Vibration

The transmission error is widely regarded as one of the main causes of gear noise. The transmission error was defined first by Harris in 1958, who started its analytical investigation. Nevertheless, overview of references prove that this concept was already applied before, but using an empirical approach. The two main factors affecting the transmission error are the mesh stiffness, which accounts for gear tooth flexibility and number of meshing gear tooth pairs, and the gear tooth micro geometry, in terms of intentional modifications and manufacturing errors. Variations in the transmission error, during the gear meshing, trigger vibrations and then provoked noise, as shown by Smith (2003). The noise level and vibration of the transmitter depends on a number of factors such as: speed, degree of balance of certain elements of the transmitter and the electromotor, quality of design of toothed elements, irregular kinematic coupling, lessened axial distance etc., so the noise control is one of the important indicants of the irregular work of the transmitter, as mentioned in literature (Ilić and Josifović 2008 and Sawhney 2009). The tested power transmitter is considered to be regular if it operates with equal

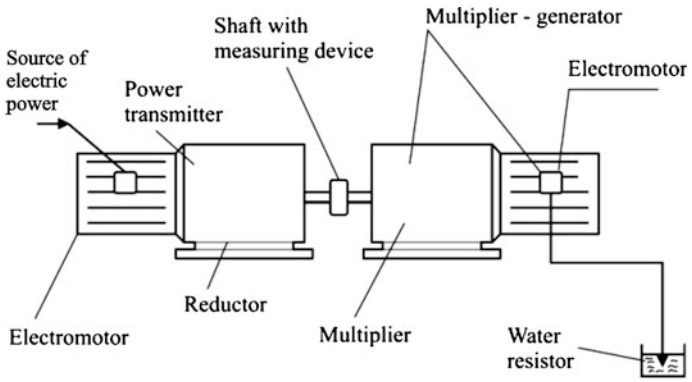

Fig. 1 Scheme of the testing device

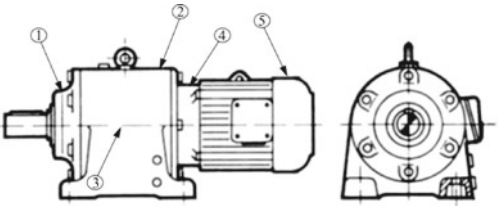

- Power $P = 1.5$ kW;
- Torque $T = 600$ Nm;
- Speed ratio $u = 70.73$;
- Output number of rotation $n = 20$ min^{-1};
- Number of electromotor rotation $n_m = 1420$ min^{-1};
- Electrical voltage $U = 380$ V;
- Frequency $f = 50$ Hz and
- Mechanical protection IP55.

Fig. 2 The tested electromotor power transmitter with technical characteristic and measure position

noise, and the level of noise does not exceed 71 ± 2 db measured from 1 m distance. The noise control is conducted according to the standard DIN 45635 and recommendations IEC–34–9. The noise measuring was conducted in the special room which is completely isolated from all external influences of noise with a digital noise meter from Brüel and Kjær type Integrating Sound Level Meter—Type 2239 A. During the noise measuring, environmental noise level was 37 db. The measuring is done by pointing the noise meter, which has a microphone, to measuring points. Vibration measuring was conducted with digital vibro—controller, by a direct contact in certain points. For vibration testing of the electromotor power transmitter Vibration Analyzer Type 2250 H from Brüel and Kjær is used. In the examined series of the motor transmitters two of five examined transmitters did not satisfy because the level of noise exceeded allowed values.

2.2 Measuring of Output Number of Rotation and Electrical Characteristics of Electromotor

The output number of rotation is set up by the number of electromotor rotations and the speed ratio of the power transmitter. The obtained value while testing is higher than the catalogue value. This was explained by the increased rotations number of the driving electromotor, because it is working without load. The allowed deviation of the measured output rotation number in idle to the catalogue value is 5 %. For number of rotation measurement in the presented testing procedure the digital tachometer type HHT-1501 producer Omega Electronic is used. The actual number of rotation is obtained by testing is n = 20.5 min-1 with the error of 2.5 %, so determined deviation was allowed.

Measuring of the electrical characteristics of electromotor is performed in idle, with the aim of determining functionality of all elements of the transmitter and the motor. The usual characteristics which are tested are: voltage, intensity of electric

current and power. The voltage testing is conducted in idle with the constant nominal voltage and direct switching of the motor. The intensity of electric current which the motor uses is obtained using ampermeter for every electric phase. The power which motor uses is obtained using wattmeter on the testing device. The variation of the electrical characteristics during the work of power transmitter cannot pass definite limits. Testing was performed in both directions of rotation and it lasted 120 s for every rotation direction.

During this testing procedure, control of seal and oil level was done. Control of seal and oil level was performed visually during testing and it was concluded that there was no leakage in any of the tested transmitters. The critical points concerning leakage are: bearing seals, blind openings, paper seals. This control is important due to lubricant provides two primary benefits: to lubricate the gears and to transfer and remove heat generated from the gears operation, so as to lubricate the bearings in the power transmitter. Losses of lubrication oil lead to conditions which provoked failure of power transmitter.

2.3 Standard Test of Electromotor

The output parameters of the transmitter can always be measured, while the input parameters, which are actually the output parameters of electromotor, must be known before starting any tests on motor transmitters. That is why the standard test of electromotor was conducted. The following characteristics of motor were determined: source power, output power of electromotor, the output number of electromotor rotations, intensity of electric current and the degree of efficiency of the electromotor was determined. It was concluded that the electromotor satisfies the demands.

Testing results are shown by diagrams in Figs. 3 and 4 and obtained values are used for further evaluation in electromotor power transmitter testing procedure.

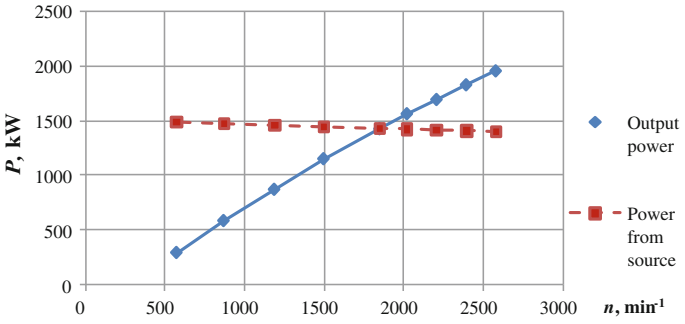

Fig. 3 Output power and power from source dependence of number of rotations

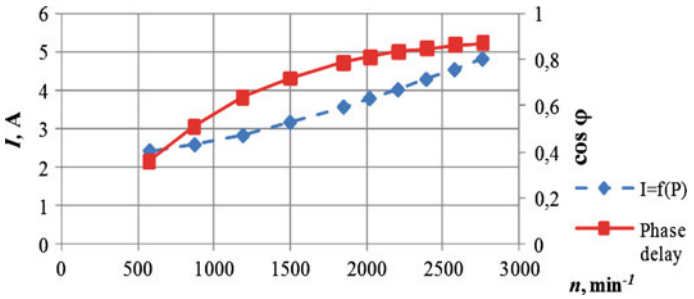

Fig. 4 Current and phase delay dependence of number of rotations

2.4 Control of Torque on Output Shaft and Thermal Loading of the Transmitter

During examination of the electromotor power transmitter torque was determined and the output rotation number of the transmitter, for both rotation directions, in the regime of permanent driving with leveled load up to the value of nominal torque. First, the power transmitter was loaded with 25 % of nominal torque, then with 50 and 75 % of nominal torque, each in a period of 7 h. Finally, it was loaded with the nominal torque until it came to a thermally stationary state. For torque measurement in this testing procedure the torque transducer type DRBK producer ETH Messtechnik is used.

The operation temperature of power transmitter is dependent on a large number of parameters, as shown in literature (Petry-Johnson et al. 2007 and Höhn et al. 1996). In this testing operation temperature was measured under different load level to analyze load level parameter as main factor of operation temperature increase. Temperature was measured according to IEC recommendations and regulations VDE 0530. The oil temperature in the housing (T_1), temperature of the housing of the transmitter (T_2) and temperature of the housing of the electromotor (T_3) were measured by thermocouple probe with universal serial bus interface linked to computer for data acquisition produced by Omega Engineering Inc., Europe. Temperature was measured for every load levels used in previous control, each in a period of 7 h, shown in Fig. 5.

2.5 Degree of Efficiency Control of the Transmitter

A large number of theoretical studies have been published on the efficiency of gear trains used in power transmitters. A group of gear efficiency models in power transmitters used a constant friction coefficient along the entire contact surface gears. Another group of the models modified the same approach with the exception that their formulation for friction coefficient was not constant, but was based on

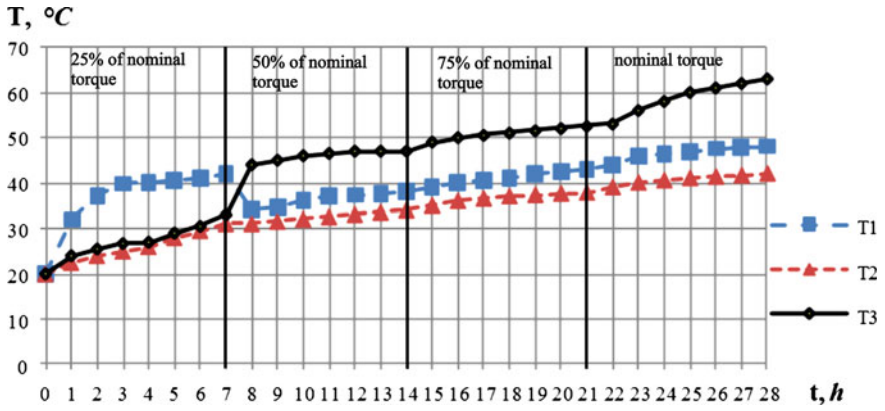

Fig. 5 Diagram of temperature with load of 25, 50, and 75 % of nominal torque and nominal torque for 7 h of each load level

various empirical formulae obtained from experimental tests. Most recently developed mathematical model used such friction formulae to compute the dynamic friction forces and power loss. Approaches based on elastohydrodynamic (EHL) lubrication models are varying in its complexity and were developed in order to compute friction coefficient without the need of empirical formulae. Some of these studies considered smooth surface EHL formulae to determine the surface shear stress distribution caused by the fluid film, from which instantaneous friction coefficients were calculated. While these models were sophisticated in handling EHL aspects of the problem in the gear mesh, they did not consider load-independent power loss, and are thus insufficient to predict total power transmitter efficiency. While there is large number of theoretical work on mechanical efficiency is extensive in modern literature, for experimental approach of the problem it cannot be said. Most experimental studies have been limited to estimating average gear mesh friction coefficient under low to medium speeds and correlating this to gear operating characteristics such as sliding velocity, torque transmitted, kind of lubrication and lubricant type. Those studies showed that reducing gear module used in power transmitter can have a significant influence on efficiency losses. The friction coefficient decreases with increases of lubricating oil, while literature review reported that the overall power efficiency of a power transmitters generally decreased with increasing viscosity of used oil. Most of the previous studies on power transmitter efficiency did not refer to other sources of power losses, especially load independent losses. Various models have been developed to quantify these sources of power loss, as shown in literature (Höhn 2000; Kollmann 2000; Josifović et al. 2010 and Höhn et al. 1996). It was practically proven that losses per one toothed pair, after the period of adaptation using nominal load are about 2 % so it would be expected for it to have the degree of efficiency of 94 % for the examined three grade motor transmitters (Fig. 6).

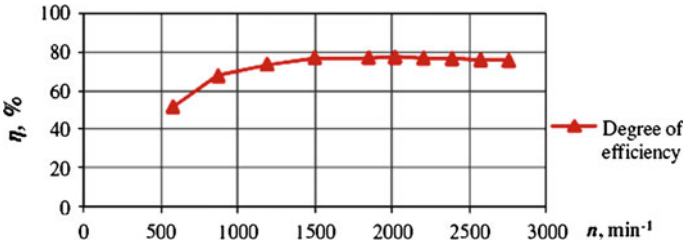

Fig. 6 Degree of efficiency dependence of number of rotations

3 Conclusion

On the basis of the conducted measuring and testing, it was concluded that the examined electromotor power transmitter satisfies the quality criteria as summary result of construction, production and working conditions. The failure of electromotor power transmitter units is directly related to its conceptual design, used production processes and the combination of both static and dynamic loadings. High stresses arise in the elements of power transmitter from both improper sizes of the components, improper gear meshing and impact and from vibrations coming from the system. Arise of noise level and temperature increases are the early signs of failure, so testing methodology must handle these parameters with respect. The electromotor power transmitters' degree of efficiency is important influential factor on the mechanical energy balance therefore it must be determined in real exploitation conditions. The conducted examinations point out the need for standardization of the processes of quality testing of electromotor power transmitter and defining the parameters of safety and reliability of the construction, which could guarantee stable and safe work of electromotor power transmitter in exploitative conditions. Considering the electromotor power transmitters' reliability, its' summary costs, computerization of the design process development of its' testing method must be done.

References

Chase D (2005) The development of an efficiency test methodology for high-speed gearboxes. Ph D thesis, The Ohio State University. (in English)

Davis JR (2005) Gear materials, properties, and manufacture. ASM International, United States of America. (in English)

Höhn BR, Michaelis K, Vollmer T (1996) Thermal rating of gear drives—balance between power loss and heat dissipation. AGMA Technical Paper 96FTM8. (in English)

Höhn BR (2000) Europe trends in transmission development. Tagung Antriebstechnik/ Zahnradgetriebe, TU Dresden. (in German)

Ilić A, Josifović D (2008) Measurement and testing of the electromotor power transmitter working characteristics. In: XII International conference on mechanical engineering, Bratislava, Proceedings of abstracts, pp 7–8. (in English)

Josifović D (2000) Examinations of mechanical constructions. Faculty of mechanical engineering in Kragujevac. (in Serbian)
Josifović D, Ivanović L, Ilić A (2010) Tribological aspects of contemporary gear materials. J Balkan Tribological Assoc 16(4):471–483 (in English)
Kollmann FG (2000) Modern method of noise reduction on gears. Tagung Antriebstechnik/ Zahnradgetriebe, TU Dresden, Vortragsband, pp 560–574. (in German)
Litvin FL, Fuentes A (2004) Gear geometry and applied theory. Cambridge University Press, Cambridge. (in English)
Meltzer G (2000) Innovative methods for the diagnosis of gear systems. Tagung Antriebstechnik/ Zahnradgetriebe, TU Dresden, Vortragsband, pp 525–541. (in German)
Petry-Johnson TT, Kahraman A, Anderson NE, Chase DR (2007) Experimental investigation of spur gear efficiency. In: Proceedings of the ASME 2007 international design engineering technical conferences. (in English)
Rešetov DN (1979) Machine and testing devices for elements testing. Mašinostroenie, Moscow. (in Russian)
Sawhney GS (2009) Mechanical experiments and workshop practice. IK International Publishing House. (in English)
Smith JD (2003) Gear noise and vibration. Marcel Dekker, Cambridge. (in English)
Trbojević M, Janković M, Vukdelija J, Ivković S, Latinović V (1988) Power transmitter. Scientific Book, Belgrade. (in Serbian)

The New Approach for Calculation of Total Mesh Stiffness and Nonlinear Load Distribution for Helical Gears

Miloš Jelić and Ivana Atanasovska

Abstract This paper described a new approach for calculation of mesh teeth stiffness and load distribution for helical gears. The mesh teeth pair stiffness is a parameter that varies both during a teeth pair mesh period and along teeth pair contact line, and can be work out only by simultaneously solving both these tasks. The Finite Element Analysis (FEA) is performed to calculate the gear teeth pair's total deformations and normal load functions in time and along teeth pair contact lines. The specific iteration procedure is used, too. The total mesh stiffness and normal load distribution calculated with this procedure can be used for precise helical gears load capacity calculations and evaluation of nonlinear dynamic model of helical gears motion.

Keywords Helical gears · Stiffness · Load distribution · FEA

List of Symbols

B	Gear facewidth
B	Length of line of contact
C	Tooth stiffness
c'	Average teeth pair stiffness
c_{sp}	Specific tooth stiffness
c_0	Total mesh stiffness
F_{bt}	Normal load in tooth face plane section
$F_{\beta i}$	Mesh initial misalignment
K_i	Ratio between elastic deformation at one particular point on the contact pattern i and unit concentrated load at the same point

M. Jelić (✉) · I. Atanasovska
Institute Kirilo Savić, Belgrade, Serbia
e-mail: milos.jelic@iks.rs

I. Atanasovska
e-mail: iviatanasov@yahoo.com

G. Dobre (ed.), *Power Transmissions*,
Mechanisms and Machine Science 13, DOI: 10.1007/978-94-007-6558-0_52,

M Number of simultaneously meshed teeth pairs
n_i Number of segments on the ith teeth pair contact line
P Contact position
Q Unit normal load
U Tooth elastic deformation
z Coordinate along contact pattern
Δ Total teeth pair deformation in the direction normal to teeth pair contact pattern

1 Introduction

In recent years, the constraints in gear design process are concentrated on lightweight and defined size of gears thus to reach—efficient gear power transmission system. To achieve this objective, it is essential to understand the dynamic behaviour of gears. In general, a pair of gears is simulated with two disks coupled with non-linear mesh stiffness and mesh damping, (Umezawa et al. 1986; Parker et al. 2000). Many authors confirmed this simplified dynamic model and focus their investigation resources on various influence factors (Walha et al. 2011; Atanasovska et al. 2012). Moradi and Salarieh (2012) in their latest paper point out the importance of studying the nonlinear oscillations of gears from aspect of competitive limitations of noise level and vibrations in last decade. However, solution for helical gears oscillations can be obtained only if non-linear functions of stiffness and load are known.

In the literature, the tooth stiffness and mesh stiffness are treated in different ways. In the simpler models, the gear mesh stiffness is assumed to be constant. In last decade, authors overcame this simplification and presented various methods for teeth deformation teeth stiffness and load calculation. Thus, Andersson and Vedmar (2003) determined the dynamic load between two elastic helical gears with excitation from new incoming contacts and calculated the total deformation of contact teeth as sum of numerical calculated (with Finite Element Method) teeth bending deformations and analytical calculated Hertz's teeth contact deformations. But, they neglected influence of load value on contact deformations. The importance of determination of variable contact area in simulation of contact problems in gears is discussed by Ulaga et al. (1999). They presented a new Finite element technique for more accurate contact stress predictions, while Pedrero et al. (2007, 2011) described minimum elastic potential criterion as method for calculation of load distribution in involute gears mesh. But they still used Hertz's formulae for contact in one point and neglected influence of load value. This is not appropriate calculation methods for teeth total deformations, because contact deformation depends of the magnitude of load and must be determined through iterative procedure (Atanasovska et al. 2010).

In two new series of papers, Li (2007, 2008) and Atanasovska and Nikolić (2007b; Atanasovska et al. 2008, 2010) have been confirmed the Finite Element Method (FEM) as out of competition method for investigations of deformations and load distribution for spur gears. Pimsarn and Kazerounian (2002) present comparative analysis that give one more confirmation for FEM usage in evaluation of spur gear tooth mesh load.

The main objective of this paper is to present a method to determine the load in a helical gear pair considering the actual positions of the contacts and the actual deformations of the gear teeth. With this method, the transient loading and unloading is avoided. In the presented analysis, the positions of the contacts and the actual deformations of the gear teeth can be determined. This analysis is carried out each time the contact force changes, i.e., in every time increment in the dynamic simulation process and give quasi-static analysis of helical gears motion. The obtained deformations are then used to determine the mesh stiffness and load distribution between the meshed teeth pairs.

2 Theoretical Considerations

2.1 Teeth Stiffness and Mesh Stiffness

In general, stiffness is the force that causes unit deformation. There are different variables that describe stiffness for helical gears. In this paper, the few of them are used. The tooth stiffness for helical gears can be defined as ratio of differential of unit normal load in tooth face plane section $d(F_{bt}/b)$ and appropriate elastic deformation:

$$c = \frac{d(F_{bt}/b)}{du} \tag{1}$$

The tooth stiffness depends of many influence factors (gears geometry, load value, material characteristics etc.) and varies along length of action, as well as along line of contact of a teeth pair. Determination of tooth stiffness function is very important point in helical gears investigations. The complex helical gears geometry and variable length and position of teeth contact lines during mesh period require complex study of teeth contact. During meshing period for helical gears lines of contact are not parallel to gears axis. Therefore, teeth pairs coming in mesh gradually. Contact starts at pinion tooth root on one face of gears and propagates through face width towards pinion tooth top on another face of gears. This leads to continuously changing of contact line length and makes load distribution calculation very complex. Zone of action (contact zone) for involute parallel-axis gears with helical teeth is the rectangular area in the plane of action bounded by the length of action and the effective face width, Fig. 1.

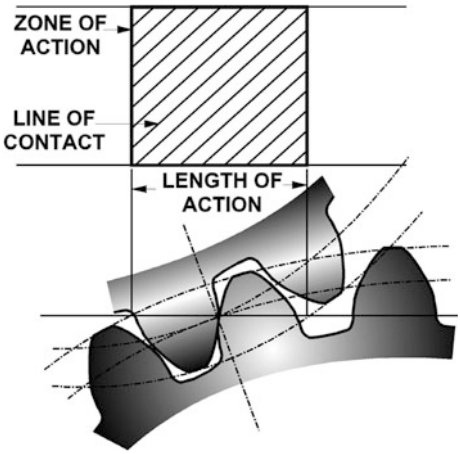

Fig. 1 Zone of action for involute parallel-axis gears with helical teeth

The tooth stiffness at each point of line of teeth pair contact is called **specific tooth stiffness** and can be obtained as ratio of unit load and tooth deformation for any specific point:

$$c_{sp} = q/u \tag{2}$$

For calculation of unit stiffness for *i*th teeth pair (when *m* teeth pair are simultaneously in contact), contact is simulated with serially connected springs, which is in accordance with contact modelling in mechanics. So, the **specific teeth pair stiffness** for any contact point when unit specific tooth stiffness for pinion tooth c_{sp1}, and wheel tooth c_{sp2} are known has following form:

$$c_{sp(i)} = \frac{c_{sp1} \cdot c_{sp2}}{c_{sp1} + c_{sp2}} \tag{3}$$

In many theoretical calculations, the assumption of constant teeth stiffness along line of contact exists. The **average teeth pair stiffness** along line of contact is used as constant teeth stiffness and for helical gears can be calculated for every of *m* teeth pair in contact as average value of specific teeth pair stiffness along line of contact:

$$c' = \overline{q/u} \tag{4}$$

The previous mentioned dynamic models of helical gears motion (Walha et al. 2011; Atanasovska et al. 2012), use simplified stiffness variable called **total mesh stiffness c_0** that is sum of total teeth pair stiffness for all simultaneously meshed teeth pairs. For involute helical gears, that means:

$$\begin{aligned} c_0 &= \sum (c_i' \cdot B_i),\ i = 1,2 \ \text{ for two teeth pair in contact} \\ c_0 &= \sum (c_i' \cdot B_i),\ i = 1,2,3 \ \text{ for three teeth pair in contact} \end{aligned} \tag{5}$$

where: c_i' is average teeth pair stiffness for ith teeth pair in contact and B_i is length of line of contact for ith teeth pair.

2.2 Analytical Model for Load Distribution

The load distribution is more complex task for involute cylindrical gears with helical teeth in comparison with the same task for the involute straight spur gears, and could not been solved with procedures published so far. Lines of teeth contact for helical gears are inclined and are not parallel with gear axis of rotation and length of contact line varies along length of contact, Fig. 1. Also, for one particular contact position contact points lie on different radius and have different deformations and stiffness. The nonlinear load distribution in helical gear mesh could be solved only by resolving the load distribution between simultaneously meshed teeth pairs and the load distribution along each of teeth pair contact line, at the same time. In this paper, for analytical definition of load distribution in helical gear mesh, the expanded procedure for load distribution over gear facewidth for involute spur gear have been used (Atanasovska and Nikolic 2006).

For every moment (contact position P) during helical gears mesh m tooth pairs are simultaneously in contact. System of integral equations, which consists of the contact equation and balance equation, can be defined for each ith of m simultaneously meshed teeth pairs for the contact position. This system can be presented in the following form:

$$\int_0^{B_i} q_i(z) \cdot K_i(z,u)dz = \Delta_i + F_{\beta i}(z); \quad \int_0^{B_i} q_i(z)dz = F_{bti} \tag{6}$$

where: $q_i(z)$—is function of unit load change along the ith teeth pair contact line, B_i—is length of ith teeth pair contact line for position P, $K_i(z,u)$—is influence function, which defines relation between u (elastic deformation at one particular point on the contact pattern) and $q_i(z)dz$ (unit concentrated load at the same point), z—is coordinate of studied point along contact pattern, Δ_i—is total teeth pair deformation in the direction normal to teeth pair contact pattern, $F_{\beta i}(z)$—is mesh initial misalignment (deviation between pinion tooth face width direction and wheel tooth face width direction when the gear pair is unloaded), F_{bti}—is total normal load value for ith teeth pair in mesh. Systems of Eq. (6) for all m simultaneously meshed tooth pairs and equation of load balance

$$F_{bt1} + F_{bt2} + \ldots + F_{btm} = F_{bt} \tag{7}$$

yield the $(2m + 1)$ equation system for load distribution solution. It's very hard or almost impossible to determine real values for many factors and variables that have crucial influence on accurate form of the function $q_i(z)$, as well as on value of

real teeth pair bearing pattern length B_i. Therefore, this equation system can be solved only by numerical methods with same simplification and assumptions.

The discrete method is a simplification model chosen for solving the load distribution in gear mesh, (Atanasovska and Nikolic 2007b). The main principle of this method defines teeth pairs contact lines like finale number of equal segments. A length of these segments is nearly a value of gear pair module and the n_i is the number of segments on the ith teeth pair contact line, so the Eq. (7) takes the following form:

$$\sum_{i=1}^{m} \sum_{j=1}^{n_i} q_{ij} \cdot B_{ij} = F_{bn} \tag{8}$$

where q_{ij}—is normal unit load along the jth segment of ith teeth pair contact line; B_{ij}—is length of the contact line segment. The numerical Finite Element Method is used for calculation of these values. In this way the nonlinear load distribution in helical gears mesh can be solved with some assumptions and simplifications: only normal load acts on teeth flanks, friction is neglected, deformations of shafts and bearings are neglected and the initial misalignment is neglected in the first step of the load distribution calculation.

3 Results and Discusion

3.1 Finite Element Analysis

The precise calculation of helical gear teeth deformations can be carried out by three-dimensional Finite Element Model (FEM) only. To develop such a model, authors defined the procedure of numerical calculations (Atanasovska et al. 2009). The commercial software Ansys 11.0 has been used. With the analysis of different models, and with emphasize on balance between accuracy and FEM calculation time, the physical models of gear segments with three teeth were adopted. The verification of FEM models is performed by strain gauges experiment on the tooth root and analytical contact stress calculation, and explained in paper Atanasovska et al. 2007a.

3D iso-parametric structural solid element defined by eight points (for 3D gear modelling) and 3D point to surface contact element (for teeth contact modelling) are used for 3D FEM helical gear pair model developing. Quasi static numerical model of helical gears are chosen for Finite Element Analysis (FEA). For every simulated contact position P two models are developed: one for the pinion, Fig. 2a and second for the wheel, sl.2.b. Figure 2 shows models for one particular contact position through period with three teeth pairs in contact. Results of FEA for this contact position are shown in Figs. 3 and 4. Figure 3 is the contour plot of deformation vector for pinion and for wheel, and Fig. 4 shows the reaction forces

in teeth contacts (normal load distribution). Such results are obtained for all modelled contact position and total deformations of pinion teeth and wheel teeth are read from them. Also, the distribution of normal load is obtained for all modelled contact line positions. The obtained results are then used for determination of mesh stiffness and load distribution in accordance with procedure explained in following chapter.

3.2 Calculation of Mesh Stiffness and Load Distribution

The appropriate investigations (Atanasovska et al. 2010) showed that gear teeth stiffness and load distribution in mesh depend on the magnitude of normal contact load. So, the iteration procedure is used for determination of teeth pair stiffness and load distribution. In the first step (iteration), total normal load for each teeth pair contact position is divided on simultaneously meshed teeth pairs in proportion of appropriate length of teeth pair contact lines, which are scanned from FEM model. After nonlinear FEA calculation, specific teeth pair stiffness of every *j*th segment on *i*th line of contact is calculated:

$$c_{ij} = \frac{F_{ij}}{u'_{ij} \cdot B_{ij}} \tag{9}$$

Total teeth pair deformation on *j*th segment of *i*th line of contact u_{ij}', length of *j*th segment on *i*th line of contact—B_{ij} and total contact force (sum of all reactions) on *j*th segment of *i*th line of contact—F_{ij} are scanned from FEA results. Then

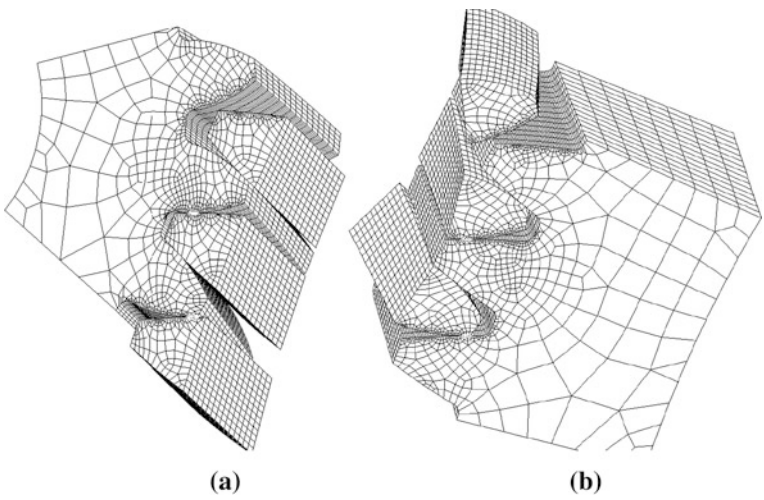

Fig. 2 FEM models for pinion and wheel

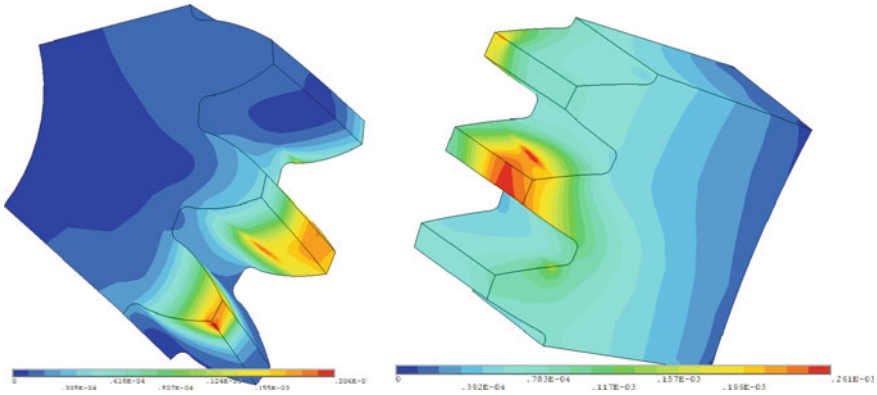

Fig. 3 Contour plot of deformation vectors for the pinion and the wheel

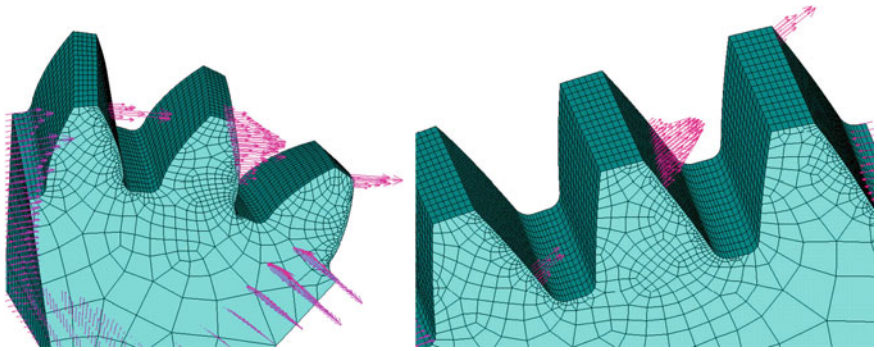

Fig. 4 Contact forces on the pinion tooth and the wheel tooth

average teeth pair stiffness for all lines of contact and total mesh stiffness for all calculated contact positions P in zone of action could be calculated.

For any next iteration normal load is divided on teeth pairs in mesh following the fact that continuous contact is possible only when total teeth deformations in contact point of all teeth pairs in contact in direction of normal load are equal. The equations for calculation of normal loads on m meshed teeth pairs for next iteration have following form:

$$F_{bti} = \frac{c_i' \cdot F_{bt}}{\sum_{i=1}^{m} (c_i' \cdot B_i)} \cdot B_i, \; i = 1, m \tag{10}$$

The final results for the modelled gear pair are given in diagrams in Fig. 5.

The total mesh stiffness and normal load distribution calculated with this procedure can be used for helical gears load capacity calculations and for modelling of nonlinear dynamic behaviour of helical gears.

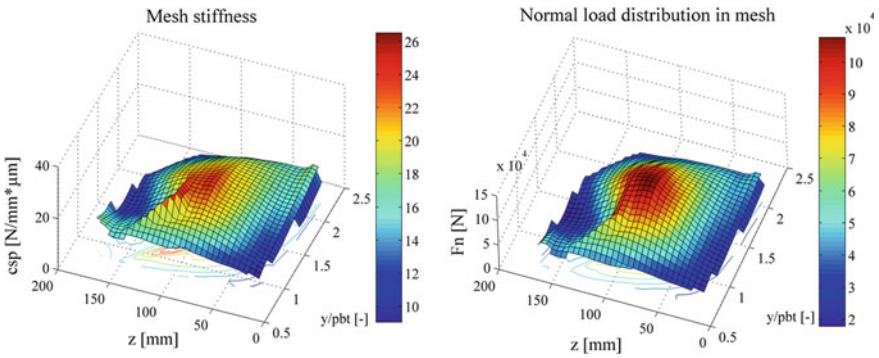

Fig. 5 Specific teeth pair stiffness and normal load distribution in zone of action

4 Conclusion

A new approach for calculation of mesh teeth stiffness and load distribution for helical gears takes in consideration real gear teeth contact without usage of traditional Hertz's solution for two cylinders in contact. The tooth deformation and mesh teeth pair stiffness are calculated in time and along contact lines at the same time. Helical gears transfer load with low noise and wear compare with spur gears. In coming years, efficiency will be one of the most important reasons for gear power transmission systems design and the application of helical gears will be increased. The research presented in this paper can help to gear researchers and green engineers to calculate helical gears with optimal parameters. The goal is to obtain gears with high level of both reliability and efficiency. In addition, the improved calculations of helical gears dynamics may lead to decrease of transmission systems vibrations and their longer life cycles.

Acknowledgments The work has been funded by the Ministry of Education and Science of Republic of Serbia Grant OI 174001 Dynamics of hybrid systems with complex structures. Mechanics of materials.

References

Andersson A, Vedmar L (2003) A dynamic model to determine vibrations in involute helical gears. J Sound Vibr 260:195–212

Atanasovska I, Nikolić V (2006) Developing of the 3D gear pair model for load distribution monitoring. In: Proceedings of 2nd international conference "Power Transmissions 2006", N. Sad, 25-26.04.2006 pp 45–50

Atanasovska I et al (2007a) Developing of gear FEM model for nonlinear contact analysis. In: Proceedings of 1st international congress of Serbian society of mechanics, pp 695–703

Atanasovska I, Nikolić V (2007) 3D spur gear FEM model for the numerical calculation of face load factor. Sci J Facta Univer Series Mech Autom Control Rob 6(1):131–143

Atanasovska I et al (2008) The methodology for helical gear teeth profile optimization. In: Proceedings of KOD 2008, pp 73–76

Atanasovska I et al (2009) Finite element model for stress analysis and nonlinear contact analysis of helical gears. Sci Tech Rev 59(1):61–69

Atanasovska I et al (2010). Analysis of the nominal load effects on gear load capacity using the finite element method. Proc Inst Mech Eng Part C J Mech Eng Sci 224(11):2539–2548

Atanasovska I, Vuksic-Popovic M, Starcevic Z (2012) The dynamic behaviour of gears with high transmission ratio. Int J Traffic Transp Eng (in press) http://www.ijtte.com/article/100/Papers_Accepted_for_Publication.html

Li S (2007) Finite element analyses for contact strength and bending strength of a pair of spur gears with machining errors, assembly errors and tooth modifications. Mech Mach Theory 42:88–114

Li S (2008) Effect of addendum on contact strength, bending strength and basic performance parameters of a pair of spur gears. Mech Mach Theory 43:1557–1584

Moradi H, Salarieh H (2012) Analysis of nonlinear oscillations in spur gear pairs with approximated modelling of backlash nonlinearity. Mech Mach Theory 51:14–31

Parker RG et al (2000) Non-linear dynamic response of a spur gear pair: modelling and experimental comparisons. J Sound Vib 237(3):435–455

Pedrero JI, Pleguezuelos M, Aguiriano S (2007) Load distribution model of minimum elastic potential for involute internal gears. Mach Des 245–250

Pedrero JI, Pleguezuelos M, Muñoz M (2011) Contact stress calculation of undercut spur and helical gear teeth. Mech Mach Theory 46:1633–1646

Pimsarn M, Kazerounian K (2002) Efficient evaluation of spur gear tooth mesh load using pseudo-interference stiffness estimation method. Mech Mach Theory 37:769–786

Ulaga S, Ulbin M, Flasker J (1999) Contact problems of gears using overhauser splines. Int J Mech Sci 41:385–395

Umezawa K, Suzuki T, Sato T (1986) Vibration of power transmission helical gears (approximate equation of tooth stiffness). Bull JSME 29:1605–1611

Walha L et al (2011) Effects of eccentricity defect on the nonlinear dynamic behavior of the mechanism clutch-helical two stage gear. Mech Mach Theory 46:986–997

Part V
Maintenance, Operating and Industrial Applications

The Influence of Corrosion on Stress Concentration Factor at Shaft to Flange Radius

Ivana Atanasovska, Miloš Jelić, Radivoje Mitrović and Dejan Momčilović

Abstract This paper describes the influence of corrosion on stress concentration factor and crack initiation at shaft-flange transition section. The real turbine shaft failure case study is used for research. This case study and numerical calculations show that the seal box solution led to constant leakage of river water in the zone of critical radius and resulted in corrosion fatigue cracks and turbine shaft failure. Thus, the Finite Element Analysis is performed to calculate the stress concentration factor increase as a result of corrosion occurrence. The corrosion at shaft-flange transition section is modelled in the zone with maximum stresses with a corrosion pit dimensioned to comply with real in situ dimension of pits. The presented research points new trends in stress concentration factor calculation. The obtained numerical results for maximum stress and stress concentration factor in critical zone confirmed failure analysis study outcome.

Keywords Stress concentration · Shafts · Corrosion · FEA

List of Symbols

d	Smaller shaft diameter
D	Larger shaft diameter
E	Young modulus of elasticity
F_a	Axial hydraulic force
G	Runner's weight

I. Atanasovska (✉) · M. Jelić
Institute "Kirilo Savić", Belgrade, Serbia
e-mail: iviatanasov@yahoo.com

M. Jelić
e-mail: milos.jelic@iks.rs

R. Mitrović
Faculty of Mechanical Engineering, Belgrade, Serbia

D. Momčilović
Institute for Material Testing, Belgrade, Serbia

G. Dobre (ed.), *Power Transmissions*,
Mechanisms and Machine Science 13, DOI: 10.1007/978-94-007-6558-0_53,

K_t	Stress concentration factor
M_t	Torque on the runner
q	Pressure in servomotor
r	Fillet radius
R_e	Yield strength
x, y, z	Axis of coordinate system
v	Poisson's rate
σ_{eqv}	Von Mises's equivalent stress
σ_{max}	Maximum stress for actual loads
σ_{nom}	Reference normal stress for machine parts without geometry modifications
σ_M	Tensile strength
σ_{Df}	Fatigue strength.

1 Introduction

Common parts of mechanical systems are shafts and axles and any damage on them may lead to systems failure. The most frequent causes of damage and fracture of shaft or axle are incorrect design or operation in chemical aggressive environment. Incorrect design may lead to low load capacity of shafts and may cause stress concentration exceeding material strength characteristics, especially in case of high cycle loading. Usual stress concentration zones on shafts are results of shoulder fillets and transition zones on shaft to flange joint. Stress concentration factor (SCF) is defined by Peterson and has been published in mechanical-design textbooks and handbooks ever since its original appearance in 1953. Its main goal is to determinate the influence of different fillets shapes on stress on shafts under real load conditions. SCFs are defined and published in form of formulae and graphs help to designers. However, in recent years many authors have raised the question of misalignments of Peterson's Stress Concentration Factors for the purpose of precise and detail shaft calculations. Such trend is increasing due to high efficiency requirements in modern technologies.

The initiation of the fatigue process for shafts starts at the location of geometrical or structural discontinuities, secondary phases, voids, making flaws and dimension variation of the machine part. These areas may act like stress concentrators that lead to local plastic deformation. Under corrosion conditions, this kind of non-homogeneities and discontinuities appear more frequent on material surface as a result of corrosion processes, amplified by static or variable mechanical loads. This leads to the so-called damage by corrosion under stress and corrosion fatigue. This paper presents results for a failure of the shaft with flange, subjected to design and corrosion protection issues. The selected shaft is a real horizontal hydro turbine shaft with significant radius change at transition zone from shaft to runner flange.

2 Theory of Stress Concentration Factor

The elementary stress formulas used in the design of structural members are based on the simplified geometry with a constant section or a section with gradual change of contour. Such conditions, however, are hardly ever attained throughout the highly stressed region of actual machine parts. The shoulders, grooves, holes, keyways, threads, etc., result in modifications of the simple stress distributions and localized high stresses occur. The localization of high stress is known as stress concentration, measured by the stress concentration factor.

The stress concentration factor K_t can be defined as the ratio of the peak stress in the zone with modifications to the nominal stress:

$$K_t = \frac{\sigma_{\max}}{\sigma_{nom}} \tag{1}$$

The long-held engineering practice uses standard analytical methods and Peterson's stress concentration factors (SCFs). Peterson's stress concentration factors (Pilkey and Pilkey 2008) are aimed for shafts with standard dimensions and may be accepted as rough engineering estimate. The analytical tools available at the time when Peterson compiled his stress-concentration factors made him to ground his calculations for shoulder fillets on solutions for similar geometries, instead of directly computing the stress state. Peterson formed a series of curves for K_t as a function of fillet radius—r, over the smaller shaft diameter—d. Curves represent different ratio of the larger shaft diameter, D, to d. The solution is only applicable over limited ranges of r/d. Peterson developed a separate set of curves for each loading scenario: bending, tension, and torsion.

Theoretical expressions for stress concentration factors for shoulder fillets in round and flat bars subject to various loads are developed by Noda et al. (1997). However, their flat-plate fillet solution was not translated into a 3D round shaft and could not include all contemporary shaft designs today. Modern analytical techniques can provide a more accurate solution. In fact, the edition of Peterson's Stress Concentration Factors by Pilkey and Pilkey (2008) cites work that used Finite Element Analysis (FEA) to overcome many of the inaccuracies of the previous method. With the FEA, designers could use numerical equations to calculate SCFs instead of relying on Peterson's curves and tables. But, they still needed a separate design equation for each loading mode (Tipton et al. 1997). Researchers made efforts to develop a simpler design equation that would cover all loading regimes. The question arises whether it is preferential to calculate stresses for every external load separately (Tipton et al. 1997) or for complex loads at once (Djordjevic et al. 1996). Different authors acquired no agreement on this issue. For SCFs and maximum stress calculation of non-standard shafts that required a high level of energy efficiency, and at the same time high level of reliability and safety, the calculations under complex loads at once appear to be more accurate.

3 FEA for the Shaft with Flange

3.1 Finite Element Model

During failure analysis case study, it is very important to properly identify the reference stress and the stress concentration factor of interest. Stress concentration factors can be obtained analytically from the elasticity theory, either computationally from the Finite Element Method, or experimentally. The recommended tabular value for the geometrical stress concentration factor for the described hollow shaft with flange in complex loading conditions is not available. Therefore, Finite Element Model described by Atanasovska et al. (2010) is used for identification of nominal and maximum stresses for calculation of stress concentration factor of shaft-flange transition zone. Due to complex loading conditions, stress concentration factor has been calculated from the intensities of equivalent stresses. Before expiration of the guarantied working period, crack appeared on shaft-flange radius (Momčilović et al. 2012). The shaft material is steel 20GSL with: Young modulus of elasticity $E = 2.04 \times 10^5$ MPa; Poisson's rate $v = 0.3$; yield strength $R_e = 310$ MPa; tensile strength $\sigma_M = 509$ MPa; fatigue strength $\sigma_{Df} = 225$ MPa (on air) and $\sigma_{Df} = 140$ MPa (in water), (Momčilović et al. 2012). It is necessary to emphasise that the mechanical properties obtained by testing exhibit significant scatter which implies that microstructure have increased inhomogeneity.

The original turbine shaft geometry with transition radius $r = 80$ mm in crack zone is simulated on the FEM model, Fig. 1. Figure 1 presents the 3D finite element model of analyzed shaft with flange, made with continuum discretized by the 3D structural solid defined by 8 nodes that had three degrees of freedom at each node (translations in the nodal x, y and z directions). The FEM model has 59,120 nodes and 47,547 elements. The boundary conditions and external loads are defined on FEM model as shown on Fig. 1 (Atanasovska et al. 2010).

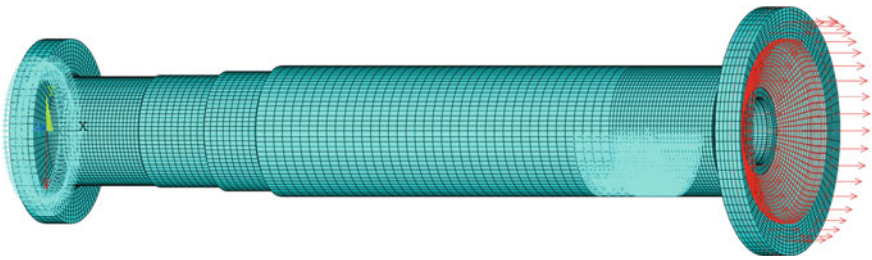

Fig. 1 Finite element model for only tension

3.2 Finite Element Analysis

For Finite Element Analysis (FEA), the load conditions were taken from the original shaft manufacturer's documentation. The numerical calculations are performed for two main load cases: regime during starting (LC1), regular operation regime (LC2). Through separate investigation of three more load cases: only bending from shaft's and runner's weight (LC3), only torsion from runner torque moment (LC4) and only tension from axial hydraulic force during starting regime (LC5), and results comparison, conclusions about decisive influence of tension on damages occurrence is obtained (Atanasovska et al. 2011).

Load case 1 corresponds to the static load during start of operation and change of the operating runner's blades position and it is defined by: the maximum axial hydraulic force of $F_a = 5{,}542.65 \times 10^3$ N, pressure in servomotor $q = 40$ bar, own shaft's weight, runner's weight of $G = 1 \times 10^6$ N and the torque on the runner of $M_t = 4{,}280.5935 \times 10^3$ Nm. The total axial hydraulic force F_a is simulated by the forces in axial direction at points of connecting the shaft flange to the runner. The pressure in servomotor is simulated by surface pressure inside of flange. The shaft weight was simulated by gravitational acceleration. Load case 2 corresponds to the dynamic, time-variable load in the course of normal operating regime and it is defined by: axial hydraulic force of $F_a = 392.4 \times 10^3$ N, own shaft's weight, runner's weight of $G = 1 \times 10^6$ N and the torque on the runner of $M_t = 4{,}280.5935 \times 10^3$ Nm, defined in the some way as for load case 1. The Finite Element Analysis (FEA) of analyzed turbine shaft was performed for all defined load cases. The obtained numerical results for maximum stresses in shaft to flange transition zone are shown in Table 1. For tension load (load case 5), nominal stress $\sigma_{eqv\text{-}nom} = 5$ MPa and maximum stress $\sigma_{eqv\text{-}max} = 38.5$ MPa can be read from numerical results, Fig. 2.

3.3 Shaft Failure Analysis Conclusions

Grounded on the finite element analysis for the turbine shaft described in the paper, it may be concluded that the extreme stress concentration occurs in the failure zone of shaft-flange radius. This fact confirms that the finite element model

Table 1 Maximum von Mises's stresses and stress concentration factors for variable transition radius

	FEA $\sigma_{eqv(70)}$ (MPa)	FEA $K_{t(70)}$ (/)	FEA $\sigma_{eqv(80)}$ (MPa)	FEA $K_{t(80)}$ (/)	Peterson K_t
LC1	136	4.25	127	3.97	/
LC2	58.8	2.1	57.6	2.057	/
LC3	44.8	2.97	41.6	2.75	2.1
LC4	36.2	1.54	35.5	1.52	/
LC5	41.5	8.3	38.5	7.7	2.24

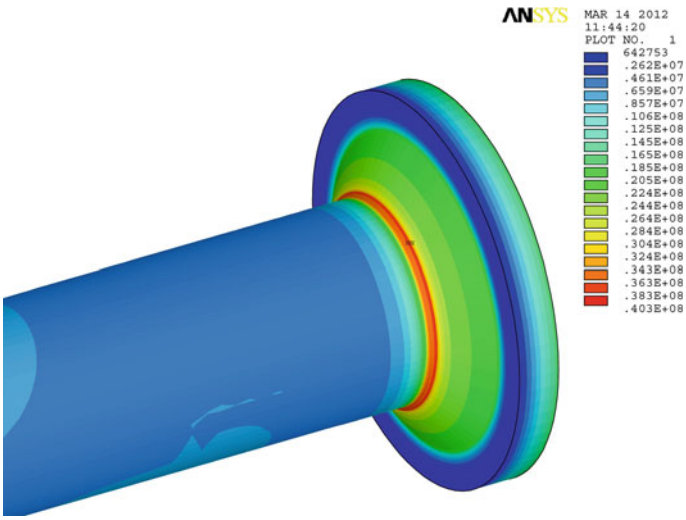

Fig. 2 VM equivalent stresses for tension (LC5), in Pa

of shaft with flange is developed in accordance with real working conditions. Obtained tension normal stress amplitude in critical radius during regular operation regime is under fatigue strength and doesn't create conditions for initial crack. Also, stress concentration factor obtained from finite element results and nominal stress calculation has a value in expected range. The maximum equivalent stresses in critical shaft-flange transition zone obtained by FEA and presented in previous paper don't exceed tensile strength of $\sigma_M = 509$ MPa for load regime during starting turbine (maximum static load), as well as fatigue strength of $\sigma_{Df} = 225$ (140) MPa for regular operation regime (dynamic cycling loading).

In conclusion, the analyzed shaft has construction in accordance with required conditions and therefore the cause for crack appearance has to be found in material characteristics or working conditions and maintenance, Atanasovska et al. 2010. The detailed research of the failure analysis case study and numerical calculations shows that the seal box solution led to constant leakage of river water in zone of critical radius which resulted in corrosion fatigue cracks and turbine shaft major failure (Momčilović et al. 2012).

4 FEA for the Shaft with Cracks

4.1 Corrosion Damages

Simultaneously with this failure analysis, the non-destructive testing of other turbine shafts of the same type revealed numerous cracks, Fig. 3. The cracks were found in zone of the same width as obtained by Finite element calculation for the

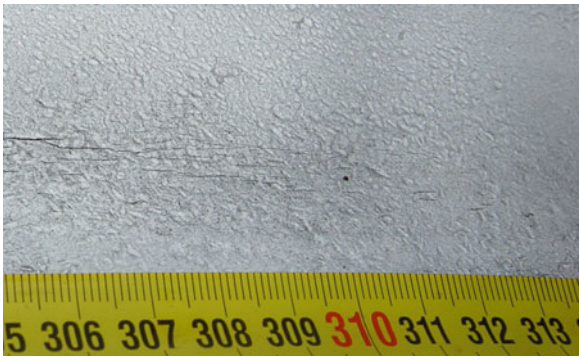

Fig. 3 Corrosion cracks at shaft to flange radius

load case 2. The pattern of the cracks at the metal surface and the presence of the one major crack accounting for failure indicate corrosion fatigue as the cause of the failure (Momčilović et al. 2012).

Thus, the Finite Element Analysis is performed to calculate the change of stress concentration factor at shaft-to-flange radius as a result of corrosion occurrence. Non-uniform corrosion and formation of pits, as a result of microstructure inhomogeneity is evident on Fig. 3, too.

4.2 FEA and SCF for the Shaft with Damages

In recent years, new commercial FEA software provide to researchers an improved tool for create the finite element mesh that may continuously change from course to very fine. Thus, stress distribution at the corrosion pits could be investigated by FEA very successfully and precise. Cerit et al. 2009 and Turnbull et al. 2009, chose FEA for calculations of stress distribution at the corrosion pits and for calculations of SCFs. The tension loading is subject of interest in research of Cerit et al. 2009, as well as in research presented in this paper.

For particular turbine shaft, the corrosion at shaft-flange transition section is modelled with a corrosion crack dimensioned to comply with real cracks dimension, Fig. 3 and theoretical papers (Turnbull et al. 2009). The crack form by hemisphere with radius of 300 μm is modelled in the zone with maximum stresses Fig. 4.

The load case with only tension from axial hydraulic force during starting regime (LC5) is investigated by FEA with corrosion crack simulated. The obtained numerical results for stress state in critical zone shows maximum Von Mises equivalent stress of $\sigma_{eqv\text{-}max} = 230$ MPa, Fig. 5. Then, the stress concentration factor for corrosion crack may be calculated as the ratio of maximum stress with crack occurrences and maximum stress at the same position on transition zone without cracks: $K_t = 5.97$.

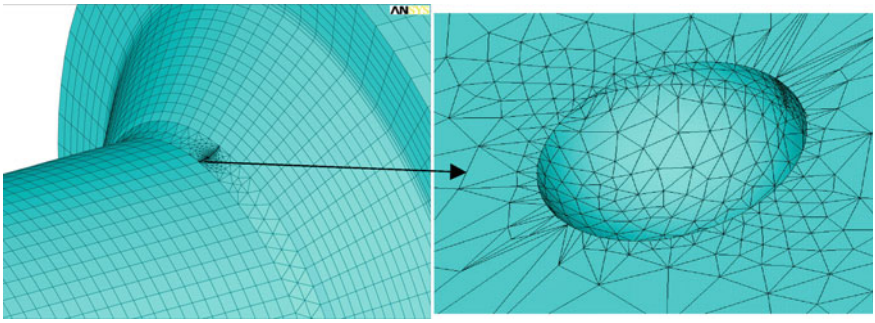

Fig. 4 Finite element model for hydraulic turbine shaft with a corrosion crack of $r = 300$ μm

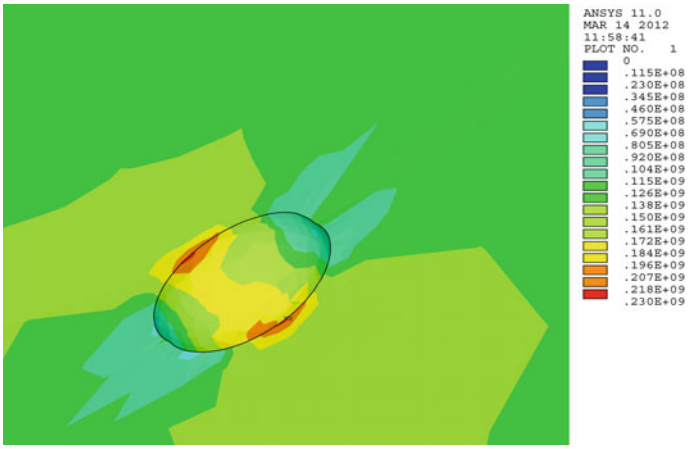

Fig. 5 Equivalent stresses in the zone of corrosion crack

5 Discussion and Conclusions

For the other turbine shafts of the same type having numerous cracks, the cracks were found in the zone of maximum stresses obtained by Finite element calculation. Then, the research of shaft-flange transition section influence on stress concentration factor has been performed (Atanasovska et al. 2011) to determine the best repair procedure for damaged shafts in order to increase their working life. The numerical calculations were performed for real shaft transition radius $r = 80$ mm and also for radii of 70 mm, that could be real shaft to flange transition radius after removal the surface zone with cracks. Figure 6 shows the comparative results for von Mises equivalent stresses for tension from axial hydraulic force during starting regime (LC5) and Table 1 shows comparative results for maximum von Mises's (VM) stresses and stress concentration factors for variable transition radius (70 and 80 mm) for all load cases in calculation.

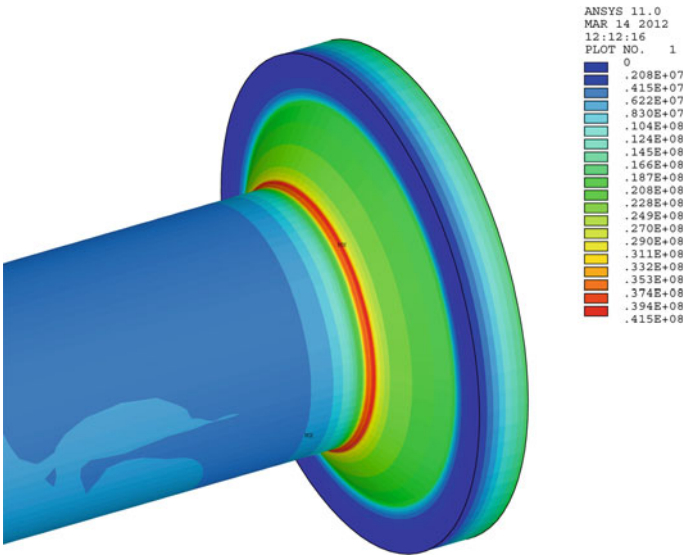

Fig. 6 VM equivalent stresses for tension (LC5), in Pa, for $r = 70$ mm

It is obvious that cutting the zone with cracks in depth of 10 mm does not influence load capacity of turbine shafts and may be recommended as the best and the most expensive solution for damage shafts repair before they are replaced. Similar results and conclusions are obtained by Bordeasu et al. (2009), but this group of authors used entirely fracture mechanic approach. The numerical Finite Element Analysis is performed for the simulation of shaft stress state under real conditions of complex load and shaft to flange radius without damages. The comparisons between stress concentration factors and stress states obtained by Finite Element Analysis and analytical stress calculations that used the Peterson's elastic stress concentration factor charts for conventional values of fillet shaft's transition radii led to conclusion that analytical approach was not suitable for calculation of load capacity of such turbine shaft with flange (Atanasovska et al. 2011). The presented research points out the new trend in stress concentration factor calculation. This procedure is particularly suitable and important for machine parts with non-standard geometry and specific operating conditions.

Acknowledgments The work has been funded by the Ministry of Education and Science of Republic of Serbia, Grant TR 35029: Development of the methodology for working capacity, reliability and energy efficiency improvement of energetic mechanical systems.

References

Atanasovska I, Mitrović R, Momčilović D (2010) FEM model for calculation of hydro turbine shaft. Proceedings of the sixth international symposium KOD 2010, Palić, Serbia, pp 183–188

Atanasovska I, Mitrović R, Momčilović D (2011) Influence of transition section of shaft with flange on stress concentration factor. The 7th international scientific conference research and development of mechanical elements and systems, April 2011. Zlatibor, Serbia, pp 213–218

Bordeasu I, Popovicu MO, Marsavina L (2009) Numerical simulation of fatigue cracks initiation and propagation for horizontal axial turbine shafts. Book series: annals of DAAAM proceedings, vol 20. pp 407–408

Cerit M, Genel K, Eksi S (2009) Numerical investigation on stress concentration of corrosion pit. Eng Fail Anal 16:2467–2472

Djordjevic Z, Nikolic V, Atanasovska I (1996) Finite element analysis of deformation and stress state of hollow shaft. IX simposium MVM, Kragujevac, Serbia, pp 156–159

Momčilović D et al (2012) Failure analysis of hydraulic turbine shaft. Engineering failure analysis, March 2012, vol 20. Elsevier, pp 54–66

Noda N-A, Takase Y, Monda K (1997) Stress concentration factors for shoulder fillets in round and flat bars under various loads. Int J Fatigue 19(1):75–84

Pilkey WD, Pilkey DF (2008) Peterson's stress concentration factors, Wiley, Inc

Tipton SM, Sorem JR, Rolovic RD (1997) Updated stress concentration factors for filleted shafts in bending and tension. J Mech Des Trans ASME 118:321–327

Turnbull A, Horner DA, Connolly BJ (2009) Challenges in modelling the evolution of stress corrosion cracks from pits. Eng Fract Mech 76:633–640

Noncircular Planetary Gears Applied to Scissors

Alexandru Pozdîrcă

Abstract The article presents the calculus of a noncircular planetary gear applied to scissors for cutting hard materials (metal plates, branches). The advantage of using the presented mechanism consists in the reduction of the necessary effort for cutting and the equal distribution of the effort during cutting. We have in view that for different openings of a person's arms, the capacity to develop force is not constant and that in cutting the resisting moment is modified by alteration of the size of the cut section and its position to the edge articulations. Starting from the zero order transmission function, the centrodes are calculated as well as the conjugate curves of the gears. The limits of nonundercuttings are also highlighted. For the calculus and representation of the gears AutoLISP programs were written, with graphic representation in AutoCAD.

Keywords Planetary gears · Noncircular gears · Scissor · Cutting

1 Introduction

Let there be a sketch of a scissors, as a mechanism made of the following three elements (Fig. 1):

- Element 0, considered fixed, on which there is a toothed area represented through centrode (C_0); on this element is the cutting edge (T_0).
- Element 1, articulated in O_0 to element 0 and in O_2 to element 2; to this the second edge of the blade is fixed, noted (T_1).
- Element 2, on which there is a toothed sector represented through centrode (C_2); this element is the mobile arm of the cutting scissors.

A. Pozdîrcă (✉)
Petru Maior University of Tîrgu Mureş, Tîrgu Mureş, Romania
e-mail: alexandru.pozdirca@yahoo.com

G. Dobre (ed.), *Power Transmissions*,
Mechanisms and Machine Science 13, DOI: 10.1007/978-94-007-6558-0_54,

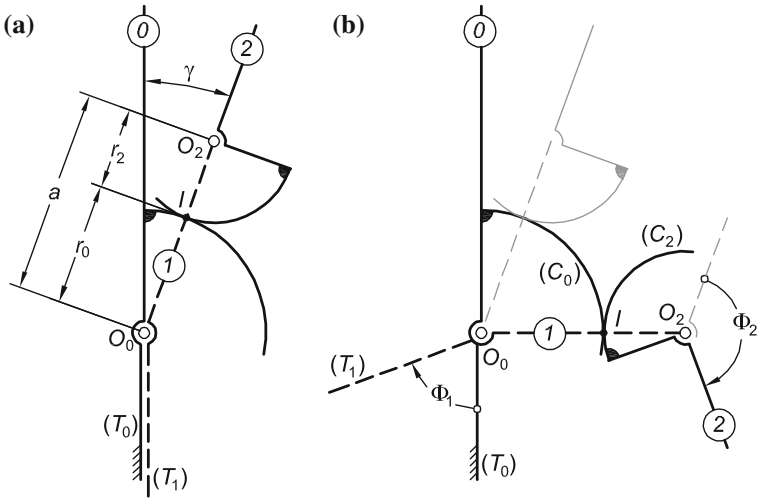

Fig. 1 The mechanism of a scissor and his geometrical parameters: **a**, **b**

This mechanism is a planetary one with gears, capable of multiplying the force. This is supposed to work as a reductor whose gear ratio is marked T.

Figure 1a, b represent this mechanism in initial position, respectively displaced. The initial position is considered to correspond to a closed scissors. The initial data of this mechanism are:

- Distance between joints O_0 and O_2, noted with a;
- Angle γ between elements 0 and 2 for initial position—scissors are closed;
- Maximum opening of arms 0 and 1, noted with Φ_2, as well as the corresponding opening of the edges (T_0) and (T_1), noted with Φ_1.

Mark φ_1 the angle of rotation of element 1 around the fixed joint O_0 and φ_2 the angle of rotation of element 2 around the mobile joint O_2.

2 Transmission Function

Within the stroke limits of Φ_1 si Φ_2, a zero order transmission ratio is sought that will lead to optimum distribution of the transmission ratio, to give the edged force when needed. Zero order transmission ratio and its derivates of order one and two are noted:

$$\varphi_2 = \varphi_2(\varphi_1),\ \varphi_2' = \frac{\mathrm{d}\varphi_2}{\mathrm{d}\varphi_1},\ \varphi_2'' = \frac{\mathrm{d}^2\varphi_2}{\mathrm{d}\varphi_1^2} \tag{1}$$

In selecting the transmission ratio, we need to take into account the following: (1) for different openings of the scissors' arms, the force that we can apply through

the arms modifies; (2) during cutting, the necessary force is not the same, due to alterations of the size of the cut section, as well as removing the section from articulation O_0.

These force diagrams can be determined through calculation and on basis of measurements taken on trial stands.

The studied transmission functions were first, second, third and fourth degree polynomials. The first degree polynomial leads to a planetary gearing with *circular gears*, and the mechanisms works as a gear assembly with constant transmission ratio. The transmission function slope, defined by the angle α is connected to the transmission ratio T of the planetary gear under the relation:

$$\tan\alpha = \varphi_2' = \frac{d\varphi_2}{d\varphi_1} = \frac{\omega_2}{\omega_1} = T. \tag{2}$$

The choice of polynomials of superior order can optimize the mechanism and will lead towards a mechanism with *noncircular gears*. Let there be A, M and B points on the transmission function considered starting, middle and end moments of cutting. The second degree polynomial can determine a transmission ration in A. The third degree polynomial can determine a transmission ration in two out of the three points. The fourth degree polynomial can determine the transmission ratio to impose in all three moments of cutting (Fig. 2).

3 Centrodes of Noncircular Gears

The trasmission function imposed, given by relation (1), leads to the calculus of relative centrodes associated to noncircular gears in the mechanism. Let there be the planetary mechanism in Fig. 3a, made of the three elements and the angular velocities associated to them. By overlapping of rotary movement this planetary gearing can transform into an ordinary one, characterised by such angular velocities as in Fig. 3b—see Voinea et al. (1983), pp 245–249.

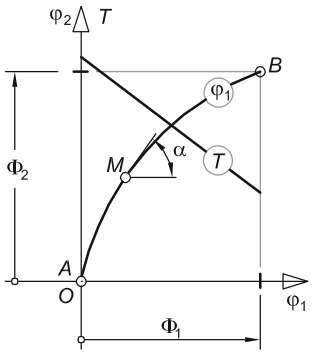

Fig. 2 Transmission function and the variation of the gear ratio

The radii of the two relative centrodes were noted with r_0 and r_2, and the instantaneous rotation centre was noted with I, in movement on the line of the centres—see Maros (1980), p 19. For the gearing in Fig. 3b, the transmission ration is given by the relation:

$$\frac{\omega_2 - \omega_1}{\omega_0 - \omega_1} = -\frac{r_0}{r_2}. \tag{3}$$

On the other hand, the sum of the centrode radii towards the instantaneous rotation centre is constant and equal to the distance between the two joints:

$$r_0 + r_2 = a. \tag{4}$$

Out of relations (3) si (4), we obtain:

$$r_2(\varphi_1) = \frac{a}{\varphi_2'} \text{ and } r_0(\varphi_1) = a - \frac{a}{\varphi_2'}. \tag{5}$$

Parametric equations of the centrode (C_0) can be expressed as a ratio to the system of the element 0. The parameter of these equations is the angle φ_1 (Fig. 3b):

$$\begin{cases} x_0(\varphi_1) = r_0 \sin \varphi_1 \\ y_0(\varphi_1) = r_0 \cos \varphi_1 \end{cases}. \tag{6}$$

Similarly, parametric equations of the centrode (C_2) expressed in rapport to the system of element 2 will be:

$$\begin{cases} x_2(\varphi_1) = r_2 \sin(\varphi_2 - \varphi_1) \\ y_2(\varphi_1) = -r_2 \cos(\varphi_2 - \varphi_1) \end{cases}. \tag{7}$$

4 Generation of Noncircular Gears

Figure 4 illustrates the principle of conjugation of tooth shapes for two mating noncircular gears that are generated by a rack-cutter. The gear centrodes (C_0) and (C_2) and the rack-cutter centrode (C_3) are in tangency at the instantaneous center of rotation I. The rack-cutter centrode is a straight line.

Pure rolling of each centrode over the other one is provided if the instantaneous linear velocities of point I of each centrode are equal under the magnitude and direction. While the gears 0 and 2 perform rotation about O_0 and O_2, respectively, the rack-cutter translates along the tangent (T) to the gear centrodes and along the center distance a and rotates about I. The pure rolling of the rack-cutter over the gear centrodes is provided if the following vector equations are observed—see Litvin (1994), pp 366–368:

$$\mathbf{v}_0 = \mathbf{v}_2 = \mathbf{v}_3 \tag{8}$$

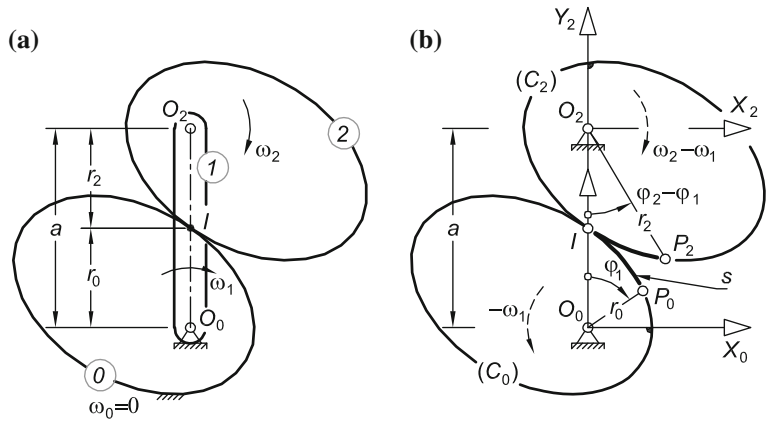

Fig. 3 Determination of relative centrodes: **a**, **b**

here $\mathbf{v}_0$ and $\mathbf{v}_2$ are the gear 0 and 2 velocity in rotation about they center, and $\mathbf{v}_3$ is the velocity of the rack-cutter, given by:

$$\mathbf{v}_0 = \boldsymbol{\omega}_1 \times \overline{O_0 I};\ \mathbf{v}_2 = (\boldsymbol{\omega}_2 - \boldsymbol{\omega}_1) \times \overline{O_2 I};\ \mathbf{v}_3 = \mathbf{v}_t + \mathbf{v}_a \tag{9}$$

where $\mathbf{v}_t$ and $\mathbf{v}_a$ is the rack-cutter velocities in the direction of (T) and O_0O_2, respectively. While the rack-cutter and the gears being generated perform the related motions described above, the rack-cutter will generate conjugate tooth profiles for gears 0 and 2.

Under these generation conditions, the angle of the common tangent to the relative centrodes can be calculated through successive relations:

$$\tan\theta = \frac{v_a}{v_0} = \frac{r_0'}{r_0}. \tag{10}$$

On the other hand, the reduced velocity s' of the rack cutter along the common tangent and space s corresponding will be:

$$v_t = \frac{ds}{dt} = \frac{v_0}{\cos\theta},\ s' = \frac{ds}{d\varphi_1} = \frac{r_0}{\cos\theta},\ s = \int_{\varphi_1} \frac{r_0}{\cos\theta} \cdot \mathrm{d}\varphi_1. \tag{11}$$

Calculation of the space can be made by numerical integration of the above relation or by approximation, having in view that the space travelled by rolling centrode (C_3) over (C_0) is equal to the length of the curve arch s measured on (C_0) corresponding to a centre angle φ_1 (Fig. 3b). Having in view that through relations (6) points can be calculated on (C_0) no matter how frequent, the cumulated distance of these points will be approximately space s.

5 Tooth Profile of Noncircular Gears

The rack cutter is associated with an own system S_3. The parametric equations of the rack cutter profile (Γ_3) compared to its own system are given by the relations (Fig. 5):

$$\begin{cases} x_3(t) = t\tan\alpha \\ y_3(t) = t \end{cases}. \tag{12}$$

To calculate the conjugate profile of the gear 0, we write the parametric Eq. (12) in the system of the gear 0 on basis of coordinate transformations of type $r_3^{(0)} = M^{(0,3)} \cdot r_3^{(3)}$. Calculating the transformations, the parametric equations obtained look like the following:

$$\begin{cases} x_3^{(0)}(t,\varphi_1) = (t\tan\alpha - s)\cos(\varphi_1 - \theta) + t\sin(\varphi_1 - \theta) + r_0\sin\varphi_1 \\ y_3^{(0)}(t,\varphi_1) = -(t\tan\alpha - s)\sin(\varphi_1 - \theta) + t\cos(\varphi_1 - \theta) + r_0\cos\varphi_1 \end{cases} \tag{13}$$

Equation (13) describe a lines family of type (Γ_3), who's enveloping (Γ_0) gives the profile of the wanted gear 0. The parameter of the generating curve is t and that of the family is φ_1. A connection is sought between the two parameters, according to the theory of enveloping curves (Ionescu 1975, pp 102–103):

$$\frac{\partial x_3^{(0)}}{\partial\varphi_1}\cdot\frac{\partial y_3^{(0)}}{\partial t} = \frac{\partial y_3^{(0)}}{\partial\varphi_1}\cdot\frac{\partial x_3^{(0)}}{\partial t}. \tag{14}$$

Replacing the partial derivates of the parametric equation (13) in relation (14) and making calculations, the relationship between the two parameters t and φ_1 can be obtained as illustrated here:

$$t = \frac{s(1-\theta')\tan\alpha + \left(r_0'\tan\alpha - r_0\right)\cos\theta - \left(r_0\tan\alpha + r_0'\right)\sin\theta + s'}{(1-\theta')(\tan^2\alpha + 1)}. \tag{15}$$

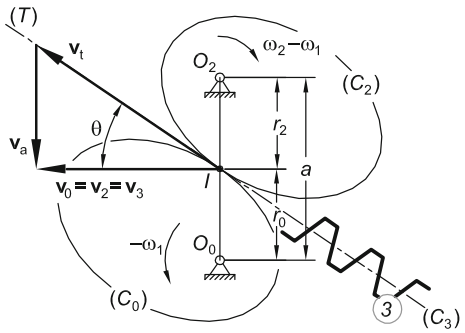

Fig. 4 General principle of generation of noncircular gears

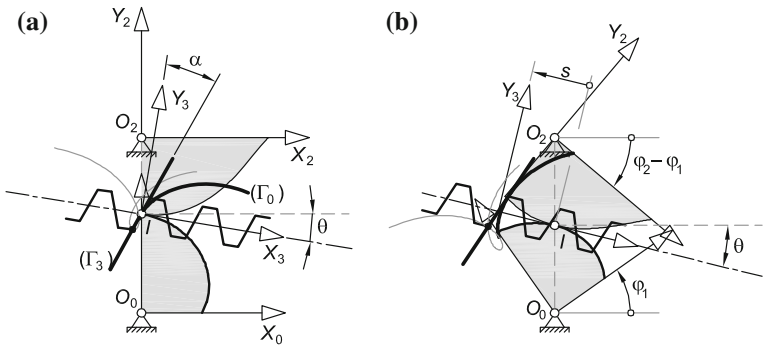

Fig. 5 Transformation of coordinates associated to the calculus of the gear profile 0: **a**, **b**

Replacing relation (15) and (13) the parametric equations of the profile of the gear 0, marked (Γ_0) in Fig. 5. In a similar manner, the profile of gear 2 can be obtained.

6 Limits of Nonundercutting

In view of studying the mechanism programs were written in AutoLISP, and the graphics were made in AutoCAD. Representations highlighted the existence of envelope as well as undercutting in generation with rack cutter of the two noncircular gears.

The example in Fig. 6 corresponds to initial data: a = 70 mm, $\Phi_1 = 67°$, $\Phi_2 = 146°$, $\gamma = 23°$, α =25°. As transmission function the second degree polynomial was chosen, which imposed the transmission ration in point A in two variants: T=3.00 respectively 2.45 (Fig. 2). In the first case, it lead to phenomena

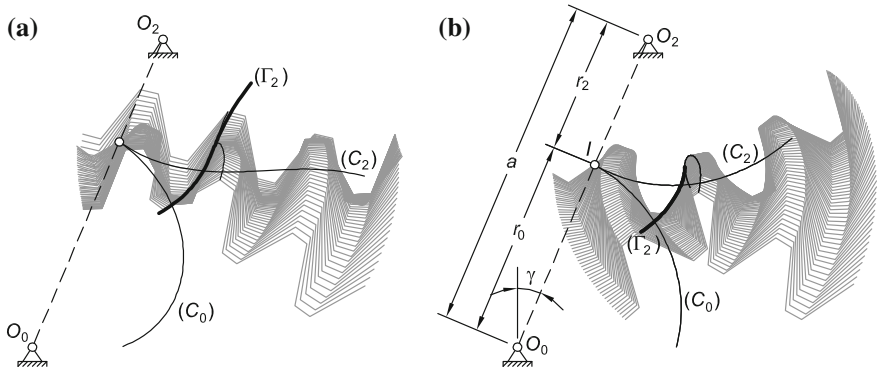

Fig. 6 Limits of nonundercutting: **a**, **b**

of interference, shown in Fig. 5a. Profile (Γ_2) was drawn as well as the connection buckle to the base of the gear tooth 2.

7 Conclusions

The presented calculations are the support for very important practical applications in the field of scissors or manual cutters. A series of results exist in brand products on the market (see www.fiskars.com), but the range of applications can be extended. The program created by the author leads the profiling calculus of non-circular gears and allows for optimization of the planetary mechanism.

References

Ionescu GhD (1975) Teoria diferenţială a curbelor şi suprafeţelor cu aplicaţii tehnice. Editura Didactică şi Pedagogică, Bucureşti
Litvin FL (1994) Gear geometry and applied theory. PTR Prentice Hall
Maros D (1980) Mecanisme. Institutul Politehnic Cluj-Napoca
Voinea R, Voiculescu D, Ceausu V (1983) Mecanica. Editura Didactica si Pedagogica, Bucuresti
http://www.fiskars.com (read on 2011.10)

Optimal Damping Constant Investigation on a Quarter-Car

Mihai Tica, George Dobre, Gabriele Barbaraci and Gabriele Virzi' Mariotti

Abstract This paper shows an investigation on optimal damping constant performed in the frequency domain. The optimal damping constant is meant as that value that minimizes the acceleration of all connected bodies characterizing a two degree of freedom system sketching a quarter car. The connected bodies are sprung and unsprung mass respectively for quarter of chassis and tire, this last keeps the contact with the ground and it is connected with the sprung mass through a shock absorber characterized by spring and fluid damper. Optimal damping constant was determined by imposing analytical conditions on the expression of acceleration of two masses. Afterwards, the variation of acceleration and position in function of frequency for the obtained value of damping constant is plotted numerically in two ways using Wolfram Mathematica and MSC Adams software.

Keywords Shock absorber · Damping constant · Sprung mass · Unsprung mass · Road disturbance

List of Symbols

c_s	Damping coefficient of shock absorber
k_T	Spring constant of tire
k_S	Spring constant of shock absorber

M. Tica (✉) · G. Dobre
University Politehnica of Bucharest, Bucharest, Romania
e-mail: ticamihai0@yahoo.co.uk

G. Dobre
e-mail: G.Dobre@gmail.com

G. Barbaraci · G. V. Mariotti
Dipartimento di Ingegneria Chimica, University of Palermo, Gestionale, Informatica e Meccanica, Palermo, Italy
e-mail: gabriele.barbaraci@unipa.it

G. V. Mariotti
e-mail: gabriele.virzimariotti@unipa.it

G. Dobre (ed.), *Power Transmissions*,
Mechanisms and Machine Science 13, DOI: 10.1007/978-94-007-6558-0_55,

m_s Sprung mass
m_U Sprung mass
$x_S(t)$ Displacement of sprung mass
$x_U(t)$ Displacement of unsprung mass
$\dot{x}_S(t)$ Velocity of sprung mass
$\dot{x}_U(t)$ Velocity of unsprung mass
$\ddot{x}_S(t)$ Acceleration of sprung mass
$\ddot{x}_U(t)$ Acceleration of unsprung mass
$y(t)$ Road disturbance

1 Introduction

The shock absorber is a component of dynamic system. It provides a dissipative effect against exogenous excitation that produces a relative motion between the bodies connected by the shock absorber. The dissipative effect can be made by a fluid damper characterized by a certain value of viscosity and so the damping characteristic. In the second half of previous century the improvements in technological field led the engineers to develop actuators able to produce the same effect of a common shock absorber. These actuators were built according to magnetic field theory and constitute another way to produce a dissipative effect on systems. In this paper we focus all attention on the first category that is a passive system, in order to produce an analytical investigation to show the values of optimal damping constant and plot the variation of acceleration and position relative to the frequency in two way: using Wolfram Mathematica and MSC Adams. The damping constant can be chosen in order to get the minimum acceleration of all masses so that the passenger driving a car, for example, is not subject to the excessive road disturbance. The damping constant is an important and useful parameter in order o understands the dynamic behavior of a system. It also used for different purpose for example it is used in a microstructure for the protection of electronic-packaging components in vibration-impact environments shown in Ping (2005) and Ping et al. (2008). In the military field a damping action is used in the guns and heavy vehicle so that the produced load must be compensated in order to get the less disturbances as possible on the structure mentioned in Samantaray (2009). In automotive research field a particular value of damping constant is reached build up a displacement-sensitive shock absorber (DSSA) in order to get a desired ride comfort of the passenger (Lee and Moon 2006). The research of optimal damping constant is already present in the automotive to verify shock absorber's ability to transfer the mid- and high-frequency content of the vibrations passing from the road profile, through the suspension, to the vehicle body as mentioned in literature (Czop and Stawik 2011). These study led the engineer to develop two different way to transmit the exogenous excitation on the vehicle or rather the acceleration dependent method (ADM) and conventional method (CM).

The interest on this methods was born from the observation that a variation of damping constant is feasible thanks to the technological development due to the mechatronic systems that relate the passive systems with active ones characterized by the introduction of control systems and electronic devices. There are many way to modify the damping constant in order to reach a desired value of power transmission produced by the exogenous excitation on a system. Eddy current can provide a modification of damping constant. A such system is built up by two permanent magnets and a conductive aluminum plate to generate both spring and variable damping effects. Eddy currents are generated in the aluminum plate due to its relative motion with respect to the magnets. These eddy currents produce a repulsive force that is proportional to the velocity of the conductor such that the moving magnet and conductor act as a viscous damper shown in Ebrahimi et al. (2008). Another way to modify the damping constant is characterized by the introduction of nanotechnology with materials in micro scale. The presence of these two different dimensions of solid part realizes a resistance force when a magnetic field is injected in the mixture hold by fluid as mentioned in Hayashi et al. (2010). The most common and famous way to modify the damping characteristic is the introduction of iron particle in a fluid damper with presence of magnetic field. Sometimes the electric field is used in order to build a comparison with the results produced with the magnetic field even whether the use of electric field imply the use of more electric power than magnetic field needs, that's why this last is preferred.

2 Mathematical Model

This paper introduces the mathematical model of system vibration according to Guglielmino et al. (2005, 2008), Guiggiani (2007). The simplest system of two degree of freedom quarter car is reproduced with minor modifications in Fig. 1.

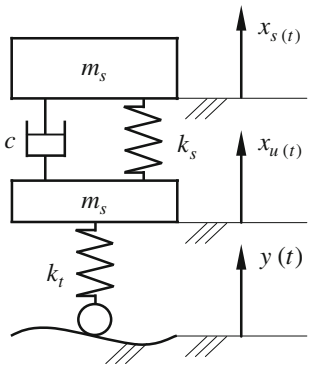

Fig. 1 Simplest system of two degree freedom of the quarter car automotive suspension

It is characterized by a system of two ordinary differential matrix Eq. (1) where the input is the road disturbance $y(t)$ according to the known vibration theories of dynamic motions:

$$\begin{bmatrix} m_S & 0 \\ 0 & m_U \end{bmatrix} \begin{bmatrix} \ddot{x}_s(t) \\ \ddot{x}_u(t) \end{bmatrix} + \begin{bmatrix} c & -c \\ -c & c \end{bmatrix} \begin{bmatrix} \dot{x}_s(t) \\ \dot{x}_u(t) \end{bmatrix} + \begin{bmatrix} k_S & -k_S \\ -k_S & k_S + k_T \end{bmatrix} \begin{bmatrix} x_s(t) \\ x_u(t) \end{bmatrix} = \begin{bmatrix} 0 \\ k_T \end{bmatrix} y(t) \tag{1}$$

The introduction of road disturbance $y(t)$ is essential to carry out all information about dynamic behavior of system. The dynamic behavior is analyzed by considering the transfer function that relates the road disturbance to the outputs. In this case the outputs are the acceleration of two masses analyzed in the frequency domain and time domain. It is important to understand that minimization of acceleration can be done in the frequency domain or in time domain, aspect mentioned in Savaresi et al. (2010). This two different ways to proceed are strictly depended on the particular input, whether the input is harmonic or time depended. In this paper an analytical investigation on damping constant is built up in order to get the optimal value that minimizes the acceleration of the sprung mass so that the entire structure, where the shock absorber is fixed, supports a lower mechanical excitation in order to get the best drive comfort and stability performance. In particular the stability performance is the mean goal of this paper or rather when the landing gear impacts on the ground, the entire structure receives a force directed on upper direction that leads the aircraft to lose the friction force of the wheel rolling on the ground and so a certain delay is introduced for arrest the plane. Moreover the same force lead the aircraft to produce a certain vibration of its structure such as fuselage and wings. This effect is present whatever is the value of damping coefficient but the less force is the less mechanical excitation is on the structure so that life cycle is higher than the others value of damping constant outside the optimal one. Usually a mechanical system is characterized by some variable masses so that the optimal damping constant modifies its value since the minimum of acceleration must be reached. There are dynamic systems that provide the variation of damping constant by using magnetic or electric field. The electro rheological systems use the electric field to increase the damping constant but it cause a huge use of power since that it is based on separation of charge from a plate to the other one in opposite side (Namuduri et al. 2003). The magneto rheological fluids are more suitable when a lower energy must be used. The work in such way the iron particle are subjected to magnetic field so that a long chain of particles produces an increasing of tensile stress, aspect mentioned in Namuduri et al. (2003). The magnetic field is produced by the introduction of control current in coil winding the iron. The gap is filled by the magneto rheological fluid characterized by a certain fraction of iron particles. The injection of control current can be typically switch on/off as in Barabaraci and Virzi' Mariotti (2011) or by a proportional state feedback. The former is characterized by the introduction of a fixed value of control current and injected once a certain value of relative speed between the sprung and unsprung mass is captured by the sensors. In this case the

sensors are accelerometer able to calculate the speed as a function of acceleration. Another way to introduce the control current is characterized by a proportional value of magnetic field to the relative speed between the sprung and unsprung mass. In this case a linearization study must be introduced in order to delete the complication due to the nonlinearity of magnetic field that is characterized by the saturation problem. The mathematical model (1) is characterized by a vector containing the kinematic variable with regard the sprung and unsprung mass that are the outputs of system shown in this paper. Its dynamic behavior is analyzed according the transfer function that relates the road disturbances to the masses. The transfer function is obtained by Laplace transform according (2) with zero initial conditions:

$$\left(s^2\mathbf{M} + s\mathbf{C} + \mathbf{K}\right)\mathbf{q}(s) - s\mathbf{q}(0_-) - \dot{\mathbf{q}}(0_-) = \begin{bmatrix} 0 \\ k_T \end{bmatrix} y(s) \tag{2}$$

The transfer function does have the form (3) and it is strictly proper because it represent a typical casual system where the order of derivative input is lower than kinematic variable ones

$$\mathbf{W}(s) = \left\{ w_{ik} = \left(\frac{\prod_{l=1}^{h} (s + z_l(c))}{\prod_{r=1}^{n} (s + p_r(c))} /h<n \right)_{ik} /w_{ik} = w_{ki}\,\forall i, \quad k = 1\ldots2 \right\} \tag{3}$$

in which: h < n and $w_{ik} = w_{ki} \forall i, \quad k = 1\ldots2$.

In particular for the sprung and unsprung mass the transfer function are respectively (4) and (5):

$$\mathrm{W(s)} = \frac{\mathrm{k_T(k_s + c \times s)}}{\mathrm{k_s(k_T + (m_s + m_U)s^2) + s(m_s s(k_t + m_U s^2) + c \times s(k_t + (m_s + m_U)s^2))}}. \tag{4}$$

$$\mathrm{W(s)} = \frac{\mathrm{k_T(k_s + s(c + m_s s))}}{\mathrm{k_s(k_T + (m_s + m_U)s^2) + s(m_s s(k_t + m_U s^2) + c \times s(k_t + (m_s + m_U)s^2))}}. \tag{5}$$

The optimal damping constant is carried out from a study of the acceleration in the frequency domain and it is based on the research of that point of acceleration plot that are maximum in a derivative sense. It is constituted by the substitution of Laplace variable with and the calculation of second derivative for each transfer function as in (6) and (7) respectively for the sprung and unsprung mass.

$$W(j\omega)_{acc\_S} = \omega^2 \frac{\sqrt{(k_S k_T)^2 + (c k_T \omega)^2}}{\sqrt{(k_S k_T + m_S m_U \omega^4 - (k_T m_S + k_S(m_S + m_U))\omega^2)^2 + (-c(m_S + m_U)\omega^3 + c k_T \omega)^2}} \tag{6}$$

Table 1 Optimal damping constant

Symbols	Description	S.I.
m_S	Sprung mass	400 kg
m_U	Unsprung mass	12 kg
k_S	Stiffness of shock absorber	50,000 N/m
k_T	Stiffness of tire	300,000 N/m

$$W(j\omega)_{acc\_U} = \omega^2 \frac{\sqrt{(k_S k_T - k_T m_S \omega^2)^2 + (c k_T \omega)^2}}{\sqrt{(k_S k_T + m_S m_U \omega^4 - (k_T m_S + k_S(m_S + m_U))\omega^2)^2 + (-c(m_S + m_U)\omega^3 + c k_T \omega)^2}} \tag{7}$$

The investigation starts by considering the intersection points of (6) and (7) for with the transfer function (8) obtained by tending the relation (6) and (7) [11]:

$$\mathrm{W}(j\omega) = \omega^2 \frac{\sqrt{\mathrm{k_T^2}\omega^2}}{\sqrt{\omega^2(\mathrm{k_T} - (\mathrm{m_S} + \mathrm{m_U})\omega^2)^2}} \tag{8}$$

Those intersection points are very important because the calculation of maximum point to reach the minimum of acceleration must be performed on them by the relation the intersection between (8) and (9);

$$\left.\frac{\mathrm{d}(\omega^2 \mathrm{W}(\mathrm{c}, \omega))}{\mathrm{d}\omega}\right|_{\omega=\Omega} = 0. \tag{9}$$

3 Optimal Damping Constant

In order to calculate the optimal damping constant with regards to the dynamic system a set of data are used and showed in the Table 1 under the assumption of passive system.

According to the expressions 6 and 7 the frequency response of the acceleration is shown for both masses as in Figs. 2 and 3 we can see the graphical representation of our previous speech. They show the graphical starting point of procedure in order to investigate the optimal damping constant value. This is made at first in order to produce a comparison with the approximated formula produced with the literature of the past.

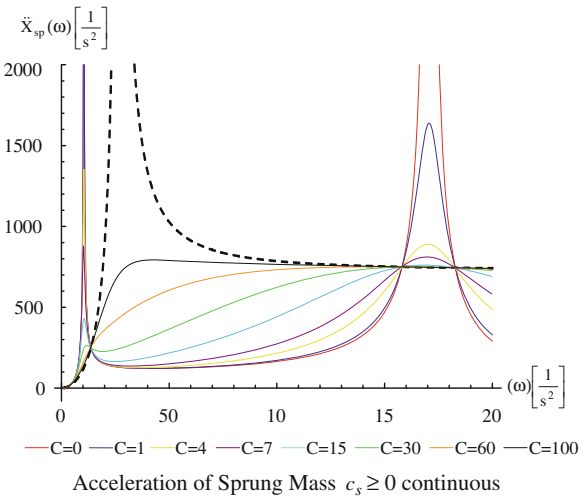

Fig. 2 Frequency response of sprung mass for $c = 0$ and $c \to \infty$

In the Figs. 7 and 8 are clear the intersection point that are significative for purpose of this study, in particular it must be shown that the intersection points in frequency domain leads to set of data, one for sprung mass and one for the unsprung mass. For the sprung and unsprung mass we refers the intersection points corresponding to the frequencies shown in the vectors (10) and (11):

$$\omega_{1s} = \sqrt{\frac{k_t}{m_u}} = 158.114$$

$$\omega_{2s} = \frac{1}{\sqrt{2}}\sqrt{\frac{2k_s m_s + k_t m_s + 2k_s m_u - \sqrt{-8k_s k_t m_s m_u + (k_t m_s + 2k_s(m_s + m_u))^2}}{m_s m_u}}$$
$$= 13.6802$$

$$\omega_{2s} = \frac{1}{\sqrt{2}}\sqrt{\frac{2k_s m_s + k_t m_s + 2k_s m_u + \sqrt{-8k_s k_t m_s m_u + (k_t m_s + 2k_s(m_s + m_u))^2}}{m_s m_u}}$$
$$= 182.746$$

$$\omega_{3s} = \frac{1}{\sqrt{2}}\sqrt{\frac{2k_s m_s + k_t m_s + 2k_s m_u + \sqrt{-8k_s k_t m_s m_u + (k_t m_s + 2k_s(m_s + m_u))^2}}{m_s m_u}} \tag{10}$$

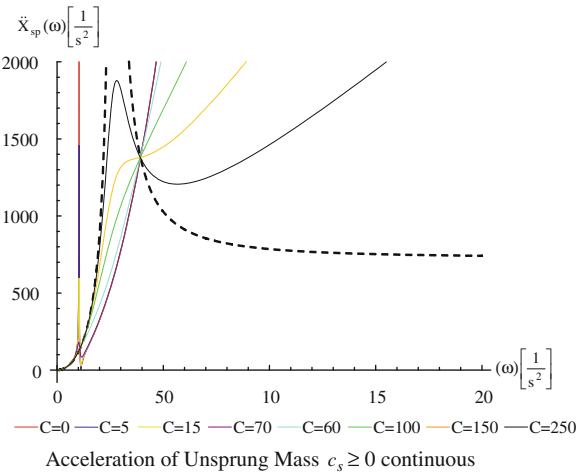

Fig. 3 Frequency response of unsprung mass for c = 0 and c → ∞

$$\omega_{1u} = \sqrt{\frac{k_s m_s + k_t m_s + 2k_s m_u}{m_s^2 + 2m_s m_u}} - \frac{\sqrt{(-2k_s m_s - 2k_t m_s - 2k_s m_u)^2 - 8k_s k_t (m_s^2 + 2m_s m_u)}}{2(m_s^2 + 2m_s m_u)} = 10.7055$$
$$\omega_{1u} = \sqrt{\frac{k_s m_s + k_t m_s + 2k_s m_u}{m_s^2 + 2m_s m_u}} + \frac{\sqrt{(-2k_s m_s - 2k_t m_s - 2k_s m_u)^2 - 8k_s k_t (m_s^2 + 2m_s m_u)}}{2(m_s^2 + 2m_s m_u)} = 39.2863 \quad (11)$$

Since that minimum acceleration is verified for the intersection point, the first derivative of acceleration function in the frequency domain must be calculated in order to get the damping constant in those points (insert the book theory Dinamica del Veicolo).

The first derivative of both functions are referred to the expression (12) and (13)

$$\frac{\partial\left(\omega^2 W(c,\omega)_{sprung}\right)}{\partial\omega}_{\omega=\omega_f} = 0 \quad (12)$$

$$\frac{\partial\left(\omega^2 W(c,\omega)_{unsprung}\right)}{\partial\omega}_{\omega=\omega_f} = 0 \quad (13)$$

where ω_f is the value of frequency relative to the best compromise between maximum and minimum acceleration taken with positive sign. The solutions of (12) and (13) are shown in a vector form as ();

The approximation formula of damping constant produced by Guiggiani (2007), is obtained by simplifying the expression used here that is carried out by MATHEMATICA but since that is too complicated and very long we report only the numerical value of it. The symbolic value of the frequencies where the intersections point exist as follows:

$$c_s = \begin{bmatrix} 3634.39 \\ 4460.94 \end{bmatrix} \left[\frac{Ns}{m}\right] \tag{14}$$

$$c_u = \begin{bmatrix} 1790.8 \\ 15802.6 \end{bmatrix} \left[\frac{Ns}{m}\right] \tag{15}$$

The Fig. 4 shows the comparison of optimal damping constant between sprung and unsprung mass:

The Fig. 4 show an important result, or rather. One can minimize the acceleration of sprung mass by using the minimum value relative to the blue bar or one can minimize the acceleration of unsprung mass by using the minimum value relative to the red one.

The frequency response has been developed considering a time varying frequency in a simulation where the frequency is vs. time simulation. The simulations were conducted assuming the time scale is been scaled by a factor of 10 according the Nyquist sampling theory.

In the Fig. 5 the value of the damping constant $c = 3634.39$ Ns/m shows a minimum of acceleration at 8.5 rad/s and it reaches the maximum displacement at 5 rad/s.

The unsprung mass acceleration increases until the end the simulation time while his displacement reaches a maximum at the same frequency shown by the displacement of the sprung mass.

In the Fig. 6 the mass suspended detects a decrease in the gradient id acceleration corresponding to the value of 8.5 rad/s which is the frequency acceleration

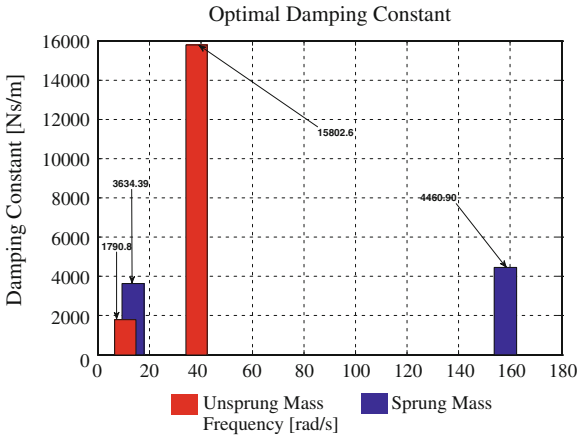

Fig. 4 Optimal damping constant value of sprung and unsprung mass

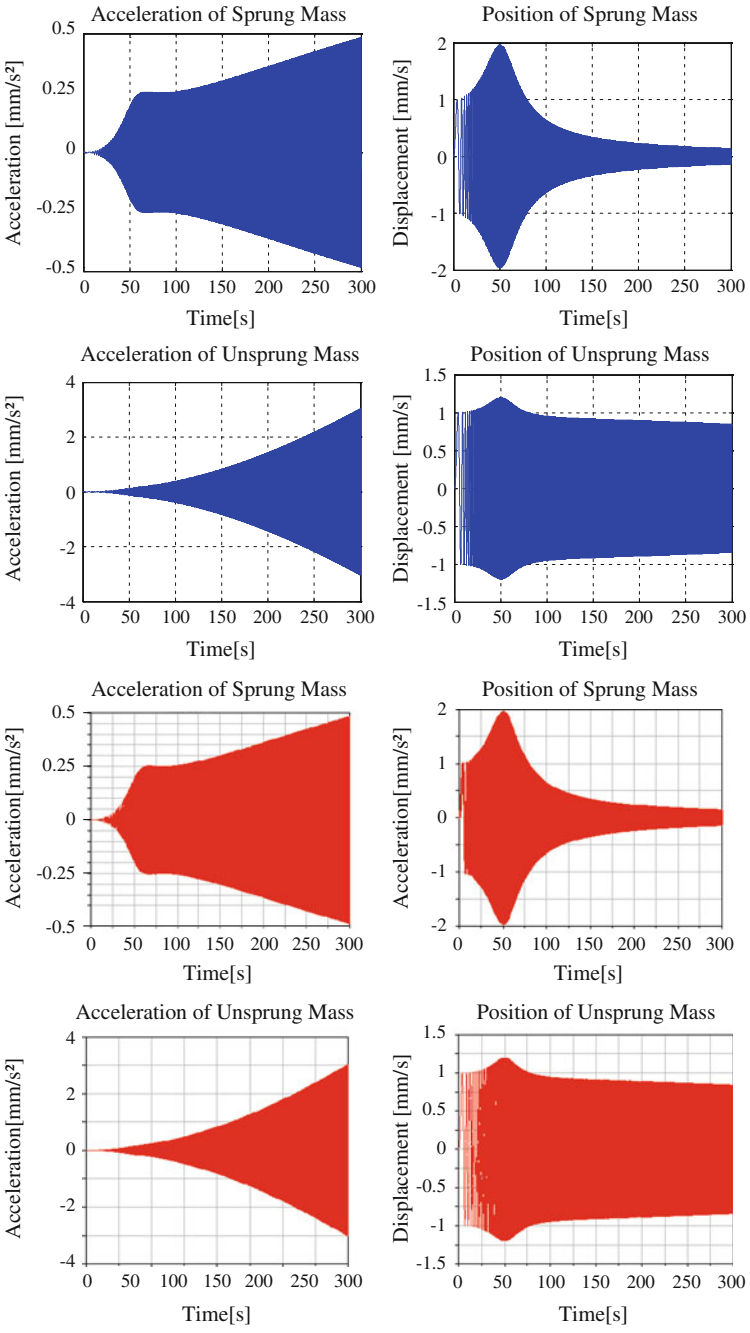

Fig. 5 Simulation to the step response of 2DOF with $c = 3634.39\,\text{Ns/m}$

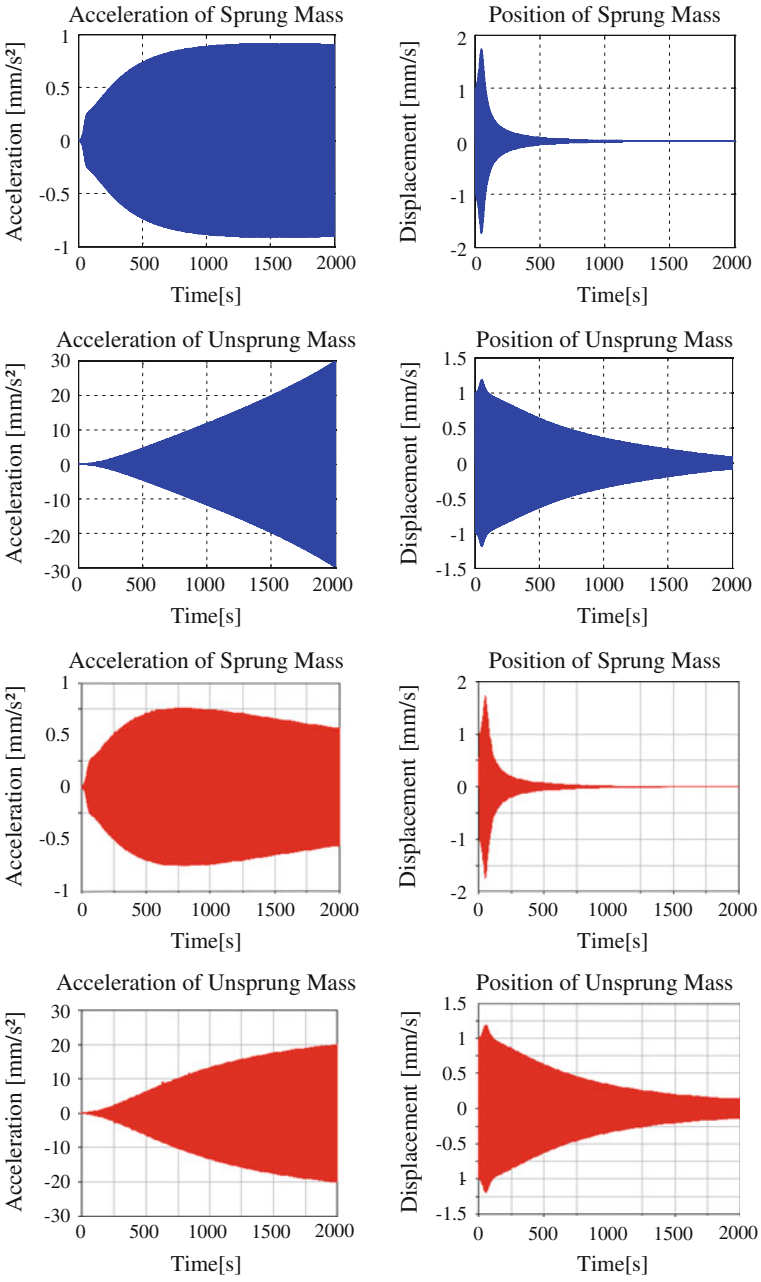

Fig. 6 Simulation to the step response of 2DOF with $c = 4460\,\text{Ns/m}$

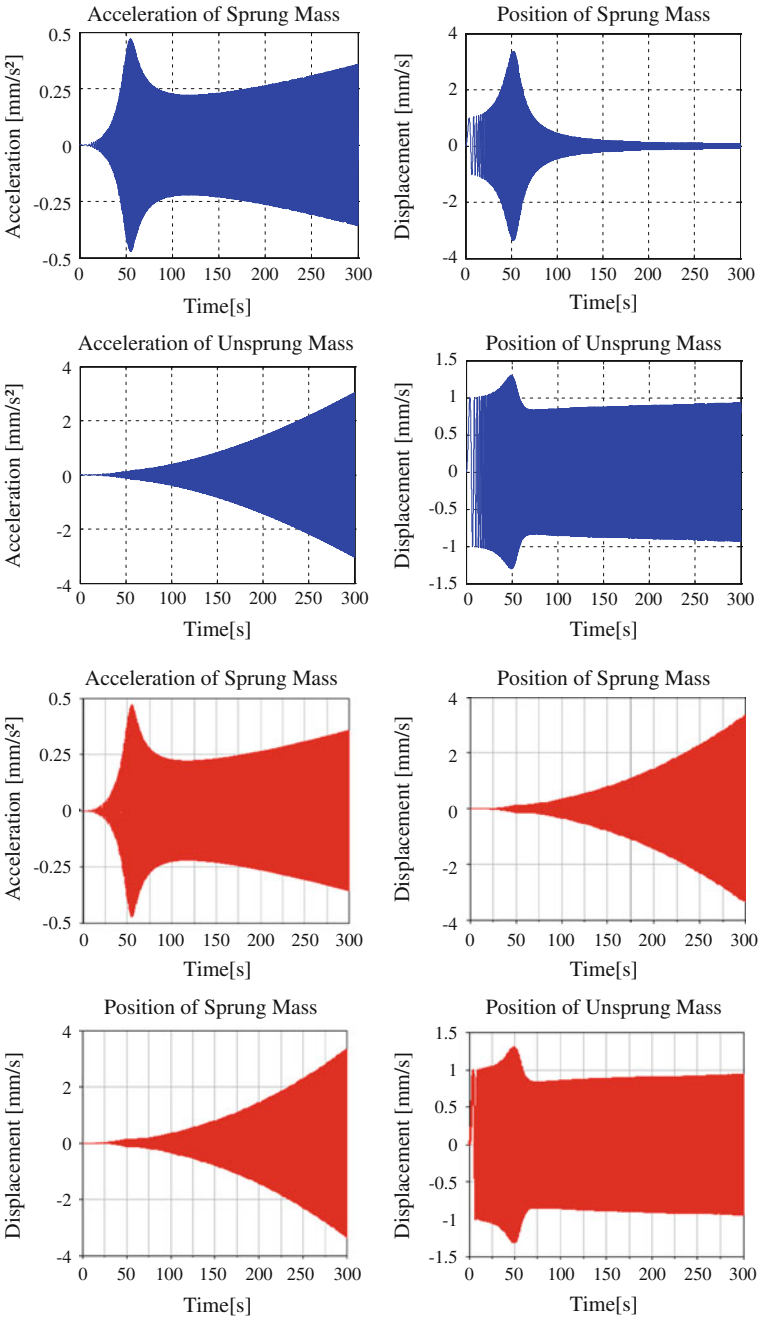

Fig. 7 Simulation to the step response of 2DOF with $c = 1790.8\,\text{Ns/m}$

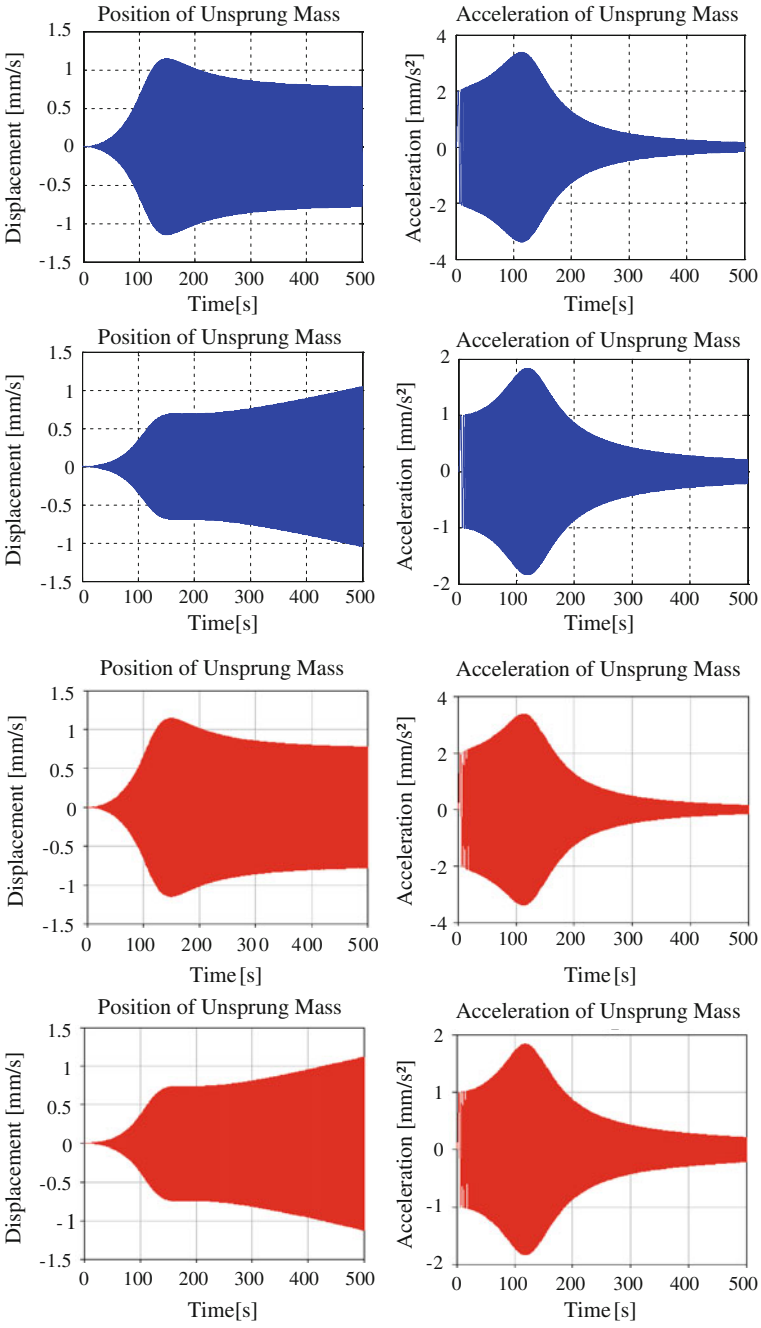

Fig. 8 Simulation to the step response of 2DOF with $c = 15802.6\,\text{Ns/m}$

the minimum reached by the suspended mass at the previous value of the damping constant. However, at 158.114 rad/s its acceleration reaches the maximum. Its displacement reaches the maximum value correspondence 5 rad/s as in the previous value of constant damping. The unsprung mass exhibits same behavior of previous case for acceleration and displacement.

In the Fig. 7 exhibits the sprung mass acceleration in Minmi corresponding to the value of 10.7 rad/s the numerical analysis performed by MATHEMATICA. Also in this case the maximum of displacement is at 5 rad/s. The unsprung mass reaches a minimum acceleration at 6 rad/s and then increases by the increasing the exogenous frequency excitation. Its displacement reaches a maximum at 5 rad/s, a minimum at 7.5 rad/s and then increase till the end of simulation.

In the Fig. 8 the sprung mass exhibits a maximum of acceleration and displacement respectively at 15 rad/s and 11.4 rad/s. Unsprung mass reaches a minimum acceleration at 19.5 rad/s and then increases by the increasing the exogenous frequency excitation. Its displacement reaches a maximum at 11.8 rad/s and then decreases till the end of simulation.

Acknowledgments The work has been funded by the Sectoral Operational Programme Human Resources Development 2007–2013 of the Romanian Ministry of Labour, Family and Social Protection through the Financial Agreement POSDRU/88/1.5/S/60203.

References

Barabaraci G, Virzi' Mariotti G (2011) Influence on the dynamic behavior of full car equipped by magneto rheological damper via switch on/off and h∞ Controller, Science and Motor vehicles, Belgrado, 19–21 April 2011

Czop P, Stawik D (2011) A high-frequency first-principle model of a shock absorber and servo-hydraulic tester. Mech Sys Signal Process 25:1937–1955

Ebrahimi B, Khamesee MB, Golnaraghi MF (2008) Design and modeling of a magnetic shock absorber based on eddy current damping effect. J Sound Vibr 315:875–889

Guglielmino E, Stammers CW, Sireteanu T, Stancioiu D (2005) Int J Veh Auton Sys 3(2/3/4): 216–229

Guglielmino E, Sireteanu T, Stammers CW, Ghita G, Giuclea M (2008) Semi-active suspension control, Springer, ISBN 978-1-84800-230-2, e-ISBN 978-1-84800-231-9. doi 10.1007/978-1-84800-231-9

Guiggiani M (2007) Dinamica del Veicolo Città Studi Edizioni. Torino

Hayashi K, Yamada T, Ido Y (2010) Resistance force of a shock absorber using magnetic functional fluids containing both micrometer-sized and nanometer-sized magnetic particles. Phys Procedia 9:243–247

Lee CT, Moon BY (2006) Simulation and experimental validation of vehicle dynamic characteristics for displacement-sensitive shock absorber using fluid-flow modeling. Mech Sys Signal Process 20:373–388

Namuduri CS, Golden MA, Praeckel J (2003) Concurrent research and development of a magnetic ride control system. IEEE 3:2853–2858

Ping Y (2005) Mechanical characteristics of oil-damping shock absorber for protection of electronic-packaging components. Tsinghua Sci Technol 10(2):216–220. Issn 1007-0214 14/23

Ping Y, Liao N, Jianbo Yang J (2008) Design, test and modelling evaluation approach of a novel Si-oil shock absorber for protection of electronic equipment in moving vehicles. Mech Mach Theor 43(1):18–32

Samantaray AK (2009) Modeling and analysis of preloaded liquid spring/damper shock absorbers. Simul Model Pract Theor 17:309–325

Savaresi SM, Poussot-Vassal C, Spelta C, Sename O, Dugard L (2010) Semi-active suspension control design for vehicles. Elsevier, ISBN: 978-0-08-096678-6

Vibration Impact on Life Bearings from Fan Unit for Fresh Air in Thermo Power Plant REK Bitola

Tale Geramitchioski and Ljupco Trajcevski

Abstract This paper contains the results and the important conclusions of the permanent vibration measuring of the bearings as a part of the fan unit for fresh air used at Thermo Plant REK Bitola, R. Macedonia—the biggest energetic institution for energy production in the country. The result, presented trough various statistical analysis is a key factor for increasing the bearing loads and evidently decreasing the bearing life. By using an appropriate mathematical-numerical method and time-frequency analysis using WVD distribution, the bearings life prediction versus the increase of the vibrations is possible.

Keywords Vibration · Bearing · Wigner-Ville distribution · Kurtosis · NP4

List of Symbols

WVD	Wigner-Ville distribution
NP4	Non-dimensional parameter.

1 Introduction

The presence of a superficial defect in a rolling element generates a shock every time that the rotating element ways on the defect. It generates periodical impulsive excitation force which excites structural resonances and mounted resonance frequency transducer (Tandon and Choudhury 1997; Kiral and Karagulle 2003). These

T. Geramitchioski (✉) · L. Trajcevski
Faculty of Technical Sciences, University St.Kliment Ohridski, Bitola, Republic of Macedonia
e-mail: tale.geramitcioski@uklo.edu.mk

L. Trajcevski
e-mail: ljupco.trajcevski@uklo.edu.mk

G. Dobre (ed.), *Power Transmissions*,
Mechanisms and Machine Science 13, DOI: 10.1007/978-94-007-6558-0_56,

characteristic frequencies depend on the speed of rotation, the location of the damage and in the case of damage on a ring, from the number of rolling elements.

By analyzing vibration generated by shock is possible to identify the damaged bearing and the element on which the damage is located (Martin and Honarvar 1995; Mathew and Alfredson 1988). Shock produces waves of expansion and deformation exciting structure frequencies: shock produces transitory vibration within high frequency, with high first peak and fast decadence, characterized by shock's period (McFadden and Smith 1984).

The statistic index Kurtosis represents a very good indicator for the analysis of damages in low speeds machineries with no continuous shocks (gears of rotating ovens, reduction gears for heavy cycles, etc.). Normally, this indicator must be used with global values rms (Boulenger and Pachaud 2003). Statistic index Kurtosis will be used with the FFT analysis integrated with time-frequency distribution Wigner-Ville and defined new statistic index NP4. It is non-dimensional, it is defined as the fourth statistic moment of the distribution. It is positive for distribution consisting of a sharp single peak and is increasing with an increase in peak of a distribution. This property of the kurtosis was employed in construction of the NP4 detection parameter.

2 Bearing Life and Monitoring of Bearing Vibrations

Mining and Power Company ELEM REK "Bitola" is the largest power generating capacity in Macedonia. It provides more than 70 % of power and part of the coal needed for the industry and households in Macedonia.

Monitoring refers to the analysis of vibrations measured at bearings of fan fresh air in REK Bitola. The fan for fresh air consists of the following main parts: body-shaped spiral impeller, shaft with bearings and regulatory apparatus (Fig. 1).

The rolling bearing used in this analysis is bearing number 4, type NU 244MA-cylindrical rollers bearings (Fig. 2).

To calculate the generate frequency we used the software GEARBOX (Fig. 3).

The measuring vibration instrument used the model of SKF CMVA60 working with software PRISM4 (SKF software). Also, the REK Bitola adopted the ISO 10816 standard by which a certain number and measuring points are set for measuring vibration in horizontal and vertical machines. For analysis of the dynamic state of 3VSV-A, a total 99 measurements of vibration were measured on the fan for fresh air branch-A TE Bitola. The time period is from 09.06.2003 to 10.03.2011. Each measure has a total of eighteen measurement data (Fig. 4).

The analysis shows the display of the spectrum in the time when bearing working in failure period and period after replacement of the bearing with new. Figure 5 shows the spectrum 10 Mart 2010 (period when bearing working in failure period) and 16 May 2011 (period after replacement the bearing with new).

On Fig. 5 we can see that the maximum peak of the spectrum is the frequency of 4.35 Hz that is corresponding to the fundamental train frequency

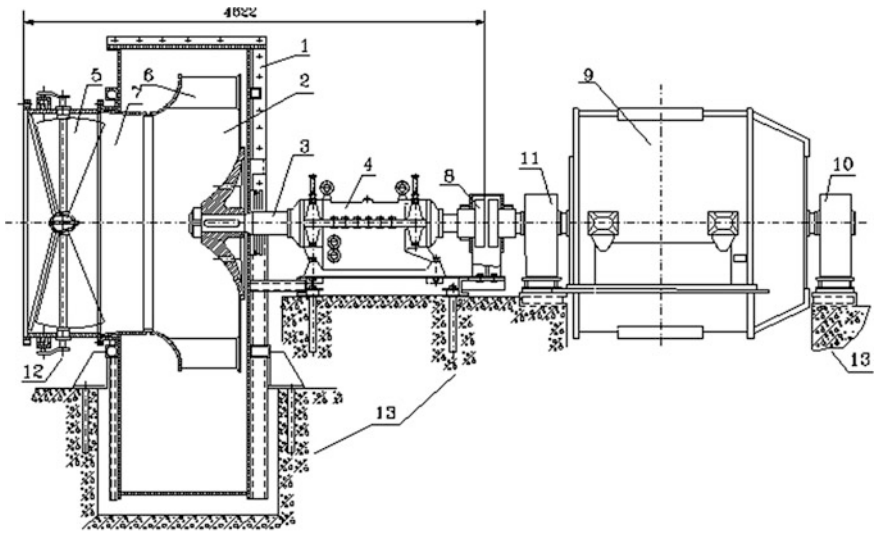

Fig. 1 The fan unit for fresh air BCB type B,[H-32b (Russian)

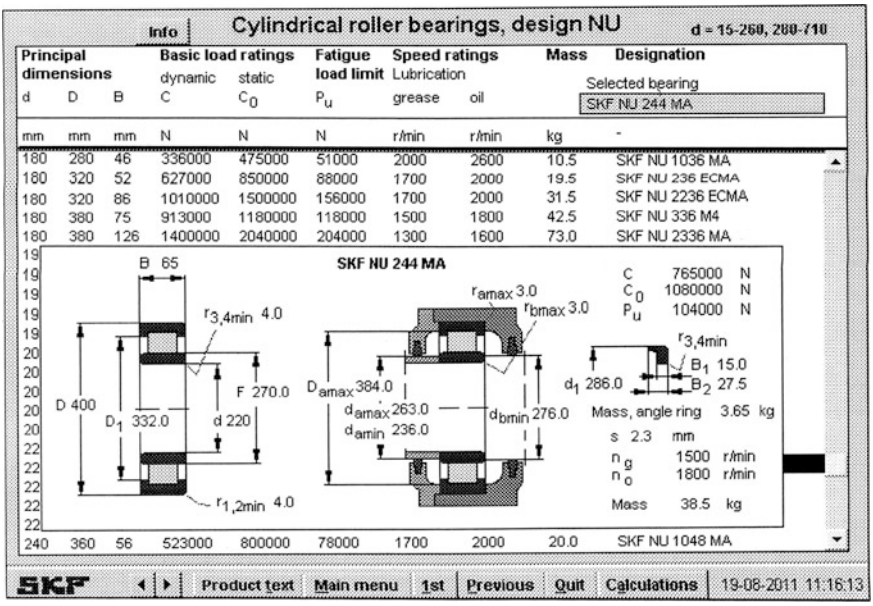

Fig. 2 Bearing SKF NU 244MA

FTF = 4.4 Hz. When in a bearing show's a defective rotating elements, then the frequency must pass through more mechanical interfaces and ball's generate FTF frequency which is rarely presented as a discrete frequency. The modulated

Fig. 3 Calculate general frequency for SKF 7338 and NU244 bearings

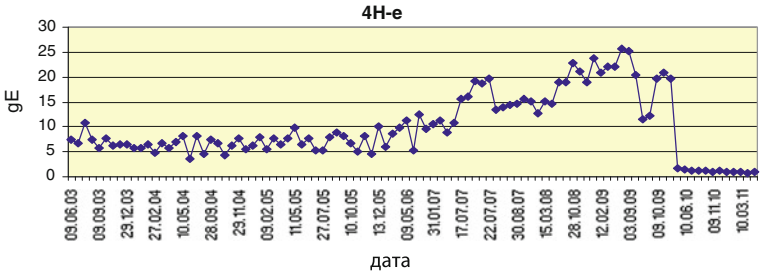

Fig. 4 The data of 99 measurements on SKF NU244 using envelope gE

frequency in this way generates other frequencies such as the rotation frequencies of 10 Hz. Since the value of the rotation frequency is small, it indicates that the rolling balls are not always in loading zone at the outer or inner ring. Also, we may notice the absence of the BSF frequency as a result of the damaged roll of balls at the bearing that can spin only in one direction. It can also be observed from the elevated amplitudes of all the other frequencies that there are serious problems with the given bearing. From the spectrum, we can see that the dominant frequency is the rotating frequency of 10 Hz with its harmonics, as well as the other frequencies FTF = 4.4 Hz, BPFI = 107.3 Hz, BPFO = 82.7 Hz and BSF = 38.1 Hz. We can conclude that for performing the analyses of the spectrum is required possessing a professional knowledge, as well as adequate knowledge for the signal processing techniques.

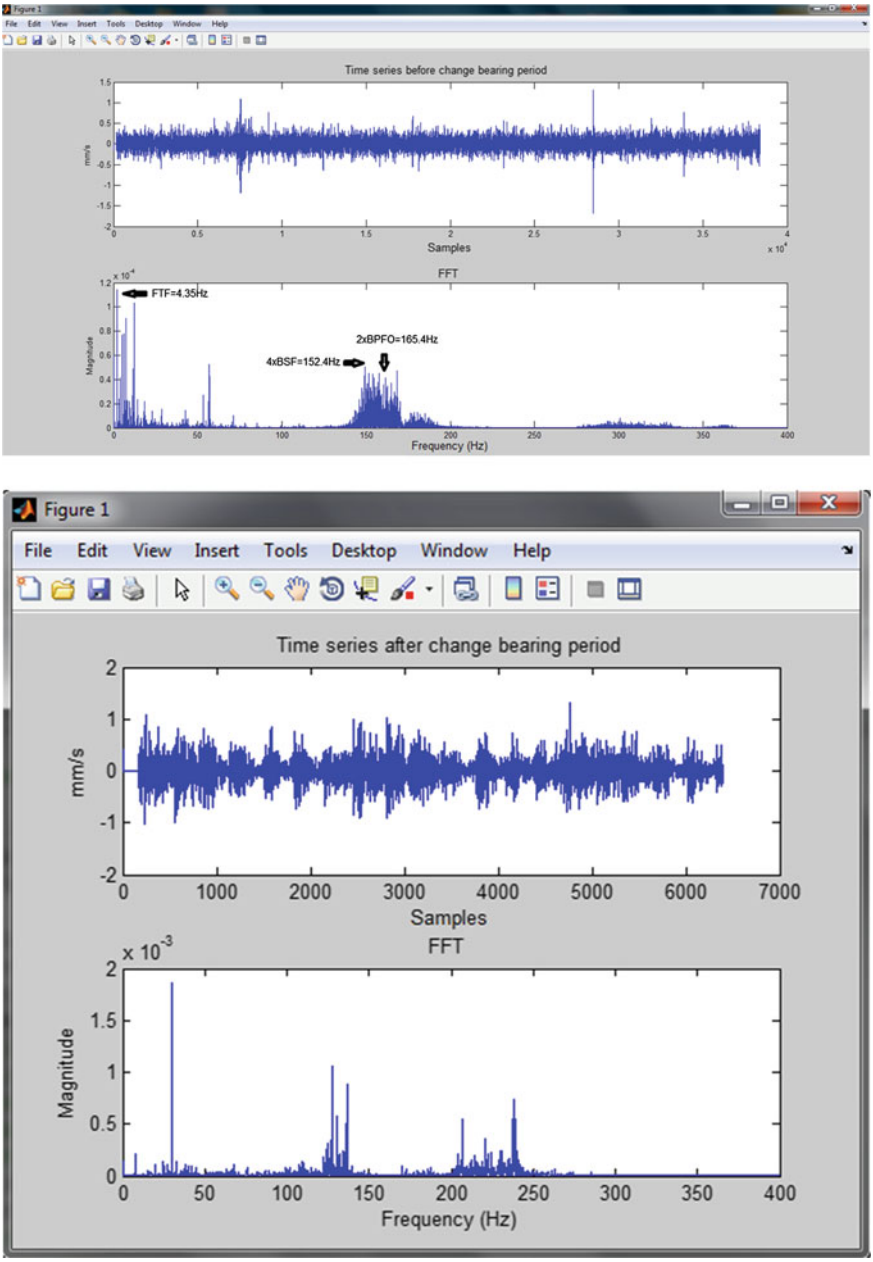

Fig. 5 Spectrum for the bearing NU244MA in a failure period and the period after replacement

We can obtain a better review of the bearing condition by using the time-frequency analyses of the Wigner-Ville distribution (WVD).

The Wigner-Ville distribution (WVD) is a general time-frequency analysis tehnique that provides good resolution along both time and frequency scales in comparision with other joint time-frequency transforms such as short time Fourier transform and wavelet transforms. Another major obstacle in the application of the WVD is due to its non-linear behavior. The non-linearity of the WVD causes the interference between different signal components. The WVD can be written as,

$$W_{xx}(t,f) = \int_{-\infty}^{+\infty} x(t+\tau/2)x^*(t-\tau/2)e^{-j2\pi f\tau}d\tau. \tag{1}$$

The Winer-Ville distribution satisfies the frequency marginal condition

$$|X(\omega)|^2 = \frac{1}{2\pi}\int_{-\infty}^{\infty} W_{xx}(t,\omega)dt. \tag{2}$$

This equation means that the integral of te WVD over the time variable at a certain frequency ω yields the energy density spectrum of x(t) at this frequency. The WVD also satisfies the time marginal condition

$$|x(t)|^2 = \frac{1}{2\pi}\int_{-\infty}^{\infty} W_{xx}(t,\omega)d\omega. \tag{3}$$

These proporties indicate that the WVD can be interreted as the energy distribution of signal. Other importanat signal characteristics that can be defined from the WVD include the instantaneous energy of the signal or signal power

$$P(t) = \int |W_{xx}(t,f)|df. \tag{4}$$

The statistic index Kurtosis represents a very good indicator for the analysis of damages in low speeds machineries with no continuous shocks. It is adimensional, it is defined as the fourth statistic moment of the distribution. The normalized kurtosis for a distribution y(t) given by its N values can be defined as

$$NK(x(t)) = \frac{1}{N}\sum_{i-1}^{N}\left(\frac{x_i - x_{sr}}{\sigma}\right)^4 - 3. \tag{5}$$

It is positive for distribution consisting of a sharp single peak and is increasing with an increase in peak of a distribution. This property of the kurtosis was employed in construction of the NP4 detection parameter. This parameter is a normalized kurtosis of signal power P (t) given by Eq. (6) as

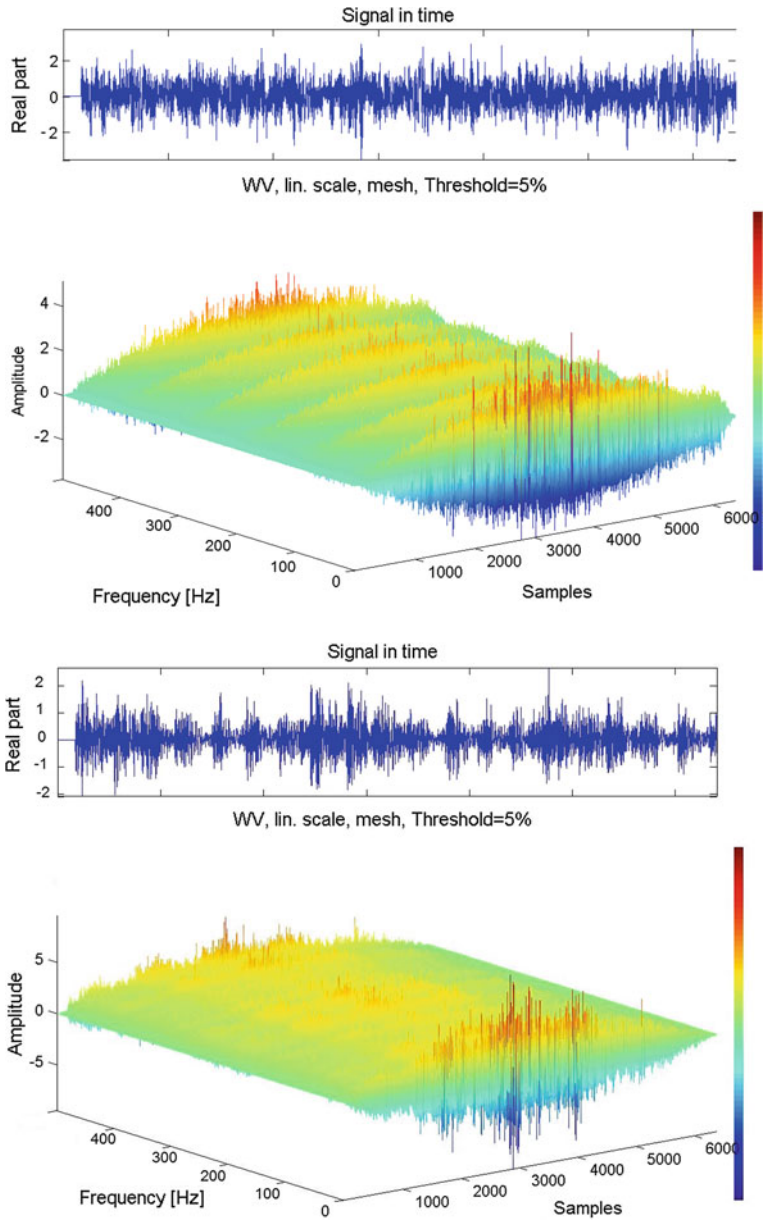

Fig. 6 WVD image of the bearing SKF NU244MA working in a failure period and the period after replacement

$$NP4 = \frac{1}{N}\sum_{i=1}^{N}\left(\frac{P(t_i) - \overline{P}}{\sigma}\right)^4 - 3. \tag{6}$$

Fig. 7 The damage on the cylinder SKF NU244MA after repairing

This NP4 is a non-dimensional parameter. The parameter NP4 depends only on the shape of the power distribution P (t).

The WVD image of the bearing NU244MA, in a failure period and the period after the replacement with a new one (Fig. 6).

When the bearing is in failure period, the normalized kurtosis is 3.2066 and the normalization of the NP4 is 1.9193. For the period after replacing the bearing, the new normalized kurtosis is −0.4905, while the normalization of the NP4 is −0.3615. From this values we can conclude that: whenever the kurtosis is positive or negative we need to calculate the parameter of NP4. When the normalized kurtosis and the NP4 are equal to zero, we have a normal distribution with a certainty claim that there are no damages. When the NP4 < 0 but the NP4 > -1, we have a confirmation of a damaged bearing. If the NP4 < 0 but the NP4 < -1 we can't confirm the damage of the bearing with the NP4 parameter. When the NP4 > 0 there is confirmed damage of the bearing.

After repairing the rolling bearings, visual inspection of the bearing elements show the condition of SKF NU244MA given in Fig. 7.

The simplest way of calculating the L10 bearing life by the ISO suggestions, is using the basic equation which takes the three factors: speed, load and type of the bearing.

$$\mathrm{L10} = (\mathrm{C}/\mathrm{P})\mathrm{p} \tag{7}$$

From the calculations we can observe that the theoretical life of the bearings is 242,528 h. Also, according to the results analyzed in the period from 2003 to 2010 in Table 1, we can conclude that the total life of the fourth bearing is 60,148 h. When comparing the theoretical life of the bearings with the working hours of the bearing fan for fresh air, we noticed that only 25 % of the bearings are working in that period.

Table 1 Working hours on the third and fourth bearings

Years	Repair	Repair bearing	Rh [h]
2002	From 16.04.2002 to 17.06.2002	Repair	4710
2003	From 22.07.2003 to 21.08.2003	/	8006
2004	From 16.06.2004 to 21.07.2004	/	7529
2005	From 28.07.2005 to 17.08.2005	/	7910
2006	From 07.07.2006 to 04.09.2006	/	7215
2007	From 02.06.2007 to 16.07.2007	/	7572
2008	From 15.08.2008 to 12.10.2008	/	7299
2009	From 13.04.2009 to 19.05.2009	/	7822
2010	From 29.03.2010 г. to 16.05.2010	Repair	2085
Total working hours for rolling bearings 3BCB-A			60148

This small percentage of working hours of the rolling bearings is to a sharp deterioration in the vibration condition of the rolling bearings after the repair, dated on 17.07.2007 and it most pronounced in envelope the acceleration in bearings, which is a indication that there is a fault.

With increasing the kurtosis twice then normal (Takeyashi and Highuchi 2004), the coefficient of vibration increasing is 1.49, i.e. 49 %.

According with the formulas (Douglas Berry 1995 12/95) for the cylindrical bearings, the percent of decreasing the bearing life depending of the percent of increasing the loading/vibrations is calculated with this formulation:

% bearing life decreasing = (1 − (1/(1 + (% vibrations increasing/100)))3 1/3) × 100.

For our case, according to the analysis that shows the kurtosis increasing on 3,2066 (twice then normal) which is 49 % increasing the vibrations than normal situation, there is a 74 % of bearing life decrease.

3 Conclusion

Using the statistical analysis of the maximum peak from the vibrations in the period 2003–2011, taken by the constant measurement of the bearing type SKF NU244MA, theoretically and practically calculating its bearing life by using the time-frequency analysis of the Wigner-Ville distribution, we obtained the following conclusions:

There are three periods of a bearing vibration condition (see Fig. 4): 2003–2007 high level of vibrations but still in the normal border, 2007–2010 rapid increase of the vibration level, and 2010–2011 after repairing the bearing. By analyzing the level of vibration through the post—repair period, we detected an error at the beginning of the construction.

- In the comparison of the theoretical life of the bearings of 242,528 h (calculated with the MITCALC) with the working hours of the bearing fan for fresh air of

60,146 h (Table 1), we noted that the bearings actually worked only 25 % of their theoretical life. This conclusion provoked deeper analyses of the bearing vibration condition and discovering the reason for this failure.

- The analysis with the WVD image, together with the normalized kurtosis and the NP4 parameter, give us full confirmation of the occurred errors on the rotation element of the machine (see Fig. 7).

After the review of the bearing reparation on Fig. 7, we conclude the following research studies:

Prolonging the bearing life may depend of choosing the proper type of bearing and the location where it will be placed. The bearing marked with the number 4 on the Fig. 2 is placed radial near the working circuit of the fan, where the axial forces are strongest. Because of the radial type of the bearing that contains cylindrical rollers that are extremely sensitive to the axial forces, it is clear that it will lead in further abrasion of the rollers as a result of the tilt in the rotating paths.

We recommend changing the cylindrical rolling bearing type with barrel or spherical roller bearing, or switching the places of the bearing number 3 (angular contact ball bearing—double row) with the bearing marked under number 4 (cylindrical roller bearing—double row).

References

Boulenger A, Pachaud C (2003) Analyse vibratoire en maintence: surveillance et diagnostic des machines, Sditeur: Dunod—L'Usine 15 janvier

Douglas Berry L (1995) Vibration versus bearing life. Reliability Magazine, 12/95 issue

Kiral Z, Karagulle H (2003) Simulation and analysis of vibration signals generated by rolling element bearing with defect, Tribology International 36

Martin HR,Honarvar F (1995) Aplication of statistical moments to bearing failure detection, Applied acoustics 44

Mathew J, Alfredson RJ (1988) The condition monitoring of rolling element bearings using vibration analysis. J Mecanical Des

MC Fadden PD, Smith JD (1984) Model for the vibration produced by a single point defect in rolling element bearing. J Sound Vibr

Takeyashi K, Highuchi Y (2004) Analysis of the behaviour of kurtosis by simplified model of one sided affiliated impact. Fifth Asia Pacific Industrial Engineering and Management Systems Conference, 25.2.1–25.2.11

Tandon N, Choudhury A (1997) An analytical model for the prediction of the vibration response of rolling element bearings due to localized defect. J Sound Vibr

Taylor IJ (1980) Identification of bearing defects by spectral analysis. J Mech Des 1:199–204

www.mitcalc.com

www.skf.cmva60

www.gearbox.com

On Measurement and Processing Data of the Real Loading: Application to Cement Equipment Components

Radu Onofrei, George Dobre, Radu Florin Mirică and Mihai Pali

Abstract Considering the real task of modern calculations of strength, reliability and durability of a system (or its components) is an actual and important means to achieve many advantages: (a) more precise calculations of the strength, leading to more accurate dimensions (in general—lower) of the product which in turn causes other cost advantages: lower manufacturing cost and lower operational energy costs; (b) a good assessment of the reliability and durability of the product; (c) as a result a better planned and predictive maintenance. The research in field remains open today because the literature does not provide accurate indications regarding: (a) consideration of real loading in calculations, (b) measuring, processing and interpretation of experimental data to develop models of loading. Research objectives in this field were developed to a good investment programming to modernize or rehabilitate a vibrating screen (1,000 … 1,200 t/h) integrated in cement fabrication flow sheet. Measurements of un-modulated real loadings on one of the lateral case wall of the vibrating screen were made. A measuring methodology procedure and an appropriate measuring chain proposed previously by authors (Dobre et al., On the methods to measure the real loading at mechanical systems. In: The 7th international conference research and development of mechanical elements and systems—IRMES, Nis, Serbia, pp 395–400, 2011). The measurement chain was configured by high performance components with relative

R. Onofrei (✉)
Complex Project Division, IMSAT Group SNEF, Bucharest, Romania
e-mail: onofrei.radu@gmail.com

G. Dobre · R. F. Mirică
University Politehnica of Bucharest, Bucharest, Romania
e-mail: G.Dobre@gmail.com

R. F. Mirică
e-mail: mirica@omtr.pub.ro

M. Pali
Transport Automation Installations Division, IMSAT Group SNEF, Bucharest, Romania
e-mail: mihai.pali@imsat.ro

G. Dobre (ed.), *Power Transmissions*,
Mechanisms and Machine Science 13, DOI: 10.1007/978-94-007-6558-0_57,

low costs (strain gauge signal amplifier, acquisition card, computer with large memory, high frequency processor, etc.). The experimental data are counted after this measurement and mean-amplitude frequency matrix is obtained. The loading spectrum for different stages and conditions of operating resulted. Finally conclusions about the main approaches and results of the paper are noted. The processing methodology of the experimental data could be extended to the entire structure of the cement equipment. The paper continues previous researches developed by the Romanian school in this area (Dobre et al., On the Real loading modelling of the mechanical systems. Fiabilitate şi Durabilitate/Fiability and Durability, Nr 1, pp 1–6, Editura Academică Brâncuşi, Târgu Jiu, ISSN 1844-640X, 2010), (Mirică et al., On the theoretical-experimental modeling of loading of the mechanical transmissions. In: Proceedings of 3rd international conference on power transmissions, Kallithea—Chalkidiki, Greece, pp 291–296, ISBN 978-960-242-662-2, 2009), (Dobre et al., On the loading modeling of the mechanical systems. In: The 13th international conference on machine design and production, 03–05 Sep 2008, Istanbul, Turkey, vol II, pp 417–480, 2008).

1 Introduction

The new development programs in the field of industrial equipment take into consideration the accumulated experience in mechanical design using real loading data of machine elements during operating. The equipment of cement industry operate in very hard conditions, the machine elements being under great stress depending on raw material processing methods, kind of raw materials, atmospheric condition, etc.

The first registrations of real loading were realized by Gassner approximately in 1935 (Haibach 1989). Loading spectra were used initially for the real loading modeling; after 1972 till present different versions of Rainflow matrices (Haibach 1989; Buxbaum 1992) are also approached. A valued analysis of the models developed for modeling the real loading and the procedures for achieving them was presented by Günther et al. (1973). Currently research is focused mainly towards elaborating models of loading in different areas of machinery and equipment construction and high buildings subject to wind action, drilling platforms subject to wave action, etc. Another direction is the extrapolation of these models.

This paper presents some results obtained by measuring the load of a vibrating screen used to classify raw material in a cement factory. The paper is structured in two main parts. The first one describes the construction of the vibrating screen and its operation. Forward is presented the measuring chain and its components. The second part describes sequences of registered loading history for main operating stages, from plug-into stop function (start-up stage, idle running, load running with raw material, idle running after raw material supply is cut-off and damping time

stage after plug-off the machine). It is described the registered data processing in order to classify the loading values by obtaining the mean-amplitude matrix, a variant of Rainflow matrix (AFNOR A 03-406: 1993), which represents in fact the occurrence frequency matrix. After this, a method of matrix data filtering is described in order to eliminate the non-damaging cycles and how is verified the recommendation that the registration of pair of values mean-amplitude to be done for either rising or decreasing semi-oscillations (Günther et al. 1973).

Finally, the loading spectrum is presented with the two components: (a) the main one in the range of high stress corresponding to operating processes, start-up and stop one; (b) the secondary one with the mean in the negative stress range (compression), corresponding to non-steady and short period of time processes which mainly occurs at start-up and stop. It is described the method of average mean calculated for each amplitude level to realize the loading spectrum (Haibach 1989) and comparison with methods used and presented by professional literature is made.

2 The Analyzed Vibrating Screen

The layout of the analyzed vibrating screen with the main assemblies is presented in Fig. 1.

The circular motion of the electrical motor is transmitted by V-belts and a cardan shaft to the Eccenter. The two rotary drives and the twin-type unbalance gear produce directive vibrations because of rotation in counter sense only (see Fig. 2). It takes some time for the machine to run smoothly after it has been switched on.

The buffer elements, which in this case are helical springs, transmit nearly static forces (consisting of machine weight and material load) to the supporting structure of the screen. These flexible elements reduce the alternating dynamic forces which are generated by the vibrating movement to the residual values.

The screening machine operates with two superimposed screen lining which are attached by an appropriate clamping mechanism. There were two types of screening lining which were used during measuring process—wire mesh and perforated plate.

Some technical data of the vibrating screen follows:

- weight of screening machine: approximately 9,800 kg with drive;
- operational vibration frequency, 750 min^{-1};
- stroke of screen: maximum 16 mm;
- inclination of drive towards horizontal: 50°;
- motor: power 22 kW, speed 1,500 min^{-1};
- excitation is by the twin-type unbalance gears;
- type of drive: via V-belt gear.

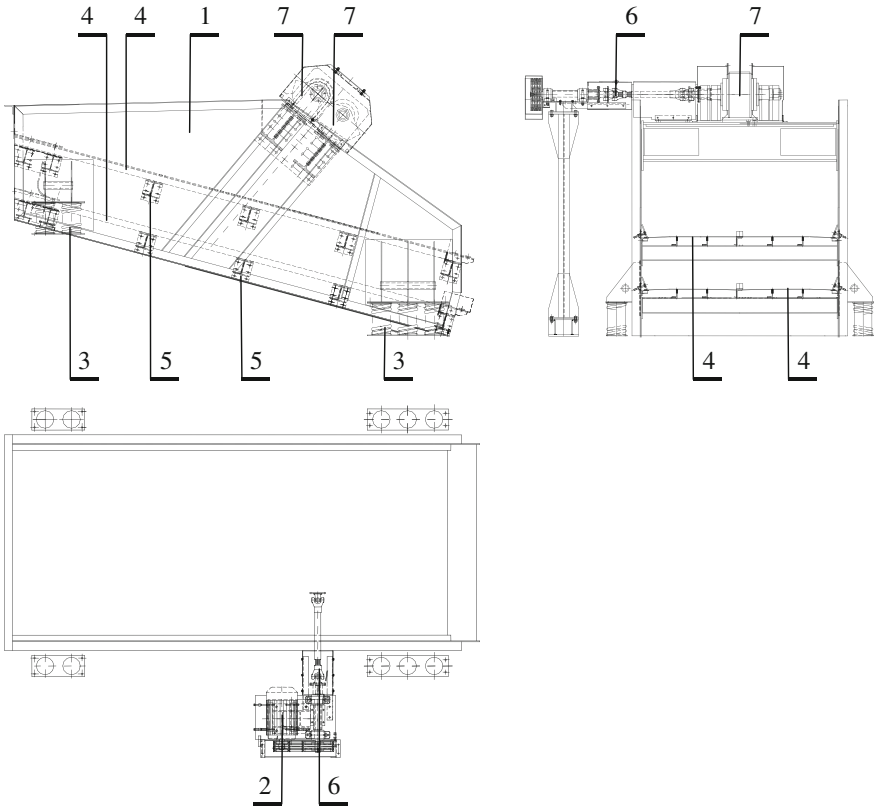

Fig. 1 Vibrating screen layout. *1*—Screen box. *2*—Unbalance drive. *3*—Buffer elements. *4*—Screen lining. *5*—Supporting structure. *6*—Cardan shaft. *7*—Eccenter

Frame and housing structures of industrial equipment come generally during operation under non-modulated loadings which has the variation cycles not univocally determined (Dobre et al. 2011). The un-modulated loading can be modeled by several methods, the obtained models being considerable different one to each other (Buxbaum 1992).

3 Measuring Instrumentation

The measuring chain adopted for this application is described in Fig. 3. To collect the signal a full strain gauge bridge is used with configuration including two strain gauges of 120 Ω and nominal gauge factor of 2.0 and two fixed precise resistances of 120 Ω in opposite sides. The strain gauges are positioned in order to be tensile stressed and they were glued on the lateral wall of the screen box. The bridge excitation of ±2.5 V is delivered by the strain gauge amplifier.

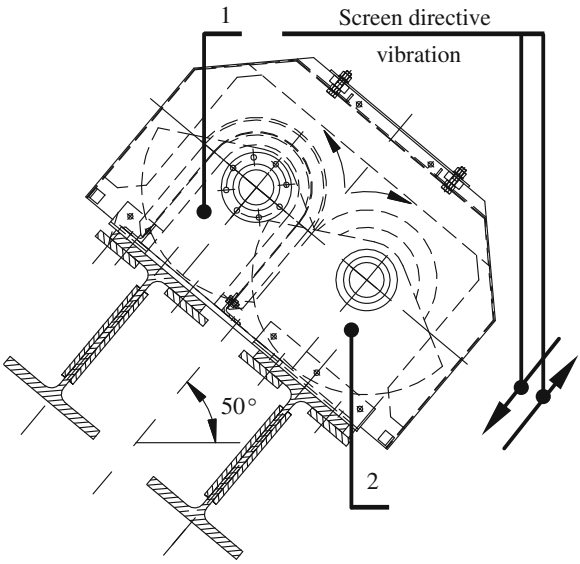

Fig. 2 Drive of the eccentrics in counter sense of rotation generates directive vibration of the screen (*1, 2*—eccentric pulleys)

The strain gauge bridge signal is amplified and delivered to the acquisition card NI 6008 from National Instruments.

The analog signal registration of un-modulated loadings is performed with sampling clock generated at equal time intervals (Dobre et al. 2011).

The acquisition software is written in LabView and permits to visualize the evolution of the signal during the acquisition process as shown in Fig. 4. The level of reference signal adjusted at 5 V and the variation of the signal amplitude in time can be seen.

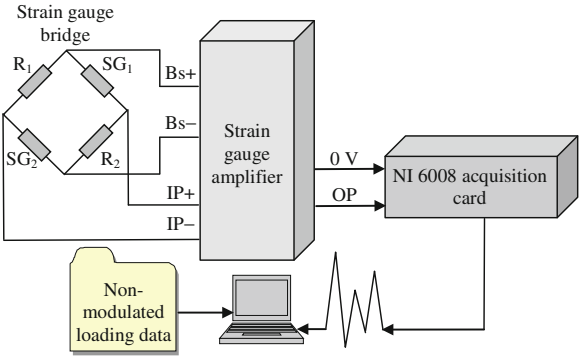

Fig. 3 The measuring system of un-modulated real loading. SG_1, SG_2—strain gauges of 120 Ω and nominal gauge factor of 2.0; *R1, R2*—120 Ω precise resistors; *Bs+*, *Bs*—supply bridge; *IP+*, *IP*—amplifier input signal; *OP*—amplifier output signal (positive potential)

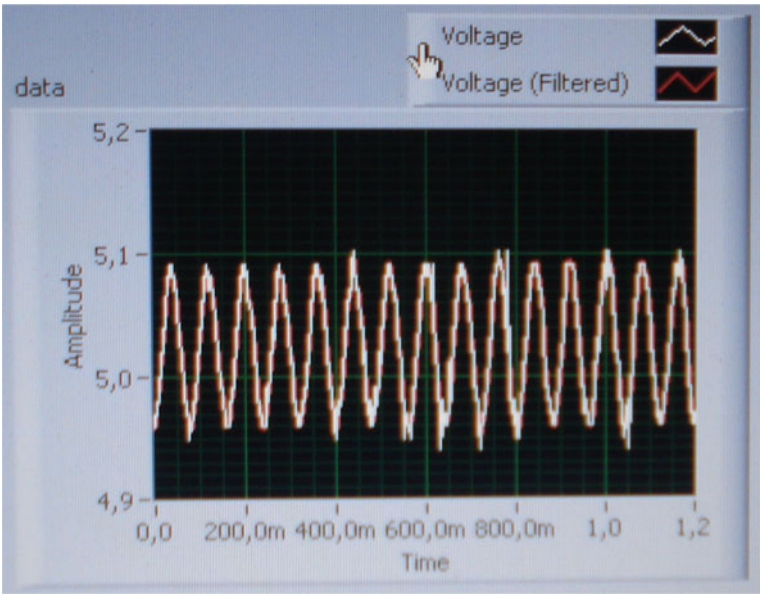

Fig. 4 Example of acquisition and registration process evolution for the screening machine

4 Vibrating Screen Operating

The transport and sorting flow sheet of limestone from the limestone quarry to the cement factory integrates the vibrating screen into the limestone waste dump sorting station. The raw material is transported and supplied by a system of ten belt conveyors to the vibrating screen, to sort it into three granulation classes. The sorted raw material is sent to the factory and used to cement and lime production.

The vibrating screen operating in time can be divided in the following main stages, from plug-into stop function: start-up stage, idle running, load running with raw material, idle running after raw material supply is cut-off and damping time stage after plug-off the machine.

The start-up stage is characterized by increasing step by step of the loading amplitude, as it is shown in Fig. 5, till the machine touches the idle running stage. On abscise is given the time in seconds and on ordinate is the relative level of loading history.

The idle running stage shows quasi-constant amplitude because of constant loading represented by own inertial mass.

The loading behavior changes when the raw material supply starts. Figure 6 shows a deep random variation of the loading amplitude when the raw material supply starts and in Fig. 7 is represented a detail of the signal between second 4 and 5 were low oscillations superimposed on main oscillations can be observed. It can be seen the excitatory succeed to set its operating frequency to the entire assembly and so, the period of the main cycles is approximately constant.

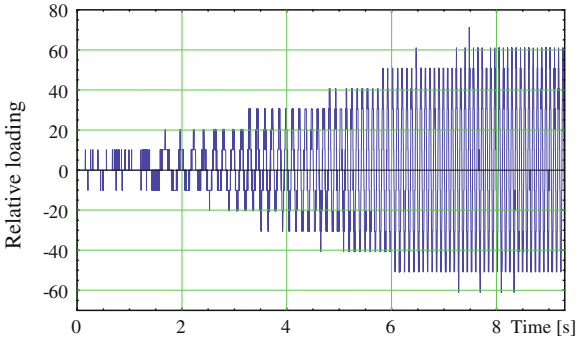

Fig. 5 Loading history sequence for the start-up stage

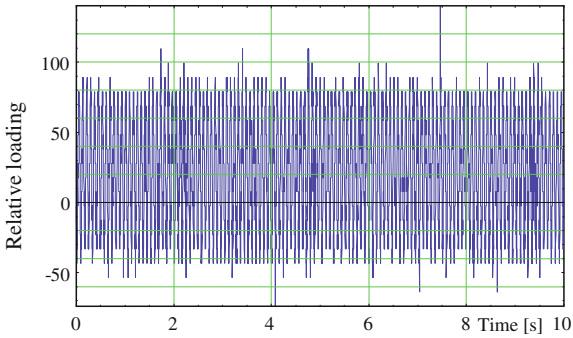

Fig. 6 Example of loading history sequence for the start of load running stage

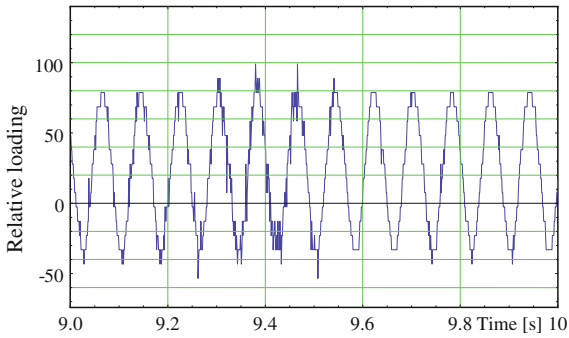

Fig. 7 Detail between second 4 and 5 of loading history sequence from Fig. 6

It can be remarked also a deep random variation of the amplitude approximately symmetric around the mean value during the load running stage. However, raw material debit fluctuation gives changes of mean loading value level. Two sequences of loading history for this stage are presented in Fig. 8 for low level of raw material debit and in Fig. 9 for a high level one.

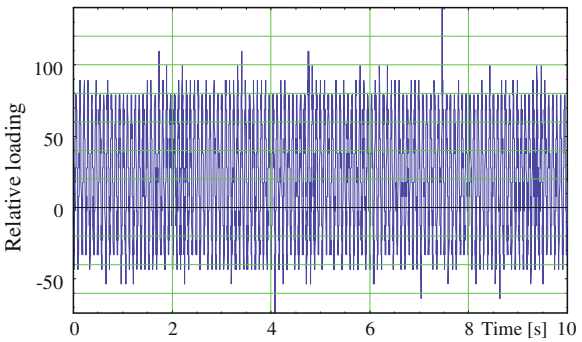

Fig. 8 Loading history sequence for the load running stage with low raw material supply debit

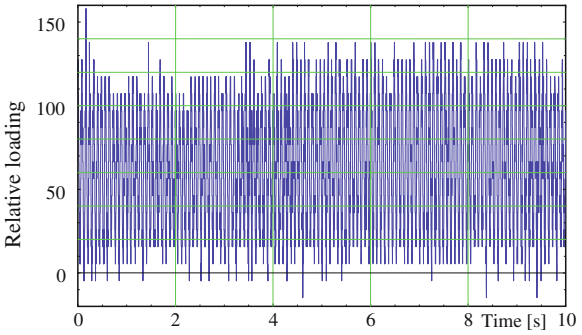

Fig. 9 Loading history sequence for the load running stage with high raw material supply debit

5 Loading Counting

The loading raw data are registered in sets of files. Non-filtered signal was registered to allow a later analysis by several methods including filtering. The chosen sampling frequency was enough for accurate record of measured signal. So, sets of peak and valley loading values were obtained for each operating stage of vibrating screen.

A vector for the entire loading history, were considered,

$$X = \{x_1, x_2, \ldots, x_n\}. \tag{1}$$

$x_1, x_2, \ldots, x_n$ are the loading samples either peak or valley, in order of appearance and register.

A new vector with components formed by two elements were generated,

$$Y = \{[mean_1, amplitude_1], [mean_2, amplitude_2], \ldots, [mean_n, amplitude_n]\}. \tag{2}$$

The mean and amplitude, of the Y vector components, were calculated as indicated below.

$$mean_i = \frac{x_i + x_{i+1}}{2},\ amplitude_i = \frac{x_{i+1} - x_i}{2},\ x_i, x_{i+1} \in X \tag{3}$$

The values of mean and amplitude were rounded by a coefficient and a new vector with the components formed by rounded mean and rounded amplitude was generated. In this way, the classification of values can be realized.

The values of minimum mean, maximum mean, minimum amplitude and maximum amplitude were kept in. These are in fact the mean-amplitude matrix dimensions (the number of rows and columns) can be calculated by dividing the difference between maximum and minimum of mean or amplitude to the above rounding coefficient. The number of classes is the number of the matrix lines and columns and the mean-amplitude matrix is the occurrence frequency matrix.

The pair of rounded values $[mean_i, amplitude_i]$, part of the Y vector, were counted and the loading history occurrence frequency matrix of the current measuring point were obtained. According to AFNOR A 03-406, this matrix is one of the Rainflow matrix versions.

Because of an easier counting algorithm and making sure of the affirmation by which there is necessary to count either the rising or decreasing semi-oscillations (Günther et al. 1973), both of them were counted. An approximately symmetric matrix shown in Fig. 10 was obtained.

Although the semi-oscillations are random succeeded, if the measuring time is long enough, the probability to find for each rising semi-oscillation (characterized by the pair mean-amplitude) a decreasing semi-oscillation (with the same mean and amplitude) is very high. The negative amplitudes from Fig. 10 are calculated with the expression (3) for decreasing semi-oscillations i.e., for $x_{i+1} < x_i$.

The range (class) of the null amplitude is between the two sides of the matrix and there was counted the lowest oscillations for which the picks become equal by including them in the same class. In this way the oscillations "filtering" with very low amplitude is realized. Forward it was used only the rising semi-oscillations matrix shown in Fig. 11.

The matrix in Fig. 11 shows very high occurrence frequencies in the low amplitude range. This means the measured signal was not filtered. The most high amplitude oscillations are in the range of positive oscillations because of the load

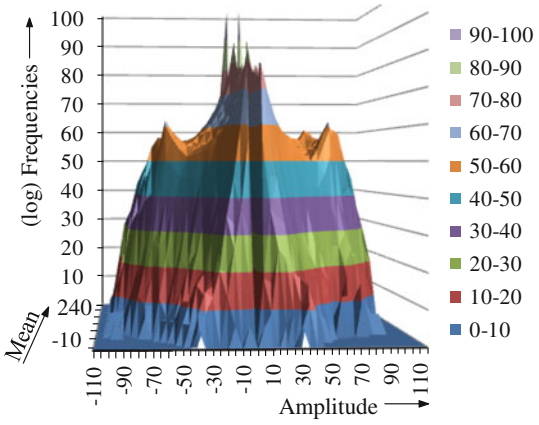

Fig. 10 Symmetrical mean-amplitude-frequency matrix of counted semi-oscillations of the loading (mean and amplitude are dimensionless)

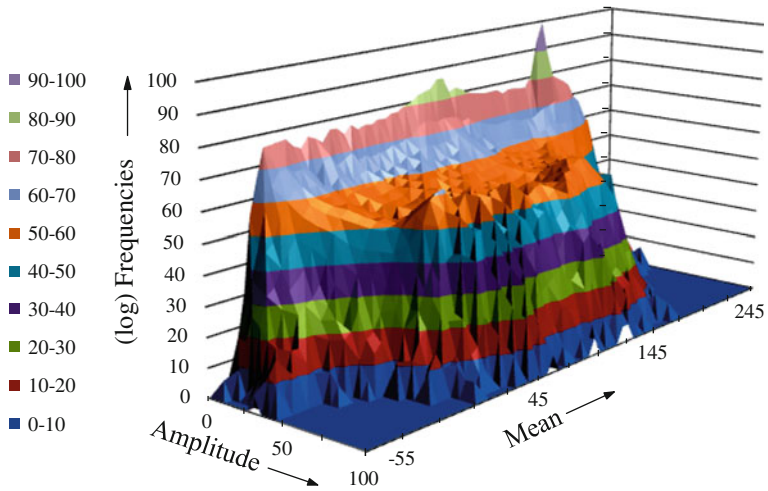

Fig. 11 Content of used mean-amplitude-frequency matrix of the counted loading semi-oscillations (mean and amplitude are dimensionless)

during operating. Multiple low amplitude oscillations are in the negative range of the mean because of non-filtered high frequency oscillations superimposed by negative portion of some high amplitude oscillations corresponding to start-up, idle running and stop stage.

The filtering of the signal can be performed by eliminating the low amplitude oscillations with high frequency. Anyway, if a very low amplitude oscillation has high level mean value then it can have important damaging effect and it will be not eliminate.

The authors consider that the signal "filtering" can be more adequately realized by choosing the counting class width and eliminating of undamaging oscillations. So, a proper algorithm of undamaging oscillations removal can be made using the sum of the two values (mean and amplitude).

If it is accepted that the maximum sum value of mean and amplitude doesn't have to pass the material flow limit, the endurance limit of the welded steel is a half of flowing limit (see DIN 743-3: 2008), the tensile less than half of fatigue stress are considered as undamaging and taking into consideration the safety factor of 1.25 for such equipment, the authors consider, having their own experience, that the oscillations with the sum of mean and amplitude less than 0.33 by the maximum value of this sum and for which were counted oscillations, can be removed from the matrix.

Figure 12 shows the matrix content after removing the oscillations considered un-damaging. Comparing Figs. 12 and 11 it can be seen the removed part of the matrix. Oscillations with negative mean derived from the start–stop non-steady process remained. The most damaging oscillations are in the positive range of the mean.

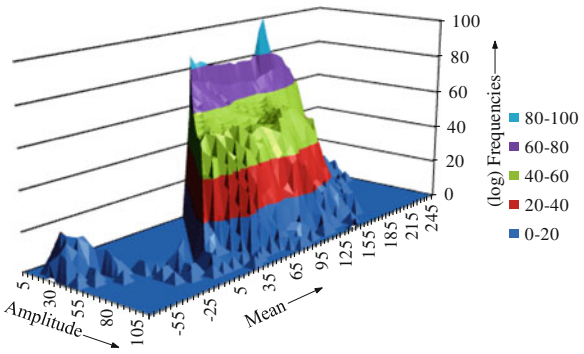

Fig. 12 The matrix of mean-amplitude-frequency from Fig. 11 after elimination of cycles considered as undamaging

A representation and a simplified model towards the mean-amplitude matrix is the loading spectrum. Being a simplified model, it is easier to use in calculations and experiments, but it is less precise.

6 The Obtained Loading Spectrum

The method using an average mean calculated for each amplitude level (Haibach 1989) was adopted to realize the loading spectrum from Fig. 13. This is justified because different operating phases with different average mean (start-up and stop, idle running, load running with fluctuant raw material debit) are included in the loading spectrum. A similar representation with variable average mean was used in NLR-TR-84043 for the loading spectra HELIX and FELIX (Edwards et al. 1984) probably for the same reason mentioned before.

The determinations of average mean using the simplified matrix (after elimination of undamaging cycles) carry on to a little bit higher mean values only in the range of low amplitudes which are considered enclosure. However, the method of averaging all mean values corresponding to amplitude introduces a certain error

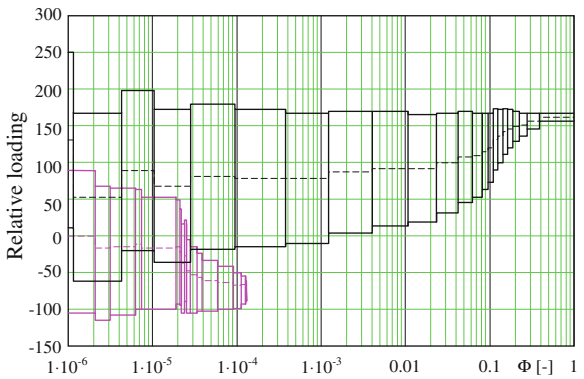

Fig. 13 The obtained loading spectrum

because of this approximation, even if the loading mean value variation has a lower influence than amplitude variation.

Figure 13 shows two components of the proposed loading spectrum for modeling the real loading measured in situ:

- the main one in the range of high stress corresponding to operating processes, start-up and stop one;
- the secondary one with the mean in the negative stress range (compression—in the realized experiment), corresponding to non-steady and short period of time processes which mainly occurs at start-up and stop.

7 Conclusions

1. The loading of the analyzed vibrating screen is non-modulated and can be built by several methods, the obtained models being considerably different one of other.
2. The vibrating screen oscillation ranges of the recorded loading history sequences are quasi-stochastic because of operating with fluctuant raw material debit (calk stones).
3. The excitatory succeed to set the operating with the own rotation frequency. That is why the main cycle period is approximately constant. Low oscillations superimposed on main oscillations can be observed.
4. The recommendation that the registration of pair of values mean-amplitude to be done for rising or decreasing semi-oscillations (semi-cycles) was verified by statistical processing of both types of semi-cycles. A quasi-symmetric matrix (on the amplitude direction) was obtained because of long enough measuring time.
5. The non-filtering raw signal registration permits to keep in some low damaging oscillations and allows later processing by various methods including by filtering.
6. The classification of means and amplitudes are carried out by rounding with a coefficient which depends on the adopted number of classes of the variation range of them.
7. The oscillations with very low amplitude are eliminated if they do not pass the class range, being counted as having null amplitude.
8. The authors proposed a simple method of eliminating the cycles considered undamaging.
9. The loading spectrum includes besides the main component due to the operation, a component of short-term start-up and stop processes, too.
10. It is recommended for calculations the data contained in mean-amplitude occurrence frequency matrix to be used, because the loading spectrum is less precise due to means averaging.

References

AFNOR A 03-406:1993. Produits métalliques. Fatigue sous sollicitations d'amplitude variable. Méthode Rainflow de comptage des cycles

Buxbaum O (1992) Betriebsfestigkeit: Sichere und wirtschaftliche Bemessung schwingbeanspruchgefährdeter Bauteile, Verlag Stahleisen, Düsseldorf

DIN 743-3:2008. Tragfähigkeitsberechnung von Wellen und Achsen. Werkstoff-Festigkeitswerte

Dobre G, Mirică RF, Miloiu G, Itu V, Dumitrescu I (2008) On the loading modeling of the mechanical systems. In: The 13th international conference on machine design and production, 03–05 Sep 2008, Istanbul, Turkey, vol II, pp 417–480

Dobre G, Mirică RF, Cănănău S (2010) On the Real Loading Modelling of the Mechanical Systems. Fiabilitate şi Durabilitate/Fiability and Durability, Nr 1, pp 1–6, Editura Academică Brâncuşi, Târgu Jiu, ISSN 1844-640X

Dobre G, Mirica RF, Onofrei RF (2011) On the methods to measure the real loading at mechanical systems. In: The 7th international conference research and development of mechanical elements and systems—IRMES 2011, Nis, Serbia, pp 395–400

Edwards PR, Darts J et al (1984) Standardized fatigue loading sequences for helicopter rotors (Helix and Felix). Part 1: Background and fatigue evaluation Part 2: Final definition of Helix and Felix

Günther W et al (1973) Schwingfestigkeit. VEB Deutscher Verlag für Grundstoffindustrie, Leipzig

Haibach E (1989) Betriebsfestigkeit: Verfahren und Daten zur Bauteilberechnung. VDI-Verlag, Düsseldorf

Mirică RF, Dobre G, Itu V, Dumitrescu I (2009) On the theoretical-experimental modeling of loading of the mechanical transmissions. In: Proceedings of 3rd international conference on power transmissions, Kallithea—Chalkidiki, Greece, pp 291–296, ISBN 978-960-242-662-2

Design of a Mechatronic System for Recovery of the Disabled Persons

Petre Lucian Seiciu

Abstract The paper presents a state-of-the-art mechatronic system for recovery of the locomotory disabled persons: SIMESIM. SIMESIM's proper design has to take into account the state-of-the-art theoretical aspects of human walking. There are two main theories to be taken into account: "The Six Determinants of Gait (SDG)" theory and "The Inverted Pendulum Analogy (IPA)" theory. Both theories explain human walking but have shortcomings that may be solved through a new theory: "The Dynamic Walking Theory (DWT)". These theories describe, more or less, appropriate walking of healthy persons. The presented theoretical aspects are to be considered at the special mechanical transmissions design of the mechatronic system for the locomotory disabled persons.

Keywords Mechatronic system · Special transmission · Rehabilitation

List of symbols

c_{et}	Energetic cost
c_{mt}	Theoretical lower limit for the cost of transport
CAD	Computer aided design
COM	Center of mass
$\vec{F}_1$, $\vec{F}_2$	Forces on the legs
$\vec{F}_x$, $\vec{F}_y$	Horizontal and vertical reaction forces
$\vec{F}_{1x}$	Vertical force of the trailing leg during double support
g	Gravity constant
GRF	Ground reaction forces
h	Height
IPA	The "Inverted Pendulum Analogy" theory
J	Collision reduction factor

P. L. Seiciu (✉)
University POLITEHNICA of Bucharest, Bucharest, Romania
e-mail: lucian.seiciu@as.info.ro

G. Dobre (ed.), *Power Transmissions*,
Mechanisms and Machine Science 13, DOI: 10.1007/978-94-007-6558-0_58,

l	Leg length
r	Momentum arm of body weight about the knee
s	Step length
sf	Foot length
SDG	The "Six Determinants of Gait" theory
STS	Step-to-step model
v	Average velocity
$\vec{v}_{COM}$	Center of mass speed
VR	Virtual reality
W_1	Negative work
W_2	Positive work
WR	Positive work rate
α	Leg angle related to vertical position

1 Introduction

Walking is one of the most important features of humans. Therefore, the scientific study of the human movement is mandatory both for its theoretical understanding and for medical purposes.

Walking failure leads to serious problems in fulfilling the most common daily activities such as stair climbing, sidewalk walking and street crossing leading in time to total loss of the limb control.

The mechatronic technology and virtual reality in rehabilitation proved to be promising research directions.

The number of people that need this type of rehabilitation is larger and the request of therapy at lower costs is higher.

The social and the material costs are huge, and most of the times the patients lives are changing dramatically.

The system users can be found in very wide domains starting with the health system (hospitals, rehabilitation centers), and finishing with the persons with disabilities themselves.

Several scientists showed that training reduce disabilities provoked by stroke, even if the rehabilitation takes place in the chronic phase (several months after the date of the stroke).

Theoretically, prolonged and intensive rehabilitation is needed to treat post–stroke patients but the real life situation is different for most of them.

This is why virtual reality (VR) is a technology suitable for rehabilitation therapy.

VR has the capacity to simulate real–life tasks while providing the means to better measure and evaluate the patient's performance.

VR also provides real-time data collection from the sensors attached to the patient's body.

These data are used for the requested feedback and for recording in databases for future evaluation.

The modern rehabilitation methods were used only in the last period at a small level, due to a lack of equipments.

The use of the gait trainers, as a new method appeared like an alternative to the classical rehabilitation (Hesse et al. 2000a and b). The results are similar to the classical methods.

A consistent difference appeared with the use of the mechatronic gait simulation systems (Mauritz 2002; Tong and Granat 1999; Uhlenbrock et al. 1997). In this moment there are only a few systems operating (in Germany, Switzerland, USA).

The paper mainly aims to cover new aspects of the design and assembly of state-of-the-art mechatronic system (MS). Two theories are taken into account in developing the paper: "The Six Determinants of Gait (SDG)" and "The Inverted Pendulum Analogy (IPA)", their shortcomings being solved through a brand new theory "The Dynamic Walking Theory (DWT)". The hereby proposed solutions lead the author to the conclusion that, in order to improve MS functioning, a more thorough scientific study of walking is needed.

2 Walking Efficiency Aspects

Human walking is theoretically explained by two prevailing, but contradictory theories. The first theory called "The Six Determinants of Gait" (SDG) aims to minimize the energetic cost of locomotion by reducing the vertical displacement of the body center of mass (COM). The second theory called "The Inverted Pendulum Analogy (IPA)" suggests that walking is a movement combination of two pendulums: the inverted pendulum for the stance leg and a direct pendulum for the swing leg.

For a proper design of the mechatronic system, walking efficiency was considered for both theories.

2.1 The Six Determinants of Gait Theory

The six determinants of gait theory (Saunders et al. 1953; Zajak et al. 2002 and 2003) are based by the model in which the gate is fragmented in six different phases due to the relative position of the legs. For example, one of the determinants is the stance phase knee flexion.

The main idea is that vertical and horizontal displacements of the body center of mass (COM) are energetically costly. This leads to a set of kinematic features

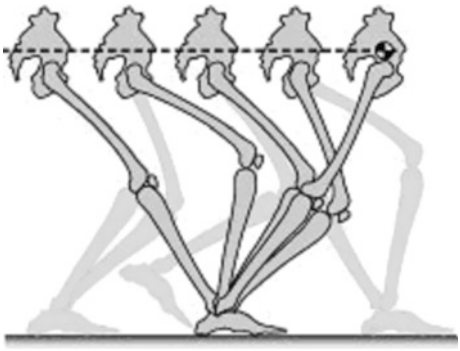

Fig. 1 The six determinants of gait (Kuo 2007)

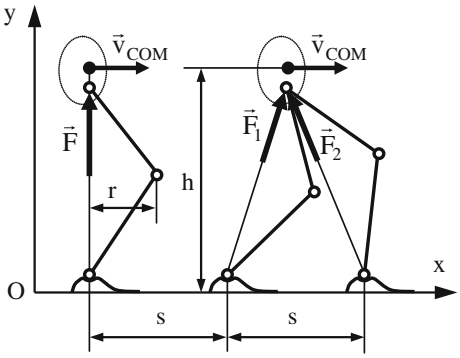

Fig. 2 Simple walking SDG model

that help to reduce the COM displacement. Motions such as flexion of the knee during the stance phase and rotations of the pelvis are therefore coordinated so as to reduce displacements of the COM (as seen in Fig. 1) so that it follows a flat trajectory.

The analysis is made with a simple walking model presented in Fig. 2 (Seiciu et al. 2008a, b). COM moves at constant height h with constant speed $\vec{v}_{COM}$. The two legs produce the forces $\vec{F}_1$ and $\vec{F}_2$. The geometric variables are the height h of the COM, the step length s, and the moment arm of body weight about the knee r, all normalized by leg length. $\vec{F}_x$ and $\vec{F}_y$ are the reaction forces in the horizontal and vertical directions for the single support. $\vec{F}_{1x}$ is the vertical force of the trailing leg during double support. All forces are normalized by body weight, and all length measurements are normalized by leg length. The work performed per step may be calculated as follows. The vertical force must equal body weight, and the ground reaction force must be directed along the leg. It results:

$$\begin{cases} F_y = 1 \\ \dfrac{F_x}{F_y} = \dfrac{x}{h}. \end{cases} \tag{1}$$

The leg will perform first negative work on the COM line and following mid-stance, positive work. The positive work per step during single support is:

$$W_1 = \int_0^{\frac{s_1}{2}} F_x dx = \frac{s_1^2}{8 \cdot h}, \tag{2}$$

where the integration bounds are restricted to the displacements following mid-stance. Negative work, which is entirely performed prior to mid-stance, equals W_1. Both legs produce forces along themselves and perform work against each other during double support. The total vertical leg force must equal body weight. The total horizontal leg forces must produce zero net acceleration over double support. This may be accomplished by equating the forward and backward components of force from the two legs, so:

$$\begin{cases} F_{1x} - F_{2y} = 0 \\ F_{1y} + F_{2y} = 1 \end{cases}. \tag{3}$$

These lead to:

$$\begin{cases} \frac{F_{1x}}{F_{1y}} = \frac{x}{h} \\ \frac{F_{2x}}{F_{2y}} = \frac{s-x}{h} \end{cases}. \tag{4}$$

Combining the above equations yields the leg forces:

$$\begin{cases} F_{1x} = F_{2x} = \frac{-x^2+s \cdot x}{s \cdot h} \\ F_{1y} = \frac{s-x}{h} \\ F_{2y} = \frac{x}{s} \end{cases}. \tag{5}$$

The positive work performed is found by integrating from the end of single support to the beginning of the next single support,

$$W_2 = \int_{\frac{s_1}{2}}^{s-\frac{s_1}{2}} F_{1x} dx = \frac{2 \cdot s^3 - 3 \cdot s \cdot s_1^2 + s_1^3}{12 \cdot s \cdot h}. \tag{6}$$

The total work per step is:

$$W = W_1 + W_2 = \frac{4 \cdot s^3 - 3 \cdot s \cdot s_1^2 + s_1^3}{24 \cdot s \cdot h}. \tag{7}$$

The mechanical cost of transport is the total work per step divided by s. If h is large, the cost is low. This may be accomplished by constraining double support to begin and end with one leg straight:

$$h = \sqrt{1 - \left(s - \frac{s_1}{2}\right)^2}. \tag{8}$$

The cost of transport also depends on the relative proportions of single and double support. Double support is more costly than single support. The most economical flat COM trajectory is achieved with single support dominating the step ($s_1 = s$) and with an instantaneous double support phase. The dimensionless positive work rate is (Kuo 2007):

$$WR = \frac{s^2 \cdot f}{4 \cdot \sqrt{4 - s^2}}. \tag{9}$$

where f is step frequency, normalized by the natural frequency of the leg, $g^{0.5} \cdot L^{-0.5}$.

Real walking presents a non-flat COM trajectory and also experiments confirm the high cost of transport with flat COM trajectory.

2.2 The Inverted Pendulum Theory

The inverted pendulum theory states that the stance leg is relatively straight and supports the COM. The COM moves in a pendular arc, with no mechanical work needed to sustain the motion (Fig. 3).

The simple walking IPA model presents a different approach than SDG theory. In this case, the COM is supported by a weightless leg acting as an inverse pendulum during single support. The stance leg the stance leg remains fairly

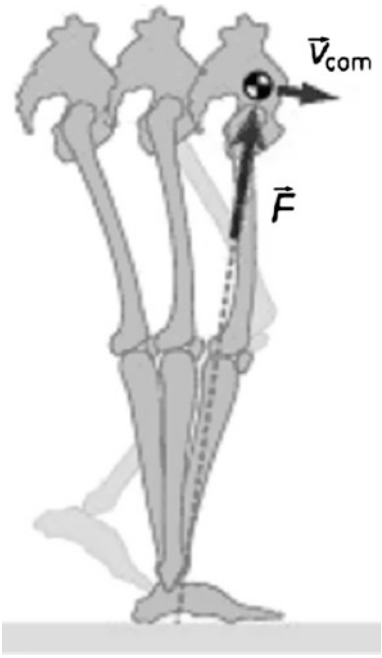

Fig. 3 The inverted pendulum (Kuo 2007)

straight during single support (SS), so little knee torque is needed to support body weight. In midpoint the ground reaction force is directed from the center of pressure to the COM. Along the whole length of the SS line, the COM velocity is directed perpendicular to the ground reaction force and no work is performed on the COM, which may be transported along the pendular arc with no energy input. At the same time, the swing leg moves like a pendulum and this leads to the conclusion that the energy-conserving properties of both require no work. This is in direct conflict with the SDG theory. The pendulum analogy therefore offers multiple explanations for why walking should cost no energy whatsoever, and not why it costs any energy at all. It is therefore necessary to consider how walking deviates from pendulum behavior, and whether this deviation might cost energy.

This model offers a strategy for reducing energy expenditure to zero which is not logical since it doesn't explain the actual energy cost of walking.

In fact the IPA model can be considered only a start model for a realistic energy efficiency walking analysis. A more realistic model is the step-to-step (STS) model, presented in Fig. 4 (Seiciu et al. 2008a, b). This model states that the energetic cost occurs only in step-to-step transitions. With the same method used with the SDG model, the positive work per step performed by the trailing leg (Kuo 2002) is:

$$W_1 = \frac{1}{2} v^2 \cdot \tan^2 \alpha \approx \frac{1}{2} \cdot v^2 \cdot \left(\frac{s}{2}\right)^2 = \frac{1}{8} \cdot f^2 \cdot s^4. \tag{10}$$

The dimensionless positive work rate is (Kuo 2007):

$$WR = \frac{1}{8} \cdot f^2 \cdot s^4. \tag{11}$$

The theoretical lower limit for the cost of transport (Collins et al. 2005) in walking models is $c_{mt} = 0$. This can be achieved by swaying the upper body with springs in such a manner as to totally eliminate the collision losses. Without swaying the upper body, a motion that would have significant energetic cost in humans, a rough lower bound on energetic cost can be estimated from the point-mass small-angle model

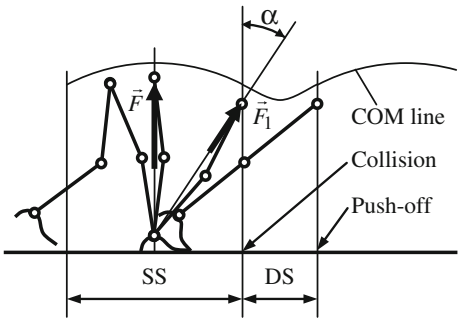

Fig. 4 Simple walking STS model

$$c_{et} \geq c_{mt} \geq J \frac{(s - s_f)^2 \cdot v^2}{2 \cdot g \cdot d \cdot l^2} \approx 0.0003. \quad (11)$$

where J is the collision reduction factor, which is 1/4 for push-off before heel-strike, $s \approx 04\ m$ is the step length, $s_f \approx 0.2\ m$ is the foot length, $l \approx 0.8\ m$ is the leg length, $v = 0.2\ m/s$ is the average velocity, and $g = 10\ m/s^2$ is the gravity constant. Other values of c_{et} for real models (Collins et al. 2005) are presented in Table 1.

Of the two important walking theories, the author uses the SDG theory to compute the work efficiency, the results being used for the mechatronic system design.

The design also must take into account some cinematic particularities that result from the use of a special developed crank-reciprocating rod mechanism.

2.3 Ground Reaction Force

The design of the mechatronic design must take into account the variation of the ground reaction force during the gate. Ground reaction forces (GRF) have been used widely to assess and characterize the walking (Damavandi et al. 2012). The measurements in turn may be used to calculate joint forces, muscle, moments, and segment mechanical energy during normal and abnormal movements, as well as to be used at the design of the rehabilitation mechatronic systems. These data are essential to understand the mechanics of human locomotion in various conditions.

During gate GRF presents large variations that must be compensated by a special design transmission connected to the foot support transmission of the mechatronic system.

3 The Mechatronic System

SIMESIM is based on a basic training gait at which there were added several subsystems necessary for a complex and full recovery (Seiciu et al. 2006, 2007). The importance of the research consists in developing a state-of-the-art mechatronic system able to respond to the utmost complex requirements. For example, in addition to the normal walking movement (limbs opposition), the system allows,

Table 1 Estimated cost of transportation for various robots

Cornel biped	Deft robot	MIT learning robot
0.2	5.3	10.5

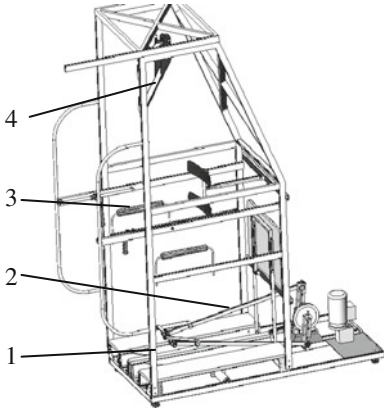

Fig. 5 SIMESIM (mechanical part)

for the first time, a tandem (skier) movement: simultaneous movement of the side limbs (right hand-leg and left hand-leg).

In this respect, the system was designed and developed based on the latest achievements of human movement science, transmission and mechanism theory as well as medical science and IT.

The system has several important parts: mechanical, electronic, measurement, control.

The mechanical part (main rig) is presented as a CAD view in Fig. 5. It comprises: 1—the patient positioning frame; 2—the feet driving module; 3—the hand guiding system; 4—the oscillating lift mechanism (harness, pulleys and a winch).

The feet driving mechanism presented as a CAD view in Fig. 6 is composed of: 1—the feet rest plates with built-in safety device; 2—the double-crank mechanism. The system has 2 original toes and heel independent sliders used to replicate the correct walking positions of the feet.

The electronic, measurement and, control parts of the system were designed to match the requirements requested.

4 System Functions and Signals

The general functions of the mechatronic system are:

- system preparation for the treatment session;
- placing the patient in the system;
- legs movement;

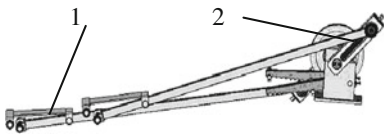

Fig. 6 Feet driving mechanism

- hip movement;
- arms movement;
- patient monitoring;
- active and passive protection of the patient;
- patient muscles' simulations.

The information monitoring system functions are:

- acquisition, computing and displaying of the sensor signals;
- date base management;
- steady and time dependent graph design;
- acquisition, computing and displaying of the function parameters;
- management of the commands to the system rendering actuators and sub-systems;
- management of the optical and/or visual warnings;
- management and display of the patient progress.

The acquired digital signals of the systems are:

- step count;
- system stand-by;
- frequency converter start;
- frequency converter damage;
- speed in steps per minute;
- urgent stop by the patient;
- accidental leg detachment;
- accidental hand detachment.

The acquired analogical signals of the systems are:

- patient weight;
- engine speed;
- analogical inputs (force transducers).

The system functionality comprises:

- the patient wearing a parachute like harness is lift from the wheelchair and is translated to the training position;
- the feet are linked to their corresponding plates;
- particular adjustments are made;
- optionally, for the case of total paralyzed patients, the knees and the pelvis are linked to supplementary guides;
- the hands may also be positioned to the hands guiding system;
- the feet are driven to produce walking movements.

The parameters to be measured are:

- the ground reaction forces;
- the body segments accelerations;
- the muscular response due to electrical stimulation.

Picture 1 SIMESIM—present state

The parameters that can be tuned are:

- the patient height displacement;
- the force on the feet rest plates;
- the length and height of the pace;
- the walking speed (Picture 1).

5 Conclusions

Of the two important walking theories, the authors use the SDG theory to compute the work efficiency, the results been used for the mechatronic system design.

The cost of transport can easily be estimate, but the results vary largely from one application to another. The authors aim to reach low cost of transport values with the newly designed MS.

The design also must take into account some cinematic particularities that result from the use of a special developed crank-reciprocating rod mechanism. The gait trainer enables severely disabled patients the repetitive practice of a physiologic walking movement.

SIMESIM will allow locomotory disabled subjects to practice the gait-like movement without overstressing therapists. The device simulates the phases of gait, supports the subject's weight according to their abilities, and controls the body movement in the vertical and horizontal directions.

Video analysis of gait and the kinesiological EMG will be use to assess the pattern of movement and the corresponding muscle activity. Walking on the gait trainer is characterized by a symmetrical, sinusoidal movement. In summary, the new gait trainer generates physiological gait-like movement which is important for the restoration of walking ability.

References

Collins S, Ruina A, Tedrake R, Wisse M (2005) Efficient bipedal based on passive-dynamic walkers. Sci Mag 307(5712):1082–1805, ISSN: 0036-8075

Damavandi M, Dixon PC, Pearsall DJ (2012) Ground reaction force adaptations during cross-slope walking and running. Hum Mov Sci 31:182–189, ISSN: 0167-9457

Hesse S, Uhlenbrock D, Werner C, Bardeleben A (2000a) A mechanized gait trainer for restoring gait in nonambulatory subjects. Arch Phys Med Rehabil 8:11158–11161

Hesse S, Uhlenbrock D (2000b) A mechanized gait trainer for restoration of gait. J Rehab Res Dev 37(6):701–708

Kuo AD (2002) Energetics of actively powered locomotion using the simplest walking model. J Biomech Eng ASME 124(1):113–120, ISSN: 0148-0731

Kuo AD (2007) The six determinants of gait and the inverted pendulum analogy: a dynamic walking perspective. Hum mov Sci 26(4):617–656

Mauritz KH (2002) Gait training in Hemiplegia. Eur J Neurol Suppl 1:23–29; discussion 53–61

Saunders J, Inman V, Eberhart H (1953) The major determinants in normal and pathological gait. Am J Bone and Joint Sur 35:543–558

Seiciu PL, Laurian T, Filipoiu D (2006) Special training gait for locomotion disabled persons. European workshop on movement science, Sportverlag Strauß

Seiciu PL, Filipoiu ID, Laurian T, Alionte CG, Barbu V (2007) Monitoring equipment for patients using SIMESIM mechatronic system. Mecatronica 56–59, ISSN 1583-7653

Seiciu PL, Filipoiu ID, Laurian T (2008a) Theoretical aspects related to the design of a mechatronic system for recovery of the disabled persons. In: Proceedings of the "9th WSEAS international conference on automation and information (ICAI '08)". WSEAS Press, Bucharest, Romania, pp 230–235, ISBN 978-960-6766-77-0, ISSN 1790-5117

Seiciu PL, Laurian T, Filipoiu ID, Parvu F (2008b) New design aspects of a locomotory rehabilitation mechatronic system. In: Katalinic B (ed) Annals of DAAM for 2008 and proceedings of the 19th international DAAAM symposium. DAAAM International, Vienna, Austria, pp 1241–1242, ISSN: 1726-9679, ISBN 978-3-901509-68-1

Tong K, Granat MH (1999) A practical gait analysis system using gyroscopes. Med Eng Phy 21(2):87–94

Uhlenbrock D, Sarkodie-Gyan T, Reiter F, Konrad M, Hesse S (1997) Development of a servo-controlled gait trainer for the rehabilitation of non-ambulatory patients. Biomed Tech 42:196–202

Zajak FE, Neptune RR, Kautz SA (2002) Biomechanics and muscle coordination of human walking. Part I Gait Posture 16(3):215–232, ISSN: 0966-6362

Zajak FE, Neptune RR, Kautz SA (2003) Biomechanics and muscle coordination of human walking. Part II Gait Posture 17(1):1–17, ISSN: 0966-636

Part VI
Education

The New Engineering Education Model on University of Niš

Vojislav Miltenović, Milan Banić and Aleksandar Miltenović

Abstract The engineer must be able to present his work and his position, to defend his opinion and to record it in written form. Therefore, engineers, educated on universities, have to be capable to work with experts from other disciplines in order to take advantage of new technologies and to use them in environmentally friendly products and production processes. This paper presents the university education model in the field of product development.

Keywords Engineer · Education · Product development

1 Introduction

The word engineer is derived from the Latin root *ingenium*, meaning "cleverness". Engineers are today researchers, designers, technologists, analysts, managers, agricultural (and bio) engineers, architects and builders of roads, bridges, railways, machinery, tools, buildings and equipment for various purposes.

Mechanical Engineering is the most reliable engine of the economy. Based on these industrial pioneer work is a basic research that combine the will and ability to transfer the knowledge into innovative technology products. This combination is strength of engineers. It gives to the engineer a key role as an indispensable link between science, industry and society.

V. Miltenović (✉) · M. Banić · A. Miltenović
Mechanical Engineering Faculty, University of Niš, Niš, Serbia
e-mail: vojamiltenovic@yahoo.com

M. Banić
e-mail: banicmilan@hotmail.com

A. Miltenović
e-mail: amiltenovic@yahoo.com

G. Dobre (ed.), *Power Transmissions*,
Mechanisms and Machine Science 13, DOI: 10.1007/978-94-007-6558-0_59,

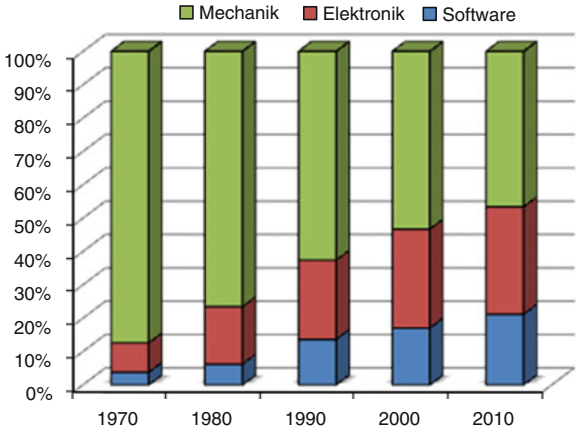

Fig. 1 Share of development in mechanical engineering

Engineers today have to consider many aspects during development of new products and systems. Demands on their knowledge are going to increase. For example, machines and devices are going to be made with more software and electronics (Fig. 1).

The engineer tasks in the field of product development in the future are varied. They deal with the entire life cycle of a product, from a product idea to its concretization through manufacturing, distribution and recycling. The development is about developing new products or improving existing products and to fulfill market needs through creativity, innovation and technology. The implementation of the product idea is in the design and for that are used advanced methods and technologies like 3D graphics systems, simulation software and virtual and physical prototypes. The results are base for the later production. Many modern products are developed in an interdisciplinary and international environment.

2 Corporate Strategy and Product Development

Current economic weakness makes the construction of machinery and equipment with its typical mid-sized structure especially hard. Therefore, the companies are forced to use more and more innovations in order to lunch new and quality products to market. Here, new ideas have to be realized and complex tasks and problems to be solved. The company has always less time available. This requires a fast and accurate development of ideas and its realization on market. Problems that can occur have to be solved as quickly as possible and without any mistake. This leads to parallel and complex processes in product development and production. This requires a methodical approach in solving problems, where teamwork is increasingly required.

Individual decisions are rare and usually risky because the performance advantage of the creativity and experience of a single person is less. Because of this, the tendency is to make decisions in groups and teams and to seek solutions to complex problems. A person's ability to work effectively in a team come more and more to the fore, since the role of the team in a company is growing.

Optimal products are not only free from defects, but above all, customer-oriented products. This provides quality management with a wide range of methods and tools. The premise is that the methods and tools can be used in the early stages of the product life cycle.

The modern prototype has accelerated the product development process. The designers are using simulation and virtual reality.

The strategic planning specified the products and processes for the future markets. Based on the company's strategy, the new business opportunities are analyzed in order to identify product and process ideas as well as evaluation of product concepts. Result of the strategic product and process planning are development orders and production changes.

Product and service innovations have to exist to ensure the competitiveness of products. The goal is to early identify the potential for future success and to develop it in time. With the help of strategic product and process planning it can be possible to systematically complete this challenging business task. New sales potential will be recognized through continuous innovation in interaction with the market.

The cycle of strategic product planning is divided into phases:

- potential determination,
- product and process determination,
- product and process design,
- business planning.

Thereby, the cycle cannot be understood as a mere sequence of individual steps. Rather, the stages are run through iterative.

2.1 Identification of Potential Success at an Early Stage

The "discovery potential" identified so-called potential for success. Potential for success describe a new or previously unsolved problem, a latent or future market respectively customer needs, a new, previously unknown technical solution, a potential new use for a known solution, etc. For that are analyzed, for example, trends in various fields (market, competitors, technology, etc.) in order to determine the impact on the design. Conversely, the in-house expertise has to be analyzed, on which is going to be made appropriate search fields and from that are generated potentials for success. Results of the potential discovery are potentials for success, which are described by request segments or product positioning in the market (e.g. product cost, low-, low-noise product).

2.2 Derivation of Innovation Ideas

The aim of the 'product and process development' is to identify potential for success with demand-driven product and production ideas. For that, based on the requirement segments, are going to be produced product and production ideas depending on the dominant drivers of innovation. If driver of innovations is the product, it will be build for full product based on solutions for the identified product potential. When a driver of innovation is production, solutions have to be developed for the whole production process. From the production ideas are then generated new product ideas. As a result of verified product and process development on the one hand the potential for success and shows on the other alternative principle solutions for new products.

2.3 Concretisations of Concepts

The product and process design of the concrete product ideas for development proposals and changes in production technology concepts. For that are first of all specified the generated solutions to the assembly concept. On the market side are determined features and requirements of individual product variants and converted into appropriate assemblies concepts and their variants. It is also important to derive the required production program. The resulting detailed production requirements (e.g. technology, infrastructure) for the definition of production structures (e.g. line number and design, customer-neutral/specific segments of production, assembly sequence) are used. Result of product and process design is all product and technical information about production that are needed as a base for the initiation of development projects and investment projects.

2.4 Evaluation and Selection

The business plan concludes the cycle of strategic product and process planning. Results of business planning are development contracts for developed production concepts or requests for production changes (investment plan). For this, the business plan support selection of the optimal product and production concepts considering cost and revenue. In addition development and market launch dates has to be determined and needed resources has to be estimated. This includes, if it is necessary, planning and also considerate technology readiness level. Task of business plan is also to develop strategies for corporate competencies. The joint project "Strategic product and process planning" assigned the individual phase methods and linked to each other. With this is now possible to organize and control the complex product development process systematically.

3 New Educational Model

In order to achieve above mentioned goals the new educational model in field of product development was defined at Mechanical Engineering Faculty, University of Nis. The new education model is based on KaLeP (The Karlsruhe education model for industrial product development) developed at Institute for Product Development of Karlsruhe Institute of Technology, but takes into account cultural and social characteristics of Western Balkans Countries region and previous experience in product development education. Implementation of new education model was preformed through several subjects already existing in the curriculum of Mechanical Engineering Faculty, University of Nis since year 2005.

Table 1 gives an overview of directly and indirectly related subjects to the core module "machine design and product development" at the bachelor (BA) and master (MSc) studies in which the implementation of the new educational model was performed.

In order to prepare future engineers to their industrial positions a special focus is given to subjects that offer a broad basic understanding of development-related aspects. The basic subjects in the bachelor degree program "machine design and product development" represent an ideal base for a structured and methodical development of products. The electoral subjects depend of personal interests and preferences of students. Theoretical education is contributed with practical experience and this knowledge is implemented during seminars and praxis with real examples from industry.

Table 1 Selected subjects from curriculum of University of Niš—Faculty of mechanical engineering

Subject	Sem.	L/W/E/P	Credits
Strength of materials	2	2.7/0/2.7/0.6	6
Material science	2	1.8/0/2.6/0.6	6
CAD and technical drawing	2	2.7/0/2.7/0.6	6
Machine elements 1	3	2/0/2/0	5
Machine elements 2	4	2/0/2/0	4
Machine elements 3	5	2/0/2/0	6
Basis of design	4	2.6/0/1.8/0.6	6
Virtual design	5	1.8/0/2.6/0.6	6
CAD—Geometric modeling	5	1.8/0/2.6/0.6	6
Tribology	7	2.6/0.6/1.8/0	6
Basics of product development	7	1.3/1/0/2.7	6
CAPD—Computer application in product development	7	2.6/0/1.8/2.4	6
Modeling and simulation	8	2.6/0/1.8/0.6	6
Finite element method	8	2.8/0/1.8/0.6	6
CAD/CAM/CAE	9	2.6/0/1.8/0.6	6
Methods of product development	9	1.3/1/0/2.7	6
Integrated product development	9	1.3/1/0/2.7	6

L lectures, *W* workshops, *E* exercises, *P* practical work

The courses integrate theoretical and methodological knowledge aimed to make a decisive contribution to the promotion of theoretical and methodological competence. Courses programmes are designed to promote the development of creativity and the potential to elaborate by combining the lecture with independent development work of the students.

To accomplish that goal course is divided into three different components:

- Lectures,
- Workshops, and
- Student work on development project.

These components cover different educational goals. The lecture, always the major component of the education concept, provides the theoretical fundamentals for both the other educational components. Purpose of other components is to enable students to in practice implement their knowledge because in that way best education results are achieved.

3.1 Lectures

In Lectures students are introduced to product development of industrial enterprises with particular reference to the requirements of small and medium sized companies. Based on practical experiences and examples from industry, the theory of planning, design, cost control and management of the development and innovation process knowledge is introduced and discussed. Problem solving processes, system analysis, team leading, product lifecycle and development strategies are presented and discussed, as well. Students are taught how to define profile of the product and product concept from ideas and how to efficiently evaluate different concepts and variant solutions.

During lectures teacher actively communicate with the students by discussing of all the topics presented during lectures. The lecture is designed for a limited number of students (maximally 30) to ensure interactive contact of professor and students.

This offers the possibility of teaching in discursive form with the use of multimedia tools to aid better presentation of the subject. If necessary the official time allotted to lecture is relaxed to enable open-end discussions.

Teaching process must be in accordance with development project and effectively accompanies phases of the student's development project.

3.2 Workshops

In the workshops knowledge is actively built up and developed with the first real application experiences. This is achieved through:

- A direct and practical translation of the learnt methods directed to the industrial product development process.
- Simulation of team work during solving of practical problems on the workshop.

A total of 13 Workshops cover and expand knowledge in the following topics:

- Team processes,
- Product lifecycle,
- Project management,
- Definition of product profile, check list, design process,
- Presentation technique,
- Evaluation of concepts and variant problem solution,
- CAD,
- Simulation,
- Organisation processes in enterprises, procurement process
- Validation of mechanical systems.

Certain workshops are led by guest professors and industrial engineers, depended by topic covered by a workshop. Guest professors are often presenting via audio–video link which enable engagement of international leading experts which significantly improve quality of the course.

These workshops are set up to deepen and extend knowledge and are not used for the direct concurrent support of the student project work.

3.3 Student Development Project

The aim of student project is the development of realistic industrial product from product profile up to the virtual prototype (3D-CAD Model) or from the idea up to the validation of manufactured prototype (Fig. 2) by independent student team.

Provider of the development task is always an industrial company which defines either the development area (if projects start from product profile) or an idea (if project starts from the idea). The number of participants in the project work, and by that in the course, is limited to 30.

The project work is so extensive, that it can only be solved by division of labour within the team.

On project start, based on set of predefined tests, course professor and his assistants select candidates for the course. Teams are formed by course professor based on the results which determine personal profile of the students from the aspect of team work.

Students work in the simulated environment of the midsized enterprise in which the virtual management is composed of course professor, his assistants, project sponsor represantives and guest professors. Management role is to ensure all recourses needed for successful project work as students are actually employed in midsized enterprise. Student teams are located into separated virtual offices in

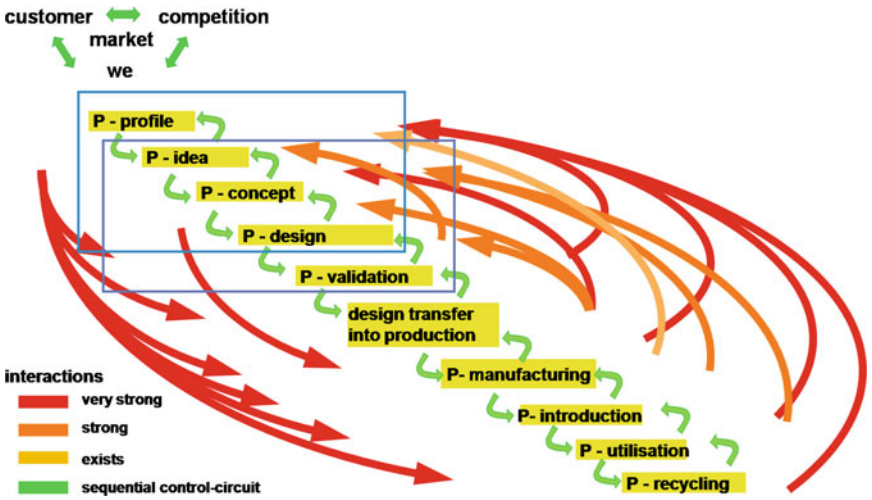

Fig. 2 Two variants of the development project: from product profile to virtual prototype and from idea to validation of actually manufactured prototype

which they dispose with all hardware and software tools necessary for project work. Students have to think about the whole project when they generate a solution for a small part, they have to think about system correlations and interfaces and the problems that they have to solve are mostly evolved from the project itself and not given in the task itself. So they get a very high self-reliance of their learning process and the motivation for understanding and learning is quite high. This requires a bigger autonomy of the students than a "classical" way of education as it is practiced in most fields of academic studies, but it gives the students the best chance to understand the things they are learning. The basic task of management is to control and evaluate student's project work. The project is divided into four phases. At the end of each phase a milestone is predicted in which students present their project work to virtual management which decides on future course of the project based on these presentations. On the project end student teams present the whole development project to virtual management and represantives of regional industrial companies. In certain cases the management awards prizes for the best solutions. Each team makes an evaluation of their group performance and their individual team members in a feed-back briefing. The results are handed to the management for an assessment (Fig. 3).

Based on assessment of virtual management and student's engagement on lectures and workshops, the work, knowledge and degree of understanding of course problematic of individual students is evaluated. In that way, students are evaluated not only by course professor and in that way additional objectivity is added to evaluation process.

Fig. 3 Final project presentation

4 New Educational Model Implementation Expiriences

Since winter semester 2006/2007, lectures in the Mechanical Engineering Faculty in Nis were held according to newly implemented educational model. Educational process was organized and executed in the two years in cooperation with IPEK. In the first year two undergraduate student teams from Mechanical Engineering Faculty in Nis, together with two teams from Karlsruhe Institute of Technology, were involved in the product development project defined by German company Kärcher (Fig. 4).

In 5 years of realization of the new education model 10 product prototypes (real or virtual) were developed by student teams. Those product prototypes could be implemented in the manufacturing program of the companies which defined the development tasks, and thus the quality and the effectiveness of the new education model are proven in the best possible way (Fig. 5).

Students demonstrated strong motivation and achievement orientation. Their presence on the lectures was over 95 %, so in some critical phases of the development project they demonstrated the behavior that exceeded demands of a new educational model. Although the involvement in this education model is based on a hard work, the knowledge and experience gained in this way can be directly applied in practice after graduation. That makes great benefit for future engineers once they graduate (Fig. 6).

Final presentation of student development always attracts attention of industry representatives and has significant media coverage. Participants in final presentation evaluate the elaboration potential and quality of performed work on a student

Fig. 4 Student team WAFIPO prototype year 2006/2007. (Device for drinking water sterilisation)

Fig. 5 Student team CFS prototype 2006/2007 (device for drinking water sterilisation)

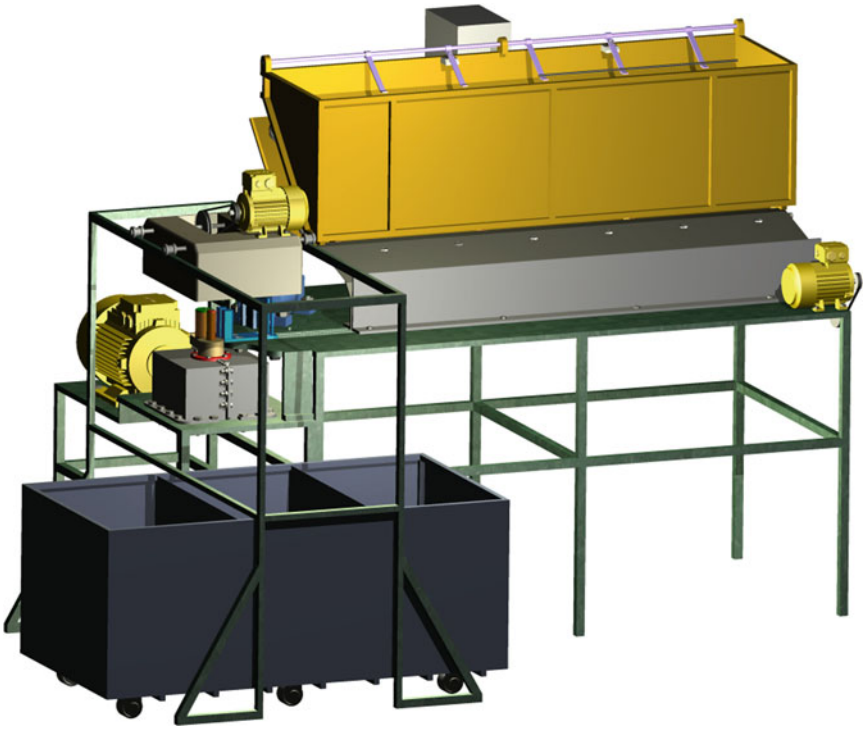

Fig. 6 Student team ABM virtual prototype 2008/2009. (Machine for steel armature bending)

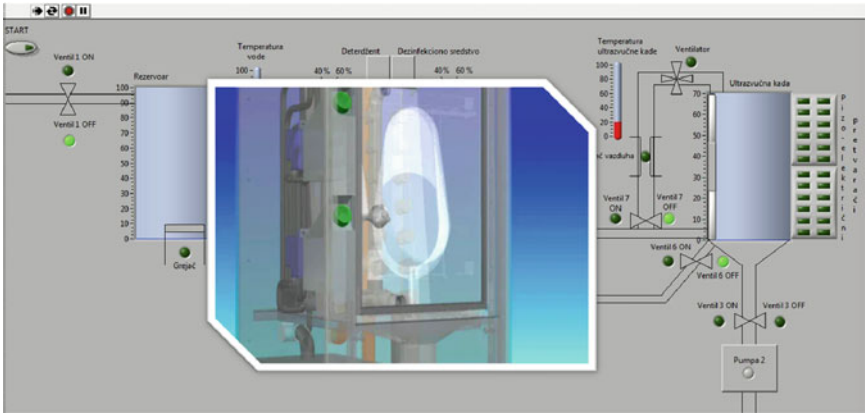

Fig. 7 Student team APEX prototype 2010/2011. (Device for ultrasonic washing of medical equipment)

Fig. 8 Final presentation of 2006/2007 development project, Karlsruhe, Germany

development project through a questionnaire which later serves for definition of student grades as well as review and revision of the education model (Figs. 7, 8).

5 Conclusion

Mechanical Engineering Faculty of University of Nis currently realizes the novel education model in the field of product development. The new education model has a primary goal to educate future engineers to the education level necessary to respond to modern demands and challenges.

Engineers today are the initiators of the knowledge society. Challenges in time will be made by 2020, that knowledge will require even more. The engineering work is not sufficiently appreciated in the modern conditions. Therefore it is necessary that we emphasized the importance of the engineers achieved results because these results make life easier and more comfortable.

For continuous innovation, the engineers can help only if they have scope and motivation. The team spirit is mentioned repeatedly as an essential key skill. The cooperation of different characters, different expertise from different cultures is indeed the reality of everyday work.

The ability to systematically assess and networked thinking is compared to the pure factual knowledge very highly. The methods should include technical competence in their own motivation and ability for life-long learning.

The engineer needs to do more than in the past, acknowledge its responsibility to society. He has to overlook the social, the political, the economic, environmental, and which has the ethical dimensions of his work.

Acknowledgments The work has been funded through the Financial Agreement TR35005 with Ministry of Education and Science of Republic of Serbia.

References

Albers A, Burkardt N (2001) MKL an der Universität Karlsruhe Block 10- Teammanagement. 2001

Albers A, Burkardt N, Matthiasen S, Schweinberger D (2000) "The Karlsruhe Model"—A successful approach to an academic education in industrial product development. Proceedings of engineering and product design education conference, University of Sussex, Brighton

Albers A, Burkardt N, Matthiasen S (2000) New education concepts for the training of creative engineers—The Karlsruhe education model for industrial product development—KaLeP. Proceedings of engineering and product design education conference, University of Sussex, Brighton

Albers A, Burkardt N, Ohmer M (2005) The constructivist aspect of design education in the karlsruhe education model for industrial product development KALEP. Proceedings of international engineering and product design education conference, Delft, The Netherlands

ETH Ingenieurprofil der Zukunft (2005) Aus Anlass des 150 Jahr-Jubiläums der ETH Zürich

Marković B, Miltenović V (2006) Significance and role of team work in product development. Scientific-expert gathering with international participation research and development of mechanical elements and systems—IRMES'06, Banja Luka, Bosnia and Herzegovina

Miltenović V (2003) Razvoj proizvoda—strategija, metode, primena. Univerzitet u Nišu—Mašinski fakultet, Niš, I—izdanje 2003. str. 293

Miltenović V, Banić M (2007) The methodological approach to product development, TEPMUS project multidisciplinary studies of design in mechanical engineering, II Workshop, Beograd, Republic of Serbia

Studienschwerpunkt Konstruktionstechnik (2005) Fakultät für Maschinenbau, Ruhr Universität Bochum

Svejda P, Scherer V (2004) Maschinenbau—Schlüssel zur Innovation. Maschinenbau RUBIN 2004

Index

G. Dobre (ed.), *Power Transmissions*,
Mechanisms and Machine Science 13, DOI: 10.1007/978-94-007-6558-0,